ACCSCIENCE PUBLISHING

International Journal of BIOPRINTING

ACCSCIENCE PUBLISHING
Volume 10 Issue 6, 2024
ISSN: 2424-8002 (Online) ISSN: 2424-7723 (Print)

ACCSCIENCE PUBLISHING

International Journal of Bioprinting

Print ISSN: 2424-7723

Online ISSN: 2424-8002

International Journal of Bioprinting is an international journal covering the technology, science and clinical application of the broadly defined field of Bioprinting. Bioprinting is defined as the use of 3D printing technology with materials that incorporate viable living cells or biological elements to produce tissue or biotechnological products. We are interested in the scientific topics spanning all stages of bioprinting process from concept creation to fabrication and beyond.

Scan to access website:

Scan to submit papers:

About the Publisher

AccScience Publishing is a publishing company based in Singapore. We publish a range of high-quality, open-access, peer-reviewed journals and books from a broad spectrum of disciplines.

Contact Us

Managing Editor
ijb.office@accscience.sg

AccScience Publishing
8 Burn Road, #15-03 Trivex, Singapore 369977.

Volume 10 • Issue 6 • December 2024
ISSN 2424-7723 (print) ISSN 2424-8002 (online)

INTERNATIONAL JOURNAL OF BIOPRINTING

Editor-in-Chief

Chee Kai Chua

Singapore University of Technology and Design, Singapore

ACCSCIENCE PUBLISHING

Access Science Without Barriers

Full issue copyright © 2024 AccScience Publishing
All rights reserved. Without permission in writing from the publisher, this full issue publication in its entirety may not be reproduced or transmitted for commercial purposes in any form or by any means, electronic or mechanical, including photocopying, recording, or any information storage and retrieval system. Permissions may be sought from ijb.office@accscience.sg.

Article copyright © Respective Author(s)
See articles for copyright year. All articles in this full issue publication are open-access. There are no restrictions in the distribution and reproduction of individual articles, provided the original work is properly cited. However, permission to reuse copyrighted materials of an article for commercial purposes is applicable if the article is licensed under Creative Commons Attribution-NonCommercial License. Check the specific license before reusing.

INTERNATIONAL JOURNAL OF BIOPRINTING

ISSN: 2424-7723 (print)
ISSN: 2424-8002 (online)

Editorial and Production Credits

Publisher: AccScience Publishing
Managing Editor: Cathy Huang
Editorial Assistants: Puva Ramakrishnan, Flora Kang
Production Editor: Puva Ramakrishnan
Special Issue Commissioning Editors: Shirley Song, Terra Shi
Article Layout and Typeset: Bsmart Publishing (India)

For all advertising queries, contact ijb.office@accscience.sg.

Supplementary file

Supplementary files of articles can be obtained at https://accscience.com/journal/IJB/10/6.

Disclaimer

AccScience Publishing is not liable to the statements, perspectives, and opinions contained in the publications. The appearance of advertisements in the journal shall not be construed as a warranty, endorsement, or approval of the products or services advertised and/or the safety thereof. AccScience Publishing disclaims responsibility for any injury to persons or property resulting from any ideas or products referred to in the publications or advertisements. AccScience Publishing remains neutral with regard to jurisdictional claims in published maps and institutional affiliations.

International Journal of Bioprinting

Editorial Board

Editor-in-Chief

Chee Kai Chua
Singapore University of Technology and Design, Singapore

Associate Editors

Maling Gou
Sichuan University, China

Jiankang He
Xi'an Jiaotong University, China

Liliang Ouyang
Tsinghua University, China

Wai Yee Yeong
Nanyang Technological University, Singapore

Yongqiang Hao (Clinician)
Shanghai Jiao Tong University School of Medicine, China

*Editorial Board Members**

Jason A. Burdick, *USA*

Shweta Agarwala, *Denmark*

Eben Alsberg, *USA*

Anthony Atala, *USA*

Douglas B. Chrisey, *USA*

Amit Bandyopadhyay, *USA*

Andrea Barbetta, *Italy*

Mikhael Bechelany, *France*

Martin Birchall, *UK*

Paulo J.D.S. Bártolo, *Singapore*

Christian Celia, *Italy*

Maria Chatzinikolaidou, *Greece*

Daniel Chen, *Canada*

Boris Chichkov, *Germany*

Gianluca Ciardelli, *Italy*

Jeremy Crook, *Australia*

Cédric Delattre, *France*

Rui Domingues, *Portugal*

Dennis Douroumis, *UK*

Tal Dvir, *Israel*

Eleonora Ferraris, *Belgium*

Gunter Finkenzeller, *Germany*

Sanjay Garg, *Australia*

Antonio Gloria, *Italy*

Manuela Gomes, *Portugal*

Brunella Grigolo, *Italy*

Michinao Hashimoto, *Singapore*

Charlotte Hauser, *Saudi Arabia*

Dong Nyoung Heo, *Korea*

Raymund E. Horch, *Germany*

Geun Hyung Kim, *Korea*

Richard James Bibb, *UK*

Jinah Jang, *South Korea*

Jingchao Jiang, *China*

Qing Jiang, *China*

Hyun-Do Jung, *Korea*

Lifeng Kang, *Australia*

Ali Khademhosseini, *USA*

Jangho Kim, *South Korea*

Bahattin Koç, *Turkey*

Dimitrios A. Lamprou, *UK*

Junmin Lee, *South Korea*

Khoon Lim, *Australia*

Ki-Taek Lim, *South Korea*

Fengyuan Liu, *UK*

Veronica MacChi, *Italy*

Carmelo De Maria, *Italy*

Elena Martínez Fraiz, *Spain*

Laurence Meagher, *Australia*

Ferry Melchels, *Australia*

Nikolaos Michailidis, *Greece*

David K. Mills, *USA*

Vladimir Mironov, *Russia*

Mario Moisés Alvarez, *Mexico*

Maurice N Collins, *Ireland*

Makoto Nakamura, *Japan*

Roger Narayan, *USA*

Insup Noh, *Korea*

Ali Nokhodchi, *UK*

J.M.A.C. de Oliveira, *Portugal*

Aleksandr Ovsianikov, *Austria*

Sang-Hyug Park, *Korea*

Alokesh Pramanik, *Australia*

Aldo R. Boccaccini, *Germany*

Michael Raghunath, *Switzerland*

Anabela Raymundo, *Portugal*

Shinji Sakai, *Japan*

Thomas Scheibel, *Germany*

Cijun Shuai, *China*

Swee Leong Sing, *Singapore*

Kedong Song, *China*

Jie Sun, *China*

Zhonghua Sun, *Australia*

Ergün Süleyman, *Germany*

Ibrahim Tarik Ozbolat, *USA*

Savas Tasoglu, *Turkey*

S. Vijayavenkataraman, *UAE*

Giovanni Vozzi, *Italy*

Liqiang Wang, *China*

Yin Xiao, *Australia*

Seung-Schik Yoo, *USA*

Barbara Zavan, *Italy*

Ioanna Zergioti, *Greece*

Yi Zhang, *China*

Yu Shrike Zhang, *USA*

Hala Zreiqat, *Australia*

Assistant Editor

Jia An, *Singapore*

Youth Editorial Board Members

Tanveer Ahmad, *Saudi Arabia*

Shivesh Anand, *Denmark*

Gokhan Bahcecioglu, *USA*

Gianluca Cidonio, *Italy*

Giovanni Falcone, *Italy*

Ruben Foresti, *Italy*

Gabriele Maria Fortunato, *Italy*

Paola Serena Ginestra, *Italy*

Xulin Hu, *China*

Anna Jezierski, *Canada*

Yiting Lei, *China*

Lan Li, *China*

Huixin Liang, *China*

Elena Marcello, *Italy*

Wei Long Ng, *Singapore*

Egor Osidak, *Russia*

Chenxi Peng, *Australia*

Rúben Pereira, *Portugal*

João Carlos Silva, *Portugal*

Yogendra Pratap Singh, *USA*

Thiago Domingues Stocco, *Brazil*

Binbin Sun, *China*

Aitor Tejo-Otero, *Spain*

Hui Zhu, *China*

*Editorial Board Members as of December 20, 2024

ACCSCIENCE PUBLISHING

Volume 10 | Issue 6 | December 2024 | Page 1 – 581 |

International Journal of Bioprinting

https://accscience.com/journal/IJB

CONTENTS

REVIEW ARTICLES

1 **3D bioprinting technologies for the enhancement and application of functional lung organoid models**
Jimin Jang, Jooyoung Lee, Sangryul Cha, Minkyoung Lee, Hyungseok Lee, Se-Ran Yang

16 **Bioprinting of wearable sensors, brain-machine interfaces, and exoskeleton robots**
Xinrui Wang, Wei Dong, Hui Dong, Yongzhuo Gao, Jiawen Lin, Haichao Jia, Yihui Tao, Hao Sun

38 **The promising role of semi-solid extrusion technology in custom drug formulation for pediatric medicine**
Thomas Cerveto, Lucas Denis, Maxime Stoops, Anna Lechanteur, Christine Jérôme, Julien Leenhardt, Stephen Flynn, Alvaro Goyanes, Roseline Mazet, Maxime Annereau, Luc Choisnard

67 **3D bioprinting techniques and hydrogels for osteochondral integration regeneration**
Haiwei Tang, Enze Zhao, Yahao Lai, Anjin Chen, Xiaoting Chen, Weinan Zeng, Xulin Hu, Kai Zhou, Zongke Zhou

95 **3D-printed electronics for biomedical applications**
Minsu Ryoo, Daeho Kim, Junseop Noh, Song Ih Ahn

114 **Extrusion bioprinting from a fluid mechanics perspective**
Reza Gharraei, Donald J. Bergstrom, Xiongbiao Chen

154 **Comprehensive insight into 3D bioprinting technology for brain tumor modeling**
Ayoung Kim, Kyumin Mo, Soohyun Choe, Miyoung Shin, Hyunho Yoon

RESEARCH ARTICLES

174 **Electrospun polylactic acid-glycolic acid composite hydrogel scaffold loaded with 3D extracellular vesicles for nasal septal cartilage defect repair**
Jie Yang, Haolei Hu, Qiang Guo, Xiaolei Chen, Shuo Li, Gang Yin, Wei Yue, Yi Zhang, Boxun Liu, Jianwei Chen, Tao Xu, Yi Li

194 **Effect of graphene and graphene oxide addition on crosslinking and mechanical properties of photocurable resins for stereolithography**
Sara Lopez de Armentia, Raquel Giménez, Juan Carlos del Real, Berna Serrano, Juan Carlos Cabanelas, Eva Paz

209 **Application of 3D-printed individualized porous tantalum buttress in shelf acetabuloplasty for developmental dysplasia of the hip**
Yang Peng, Xin Chen, Juncai Xu, Ran Xiong, Chengjun Huang, Liu Yang, Guangxing Chen

224 **Direct ink writing of biomimetic hydroxyapatite scaffolds with tailored concave porosity**
Laura del-Mazo-Barbara, Anna Diez-Escudero, Irene Lodoso-Torrecilla, Morteza Aramesh, Cecilia Persson, Maria-Pau Ginebra

245 **3D-bioprinted *in vitro* skeletal muscle with pennate fiber architecture to enhance contractile function**
Lin Gao, Liuhe Li, Wenze Wu, Junnan Feng, Ziwei Liu, Jiankang He, Dichen Li

260 **Bioprinted keratinocyte and stem cell-laden constructs for skin tissue engineering**
Eva Bettendorf, Rafael Schmid, Raymund E. Horch, Annika Kengelbach-Weigand, Yvonne Kulicke, Stefan Schrüfer, Dirk W. Schubert, Zan Lamberger, Philipp Stahlhut, Gregor Lang, Celena A. Sörgel

282 **3D-printed zinc/magnesium-doped hydroxyapatite-polycaprolactone composite scaffolds for angiogenesis and osteogenesis**
Lei Qiang, Hao Huang, Jing Shan, Guanlu Shen, Quan Zhang, Weize Kong, Ya Fang, Yiwei Zhang, Jinwu Wang, Yihao Liu, Chengwei Wang, Pengfei Zheng, Jie Weng

300 **Development and *in vitro* evaluation of bioprinted plasma-infused biocarriers for mesenchymal stromal cell delivery in musculoskeletal disorder treatment**
Cristina Del Amo, Miguel Perez Garrastachu, Inés Jaúregui, Francisco J. Alvarez, Isabel Andia

317 **3D-printed poly(*p*-dioxanone)/graphene oxide composite bioresorbable stents for congenital heart disease treatment**
Enrong Chen, Xiji Qin, Zhihui Xiong, Xiaorong Cai, Xuejun Jin, Kun Sun, Jing Sun

338 **3D-printed scaffold of dopamine methacrylate oligomer grafted on PEGDMA incorporated with collagen hydrolysate for engineering cartilage tissue**
Kitipong Pasanaphong, Acharee Suksuwan, Narongrit Srikaew, Ruedee Hemstapat, Tulyapruek Tawonsawatruk, Sutee Wangtueai, Nanthaphong Khamthong, Sani Boonyagul, Phavit Wongsirichot, Nuttapol Tanadchangsaeng

360 **Development and applications of an *in vitro* non-alcoholic fatty liver disease model based on 3D-printed liver tissue**
Kun Du, Wei Peng, Ying Zhao, Tianma He, Tao Ding, Feifei Pu, Zibei Ming, Renquan Ruan, Jing Liu

373 **ChocOmega-3: Innovative manufacturing of ω-3-enriched chocolate**
Esra Pilavci, Dilruba Baykara, Kubra Ozkan, Ayşegul Tiryaki, Melih Musa Ayran, Gozde Enguven, Tufan Arslan Tut, Mehmet Murat Bozdag, Osman Sagdic, Oguzhan Gunduz, Roger J. Narayan, Canan Dogan

391 **3D-printed polycaprolactone-magnetic nanoparticles composite multifunctional scaffolds for bone tissue regeneration and hyperthermia treatment**
Susheem Kanwar, Sanjairaj Vijayavenkataraman

407 **3D-bioprinted respiratory disease model: Exploring the importance of culture conditions and controlled release in modeling infection**
Amanda Zimmerling, Lauren Aubrey, Kathryn Avery, Xavier Tabil, Jim Boire, Xiongbiao Chen, Yan Zhou

430 **Evaluation of 3D-bioprinted skin scaffolds in mice along with gold nanoparticle exposure**
Yi Wang, Xin Ma, Xu Wu, Shuaideng Wang, Peng Peng, Guozhang Tang, Xinya Qin, Xinmeng Wang, Chenwei Wang, Jiangning Zhou

444 **Development of multi-layered 3D-printed scaffold for sequential delivery of biomolecules**
Jong-Eun Won, Hyun Kyung Moon, Hae-Won Kim, Ji Suk Shim

457 **Deformation monitoring and stress distribution prediction of 3D-printed hydroxyapatite scaffolds**
Danyu Yao, Luge Zhang, Hong Liu, Ming Liu, Ling Wang, Mingen Xu

471 **Nanomaterial-modified bioinks for DLP-based bioprinting of bone constructs: Impact on mechanical properties and mesenchymal stem cell function**
Julie Kühl, Sven Malte Krümpelmann, Larissa Hildebrandt, Malte Bruhn, Jan-Bernd Hövener, Ronald Seidel, Stanislav Gorb, Fabian Schütt, Rainer Adelung, Andreas Seekamp, Leonard Siebert, Sabine Fuchs

496 **Collagen bioinks redefined: Optimizing ionic strength and growth factor delivery for cartilage tissue engineering**
Murad Redzheb, Yordan Sbirkov, Atanas Valev, Vasil Dzharov, Hristi Petrova, Tatyana Damyanova, Ani Georgieva, Victoria Sarafian

516 **Fabrication of bacteriorhodopsin-embedded hydrogel construct for biocompatible photosensitive device**
Mian Wu, Feng Lin, Yu Song

532 **Design, fabrication, and biocompatibility of 3D-printed poly(LLA-ran-PDO-ran-GA)/poly (D-lactide) composite scaffolds for bone tissue engineering**
Tiantang Fan, Xiao Meng, Ruishen Zhuge, Jingwen Qin, Yutong Wang, Chunyu Zhang, Yiqiao Yin, Jianru Liu, Tianyun Fan, Dongya Liu

544 **Internally-crosslinked alginate dialdehyde/alginate/gelatin-based hydrogels as bioinks for prospective cardiac tissue engineering applications**
Giovanni Paolo Stola, Camilla Paoletti, Letizia Nicoletti, Geo Paul, Claudio Cassino, Leonardo Marchese, Valeria Chiono, Elena Marcello

567 **Biomechanical analysis of partial mandibular implants with various lattice designs of different material properties: *In vitro* study and finite element analysis**
Hao Zhang, Lih Jyh Fuh, Jui Ting Hsu, Zhe Min Lim, Heng Li Huang

ACCSCIENCE PUBLISHING

International Journal of Bioprinting

REVIEW ARTICLE

3D bioprinting technologies for the enhancement and application of functional lung organoid models

Jimin Jang[1†], Jooyoung Lee[2†], Sangryul Cha[1], Minkyoung Lee[2], Hyungseok Lee[2,3*], and Se-Ran Yang[1*]

[1]Department of Thoracic and Cardiovascular Surgery, School of Medicine, Kangwon National University, Chuncheon, Gangwon State, Republic of Korea

[2]Department of Smart Health Science and Technology, College of Engineering Kangwon National University, Chuncheon, Gangwon State, Republic of Korea

[3]Department of Mechanical and Biomedical, Mechatronics Engineering, College of Engineering, Kangwon National University, Chuncheon, Gangwon State, Republic of Korea

(This article belongs to the Special Issue: *The latest advancements in bioprinting technology*)

Abstract

Respiratory diseases, ranging from minor infections to serious chronic diseases and malignancies, negatively affect the respiratory system and are influenced by various environmental factors such as air pollution, occupational hazards, and tobacco smoke, as well as lifestyle, genetic causes, and infectious agents. The prevalence and severity of respiratory diseases require the development of advanced models to better understand their pathophysiology and develop effective treatments. In this context, 3D bioprinting technology emerges as an innovative tool to create functional lung organoid models. The use of induced pluripotent stem cells and extracellular matrix in bioprinting enables the development of organoids that closely mimic human lung tissue. Bioprinting-based organoids can better replicate the dynamic environment of the human lung, facilitating more accurate disease modeling and drug testing. In this review, we highlight the potential of bioprinted lung organoids in understanding the mechanisms of chronic respiratory diseases, testing the efficacy and safety of new drugs, and exploring regenerative medicine approaches. The integration of advanced bioprinting and organoid technologies is a promising field in respiratory disease research and treatment, offering new hope for patients suffering from lung diseases.

Keywords: Alveolar organoid; Chronic respiratory disease; Bioprinting; Extracellular matrix; Induced pluripotent stem cells

[†]These authors contributed equally to this work.

***Corresponding authors:**
Hyungseok Lee
(ahl@kangwon.ac.kr)

Se-Ran Yang
(seran@kangwon.ac.kr)

Citation: Jang J, Lee J, Cha S, Lee M, Lee H, Yang S. 3D Bioprinting technologies for the enhancement and application of functional lung organoid models. *Int J Bioprint.* 2024;10(6):4092. doi: 10.36922/ijb.4092

Received: June 30, 2024
Revised: August 14, 2024
Accepted: August 14, 2024
Published Online: August 16, 2024

Copyright: © 2024 Author(s). This is an Open Access article distributed under the terms of the Creative Commons Attribution License, permitting distribution, and reproduction in any medium, provided the original work is properly cited.

Publisher's Note: AccScience Publishing remains neutral with regard to jurisdictional claims in published maps and institutional affiliations.

1. Introduction

1.1. Traditional animal models in pulmonary disease research and limitations

Respiratory diseases constitute a significant part of the global health challenges, encompassing a wide range of conditions that adversely impact the respiratory system.[1] These conditions vary from mild infections to severe chronic disorders and malignancies, which significantly affect the quality of life and, in many instances, lead to considerable morbidity and mortality.[2]

In the realm of drug development and respiratory research, creating and utilizing accurate disease models is crucial for understanding disease mechanisms and testing potential treatments. To replicate actual respiratory diseases, various agents including bleomycin (BLM), particulate matter (PM2.5), tobacco smoke, and porcine pancreatic elastase (PPE) have long been fundamental tools in the study of pulmonary diseases.[3–6] While the BLM model is widely used to study pulmonary fibrosis, it primarily induces acute lung injury, which typically resolves over time in mice.[7] Models utilizing tobacco smoke, PM2.5, and PPE exposure are essential for studying diseases like COPD.[8] In addition, lung cancer mouse models induced by gene mutations such as *EGFR* and *P53* are also significant in research.[9] However, these models present substantial limitations that can hinder the translation of research findings to human applications. The rapid clearance mechanisms in mice contrast with the slower, more cumulative effects observed in human lungs, leading to differences in disease manifestation and severity. The differences in metabolism and immune responses between mice and humans can also result in variations in drug processing and side effects.[10,11] Compounds metabolized differently can demonstrate efficacy or toxicity in mice that do not translate to humans.[12] This discrepancy poses a significant challenge to the predictive value of mouse models for human pharmacology.

The use of animals in research, especially for conditions that could be studied through alternative methods, also raises ethical concerns. Furthermore, maintaining animal facilities is costly and resource-intensive, which could otherwise be allocated towards developing and refining alternative models. Given these limitations, there is an increasing emphasis on developing alternative models that can better mimic human lung diseases. Advances in organ-on-a-chip technology, three-dimensional (3D) bioprinting, and *ex vivo* human lung tissue cultures offer promising avenues. These technologies not only replicate human tissue architecture and physiological responses more accurately but also allow for the study of human-specific disease processes and treatment responses.[13–15] The shift towards these innovative models could significantly improve the predictive accuracy of preclinical trials and enhance the development of more effective therapies.

Hence, while traditional *in vivo* mouse models have provided foundational insights into pulmonary diseases, their limitations in translating findings to human conditions necessitate the development of advanced, human-relevant models. The integration of these new technologies into respiratory research and drug development is crucial for making significant strides in treating lung diseases.

1.2. The emergence of bioprinting technology for lung models

Previous studies have used either two-dimensional (2D) cell culture methods or 3D constructs to create *in vitro* alveolar models. 2D cell culture methods involve growing cells in a flat, 2D layer, which allows for easy observation and manipulation of cells.[16] These methods are cost-effective and relatively simple, making them a popular choice for initial studies. However, 2D cultures fail to replicate the 3D environment of tissues, leading to differences in cell morphology, polarization, and function compared to *in vivo* conditions. This limitation hampers the study of cell–cell and cell–matrix interactions, which are crucial for understanding cellular behavior in a more physiologically relevant context.[17]

On the other hand, 3D constructs provide a 3D scaffold that supports more complex cell growth, allowing cells to interact with their surroundings in a manner more akin to natural tissues. These constructs can be created using a variety of materials, including hydrogels, which mimic the extracellular matrix (ECM) and provide biochemical cues to the cells.[18] 3D culture systems can better simulate the physical and biochemical environment of tissues, resulting in more accurate representations of cellular functions, differentiation patterns, and responses to stimuli. However, these approaches still face limitations, such as the difficulty in precisely controlling the spatial distribution of cells and materials, as well as the challenge of replicating the intricate architecture of native tissues at a high resolution.[19] To address these limitations, 3D bioprinting technology has emerged. This technology allows for precise control over the spatial distribution of materials and cells, enabling the recreation of complex tissue structures using a variety of materials, including hydrogels and polymers.[20] Consequently, 3D bioprinting offers significant advantages for the development of *in vitro* alveolar models by better replicating the structural complexity of alveoli and enhancing the cellular environment. This is crucial for accurately representing cell growth, differentiation, and native physiological conditions, which are essential for applications such as drug screening and disease research.[21]

This review focuses on the application of bioprinting technologies in modeling lung disease. Firstly, we examine organoids for disease modeling in the lung, discussing their advantages and limitations. Following this, we explore research involving 3D bioprinting technology, proposing strategies to overcome the aforementioned challenges. Despite the promise of these technologies, there are inherent limitations that need to be addressed. Finally, we delve into bioprinting-based lung organoid disease modeling techniques and strategies, discussing their potential and the future directions for this field.

2. Organoids

2.1. Lung structure and cellular function

The lungs are intricately structured and play a crucial role in the gas exchange processes essential to our body.[22] This vital function is enabled by the unique anatomical architecture and complex cellular composition of the lungs, which are divided into distinct parts: airways, alveoli, and blood vessels, with each component made up of highly specialized cells.[23] The primary gas exchange occurs in the alveoli, where a variety of cells and blood vessels, such as alveolar type I (AT1) cells, alveolar type II (AT2) cells, fibroblasts, and vascular endothelial cells (ECs), perform essential roles.[24]

AT1 cells cover most of the alveolar wall and are flat and thin, maximizing the efficiency of gas exchange.[25] Their extremely thin cell membranes allow oxygen and carbon dioxide to move rapidly between the blood and the alveoli.[26] While AT1 cells are essential for efficient gas exchange, they have limited regenerative capabilities.[27] Therefore, recovery from damage to these cells can be slow and sometimes incomplete, complicating lung repair processes.[28] AT2 cells play a critical role in regulating the microenvironment within the alveoli and are primarily responsible for the production and secretion of surfactant, which reduces surface tension within the alveoli to prevent collapse.[29] In addition, AT2 cells have the potential to differentiate into type I cells when necessary, thereby playing a critical role in lung tissue repair and regeneration.[30] The surfactant production and regenerative capabilities of AT2 cells are essential for maintaining overall lung health (Figure 1A).[31]

Fibroblasts provide structural support to lung tissue by producing fibrous proteins such as collagen and elastin, and are crucial for maintaining the elasticity and structural integrity of the lungs.[32] However, excessive activation or abnormal proliferation of fibroblasts can lead to diseases such as pulmonary fibrosis.[33] Pulmonary fibrosis involves the abnormal hardening and functional degradation of lung tissue, primarily caused by the overactivity of fibroblasts.[34] ECs are essential for maintaining lung function by optimizing gas exchange in the lungs, regulating the transfer of substances between blood and tissue, and modulating inflammatory responses and blood clotting (Figure 1B).[35] In particular, disruption of the blood-air barrier due to damage or dysfunction of endothelial cells can be associated with a variety of pathological conditions,

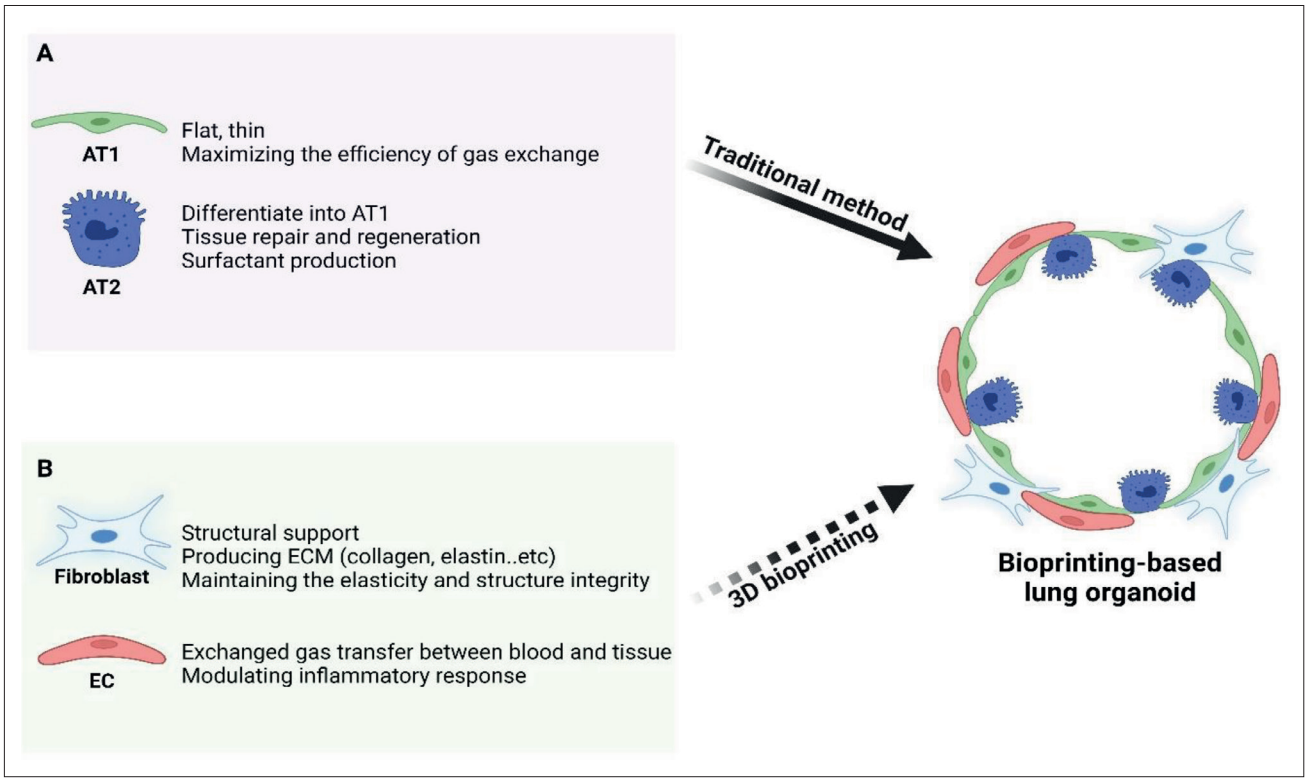

Figure 1. Schematic of lung cellular function and lung organoid. The structure of the lung is largely composed of alveolar type I (AT1) cells, alveolar type II (AT2) cells, fibroblasts, and vascular endothelial cells (ECs). Each cell has a unique function and regulates the microenvironment within the lung parenchyma. Generally, lung organoids are developed by harnessing the differentiation of only AT1 and AT2 cells, whereas organoids containing fibroblasts and ECs are constructed using 3D bioprinting. This diagram was created with BioRender.com.

including various inflammatory lung diseases such as pulmonary hypertension and pulmonary edema.[36,37]

The interactions among these various cell types help maintain proper lung functions and enable recovery from environmental damage. A deep understanding of the lungs' anatomical structure and the functions of these cells provides foundational knowledge that is crucial for the treatment and management of respiratory diseases.[38] This comprehensive understanding is essential for optimizing clinical interventions and developing more effective treatments for specific respiratory conditions.

2.2. Definition and description of organoids

An organoid is an assembly of cells cultured in 3D environments to mimic the structure and function of a human organ or tissue.[39] This advanced technology is useful in various fields such as regenerative medicine, disease modeling, and drug development.[40] Traditional animal disease modeling and 2D cell cultures are limited in their ability to accurately mimic human organs or disease pathogenesis. For example, lung diseases in humans are often mostly irreversible, whereas mouse animal models have a rapid recovery, which limits their ability to simulate diseases caused by cellular senescence and viral infections.[41–43] In addition, due to differences in gene and protein structures from humans, it is difficult to apply therapeutic strategies from animal disease models to humans due to clear differences in mechanisms.[44] Traditional 2D cell cultures are grown as monolayers of cells on flat surfaces, which limits cell–cell interactions and spatial arrangements compared to real human organs and tissue. In contrast, organoids are made using real human cells, so they have the same genes as humans, and the tissue environment they create can more accurately mimic disease, enabling precise prediction of how they will respond in the organ.[45,46] They also use complex culture media, including ECM, to simulate the cells' natural environment. This not only provides physical support for the cells but also a variety of biochemical signals that regulate their differentiation and function.[47]

2.3. Advantages and limitation of 3D lung organoid models

Lung organoids are primarily generated using human pluripotent stem cells (hPSCs), which form the various cell types that compose lung tissue.[48,49] During this process, they use the ECM to form 3D structures, which can recreate various functions of the lungs. For example, the development of lung alveolar organoids can simulate the structure of air sacs in the lungs by inducing differentiation into AT1 cells for gas exchange and AT2 cells for repairing AT1 cells.[50,51] In other studies, organoid models have also been reported to identify fibroblast activation, which is important for lung tissue repair and wound healing.[52,53] Therefore, the main challenge in developing lung organoids is to simulate the developmental process and complex structure and function of the real human lung. In addition, bronchial organoids can be differentiated into various epithelial cells, including club cells, basal cells, and other cell types that exist in the real bronchi, to reproduce the secretion and function of mucus in the real bronchi.[54,55] Recently, they have also been used to simulate lung development to study the mechanisms of genetic and infantile lung diseases such as bronchopulmonary dysplasia.[56–58]

Currently, researchers are trying to overcome this challenge by optimizing the type of cells, 3D culture conditions, and composition of the ECM. However, the existing studies present several limitations. First, there are limitations in perfectly recreating the structure of alveoli and bronchioles. For example, the significantly higher proportion of AT2/AT1 cells in alveolar organoids compared to human lung tissue indicates that organoids are not yet perfect mimics. This is probably because most organoids are made by inducing a certain amount of differentiation of AT2 into AT1 cells.[59–61] Second, lung organoids are mainly composed of cells derived from specific stem cells. Therefore, it is difficult to differentiate all cell types present in the lungs from stem cells. For example, ECs are key regulators of interleukins, which are important for homeostasis and inflammation.[62–64] In addition, immune cells such as macrophages regulate the lung microenvironment through the release of pro-inflammatory cytokines and chemokines.[65–67] The absence of these cells can lead to inaccurate results in drug efficacy testing and disease mechanism studies using organoids. Therefore, increasing the similarity of lung organoids to actual lung tissue is essential to enhance their potential. In addition, developing lung organoid models for reproducible organoid production and mass production for high-throughput drug efficacy validation systems will improve their utility.[68]

Recently, several studies have been reported to overcome these challenges. To overcome the limitation of alveolar organoids consisting of only AT1 and AT2 cells, da Rosa et al. cultured Wharton's jelly mesenchymal stem cells using sodium alginate and gelatin matrix bioprinting, and confirmed their differentiation into ciliated and goblet cells.[69] There is also active research to validate alveolar organoids to mimic the tumor microenvironment. Mu et al. co-cultured PBMCs from peripheral blood with patient-derived NSCLC organoids and demonstrated tumor suppression by T-cell responses.[70] The potential of lung organoids depends on their similarity to real lung tissue, and the composition of the microenvironment must continue to be studied.

3. Bioprinting techniques for lung model fabrication

Additive manufacturing, also known as 3D printing, involves creating components by layering materials.[71] Additive manufacturing systems are categorized into seven distinct processes based on how material layers are formed: (1) material extrusion (MEX), where material is selectively dispensed through a nozzle or orifice; (2) vat photopolymerization (VPP), which uses a vat of liquid photopolymer selectively cured by light-activated polymerization; (3) powder bed fusion (PBF), where thermal energy selectively fuses regions of a powder bed; (4) binder jetting (BJT), in which a liquid binder is selectively deposited to bind powder materials; (5) material jetting (MJT), where droplets of build material are selectively deposited using an inkjet print head; (6) directed energy deposition (DED), which utilizes focused thermal energy to fuse materials by melting them as they are being deposited; and (7) sheet lamination (SHL), where sheets of material are bonded together to form a part. Among these seven methods, those applicable to bioprinting technology using living cells are MEX, VPP, and MJT.

3D printing and bioprinting, while similar in their layer-by-layer fabrication approach, differ significantly in their applications and materials used. 3D printing is primarily used for creating non-biological objects from materials such as plastics, metals, and ceramics, with common applications in manufacturing, prototyping, and the creation of complex mechanical parts.[72] It utilizes materials that are often rigid and non-living, focusing on the structural integrity and functional aspects of the printed object. In contrast, bioprinting is specifically designed for creating biological constructs, including tissues and organs, using bioinks composed of living cells and biomaterials.[73–75] It aims to replicate the complex architecture of biological tissues, facilitating cell growth and function, with applications predominantly in the field of medicine and biological research, such as tissue engineering, regenerative medicine, and the development of *in vitro* models for drug testing. Bioprinting technology can be broadly categorized into three main types: extrusion-based bioprinting (EBB), inkjet-based bioprinting (IBB), and laser-based bioprinting (LBB). These three bioprinting methods each have unique advantages and are chosen based on the specific requirements of the tissue engineering application (Figure 2). These technologies hold significant potential for advancing tissue engineering, as it enables the creation of complex structures that closely mimic the natural architecture of biological tissues, such as lung tissue.[76]

3.1. Extrusion-based bioprinting

EBB is one of the most commonly employed methods in the field of bioprinting due to its versatility and ability to handle a broad range of biomaterials, including hydrogels, biopolymers, and cell-laden bioinks.[19,77] This technique operates by the controlled extrusion of bioink through a nozzle, which deposits material layer by layer to construct 3D structures.[78] The continuous filament formation under regulated pressure allows EBB to effectively create scaffolds embedded with cells, resulting in complex tissue constructs.[75]

For instance, Miller et al. demonstrated the use of EBB to fabricate a lung model integrated with a perfusable vascular

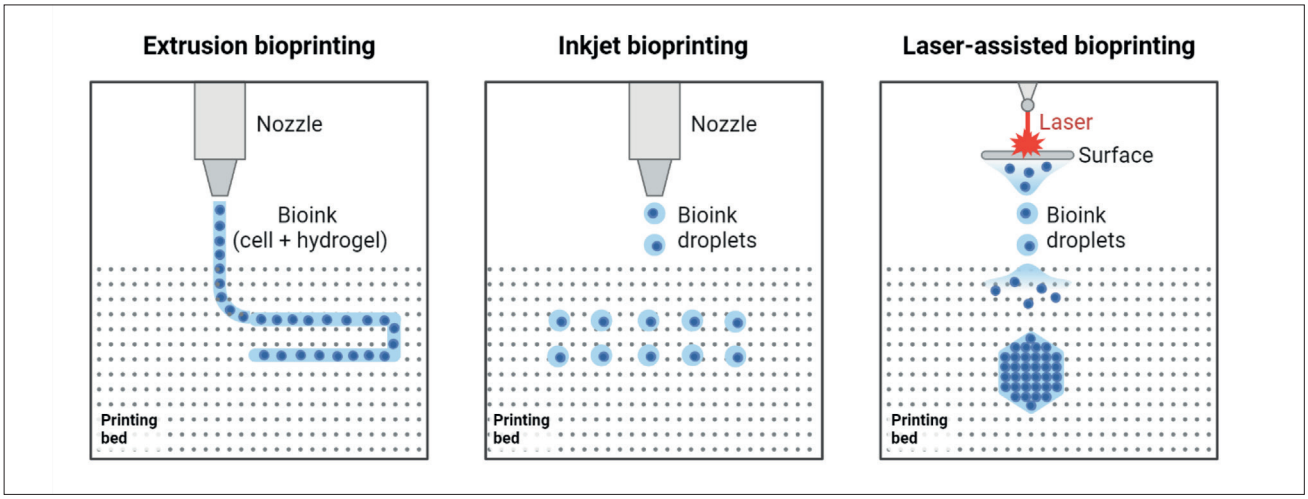

Figure 2. Schematic of three main bioprinting techniques. The three main bioprinting techniques include extrusion-based, inkjet-based, and laser-based bioprintings. This diagram was created with BioRender.com (adapted from "Types of Additive Manufacturing in Bioprinting Processes"; retrieved from https://app.biorender.com/biorender-templates).

network.[79] This development is critical for replicating the oxygenation functions of the lungs, as the vascular network facilitates efficient nutrient and oxygen delivery throughout the tissue. Additionally, EBB supports the integration of high cell densities and various biomaterials, making it suitable for the fabrication of large and intricate structures.[80,81] It also allows for the incorporation of mechanical and biochemical cues within the printed scaffolds.[82] The capability to incorporate mechanical and biochemical cues within printed scaffolds further enhances the potential of EBB in tissue engineering applications.

Despite its advantages, EBB typically produces structures with lower resolution compared to other bioprinting techniques. The necessity for high-viscosity bioinks, which are required to maintain the structure's integrity during printing, can lead to challenges such as nozzle clogging and uneven cell distribution.[78] Moreover, the precision of cell placement and the fine resolution of the printed constructs are often compromised, potentially affecting the overall functionality and replicability of the bioprinted tissue.

3.2. Inkjet-based bioprinting

IBB utilizes droplets of bioink ejected from a printhead to build structures layer by layer.[83] This method is known for its high resolution and ability to deposit small volumes of bioink with precise control.[19] Also, this technique uses thermal or piezoelectric actuators to generate droplets of bioink, which are then ejected onto a substrate in a controlled manner.[84] Inkjet bioprinting is particularly suitable for creating detailed tissue constructs and high-throughput applications.[85]

Researchers have utilized inkjet bioprinting to create high-resolution lung models with precise cell placement. Kang et al. developed a 3D pulmonary fibrosis model using inkjet bioprinting.[86] They layered endothelial cells, type I collagen, fibroblasts, AT1 and AT2 cells using inkjet bioprinting technology. In addition, they achieved high precision in cell placement and tissue architecture by creating microfabricated lung models with inkjet bioprinting. They reported that this layered structure mimics the alveolar barrier model and can easily induce epithelial-mesenchymal transition, which is an important pathogenic mechanism in pulmonary fibrosis, and identify biomarker expression, allowing for quick and effective simulation of pulmonary fibrosis therapeutics.

Inkjet bioprinting offers high precision and resolution, making it suitable for fabricating intricate tissue structures.[87] It also allows for the use of low-viscosity bioinks, which can improve cell viability and functionality.[85] However, the low viscosity requirement limits the range of usable bioinks, and the shear forces generated during droplet ejection can potentially damage cells.[83] In addition, the technique is generally limited to producing relatively thin layers of tissue.

3.3. Laser-based bioprinting

LBB, including laser-induced forward transfer (LIFT) and stereolithography (SLA), uses laser energy to pattern bioinks with high precision.[88] These methods leverage laser energy to pattern bioinks with high precision and resolution, making them particularly suitable for creating complex and detailed tissue constructs.[89] LBB offers unparalleled control over the microarchitecture of printed tissues, which is essential for replicating the intricate structures of lung tissue.[90] LIFT is a non-contact bioprinting method that uses a pulsed laser to transfer bioink from a donor substrate to a receiver substrate. The laser energy creates a focused microbubble at the interface of the bioink and the donor substrate, propelling a droplet of bioink towards the receiver substrate.[81] This technique allows for high precision in droplet placement and minimal damage to cells due to the gentle transfer process. SLA is a photopolymerization-based bioprinting technique that uses a laser to selectively cure photo-crosslinkable bioinks layer by layer.[88] This method is highly precise and can produce structures with intricate details and smooth surfaces. SLA is particularly advantageous for fabricating scaffolds with complex geometries and internal features that are challenging to achieve with other bioprinting methods.

Guillotin et al. demonstrated the use of LIFT to create high-resolution alveolar structures.[91] The precise control offered by LIFT allowed for the deposition of alveolar epithelial cells in defined patterns, closely mimicking the native architecture of lung alveoli. This approach enabled the formation of functional alveolar units with enhanced gas exchange capabilities. Zhu et al. utilized stereolithography to print lung models with detailed vascular networks.[92] By carefully controlling the laser parameters and the properties of the photo-crosslinkable bioinks, they were able to create microvascular structures that supported perfusion and enhanced the functionality of the printed lung tissue. These vascular networks are essential for providing nutrients and oxygen to the cells, thereby improving cell viability and tissue integration.

LBB offers high precision and resolution, enabling the creation of intricate and detailed tissue structures.[93] The non-contact nature of LIFT minimizes cell damage, while the layer-by-layer approach of SLA allows for the fabrication of complex geometries.[89] These techniques also support the use of photo-crosslinkable bioinks, which can enhance the stability and functionality of

the printed constructs.[91] However, the requirement for photo-crosslinkable materials in SLA limits the range of usable bioinks.[83] In addition, the high cost and complexity of laser-based systems can be a barrier to widespread adoption.[94] The scalability of these methods for large-scale tissue production also remains a challenge.[93]

3.4. Three-dimensional lung bioprinting and its considerations

When developing a lung model using 3D bioprinting, several critical considerations must be taken into account to ensure the model's functionality and relevance. One of the primary considerations is the selection of bioink, which must be carefully chosen to support cell viability, proliferation, and differentiation.[19,73] The bioink should closely mimic the ECM of lung tissue, providing the necessary biochemical and mechanical cues for appropriate cell behavior, including attachment, migration, and differentiation into specific lung cell types. The bioink composition often includes natural polymers like collagen, gelatin, and hyaluronic acid, which are known for their biocompatibility and ability to promote cell growth. The lung's complex and hierarchical structure, with its branched airways and alveoli, poses a significant challenge for bioprinting. Precise control over the bioprinting process is essential to ensure that the printed structures accurately replicate the native tissue's intricate geometry and functionality. This involves optimizing the printing resolution and layer thickness to create detailed and functional lung models. Techniques such as multi-material bioprinting can be employed to print different cell types and ECM components in a spatially controlled manner, closely mimicking the heterogeneous composition of lung tissue.[74,95]

Another important consideration is the mechanical properties of the printed lung model. The lung tissue is subjected to cyclic stretching and relaxation during respiration, so the printed structures must exhibit similar mechanical behavior to native lung tissue. This requires careful tuning of the bioink formulation and scaffold design to achieve the appropriate elasticity and strength. Incorporating materials that can undergo dynamic mechanical stimulation can help in replicating the physiological conditions of the lung, thereby enhancing the functionality and longevity of the bioprinted lung model.

Furthermore, vascularization is a critical aspect of lung tissue engineering. The printed lung model must include a perfusable vascular network to ensure the delivery of nutrients and oxygen to the cells, as well as the removal of metabolic waste. This can be achieved through advanced bioprinting techniques that allow for the incorporation of endothelial cells and the creation of microvascular structures within the lung model. The inclusion of vascular networks not only improves cell viability but also enhances the overall functionality of the bioprinted lung tissue.

To facilitate widespread adoption and practical application, the bioprinting process must be both scalable and reproducible. This entails standardizing bioink formulations, printing parameters, and post-processing steps to ensure consistent and reliable results across different batches. Developing robust protocols for bioink preparation, bioprinting, and subsequent tissue maturation is crucial for achieving reproducibility. Additionally, integrating automated systems and real-time monitoring during the bioprinting process can further enhance the precision and consistency of the printed lung models.[75,96,97]

4. Research on bioprinting-based 3D organoid and tissue modeling

Recently, there has been significant progress in utilizing 3D bioprinting technology to replicate the structure and function of lungs, thereby enhancing the ease of organoid creation. Krakos et al. used EBB to develop a lab-on-a-chip device that simulates the mechanical and biological environment of the lung.[98] The researchers created six different hydrogel inks by varying the proportions of sodium alginate, agar, chitosan, gelatin, and methylcellulose, and optimized them with different bioprinting parameters. The hydrogel-based lab-on-chip composed of 3% sodium alginate, 7% gelatin, and 90% NaCl showed the highest cell viability and had similar elasticity modulus values to biological tissues (0.060–0.512 MPa) at 37°C conditions.[98]

While bioprinting has not yet fully simulated lung structure, scaffolds have been developed that are conducive to cell culture for use in *in vitro* studies. Gerbolés et al. created a hydrogel mixture by combining Matrigel, porcine skin gelatin, and sodium alginate.[99] To conduct 3D bioprinting of organoid-based scaffolds (OBST), the layered structure was based on 10% porcine skin gelatin and 10% Matrigel, with variable proportions of sodium alginate. Considering the viscosity to maintain cell comfort, the sodium alginate concentration was fixed at 2% at 35°C and the extrusion speed at 13 mm/s. The hydrogel mixture was then combined with Calu-3 cells, a human lung adenocarcinoma cell line, prior to bioprinting. They reported that bioprinted Calu-3 cells treated with colloidal toxic silver nanoparticles (AgNPs), known for their potential antitumor properties, exhibited half maximal inhibitory concentration (IC_{50}) values similar to toxicological studies conducted in mice.[99]

Urciuolo et al. demonstrated that a photosensitive polymer, 7-hydroxycoumarin-3-carboxylic acid (HCCA)-gelatin, can be added to Matrigel and subsequently

Table 1. Bioprinting-based 3D lung modeling

Bioprinting	Cells or materials	Printing parameters	Mimicry or improvement	Results	Ref.
IBB	• Epithelial cells • Endothelial cells • Type I collagen • Fibroblasts	• Piezoelectric nozzle: 80 μm sized • Jet speed: 3 m/s • Rise, fall, dwell time: 10 μs • Peak drive voltage: ±80 V	Alveolar barrier models	Easily induce epithelial-mesenchymal transition	86
EBB	• Sodium alginate • Agar • Chitosan • Gelatin • Methylcellulose • NaCl	• Ink: 28°C • Printhead speed :13–15 mm/s • Extrusion pressure: 10–12 kPa • Table: 27°C • Head: 60°C	LOC	Lung cancer-based LOC analysis	98
EBB	Hydrogel (Calu-3 cells, AgNPs)	• 10% porcine skin gelatin • 10% Matrigel • 2% Sodium alginate • Ink: 35°C • Extrusion speed: 13 mm/s	Technology for cell culture	Long-term culturing of cell lines due to the reduction in oxidative stress	99
LBB	Hydrogel (HCCA-gelatin-Matrigel crosslinked)	• Laser power: 1 mW • Wavelength: 800 nm	Lung development (bud tip)	Dynamic fabrication, Live modulation	100
EBB	PEVA LudECM	• 25 G metal nozzle, 500 kPA (PEVA Chamber) • Extrusion pressure: 5–12 kPa • 1% w/v LudECM within the ILFs region	Vascularized lung cancer	Anti-cancer drug evaluation	101
LBB	Hydrogel (water and poly-ethylene glycol-diacrylate)	• 20 wt%, 6 kDa PEGDA • Voxel resolution: 5 pl • Print time: 1 h	Vascularized alveolar model topology	Control over tissue architecture and design of regenerative tissues	105

Abbreviations: EBB, extrusion-based bioprinting; IBB, inkjet-based bioprinting; ILFs, IPF-derived lung fibroblasts; LBB, laser-based bioprinting; LOC, Lab-on-a-chip; LudECM, lung-derived decellularized extracellular matrix; PEGDA, polyethylene glycol diacrylate.

crosslinked during cell culture using two-photon mediated bioprinting.[100] The researchers added liquid HCC-Gelatin to the existing matrigel and incubated it for 15 min before photocrosslinking using bioprinting. The crosslinked hydrogel maintained structural integrity after incubating the matrigel droplets in Dulbecco's Modified Eagle Medium (DMEM) for 2 days and showed accuracy with minimal linewidth (1.5 ± 0.8 μm), even when multiple hydrogel parallelepipeds of different heights were fabricated and then compared. This technique can be utilized to crosslink tissue constructs in cell culture to mimic geometric constraints such as cell migration or structural features in bud-tip real-time as the lung develops (Figure 4C).

Choi et al. incorporated patient-derived lung cancer organoids with porcine lung-derived decellularized extracellular matrix (LudECM) hydrogel to establish a lung cancer microenvironment and provide physical and biochemical signals.[101] In this particular study, bioprinting demonstrated a new potential to furnish lung organoids with blood vessel network, which is otherwise, typically, absent in the pre-existing organoids (Figure 4D). Resistance to targeted anti-cancer drugs in lung cancer organoids was significantly higher in LudECM compared to conventional Matrigel. In addition, they demonstrated the creation a lung model with a perfusable vascular network by use of EBB. This model is crucial for mimicking the oxygenation function of the lungs, as it allows for the integration of a functional blood supply within the organoid. Chambers for culturing lung cancer organoids (LCOs), IPF-derived lung fibroblasts (ILFs), and ECs were printed in PEVA blood vessel constructs and were then printed in gelatin, after which the ILF bioink was treated and the gelatin was removed. These ILFs were cultured in LudECM for one day and then further cultured with ECs. Finally, LCOs were printed in the fibroblast area in the blood vessels. The resulting bioprinting-based vascular constructs were

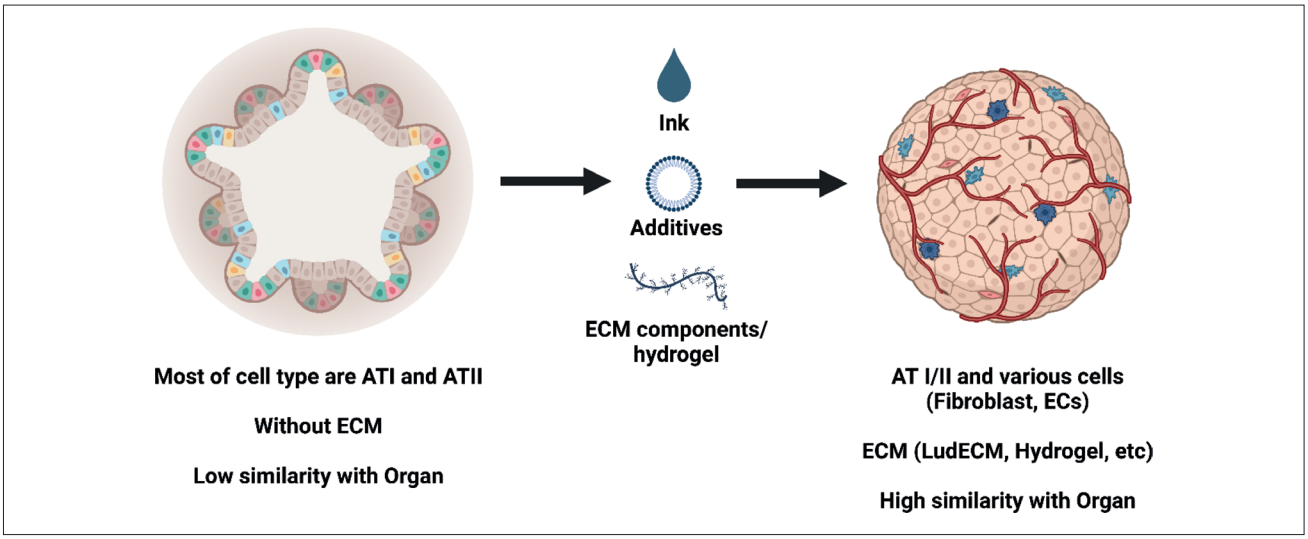

Figure 3. Improved structure of a lung organoid using 3D bioprinting. Traditional organoids generally consist of only alveolar type I (AT1) and alveolar type II (AT2) cells without extracellular matrix (ECM), resulting in a low similarity to the lung. On the other hand, 3D bioprinting-based lung organoid containing ECM and various cell types such as fibroblasts and vascular endothelial cells (ECs) has a high-degree resemblance to the organ. This diagram was created with BioRender.com.

stable in shear recovery evaluation. This study highlights the potential of 3D bioprinting in creating complex, multi-cellular structures that are essential for accurately replicating lung physiology.[102]

The field of 3D bioprinting for organoid and tissue modeling is poised for remarkable advancements, driven by ongoing research and technological innovation. One promising direction is the integration of advanced bioinks, which can provide better support for cell viability and functionality. These bioinks, enriched with growth factors, ECM components, and other biomolecules, could significantly enhance the complexity and functionality of bioprinted tissues.[103,104] In addition, the development of more sophisticated bioprinting techniques, such as light-assisted bioprinting,[105] volumetric bioprinting,[106] and microfluidics-assisted bioprinting,[107] can improve the precision and resolution of tissue structures, enabling the reproduction of complex vascular networks and organ-specific microstructures. These advancements are crucial for overcoming current limitations in vascularization and tissue complexity. The various bioprinting-based 3D lung modeling approaches are summarized in Table 1 and Figures 3 and 4.

Despite these advancements, several limitations and challenges remain in the development of vascularized lung organoid models. Replicating the complex branching and hierarchical structure of native blood vessels is particularly challenging. Current bioprinting techniques often struggle to achieve the fine resolution required to accurately recreate these intricate networks. Maintaining perfusion and ensuring the long-term culture of vascularized lung organoids are additional challenges.[108] The development of bioreactors and dynamic culture systems that can provide a continuous supply of nutrients and oxygen is essential for addressing these issues. Collaboration between biologists, engineers, and clinicians will be crucial for translating bioprinting advancements into clinical settings. Regulatory frameworks and ethical guidelines will need to evolve in tandem with technological progress to ensure the safe and effective use of bioprinted tissues in regenerative medicine, drug testing, and disease modeling.[109]

5. Conclusion

In summary, organoid and tissue modeling research using 3D bioprinting has shown significant progress in recreating complex tissue structures and modeling disease environments. By applying bioprinting technologies, these studies overcome the limitations of conventional 3D tissue modeling and pave the way for future innovations towards the bioprinting of therapeutic functional organs.[110] However, many challenges remain, such as improving the similarity and stability of bioprinted structures and integrating functional vascular networks.[111] In addition, significant improvements are needed in achieving uniform cell distribution and vascularization within the printed structures. Continued research and collaboration between biomedical engineering, materials science, and clinical disciplines are essential to resolve these challenges and fully realize the potential of bioprinting in medical science.

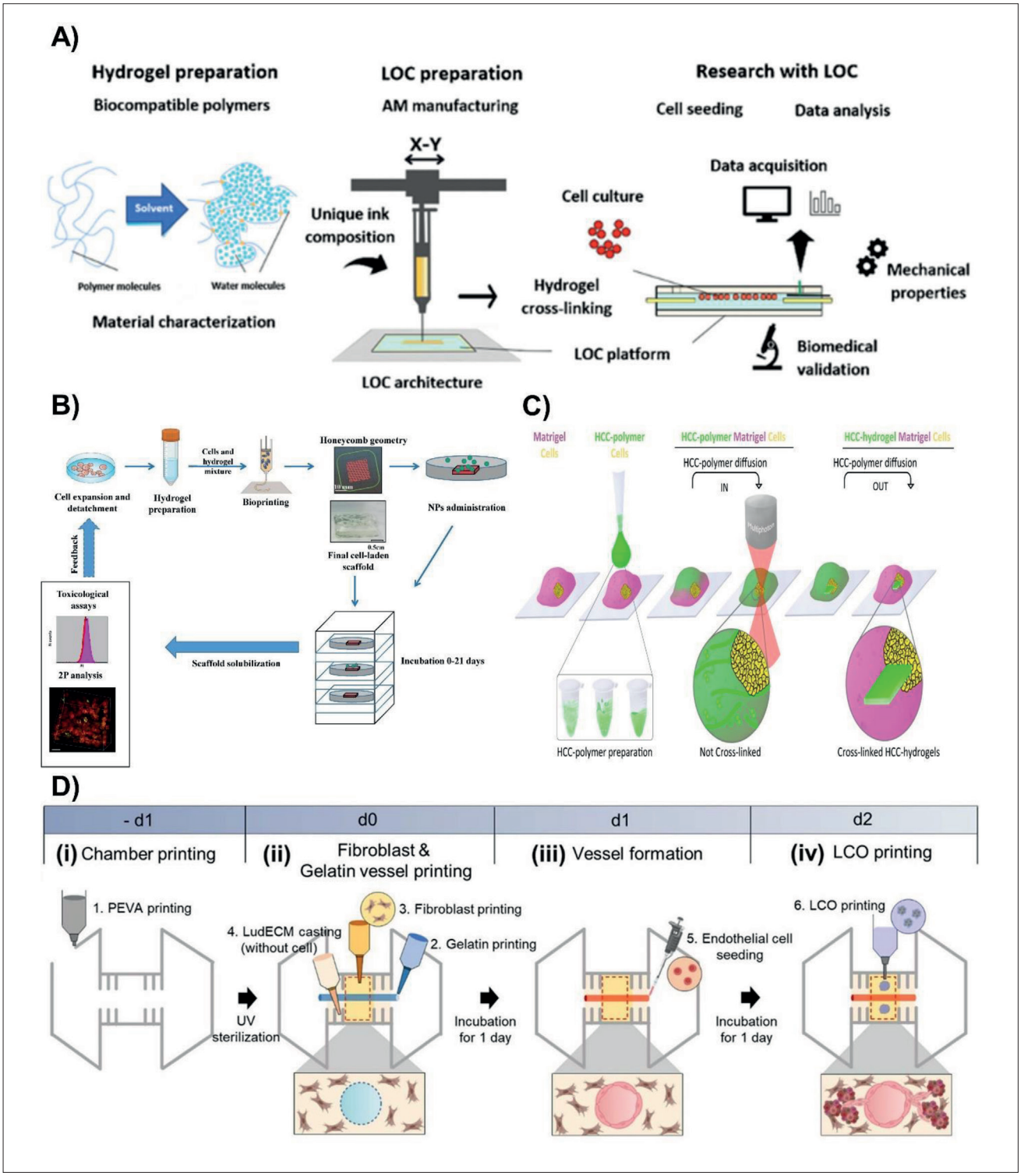

Figure 4. Researches for the production of 3D lung models. (A) Schematic overview of the study showing the development of a lab-on-chip (LOC) platform using six hydrogel inks Adapted from Krakos et al.[98] (B) Protocol for the toxicological study of silver nanoparticles (AgNPs) using organoid-based scaffold Adapted from Gerboles et al.[99] (C) Method for hydrogel-in-hydrogel live bioprinting using two-photon (2P) bioprinting Adapted from Urciuolo et al.[100] (D) Schematic of fabrication of vascularized lung cancer organoids (LCO) models including lung tissue-specific extracellular matrix (ECM) components and LCOs, stroma cells, and blood vessel.[101] Copyright © 2023 IOP Publishing. Reproduced with permission of IOP Publishing, Ltd. All rights reserved.

Acknowledgments

None.

Funding

This work was supported by the National Research Foundation of Korea (NRF) grant funded by the Korea government (2020R1A5A8019180), the Ministry of Education (MOE) (2022RIS-005).

Conflict of interest

The authors declare they have no competing interests

Author contributions

Conceptualization: Jimin Jang, Jooyoung Lee, Se-Ran Yang, Hyungseok Lee *Visualization:* Jimin Jang, Jooyoung Lee
Writing–original draft: Jimin Jang, Jooyoung Lee, Sangryul Cha, Minkyong Lee
Writing–review & editing: Se-Ran Yang, Hyungseok Lee

Ethics approval and consent to participate

Not applicable.

Consent for publication

Not applicable.

Availability of data

Not applicable.

References

1. Levine SM, Marciniuk DD. Global impact of respiratory disease: what can we do, together, to make a difference? *Chest*. 2022;161(5):1153-1154.
doi: 10.1016/j.chest.2022.01.014

2. Shukla SD, Swaroop Vanka K, Chavelier A, et al. Chronic respiratory diseases: an introduction and need for novel drug delivery approaches. In: Targeting Chronic Inflammatory Lung Diseases Using Advanced Drug Delivery Systems; 2020:1-31.
doi: 10.1016/B978-0-12-820658-4.00001-7

3. Ayilya BL, Balde A, Ramya M, Benjakul S, Kim SK, Nazeer RA. Insights on the mechanism of bleomycin to induce lung injury and associated in vivo models: a review. *Int Immunopharmacol*. 2023;121:110493.
doi: 10.1016/j.intimp.2023.110493

4. Ribble A, Hellmann J, Conklin DJ, Bhatnagar A, Haberzettl P. Fine particulate matter (PM(2.5))-induced pulmonary oxidative stress contributes to increases in glucose intolerance and insulin resistance in a mouse model of circadian dyssynchrony. *Sci Total Environ*. 2023;877:162934.
doi: 10.1016/j.scitotenv.2023.162934

5. John G, Kohse K, Orasche J, et al. The composition of cigarette smoke determines inflammatory cell recruitment to the lung in COPD mouse models. *Clin Sci (Lond)*. 2014;126(3):207-221.
doi: 10.1042/cs20130117

6. Khedoe PP, Wong MC, Wagenaar GT, et al. The effect of PPE-induced emphysema and chronic LPS-induced pulmonary inflammation on atherosclerosis development in APOE*3-LEIDEN mice. *PLoS One*. 2013;8(11):e80196.
doi: 10.1371/journal.pone.0080196

7. Ishida Y, Kuninaka Y, Mukaida N, Kondo T. Immune mechanisms of pulmonary fibrosis with bleomycin. *Int J Mol Sci*. 2023;24(4):3149.
doi: 10.3390/ijms24043149

8. Su J, Ye Q, Zhang D, et al. Joint association of cigarette smoking and PM(2.5) with COPD among urban and rural adults in regional China. *BMC Pulm Med*. 2021;21(1):87.
doi: 10.1186/s12890-021-01465-y

9. Kwon MC, Berns A. Mouse models for lung cancer. *Mol Oncol*. 2013;7(2):165-177.
doi: 10.1016/j.molonc.2013.02.010

10. Uhl EW, Warner NJ. Mouse models as predictors of human responses: evolutionary medicine. *Curr Pathobiol Rep*. 2015;3(3):219-223.
doi: 10.1007/s40139-015-0086-y

11. Rydell-Törmänen K, Johnson JR. The applicability of mouse models to the study of human disease. *Methods Mol Biol*. 2019;1940:3-22.
doi: 10.1007/978-1-4939-9086-3_1

12. Patisaul HB, Fenton SE, Aylor D. Animal models of endocrine disruption. *Best Pract Res Clin Endocrinol Metab*. 2018;32(3):283-297.
doi: 10.1016/j.beem.2018.03.011

13. Chae S, Ha DH, Lee H. 3D bioprinting strategy for engineering vascularized tissue models. *Int J Bioprint*. 2023;9(5):748.
doi: 10.18063/ijb.748

14. Bosáková V, De Zuani M, Sládková L, et al. Lung organoids-the ultimate tool to dissect pulmonary diseases? *Front Cell Dev Biol*. 2022;10:899368.
doi: 10.3389/fcell.2022.899368

15. Shrestha J, Razavi Bazaz S, Aboulkheyr Es H, et al. Lung-on-a-chip: the future of respiratory disease models and pharmacological studies. *Crit Rev Biotechnol*. 2020;40(2):213-230.
doi: 10.1080/07388551.2019.1710458

16. Hermanns MI, Unger RE, Kehe K, Peters K, Kirkpatrick CJ. Lung epithelial cell lines in coculture with human pulmonary microvascular endothelial cells: development of an alveolo-capillary barrier in vitro. *Lab Invest*. 2004;84(6):736-752.
doi: 10.1038/labinvest.3700081

17. Birgersdotter A, Sandberg R, Ernberg I. Gene expression perturbation in vitro—a growing case for three-dimensional (3D) culture systems. Semin Cancer Biol. 2005;15(5):405-412.
doi: 10.1016/j.semcancer.2005.06.009

18. Pampaloni F, Reynaud EG, Stelzer EH. The third dimension bridges the gap between cell culture and live tissue. *Nat Rev Mol Cell Biol*. 2007;8(10):839-845.
doi: 10.1038/nrm2236

19. Murphy SV, Atala A. 3D bioprinting of tissues and organs. *Nat Biotechnol*. 2014;32(8):773-785.
doi: 10.1038/nbt.2958

20. Zou S, Ye J, Wei Y, Xu J. Characterization of 3D-bioprinted in vitro lung cancer models using RNA-sequencing techniques. *Bioengineering (Basel)*. 2023;10(6):667.
doi: 10.3390/bioengineering10060667

21. Wang X, Zhang X, Dai X, et al. Tumor-like lung cancer model based on 3D bioprinting. *3 Biotech*. 2018;8:501.
doi: 10.1007/s13205-018-1519-1

22. Maina JN. Fundamental structural aspects and features in the bioengineering of the gas exchangers: comparative perspectives. *Adv Anat Embryol Cell Biol*. 2002;163:Iii-xii, 1-108.
doi: 10.1007/978-3-642-55917-4

23. Khan YS, Lynch DT. Histology, Lung. 2023. In: StatPearls [Internet]. Treasure Island (FL): StatPearls Publishing; 2024.

24. Brownfield DG, de Arce AD, Ghelfi E, Gillich A, Desai TJ, Krasnow MA. Alveolar cell fate selection and lifelong maintenance of AT2 cells by FGF signaling. *Nat Commun*. 2022;13(1):7137.
doi: 10.1038/s41467-022-34059-1

25. Yang J, Hernandez BJ, Martinez Alanis D, et al. The development and plasticity of alveolar type 1 cells. *Development*. 2016;143(1):54-65.
doi: 10.1242/dev.130005

26. Han S, Lee M, Shin Y, et al. Mitochondrial integrated stress response controls lung epithelial cell fate. *Nature*. 2023;620(7975):890-897.
doi: 10.1038/s41586-023-06423-8

27. Quan R, Shi C, Fang B, et al. Age-dependent inflammatory microenvironment mediates alveolar regeneration. *Int J Mol Sci*. 2024;25(6):3476.
doi: 10.3390/ijms25063476

28. Basil MC, Katzen J, Engler AE, et al. The cellular and physiological basis for lung repair and regeneration: past, present, and future. *Cell Stem Cell*. 2020;26(4):482-502.
doi: 10.1016/j.stem.2020.03.009

29. Ruaro B, Salton F, Braga L, et al. The history and mystery of alveolar epithelial type II cells: focus on their physiologic and pathologic role in lung. *Int J Mol Sci*. 2021;22(5):2566.
doi: 10.3390/ijms22052566

30. Zhang J, Liu Y. Epithelial stem cells and niches in lung alveolar regeneration and diseases. *Chin Med J Pulm Crit Care Med*. 2024;2(1):17-26.
doi: 10.1016/j.pccm.2023.10.007

31. Beers MF, Moodley Y. When is an alveolar type 2 cell an alveolar type 2 cell? A conundrum for lung stem cell biology and regenerative medicine. *Am J Respir Cell Mol Biol*. 2017;57(1):18-27.
doi: 10.1165/rcmb.2016-0426PS

32. Kendall RT, Feghali-Bostwick CA. Fibroblasts in fibrosis: novel roles and mediators. *Front Pharmacol*. 2014;5:123.
doi: 10.3389/fphar.2014.00123

33. Fu Z, Xu YS, Cai CQ. Ginsenoside Rg3 inhibits pulmonary fibrosis by preventing HIF-1α nuclear localisation. *BMC Pulm Med*. 2021;21(1):70.
doi: 10.1186/s12890-021-01426-5

34. Wilson MS, Wynn TA. Pulmonary fibrosis: pathogenesis, etiology and regulation. *Mucosal Immunol*. 2009;2(2):103-121.
doi: 10.1038/mi.2008.85

35. Li YX, Wang HB, Li J, Jin JB, Hu JB, Yang CL. Targeting pulmonary vascular endothelial cells for the treatment of respiratory diseases. *Front Pharmacol*. 2022;13:983816.
doi: 10.3389/fphar.2022.983816

36. Vassiliou AG, Kotanidou A, Dimopoulou I, Orfanos SE. Endothelial damage in acute respiratory distress syndrome. *Int J Mol Sci*. 2020;21(22):8793.
doi: 10.3390/ijms21228793

37. Correale M, Chirivi F, Bevere EML, et al. Endothelial function in pulmonary arterial hypertension: from bench to bedside. *J Clin Med*. 2024;13(8):2444.
doi: 10.3390/jcm13082444

38. Meng X, Cui G, Peng G. Lung development and regeneration: newly defined cell types and progenitor status. *Cell Regen*. 2023;12(1):5.
doi: 10.1186/s13619-022-00149-0

39. Zhao Z, Chen X, Dowbaj AM, et al. Organoids. *Nat Rev Methods Primers*. 2022;2:94.
doi: 10.1038/s43586-022-00174-y

40. Arjmand B, Rabbani Z, Soveyzi F, et al. Advancement of organoid technology in regenerative medicine. *Regen Eng Transl Med*. 2023;9(1):83-96.
doi: 10.1007/s40883-022-00271-0

41. Parikh P, Wicher S, Khandalavala K, Pabelick CM, Britt RD, Jr., Prakash YS. Cellular senescence in the lung across the age spectrum. *Am J Physiol Lung Cell Mol Physiol*. 2019;316(5):L826-L842.
doi: 10.1152/ajplung.00424.2018

42. Koks S, Dogan S, Tuna BG, Gonzalez-Navarro H, Potter P, Vandenbroucke RE. Mouse models of ageing and their relevance to disease. *Mech Ageing Dev*. 2016;160:41-53.
doi: 10.1016/j.mad.2016.10.001

43. Fan C, Wu Y, Rui X, et al. Animal models for COVID-19: advances, gaps and perspectives. *Signal Transduct Target Ther*. 2022;7(1):220.
doi: 10.1038/s41392-022-01087-8

44. Cox TC. Utility and limitations of animal models for the functional validation of human sequence variants. *Mol Genet Genomic Med*. 2015;3(5):375-382.
doi: 10.1002/mgg3.167

45. Duval K, Grover H, Han LH, et al. Modeling physiological events in 2D vs. 3D cell culture. *Physiology (Bethesda)*. 2017;32(4):266-277.
doi: 10.1152/physiol.00036.2016

46. Jubelin C, Munoz-Garcia J, Griscom L, et al. Three-dimensional in vitro culture models in oncology research. *Cell Biosci*. 2022;12(1):155.
doi: 10.1186/s13578-022-00887-3

47. Cacciamali A, Villa R, Dotti S. 3D cell cultures: evolution of an ancient tool for new applications. *Front Physiol*. 2022;13:836480.
doi: 10.3389/fphys.2022.836480

48. Miller AJ, Dye BR, Ferrer-Torres D, et al. Generation of lung organoids from human pluripotent stem cells in vitro. *Nat Protoc*. 2019;14(2):518-540.
doi: 10.1038/s41596-018-0104-8

49. Kong J, Wen S, Cao W, et al. Lung organoids, useful tools for investigating epithelial repair after lung injury. *Stem Cell Res Ther*. 2021;12(1):95.
doi: 10.1186/s13287-021-02172-5

50. Hein RFC, Conchola AS, Fine AS, et al. Stable iPSC-derived NKX2-1+ lung bud tip progenitor organoids give rise to airway and alveolar cell types. *Development*. 2022;149(20):dev200693.
doi: 10.1242/dev.200693

51. Chiu MC, Li C, Liu X, et al. A bipotential organoid model of respiratory epithelium recapitulates high infectivity of SARS-CoV-2 Omicron variant. *Cell Discov*. 2022;8(1):57.
doi: 10.1038/s41421-022-00422-1

52. Sucre JM, Wilkinson D, Vijayaraj P, et al. A three-dimensional human model of the fibroblast activation that accompanies bronchopulmonary dysplasia identifies Notch-mediated pathophysiology. *Am J Physiol Lung Cell Mol Physiol*. 2016;310(10):L889-L898.
doi: 10.1152/ajplung.00446.2015

53. Ng-Blichfeldt JP, de Jong T, Kortekaas RK, et al. TGF-beta activation impairs fibroblast ability to support adult lung epithelial progenitor cell organoid formation. *Am J Physiol Lung Cell Mol Physiol*. 2019;317(1):L14-L28.
doi: 10.1152/ajplung.00400.2018

54. Sachs N, Papaspyropoulos A, Zomer-van Ommen DD, et al. Long-term expanding human airway organoids for disease modeling. *EMBO J*. 2019;38(4):e100300.
doi: 10.15252/embj.2018100300

55. Chan LLY, Anderson DE, Cheng HS, et al. The establishment of COPD organoids to study host-pathogen interaction reveals enhanced viral fitness of SARS-CoV-2 in bronchi. *Nat Commun*. 2022;13(1):7635.
doi: 10.1038/s41467-022-35253-x

56. Laube M, Pietsch S, Pannicke T, Thome UH, Fabian C. Development and functional characterization of fetal lung organoids. *Front Med (Lausanne)*. 2021;8:678438.
doi: 10.3389/fmed.2021.678438

57. Matkovic Leko I, Schneider RT, Thimraj TA, et al. A distal lung organoid model to study interstitial lung disease, viral infection and human lung development. *Nat Protoc*. 2023;18(7):2283-2312.
doi: 10.1038/s41596-023-00827-6

58. Vazquez-Armendariz AI, Herold S. From clones to buds and branches: the use of lung organoids to model branching morphogenesis ex vivo. *Front Cell Dev Biol*. 2021;9:631579.
doi: 10.3389/fcell.2021.631579

59. Jain KG, Xi NM, Zhao R, Ahmad W, Ali G, Ji HL. Alveolar type 2 epithelial cell organoids: focus on culture methods. *Biomedicines*. 2023;11(11):3034.
doi: 10.3390/biomedicines11113034

60. Mulay A, Konda B, Garcia G, Jr., et al. SARS-CoV-2 infection of primary human lung epithelium for COVID-19 modeling and drug discovery. *Cell Rep*. 2021;35(5):109055.
doi: 10.1016/j.celrep.2021.109055

61. Konda B, Mulay A, Yao C, Beil S, Israely E, Stripp BR. Isolation and enrichment of human lung epithelial progenitor cells for organoid culture. *J Vis Exp*. 2020;(161).
doi: 10.3791/61541

62. Van Hung T, Emoto N, Vignon-Zellweger N, et al. Inhibition of vascular endothelial growth factor receptor under hypoxia causes severe, human-like pulmonary arterial hypertension in mice: potential roles of interleukin-6 and endothelin. *Life Sci*. 2014;118(2):313-328.
doi: 10.1016/j.lfs.2013.12.215

63. Zhang Y, Zhang H, Li S, Huang K, Jiang L, Wang Y. Metformin alleviates LPS-induced acute lung injury by regulating the SIRT1/NF-kappaB/NLRP3 pathway and inhibiting endothelial cell pyroptosis. *Front Pharmacol*. 2022;13:801337.
doi: 10.3389/fphar.2022.801337

64. Selimovic N, Bergh CH, Andersson B, Sakiniene E, Carlsten H, Rundqvist B. Growth factors and interleukin-6 across the lung circulation in pulmonary hypertension. *Eur Respir J*. 2009;34(3):662-668.
doi: 10.1183/09031936.00174908

65. Finicelli M, Digilio FA, Galderisi U, Peluso G. The emerging role of macrophages in chronic obstructive pulmonary disease: the potential impact of oxidative stress and extracellular vesicle on macrophage polarization and function. *Antioxidants (Basel)*. 2022;11(3):464.
doi: 10.3390/antiox11030464

66. Osorio-Valencia S, Zhou B. Roles of macrophages and endothelial cells and their crosstalk in acute lung injury. *Biomedicines*. 2024;12(3):632. doi: 10.3390/biomedicines12030632

67. Ramachandran S, Verma AK, Dev K, et al. Role of cytokines and chemokines in NSCLC immune navigation and proliferation. *Oxid Med Cell Longev*. 2021;2021:5563746. doi: 10.1155/2021/5563746

68. Huskin G, Chen J, Davis T, Jun HW. Tissue-engineered 3D in vitro disease models for high-throughput drug screening. *Tissue Eng Regen Med*. 2023;20(4):523-538. doi: 10.1007/s13770-023-00522-3

69. da Rosa NN, Appel JM, Irioda AC, et al. Three-dimensional bioprinting of an in vitro lung model. *Int J Mol Sci*. 2023;24(6):5852. doi: 10.3390/ijms24065852

70. Mu P, Zhou S, Lv T, et al. Newly developed 3D in vitro models to study tumor-immune interaction. *J Exp Clin Cancer Res*. 2023;42(1):81. doi: 10.1186/s13046-023-02653-w

71. Gibson I, Rosen DW, Stucker B, et al. *Additive Manufacturing Technologies*, vol 17. Springer; 2021. doi: 10.1007/978-1-4419-1120-9

72. Shahrubudin N, Lee TC, Ramlan R. An overview on 3D printing technology: technological, materials, and applications. *Procedia Manufact*. 2019;35:1286-1296. doi: 10.1016/j.promfg.2019.06.089

73. Gopinathan J, Noh I. Recent trends in bioinks for 3D printing. *Biomater Res*. 2018;22(1):11. doi: 10.1186/s40824-018-0122-1

74. Jakab K, Norotte C, Marga F, Murphy K, Vunjak-Novakovic G, Forgacs G. Tissue engineering by self-assembly and bio-printing of living cells. *Biofabrication*. 2010;2(2):022001. doi: 10.1088/1758-5082/2/2/022001

75. Mandrycky C, Wang Z, Kim K, Kim D-H. 3D bioprinting for engineering complex tissues. *Biotechnol Adv*. 2016;34(4):422-434. doi: 10.1016/j.biotechadv.2015.12.011

76. Fan P, Jin F, Qin Y, et al. Multiscale 3D bioprinting for the recapitulation of lung tissue. *IJB*. 2023;9(6):1166. doi: 10.36922/ijb.1166

77. Ozbolat IT. Bioprinting scale-up tissue and organ constructs for transplantation. *Trends Biotechnol*. 2015;33(7):395-400. doi: 10.1016/j.tibtech.2015.04.005

78. Groll J, Boland T, Blunk T, et al. Biofabrication: reappraising the definition of an evolving field. *Biofabrication*. 2016;8(1):013001. doi: 10.1088/1758-5090/8/1/013001

79. Miller AJ, Spence JR. In vitro models to study human lung development, disease and homeostasis. *Physiology (Bethesda)*. 2017;32(3):246-260. doi: 10.1152/physiol.00041.2016

80. Matai I, Kaur G, Seyedsalehi A, McClinton A, Laurencin CT. Progress in 3D bioprinting technology for tissue/organ regenerative engineering. *Biomaterials*. 2020;226:119536. doi: 10.1016/j.biomaterials.2019.119536

81. Ozbolat IT, Hospodiuk M. Current advances and future perspectives in extrusion-based bioprinting. *Biomaterials*. 2016;76:321-343. doi: 10.1016/j.biomaterials.2015.10.076

82. Gungor-Ozkerim PS, Inci I, Zhang YS, Khademhosseini A, Dokmeci MR. Bioinks for 3D bioprinting: an overview. *Biomater Sci*. 2018;6(5):915-946. doi: 10.1039/c7bm00765e

83. Derby B. Printing and prototyping of tissues and scaffolds. *Science*. 2012;338(6109):921-926. doi: 10.1126/science.1226340

84. Ning L, Chen X. A brief review of extrusion-based tissue scaffold bio-printing. *Biotechnol J*. 2017;12(8):1600671. doi: 10.1002/biot.201600671

85. Xu T, Jin J, Gregory C, Hickman JJ, Boland T. Inkjet printing of viable mammalian cells. *Biomaterials*. 2005;26(1):93-99. doi: 10.1016/j.biomaterials.2004.04.011

86. Kang D, Park JA, Kim W, et al. All-inkjet-printed 3D alveolar barrier model with physiologically relevant microarchitecture. *Adv Sci (Weinh)*. 2021;8(10):2004990. doi: 10.1002/advs.202004990

87. Scoutaris N, Ross S, Douroumis D. Current trends on medical and pharmaceutical applications of inkjet printing technology. *Pharm Res*. 2016;33(8):1799-1816. doi: 10.1007/s11095-016-1931-3

88. Yang H, Yang K-H, Narayan RJ, Ma S. Laser-based bioprinting for multilayer cell patterning in tissue engineering and cancer research. *Essays Biochem*. 2021;65(3):409-416. doi: 10.1042/EBC20200093

89. Gruene M, Pflaum M, Hess C, et al. Laser printing of three-dimensional multicellular arrays for studies of cell–cell and cell–environment interactions. *Tissue Eng Part C: Methods*. 2011;17(10):973-982. doi: 10.1089/ten.TEC.2011.0185

90. Catros S, Guillotin B, Bačáková M, Fricain J-C, Guillemot F. Effect of laser energy, substrate film thickness and bioink viscosity on viability of endothelial cells printed by laser-assisted bioprinting. *Appl Surf Sci*. 2011;257(12):5142-5147. doi: 10.1016/j.apsusc.2010.11.049

91. Guillotin B, Souquet A, Catros S, et al. Laser assisted bioprinting of engineered tissue with high cell density and microscale organization. *Biomaterials*. 2010;31(28):7250-7256. doi: 10.1016/j.biomaterials.2010.05.055

92. Zhu W, Qu X, Zhu J, et al. Direct 3D bioprinting of prevascularized tissue constructs with complex microarchitecture. *Biomaterials*. 2017;124:106-115. doi: 10.1016/j.biomaterials.2017.01.042

93. Li J, Chen M, Fan X, Zhou H. Recent advances in bioprinting techniques: approaches, applications and future prospects. *J Transl Med*. 2016;14:271. doi: 10.1186/s12967-016-1028-0

94. Geckil H, Xu F, Zhang X, Moon S, Demirci U. Engineering hydrogels as extracellular matrix mimics. *Nanomedicine (Lond)*. 2010;5(3):469-484. doi: 10.2217/nnm.10.12

95. Hinton TJ, Jallerat Q, Palchesko RN, et al. Three-dimensional printing of complex biological structures by freeform reversible embedding of suspended hydrogels. *Sci Adv*. 2015;1(9):e1500758. doi: 10.1126/sciadv.1500758

96. Kang H-W, Lee SJ, Ko IK, Kengla C, Yoo JJ, Atala A. A 3D bioprinting system to produce human-scale tissue constructs with structural integrity. *Nat Biotechnol*. 2016;34(3):312-319. doi: 10.1038/nbt.3413

97. Wang X, Ao Q, Tian X, et al. 3D bioprinting technologies for hard tissue and organ engineering. *Materials (Basel)*. 2016;9(10):802. doi: 10.3390/ma9110911

98. Krakos A, Cieslak A, Hartel E, Labowska MB, Kulbacka J, Detyna J. 3D bio-printed hydrogel inks promoting lung cancer cell growth in a lab-on-chip culturing platform. *Mikrochim Acta*. 2023;190(9):349. doi: 10.1007/s00604-023-05931-8

99. Gerboles AG, Galetti M, Rossi S, et al. Three-dimensional bioprinting of organoid-based scaffolds (OBST) for long-term nanoparticle toxicology investigation. *Int J Mol Sci*. 2023;24(7):6595. doi: 10.3390/ijms24076595

100. Urciuolo A, Giobbe GG, Dong Y, et al. Hydrogel-in-hydrogel live bioprinting for guidance and control of organoids and organotypic cultures. *Nat Commun*. 2023;14(1):3128. doi: 10.1038/s41467-023-37953-4

101. Choi YM, Lee H, Ann M, Song M, Rheey J, Jang J. 3D bioprinted vascularized lung cancer organoid models with underlying disease capable of more precise drug evaluation. *Biofabrication*. 2023;15(3):4104. doi: 10.1088/1758-5090/acd95f

102. Ma X, Liu J, Zhu W, et al. 3D bioprinting of functional tissue models for personalized drug screening and in vitro disease modeling. *Adv Drug Deliv Rev*. 2018;132:235-251. doi: 10.1016/j.addr.2018.06.011

103. Ashammakhi N, Ahadian S, Xu C, et al. Bioinks and bioprinting technologies to make heterogeneous and biomimetic tissue constructs. *Mater Today Bio*. 2019;1:100008. doi: 10.1016/j.mtbio.2019.100008

104. Chen XB, Fazel Anvari-Yazdi A, Duan X, et al. Biomaterials / bioinks and extrusion bioprinting. *Bioact Mater*. 2023;28:511-536. doi: 10.1016/j.bioactmat.2023.06.006

105. Grigoryan B, Paulsen SJ, Corbett DC, et al. Multivascular networks and functional intravascular topologies within biocompatible hydrogels. *Science*. 2019;364(6439):458-464. doi: 10.1126/science.aav9750

106. Bernal PN, Delrot P, Loterie D, et al. Volumetric bioprinting of complex living-tissue constructs within seconds. *Adv Mater*. 2019;31(42):e1904209. doi: 10.1002/adma.201904209

107. Richard C, Neild A, Cadarso VJ. The emerging role of microfluidics in multi-material 3D bioprinting. *Lab Chip*. 2020;20(12):2044-2056. doi: 10.1039/c9lc01184f

108. Mironov V, Kasyanov V, Drake C, Markwald RR. Organ printing: promises and challenges. *Regen Med*. 2008;3(1):93-103. doi: 10.2217/17460751.3.1.93

109. Sekar MP, Budharaju H, Zennifer A, et al. Current standards and ethical landscape of engineered tissues-3D bioprinting perspective. *J Tissue Eng*. 2021;12:20417314211027677. doi: 10.1177/20417314211027677

110. Saini G, Segaran N, Mayer JL, Saini A, Albadawi H, Oklu R. Applications of 3D bioprinting in tissue engineering and regenerative medicine. *J Clin Med*. 2021;10(21):4966. doi: 10.3390/jcm10214966

111. Huang G, Zhao Y, Chen D, et al. Applications, advancements, and challenges of 3D bioprinting in organ transplantation. *Biomater Sci*. 2024;12(6):1425-1448. doi: 10.1039/d3bm01934a

ACCSCIENCE PUBLISHING

International Journal of Bioprinting

REVIEW ARTICLE

Bioprinting of wearable sensors, brain-machine interfaces, and exoskeleton robots

Xinrui Wang[1,2], Wei Dong[1], Hui Dong[1]*, Yongzhuo Gao[1]*, Jiawen Lin[3], Haichao Jia[3], Yihui Tao[4], and Hao Sun[3]*

[1] School of Mechatronics Engineering, Harbin Institute of Technology, Harbin, 150001, China

[2] Weapon Equipment Research Institute, China South Industries Group Corp., Beijing, 102202, China

[3] College of Mechanical Engineering, Fuzhou University, Fuzhou, 350001, China

[4] College of Big Data and Internet, Shenzhen Technology University, Shenzhen, 518118, China

(This article belongs to the *Special Issue: Biomimetic and bioinspired printed structures*)

Abstract

Bioprinting holds the promise of producing biocompatible structures capable of seamlessly integrating with human physiology, improving human health by enabling the precise fabrication of tissue models that closely mimic the architecture and functions of human skin, brain, and bone. Building on the advancements of bioprinting, there has been a corresponding increase in cross-disciplinary innovations in wearable technologies, brain-machine interfaces, and exoskeleton robotics. Given the progress of bioprinting in skin study, wearable electronics are expected to have improved biocompatibility and integration with the human body. For patient-specific neural tissues created using bioprinting, the potential to replicate neural activities through the synergy of bioprinting and brain-machine interfaces presents opportunities to enhance the performance of more advanced neuromorphic systems. Inspired by the advancements of bioprinting in producing patient-specific bone grafts and scaffolds, this technology could bridge the gap between mechanical systems and biomechanics, redefining the limits of skeleton robotics. This review explores the advancements of bioprinting in wearable sensors, brain-machine interfaces, and exoskeleton robots, and briefly addresses the existing and potential challenges in interdisciplinary research.

Keywords: Bioprinting; Wearable sensor; Brain-machine interface; Exoskeleton robot

***Corresponding authors:**
Hui Dong (dongh@hit.edu.cn)

Yongzhuo Gao (gaoyongzhuo@hit.edu.cn)

Hao Sun (sh@fzu.edu.cn)

Citation: Wang X, Dong W, Dong H, et al. Bioprinting of wearable sensors, brain-machine interfaces, and exoskeleton robots. *Int J Bioprint*. 2024;10(6):3590. doi: 10.36922/ijb.3590

Received: May 6, 2024
Revised: July 20, 2024
Accepted: July 24, 2024
Published Online: July 31, 2024

Copyright: © 2024 Author(s). This is an Open Access article distributed under the terms of the Creative Commons Attribution License, permitting distribution, and reproduction in any medium, provided the original work is properly cited.

Publisher's Note: AccScience Publishing remains neutral with regard to jurisdictional claims in published maps and institutional affiliations.

1. Introduction

Advancements in 3D bioprinting are transforming various fields, such as regenerative and rehabilitation medicine, bionics, and biomimetic engineering. With precise placement of cells and supporting biomaterials, bioprinting enables the fabrication of complex and functional tissues that closely mimic native structures.[1,2] This precision offers promising avenues for treating degenerative diseases or injuries and constructing more advanced bionic systems.[3,4] The impact of bioprinting extends beyond medicine. Over the past 20 years, academic and industrialized bioprinting technologies have evolved from high-cost, specialized applications to more accessible,

cost-effective solutions due to advancements in print technologies, material science, and digital design tools. Corporations and research institutions are improving existing bioprinting applications and investigating new uses, expanding its potential. Following successes in skin,[5] bone,[6] and neural systems,[7] we anticipate the significant applications of bioprinting in wearable sensors, brain-machine interfaces (BMIs), and exoskeleton robots – key areas in informatics, robotics, and artificial intelligence (AI).[8–10] This cross-disciplinary synergy is paving new pathways for scientific endeavors and redefining the possibilities in advanced fabrication technologies. The integration of bioprinting with these emerging fields highlights its interdisciplinary significance.

The successful application of bioprinting in skin repair has provided insights for further developing wearable bioelectronic skin and constructing body area networks. Wearable devices are based on electronic technologies and incorporated into clothing and accessories that can be comfortably worn on the body to enhance daily activities.[11] These devices can track various health metrics like heart rate and glucose levels. Similar to wearable devices but with enhanced flexibility and adaptability, electronic skin (e-skin) utilizes thin materials that mimic the properties of human skin.[12] It is equipped to sense pressure, temperature, and other stimuli and can be directly applied to human skin or integrated into prosthetics. Bioprinting is enabling unprecedented customization for developing advanced wearable devices and e-skin.[13] By printing biocompatible materials in intricate designs, the wearable devices can conform perfectly to an individual's anatomy. The integration of printed biological constructs with wearables opens new opportunities for tailored medical interventions and expands the scope of personalized treatment. These personalized wearable devices can transcend their function as mere extensions of the human body, incorporating skin sensors and patches to monitor physiological parameters (Figure 1).

Bioprinting in brain sciences has paved the way for further advancements in biological BMIs, which are technologically mediated forms of communication that establish a direct conduit between the biological brain and external devices,[14] surpassing traditional interaction methodologies reliant on peripheral neuromuscular outputs. Moreover, bioprinting of BMIs can seamlessly connect the human nervous system with electronic devices.[15] Bioprinted neural interfaces crafted to interact delicately with the brain's complex structures could lead

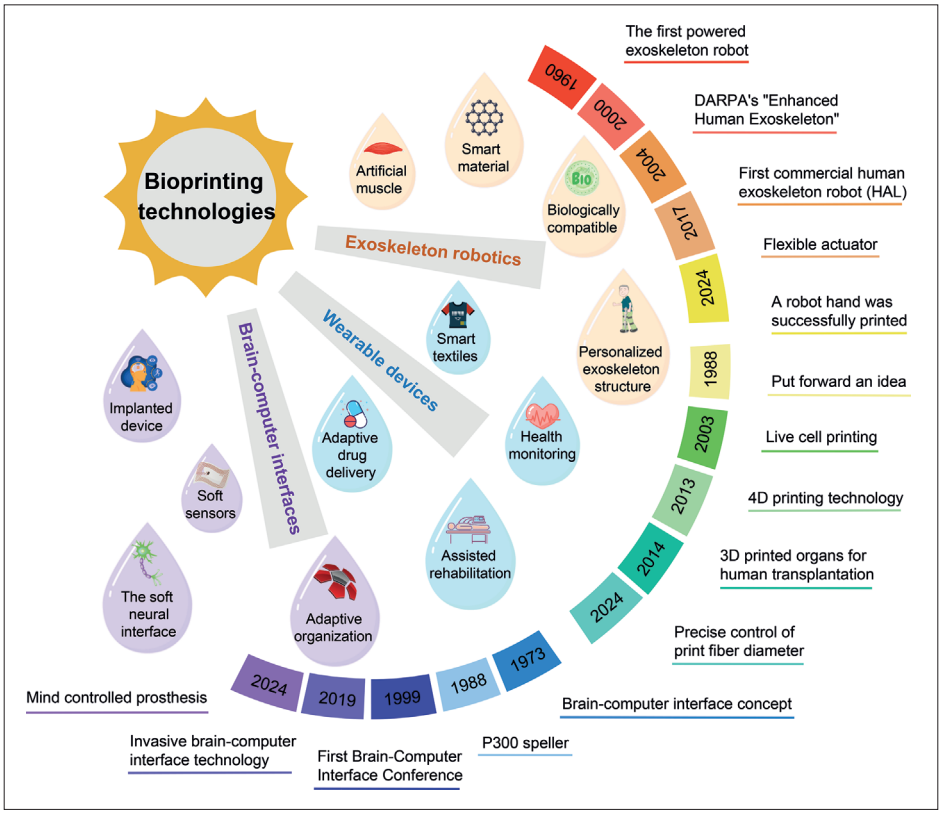

Figure 1. Bioprinting enhances the performance and application of wearable sensors, brain-machine interfaces, and exoskeleton robotics, aligning them with human physiology. Figure created using WPS PPT by Kingsoft Office.

to significant advancements in treating neurological disorders, enhancing cognitive abilities, and restoring function to individuals with spinal cord injuries. Bioprinting also ensures compatibility and minimizes the potential for immune rejection.[16] Such interdisciplinary integration is poised to redefine the boundaries of human-machine interaction and explore new frontiers in enhancing human capabilities.

The advancement of bioprinting in bone research suggests that it could provide new approaches for fabricating user-friendly exoskeleton robots. Exoskeleton robotics, an intriguing subset of biomechatronics, pertains to the design, development, and deployment of wearable robotic apparatus that are in sync with the intents and movements of the human body.[17] These devices are meticulously engineered to augment, assist, enable, or enhance physical activity through direct interaction with the limbs or other body parts. Exoskeleton robotics stands to benefit from the advances in bioprinting as well.[18] Ideally, lightweight, adaptive exoskeletons with "bio-actuators" are capable of responsive and organic movements that mimic natural muscle contractions. These innovations could transform rehabilitation therapies and enhance mobility for individuals with impairments.[19] The integration of biologically inspired printing and robotic exoskeletons promises a future wherein assistive devices seamlessly harmonize with the human body, blurring the lines between biological and mechanical components and function (Figure 2).[20]

Bioprinting is established on a comprehensive multidisciplinary framework, offering significant benefits for the advancement of various fields. In this review, we first introduce the methodologies, materials, and instrumental equipment that constitute the development of bioprinting. Thereafter, we discuss the association of bioprinting with wearable sensors, BMIs, and exoskeleton robots. For wearable technology, we analyze the current and prospective contributions of bioprinting to the development of electronic skin and body area networks based on the utilization of bioprinted bionic skin. Similarly, we investigate the prospects of bioprinting with exoskeleton and humanoid robots, based on current evidence on bioprinted bone and cartilage. Finally, anchored on the utilization of bioprinted nerve conduits, we elaborate on the prospects of bioprinting technology to advance BMIs and neuromorphic systems. This review is the first to explore bioprinting applications across diverse cutting-edge fields. Although interdisciplinary studies are still at a nascent stage, bioprinting technology could potentially serve as the key link between carbon-based and silicon-based life forms.

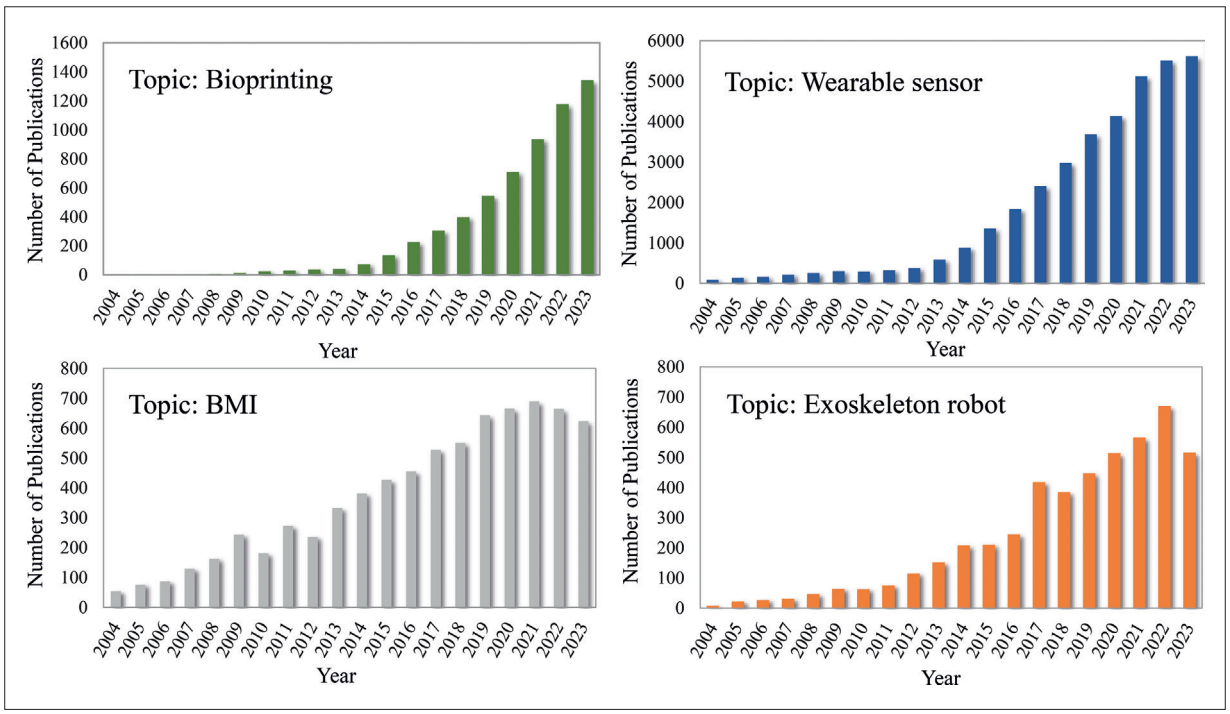

Figure 2. The total annual publications related to bioprinting, wearable sensors, brain-machine interfaces (BMIs), and exoskeleton robots have displayed sequential growth over the past 20 years. Data sourced from the Web of Science Core Collection.

2. Bioprinting process

2.1. Bioprinting methods

Principal bioprinting methods include inkjet, extrusion, laser, and stereolithography (SLA)-based approaches. In this section, we categorize the various bioprinting methods based on the type of physical field used. For example, extrusion and inkjet printing are classified as force-controlled methods, whereas laser and SLA printing are considered light-controlled methods.

2.1.1. Extrusion and inkjet bioprinting

Extrusion and inkjet bioprinting fundamentally share several similarities.[21,22] The techniques involve the precise deposition of bioinks, consisting of living cells and biomaterials, through a computer-controlled delivery system. Recently, Yang et al. proposed a mechanical extrusion-based bioprinting strategy to load cells into hollow hydrogel-based scaffolds (HHSs). The scaffolds had high mechanical responsiveness to load cells and provided an efficient and promising way for cell-based therapy.[23] Both extrusion and inkjet methods require careful tuning of printing parameters, including pressure, speed, and resolution, to ensure high cell viability and precise control over the mechanical and structural properties of the final construct. Another similarity of both approaches is their capability to print a wide range of biomaterials, including hydrogels, polymers, and ceramics, for fabricating various tissue types. Buduo et al. utilized inkjet bioprinting to print silk fibroin, a natural protein derived from *Bombyx mori* cocoons. The printed structure had viscoelastic, shear-thinning, thixotropic, and transparent features, and was employed as enzymatic sensors for quantitative analysis.[24]

There are also several differences between the two modalities.[25,26] Extrusion-based bioprinting utilizes a process where a continuous stream of biomaterials is extruded through a nozzle and deposited in a predetermined pattern.[27] Conversely, inkjet printing utilizes the deposition of small droplets of bioink. Inkjet printing features higher printing precision but may result in lower cell viability due to the forces exerted during droplet formation.[28] In contrast, extrusion-based printing offers better control over the printing process, enabling the printing of highly complex structures with high cell viability. Additionally, extrusion-based bioprinting is known for its ability to print more complex biomaterials, such as thermoplastic polymers and alginate gels, which may be challenging to deposit using inkjet printing.[29,30]

2.1.2. Laser and stereolithography-based bioprinting

Laser and SLA-based bioprinting are two advanced biofabrication techniques that conceptually emphasize light-initiated polymerization or crosslinking as the pivotal element in the bioprinting process.[31] The laser-based approach utilizes a focused laser beam to locally cure bioinks through a process known as laser-induced forward transfer (LIFT).[32] Conversely, SLA typically involves the use of a digital light projector or laser that scans across the surface of a photopolymer resin, curing it layer-by-layer to form the desired 3D structure.[33] Compared with extrusion or inkjet bioprinting, the use of optics usually enables higher-resolution patterning, necessary for producing constructs with finely detailed architecture.

Laser and SLA-based methods can be distinguished based on their requirements in printing materials and preservation of biological activity within the printed structures. Laser-based bioprinting requires bioinks that are suitable for accurate LIFT and enable rapid solidification without compromising the viability of encapsulated cells. Afting et al. proposed a platform for minimally invasive microimplant manufacturing based on one-photon photopolymerization and multi-photon 3D laser printing, displaying significant promise for engineering complex microarchitectures.[34] SLA often requires selective curing of the material within a container to develop the desired structure in a layer-by-layer manner. Nonetheless, the SLA method surpasses the laser-based method in terms of printing efficiency by allowing multiple structures to be printed in a single run without vat cleaning, which reduces the printing time and increases productivity.[35] Kam et al. presented a thermal initiator for 3D printing that enabled localized polymerization using near-infrared and visible light. The proof-of-concept successfully fabricated hydrogel and polymeric objects using SLA and two-photon printing techniques, offering versatility and potential for new applications, especially in creating scaffolds for bioprinting.[36]

Laser and SLA-based bioprinting offers high resolution and precision for fabricating intricate tissue structures. In contrast, extrusion and inkjet methods are more scalable and versatile but may lack the level of detail and accuracy. Additionally, electrospinning,[37] magnetic,[38] and acoustic printing[39] have also been used in bioprinting. These methods incorporate diverse principles and techniques, including magnetic fields, ultrasonic vibrations, and electromagnetic forces, for controlled deposition of cells and biomaterials. The key criteria for selecting a bioprinting method include features like accuracy, resolution, speed, capacity for creating complex structures, material biocompatibility, and potential for scalability in manufacturing.[40]

2.2. Bioprinting materials

The progress and innovation in bioprinting have fundamentally relied on advancements in material science. The development of materials with specific properties has

been crucial for optimizing bioprinting processes and creating superior biological constructs. Characteristics of materials, such as viscosity, morphology, and biocompatibility, govern the technological advancement and improvements in bioprinting. The selection or design of materials with suitable properties has become increasingly significant to ensure successful bioprinting. Of these, cells and the extracellular matrix (ECM) are the most commonly used and fundamental materials in bioprinting, while hydrogels and synthetic polymers serve as essential supporting materials. Likewise, nanocomposites and bioactive materials are considered functional modulatory components.

2.2.1. Cells and extracellular matrix components

Cells and ECM components are distinct bioprinting materials that confer numerous advantages.[41] Cells serve as functional units that drive tissue development and function. Bioprinting enables the precise positioning of cells within 3D structures, allowing for the creation of complex tissue architectures that can potentially recapitulate *in vivo* function.[42] The ECM, a complex mixture of structural and functional molecules secreted by cells, serves as a scaffold for cell adhesion, proliferation, and differentiation. Bioprinting with ECM components produces tissues that closely resemble engineered structures, with precise biomechanics and biochemical content.[43] Combining cells and ECM components in bioprinting facilitates the creation of functional tissues with biomimetic properties.

When using both components in bioprinting, several factors should be considered, such as careful handling of live cells, maintaining correct temperature and a nutrient-rich environment, and suppressing immune responses to printed ECM components or cells in tissue engineering. Therefore, sophisticated planning and a thorough understanding of materials and techniques are essential for creating complex, functional structures.[44]

2.2.2. Hydrogels and synthetic polymers

Hydrogels are hydrophilic polymers with the ability to retain a substantial volume of water within their networks, and they are the most commonly used biomaterials in 3D bioprinting. Hydrogels feature a high degree of biocompatibility, which minimizes negative immune responses upon implantation. Additionally, they provide a soft and pliable consistency that resembles the texture of soft tissues. The porous structure of hydrogels also facilitates efficient nutrient and waste exchange, making them ideal for tissue engineering applications that necessitate a semblance to physiological conditions.[45] Hydrogels face challenges due to their high-water content and elasticity, which can limit their mechanical strength and structural integrity, affecting shape fidelity post-printing and during *in vitro* culture or *in vivo* implantation.[46]

Synthetic polymers are engineered polymeric materials that offer a broader range of mechanical properties and degradation profiles. Moreover, their specific mechanical strength, elasticity, and biodegradability make them highly versatile in fabricating scaffolds for tissue engineering.[47] Synthetic polymers can be customized for specific applications and degrade at controlled rates, allowing temporal control over scaffold stability. It is crucial to tailor polymerization and crosslinking processes to minimize residual monomers and potentially harmful additives and to precisely control the degradation rates of synthetic polymers to match tissue kinetics.[48]

2.2.3. Nanocomposites

Nanocomposites incorporate nanoparticles into a bulk matrix to enhance its physical and chemical properties. In 3D printing, they offer enhanced mechanical properties, biocompatibility, and bioactivity.[49] Additionally, nanocomposites can alter mechanical properties, such as strength, elasticity, and toughness, making them suitable for a wide range of biomedical applications, including bone and dental implants.[50] The presence of nanoparticles within the matrix can significantly alter surface characteristics, which is crucial for cell attachment and proliferation. Furthermore, nanocomposites can be engineered for specific antibacterial properties, facilitating their application in patient-specific implants and devices in clinical settings. Several key considerations should be addressed to ensure optimal performance and safety when incorporating nanocomposites in bioprinting, such as nanocomposite stability, as nanoparticles may shift or react under physiological conditions, affecting the long-term reliability of printed structures.[51]

2.2.4. Bioactive materials

Bioactive materials are engineered to induce specific biological reactions at their interface, developing a connection between the material and living tissues. In bioprinting, the primary characteristic of bioactive materials is their ability to support cell adhesion, proliferation, and differentiation. These materials often undergo surface modifications to enhance their bioactivity and promote tissue repair.[52] Additionally, their inherent degradability allows for their gradual replacement by native tissues, thereby reducing the need for secondary surgeries.[53] Bioactive materials can be precisely printed into complex, porous structures that mimic the natural ECM to support cell growth and vascularization, making them particularly effective for creating scaffolds for bone and dental regeneration.[54] However, employing bioactive materials in bioprinting demands careful consideration

of several factors, such as their chemical composition that directly affects bioactivity and resorption rates. The manufacturing process also affects material properties. Moreover, the structural integrity and resolution of the printed objects should be optimized to accurately replicate the complex internal architectures for effective biological integration.[55]

The correlation between materials, bioprinting methods, and their corresponding biomedical applications is presented in Table 1.

2.3. Machinery

Compared to conventional additive manufacturing equipment, bioprinters require optimization to ensure cell viability and function while meeting the demands for precise and rapid fabrication. Apart from the various bioprinting techniques (**Section 2.1**), crosslinking and microfluidic systems are also commonly used as hardware for constructing biological structures.

2.3.1. Bioprinters

The evolution of bioprinting technology from basic designs to advanced, intelligent systems highlights a significant technological trajectory.[70] Extrusion-based bioprinters offer a basic yet effective approach for depositing bioinks in a layer-by-layer manner. Inkjet bioprinters complement extrusion-based bioprinters by providing higher resolution patterns but face limitations with viscous materials. SLA-based printers are known for their capability to achieve fine resolution and print complex geometries by curing photosensitive resins with ultraviolet (UV) light, suitable for fabricating intricate tissue scaffolds. The capabilities of commercial bioprinters have transformed from basic mechanical deposition to sophisticated integrated systems endowed with intelligent features. Bioprinters integrated with automation, sophisticated software, and feedback systems enable real-time adjustments during the printing process.[71] These advancements highlight the increasingly complex applications in the field of medical science. Some of these commercial 3D bioprinters are illustrated in Table 2.

2.3.2. Microfluidic systems

Microfluidics refers to the science and technology of systems that process or manipulate small amounts of fluids using microscale channels.[72] The interdisciplinary aspects of microfluidics enable the precise control and manipulation of fluidic environments for various applications, including bioprinting.[73] Additionally, microfluidic systems have been employed as delivery systems to facilitate the precise and controlled transport of biomaterials to the printhead of the bioprinter for subsequent layer-by-layer fabrication of 3D biological tissues. Further applications of microfluidics in bioprinting include the development of gradient materials, where different types of cells or growth factors are precisely positioned within the printed structure.[74] These gradients are essential for mimicking the natural composition of tissues, where multiple cell types coexist in a spatially organized manner. Microfluidic channels can be designed to combine different bioinks in predefined ratios before deposition, enabling seamless integration of different materials within a single printed construct.[75] Additionally, microfluidics can be explored for its potential in on-chip bioprinting, which holds significant potential in developing implantable medical devices.[76]

2.3.3. Intelligent control

Intelligent algorithms can be used to tune the motions of the bioprinter. By synchronizing the movement of multiple printheads and modulating printing parameters (e.g., speed, pressure, and pathway) in real-time, these systems can accommodate the variable behaviors of various bioinks.

Among the intelligent methods, machine vision algorithms, including convolutional, transformer, and graph neural networks, can be integrated into printers to enable real-time monitoring and precise process control.[77,78] By continuously capturing high-resolution images of the bioprinted structures during the printing operation, these systems provide valuable feedback on the accuracy of bioink deposition, supplemented with automatic adjustments of the motion path, speed, and material flow rate. Dynamic corrections using machine vision-based

Table 1. Materials used for different bioprinting techniques and applications.

Material	Bioprinting technique	Applications
Cells and extracellular matrix components	Inkjet[56]; extrusion[57,58]	Bone[56]; liver[57]; glands[58]
Hydrogels	Extrusion[59,60]; inkjet[61]; laser[62]	Cartilage[59]; neural[60]; microsphere[61]; Y-shaped vessel[62]
Polymers	Extrusion[63]; stereolithography (SLA)[64]	Cornea[63,64]
Nanocomposites	Extrusion[65,66]; SLA[67]	Muscle[65]; cardiovascular[66]; heart[67]
Bioactive materials	Extrusion[68]; SLA[69]	Skin[68]; brain[69]

Table 2. Commercial 3D printers for bioprinting.

Product	Company	Country	Bioprinting technique	Materials	Resolution	Speed
TissueStart™	Tissuelabs	Brazilian	Extrusion	Cell, extracellular matrix (ECM), hydrogels, nanocomposites, bioactive materials	25 μm	40 mm/s
Bio X	CELLINK	Sweden	Extrusion; stereolithography (SLA)	Hydrogels, synthetic polymers	1 μm	1–40 mm/s
LUMEN X™	CELLINK	Sweden	SLA	Cells, ECM, hydrogels, nanocomposites, bioactive materials	35 μm	—
R-GEN 200	REGEN+IU	Switzerland	Extrusion; inkjet; SLA	Ceramic pastes, cement for bone/dental	5 μm	5–100 mm/s
SunP ALPHA-CPT2	SunP Biotech	China	Extrusion	Hydrogels, biopolymers, bone cement paste, silicones, polymer pastes	1 μm	0.1–50 mm/s
BiopixlarAER	Fluicell	Sweden	Microfluidics;	Cells	5 μm	—
BioScaffolder	GEISM	Germany	Extrusion; inkjet; microfluidics	Hydrogels, biopolymers, nanocomposites, cells	1 μm	10 μl/min
BioAssemblyBot 500 (BAB500)	Advanced Solutions	United States of America (USA)	Extrusion	Hydrogels, synthetic polymers, cells	20 μm	—
3D-bioplotter	Envision TEC	Germany	Extrusion	Hydrogels	1 μm	0.1–150mm/s
Allevi3	ALLEVI	USA	Extrusion	Synthetic polymers	1 μm	—
Melt electrowriting	University of Oregon	USA	Microfluidics	Synthetic polymers, hydrogels, ECM, bioactive materials	X/Y-accuracy: 5μm; Y-accuracy: 1.25 μm	125 mm/s
Rastrum	Inventia Life Science	Australia	Inkjet; microfluidic printhead	Cells, ECM	20 μm	20–25 nL/s
NGB-R bioprinter	Poietis	France	Laser, extrusion, inkjet, microfluidic printhead	Hydrogels	10 μm	40–50 mL/s

doi: 10.36922/ijb.3590

motion control minimize errors and inconsistencies, preserving cell viability and the mechanical properties of printed tissues.[79] In particular, the integration of machine vision algorithms into *in situ* bioprinting stands as a significant advancement within the field.[80] Based on clinical data by magnetic resonance imaging (MRI) and computed tomography (CT) scans, machine vision provides bioprinters with dynamic control over printing processes, tailored to individual patient anatomies. These intelligent algorithms use imaging inputs to automatically construct accurate 3D models of the target area and ensure that the bioprinted cells and biomaterials are precisely deposited. This adaptive printing process can enhance surgical applications and regenerative medicine, paving the way for advanced personalized medical treatments and interventions.[81]

3. Wearable sensors

3.1. Bioprinted skin

The skin is the largest organ of the human body and is essential for survival and maintaining physiological balance. It acts as a crucial barrier, shielding the internal environment from pathogens, chemicals, and physical injuries, and plays significant roles in thermoregulation, vitamin D synthesis, and sensory perception.

Artificial skin research represents one of the earliest and most successful applications of bioprinting.[82] Bioprinting has been applied in dermatological research for skin repair, regeneration, and *in situ* healing, surpassing the capabilities of traditional approaches. One major benefit of 3D-bioprinted structures is their ability to be tailored to individual wound topographies, effectively overcoming the limitations of traditional skin grafts that might not conform perfectly to wound sites. Catarino et al. utilized 3D bioprinting to embed specific structures within artificially fabricated skin. By printing spheroids formed from dermal papilla cells (DPCs) and human umbilical vein cells (HUVECs) into a pre-gelled dermal layer containing fibroblasts, multiple elements can be positioned with high accuracy. As the tissue matures, it forms structures resembling hair follicles, facilitated by the migration of keratinocytes and melanocytes. Creating sophisticated skin models that closely resemble natural skin structures could significantly advance regenerative medicine, enhancing both grafts and testing chemical safety (Figure 3a).[83] The high accuracy of 3D bioprinting various cell types and structural proteins in defined spatial distributions can produce the desired skin heterogeneity. Thus, the complex multi-layered skin architecture can be replicated. Zhang et al. proposed a method for moisture-permeable wearable electronics using a 3D liquid diode (LD). The detachable design was integrated into advanced skin- and textile-based electronics with the potential for developing scalable wearables, emphasizing sustainability and cost-effectiveness.[84] Jorgensen et al. used six types of primary human skin cells to bioprint a tri-layer skin construct, including the epidermal, dermal, and hypodermal layers. Transplantation of bioprinted skin onto mice and porcine models enhanced wound healing, promoted vascularization, and supported normal skin structure and function, suggesting potential clinical applications for wound treatment.[85]

The future of bioprinting in skin research is striving towards creating fully functional and vascularized skin, emphasizing the integration with native tissues and enhanced survival rates for more advanced medical treatment applications.

3.2. Bioprinting of electronic skin and wearable sensors

The successful applications of bioprinting in skin research have provided valuable insights for the development of wearable e-skin and electronic sensors. E-skin, inspired by natural skin, is engineered to endow humans with unprecedented multi-sensory perceptions that surpass our inherent abilities. This innovative technology integrates environmental sensing functions of human skin, expanding the spectrum of perceptual abilities.[86] Bioprinting stands as a transformative tool in the evolution of e-skin, offering high precision and versatility in developing biomedical devices on/in the skin. Through the synchronous deposition of cells and electronic components, bioprinting has the potential to incorporate advanced sensory technologies into skin repair.[87] Likewise, bioprinting addresses the challenges in fabricating compatible e-skin, particularly for measuring body motion-related signals (e.g., pressure and temperature).[88] The combination of bioprinting and implantable sensor technology, particularly for glucose and oxygen monitoring, holds significant research value. Functional bioprinted implantable sensors that minimize immune response and ensure long-term stability can be utilized for collecting biomedical data (e.g., glucose and oxygen).[89] In this regard, chronic conditions, such as diabetes and hypoxia, can be better managed. Additionally, advancements in the Internet of Things (IoT) have increased the prevalence and accelerated the development of wearable devices for personalized healthcare. The integration of bioprinting in the design and development of wearable devices enables precise adjustments of key factors, including flexibility, stretchability, implantability, biocompatibility, and biodegradability.

Bioprinting has established the foundation for developing advanced wearable devices. Agarwala et al. presented a low-cost bioprinting method to fabricate a

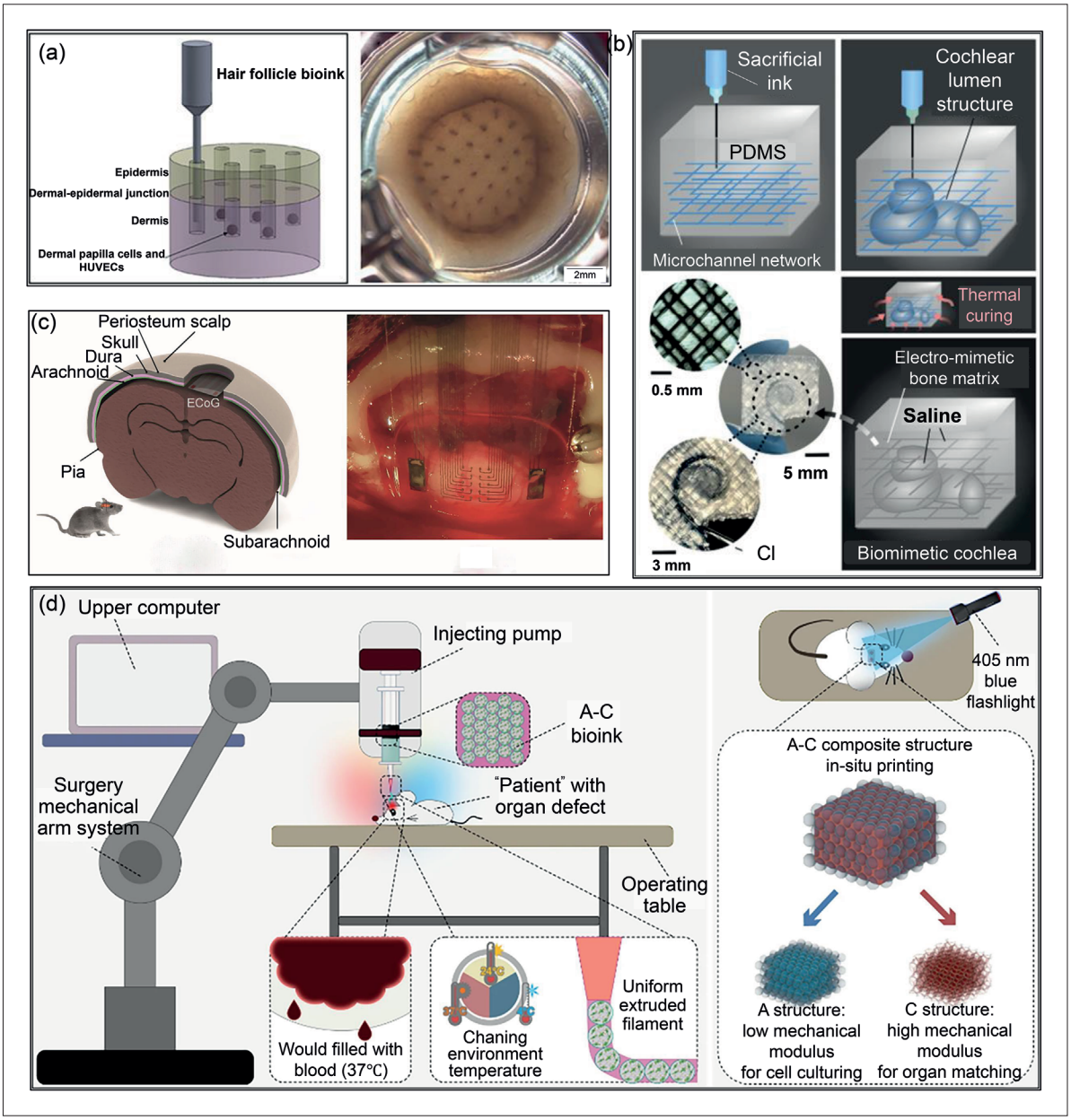

Figure 3. Bioprinting for e-skin and wearable sensors (a) 3D bioprinting of hair follicles within the skin. Adapted with permission from Motter Catarino et al.[83] (b) Diagram illustrating the embedded printing to create electro-mimetic structures and biomimetic cochleae. Adapted with permission from Lei et al.[92] (c) A parylene electrocorticography electrode array implanted on the surface of a rat's cortex. Adapted with permission from Kim et al.[95] (d) Schematic of *in situ* bioprinting and photocrosslinking using bioconcrete bioink. Adapted with permission from Xie et al.[96] Abbreviations: PDMS: Polydimethylsiloxane; ECoG: Electrocorticography; HUVECs: Human Umbilical Vein Endothelial Cells.

biocompatible hydrogel-based bioelectronics platform. They used silver nanoparticles to print electronic circuits between two gelatin methacryloyl (GelMA) hydrogel layers and tested the effects of electrical stimulation and temperature of the circuit designs on cells. This platform could potentially be used to study cell behavior under external stimuli and for biomedical applications, such as organ printing and wound management.[90] Krishnadoss et al. developed a flexible and biocompatible platform using 3D *in situ* bioprinting that is capable of fabricating implantable soft micro-supercapacitors (MSCs). The platform uses bio-ionic liquid-functionalized biopolymers that form a hydrogel electrolyte when exposed to visible light. The MSC has a specific capacitance of 16 μF/g, a volumetric

capacitance of 44 μF/cm^3, and was cyclically stable for up to 10,000 cycles. The reported technology can be employed as a life-long power source for implantable bioelectronic devices.[91] Lei et al. developed a framework from printed neural networks for electric field imaging of cochlear implants. This approach facilitated the construction of tunable and customizable 3D-printed cochleae, which can emulate realistic scenarios at various stimulation levels. The system can identify the causes of current dispersion and measure *in vivo* cochlear tissue resistivity (estimated average of 6.6 kΩ·cm). Furthermore, this technology can improve physical modeling and digital twin applications in neuromodulation implants (Figure 3b).[92] Xu et al. proposed a synthesis method for creating complex polymer networks in biomimetic electroconductive liquid metal hydrogels. By synthesizing four precursors within two steps, hydrogel adhesives with strong adhesion, high electroconductivity, and excellent compatibility both *in vitro* and *in vivo* were produced. These hydrogels can self-heal and possess shear-thinning properties that may be suitable for minimally invasive bioprinting in *in vivo* experiments.[93]

In the future, bioprinting is expected to revolutionize the development of implantable and wearable devices with integrated soft electronics. Advancements in scalability, regulatory frameworks, and long-term functionality will enable the widespread implementation of bioprinted wearable devices.

3.3. Bioprinting of body area network

Body area network (BAN) refers to a network of wearable devices within or on the human body. BAN elevates wearable devices to the systemic level by integrating devices into a cohesive framework that enables sophisticated monitoring, data collection, and communication interfaced with physiological processes. The synergy between bioprinting and BAN offers numerous research opportunities. For instance, bioprinting facilitates the creation of personalized prosthetic devices with BAN functionalities. These biocompatible prostheses may interact with the patient's nervous system, enhancing proprioceptive feedback and motor control for better quality of life and functionality. Moreover, the capacity of bioprinting to produce personalized implantable devices that communicate through BAN paves the way for monitoring platforms and sophisticated drug delivery systems. For general healthcare, implantable sensors are used to monitor various biomarkers, such as glucose, electrolytes, and hormones. The incorporation of biosensors with BAN enables a remote monitoring system that alerts healthcare professionals to any deviations.[94] Kim et al. created a 22-channel, highly flexible electrocorticography microelectrode array on a parylene film. The microelectrode patterns were printed on Polydimethylsiloxane (PDMS), transferred to parylene films, and connected using a custom 3D-printed connector. The device successfully recorded brain signals in rat models (Figure 3c).[95] Likewise, Xie et al. developed a bioconcrete bioink featuring electrosprayed cell-laden microgels as an "aggregate" and GelMA as the "cement." Portable and easily prepared, this bioink enabled the pre-culturing of microgels into mini tissues. Its effectiveness in repairing cranial defects demonstrated its clinical potential for *in situ* treatment (Figure 3d).[96] The fusion of bioprinting with BAN constitutes a cutting-edge technological domain that could lead to next-generation healthcare with increased personalization and integrated therapeutic systems. This synergy promises to improve individual health outcomes and advance more patient-centric systems.

4. Brain-machine interfaces

4.1. Bioprinted nerve conduits

In brain science and neural repair in clinical interventions, nerve conduits are instrumental in promoting the precise and targeted regeneration of damaged neural pathways. Peripheral and central (brain) nerves have complex interactions and differences in regenerative capacities. The peripheral nervous system (PNS) has a greater ability to regenerate after injury, aided by the presence of Schwann cells, which support axonal growth and promote a more permissive environment.[97] In contrast, the central nervous system (CNS), which includes the brain and spinal cord, has limited regeneration capability due to inhibitory molecules.[98]

Bioprinted nerve conduits have a significant impact on studies of the PNS and CNS. For PNS, bioprinted nerve conduits provide a platform for the regeneration of damaged nerve tissues that facilitate the effective repair of traumatic nerve injuries. Furthermore, these conduits can be tailored to match the diameter and length of damaged nerves, promoting successful regrowth and functional recovery. For CNS studies, bioprinted nerve conduits have the potential to enhance tissue engineering and drug development for neural disorders, such as Alzheimer's and Parkinson's disease. The ability to control the composition and architecture of these conduits enables the creation of models that mimic the complexity and functionality of the CNS. Hu et al. utilized bioprinting to fabricate a bio-conduit with cryo-polymerized GelMA (cryoGelMA) and adipose-derived stem cells for peripheral nerve regeneration. This customizable and biodegradable conduit supported cell attachment, proliferation, and neurotrophic factor expression. After implantation in a rat sciatic nerve model, the bio-conduit effectively supported re-innervation across a 10 mm gap (Figure 4a).[99] Hsu et al. introduced a conductive microporous hydrogel composed

of gold nanoyarn balls-coated injectable building blocks, which enhanced angiogenesis and brain function recovery following traumatic brain injury. This hydrogel can be used as bioink to fill complex defect shapes through minimally invasive implantation and modulate the injury environment. Functional neuroimaging indicated restored connectivity in critical brain circuits post-treatment with the hydrogel (Figure 4b).[100] Fang et al. developed a conductive multiscale-filled nerve guidance conduit (MF-NGC) featuring a hierarchical structure of electrospun poly(lactide-co-caprolactone) (PCL)/collagen nanofibers, reduced graphene oxide/PCL microfibers, and PCL microfibers. The bioprinted MF-NGCs exhibited fine permeability, mechanical stability, and electrical conductivity. Within a rat sciatic nerve model, MF-NGCs encouraged neovascularization, leading to significant peripheral nerve regeneration and better sciatic nerve function (Figure 4c).[101]

4.2. Bioprinting of brain-machine interfaces

Effective peripheral nerve regenerative techniques, including synthetic conduits and bioactive scaffolds, are essential for restoring the bidirectional communication pathways necessary for the optimal functioning of BMI.[102] Precise transmission of motor commands and sensory feedback between the brain and peripheral devices can be facilitated by these methods which reduce signal latency and improve control accuracy.[103] Innovations in nerve repair that incorporate cutting-edge biomaterials and neurotrophic factors expedite axonal regrowth while enhancing the long-term stability and compatibility of neural interfaces.[104] This symbiotic relationship between peripheral nerve repair and BMI development underscores the importance of an interdisciplinary paradigm that combines neurobiology, materials science, and bioengineering.[105] Refining repair techniques enhance the reliability and durability of BMIs. Ongoing research is crucial for advancing neural rehabilitation and human-technology innovation.[106] Achievements in bioprinting for nerve repair further facilitate the exploration of BMI development.

A primary challenge in developing BMIs is creating robust, biocompatible connections between electronic interfaces and neural tissues. These connections must function consistently over long periods without damaging the brain's soft tissues or causing adverse biological responses. Bioprinting may address these hurdles by enabling the fabrication of custom-designed tissues with built-in electronic sensors and wiring. Moreover, by precisely arranging different cell types and materials, bioprinting can achieve the requisite sensitivity and specificity needed for effective signaling and connectivity in BMIs. Recently, bioprinting has enabled the fabrication of conductive, soft, and biocompatible electrodes. This biomimicry may potentially reduce the foreign body response, enhance signal fidelity, and ensure more stable long-term integration with neural circuits. Adewole et al. developed "living electrodes," consisting of living cortical neurons and axonal tracts encased in hydrogel cylinders, for brain activity modulation and optobiological monitoring. These engineered constructs demonstrated rapid axonal growth and consistent cytoarchitecture. Transplantation into the rat cortex revealed successful integration, survival, and function, validating the approach as an effective neural interface. These optically controllable living electrodes represented critical advancements in developing novel optobiological interfacing tools (Figure 4d).[107] Using conductive inks, silicone insulations, and cold-air plasma-activated electrodes, Afanasenkau et al. proposed a method for printing biocompatible and customized electrode arrays. These printed bioelectronic interfaces were tested in the neuronal pathways of cats, rats, and zebrafish. The results demonstrated prolonged integration and functional stability, highlighting the ability of bioprinting for personalized neuroprosthetic applications.[108]

By adjusting the mechanical properties to match those of the brain, bioprinted electrodes can record and stimulate neural activity, as well as support neural growth and healing. Liu et al. introduced a hydrogel-based elastic microelectronics system with conductive hydrogel as the conductor and an elastic fluorinated photoresist as the passivation insulation layer. The system exhibited reduced interfacial impedance, improved current-injection density, and stable electrical performance under strain. It can be used for low-voltage electrical stimulation of live mice sciatic nerve. The demonstrated properties of the soft arrays provided promising applications in BMI research.[109] Additionally, the capability of bioprinting to create layered structures with spatial biochemical gradients offers a strategic advantage in designing electrodes that can interface with multiple types of neural cells. Roth et al. introduced a platform called spatially patterned organoid transfer (SPOT), which utilizes a hydrogel embedded with iron-oxide nanoparticles. This setup facilitated the precise spatial arrangement of organoids and fabricated assembloids from human pluripotent stem cell-derived neural organoids.[110] Although the correlation between BMIs and bioprinting is still in its experimental stage and far from practical application, the combination will undoubtedly advance neuroscience and rehabilitation medicine.

4.3. Bioprinting of neuromorphic systems

While bioprinting has traditionally focused on regenerative medicine and tissue engineering, its potential for developing neuromorphic systems introduces an exciting interdisciplinary field. With the rapid advancement

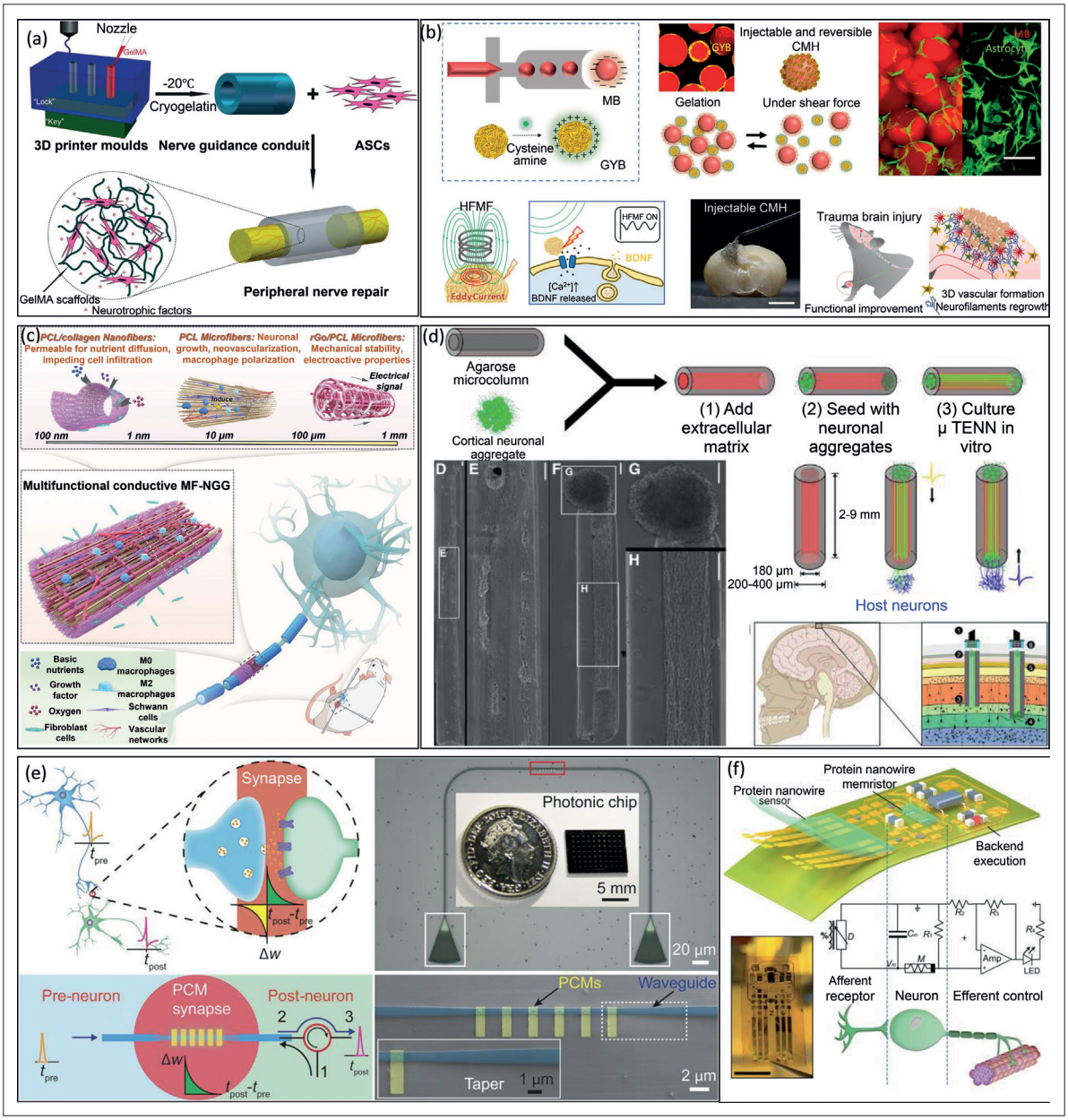

Figure 4. Bioprinting of brain-machine interfaces. (a) Schematic of engineered bio-conduit for peripheral nerve regeneration. Adapted with permission from Hu et al.[99] (b) Fabrication of a flexible conductive microporous hydrogel. Adapted with permission from Hsu et al.[100] (c) Multifunctional, conductive nerve guidance conduits with hierarchical fibers for treating peripheral nerve injuries. Adapted with permission from Fang et al.[101] (d) Fabrication of aggregated, microtissue-engineered neural network and living electrodes. Adapted with permission from Adewole et al.[107] (e) Photonic synapse integrated on a chip. Adapted with permission from Cheng et al.[112] (f) Integrated neuromorphic interface. Adapted with permission from Fu et al.[113] Abbreviation: PCM: phase-change materials.

of big data and large models, sustainable computing – harmonizing advanced computational practices with environmental responsibility – becomes increasingly critical. Neuromorphic systems, emulating neural architectures and functionalities of the brain, designed to mimic human data processing and storage methodologies could be particularly valuable in this context. Nevertheless, despite advanced bio-inspired algorithms, AI systems built on existing neuromorphic circuits still underperform when compared with the complexity of natural biological neural networks.[111]

Bioprinting can further enhance the development of neuromorphic systems. Firstly, soft biomaterials, such as biocompatible hydrogels and organic polymers, can mimic the pliable and dynamic characteristics of biological synapses. Cheng et al. reported a hardware synapse that utilizes a photonic integrated-circuit approach. The synapse incorporates phase-change materials with silicon nitride waveguides, where synaptic weight can be adjusted by the number of optical pulses applied. The research offers a simple but effective method to achieve synaptic plasticity that closely mimics the analog behavior of biological synapses (Figure 4e).[112] In parallel, advances in bioprinting enable the creation of customized neural networks (i.e., brain-on-chip models), where specific neuronal types and connections can be accurately positioned according to predefined designs. This capability allows researchers to explore various neural configurations and their impact on neuromorphic system behaviors, providing more effective solutions in neurocomputing applications. Fu et al. presented self-powered neuromorphic interfaces for biological signal matching through synthesized protein nanowires. Based on these protein nanowires, flexible neuromorphic systems capable of intelligently processing biologically relevant stimuli for adaptive responses have also been developed. The sustainable nature and potential multifunctionality of protein nanowires enhance the potential for biological integration of these interfaces (Figure 4f).[113]

Although the interdisciplinary study of bioprinting and neuromorphic technology is still in its nascent stages, it presents a promising frontier for future exploration. Likewise, bioprinting applications in the brain may extend to the development of brain organoids, personalized medicine, neurodegenerative disease models, and drug testing platforms. Its ability to create intricate neural networks and complex tissue structures opens diverse possibilities for both basic research and clinical applications in neuroscience.

5. Exoskeleton robots

5.1. Bioprinted skeleton

The skeletal system, consisting of bones and cartilage, serves crucial functions within the human body. Bones provide a rigid framework for the body and enable movement, support, and protection of organs and tissues. Additionally, bones play critical roles in hematopoiesis, calcium homeostasis, and regulation of acid-base balance. Cartilage is a critical connective tissue that covers bone surfaces in joints, supporting load transmission and lubrication. Furthermore, cartilage serves as a shock absorber and enables smooth movement in joints.

Bioprinting for bone and cartilage repair and regeneration is currently a flourishing area of interest.[114] By using customized biomaterials and bioinks, researchers can create scaffold-like structures that mimic the natural ECM of bone and cartilage for cell growth and tissue stimulation. Li et al. used bioprinting to fabricate a biomimetic scaffold for humeral head regeneration. The strategy was versatile and scalable for repairing large joints and represented a modulation of endochondral ossification for bioprinted anisotropic scaffolds (Figure 5a).[115] Liu et al. proposed a hierarchical fabrication strategy for ceramic-reinforced organo-hydrogels, which exhibited high stiffness, strength, and toughness through multi-scale energy dissipation. The study extended the design principles of natural materials to fabricate composite hydrogels with mechanical and functional enhancement (Figure 5b).[116] Du et al. combined manganese silicate (MS) nanoparticles with tendon/bone-related cells to create immunomodulatory multicellular scaffolds for tendon-to-bone regeneration. These scaffolds, leveraging biomimetic cellular distribution and MS nanoparticles, exhibited enhanced cellular differentiation. Animal studies confirmed that these scaffolds effectively achieved immunomodulation, regeneration, and functional recovery at tendon-to-bone interfaces.[117] Jo et al. developed a bioink by integrating MXene nanoparticles with GelMA and Hyaluronic Acid Methacrylated

(HAMA)hydrogels to enhance myogenesis in 3D-bioprinted constructs. These bioinks demonstrated excellent printability and cytocompatibility, as well as promoted skeletal muscle cell differentiation without additional agents (Figure 5c).[118] Huan et al. developed a bioprinted autologous bone (AB) scaffold for bone regeneration using a PCL shell and bone marrow-derived mesenchymal stem cell (BMSC) hydrogel. The scaffold demonstrated excellent cellular affinity and enhanced osteogenic differentiation. It also promoted new bone and osteoid formation in beagle dog cranial defects over nine months. Further *in vivo* results indicated BMSC differentiation into various tissues, highlighting the potential of the bioprinting approach in clinical applications (Figure 5d).[119]

Future research in the bioprinting of bone and cartilage will likely emphasize the development of innovative biomaterials, improvement of printing technologies for higher-resolution structures, and exploration of dynamic biophysical stimuli to enhance tissue functionality.

5.2. Bioprinting of exoskeleton

The significant contributions of bioprinting in bone research suggest its potential for developing user-friendly and customizable exoskeleton robots. Exoskeleton robots are wearable apparatuses that function as external

frameworks to enhance the biomechanical capabilities of the human body. These robotic suits display increased strength, endurance, and protection, aiding individuals in physically demanding or repetitive tasks. Key applications include rehabilitation therapy where they assist with movement and strength recovery, industrial sectors for lifting heavy loads, and assistive living technologies that provide support for the elderly or those with mobility impairments. The interplay between motor system repair and bioprinted exoskeleton robotics represents significant advancements in regenerative medicine and biomedical engineering.

Biofabrication allows for the integration of tailored, biomechanically compatible soft tissues or cushions into exoskeleton designs, enhancing comfort and functionality, as well as reducing the weight of the apparatus. He et al. used metal-organic framework exoskeletons and live cells to investigate the survival and efficacy of BMSCs in cardiac therapy. These partially coated exoskeletons improved BMSC survival by supporting the cells while retaining their

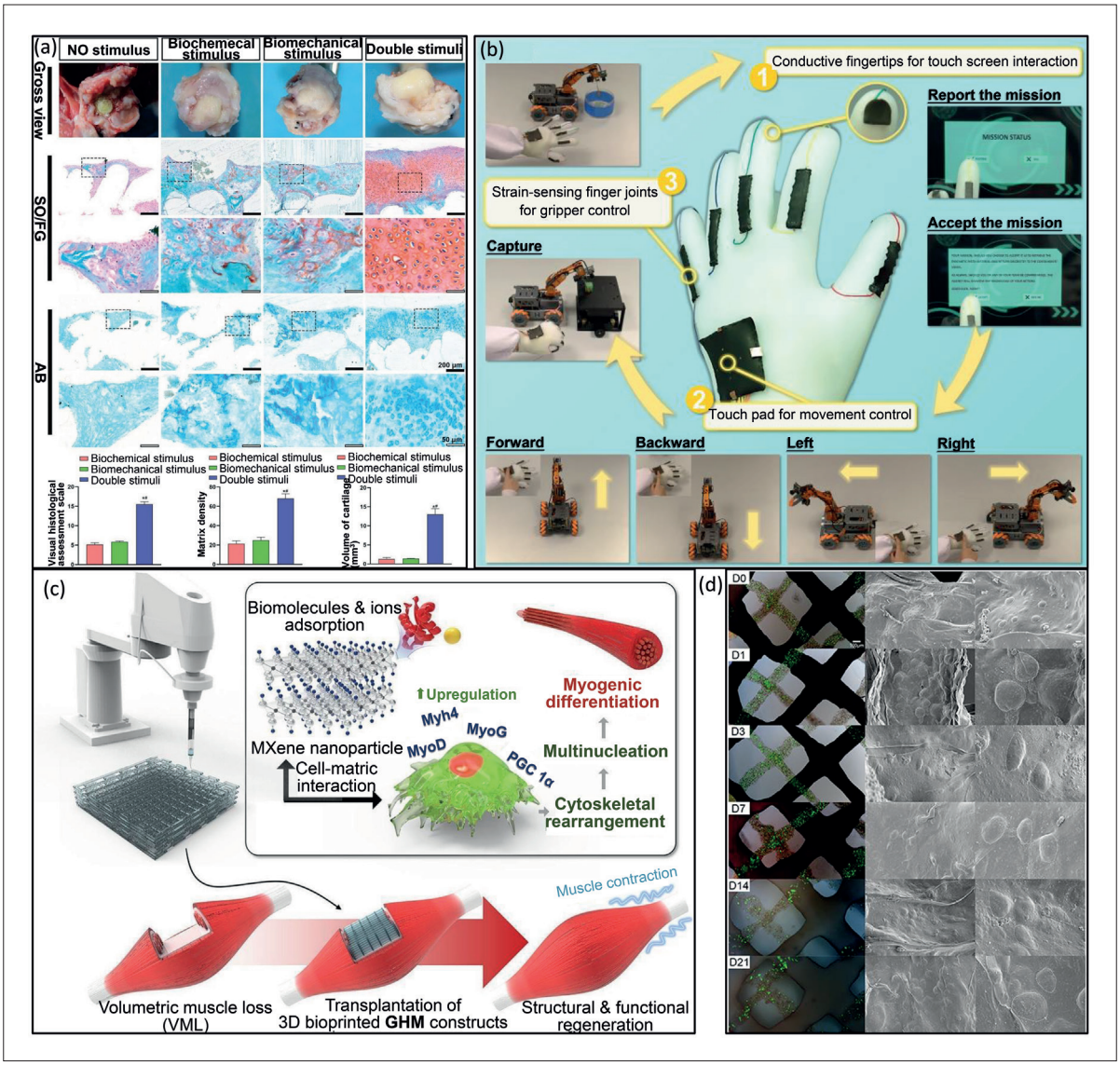

Figure 5. Bioprinting of exoskeleton. (a) Histological analysis of cartilage regeneration in the humeral head following *in vivo* semi-shoulder arthroplasty. Adapted with permission from Li et al.[115] (b) A versatile smart glove equipped with conductive fingertips and strain sensors made from composite organo-hydrogels for controlling touch screens and robotics. Adapted with permission from Liu et al.[116] (c) Skeletal muscle regeneration using bioprinted hyaluronate/gelatin hydrogels embedded with MXene nanoparticles. Adapted with permission from Jo et al.[118] (d) Images of calcein-AM/propidium iodide (PI) staining (live/dead) and surface morphology across various groups. Adapted with permission from Huan et al.[119] Abbreviations: SO/FG: safranin O/fast green staining; AB:alcian blue staining; GHM: gelatin methacryloyl and hyaluronic acid methacryloyl composite hydrogels; MyoD: myoblast determination protein 1; MyoG: myogenin; Myh4: myosin heavy chain 4; PGC 1α: peroxisome proliferator-activated receptor-gamma coactivator.

natural properties. The approach enhanced cell adhesion and prevented cell loss during therapy, providing insights into cell-exoskeleton interactions for future biohybrid designs.[120] Additionally, bioprinted sensors embedded within exoskeletons could provide real-time feedback on muscle engagement and biomechanical strain, which may promote optimal alignment and movement patterns. Zhao et al. developed biomass-based conductive polymer hydrogels, consisting of a polyacrylamide/2-hydroxypropyl trimethyl ammonium chloride chitosan (PAM/HACC) network, to enhance the functionality and sustainability of wearable apparatus. The integration of HACC boosted the hydrogel's mechanical strength and stability. Embedding polypyrrole (PPy) into these networks provided the hydrogels with excellent electromagnetic shielding (40 dB) and strain sensitivity (gauge factor = 2.56). Based on these properties, the novel material is suitable for developing exoskeletal equipment.[121] Particularly, the combination of motor system repair and bioprinted exoskeleton robotics exemplifies the convergence of regenerative medicine and biomedical engineering. The skeleton motor system comprises three parts: bones, bone connections (joints), and skeletal muscles. Bones form the skeleton through bone connections, while skeletal muscles attach to bones, spanning across joints and pulling on bones to generate movement. Extensive tissue damage to the musculoskeletal system has long been a challenge in clinical treatment. Autologous bone grafting is commonly used to treat bone tissue injuries but is limited by the availability of donor site grafts. Bioprinting can emulate the hierarchical structure and function of natural bone by combining hydrogels with various cells and growth factors to create tissue engineering scaffolds that enhance bone regeneration.[122] Similarly, the development of exoskeleton robots will benefit from bioprinting by providing highly customized and biocompatible structures that enhance the user's natural movements. This synergy leverages the cutting-edge capabilities of bioprinting and robotic technologies to create integrated therapeutic solutions for individuals suffering from motor system impairments.[123]

Although bioprinting and exoskeleton research currently exhibit minimal convergence, the escalating demands for smarter, lighter, and more comfortable multifunctional exoskeletons are likely to drive a significant increase in bioprinting applications.

5.3. Bioprinting of humanoid robots

The framework of robots is conceptually analogous to the human skeletal structure, as both serve as foundational supports that facilitate movement and structural integrity. Nowadays, the development of humanoid robots is being positioned at the forefront in the field of robotics, as they epitomize the convergence of advanced multidisciplinary approaches to achieve human-like functionality and autonomy. Such robots are of particular interest due to their potential applications in diverse fields, such as industry and service.[124]

Traditionally, robotic technology has played a crucial role in bioprinting by facilitating practical applications of new concepts and materials.[125] Incorporated with precise and automated systems, robotics has enabled the intricate and reproducible layering necessary for creating complex biological structures. This contribution is crucial for positioning biomaterials with high precision, which is essential for maintaining viability and functional integrity. Advances in bioprinting offer intriguing prospects for enhancing robotics, particularly in the development of human-like robots.[126] Conventional robotic systems mainly rely on solid materials that may lack the biomechanical intricacy and adaptability of natural biological systems. Bioprinting is capable of fabricating biohybrid components that mimic the structure and function of the human body. Moreover, bioprinting can create artificial skin, muscles, or sensory organs that are biomechanically and biochemically akin to their natural counterparts.[127] These biofabricated components can be integrated into humanoid robots, rendering them more lifelike in appearance and functionality. Such components could be crucial in creating robots capable of more natural interactions within human environments or for specialized tasks in hazardous conditions where conventional robots might fail. The combination of bioprinting and robotics has the potential to advance both fields and transform societal perceptions and applications of robots.

The integration of AI and robotics into various fields can further promote the prospect of interdisciplinary applications. Embodied intelligence is often considered a quintessential goal in AI and robotics, representing the development of cognitive processes with physical action within an environment.[128] This concept refers to the ability of an AI system to interact with the world through a physically instantiated system, such as a robot, which integrates sensory feedback into its decision-making processes. The connection between embodied intelligence and bioprinting might not be immediately or easily obvious, but it holds profound implications.[129] For instance, bioprinted actuators or sensors can enhance the physical capabilities of robots, leading to more responsive and adaptable embodied agents.

Bioprinting could bridge the gaps between mechanical systems and biomechanical factors,[130] pushing the boundaries of robot capabilities and reshaping the scope of AI in embodied systems.

6. Challenges and future direction

Bioprinting is driving numerous innovations and exploratory applications across various fields, including skin, brain, and bone research, inspiring cutting-edge technological advances. Its integration with wearable sensors, BMIs, and exoskeleton robots shares common challenges that encompass material biocompatibility and structural integrity, which are crucial for ensuring seamless human interfaces without inducing adverse reactions.

6.1. Challenges

6.1.1. Wearable sensors

In developing advanced wearable sensors with bioprinting, the major challenge is integrating biological components with electronic systems while maintaining functionality and stability. The biocompatibility of materials utilized in the sensor is crucial, as they should not provoke any adverse reactions from the skin. These materials need to be durable to withstand environmental factors, including moisture, temperature variations, and mechanical stress. In parallel, bioprinted wearable sensors may face challenges with signal integrity and sensitivity. The sensors should be capable of accurately measuring physiological data without interference from body movements or external noise. Manufacturing scalability also poses extensive challenges. Bioprinting processes should be optimized to enable mass production of wearable sensors at a reasonable cost with consistent quality. This requires highly controlled and repeatable manufacturing processes, which is difficult to achieve given the inherent variability of biological materials.[131] Regulatory and ethical considerations are crucial aspects as well. Data collected by bioprinted wearable sensors often involve sensitive health information that must be handled with strict confidentiality to comply with medical data protection regulations. Additionally, the approval and commercial use of biointegrated devices is still under development, necessitating close attention to developing standards and legal requirements.

6.1.2. Brain-machine interfaces

The utilization of bioprinting in developing BMIs introduces complex challenges that must be addressed to realize their full potential. The primary issue is the selection and development of materials that are both biocompatible and capable of effectively interfacing with neural systems. These materials should promote neuronal growth and support their functions, as well as possess the durability required to uphold structural and functional integrity over time, which are inherently challenging due to the brain's delicate nature. The materials should integrate electrical and biological functionalities to ensure dependable signal transduction between neurons and the machine interface. Another significant challenge is regulating the brain's immune response to foreign entities. Brain tissues are extremely sensitive to inflammation, and even a minor immunogenic response can potentially lead to severe complications. Furthermore, regulatory frameworks are still evolving in response to technological advances in BMIs. Therefore, ethical considerations concerning privacy, consent, and potential cognitive enhancement must be rigorously managed.

6.1.3. Exoskeleton robots

Combining bioprinting with exoskeleton robots presents several significant challenges. The primary challenge is developing bioprinted materials that are both biocompatible and robust enough to withstand the mechanical stresses involved in exoskeleton operations. These bioprinted materials must be capable of enduring repetitive use in varying environmental conditions. Additionally, these materials should adapt to the unique biomechanical movements and avoid injury. Another significant challenge is ensuring seamless integration between the bioprinted components and traditional mechanical elements of the robots. The interfaces between the bioprinted soft structures and the hard exoskeleton components must withstand dynamic stress and strain during movement. Furthermore, the bioprinted sensors in exoskeletons should be capable of monitoring physiological responses without disrupting the user's physiological functions. Finally, the deployment of bioprinted exoskeletons involves ethical and regulatory considerations, including medical safety standards, data security, establishment of user privacy, and the potential socio-cultural impacts of using advanced technologies to enhance human capability.

6.2. Future direction

Addressing these challenges demands a novel interdisciplinary paradigm that combines expertise across various fields, including biology, materials science, electronics, data analytics, and regulatory affairs. Insights from biology enhance our understanding of interactions between bioprinted materials and living tissues. Materials science contributes to the development of robust, flexible, and durable materials tailored for specific biomedical applications. The integration of cutting-edge electronics enables the creation of sophisticated sensors and BMIs that can accurately interpret and respond to biological signals. Data analytics play a crucial role in processing complex datasets, facilitating optimization and real-time decision-making. Furthermore, expertise in regulatory affairs is essential to navigate the stringent approval processes and ensure compliance with safety standards, thus accelerating the transition from research to clinical and commercial use. Such interdisciplinary collaborations will enable more

effective integration of bioprinting into wearable sensors, BMIs, exoskeleton robots, and other human-centric fields.

7. Conclusion

Bioprinting promises to produce biocompatible structures that integrate seamlessly with human physiology. This technology enables the precise creation of tissue models closely mimicking the architecture and function of human skin, brain, and bone. Advances in bioprinting have led to innovations in wearable technologies, brain-machine interfaces, and exoskeleton robotics. With progress in skin studies, bioprinting is expected to enhance the biocompatibility of wearable electronics. Patient-specific neural tissues offer the potential to replicate neural activities that enhance brain-machine interfaces. Similarly, bioprinted bone grafts could redefine exoskeleton robotics by bridging mechanical systems and biomechanics. This review explores bioprinting advancements in these areas and discusses interdisciplinary challenges.

Acknowledgments

None.

Funding

This work was supported by the National Natural Science Foundation of China (grant numbers: 62173093; 61604042).

Conflict of interest

The authors declare they have no competing interests.

Author contributions

Conceptualization: Xinrui Wang, Wei Dong, Hao Sun
Funding acquisition: Hao Sun, Wei Dong
Investigation: Xinrui Wang, Hui Dong, Yongzhuo Gao, Jiawen Lin, Haichao Jia, Yihui Tao
Supervision: Wei Dong
Writing – original draft: Hao Sun
Writing – review & editing: Wei Dong

Ethics approval and consent to participate

Not applicable.

Consent for publication

Not applicable.

Availability of data

Not applicable.

References

1. Murphy SV, Atala A. 3D bioprinting of tissues and organs. *Nat Biotechnol.* 2014;32(8):773-785.
doi: 10.1038/nbt.2958

2. Budharaju H, Sundaramurthi D, Sethuraman S. Embedded 3D bioprinting-an emerging strategy to fabricate biomimetic and large vascularized tissue constructs. *Bioact Mater.* 2024;32:356-384.
doi: 10.1016/j.bioactmat.2023.10.012

3. Vijayavenkataraman S, Yan W C, Lu W F, et al. 3D bioprinting of tissues and organs for regenerative medicine. *Adv Drug Deliv Rev.* 2018;132:296-332.
doi: 10.1016/j.addr.2018.07.004

4. Dornhof J, Zieger V, Kieninger J, et al. Bioprinting-based automated deposition of single cancer cell spheroids into oxygen sensor microelectrode wells. *Lab Chip.* 2022;22(22):4369-4381.
doi: 10.1039/D2LC00705C

5. Liu H, Xing F, Yu P, et al. A review of biomacromolecule-based 3D bioprinting strategies for structure-function integrated repair of skin tissues. *Int J Biol Macromol.* 2024;268:131623.
doi: 10.1016/j.ijbiomac.2024.131623

6. Abbadessa A, Ronca A, Salerno A. Integrating bioprinting, cell therapies and drug delivery towards *in vivo* regeneration of cartilage, bone and osteochondral tissue. *Drug Deliv Transl Res.* 2024;14:858-894.
doi: 10.1007/s13346-023-01437-1

7. Lee S J, Esworthy T, Stake S, et al. Advances in 3D bioprinting for neural tissue engineering. *Adv Biosyst.* 2018;2(4):1700213.
doi: 10.1002/adbi.201700213

8. Gravina R, Fortino G. Wearable body sensor networks: state-of-the-art and research directions. *IEEE Sens J.* 2020;21(11):12511-12522.
doi: 10.1109/JSEN.2020.3044447

9. Vasilopoulou M, Mohd Yusoff AR, Chai Y, et al. Neuromorphic computing based on halide perovskites. *Nat Electron.* 2023;6(12):949-962.
doi: 10.1038/s41928-023-01082-z

10. Spezialetti M, Placidi G, Rossi S. Emotion recognition for human-robot interaction: recent advances and future perspectives. *Front Robot AI.* 2020;7:532279.
doi: 10.3389/frobt.2020.532279

11. Ates HC, Nguyen PQ, Gonzalez-Macia L, et al. End-to-end design of wearable sensors. *Nat Rev Mater.* 2022;7(11):887-907.
doi: 10.1038/s41578-022-00460-x

12. Liu F, Deswal S, Christou A, et al. Neuro-inspired electronic skin for robots. *Sci Robot.* 2022;7(67):eabl7344.
doi: 10.1126/scirobotics.abl7344

13. Li D, Yao K, Gao Z, et al. Recent progress of skin-integrated electronics for intelligent sensing. *Light: Advanced Manufacturing.* 2021;2(1):39-58. doi: 10.37188/lam.2021.004

14. Shanechi MM. Brain–machine interfaces from motor to mood. *Nat Neurosci.* 2019;22(10):1554-1564. doi: 10.1038/s41593-019-0488-y

15. Ziai Y, Zargarian SS, Rinoldi C, et al. Conducting polymer-based nanostructured materials for brain–machine interfaces. *Wiley Interdiscip Rev Nanomed Nanobiotechnol.* 2023;15(5):e1895. doi: 10.1002/wnan.1895

16. Portillo-Lara R, Goding JA, Green RA. Adaptive biomimicry: design of neural interfaces with enhanced biointegration. *Curr Opin Biotechnol.* 2021;72:62-68. doi: 10.1016/j.copbio.2021.10.004

17. Shi D, Zhang W, Zhang W, et al. A review on lower limb rehabilitation exoskeleton robots. *Chin J Mech Eng.* 2019;32(1):1-11. doi: 10.1186/s10033-019-0389-8

18. Selvam A, Aggarwal T, Mukherjee M, et al. Humans and robots: friends of the future? a bird's eye view of biomanufacturing industry 5.0. *Biotechnol Adv.* 2023;68:108237. doi: 10.1016/j.biotechadv.2023.108237

19. da Silva JLGF, Gonçalves SMB, da Silva HHP, et al. Three-dimensional printed exoskeletons and orthoses for the upper limb – a systematic review. *Prosthet Orthot Int.* 2022;10:1097. doi: 10.1097/PXR.0000000000000318

20. Popov A, Malferrari S, Kalaskar DM. 3D bioprinting for musculoskeletal applications. *J 3D Print Med.* 2017;1(3): 191-211. doi: 10.2217/3dp-2017-0004

21. Zhang YS, Haghiashtiani G, Hübscher T, et al. 3D extrusion bioprinting. *Nat Rev Methods Primers.* 2021;1(1):75. doi: 10.1038/s43586-021-00073-8

22. Li X, Liu B, Pei B, et al. Inkjet bioprinting of biomaterials. *Chem Rev.* 2020;120(9):10793-10833. doi: 10.1021/acs.chemrev.0c00008

23. Yang J, Chen Z, Gao C, et al. A mechanical-assisted post-bioprinting strategy for challenging bone defects repair. *Nat Commun.* 2024;15(1):3565. doi: 10.1038/s41467-024-48023-8

24. Di Buduo CA, Lunghi M, Kuzmenko V, et al. Bioprinting soft 3D models of hematopoiesis using natural silk fibroin-based bioink efficiently supports platelet differentiation. *Adv Sci.* 2024;11:2308276. doi: 10.1002/advs.202308276

25. Gillispie G, Prim P, Copus J, et al. Assessment methodologies for extrusion-based bioink printability. *Biofabrication.* 2020;12(2):022003. doi: 10.1088/1758-5090/ab6f0d

26. Schwab A, Levato R, D'Este M, et al. Printability and shape fidelity of bioinks in 3D bioprinting. *Chem Rev.* 2020;120(19):11028-11055. doi: 10.1021/acs.chemrev.0c00084

27. Cooke ME, Rosenzweig DH. The rheology of direct and suspended extrusion bioprinting. *APL Bioengineering.* 2021;5(1):011502. doi: 10.1063/5.0031475

28. Gudapati H, Dey M, Ozbolat I. A comprehensive review on droplet-based bioprinting: past, present and future. *Biomaterials.* 2016;102:20-42. doi: 10.1016/j.biomaterials.2016.06.012

29. Shah PP, Shah HB, Maniar KK, et al. Extrusion-based 3D bioprinting of alginate-based tissue constructs. *Procedia CIRP.* 2020;95:143-148. doi: 10.1016/j.procir.2020.06.007

30. Kačarević ŽP, Rider PM, Alkildani S, et al. An introduction to 3D bioprinting: possibilities, challenges and future aspects. *Materials.* 2018;11(11):2199. doi: 10.3390/ma11112199

31. Levato R, Dudaryeva O, Garciamendez-Mijares CE, et al. Light-based vat-polymerization bioprinting. *Nat Rev Methods Primers.* 2023;3(1):47. doi: 10.1038/s43586-023-00231-0

32. Chang J, Sun X. Laser-induced forward transfer based laser bioprinting in biomedical applications. *Front Bioeng Biotechnol.* 2023;11:1255782. doi: 10.3389/fbioe.2023.1255782

33. Wu Y, Su H, Li M, et al. Digital light processing-based multi-material bioprinting: processes, applications, and perspectives. *J Biomed Mater Res A.* 2023;111(4):527-542. doi: 10.1002/jbm.a.37473

34. Afting C, Mainik P, Vazquez-Martel C, et al. Minimal-invasive 3D laser printing of microimplants in organismo. *Adv Sci.* 2024:2401110. doi: 10.1002/advs.202401110

35. Zennifer A, Manivannan S, Sethuraman S, et al. 3D bioprinting and photocrosslinking: emerging strategies & future perspectives. *Biomater Adv.* 2022;134:112576. doi: 10.1016/j.msec.2021.112576

36. Kam D, Rulf O, Reisinger A, et al. 3D printing by stereolithography using thermal initiators. *Nat Commun.* 2024;15(1):2285. doi: 10.1038/s41467-024-46532-0

37. Thangadurai M, Ajith A, Budharaju H, et al. Advances in electrospinning and 3D bioprinting strategies to enhance functional regeneration of skeletal muscle tissue, *Biomater Adv*. 2022;142:213135. doi: 10.1016/j.bioadv.2022.213135

38. Van de Walle A, Perez J E, Wilhelm C. Magnetic bioprinting of stem cell-based tissues. *Bioprinting,* 2023;30:e00265.

doi: 10.1016/j.bprint.2023.e00265

39. Rasouli R, Villegas KM, Tabrizian M. Acoustofluidics–changing paradigm in tissue engineering, therapeutics development, and biosensing. *Lab Chip*. 2023;23(5): 1300-1338. doi: 10.1039/D2LC00439A

40. Raees S, Ullah F, Javed F, et al. Classification, processing, and applications of bioink and 3D bioprinting: a detailed review. *Int J Biol Macromol.* 2023;232:123476. doi: 10.1016/j.ijbiomac.2023.123476

41. Wang H, Yu H, Zhou X, et al. An overview of extracellular matrix-based bioinks for 3D bioprinting. *Front Bioeng Biotechnol.* 2022;10:905438. doi: 10.3389/fbioe.2022.905438

42. Ong CS, Yesantharao P, Huang CY, et al. 3D bioprinting using stem cells. *Pediatr Res.* 2018;83(1):223-231. doi: 10.1038/pr.2017.252

43. Zhang H, Wang Y, Zheng Z, et al. Strategies for improving the 3D printability of decellularized extracellular matrix bioink. *Theranostics.* 2023;13(8):2562. doi: 10.7150/thno.81785

44. Tang M, Rich JN, Chen S. Biomaterials and 3D bioprinting strategies to model glioblastoma and the blood-brain barrier. *Adv. Mater.* 2021;33(5):2004776. doi: 10.1002/adma.202004776

45. Hull SM, Brunel LG, Heilshorn SC. 3D bioprinting of cell-laden hydrogels for improved biological functionality. *Adv. Mater.* 2022;34(2):2103691. doi: 10.1002/adma.202103691

46. Mancha Sánchez E, Gómez-Blanco JC, López Nieto E, et al. Hydrogels for bioprinting: a systematic review of hydrogels synthesis, bioprinting parameters, and bioprinted structures behavior. *Front Bioeng Biotechnol.* 2020;8:776. doi: 10.3389/fbioe.2020.00776

47. Liu F, Wang X. Synthetic polymers for organ 3D printing. *Polymers.* 2020;12(8):1765. doi: 10.3390/polym12081765

48. Muthukrishnan L. Imminent antimicrobial bioink deploying cellulose, alginate, EPS and synthetic polymers for 3D bioprinting of tissue constructs. *Carbohydr Polym.* 2021;260:117774. doi: 10.1016/j.carbpol.2021.117774

49. Cai Y, Chang SY, Gan SW, et al. Nanocomposite bioinks for 3D bioprinting. *Acta Biomater.* 2022;151:45-69. doi: 10.1016/j.actbio.2022.08.014

50. Loukelis K, Helal ZA, Mikos AG, et al. Nanocomposite bioprinting for tissue engineering applications. *Gels.* 2023;9(2):103. doi: 10.3390/gels9020103

51. Dong H, Lin J, Tao Y, et al. AI-enhanced biomedical micro/nanorobots in microfluidics. *Lab Chip.* 2024;24: 1419-1440. doi: 10.1039/D3LC00909B

52. Heid S, Boccaccini AR. Advancing bioinks for 3D bioprinting using reactive fillers: a review. *Acta Biomater.* 2020; 113:1-22. doi: 10.1016/j.actbio.2020.06.040

53. Kolan KCR, Semon JA, Bindbeutel AT, et al. Bioprinting with bioactive glass loaded polylactic acid composite and human adipose stem cells. *Bioprinting.* 2020;18:e00075. doi: 10.1016/j.bprint.2020.e00075

54. Sordi MB, Cruz A, Fredel MC, et al. Three-dimensional bioactive hydrogel-based scaffolds for bone regeneration in implant dentistry. *Mater Sci Eng C Mater Biol Appl.* 2021;124:112055. doi: 10.1016/j.msec.2021.112055

55. Murphy SV, De Coppi P, Atala A. Opportunities and challenges of translational 3D bioprinting. *Nat Biomed Eng.* 2020;4(4):370-380. doi: 10.1038/s41551-019-0471-7

56. Xu H, Zhang Y, Zhang Y, et al. 3D bioprinting advanced biomaterials for craniofacial and dental tissue engineering – a review. *Materials & Design.* 2024;241:112886. doi: 10.1016/j.matdes.2024.112886

57. Khati, V, Ramachandraiah, H, et al. 3D Bioprinting of multi-material decellularized liver matrix hydrogel at physiological temperatures. *Biosensors.* 2022;12(7):521. doi: 10.3390/bios12070521

58. Zhang Y, Enhejirigala, Yao B, et al. Using bioprinting and spheroid culture to create a skin model with sweat glands and hair follicles. *Burns Trauma.* 2021;9:tkab013. doi: 10.1093/burnst/tkab013

59. O'Shea DG, Hodgkinson T, Curtin CM, et al. An injectable and 3D printable pro-chondrogenic hyaluronic acid and collagen type II composite hydrogel for the repair of articular cartilage defects. *Biofabrication.* 2023;16(1):015007. doi: 10.1088/1758-5090/ad047a

60. Cruz EM, Machado LS, Zamproni LN, et al. A gelatin methacrylate-based hydrogel as a potential bioink for 3D bioprinting and neuronal differentiation. *Pharmaceutics.* 2023;15(2):627. doi: 10.3390/pharmaceutics15020627

61. Xiong R, Zhang Z, Chai W, et al. Freeform drop-on-demand laser printing of 3D alginate and cellular constructs. *Biofabrication.* 2015;7:045011. doi: 10.1088/1758-5090/7/4/045011

62. Xie M, Gao Q, Zhao H, et al. Electro-assisted bioprinting of low-concentration GelMA microdroplets. *Small.* 2019;15:1804216. doi: 10.1002/smll.201804216

63. Puistola P, Miettinen S, Skottman H, et al. Novel strategy for multi-material 3D bioprinting of human stem cell based corneal stroma with heterogenous design. *Mater Today Bio.* 2024;24:100924.

doi: 10.1016/j.mtbio.2023.100924

64. Mahdavi SS, Abdekhodaie MJ, Kumar H, et al. Stereolithography 3D bioprinting method for fabrication of human corneal stroma equivalent. *Ann Biomed Eng.* 2020;48:1955-1970. doi: 10.1007/s10439-020-02537-6

65. Boularaoui S, Shanti A, Lanotte M, et al. Nanocomposite conductive bioinks based on low-concentration GelMA and MXene nanosheets/gold nanoparticles providing enhanced printability of functional skeletal muscle tissues. *ACS Biomater Sci Eng.* 2021;7(12):5810-5822. doi: 10.1021/acsbiomaterials.1c01193

66. Lackner F, Šurina P, Fink J, et al. 4-axis 3D-printed tubular biomaterials imitating the anisotropic nanofiber orientation of porcine aortae. *Adv Healthc Mater.* 2024;13(2):2302348. doi: 10.1002/adhm.202302348

67. Mousavi A, Hedayatnia A, van Vliet PP, et al. Development of photocrosslinkable bioinks with improved electromechanical properties for 3D bioprinting of cardiac BioRings. *Applied Materials Today.* 2024;36:102035. doi: 10.1016/j.apmt.2023.102035

68. Wang Y, Yuan X, Yao B, et al. Tailoring bioinks of extrusion-based bioprinting for cutaneous wound healing. *Bioact Mater.* 2022;17:178-194. doi: 10.1016/j.bioactmat.2022.01.024

69. Ozbek II, Saybasili H, Ulgen KO. Applications of 3D bioprinting technology to brain cells and brain tumor models: special emphasis to glioblastoma. *ACS Biomater Sci Eng.* 2024;10(5):2616-2635. doi: 10.1021/acsbiomaterials.3c01569

70. Daly AC, Prendergast ME, Hughes AJ, et al. Bioprinting for the biologist. *Cell.* 2021;184:18-32. doi: 10.1016/j.cell.2020.12.002

71. Ramesh S, Deep A, Tamayol A, et al. Advancing 3D bioprinting through machine learning and artificial intelligence. *Bioprinting.* 2024:e00331. doi: 10.1016/j.bprint.2024.e00331

72. Manz A, Graber N, Widmer HM. Miniaturized total chemical analysis systems: a novel concept for chemical sensing. *Sens Actuators B Chem.* 1990;1(1-6):244-248. doi: 10.1016/0925-4005(90)80209-I

73. Sun H, Jia Y, Dong H, et al. Combining additive manufacturing with microfluidics: an emerging method for developing novel organs-on-chips. *Curr Opin Chem Eng.* 2020;28:1-9. doi: 10.1016/j.coche.2019.10.006

74. Yu S, Jing Y, Fan Y, et al. Ultrahigh efficient emulsification with drag-reducing liquid gating interfacial behavior. *Proc Natl Acad Sci USA*. 2022;119(29):e2206462119. doi: 10.1073/pnas.2206462119

75. Cai B, Kilian D, Ramos Mejia D, et al. Diffusion-based 3D bioprinting strategies. *Adv Sci.* 2024;11(8):2306470. doi: 10.1002/advs.202306470

76. Sun H, Xiong L, Huang Y, et al. AI-aided on-chip nucleic acid assay for smart diagnosis of infectious disease. *Fundam Res.* 2022;2(3):476-486. doi: 10.1016/j.fmre.2021.12.005

77. Sujigarasharma K, Sharulatha S, Lawanya Shri M, et al. Optimizing 3D bioprinting using advanced deep learning techniques a comparative study of CNN, RNN, and GAN. *Comput Intell Bioprint.* 2024;8: 157-173. doi: 10.1002/9781394204878.ch8

78. Ramesh S, Deep A, Tamayol A, et al. Advancing 3D bioprinting through machine learning and artificial intelligence. *Bioprinting.* 2024;38:e00331. doi: 10.1016/j.bprint.2024.e00331

79. Sun H, Xie W, Mo J, et al. Deep learning with microfluidics for on-chip droplet generation, control, and analysis. *Front Bioeng Biotechnol.* 2023;11:1208648. doi: 10.3389/fbioe.2023.1208648

80. Liu C, Wang L, Lu W, et al. Computer vision-aided bioprinting for bone research. *Bone Res.* 2022;10(1):21. doi: 10.1038/s41413-022-00192-2

81. Thai MT, Phan PT, Tran HA, et al. Advanced soft robotic system for in situ 3D bioprinting and endoscopic surgery. *Adv Sci.* 2023;10(12):2205656. doi: 10.1002/advs.202205656

82. Wang Z, Xiao C, Roy M, et al. Bioinspired skin towards next-generation rehabilitation medicine. *Front Bioeng Biotechnol.* 2023;11:1196174. doi: 10.3389/fbioe.2023.1196174

83. Motter Catarino C, Cigaran Schuck D, Dechiario L, et al. Incorporation of hair follicles in 3D bioprinted models of human skin. *Sci Adv.* 2023;9(41):eadg0297. doi: 10.1126/sciadv.adg0297

84. Zhang B, Li J, Zhou J, et al. A three-dimensional liquid diode for soft, integrated permeable electronics. *Nature.* 2024;628:84-92. doi: 10.1038/s41586-024-07161-1

85. Jorgensen AM, Gorkun A, Mahajan N, et al. Multicellular bioprinted skin facilitates human-like skin architecture *in vivo. Sci Transl Med.* 2023;15(716):eadf7547. doi: 10.1126/scitranslmed.adf7547

86. Chortos A, Liu J, Bao Z. Pursuing prosthetic electronic skin. *Nat Mater.* 2016;15(9):937-950. doi: 10.1038/nmat4671

87. Dong T, Hu J, Dong Y, et al. Advanced biomedical and electronic dual-function skin patch created through microfluidic-regulated 3D bioprinting. *Bioact Mater.* 2024;40:261-274. doi: 10.1016/j.bioactmat.2024.06.015

88. Yang JC, Mun J, Kwon SY, et al. Electronic skin: recent progress and future prospects for skin-attachable devices

for health monitoring, robotics, and prosthetics. *Adv. Mater.* 2019;31:1904765.
doi: 10.1002/adma.201904765

89. Apelgren P, Amoroso M, Säljö K, et al. Long-term *in vivo* integrity and safety of 3D-bioprinted cartilaginous constructs. *J Biomed Mater Res B Appl Biomater.* 2021;109:126-136.
doi: 10.1002/jbm.b.34687

90. Agarwala S, Lee JM, Ng WL, et al. A novel 3D bioprinted flexible and biocompatible hydrogel bioelectronic platform. *Biosens Bioelectron.* 2018;102:365-371.
doi: 10.1016/j.bios.2017.11.039

91. Krishnadoss V, Kanjilal B, Hesketh A, et al. *In situ* 3D printing of implantable energy storage devices. *Chem Eng J.* 2021;409:128213.
doi: 10.1016/j.cej.2020.128213

92. Lei IM, Jiang C, Lei CL, et al. 3D printed biomimetic cochleae and machine learning co-modelling provides clinical informatics for cochlear implant patients. *Nat Commun.* 2021;12:6260.
doi: 10.1038/s41467-021-26491-6

93. Xu Y, Rothe R, Voigt D, et al. Convergent synthesis of diversified reversible network leads to liquid metal-containing conductive hydrogel adhesives. *Nat Commun.* 2021;12(1):2407.
doi: 10.1038/s41467-021-22675-2

94. Chatterjee B, Mohseni P, Sen S. Bioelectronic sensor nodes for the internet of bodies. *Annu Rev Biomed Eng.* 2023;25:101-129.
doi: 10.1146/annurev-bioeng-110220-112448

95. Kim Y, Alimperti S, Choi P, et al. An inkjet printed flexible electrocorticography (ECoG) microelectrode array on a thin parylene-C film. *Sensors.* 2022;22(3):1277.
doi: 10.3390/s22031277

96. Xie M, Shi Y, Zhang C, et al. *In situ* 3D bioprinting with bioconcrete bioink. *Nat Commun.* 2022;13(1):3597.
doi: 10.1038/s41467-022-30997-y

97. Sondell M, Lundborg G, Kanje M. Vascular endothelial growth factor has neurotrophic activity and stimulates axonal outgrowth, enhancing cell survival and Schwann cell proliferation in the peripheral nervous system. *J Neurosci.* 1999;19:5731-5740.
doi: 10.1523/JNEUROSCI.19-14-05731.1999

98. Carpanini SM, Torvell M, Morgan BP. Therapeutic inhibition of the complement system in diseases of the central nervous system. *Front Immunol.* 2019;10:362.
doi: 10.3389/fimmu.2019.00362

99. Hu Y, Wu Y, Gou Z, et al. 3D-engineering of cellularized conduits for peripheral nerve regeneration. *Sci Rep.* 2016;6(1):32184.
doi: 10.1038/srep32184

100. Hsu RS, Li SJ, Fang JH, et al. Wireless charging-mediated angiogenesis and nerve repair by adaptable microporous hydrogels from conductive building blocks. *Nat Commun.* 2022;13(1):5172.
doi: 10.1038/s41467-022-32912-x

101. Fang Y, Wang C, Liu Z, et al. 3D printed conductive multiscale nerve guidance conduit with hierarchical fibers for peripheral nerve regeneration. *Adv Sci.* 2023;10(12):2205744.
doi: 10.1002/advs.202205744

102. Courtine G, Micera S, DiGiovanna J, et al. Brain-machine interface: closer to therapeutic reality?. *Lancet.* 2013;381(9866):515-517.
doi: 10.1016/S0140-6736(12)62164-3

103. Zhang Q, Hu S, Talay R, et al. A prototype closed-loop brain–machine interface for the study and treatment of pain. *Nat Biomed Eng.* 2023;7(4):533-545.
doi: 10.1038/s41551-021-00736-7

104. Kantawala B, Hamitoglu AE, Nohra L, et al. Microengineered neuronal networks: enhancing brain-machine interfaces. *Ann Med Surg.* 2024;86(6):3535-3542.
doi: 10.1097/MS9.0000000000002130

105. Ghafoor U, Kim S, Hong KS. Selectivity and longevity of peripheral-nerve and machine interfaces: a review. *Front Neurorobot.* 2017;11:59.
doi: 10.3389/fnbot.2017.00059

106. Sun G, Zeng F, McCartin M, et al. Closed-loop stimulation using a multiregion brain-machine interface has analgesic effects in rodents. *Sci Transl Med.* 2022;14(651):eabm5868.
doi: 10.1126/scitranslmed.abm5868

107. Adewole DO, Struzyna LA, Burrell JC, et al. Development of optically controlled "living electrodes" with long-projecting axon tracts for a synaptic brain-machine interface. *Sci Adv.* 2021;7(4):eaay5347.
doi: 10.1126/sciadv.aay5347

108. Afanasenkau D, Kalinina D, Lyakhovetskii V, et al. Rapid prototyping of soft bioelectronic implants for use as neuromuscular interfaces. *Nat Biomed Eng.* 2020;4(10):1010-1022.
doi: 10.1038/s41551-020-00615-7

109. Liu Y, Liu J, Chen S, et al. Soft and elastic hydrogel-based microelectronics for localized low-voltage neuromodulation. *Nat Biomed Eng.* 2019;3(1):58-68.
doi: 10.1038/s41551-018-0335-6

110. Roth JG, Brunel LG, Huang MS, et al. Spatially controlled construction of assembloids using bioprinting. *Nat Commun.* 2023;14(1):4346.
doi: 10.1038/s41467-023-40006-5

111. Ahmed T. Bio-inspired artificial synapses: neuromorphic computing chip engineering with soft biomaterials, memories-materials, devices. *Circuits Syst.* 2023;6:100088.
doi: 10.1016/j.memori.2023.100088

112. Cheng Z, Ríos C, Pernice WHP, et al. On-chip photonic synapse. *Sci Adv.* 2017;3(9):e1700160. doi: 10.1126/sciadv.1700160

113. Fu T, Liu X, Fu S, et al. Self-sustained green neuromorphic interfaces. *Nat Commun.* 2021;12(1):3351. doi: 10.1038/s41467-021-23744-2

114. Abdollahiyan P, Oroojalian F, Mokhtarzadeh A, et al. Hydrogel-based 3D bioprinting for bone and cartilage tissue engineering. *Biotechnol J.* 2020;15(12):2000095. doi: 10.1002/biot.202000095

115. Li T, Ma Z, Zhang Y, et al. Regeneration of humeral head using a 3D bioprinted anisotropic scaffold with dual modulation of endochondral ossification. *Adv Sci.* 2023;10(12): 2205059. doi: 10.1002/advs.202205059

116. Liu Q, Dong X, Qi H, et al. 3D printable strong and tough composite organo-hydrogels inspired by natural hierarchical composite design principle. *Nat Commun.* 2024;1 5(1):3237. doi: 10.1038/s41467-024-47597-7

117. Du L, Wu J, Han Y, et al. Immunomodulatory multicellular scaffolds for tendon-to-bone regeneration. *Sci Adv.* 2024;10(10):eadk6610. doi: 10.1126/sciadv.adk6610

118. Jo HJ, Kang MS, Heo HJ, et al. Skeletal muscle regeneration with 3D bioprinted hyaluronate/gelatin hydrogels incorporating MXene nanoparticles. *Int J Biol Macromol.* 2024;265:130696. doi: 10.1016/j.ijbiomac.2024.130696

119. Huan Y, Zhou D, Wu X, et al. 3D bioprinted autologous bone particle scaffolds for cranioplasty promote bone regeneration with both implanted and native BMSCs. *Biofabrication.* 2023;15(2):025016. doi: 10.1088/1758-5090/acbe21

120. He H, Yuan Y, Wu Y, et al. Exoskeleton partial-coated stem cells for infarcted myocardium restoring. *Adv. Mater.* 2023;35(52):2307169. doi: 10.1002/adma.202307169

121. Zhao T, Zhou J, Wu W, et al. Antibacterial conductive polyacrylamide/quaternary ammonium chitosan hydrogel for electromagnetic interference shielding and strain sensing. *Int J Biol Macromol.* 2024;265:130795. doi: 10.1016/j.ijbiomac.2024.130795

122. Wu J, Zhu Z, Pei X. 3D-printed biomimetic hydrogel for repairing tissue damage in motor systems. *Chin J Tissue Eng Res.* 2024;28:4703. doi: 10.12307/2024.535

123. Xue Q, Ma L, Hu H, et al. 3D bioprinting as a prospective therapeutic strategy for corneal limbal epithelial stem cell deficiency. *Int J Bioprint.* 2023;9(3):710. doi: 10.18063/ijb.710

124. Panagou S, Neumann WP, Fruggiero F. A scoping review of human robot interaction research towards Industry 5.0 human-centric workplaces. *Int J Product Res.* 2024;62(3): 974-990. doi: 10.1080/00207543.2023.2172473

125. Dong H, Hu B, Zhang W, et al. Robotic-assisted automated in situ bioprinting. *Int J Bioprint.* 2023;9(1):629. doi: 10.18063/ijb.v9i1.629

126. Guix M, Mestre R, Patiño T, et al. Biohybrid soft robots with self-stimulating skeletons. *Sci Robot.* 2021;6(53):eabe7577. doi: 10.1126/scirobotics.abe7577

127. Mestre R, Patiño T, Sánchez S. Biohybrid robotics: from the nanoscale to the macroscale. *Wiley Interdiscip Rev Nanomed Nanobiotechnol.* 2021;13(5):e1703. doi: 10.1002/wnan.1703

128. Jin D, Zhang L. Embodied intelligence weaves a better future. *Nat Machine Intell.* 2020;2(11):663-664. doi: 10.1038/s42256-020-00250-6

129. Smirnova L, Caffo BS, Gracias DH, et al. Organoid intelligence (OI): the new frontier in biocomputing and intelligence-in-a-dish. *Front Sci.* 2023; 1:1017235. doi: 10.3389/fsci.2023.1017235

130. Lee W, Xu C, Fu H, et al. 3D bioprinting highly elastic PEG-PCL-DA hydrogel for soft tissue fabrication and biomechanical stimulation. *Adv Funct Mater.* 2024;34:2313942. doi: 10.1002/adfm.202313942

131. Kronenfeld JM, Rother L, Saccone MA, et al. Roll-to-roll, high-resolution 3D printing of shape-specific particles. *Nature.* 2024;627(8003):306-312. doi: 10.1038/s41586-024-07061-4

ACCSCIENCE PUBLISHING

International Journal of Bioprinting

REVIEW ARTICLE

The promising role of semi-solid extrusion technology in custom drug formulation for pediatric medicine

Thomas Cerveto[1], Lucas Denis[2,3], Maxime Stoops[2], Anna Lechanteur[4], Christine Jérôme[5], Julien Leenhardt[6,7,8], Stephen Flynn[9], Alvaro Goyanes[10,11,12], Roseline Mazet[6]*, Maxime Annereau[2]*, and Luc Choisnard[1]

[1]Grenoble Alpes University and Centre National de la Recherche Scientifique (CNRS; French National Centre for Scientific Research), Département de Pharmacochimie Moléculaire (DPM; Department of Molecular Pharmacochemistry), Unité Mixte de Recherche (UMR; Mixed Research Unit), Grenoble, France

[2]Clinical Pharmacy Department, Gustave Roussy Cancer Campus, Villejuif, France

[3]Paris-Saclay University and CNRS, Institut Galien Paris-Saclay, UMR, Orsay, France

[4]Laboratory of Pharmaceutical Technology and Biopharmacy, Center for Interdisciplinary Research on Medicines (CIRM), University of Liège, Liège, Belgium

[5]CESAM Research Unit, Center for Education and Research on Macromolecules (CERM), University of Liège, Liège, Belgium

[6]Pharmacy Department, Centre Hospitalier Universitaire (CHU; University Hospital Center) Grenoble Alpes, Grenoble, France

[7]Nuclear Medicine Department, CHU Grenoble Alpes, Grenoble, France

[8]Grenoble Alpes University, Institut National de la Santé et de la Recherche Médicale (INSERM; National Institute of Health and Medical Research), Laboratoire de Recherche sur les Maladies Cardiovasculaires (LRB; Cardiovascular Diseases Research Laboratory), UMR, Grenoble, France

[9]Global Pharma Marketing service, Roquette Frères, Lestrem, France

[10]Departamento de Farmacología, Farmacia y Tecnología Farmacéutica, I+D Farma (GI-1645), Facultad de Farmacia, Instituto de Materiales (iMATUS) and Health Research Institute of Santiago de Compostela (IDIS), Universidade de Santiago de Compostela, Santiago de Compostela, Spain

[11] Department of Pharmaceutics, UCL School of Pharmacy, University College London, Brunswick Square, London, UK

[12]FABRX Ltd., Henwood House, Henwood, Ashford, Kent, UK

***Corresponding authors:**
Roseline Mazet
(RMazet@chu-grenoble.fr)

Maxime Annereau
(Maxime.ANNEREAU@gustaveroussy.fr)

Citation: Cerveto T, Denis L, Stoops M, et al. The promising role of semi-solid extrusion technology in custom drug formulation for pediatric medicine. *Int J Bioprint*. 2024;10(6):4063. doi: 10.36922/ijb.4063

Received: June 27, 2024
Revised: August 6, 2024
Accepted: August 7, 2024
Published Online: August 29, 2024

Copyright: © 2024 Author(s). This is an Open Access article distributed under the terms of the Creative Commons Attribution License, permitting distribution, and reproduction in any medium, provided the original work is properly cited.

Publisher's Note: AccScience Publishing remains neutral with regard to jurisdictional claims in published maps and institutional affiliations.

(This article belongs to the Special Issue: *Advanced Biomaterials for 3D Printing and Healthcare Application*)

Abstract

The long-standing issue of inadequate medicine formulations has been a focus of regulatory bodies and pharmaceutical research, particularly in adapting medicines for children's unique requirements. The pediatric population presents diverse challenges in pharmacotherapy due to their varying age-related physiological differences, and taste and dosage form preferences. Conventional formulations often fail to meet these needs, leading to a high prevalence of off-label medication use and modifications by caregivers, which can compromise drug efficacy and safety. The well-known challenges of managing children's medication are similar to those in geriatrics, both of which require dose adjustments to accommodate the patient's pathophysiological characteristics and prevent deglutination problems. This paper explores recent innovations in drug formulations, highlighting the shift from traditional liquid formulations to solid dosages through three-dimensional (3D)

printing technology. Recent advancements in 3D printing technology offer promising solutions to these challenges. Additive manufacturing (AM), or 3D printing, facilitates the creation of complex objects (e.g., drug formulations) directly from digital models, allowing for high precision and customization. 3D-printed formulations have displayed considerable promise in improving palatability, adherence, and dose accuracy for pediatric use. Innovations like chewable tablets and taste-masked formulations make medications more acceptable to children. Moreover, the ability of 3D printing to adjust drug release profiles and doses offers a personalized approach to pediatric and geriatric pharmacotherapy, which is essential for managing conditions that require precise therapeutic control. The paper discusses several case studies using the semi-solid extrusion (SSE) process for producing personalized dosage forms, along with various technical and regulatory challenges associated with implementing this process in hospital-based drug manufacturing. In conclusion, while 3D printing in pediatric and geriatric pharmacotherapy addresses many challenges of traditional drug formulations, ongoing research and adaptation of regulatory frameworks are necessary to expand its application, ensuring safer, more effective, and more acceptable medication.

***Keywords*:** Unlicensed preparation; 3D printing; Pediatrics; Semi-solid extrusion; Hospital preparation; Personalized medicines

1. Introduction

The lack of availability of appropriate medicines for children has been an extensive and well-known problem for many years.[1] Children require medicines that are adapted to each age group, due to the remarkable heterogeneity of this population, which ranges from premature infants to young adults. Some medicines are not suitable for young children, and even less so for premature infants.[2–4] Furthermore, differences in the pharmacokinetic and pharmacodynamic profiles of children and adults necessitate different dosage strengths for children. Moreover, the preferred dosage form for children evolves with age and must be adapted to account for varying weights, forms, and taste preferences, which can differ from country to country.[5] Consequently, there is a strong demand for medicines that are suitable for children, easy to administer, use non-toxic excipients, reduced dosage frequency, good palatability, and flexible dosing.[6,7] When developing a medicine, the choice of pediatric forms is most often made in favor of oral liquid forms, despite their limitations, including stability issues, difficulty in achieving controlled-release formulations, the need for multiple-day dosing, exposure to potentially harmful excipients, poorer palatability, and higher costs. From an industrial perspective, these constraints represent a significant challenge.[8–11]

Numerous incentives from the United States (US) Food and Drug Administration (FDA) and the European Medicines Agency (EMA), such as Pediatric Investigation Plans, are mobilized in order to develop new formulations adapted for children with specific indications, allowing them to achieve Pediatric-Use Marketing Authorization (PUMA) status. In contrast, pediatric formulations of drugs already on the market typically receive only hybrid generic status and are priced similarly to the original drug. Between 2007 and 2016, 267 new medicines and 43 new dosage forms for children's use were authorized. Unfortunately, despite these incentives, only seven PUMAs have been obtained since 2006.[12] Pediatric medicines remain underdeveloped, particularly in areas such as anticancer drugs, cardiology, or diseases affecting only children.[10,13–19] To achieve better results, Europe is in the process of amending its incentive rules (Regulation 726/2004 and Directive 2001/83/EC) and the legislation on medicines for children and rare diseases (Regulation 1901/2006 and Regulation 141/2000/EC, respectively).

Children are a particularly vulnerable patient group with limited pharmaceutical treatment options. Drug shortages have been associated with higher relapse rates in children with cancer, the use of less effective agents, off-label use, and a greater risk of both short- and long-term toxicity.[20] Drug shortages negatively impact patients by affecting drug therapy, causing delays in medical procedures or therapy, and contributing to medication errors.[21,22] Therapeutic alternatives, where they exist, are often associated with higher cost, lower efficacy, increased side effects, off-label use, and medication errors due to inexperience and lack of knowledge.[23,24]

Despite efforts by health authorities to promote the development of pediatric medicines, many medicinal products are authorized only for adults and are not currently available in formulations suitable for administration to the pediatric population. As a consequence, off-label or even unlicensed practices are frequent and their prevalence has been estimated to range from 3.2% to 95% overall, 26–95% in neonates,[25–27] 2.7–51.2% in outpatients, and 9.0–79.0% in inpatients.[28,29] Caregivers or parents often modify off-

label medicines before administration, such as crushing tablets into powder, opening capsules and diluting the powder in a liquid, or drinking injectable drugs. However, such modifications can have potentially harmful consequences for a pediatric patient.[30] These practices may affect the efficacy and safety parameters of the medicinal product by altering its absorption characteristics, stability, and palatability.[31–33] Such manipulation presents a risk of medication errors in dose calculation or preparation, leading to inaccurate dosing and undetermined effects on the product's stability.[30,34] Additionally, crushing tablets or opening capsules exposes caregivers or family members to chemical risks associated with the active substance, particularly when it is carcinogenic.

Due to the lack of appropriate medicines for children, compounded medicines (i.e., unlicensed preparation) can play an important role in addressing needs unmet by commercial medicines or during drug shortage.[35,36] Unlicensed preparations are produced by the community and hospital pharmacies, offering capsules or oral liquid formulations adapted to patients' needs. The need for adapted treatment through compounding is significant, especially in conditions with narrow therapeutic margins, long-term treatments, and medications where non-adapted dosages or non-compliance can jeopardize patient survival, such as cancer, autoimmune diseases, and cardiology.[10,34] For example, a recent study on hospital preparations in oncology by the European Society for Paediatric Oncology (SIOPE) and the European Society of Oncology Pharmacy (ESOP) identified 28 formulations for 13 different active pharmaceutical ingredients (APIs) used in chemotherapy and 35 formulations for 16 different APIs used in supportive therapy, each with a sufficient level of evidence.[37] In some cases, more sophisticated formulation strategies, such as encapsulation of drug particles or 3D medicine printing, are highly promising and have demonstrated a significant benefit over traditional extemporaneous preparation.[37] Such robust and adaptive techniques could facilitate access to personalized therapy for all pediatric patients.[38,39] Scientific publications and recent industry strategies indicate a clear shift from liquid dosage forms to novel solid dosage forms.[40] This new technology improves palatability, provides flexibility in the design of child-friendly dosage forms, and could enable cost-effective, individualized treatment options. However, further research in this field is evident.[41–43]

The common challenges of managing children's medication are similar to those encountered in geriatrics. Similarly, geriatric patients require dose adjustments according to their physiological characteristics and galenic compounding to compensate for deglutination problems. Swallowing difficulties in older adults present challenges for medication management, particularly as polypharmacy is so common.[44] Therefore, geriatric patients require personalized treatment using compounded medicines, just as pediatric patients do.[45]

Overall, the use of unlicensed preparations has increased over the last 10 years, especially as they are also used to compensate for drug shortages, such as anesthetic drugs during the COVID-19 crisis or amoxicillin since 2022.[46]

Furthermore, unlicensed preparations can be tailored to individual patients or produced at a larger semi-industrial scale. Since compounding carries the risk of contamination and supra- and subtherapeutic errors,[47] it demands highly trained personnel and premises that are no longer available in all pharmacies in many countries. To ensure the quality of the preparations and their safe use, regulations must be adapted to these different production scales. For example, the FDA has revised its recommendations to provide more flexibility to hospital pharmacies and health systems in the distribution of compounded drugs, while emphasizing the importance of ensuring their safety and efficacy.[48] In France, new regulations allow for the production of medium-sized batches, with a corresponding increase in quality towards Good Manufacturing Practice (GMP) standards.[49] In this context, 3D printing emerges as a valuable tool for creating custom shapes and doses, enhancing the quality of pediatric preparations.[42]

Since the 2010s, there has been increasing enthusiasm among academic, hospital, and community pharmacies, as well as the industry, for additive manufacturing (AM) of drugs.[50,51] Better known as 3D printing, AM is a process of creating a physical object by joining materials layer by layer from a digital 3D model.[52] All AM processes can be divided into a sequence of operations integrated within a digital chain, which comprises four distinct stages.[53–55] The first stage is computer-aided design (CAD), which involves creating a 3D digital model and converting its surfaces into a network of polygons, typically triangular facets. The positions of these facets are then translated into instructions for the 3D printer, written in G-code. The second stage is the preparation of the digital model prior to manufacturing, which involves optimizing and repairing the digital model before slicing it into layers. The third stage is computer-aided manufacturing (CAM), which involves manufacturing the physical object layer by layer. The fourth stage is post-processing, which is optional depending on the objects manufactured and the technology used. This stage consists of a series of steps carried out after the completion of a manufacturing cycle to ensure the finished product has the desired properties (e.g., support removal, drying, coating, polishing, coloring, smoothing, etc.).

Additive manufacturing (AM) processes offer several advantages over traditional methods. They enable complex objects to be manufactured with high precision and enable flexible modifications to the object's characteristics by adjusting the parameters of the digital model. This capability allows the creation of various versions of the same model. Therefore, AM processes are well-suited for the on-demand production of small batches.

This review presents a brief overview of the various technological aspects and materials used in the 3D printing of drugs, utilizing the Web of Science (WoS) and PubMed bibliographic tools. It provides a state-of-the-art bibliographic overview (2021–2024) of the latest advances in the field, focusing on drug 3D printing using semi-solid extrusion (SSE) technology, which is one of the most promising technologies for 3D-printed medicines. The aspects related to the manufacturing processes and post-treatment of the preparations are addressed. Finally, the application of SSE-printed compounds in a hospital setting is discussed.

2. Additive manufacturing processes for drugs

2.1. Processes overview

Additive manufacturing (AM) processes have been classified by ISO/ASTM 52900 into seven families according to the binding or solidifying agent, the raw material (polymer, metallic, ceramic, and composites), and the material distribution technique used (Figure 1).[56] The processes applicable to drug product manufacturing utilize polymers or photopolymers (resins). Five families using polymers or resins as raw material have been researched for drug manufacturing: powder bed fusion, material extrusion, material jetting, vat photopolymerization, and binder jetting (Figure 1).[57–59] The remaining processes, directed energy deposition and sheet lamination, are not designed for drug manufacturing but are instead for metallic parts manufacturing. Each process has its respective characteristics, advantages, and drawbacks that influence the quality and printability of drugs, as well as the organization of the production process.

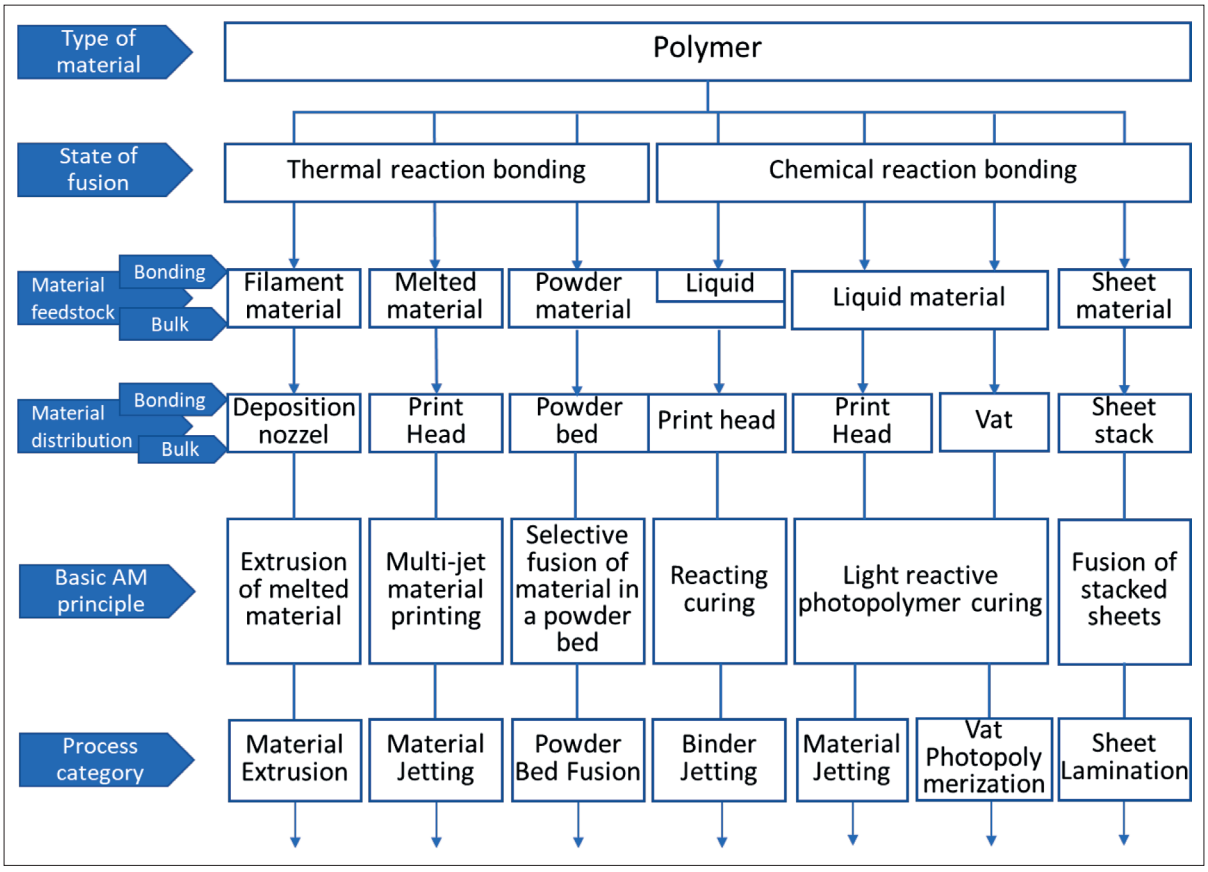

Figure 1. Diagram of additive manufacturing processes according to the ISO/ASTM 52900 nomenclature. Adapted with permission from ref.[52] Copyright © 2021 ISO/ASTM.

The processes can be divided into three major groups, depending on the characteristics of the raw material and the manufacturing requirements[60]: (i) powder agglomeration processes with powder bed fusion and binder jetting; (ii) liquid material solidification processes with material jetting and vat photopolymerization; and (iii) extrusion processes from solid or semi-solid materials.

To determine which of these processes would be most suitable for hospital and community pharmacy use in the coming years, the process should meet the following criteria:

(i) The process must be perfectly suited for manufacturing a wide range of different products, with minimal cleaning constraints and a low risk of cross-contamination between batches. This is crucial for hospital confounding, where equipment is used to produce various medications tailored to individual patient needs. If this criterion is not met, the process is excluded.

(ii) The materials used in the process (i.e., equipment and pharmaceutical raw materials) must be well-established for clinical use. The process should utilize a variety of excipients that are biocompatible and readily available. The process should be capable of handling and processing thermosensitive or photosensitive APIs or excipients.

(iii) The process must enable the manufacture of dosage forms suitable for specific populations. Considering oral dosage forms particularly suited for children, mini-printlets (mini 3D-printed tablets), orodispersible, fast disintegrating printlets, and chewable printlets have to be printable. These shapes must be appropriately sized for children's mouths and esophagus to ensure ease of administration. Suppositories are another type of solid dosage form suitable for children that are administered rectally. In addition, the selected process should ideally facilitate the production of drugs with different API release kinetics (immediate and controlled release). The process is excluded if this criterion is not met.

In the following sections, we will discuss the different criteria for each process. Processes that are unsuitable for manufacturing printed medicines in hospitals are excluded from the evaluation, with justification for their exclusion. Finally, we will identify and detail the most appropriate process.

2.1.1. Powder agglomeration processes

Powder bed fusion involves using thermal energy (e.g., scanning laser) to selectively melt areas of powder which is placed in excess within a container.[52,55] This process does not meet the aforementioned criteria. Firstly, it is not suitable for manufacturing multiple different products for various patients. The use of a large quantity of powder implies significant constraints for product changeovers, with extensive cleaning required for the powder container. Therefore, the risk of cross-contamination is high. This process is better suited for large-scale industrial production of a single product. In addition, hospital premises would need to handle the use and storage of large quantities of powder in controlled atmosphere zones, requiring extensive personal protective equipment, particularly for chemotherapy drugs, which present a major risk to operators. The process also does not accommodate heat-sensitive materials. Furthermore, only a small proportion (10–15%) of the powder is sintered during the process.[61,62] The rest is recovered, but not all of it can be recycled. Each pass through the 3D printer deteriorates the quality of the powder, necessitating the mixing of recycled powder with approximately 50% or more fresh powder,[61,62] resulting in significant material loss. For all these reasons, this process may not be suitable for manufacturing drug products in hospitals.

Binder jetting involves selectively depositing a liquid binding agent on a powder bed to agglomerate the powder particles.[52,55] This process is used to produce Spritam®, the first and only 3D-printed medicine commercially available in the United States of America (USA). Spritam® is prepared using the patented ZipDose® technology,[63] which allows the drug formulation to disintegrate extremely rapidly.[64] Binder jetting is similar to the powder bed melting process, except that it uses a solvent to bind the powder instead of thermal energy. The powder is also placed in excess in a container. Unlike the powder bed melting process, thermosensitive or photosensitive materials can be used, as binder jetting does not require thermal energy or a light source for production. However, like powder-bed fusion, the substantial use of powder is not suitable for hospital compounding, but rather for industrial manufacturing. Therefore, this process is excluded.

2.1.2. Liquid photoreactive material solidification processes

Vat photopolymerization is an AM process where a liquid photopolymer is placed in a vat and selectively exposed to a light source to create an object via light-induced curing.[52,55] However, this process has two main issues. First, there are limited biocompatible photopolymerizable materials available for drug production,[65] and there is insufficient information on their safety for human consumption. There may also be a risk of undesirable chemical reactions between the API and photopolymers.[65,66] As a result, the process may not yet be for drug manufacturing. Second,

the need to place the raw material (in liquid form) in large quantities in a tank and cure it with ultraviolet (UV) light precludes the use of photosensitive materials and complicates product changeovers. This results in extensive cleaning requirements and an increased risk of cross-contamination. For these reasons, this process is also not suitable for drug manufacturing in hospitals.

Material jetting is an AM process that involves spraying a liquid onto a substrate in droplets, triggered by either piezoelectric or thermal stimulation. This process includes two main types: (i) continuous inkjet printing (where ink flow is continuous) and (ii) drop-on-demand (where ink is jetted on demand).[67] Depending on the technology used, the drops could either solidify spontaneously or with the aid of heat or UV light.[65] Among the reported dosage forms, oral and buccal films have demonstrated significant promise for this technology.[67,68] In 2024, material jetting meets most of our criteria except the second one. Inkjet 3D printers currently used in pharmaceutical research are still in the early stages of development[68] and are essentially derived from conventional desktop printers, which are not yet suitable for clinical use. Therefore, despite its potential, this process is also excluded for hospital and pharmacy use.

2.1.3. Extrusion processes

Extrusion is a mechanical manufacturing process where the material is forced through a small hole (the die) under pressure, transforming it into a homogeneous, plastic, semi-solid mass, known as the extrudate (typically a filament). In AM based on extrusion processes, the raw material is passed through a nozzle orifice and selectively deposited layer by layer.[52] The raw material may be in solid form or semi-solid form. All extrusion-based AM processes follow the same successive operations[55]: material loading, liquefaction, pressure application to move the material through the nozzle, extrusion, and controlled layer-by-layer deposition along a predefined path, followed by bonding the successive layers. The specifics of SSE are discussed in the next section.

In fused filament fabrication (FFF), also known as fused deposition modeling (FDM), the material is a solid thermoplastic filament obtained through hot melt extrusion (HME). HME uses a heat input to melt thermoplastic materials, which may initially be in various forms, such as powders, granules, flakes, pastes, etc. The extrudate is produced continuously, and the size and shape of its cross-section are defined by those of the die.[55] Established in the pharmaceutical industry in the 1980s, HME is used to produce a variety of dosage forms (e.g., pellets, granules, implants, etc.).[60] HME can also be used to produce controlled-release forms and increase the apparent solubility of APIs by promoting the formation of amorphous solid dispersions.[60,69] Additionally, HME can be used to produce solid thermoplastic filament suitable for FFF/FDM. In FFF/FDM, the filament is fed through a print head with a heated nozzle that melts the material and deposits it layer-by-layer on the manufacturing platform.[52,53,55] Among the AM processes discussed, FFF/FDM is one of the least costly and easiest to operate, providing good precision and versatility,[60,64,70–78] and remains the most frequently used AM process in the market.[55]

Fused filament fabrication/fused deposition modeling (FFF/FDM) offers several significant advantages. First, it uses solid filament that can be easily stored and handled during production, making it easy to set up on hospital premises. The filament is consumed precisely by the 3D printer for parts manufacturing, minimizing waste and simplifying cleaning, which involves only the nozzle and build platform onto which the material is deposited. This helps manage the risk of cross-contamination. Moreover, HME has long been used in the pharmaceutical sector, providing access to a wide range of biocompatible excipients for use in FFF. The process does not require light exposure, enabling the use of photosensitive materials and eliminating the need for post-printing treatments.

However, this process has significant limitations. Firstly, filament manufacturing by HME can be challenging to manage within hospitals due to the complexity of achieving homogeneous distribution of APIs, making it difficult to achieve at the point of care. The API can be incorporated either with the excipients in the extruder or post-extrusion, which complicates the process.[70] Additionally, HME equipment is costly and bulky. FFF also has a low printing speed, i.e., 2–5 min to manufacture a single tablet, or >1 h for a single batch of 30 prints.[70] It is difficult to improve this speed due to the constraints of filament flow, which requires a balance between low viscosity for extrusion and high viscosity for layer adhesion.[60,70,76] Another drawback is the need for high temperatures to melt the thermoplastic filament, typically ranging from 100 to 250°C,[70] which makes it difficult to manufacture drugs containing heat-sensitive APIs.

In terms of feasible dosage forms suitable for children or the elderly, the FFF process is well-suited for manufacturing solid dosage forms for swallowing, including chewable forms, such as the mini-tablets developed by Parulski et al.[79] However, formulations produced using this process often result in dosage forms with high hardness and melting temperatures higher than 100°C, which makes them unsuitable for suppositories or orodispersible forms.

In view of these drawbacks, we consider that the FFF process is not currently the most suitable option for compounding in pediatric oncology hospitals.

2.2. Semi-solid extrusion

2.2.1. Process overview

The other extrusion-based AM process is SSE. Unlike FFF, SSE uses a semi-solid (or semi-molten) raw material, usually placed in a syringe or cartridge and extruded at low temperatures,[80] generally between ambient temperature and 80°C (Table 1).[81] The material is extruded by applying sufficient pressure in two main ways. The first approach is pneumatic extrusion, whereby the piston of the syringe containing the pharmaceutical ink is pushed by compressed air pressure. The pressurized air is connected directly to the syringe body, whose nozzle can incorporate a valve to control the air channel into the printhead via an on-off switch, closing the channel when the valve is switched off[80] (Figure 2). The advantages of this system are high precision in material extrusion, fast response time as the syringe body can be instantly pressurized, and suitability for viscous materials (as the gas can reach high pressures without compromising system integrity). However, it is less effective for low-viscosity materials and is more complex compared to mechanical systems.[80,81] The second approach is mechanical extrusion, utilizing either a piston or a screw controlled by stepper motors to push the material through the nozzle (Figure 3). Mechanical extrusion is more affordable and easier to transport than the pneumatic system, as it does not require an air compressor. Furthermore, syringes can be replaced quickly and easily, speeding up the printing process. However, it is not suited for high-viscosity materials.[80]

The quality of dosage forms manufactured by SSE is influenced by three categories of parameters: material parameters, operating parameters, and machine parameters. These parameters interact with each other and influence the quality of the finished products, including API content and uniformity, release kinetics, mass and mass uniformity of printed products, product appearance, and mechanical properties (e.g., surface roughness, dimensional accuracy, hardness, etc.). Material parameters refer to the formulation, particularly the material's rheological properties and, to a lesser extent, its thermal properties. Operating parameters are those that can be modified during print production, i.e., numerical parameters and physical parameters. Numerical parameters enable modulation of the dosage and kinetics of print release from the 3D model; physical parameters designate the selection of optimal temperature, pressure, and print speed as a function of material and numerical parameters. Machine parameters are the characteristics of the equipment used to print the drug, such as the design and number of printheads or the diameter of the nozzle.

2.2.2. Dosage form design by computer-aided design

Operating parameters affect the quality attributes of the finished product. The design of the dosage form mainly includes its geometry, dimensions, and infill density. Design geometry is an editable parameter, where the exchange surface can be adjusted to modify the API release kinetics. Different dosage form dimensions can alter the quantity of API in the finished product (e.g., larger dosage forms contain more API). Additionally, the size of the dosage form is strongly correlated with its mass.[110] The infill density of the dosage form can be varied to obtain different properties and release profiles. Generally, porosity is retained to facilitate API release; thus, infill density rarely reaches 100%. By adjusting these parameters during drug production via SSE, it is possible to tailor the dosage form to meet the specific needs of the patient, ensuring precise control over the drug's characteristics and performance.

2.2.3. Pharma-ink and dosage forms

The 3D printing material, also called the Pharma-ink (a mixture of drugs and excipients), should possess several ideal characteristics: it should be easy to prepare without using heat, adhere minimally to facilitate packaging in the 3D printer while ensuring sufficient adhesion of the semi-solid mass to the printing bed, be smooth and free of lumps, and be easily incorporated into a syringe. Finally, the dynamic viscosity of the ink must be sufficiently high, with shear-thinning properties, to be printable without collapsing once extruded.[110] Table 1 provides a non-exhaustive literature review of articles published between 2021 and 2024 on drugs manufactured via SSE. The most common dosage forms are solid oral forms, predominantly swallowable dosage forms (films or tablets). Other solid oral dosage forms produced by SSE include orodispersible and chewable forms. One advantage of SSE over FFF is its ability to manufacture solid dosage forms with a soft texture, allowing for the creation of chewable printlets. For example, gummies made by Rouaz-El Hajoui et al. contain gastro-resistant pellets with the API,[100] enabling the modified release of the API while still allowing chewing of the dosage form (Figure 4). While most of these solid oral dosage forms are designed for systemic pharmacological action, there are a few examples intended for local action in the stomach, such as gastro-floating devices. Other notable forms include mucoadhesive films like vaginal ovules made by Teworte et al.,[123] rectal forms, such as infliximab suppositories made by Awad et al.[121] (Figure 5), and medical devices impregnated with active substances,

Table 1. Commented bibliographical review (2021–2024) on the use of 3D printing for semi-solid extrusion (SSE) according to the different pharmaceutical forms produced and their composition (active pharmaceutical ingredient [API] and excipients)

Formulation type	Formulation details and properties	API	Excipients	Commentaries	Ref.
Oral dosage forms					
Swallowable printlets	Immediate release printlets	Caffeine	Sodium alginate; HPMC; sodium croscarmellose	Development of caffeine-containing printlets for neonates suffering from apnea of prematurity	[82]
	Immediate release printlets	Cranberry leaf extracts	Polyethylene oxide	*In vivo* assessment (in rats) of L-arginine-loaded cranberry leaf extract bioactivity on insulin resistance and development of 3D-printed dosage forms	[83]
	Immediate release printlets	Sildenafil citrate (10 mg)	Gelucire® 48/16; glycerol	Bioequivalence assessment of solid oral dosage forms of sildenafil manufactured by SSE within hospital pharmacy vs. industrial sildenafil tablets; sildenafil was selected for its treatment of pulmonary arterial hypertension in children, which requires a low dosage that can be adapted from one individual to another according to their pathophysiological characteristics	[84]
	Gastro-resistant delayed-release printlets	Octréotide acetate (3.4%)	Carbopol 974P NF, HPMC 2910, corn starch	Evaluation of the ability of SSE to manufacture swallowable dosage forms containing biological macromolecules	[85]
	Immediate-release printlets with porous geometry	Paracetamol	HPMC	Evaluation of the effects of solid drug particles in inks on the quality of printed parts with porous geometry	[86]
	Controlled release re-dispersible 3D-printed nanomedicines	Resveratrol, curcumin	Carboxymethyl cellulose sodium, glycerin, water, poly(ε-caprolactone), medium chain triglycerides, polysorbate 80	Feasibility assessment of manufacturing oral solid dosage forms containing two API co-encapsulated in polymeric nanocapsules using SSE; different *in vitro* release profiles were obtained depending on the polymer used, the infill density, and the presence/absence of a channeling agent	[87]
	Immediate-release printlets	Flurbiprofen (15%)	Sodium alginate, mannitol	Evaluation of the effects of pre-crosslinking alginate ink-gel on preventing matrix collapse after drying the printed dosage form	[88]
	Immediate-release printlets	Albendazole	Polyethylene glycol 1500, propylene glycol, poloxamer 188, ultrapure water	Inclusion of nanocrystals within printlets made by SSE and MESO-PP	[89]
	Swallowable printlets with several drug release profiles	Tranexamic acid or paracetamol	HPMC, PVP, SiO_2	Printability assessment of different formulations (particularly their rheological properties) and the impact of structural design and formulation on the quality of printed dosage forms (drug release kinetics, dimensions, mass)	[90]
	Gastric floating delivery system with 8 h sustained-release and immediate and prolonged floating (>10 h)	Clarithromycin	HPMC K15M CR, EC 20, PVP k30, poloxamer 188, carbomer 934P, nano-$CaCO_3$	Evaluation of the effects of a core-shell system made using multi-nozzle SSE 3D printing on the floating time and drug release	[91]

Continued

Table 1. Continued

Formulation type	Formulation details and properties	API	Excipients	Commentaries	Ref.
Swallowable printlets	Gastric floating delivery system	Propranolol hydrochloride (12.5%)	Sodium alginate, hydroxyethyl cellulose, calcium chloride, Tween 85	Formulation of a floating drug delivery system in a single step with coaxial SSE 3D printing using ionotropic gelation of sodium alginate	[92]
	Controlled-release intragastric floating printlets	Furosemide and sildenafil citrate	Polysorbate 80; Gelucire® 48/16	Manufacturing parameters and quality control of 3D printed dosage forms based on EP; the study demonstrated the suitability of testing for dissolution, uniformity of mass, and content uniformity according to EP tests.	[93]
	Controlled-release gastro-floating printlets	Famotidine	HPMC; alpha-lactose monohydrate; microcrystalline cellulose; PVP	The dosage form demonstrated sufficient buoyancy after 10 h	[94]
	Gastroretentive printlets	Niclosamide	Gelucire 50/13	Dosage form made using MESO-PP	[95]
	Gastro-floating printlets	Ricobendazole	Crosslinking ink: water; ethanol; calcium chloride; hydroxyethyl cellulose; Tween®85 Alginate ink: sodium alginate solution	Co-extrusion of crosslinking ink and sodium alginate ink feeds	[96]
Chewable printlets	Pectin-based drug-loaded gummies	Simethicone	Pectin, sorbitol, citric acid anhydrous, maltitol	Formulation of sugar-free gummy dosage form for adults and children	[97]
	3D-printed chewable medicines containing amino acids	Isoleucine or valine or citrulline	Sucrose, pectin, maltodextrin, water, maltitol, flavorings (lemon, vanilla, peach), colorants, citric acid	This study evaluated the efficacy and acceptability of 3D-printed drugs (made in a hospital setting) vs. conventional compounded medicines in six children; the printed drugs were well-accepted and displayed improved adherence	[98]
	Emulsion gel for solid dosage forms (immediate release)	Fenofibrate	Formulation 1: Water, soybean oil, Maisine® CC, stearic acid, silica suspension, Methocel™ A4M, Methocel™ E4M, Ac-Di-Sol SD-711 (croscarmellose sodium) Formulation 2: Water, soybean oil, Maisine® CC, Tween 85, stearic acid, silica suspension, Methocel™ A4M, Ac-Di-Sol SD-711 (croscarmellose sodium)	This study evaluated a lipid-based formulation within an emulsion gel stabilized with solid particles and a surfactant; the aim was to develop a formulation adapted for poor water-soluble API for SSE 3D printing	[99]
	Formulation of gastro-resistant chewable printlets from enteric omeprazole pellets	Omeprazole (7 mg)	Formulation 1: omeprazole powder, carboxymethyl cellulose, carrageenan, xanthan gum, sodium bicarbonate, glycerol, liquid sweetener, essence, purified water Formulation 2: omeprazole pellets, gelatine, carrageenan, xanthan gum, liquid sweetener, essence, lemon juice, purified water	Comparison of formulation 1 (3D-printed hydrogels with dissolved omeprazole powder) vs. formulation 2 (3D-printed hydrogels loaded with gastro-resistant omeprazole pellets); both demonstrated appropriate properties for 3D printing (especially rheological properties) and conformed with pharmacopeia specifications for content and mass uniformity; formulation 2 exhibits high gastro-resistance	[100]
	Immediate-release printlets for pediatric use	Isoniazid	Corn starch, distilled water	Development of a pediatric-friendly formulation in low-resource settings	[101]

Continued

Table 1. Continued

Formulation type	Formulation details and properties	API	Excipients	Commentaries	Ref.
	Immediate-release printlets for pediatric use	Amlodipine besylate	D-mannitol, maltitol, carboxymethyl cellulose sodium type 800 mPa/s, sodium starch glycolate type lippin, sucralose, methylparaben, soybean oil, anhydrous citric acid, sodium citrate, FD&C yellow n°5	Evaluation of the feasibility of SSE 3D printing hospital preparations for children	[102]
Chewable printlets	Immediate-release gummy chewable printlets for pediatrics	Propranolol hydrochloride	Sodium carboxymethyl starch; gelatin; carrageenan; γ-aminobutyric acid	Evaluation of different gum formulations; gelatin improves printability; carrageenan improves thermal stability and disintegration rate of dosage forms	[103]
Polypill (printlet)	pH-responsive polypills for delayed drug release	Bovine serum protein	Carboxymethyl chitosan, sodium alginate, PEGDA, TPO	Development of a dosage form for API release, modified by modulating the carboxymethyl chitosan/sodium alginate ratio and the filling density using SSE 3D printing	[104]
Swallowable films	Swallowable films with several modified drug release profiles	Hydrochlorothiazide	Copolymer PVA/PVAc	Evaluation of five PVA/PVAc copolymers with different ratios of PVA to PVAc monomers to adjust API release rate	[105]
	Immediate-release printlets	Loratadine	Cellulose; manitole; CMS-Na; PVP	Preparation of orodispersible printlets containing water-insoluble and thermally unstable drugs	[106]
	Immediate-release swallowable films	Eucalyptus extract	Tween 80, esters of polyglycerol and stearic acid, Eumulgin SMO 20, polyethylene oxide	Formulation of a stable aqueous nanoemulsion based on modified lipophilic eucalypt extract applicable in the SSE 3D printing process, without losing the antimicrobial activity of the original eucalyptus extract.	[107]
	Sustained release swallowable films	Triamcinolone acetonide	Carboxymethyl cellulose 4000, tetraethyl orthosilicate 98%, pluronic P123	Feasibility assessment of producing pharmaceutical films using a hydrophilic ink containing mesoporous silica with nanostructured pores as a drug carrier for hydrophobic API	[108]
	Films with four different structures based on carboxymethyl cellulose ink from durian rind wastes	Theophylline	Carboxymethyl cellulose derived from durian rind wastes	The aim of this study was to assess the recyclability of agri-food waste (durian rind) as an excipient used in the manufacture of films by 3D printing	[109]
	Immediate-release films of nano-piroxicam via supercritical carbon dioxide technology	Nano-piroxicam (7.5%)	HPMC, Tween 80, eau purifiée, glycerol	The aim of the study was to produce a printable ink that stabilizes API nanoparticles to conserve API original polymorph	[110]

Continued

Table 1. Continued

Formulation type	Formulation details and properties	API	Excipients	Commentaries	Ref.
Orodispersible dosage forms	Immediate release printlets from emulsion gels.	Fenofibrate	Capmul MGM EP, Captex 355 EP/NF, Kolliphor EL, purified water, Methocel A4M, Ac-Di-Sol SD-711	Quality assessment of SSE additive manufacturing of lipid-based emulsion gels for poorly water-soluble drugs; printlets that disintegrate within 3 min are considered orodispersible	[111]
	Immediate release printlets	Hydrochlorothiazide	Lactose monohydrate, croscarmellose sodium, PVP, flavoring essence	Comparative study of the suitability of the molding for SSE 3D printing to produce pediatric dosage forms	[112]
		Carbamazepine	Ac-Di-Sol; Kollidon® 30; lactose monohydrate; sucralose; water	Development of small dosage forms (mini-tablets) for pediatric use	[113]
	Orodispersible films	No API used	HPMC; PVA; glycerol; sodium starch glycolate; porogen agents (Aeroperl® 300, Fujisil®, Syloid® 244 FP, Syloid® XDP 3050, Neusilin® S2, Neusilin® US2, and Neusilin® UFL2)	Multi-layered films with porous structures used as substrates for inkjet printing	[114]
		No API used	Maltodextrin; sorbitol; hydroxyethyl cellulose; purified water	Evaluation of different drying times on the properties of orodispersible films made by additive manufacturing	[115]
	Fast-disintegrating tablets	Phenytoin sodium	HPMC E15; sodium starch glycolate	Feasibility assessment of manufacturing fast-disintegrating tablets via SSE that were filled in dosing syringes	[116]
Others dosage forms					
Mucoadhesive films	Mucoadhesive buccal films	Estradiol	D-sorbitol; polyoxyethylene sorbitan monooleate; acetonitrile; glycerin; gelatin; polyethylene glycol; hydroxypropyl cellulose; transcutol P oil.	Different release rates observed depending on the infill pattern (rectangular, honeycomb, and plain); plain infill had the lowest drug release rate; rectangular infill had the highest drug release rate	[117]
	Mucoadhesive films	Apigenin	Ethanol; water; carboxyvinyl polymer; poloxamer; HPMC	Development of apigenin-loaded printed films to prevent carcinogenesis in patients suffering oral leukoplakia	[118]

Continued

doi: 10.36922/ijb.4063

Table 1. Continued

Formulation type	Formulation details and properties	API	Excipients	Commentaries	Ref.
Suppositories or ovules	Suppositories made with laponite-alginate hydrogel	Methylene blue as the drug model	Laponite; alginate	Feasibility assessment of manufacturing suppositories using SSE, with post-printing API loading via adsorption	[119]
	Suppositories for local multidrug delivery	Tofacitinib citrate; budesonide	Lauroyl macrogol-32 glycerides (Gelucire® 44/14); coconut oil; N,N-dimethylacetamide	Poor water-soluble drugs; good self-emulsification; printing temperature (29°C) close to ambient temperature; an evaporative air cooler placed in front of the printer to ensure printing consistency	[120]
	Suppositories for local drug delivery	Infliximab	Gelucire® 44/14 or Gelucire® 48/16; coconut oil; purified water	Successful printing of well-defined suppositories containing biological, thermosensitive, and hydrosensitive API	[121]
	Vaginal ovules	Metronidazole	Polycaprolactone; Gantrez™-AN119	Disc- and mesh-shaped intravaginal devices developed for the sustained release of antibiotics; the aim was to reduce the frequency of administration	[122]
	Vaginal mucoadhesive ovules	Pirfenidone	Sodium alginate; HPMC; aqueous solution: HEPES, $CaCl_2$ crosslinker	Ovules demonstrated sustained release with mucoadhesive properties	[123]
Medical devices	Skin patches for wound application	Not available	Corn starch; β-glucan water suspension; glycerol; distilled water	Extrusion over an alginate support of the corn starch-based ink for wound treatment by SSE	[124]
	3D-printed silicone scaffolds for sustained release (intravaginal use)	Metronidazole	Mixture of vinyl-terminated polydimethylsiloxane (70%) and vinyl-methyl-modified silica (30%); methylhydrosiloxane-dimethylsiloxane copolymer, trimethylsiloxane	Successful sustained release (14 days) of metronidazole contained within a 3D-printed silicone-based scaffold for intravaginal use	[125]
	Anti-infective urinary catheter	Secnidazole	PVA; sodium alginate; methylcellulose; polyethylene glycol	Characterization of stability and suitability of secnidazole-impregnated PVA-based urinary catheter; the device demonstrated anti-biofilm activity	[126]

Abbreviations: EC, ethylcellulose; EP, European Pharmacopeia; HPMC, hydroxypropyl methylcellulose; MESO-PP, melting solidification printing process; PEGDA, polyethylene glycol diacrylate; PVA/PVAc, poly(vinyl alcohol-co-vinyl acetate); PVA, polyvinyl alcohol; PVP, pyrrolidone; TPO, Diphenyl (2,4,6-trimethylbenzoyl) phosphine oxide.

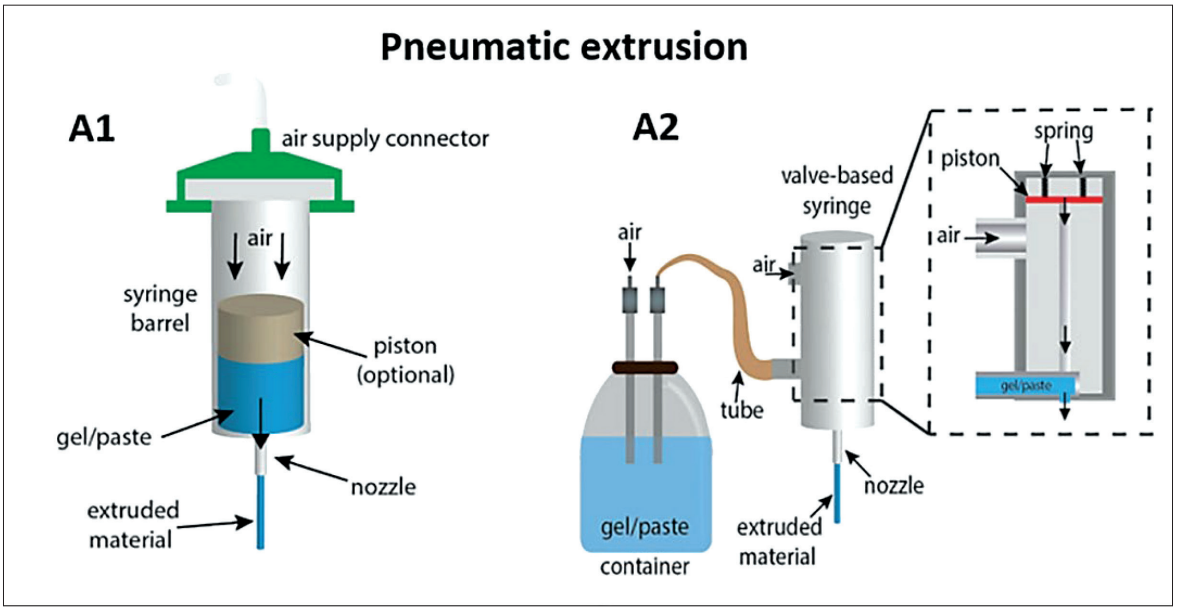

Figure 2. SSE 3D printing extrusion mechanisms: pneumatic extrusion including (A1) valve-free and (A2) valve-based. Adapted with permission from ref.[80] Copyright © 2024 Elsevier.

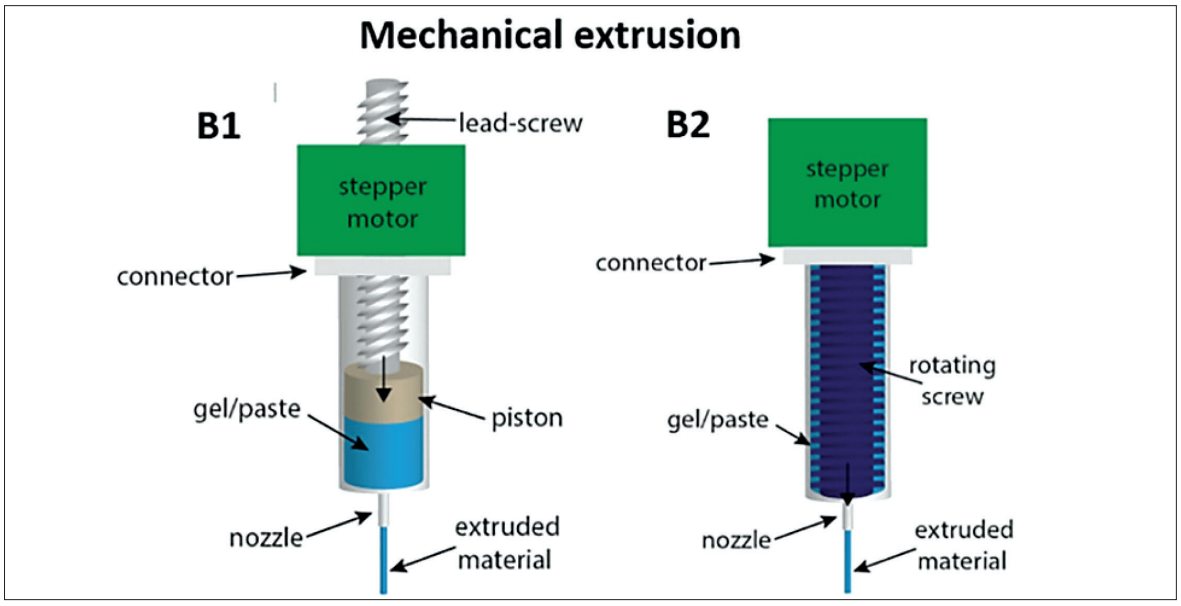

Figure 3. SSE 3D printing extrusion mechanisms: mechanical extrusion including (B1) piston- or (B2) screw-driven. Adapted with permission from ref.[80] Copyright © 2024 Elsevier.

like the anti-infective drug-loaded urinary catheter made by Archana et al.[126] The articles reviewed report different drug release kinetics (immediate or controlled release), demonstrating the versatility of SSE for producing variants of the same drug. Except for orodispersible forms, which are primarily advantageous for their rapid release of APIs, controlled release kinetics are found among all the solid oral dosage forms (Table 1), including chewable formulations. For example, Rouaz-El Hajoui et al.[100] developed a gastro-resistant form produced by SSE from a hydrogel loaded with pellets containing an API sensitive to the stomach's acidic pH. This example demonstrates that the formulation of a chewable form is compatible with modified release kinetics.

Figure 4. Pictures of 3D-printed gummies. Adapted with permission from ref.[100] Copyright © 2023 The Authors. Published by Elsevier B.V.

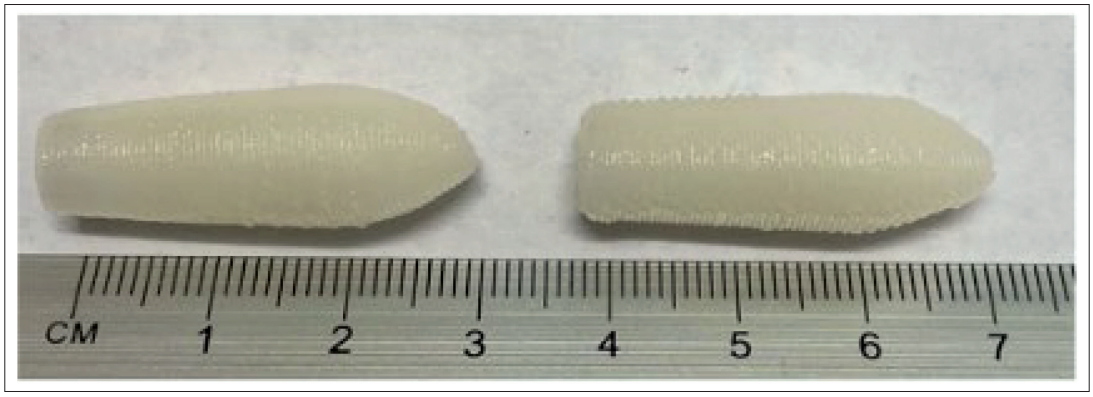

Figure 5. Picture of 3D-printed suppositories. Adapted from ref.[85]

2.2.4. Rheological properties

The rheological properties of the material are central to the successful execution of the SSE process and to obtaining finished products of the desired quality.[80] A notable prerequisite for successful printing is that the raw material should ideally be shear-thinning[80,110,85,108,118] (i.e., the viscosity of the material decreases as shear strain increases) and without thixotropy[80,85,127,128] (i.e., the viscosity of the material should not decrease under constant stress over time). The absence of thixotropy is important because the viscosity of the material should not be time-dependent, and the successive layers should recover their initial structure within a few seconds after extrusion.[80,85,127,128] A thixotropic material is likely to have a viscosity that decreases as printing progresses, causing the dosage form to collapse. Shear-thinning behavior ensures uniform extrusion with smooth extrudates,[85] preventing nozzle clogging. Conversely, if the viscosity is too low, there is a risk of collapse of the dosage form.[81,118] Therefore, it is necessary to formulate a semi-solid raw material with appropriate viscosity, neither too high to impede extrusion nor too low to prevent collapse. The viscosity of the material should allow extrusion only when pressure is applied and ensure a consistent extrusion rate so that the dosage form obtained meets specified

requirements (e.g., API content, release kinetics, etc.).[80] Rheological properties also influence the nozzle and print bed temperatures: higher viscosity typically requires higher printing temperatures for extrusion. Compared to FFF, SSE has two main advantages: the required temperatures are lower, generally between ambient temperature and 80°C[81] (Table 1); and the printing rate is generally faster. For instance, Hu *et al.* reported that 50 dosage forms can be printed in 13–15 min.[113] To facilitate technology transfer between teams, it is important to translate these rheological properties into force parameters for the printer system. This data allows for the calibration of the printers to obtain consistent results.[129,130] Additionally, it is crucial that the pharma-ink remains stable in terms of its rheological properties in the cartridge before printing, enabling on-demand printing without the need to prepare the pharma-ink each time.

2.2.5. Printheads and nozzle

The nozzle diameter must be sufficiently precise to achieve high resolution for the dosage form, ensuring accurate dosage and API release kinetics while minimizing the risk of obstruction due to the size of the raw material components or the rheological properties of the material.[80,85] Consequently, the mean particle size of the API should be smaller than a few hundred micrometers.[80]

The number of print heads determines the range of printed products that can be produced by the machine. Each nozzle can only handle one filament. Machines with at least two nozzles are particularly advantageous for multi-layer printed products (also known as polypills). These machines can alternate between layers containing two different APIs or between an API and an excipient. There are several examples of polypills produced using SSE technology.[131,132]

2.2.6. Extrusion pressure

Pressure is a critical parameter in the SSE process.[81] The pressure applied to the top of the syringe containing the raw material increases progressively until a certain threshold is reached, at which point the material begins to be extruded. The extrusion rate is directly correlated with the pressure applied, making it essential for this pressure to remain constant with only slight fluctuations to ensure the quality of the finished product.[81] Poorly controlled pressure would lead to inconsistencies in material flow, potentially affecting API content. Therefore, pressure must be accurately measured using sensors integrated into the 3D printer. These sensors can detect process problems, e.g., a clogged nozzle would be signaled by an unexpected increase in pressure or the presence of air in the syringe that would be indicated by an unexpected drop in pressure.[81] In general, pressure measurement can be used to establish correlations between pressure and critical quality attributes of the finished product (e.g., mass, dimensions, etc.).[81]

2.3. Post-processing steps

Post-processing is an optional stage in the 3D printing process. For SSE, when post-treatment is necessary, it is almost always drying (Table 2). Drying involves removing water or other volatile liquids from a product, either in a free or adsorbed state. This step is often critical depending on the quality attributes of the dosage form.[80] The need for drying depends on material parameters, i.e., the quantitative and qualitative composition of the pharma-ink, as well as the thermal and rheological properties of the material. It also depends on the printing temperature.

Drying influences the residual moisture content, which affects various parameters of the product. For example, the limits of residual moisture content for orodispersible films are in the range of 3–6%.[133] The moisture content within orodispersible films influences their chemical and microbiological stability, as well as properties like stickiness, tensile strength, flexibility, and disintegration time.[115] Microbiological stability is a particularly important parameter, given the transition from a semi-solid gel containing a significant amount of water to a solid oral dosage form, where the water activity must be reduced to less than 0.6 to minimize the risk of biological contamination.[111,134]

In the reviewed articles, three possibilities regarding post-processing are noted: (i) obtaining a finished product without post-processing[83,84,89,93,95,100,101,103,107,120,121]; (ii) drying is necessary (Table 2); and (iii) other post-treatment operations, besides drying, are necessary, such as crosslinking the printed parts,[104,123] adsorption of the active substance[119] or coating.[126]

The most common drying method is open-air drying at room temperature, with drying times generally between 12 and 48 h. Drying is also carried out in an oven (sometimes under vacuum), at low temperatures (20–80°C), for periods ranging from a few hours to 24 h. The printing bed is sometimes used to dry printed materials, with temperatures of 60–70°C for 10 min to 2 h. Desiccators or freeze-drying are sometimes used. Some studies combined different drying techniques. Falcone et al. used a combination of open-air drying, a low-power microwave (200–400 W), an oven, and a desiccator.[92] Except for freeze-drying, most drying techniques are simple and do not require complex equipment, making them feasible to use with SSE in hospitals. However, these methods generally require several hours to complete.

Table 2. Drying conditions

Drying method	Temperature	Time	Commentaries	Ref.
(i) Air-dried at 22.2°C for 48 h (ii) Freeze-drying at -80°C for 15 min; 15 h vacuum			Long drying times can increase the risk of recrystallization	[110]
Freeze-drying	-80°C	Overnight	Freeze-drying creates a porous network accessible to water; hydration of the dosage form produces a thick gel, enabling longer active pharmaceutical ingredient (API) release	[85]
	-80°C	20 h	The drying step follows an ionic crosslinking step	[104]
Air-dried	Room temperature	24 h		86
	Room temperature	Until obtaining a constant weight		88
	Room temperature	48 h		108
	Room temperature	6 h		112
	Room temperature	Overnight		113
	Room temperature	Overnight		118
	Room temperature	24 h	Drying is necessary for the evaporation of acetone	[122]
	19.2 ± 0.9°C	48 h		87
	Ambient temperature	12 h		90
Oven-dried	37°C	24 h	Three drying conditions were tested: 70°C for 12 h, 40°C for 16h, and 37°C for 24 h; 37°C for 24 h demonstrated the easiest removal from printlet supports	[124]
	55°C	No data	The drying step is followed by dip-coating of the printed parts with 2% Eudragit E100 in methanol in order to prevent humidity uptake	[126]
(i) Oven-dried at 50°C for 4 h; then stored in the desiccator at 20°C for 24 h or refrigerated at 4°C for 72 h (ii) Oven-dried at 50°C for 24 h			Printlets dried at 50°C for 4h, followed by refrigeration at 4°C for 72 h demonstrated the highest sustained API release after 24 h and 14 days.	[125]
Oven-dried	50°C	4 h		91
	80°C	2 h		
Oven-dried	50°C	24 h		94
Vacuum oven drying	40°C	2.5 h	Dosage form cracking at > 40°C	[111]
Ventilated oven-dried	40°C	12 h		82
(i) Air-dried at room temperature (ii) Microwave 200 W for 15 min (iii) Microwave 300 W for 10 min (iv) Microwave 400 W for 5 min (v) Oven-dried at 40°C for 7 h (vi) Vacuum drying at room temperature for 6 h (vii) Desiccator overnight				92

Continued

doi: 10.36922/ijb.4063

Table 2. Continued

Drying method	Temperature	Time	Commentaries	Ref.
Drying is mentioned but without specific data about the process				96
				97
(i) Vacuum oven	22°C	Overnight	Vacuum oven at 400 mbar pressure	[99]
(ii) Air-dried	Room temperature	24 h		
In-process drying with a heated bed	60°C	2 h		102
In-process drying with a heated bed	70°C	10 min		114
In-process drying with a heated bed	70°C	41–114 min post-printing		115

3. Discussion

3.1. Challenges

Based on the literature review on the SSE process for AM of drugs, it is evident that the SSE process is currently the most suitable and mature technology for manufacturing compounded preparations. The SSE process enables the manufacturing of many different products, allowing for easy product changeovers. Additionally, it offers easy-to-use technology with equipment and excipients adapted to clinical use. Finally, SSE makes it possible to design a wide range of dosage forms tailored to each patient's needs, mainly for oral administration, with immediate or modified release kinetics. Therefore, this technology could significantly benefit patients whose medical needs are unmet by existing industrial therapies or conventional compounding methods. Currently, the design and production of compounded medicines are subject to various constraints, which can be classified into three categories: (i) scientific and technical aspects, (ii) regulatory aspects, and (iii) personnel-related aspects (i.e., involved in design and manufacturing).[135]

3.1.1. Scientific and technical aspects

According to Pluta,[135] the scientific and technical aspects of compounded medicines encompass several critical factors: (i) formulation quality (i.e., ensuring the dosage form meets the patient's needs and is stable), (ii) formulation calculations (e.g., renal clearance, the half-life of the API, stability data, etc.), (iii) operating procedures, and (iv) post-preparation steps (e.g., control preparation, pharmacopeial standards, etc.). The SSE process introduces several technical challenges to these factors. The first challenge is related to the CAD, which is the model on which printed medicines are based. In particular, 3D modeling provides the flexibility to produce different dosages by modifying parameters, such as size or filling density. However, the resolution of the infill pattern is less precise compared to FFF, and the extruded gel tends to be more cohesive. This can make it difficult to obtain a porous dosage form, potentially affecting the release kinetics.

As a result, the computational aspects of compounding become more complex, with mathematical modeling playing a crucial role in the drug development process. This complexity highlights the importance of adopting a Quality by Design (QbD) approach, which integrates comprehensive modeling aspects and the use of experimental designs in drug development. In parallel, the formulation must not only be compatible with these numerical aspects but also satisfy rheological constraints. As highlighted in the technical aspects of SSE, formulations for drug production can be highly diverse and complex. In this context, the development of formulations using

SSE should be based on mathematical modeling, enabling adjustments of numerous variables to achieve desired outcomes, such as specific dosages and targeted drug release kinetics. Consequently, adopting the QbD approach is a key to the success of SSE in drug manufacturing. This approach involves developing a control strategy defined in ICH Q10 as "a planned set of controls, resulting from the understanding of the product and the manufacturing process, which ensures the performance of the process and the quality of the product."[136] The control strategy should ideally favor non-destructive quality controls conducted "in line" during the manufacturing process. Such controls are technically through the use of process analytical technology (PAT). PAT is defined in ICH Q8(R2) as "a system of design, analysis, and control of production through the in-production measurement of critical quality and performance attributes of raw materials and materials in use, with the aim of ensuring the quality of the finished product."[137] In essence, PAT enables the design, analysis, and control of pharmaceutical manufacturing processes by measuring process variables, ensuring that they conform to the parameters set by mathematical modeling and that the quality of the finished product meets the expected standards. The key advantage of PAT in the context of SSE is its ability to provide non-destructive controls. This is particularly valuable as the batches produced for each patient are often very small in size and may not be adequate for statistical analysis of the batch by representative sampling. For instance, in the SSE process, pressure sensors integrated into printers can measure extrusion pressure, facilitating control of the drug's quality attributes (e.g., dose, size, and weight).[81] On-line near-infrared spectroscopy can be employed to quantify API content.[138] Likewise, integrating an in-built balance within 3D printers allows for precise control over the mass of medicines manufactured.

3.1.2. Regulatory aspects

From a regulatory standpoint, current regulations in both Europe and the USA do not require compliance with GMP,[135,139] as they are designed to regulate the mass manufacturing of standardized products. Hospital preparations are typically made in small batches for a small number of patients. This approach allows for the control of associated risks and ensures the maintenance of an appropriate level of quality. However, the FDA and the French Medicines Agency have recently revised their quality recommendations, raising the required standards closer to those of GMP.[49]

As a result, batch-release controls for compounding are not required. However, the 3D printing of drugs at the point of care may necessitate regulatory changes. AM enables the production of highly sophisticated dosage forms with highly complex release kinetic profiles (e.g., different kinetics for different APIs) through a process based on digital technology. The benefit for patients lies specifically in the precision and flexibility of the products manufactured, which can vary significantly from one patient to another. Given these factors, it would be surprising if release quality controls were not implemented for printed drugs, as the risks to patient safety and drug efficacy are substantial. Therefore, incorporating PAT into 3D printers seems essential.

3.1.3. Personnel

Compounding requires qualified personnel with expertise in technical, scientific, and quality aspects. Drug AM via SSE will require in-depth training to fully understand and master the technology. Specific training on the machinery (particularly its use, control, cleaning, and maintenance) should be provided to all staff involved in this process. In addition, staff should also comprehensive training on slicing software that enables treatment customization to ensure the quality and safety of the drugs produced.

3.2. Manufacturing scenarios

Currently, "traditional" compounded medicines are manufactured at the point of care using pharmacy or hospital staff and equipment (and regulated by section 503A of the Federal Food, Drug, and Cosmetic Act). Bearing in mind what has been said above, the crucial question is whether hospital premises and the staff who work there can manufacture these SSE-printed medicines, guaranteeing their safety, efficacy, and quality. We can identify the following players involved in the development and production of printed dosage forms.

The structure responsible for drug development follows a Quality by Design approach, ensuring the development of the drug formulation, the design of the 3D digital model at the origin of the dosage form, and different calculations and mathematical modeling allowing the prediction of critical quality attributes of the product from input variables. This structure will thus oversee defining and validating the production procedure, ensuring the quality of the process, its reliability, and its performance. In the remainder of this text, this structure will be referred to as "structure (a)."

The structure responsible for manufacturing the intermediate pharma-ink (the gel or paste placed in a cartridge or syringe, mixture of drug and excipients). In the remainder of this text, this structure will be referred to as "structure (b)."

The structure responsible for 3D printing is the pharma-ink, the post-processing, and the batch release.

We have seen that generally post-processing consists of a simple drying operation in the open air or in an oven. Freeze-drying is probably the most sophisticated drying process found in the literature for SSE, but it remains little used (see Table 1). This is why it is very likely that the structure that prints the drugs is the same as that which carries out post-processing. In the remainder of this text, this structure will be referred to as "structure (c)."

We can identify different scenarios for pharmaceutical 3D printing at the point of care, which are being considered by regulatory agencies such as the FDA[140] or in other works such as Jørgensen et al.[141]

Development and production at the point of care: In this first scenario, the hospital or pharmacy the hospital would bring together the activities of structures (a), (b), and (c). Printed medicines would therefore be developed, manufactured, and distributed in the same way as other compounded medicines made within hospitals. The pharma-ink would be prepared at the point of care before printing the medicines. This would imply a certain number of constraints for hospitals, like maintaining qualified personnel for ensuring the development of printed dosage forms as well as maintaining the equipment in a state of qualification that ensures its operability and performance.

Point of care ensures only manufacturing of the final product: the second scenario separates the development and production of the pharma-ink from the production of the finished product between two different structures. In this case, we could imagine that a pharmaceutical company would bring together the activities of structures (a) and (b), and oversee the research and development (R&D) for printed medicines, in collaboration with health authorities, 3D printer manufacturers, and hospitals. Hospitals would only ensure that they manufacture the finished product. A case study carried out by Seoane et al. and published in 2023 studies the feasibility of decentralized production of printed medicines in hospitals based on 3D printer pharma-ink manufactured by a third party.[138] On this basis, a pharmaceutical company could take on the task of manufacturing the pharmaceutical ink and distributing it to hospitals. The commercialization of the pharma-inks may require the need for new regulations, as the pharma-in is not a final medicine nor a raw material.

Outsourced development and manufacturing: An alternative business model to the production of medicines in a hospital or pharmacy would be one where the hospital outsources the development and manufacturing of the printed drug to a third party that would be structures (a), (b), and (c) all in one. The latter is a traditional industrial manufacturer subject to GMP or another hospital that has the capacity to develop and manufacture the printed drugs.

These scenarios are likely to coexist, depending on the hospitals' ability to manage the development and manufacture of printed drugs. For a hospital, the use of a third party for the development and/or manufacture of pharmaceutical inks should be based on a risk assessment that will determine if the hospital can perform these activities while ensuring the quality, safety, and efficacy of the printed medicine.

3.3. Applications of 3D printing technology in the compounding unit

Chronic conditions have been estimated to affect 10–30% of children, depending on the criteria used.[142] Examples of chronic diseases include asthma, cystic fibrosis, HIV, congenital heart disease, diabetes, attention-deficit/hyperactivity disorder, depression, and cancer. For these patients, as with adults, personalized medication based on genetic and physiological parameters is increasingly feasible. However, this often requires adjustments to the treatment, risking non-adherence or sub/supra therapeutic effects. In many cases, it necessitates adapting the form and strength of a licensed medicine.[143] For example, in a phase I–II trial evaluating metronomic chemotherapy in patients with a relapsed or refractory Wilms tumor (MetroWilms), there was a need to administer adjusted doses of cis-retinoic acid or etoposide. The dosage forms in the market did not accommodate these adjustments, and patients were even required to drink an injectable solution of irinotecan due to the lack of an oral form for the product.[144] Changing the route of administration of a medicinal product is not a recommended practice, as it may have harmful consequences for pediatric patients.[30] Indeed, these practices may alter the efficacy and safety parameters of the medication by modifying its absorption characteristics, stability, and palatability.[31–33] For instance, in the MetroWilms clinical trial, the etoposide injection was unsuitable for children because it contained alcohol and had an unpleasant taste, which significantly reduced patient compliance.

To reduce this practice, hospital pharmacies are currently producing various capsules and liquid forms to meet patient needs with specific doses.[145] As described by Curti et al., compounding does not have high dose accuracy, which is a problem for drugs with a narrow therapeutic index.[146] With 3D printing, it is possible to manufacture medicines in more accurate doses for patients based on their weight, age, and specific needs.[147] The accuracy and flexibility of 3D printing have been studied for low-dose formulations for neonates[82] and high-dose medications to reduce the number of tablets required.[148] For certain anticancer drugs or medications used in cardiology with

a narrow therapeutic index, 3D printing could provide a viable solution.

3D printing can also improve patient compliance by reducing the number of tablets to be taken. For example, polypills that combine multiple APIs with different release profiles into a single dosage form offer a practical solution. An example is a polypill that incorporates nifedipine and captopril, both used to treat arterial hypertension in patients with type II diabetes, along with glipizide, which is used for the treatment of type II diabetes.[131] Incorporating all three drugs into a single solid dosage form would be highly beneficial in treating diabetic patients; however, the formulation would require the distinct release profile of each drug. Additionally, polypills that combine, for example, an antiemetic with an oral anticancer drug or two antibiotics in one dose could improve compliance, which is a major factor in managing pediatric chronic diseases.

One of the significant advantages of 3D printing is its ability to enhance adherence by developing novel dosage forms that are easy to administer and designed with child-friendly formulations.[149] These can include different flavors and color profiles,[80] addressing one of the major challenges in pediatrics, i.e., making medicines acceptable to children who are often reluctant to swallow bitter tablets. For example, BACTRIM® (40 mg/mL trimethoprim + 8 mg/mL sulfamethoxazole, oral suspension) and DALACIN® (75 mg/5 mL clindamycin granules for suspension) are marketed in liquid oral form but are often poorly tolerated due to their unpleasant taste and large volumes required for administration.[150,151] This can lead to non-compliance, increasing the risk of opportunistic diseases or the development of antibiotic resistance.

3D printing can make oral dosage forms more appealing for children by producing tablets with eye-catching appearances and favorable palatability. Some studies have produced chewable dosage forms, while others focused on taste-masking by adjusting excipients and incorporating pleasant flavors, which can increase adherence to treatment.[42] For example, Karavasili et al. produced pediatric-friendly chocolate-based dosage forms of paracetamol and ibuprofen, suggesting the possibility of encapsulating the drug paste within a matrix that masks its unpleasant flavor, as in the case of some bitter-tasting drugs.[80]

Following these strategies to make medicines more pleasant for children, 3D-printed gummies were fabricated with different shapes (heart, bear, and disc) and colors using mixtures of gelatin, carrageenan, xanthan gum, and sweeteners. Additionally, gelatin and hydroxypropyl methylcellulose (HPMC) hydrogels were used to prepare gummies with lamotrigine.[39] The viscosity and strength of the formulation were easily modified by varying the amounts of the two main excipients, HPMC and gelatin. Moreover, the production of dispersible film with personalized doses, such as hydrocortisone, can enhance dose accuracy while improving patient compliance.[152]

An important benefit of AM in drug manufacturing is the possibility to tailor treatments to individual patient requirements and adapt drug release profiles as needed. For example, ranitidine hydrochloride was used as a model drug, and it was observed that the addition of corn starch among the components resulted in a greater extended release of the drug. [153] Similarly, a study prepared immediate-release levetiracetam tablets to treat epilepsy, where the dose in pediatric patients is subsequently increased over time.[134] This flexibility offered by AM enables tablet preparation that can be easily modified to follow the required dosage regimen.[154] In France, for example, the preparation most frequently made in hospitals is an immediate-release melatonin capsule for various uses, such as alleviating stress before imaging exams or aiding sleep during hospitalization.[155] However, this formulation often requires adjustments (i.e., frequently opened) before administration, which can compromise the stability of the drug.

An alternative approach to enhance compliance involves preparing solid lipid tablets based on emulsion gels.[111] Unlike previous approaches where blends of lipid excipients are directly printed, these formulations are printed using preformed oil-in-water (O/W) emulsions loaded with the poorly soluble drug fenofibrate. The resulting formulations disintegrated in less than 15 min. Besides printing the tablets at room temperature, which is particularly useful for thermolabile compounds, these formulations are effective for poorly water-soluble drugs, as they help improve their oral bioavailability. The low temperatures required for material extrusion make this technique suitable for printing proteins and other thermosensitive drugs.[80]

Due to the lack of commercially available tacrolimus suppositories, these are commonly compounded in hospital pharmacy settings using a molding technique, which requires several steps and long periods of solidification. Suppositories loaded with the immunosuppressant tacrolimus, which are commonly used in patients with therapy-resistant inflammatory bowel disease (IBD), have already been prepared.[156] Using SSE and a suitable combination of lipid excipients, self-supporting suppositories were directly printed without the aid of molds. Moreover, the suppositories were fabricated in various sizes to accommodate patient comfort and dosage requirements. They were prepared using a mixture of Gelucire 44/14 or Gelucire 48/16 and coconut oil, the latter served as a plasticizer. Both pharma-inks displayed

good printability without the need for solid-phase carriers or a cooling system on the build plate. These active substances, for which pharmacies already produce various preparations, are excellent candidates for the approach.

The application of 3D printing in pharmaceutical manufacturing minimizes the need for excessive excipients. The two major components of a 3D-printed tablet or dosage form are the polymer matrix and drug component. Hence, the use of 3D-printed dosage forms for disease treatment reduces the risk of unwanted side effects and enhances therapeutic efficacy.[157] Personalized medicine demands tailored treatments, which can be provided by compounding. Besides an individualized dose, other specific patient needs, such as sensory processing disorders, food allergies, and dietary needs, can be accommodated by compounding.[158]

Due to their ease of administration, absence of toxic excipients, improved palatability, and flexible dosing, 3D printing has demonstrated its significant value across various pharmaceutical applications. 3D-printed tablets can be produced to avoid swallowing issues (chewable tablets), with different release profiles (e.g., immediate or controlled release), unique features (e.g., high drug loads), and better palatability that can be tailored to individual patient needs.[80]

Despite the technological challenges, several teams have successfully addressed these issues in real-world applications, particularly focusing on rare diseases with low therapeutic indices. This approach optimizes treatment effectiveness while reducing undesirable effects.[131,134,159] Although current technology exhibits limitations with regard to its applications, enhancements in printing velocity and the concurrent utilization of multiple printheads are expected to improve the quantity of material that can be produced.

In the forthcoming years, the capacity to optimize these parameters will prove pivotal in determining whether the focus remains on rare diseases, where the demand is high, or shifts to more prevalent diseases with similarly high demand. Nevertheless, the ability to meet the demand will remain a crucial consideration.

4. Conclusion

This review highlights significant advancements in pediatric pharmacotherapy through 3D printing technology. Traditional formulations have long struggled to meet the specific needs of the populations, leading to off-label use and potential safety risks. In contrast, 3D printing, particularly SSE technology, offers promising solutions by enabling the production of customized drug formulations tailored to individual patient needs. This technology addresses critical issues for small-scale production, such as dose accuracy, palatability, and ease of administration, thereby improving adherence and therapeutic outcomes.

The ability to produce polypills with varying release profiles and chewable, taste-masked formulations demonstrates 3D printing's potential to revolutionize medication for conditions requiring precise therapeutic control. Moreover, the flexibility and precision of 3D printing make it an invaluable tool for creating personalized treatments that traditional compounding methods cannot achieve with the same efficiency or safety.

Despite these promising developments, the practical production of these drugs will depend on the pharmacies' and hospitals' ability to manage the risks involved in production, considering the criticality of the drug and the hospital's resources for development and production. Furthermore, the successful integration of 3D printing into routine clinical practice requires ongoing research, as well as clarification of legislation and harmonization between countries. Ensuring the safety, efficacy, and quality of 3D-printed medications will involve robust quality control measures and specialized training for personnel involved in the drug manufacturing process.

The challenges associated with this novel production method include the need for personalization, ease of administration, and long-term patient compliance. It is of paramount importance to monitor patient compliance with these novel drugs, even if initial studies yield favorable feedback indicating that these personalized forms are well adhered to by patients.[98]

In conclusion, 3D printing technology represents a transformative approach to personalized medicine, addressing long-standing formulation challenges and paving the way for safer, more effective, and more acceptable medications. Continued innovation and regulatory support will be essential to fully realize its potential in improving patient care and outcomes.

Acknowledgments

This review was produced as part of the 13th Journée Scientifique du Médicament, organized by the Département de Pharmacochimie Moléculaire (UMR CNRS-UGA 5063) and the Grenoble University Hospital Center (CHUGA). The event, which focused on the 3D printing of medicinal products, was held on June 13, 2024.

Funding

This work was partially supported by Agence Nationale de la Recherche through Labex ARCANE and CBH-EUR-GS (ANR-17-EURE-0003).

Conflict of interest

The authors declare they have no competing interests.

Author contributions

Conceptualization: Thomas Cerveto, Roseline Mazet, Maxime Annereau, Luc Choisnard
Writing – original draft: All authors
Writing – review & editing: All authors

Ethics approval and consent to participate

Not applicable.

Consent for publication

Not applicable.

Availability of data

None.

References

1. Rocchi F, Tomasi P. The development of medicines for children. Part of a series on Pediatric Pharmacology, guest edited by Gianvincenzo Zuccotti, Emilio Clementi, and Massimo Molteni. *Pharmacol Res.* 2011;64(3):169-175. doi: 10.1016/j.phrs.2011.01.016
2. O'Brien F, Clapham D, Krysiak K, et al. Making medicines baby size: the challenges in bridging the formulation gap in neonatal medicine. *Int J Mol Sci.* 2019;20(11):2688. doi: 10.3390/ijms20112688
3. Kogermann K, Lass J, Nellis G, Metsvaht T, Lutsar I. Age-appropriate formulations including pharmaceutical excipients in neonatal medicines. *Curr Pharm Des.* 2017;23(38):5779-5789. doi: 10.2174/1381612823666170926122613
4. Nunn T, Williams J. Formulation of medicines for children. *Br J Clin Pharmacol.* 2005;59(6):674-676. doi: 10.1111/j.1365-2125.2005.02410.x
5. Ranmal SR, Cram A, Tuleu C. Age-appropriate and acceptable paediatric dosage forms: insights into end-user perceptions, preferences and practices from the Children's Acceptability of Oral Formulations (CALF) Study. *Int J Pharm.* 2016;514(1):296-307. doi: 10.1016/j.ijpharm.2016.07.054
6. Ivanovska V, Rademaker CMA, van Dijk L, Mantel-Teeuwisse AK. Pediatric drug formulations: a review of challenges and progress. *Pediatrics.* 2014;134(2):361-372. doi: 10.1542/peds.2013-3225
7. Joosse IR, Mantel-Teeuwisse AK, Wirtz VJ, Suleman F, van den Ham HA. Missing data on accessibility of children's medicines. *Bull World Health Organ.* 2022;100(10): 636-642. doi: 10.2471/BLT.22.288137
8. Mfoafo KA, Omidian M, Bertol CD, Omidi Y, Omidian H. Neonatal and pediatric oral drug delivery: Hopes and hurdles. *Int J Pharm.* 2021;597:120296. doi: 10.1016/j.ijpharm.2021.120296
9. Alessandrini E, Brako F, Scarpa M, et al. Children's preferences for oral dosage forms and their involvement in formulation research via EPTRI (European Paediatric Translational Research Infrastructure). *Pharmaceutics.* 2021;13(5):730. doi: 10.3390/pharmaceutics13050730
10. Jîtcă CM, Jîtcă G, Ősz BE, Pușcaș A, Imre S. Stability of oral liquid dosage forms in pediatric cardiology: a prerequisite for patient's safety—a narrative review. *Pharmaceutics.* 2023;15(4):1306. doi: 10.3390/pharmaceutics15041306
11. Batchelor HK, Marriott JF. Formulations for children: problems and solutions. *Br J Clin Pharmacol.* 2015;79(3):405-418. doi: 10.1111/bcp.12268
12. Litalien C, Bérubé S, Tuleu C, et al. From paediatric formulations development to access: Advances made and remaining challenges. *Br J Clin Pharmacol.* 2022;88(10):4349-4383. doi: 10.1111/bcp.15293
13. US Food and Drug Administration. Qualifying for pediatric exclusivity under Section 505A of the Federal Food, Drug, and Cosmetic Act: frequently asked questions on pediatric exclusivity (505A). The Pediatric "Rule," and their Interaction. Q1–Q14: Exclusivity. http://www.fda.gov/Drugs/DevelopmentApprovalProcess/DevelopmentResources/ucm077915.htm.
14. US Food and Drug Administration. Pediatric Research Equity Act of 2003.
15. Regulation (EC) No 1901/2006 of the European Parliament and of the Council of 12 December 2006 on medicinal products for paediatric use and amending Regulation (EEC) No 1768/92, Directive 2001/20/EC, Directive 2001/83/EC and Regulation (EC) No 726/2004.
16. Regulation (EC) No 1902/2006 of the European Parliament and of the Council of 12 December 2006 amending Regulation 1901/2006 on medicinal products for paediatric use.
17. Commission, to the European Parliament, and the Council. 10 years of the EU Paediatric Regulation - State of Paediatric Medicines in the EU; 2017. Accessed April 20, 2021. https://health.ec.europa.eu/system/files/2017-11/2017_childrensmedicines_report_en_0.pdf
18. Kaguelidou F, Ouèdraogo M, Treluyer JM, et al. Développement des médicaments en pédiatrie: défis existants et recommandations. *Therapies.* 2023;78(1): 95-104. doi: 10.1016/j.therap.2022.12.002

19. Vieira I, Sousa JJ, Vitorino C. Paediatric medicines – regulatory drivers, restraints, opportunities and challenges. *J Pharm Sci*. 2021;110(4):1545-1556. doi: 10.1016/j.xphs.2020.12.036

20. Huss G, Barak S, Reali L, et al. Drug Shortages in Pediatrics in Europe: the position of the European Pediatric Societies. *J Pediatr*. 2023;261:113472 doi: 10.1016/j.jpeds.2023.11347

21. Atif M, Sehar A, Malik I, Mushtaq I, Ahmad N, Babar ZUD. What impact does medicines shortages have on patients? A qualitative study exploring patients' experience and views of healthcare professionals. *BMC Health Serv Res*. 2021;21(1):827. doi: 10.1186/s12913-021-06812-7

22. ASHP Expert Panel on Drug Product Shortages, Fox ER, Birt A, et al. ASHP guidelines on managing drug product shortages in hospitals and health systems. *Am J Health-Syst Pharm AJHP Off J Am Soc Health-Syst Pharm*. 2009;66(15):1399-1406. doi: 10.2146/ajhp090026

23. Butterfield L, Cash J, Pham K, Advocacy Committee for the Pediatric Pharmacy Advocacy Group. Drug shortages and implications for pediatric patients. *J Pediatr Pharmacol Ther JPPT Off J PPAG*. 2015;20(2):149-152. doi: 10.5863/1551-6776-20.2.149

24. Metzger ML, Billett A, Link MP. The impact of drug shortages on children with cancer--the example of mechlorethamine. *N Engl J Med*. 2012;367(26):2461-2463. doi: 10.1056/NEJMp1212468

25. Allen HC, Garbe MC, Lees J, et al. Off-label medication use in children, more common than we think: a systematic review of the literature. *J Okla State Med Assoc*. 2018; 111(8):776-783.

26. Balan S, Hassali MAA, Mak VSL. Two decades of off-label prescribing in children: a literature review. *World J Pediatr WJP*. 2018;14(6):528-540. doi: 10.1007/s12519-018-0186-y

27. Koszma EIA, Bispo AJB, Santana IA de O, dos Santos CNODB. Use of off-label medications in a neonatal intensive care unit. *Rev Paul Pediatr*. 2021;39:e2020063. doi: 10.1590/1984-0462/2021/39/2020063

28. Meng M, Lv M, Wang L, et al. Off-label use of drugs in pediatrics: a scoping review. *Eur J Pediatr*. 2022;181(9):3259-3269. doi: 10.1007/s00431-022-04515-7

29. Meng M, Zhou Q, Lei W, et al. Recommendations on off-label drug use in pediatric guidelines. *Front Pharmacol*. 2022;13:892574. doi: 10.3389/fphar.2022.892574

30. Richey RH, Craig JV, Shah UU, et al. MODRIC - Manipulation of drugs in children. *Int J Pharm*. 2013;457(1):339-341. doi: 10.1016/j.ijpharm.2013.08.061

31. Kirkevold Ø, Engedal K. Concealment of drugs in food and beverages in nursing homes: cross sectional study. *BMJ*. 2005;330(7481):20. doi: 10.1136/bmj.38268.579097.55

32. Mercovich N, Kyle GJ, Naunton M. Safe to crush? A pilot study into solid dosage form modification in aged care. *Australas J Ageing*. 2014;33(3):180-184. doi: 10.1111/ajag.12037

33. Kelly J, Wright D. Administering medication to adult patients with dysphagia. *Nurs Stand R Coll Nurs G B 1987*. 2009;23(29):62-68. doi: 10.7748/ns2009.03.23.29.62.c6928

34. Lemarchand C, Bienaymé H, Rieutord A, Abbou S, Annereau M, Bastid J. Dispensing oral temozolomide in children: precision and stability of a novel and ready to use liquid formulation in comparison with capsule derived mixtures. *Pharmaceutics*. 2023;15(12):2711. doi: 10.3390/pharmaceutics15122711

35. ANSM. Monographie Préparation magistrale Amoxicilline 125 mg, 250 mg et 500 mg, gélules réalisées à partir de MPUP d'Amoxicilline trihydratée; 2023. Accessed December 12, 2023. https://ansm.sante.fr/uploads/2023/12/26/20231226-amoxicilline-trihydratee-monographie.pdf

36. EDS Form Group. Aprépitant : avis d'expert sur les formulations extemporanées;2024. Accessed May 16, 2024. https://www.edqm.eu/documents/52006/1912832/Apr%C3%A9pitant%20-%20Avis%20d%E2%80%99expert%20sur%20les%20formulations%20extemporan%C3%A9es.pdf/02dc9885-c08b-e8f3-4554-b46bec47014a?t=1713795079735

37. Otsokolhich M, Annereau M, Bauters T, et al. SIOPE and ESOP recommendations for extemporaneous compounding of oral liquid medicine formulations in paediatric oncology. *EJC Paediatr Oncol*. 2024;3:100163. doi: 10.1016/j.ejcped.2024.100163

38. Annereau M, Toussaint B, Dufaÿ Wojcicki A, Dufaÿ S, Diaz Salmeron R, Boudy V. [2D-3D printing in hospital pharmacies, what roles and challenges?]. *Ann Pharm Fr*. 2021;79(4):361-374. doi: 10.1016/j.pharma.2021.01.002

39. Tagami T, Ito E, Kida R, Hirose K, Noda T, Ozeki T. 3D printing of gummy drug formulations composed of gelatin and an HPMC-based hydrogel for pediatric use. *Int J Pharm*. 2021;594:120118. doi: 10.1016/j.ijpharm.2020.120118

40. Thabet Y, Klingmann V, Breitkreutz J. Drug formulations: standards and novel strategies for drug administration in pediatrics. *J Clin Pharmacol*. 2018;58(S10):S26-S35. doi: 10.1002/jcph.1138

41. Vijayavenkataraman S, Fuh JYH, Lu WF. 3D printing and 3d bioprinting in pediatrics. *Bioengineering*. 2017;4(3):63. doi: 10.3390/bioengineering4030063

42. Lafeber I, Ruijgrok EJ, Guchelaar HJ, Schimmel KJM. 3D printing of pediatric medication: the end of bad tasting oral liquids?—A scoping review. *Pharmaceutics*. 2022;14(2):416. doi: 10.3390/pharmaceutics14020416

43. Sukanya VS, Panigrahy N, Rath SN. Recent approaches in clinical applications of 3D printing in neonates and pediatrics. *Eur J Pediatr*. 2021;180(2):323-332. doi: 10.1007/s00431-020-03819-w

44. Taylor S, Glass BD. Altering dosage forms for older adults. *Aust Prescr*. 2018;41(6):191-193. doi: 10.18773/austprescr.2018.063

45. Gauthier P. État des lieux des besoins en préparation magistrale gériatrique pour la voie orale; 2021. Accessed May 25, 2022. https://dumas.ccsd.cnrs.fr/dumas-03736513

46. Thakar N, Rajab I, Moozhayil S. Extemporaneous compounding of amoxicillin suspensions during national shortage. *Pharmacy Times*. https://www.pharmacytimes.com/view/extemporaneous-compounding-of-amoxicillin-suspensions-during-national-shortage. Published 2023. Accessed April 4, 2024.

47. Watson CP, Tyler KL, Bickers DR, Millikan LE, Smith S, Coleman E. A randomized vehicle-controlled trial of topical capsaicin in the treatment of postherpetic neuralgia. *Clin Ther*. 1993;15(3):510-526.

48. Ashley DD. FDA Revises Hospital and Health System Compounding Guidance to Help Preserve Patient Access to Compounded Drugs; 2021. Accessed May 10, 2024. https://www.fda.gov/news-events/press-announcements/fda-revises-hospital-and-health-system-compounding-guidance-help-preserve-patient-access-compounded

49. ANSM. Bonnes Pratiques de Préparation; 2022. Accessed September 20, 2022. https://ansm.sante.fr/documents/reference/bonnes-pratiques-de-preparation

50. Beer N, Hegger I, Kaae S, et al. Scenarios for 3D printing of personalized medicines - a case study. *Explor Res Clin Soc Pharm*. 2021;4:100073. doi: 10.1016/j.rcsop.2021.100073

51. Warsi MH, Yusuf M, Robaian MA, Khan M, Muheem A, Khan S. 3D printing methods for pharmaceutical manufacturing: opportunity and challenges. *Curr Pharm Des*. 2023;24(42):4949-4956. Accessed January 5, 2023. https://www.eurekaselect.com/article/95074

52. International Organization for Standardization [ISO]. *ISO/ASTM 52900:2021(Fr), Fabrication Additive — Principes Généraux — Fondamentaux et Vocabulaire*; 2021. Accessed November 22, 2022. https://www.iso.org/obp/ui/#iso:std:iso-astm:52900:ed-2:v1:fr

53. Barlier C, Bernard A. *Fabrication Additive : Du Prototypage Rapide à l'impression 3D Ed. 2*. Dunod; 2020.

54. Laverne F, Segonds F, Dubois P. *Fabrication Additive - Principes Généraux*. Editions T.I.; 2016.

55. Gibson I, Rosen D, Stucker B. *Additive Manufacturing Technologies. 3D Printing, Rapid Prototyping, and Direct Digital Manufacturing*. 2nded. Springer; 2015.

56. International Organization for Standardization [ISO]. *Norme internationale ISO/ASTM 52900 Fabrication additive — Principes généraux — Fondamentaux et vocabulaire*. Accessed July 26, 2022. https://www.iso.org/cms/render/live/fr/sites/isoorg/contents/data/standard/07/45/74514.html

57. Auriemma G, Tommasino C, Falcone G, Esposito T, Sardo C, Aquino RP. Additive manufacturing strategies for personalized drug delivery systems and medical devices: fused filament fabrication and semi solid extrusion. *Molecules*. 2022;27(9):2784. doi: 10.3390/molecules27092784

58. Trenfield SJ, Awad A, Goyanes A, Gaisford S, Basit AW. 3D printing pharmaceuticals: drug development to frontline care. *Trends Pharmacol Sci*. 2018;39(5):440-451. doi: 10.1016/j.tips.2018.02.006

59. Pou J, Riveiro A, Davim JP. *Additive Manufacturing*. Elsevier Science; 2021.

60. Dumpa N, Butreddy A, Wang H, Komanduri N, Bandari S, Repka MA. 3D printing in personalized drug delivery: an overview of hot-melt extrusion-based fused deposition modeling. *Int J Pharm*. 2021;600:120501. doi: 10.1016/j.ijpharm.2021.120501

61. Dotchev K, Yusoff W. Recycling of polyamide 12 based powders in the laser sintering process. *Rapid Prototyp J*. 2009;15(3):192-203. doi: 10.1108/13552540910960299

62. Kellens K, Renaldi R, Dewulf W, Kruth J pierre, Duflou JR. Environmental impact modeling of selective laser sintering processes. *Rapid Prototyp J*. 2014;20(6):459-470. doi: 10.1108/RPJ-02-2013-0018

63. ZipDose Technology | Spritam | Aprecia. Accessed December 15, 2022. https://www.aprecia.com/technology/zipdose

64. Melocchi A, Briatico-Vangosa F, Uboldi M, et al. Quality considerations on the pharmaceutical applications of fused deposition modeling 3D printing. *Int J Pharm*. 2021;592:119901. doi: 10.1016/j.ijpharm.2020.119901

65. Seoane-Viaño I, Trenfield SJ, Basit AW, Goyanes A. Translating 3D printed pharmaceuticals: fFrom hype to real-world clinical applications. *Adv Drug Deliv Rev*. 2021;174:553-575. doi: 10.1016/j.addr.2021.05.003

66. Xu X, Awad A, Robles-Martinez P, Gaisford S, Goyanes A, Basit AW. Vat photopolymerization 3D printing for

advanced drug delivery and medical device applications. *J Controlled Release*. 2021;329:743-757.
doi: 10.1016/j.jconrel.2020.10.008

67. Uddin MJ, Hassan J, Douroumis D. Thermal inkjet printing: prospects and applications in the development of medicine. *Technologies*. 2022;10(5):108.
doi: 10.3390/technologies10050108

68. Carou-Senra P, Rodríguez-Pombo L, Awad A, Basit AW, Alvarez-Lorenzo C, Goyanes A. Inkjet printing of pharmaceuticals. *Adv Mater*. 2024;36(11):2309164.
doi: 10.1002/adma.202309164

69. Académie de Pharmacie. *Dictionnaire de l'académie de Pharmacie.*
https://dictionnaire.acadpharm.org/w/Extrusion

70. Cailleaux S, Sanchez-Ballester NM, Gueche YA, Bataille B, Soulairol I. Fused Deposition Modeling (FDM), the new asset for the production of tailored medicines. *J Controlled Release*. 2021;330:821-841.
doi: 10.1016/j.jconrel.2020.10.056

71. Cano-Vicent A, Tambuwala MM, Hassan SkS, et al. Fused deposition modelling: Current status, methodology, applications and future prospects. *Addit Manuf.* 2021;47:102378.
doi: 10.1016/j.addma.2021.102378

72. Eleftheriadis GK, Ritzoulis C, Bouropoulos N, et al. Unidirectional drug release from 3D printed mucoadhesive buccal films using FDM technology: in vitro and ex vivo evaluation. *Eur J Pharm Biopharm*. 2019;144:180-192.
doi: 10.1016/j.ejpb.2019.09.018

73. Goyanes A, Allahham N, Trenfield SJ, Stoyanov E, Gaisford S, Basit AW. Direct powder extrusion 3D printing: Fabrication of drug products using a novel single-step process. *Int J Pharm*. 2019;567:118471.
doi: 10.1016/j.ijpharm.2019.118471

74. Isreb A, Baj K, Wojsz M, Isreb M, Peak M, Alhnan MA. 3D printed oral theophylline doses with innovative 'radiator-like' design: Impact of polyethylene oxide (PEO) molecular weight. *Int J Pharm*. 2019;564:98-105.
doi: 10.1016/j.ijpharm.2019.04.017

75. Nober C, Manini G, Carlier E, et al. Feasibility study into the potential use of fused-deposition modeling to manufacture 3D-printed enteric capsules in compounding pharmacies. *Int J Pharm*. 2019;569:118581.
doi: 10.1016/j.ijpharm.2019.118581

76. Parulski C, Jennotte O, Lechanteur A, Evrard B. Challenges of fused deposition modeling 3D printing in pharmaceutical applications: where are we now? *Adv Drug Deliv Rev.* 2021;175:113810.
doi: 10.1016/j.addr.2021.05.020

77. Quodbach J, Bogdahn M, Breitkreutz J, et al. Quality of FDM 3D printed medicines for pediatrics: considerations for formulation development, filament extrusion, printing process and printer design. *Ther Innov Regul Sci.* 2022;56(6):910-928.
doi: 10.1007/s43441-021-00354-0

78. Tagami T, Yoshimura N, Goto E, Noda T, Ozeki T. Fabrication of muco-adhesive oral films by the 3D printing of hydroxypropyl methylcellulose-based catechin-loaded formulations. *Biol Pharm Bull*. 2019;42(11): 1898-1905.
doi: 10.1248/bpb.b19-00481

79. Parulski C, Bya LA, Goebel J, Servais AC, Lechanteur A, Evrard B. Development of 3D printed mini-waffle shapes containing hydrocortisone for children's personalized medicine. *Int J Pharm*. 2023;642:123131.
doi: 10.1016/j.ijpharm.2023.123131

80. Seoane-Viaño I, Januskaite P, Alvarez-Lorenzo C, Basit AW, Goyanes A. Semi-solid extrusion 3D printing in drug delivery and biomedicine: personalised solutions for healthcare challenges. *J Controlled Release*. 2021;332:367-389.
doi: 10.1016/j.jconrel.2021.02.027

81. Díaz-Torres E, Rodríguez-Pombo L, Ong JJ, et al. Integrating pressure sensor control into semi-solid extrusion 3D printing to optimize medicine manufacturing. *Int J Pharm* X. 2022;4:100133.
doi: 10.1016/j.ijpx.2022.100133

82. Roche A, Sanchez-Ballester NM, Aubert A, Rossi JC, Begu S, Soulairol I. Preliminary Study on the development of caffeine oral solid form 3D printed by semi-solid extrusion for application in neonates. *AAPS PharmSciTech.* 2023;24(5):122.
doi: 10.1208/s12249-023-02582-z

83. Koshovyi O, Vlasova I, Laur H, et al. Chemical composition and insulin-resistance activity of arginine-loaded american cranberry (Vaccinium macrocarpon Aiton, Ericaceae) Leaf Extracts. *Pharmaceutics*. 2023;15(11):2528.
doi: 10.3390/pharmaceutics15112528

84. Lyousoufi M, Lafeber I, Kweekel D, et al. Development and bioequivalence of 3D-printed medication at the point-of-care: bridging the gap toward personalized medicine. *Clin Pharmacol Ther*. 2023;113(5):1125-1131.
doi: 10.1002/cpt.2870

85. Chatzitaki AT, Eleftheriadis G, Tsongas K, et al. Fabrication of 3D-printed octreotide acetate-loaded oral solid dosage forms by means of semi-solid extrusion printing. *Int J Pharm.* 2023;632:122569.
doi: 10.1016/j.ijpharm.2022.122569

86. Teoh XY, Zhang B, Belton P, Chan SY, Qi S. The effects of solid particle containing inks on the printing quality of porous pharmaceutical structures fabricated by 3d semi-solid extrusion printing. *Pharm Res.* 2022;39(6):1267-1279.
doi: 10.1007/s11095-022-03299-7

87. de Oliveira TV, de Oliveira RS, dos Santos J, Funk NL, Petzhold CL, Beck RCR. Redispersible 3D printed

nanomedicines: an original application of the semisolid extrusion technique. *Int J Pharm.* 2022;624:122029. doi: 10.1016/j.ijpharm.2022.122029

88. Falcone G, Mazzei P, Piccolo A, et al. Advanced printable hydrogels from pre-crosslinked alginate as a new tool in semi solid extrusion 3D printing process. *Carbohydr Polym.* 2022;276:118746. doi: 10.1016/j.carbpol.2021.118746

89. Lopez-Vidal L, Real JP, Real DA, et al. Nanocrystal-based 3D-printed tablets: semi-solid extrusion using melting solidification printing process (MESO-PP) for oral administration of poorly soluble drugs. *Int J Pharm.* 2022;611:121311. doi: 10.1016/j.ijpharm.2021.121311

90. Zhang B, Belton P, Teoh XY, Gleadall A, Bibb R, Qi S. An investigation into the effects of ink formulations of semi-solid extrusion 3D printing on the performance of printed solid dosage forms. *J Mater Chem B*. 2023;12(1):131-144. doi: 10.1039/D3TB01868G

91. Chen P, Liu J, Zhang K, et al. Preparation of clarithromycin floating core-shell systems (CSS) using multi-nozzle semi-solid extrusion-based 3D printing. *Int J Pharm.* 2021;605:120837. doi: 10.1016/j.ijpharm.2021.120837

92. Falcone G, Saviano M, Aquino RP, Del Gaudio P, Russo P. Coaxial semi-solid extrusion and ionotropic alginate gelation: a successful duo for personalized floating formulations via 3D printing. *Carbohydr Polym*. 2021;260:117791. doi: 10.1016/j.carbpol.2021.117791

93. Lafeber I, Tichem JM, Ouwerkerk N, et al. 3D printed furosemide and sildenafil tablets: Innovative production and quality control. *Int J Pharm.* 2021;603:120694. doi: 10.1016/j.ijpharm.2021.120694

94. Yang HS, Kim DW. Fabrication of gastro-floating famotidine tablets: hydroxypropyl methylcellulose-based semisolid extrusion 3D printing. *Pharmaceutics*. 2023; 15(2):316. doi: 10.3390/pharmaceutics15020316

95. Real JP, Real DA, Lopez-Vidal L, et al. 3D-printed gastroretentive tablets loaded with niclosamide nanocrystals by the melting solidification printing process (MESO-PP). *Pharmaceutics*. 2023;15(5):1387. doi: 10.3390/pharmaceutics15051387

96. Falcone G, Real JP, Palma SD, et al. Floating ricobendazole delivery systems: a 3D printing method by co-extrusion of sodium alginate and calcium chloride. *Int J Mol Sci.* 2022;23(3):1280. doi: 10.3390/ijms23031280

97. Ganatra P, Jyothish L, Mahankal V, Sawant T, Dandekar P, Jain R. Drug-loaded vegan gummies for personalized dosing of simethicone: a feasibility study of semi-solid extrusion-based 3D printing of pectin-based low-calorie drug gummies. *Int J Pharm.* 2024;651:123777. doi: 10.1016/j.ijpharm.2024.123777

98. Rodríguez-Pombo L, de Castro-López MJ, Sánchez-Pintos P, et al. Paediatric clinical study of 3D printed personalised medicines for rare metabolic disorders. *Int J Pharm*. 2024;657:124140. doi: 10.1016/j.ijpharm.2024.124140

99. Johannesson J, Pathare MM, Johansson M, Bergström CAS, Teleki A. Synergistic stabilization of emulsion gel by nanoparticles and surfactant enables 3D printing of lipid-rich solid oral dosage forms. *J Colloid Interface Sci.* 2023;650:1253-1264. doi: 10.1016/j.jcis.2023.07.055

100. Rouaz-El Hajoui K, Herrada-Manchón H, Rodríguez-González D, et al. Pellets and gummies: seeking a 3D printed gastro-resistant omeprazole dosage for paediatric administration. *Int J Pharm*. 2023;643:123289. doi: 10.1016/j.ijpharm.2023.123289

101. Chatzitaki AT, Mystiridou E, Bouropoulos N, Ritzoulis C, Karavasili C, Fatouros DG. Semi-solid extrusion 3D printing of starch-based soft dosage forms for the treatment of paediatric latent tuberculosis infection. *J Pharm Pharmacol.* 2022;74(10):1498-1506. doi: 10.1093/jpp/rgab121

102. Han X, Kang D, Liu B, et al. Feasibility of developing hospital preparation by semisolid extrusion 3D printing: personalized amlodipine besylate chewable tablets. *Pharm Dev Technol*. 2022;27(2):164-174. doi: 10.1080/10837450.2022.2027965

103. Zhu C, Tian Y, Zhang E, et al. Semisolid extrusion 3D printing of propranolol hydrochloride gummy chewable tablets: an innovative approach to prepare personalized medicine for pediatrics. *AAPS PharmSciTech*. 2022;23(5):166. doi: 10.1208/s12249-022-02304-x

104. Wang F, Li L, Zhu X, Chen F, Han X. Development of pH-responsive polypills via semi-solid extrusion 3D printing. *Bioengineering*. 2023;10(4):402. doi: 10.3390/bioengineering10040402

105. Korelc K, Larsen BS, Heintze AL, et al. Towards personalized drug delivery via semi-solid extrusion: exploring poly(vinyl alcohol-co-vinyl acetate) copolymers for hydrochlorothiazide-loaded films. *Eur J Pharm Sci.* 2024;192:106645. doi: 10.1016/j.ejps.2023.106645

106. Yi S, Xie J, Chen L, Xu F. Preparation of loratadine orally disintegrating tablets by semi-solid extrusion 3D printing. *Curr Drug Deliv*. 2023;20(6):818-829. doi: 10.2174/1567201819666221011094913

107. Koshovyi O, Heinämäki J, Raal A, et al. Pharmaceutical 3D-printing of nanoemulsified eucalypt extracts and their antimicrobial activity. *Eur J Pharm Sci.* 2023;187:106487. doi: 10.1016/j.ejps.2023.106487

108. Schmidt LM, dos Santos J, de Oliveira TV, et al. Drug-loaded mesoporous silica on carboxymethyl cellulose hydrogel:

Development of innovative 3D printed hydrophilic films. *Int J Pharm*. 2022;620:121750.
doi: 10.1016/j.ijpharm.2022.121750

109. Panraksa P, Rachtanapun P, Thipchai P, et al. Sustainable 3D printing of oral films with tunable characteristics using CMC-based inks from durian rind wastes. *Eur J Pharm Biopharm*. 2023;186:30-42.
doi: 10.1016/j.ejpb.2023.03.006

110 Mathiyalagan R, Sjöholm E, Manandhar S, et al. Personalizing oral delivery of nanoformed piroxicam by semi-solid extrusion 3D printing. *Eur J Pharm Sci*. 2023; 188:106497.
doi: 10.1016/j.ejps.2023.106497

111. Johannesson J, Wu M, Johansson M, Bergström CAS. Quality attributes for printable emulsion gels and 3D-printed tablets: towards production of personalized dosage forms. *Int J Pharm*. 2023;646:123413.
doi: 10.1016/j.ijpharm.2023.123413

112. Suárez-González J, Magariños-Triviño M, Díaz-Torres E, Cáceres-Pérez AR, Santoveña-Estévez A, Fariña JB. Individualized orodispersible pediatric dosage forms obtained by molding and semi-solid extrusion by 3D printing: a comparative study for hydrochlorothiazide. *J Drug Deliv Sci Technol*. 2021;66:102884.
doi: 10.1016/j.jddst.2021.102884

113. Hu J, Fitaihi R, Abukhamees S, Abdelhakim HE. Formulation and characterisation of carbamazepine orodispersible 3D-printed mini-tablets for paediatric use. *Pharmaceutics*. 2023;15(1):250.
doi: 10.3390/pharmaceutics15010250

114. Elbl J, Veselý M, Blaháčková D, et al. Development of 3D printed multi-layered orodispersible films with porous structure applicable as a substrate for inkjet printing. *Pharmaceutics*. 2023;15(2):714.
doi: 10.3390/pharmaceutics15020714

115. Janigová N, Elbl J, Pavloková S, Gajdziok J. Effects of various drying times on the properties of 3D printed orodispersible films. *Pharmaceutics*. 2022;14(2):250.
doi: 10.3390/pharmaceutics14020250

116. Panraksa P, Zhang B, Rachtanapun P, Jantanasakulwong K, Qi S, Jantrawut P. 'Tablet-in-Syringe': a novel dosing mechanism for dysphagic patients containing fast-disintegrating tablets fabricated using semisolid extrusion 3D printing. *Pharmaceutics*. 2022;14(2):443.
doi: 10.3390/pharmaceutics14020443

117. Abdella S, Afinjuomo F, Song Y, Upton R, Garg S. 3D printed bilayer mucoadhesive buccal film of estradiol: Impact of design on film properties, release kinetics and predicted in vivo performance. *Int J Pharm*. 2022;628:122324.
doi: 10.1016/j.ijpharm.2022.122324

118. Takashima H, Tagami T, Kato S, Pae H, Ozeki T, Shibuya Y. Three-dimensional printing of an apigenin-loaded mucoadhesive film for tailored therapy to oral leukoplakia and the chemopreventive effect on a rat model of oral carcinogenesis. *Pharmaceutics*. 2022;14(8):1575.
doi: 10.3390/pharmaceutics14081575

119. Munoz-Perez E, Rubio-Retama J, Cussó L, Igartua M, Hernandez RM, Santos-Vizcaino E. 3D-printed Laponite/Alginate hydrogel-based suppositories for versatile drug loading and release. *Drug Deliv Transl Res*. 2024.
doi: 10.1007/s13346-023-01506-5

120. Awad A, Hollis E, Goyanes A, Orlu M, Gaisford S, Basit AW. 3D printed multi-drug-loaded suppositories for acute severe ulcerative colitis. *Int J Pharm X*. 2023; 5:100165.
doi: 10.1016/j.ijpx.2023.100165

121. Awad A, Goyanes A, Orlu M, Gaisford S, Basit AW. 3D printed infliximab suppositories for rectal biologic delivery. *Int J Pharm X*. 2023;5:100176.
doi: 10.1016/j.ijpx.2023.100176

122. Utomo E, Domínguez-Robles J, Anjani QK, et al. Development of 3D-printed vaginal devices containing metronidazole for alternative bacterial vaginosis treatment. *Int J Pharm X*. 2022;5:100142.
doi: 10.1016/j.ijpx.2022.100142

123. Teworte S, Aleandri S, Weber JR, Carone M, Luciani P. Mucoadhesive 3D printed vaginal ovules to treat endometriosis and fibrotic uterine diseases. E*ur J Pharm Sci*. 2023;188:106501.
doi: 10.1016/j.ejps.2023.106501

124. Pérez Gutiérrez CL, Cottone F, Pagano C, et al. The Optimization of Pressure-Assisted Microsyringe (PAM) 3D printing parameters for the development of sustainable starch-based patches. *Polymers*. 2023;15(18):3792.
doi: 10.3390/polym15183792

125. Kyser AJ, Mahmoud MY, Herold SE, et al. Formulation and characterization of pressure-assisted microsyringe 3D-printed scaffolds for controlled intravaginal antibiotic release. *Int J Pharm*. 2023;641:123054.
doi: 10.1016/j.ijpharm.2023.123054

126. Archana M, Rubini D, Dharshini KP, et al. Development of an anti-infective urinary catheter composed of polyvinyl alcohol/sodium alginate/methylcellulose/polyethylene glycol by using a pressure-assisted 3D-printing technique. *Int J Biol Macromol*. 2023;249:126029.
doi: 10.1016/j.ijbiomac.2023.126029

127. Conceição J, Farto-Vaamonde X, Goyanes A, et al. Hydroxypropyl-β-cyclodextrin-based fast dissolving carbamazepine printlets prepared by semisolid extrusion 3D printing. *Carbohydr Polym*. 2019;221:55-62.
doi: 10.1016/j.carbpol.2019.05.084

128. Rahman J, Quodbach J. Versatility on demand – the case for semi-solid micro-extrusion in pharmaceutics. *Adv Drug Deliv Rev*. 2021;172:104-126.
doi: 10.1016/j.addr.2021.02.013

129. Elbadawi M, Gustaffson T, Gaisford S, Basit AW. 3D printing tablets: predicting printability and drug dissolution from rheological data. *Int J Pharm.* 2020; 590:119868.
doi: 10.1016/j.ijpharm.2020.119868

130. Suárez-González J, Díaz-Torres E, Monzón-Rodríguez CN, Santoveña-Estévez A, Fariña JB. Revolutionizing three-dimensional printing: enhancing quality assurance and point-of-care integration through instrumentation. *Pharmaceutics*. 2024;16(3):408.
doi: 10.3390/pharmaceutics16030408

131. Khaled SA, Burley JC, Alexander MR, Yang J, Roberts CJ. 3D printing of tablets containing multiple drugs with defined release profiles. *Int J Pharm.* 2015;494(2):643-650.
doi: 10.1016/j.ijpharm.2015.07.067

132. Haring AP, Tong Y, Halper J, Johnson BN. Programming of multicomponent temporal release profiles in 3D printed polypills via core–shell, multilayer, and gradient concentration profiles. *Adv Healthc Mater.* 2018;7(16):1800213.
doi: 10.1002/adhm.201800213

133. Borges AF, Silva C, Coelho JFJ, Simões S. Outlining critical quality attributes (CQAs) as guidance for the development of orodispersible films. *Pharm Dev Technol.* 2017;22(2):237-245.
doi: 10.1080/10837450.2016.1199567

134. El Aita I, Breitkreutz J, Quodbach J. On-demand manufacturing of immediate release levetiracetam tablets using pressure-assisted microsyringe printing. *Eur J Pharm Biopharm*. 2019;134:29-36.
doi: 10.1016/j.ejpb.2018.11.008

135. Pluta P. Compounding overview: primary considerations for the workplace. *Pharm Technol*. 2024;48(2):18-22. Accessed April 10, 2024.
https://www.pharmtech.com/view/compounding-overview-primary-considerations-for-the-workplace

136. European Medicines Agency. ICH guideline Q10 on pharmaceutical quality system; 2007.
https://www.ema.europa.eu/en/documents/scientific-guideline/international-conference-harmonisation-technical-requirements-registration-pharmaceuticals-human_en.pdf

137. European Medicines Agency. ICH guideline Q8 (R2) on pharmaceutical development; 2004.
https://www.ema.europa.eu/en/documents/scientific-guideline/international-conference-harmonisation-technical-requirements-registration-pharmaceuticals-human-use_en-11.pdf

138. Seoane-Viaño I, Xu X, Ong JJ, et al. A case study on decentralized manufacturing of 3D printed medicines. *Int J Pharm X*. 2023;5:100184.
doi: 10.1016/j.ijpx.2023.100184

139. Section 503A of the Federal Food, Drug, and Cosmetic Act. *FDA*; 2018. Accessed April 12, 2024.
https://www.fda.gov/drugs/human-drug-compounding/section-503a-federal-food-drug-and-cosmetic-act

140. Beitler BG, Abraham PF, Glennon AR, et al. Interpretation of regulatory factors for 3D printing at hospitals and medical centers, or at the point of care. *3D Print Med*. 2022;8(1):7.
doi: 10.1186/s41205-022-00134-y

141. Jørgensen AK, Ong JJ, Parhizkar M, Goyanes A, Basit AW. Advancing non-destructive analysis of 3D printed medicines. *Trends Pharmacol Sci*. 2023;44(6):379-393.
doi: 10.1016/j.tips.2023.03.006

142. Miller GF, Coffield E, Leroy Z, Wallin R. Prevalence and costs of five chronic conditions in children. *J Sch Nurs Off Publ Natl Assoc Sch Nurses.* 2016;32(5):357-364.
doi: 10.1177/1059840516641190

143. Bg PK, Mehrotra S, Marques SM, Kumar L, Verma R. 3D printing in personalized medicines: a focus on applications of the technology. *Mater Today Commun.* 2023;35:105875.
doi: 10.1016/j.mtcomm.2023.105875

144. ClinicalTrials.gov. Metronomic Chemotherapy in Wilms Tumor (MetroWilms-1906) (MetroWilms); 2022. Accessed April 30, 2024.
https://classic.clinicaltrials.gov/ct2/show/NCT05384821

145. Binson G, Sanchez C, Waton K, et al. Accuracy of dose administered to children using off-labelled or unlicensed oral dosage forms. *Pharmaceutics.* 2021;13(7):1014.
doi: 10.3390/pharmaceutics13071014

146. Curti C, Brandin T, Kabac T, et al. Contrôle qualité des préparations magistrales en officine: contraintes réglementaires et pistes d'amélioration. *Pharm Hosp Clin.* 2020;55(3):268-274.
doi: 10.1016/j.phclin.2020.04.009

147. Zheng Z, Lv J, Yang W, et al. Preparation and application of subdivided tablets using 3D printing for precise hospital dispensing. *Eur J Pharm Sci.* 2020;149:105293.
doi: 10.1016/j.ejps.2020.105293

148. Cui M, Pan H, Fang D, Sun H, Qiao S, Pan W. Exploration and evaluation of dynamic dose-control platform for pediatric medicine based on Drop-on-Powder 3D printing technology. *Int J Pharm*. 2021;596:120201.
doi: 10.1016/j.ijpharm.2021.120201

149. Park BJ, Choi HJ, Moon SJ, et al. Pharmaceutical applications of 3D printing technology: current understanding and future perspectives. *J Pharm Investig*. 2019;49:575-585.
doi: 10.1007/s40005-018-00414-y

150. de Groot MCH, van Puijenbroek EP. Clindamycin and taste disorders. *Br J Clin Pharmacol*. 2007;64(4):542-545.
doi: 10.1111/j.1365-2125.2007.02908.x

151. Shinotsuka H, Mizutani N, Aikawa S, Kimura G. Palatability evaluation of sulfamethoxazole/trimethoprim with

sweetener using the two-bottle choice test. *Chem Pharm Bull (Tokyo)*. 2023;71(12):906-908.
doi: 10.1248/cpb.c23-00428

152. Protopapa C, Siamidi A, Kolipaka SS, Junqueira LA, Douroumis D, Vlachou M. In vitro profile of hydrocortisone release from three-dimensionally printed paediatric mini-tablets. *Pharmaceutics*. 2024;16(3):385.
doi: 10.3390/pharmaceutics16030385

153. Herrada-Manchón H, Rodríguez-González D, Alejandro Fernández M, et al. 3D printed gummies: personalized drug dosage in a safe and appealing way. *Int J Pharm*. 2020;587:119687.
doi: 10.1016/j.ijpharm.2020.119687

154. Godoi FC, Prakash S, Bhandari BR. 3d printing technologies applied for food design: Status and prospects. *J Food Eng*. 2016;179:44-54.
doi: 10.1016/j.jfoodeng.2016.01.025

155. Schmidt CM, Knief A, Deuster D, Matulat P, Zehnhoff-Dinnesen A. Melatonin is a useful alternative to sedation in children undergoing brainstem audiometry with an age dependent success rate - a field report of 250 investigations. *Neuropediatrics*. 2007;38:2-4.
doi: 10.1055/s-2007-981467

156. Seoane-Viaño I, Ong JJ, Luzardo-Álvarez A, et al. 3D printed tacrolimus suppositories for the treatment of ulcerative colitis. *Asian J Pharm Sci*. 2021;16(1):110-119.
doi: 10.1016/j.ajps.2020.06.003

157. Chakka LRJ, Chede S. 3D printing of pharmaceuticals for disease treatment. *Front Med Technol*. 2023;4: 1040052.
doi: 10.3389/fmedt.2022.1040052

158. Heitman T, Day AJ, Bassani AS. Pediatric compounding pharmacy: taking on the responsibility of providing quality customized prescriptions. *Children*. 2019;6(5):66.
doi: 10.3390/children6050066

159. Skowyra J, Pietrzak K, Alhnan MA. Fabrication of extended-release patient-tailored prednisolone tablets via fused deposition modelling (FDM) 3D printing. *Eur J Pharm Sci*. 2015;68:11-17.
doi: 10.1016/j.ejps.2014.11.009

ACCSCIENCE PUBLISHING

International Journal of Bioprinting

REVIEW ARTICLE

3D bioprinting techniques and hydrogels for osteochondral integration regeneration

Haiwei Tang[1†], Enze Zhao[1†], Yahao Lai[1], Anjin Chen[1], Xiaoting Chen[1], Weinan Zeng[1], Xulin Hu[2*], Kai Zhou[1*], and Zongke Zhou[1*]

[1] Department of Orthopedics and Orthopedic Research Institute, West China Hospital, Sichuan University, Chengdu, Sichuan, China

[2] Department of Orthopaedics, Clinical Medical College and Affiliated Hospital of Chengdu University, Chengdu, Sichuan, China

Abstract

Despite considerable advancements in regenerative medicine, restoring the osteochondral interface and facilitating the integration of osteochondral regeneration remain significant clinical conundrums. This challenge is predominantly attributed to the scarcity of appropriate tissue engineering materials for replacing osteochondral defects and facilitating tissue regeneration. 3D bioprinting constitutes a promising approach for bone fabrication, as it not only allows for the design of precise personalized scaffolds but also encapsulates cells and growth factors, with the potential to replicate the functions of native tissues. Many critical properties of hydrogels, such as their mechanical properties, elasticity, and bioactivity, make them the most prevalently utilized bioinks in tissue engineering. In addition, their structure can be easily adjusted to meet the needs of different situations. Therefore, 3D-bioprinted hydrogel scaffolds may have promising prospects for integrated osteochondral repair and are receiving increasing attention. In this review, we describe the current problems encountered in the field of osteochondral integration repair and review the latest advances in current 3D printing technology and 3D bioprinting hydrogel scaffolds. We propose prospects for the development of novel 3D-bioprinted hydrogel scaffolds, providing cues for future research directions.

Keywords: Osteochondral integration repair; 3D-bioprinted; Hydrogels

†These authors contributed equally to this work.

***Corresponding authors:**
Xulin Hu
(huxulin1993@cdu.edu.cn)

Kai Zhou
(zhoukai_scu@scu.edu.cn)

Zongke Zhou
(zhouzongke@scu.edu.cn)

Citation: Tang H, Zhao E, Lai Y, et al. 3D bioprinting techniques and hydrogels for osteochondral integration regeneration. *Int J Bioprint*. 2024;10(6):4472. doi: 10.36922/ijb.4472

Received: August 7, 2024
Revised: August 27, 2024
Accepted: September 9, 2024
Published Online: September 10, 2024

Copyright: © 2024 Author(s). This is an Open Access article distributed under the terms of the Creative Commons Attribution License, permitting distribution, and reproduction in any medium, provided the original work is properly cited.

Publisher's Note: AccScience Publishing remains neutral with regard to jurisdictional claims in published maps and institutional affiliations.

1. Introduction

The osteochondral tissue is composed of a cartilage layer, a bone-cartilage interface, and subchondral bone. Articular cartilage, when involved in joint function, is capable of enduring mechanical load stress and lubricating friction during movement.[1,2] Owing to its close structural connection, cartilage damage caused by trauma, aging, and degeneration often extends to the interface and subchondral bone layers, leading to the formation of osteochondral defects (OCDs).[3,4] As OCDs progress, they can result in joint pain, deformity, limited range of motion, and even dysfunction, eventually leading to osteoarthritis (OA).[5] In general, there are many differences in chemical composition and mechanical, structural, electrical, and oxygen and nutritional consumption between articular and subchondral bone.[6,7] The cartilage layer is characterized by a soft and

smooth tissue surface devoid of blood vessels, nerves, and lymphatics. In contrast, the subchondral bone layer is rich in blood vessels and nerves, with a calcified hard texture that plays a crucial role in buffering mechanical stress.[8-10] Thus, owing to the inherent differences between bone and cartilage, simultaneous regeneration of both tissues is often challenging and requires spatially targeted delivery of different stimulus factors within the scaffold for sustained and responsive repair.[11,12] Currently, common surgical treatments for OCD include autologous chondrocyte implantation (ACI), matrix-induced autologous chondrocyte implantation (MACI), osteochondral autografts and allografts, microfracture and total articular replacement.[13-18] Although these treatment methods are widely used in clinical practice, there are still many defects and deficiencies. The principle of ACI lies in restoring the integrity of cartilage lesions by inducing the formation of hyaline-like cartilage, and it has been clinically applied for more than 20 years.[19] Nevertheless, there are still drawbacks, such as the scarcity of chondrocyte sources, the prolonged time for obtaining chondrocytes, the difficulty in immobilizing the chondrocyte solution,[20] and the poor efficacy for older individuals[21] and patients with a long duration of symptoms.[22] Notably, ACI is unable to repair the osteochondral interface and achieve integrated osteochondral regeneration. MACI is an enhanced method of ACI, where a cell-loaded membrane is employed to evenly distribute chondrocytes and mitigate the risk of graft hypertrophy, demonstrating a superior therapeutic outcome and minor trauma as it can be applied via arthroscopic technology.[23,24] However, it still does not fully meet the requirements for osteochondral integrative repair. Osteochondral autografts and allografts are therapeutic strategies for direct cartilage repair, which immediately fills the defect with mature articular cartilage. However, autografts are not only difficult to perform but may also cause complications at the donor site. Furthermore, challenges persist in restoring the surfaces of both the cartilage and bone to form a smooth, convex joint surface.[25] For allografts, challenges include limited tissue supply, immune rejection, inadequate integration, low cell viability due to graft storage, and the possibility of disease transmission.[26] Microfractures are treated by drilling holes in cartilage and subchondral bone areas to increase blood flow and bone marrow supply to the defect site. Recently, there has been extensive research on the potential of injecting stem cells or biomolecules into defect sites to increase the efficacy of microfractures. However, it may lead to the formation of less functional fibrocartilage.[27] Total articular replacement is considered the gold standard for various joint diseases but often requires more than one revision for young people. For mildly damaged joints, joint replacement is often too aggressive[14] (Table 1).

Owing to these limitations, more novel and effective therapeutic approaches need to be developed. Tissue engineering can generate functional substitutes resembling natural tissues for restoring or replacing damaged tissues. Additionally, it possesses the advantages of accessible materials, straightforward operation, and excellent biocompatibility, thereby becoming a promising therapeutic approach for clinical tissue defects.[28-30] Currently, there are two principal approaches for repairing OCDs through tissue engineering. The first involves creating artificial cartilage structures that mimic the structural traits, mechanical strength, and biological functions of natural cartilage tissues. And the second approach emphasizes regenerative medicine by employing appropriate biological materials as artificial extracellular matrices or loading with biological factors (cells or growth factors) to facilitate cell growth, proliferation, and differentiation at the defect site.[31-34] Generally, to ensure the uniform distribution of biological factors within the matrix, conventional tissue engineering is typically characterized by a homogeneous composition.[35,36] Nevertheless, given the significant anisotropy of articular cartilage, it is widely acknowledged that the field requires more effective strategies to capture the spatial complexity of natural tissues and their subchondral bone interfaces.[37] Another challenge in cartilage tissue engineering lies in the fact that the mechanical properties of tissue-engineered cartilage tend to be relatively weak and are unable to withstand the high levels of compression and shear loads that occur in the joint after implantation.[35] Therefore, the fabrication of osteochondral engineering scaffolds requires flexible and high-precision machining.

3D bioprinting, also known as additive manufacturing (AM), is based on the digital model created through computer-aided design. By employing various 3D printers and computer-aided manufacturing, materials are accurately and rapidly accumulated layer by layer to obtain a genuine, physical 3D entity. The application of 3D printing technology in bone and cartilage tissue engineering presents several advantages. Firstly, by leveraging patient-specific medical imaging data, such as computed tomography (CT) or magnetic resonance imaging (MRI) scans, personalized scaffolds can be developed in accordance with individual requirements. Secondly, 3D printing facilitates the fabrication of complex geometric structures, particularly complex layered porous structures, which are challenging to achieve through traditional manufacturing approaches.[35,38,39] The precision of 3D printing makes the fabricated scaffold closer to the structure of natural cartilage, which is more conducive to cartilage integration. Thirdly, 3D printing exhibits flexibility and compatibility with a variety of biocompatible materials, guaranteeing an efficient manufacturing process for structures composed

Table 1. Advantages and disadvantages of current clinical treatments for osteochondral defects (OCD).

Treatments	Mechanism	Advantages	Disadvantages	Complications	Ref.
ACI	Induce the formation of hyaline-like cartilage and restore the integrity of cartilage lesions	Promote cartilage regeneration	Cannot repair the osteochondral interface; lack of chondrocyte source; long acquisition time of chondrocytes; difficult to fix chondrocyte solution; young adults have better efficacy	Graft hypertrophy; arthrofibrosis; graft breakdown; etc.	[19-22]
MACI	Induce the formation of hyaline-like cartilage and restore the integrity of cartilage lesions	Chondrocytes evenly distributed; low risk associated with implants; relatively minor trauma	Cannot repair the osteochondral interface; lack of chondrocyte source; long acquisition time of chondrocytes; difficult to fix chondrocyte solution; different effects in various people	Graft breakdown; wound complications	[23,24]
Osteochondral autografts	Fill the defect directly	Defects can be filled immediately with mature, hyaline articular cartilage	High surgical difficulty; donor site complications; uneven joint surface	Donor site pain; donor site infection; etc.	[25]
Osteochondral allografts	Fill the defect directly	Defects can be filled immediately with mature, hyaline articular cartilage	Limited tissue source; immune rejection; insufficient integration; low cell viability; disease transmission	Immune rejection; transplantation failure; disease transmission	[26]
Microfracture	Increase blood flow and bone marrow supply to the defect site	Simple	Possibility of less functional fibrocartilage formation; young adults have better efficacy	Worse joint function; wound complications	[27]
Total articular replacement	Prostheses replace damaged joints	Excellent joint function; high long-term survival rate	Young adults need more than one revision for total articular replacement	Periprosthetic infection; prosthesis loosening	[14]

Abbreviations: ACI: Autologous chondrocyte implantation; MACI: Matrix-induced autologous chondrocyte implantation.

of multiple materials. It can be tailored by combining different materials to fulfill the specific requirements of the scaffold.[40,41] Additionally, various cells and bioactive factors can be loaded in the scaffold and even form gradients, which can better promote regeneration.[42,43] Therefore, 3D printing technology has brought a new dawn to bone and cartilage tissue engineering.

Bioinks are the most critical component in 3D bioprinting. The ideal 3D bioink for osteochondral engineering should be capable of supporting cell growth and proliferation, maintaining the phenotype of chondrocytes and osteoblasts, facilitating the osteogenic and chondrogenic differentiation of stem cells, and replicating the osteochondral interface or cartilage tissue. Moreover, it must possess mechanical strength analogous to that of natural tissues.[32] Hydrogels, which are composed of highly hydrated, natural extracellular matrix (ECM)-mimicking polymeric networks, are multifunctional biomaterials that play important roles in 3D bioprinting.[44,45] Their unique properties, such as outstanding water retention, biodegradability, porous 3D grid structure, and biocompatibility, enable them to provide a 3D environment similar to that of the ECM, ensuring cell proliferation, differentiation, and even delivery of biomolecules, such as growth factors, drugs, and cells. In addition, its composition, structure, mechanical properties, and biochemical properties can be easily adjusted to meet the specific requirements of osteochondral tissue engineering.[46-49] These properties combined with 3D bioprinting technology facilitate a homogeneous distribution of biological components within the biomaterial matrix and spatial complexity, rendering them highly suitable for tissue engineering.[33] Depending on their source, hydrogels can be further divided into natural and synthetic hydrogels. Natural hydrogels derived from biological sources, such as alginate and hyaluronic acid (HA), have excellent biocompatibility and biodegradability and are often used as biomaterials for OCD tissue engineering.[50,51] Nevertheless, their mechanical properties typically do not satisfy the requirements of OCD therapy; thus, various strategies are adopted to increase their strength and toughness.[52] Synthetic hydrogels are hydrated networks of polymers synthesized via chemical methods and can be tailored according to specific physical and chemical properties, ensuring they meet the requirements of their intended applications.[53] Crosslinking is a key step in controlling the properties of the printed

material, and a variety of crosslinking methods, such as covalent bonding, thermogelation, cryogelation, and other noncovalent bonding methods, have been widely used in the 3D bioprinting of hydrogels.[54] Furthermore, novel preparation methods, such as photo-crosslinking and click chemistry, can be used to fabricate hydrogels with adjustable mechanical strength and degradability.[55,56] However, synthetic hydrogels are limited by poor biocompatibility, toxic degradation products, and loss of mechanical properties during degradation.

Owing to the significant potential of 3D-bioprinted hydrogel materials in osteochondral repair, we conducted a review of its related applications. Firstly, we summarize the diverse 3D printing approaches and analyze their advantages and defects. Secondly, the current clinical applications are summarized in accordance with the three segments of tissue engineering: scaffolds, cells, and bioactive factors. Finally, this review discusses the development prospects and current challenges regarding the 3D bioprinting hydrogel system.

2. 3D printing methods

The field of osteochondral repair features a variety of 3D printing technologies, each with its own advantages and disadvantages. In this section, we provide a comprehensive overview of the advantages and disadvantages associated with traditional 3D printing technology as well as its latest advancements (Table 2; Figure 1).[7,57,58] Moreover, bioinks are essential for the successful printing of tissue and organ structures. Different 3D printing technologies have distinct requirements for bioinks based on their respective principles.[59] Thus, we have also summarized the adaptability of 3D bioinks.

2.1. Inkjet printing

Inkjet 3D printing technology is an advancement of traditional inkjet printing that uses microtriggers in the print head to precisely control the spray and solidification speed of ink to achieve 3D printing. This non-contact printing method offers high precision and efficiency in depositing various materials, making it one of the most widely used forms of 3D printing.[60,61] Based on the ink droplets formed in printers, inkjet printing can be divided into two types: continuous inkjet (CIJ) printing and drop-on-demand inkjet (DOD) printing.[7] In CIJ printing, the bioink is forced through the nozzle under pressure, causing the nozzle to extrude into a stream of droplets due to Rayleigh-Plateau instability.[62] However, the use of CIJ printing is severely limited due to the complexity of its equipment, bioink wastage, and potential contamination of biomaterials.[63] In DOD printing, its simplicity, precision, and equipment efficiency, as well as the ability to minimize waste through the targeted spraying of ink droplets, led to its widespread adoption.[63,64] In order to meet the electronic control requirements of inkjet printing equipment, inkjet bioinks must possess a certain level of conductivity. In addition, due to the small deformation at the outlet of the inkjet print nozzle, inkjet printing is not suitable for high-viscosity bioinks with high cell density because the high viscosity can cause frequent clogging of the print nozzle.[65,66]

2.2. Extrusion printing

Extrusion printing technology, which has high precision and accessibility, is the most commonly utilized method for creating 3D scaffold structures by extruding or dispersing continuous biomaterial strands or fibers layer-by-layer.[49,67,68] It is widely used in the field of biomanufacturing and can be applied to almost all types of hydrogel polymer solutions with different viscosities, as well as bioinks encapsulated with high cell density.[66,69] Generally, materials with higher viscosity are utilized to offer structural support, whereas materials with lower viscosity establish critical conditions to preserve cell viability and function. The main advantage of this technology is that it can utilize a variety of materials and cell types to fabricate tissue scaffolds.[70] In addition, it is able to deposit biological materials with physiological cell density layer-by-layer in a designed way.[71] However, the high pressure and shear stress generated by the nozzle during printing may cause a decrease in cell viability; thus, it is crucial to balance printability and cell viability, which may require the incorporation of various bioinks with special rheological properties to prevent cell damage.[72-75] Moreover, the limited strand resolution (typically greater than 100 μm) is another inadequacy.[76,77]

Fused deposition modeling (FDM) is a special extrusion technology, in which the material is melted at high temperatures to transform it into a liquid state, extruded through a printer nozzle, cured, and easily used to fabricate scaffolds with excellent structural integrity.[78] The main drawback of this technology is the lack of suitable biocompatible and bioactive materials. In addition, the printing parameters of the bone scaffold that produces the strongest mechanical properties remain unknown.[79] Currently, in the field of FDM, traditional prototype printing methods, such as the use of semi-molten polymers and hydrogels, are gradually being developed for high-performance composite material fabrication to improve material function.[80,81] Moreover, Junqueira et al. created personalized drug dosage forms by combining FDM with inkjet printing.[82] FDM is becoming one of the most widely used AM technologies.

2.3. Laser-assisted printing

Laser-assisted printing, also known as laser-induced forward transfer, uses laser pulses to vaporize the

bioink liquid and deposit it at the desired location.[83,84] The printers typically comprise three layers: an energy-absorbing layer, a ribbon layer consisting of bioinks, and a substrate layer.[85] Since this printing method utilizes laser deposition of bioink, it eliminates the need for a nozzle, thereby significantly reducing shear stress on the cells within the bioink. This guarantees that even with highly viscous bioink, the printer can process it without clogging problems.[86] Furthermore, high printing accuracy and resolution are among the advantages of this method.[87] However, it is worth noting that the laser produces a thermal effect, which can cause thermal damage to cells and affect cell survival. Its high cost limits its wide application as well.[88] Recently, to fully leverage the dynamic properties of cells and living biomaterials, "time" has been considered the fourth dimension, especially for soft tissue design. Through laser-assisted printing, Douillet et al. successfully developed a new model that can replicate the dynamic remodeling of fibroblasts *in vitro*, providing a new tool for the future study of *in vitro* dermal tissue.[89]

2.4. Vat polymerization-based printing

Vat polymerization (VP)-based printing is a cutting-edge 3D printing method that uses light of a specific wavelength to induce a photopolymerization reaction, resulting in the formation of intricate 3D structures from a liquid bioresin.[101,102] Therefore, this 3D printing technology is only compatible with photo-crosslinked bioinks or resins.[103] Over the past decade, several new technologies have been developed depending on the type of light used, including stereolithography (SLA), digital light processing (DLP), and two-photon polymerization (2PP).

The SLA system uses a laser source to refract and scan the material in a vat to cure the bioresin. Generally, when exposed to a light source, the photoinitiator generates free radicals or other reactive substances, initiating the polymerization of the resin into a predetermined 2D shape via a digital micromirror device (DMD); this process occurs layer by layer.[104] Depending on the location of the laser source, the SLA system can be divided into top-down and bottom-up printing.[101] Top-down printing, which is a traditional method, involves printing a support structure and the target structure together to form an accurately designed construct. During bottom-up printing, the printer draws a section of the component on the bottom layer of the resin, and as the building platform rises, the liquid resin flows beneath the previously cured layer, backfilling the resin layer.[57] The inverted SLA system only requires a thin layer of bioresin; thus, larger molding volumes can be printed without a

Table 2. Summary of the comparative characteristics of common printing techniques.

Parameters	Printing method					Ref.
	Inject printing	Extrusion printing	Laser-assisted printing	Vat polymerization (VP)-based printing	Tomographic volumetric printing	
Materials	Biomolecules; growth factors	Hydrogel; ceramics	Biomolecules; cells	Liquid bioresin; hydrogel	Liquid bioresin; hydrogel	90-92
Resolution or droplet size	≈ 50 μm	≈ 200–1000 μm	≈ 10–100 μm	≈ 10–100 μm	≈ 80 μm	92-95
Material viscosities	3.5–12 mPa/s	30 to 6 × 10^7 mPa/s	1–300 mPa/s	Up to 5 Pa/s	4–93 Pa/s	91,92,96,97
Print speed	Fast (up to 10,000 droplets per second)	Slow (10–50 μm/s)	Fast (1.6 μm/s)	Fast (>10^5 mm^3/h)	Fast (>10^5 mm^3/h)	91,92,95
Advantages	Wide availability; low cost; high resolution; high printing speed; ability to introduce concentration gradients in 3D construct	High cell density; high cell viability; wide viscosity	Low shear stress; wide viscosity; high printing speed; high resolution	High resolution; high printing speed; high cell viability	High resolution; high printing speed;	96,98,99
Disadvantages	Poor vertical structure clogging characteristics; thermal and mechanical stress to cells; limited printable materials	Limited resolution; shear forces can damage cells	Low cell viability; relatively high cost	Cumulative ultraviolet light (UV) exposure; restrictive multi-material functionality; high cost; high complexity	High cost; high complexity	88,99,100

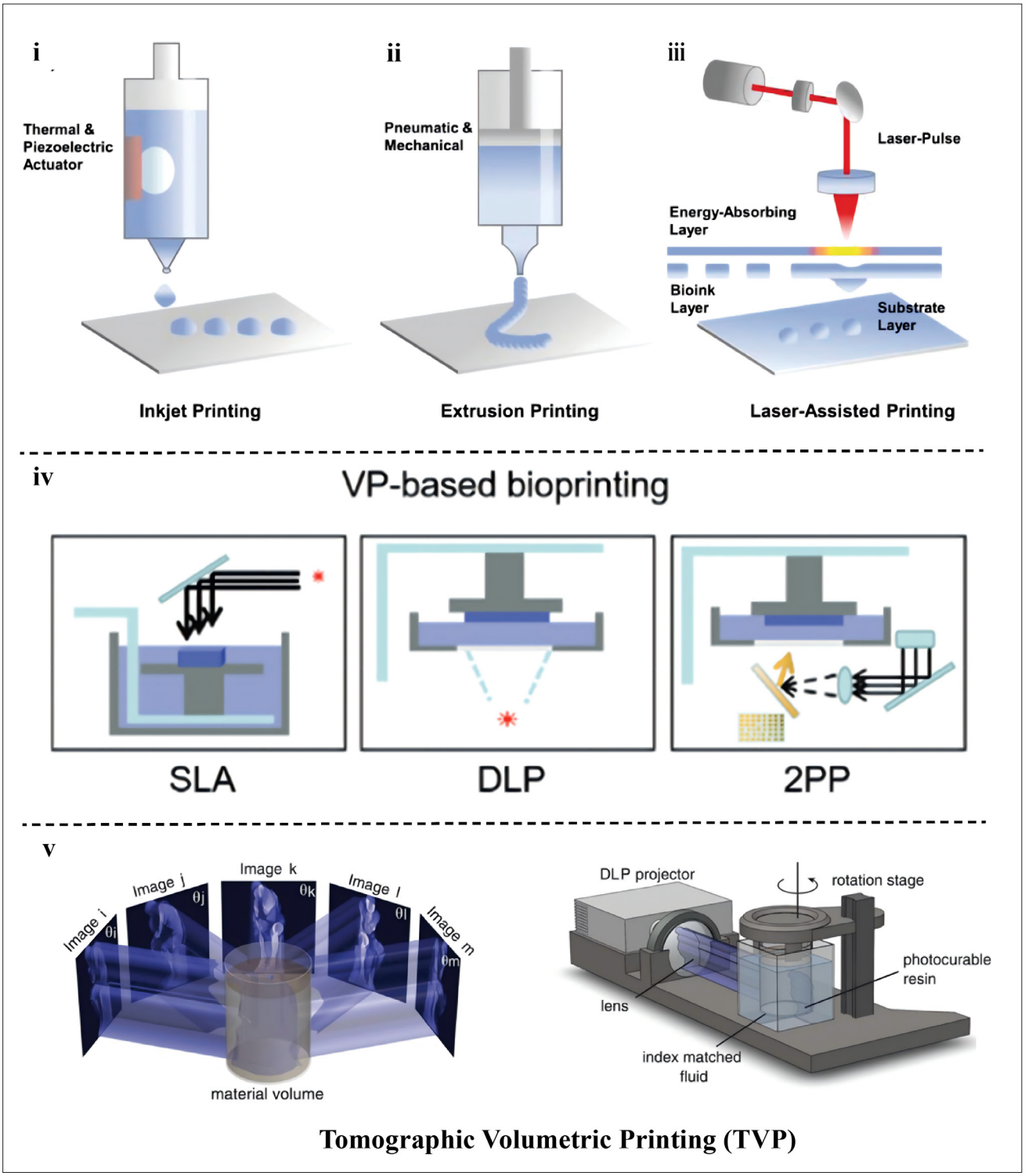

Figure 1. 3D printing methods. (i) Inkjet printing. (ii) Extrusion printing. (iii) Laser-assisted printing. Reprinted with permission from Wang et al.[7] Copyright © 2022 Wiley. (iv) Vat-polymerization (VP)-based printing. Reprinted with permission from Wang et al.[57] Copyright © 2022 AccScience Publishing. (v) Tomographic volumetric printing. Reprinted with permission from Kelly et al.[58] Copyright © 2019 Science. Abbreviations: SLA: Stereolithography; DLP: Digital light processing; 2PP: Two-photon polymerization.

large printer, making it more convenient, but the printing speed is relatively slow. During the printing process, the planar configuration of each layer is determined by the projected light, and the 3D structure can be manipulated via a light absorber that attenuates the light, resulting in high resolution.[105,106] Furthermore, since the entire layer of bioresin can be polymerized immediately, SLA results in higher printing speeds compared to both nozzle-related and nozzle-free methods.[107,108]

Digital light processing (DLP) printing is predicated on the local photopolymerization of liquid monomers or oligomers triggered by ultraviolet light in the presence of photoinitiators, which involves the utilization of a DMD to project the entire optical pattern plane onto the optical polymer solution for concurrent printing, accelerating the printing process.[109-111] Furthermore, the continuous updating of the projected optical pattern enables the movement of the platform carrying the printed object, thereby facilitating the printing of smooth 3D objects without artificial interfaces.[112] The greatest advantage of DLP technology is its high printing speed and geometric resolution (up to the nanoscale).[113,114] Thus, it is more appropriate for printing large structures at the micron level than SLA.

The 2PP system is capable of fabricating high-resolution arbitrary 3D microstructures at the nanoscale through the utilization of a near-infrared laser femtosecond light source.[115] The femtosecond laser is focused precisely onto the bioresin, and its movement is governed by an oil-immersed objective. Moreover, the polymerization process is initiated by two-photon absorption. The system can be accomplished within a remarkably short period of time. Nevertheless, the application of this system is restricted by material degradation and bubble damage caused by high laser power.[57]

2.5. Tomographic volumetric printing

Tomographic volumetric printing (TVP) is an emerging printing approach that constructs entire 3D objects by projecting light patterns from various angles, rather than through iterative layer-by-layer polymerization, and the method features a resolution of up to 80 μm.[116] As TVP technology advances, it becomes feasible to build structures that accommodate arbitrary cells.[117] The high cost and complexity are the main limitations of its application. Additionally, continuous chaotic printing has been developed to fabricate layered structures. A print head equipped with a static mixer is utilized to generate a mixed bioink, and a defined internal layer is extruded to exponentially expand the interface area between adjacent bioinks.[99] These approaches could provide efficient methods for creating heterogeneous tissues, such as osteochondral tissue and bone.

3. 3D-bioprinted hydrogel system for osteochondral integration repair

In this section, we summarize the application of 3D-printed hydrogel systems in osteochondral integrated repair from three aspects: scaffold, cells, and bioactive factors. Hydrogels are the most commonly used materials in 3D bioprinting due to their ability to control printability and viscosity and mimic native tissues.[118,119] As hydrogels alone also promote cell differentiation and tissue regeneration *in vivo*, this review will give an overview of hydrogel substrates in the stent section and then summarize the application of composite hydrogels.

3.1. Hydrogel substrates

3.1.1. Alginate-based hydrogels

Alginate contains two distinct guluronic acids that are found naturally in the cell walls of algae and the capsules of *Azotobacteria* and *Pseudomonas*, and can thus be produced from brown seaweed and bacteria.[120,121] Owing to its excellent biocompatibility, degradability, and ability to form gels, it is widely used in tissue engineering.[122] In osteochondral repair, alginate hydrogels are commonly employed as bioinks to fabricate scaffolds via 3D printing. Chawla et al. fabricated an alginate scaffold that is compatible with blood and cells and facilitates the survival and proliferation of osteoblasts *in vitro*, verifying its biological activity. Moreover, they also demonstrated that the solution formulated with 2.5% alginate and 5% gelatin exhibited optimal viscosity.[123]

Despite these benefits, poor cellular adhesion, migration, and viability may affect cell proliferation and survival.[124] In addition, its weak mechanical properties may compromise its shape fidelity and integrity after printing. To address these shortcomings, alginate has been incorporated with a variety of bioactive molecules, such as bioactive proteins (collagen and fibrin) and cell-adhesion peptides (arginine-glycine-aspartic acid), to improve its ability to promote cell proliferation.[125-127] Additionally, some bioactive inorganic materials (calcium carbonate) and polymers (chitosan) are employed to enhance the mechanical properties of these materials.[128-130] Furthermore, Chawla et al. reported that loading cells in alginate hydrogels also increased their mechanical strength, as the cells secreted matrix.[123]

Owing to the inherent defects of alginate gel, 3D-printed pure alginate hydrogels may not meet the requirements of osteochondral repair, warranting further research into

composite alginate hydrogels for osteochondral repair in future developments.

3.1.2. Methacryloyl-modified gelatin hydrogels

Methacryloyl-modified gelatin (GelMA) is a gelatin derivative composed of methacryloyl side groups (methacrylamide and methacrylate [MA]), with excellent cell adhesion properties due to its retention of most functional amino acid motifs (e.g., RGD motifs).[131,132] GelMA hydrogels have excellent biocompatibility, can load cells, and maintain the controlled release of growth factors, as well as the advantage of low immunogenicity, making them widely used.[133] Jiang et al. fabricated a 3D-printed platelet-rich plasma (PRP)-GelMA hydrogel scaffold using DMD for osteochondral repair in a rabbit model and compared the therapeutic effects of different concentrations of PRP on osteochondral repair. They found that 20% of PRP exhibited the strongest repair effect and could promote the polarization of M2 macrophages.[40]

However, Enhancing the mechanical strength of 3D printed GelMA for soft tissue engineering applications. Current methods to enhance their mechanical properties are mainly through crosslinking with other substances, such as nanomaterials and polymers.[134] Dong et al. prepared a GelMA-GelMA (G-G) homogeneous double-network hydrogel based on DLP 3D printing to improve its mechanical strength. In addition, hydrogen bonding and crosslinking between HA and GelMA hydrogel can also play a role in enhancing mechanical properties[135] (Figure 2i).

3.1.3. Chitosan hydrogels

Chitosan is derived from chitin, which is abundant in nature and has satisfactory biocompatibility and biodegradability. It is an attractive candidate material for tissue engineering.[136] Chitosan hydrogels prepared by enzyme crosslinking can support the proliferation of chondrocytes and mesenchymal stem cells (MSCs), maintain the phenotype and morphology of chondrocytes, and promote the deposition of cartilage ECM *in vitro*.[137] Sheehy et al. verified their capacity to support chondrogenesis and hypertrophy of MSCs. The chondroblast phenotype of MSCs was well retained after 8 weeks of chondrogenesis *in vitro*. *In vivo*, it was discovered that it promoted neither vascularization nor endochondral ossification, suggesting that it is a suitable material for articular cartilage engineering.[138]

However, chitosan possesses poor water solubility under physiological conditions and low cell adhesion, which constitutes the primary reason restricting its application. Currently, the solubility and cell adhesion of chitosan derivatives are regulated by introducing functional groups, ligands, macromolecular side chains, etc.[139,140] Chitosan derivatives demonstrate excellent biological characteristics. Additionally, as chitosan is derived from shellfish or shrimp, the allergic reaction might also impact its clinical transformation. Waibel et al. evaluated its biosafety, and no adverse effects were found in the subjects.[141] Further research is warranted to clarify this issue in the future.

3.1.4. Hyaluronic acid hydrogels

Hyaluronic acid (HA) is an essential constituent of the ECM, and its molecular chain is alternately composed of repeating disaccharide units of β-1,4-D-glucuronate-β-1,3-n-acetyl-d-glucosamine.[142,143] Owing to the diversity of the repeating disaccharide unit, the HA molecule does not induce an immune response. In addition, HA can cause macrophages to polarize from M1 type to M2 type by targeting CD44 *in vivo*, exerting anti-inflammatory effects.[144] HA also has inherent properties against certain strains and antimicrobial delivery. Coupled with its outstanding water retention capacity, biodegradability, and designability, it is extensively utilized in the fields of drug delivery, cell culture, and regenerative medicine.[145,146]

Nevertheless, its high vulnerability to enzymes and weak mechanical properties impede its broader application.[147] Fortunately, there are numerous multifunctional reactive groups in HA, and diverse HA derivatives can be obtained by employing various chemical modification and crosslinking strategies to enhance their mechanical strength and stability[148] (Figure 2i). For instance, HA can be chemically modified with photo-crosslinkable functional groups, such as MA, to facilitate photo-crosslinking between HA molecules.[149] A HAMA hydrogel possesses enhanced mechanical strength, making it suitable for constructing a variety of hydrogels, such as microparticles, microneedles, and 3D-printed scaffolds.[150] The biological properties of HA can also be improved via oxidation or the introduction of sulfhydryl and catechol, etc.[151-153]

3.2. Hydrogel composition

3.2.1. Hydrogel mixed with bioceramics

Bioceramic materials, exemplified by calcium carbonate, calcium phosphate, calcium sulfate, and their derivatives, possess excellent mechanical properties, which can compensate for the weak mechanical properties of hydrogels.[154] Furthermore, the inherent bone inducibility and conductivity of bioceramics facilitate the proliferation and differentiation of MSCs in both scaffold-loaded and bone defect sites, enhancing the repair capacity when combined with hydrogels to form bioinks.[155,156] The common applications of 3D bioprinting of hydrogel in

combination with bioceramics in integrated osteochondral repair are as follows:

(i) Hydroxyapatite (HAP): HAP, the most widely used bioactive material in calcium carbonate ceramics, has outstanding biocompatibility and mechanical properties, which can compensate for the deficiencies in the mechanical properties of hydrogels. In addition, its porous structure is conducive to the growth of bone tissue and vessels.[157] Recently, researchers have endeavored to print scaffolds appropriate for osteochondral repair through the combination of hydrogels and HAP. You et al. compared the biological properties of pure alginate hydrogel scaffolds and alginate hydrogels combined with HAP composite scaffolds. They discovered that chondrocytes exhibited a higher survival rate and proliferation efficiency in the composite scaffolds, as well as a higher level of mineralized matrix, revealing their potential in the integrated repair of osteochondral tissues.[158] Liu et al. employed a composite material consisting of GelMA and nanoHAP (nHAP) to fabricate a three-layer scaffold for repairing OCDs in rabbits and demonstrated a favorable therapeutic effect[134] (Figure 2ii). Furthermore, Wang et al. reported that HAP content and hypoxia are important factors for osteogenic differentiation, hypertrophy, and endochondrosis of adipose MSCs (ADMSCs), but the optimal HAP content has not yet been determined.[159] HAP and hydrogel composite scaffolds demonstrate great potential in osteochondral repair, but the optimal ratio of mixing is still uncertain, and further studies are warranted to determine whether this combination can enhance efficacy.

(ii) β-Tricalcium phosphate (TCP) and magnesium phosphate: The most commonly utilized calcium phosphate derivative is TCP. Among its forms, β-TCP, which has an inorganic composition similar to that of the bone matrix, is widely used in biomaterials due to its ability to effectively bind to bone and ensure normal cell growth and differentiation. In osteochondral repair, Kosik-Kozioł et al. designed a 3D hydrogel scaffold containing β-TCP that can promote the proliferation and differentiation of bone marrow-derived MSCs (BMSCs) and reported that 0.5% w/v TCP was the optimal concentration for the formation of a stable scaffold.[160] Approximately 60% of magnesium in the human body is found in the bone matrix, where it facilitates cell adhesion, proliferation, and differentiation; induces bone mineral deposition; and promotes bone formation.[161] Chen et al. combined a thixotropic magnesium phosphate-based hydrogel material with gellan/alginate to produce bioink, and the printed scaffold exhibited outstanding osteogenic activity.[162]

(iii) The combination of bioceramics and hydrogels as bioinks holds significant potential for 3D printing in osteochondral repair. However, the current number of studies is rather limited, warranting further research to derive more precise conclusions.

3.2.2. Synthetic polymer-reinforced hydrogels

Synthetic polymers, such as polycaprolactone (PCL) and polylactic acid (PLA), are extensively employed as tissue engineering materials due to their plasticity and controllable degradation rate. These polymers are often combined with hydrogels to develop composite materials. Gao et al. combined poly(*N*-acryloyl 2-glycine) (PACG) and GelMA to develop a biodegradable, high-strength molecular polymer-reinforced biohybrid gradient scaffold that promoted the simultaneous regeneration of cartilage and subchondral bone in rats[163] (Figure 2ii). *N*-acryloyl glycinamide (NAGA) is also compounded into a GelMA hydrogel and printed as a scaffold, which has great potential for treating OCDs under OA conditions and exhibits excellent antifatigue and antioxidation properties, as well as printability.[164] In addition, Antich et al. utilized HA and PLA to print a composite scaffold with excellent mechanical properties that can promote cartilage regeneration by increasing the expression of chondrogenic gene markers and specific matrix deposition.[165]

Due to the large amount of equipment required, difficulties with bioink crosslinking, and other issues, traditional 3D bioprinting methods are generally printed *in vitro* before implantation in the body to repair the damaged area. Its long waiting time without treatment makes it a major flaw. As an emerging technology, *in situ* 3D printing can be implemented to greatly reduce the waiting time.[166] Ma et al. 3D printed a four-arm pegylated hydrogel hybrid scaffold *in situ* with robotic assistance, and OCDs could be repaired in approximately 60 s.[167]

Although many studies have explored the use of polymer hydrogel composites in osteochondral integrative repair, many problems remain in their clinical application. For example, further extensive and clinical translational research is required to determine how to better control the degradation rate to match bone growth and identify optimal porosity. Furthermore, while *in situ* 3D printing technology has begun to be applied, more relevant research and better technology are needed to improve repair results in the future.

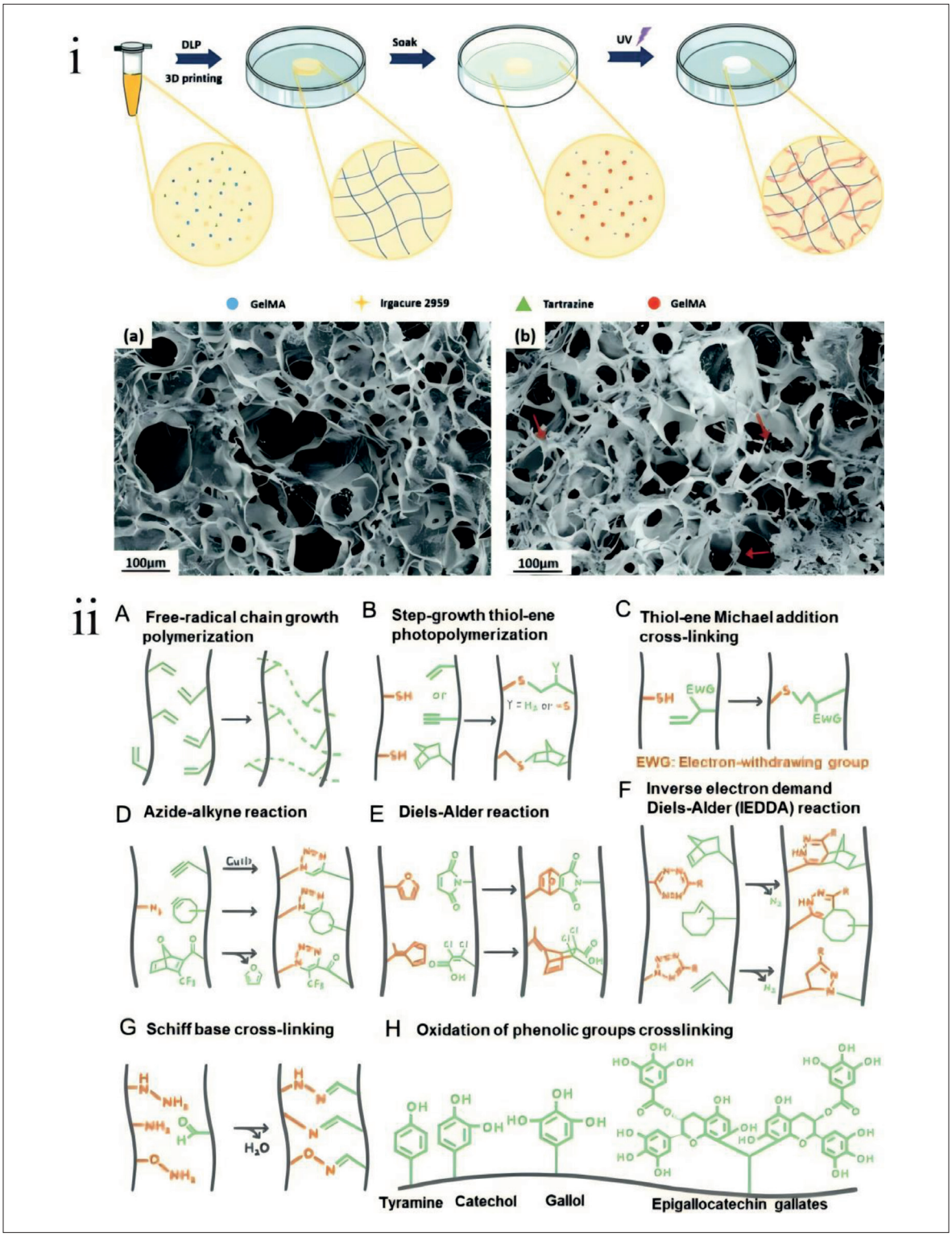

Figure 2. Methods for strengthening the mechanical strength of hydrogel. (i) Schematic illustration of the preparation of G–G DN hydrogels, and SEM photographs of GelMA and G–G hydrogel (the scale bar is 100 μm). (a) GelMA, (b) G–G (the red arrow indicates the second network). Both hydrogels showed a porous three-dimensional network structure, but the pore sizes of pure GelMA hydrogel differed greatly and were relatively isolated. Reprinted with permission from Ref[135]. *Copyright © 2022 Royal Society of Chemistry.* (ii) Schematic representations of various chemical crosslinking strategies for inducing HA hydrogels. Reprinted with permission from Ref[148]. *Copyright © 2023 Elsevier.*"

3.2.3. Hydrogels made from various composite materials

Some researchers have attempted to use two or more composite hydrogels to treat OCDs. Polymeric scaffolds are extensively utilized in bone tissue engineering due to their biocompatibility, ductility, and customizability. Compared with other polymers, polycaprolactone (PCL) has greater toughness, elasticity, and mechanical strength and is the most prevalently employed synthetic polymer.[168,169] Chen et al. fabricated a 3D bioprinting biphasic scaffold, where the cartilage phase scaffold consisted of alginate saline gel and PCL, and the bone phase scaffold was loaded with HAP in the PCL.[170] This hybrid scaffold exhibits an ideal biological response both in the short and long term, and it has the potential to be used as an interface material for cartilage and bone.

Owing to the deficiency of bone-induced characteristics, the utilization of PCL in bone tissue engineering is limited.[171] Currently, numerous studies have endeavored to coat porous scaffolds with certain natural biological materials to enhance their cell adhesion.[172] The cartilage ECM is a special type of natural biological material and also a fiber-reinforced composite material, and it can increase the expression of collagen II and aggrecan in chondrocytes, thereby increasing cell adhesion.[173] Li et al. designed a double-layered scaffold; the cartilage layer was composed of ECM, polycaprolactone (PCL), and hydrogel, and the subchondral bone layer was composed of PCL and polydopamine (PDA) modified with magnesium oxide (MgO) nanoparticles. The scaffold effectively regenerated bone and cartilage simultaneously in rats.[174]

Additionally, researchers are applying natural compounds to bone tissue engineering. Honokiol is the main bisphenol compound isolated from *Magnolia* trees and is reported to have a wide range of biological activities and low cytotoxicity.[175] Zhu et al. used ECM, polyethylene glycol diacrylate (PEGDA), and honokiol to develop hydrogel scaffolds, and the 3D-printed hydrogel scaffolds exhibited excellent osteochondral regeneration ability.[176]

Owing to the varying advantages and disadvantages of different materials, fabricating scaffolds by combining multiple materials can address the various requirements of osteochondral repair. However, the complex fabrication process may be a major factor limiting its application. In the future, it is imperative to identify more suitable materials and simplify the production process (Table 3).

3.3. Enhancement of the biofunctions of hydrogel-based osteochondral repair

In addition to the recruitment of cells, such as MSCs, or bioactive factors to promote bone repair, the direct delivery of homologous or dissimilar MSCs and the stimulation of molecules constitute a strategy for bone tissue engineering. Herein, we will discuss enhancing the biofunctions of hydrogel-mediated osteochondral repair using cells and growth factors.

3.3.1. Mesenchymal stem cells

Mesenchymal stem cells (MSCs) come from a wide range of sources and can differentiate into bone cells and chondrocytes that play important roles in tissue repair.[177] Shim et al. 3D-printed a hydrogel scaffold containing human turbinate-derived MSCs (hTMSCs), and the scaffold demonstrated good osteochondral regeneration in rabbits.[178] Gao et al. uniformly printed human MSCs on polymerized poly(ethylene glycol) (PEG)-GelMA, and the scaffold demonstrated remarkable osteogenic and chondrogenic differentiation.[179] Zhang et al. fabricated a composite scaffold with HAP and a hydrogel and gradient-loaded BMSCs onto the scaffold in accordance with osteochondral characteristics, demonstrating favorable osteochondral repair effects in rabbit models.[180]

Furthermore, chronic inflammation within the joint reduces chondrogenesis and MSC motility, leading to cartilage matrix interpretation and thus exacerbating the progression of osteochondral injury.[181,182] Therefore, inhibiting the inflammatory microenvironment is key for effectively repairing OCDs caused by inflammatory diseases, such as OA. Liu et al. designed a 3D-printed multilayer hydrogel scaffold loaded with BMSCs. The PCL layer combines with β-TCP for bone regeneration, whereas PCL/methacrylated hyaluronic acid (MeHA) combines with Kartogenin (KGN) for cartilage regeneration. Diclofenac sodium (DC)-supported hydrogel coating was applied to the top of the articular facing stent to inhibit the inflammatory microenvironment[183] (Figure 3i). This composite scaffold can effectively promote osteochondral repair by promoting the deposition of ECM proteins and suppressing the production of interleukin-1β.

Promoting cartilage vascularization is also a major challenge in bone tissue engineering. Although cartilage templates are well-vascularized *in vivo*, vascularization begins peripherally, and the central region of cartilage remains vascular-free. To address this issue, Daly et al. developed a 3D-printed hydrogel scaffold loaded with MSCs, promoting vascularization after implantation with the potential to repair large bone defects.[184]

In bioprinting, the contact between cells and the cell contact-dependent signal is blocked due to the trapping effect of the hydrogel, resulting in the loss of their biological activity.[185] The spheroid, a multicellular aggregate with a microenvironment similar to native tissue, is an advanced printing unit with the potential to become a bioink for bone tissue engineering. Its extensive intercellular contact

Table 3. Application of various hydrogel formulations in 3D bioprinting for osteochondral repair.

Hydrogel composition	Crosslinking method	Effects	Model	Ref.
Alginate	Physical (ionic interaction)	Promote the survival and proliferation of osteoblasts	*In vitro*: MG63 osteoblasts	[123]
Hydroxyapatite (HAP); alginate	Physical	Promote the survival and proliferation of chondrocytes; stimulate chondrocytes to secrete calcified matrix	*In vitro*: Chondrocytes *In vivo*: Mouse subcutaneous implantation	[158]
Nanohydroxyapatite (nHAP); methacrylated gelatin (GelMA)	Physical	Promote osteochondral regeneration; promote the formation of cartilage-like extracellular matrix (ECM) and type II collagen	*In vitro*: Bone marrow-derived mesenchymal stem cells (BMSCs) *In vivo*: Rabbit osteochondral defect	[134]
HAP; hyaluronic acid (HA)	Physical	Promote both chondrogenic and hypertrophic differentiation of adipose mesenchymal stem cells (ADMSCs); promote osteogenic differentiation	*In vitro*: ADMSCs *In vivo*: Mouse subcutaneous implantation	[159]
β-tricalcium phosphate (TCP); GelMA; alginate	Physical and chemical (Ultraviolet [UV] radiation)	Promote the differentiation of BMSCs; promote the calcification of osteochondral region	*In vitro*: BMSCs	[160]
Alginate; gellan gum; thixotropic magnesium phosphate-based gel (TMP-BG)	Physical ($CaCl_2$)	Promote osteogenic and chondrogenic differentiation of BMSCs; upregulation of osteogenic genes	*In vitro*: MG63 osteoblasts *In vivo*: Rabbit knee defects	[162]
Poly(*N*-acryloyl 2-glycine) (PACG); GelMA; Mn^{2+}	Chemical (UV radiation)	Promote simultaneous regeneration of bone and cartilage; upregulated expression of bone-forming and cartilage-related genes in BMSCs	*In vitro*: BMSCs *In vivo*: Rat OCDs	[163]
N-acryloyl glycinamide (NAGA); Laponite; Tannic; GelMA	Chemical	Promote proliferation, chondrogenic differentiation, and osteogenic differentiation of BMSCs; oxidation resistance	*In vitro*: BMSCs	[164]
Polylactic acid (PLA); alginate; HA	Physical ($CaCl_2$)	Increased chondrogenesis marker gene expression and specific matrix deposition	*In vitro*: Chondrocytes	[165]
Four-armed polyethylene glycol-acrylate (PEG-ACLT); HAP; GelMA	Chemical	Directly obtain autogenous mesenchymal stem cells (MSCs) from the surrounding microenvironment; promote osteochondral regeneration	*In vitro*: Resin femoral condyle *In vivo*: Rabbit knee OCDs	[167]
Polycaprolactone (PCL); HAP; alginate	Physical ($CaCl_2$)	Promote chondrocyte proliferation and differentiation; promote calcium deposition	*In vitro*: Chondrocytes	[170]
PCL; MgO; polydopamine (PDA); ECM	Chemical	Stimulate proliferation, chondrogenic differentiation, and osteogenic differentiation of BMSCs	*In vitro*: BMSCs *In vivo*: Rat OCDs	[174]
Polyethylene glycol diacrylate (PEGDA); honokiol; ECM	Chemical	Inhibit macrophage release of inflammatory factors; promote osteochondral regeneration	*In vitro*: Macrophage *In vivo*: Rat OCDs	[176]

promotes cell signal transmission and maintains stem cell function.[186-188] Zhang et al. constructed a porous composite particle hydrogel loaded with ADMSC spheres, which demonstrated high levels of viability and efficient cartilage/bone differentiation after 3D printing[189] (Figure 3i).

At present, 3D-printed hydrogel scaffolds loaded with MSCs have displayed excellent osteochondral repair effects. Although they are unlikely to completely mimic the physiological and biochemical properties of natural osteochondral tissue, they have the potential for clinical applications. For example, natural tissues have an unevenly distributed porous structure, making it promising to prepare scaffolds with gradient porosity that closely mimics the porosity of each layer of bone cartilage. Research has demonstrated that scaffolds with 90–120 μm apertures facilitate the chondrogenic differentiation of MSCs,

whereas scaffolds with larger apertures (>300 μm) promote osteogenic differentiation and vascularization.[190,191] Scaffolds with vertical porosity and pore size gradients can promote the bidirectional differentiation of MSCs.[192,193] Moreover, future studies should consider both the anti-inflammatory and vascularization capabilities of stents. Given the complexity of 3D printing cellular spheres, it is necessary to develop an integrated platform to achieve efficient manufacturing of spheres through 3D printing technology.[194]

3.3.2. Chondrocytes and osteocytes

Although scaffold-coated MSCs exhibit high cell viability in bone repair, they may still lack the ability to promote cell differentiation and new bone formation in the absence of growth factors. Therefore, chondrocytes or osteoblasts are sometimes loaded directly onto the scaffold to enhance bone repair. Diloksumpan et al. utilized chondrocytes containing hydrogels, bioceramics, and polymers to design a hybrid 3D-printed scaffold with a mechanically strengthened osteochondral interface, offering valuable insights for designing interfaces and materials in regenerative medicine.[195] Zhai et al. created a PEG-clay nanocomposite crosslinked hydrogel scaffold with osteoblasts via a two-channel 3D printing technique. The scaffold allows osteoblasts to obtain oxygen and nutrients, providing superior bone protection.[196]

Studies have demonstrated that chondrocytes exhibit superior proliferation and cell functionality on HA hydrogels, whereas osteoblasts exhibit better proliferation and cell function on type I collagen (COL I) hydrogels.[197] Therefore, to achieve better repair results, it is necessary to choose the appropriate hydrogel material for the loaded cells. Further studies are warranted to verify the efficacy of the direct loading of chondrocytes or osteoblasts.

3.3.3. Mixed cells

Given that bone cartilage inherently possesses a layered structure, researchers have endeavored to load distinct cells at various levels to fabricate 3D-printed scaffolds loaded with multiple types of cells to augment the effect of bone cartilage repair. Critchley et al. designed a 3D-printed biphasic fiber-reinforced hydrogel scaffold loaded with MSCs while highlighting its cartilage layer with infrapatellar fat pad-derived stem/stromal cells (FPSCs) and chondrocytes, achieving favorable therapeutic effects in a goat model.[198] Zhang et al. employed dual-channel extrusion bioprinting technology to generate innovative anisotropic bicellular living hydrogels (ABLHs). The upper layer is embedded with articular cartilage progenitor cells (ACPCs) derived from cartilage to promote cartilage formation, and the lower layer is populated with BMSCs to promote bone formation.[199]

3.3.4. Growth factors

The cytokine TGF-β, belonging to the TGF-β superfamily, plays a crucial role in embryonic bone development and the homeostasis of bone and cartilage after birth; it is also capable of facilitating the early development of chondrocytes.[200] In osteochondral tissue engineering, Gao et al. 3D-printed a double-layer hydrogel scaffold; the upper layer was loaded with TGF-β to facilitate cartilage differentiation, and the lower layer employed TCP to enhance the mechanical properties of the hydrogel.[201]

Bone morphometric proteins (BMPs) are cytokines also from the TGF-β family that exhibit structural similarities. In contrast to TGF-β, BMPs facilitate differentiation at all stages of chondrocyte cell differentiation. The spatiotemporal integration of these growth factors can also restore osteochondral tissue by inducing cartilage formation and osteogenesis within a single scaffold.[202] Qiao et al. fabricated a three-layer scaffold through 3D printing, in which BMP-7 and TGF-β1 were contained in the cartilage surface layer; TGF-β1 was present in the calcified cartilage layer; BMP-2 was located in the subchondral bone layer. This successfully enabled the precise delivery of various cytokines to the three-layer structure of osteochondral tissue and enhanced bone regeneration[203] (Figure 3i).

However, questions remain regarding the application of TGF-β. Excessive TGF-β can lead to side effects on bone tissue, possibly worsening OA; thus, further research is warranted to determine the appropriate dosage. Additionally, more investigation is required to effectively promote bone regeneration.

Stromal cell-derived factor-1α (SDF-1α) is a potent chemokine that can recruit BMSCs and plays a pivotal role in endogenous tissue repair, as demonstrated in a rotator cuff injury model.[204,205] The conventional approach for incorporating SDF-1α into scaffolds involves direct protein integration, but rapid double osmosis and degradation limit its sustained impact on stem cell recruitment. To address this issue, researchers have explored various methods, such as chemical fixation and co-encapsulation with other growth factors, to enhance cartilage repair.[206,207] However, these methods may inadvertently recruit other cells, such as endothelial progenitor cells, lymphocytes, and macrophages, which can impede the efficacy of cartilage regeneration.[208] In order to overcome this challenge, Zeng et al. chemically crosslinked HAP and hydrogel to create a mechanically robust scaffold. Subsequently, they chemically crosslinked ligands and loaded SDF-1α-coated poly(lactide-co-acetic acid) (PLGA) nanospheres to specifically capture BMSCs *in vivo* (Figure 3ii).[130] Additionally, they utilized pre-designed bioinks for *in situ*

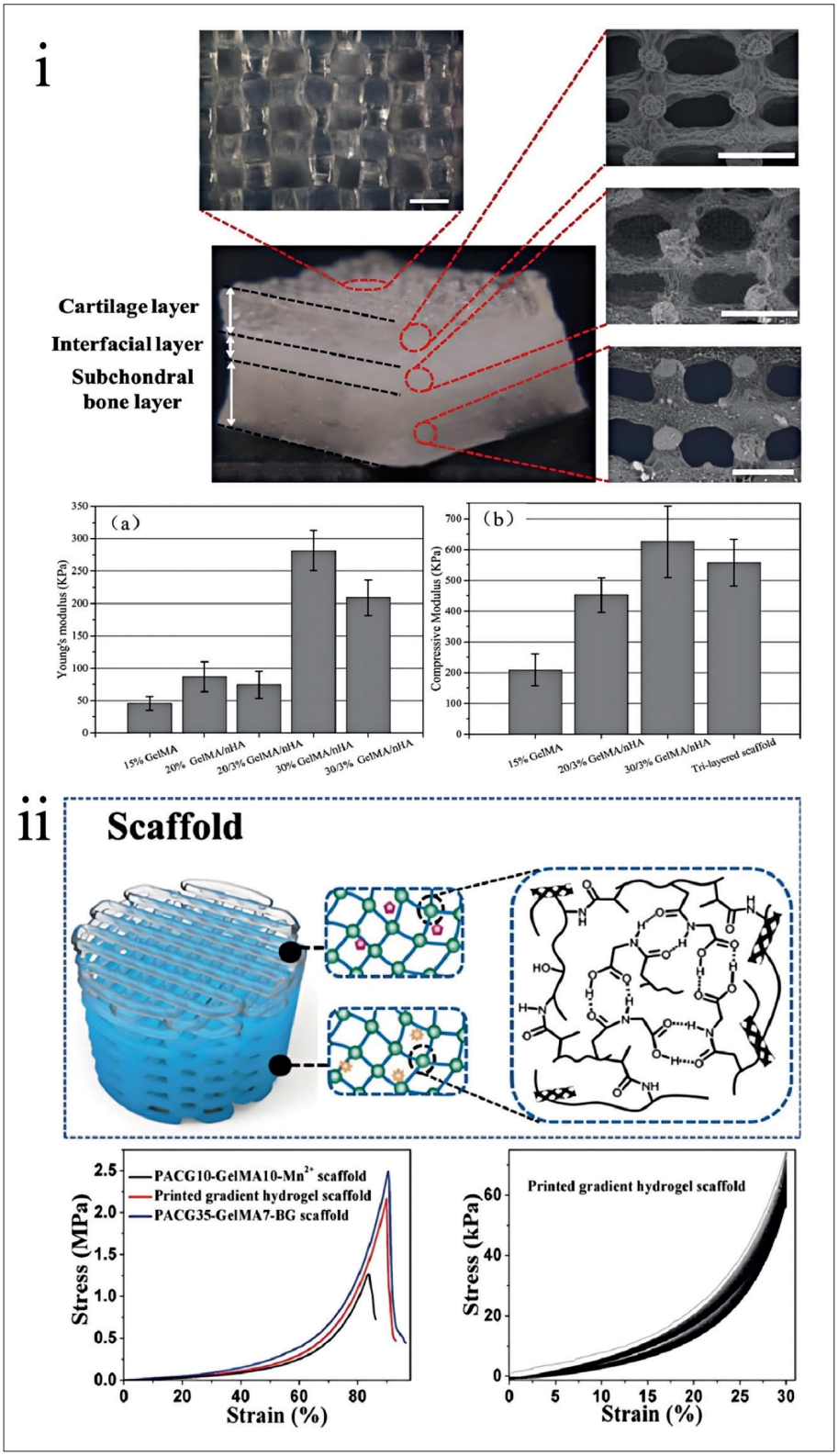

Figure 3. Methods to further enhance the osteochondral regeneration effect of hydrogel scaffolds. (i) The Schematic diagram of the preparation process and application scenario of the tri-layered fiber-reinforced and GF-loaded hydrogel construct, and its osteochondral repair effects. Reprinted with permission from Ref[203]. *Copyright © 2021 Elsevier*. (ii) Schematic diagrams of A) the composition of pre-designed bioink modular units and manufacturing process and B) the in situ inductive regeneration process of OC defects. Reprinted with permission from Ref[130]. *Copyright © 2024 Wiley.*"

printing to bypass the need for prior *in vitro* culture while preserving the dryness and homing ability of BMSCs.[209,210]

Several studies have evaluated growth factor-loaded hydrogel scaffolds for 3D-printed osteochondral repair, indicating a potential future research direction.

3.3.5. Exosomes

Exosomes (exos) are extracellular vesicles secreted by cells, with a diameter of 40–160 nm. They are rich in a variety of cytokines and growth factors and are often involved in intercellular communication.[211] Exos derived from MSCs have been reported to accelerate cartilage and subchondral bone regeneration; thus, the development of bioactive materials based on exos has broad clinical application prospects.[212,213] Sun et al. loaded the exos of MSCs onto the upper layer of a double-layer 3D-printed hydrogel scaffold, achieving a near-normal tissue repair effect in a rabbit osteochondral injury model.[214] Li et al. combined decellularized ECM (dECM) and exos for the first time to construct a spatially biomimetic scaffold by employing 3D printing technology; the dCEM is capable of promoting cartilage and bone formation, BMSC seeding, and the continuous release of exos, effectively accelerating osteochondral regeneration in rat models.[215] Moreover, several studies have demonstrated that specific vesicle subtypes encompass complete mitochondria or mitochondrial components, which can enhance the functional status of target cells and restore mitochondrial function via mitochondrial transfer among cells.[216-218] On this basis, Chen et al. fabricated an oriented scaffold through 3D printing of exos derived from MSCs, GelMA hydrogels, and ECM, and the scaffold could ameliorate mitochondrial dysfunction in chondrocytes, enhance chondrocyte migration, and facilitate the polarization of synovial macrophages to the M2 phenotype, which is beneficial for osteochondral tissue regeneration.[219] However, given the profusion of bioactive molecules in exos, the mechanism of osteogenesis and chondrogenesis induced by exos remains ambiguous, and further studies are required to validate this mechanism. The correlation between the exos release curve and the scaffold degradation rate merits optimization to determine the optimal effect on bone repair. Additionally, to increase their efficacy, exos with targeted delivery functionality constitute a promising research direction (Table 4).

4. Conclusion and future perspectives

Articular cartilage and subchondral bone constitute unified functional units, and the notion of "osteochondral unit repair and regeneration" has endured for a considerable period. Nevertheless, owing to the disparity between ischemic and non-neurogenic hyaline cartilage and the vascular abundance of subchondral bone, the reconstruction of damaged tissue persists as a significant clinical conundrum.[37] The innovative manufacturing process known as 3D printing offers numerous opportunities for advancing osteochondral tissue engineering.[220] Given the critical need for precision in fabricating osteochondral scaffold structures, enhancing print resolution stands out as a key technical challenge alongside considerations related to print speed and processing costs.[221] Electrodynamic printing technology is an innovative printing method, which has a superior resolution compared to traditional printing technology. However, limited research currently exists in this area. Future investigations into this technology are anticipated to fabricate scaffolds with improved osteochondral tissue properties.[41] *In situ* 3D printing technology eliminates the need for *in vitro* cell culture, reducing complexity and the risk of cell contamination while enhancing repair capabilities, making it another key focus for future research.

For multilayer scaffolds, mismatched strain poses a significant challenge and may result in design failures if not appropriately addressed. It is crucial to align the mechanical properties across layers for enhanced bonding strength.[4,222] However, the current literature lacks comprehensive studies on this aspect. Furthermore, natural osteochondral tissue exhibits an unevenly distributed porous structure, which has been reported to promote the bidirectional differentiation of MSCs and osteochondral regeneration.[192] Given these findings, focusing on gradient porosity structures could offer more promising avenues for future research. Besides its porosity, the two-layer structure of bone cartilage also has distinct mechanical properties. Substrate stiffness influences the migration of MSCs and their differentiation into various cell types.[223] Therefore, the uneven mechanical distribution should be controlled more precisely through 3D printing. One method involves printing gradient structures by altering the ratio of hydrogels and bioactive nanomaterials in different layers[201]; the other method involves printing gradient structures by patterning diverse bioinks or crosslinking densities.[224]

Recently, researchers have expressed significant interest in the 4D bioprinting of multifunctional bone scaffolds, which incorporates time as the fourth dimension.[225] Unlike traditional 3D printing, scaffolds produced through 4D technology exhibit predictable transformations over time concerning their form or functionality when subjected to specific external stimuli like pH levels or changes in humidity and temperature conditions.[226] Notably, it can furnish original-shaped osteochondral tissue scaffolds suitable for minimally invasive placement in host environments. Materials applicable for use in 4D

Table 4. Application of 3D-printed bioactive hydrogels in osteochondral repair.

Hydrogel composition	Bioactive factor	Crosslinking method	Effects	Model	Ref.
GelMA	PRP	N/A	Promote the polarization of M2 macrophages; promote osteochondral regeneration	*In vitro*: BMSCs *In vivo*: Rabbits	40
Atelocollagen; HA	hTMSCs	N/A	Promote osteochondral regeneration	*In vitro*: hTMSCs *In vivo*: Rabbit OCDs	178
PEG-GelMA	hMSCs	Chemical (photo-crosslinked)	Promote early differentiation of hMSCs; excellent osteogenic and cartilage differentiation ability	*In vitro*: hMSCs	179
nHA	BMSCs	Physical ($CaCl_2$)	Create nHA gradients; promote osteochondral regeneration	*In vitro*: BMSCs *In vivo*: Rat OCDs	180
PCL; KGN; β-TCP; DC; HeMA	BMSCs	Chemical	Promote type II collagen and inhibit interleukin-1β; promote osteochondral regeneration; promote the deposition of ECM protein	*In vitro*: BMSCs *In vivo*: Rat OCDs	183
GelMA	MSCs	Physical	Improve the vascularization level in the core area of bone defect; promote osteochondral regeneration	*In vitro*: MSCs *In vivo*: Rat OCDs	184
NIPAM; SBMA	ASCs spheres	Chemical	High level of viability and stemness; efficient chondrogenic/osteogenic/adipogenic differentiation	*In vitro*: ASC spheres *In vivo*: Rabbit OCDs	189
Bioceramic; polymers; GelMA	Chondroprogenitor cells	Physical	Hydrogel-ceramic interfaces; multiscale 3D printing; promote osteochondral regeneration	*In vitro*: MSCs; chondrocytes	195
PEGDA; XLG nanoclay; HA	Osteoblasts	Chemical (photo-crosslinked)	Two-channel 3D printing; deliver oxygen and nutrients; promote osteoblast proliferation and differentiation.	*In vitro*: Osteoblast *In vivo*: Rat tibia defect	196
PCL; PLA; PLGA; alginate	BMSCs; FPSCs; Chondrocytes	Chemical	Biphasic, fiber-reinforced cartilaginous templates; promote osteochondral regeneration	*In vitro*: BMSCs *In vivo*: Mouse subcutaneous implantation; goat OCDs	198
GelMA; alginate	ACPCs; BMSCs	Chemical (photo-crosslinked)	Two-channel extrusion bioprinting; anisotropic bicellular living hydrogels; promote osteochondral regeneration	*In vitro*: ACPCs; BMSCs *In vivo*: Rabbit OCDs	199
HA-DA; oxidized HA; GelMA	MSCs-derived exos; dECM	Chemical (UV-radiation)	Novel cell-free recipe for stem cell therapy; promote osteochondral regeneration	*In vitro*: Rat BMSCs *In vivo*: Rat OCDs	215
GelMA	ECM; MSCs-derived exos	Chemical (photo-crosslinked)	Restore chondrocyte mitochondrial dysfunction; enhance chondrocyte migration; polarize the synovial macrophage response toward an M2 phenotype	*In vitro*: Chondrocytes *In vivo*: Rabbit OCDs	219

(Continued)

Table 4. Continued

PNAGA	TGF-β	Chemical	High-strength biohybrid gradient hydrogel; promote osteochondral regeneration	*In vitro*: Human BMSCs *In vivo*: Rat OCDs	[201]
PCEC; PLGA microspheres; GelMA	TGF-β; BMP-7; BMP-2	Chemical (UV-radiation)	Tri-layered biohybrid scaffold with zone-specific GF delivery; promote osteochondral regeneration; the superficial cartilage layer increases surface lubricity and friction resistance	*In vitro*: MSCs *In vivo*: Rabbit OCDs	[203]
HAP; PLGA nanospheres; alginate	SDF-1α	Chemical	*In situ* printing; sustained, slow release of SDF-1α; specific recruitment of BMSCs	*In vitro*: BMSCs *In vivo*: Rabbit OCDs	[130]

Abbreviations: GelMA: Methacrylated gelatin; PRP: Platelet-rich plasma; N/A: Not mentioned; BMSCs: Bone marrow-derived mesenchymal stem cells; HA: Hyaluronic acid; hTMSCs: Human turbinate-derived mesenchymal stem cells; PEG: Polyethylene glycol; hMSCs: Human mesenchymal stem cells; nHA: XXX; PCL: Polycaprolactone; KGN: Kartogenin; TCP: Tricalcium phosphate; DC: Diclofenac sodium; HEMA: XXX; ECM: Extracellular matrix; NIPAM: *N*-isopropylacrylamide; SBMA: sulfobetaine methacrylate; ASCs: Adipose-derived mesenchymal stem cells; PEGDA: Polyethylene glycol diacrylate; XLG: laponite XLG nanoclay; PLA: Polylactic acid; PLGA: Polylactic-co-glycolic acid; FPSCs: Fat pad-derived stem/stromal cells; ACPCs: Articular cartilage progenitor cells; UV: Ultraviolet; HA-DA: dopamine-conjugated HA; dECM: Decellularized extracellular matrix; PNAGA: polymer (*N*-acryloyl glycinamide); PCEC: triblock polymer of poly(ε-caprolactone) and poly(ethylene glycol); HAP: Hydroxyapatite; GF: Growth factor.

bioprinting include shape-memory alloys (SMA), shape-memory ceramics (SMC), shape-memory polymers (SMPs), and shape-memory hydrogels (SMH).[227] This research area holds promise as a potential focal point for future studies.

Equally vital are aspects such as expanding biological materials options, selecting appropriate seed cells, and adapting bioactive substances.[36] Hydrogels have excellent elastic and hydration properties that mimic the crosslinked network structure of the ECM, enabling cells to survive and maintain their function. Therefore, hydrogels are the most commonly used biomaterials in 3D printing. At present, there have been steady changes and improvements in improving the mechanical properties of hydrogels by crosslinking them with different substances, such as TCP and synthetic polymers. However, the composition and structure of the material optimization have not been fully investigated and clarified. Particularly, developing a scaffold that enables cell infiltration while providing mechanical stability in the early stages of healing poses an extremely challenging task. The alignment of the tide line between bone and cartilage remains unresolved when fabricating osteochondral implants. Future efforts should focus on further optimizing 3D-printed hydrogel scaffolds.

In addition to scaffold materials, the cell source is also a crucial factor affecting the treatment efficacy of OCD with tissue engineering. Currently, most researchers have shifted their focus from tissue-specific cells to progenitor cells.[228] The osteogenic and chondrogenic differentiation of MSCs has been extensively investigated, but the heterogeneity in origin, separation methods, and differentiation mechanism of MSCs still needs to be addressed.[229] Aging,[230] continuous passage,[231] and donor parameters[232] can also impact the regenerative potential of MSCs. For scaffold-loaded bioactive factor strategies, the dose profiles and release curves of bioactive factors should be optimized and rigorously validated methodologically.

In addition to the physical properties of bioinks, certain effects and mechanisms should also be considered. Bioelectric effects in bone play a highly important role in bone development and fracture healing, and their endogenous electric fields contribute to cell proliferation, differentiation, and migration.[233] Consequently, researchers can attempt to construct bone tissue scaffolds with a biomimetic electric microenvironment.[234] Additionally, self-healing enables hydrogels to withstand repeated damage. Therefore, self-healing mechanisms, such as host-guest noncovalent interactions, ionic bonding, and hydrogen bonding, can be incorporated into hydrogels to restore their original properties after damage. Wei et

al. introduced host-guest noncovalent interactions into photo-crosslinked HA hydrogels and developed a dual-network dynamic hydrogel with excellent self-healing ability.[235] Moreover, the integration of hydrogels with surrounding tissue after implantation is particularly important for bone regeneration. Thus, researchers can attempt to develop adhesive hydrogels to improve the mechanical integrity between hydrogels and tissues in future research.[236] Moreover, the piezoelectric effect can also regulate cell function and contribute to bone tissue repair and regeneration.[237] Introducing piezoelectric materials (such as zinc oxide[237] and barium titanate[238]) into 3D-printed hydrogels may be a promising approach in the future. Chronic inflammation and excessive reactive oxygen species (ROS) within the joint can exacerbate the progression of osteochondral injury. Hence, incorporating certain anti-inflammatory substances into hydrogels to decrease the generation of inflammatory mediators and ROS and facilitate osteochondral regeneration is feasible.[183,239]

In conclusion, 3D printing is an emerging technology that has attracted increasing interest in the clinical setting due to its high resolution, tunable composition, and mechanical properties. Although 3D printing technology cannot yet fully replicate the characteristics of natural osteochondral tissue, it holds great promise for effectively regenerating osteochondral tissue with advancements in new technologies and biomaterials.

Acknowledgments

None.

Funding

The authors would like to thank the following funding sources: The National Natural Science Foundation of China (82002304, 82172394, U22A20280); 1.3.5 Project for Disciplines of Excellence, West China Hospital, Sichuan University (2023HXFH012 and ZYGD23033).

Conflicts of interest

Xulin Hu serves as the Editorial Board Member of the journal but was not in any way involved in the editorial and peer-review process conducted for this paper, directly or indirectly. Other authors declare they have no competing interests.

Author contributions

Conceptualization: Haiwei Tang, Enze Zhao
Investigation: Haiwei Tang, Enze Zhao, Yahao Lai, Xiaoting Chen
Methodology: Yahao Lai, Anjin Chen, Weinan Zeng
Formal analysis: Haiwei Tang, Enze Zhao, Yahao Lai
Writing – original draft: Haiwei Tang, Enze Zhao
Writing – review & editing: Xulin Hu, Kai Zhou, Zongke Zhou

Ethics approval and consent to participate

Not applicable.

Consent for publication

Not applicable.

Availability of data

Not applicable.

References

1. Wu J, Kuang L, Chen C, et al. miR-100-5p-abundant exosomes derived from infrapatellar fat pad MSCs protect articular cartilage and ameliorate gait abnormalities via inhibition of mTOR in osteoarthritis. *Biomaterials.* 2019;206:87-100. doi: 10.1016/j.biomaterials.2019.03.022
2. Lin W, Kluzek M, Iuster N, et al. Cartilage-inspired, lipid-based boundary-lubricated hydrogels. *Science.* 2020;370(6514):335-338. doi: 10.1126/science.aay8276
3. Lesage C, Lafont M, Guihard P, Weiss P, Guicheux J, Delplace V. Material-assisted strategies for osteochondral defect repair. *Adv Sci (Weinh).* 2022;9(16):e2200050. doi: 10.1002/advs.202200050
4. Zhou L, Gjvm VO, Malda J, et al. Innovative tissue-engineered strategies for osteochondral defect repair and regeneration: current progress and challenges. *Adv Healthc Mater.* 2020;9(23):e2001008. doi: 10.1002/adhm.202001008
5. Deng C, Chang J, Wu C. Bioactive scaffolds for osteochondral regeneration. *J Orthop Translat.* 2019;17:15-25. doi: 10.1016/j.jot.2018.11.006
6. Ansari S, Khorshidi S, Karkhaneh A. Engineering of gradient osteochondral tissue: from nature to lab. *Acta Biomater.* 2019;87:41-54. doi: 10.1016/j.actbio.2019.01.071
7. Wang S, Zhao S, Yu J, Gu Z, Zhang Y. Advances in translational 3D printing for cartilage, bone, and osteochondral tissue engineering. *Small.* 2022;18(36):e2201869. doi: 10.1002/smll.202201869
8. Wei W, Dai H. Articular cartilage and osteochondral tissue engineering techniques: recent advances and challenges. *Bioact Mater.* 2021;6(12):4830-4855. doi: 10.1016/j.bioactmat.2021.05.011
9. Hu W, Chen Y, Dou C, Dong S. Microenvironment in subchondral bone: predominant regulator for the treatment of osteoarthritis. *Ann Rheum Dis.* 2021;80(4):413-422.

doi: 10.1136/annrheumdis-2020-218089

10. Zhang H, Wang L, Cui J, et al. Maintaining hypoxia environment of subchondral bone alleviates osteoarthritis progression. *Sci Adv.* 2023;9(14):eabo7868. doi: 10.1126/sciadv.abo7868

11. Kang J, Li Y, Qin Y, et al. *In situ* deposition of drug and gene nanoparticles on a patterned supramolecular hydrogel to construct a directionally osteochondral plug. *Nanomicro Lett.* 2023;16(1):18. doi: 10.1007/s40820-023-01228-w

12. Niu X, Li N, Du Z, Li X. Integrated gradient tissue-engineered osteochondral scaffolds: challenges, current efforts and future perspectives. *Bioact Mater.* 2023;20:574-597. doi: 10.1016/j.bioactmat.2022.06.011

13. Li H, He Z, Li W, et al. Exploring the mechanism of microfracture in the treatment of porcine full-thickness cartilage defect. *Am J Sports Med.* 2023;51(4): 1033-1046. doi: 10.1177/03635465231153630

14. Ghouri A, Muzumdar S, Barr AJ, et al. The relationship between meniscal pathologies, cartilage loss, joint replacement and pain in knee osteoarthritis: a systematic review. *Osteoarthritis Cartilage.* 2022;30(10):1287-1327. doi: 10.1016/j.joca.2022.08.002

15. Kubosch EJ, Lang G, Furst D, et al. The potential for synovium-derived stem cells in cartilage repair. *Curr Stem Cell Res Ther.* 2018;13(3):174-184. doi: 10.2174/1574888x12666171002111026

16. Schuette HB, Kraeutler MJ, Schrock JB, McCarty EC. Primary autologous chondrocyte implantation of the knee versus autologous chondrocyte implantation after failed marrow stimulation: a systematic review. *Am J Sports Med.* 2021;49(9):2536-2541. doi: 10.1177/0363546520968284

17. Gilat R, Haunschild ED, Huddleston H, et al. Osteochondral allograft transplantation of the knee in adolescent patients and the effect of physeal closure. *Arthroscopy.* 2021;37(5):1588-1596. doi: 10.1016/j.arthro.2020.12.204

18. Gao L, Orth P, Cucchiarini M, Madry H. Autologous matrix-induced chondrogenesis: a systematic review of the clinical evidence. *Am J Sports Med.* 2019;47(1):222-231. doi: 10.1177/0363546517740575

19. Welch T, Mandelbaum B, Tom M. Autologous chondrocyte implantation: past, present, and future. *Sports Med Arthrosc Rev.* 2016;24(2):85-91. doi: 10.1097/jsa.0000000000000115

20. Tuan RS. A second-generation autologous chondrocyte implantation approach to the treatment of focal articular cartilage defects. *Arthritis Res Ther.* 2007;9(5):109. doi: 10.1186/ar2310

21. Niemeyer P, Köstler W, Salzmann GM, Lenz P, Kreuz PC, Südkamp NP. Autologous chondrocyte implantation for treatment of focal cartilage defects in patients age 40 years and older: a matched-pair analysis with 2-year follow-up. *Am J Sports Med.* 2010;38(12):2410-2416. doi: 10.1177/0363546510376742

22. Saris DB, Vanlauwe J, Victor J, et al. Treatment of symptomatic cartilage defects of the knee: characterized chondrocyte implantation results in better clinical outcome at 36 months in a randomized trial compared to microfracture. *Am J Sports Med.* 2009;37(Suppl 1):10s-19s. doi: 10.1177/0363546509350694

23. Jones KJ, Cash BM. Matrix-induced autologous chondrocyte implantation with autologous bone grafting for osteochondral lesions of the femoral trochlea. *Arthrosc Tech.* 2019;8(3):e259-e266. doi: 10.1016/j.eats.2018.10.022

24. Nixon AJ, Sparks HD, Begum L, et al. Matrix-induced autologous chondrocyte implantation (MACI) using a cell-seeded collagen membrane improves cartilage healing in the equine model. *J Bone Joint Surg Am*. 2017;99(23):1987-1998. doi: 10.2106/jbjs.16.00603

25. Richter DL, Tanksley JA, Miller MD. Osteochondral autograft transplantation: a review of the surgical technique and outcomes. *Sports Med Arthrosc Rev.* 2016;24(2):74-78. doi: 10.1097/jsa.0000000000000099

26. Zouzias IC, Bugbee WD. Osteochondral allograft transplantation in the knee. *Sports Med Arthrosc Rev*. 2016;24(2):79-84. doi: 10.1097/jsa.0000000000000109

27. Borodi PG, Russu OM, Feier AM, Georgeanu VA, Zuh SG, Pop TS. Is microfracture alone enough? *Appl. Sci.* 2021;11(16):7309. doi: 10.3390/app11167309

28. Lee SS, Du X, Kim I, Ferguson SJ. Scaffolds for bone-tissue engineering. *Matter.* 2022;5(9):2722-2759. doi: 10.1016/j.matt.2022.06.003

29. Bian Y, Hu T, Lv Z, et al. Bone tissue engineering for treating osteonecrosis of the femoral head. *Exploration (Beijing).* 2023;3(2):20210105. doi: 10.1002/exp.20210105

30. Qin L, Yang S, Zhao C, et al. Prospects and challenges for the application of tissue engineering technologies in the treatment of bone infections. *Bone Res.* 2024;12(1):28. doi: 10.1038/s41413-024-00332-w

31. Kwon H, Brown WE, Lee CA, et al. Surgical and tissue engineering strategies for articular cartilage and meniscus repair. *Nat Rev Rheumatol.* 2019;15(9):550-570. doi: 10.1038/s41584-019-0255-1

32. Yang J, Zhang YS, Yue K, Khademhosseini A. Cell-laden hydrogels for osteochondral and cartilage tissue engineering. *Acta Biomater.* 2017;57:1-25.

doi: 10.1016/j.actbio.2017.01.036

33. Huang BJ, Hu JC, Athanasiou KA. Cell-based tissue engineering strategies used in the clinical repair of articular cartilage. *Biomaterials.* 2016;98:1-22. doi: 10.1016/j.biomaterials.2016.04.018

34. Yang Z, Yi P, Liu Z, et al. Stem cell-laden hydrogel-based 3D bioprinting for bone and cartilage tissue engineering. *Front Bioeng Biotechnol.* 2022;10:865770. doi: 10.3389/fbioe.2022.865770

35. Daly AC, Freeman FE, Gonzalez-Fernandez T, Critchley SE, Nulty J, Kelly DJ. 3D bioprinting for cartilage and osteochondral tissue engineering. *Adv Healthc Mater.* 2017;6(22):1700298. doi: 10.1002/adhm.201700298

36. Zhang H, Wang M, Wu R, et al. From materials to clinical use: advances in 3D-printed scaffolds for cartilage tissue engineering. *Phys Chem Chem Phys.* 2023;25(36):24244-24263. doi: 10.1039/d3cp00921a

37. Huey DJ, Hu JC, Athanasiou KA. Unlike bone, cartilage regeneration remains elusive. *Science.* 2012;338(6109):917-921. doi: 10.1126/science.1222454

38. Mouser VHM, Levato R, Bonassar LJ, et al. Three-dimensional bioprinting and its potential in the field of articular cartilage regeneration. *Cartilage.* 2017;8(4):327-340. doi: 10.1177/1947603516665445

39. Schon BS, Hooper GJ, Woodfield TB. Modular tissue assembly strategies for biofabrication of engineered cartilage. *Ann Biomed Eng.* 2017;45(1):100-114. doi: 10.1007/s10439-016-1609-3

40. Jiang G, Li S, Yu K, et al. A 3D-printed PRP-GelMA hydrogel promotes osteochondral regeneration through M2 macrophage polarization in a rabbit model. *Acta Biomater.* 2021;128:150-162. doi: 10.1016/j.actbio.2021.04.010

41. Ege D, Hasirci V. Is 3D printing promising for osteochondral tissue regeneration? *ACS Appl Bio Mater.* 2023;6(4):1431-1444. doi: 10.1021/acsabm.3c00093

42. Visser J, Melchels FP, Jeon JE, et al. Reinforcement of hydrogels using three-dimensionally printed microfibres. *Nat Commun.* 2015;6:6933. doi: 10.1038/ncomms7933

43. Baur E, Hirsch M, Amstad E. Porous 3D printable hydrogels. *Adv Mater Technol.* 2023;8(9):2201763. doi: 10.1002/admt.202201763

44. Yue K, Trujillo-de Santiago G, Alvarez MM, Tamayol A, Annabi N, Khademhosseini A. Synthesis, properties, and biomedical applications of gelatin methacryloyl (GelMA) hydrogels. *Biomaterials.* 2015;73:254-271. doi: 10.1016/j.biomaterials.2015.08.045

45. Geckil H, Xu F, Zhang X, Moon S, Demirci U. Engineering hydrogels as extracellular matrix mimics. *Nanomedicine (Lond).* 2010;5(3):469-484. doi: 10.2217/nnm.10.12

46. Castilho M, Mouser V, Chen M, Malda J, Ito K. Bi-layered micro-fibre reinforced hydrogels for articular cartilage regeneration. *Acta Biomater.* 2019;95:297-306. doi: 10.1016/j.actbio.2019.06.030

47. Liang Y, He J, Guo B. Functional hydrogels as wound dressing to enhance wound healing. *ACS Nano.* 2021;15(8):12687-12722. doi: 10.1021/acsnano.1c04206

48. Olov N, Bagheri-Khoulenjani S, Mirzadeh H. Injectable hydrogels for bone and cartilage tissue engineering: a review. *Prog Biomater.* 2022;11(2):113-135. doi: 10.1007/s40204-022-00185-8

49. Askari M, Afzali Naniz M, Kouhi M, Saberi A, Zolfagharian A, Bodaghi M. Recent progress in extrusion 3D bioprinting of hydrogel biomaterials for tissue regeneration: a comprehensive review with focus on advanced fabrication techniques. *Biomater Sci.* 2021;9(3):535-573. doi: 10.1039/d0bm00973c

50. Elkhoury K, Morsink M, Sanchez-Gonzalez L, Kahn C, Tamayol A, Arab-Tehrany E. Biofabrication of natural hydrogels for cardiac, neural, and bone tissue engineering applications. *Bioact Mater.* 2021;6(11):3904-3923. doi: 10.1016/j.bioactmat.2021.03.040

51. Singh YP, Moses JC, Bhardwaj N, Mandal BB. Injectable hydrogels: a new paradigm for osteochondral tissue engineering. *J Mater Chem B.* 2018;6(35):5499-5529. doi: 10.1039/c8tb01430b

52. Lin X, Zhang L, Duan B. Polyphenol-mediated chitin self-assembly for constructing a fully naturally resourced hydrogel with high strength and toughness. *Mater Horiz.* 2021;8(9):2503-2512. doi: 10.1039/d1mh00878a

53. Qin XH, Wang X, Rottmar M, Nelson BJ, Maniura-Weber K. Near-infrared light-sensitive polyvinyl alcohol hydrogel photoresist for spatiotemporal control of cell-instructive 3D microenvironments. *Adv Mater.* 2018;30(10):1705564. doi: 10.1002/adma.201705564

54. Huang Q, Zou Y, Arno MC, et al. Hydrogel scaffolds for differentiation of adipose-derived stem cells. *Chem Soc Rev.* 2017;46(20):6255-6275. doi: 10.1039/c6cs00052e

55. Beninatto R, Barbera C, De Lucchi O, et al. Photocrosslinked hydrogels from coumarin derivatives of hyaluronic acid for tissue engineering applications. *Mater Sci Eng C Mater Biol Appl.* 2019;96:625-634. doi: 10.1016/j.msec.2018.11.052

56. Rosenquist J, Folkesson M, Höglund L, Pupkaite J, Hilborn J, Samanta A. An injectable, shape-retaining collagen hydrogel

cross-linked using thiol-maleimide click chemistry for sealing corneal perforations. *ACS Appl Mater Interfaces.* 2023;15(29):34407-34418.
doi: 10.1021/acsami.3c03963

57. Wang Y, Wang J, Ji Z, et al. Application of bioprinting in ophthalmology. *Int J Bioprint.* 2022;8(2):552.
doi: 10.18063/ijb.v8i2.552

58. Kelly BE, Bhattacharya I, Heidari H, Shusteff M, Spadaccini CM, Taylor HK. Volumetric additive manufacturing via tomographic reconstruction. *Science.* 2019;363(6431):1075-1079.
doi: 10.1126/science.aau7114

59. He W, Deng J, Ma B, et al. Recent advancements of bioinks for 3D bioprinting of human tissues and organs. *ACS Appl Bio Mater.* 2024;7(1):17-43.
doi: 10.1021/acsabm.3c00806

60. Li X, Liu B, Pei B, et al. Inkjet bioprinting of biomaterials. *Chem Rev.* 2020;120(19):10793-10833.
doi: 10.1021/acs.chemrev.0c00008

61. Heinrich MA, Liu W, Jimenez A, et al. 3D bioprinting: from benches to translational applications. *Small.* 2019;15(23):e1805510.
doi: 10.1002/smll.201805510

62. Gudapati H, Dey M, Ozbolat I. A comprehensive review on droplet-based bioprinting: past, present and future. *Biomaterials.* 2016;102:20-42.
doi: 10.1016/j.biomaterials.2016.06.012

63. Matai I, Kaur G, Seyedsalehi A, McClinton A, Laurencin CT. Progress in 3D bioprinting technology for tissue/organ regenerative engineering. *Biomaterials.* 2020;226:119536.
doi: 10.1016/j.biomaterials.2019.119536

64. Saunders RE, Gough JE, Derby B. Delivery of human fibroblast cells by piezoelectric drop-on-demand inkjet printing. *Biomaterials.* 2008;29(2):193-203.
doi: 10.1016/j.biomaterials.2007.09.032

65. Zandrini T, Florczak S, Levato R, Ovsianikov A. Breaking the resolution limits of 3D bioprinting: future opportunities and present challenges. *Trends Biotechnol.* 2023;41(5):604-614.
doi: 10.1016/j.tibtech.2022.10.009

66. Mandrycky C, Wang Z, Kim K, Kim DH. 3D bioprinting for engineering complex tissues. *Biotechnol Adv.* 2016;34(4):422-434.
doi: 10.1016/j.biotechadv.2015.12.011

67. Lee JM, Sing SL, Zhou M, Yeong WY. 3D bioprinting processes: a perspective on classification and terminology. *Int J Bioprint.* 2018;4(2):151.
doi: 10.18063/IJB.v4i2.151

68. Lawlor KT, Vanslambrouck JM, Higgins JW, et al. Cellular extrusion bioprinting improves kidney organoid reproducibility and conformation. *Nat Mater.* 2021;20(2):260-271.
doi: 10.1038/s41563-020-00853-9

69. Ozbolat IT, Hospodiuk M. Current advances and future perspectives in extrusion-based bioprinting. *Biomaterials.* 2016;76:321-343.
doi: 10.1016/j.biomaterials.2015.10.076

70. Pati F, Jang J, Ha DH, et al. Printing three-dimensional tissue analogues with decellularized extracellular matrix bioink. *Nat Commun.* 2014;5:3935.
doi: 10.1038/ncomms4935

71. Mironov V, Trusk T, Kasyanov V, Little S, Swaja R, Markwald R. Biofabrication: a 21st century manufacturing paradigm. *Biofabrication.* 2009;1(2):022001.
doi: 10.1088/1758-5082/1/2/022001

72. Liu W, Heinrich MA, Zhou Y, et al. Extrusion bioprinting of shear-thinning gelatin methacryloyl bioinks. *Adv Healthc Mater.* 2017;6(12):1601451.
doi: 10.1002/adhm.201601451

73. Zandi N, Sani ES, Mostafavi E, et al. Nanoengineered shear-thinning and bioprintable hydrogel as a versatile platform for biomedical applications. *Biomaterials.* 2021; 267:120476.
doi: 10.1016/j.biomaterials.2020.120476

74. Loebel C, Rodell CB, Chen MH, Burdick JA. Shear-thinning and self-healing hydrogels as injectable therapeutics and for 3D-printing. *Nat Protoc.* 2017;12(8):1521-1541.
doi: 10.1038/nprot.2017.053

75. Xin S, Deo KA, Dai J, et al. Generalizing hydrogel microparticles into a new class of bioinks for extrusion bioprinting. *Sci Adv.* 2021;7(42):eabk3087.
doi: 10.1126/sciadv.abk3087

76. Liu W, Zhang YS, Heinrich MA, et al. Rapid continuous multimaterial extrusion bioprinting. *Adv Mater.* 2017;29(3):.
doi: 10.1002/adma.201604630

77. Kyle S, Jessop ZM, Al-Sabah A, Whitaker IS. 'Printability' of candidate biomaterials for extrusion based 3D printing: state-of-the-art. *Adv Healthc Mater.* 2017;6(16): 1604630.
doi: 10.1002/adhm.201700264

78. Kosorn W, Sakulsumbat M, Uppanan P, et al. PCL/PHBV blended three dimensional scaffolds fabricated by fused deposition modeling and responses of chondrocytes to the scaffolds. *J Biomed Mater Res B Appl Biomater.* 2017;105(5):1141-1150.
doi: 10.1002/jbm.b.33658

79. Winarso R, Anggoro PW, Ismail R, Jamari J, Bayuseno AP. Application of fused deposition modeling (FDM) on bone scaffold manufacturing process: a review. *Heliyon.* 2022;8(11):e11701.
doi: 10.1016/j.heliyon.2022.e11701

80. Turnbull G, Clarke J, Picard F, et al. 3D bioactive composite scaffolds for bone tissue engineering. *Bioact Mater.* 2018;3(3):278-314.
doi: 10.1016/j.bioactmat.2017.10.001

81. Park MJ, Bae J, Ju YK. Structural behavior of a composite curtain wall fabricated by the fused deposition modeling 3D printing method. *Polymers (Basel).* 2022;14(7):1431. doi: 10.3390/polym14071431

82. Junqueira LA, Tabriz AG, Raposo FJ, et al. Coupling of fused deposition modeling and inkjet printing to produce drug loaded 3D printed tablets. *Pharmaceutics.* 2022;14(1). doi: 10.3390/pharmaceutics14010159

83. Guillotin B, Souquet A, Catros S, et al. Laser assisted bioprinting of engineered tissue with high cell density and microscale organization. *Biomaterials.* 2010;31(28):7250-7256. doi: 10.1016/j.biomaterials.2010.05.055

84. Mézel C, Souquet A, Hallo L, Guillemot F. Bioprinting by laser-induced forward transfer for tissue engineering applications: jet formation modeling. *Biofabrication.* 2010;2(1):014103. doi: 10.1088/1758-5082/2/1/014103

85. Derakhshanfar S, Mbeleck R, Xu K, Zhang X, Zhong W, Xing M. 3D bioprinting for biomedical devices and tissue engineering: a review of recent trends and advances. *Bioact Mater.* 2018;3(2):144-156. doi: 10.1016/j.bioactmat.2017.11.008

86. Dou C, Perez V, Qu J, Tsin A, Xu B, Li J. A state-of-the-art review of laser-assisted bioprinting and its future research trends. *Chem Bio Eng Rev.* 2021;8(5):517-534. doi: 10.1002/cben.202000037

87. Cheptsov VS, Tsypina SI, Minaev NV, Yusupov VI, Chichkov BN. New microorganism isolation techniques with emphasis on laser printing. *Int J Bioprint.* 2019;5(1):165. doi: 10.18063/ijb.v5i1.165

88. Bedell ML, Navara AM, Du Y, Zhang S, Mikos AG. Polymeric systems for bioprinting. *Chem Rev.* 2020;120(19):10744-10792. doi: 10.1021/acs.chemrev.9b00834

89. Douillet C, Nicodeme M, Hermant L, et al. From local to global matrix organization by fibroblasts: a 4D laser-assisted bioprinting approach. *Biofabrication.* 2022;14(2):025006. doi: 10.1088/1758-5090/ac40ed

90. Li J, Chen M, Fan X, Zhou H. Recent advances in bioprinting techniques: approaches, applications and future prospects. *J Transl Med.* 2016;14:271. doi: 10.1186/s12967-016-1028-0

91. Murphy SV, Atala A. 3D bioprinting of tissues and organs. *Nat Biotechnol.* 2014;32(8):773-785. doi: 10.1038/nbt.2958

92. Loterie D, Delrot P, Moser C. High-resolution tomographic volumetric additive manufacturing. *Nat Commun.* 2020;11(1):852. doi: 10.1038/s41467-020-14630-4

93. Hochleitner G, Jüngst T, Brown TD, et al. Additive manufacturing of scaffolds with sub-micron filaments via melt electrospinning writing. *Biofabrication.* 2015;7(3):035002. doi: 10.1088/1758-5090/7/3/035002

94. Li K, Wang C, Sun L, et al. Laser-assisted electrohydrodynamic jet printing of hierarchical nanostructure. *Appl Therm Eng.* 2024;253:123659. doi: 10.1016/j.applthermaleng.2024.123659

95. Huang J, Qin Q, Wang J. A review of stereolithography: processes and systems. *Processes.* 2020;8(9):1138. doi: 10.3390/pr8091138

96. Jana S, Lerman A. Bioprinting a cardiac valve. *Biotechnol Adv.* 2015;33(8):1503-1521. doi: 10.1016/j.biotechadv.2015.07.006

97. Hinczewski C, Corbel S, Chartier T. Ceramic suspensions suitable for stereolithography. *J Eur Ceram Soc.* 1998;18(6):583-590. doi: 10.1016/S0955-2219(97)00186-6

98. Gruene M, Deiwick A, Koch L, et al. Laser printing of stem cells for biofabrication of scaffold-free autologous grafts. *Tissue Eng Part C Methods.* 2011;17(1):79-87. doi: 10.1089/ten.TEC.2010.0359

99. Ceballos-González CF, Bolívar-Monsalve EJ, Quevedo-Moreno DA, et al. High-throughput and continuous chaotic bioprinting of spatially controlled bacterial microcosms. *ACS Biomater Sci Eng.* 2021;7(6):2408-2419. doi: 10.1021/acsbiomaterials.0c01646

100. Han Y, Jia B, Lian M, et al. High-precision, gelatin-based, hybrid, bilayer scaffolds using melt electro-writing to repair cartilage injury. *Bioact Mater.* 2021;6(7): 2173-2186. doi: 10.1016/j.bioactmat.2020.12.018

101. Ng WL, Lee JM, Zhou M, et al. Vat polymerization-based bioprinting-process, materials, applications and regulatory challenges. *Biofabrication.* 2020;12(2):022001. doi: 10.1016/j.addma.2024.104189

102. Chekkaramkodi D, Jacob L, C MS, Umer R, Butt H. Review of vat photopolymerization 3D printing of photonic devices. *Addit Mfg.* 2024;86:104189 doi: 10.1016/j.addma.2024.104189

103. Daly AC, Prendergast ME, Hughes AJ, Burdick JA. Bioprinting for the biologist. *Cell.* 2021;184(1):18-32. doi: 10.1016/j.cell.2020.12.002

104. Miri AK, Nieto D, Iglesias L, et al. Microfluidics-enabled multimaterial maskless stereolithographic bioprinting. *Adv Mater.* 2018;30(27):e1800242. doi: 10.1002/adma.201800242

105. Creff J, Courson R, Mangeat T, et al. Fabrication of 3D scaffolds reproducing intestinal epithelium topography by high-resolution 3D stereolithography. *Biomaterials.* 2019;221:119404. doi: 10.1016/j.biomaterials.2019.119404

106. Wang Z, Abdulla R, Parker B, Samanipour R, Ghosh S, Kim K. A simple and high-resolution stereolithography-based 3D bioprinting system using visible light crosslinkable bioinks. *Biofabrication.* 2015;7(4):045009. doi: 10.1088/1758-5090/7/4/045009

107. Anandakrishnan N, Ye H, Guo Z, et al. Fast stereolithography printing of large-scale biocompatible hydrogel models. *Adv Healthc Mater.* 2021;10(10):e2002103. doi: 10.1002/adhm.202002103

108. Walker DA, Hedrick JL, Mirkin CA. Rapid, large-volume, thermally controlled 3D printing using a mobile liquid interface. *Science.* 2019;366(6463):360-364. doi: 10.1126/science.aax1562

109. Zhang AP, Qu X, Soman P, et al. Rapid fabrication of complex 3D extracellular microenvironments by dynamic optical projection stereolithography. *Adv Mater.* 2012;24(31):4266-4270. doi: 10.1002/adma.201202024

110. Zhang Z, Yao S, Hu X, et al. Sacrificial synthesis of supported ru single atoms and clusters on N-doped carbon derived from covalent triazine frameworks: a charge modulation approach. *Adv Sci (Weinh).* 2021;8(3):2001493. doi: 10.1002/advs.202001493

111. Li W, Wang M, Mille LS, et al. A smartphone-enabled portable digital light processing 3D printer. *Adv Mater.* 2021;33(35):e2102153. doi: 10.1002/adma.202102153

112. Tumbleston JR, Shirvanyants D, Ermoshkin N, et al. Additive manufacturing. Continuous liquid interface production of 3D objects. *Science.* 2015;347(6228):1349-1352. doi: 10.1126/science.aaa2397

113. Zhu W, Ma X, Gou M, Mei D, Zhang K, Chen S. 3D printing of functional biomaterials for tissue engineering. *Curr Opin Biotechnol.* 2016;40:103-112. doi: 10.1016/j.copbio.2016.03.014

114. Wang M, Li W, Mille LS, et al. Digital light processing based bioprinting with composable gradients. *Adv Mater.* 2022;34(1):e2107038. doi: 10.1002/adma.202107038

115. Xing JF, Zheng ML, Duan XM. Two-photon polymerization microfabrication of hydrogels: an advanced 3D printing technology for tissue engineering and drug delivery. *Chem Soc Rev.* 2015;44(15):5031-5039. doi: 10.1039/c5cs00278h

116. Wang B, Engay E, Stubbe PR, et al. Stiffness control in dual color tomographic volumetric 3D printing. *Nat Commun.* 2022;13(1):367. doi: 10.1038/s41467-022-28013-4

117. Bernal PN, Delrot P, Loterie D, et al. Volumetric bioprinting of complex living-tissue constructs within seconds. *Adv Mater.* 2019;31(42):e1904209. doi: 10.1002/adma.201904209

118. Li H, Wang J, Yang G, Pei X, Zhang X. Advances of mussel-inspired hydrogels for bone/cartilage regeneration. *Chem Eng J.* 2024;487:150560. doi: 10.1016/j.cej.2024.150560

119. Lee KY, Mooney DJ. Hydrogels for tissue engineering. *Chem Rev.* 2001;101(7):1869-1879. doi: 10.1021/cr000108x

120. Trica B, Delattre C, Gros F, et al. Extraction and Characterization of alginate from an edible brown seaweed (*cystoseira barbata*) harvested in the Romanian black sea. *Mar Drugs.* 2019;17(7):405. doi: 10.3390/md17070405

121. Ahmad Raus R, Wan Nawawi WMF, Nasaruddin RR. Alginate and alginate composites for biomedical applications. *Asian J Pharm Sci.* 2021;16(3):280-306. doi: 10.1016/j.ajps.2020.10.001

122. Rastogi P, Kandasubramanian B. Review of alginate-based hydrogel bioprinting for application in tissue engineering. *Biofabrication.* 2019;11(4):042001. doi: 10.1088/1758-5090/ab331e

123. Chawla D, Kaur T, Joshi A, Singh N. 3D bioprinted alginate-gelatin based scaffolds for soft tissue engineering. *Int J Biol Macromol.* 2020;144:560-567. doi: 10.1016/j.ijbiomac.2019.12.127

124. Kulanthaivel S, Rathnam VSS, Agarwal T, et al. Gum tragacanth-alginate beads as proangiogenic-osteogenic cell encapsulation systems for bone tissue engineering. *J Mater Chem B.* 2017;5(22):4177-4189. doi: 10.1039/c7tb00390k

125. Tiwari S, Patil R, Bahadur P. Polysaccharide based scaffolds for soft tissue engineering applications. *Polymers (Basel).* 2018;11(1). doi: 10.3390/polym11010001

126. Sarker B, Rompf J, Silva R, et al. Alginate-based hydrogels with improved adhesive properties for cell encapsulation. *Int J Biol Macromol.* 2015;78:72-78. doi: 10.1016/j.ijbiomac.2015.03.061

127. Diniz IM, Chen C, Ansari S, et al. Gingival mesenchymal stem cell (GMSC) delivery system based on RGD-coupled alginate hydrogel with antimicrobial properties: a novel treatment modality for peri-implantitis. *J Prosthodont.* 2016;25(2):105-115. doi: 10.1111/jopr.12316

128. Endo K, Anada T, Yamada M, Seki M, Sasaki K, Suzuki O. Enhancement of osteoblastic differentiation in alginate gel beads with bioactive octacalcium phosphate particles. *Biomed Mater.* 2015;10(6):065019. doi: 10.1088/1748-6041/10/6/065019

129. Popa EG, Gomes ME, Reis RL. Cell delivery systems using alginate–carrageenan hydrogel beads and fibers for regenerative medicine applications. *Biomacromolecules.* 2011;12(11):3952-3961.

doi: 10.1021/bm200965x

130. Zeng H, Chen Z, Wei P, Huang H, Liu B, Fan Z. Rapid customization of biomimetic cartilage scaffold with stem cell capturing and homing capabilities for *in situ* inductive regeneration of osteochondral defects. *Adv. Funct. Mater.* 2024;34(28):2400608. doi: 10.1002/adfm.202400608

131. Klotz BJ, Gawlitta D, Rosenberg A, Malda J, Melchels FPW. Gelatin-methacryloyl hydrogels: towards biofabrication-based tissue repair. *Trends Biotechnol.* 2016;34(5):394-407. doi: 10.1016/j.tibtech.2016.01.002

132. Bellis SL. Advantages of RGD peptides for directing cell association with biomaterials. *Biomaterials.* 2011;32(18):4205-4210. doi: 10.1016/j.biomaterials.2011.02.029

133. Samorezov JE, Headley EB, Everett CR, Alsberg E. Sustained presentation of BMP-2 enhances osteogenic differentiation of human adipose-derived stem cells in gelatin hydrogels. *J Biomed Mater Res A.* 2016;104(6):1387-1397. doi: 10.1002/jbm.a.35668

134. Liu J, Li L, Suo H, Yan M, Yin J, Fu J. 3D printing of biomimetic multi-layered GelMA/nHA scaffold for osteochondral defect repair. *Mater Des.* 2019;171:107708. doi: 10.1016/j.matdes.2019.107708

135. Dong Y, Zhang M, Han D, et al. A high-performance GelMA-GelMA homogeneous double-network hydrogel assisted by 3D printing. *J Mater Chem B.* 2022;10(20):3906-3915. doi: 10.1039/d2tb00330a

136. Rajabi M, McConnell M, Cabral J, Ali MA. Chitosan hydrogels in 3D printing for biomedical applications. *Carbohydr Polym.* 2021;260:117768. doi: 10.1016/j.carbpol.2021.117768

137. Choi B, Kim S, Lin B, Wu BM, Lee M. Cartilaginous extracellular matrix-modified chitosan hydrogels for cartilage tissue engineering. *ACS Appl Mater Interfaces.* 2014;6(22):20110-20121. doi: 10.1021/am505723k

138. Sheehy EJ, Mesallati T, Vinardell T, Kelly DJ. Engineering cartilage or endochondral bone: a comparison of different naturally derived hydrogels. *Acta Biomater.* 2015;13:245-253. doi: 10.1016/j.actbio.2014.11.031

139. Fu J, Yang F, Guo Z. The chitosan hydrogels: from structure to function. *New J Chem.* 2018;42(21):17162-17180. doi: 10.1039/C8NJ03482F

140. Mourya VK, Inamdar NN. Trimethyl chitosan and its applications in drug delivery. *J Mater Sci Mater Med.* 2009;20(5):1057-1079. doi: 10.1007/s10856-008-3659-z

141. Waibel KH, Haney B, Moore M, Whisman B, Gomez R. Safety of chitosan bandages in shellfish allergic patients. *Mil Med.* 2011;176(10):1153-1156. doi: 10.7205/milmed-d-11-00150

142. Maloney FP, Kuklewicz J, Corey RA, et al. Structure, substrate recognition and initiation of hyaluronan synthase. *Nature.* 2022;604(7904):195-201. doi: 10.1038/s41586-022-04534-2

143. Zamboni F, Wong CK, Collins MN. Hyaluronic acid association with bacterial, fungal and viral infections: can hyaluronic acid be used as an antimicrobial polymer for biomedical and pharmaceutical applications? *Bioact Mater.* 2023;19:458-473. doi: 10.1016/j.bioactmat.2022.04.023

144. Ding YW, Wang ZY, Ren ZW, Zhang XW, Wei DX. Advances in modified hyaluronic acid-based hydrogels for skin wound healing. *Biomater Sci.* 2022;10(13):3393-3409. doi: 10.1039/d2bm00397j

145. Yang X, Wang B, Peng D, et al. Hyaluronic acid-based injectable hydrogels for wound dressing and localized tumor therapy: a review. *Adv Nanobiomed Res.* 2022;2(12):2200124. doi: 10.1002/anbr.202200124

146. Shebl RI, Amer ME, Abuamara TMM, et al. Staphylococcus aureus derived hyaluronic acid and bacillus Calmette-Guérin purified proteins as immune enhancers to rabies vaccine and related immuno-histopathological alterations. *Clin Exp Vaccine Res.* 2021;10(3):229-239. doi: 10.7774/cevr.2021.10.3.229

147. Trombino S, Servidio C, Curcio F, Cassano R. Strategies for hyaluronic acid-based hydrogel design in drug delivery. *Pharmaceutics.* 2019;11(8):407. doi: 10.3390/pharmaceutics11080407

148. Kotla NG, Mohd Isa IL, Larrañaga A, et al. Hyaluronic acid-based bioconjugate systems, scaffolds, and their therapeutic potential. *Adv Healthc Mater.* 2023;12(20):e2203104. doi: 10.1002/adhm.202203104

149. Schuurmans CCL, Mihajlovic M, Hiemstra C, Ito K, Hennink WE, Vermonden T. Hyaluronic acid and chondroitin sulfate (meth)acrylate-based hydrogels for tissue engineering: synthesis, characteristics and pre-clinical evaluation. *Biomaterials.* 2021;268:120602. doi: 10.1016/j.biomaterials.2020.120602

150. An C, Li H, Zhao Y, et al. Hyaluronic acid-based multifunctional carriers for applications in regenerative medicine: a review. *Int J Biol Macromol.* 2023;231:123307. doi: 10.1016/j.ijbiomac.2023.123307

151. Pandit AH, Mazumdar N, Ahmad S. Periodate oxidized hyaluronic acid-based hydrogel scaffolds for tissue engineering applications. *Int J Biol Macromol.* 2019;137:853-869. doi: 10.1016/j.ijbiomac.2019.07.014

152. Zhou D, Li S, Pei M, et al. Dopamine-modified hyaluronic acid hydrogel adhesives with fast-forming and high tissue adhesion. *ACS Appl Mater Interfaces.* 2020;12(16):18225-18234. doi: 10.1021/acsami.9b22120

153. Zhou M, Wei W, Chen X, Xu X, Zhang X, Zhang X. pH and redox dual responsive carrier-free anticancer drug nanoparticles for targeted delivery and synergistic therapy. *Nanomedicine.* 2019;20:102008. doi: 10.1016/j.nano.2019.04.011

154. Palmese LL, Thapa RK, Sullivan MO, Kiick KL. Hybrid hydrogels for biomedical applications. *Curr Opin Chem Eng.* 2019;24:143-157. doi: 10.1016/j.coche.2019.02.010

155. Wang H, Xu Y, Wang P, et al. Cell-mediated injectable blend hydrogel-BCP ceramic scaffold for *in situ* condylar osteochondral repair. *Acta Biomater.* 2021;123:364-378. doi: 10.1016/j.actbio.2020.12.056

156. Seol YJ, Park JY, Jeong W, Kim TH, Kim SY, Cho DW. Development of hybrid scaffolds using ceramic and hydrogel for articular cartilage tissue regeneration. *J Biomed Mater Res A.* 2015;103(4):1404-1413. doi: 10.1002/jbm.a.35276

157. Li J, Zhi W, Xu T, et al. Ectopic osteogenesis and angiogenesis regulated by porous architecture of hydroxyapatite scaffolds with similar interconnecting structure *in vivo*. *Regen Biomater.* 2016;3(5):285-297. doi: 10.1093/rb/rbw031

158. You F, Chen X, Cooper DML, Chang T, Eames BF. Homogeneous hydroxyapatite/alginate composite hydrogel promotes calcified cartilage matrix deposition with potential for three-dimensional bioprinting. *Biofabrication.* 2018;11(1):015015. doi: 10.1088/1758-5090/aaf44a

159. Wang Y, Wu S, Kuss MA, Streubel PN, Duan B. Effects of hydroxyapatite and hypoxia on chondrogenesis and hypertrophy in 3D bioprinted ADMSC laden constructs. *ACS Biomater Sci Eng.* 2017;3(5):826-835. doi: 10.1021/acsbiomaterials.7b00101

160. Kosik-Kozioł A, Costantini M, Mróz A, et al. 3D bioprinted hydrogel model incorporating β-tricalcium phosphate for calcified cartilage tissue engineering. *Biofabrication.* 2019;11(3):035016. doi: 10.1088/1758-5090/ab15cb

161. Wang W, Shen J, Meng Y, et al. Magnesium cationic cue enriched interfacial tissue microenvironment nurtures the osseointegration of gamma-irradiated allograft bone. *Bioact Mater.* 2022;10:32-47. doi: 10.1016/j.bioactmat.2021.08.027

162. Chen Y, Chen Y, Xiong X, et al. Hybridizing gellan/alginate and thixotropic magnesium phosphate-based hydrogel scaffolds for enhanced osteochondral repair. *Mater Today Bio.* 2022;14:100261. doi: 10.1016/j.mtbio.2022.100261

163. Gao F, Xu Z, Liang Q, et al. Osteochondral regeneration with 3D-printed biodegradable high-strength supramolecular polymer reinforced-gelatin hydrogel scaffolds. *Adv Sci (Weinh).* 2019;6(15):1900867. doi: 10.1002/advs.201900867

164. Dong L, Han Z, Li X. Tannic acid-mediated multifunctional 3D printed composite hydrogel for osteochondral regeneration. *Int J Bioprint.* 2022;8(3):587. doi: 10.18063/ijb.v8i3.587

165. Antich C, de Vicente J, Jiménez G, et al. Bio-inspired hydrogel composed of hyaluronic acid and alginate as a potential bioink for 3D bioprinting of articular cartilage engineering constructs. *Acta Biomater.* 2020;106:114-123. doi: 10.1016/j.actbio.2020.01.046

166. Agostinacchio F, Mu X, Dirè S, Motta A, Kaplan DL. *In situ* 3D printing: opportunities with silk inks. *Trends Biotechnol.* 2021;39(7):719-730. doi: 10.1016/j.tibtech.2020.11.003

167. Ma K, Zhao T, Yang L, et al. Application of robotic-assisted *in situ* 3D printing in cartilage regeneration with HAMA hydrogel: an *in vivo* study. *J Adv Res.* 2020;23:123-132. doi: 10.1016/j.jare.2020.01.010

168. Motloung MP, Mofokeng TG, Ray SS. Viscoelastic, thermal, and mechanical properties of melt-processed poly (ε-Caprolactone) (PCL)/hydroxyapatite (HAP) composites. *Materials (Basel).* 2021;15(1). doi: 10.3390/ma15010104

169. Rahmani S, Maroufkhani M, Mohammadzadeh-Komuleh S, Khoubi-Arani Z. Chapter 7 – polymer nanocomposites for biomedical applications. In: Barhoum A, Jeevanandam J, Danquah MK, eds. *Fundamentals of Bionanomaterials.* Elsevier; 2022:175-215. doi: 10.1016/B978-0-12-824147-9.00007-8

170. Chen H, Gonnella G, Huang J, Di-Silvio L. Fabrication of 3D bioprinted bi-phasic scaffold for bone-cartilage interface regeneration. *Biomimetics (Basel).* 2023;8(1):87. doi: 10.3390/biomimetics8010087

171. Wang S, Gu R, Wang F, et al. 3D-printed PCL/Zn scaffolds for bone regeneration with a dose-dependent effect on osteogenesis and osteoclastogenesis. *Mater Today Bio.* 2022;13:100202. doi: 10.1016/j.mtbio.2021.100202

172. Tabatabaei F, Gelin A, Rasoulianboroujeni M, Tayebi L. Coating of 3D printed PCL/TCP scaffolds using homogenized-fibrillated collagen. *Colloids Surf B Biointerfaces.* 2022;217:112670. doi: 10.1016/j.colsurfb.2022.112670

173. Thakkar S, Ghebes CA, Ahmed M, et al. Mesenchymal stromal cell-derived extracellular matrix influences gene expression of chondrocytes. *Biofabrication.* 2013;5(2):025003. doi: 10.1088/1758-5082/5/2/025003

174. Li C, Zhang W, Nie Y, et al. Integrated and bifunctional bilayer 3D printing scaffold for osteochondral defect repair. *Adv Funct Mater.* 2023;33(20):2214158. doi: 10.1002/adfm.202214158

175. Chen C, Zhang QW, Ye Y, Lin LG. Honokiol: a naturally occurring lignan with pleiotropic bioactivities. *Chin J Nat Med.* 2021;19(7):481-490. doi: 10.1016/S1875-5364(21)60047-X

176. Zhu S, Chen P, Chen Y, Li M, Chen C, Lu H. 3D-printed extracellular matrix/polyethylene glycol diacrylate hydrogel incorporating the anti-inflammatory phytomolecule honokiol for regeneration of osteochondral defects. *Am J Sports Med.* 2020;48(11):2808-2818. doi: 10.1177/0363546520941842

177. Liu J, Gao J, Liang Z, et al. Mesenchymal stem cells and their microenvironment. *Stem Cell Res Ther.* 2022;13(1):429. doi: 10.1186/s13287-022-02985-y

178. Shim JH, Jang KM, Hahn SK, et al. Three-dimensional bioprinting of multilayered constructs containing human mesenchymal stromal cells for osteochondral tissue regeneration in the rabbit knee joint. *Biofabrication.* 2016;8(1):014102. doi: 10.1088/1758-5090/8/1/014102

179. Gao G, Schilling AF, Hubbell K, et al. Improved properties of bone and cartilage tissue from 3D inkjet-bioprinted human mesenchymal stem cells by simultaneous deposition and photocrosslinking in PEG-GelMA. *Biotechnol Lett.* 2015;37(11):2349-2355. doi: 10.1007/s10529-015-1921-2

180. Zhang H, Huang H, Hao G, et al. 3D printing hydrogel scaffolds with nanohydroxyapatite gradient to effectively repair osteochondral defects in rats. *Adv Funct Mater.* 2021;31(1):2006697. doi: 10.1002/adfm.202006697

181. Reesink HL, Sutton RM, Shurer CR, et al. Galectin-1 and galectin-3 expression in equine mesenchymal stromal cells (MSCs), synovial fibroblasts and chondrocytes, and the effect of inflammation on MSC motility. *Stem Cell Res Ther.* 2017;8(1). doi: 10.1186/s13287-017-0691-2

182. Loeser RF, Goldring SR, Scanzello CR, Goldring MB. Osteoarthritis: a disease of the joint as an organ. *Arthritis Rheum.* 2012;64(6):1697-1707. doi: 10.1002/art.34453

183. Liu Y, Peng L, Li L, et al. 3D-bioprinted BMSC-laden biomimetic multiphasic scaffolds for efficient repair of osteochondral defects in an osteoarthritic rat model. *Biomaterials.* 2021;279:121216. doi: 10.1016/j.biomaterials.2021.121216

184. Daly AC, Pitacco P, Nulty J, Cunniffe GM, Kelly DJ. 3D printed microchannel networks to direct vascularisation during endochondral bone repair. *Biomaterials.* 2018;162:34-46. doi: 10.1016/j.biomaterials.2018.01.057

185. Galle J, Hoffmann M, Aust G. From single cells to tissue architecture-a bottom-up approach to modelling the spatio-temporal organisation of complex multi-cellular systems. *J Mathematical Biology.* 2009;58(1-2):261-283. doi: 10.1007/s00285-008-0172-4

186. Zhuang P, Sun AX, An J, Chua CK, Chew SY. 3D neural tissue models: from spheroids to bioprinting. *Biomaterials.* 2018;154:113-133. doi: 10.1016/j.biomaterials.2017.10.002

187. Lee EJ, Park SJ, Kang SK, et al. Spherical bullet formation via E-cadherin promotes therapeutic potency of mesenchymal stem cells derived from human umbilical cord blood for myocardial infarction. *Mol Ther.* 2012;20(7):1424-1433. doi: 10.1038/mt.2012.58

188. Fennema E, Rivron N, Rouwkema J, van Blitterswijk C, De Boer J. Spheroid culture as a tool for creating 3D complex tissues. *Trends Biotechnol.* 2013;31(2):108-115. doi: 10.1016/j.tibtech.2012.12.003

189. Zhang J, Xin W, Qin Y, et al. "All-in-one" zwitterionic granular hydrogel bioink for stem cell spheroids production and 3D bioprinting. *Chem Eng J.* 2022;430:132713. doi: 10.1016/j.cej.2021.132713

190. Kim K, Yeatts A, Dean D, Fisher JP. Stereolithographic bone scaffold design parameters: osteogenic differentiation and signal expression. *Tissue Eng Part B Rev.* 2010;16(5):523-539. doi: 10.1089/ten.TEB.2010.0171

191. Karageorgiou V, Kaplan D. Porosity of 3D biomaterial scaffolds and osteogenesis. *Biomaterials.* 2005;26(27):5474-5491. doi: 10.1016/j.biomaterials.2005.02.002

192. Nowicki MA, Castro NJ, Plesniak MW, Zhang LG. 3D printing of novel osteochondral scaffolds with graded microstructure. *Nanotechnology.* 2016;27(41):414001. doi: 10.1088/0957-4484/27/41/414001

193. Peng Y, Zhuang Y, Liu Y, et al. Bioinspired gradient scaffolds for osteochondral tissue engineering. *Exploration (Beijing).* 2023;3(4):20210043. doi: 10.1002/exp.20210043

194. Mironov V, Visconti RP, Kasyanov V, Forgacs G, Drake CJ, Markwald RR. Organ printing: tissue spheroids as building blocks. *Biomaterials.* 2009;30(12):2164-2174. doi: 10.1016/j.biomaterials.2008.12.084

195. Diloksumpan P, de Ruijter M, Castilho M, et al. Combining multi-scale 3D printing technologies to engineer reinforced hydrogel-ceramic interfaces. *Biofabrication.* 2020;12(2):025014. doi: 10.1088/1758-5090/ab69d9

196. Zhai X, Ruan C, Ma Y, et al. 3D-bioprinted osteoblast-laden nanocomposite hydrogel constructs with induced microenvironments promote cell viability, differentiation, and osteogenesis both *in vitro* and *in vivo*. *Adv Sci (Weinh).* 2018;5(3):1700550. doi: 10.1002/advs.201700550

197. Park JY, Choi JC, Shim JH, et al. A comparative study on collagen type I and hyaluronic acid dependent cell behavior for osteochondral tissue bioprinting. *Biofabrication.* 2014;6(3):035004. doi: 10.1088/1758-5082/6/3/035004

198. Critchley S, Sheehy EJ, Cunniffe G, et al. 3D printing of fibre-reinforced cartilaginous templates for the regeneration of osteochondral defects. *Acta Biomater.* 2020; 113:130-143.
doi: 10.1016/j.actbio.2020.05.040

199. Zhang Y, Li D, Liu Y, et al. 3D-bioprinted anisotropic bicellular living hydrogels boost osteochondral regeneration via reconstruction of cartilage-bone interface. *Innovation (Camb).* 2024;5(1):100542.
doi: 10.1016/j.xinn.2023.100542

200. Wu M, Wu S, Chen W, Li Y-P. The roles and regulatory mechanisms of TGF-β and BMP signaling in bone and cartilage development, homeostasis and disease. *Cell Res.* 2024;34(2):101-123.
doi: 10.1038/s41422-023-00918-9

201. Gao F, Xu Z, Liang Q, et al. Direct 3D printing of high strength biohybrid gradient hydrogel scaffolds for efficient repair of osteochondral defect. *Adv Funct Mater.* 2018;28(13):1706644.
doi: 10.1002/adfm.201706644

202. Dorcemus DL, Kim HS, Nukavarapu SP. Gradient scaffold with spatial growth factor profile for osteochondral interface engineering. *Biomed Mater.* 2021;16(3):035021.
doi: 10.1088/1748-605X/abd1ba

203. Qiao Z, Lian M, Han Y, et al. Bioinspired stratified electrowritten fiber-reinforced hydrogel constructs with layer-specific induction capacity for functional osteochondral regeneration. *Biomaterials.* 2021;266:120385.
doi: 10.1016/j.biomaterials.2020.120385

204. Chen C, Chen Y, Li M, et al. Functional decellularized fibrocartilaginous matrix graft for rotator cuff enthesis regeneration: a novel technique to avoid *in-vitro* loading of cells. *Biomaterials.* 2020;250:119996.
doi: 10.1016/j.biomaterials.2020.119996

205. Askari AT, Unzek S, Popovic ZB, et al. Effect of stromal-cell-derived factor 1 on stem-cell homing and tissue regeneration in ischaemic cardiomyopathy. *Lancet.* 2003;362(9385):697-703.
doi: 10.1016/s0140-6736(03)14232-8

206. Wang C, Dong J, Liu F, Liu N, Li L. 3D-printed PCL@BG scaffold integrated with SDF-1α-loaded hydrogel for enhancing local treatment of bone defects. *J Biol Eng.* 2024;18(1):1.
doi: 10.1186/s13036-023-00401-4

207. Luo H, Wang Z, Yu F, et al. Injectable and microporous microgel assembly with sequential bioactive factor release for the endogenous repair of nucleus pulposus. *Adv Funct Mater.* 2024;34(25):2315592.
doi: 10.1002/adfm.202315592

208. Li JH, Li Y, Huang D, Yao M. Role of stromal cell-derived factor-1 in endothelial progenitor cell-mediated vascular repair and regeneration. *Tissue Eng Regen Med.* 2021;18(5):747-758.
doi: 10.1007/s13770-021-00366-9

209. Zhou J, Li Q, Tian Z, Yao Q, Zhang M. Recent advances in 3D bioprinted cartilage-mimicking constructs for applications in tissue engineering. *Mater Today Bio.* 2023;23:100870.
doi: 10.1016/j.mtbio.2023.100870

210. Hoang DM, Pham PT, Bach TQ, et al. Stem cell-based therapy for human diseases. *Signal Transduct Target Ther.* 2022;7(1):272.
doi: 10.1038/s41392-022-01134-4

211. Kalluri R, LeBleu VS. The biology, function, and biomedical applications of exosomes. 2020;367(6478):eaau6977.
doi: 10.1126/science.aau6977

212. Kilian D, Ahlfeld T, Akkineni AR, Bernhardt A, Gelinsky M, Lode A. 3D bioprinting of osteochondral tissue substitutes – *in vitro*-chondrogenesis in multi-layered mineralized constructs. *Sci Rep.* 2020;10(1):8277.
doi: 10.1038/s41598-020-65050-9

213. Zhang S, Chuah SJ, Lai RC, Hui JHP, Lim SK, Toh WS. MSC exosomes mediate cartilage repair by enhancing proliferation, attenuating apoptosis and modulating immune reactivity. *Biomaterials.* 2018;156:16-27.
doi: 10.1016/j.biomaterials.2017.11.028

214. Sun T, Feng Z, He W, et al. Novel 3D-printing bilayer GelMA-based hydrogel containing BP, β-TCP and exosomes for cartilage-bone integrated repair. *Biofabrication.* 2023;16(1):015008.
doi: 10.1088/1758-5090/ad04fe

215. Li Q, Yu H, Zhao F, et al. 3D printing of microenvironment-specific bioinspired and exosome-reinforced hydrogel scaffolds for efficient cartilage and subchondral bone regeneration. *Adv Sci (Weinh).* 2023;10(26):e2303650.
doi: 10.1002/advs.202303650

216. Zhou X, Liu S, Lu Y, Wan M, Cheng J, Liu J. MitoEVs: a new player in multiple disease pathology and treatment. *J Extracell Vesicles.* 2023;12(4):e12320.
doi: 10.1002/jev2.12320

217. Sanz-Ros J, Mas-Bargues C, Romero-García N, Huete-Acevedo J, Dromant M, Borrás C. The potential use of mitochondrial extracellular vesicles as biomarkers or therapeutical tools. *Int J Mol Sci.* 2023;24(8):7005.
doi: 10.3390/ijms24087005

218. König T, McBride HM. Mitochondrial-derived vesicles in metabolism, disease, and aging. *Cell Metab.* 2024;36(1):21-35.
doi: 10.1016/j.cmet.2023.11.014

219. Chen P, Zheng L, Wang Y, et al. Desktop-stereolithography 3D printing of a radially oriented extracellular matrix/mesenchymal stem cell exosome bioink for osteochondral defect regeneration. *Theranostics.* 2019;9(9):2439-2459.
doi: 10.7150/thno.31017

220. Stichler S, Jungst T, Schamel M, et al. Thiol-ene clickable poly(glycidol) hydrogels for biofabrication. *Ann Biomed Eng.* 2017;45(1):273-285.
doi: 10.1007/s10439-016-1633-3

221. Collins MN, Ren G, Young K, Pina S, Reis RL, Oliveira JM. Scaffold fabrication technologies and structure/function properties in bone tissue engineering. *Adv Funct Mater.* 2021;31(21):2010609.
doi: 10.1002/adfm.202010609

222. Xu W, Jambhulkar S, Zhu Y, et al. 3D printing for polymer/particle-based processing: a review. *Compos. B Eng.* 2021;223:109102.
doi: 10.1016/j.compositesb.2021.109102

223. Engler AJ, Sen S, Sweeney HL, Discher DE. Matrix elasticity directs stem cell lineage specification. *Cell.* 2006;126(4):677-689.
doi: 10.1016/j.cell.2006.06.044

224. Zhou X, Tenaglio S, Esworthy T, et al. Three-dimensional printing biologically inspired DNA-based gradient scaffolds for cartilage tissue regeneration. *ACS Appl Mater Interfaces.* 2020;12(29):33219-33228.
doi: 10.1021/acsami.0c07918

225. Demoly F, Dunn ML, Wood KL, Qi HJ, André JC. The status, barriers, challenges, and future in design for 4D printing. *Mater Des.* 2021;212:110193.
doi: 10.1016/j.matdes.2021.110193

226. Agarwala S, Goh GL, Goh GD, Dikshit V, Yeong WY. Chapter 10 – 3D and 4D printing of polymer/CNTs-based conductive composites. In: Sadasivuni KK, Deshmukh K, Almaadeed MA, eds. *3D and 4D Printing of Polymer Nanocomposite Materials*. Elsevier; 2020:297-324.
doi:10.1016/B978-0-12-816805-9.00010-7

227. Ryan KR, Down MP, Banks CE. Future of additive manufacturing: overview of 4D and 3D printed smart and advanced materials and their applications. *Chem Eng J.* 2021;403:126162.
doi: 10.1016/j.cej.2020.126162

228. Pintus E, Baldassarri M, Perazzo L, Natali S, Ghinelli D, Buda R. Stem cells in osteochondral tissue engineering. *Adv Exp Med Biol.* 2018;1058:359-372.
doi: 10.1007/978-3-319-76711-6_16

229. Rennerfeldt DA, Van Vliet KJ. Concise review: when colonies are not clones: evidence and implications of intracolony heterogeneity in mesenchymal stem cells. *Stem Cells.* 2016;34(5):1135-1141.
doi: 10.1002/stem.2296

230. Marędziak M, Marycz K, Tomaszewski KA, Kornicka K, Henry BM. The influence of aging on the regenerative potential of human adipose derived mesenchymal stem cells. *Stem Cells Int.* 2016;2016:2152435.
doi: 10.1155/2016/2152435

231. Elkhenany H, Amelse L, Caldwell M, Abdelwahed R, Dhar M. Impact of the source and serial passaging of goat mesenchymal stem cells on osteogenic differentiation potential: implications for bone tissue engineering. *J Anim Sci Biotechnol.* 2016;7:16.
doi: 10.1186/s40104-016-0074-z

232. Volk SW, Wang Y, Hankenson KD. Effects of donor characteristics and *ex vivo* expansion on canine mesenchymal stem cell properties: implications for MSC-based therapies. *Cell Transplant.* 2012;21(10):2189-2200.
doi: 10.3727/096368912x636821

233. Baxter FR, Bowen CR, Turner IG, Dent AC. Electrically active bioceramics: a review of interfacial responses. *Ann Biomed Eng.* 2010;38(6):2079-2092.
doi: 10.1007/s10439-010-9977-6

234. Jiang L, Wang Y, Liu Z, et al. Three-dimensional printing and injectable conductive hydrogels for tissue engineering application. *Tissue Eng Part B Rev.* 2019;25(5):398-411.
doi: 10.1089/ten.TEB.2019.0100

235. Wei K, Zhu M, Sun Y, et al. Robust biopolymeric supramolecular "Host–Guest Macromer" hydrogels reinforced by *in situ* formed multivalent nanoclusters for cartilage regeneration. *Macromolecules.* 2016;49(3):866-875.
doi: 10.1021/acs.macromol.5b02527

236. Salzlechner C, Haghighi T, Huebscher I, et al. Adhesive hydrogels for maxillofacial tissue regeneration using minimally invasive procedures. *Adv Healthc Mater.* 2020;9(4):e1901134.
doi: 10.1002/adhm.201901134

237. Khare D, Basu B, Dubey AK. Electrical stimulation and piezoelectric biomaterials for bone tissue engineering applications. *Biomaterials.* 2020;258:120280.
doi: 10.1016/j.biomaterials.2020.120280

238. Zhang X, Zhang C, Lin Y, et al. Nanocomposite membranes enhance bone regeneration through restoring physiological electric microenvironment. *ACS Nano.* 2016;10(8):7279-7286.
doi: 10.1021/acsnano.6b02247

239. Deng C, Zhou Q, Zhang M, et al. Bioceramic scaffolds with antioxidative functions for ROS scavenging and osteochondral regeneration. *Adv Sci (Weinh).* 2022;9(12):e2105727.
doi: 10.1002/advs.202105727

ACCSCIENCE PUBLISHING

International Journal of Bioprinting

REVIEW ARTICLE

3D-printed electronics for biomedical applications

Minsu Ryoo[1], Daeho Kim[1], Junseop Noh[1], and Song Ih Ahn[2]*

[1]School of Mechanical Engineering, Pusan National University, Pusan, Republic of Korea

[2]Department of Mechanical Engineering, Korea Advanced Institute of Science and Technology (KAIST), Daejeon, Republic of Korea

Abstract

Biomedical electronics have garnered significant interest due to the rising demand for advanced healthcare devices for diagnosis, monitoring, and treatment. Three-dimensional (3D) printing, or additive manufacturing, has emerged as an attractive fabrication method for developing these advanced biomedical devices. Its unique features, such as versatility, cost-effectiveness, and rapid prototyping capabilities, when combined with medical imaging technologies enable the creation of highly precise and customized patient-specific structures. Extensive research in the field of 3D printing has focused on developing biomedical devices, including wearable and implantable devices, as well as scaffolds or platforms. Recently, the integration of 3D printing with state-of-the-art electronic materials, known for their high flexibility, conductivity, stretchability, stability, and biocompatibility, has led to the development of innovative biomedical electronics. In this review, we outline the recent advancements in 3D printing technologies and their applications in bioelectronic devices. Firstly, we describe various 3D printing methods and printable electronic materials, highlighting their advantages and limitations. Subsequently, we explore the applications of these technologies in biomedical research, spanning from surgical guidance and prosthetics to health monitoring devices and tissue-engineered scaffolds. Finally, this review discusses the current challenges and future directions to fully exploit the potential of 3D-printed bioelectronic devices, aimed at transforming personalized healthcare.

Keywords: Bioelectronics; Biomedical electronics; 3D printing; Biomedical devices; Personalized healthcare

***Corresponding author:**
Song Ih Ahn (siahn@kaist.ac.kr)

Citation: Ryoo M, Kim D, Noh J, Ahn SI. 3D-printed electronics for biomedical applications. *Int J Bioprint*. 22024;10(6):4139. doi: 10.36922/ijb.4139

Received: July 3, 2024
Revised: August 2, 2024
Accepted: August 2, 2024
Published Online: August 7, 2024

Copyright: © 2024 Author(s). This is an Open Access article distributed under the terms of the Creative Commons Attribution License, permitting distribution, and reproduction in any medium, provided the original work is properly cited.

Publisher's Note: AccScience Publishing remains neutral with regard to jurisdictional claims in published maps and institutional affiliations.

1. Introduction

Three-dimensional (3D) printing has emerged as an innovative technology in biomedical engineering, profoundly impacting personalized medicine and medical device fabrication. The ability of 3D printing to fabricate complex patient-specific structures with high precision and customization has attracted significant attention from researchers. Moreover, the inherent versatility of material options, design flexibility, cost-effectiveness, and rapid fabrication have led to widespread applications in biomedical devices. By layering materials in a controlled manner, 3D printing enables the creation of

anatomically accurate pre-surgical models,[1–3] implantable devices,[4–6] biosensors,[7–10] and multifunctional tissue and organ models.[11–13]

The growing interest in personalized health monitoring and feedback therapy underscores the need to integrate electronics into biomedical devices. Despite significant advancements in conventional microfabrication, 3D printing emerges as an innovative technology that offers enhanced design flexibility for fabricating constructs within a shorter fabrication time at a lower cost. This technology enables electronics to be deposited on the 3D surface of a device or fully 3D-printed with other components of the device. The direct deposition of electronic materials on devices using inkjet- or extrusion-based 3D printing allows complex patterning, even on moving freeform surfaces.[14] Fully 3D-printed electronics enable the real-time interweaving of electronic materials with biological components. Various 3D printing techniques have been used to fabricate bioelectronic devices, demonstrating the versatility and potential of 3D printing in advancing bioelectronic devices.

The design and materials of bioelectronic devices need to be carefully considered to establish a stable interface between the device and the body. Considering the 3D structure and motion of the human body, many types of bioinspired structures have been introduced.[15–17] These structures have provided enhanced device stability and functionality for specific applications. Moreover, the development of electrically conductive materials that exhibit printability and biocompatibility has improved the functionality and biointegration capabilities of devices.[18,19] Mechanical flexibility and robustness are also critical for ensuring device stability and reliability.[20]

The convergence of 3D printing technologies, electronic materials, and medical imaging techniques has paved the way for developing a wide range of bioelectronic devices. Moreover, advances in signal processing techniques have further enhanced the development of biomedical sensors, wearables, and multifunctional biomedical platforms for real-time monitoring of physiological signals. Recently, artificial intelligence (AI) has been applied to enhance the capabilities and functionalities of these devices, offering improved data analysis, predictive analytics, and adaptive responses for medical applications.[21]

This review aims to describe recent progress in the 3D printing of bioelectronic devices. First, different types of 3D printing techniques and electronic materials widely used in the fabrication of bioelectronic devices are introduced. We then explore recent advancements in 3D-printed bioelectronic devices across various biomedical applications, highlighting the advantages of 3D printing, such as design flexibility, cost-effectiveness, rapid prototyping, and personalized fabrication. Finally, we address the current challenges of 3D-printed bioelectronics, including device structures and materials, suggesting future directions for bioelectronic applications.

2. 3D printing technologies

According to the International Organization for Standardization, 3D printing techniques can be categorized into seven different types. Here, we describe three types of 3D printing methods (inkjet-based printing, vat photopolymerization-based printing, and extrusion-based printing) that provide high precision, biocompatibility, and minimal post-processing, allowing for bioelectronic fabrication. Each printing method has its advantages and limitations, as summarized in Table 1.

2.1. Material jetting

Material jetting method, which ejects ink droplets from nozzles onto a substrate, is characterized by high fabrication speed, low cost, and high printing resolution. Its low material usage makes it suitable for fabricating large objects.[22,23] There are two conventional methods for generating energy at the nozzles for ink ejection: thermal and piezoelectric inkjet methods (Figure 1A).[24] Thermal inkjet printing applies thermal energy to generate air bubbles within the print head, creating a pressure pulse that produces and pushes ink droplets.[25,26] Due to its fast printing speed, low cost, and wide availability,[27] this method has been used to fabricate various electronic devices, such as inorganic quantum-dot light-emitting diodes (QD-LEDs),[28] 3D structure of conductive hydrogel,[29] neuromorphic transistors,[30] field-effect transistors,[31] and fully printed capacitors.[32] However, during ink jetting, the thermal and mechanical stresses generated at the nozzle can cause damage to materials, inaccurate droplet direction, non-uniform droplet size, and nozzle clogging.[33–37] Vaporizable and thermally stable materials should be used to avoid printing errors. In a piezoelectric inkjet printing system, voltage is applied to the piezoelectric actuator to generate a mechanical pulse that creates ink droplets.[38,39] Using a piezoelectric inkjet printer, it is relatively easy to control the size of the ink droplets and the jetting direction.[40] Moreover, a broader range of materials, including thermally sensitive materials, can be used because the printer does not apply high temperatures to materials.[41]

For inkjet printing, ink properties such as viscosity and surface tension must be considered to generate ink droplets. Inks with low viscosity (under 20 mPa·s) are capable of creating droplets without excessive force.[24] For example, materials with low viscosity, such as $AgNO_3$,[42]

Table 1. Key features of different 3D printing methods for bioelectronic fabrication.

3D printing method	Techniques	Operation principle	Advantages		Disadvantages	
Material jetting	Thermal inkjet printing	Pressure pulse generated by air bubbles created from thermal energy	High fabrication speed High printing resolution Low cost	Relatively simple	Limited choice of materials Support structure required depending on printing structure	Generated heat could cause damage to materials
	Piezoelectric inkjet printing	Mechanical pulse generated by a piezoelectric actuator		Controllable droplet size		Relatively expensive compared to thermal inkjet-based printing
	Aerosol jet printing	Precise deposition of aerosolized ink containing fine particles onto a substrate	High resolution Versatile material usage Capable of creating complex structures		High initial and maintenance costs Low printing speed Requirement of specific substrates	
VAT photopolymerization	SLA	Photocuring resin through a concentrated laser beam	Support-free system High printing resolution High level of accuracy	Smooth printed surface	Limited choice of materials (photoresins) Large amount of waste Limited printing size	Relatively low printing speed compared to DLP
	DLP	Photocuring resin by projecting an image of a printing layer onto the resin		High printing speed Simple replacement of light source compared to SLA		Smaller object size compared to SLA
Extrusion-based printing	FDM	Depositing melted thermoplastic materials in filament form	Low cost Large object size Accessibility Less waste Printable on various substrates		Relatively low resolution Limited choice of materials Post-processing requirements Low printing speed	
	DIW	Depositing inks using extruders (pneumatic, syringe, and progressive cavity)	High fabrication speed Simple to perform multi-material printing Highly customizable Material flexibility Printable on various substrates		Support structure required depending on printing structure Relatively low resolution	

Abbreviations: DIW, direct ink writing; DLP, digital light processing; FDM, fused deposition method; SLA, stereolithography.

PEDOT:PSS,[43] graphene,[44] gold nanoparticles,[45] and MnO_2,[46] have been used for inkjet printing of electronics. The surface tension should also be within a suitable range (30–70 mN/m) to eject ink without forming satellite droplets in the nozzle.[47]

2.2. Vat photopolymerization-based 3D printing

Vat photopolymerization-based 3D printing produces objects by selectively curing a photocurable resin in a vat using a light source. Vat photopolymerization-based 3D printing has gained considerable attention due to its high precision, high printing speed, and smooth printed surfaces. The photopolymerization process can generally be classified according to the light source used for curing: stereolithography appearance (SLA), which uses lasers, and digital light processing (DLP), which operates with a projector (Figure 1B).[48]

SLA is one of the earliest and most widely used additive manufacturing (AM) techniques.[49] This technique uses a concentrated laser beam on the surface of a photocurable resin to create a pattern in each layer. After one layer of resin is cured, the platform moves downward to fabricate another layer of resin, and this layer-by-layer photocuring step is repeated to construct a 3D object.[50] A recent study demonstrated its application in the fabrication of multi-material actuators using a combination of hard and flexible material resin formulations.[51] DLP uses a digital light projector to project the image of a printing layer onto a liquid resin.[48] As the entire layer of liquid resin can be cured simultaneously, the printing speed is relatively fast compared to other methods.[52] One major challenge of vat photopolymerization-based 3D printing is its limited choice of materials. To overcome this challenge while preserving its advantages of printing speed and resolution, DLP has been integrated with other printing methods to

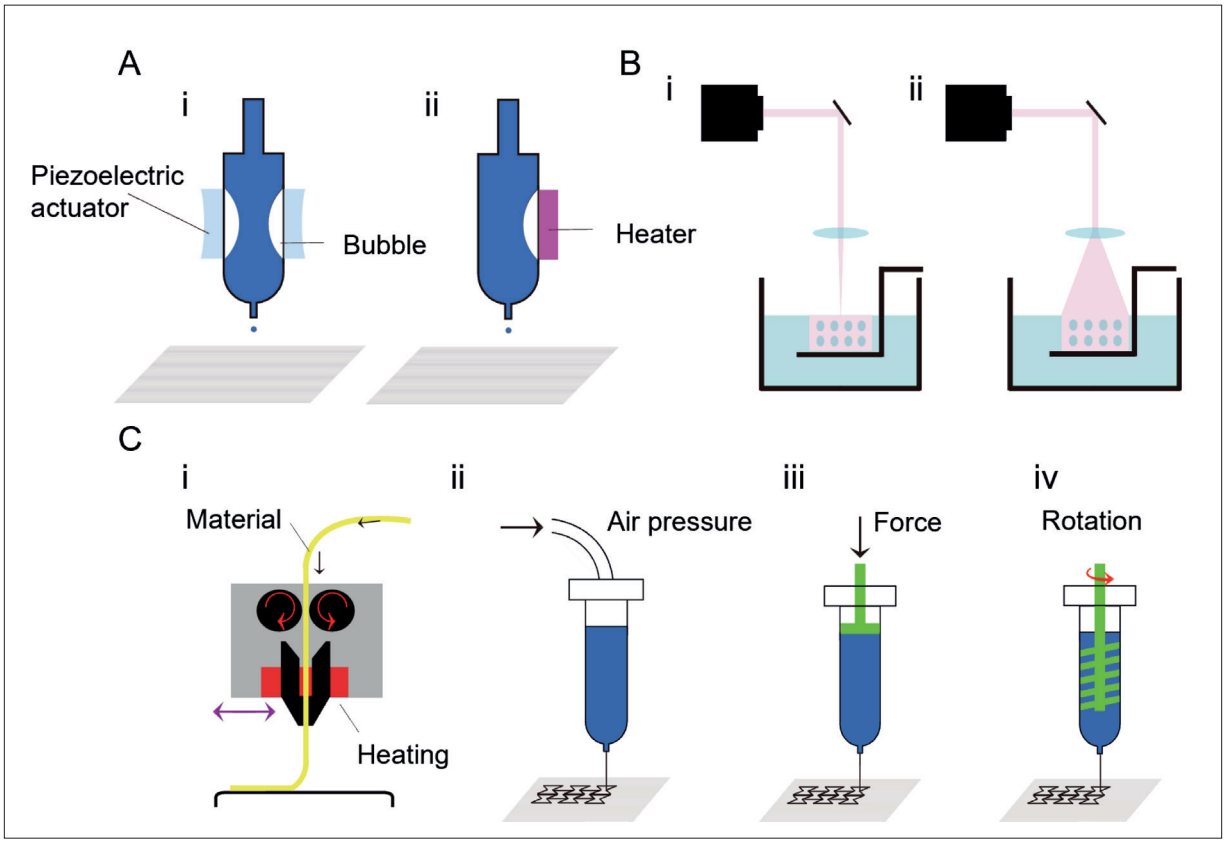

Figure 1. Various 3D printing methods. (A) Inkjet-based printing can be categorized into piezoelectric inkjet printing (i) and thermal inkjet printing (ii), based on the energy generation methods. (B) Vat photopolymerization printing create objects by curing photocurable resin using lasers (stereolithography) (i) or a projector (digital light processing [DLP]) (ii). (C) Extrusion-based printing applies pressure at a nozzle to extrude materials, and this method can be divided into fused deposition modeling (FDM) (i) and direct ink writing (DIW) (ii–iv).

achieve synergistic effects, leveraging the strengths of each technique.[53,54] For instance, a hybrid 3D printing system combining DLP and direct ink writing (DIW) systems has enabled high-speed and high-resolution printing of a wide range of functional materials.

2.3. Extrusion-based printing

In extrusion-based printing, a continuous stream of material is extruded through a nozzle using a pressure gradient. Pneumatic, mechanical (piston- and screw-based), and solenoid mechanisms are used to generate a pressure gradient in the printing nozzle.[55–57] Despite limitations in printing speed and resolution, extrusion-based printing allows for the printing of versatile structures with relatively high structural integrity through the continuous deposition of inks at desired locations.[58,59] Owing to these advantageous characteristics, extrusion-based printing has been used to print electronics with complex structures,[60,61] 3D-structured electronic devices on nonplanar substrates,[62] and ionic hydrogel-based electrical impedance tomography (EIT) sensors on deforming surfaces.[63]

Several extrusion-based 3D printing methods exist, including fused deposition modeling (FDM) and DIW (Figure 1C).[64] FDM fabricates objects by melting and depositing thermoplastic materials through a temperature-controlled nozzle. The nozzle extrudes materials in filament form to produce layer-by-layer elements. Moreover, by combining with other types of 3D printing method such as inkjet printing, FDM could rapidly fabricate a base structure while utilizing commercialized ink for inkjet printing.[30] DIW extrudes inks using various types of extruders (pneumatic, syringe, or progressive cavity). DIW enables the printing of a wide range of materials as long as the material exhibits proper rheological behavior.[65–67] Moreover, DIW offers highly customizable settings that can be easily modified for the controlled fabrication of multi-material structures.

3. 3D-printable materials

Material selection is a critical and challenging task in the 3D printing of bioelectronic devices. These materials should exhibit mechanical properties conducive to 3D

printing and high electrical conductivity for electronic functionality. Biocompatibility is also crucial for biomedical applications.

3.1. Metallic materials

Electronic devices benefit greatly from materials with high electrical conductivity.[68] Among the wide range of materials, metals exhibit the highest electrical conductivity. However, not all metals are suitable for 3D printing due to their high melting temperatures. Thus, liquid metals and metal nanoparticles with relatively low melting points are commonly used in 3D printing.[69,70]

Liquid metals have gained attention owing to their flexibility in modification and their high thermal and electrical conductivities. Among various liquid metals, gallium-based alloys, such as eutectic gallium indium (EGaIn) and gallium indium tin alloys (Galinstan) are biocompatible, highly conductive, and stable at room temperature (Figure 2A).[69,71–73] Their ease of printability has led to their use in the 3D printing of various bioelectronic devices, including smart electronic clothes,[74] electrodes for soft sensor systems,[75] wearable heaters,[76] and haptic feedback multimodal sensor devices.[77] Liquid metals are mostly 3D-printed using inkjet printing and DIW, as they are not photocurable.

Metal nanoparticles offer unique properties compared to bulk metals.[78] Their nanoscale size reduces their melting temperature, enabling their use in diverse biomedical applications. Highly conductive metal nanoparticles, such as silver nanoparticles (AgNPs), silver nanowires (AgNWs), and gold nanoparticles (AuNPs) are commonly used to fabricate bioelectronic devices.[79–83] For example, AgNPs have been employed in the fabrication of optoelectronic devices,[62,84] flexible electrochemical biosensors,[85] and strain sensors.[86,87] Similarly, AuNPs have been utilized for the biosensing platform that detects COVID-19 antibodies.[88]

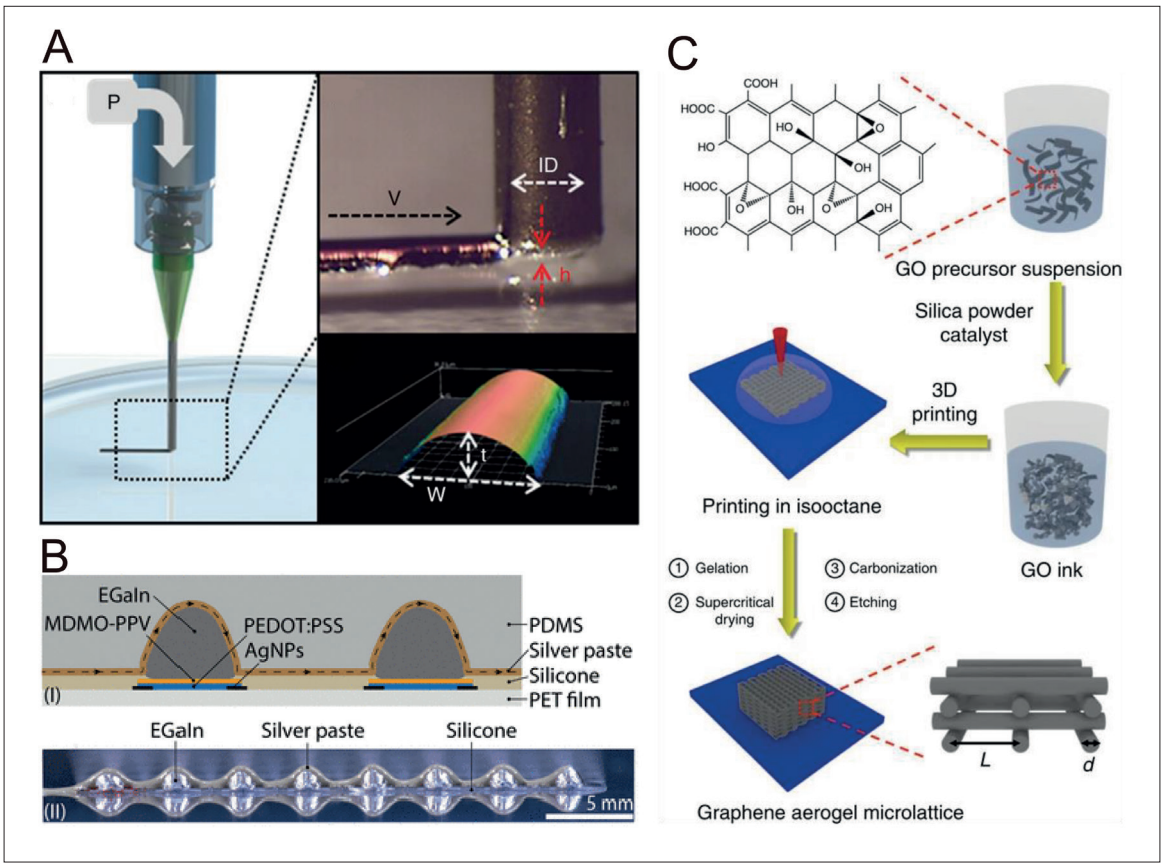

Figure 2. 3D printing of metallic materials. (A) 3D printing of gallium-based liquid metal via the direct ink writing (DIW) method.[73] Reproduced with permission from Wiley. Copyright © 2019 Wiley. (B) 3D-printed gallium-based liquid metal to form electrodes in organic light-emitting diode array.[103] Reprinted with permission from AAAS. Copyright © 2022. The Authors, some rights reserved; exclusive licensee AAAS. Distributed under a CC BY-NC 4.0 license (http://creativecommons.org/licenses/by-nc/4.0/). (C) 3D printing of graphene oxide-based ink filaments to construct a graphene aerogel microlattice with excellent conductivity and light weight.[89] Reproduced with permission from Springer Nature. Copyright © 2015 Nature.

3.2. Non-metallic materials

3.2.1. Carbon-based materials

Carbon-based materials such as graphene and carbon nanotubes are electrically conductive nonmetallic materials. Graphene exhibits excellent electrical and thermal conductivities, high light transmittance, biocompatibility, and superior mechanical flexibility (Figure 2B).[89–91] These properties enable a broad range of applications in bioelectronics. Since graphene has low solubility in solvents, it is often modified to enhance its solubility while maintaining its functional properties. For example, graphene oxide (GO), its oxidized form, and reduced graphene oxide (rGO) are widely used in 3D printing because their solubility and electrical properties can be easily controlled.[91]

Carbon nanotubes (CNT), which are hollow cylinders rolled from graphene sheets, exhibit remarkable mechanical, electrical, and chemical properties.[92,93] Their large surface area and extreme length-to-diameter ratio enable the construction of highly aligned structures, which is advantageous for enhancing mechanical properties, electrical performance[94] and cell adhesion.[95] CNT can be 3D-printed using diverse methods, including inkjet printing,[96] SLA,[97] and FDM.[98]

Moreover, carbon-based materials are often used as fillers in polymers to improve the mechanical, electrical, and chemical properties of other materials. For example, GO-incorporated polylactic acid (PLA) scaffolds have been synthesized to enhance the structural and mechanical properties to promote bone cell attachment, proliferation, and differentiation.[99] In another study, the addition of multi-walled carbon nanotubes (MWCNTs) to polycaprolactone scaffolds significantly increased the electrical conductivity of the scaffold, allowing for the application of electrical stimulation (ES) in bone tissue models.[100]

3.2.2. Conductive polymers

Recently, conductive polymers have attracted significant interest due to their biocompatibility, tunability, and flexibility. These polymers are composed of repetitive monomer units designed to enhance their electrical conductivity.[101] Their mechanical and electrical properties can be easily modified by incorporating other materials. The most extensively used conductive polymers include poly(3,4-ethylenedioxythiophene) polystyrene sulfonate (PEDOT:PSS), polypyrrole (PPy), polyaniline (PANI), and polyacetylene.

PEDOT:PSS exhibits high conductivity, biocompatibility, optical transparency, thermal and chemical stability, and flexibility (Figure 2C).[102,103] Its electrical properties can be further enhanced by incorporating conductive fillers such as graphene[104] and CNT.[105] By adding graphene nanoflakes to nonconductive thermoplastic polyurethane, the electrical conductivity increased to 0.59×10^{-6} S/m.[105] Additionally, the stretchability of PEDOT:PSS can be improved by adding polymer like polyethylene oxide (PEO)[43] or polyvinyl alcohol (PVA),[106] which decreases the interaction between the polymer chains and increases the free volume between PEDOT and PSS. The broad utilization of PEDOT:PSS in bioelectronic devices such as biosensors,[106] stretchable transistors,[107] temperature sensors,[108] and soft neural probes[109] is achieved through tuning the aforementioned parameters. Moreover, PEDOT:PSS can be used in diverse 3D printing methods including inkjet printing,[29] DIW,[109] and SLA.[110]

PPy exhibits high electrical conductivity and excellent chemical stability under biological conditions. Due to its ability to enhance cell growth and differentiation, PPy has been extensively used as a scaffold material for tissue engineering.[111] Beyond tissue engineering, PPy has shown great potential in electronic devices such as wearable flexible electronic sensors,[112] cardiac patches,[113] scaffolds,[114] and wearable storage devices.[115] PANI is also a promising conductive polymer for biomedical electronics owing to its ease of synthesis, low cost, and tunable conductivity.

3.2.3. Conductive hydrogel

Conductive hydrogels have emerged as favorable options for biomedical electronic interfaces owing to their soft mechanical properties, biocompatibility, and water content. Compared to conventional electrode materials, which exhibit Young's moduli several orders of magnitude higher than those of biological tissues, conductive hydrogels offer tunability to match the Young's modulus of the targeted tissues.[116,117] Especially, ionic hydrogels containing mobile nanofillers exhibit both high conductivity and tissue-like softness.[118] Furthermore, their stretchability and flexibility have led to their application in soft electronic materials.[119] Conductive hydrogel combined with 3D printing allows for the customization of electronic device; for instance, merging DLP printing technique with a conductive hydrogel elastomer assembling process can be applied to producing customized stretchable conductors.[120]

Conductive hydrogels can also be made using a variety of polymers including PEDOT:PSS,[109] PVA,[106] PPy,[114] polyethylene glycol diacrylate (PEGDA),[121] and PANI.[122] These hydrogels can be fabricated using various methods including inkjet printing, SLA, DLP, and DIW.

However, challenges remain in obtaining the desired levels of electrical conductivity and mechanical toughness while preserving their advantageous properties.[123]

Hydrogels can achieve enhanced conductivity by incorporating conductive polymers or conductive particles such as carbon-based materials, creating a conductive nanocomposite network throughout the gel.[124] By the incorporation of CNTs to PEDOT:PSS, electrical conductivity has increased up to 2000 S/m, a value that is challenging to achieve with PEDOT:PSS alone.[125] The mechanical toughness of hydrogels can be increased by introducing filler materials that enhance their storage moduli.[126]

4. Applications in biomedical research

The applications of 3D-printed electronic devices in biomedical research have ushered in a new era of innovation and customization. One notable advantage is the creation of a patient-specific architecture tailored to individual anatomies, which ensures personalization. Moreover, 3D printing enables the direct integration of electronic components into the 3D structures of biological materials, thereby enhancing the stability, robustness, and functionality of biomedical devices. Its rapid prototyping capabilities foster a more efficient and cost-effective approach to experimental setups. In this section, we discuss the diverse applications of 3D-printed electronics in biomedical research, ranging from personalized surgical guidance and medical implants to tissue engineering platforms (Table 2). We explore how these innovations are transforming healthcare, improving patient outcomes, and paving the way for future advancements in biomedicine.

4.1. 3D-printed surgical guidance

Surgical quality can be significantly enhanced through preoperative planning and rehearsal.[127] Presurgical organ models, which help in understanding a patient's specific anatomy, have been widely used to reduce operation time and improve patient outcomes. Advances in 3D printing and 3D visualization techniques, such as computed tomography (CT) and magnetic resonance imaging (MRI), have allowed the fabrication of presurgical models with patient-specific features.[128] Recent studies have integrated 3D-printed electronic sensors into presurgical organ models to provide realistic and quantitative feedback during preoperative simulations (Figure 3A and B).[129,130] These models were fabricated via DIW with ionic hydrogel to match the mechanical properties of soft tissues, allowing real-time monitoring of the pressures applied to the models.

In situ 3D printing has shown great potential for directly fabricating fragile devices on time-varying

Table 2. 3D-printed electronics for biomedical applications.

Application category	Application	3D printing method	Ref.
Surgical guidance	3D-printed patient-specific prostate model with integrated sensors having physical properties close to those of prostate tissue	DIW	129
	3D-printed patient-specific aortic root models with internal sensors	DIW	130
Bionic devices	3D-printed bionic arm	FDM	131
	Implantable wireless battery less vascular electronics with printed soft sensors sensing of hemodynamics	Aerosol jet printing	143
	3D-printed bimodal electronic skin with high resolution and breathability for hair growth	DIW	133
	Soft robots, circuit-embedding architectures, and strain sensors	DLP and FDM	53
Sensors and diagnostic devices	Wearable health monitoring device applications	Inkjet printing	43
	Conducting polymer hydrogel strain sensor for soft machines	DIW	106
	Soft neural probe capable of *in vivo* single-unit recording	DIW	109
	3D-printed stretchable and strain-insensitive temperature sensor	DIW	138
	Wireless bioelectronics for human-machine interfaces	Aerosol jet printing	10
Tissue engineering	3D-printed PCL/MWCNTs scaffolds with electrical stimulation for bone tissue engineering	DIW	100
	3D printed PLA/BFO scaffolds of electrical stimulus on human adipose-derived mesenchymal stem cells.	FDM	145
	Conductive PPy/PEGDA hydrogel for future scaffolds	DLP	121

Abbreviations: BFO, bismuth ferrite; DIW, direct ink writing; DLP, digital light processing; FDM, fused deposition method; MWCNT, multi-walled carbon nanotubes; PEGDA, polyethylene glycol diacrylate; PLA, polylactic acid; PPy, polypyrrole.

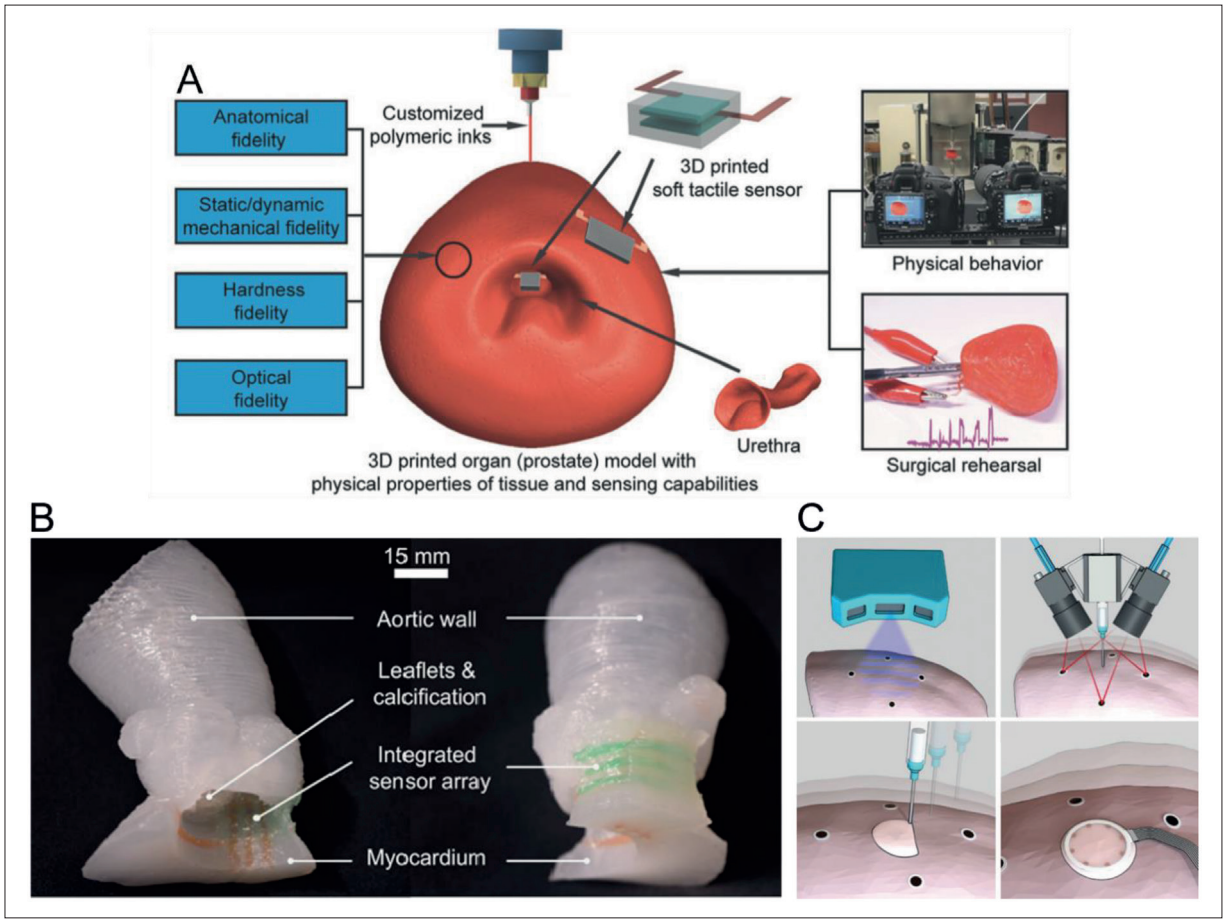

Figure 3. 3D-printed surgical guidance. (A) A 3D-printed prostate was integrated with a tactile sensor for surgical guidance.[129] Reproduced with permission from Wiley. Copyright © 2017 Wiley. (B) 3D-printed patient-specific aortic root model.[130] Reprinted with permission from AAAS. Copyright © The Authors, some rights reserved; exclusive licensee AAAS. Distributed under a CC BY-NC 4.0 license (http://creativecommons.org/licenses/by-nc/4.0/). (C) 3D printing of electrical impedance tomography sensor on a deforming tissue surface.[63] Reprinted with permission from AAAS. Copyright © The Authors, some rights reserved; exclusive licensee AAAS. Distributed under a CC BY-NC 4.0 license (http://creativecommons.org/licenses/by-nc/4.0/).

geometries, minimizing the risk associated with manual transplantation processes. The recent trend sees the combination of AI with *in situ* DIW technology to fabricate devices directly on deformed or moving surfaces by sensing the time-varying geometric states of a target surface in real time (Figure 3C).[63] For instance, an ionic hydrogel-based stretchable EIT strain sensor was directly printed onto porcine lungs under respiration-induced deformation. The EIT sensor showed stable adhesion to the lung surface during respiration and provided *in situ* spatiotemporal mapping of the 2D volumetric strain.

4.2. Prosthetics and bionic devices

3D printing facilitates the creation of personalized prostheses by reconstructing the scanned geometries of individuals. For example, the application of FDM technology has led to the design and fabrication of patient-specific customized bionic arms.[131] One arm was meticulously modeled to mirror the geometry of the other arm using computer-aided design (CAD) software, so that it is symmetrical to the other. Moreover, a 3D-printed partial hip prosthesis incorporating internal cellular structures was designed based on anatomical CT scan data.[132]

Recently, e-skin capable of monitoring temperature and external stimuli was developed using multi-material *in situ* inkjet printing (Figure 4A).[133] The e-skin is incorporated with temperature, pressure, and tactile sensors, and allowed for hair penetration and growth to enhance wearing comfort. This innovative design addresses a key challenge in wearable technology by providing both functionality and comfort to users.

Relying on characteristics of 3D printing that allows complex or out-of-plane shape fabrication, optoelectronic devices have shown significant promise for further advancement, potentially leading to ophthalmic

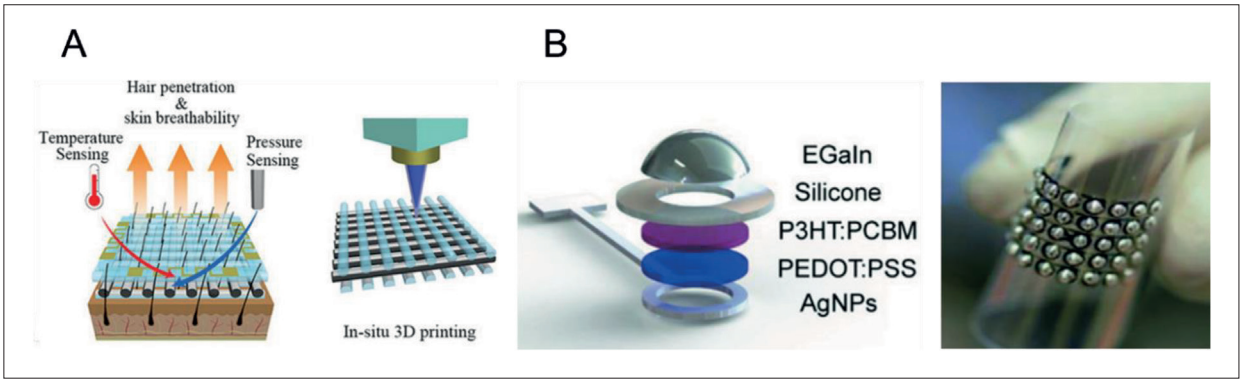

Figure 4. 3D-printed bionic devices. (A) 3D-printed electronic skin with an integrated sensor for accurate stimulus identification of hair growth.[133] Reproduced with permission from American Chemical Society . Copyright © 2022 American Chemical Society. (B) 3D-printed flexible photodetector fabricated on a curved surface.[62] Reproduced with permission from Wiley. Copyright © 2018 Wiley.

applications such as contact lenses or bionic eyes.[134] Arrays of quantum-dot-based light-emitting diodes[84] and organic photodetectors[62] have been fabricated through layer-by-layer deposition on nonflat substrates, achieved through the direct deposition of inks on curved surfaces via DIW (Figure 4B).[62]

Furthermore, 3D printing technology allows the direct interweaving of biological materials with electronic components in multiple dimensions. This integration not only mimics the functions and external appearance but also replicates the mechanical properties of specific organs.[135] For example, a 3D cyborg ear has been created by directly integrating cells and hydrogels with electronic components.[136] A chondrocyte-seeded alginate hydrogel was 3D-printed via extrusion-based printer to recreate the complex anatomical geometry of the human ear, and a silver nanoparticle-infused coil antenna was printed to receive signals with frequencies beyond the normal audible range.

4.3. Health monitoring devices

Extensive research efforts are underway in the field of wearable electronic devices, with a focus on sensing, diagnosing, and predicting health conditions through advanced human-machine interfaces.[137] Through the precise fabrication of intricate structures and incorporation of flexible electronic materials, 3D printing has enhanced the sensitivity and specificity of biosensors.[138] Various 3D-printed biosensors such as wearable ultraviolet sensors,[139] strain-insensitive temperature sensors,[140] and conformal strain and humidity sensors[141] have shown high responsivity, good stability, and robust performance even after repeated bending cycles.

When designing wearable applications, mechanical flexibility and stretchability are critical considerations to ensure adaptation to curved tissue surfaces. An inkjet-printed stretchable conductor was developed using a PEDOT:PSS/ PEO polymer blend to achieve high elasticity.[43] This device has shown potential as a wearable sensor patch, particularly for recording photoplethysmography (PPG) and electrocardiography (ECG). In another study, a highly stretchable conductive polymer composed of PEDOT:PSS nanofibers and PVA was 3D-printed via DIW to fabricate a strain sensor.[106] This strain sensor was integrated with electronic skin to identify hand gestures and has been applied to a soft gripper for object manipulation (Figure 5A).[106]

Not only can the materials be modified but the structure of the devices can also be designed to enhance their functionality. For example, auxetic structures with a negative Poisson's ratio have been used to fabricate flexible strain sensors to increase the sensing performance.[60] A skin-inspired gradient porous-structure sensor was developed to achieve high sensitivity and stability.[142] In both studies, 3D printing technique offered a high degree of design flexibility and fabrication efficiency.

Implantable monitoring devices have introduced new opportunities for directly recording biological signals. The multi-material and high-resolution DIW capability enabled the fabrication of flexible and highly conductive soft neural probes without the need for post-assembly and multi-step procedures (Figure 5B).[109] The 3D-printed soft neural probe was implanted in the dorsal hippocampus of the mice to monitor neural activity under freely moving conditions. Recently, an implantable vascular electronic system with aerosol jet-printed soft pressure sensors and a multi-material inductive stent was developed for wireless monitoring of hemodynamics (Figure 5C).[143] In this study, 3D printing allowed for the rapid fabrication of pressure

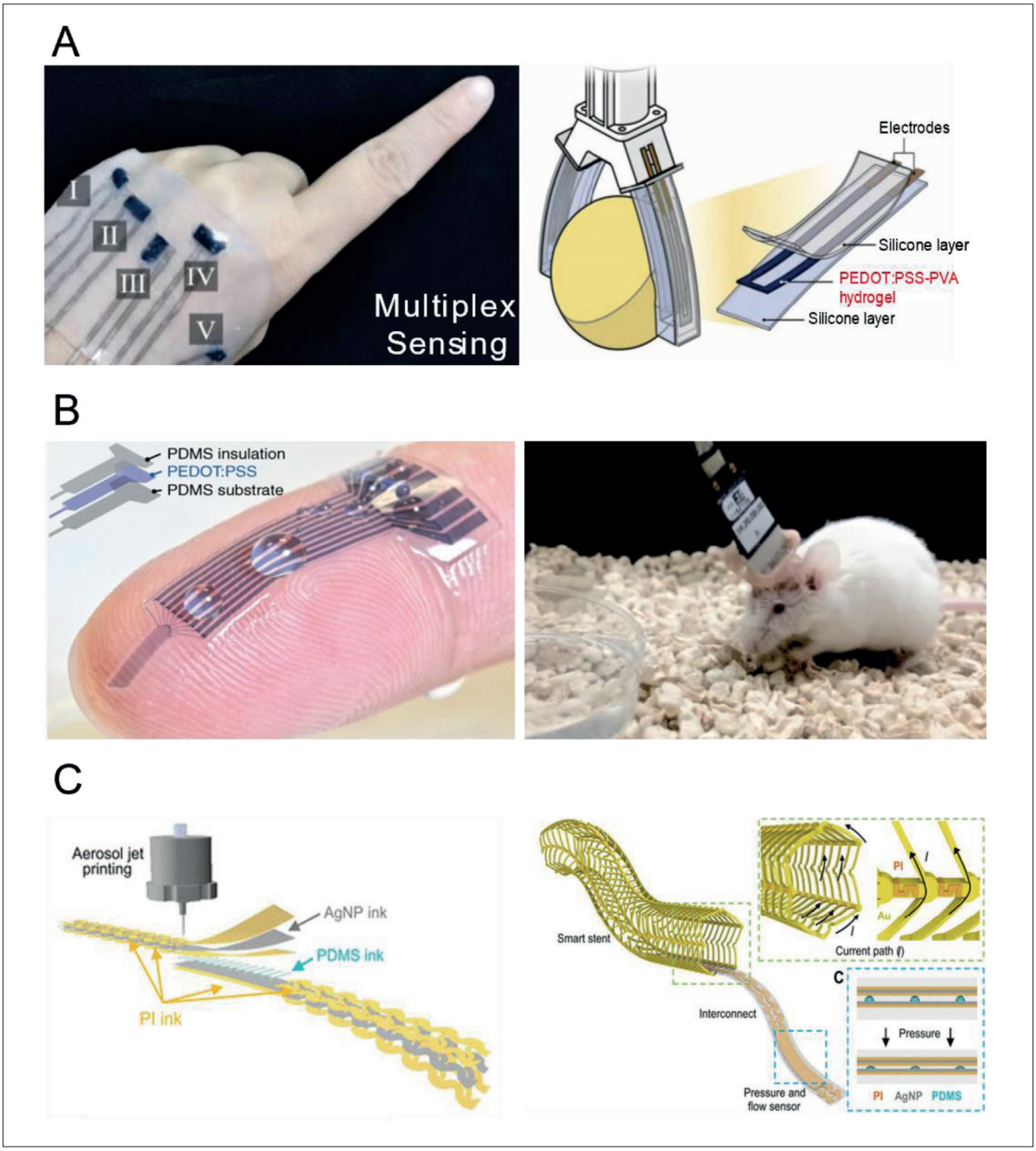

Figure 5. 3D-printed biomedical sensors. (A) A 3D-printed high-stretchable hydrogel strain sensors for soft machines.[106] Reproduced with permission from Wiley. Copyright © 2022 Wiley. (B) A 3D-printed soft hydrogel microstructure for *in vivo* signaling of neural probes.[109] Reproduced with permission from XX. Copyright © 2020 Nature. (C) 3D-printed implantable vascular electronics for multiplex sensing of hemodynamics.[143] Reprinted with permission from AAAS. Copyright © The Authors, some rights reserved; exclusive licensee AAAS. Distributed under a CC BY-NC 4.0 license (http://creativecommons.org/licenses/by-nc/4.0/).

sensors with fast response times, high durability, and sensing at small bending radii.

4.4. Tissue-engineered scaffolds

3D printing enables the construction of tissue scaffolds with sophisticated 3D tissue-specific structures. Moreover, the use of biocompatible and electrically conductive materials has led to advances in tissue regeneration technology. Cells and tissues are inherently exposed to endogenous electric fields generated on their own to regulate their functions. Furthermore, exogenous ES can enhance the tissue regenerative capacity by modulating

cellular activity. In this context, bioelectric scaffolds that can apply physiological ES to cells have been developed to investigate the underlying mechanisms of ES-mediated cellular responses and induce tissue regeneration *in vitro* or *in vivo*.[144]

For instance, a DIW 3D-printed PLA scaffold containing bismuth ferrite (BFO) nanoparticles was developed to construct a 3D cellular environment for neural tissue engineering (Figure 6A).[145] In this scaffold, the physiological level of ES applied to stem cells induced cell alignment toward BFO lines. Similarly, a conductive and biodegradable scaffold made of polycaprolactone and MWCNTs was 3D-printed using DIW for bone tissue regeneration (Figure 6B).[100] Following scaffold implantation at the bone defect site, exogenous ES was applied using a transcutaneous electrical stimulator. The combination of conductive PCL/MWCNT scaffolds with ES promotes angiogenesis and mineralized bone tissue formation.

Various types of sensors have been integrated into tissue engineering platforms to monitor biological functions in real time. An instrumented cardiac microphysiological device incorporating soft strain gauge sensors, electrical interconnects, and eight independent cell culture wells was fabricated using DIW multi-material 3D printing.[146] This device enabled the measurement of contraction strength and beat rate in drug–dose response studies within an *in vitro* environment over a long testing period. Another cardiac microphysiological platform combined 3D-printed micropillar electrodes and elastic microwires to record electrophysiological signals and contractile functions.[147] The DIW-based 3D printing method has allowed the fabrication of high-aspect-ratio micropillars by tuning the height, electrochemical properties, and elasticity of the electrodes.

5. Conclusion and future perspectives

3D printing has emerged as a state-of-the-art manufacturing technology in the biomedical field, offering patient-specific customization through low-cost and efficient fabrication processes.[148–151] Diverse printing techniques and materials have enabled the construction of functional devices tailored to individual needs. These bioelectronic devices can be seamlessly integrated into biological systems and applied to patient care. However, challenges persist as 3D-printed models strive to achieve an ideal match with the human body in terms of mechanical, chemical, and functional aspects. In this section, the current challenges in 3D-printed applications in medicine and future directions are discussed.

For practical application of wearable and implantable devices, there are several key considerations, including biocompatibility, long-term stability, sensitivity, and measurement accuracy. The device should be biocompatible to avoid chronic immune responses and to ensure stable physiological biosignal monitoring during long-term biointegration. Devices with high mechanical flexibility and stretchability should be designed for stable

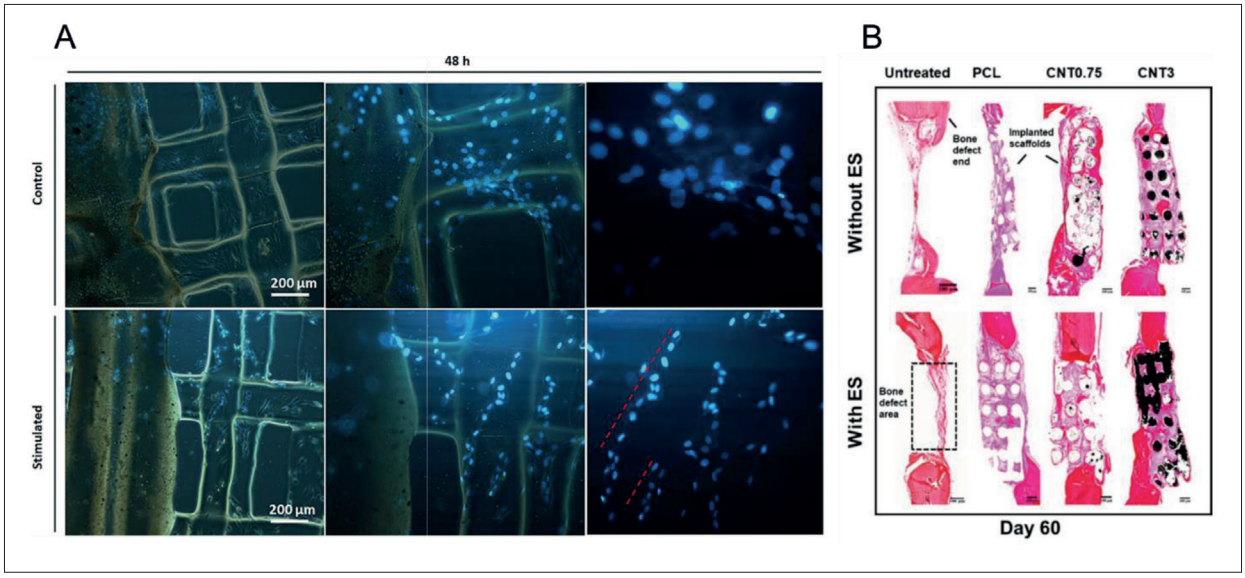

Figure 6. 3D-printed tissue-engineered scaffolds. (A) 3D-printed scaffolds for stimulating human adipose-derived mesenchymal stem cells.[145] Reproduced with permission from Wiley . Copyright © 2021 Wiley. (B) 3D-printed polycaprolactone (PCL)/multi-walled carbon nanotubes (MWCNTs) scaffolds with electrical stimulation (ES) for bone tissue regeneration.[100] Reproduced with permission from Springer Nature. Copyright © 2021 Springer.

adhesion to the human skin or tissues, which are generally curved and deformed. In addition to the adhesion between the device and human tissues, seamless adhesion between multiple layers of devices must be considered. Moreover, high sensitivity and measurement accuracy are critical for achieving high-performance devices.

Hybrid 3D printing have been widely investigated due to their potential to combine the strengths of different 3D printing methods. While advancements in individual 3D printing techniques have improved material versatility, printing resolution, and printing speed, each method still has distinct advantage and limitations. Hybrid 3D printing can foster further advancement by balancing the pros and cons of each printing method.[134] For instance, by adopting vat photopolymerization, and DIW could provide both high resolution with material versatility.[152] Therefore, it is crucial to not only advance the capabilities of each method on its own but also to amalgamate different methods to utilize their advantages.

Biocompatible 3D-printable electronic materials have been extensively explored. Significant contributions have been made toward obtaining soft electronic materials with high mechanical flexibility and stretchability.[153,154] Printable soft electronically conductive composites have been formulated by varying the types and contents of conductive materials. These composites exhibiting customizable conductivity and mechanical properties have been discovered. Using materials that exhibit mechanical properties that match the physiological properties of the target tissue can enhance the integration stability with tissues and reduce the mechanical mismatch between the device and tissue. Stable integration at the interfaces of the device tissue and layer of the device is another critical factor for attaining stable and high performance of the device.

The device structure can also improve the device performance. The dimensions and sizes should be tailored for each specific application.[155] The device's deformation behavior can be designed to match the movement and structure of the deformed surface of human tissues. Auxetic structures that exhibit negative Poisson's ratios and synclastic curvatures during deformation have been used to enhance the adaptability and sensitivity.[156,157] As the application sites of bioelectronic devices become more diverse, the device design should reflect the structure and movement of the target site. The structural design significantly influences device functions such as sensitivity, stability, and deformation behavior, which vary accordingly. Considering the limitations in building and testing devices with numerous structures, recent advances in machine-learning-based design optimization would offer great potential for creating devices with target-specific optimized designs.[158] This approach not only enhances the efficiency of the design process but also ensures that the final devices meet the specific demands of their targeted environments, leading to improved performance and reliability of the biosignals.

3D printing of bioelectronic devices holds great promise for healthcare because it offers personalized, efficient, and cost-effective solutions. Extensive studies on 3D-printable bioelectronic materials and biological tissue-tailored design fabrication could provide unprecedented technologies for personalized healthcare and therapy. Particularly, the interface between wearable or implantable devices and the target tissue surface must be carefully investigated for stable and reliable integration. Overcoming the current challenges and exploring new frontiers in bioelectronic materials, design optimization, and biomedical applications will pave the way for the next generation of innovative biomedical devices.

Acknowledgments

None.

Funding

This work was supported by the National Research Foundation of Korea (NRF) grant funded by the Korea government (MSIT) (No. 2022R1C1C1010823, No. RS-2023-00218543).

Conflict of interest

The authors declare they have no competing interests

Author contributions

Conceptualization: Minsu Ryoo, Song Ih Ahn
Visualization: Minsu Ryoo, Daeho Kim
Writing–original draft: Minsu Ryoo, Junseop Noh, Daeho Kim
Writing–review & editing: Minsu Ryoo, Daeho Kim, Song Ih Ahn

Ethics approval and consent to participate

Not applicable.

Consent for publication

Not applicable.

Availability of data

Not applicable.

References

1. Xu L, Qin H, Tan J, et al. Clinical study of 3D printed personalized prosthesis in the treatment of bone defect after pelvic tumor resection. *J Orthop Translat*. 2021;29:163-169. doi: 10.1016/j.jot.2021.05.007
2. Tejo-Otero A, Lustig-Gainza P, Fenollosa-Artés F, Valls A, Krauel L, Buj-Corral I. 3D printed soft surgical planning prototype for a biliary tract rhabdomyosarcoma. *J Mech Behav Biomed Mater*. 2020;109:103844. doi: 10.1016/j.jmbbm.2020.103844
3. Uhl JF, Sufianov A, Ruiz C, et al. The use of 3D printed models for surgical simulation of cranioplasty in craniosynostosis as training and education. *Brain Sci*. 2023;13(6):894. doi: 10.3390/brainsci13060894
4. Wang F, Xue Y, Chen X, et al. 3D printed implantable hydrogel bioelectronics for electrophysiological monitoring and electrical modulation. *Adv Funct Mater*. 2024;34(21):2314471. doi: 10.1002/adfm.202314471
5. Krishnadoss V, Kanjilal B, Hesketh A, et al. In situ 3D printing of implantable energy storage devices. *Chem Eng J*. 2021;409:128213. doi: 10.1016/j.cej.2020.128213
6. Picco CJ, Domínguez-Robles J, Utomo E, et al. 3D-printed implantable devices with biodegradable rate-controlling membrane for sustained delivery of hydrophobic drugs. *Drug Deliv*. 2022;29(1):1038-1048. doi: 10.1080/10717544.2022.2057620
7. Yi Q, Najafikhoshnoo S, Das P, et al. All-3D-printed, flexible, and hybrid wearable bioelectronic tactile sensors using biocompatible nanocomposites for health monitoring. *Adv Mater Technol*. 2022;7(5):2101034. doi: 10.1002/admt.202101034
8. Tang Z, Jia S, Zhou C, Li B. 3D printing of highly sensitive and large-measurement-range flexible pressure sensors with a positive piezoresistive effect. *ACS Appl Mater Interfaces*. 2020;12(25):28669-28680. doi: 10.1021/acsami.0c06977
9. Davoodi E, Montazerian H, Haghniaz R, et al. 3D-printed ultra-robust surface-doped porous silicone sensors for wearable biomonitoring. *ACS Nano*. 2020;14(2):1520-1532. doi: 10.1021/acsnano.9b06283
10. Kwon Y-T, Kim Y-S, Kwon S, et al. All-printed nanomembrane wireless bioelectronics using a biocompatible solderable graphene for multimodal human-machine interfaces. *Nat Commun*. 2020;11(1):3450. doi: 10.1038/s41467-020-17288-0
11. Yan W-C, Davoodi P, Vijayavenkataraman S, et al. 3D bioprinting of skin tissue: from pre-processing to final product evaluation. *Adv Drug Deliv Rev*. 2018;132: 270-295. doi: 10.1016/j.addr.2018.07.016
12. Bao G, Yang P, Yi J, et al. Full-sized realistic 3D printed models of liver and tumour anatomy: a useful tool for the clinical medicine education of beginning trainees. *BMC Med Educ*. 2023;23(1):574. doi: 10.1186/s12909-023-04535-3
13. Fu H, Zhang D, Zeng J, et al. Application of 3D-printed tissue-engineered skin substitute using innovative biomaterial loaded with human adipose-derived stem cells in wound healing. *Int J Bioprint*. 2023;9(2):674. doi: 10.18063/ijb.v9i2.674
14. Zhu Z, Guo SZ, Hirdler T, et al. 3D printed functional and biological materials on moving freeform surfaces. *Adv Mater*. 2018;30(23):e1707495. doi: 10.1002/adma.201707495
15. Guo X, Li H, Hong W, et al. 3D printed fourth-order star-like negative poisson's ratio structure for high-sensitivity bionic flexible capacitive pressure sensor. *IEEE Sens J*. 2024;24(9) 13937-13945. doi: 10.1109/JSEN.2024.3374304
16. He Q, Zeng Y, Jiang L, et al. Growing recyclable and healable piezoelectric composites in 3D printed bioinspired structure for protective wearable sensor. *Nat Commun*. 2023;14(1):6477. doi: 10.1038/s41467-023-41740-6
17. Wei J, Xie J, Zhang P, et al. Bioinspired 3D printable, self-healable, and stretchable hydrogels with multiple conductivities for skin-like wearable strain sensors. *ACS Appl Mater Interfaces*. 2021;13(2):2952-2960. doi: 10.1021/acsami.0c19512
18. Jain K, Wang Z, Garma LD, et al. 3D printable composites of modified cellulose fibers and conductive polymers and their use in wearable electronics. *Appl Mater Today*. 2023;30:101703. doi: 10.1016/j.apmt.2022.101703
19. Yu J, Tian F, Wang W, et al. Design of highly conductive, intrinsically stretchable, and 3D printable PEDOT: PSS hydrogels via PSS-chain engineering for bioelectronics. *Chem Mater*. 2023;35(15):5936-5944. doi: 10.1021/acs.chemmater.3c00844
20. Peng S, Li Y, Wu L, et al. 3D printing mechanically robust and transparent polyurethane elastomers for stretchable electronic sensors. *ACS Appl Mater Interfaces*. 2020; 12(5):6479-6488 doi: 10.1021/acsami.9b20631
21. Tan P, Xi Y, Chao S, et al. An artificial intelligence-enhanced blood pressure monitor wristband based on piezoelectric nanogenerator. *Biosensors*. 2022;12(4):234. doi: 10.3390/bios12040234
22. Kim B, Jang S, Geier ML, Prabhumirashi PL, Hersam MC, Dodabalapur A. High-speed, inkjet-printed carbon nanotube/zinc tin oxide hybrid complementary ring oscillators. *Nano Lett*. 2014;14(6):3683-3687. doi: 10.1021/nl5016014

23. Minemawari H, Yamada T, Matsui H, et al. Inkjet printing of single-crystal films. *Nature*. 2011;475(7356):364-367. doi: 10.1038/nature10313

24. De Gans BJ, Duineveld PC, Schubert US. Inkjet printing of polymers: state of the art and future developments. *Adv Mater*. 2004;16(3):203-213. doi: 10.1002/adma.200300385

25. Calvert P. Printing cells. *Science*. 2007;318(5848):208-209. doi: 10.1126/science.1144212

26. Cui X, Boland T. Human microvasculature fabrication using thermal inkjet printing technology. *Biomaterials*. 2009;30(31):6221-6227. doi: 10.1016/j.biomaterials.2009.07.056

27. Huang Z, Tang Y, Guo H, et al. 3D printing of ceramics and graphene circuits-on-ceramics by thermal bubble inkjet technology and high temperature sintering. *Ceramics Int*. 2020;46(8):10096-10104. doi: 10.1016/j.ceramint.2019.12.278

28. Wood V, Panzer MJ, Chen J, et al. Inkjet-printed quantum dot–polymer composites for full-color ac-driven displays. *Adv Mater*. 2009;21(21):2151-2155. doi: 10.1002/adma.200990078

29. Teo MY, RaviChandran N, Kim N, et al. Direct patterning of highly conductive PEDOT: PSS/ionic liquid hydrogel via microreactive inkjet printing. *ACS Appl Mater Interfaces*. 2019;11(40):37069-37076. doi: 10.1021/acsami.9b12069

30. Mangoma TN, Yamamoto S, Malliaras GG, Daly R. Hybrid 3D/Inkjet-printed organic neuromorphic transistors. *Adv Mater Technol*. 2022;7(2):2000798. doi: 10.1002/admt.202000798

31. Carey T, Cacovich S, Divitini G, et al. Fully inkjet-printed two-dimensional material field-effect heterojunctions for wearable and textile electronics. *Nat Commun*. 2017;8(1):1202. doi: 10.1038/s41467-017-01210-2

32. Gibertini E, Lissandrello F, Bertoli L, Viviani P, Magagnin L. All-inkjet-printed Ti3C2 MXene capacitor for textile energy storage. *Coatings*. 2023;13(2):230. doi: 10.3390/coatings13020230

33. Li Y, Dahhan O, Filipe CD, Brennan JD, Pelton RH. Deposited nanoparticles can promote air clogging of piezoelectric inkjet printhead nozzles. *Langmuir*. 2019;35(16): 5517-5524. doi: 10.1021/acs.langmuir.8b04335

34. Li Y, Dahhan O, Filipe CD, Brennan JD, Pelton RH. Optimizing piezoelectric inkjet printing of silica sols for biosensor production. *J Sol-Gel Sci Technol*. 2018; 87:657-664. doi: 10.1007/s10971-018-4762-3

35. Li J, Rossignol F, Macdonald J. Inkjet printing for biosensor fabrication: combining chemistry and technology for advanced manufacturing. *Lab Chip*. 2015;15(12): 2538-2558. doi: 10.1039/C5LC00235D

36. Zhu W, Ma X, Gou M, Mei D, Zhang K, Chen S. 3D printing of functional biomaterials for tissue engineering. *Curr Opin Biotechnol*. 2016;40:103-112. doi: 10.1016/j.copbio.2016.03.014

37. Yan K, Li J, Pan L, Shi Y. Inkjet printing for flexible and wearable electronics. *APL Mater*. 2020;8(12):120705. doi: 10.1063/5.0031669

38. Shah MA, Lee D-G, Lee B-Y, Hur S. Classifications and applications of inkjet printing technology: a review. IEEE Access. 2021 doi: 10.1109/ACCESS.2021.3119219

39. Tekin E, Smith PJ, Schubert US. Inkjet printing as a deposition and patterning tool for polymers and inorganic particles. *Soft Matter*. 2008;4(4):703-713. doi: 10.1039/B711984D

40. Chung S, Cho K, Lee T. Recent progress in inkjet-printed thin-film transistors. *Adv Sci (Weinh)*. 2019;6(6):1801445. doi: 10.1002/advs.201801445

41. Rahmati S, Shirazi S, Baghayeri H. Piezo-electric head application in a new 3D printing design. *Rapid Prototyping J*. 2009;15(3):187-191. doi: 10.1108/13552540910960280

42. Wang Z, Wu W, Yang Q, Li Y, Noh C-H. In-situ fabrication of flexible vertically integrated electronic circuits by inkjet printing. *J Alloys Compd*. 2009;486(1-2):706-710. doi: 10.1016/j.jallcom.2009.07.044

43. Lo L-W, Zhao J, Wan H, Wang Y, Chakrabartty S, Wang C. An inkjet-printed PEDOT: PSS-based stretchable conductor for wearable health monitoring device applications. *ACS Appl Mater Interfaces*. 2021;13(18):21693-21702. doi: 10.1021/acsami.1c00537

44. Delekta SS, Adolfsson KH, Erdal NB, Hakkarainen M, Östling M, Li J. Fully inkjet printed ultrathin microsupercapacitors based on graphene electrodes and a nano-graphene oxide electrolyte. *Nanoscale*. 2019;11(21):10172-10177. doi: 10.1039/C9NR01427F

45. Su C-H, Chiu H-L, Chen Y-C, et al. Highly responsive PEG/gold nanoparticle thin-film humidity sensor via inkjet printing technology. *Langmuir*. 2019;35(9):3256-3264. doi: 10.1021/acs.langmuir.8b03433

46. Wen D, Ying G, Liu L, et al. Flexible and high-performance MXene/MnO2 film electrodes fabricated by inkjet printing: toward a new generation supercapacitive application. *Adv Mater Interfaces*. 2021;8(21):2101453. doi: 10.1002/admi.202101453

47. Kim JD, Choi JS, Kim BS, Choi YC, Cho YW. Piezoelectric inkjet printing of polymers: stem cell patterning on polymer substrates. *Polymer*. 2010;51(10):2147-2154. doi: 10.1016/j.polymer.2010.03.038

48. Remaggi G, Zaccarelli A, Elviri L. 3D printing technologies in biosensors production: recent developments. *Chemosensors*. 2022;10(2):65. doi: 10.3390/chemosensors10020065

49. Huang J, Qin Q, Wang J. A review of stereolithography: processes and systems. *Processes*. 2020;8(9):1138. doi: 10.3390/pr8091138

50. Quan H, Zhang T, Xu H, Luo S, Nie J, Zhu X. Photo-curing 3D printing technique and its challenges. *Bioact Mater*. 2020;5(1):110-115. doi: 10.1016/j.bioactmat.2019.12.003

51. Song Q, Chen Y, Hou P, et al. Fabrication of multi-material pneumatic actuators and microactuators using stereolithography. *Micromachines*. 2023;14(2):244. doi: 10.3390/mi14020244

52. Pagac M, Hajnys J, Ma Q-P, et al. A review of vat photopolymerization technology: materials, applications, challenges, and future trends of 3D printing. *Polymers*. 2021;13(4):598. doi: 10.3390/polym13040598

53. Peng X, Kuang X, Roach DJ, et al. Integrating digital light processing with direct ink writing for hybrid 3D printing of functional structures and devices. *Addit Manuf*. 2021;40:101911. doi: 10.1016/j.addma.2021.101911

54. Liu M, Zhang Q, Shao Y, Liu C, Zhao Y. Research of a novel 3D printed strain gauge type force sensor. *Micromachines*. 2018;10(1):20. doi: 10.3390/mi10010020

55. Kim NP, Eo J-S, Cho D. Optimization of piston type extrusion (PTE) techniques for 3D printed food. *J Food Eng*. 2018;235:41-49. doi: 10.1016/j.jfoodeng.2018.04.019

56. Valkenaers H, Vogeler F, Voet A, Kruth J-P. *Screw Extrusion Based 3D Printing, A Novel Additive Manufacturing Technology*. University of Stellenbosch: Stellenbosch; 2013:97-103.

57. Seoane-Viaño I, Januskaite P, Alvarez-Lorenzo C, Basit AW, Goyanes A. Semi-solid extrusion 3D printing in drug delivery and biomedicine: personalised solutions for healthcare challenges. *J Control Release*. 2021;332:367-389. doi: 10.1016/j.jconrel.2021.02.027

58. Tetsuka H, Shin SR. Materials and technical innovations in 3D printing in biomedical applications. *J Mater Chem B*. 2020;8(15):2930-2950. doi: 10.1039/D0TB00034E

59. Dababneh AB, Ozbolat IT. Bioprinting technology: a current state-of-the-art review. *J Manuf Sci Eng*. 2014;136(6):061016. doi: 10.1115/1.4028512

60. Li B, Liang W, Zhang L, Ren F, Xuan F. TPU/CNTs flexible strain sensor with auxetic structure via a novel hybrid manufacturing process of fused deposition modeling 3D printing and ultrasonic cavitation-enabled treatment. *Sens Actuators A: Phys*. 2022;340:113526. doi: 10.1016/j.sna.2022.113526

61. Ma C, Zhu B, Qian Z, Ren L, Yuan H, Meng Y. 3D-printing of conductive inks based flexible tactile sensor for monitoring of temperature, strain and pressure. *J Manuf Processes*. 2023;87:1-10. doi: 10.1016/j.jmapro.2023.01.008

62. Park SH, Su R, Jeong J, et al. 3D printed polymer photodetectors. *Adv Mater*. 2018;30(40):1803980. doi: 10.1002/adma.201803980

63. Zhu Z, Park HS, McAlpine MC. 3D printed deformable sensors. *Sci Adv*. 2020;6(25):eaba5575. doi: 10.1126/sciadv.aba5575

64. Schouten M, Wolterink G, Dijkshoorn A, Kosmas D, Stramigioli S, Krijnen G. A review of extrusion-based 3d printing for the fabrication of electro-and biomechanical sensors. *IEEE Sens J*. 2020;21(11):12900-12912. doi: 10.1109/JSEN.2020.3042436

65. Saadi MASR, Maguire A, Pottackal NT, et al. Direct ink writing: A 3D printing technology for diverse materials. *Adv Mater*. 2022;34(28):2108855. doi: 10.1002/adma.201707495

66. Wei P, Leng H, Chen Q, Advincula RC, Pentzer EB. Reprocessable 3D-printed conductive elastomeric composite foams for strain and gas sensing. *ACS Appl Polym Mater*. 2019;1(4):885-892. doi: 10.1021/acsapm.9b00118

67. Huang K, Dong S, Yang J, et al. Three-dimensional printing of a tunable graphene-based elastomer for strain sensors with ultrahigh sensitivity. *Carbon*. 2019;143:63-72. doi: 10.1016/j.carbon.2018.11.008

68. Baker DV, Bao C, Kim WS. Highly conductive 3D printable materials for 3D structural electronics. *ACS Appl Electron Mater*. 2021;3(6):2423-2433. doi: 10.1021/acsaelm.1c00296

69. Neumann TV, Dickey MD. Liquid metal direct write and 3D printing: a review. *Adv Mater Technol*. 2020;5(9): 2000070. doi: 10.1002/admt.202000070

70. Tan HW, An J, Chua CK, Tran T. Metallic nanoparticle inks for 3D printing of electronics. *Adv Electronic Mater*. 2019;5(5):1800831. doi: 10.1002/aelm.201800831

71. Zou Z, Chen Y, Yuan S, Luo N, Li J, He Y. 3D printing of liquid metals: recent advancements and challenges. *Adv Funct Mater*. 2023;33(10):2213312. doi: 10.1002/adfm.202213312

72. Chen R. *Liquid Metal Based Flexible Pressure Sensor for Tactile Sensing of Robots*. IOP Publishing; 2021:052025. doi: 10.1088/1742-6596/1885/5/052025

73. Cook A, Parekh DP, Ladd C, et al. Shear-driven direct-write

printing of room-temperature gallium-based liquid metal alloys. *Adv Eng Mater*. 2019;21(11):1900400. doi: 10.1002/adem.201900400

74. Wu P, Fu J, Xu Y, He Y. Liquid metal microgels for three-dimensional printing of smart electronic clothes. *ACS Appl Mater Interfaces*. 2022;14(11):13458-13467. doi: 10.1021/acsami.1c22975

75. Kim S, Oh J, Jeong D, Bae J. Direct wiring of eutectic gallium–indium to a metal electrode for soft sensor systems. *ACS Appl Mater Interfaces*. 2019;11(22):20557-20565. doi: 10.1021/acsami.9b05363

76. Wang Y, Yu Z, Mao G, et al. Printable liquid-metal@ PDMS stretchable heater with high stretchability and dynamic stability for wearable thermotherapy. *Adv Mater Technol*. 2019;4(2):1800435. doi: 10.1002/admt.201800435

77. Oh J, Kim S, Lee S, Jeong S, Ko SH, Bae J. A liquid metal based multimodal sensor and haptic feedback device for thermal and tactile sensation generation in virtual reality. *Adv Funct Mater*. 2021;31(39):2007772. doi: 10.1002/adfm.202007772

78. Allen G, Bayles R, Gile W, Jesser W. Small particle melting of pure metals. *Thin Solid Films*. 1986;144(2):297-308. doi: 10.1016/0040-6090(86)90422-0

79. McNamara K, Tofail SA. Nanoparticles in biomedical applications. *Adv Phys: X*. 2017;2(1):54-88. doi: 10.1080/23746149.2016.1254570

80. Das S, Langbang L, Haque M, Belwal VK, Aguan K, Roy AS. Biocompatible silver nanoparticles: an investigation into their protein binding efficacies, anti-bacterial effects and cell cytotoxicity studies. *J Pharm Anal*. 2021;11(4):422-434. doi: 10.1016/j.jpha.2020.12.003

81. Rajendran G, Rajamuthuramalingam T, Jesse DMI, Kathiravan K. Synthesis and characterization of biocompatible acetaminophen stabilized gold nanoparticles. *Mater Res Express*. 2019;6(9):095043. doi: 10.1088/2053-1591/ab2e4d

82. Nejati K, Dadashpour M, Gharibi T, Mellatyar H, Akbarzadeh A. Biomedical applications of functionalized gold nanoparticles: a review. *J Clust Sci*. 2021;33:1-16. doi: 10.1007/s10876-020-01955-9

83. Madhavan R. Flexible and stretchable strain sensors fabricated by inkjet printing of silver nanowire-ecoflex composites. *J Mater Sci: Mater Electron*. 2022;33(7):3465-3484. doi: 10.1007/s10854-022-09087-8

84. Kong YL, Tamargo IA, Kim H, et al. 3D printed quantum dot light-emitting diodes. *Nano Lett*. 2014;14(12):7017-7023. doi: 10.1021/nl5033292

85. Rosati G, Ravarotto M, Scaramuzza M, De Toni A, Paccagnella A. Silver nanoparticles inkjet-printed flexible biosensor for rapid label-free antibiotic detection in milk. *Sens Actuators B: Chem*. 2019;280:280-289. doi: 10.1016/j.snb.2018.09.084

86. Agarwala S, Goh GL, Yap YL, et al. Development of bendable strain sensor with embedded microchannels using 3D printing. *Sens Actuators A: Phys*. 2017;263:593-599. doi: 10.1016/j.sna.2017.07.025

87. Kwon SN, Kim SW, Kim IG, Hong YK, Na SI. Direct 3D Printing of graphene nanoplatelet/silver nanoparticle-based nanocomposites for multiaxial piezoresistive sensor applications. *Adv Mater Technol*. 2019;4(2):1800500. doi: 10.1002/admt.201800500

88. Ali MA, Hu C, Jahan S, et al. Sensing of COVID-19 antibodies in seconds via aerosol jet nanoprinted reduced-graphene-oxide-coated 3D electrodes. *Adv Mater*. 2021;33(7):2006647. doi: 10.1002/adma.202006647

89. Zhu C, Han TY-J, Duoss EB, et al. Highly compressible 3D periodic graphene aerogel microlattices. *Nat Commun*. 2015;6(1):6962. doi: 10.1038/ncomms7962

90. Zhu D, Ren Y, Liao G, et al. Thermal and mechanical properties of polyamide 12/graphene nanoplatelets nanocomposites and parts fabricated by fused deposition modeling. *J Appl Polym Sci*. 2017;134(39):45332. doi: 10.1002/app.45332

91. Wang J, Liu Y, Fan Z, Wang W, Wang B, Guo Z. Ink-based 3D printing technologies for graphene-based materials: a review. *Adv Compos Hybrid Mater*. 2019;2:1-33. doi: 10.1007/s42114-018-0067-9

92. Thostenson ET, Li C, Chou T-W. Nanocomposites in context. *Compos Sci Technol*. 2005;65(3-4):491-516. doi: 10.1016/j.compscitech.2004.11.003

93. Balasubramanian K, Burghard M. Chemically functionalized carbon nanotubes. *Small*. 2005;1(2):180-192. doi: 10.1002/smll.200400118

94. Goh GL, Agarwala S, Yeong WY. Directed and on-demand alignment of carbon nanotube: a review toward 3D printing of electronics. *Adv Mater Interfaces*. 2019;6(4):1801318. doi: 10.1002/admi.201801318

95. Lee S-J, Wei Z, Nowicki M, et al. 3D printing nano conductive multi-walled carbon nanotube scaffolds for nerve regeneration. *J Neural Eng*. 2018;15(1):016018. doi: 10.1088/1741-2552/aa95a5

96. Jarosova R, Mcclure SE, Gajda M, et al. Inkjet-printed carbon nanotube electrodes for measuring pyocyanin and uric acid in a wound fluid simulant and culture media. *Anal Chem*. 2019;91(14):8835-8844. doi: 10.1021/acs.analchem.8b05591

97. Eng H, Maleksaeedi S, Yu S, et al. Development of CNTs-filled photopolymer for projection stereolithography. *Rapid Prototyping J*. 2017;23(1):129-136. doi: 10.1108/RPJ-10-2015-0148

98. Nadernezhad A, Unal S, Khani N, Koc B. Material extrusion-based additive manufacturing of structurally controlled poly (lactic acid)/carbon nanotube nanocomposites. *Int J Adv Manuf Technol*. 2019;102:2119-2132.

doi: 10.1007/s00170-018-03283-9

99. Belaid H, Nagarajan S, Teyssier C, et al. Development of new biocompatible 3D printed graphene oxide-based scaffolds. *Mater Sci Eng: C*. 2020;110:110595. doi: 10.1016/j.msec.2019.110595

100. eSilva EP, Huang B, Helaehil JV, et al. In vivo study of conductive 3D printed PCL/MWCNTs scaffolds with electrical stimulation for bone tissue engineering. *Bio-Des Manuf*. 2021;4(2):190-202. doi: 10.1007/s42242-020-00116-1

101. Ryan KR, Down MP, Hurst NJ, Keefe EM, Banks CE. Additive manufacturing (3D printing) of electrically conductive polymers and polymer nanocomposites and their applications. *eScience*. 2022;2(4):365–381. doi: 10.1016/j.esci.2022.07.003

102. Shi H, Liu C, Jiang Q, Xu J. Effective approaches to improve the electrical conductivity of PEDOT: PSS: a review. *Adv Electron Mater*. 2015;1(4):1500017. doi: 10.1002/aelm.201500017

103. Su R, Park SH, Ouyang X, Ahn SI, McAlpine MC. 3D-printed flexible organic light-emitting diode displays. *Sci Adv*. 2022;8(1):eabl8798. doi: 10.1126/sciadv.abl8798

104. Vuorinen T, Niittynen J, Kankkunen T, Kraft TM, Mäntysalo M. Inkjet-printed graphene/PEDOT: PSS temperature sensors on a skin-conformable polyurethane substrate. *Sci Rep*. 2016;6(1):35289. doi: 10.1038/srep35289

105. Yang J, Cao Q, Tang X, et al. 3D-printed highly stretchable conducting polymer electrodes for flexible supercapacitors. *J Mater Chem A*. 2021;9(35):19649-19658. doi: 10.1039/D1TA02617H

106. Shen Z, Zhang Z, Zhang N, et al. High-stretchability, ultralow-hysteresis conductingpolymer hydrogel strain sensors for soft machines. *Adv Mater*. 2022;34(32): 2203650. doi: 10.1002/adma.202203650

107. Molina-Lopez F, Gao T, Kraft U, et al. Inkjet-printed stretchable and low voltage synaptic transistor array. *Nat Commun*. 2019;10(1):2676. doi: 10.1038/s41467-019-10569-3

108. Soni M, Bhattacharjee M, Ntagios M, Dahiya R. Printed temperature sensor based on PEDOT: PSS-graphene oxide composite. *IEEE Sens J*. 2020;20(14):7525-7531. doi: 10.1109/JSEN.2020.2969667

109. Yuk H, Lu B, Lin S, et al. 3D printing of conducting polymers. *Nat Commun*. 2020;11(1):1604. doi: 10.1038/s41467-020-15316-7

110. Scordo G, Bertana V, Scaltrito L, et al. A novel highly electrically conductive composite resin for stereolithography. *Mater Today Commun*. 2019;19:12-17. doi: 10.1016/j.mtcomm.2018.12.017

111. Vijayavenkataraman S, Kannan S, Cao T, Fuh JY, Sriram G, Lu WF. 3D-printed PCL/PPy conductive scaffolds as three-dimensional porous nerve guide conduits (NGCs) for peripheral nerve injury repair. *Front Bioeng Biotechnol*. 2019;7:266. doi: 10.3389/fbioe.2019.00266

112. Qian J, Xiao R, Su F, Guo M, Liu D. 3D wet-spinning printing of wearable flexible electronic sensors of polypyrrole@ polyvinyl formate. *J Ind Eng Chem*. 2022;111:490-498. doi: 10.1016/j.jiec.2022.04.030

113. Ajdary R, Ezazi NZ, Correia A, et al. Multifunctional 3D-printed patches for long-term drug release therapies after myocardial infarction. *Adv Funct Mater*. 2020;30(34):2003440. doi: 10.1002/adfm.202003440

114. Distler T, Polley C, Shi F, et al. Electrically conductive and 3D-printable oxidized alginate-gelatin polypyrrole:PSS hydrogels for tissue engineering. *Adv Healthc Mater*. 2021;10(9):2001876. doi: 10.1002/adhm.202001876

115. Gu Y, Zhang Y, Shi Y, Zhang L, Xu X. 3D all printing of polypyrrole nanotubes for high mass loading flexible supercapacitor. *ChemistrySelect*. 2019;4(36):10902-10906. doi: 10.1002/slct.201902721

116. Li W, Liu J, Wei J, Yang Z, Ren C, Li B. Recent progress of conductive hydrogel fibers for flexible electronics: fabrications, applications, and perspectives. *Adv Funct Mater*. 2023;33(17):2213485. doi: 10.1002/adfm.202213485

117. Yuk H, Lu B, Zhao X. Hydrogel bioelectronics. *Chem Soc Rev*. 2019;48(6):1642-1667. doi: 10.1039/c8cs00595h

118. Kang M, Park J, Kim SA, et al. Modulus-tunable multifunctional hydrogel ink with nanofillers for 3D-Printed soft electronics. *Biosens Bioelectron*. 2024;255:116257. doi: 10.1016/j.bios.2024.116257

119. Zhou Y, Wan C, Yang Y, et al. Highly stretchable, elastic, and ionic conductive hydrogel for artificial soft electronics. *Adv Funct Mater*. 2019;29(1):1806220. doi: 10.1002/adfm.201806220

120. Zhou J, Yan H, Wang C, Gong H, Nie Q, Long Y. 3D printing highly stretchable conductors for flexible electronics with low signal hysteresis. *Virt Phys Prototyping*. 2022;17(1):19-32. doi: 10.1080/17452759.2021.1980283

121. Fantino E, Roppolo I, Zhang D, et al. 3D printing/interfacial polymerization coupling for the fabrication of conductive hydrogel. *Macromol Mater Eng*. 2018;303(4):1700356. doi: 10.1002/mame.201700356

122. Carcione R, Pescosolido F, Montaina L, et al. Self-standing 3D-printed PEGDA–PANIs electroconductive hydrogel composites for pH monitoring. *Gels*. 2023;9(10):784. doi: 10.3390/gels9100784

123. Distler T, Boccaccini AR. 3D printing of electrically conductive hydrogels for tissue engineering and biosensors–a review. *Acta Biomater*. 2020;101:1-13. doi: 10.1016/j.actbio.2019.08.044

124. Serafin A, Murphy C, Rubio MC, Collins MN. Printable alginate/gelatin hydrogel reinforced with carbon nanofibers as electrically conductive scaffolds for tissue engineering. *Mater Sci Eng: C*. 2021;122:111927. doi: 10.1016/j.msec.2021.111927

125. Liu J, Garcia J, Leahy LM, et al. 3D printing of multifunctional conductive polymer composite hydrogels. *Adv Funct Mater*. 2023;33(37):2214196. doi: 10.1002/adfm.202214196

126. Deng Z, Hu T, Lei Q, He J, Ma PX, Guo B. Stimuli-responsive conductive nanocomposite hydrogels with high stretchability, self-healing, adhesiveness, and 3D printability for human motion sensing. *ACS Appl Mater Interfaces*. 2019;11(7):6796-6808. doi: 10.1021/acsami.8b20178

127. Qiu K, Haghiashtiani G, McAlpine MC. 3D printed organ models for surgical applications. *Annu Rev Anal Chem (Palo Alto Calif)*. 2018;11(1):287-306. doi: 10.1146/annurev-anchem-061417-125935

128. Mitsouras D, Liacouras P, Imanzadeh A, et al. Medical 3D printing for the radiologist. *Radiographics*. 2015;35(7):1965-1988. doi: 10.1148/rg.2015140320

129. Qiu K, Zhao Z, Haghiashtiani G, et al. 3D printed organ models with physical properties of tissue and integrated sensors. *Adv Mater Technol*. 2018;3(3):1700235. doi: 10.1002/admt.201700235

130. Haghiashtiani G, Qiu K, Zhingre Sanchez JD, et al. 3D printed patient-specific aortic root models with internal sensors for minimally invasive applications. *Sci Adv*. 2020;6(35):eabb4641. doi: 10.1126/sciadv.abb4641

131. Said S, Boulkaibet I, Sheikh M, Karar AS, Alkork S, Nait-ali A. Machine-learning-based muscle control of a 3D-printed bionic arm. *Sensors*. 2020;20(11):3144. doi: 10.3390/s20113144

132. Corona-Castuera J, Rodriguez-Delgado D, Henao J, Castro-Sandoval JC, Poblano-Salas CA. Design and fabrication of a customized partial hip prosthesis employing CT-scan data and lattice porous structures. *ACS Omega*. 2021;6(10):6902-6913. doi: 10.1021/acsomega.0c06144

133. Sang S, Pei Z, Zhang F, et al. Three-dimensional printed bimodal electronic skin with high resolution and breathability for hair growth. *ACS Appl Mater Interfaces*. 2022;14(27):31493-31501. doi: 10.1021/acsami.2c09311

134. Gao H, An J, Chua CK, Bourell D, Kuo C-N, Tan DT. 3D printed optics and photonics: processes, materials and applications. *Mater Today*. 2023;69:107-132. doi: 10.1016/j.mattod.2023.06.019

135. Kong YL, Gupta MK, Johnson BN, McAlpine MC. 3D printed bionic nanodevices. *Nano Today*. 2016;11(3):330-350. doi: 10.1016/j.nantod.2016.04.007

136. Mannoor MS, Jiang Z, James T, et al. 3D printed bionic ears. *Nano Lett*. 2013;13(6):2634-2639. doi: 10.1021/nl4007744

137. Lu L, Zhang J, Xie Y, et al. Wearable health devices in health care: narrative systematic review. *JMIR mHealth uHealth*. 2020;8(11):e18907. doi: 10.2196/18907

138. Ho DH, Hong P, Han JT, et al. 3D-printed sugar scaffold for high-precision and highly sensitive active and passive wearable sensors. *Adv Sci*. 2020;7(1):1902521. doi: 10.1002/advs.201902521

139. Ouyang X, Su R, Ng DWH, Han G, Pearson DR, McAlpine MC. 3D printed skin-interfaced UV-visible hybrid photodetectors. *Adv Sci (Weinh)*. 2022;9(25):e2201275. doi: 10.1002/advs.202201275

140. Wang Z, Gao W, Zhang Q, et al. 3D-printed graphene/polydimethylsiloxane composites for stretchable and strain-insensitive temperature sensors. *ACS Appl Mater Interfaces*. 2019;11(1):1344-1352. doi: 10.1021/acsami.8b16139

141. Hou Y, Gao M, Gao J, et al. 3D printed conformal strain and humidity sensors for human motion prediction and health monitoring via machine learning. *Adv Sci (Weinh)*. 2023;10(36):e2304132. doi: 10.1002/advs.202304132

142. Zhu G, Dai H, Yao Y, et al. 3D printed skin-inspired flexible pressure sensor with gradient porous structure for tunable high sensitivity and wide linearity range. *Adv Mater Technol*. 2022;7(7):2101239. doi: 10.1002/admt.202101239

143. Herbert R, Lim H-R, Rigo B, Yeo W-H. Fully implantable wireless batteryless vascular electronics with printed soft sensors for multiplex sensing of hemodynamics. *Sci Adv*. 2022;8(19):eabm1175. doi: 10.1126/sciadv.abm1175

144. Chen C, Bai X, Ding Y, Lee I-S. Electrical stimulation as a novel tool for regulating cell behavior in tissue engineering. *Biomater Res*. 2019;23(1):1-12. doi: 10.1186/s40824-019-0176-8

145. Bedir T, Ulag S, Aydogan K, et al. Effect of electric stimulus on human adipose-derived mesenchymal stem cells cultured in 3D-printed scaffolds. *Polym Adv Technol*. 2021;32(3):1114-1125. doi: 10.1002/pat.5159

146. Lind JU, Busbee TA, Valentine AD, et al. Instrumented cardiac microphysiological devices via multimaterial three-dimensional printing. *Nat Mater*. 2017;16(3):303-308. doi: 10.1038/nmat4782

147. Wu Q, Zhang P, O'Leary G, et al. Flexible 3D printed microwires and 3D microelectrodes for heart-on-a-chip engineering. *Biofabrication*. 2023;15(3):035023. doi: 10.1088/1758-5090/acd8f4

148. Aimar A, Palermo A, Innocenti B. The role of 3D printing in medical applications: a state of the art. *J Healthc Eng*. 2019;2019:5340616. doi: 10.1155/2019/5340616

149. Yan Q, Dong H, Su J, et al. A review of 3D printing technology for medical applications. *Engineering*. 2018;4(5):729-742. doi: 10.1016/j.eng.2018.07.021

150. Ventola CL. Medical applications for 3D printing: current and projected uses. *P T*. 2014;39(10):704-711.

151. Jiang Y, Islam MN, He R, et al. Recent advances in 3D printed sensors: materials, design, and manufacturing. *Adv Mater Technol*. 2023;8(2):2200492. doi: 10.1002/admt.202200492

152. Jin J, Zhang F, Yang Y, et al. Hybrid multimaterial 3D printing using photocuring-while-dispensing. *Small*. 2023;19(50):2302405. doi: 10.1002/smll.202302405

153. Pless CJ, Nikzad S, Papiano I, et al. Soft electronic block copolymer elastomer composites for multi-material printing of stretchable physiological sensors on textiles. *Adv Electron Mater*. 2023;9(5):2201173. doi: 10.1002/aelm.202201173

154. Balakrishnan G, Song J, Mou C, Bettinger CJ. Recent progress in materials chemistry to advance flexible bioelectronics in medicine. *Adv Mater*. 2022;34(10):2106787. doi: 10.1002/adma.202106787

155. Pillai S, Upadhyay A, Sayson D, Nguyen BH, Tran SD. Advances in medical wearable biosensors: Design, fabrication and materials strategies in healthcare monitoring. *Molecules*. 2021;27(1):165. doi: 10.3390/molecules27010165

156. Chow L, Yick Kl, Wong KH, et al. 3D printing auxetic architectures for hypertrophic scar therapy. *Macromol Mater Eng*. 2022;307(5):2100866. doi: 10.1002/mame.202100866

157. Dong S, Hu H. Sensors based on auxetic materials and structures: a review. *Materials*. 2023;16(9):3603. doi: 10.3390/ma16093603

158. Ma C, Li G, Qin L, et al. Analytical model of micropyramidal capacitive pressure sensors and machine-learning-assisted design. *Adv Mater Technol*. 2021;6(12):2100634. doi: 10.1002/admt.202100634

ACCSCIENCE PUBLISHING

International Journal of Bioprinting

REVIEW ARTICLE

Extrusion bioprinting from a fluid mechanics perspective

Reza Gharraei[1], Donald J. Bergstrom[2], and Xiongbiao Chen[1,2]*

[1]Division of Biomedical Engineering, University of Saskatchewan, Saskatoon, Saskatchewan, Canada

[2]Department of Mechanical Engineering, University of Saskatchewan, Saskatoon, Saskatchewan, Canada

Abstract

Bioprinting is an emerging technology for fabricating intricate and diverse structures that closely mimic natural tissues and organs for applications, such as tissue engineering, drug delivery, and cancer research. Among the various bioprinting techniques, extrusion-based bioprinting stands out due to its capability to apply a wide range of biomaterials and living cells and its controllability over printed structures. In bioprinting, bioink stored in a syringe is extruded through a nozzle connected to the syringe and deposited onto the printing stage to form 3D structures. The bioprinting process involves the flow of bioink through the syringe and nozzle, then spreading on a printing stage. As a result, fluid mechanics plays a crucial role in extrusion bioprinting. Notably, the biomaterials used in bioprinting are typically non-Newtonian fluids, which have complex viscoelastic and thixotropic behaviors; the influence of these behaviors on the bioprinting process has garnered considerable attention, with various methods employed, including numerical simulations via computational fluid dynamics (CFD). This paper reviews the latest developments in the fluid mechanics of extrusion-based bioprinting to shed light on the challenges and key considerations involved. This review covers the topics of extrusion bioprinting (including driving mechanisms, printability, and cell viability), biomaterial rheology and its effect on bioprinting, multi-material bioprinting, and numerical simulations of bioprinting. Key issues and challenges are also discussed along with recommendations for future research.

Keywords: 3D bioprinting; Fluid Mechanics; Viscoelasticity; Tissue engineering

***Corresponding author:**
Xiongbiao Chen
(xbc719@mail.usask.ca)

Citation: Gharraei R, Bergstrom DJ, Chen X. Extrusion bioprinting from a fluid mechanics perspective. *Int J Bioprint*. 2024;10(6):3973. doi: 10.36922/ijb.3973

Received: June 18, 2024
Revised: August 9, 2024
Accepted: August 20, 2024
Published Online: August 30, 2024

Copyright: © 2024 Author(s). This is an Open Access article distributed under the terms of the Creative Commons Attribution License, permitting distribution, and reproduction in any medium, provided the original work is properly cited.

Publisher's Note: AccScience Publishing remains neutral with regard to jurisdictional claims in published maps and institutional affiliations.

1. Introduction

Biofabrication is an emerging technology aiming to address the lack of tissue/organ donors for transplantation in patients with severe injuries or diseases. Among various biofabrication techniques, three-dimensional (3D) bioprinting stands out for its ability to deposit cell-laden biomaterials (bioink) layer-by-layer to fabricate 3D constructs with spatial control over scaffold design,[1] enabling consistent production of patient-specific 3D scaffolds.[2,3] These scaffolds can be fabricated using the patient's native biological materials.[4–7]

Based on the working principle, 3D bioprinting techniques can be classified into extrusion bioprinting, inkjet printing, acoustic-droplet ejection, electrohydrodynamic (EHD) jetting, stereolithography, laser-induced forward transfer, and laser guidance direct writing.[8] Each of these techniques has its respective advantages and disadvantages. Among these, extrusion bioprinting is the most commonly used due to its high printing speed, scalability, and ability to print a wide range of bioink viscosities ($30–6 \times 10^7$ mPa·s).[9–12] Furthermore, extrusion bioprinting is a feasible method to fabricate scaffolds with high cell density and anatomical porosity, which is challenging for other bioprinting techniques.[13] However, extrusion bioprinting has its limitations, notably the difficulty in obtaining fiber diameters smaller than 100 μm. This fiber resolution is notably lower compared to those achievable by inkjet and laser-based printers, i.e., 50 and 5 μm, respectively.[8] As a result, extrusion bioprinting has limited accuracy in cell patterning and organization.[14]

Hydrogels are frequently employed as support materials in bioinks due to their advantageous properties for promoting cellular growth.[15–18] They share similarities with the extracellular matrix (ECM) in terms of high water content, porosity enabling nutrient and gas exchange, biocompatibility, and biodegradability, making them appealing for cell therapy applications.[19,20] Natural hydrogels, such as alginate, gelatin, agarose, chitosan, collagen, and hyaluronic acid, are commonly utilized in synthesizing bioinks.[21–24] Scaffolds biofabricated from natural hydrogels or synthetic bioinks are essential in tissue engineering, providing a favorable environment and physical support for cell function and interaction.[1] Besides, these scaffolds can also serve as delivery vehicles for growth factors to promote and regulate tissue growth.[25]

In the bioprinting process, constructs are typically formed through layer-by-layer deposition of bioink(s). To achieve 3D cell-laden scaffolds with good structural fidelity, the bioink should exhibit appropriate rheological behavior and rapid gelation characteristics. Besides, the bioprinting process should be benign to prevent the damage of cells during the printing process.[8] While hydrogels with high water content provide a suitable environment for cells, they also exhibit poor mechanical properties. This can be addressed by utilizing high-concentration hydrogels to improve shape fidelity in scaffold bioprinting; however, this may compromise the conditions for cell growth and viability.[26] In contrast, certain synthetic polymers offer favorable mechanical properties, but they often lack biocompatibility.[27] To enhance the mechanical stability of cell-laden constructs, researchers utilize both natural hydrogels and synthetic polymers, or composite polymers, for bioprinting. Hybrid scaffolds, printed from two or more biomaterials, synergistically enhance biological and mechanical properties.[28]

For extrusion bioprinting, bioinks should have the following properties: (i) the bioink should flow easily through the needle while also retaining its shape after extrusion, (ii) the printed filaments should exhibit and maintain good structural integrity and adhesion between the printed layers, and (iii) the bioink should support cell survival and function during and after the bioprinting process.[29,30]

Given that extrusion bioprinting relies on the flow of liquid bioinks before gelation on the printing stage, fluid mechanics is crucial for its success. It explains the process-induced forces on the cells, printability of bioinks, and instabilities that can affect the bioprinting process, as well as the mixing process in multi-material bioprinting techniques. Conversely, hydrogels and polymer melts reveal viscoelastic and thixotropic behaviors, making their fluid analysis more intricate. Despite the importance of fluid mechanics in the bioprinting process, many crucial aspects have not been discussed or documented in previous reviews on bioprinting. In this paper, we review the recent studies on the extrusion bioprinting process from the fluid mechanics viewpoint and discover how fluid mechanics can affect the outcomes of bioprinting. Dimensionless numbers are powerful, widely used tools in fluid mechanics for generalizing test results. They normalize length scales, time scales, velocities, or forces affecting a physical phenomenon, representing the geometrical, kinematic, and kinetic similarity of different flow conditions. As such, dimensionless parameters, including Reynolds, Weber, Weissenberg, Elasticity, and Péclet numbers, are used and presented in various sections, providing generalized criteria to assess the flow and mixing behavior during the bioprinting process.

2. Extrusion bioprinting

This section reviews and presents the fundamentals of extrusion bioprinting, including the extrusion driving mechanism, printability, cell viability, and bioink rheology.

2.1. Driving mechanisms for extrusion

An extrusion bioprinter typically comprises a computer-controlled printing head and a positioning system. During the printing process, the printing head is controlled to move in three directions, while the bioink, stored in a syringe that is attached to the printing head, is extruded out of a tip or needle, depositing on the printing stage to form a 3D structure. The extrusion of bioink requires energy transfer or mechanical forces, often achieved using a pneumatic system with compressed gas (e.g., air or

nitrogen) or a mechanical system with a piston or screw to drive the liquid biomaterial.

While pneumatic-driven systems are widely used in most commercial bioprinters because of their simplicity, they possess a main drawback caused by gas compressibility. As a result, pneumatic-driven systems lack accurate control over the start and stop in extrusion or printing. This can be offset by using a valve-based pneumatic system that facilitates high-precision extrusion by controlled pressure and pulse frequency.[31,32] Additionally, the pneumatic-driven system is not suitable for printing highly viscous bioinks, which requires high pressures and may lead to related issues.[33]

The piston- and screw-driven systems are more accurate in extrusion or printing as the linear displacement of the piston or rotation of the screw can be accurately controlled compared to the gas pressure in the pneumatic-driven system.[34] Moreover, both piston- and screw-driven systems are good for printing high-viscosity bioinks,[35] though it has been reported that the screw-driven system generally induces more cell damage compared to the pneumatic-driven system.[36]

2.2. Printability

During the extrusion bioprinting process, each layer is stacked on top of the previous one to construct a 3D scaffold. To ensure the stability of the printed construct, the filaments need to solidify after being deposited on the printing stage. This solidification process is achieved through a crosslinking process, which can be either physical or chemical.[36] However, the time required for crosslinking can pose challenges. During gelation, the bioink (in liquid form) may flow and spread on the printing stage, causing deformations and deviations from the intended geometry. This deviation from the designed structure is characterized by printability. In some cases, the flow of the deposited bioink can even lead to the collapse of the entire structure, rendering it unprintable.[36] Printability significantly affects the mechanical and biological properties of the printed construct, such as its mechanical strength and cellular functionality.[6–8] To evaluate printability, it is common to analyze the differences between the printed construct and the intended design, considering factors such as filament diameter and pore size.[37] These evaluations can be qualitative, relying on visual observations, or quantitative, involving the use of numerical indices.[37] There are various definitions of printability in the literature,[38,39] each considering printability from different perspectives to explain the ability to print a 3D construct that closely matches the one designed in computer-aided design (CAD) software. In this review, we adopt the definition of printability as the capability to create and uphold the 3D form of an intended structure[38]; this is characterized by factors such as extrudability, filament fidelity, and structural integrity. Printability depends on various parameters, including the viscosity and surface tension of the bioink, the crosslinking time, as well as the surface properties of the printing stage and printer nozzle.[36,39] Table 1 presents the printability criteria, the factors characterizing them, and how they affect printing outcomes. Regarding the extrudability, there are four typical cases for the extrusion of bioinks (Figure 1): (i) unextrudable, (ii) discontinuous (dripping), (iii) continuous but uncontrollable (with gobbling drop[52,53]), and (iv) continuous and controllable (jetting).[38] These cases can be recognized by comparing the effective forces on the flow of bioink. To successfully extrude bioink from the nozzle, the inertial force (characterizing the acceleration of the fluid) should dominate the capillary force from the surface tension of the bioink that tends to keep it attached to the nozzle.

The entire extrusion bioprinting process occurs within the laminar flow regime, characterized by low Reynolds number (*Re*). Reynolds number is a dimensionless quantity that compares inertial and viscous forces in the flow. For the flow of a Newtonian fluid inside a needle, *Re* is defined as[54]:

$$Re = \frac{\rho \bar{U} d}{\eta} \quad \text{(I)}$$

where ρ and η represent the density and dynamic viscosity of the fluid, respectively, d is the diameter of the needle, and $\bar{U}$ the average velocity of the flow inside the needle. Due to the relatively high viscosity, the small size of the dispensing needle, and the slow velocity of the bioink during the extrusion, extrusion bioprinting typically exhibits extremely low *Re*. This results in a special laminar flow regime known as creeping flow, characterized by the dominance of viscous forces,[54] facilitating the smooth deposition of filaments. Another important parameter in extrusion bioprinting is the Weber number, which is the ratio of inertial to capillary forces, presented as[54]:

$$We = \frac{\rho \bar{U}^2 Ri}{\zeta} \quad \text{(II)}$$

where ρ is bioink density, R_i is the internal radius of the nozzle, and ζ denotes the surface tension of the bioink. For a given nozzle radius and bioink properties, the Weber number is determined by the flow rate, which depends on the dispensing force applied by the driving mechanism to the bioink.

Table 1. Printability criteria

Criterion	Definition	Assessment method	Affecting parameters	Effect on printing results	Ref.
Extrudability	Ability of a bioink to be extruded through a nozzle continuously and controllably to form a fiber	(i) Visual inspection of fiber issuing the nozzle; (ii) analysis based on Weber number	(i) Printing pressure; (ii) surface tension of bioink; (iii) apparent viscosity of bioink; (iv) loss tangent of bioink	Continuity and smoothness of fiber	[38,40,41,42,43]
Filament fidelity	Deformation of the deposited filament as it bridges over previously printed filaments in the lower layer, with limited sagging or filling of the pores	(i) Analyzing the uniformity of the cross-section; (ii) determining the ratio of the printed filament's width or height to the theoretical diameter; (iii) examining the pore size within a layer; (iv) filament collapse test by extruding the filament over a series of pillars with progressively increasing spacing	(i) Surface tension of bioink; (ii) yield stress of bioink; (iii) storage modulus and loss tangent of bioink; (iv) elastic modulus of the printed filament after crosslinking	Altering the cross-sectional profile of the filament across different layers and locations of the printed scaffold	[44, 45–49]
Structural integrity	Capability of a printed 3D construct to maintain its shape and dimensions similar to the original design after printing	(i) Thickness of individual layers; (ii) height of the whole construct; (iii) size of pores in the vertical direction	(i) Surface tension of bioink; (ii) wettability of bioink; (iii) viscosity recovery rate of bioink; (iv) loss tangent of bioink	(i) Fusion of printed filaments at their intersections; (ii) deformation and overhang on the filaments of the lower layer	[36,38, 50,44,51]

Notably, Case A in Figure 1 corresponds to $We = 0$; the bioink does not flow out of the nozzle and is unextrudable due to either its high viscosity or clogging caused by large cells or aggregates. Increasing the dispensing force can improve extrudability, but it may result in a fractured filament morphology and even nozzle breakage. At an extremely low flow rate, $We << 1$, characterizing the dripping regime, drops of liquid periodically detach from the nozzle. This flow regime is not suitable for extrusion bioprinting as it fails to deposit a continuous filament of bioink. At $We < 1$, there is a limited continuous stream of bioink extruding from the nozzle, terminated by a terminal droplet detaching from its end in a periodic or chaotic manner. For a viscoelastic liquid, the terminal drop reaches a size larger than the nozzle diameter by "gobbling" a chain of smaller drops upstream. This flow pattern, characterized by the gobbling phenomenon, persists up to *We* of ~1.[55] The flow with gobbling drop is not suitable for bioprinting because the diameter of the liquid stream is variable and uncontrollable. At a higher flow rate, i.e., $We >1$, the droplets' detachment point abruptly shifts downstream from the nozzle exit (typically farther than $20Ri$[52,53]), resulting in the formation of a continuous jet controllable by the dispensing force and suitable for bioprinting applications. Cases C and D in Figure 1 are more associated with the viscoelastic or dynamic behavior of a bioink, as experimentally observed on the viscoelastic fluid stream (0.01 wt% polyacrylamide aqueous solution).[52]

Figure 2 illustrates the behavior of the fluid stream at various *We*, recorded using a high-speed camera. The sequential images presented in Figure 2A and B illustrate the dynamic behavior of the liquid stream at 5 ms intervals. The gobbling phenomenon is obvious for $We < 1$ and We ~1. For $We < 1$ (Figure 2A), the detachment point of the gobbling drop fluctuates periodically. Increasing the flow rate changes the dynamic of the gobbling drop, and at We ~1 (Figure 2B), the gobbling drop remains almost stationary near the detachment point.[55] Figure 2A and B both correspond to Figure 1C. Although the small spacing between the dispensing nozzle and printing stage can alter the dynamic of the dripping and gobbling flow, the discontinuous and uncontrollable nature of these regimes prevents smooth filament deposition, rendering them unsuitable for bioprinting. Figure 2C displays the jetting regime characterized with $We < 1$, corresponding to Figure 1D. While jet flow with We > 1 will break up

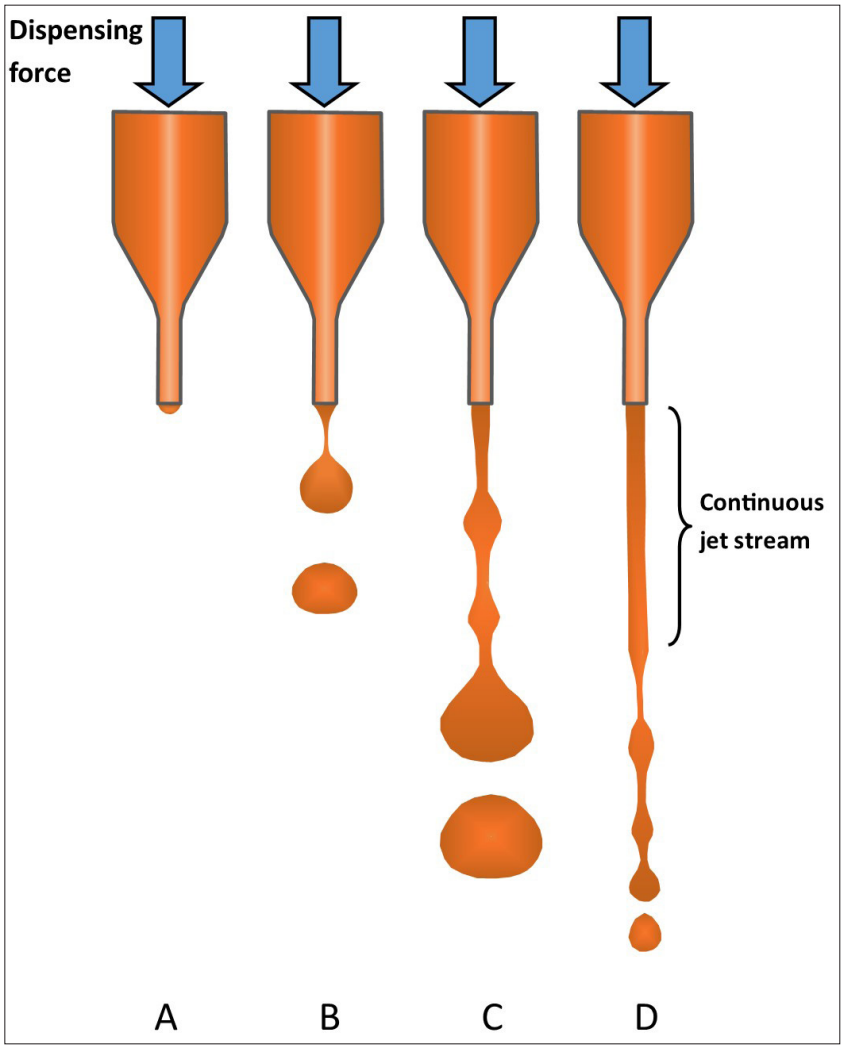

Figure 1. Filament extrudability: (A) unextrudable ($We \approx 0$), (B) discontinuous ($We \ll 1$) , (C) continuous yet uncontrollable ($We \lesssim 1$), and (D) continuous and controllable ($We > 1$). Abbreviation: *We*, Weber number. The figure is prepared by authors using Microsoft Publisher.

due to Rayleigh-Plateau capillary instability[56–58] far from the nozzle (>20 *Ri*), this process does not disrupt the deposition of bioink in bioprinting, as the nozzle-stage spacing is about 2*Ri*. The aforementioned flow regimes based on *We* can also occur due to a change in nozzle size. Considering mass conservation, for a given flow rate of bioink, an increase in nozzle diameter will decrease *We*.

The printability of a bioink is heavily influenced by its surface tension and wettability. These properties play a critical role in the formation of filaments during the printing process. On one hand, a high surface tension leads to smaller *We* at a given flow rate, causing poor extrudability with dripping extrusion or even failing to extrude.[40,41] In contrast, surface tension helps deposited filaments maintain their shape and their cross-sectional profile.[59] The wettability of a bioink, as measured by its contact angle with a solid surface, governs the contact of the first layer of the construct with the printing stage. A large contact angle improves the fidelity of the construct; conversely, a smaller contact angle helps secure the printed construct to the printing stage, preventing undesired deformations and movements during the printing process, ultimately enhancing the structural integrity.[36] Moreover, ensuring sufficient wettability between the bioink and the nozzle can prevent problems, such as leaking, flooding, or wetting the exterior surface of the nozzle tip, as the bioink is extruded from the nozzle.[40]

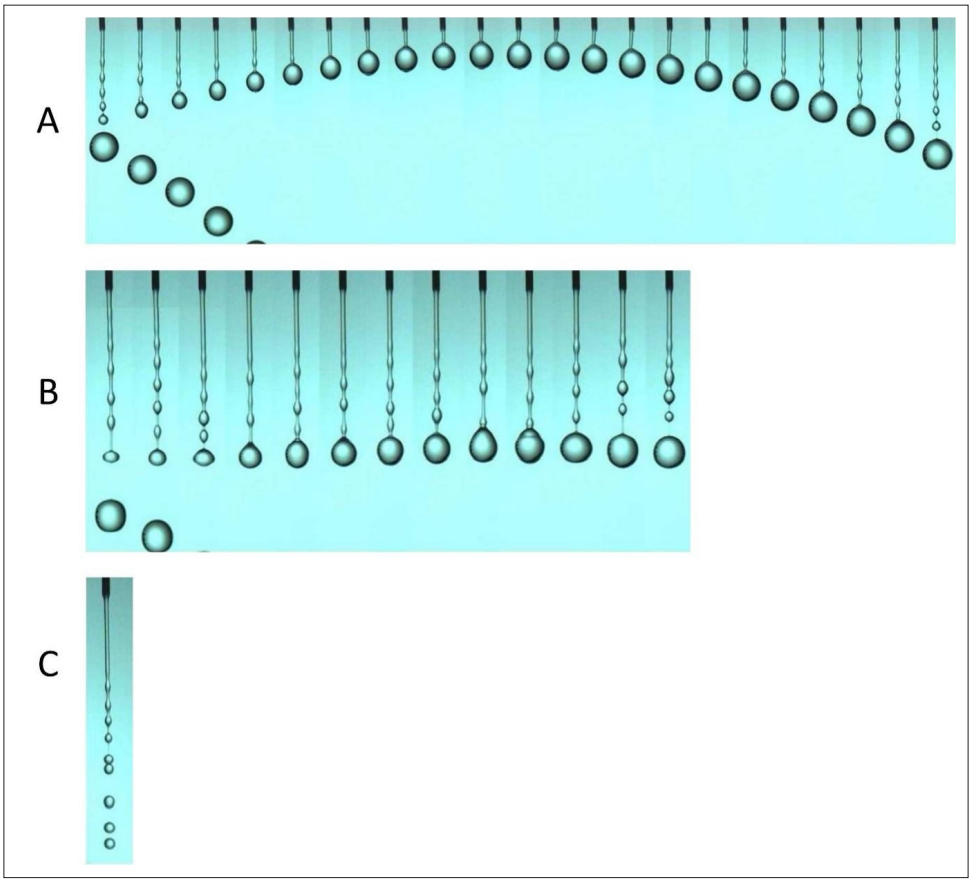

Figure 2. Different flow regimes for a fluid issuing from a nozzle with (A) $We < 1$, (B) $We \approx 1$, and (C) $We > 1$, where the interval between consecutive frames at (A) and (B) is Δt = 5 ms. Abbreviations: *We*, Weber number; Δ*t*: time interval between consecutive images. Adapted with permission from ref.[52] Copyright © 2009 Cambridge University Press.

The velocity of a filament at the outlet of the nozzle is controlled by the extrusion pressure or the piston/screw linear/angular velocity. The difference between the filament velocity (U_s) and printing head horizontal-moving speed (U_p) affects the diameter of the printed filament. Theoretically, if these velocities are equal, the diameter of the filament will be the same as that of the nozzle. If $U_p > U_s$, the filament will be stretched during printing, resulting in thinner or even discontinuous filament deposition. When $U_p < U_s$, a thicker filament and material bulge are formed at the front edge of the needle.[36]

2.3 Cell viability in extrusion bioprinting

Printing of a cell-laden fiber involves the transmission of thermal and mechanical energy from the printing head to the bioink, which can influence the cell phenotype and viability (e.g., by interacting with DNA), damage cell membrane, or alter the osmotic equilibrium between cells and the environment.[60] The primary damage to cells occurs due to the force or stresses induced within the flowing solution, leading to deformations in the cell membrane and further impacting cell viability and stability after printing.[36,61,62]

A study[34] on cell viability in pneumatic and screw-driven bioprinting processes indicate that despite the higher accuracy of screw-driven bioprinting, it can result in a higher percentage of cell damage in comparison with pneumatic bioprinting. Nevertheless, stresses inside the nozzle play a primary role in the survivability and viability of cells during the extrusion printing process. These stresses originate from the velocity gradients in the bioink flowing through the nozzle that deform the cells. The extent of cell injury depends on the magnitude and duration of the applied stresses.[63] Typically, cells can endure stresses to a certain extent through adaptation mechanisms; nonetheless, if the stresses exceed the cell's capacity to withstand them, irreversible damage can occur, resulting in cell death.[64,65] High shear stress is one of the most detrimental factors that reduces cell viability

and survivability. Several factors affect cell survival and viability in extrusion printing, including the viscosity of the bioink, the pressure used to extrude the bioink, the size of the nozzle, and the printing speed.[1,64] In addition to shear stress, cells also experience extensional stress during the bioprinting process, which plays a crucial role in determining their overall viability.[63,66,67] Extensional stress arises due to the abrupt change in velocity experienced by the cell suspension as it passes through the contractive region of the needle (Figure 3). Compared to shear stress, extensional stress can cause more severe damage to cells.[63] Therefore, it is important to examine both shear and extensional stresses when studying the relationship between cell damage and the bioprinting process.[63,68,69]

Figure 3 illustrates the stresses exerted on cells and cell deformation as they enter and then pass through the needle of a chamfered nozzle. Given the parallel flow inside the cylindrical needle (i.e., the Poiseuille flow[70]), the shear stress inside the needle can be calculated by

$$\tau_s = \left(\frac{r}{2}\right)\left(\frac{\Delta P}{L}\right) \quad \text{(III)}$$

where ΔP is the pressure drop in the needle, and r and L are the radius and length of the needle, respectively. Cogswell[71] proposed a relation to calculate the average extensional stress α magnitude $\bar{\tau}_e$ based on the pressure drop ΔP_{en} at the nozzle entrance region,

$$\bar{\tau}_e = \frac{3}{8}(n+1)\Delta P_{en} \quad \text{(IV)}$$

where n is the power-law index of the fluid. While the analysis[72] indicates that Cogswell's relation[71] is not accurate for high nozzle convergence angles, it has been widely used for estimating the extensional stress due to its simplicity. The most accurate method for calculating extensional stress involves measuring the extensional viscosity **(Section 3.3.3)**.

A previous study[63] used the Cogswell relation for extensional stress to formulate their empirical cell damage law as follows:

$$\mathcal{D}_t = \mathcal{D}_e + (1 - \mathcal{D}_e)\mathcal{D}_s \quad \text{(V)}$$

where D_t denotes total damaged cell ratio (DCR), with D_e and D_s representing DCR values originating from extensional and shear stresses, respectively[63]:

$$\mathcal{D}_s = 1 - \exp(-a_1 \tau_s^{b_1} t_s^{c_1}) \quad \text{(VI)}$$

$$\mathcal{D}_e = 1 - \exp(-a_2 \bar{\tau}_e^{b_2}) \quad \text{(VII)}$$

where $\bar{\tau}_s$ is the magnitude of shear stress at the dispensing needle with an exposure time of t_s, and $\bar{\tau}_e$ represents the average extensional stress. The model parameters of a, b, and c for Schwann (RSC96) and myoblast (L8) cell lines, as identified,[66] are listed in Table 2**.** Cells are exposed to extensional stresses as they pass through the contraction region of the nozzle at the needle entrance within a relatively short time compared to their exposure time to shear stresses. Therefore, exposure time is not included in the cell damage law for extensional stress effects.

By focusing on shear stress as the main cause of cell damage (in comparison with compressive stresses), a cell damage law based on one independent variable, i.e., pressure work (W_p), was developed:[73]

$$\mathcal{D}_t = \mathcal{D}_{max} + (\mathcal{D}_{max} - \mathcal{D}_0)\exp(-a_p W_p) \quad \text{(VIII)}$$

Pressure work is a combined index to indicate the accumulated energy of the flow pressure as bioink passes through the needle.[73]

$$W_p = \frac{1}{2}\Delta P_n A L \quad \text{(IX)}$$

where A denotes the dispensing nozzle cross-sectional area, and ΔP_n is the total pressure drop in the nozzle with a total length of L (Figure 3); $\mathcal{D}_{max}$ and $\mathcal{D}_0$ are reference measures as maximum DCR and DCR value at the needle entrance (the contraction region); a_p is the parameter that governs the cell sensitivity to pressure. While the cell damage model of Han et al.[73] has not considered extensional stress as an effective factor, its results are validated in a wide range of bioprinting conditions.

While various studies have demonstrated that cell damage increases with the printing pressure for a given needle diameter,[63,73,75] the influence of needle diameter on cell damage varies, presenting two different scenarios. For a given printing pressure, Han et al.[73] and Ning et al.[63] revealed an increase in cell damage with the needle diameter (Scenario 1). In contrast, Li et al.[75] reported a decrease in cell damage with needle diameter (Scenario 2). Chirianni et al.[74] proposed a generalized version of the cell damage model Han et al.[73] that can predict both scenarios by defining equivalent pressure work based on the equivalent nozzle area. They also added the effect of extensional stresses to the cell damage model by replacing the constant $\mathcal{D}_0$ with a non-constant term, describing the cell damage at the entrance of the needle where the cells are exposed to extensional stresses.[74]

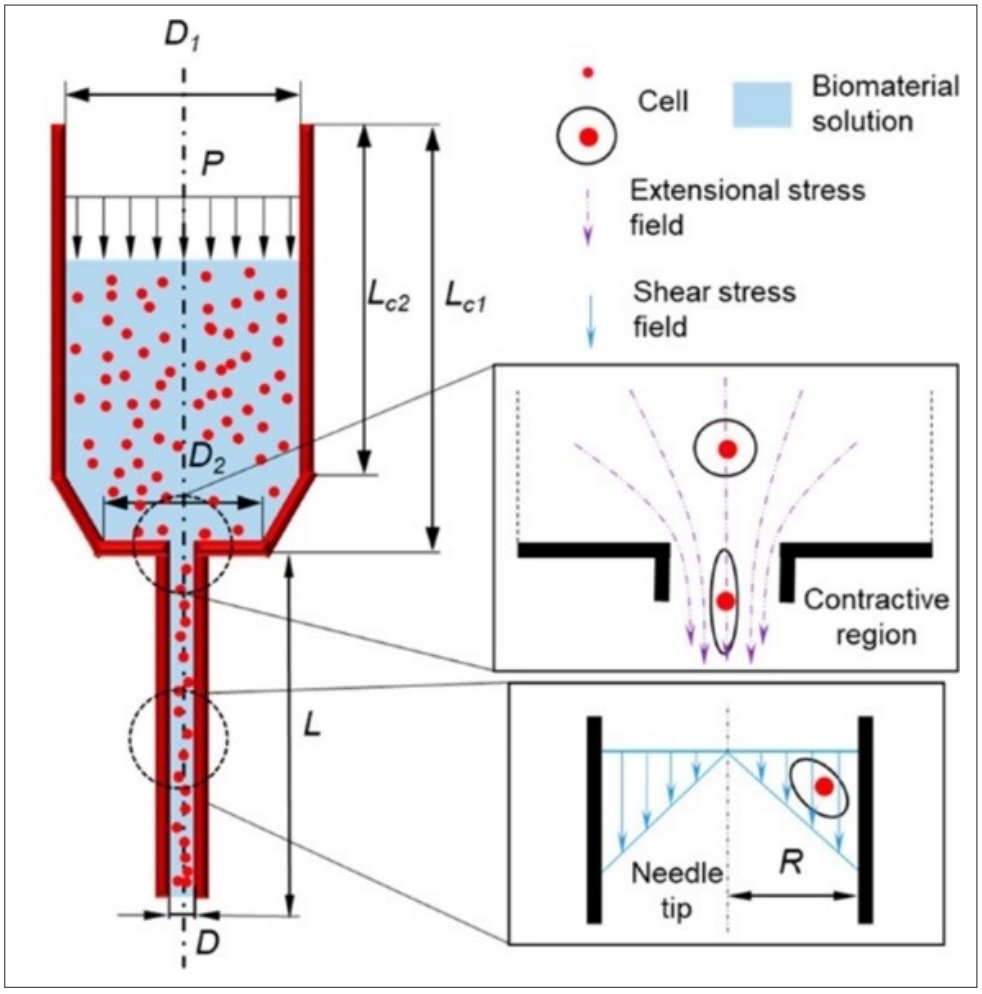

Figure 3. Schematic of cell deformation during the bioink flow through a chamfered nozzle and distribution of stresses. Adapted with permission from ref.[63] Copyright © 2018 American Chemical Society.

$$\mathcal{D}_t = \mathcal{D}_{max} - \{\mathcal{D}_{max} - \mathcal{D}_{e,max}[1-\exp(-a_e \tau_e^{b_e})]\}\exp(-a_p W_p^{eq}) \quad \text{(X)}$$

Chirianni et al.[74] defined W_p^{eq} as a generalized form of pressure work[74]:

$$W_p^{eq} = \frac{1}{2}\Delta P_n A_{eq} L \quad \text{(XI)}$$

where A_{eq} is the equivalent nozzle cross-section area. Chirianni et al.[74] described the different behavior of cell damage in Scenarios 1 and 2 based on uneven cell distribution in the nozzle cross-section. They defined equivalent area A_{eq} as[74]

$$A_{eq} = \begin{cases} A\exp(-k_1 A) & \\ A_{eq,0} + \left(A_{eq,\infty} - A_{eq,0}\right) & \\ \left[1 - exp\left(-k_2\left(A - A_0\right)\right)\right] & \end{cases} \quad \begin{matrix} \\ if\ 0 < A < A_0 \\ if\ A > A_0 \end{matrix} \quad \text{(XII)}$$

which identifies a portion of the nozzle cross-section area that is affected by cell distribution. Here, $A_0 > 0$, $A_{eq,\infty} > 0$, $k_1 \geq 0$, and $k_2 \geq 0$ are model parameters, and $A_{eq,0} = A_0 \exp(-k_2 A_0)$. Figure 4A demonstrates how these parameters affect A_{eq}, allowing for various relationships between nozzle cross-section and its equivalent area A_{eq} to reproduce a variety of outcomes from previous experimental tests on cell damage during extrusion bioprinting. Chirianni et al.[74] validated their cell

Table 2. Values of various cell damage models' parameters

Model contributors	Bioink	Cell damage model parameters		Value
Ning et al. [63]	Alginate/RSC96; Alginate/L8	Alginate/RSC96	a_1	3.9×10^{-4}
			b_1	0.48
			c_1	0.71
			a_2	-9.43×10^{-4}
			b_2	0.61
		Alginate/L8	a_1	-3.2×10^{-4}
			b_1	0.61
			c_1	0.52
			a_2	-1.43×10^{-3}
			b_2	0.55
Han et al.[73]	Alginate/human- dermal fibroblasts CCD-986sk	Alginate 2%/ CCD-986sk	$\mathcal{D}_0$	0.0693
			$\mathcal{D}_\infty$	0.4262
			ε_d	0.0419
		Alginate 3%/ CCD-986sk	$\mathcal{D}_0$	0.0828
			$\mathcal{D}_\infty$	0.3614
			ε_d	0.0283
		Alginate 4%/ CCD-986sk	$\mathcal{D}_0$	0.0861
			$\mathcal{D}_\infty$	0.3063
			ε_d	0.0257
Chirianni et al.[74]	-	DCR data from Han et al.[73] and Li et al.[75]	A_0	0.50
			$A_{eq,\infty}$	0.70
			k_1	0
			k_2	4
			a_p	0.0281
			a_e	0.4977
			e	0.1428
			$\mathcal{D}_{e,max}$	0.2795
			$\mathcal{D}_{max}$	0.4358

Abbreviation: DCR, damaged cell ratio

damage model based on the cell damage results of Han et al.[73] and Li et al.[75] (Figure 4B and C).

Considering the role of the nozzle in subjecting the cells to shear and extensional stresses, its design is among the most significant factors directly impacting cell viability. Enhancing nozzle design and minimizing the forces exerted on the bioink, in conjunction with controlling the concentration of the bioink, can greatly reduce stresses and cell injuries.[76] It should be noted that when bioprinting with cells, it is crucial to reduce or minimize the process-induced forces or stresses on the cells.[73,74] To achieve this, a straightforward method is to employ lower extrusion pressures, as elevated pressure increases shear stress within the nozzle flow, thus possibly damaging the cell membrane and reducing cell viability.

3. Bioink rheology and its effect on bioprinting outcomes

During the extrusion process, bioink flows through the syringe and the dispensing nozzle before being deposited on the printing stage. The rheology of bioink is the main factor that governs the behavior of bioink during the extrusion, thus affecting printability and cell viability to a great extent. In rheology, the flow behavior of a fluid represents the relationship between the fluid flow (or strain rate) and the stress within the fluid and can generally divided into Newtonian and non-Newtonian fluids. Figure 5 illustrates the stresses applied on an imaginary 3D element of fluid in flow, representing the stress ($\overline{\overline{\tau}}$) and strain rate ($\overline{\overline{\gamma}}$) tensors for that element. Rheological models are

mathematical equations that relate the stress and deformation tensors of the fluid. The normal components of stress are defined as[70]:

$$\begin{aligned}\sigma_{xx} &= p + \tau_{xx} \\ \sigma_{yy} &= p + \tau_{yy} \\ \sigma_{zz} &= p + \tau_{zz}\end{aligned} \quad \text{(XIII)}$$

where p is the isotropic pressure. The components τ_{xx}, τ_{yy}, and τ_{zz} are known as the deviatoric normal stresses for Newtonian fluids,[77] representing the contributions of the flow to the normal stresses on fluid elements. For an incompressible Newtonian fluid, the isotropic pressure is the average of normal stresses, and the deviatoric normal stresses are identically equal to zero.[70,78]

Newtonian fluids display a linear relationship between the stress and strain rate tensors, expressed by Newton's law of viscosity[70]:

$$\bar{\bar{\tau}} = \eta \bar{\bar{\dot{\gamma}}} \quad \text{(XIV)}$$

where η is the dynamic viscosity of the fluid. In contrast, non-Newtonian fluids cover a wide range of fluids with a non-linear relationship between their stress and strain rate.

For non-Newtonian fluid flow, the normal stress components τ_{xx}, τ_{yy}, and τ_{zz} are known as extra stresses, and they may take non-zero values (contrary to Newtonian fluid).[77] Non-Newtonian fluid can be divided into three sub-classes,[77] i.e., time-independent, time-dependent, and viscoelastic fluids. Figure 6 illustrates the characteristic behaviors of these sub-classes.

Generally, bioinks exhibit a combination of features from all three non-Newtonian sub-classes.[36] There are many studies on the rheology of bioinks that demonstrate the viscoelastic behavior of bioinks.[36,79] To understand the complex behavior of viscoelastic fluids, various rheological tests are employed to gain information on flow behavior, which can be used to predict printability and cell viability in the bioprinting process.

3.1. Time-independent flow behavior

For time-independent fluids, the instantaneous strain at each point is determined by the stress value at that moment and location. The time-independent flow behavior of a fluid can be evaluated using a steady shear test with a rotational rheometer, employing cone plates, parallel plates, or concentric cylinders (bob-cup). In this test, the shear rate is gradually increased/decreased while recording the corresponding shear stress, resulting in a flow curve that displays the variation of shear stress with strain rate (Figure 6A).

Generalizing **Equation V**, the apparent viscosity (η_{app}) can be defined as[70]

$$\eta_{app} = \frac{\bar{\bar{\tau}}}{\bar{\bar{\dot{\gamma}}}} \quad \text{(XV)}$$

By replacing the dynamic viscosity (η) with apparent viscosity (η_{app}), **Equation V** can describe the flow behavior of time-independent non-Newtonian fluids. For an isothermal flow, wherein Newtonian fluids maintain a constant η_{app}, non-Newtonian fluids exhibit η_{app} as a function of strain rate tensor magnitude and other parameters that characterize the rheological behavior of the fluid. Considering the process forces during extrusion, the shear stress level is low at the syringe barrel, increased to a maximum at the dispensing nozzle, and then decreases to very low levels as the filament is deposited on the stage. A shear-thinning bioink, whose apparent viscosity decreases with shear stress, provides favorable behavior for extrusion bioprinting, as it requires a lower driving force for extrusion and exerts lower stress on cells. After fiber deposition on the stage, the low shear stress increases the viscosity of the bioink, improving shape fidelity and printability. In contrast, a shear-thickening fluid, with viscosity that increases with shear stress, is not suitable for extrusion as its viscosity increases inside the nozzle, which compromises cell viability, and decreases after deposition, reducing shape fidelity.

There are various mathematical models to represent the flow behavior of a time-independent non-Newtonian fluid. Among these models, the power-law,[80,81] Carreau,[82] Carreau-Yasuda,[83] Cross,[84] and Herschel–Bulkley[85] models are more compatible with the flow behavior of biomaterials. Table 3 illustrates the mathematical equations and parameters governing these models.

The Herschel–Bulkley model describes the flow behavior of yield-pseudoplastic fluids characterized by the presence of a yield stress (τ_0), which must be exceeded for the fluid to deform or flow. If the externally applied stress is lower than the yield stress, the material will exhibit elastic deformation.

The determination of the yield stress typically involves conducting steady shear tests at low shear rates. The data obtained from these experiments are then utilized to extrapolate and predict the yield stress when the shear rate approaches zero.[36,77] An alternative approach to measuring the yield stress is to use vane geometries with rotational rheometers. The vane geometry enables the measurement of shear stress corresponding to the onset of flow under specified test conditions, typically within the time scale of the measurement.[77]

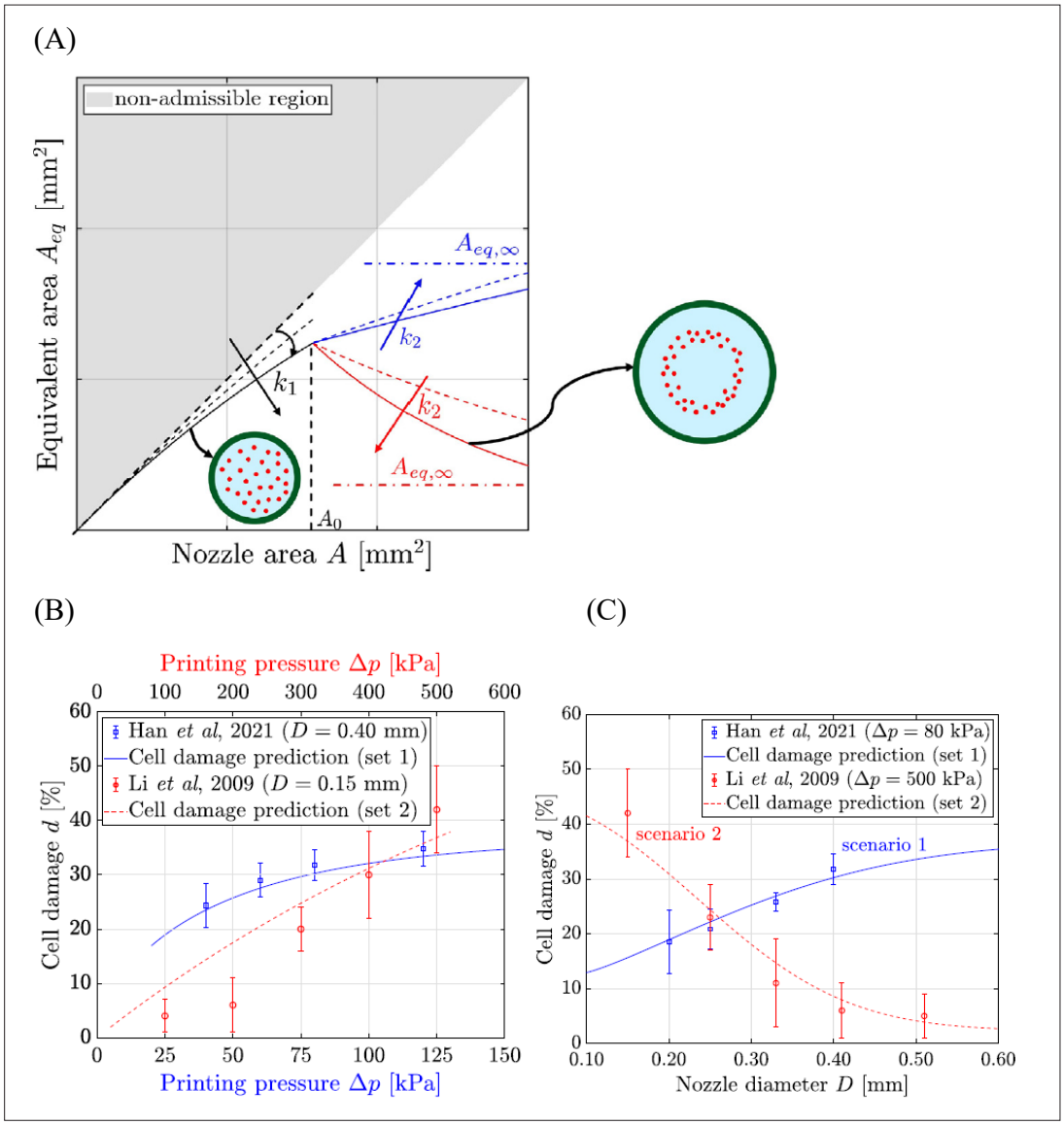

Figure 4. Parameters and outcomes of Chirianni et al.[74] model for cell damage prediction. (A) Equivalent area (A_{eq}) versus nozzle cross-sectional area (A). Qualitative description of the model parameters effect on cell distribution and A_{eq} in **Equation XII**. (B and C) Comparison of cell damage prediction by Chirianni et al.[74] using the model (or Equation X) and the experimental results reported by Han et al.[73] (Scenario 1) and Li et al.[75] (Scenario 2) for (B) printing with a given nozzle diameter and various printing pressures, and (C) given printing pressure and various nozzle diameter. Reprinted with permission from ref.[74], Copyright© (2024) Elsevier.

Herschel–Bulkley fluids are suitable for extrusion bioprinting because their viscosity changes favorably, enhancing cell viability and printability. Additionally, their yield stress prevents dripping from the nozzle, improving shape fidelity after printing. If shear stress is lower than the yield value, there is no movement in the fluid, thus preventing drips in bioprinting. Another benefit of utilizing fluids with yield stress as bioinks is the formation of a plug flow region within the central area of the dispensing needle. In this region, shear stress is reduced to zero, allowing cells to be transported without experiencing shear stress.[86] When cells are incorporated into the bioink, the yield stress helps maintain the uniform distribution of the encapsulated cells, promoting homogeneity,[87] Bioinks with low yield stress are susceptible to issues like cell settling or phase separation. Conversely, high-yield stress can potentially have adverse effects on cells when the flow is initiated.[88,89]

While power-law, Carreau, or Cross fluids are not classified as yield fluids, their high limiting zero-shear viscosity resembles yield behavior to some extent. At low

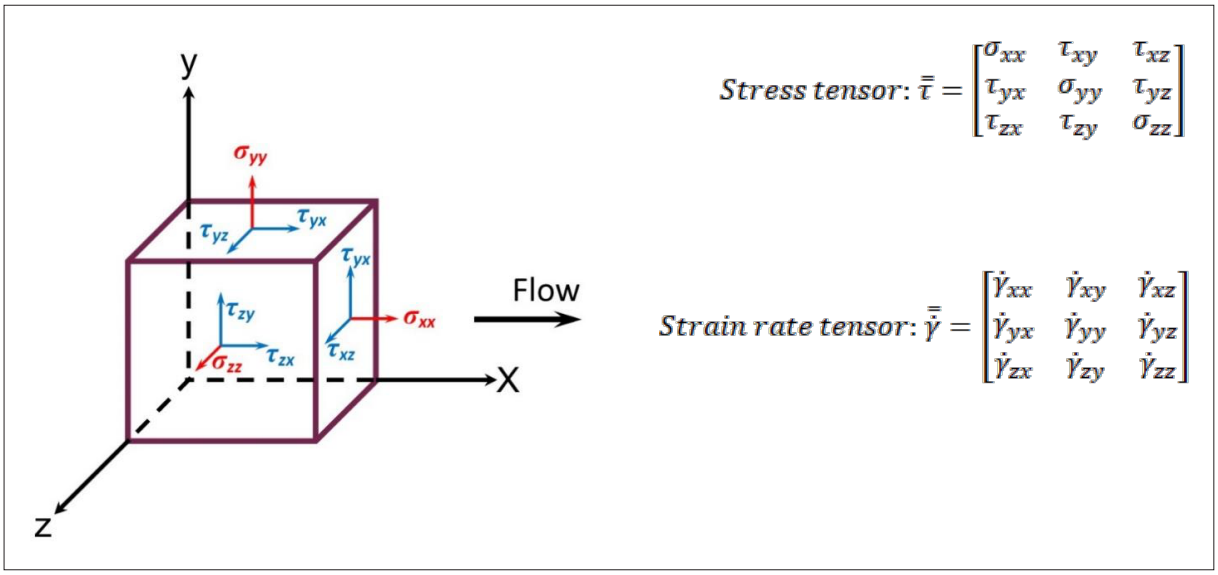

Figure 5. Stress components on a cubical fluid element; stress and strain rate tensors for a cubical fluid element. The figure was created by the authors using Microsoft Publisher.

shear stress values, the high zero-shear viscosity prevents significant shear or flow. For these fluids, the apparent yield stress or critical stress corresponds to the critical shear rate marking the onset of shear-thinning behavior after the plateau in the low-shear region.

3.2. Time-dependent flow behavior

Fluids that exhibit time-dependent behavior can have their apparent viscosities influenced not only by the shear rate but also by the duration of shearing. Time-dependent flow behavior can be classified into two main types: thixotropy and rheopexy. Thixotropy describes a material's property where its apparent viscosity or shear stress decreases over time during constant shearing (Figure 6B). When a thixotropic fluid is subjected to shearing at a constant rate after a prolonged period of rest, its apparent viscosities gradually decrease as the internal structure of the fluid is progressively disrupted. As the number of structural linkages that can be broken down reduces, the rate at which the apparent viscosity changes with time gradually diminishes.[77] Conversely, when the structure breaks down, the rate of reforming linkages increases, eventually leading to a dynamic equilibrium where the buildup and breakdown rates are balanced.

When measuring the flow curve in a single experiment, where the shear rate is continuously increased from zero to its maximum value and then decreased back to zero at the same rate, a hysteresis loop is observed (Figure 6C). The height, shape, and enclosed area of the hysteresis loop depend on factors such as the duration of shearing, the rate of shear rate increase/decrease, and the sample's previous kinematic history. Generally, the larger the enclosed area, the stronger the time-dependent behavior of the material. In contrast, the fluids that exhibit an increase in apparent viscosity or shear stress with the duration of shearing are known as rheopectic materials.[79] Similar to thixotropic materials, rheopectic fluids also exhibit hysteresis effects in their flow curves (Figure 6C).

The breakdown of the material's structure under shearing is reversible to some extent. After the shearing is stopped and a resting period is observed, the fluid can recover its initial viscosity by rebuilding its structure.[90] A printable bioink needs to exhibit low viscosity during the printing process and sufficient mechanical strength after being printed. Therefore, an ideal printable hydrogel should possess thixotropic properties and fast recovery to regain its viscosity after printing.[59] The time required for complete viscosity recovery can be considerably long (depending on the material and shear rate). Therefore, it is common to report a recovery of up to 80–90% of the initial viscosity or moduli.[91]

To assess the rate of recovery after extrusion, a three-point interval thixotropy test can be conducted using a rotational rheometer with parallel plates or cone-plate geometries. This test involves three intervals resembling the bioink condition during extrusion bioprinting. The first interval with a low shear rate represents the low shear of the bioink in the syringe, the second interval with a high

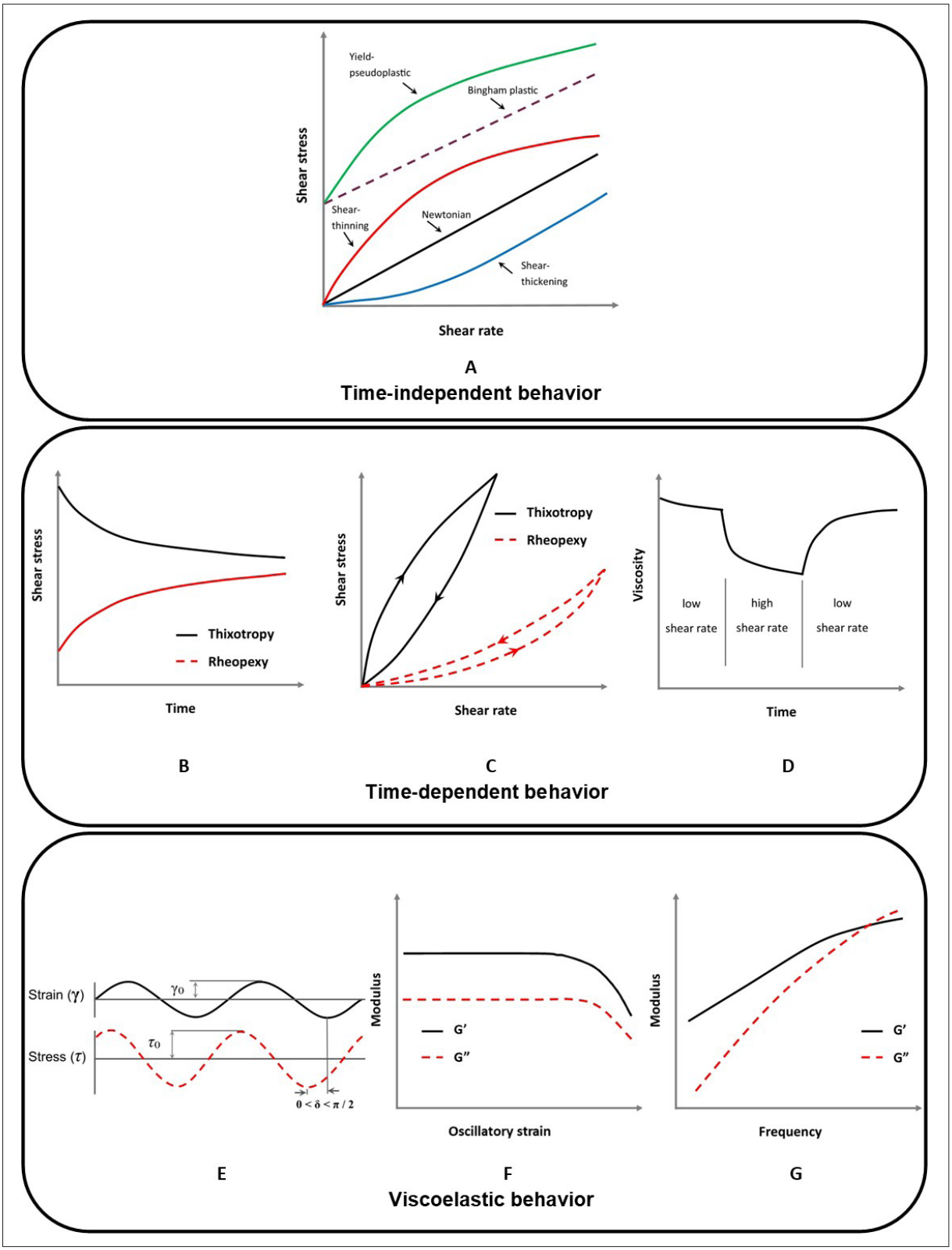

Figure 6. Rheologic behavior of fluids. Time-independent behavior: (A) Flow curves from steady shear test. Time-dependent behavior: (B) transient shear with constant shear rate, (C) hysteresis, (D) three-point interval thixotropy test. Viscoelastic behavior: (E) oscillatory shear test, (F) strain sweep test determining the linear viscoelastic region (LVR), and (G) frequency test in LVR. Abbreviations: G', storage modulus, G", loss modulus.

Table 3. Commonly used mathematical models to describe the time-independent flow behavior of bioinks[80–85]

Model	Equation	Parameters	Description
Power-law	$\bar{\bar{\tau}} = \left(K\dot{\gamma}^{n-1} \right) \bar{\bar{\dot{\gamma}}}$	K: consistency coefficient n: power-law index	$n < 1$: shear-thinning $n = 1$: Newtonian $n > 1$: shear-thickening
Carreau	$\frac{\eta - \eta_\infty}{\eta_0 - \eta_\infty} = \left[1 + k\dot{\gamma}^2 \right]^{\frac{n-1}{2}}$	k: a time constant n: power-law exponent η_0: limiting zero-shear viscosity η_∞: limiting infinite-shear viscosity	η_0 and η_∞ values are obtained from flow behavior at very low and high shear rates
Carreau-Yasuda	$\frac{\eta - \eta_\infty}{\eta_0 - \eta_\infty} = \left[1 + k\dot{\gamma}^\alpha \right]^{\frac{n-1}{\alpha}}$	k, n, η_0, η_∞: similar to Carreau model α: a dimensionless parameter characterizing the transition between the zero-shear-rate and power-law regions in flow curve	η_0 and η_∞ are the same as Carreau model α is obtained from flow curve
Cross	$\frac{\eta - \eta_\infty}{\eta_0 - \eta_\infty} = \frac{1}{1 + k\dot{\gamma}^n}$	K: consistency coefficient n: power-law index	η_0 is the same as Carreau model η_∞ is usually negligible
Herschel-Bulkley	$\bar{\bar{\tau}} - \bar{\bar{\tau}}_0 = \left(K\dot{\gamma}^{n-1} \right) \bar{\bar{\dot{\gamma}}}$	K: consistency coefficient n: power-law index τ_0: yield stress	With $n = 1$, it changes to Bingham plastic model

shear rate simulates the breakdown of the fluid structure under high shear inside the nozzle, and the third interval with a low shear rate reflects the structural recovery after hydrogel extrusion (Figure 6D).

Although time-independent shear-thinning behavior is an essential requirement for a bioink, the viscosity recovery test can provide a more realistic idea of whether a bioink is suitable for bioprinting or not. This test helps researchers predict the bioink's printability and determine if it requires additional crosslinking is needed to improve the recovery rate after deposition. For instance, Paxton et al.'s comparative analysis[92] on viscosity recovery for Poloxamer 407 and alginate indicated that 25% and 30% Poloxamer 407 biomaterials have a rapid recovery, and they exhibit good printability and shape fidelity. In contrast, 15% Poloxamer 407 was not printable because of its slow viscosity recovery. Their tests also indicated that the slow recovery of 8% alginate solution can be addressed by pre-crosslinking, which improved the viscosity recovery rate. The three-point thixotropy test of alginate-carboxymethyl cellulose (CMC) composite biomaterials by Tuladhar et al.[93] revealed that solutions with 25% alginate and 75% CMC, as well as those with 50% alginate and 50% CMC, have a good viscosity recovery rate and shape fidelity after printing.

Diañez et al.[94] and Herrada-Manchón et al.[95] successfully printed biomaterials with slow viscosity recovery by incorporating thermal gelation or *in situ* rapid crosslinking during the printing process. Thermosensitive biomaterials improve printability and shape fidelity via rapid gelation, facilitated by the temperature difference between the printing head and stage. The recovery rate of biomaterials also affects the structural integrity of the printed scaffold during the layer-by-layer deposition process. Hydrogels that rapidly develop self-supporting capacity can withstand the weight of the upper layers, preventing the deformation and collapse of the scaffold during or after printing.[50] Filaments with good shape fidelity can be achieved by bioinks that exhibit higher viscosity at lower shear rates and a greater post-printing recovery rate.[96] Conversely, the time-dependence of viscosity can lead to inhomogeneity in a printed filament.[97]

3.3. Viscoelastic behavior

Viscoelastic materials exhibit both elastic and viscous characteristics when subjected to flow or deformation. Rheological studies documented in the literature have confirmed that bioinks and polymer melts used in extrusion bioprinting are viscoelastic materials.[36,98] Therefore, they possess both energy-damping properties and the capacity to store strain energy. These materials dissipate energy during loading and unloading, resulting in a hysteresis loop in the stress–strain rate curve, which represents the energy lost during cyclic loading.

3.3.1. Dynamic moduli of a viscoelastic fluid

The dynamic moduli of storage modulus (G') and the loss modulus (G'') are typically used to represent viscoelastic properties. These moduli are commonly examined through small-amplitude- oscillatory-sweep (SAOS) tests

on a rotational rheometer.[78,93] The controlled oscillatory rotation of the shaft can generate a sinusoidal shear strain γ on the fluid stored between parallel plates or a cone and a plate.

$$\gamma = \gamma_0 \sin(\omega t) \quad \text{(XVI)}$$

where γ_0 denotes shear-strain amplitude; ω and t are angular velocity and time, respectively. The rheometer measures the transient shear stress (based on transient resistive torque),

$$\tau = \tau_0 \sin(\omega t + \delta) \quad \text{(XVII)}$$

where τ_0 is shear-stress amplitude and δ represents the phase shift between stress and strain, known as loss angle (Figure 6E). The storage and the loss moduli are defined as[36]

$$G' = \frac{\tau_0}{\gamma_0}\cos(\delta); G'' = \frac{\tau_0}{\gamma_0}\sin(\delta) \quad \text{(XVIII)}$$

The loss tangent of material is calculated by[36]

$$tan\delta = \frac{G''}{G'} \quad \text{(XIX)}$$

For a viscoelastic material, the loss angle can take values between 0 (elastic material) and π/2 (pure fluid) (Figure 6E). The storage modulus (G') indicates solid-like behavior and the material's ability to store energy, reflecting the elastic shape recovery or cell suspension capabilities of bioinks. Conversely, the loss modulus (G'') represents the liquid-like behavior of the bioink and relates to the energy dissipated during extrusion and mixing.[78]

The storage and loss moduli can vary under different conditions, including shear rate, stress, and temperature.[77] Therefore, to obtain accurate G' and G'' values as fluid properties, oscillatory tests should be performed within the linear viscoelastic region (LVR) of the bioink, where both moduli are independent of stress/shear. The LVR can be determined through an oscillatory amplitude (stress or shear) sweep, where the shear stress or shear rate gradually increases while maintaining a constant frequency (typically 1 or 2 Hz). The LVR is identified as the region where G' and G'' remain unaffected by the stress or shear amplitude (Figure 6F). Once the LVR is established, a frequency sweep test (SAOS) can be conducted by applying a fixed stress or shear amplitude within the LVR and varying the frequency. This process allows for the determination of the storage and loss moduli of the bioink at various frequencies (Figure 6G).

In addition to loss and storage moduli, researchers use the loss tangent to assess the printability of bioinks. The loss tangent indicates the balance between the elastic and viscous behaviors of the material. Biomaterials with a loss tangent of less than 0.1 act as strong gels, providing excellent structural integrity in the printed construct but potentially causing inconsistent extrusion due to gel fracture in the printing nozzle. Conversely, weak gels have a loss tangent greater than 0.1 and can be extruded uniformly, but may collapse after deposition unless crosslinked during deposition to achieve good shape fidelity.[44] Therefore, the loss tangent plays a crucial role in optimizing bioink printability. Petta et al.[42] found that tyramine hyaluronan derivative hydrogels with a loss tangent between 0.5 and 0.6 exhibited optimal printability. In a similar study, Cheng et al.[99] identified that biomaterials with a loss tangent of 0.2–0.7 are suitable for 3D printing with good printability.

Gao et al.[43] identified an optimal region for bioprinting using gelatin-alginate biomaterials. They summarized their results in a map that illustrates the optimal extrudability and cell viability based on loss and storage moduli, as well as the loss tangent (Figure 7). Their experiments with vvarious gelatin–alginate composite bioinks suggested that a loss tangent in the range of approximately 0.25–0.45 results in smooth fiber extrusion without compromising structural integrity. However, increasing the moduli raises the extrusion pressure, negatively affecting cell viability due to increased bioink viscosity.

3.3.2. Normal stress differences in a viscoelastic fluid

As aforementioned, additional stress terms in normal stresses may take non-zero values and can lead to complex behaviors in viscoelastic fluids. In these fluids, there is no simple expression for the isotropic pressure; instead, the first and second normal stress differences play a crucial role. Assuming the flow of a viscoelastic fluid in the x-direction (Figure 5), the first and second normal stress differences are defined as[78]:

$$N_1 = \tau_{xx} - \tau_{yy} \quad \text{(XX)}$$

$$N_2 = \tau_{yy} - \tau_{zz} \quad \text{(XXI)}$$

Normal stress differences are more readily measurable than the individual normal stresses,[77] and they account for most of the unusual behaviors in viscoelastic fluids, such as extrudate swell (Barus effect), rod climbing (Weissenberg effect), and the development of secondary flows at low Reynolds numbers[78] (Figure 8). Both extrudate swell and

secondary flow can significantly affect the outcomes of extrusion bioprinting.

Despite the crucial role of normal stress differences in the behavior of viscoelastic fluids, there is no published research reporting the measured values of these differences for biomaterials. Existing data come from tests on industrial polymeric fluids that differ from the biomaterials used in bioprinting. The first normal stress difference can be measured using a rotational rheometer with axial force measurement capability during a steady shear test with a cone-plate geometry.[77] The second normal stress difference N_2 is typically much smaller than N_1 and is often negligible, especially for dilute solutions. Nevertheless, for polymer melts and concentrated or entangled polymer solutions, N_2 may have a value of $-0.1N_1$ to 0.3 N_1, affecting the flow pattern by generating secondary flows.[103] Due to geometrical symmetry, N_2 does not affect flow in circular or coaxial pipes, so its effect can be ignored for the flow of biomaterial melts or concentrated bioinks within bioprinting nozzles.

Normal stress differences are characteristics of a viscoelastic fluid. Therefore, a comparison of the first normal stress difference with the shear stress can be a measure of viscoelastic behavior.[104] To quantify this behavior, the relaxation time of a fluid (λ), also known as Maxwell relaxation time, is defined as[77]:

$$\lambda = \frac{N_1}{2\tau_{yx}\,\dot{\gamma}_{yx}} \tag{XXII}$$

To compare the elastic and viscous forces in the flow, the Weissenberg number is defined as [104]:

$$Wi = \frac{\tau_{xx} - \tau_{yy}}{\tau_{yx}} = 2\lambda\,\dot{\gamma}_{yx} \tag{XXIII}$$

This number compares the first normal stress difference and shear stress as characteristic values for elastic and viscous forces. In a simple shear flow, τ_{yx} and $\dot{\gamma}_{yx}$ denote the shear stress and strain rate, respectively.

The Weissenberg number quantifies the significance of viscoelastic behavior in a flow. For example, depending on the contraction ratio, bioink flow inside a chamfered nozzle with $Wi > Wi_{cr}$ may develop symmetrical (or asymmetrical) vortices in the contraction area, even at low Reynolds numbers. The critical Weissenberg number Wi_{cr} determines when elastic forces within the viscoelastic fluid are strong enough to affect the regular viscous behavior of fluid. Conversely, for $Wi > Wi_{cr}$, the bioink may exhibit extrudate swelling at the dispensing nozzle exit due to the Barus effect.[105–107] The values of Wi_{cr} for the onset of vortices in the contraction area or extrudate swell phenomenon may differ depending on various flow parameters. Figure 8A[100] illustrates the extrudate swell effect for polymeric fluid extruding from a circular nozzle. This swelling can significantly change the filament diameter and affect printability.[97] To compensate for filament swelling, the filaments should be printed with a smaller diameter than the original design. This can be achieved by reducing extrusion pressure, increasing print speed, or using smaller nozzles.[97]

Empirical and semi-empirical correlations often relate the swell ratio (d_{ex}/d) to the first normal stress difference N_1. Tanner[108] suggested a relationship based on the Phan-Thien-Tanner (PTT) viscoelastic model that aligns with experimental observations:

$$\frac{d_{ex}}{d} = \left[1 + \frac{1}{2}\left(\frac{N_1}{2\tau}\right)_w^2\right]^{1/6} \tag{XXIV}$$

where d_{ex} represents the diameter of filament emerging from the needle; the subscript w indicates that N_1 and τ are the first normal stress difference and shear stress values at the wall of the needle.

3.3.3. Extensional viscosity in a viscoelastic fluid

The response of a viscoelastic fluid to extensional flow (as discussed in **Section 2.3**) can differ drastically from that of a Newtonian fluid. Despite the crucial role of extensional viscosity in cell viability assessments, there are no published studies on the extensional viscosity of bioinks. Extensional rheology can provide crucial data for analyzing the stresses developed in the viscoelastic bioink as it is extruded through the dispensing nozzle. The extensional viscosity can be measured using a filament stretching rheometer (FiSER).[109,110] Figure 9 illustrates a schematic of the fluid filament stretched inside a FiSER. In this method, a cylindrical bridge of liquid is created between two parallel plates. The upper plate is then moved up, stretching the liquid bridge and creating a tensile stress from the tensile force (F_E) exerted by plates. The upper plate velocity profile U_u is adjusted to create an exponential decrease in midpoint radius (R) with a constant stretching rate $\dot{\gamma}_e$ [111]:

$$\dot{\gamma}_e = -\frac{2}{R}\frac{dR}{dt} \tag{XXV}$$

The Hencky strain (γ_e) at the midpoint of the liquid bridge is influenced by the stretching history and can be

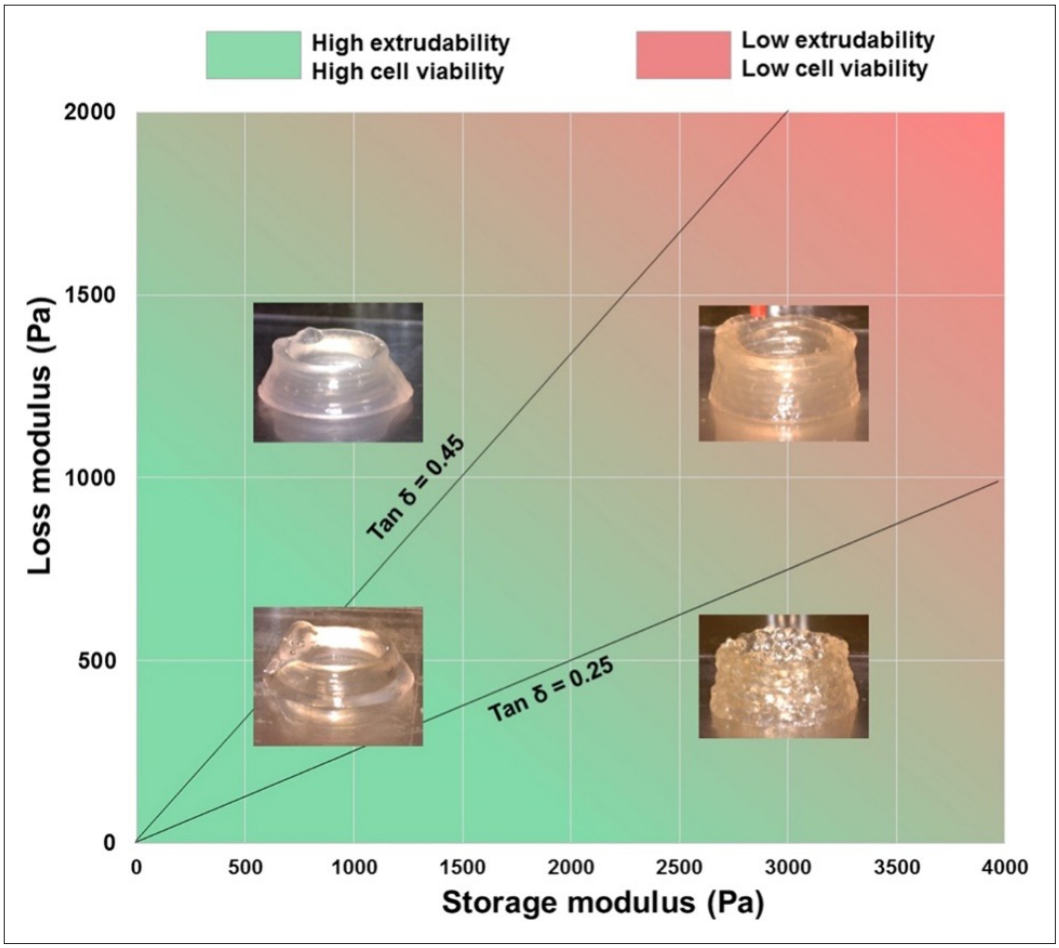

Figure 7. Optimal ranges of dynamic moduli and loss tangent for bioprinting of gelatine-alginate biomaterials. Adapted with permission from ref.[43] Copyright © 2018 IOP Publishing.

determined by integrating the stretching rate over time from the initiation of stretching[109]:

$$\gamma_e = \int_0^t \dot{\gamma}_e \, dt' = -2 \, ln\left[\frac{R_0}{R(t)}\right] \quad \text{(XXVI)}$$

where R_0 is the initial radius of the liquid bridge.

By defining the extensional stress as[109] $\tau_e = \frac{F_E}{\pi R_{mid}^2}$, the transient extensional viscosity (η_E) can be calculated as[109]

$$\eta_E = 3\eta_s + \frac{\tau_e}{\dot{\gamma}_e} \quad \text{(XXVII)}$$

where η_s is the viscosity of the solvent in a viscoelastic solution. The extensional viscosity of a bioink offers a clear understanding of the extensional stress on cells, making it a more accurate parameter for predicting cell viability than using **Equation IV**. Extensional rheology of bioink can affect the dynamics of gobbling drop and extrudability, as discussed in **Section 2.2**.

Given the significant role of extensional rheology in the behavior of a viscoelastic fluids, especially in extensional flows, some researchers define the relaxation time of the viscoelastic fluid based on the time constant (λ_e) for the exponential decay of the liquid bridge midpoint radius.

As aforementioned, bioinks may exhibit all three sub-classes of non-Newtonian rheology. Table 4 presents the rheological characteristics and flow behavior models for some common biomaterials. While most bioprinting

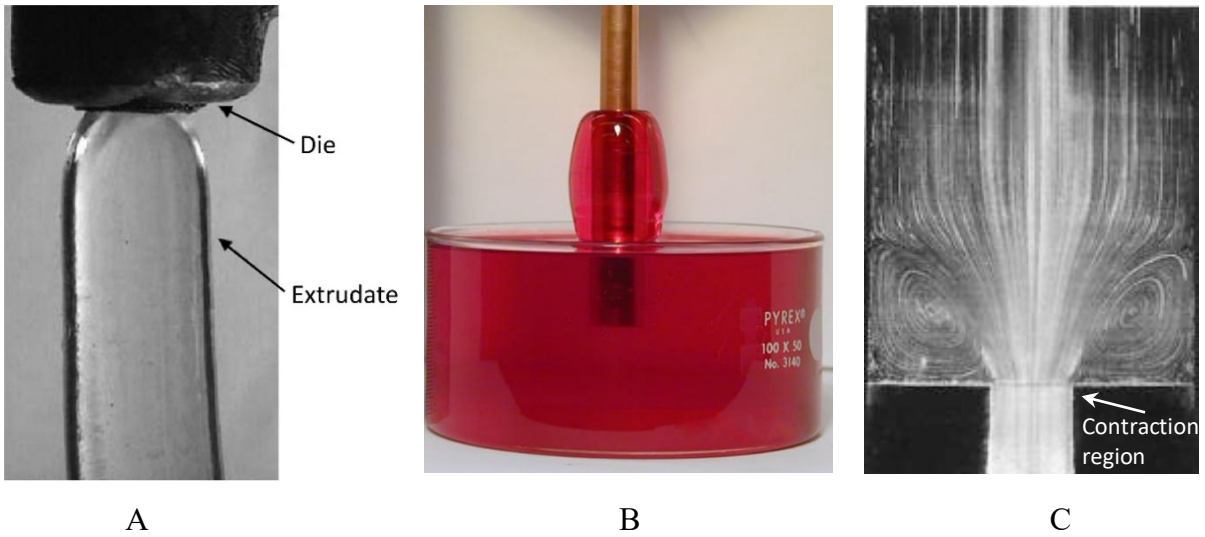

Figure 8. Visualizations of some unusual behaviors of viscoelastic fluids. (A) Extrudate swell for viscoelastic fluid issuing from a die (nozzle).[100] Reprinted with permission from ref.[100] Copyright © 2004, John Wiley and Sons. (B) Rod climbing of a viscoelastic fluid over the rotating rod. Adapted from ref.[101] (C) Development of secondary flows at contraction flow with low Reynolds numbers (the geometry is similar to that in Figure 3). Reprinted with permission from ref.[102] Copyright 1994, The Society of Rheology.

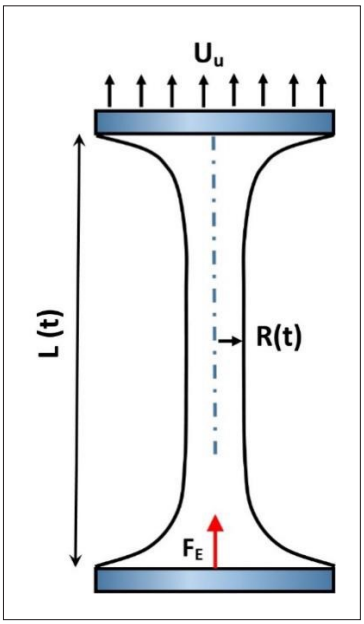

Figure 9. Schematic diagram of the liquid bridge within a filament starching rheometer (FiSER).

studies include rheological test results, only a few have fitted a flow behavior model to their data. Various models can be fitted to the flow behavior of biomaterials depending on their concentrations and compositions. The table indicates that all listed biomaterials exhibit shear-thinning and viscoelastic behavior. Additionally, the biomaterials (listed in Table 4) are natural materials that can have different compositions depending on their source and processing, which affects their rheological behavior. It is important to note that the absence of thixotropy as a listed rheological characteristic for a biomaterial in Table 4 preclude the possibility of thixotropic behavior; such behavior may emerge at certain concentrations or compositions. Regarding thixotropy and viscoelastic behavior, there is a lack of mathematical model fitted to available test results in the literature, except for an alginate-based bioink.[112]

4. Extrusion multi-material bioprinting

Native tissues possess complex structures composed of diverse types of materials and cells, with the ECM organized delicately to fulfill the specific functions of each tissue and organ.[35] To successfully replicate this complexity in bioprinting, it is necessary to combine multiple biomaterials and cell types in a single printing session. Extrusion-based multi-material bioprinting methods can fall into two main categories: (i) multi-material bioprinting without mixing and (ii) multi-material bioprinting with mixing. Over the past decade, various techniques have been developed in both categories to enhance the outcomes of bioprinting. Multi-material bioprinting methods without mixing enable independent control of the flow of different biomaterials

and cell-containing solutions, followed by their simultaneous deposition. For example, coaxial printing involves minimal contact between precursors as they exit the nozzle and to deposit on the printing stage, where crosslinking solidifies them. Other methods, like the head sweeping technique, deposit different bioinks separately. In contrast, multi-material bioprinting with mixing, such as using micromixer-equipped heads, involves contact between precursors before deposition. Depending on the design and application, the extent of mixing can vary from minimal (separated) to homogeneous. Most of these methods are designed to maximize the mixing of precursor biomaterials and cells, enabling the deposition of a homogeneous mixture with precise control over composition during the printing process.

4.1. Extrusion multi-material bioprinting without mixing

4.1.1. Swapping the dispensing heads

The simplest approach for multi-material bioprinting is swapping the dispensing heads on the bioprinter. This method enables hierarchical printing of different bioinks [62,125–127] by loading different biomaterials onto separate printing heads, which are sequentially mounted on the printing arm. This allows for specific parts of the scaffold to be printed in a predetermined manner. Hydrogels are typically pre-mixed with cells and facilitate the simultaneous printing of multiple bioinks.[27] For example, a multi-head system can be utilized to print cell-laden scaffolds using decellularized extracellular matrix (dECM)-based bioink and polycaprolactone (PCL).[128] This method has also proven successful in creating hybrid scaffolds that combine alginate and PCL, exhibiting improved mechanical properties compared to pure alginate scaffolds.[125,129] However, this method can only print one bioink at a time, resulting in a relatively slow printing process. Additionally, precise alignment of the nozzles and accurate control of the bioink flow are necessary when changing printing heads to maintain structural integrity.[130] To address the slow printing issue, some bioprinters incorporate multiple arms with independent motion paths and heads.[131] However, this approach introduces challenges in aligning the arms accurately, which can potentially impact the overall integrity of the printed scaffolds.[131]

4.1.2. Coaxial printing

Coaxial printing is an emerging technique in extrusion multi-material bioprinting[132–136] that uses coaxial needles for printing core–shell fibers. This method involves inserting small-diameter needles into larger-diameter needles, allowing for the fabrication of structures with core–shell or hollow fibers.[24] Depending on the specific application, different biomaterials and cell types can be extruded as the core or sheath layer of the filament.[11]

Coaxial bioprinting can significantly improve the mechanical properties of biomaterials by combining them with stronger biomaterials. For example, core–shell polyethylene glycol diacrylate (PEGDA)/alginate filaments, with alginate as the core and PEGDA as the shell, exhibit higher tensile moduli and strengths compared to alginate.[130] This method allows for printing a cell-laden hydrogel as the core, while the shell provides structural integrity and protection for the cell-laden hydrogel.[137] Furthermore, coaxial printing enables the creation of advanced scaffold structures, including vessel-like channels.[28,138] However, a major challenge in coaxial printing is the difficulty in using multiple coaxially assembled needles to produce small-diameter fibers, due to the requirement of larger-diameter outer needles to accommodate the internal small-diameter needles.[36] Despite this, coaxial heads can print fibers with a core–shell structure without mixing the materials.

Table 4. Rheological characteristics and models for common biomaterials

Biomaterials	Newtonian/non-Newtonian	Models	Ref.
Alginate	Non-Newtonian: (i) shear-thinning; (ii) thixotropy; (iii) viscoelastic	Power-law; cross; viscoelastic (PTT)	[112–116]
Alginate/gelatine	Non-Newtonian: (i) shear-thinning; (ii) viscoelastic	Herschel-Bulkley	[117]
Agarose	Non-Newtonian: (i) shear-thinning; (ii) viscoelastic	Power-law	[118]
Carboxymethyl cellulose (CMC)	Non-Newtonian: (i) shear-thinning; (ii) thixotropy; (iii) viscoelastic	Power-law; cross	[119]
Chitosan	Non-Newtonian: (i) shear-thinning; (ii) thixotropy; (iii) viscoelastic	Carreau-Yasuda	[120,121]
Collagen	Non-Newtonian: (i) shear-thinning; (ii) viscoelastic	Power-law; Carreau	[122]
Gelatin	Non-Newtonian: (i) shear-thinning; (ii) viscoelastic	Power-law	[123,124]

The stability of coaxial streams exiting the dispensing nozzle is crucial for successful bioprinting. Upon exiting the nozzle, biomaterials in both the core and sheath layers may experience swelling if the flow exhibits a Weissenberg number greater than the Wi_{cr}, i.e., corresponding to the onset of extrude swell. Typically, the core flow contains a low-viscosity bioink or Newtonian crosslinker with minimal swelling. However, if the viscoelastic biomaterial in the sheath layer exhibits a high swelling ratio, it can exert pressure on the core flow, potentially causing instabilities and breakup of the core into droplets. To mitigate this, most coaxial nozzles are designed with the core needle slightly longer than the sheath needle to protect the core flow from the swelling effects of the sheath flow.

4.1.3. Single-nozzle multi-material heads

Continuous single-nozzle multi-material (SNMM) bioprinting is a technique that involves dispensing different biomaterials sequentially through a single nozzle.[139] The SNMM bioprinting head may include a selector valve to control the printing of different bioinks.[139] Considering the internal volume of the head and the diffusion rate of bioinks, any change in the flow rate of precursors results in a delay in the composition of fiber, proportional to the internal volume of the head. Therefore, there is always a "transition distance" during which the composition gradually shifts from one composition to another.[139–141]

The drawback of single-nozzle methods is that they cannot print various biomaterials simultaneously. This can be addressed by using a bundle of capillary nozzles inside the printing head.[142] Liu et al.[143] developed a multi-material bioprinting platform featuring a bundle of capillaries inside a single nozzle, each connected to different bioink reservoirs. This setup allows for the continuous deposition of multiple bioinks from a single nozzle, enabling the creation of heterogeneous 3D constructs using various biomaterials and cell types.

4.1.4. Microfluidic multi-material heads with separated streams of biomaterials

Microfluidic devices offer precise control over minute volumes of fluids (10^{-9}–10^{-18} L) through intricately designed microchannels with diameters in the tens of micrometers. This level of control allows for superior management of fluids in both spatial and temporal domains. Microfluidics-assisted 3D bioprinting utilizes microchannels to guide the flow of bioink, enabling precise control over flow,[144] switching,[145] component mixing,[146,147] and print resolution.[148] The integration of a multi-nozzle system in a microfluidic head allows for separate extrusion paths for each material, which are then combined after exiting independent orifices to form desired structures, such as multi-layer constructs.[149]

The combination of microfluidic bioprinting with coaxial techniques allows for the fabrication of core–shell fibers with exceptional accuracy and control.[144,145,150] Microfluidic devices typically benefit from integrated control systems that facilitate on-the-fly switching between different biomaterial sources and precise regulation of flow rates in the channels. Multiple channels enable quick transitions between different materials or even cell-laden and cell-free filaments.[151]

While various approaches to microfluidic bioprinting have been developed, there is still potential for improving the efficiency of these processes. A major limitation of microfluidic bioprinting is the high shear stress experienced by cells within the microchannels, which can reduce cell viability. One solution to this issue involves creating a sheath flow that surrounds the laminar core flow, acting as a protective barrier for the cells.[152] Although Lee et al.[153] managed to mitigate cell stress in a microfluidic head by implementing a sheath flow to protect and center the cells within the flow, their system did not include micromixers. Furthermore, their study focused on glioblastoma multiforme (GBM) tumor cells, which are less sensitive to stress compared to normal cells.[148,154]

Y-chips can be utilized in microfluidic printing to facilitate the feeding of multiple materials into the printing head.[148,155] By employing two syringe pumps, bioinks can be sequentially pushed through two channels connected to a single nozzle. This allows for the fabrication of constructs with distinct transitions between different constituent materials.

Figure 10 illustrates various microfluidic chip designs used for multi-material bioprinting.[152,156] Design A features a Y-passage that enables the simultaneous deposition of two bioinks. Design B features a switching system that alternates between two bioinks, allowing for alternating multi-material bioprinting. Design C uses grooved-wall micromixers to blend two or more bioinks together. Design D has a serpentine micromixer, suitable for fluid–fluid and fluid–solid (cell) mixing. Design E employs a sheath flow to protect cells within the core flow by positioning them at the center, where shear stress is lower. Design F, known as the flow-focusing design, regulates the fiber diameter by adjusting the ratio between the core and sheath flow rates.

In designs E and F, coaxial flow of viscoelastic biomaterials or Newtonian crosslinkers is employed. Unlike coaxial nozzles, microfluidic sheath flow or flow-focusing chips do not utilize coaxial needles; instead, the core and sheath flow are regulated by balancing the effective forces. The elastic behavior of viscoelastic biomaterials can lead to complex behaviors inside the flow-focusing microfluidic chip. In coaxial flow, inertial, viscous, capillary, and elastic

forces can be effective. Two main regimes describe the dynamics of coaxial flow in a flow-focusing microfluidic device: (I) the dripping regime, in which the breakup of the core flow creates droplets dispersed in the sheath flow, and (ii) the jetting flow with continuous core flow (Figure 11A).[157,158] For successful coaxial bioprinting, a stable jetting flow should be maintained inside the needle.

Utada et al.[157] analyzed the transition between dripping and jetting flow regimes based on the balance of capillary, viscous shear, and inertial forces for Newtonian fluids. Derzsi et al.[158] extended this analysis to coaxial flow of Newtonian core and viscoelastic sheath flows, similar to hollow fiber printing, in a flow-focusing microfluidic chip. Their experiments, covering a wide range of viscosity and flow rate ratios, demonstrated that the Weissenberg number governs the dynamics of coaxial flows with a viscoelastic sheath layer. They defined the Weissenberg number based on extensional strain rate $\dot{\gamma}_e$ and extensional relaxation time (λ_e):

$$Wi = \dot{\gamma}_e \lambda_e \tag{XXVIII}$$

Figure 11B illustrates the results of Derzsi et al.[158] for the dripping-jetting transition, plotting the dimensionless group of volumetric flow rate (Q) and viscosity in the core and sheath flow ($Q_c\eta_c$) against the critical Weissenberg numbers (Wi_{trans}) at which the transition from dripping to jetting flow regime occurs. Their results are based on the elasticity number (El) of the focusing stream, which compares elastic and inertial forces to represent the strength of elasticity in the focusing stream[158]:

$$El = \frac{\lambda_e \eta}{\rho w^2} \tag{XXIX}$$

where w is the channel width. While the jetting regime stabilizes the continuous coaxial flow, the Rayleigh-Plateau instability[56–58] can lead to breakup of the core stream into droplets (Figure 11A). Therefore, the length of needle should be shorter than the continuous jet region to prevent the core stream breakup.

4.2. Multi-material bioprinting with mixing

The complete mixing of two fluids inside a multi-material head requires that the shortest residence time (t_{res}) of the precursors streams inside the mixer exceeds the mixing time (t_{mix}) of components. For the parallel (or coaxial) flow of two precursor fluids inside the head, the only effective mechanism of mixing is molecular diffusion. For a straight channel with hydraulic diameter d and length ℓ, the residence time (t_{res}) is given by:

$$t_{res} \approx \frac{\ell d^2}{Q} \tag{XXX}$$

The mixing time (t_{mix}) for diffusion mixing of fluids is calculated by:

$$t_{mix} \approx \frac{d_{mix}^2}{D} \tag{XXXI}$$

where D is diffusion coefficient, and the mixing distance (d_{mix}) that components must diffuse to make a homogenous mixture is proportional to the hydraulic diameter of the channel (d). Therefore, for efficient mixing inside the head,[159]

$$t_{mix} < t_{res} \Rightarrow Pe = \frac{Q}{dD} \lesssim \frac{\ell}{d} \tag{XXXII}$$

where Pe denotes the dimensionless Péclet number, which is defined as the ratio of the advective transport rate of a component to its diffusive transport rate. To enhance the mixing process of biomaterials inside a multi-material head, the process can be optimized by reducing the total flow rate, which corresponds to printing at lower speeds, or by shortening the mixing distance through increased interdigitation between the streamlines of precursor flows. Interdigitation can be achieved by passive mixing techniques, without external energy requirement, or active methods that involve external energy supply for their dynamic mechanics. While active mixing methods can provide rapid mixing of high-viscosity biomaterials,[160] passive mixing is more commonly used in multi-material heads because of its simplicity and low stress levels on the bioink.

4.2.1. Multi-material heads with static mixers

Static mixers with diverse geometries have been developed to meet the requirements of various applications. While highly efficient static mixers can effectively mix fluids, they often generate high levels of shear stress due to their complex geometry and narrow flow paths. However, helical mixers with alternating left- and right-hand twisted elements, known as Kenics type mixers (Figure 13A), offer a good balance between mixing efficiency and shear stress. Their simple geometry allows for effective mixing without excessively high shear stress.[161]

In the context of bioprinting, with creeping flow inside the dispensing nozzle ($Re \ll 1$), the mixing potential of vortices is limited. Helical mixers with twisted elements facilitate mixing through chaotic advection.[156,162]

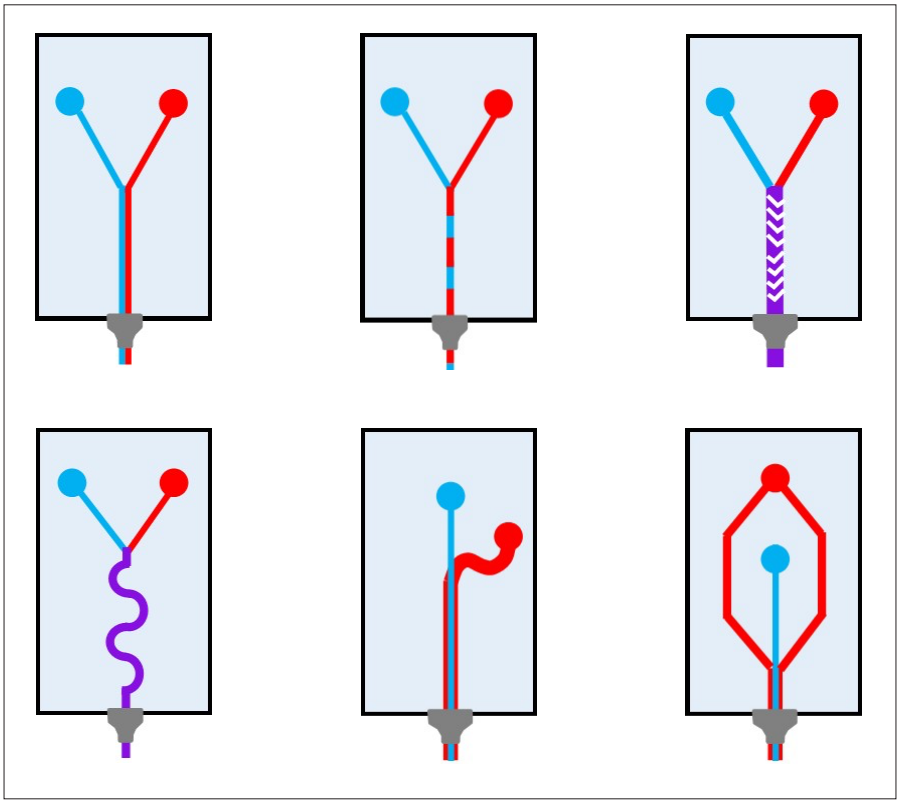

Figure 10. Various designs of microfluidic chips used in biofabrication. Microfluidic chips with (A) parallel flow, (B) switching flow, (C) grooved-wall micromixers, (D) serpentine micromixer, (E) sheath flow, and (F) flow-focusing.

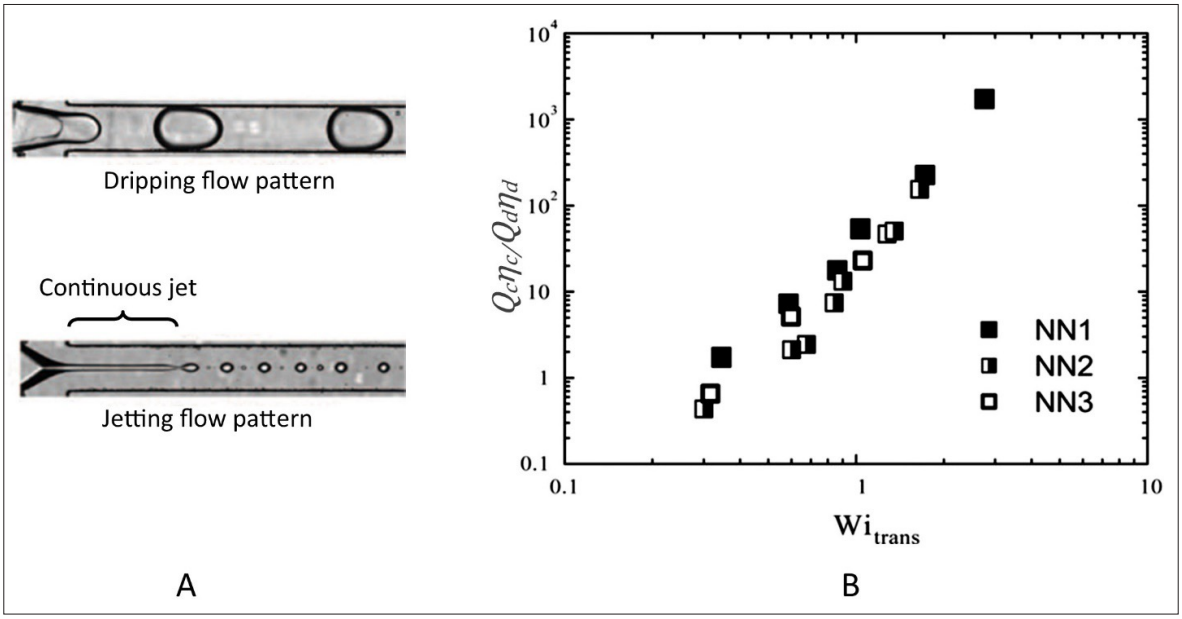

Figure 11. Dripping and jetting flow regimes, and their transition inside a flow-focusing microfluidic chip. (A) Visualization of dripping and jetting flows. (B) Ratios of the products of flow rate and viscosity vs. We_{trans} in core and focusing streams. For the focusing streams NN1: strongly elasticity liquid with, NN2: moderate elasticity liquid with and NN3: weak elasticity liquid with . The core flows are glycerin-water mixtures with Newtonian flow behavior.[158] Reprinted from Ref.[158], with the permission of AIP Publishing.

Interdigitation of streamlined precursor flows through chaotic advection provides an efficient mixing mechanism for creeping flows at extremely low Reynolds numbers.[162,163] Therefore, helical mixers have been used by researchers for mixing precursors inside multi-material heads.[141,164,165]

Helical mixers divide the streams of biomaterials into sub-streams, distribute them radially, and recombine them to produce a multi-layer structure in the flow cross section (interdigitation). A helical static mixing element divides each stream of biomaterial into two sub-streams. The average layer thickness represents the mixing distance (d_{mix}) and depends on the number of mixing elements (m) and the number of biomaterials (α):

$$d_{mix} = d/s \quad \text{(XXXIII)}$$

where s is the number of layers[162,163]

$$s = \alpha 2^{m-1} \quad \text{(XXXIV)}$$

This demonstrates how helical mixers can shorten the mixing distance of two biomaterial to $d/2^m$. Puertas et al.[141] combined a single-nozzle dual-syringe system with a helical static mixer integrated into an extrusion bioprinter. This system enabled the printing of homogeneous strands using a reactive hydrogel. The hydrogel precursors were extruded simultaneously from separate syringes, and the static mixer ensured homogeneous mixing and initiation of the crosslinking reaction before extrusion. This approach provided the bioprinter with a homogenous mixture of biomaterials and crosslinker.

Static helical mixers have also been successful in the bioprinting of constructs with gradient stiffness by mixing stiff and soft cell-containing hydrogels in appropriate ratios.[164–167] Kuzucu et al.[164] used a multi-material head with a helical mixer to print 2D and 3D structures with controlled stiffness. They utilized carboxylated agarose hydrogels with different stiffness as precursors. Figure 12 illustrates the 2D- and 3D-printed structures with medium-soft and stiff-soft carboxylated agarose-native agarose blend hydrogels, highlighting the variations in stiffness achieved by changing the flow rate of precursors during printing. Their results demonstrate the effectiveness of static helical mixers in achieving controlled mixing of biomaterials for bioprinting purposes.

Helical mixers have also been utilized in a novel technique, known as chaotic printing. The concept of chaotic printing was introduced by Chávez-Madero et al.[162] as a method for creating intricate constructs at the micrometer or even submicrometer scale within printed fibers. They utilized the chaotic flow generated by a helical mixer to print multi-material and multi-layer fibers. The multi-layer structure in the flow cross section is stabilized by crosslinking inside the printing head, preventing diffusion from completing the mixing process and achieving a homogeneous mixture. This approach demonstrated the ability to rapidly produce fine microstructures within printed fibers in a controlled and predictable manner. Utilizing the laminar chaotic flow generated by the static mixer, they achieved the stratification of different materials in 3D printing. They successfully printed well-defined multi-layer fibers using 2, 3, 4, 5, and 6 helical mixer elements with resolution of approximately 500, 250, 125, 62.5, and 31.75 μm, respectively. Similarly, Samandari et al.[168] utilized a helical mixer-integrated coaxial microfluidic device to divide alginate and GelMA solutions streams into sub-streams with desired thicknesses. This approach allowed for the fabrication of millimeter-sized fibers with intricate microscale structures, comprising successive microfilaments made of alginate and GelMA hydrogels, stabilized by UV-crosslinking. The resulting multiscale fibrous structure exhibited properties that facilitated cell spreading and alignment. The studies of Chávez-Madero et al.[163] and Samandari et al.[168] highlight the potential of continuous chaotic printing and static mixer-based approaches for the precise fabrication of complex structures with diverse material compositions and internal architectures.

Ceballos-González et al.[169] expanded on the multi-material chaotic bioprinting heads designed by Chávez-Madero et al.[162] by incorporating additional inlets to produce radial and axial micropatterns inside the printed fibers. Considering the relationship between the number of layers and the number of mixing elements, as well as the number of axial inlets, they applied more control over the multi-layer structure of fibers by altering the number and position of inlets for different precursors. Figure 13 illustrates their experimental observations and computational simulation results for the multi-layer fiber structures produced with varying numbers of mixing elements and inlet compositions. They also employed radial inlets in combination of axial ones to gain more control over the internal structure of the printed fibers. By switching between different axial and radial inlets during the printing process, they effectively controlled the internal structure of the printed fibers in both axial and radial directions.

4.2.2. Multi-material heads with microfluidic micromixers

Single-nozzle microfluidic multi-material printing heads are used in various bioprinting applications.[130] While they lack a dedicated mixing element, the co-flowing streams of bioinks inside microchannels promote some

level of mixing. These microfluidic systems draw different biomaterials from separate reservoirs and extrude them as a single multi-material fiber, ensuring precise control over the concentration of precursor biomaterials at the outlet.[143,170] Colosi[171] utilized a simple Y-shaped microfluidic chip with coaxial outlet to print a cell-laden heterogeneous construct composed of core–shell fibers. Microfluidic systems are among the fastest methods for bioprinting. However, due to the single-nozzle design, these systems can only print one bioink or a mixture of bioinks at a time.[130] While designs with co-flow of biomaterials inside a Y-microchannel (Figure 10A) promotes mixing, designs equipped with micromixer elements (Figure 10C and D) effectively facilitate the mixing of biomaterials during the extrusion process. Although both active and passive micromixers can work in microfluidic printing systems, passive micromixers are more popular due to their simplicity and relatively mild effect on cells. Passive micromixers operate based on interdigitation mechanism, which can be achieved through split-and-recombine (SAR) flow guidance methods or chaotic mixing.[160]

Strook et al.[172] demonstrated that a grooved-wall micromixer can benefit from chaotic advection to decrease the mixing distance. They reported that for grooved-wall micromixers,

$$\ln Pe \lesssim \frac{\ell}{d} \qquad \text{(XXXV)}$$

which shortens the length of mixing channel required for complete mixing of precursors.

Angelozzi et al.[152] demonstrated that adding a serpentine micromixer to the Y-shaped microfluidic chip (Figure 10D) enhances the mixing of osteoblast cells within the alginate solution and facilitates the deposition of fibers with homogeneous distribution of cells. The serpentine micromixer can facilitate the chaotic mixing process by generating Dean vortices in the flow cross-section. The straight channels (Figure 10A) were found to cause cell segregation along one side of the printed fibers due to the laminar dispersion of cells in the flow inside the microfluidic device.[148,152]

Based on the intended purpose and the desired structure of the printed scaffold, a microfluidic chip with a specialized function can be custom-designed and integrated into the printing head. For instance, combining microfluidic chips with coaxial printing heads can harness the advantages of both approaches for bioprinting. The integration of the microfluidic chip upstream of the coaxial dispensing nozzle enables the printing of low-viscosity bioinks while attaining high architectural complexity. Idaszek et al.[173] introduced an innovative coaxial 3D extrusion bioprinting system that incorporated a microfluidic mixing unit to fabricate 3D constructs with gradients of cells and biomaterials, specifically designed for chondral defect repair. This platform enabled the separate delivery of various bioinks or their quick mixing within the microfluidic mixer prior to extrusion through a coaxial nozzle. The system facilitated the generation of gradients in composition, mechanical properties, and biological cues, resulting in constructs with high structural integrity and enhanced bioactivity.

5. Numerical simulation of bioprinting

Due to the high cost of most cell-containing bioinks and the time-consuming nature of bioprinting tasks, researchers have increasingly turned to computational fluid dynamics (CFD) simulations as a valuable complementary approach. These simulations analyze the extrusion, mixing, and deposition processes involved in bioprinting by leveraging the detailed information from the numerical solutions of the governing equations.[88]

Numerical simulations of bioprinting processes allow for a deeper understanding of the relationships between nozzle geometry, bioink properties, printing parameters, and extrusion forces. These simulations play a crucial role in predicting the impact of the printing process on cell viability and the shape of the extruded fiber. CFD techniques have the potential to optimize dispenser geometry, printing conditions, and even facilitate the development of new bioink compositions, reducing the need for extensive experimental testing.[63,174]

In order to model the flow of bioinks during the extrusion bioprinting process, the governing equations of fluid flow, along with appropriate boundary conditions, should be solved numerically using commonly employed methods, such as finite-volume or finite-element approaches.

The numerical solution method enables researchers to simulate and analyze the intricate fluid dynamics within the bioprinting system, providing valuable insights into the behavior of bioinks and their interaction with the printing environment. By leveraging these simulations, researchers can make informed decisions regarding printing parameters, biomaterial compositions, and optimization strategies, ultimately advancing the capabilities of bioprinting technology.[63]

Assuming laminar, incompressible flow, the governing equations for the flow of biomaterials can be written as follows:

(i) Continuity[70]:

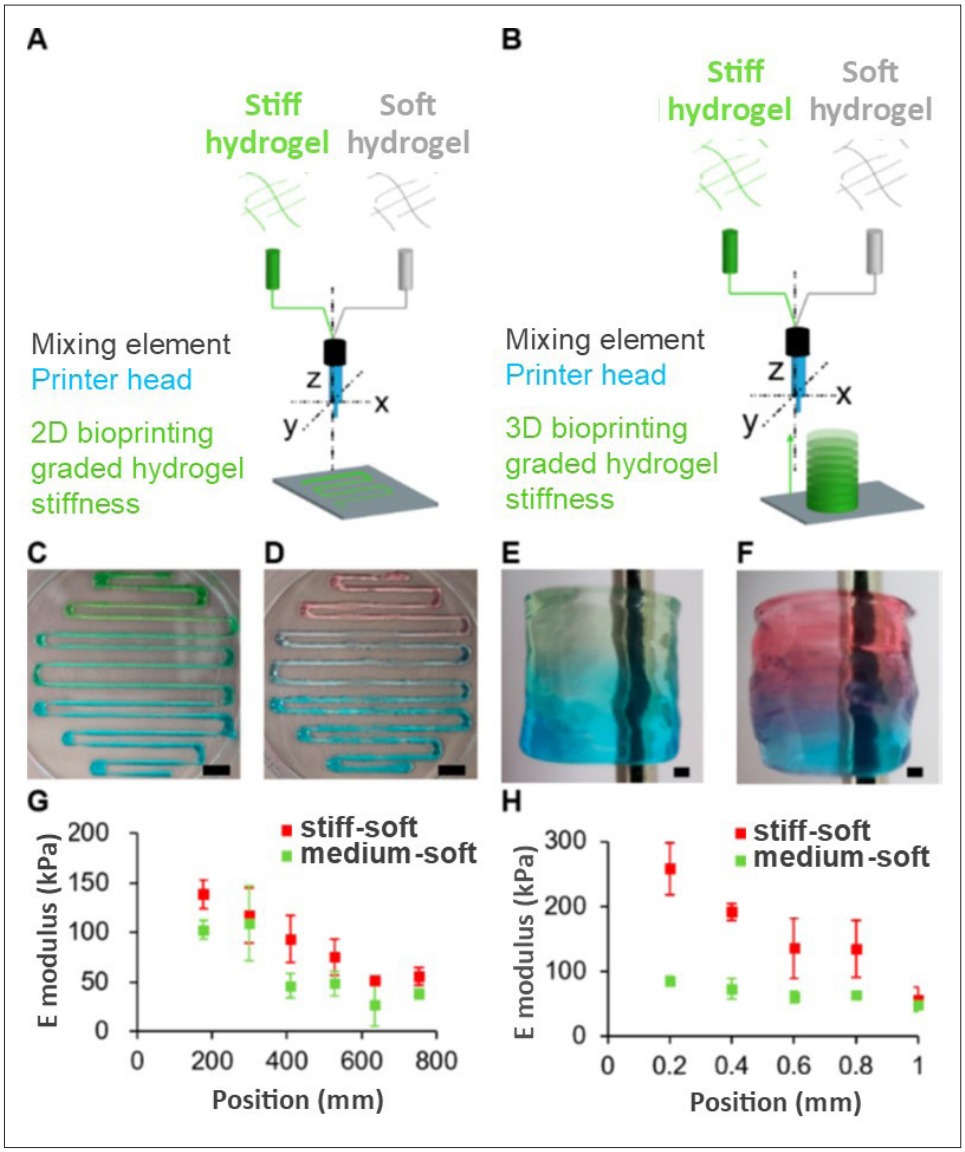

Figure 12. Multi-material bioprinting of 2D and 3D structures with a stiffness gradient, controlled by mixing two carboxylated agarose hydrogels with different stiffness. (A) printing of 2D structures with controlled stiffness gradient (B) printing of 3D structures with controlled stiffness gradient, (C) 2D structure with medium-soft stiffness gradient, (D) 2D structure with stiff-soft stiffness gradient, (E) 3D structure with medium-soft stiffness gradient, (F) 3D structure with stiff-soft stiffness gradient. (G) Variation of elastic modulus with position in 2D printed structures, (H) variation of elastic modulus with position in 3D printed structures.[164] Soft, medium, and stiff carboxylated agarose hydrogels are colored in blue, green, and red respectively. Scale bars: 10 mm for C, D, and 1 mm for E, F. Abbreviation: E modulus, elastic modulus. Adapted from ref.[164] Copyright © 2021 American Chemical Society.

$$\frac{\partial \rho}{\partial t} + \nabla \cdot \rho \vec{U} = 0 \qquad \text{(XXXVI)}$$

(ii) Momentum transport[70]:

$$\frac{D\left(\rho \vec{U}\right)}{Dt} = -\nabla p + \nabla \cdot \bar{\bar{\tau}} + \rho \vec{g} \qquad \text{(XXXVII)}$$

where $\frac{D}{Dt}$ is the material derivative; $\vec{U}$ and $\vec{g}$ are vectors representing the fluid velocity and gravitational acceleration, respectively; p and ρ denote the pressure and density of the fluid, respectively; and τ is the stress tensor.

The boundary condition at the inlet of a dispensing head is the given pressure or inlet velocity for pneumatic or piston-driven systems, respectively. The nozzle outlet is set to ambient pressure, and a no-slip boundary condition

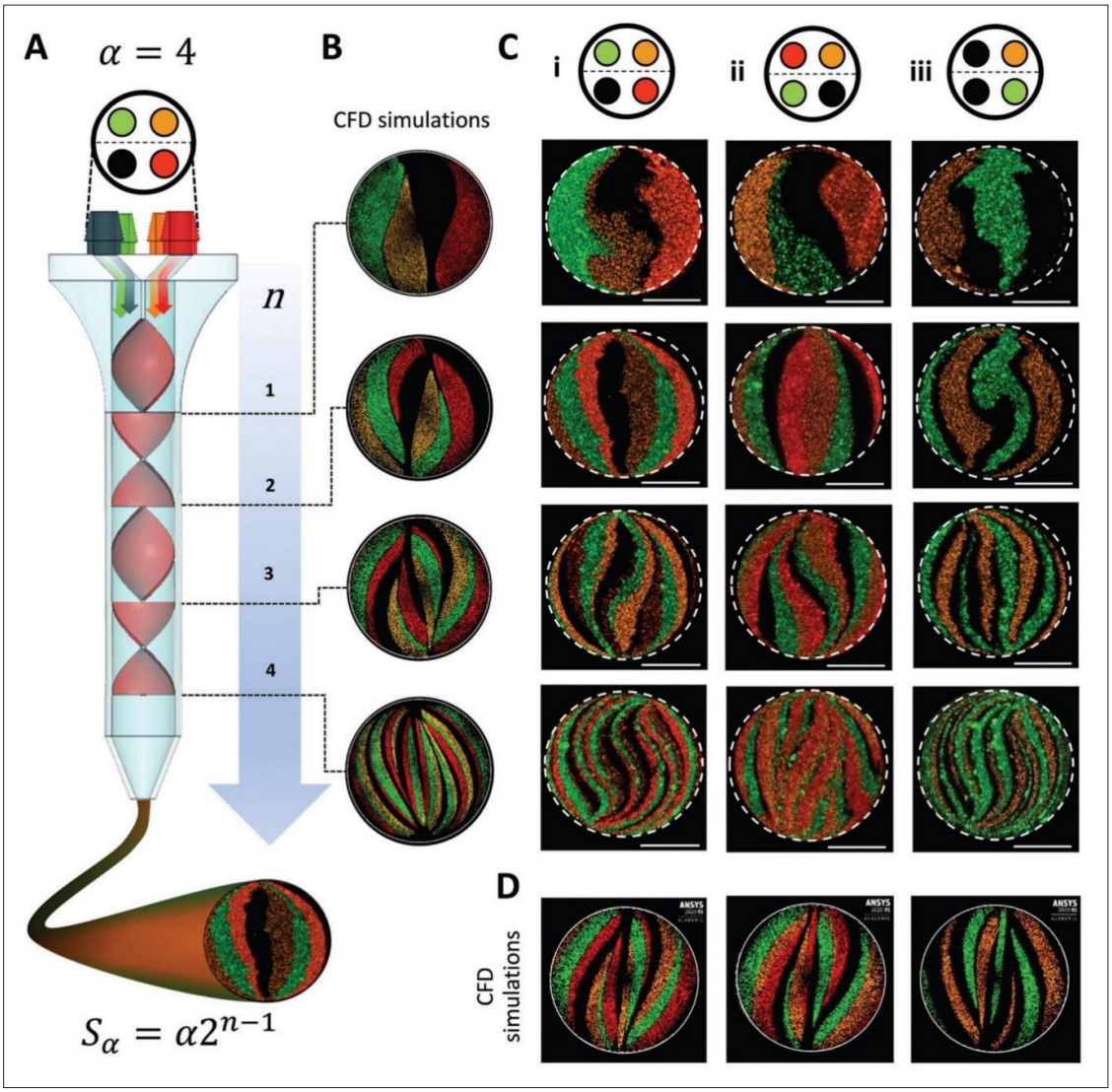

Figure 13. Chaotic multi-material printing using the various number of inlets and helical mixing elements; (A) design of head with axial inlets, (B) predictions of internal multi-layer structure inside fiber by computational simulations, (C) multi-layer structures inside the fibers printed with different numbers of mixing elements and axial inlets, and (D) computational simulation results for the case with three mixing elements. Abbreviation: CFD, computational fluid dynamics. Reprinted with permission from ref.[169] Copyright © 2023 Wiley-VCH GmbH.

is applied on solid walls. Some polymer solutions or melts may exhibit slip on the solid wall. It should be examined by performing steady shear tests with different gaps using a parallel plate rheometer.[78] Based on a power-law fluid model, the slip condition can be written as[176]:

$$U_{slip} = \frac{\delta_t \tau_w^{1/n}}{\eta_{app}^{1/n}} \quad \text{(XXXVIII)}$$

where η_{app} denotes the apparent viscosity of the fluid at the solid wall, τ_w is wall shear stress, and δ_t is the thickness of the slip layer. The solution of **Equations XXVII and XXVIII** requires a constitutive relation to relate the stress tensor ($\overline{\overline{\tau}}$) to the strain rate tensor ($\overline{\overline{\gamma}}$); it could be one of the models described in Table 3.

Numerical simulations of the bioprinting process have primarily focused on understanding the flow of biomaterials within the bioprinter head. CFD simulations have been employed to examine the impact of parameters related to the dispensing system in two main areas. One

approach explores the effect of nozzle geometry while considering specific biomaterial properties,[176–178] and the other investigates the dynamics of biomaterials for a fixed nozzle geometry.[179–181] Most studies have neglected cell-biomaterial interactions and model the bioink as a single-phase non-Newtonian fluid due to the low volume fraction of cells in bioinks.[63,182,183] However, several researchers have utilized simulations to study cell deformation during the bioprinting procedure.[177,184]

Computational fluid dynamics (CFD) simulations have been used to predict the shear stress distribution in chamfered (straight) and tapered (conical) dispensing nozzles, with results indicating a higher shear stress level inside chamfered nozzles compared to a tapered geometry.[185,186] The higher shear stress can lead to lower cell viability when using chamfered nozzles.[88] Most CFD studies have focused on the flow through the dispensing nozzle and have explored the effects of printing pressure, nozzle geometry, and rheological properties of bioinks on the shear stress exerted on the cells in the bioink.[63,182,183] The distribution of wall shear stress for different nozzle geometries suggests that optimizing nozzle geometry involves balancing printing resolution and cell viability. The nozzles featuring a smaller convergence angle tend to produce higher wall shear stress (Figure 14A–C), potentially leading to adverse effects on cell viability.[187,188]

Numerical simulations have also been employed to model the flow of bioinks inside coaxial dispensing systems. These simulations have been used to understand the parameters controlling the diameter, velocity, and mass of the gel fiber near the nozzle outlet during the extrusion of hollow strands,[189,190] using biomaterials such as alginate with a crosslinker.

In cases where extrusion involves mixing two or more biomaterials, and assuming the effect of cells in the flow of bioinks is negligible, the mixing of bioinks can be simulated by solving of the components' transport equations (excluding considerations of chemical reactions and phase changes).[191]

$$\frac{D\left(\rho Y_i\right)}{Dt} = -\nabla \cdot \vec{J}_i \qquad \text{(XXXIX)}$$

where

$$\vec{J}_i = -\rho D_{i,m} \nabla Y_i \qquad \text{(XL)}$$

and Y_i is mass fraction of component i; and $D_{i,m}$ is its diffusion coefficient.

Given the widespread use of helical mixers in industrial applications, numerous numerical simulations are available in the literature that study the performance of these mixers and the improvement of their geometry. Numerical simulations of mixing two miscible biomaterials in an extrusion bioprinting head equipped with a helical mixer revealed an improvement in mixing efficiency as the power-law index of biomaterials increases.[192]

Computational fluid dynamics (CFD) has been used to simulate the process forces or pressure work required for cell-damage predictions based on various cell damage models. Ning et al.[63] and Han et al.[73] employed CFD to provide information on the pressure drop and stress distribution in the flow of alginate-based bioinks as they are extruded through chamfered dispensing nozzles. They modeled bioinks, including alginate/RSC96 Schwann cells, alginate/L8 myoblast cells,[63] and alginate/human dermal fibroblasts cells,[73] using the power-law non-Newtonian model in their numerical simulations and analytical calculations. Chirianni et al.[74] used CFD to validate their cell-damage model with previous experimental test results. They modeled bioinks based on alginate-based human dermal fibroblasts as a Carreau-Yasuda non-Newtonian fluid in their numerical simulations. Their numerical results for the distribution of shear and extensional stresses magnitude inside the nozzle are displayed in Figure 14D and E. This figure illustrates how extensional stress peaks in the contraction region of the nozzle.

Chávez-Madero et al.[162] and Ceballos-González et al.169 used CFD simulation and massless particle tracking methods to predict the thickness and patterns of the internal multi-layer structures generated by a helical mixer. The results were in good agreement with experimental visualization and the theoretical average thickness of the internal layers (Figure 13B–D).

Computational fluid dynamics (CFD) simulations play a crucial role in microfluidic studies by providing data about the distribution of velocity, pressure, concentrations, and shear stress, which can be challenging to measure experimentally. Several computational simulations have been conducted by researchers to investigate the effects of shear stress on cell viability and explore the flow of various biomaterials inside customized nozzle geometries.[178,193]

Zaeri et al.[113] studied the flow in a coaxial microfluidic bioprinting chip numerically, where CFD was used to study the effect of printing parameters on the geometrical outcome of the printed fiber. Their simulation did not consider the deposition of fiber on the printing stage; instead, the structure of the fiber was investigated based on the flow structure at the nozzle outlet cross-section. They

modeled the alginate-based bioink as a power-law fluid and the crosslinker (calcium chloride) as a Newtonian fluid. Zarei et al.[113] illustrated the dripping and jetting flow regimes for coaxial flow of alginate in the sample (core) and calcium chloride in the sheath layer with various flow ratios (Figure 15). They correlated the droplet generation frequency to the ratio of Reynolds number for the sheath to core (sample) flows. In a similar numerical study on coaxial printing of core (inner), sample (middle), and sheath (outer) layers, Etefagh et al.[114] demonstrated that their numerical predictions for layer thickness in coaxial fibers closely matched experimental measurements, validating the capability of CFD in the design and optimization of printing parameters to achieve the desired internal structure in multi-layer fibers.

While many previous studies using CFD have focused on bioink flow inside the nozzle, numerical studies on the deposition of bioink fibers on the printing stage have been emerging recently. The deposition of fibers on the printing stage is of a two-phase flow problem, which requires managing two separate media and adding additional differential equations and boundary conditions to the governing equations. In addition to the boundary conditions, such as pressure (or velocity) inlet and solid walls, interface boundary conditions must be established to balance the forces at the interface of the fiber with the ambient fluid (air or crosslinker)[194] during fiber deposition. Moreover, methods for interface tracking/capturing, such as volume of fluid (VOF) or level-set[194] methods, are required to calculate the displacement and deformation of the fiber's interface with the ambient fluid.

Chand et al.[187] studied the deposition of fibers on the printing stage with various printing speeds. They modeled the alginate/NFC bioink (ink6040) as a power-law fluid and used the VOF method to capture the deformation of the interface between the deposited fiber and ambient air during the deposition process. Talluri et al.[195] also used the VOF method to study the effect of bioink rheology on the stability of deposited fibers and provided a stability map based on printing speed, nozzle-stage spacing, and the power-law index of the bioink. Ramezani et al.[195] used the level-set method to study the dynamics of a chitosan-based bioink fiber, modeled with the Carreau-Yasuda model, as it is deposited inside a vertical channel.

Due to the limited detailed data on the viscoelastic behavior of most bioinks, researchers often rely on time-independent models to describe their flow behavior in CFD simulations. Simulating viscoelastic biomaterials with time-independent non-Newtonian models like Herschel–Bulkley can lead to an overestimation of the mass flow rate as the printing pressure increases. The elasticity of the bioink reduces the flow rate within the printing head by hampering the flow inside the nozzle.[196] To date, no CFD studies have specifically addressed the extrusion of bioink through the nozzle of a bioprinter while considering its viscoelastic behavior. A CFD study conducted by Göhl et al.[112] incorporated the viscoelastic properties of the fluid, modeling the flow of biomaterial as it is deposited on the printing stage. While this study did not cover the flow inside the printing head, it provides valuable insights into the numerical modeling of viscoelastic biomaterial flow.

Göhl et al.[112] employed CFD to simulate viscoelastic biomaterial deposition and predict the final shape of printed filaments. They investigated various printing parameters, including printing speed and nozzle height, to understand their impact on the printing process. In their study, they modeled the rheological behavior of the bioinks, which consisted of cellulose nanofibril (CNF) dispersions in an alginate solution, using the linear PTT model.[197,198] Additionally, they modeled surface tension forces using the continuum surface force method.[199] For a solution with viscoelastic behavior, the split form of the stress tensor ($\bar{\bar{\tau}}$) is given by[78]

$$\bar{\bar{\tau}} = \bar{\bar{\tau}}_p + \eta_s \bar{\bar{\dot{\gamma}}} \tag{XLI}$$

where η_s is the solvent viscosity, and $\bar{\bar{\tau}}_p$ is the polymer contribution to the stress tensor. The polymeric portion of stress tensor ($\bar{\bar{\tau}}_p$) for a PTT fluid is defined by[197,198]

$$\lambda\left[\frac{\partial \bar{\bar{\tau}}_p}{\partial t} + \nabla\cdot\left(\vec{U}\bar{\bar{\tau}}_p\right)\right] + f\left(\tau_p\right)\bar{\bar{\tau}}_p = \eta_p \left(\nabla\vec{U} + \nabla\vec{U}^T\right) + \lambda\left(\bar{\bar{\tau}}_p.\nabla\vec{U} + \nabla\vec{U}^T\cdot\bar{\bar{\tau}}_p\right) \tag{XLII}$$

and

$$ft\left(\tau_p\right) = 1 + \frac{\lambda\varepsilon}{\eta_p}\ r\left(\bar{\bar{\tau}}_p\right) \tag{XLIII}$$

where *tr*( ) represents the trace operator; λ and ε are the relaxation time and the extension-related parameter of the PTT model, respectively. The limiting case $\varepsilon = 0$ represents the Oldroyd-B viscoelastic model,[200] while $\lambda = 0$ represents a Newtonian fluid. The numerical results from Göhl et al.[112] exhibtied excellent agreement with experimental data (Figure 16), demonstrating the capability of

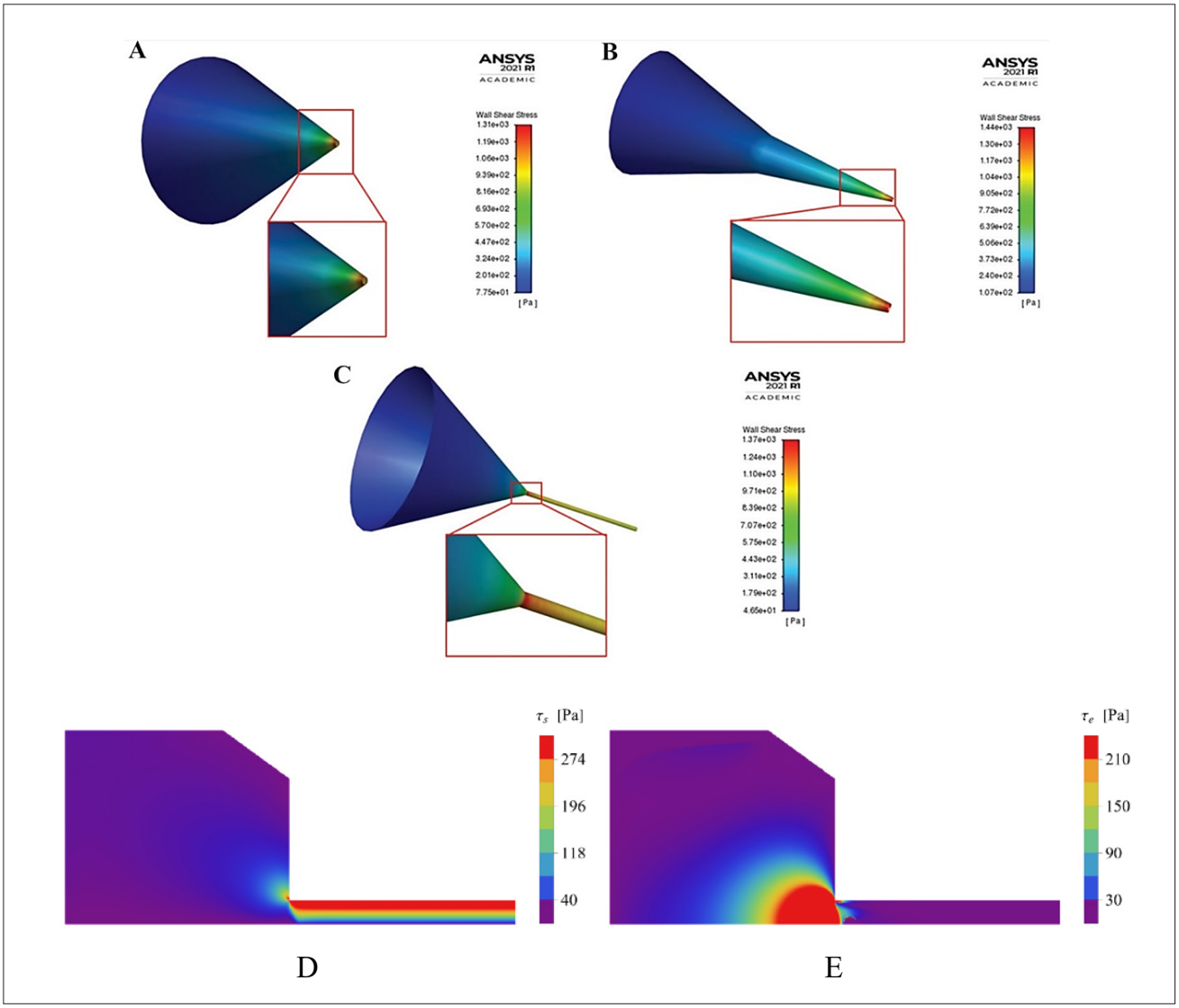

Figure 14. Numerical simulation results for the distribution of shear and extensional stresses inside the nozzle during extrusion bioprinting (A–C). Numerical results by Chand et al.[187] for extrusion through various dispensing nozzle: distribution of wall shear stress for (A) tapered conical, (B) conical, and (C) cylindrical nozzles. Reprinted with permission from ref.[187] (D and E) Numerical results of Chirianni et al.[74] for extrusion through chamfered nozzle: distribution of stresses on the middle plane of the nozzle; (D) shear stress, and (E) extensional stress in the contraction region and needle. Reprinted with permission from ref.[74] Copyright © (2024) Elsevier.

CFD to accurately predict the outcomes of the bioprinting process.

There are various viscoelastic models, each with distinct constitutive equations, that should be selected based on the results of rheological tests. The process of fitting a viscoelastic model to the results of rheological tests and determining the parameters of the constitutive equation requires sophisticated mathematical calculations.[201,202] By selecting the suitable viscoelastic model for various bioinks and using CFD for simulation of the bioink flow during the extrusion and deposition on the stage, researchers can obtain more reliable information about the process forces, fiber diameter, and even the printability of the bioink.

The constitutive equations of current viscoelastic models are developed for single-component fluids with constant or temperature-dependent viscoelastic properties. However, the simulation of multi-material bioprinting, which involves mixing miscible viscoelastic fluids, requires viscoelastic models with composition-

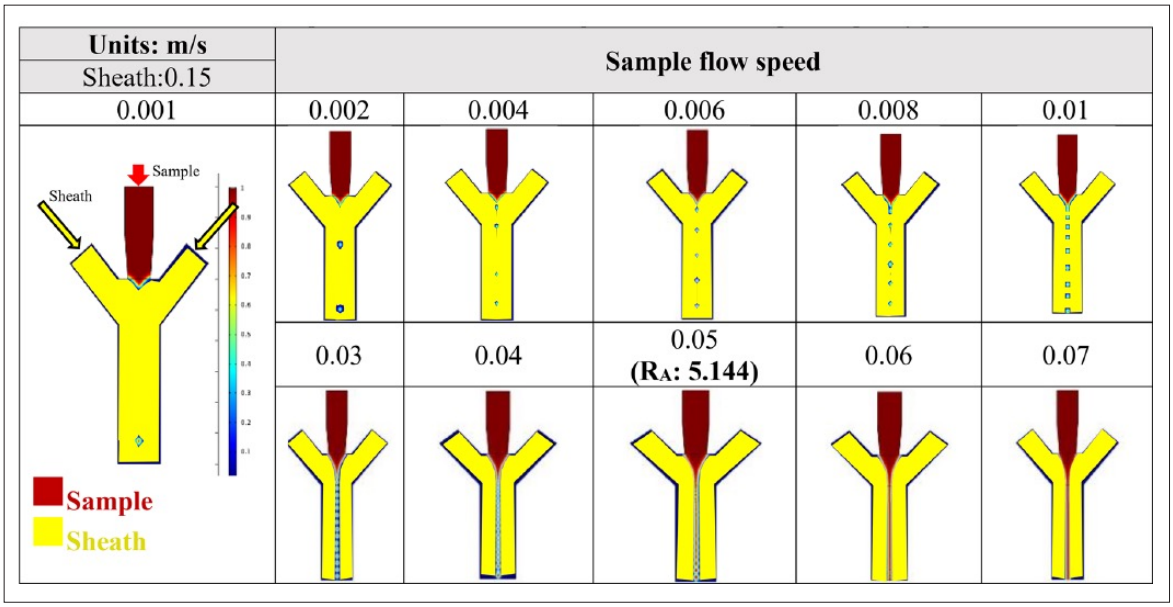

Figure 15. Numerical simulation of coaxial flow in a microfluidic chip. Transition from dripping to jetting regime by change in sample (core) stream flow velocity. Adapted from ref.[114]

dependent constitutive equations. Therefore, the accurate simulation of multi-material printing with viscoelastic models remains a significant challenge.

6. Conclusion

Extrusion bioprinting is an emerging technology for fabricating intricate and diverse structures for various biomedical engineering applications, where fluid mechanics are involved in determining the outcomes of the printed structures. This review surveys ongoing research on extrusion bioprinting, with a focus on its recent developments and advances from the perspective of fluid mechanics. During extrusion and deposition (prior to crosslinking), the biomaterial is in either fluid or semi-fluid states. Therefore, fluid mechanics plays a crucial

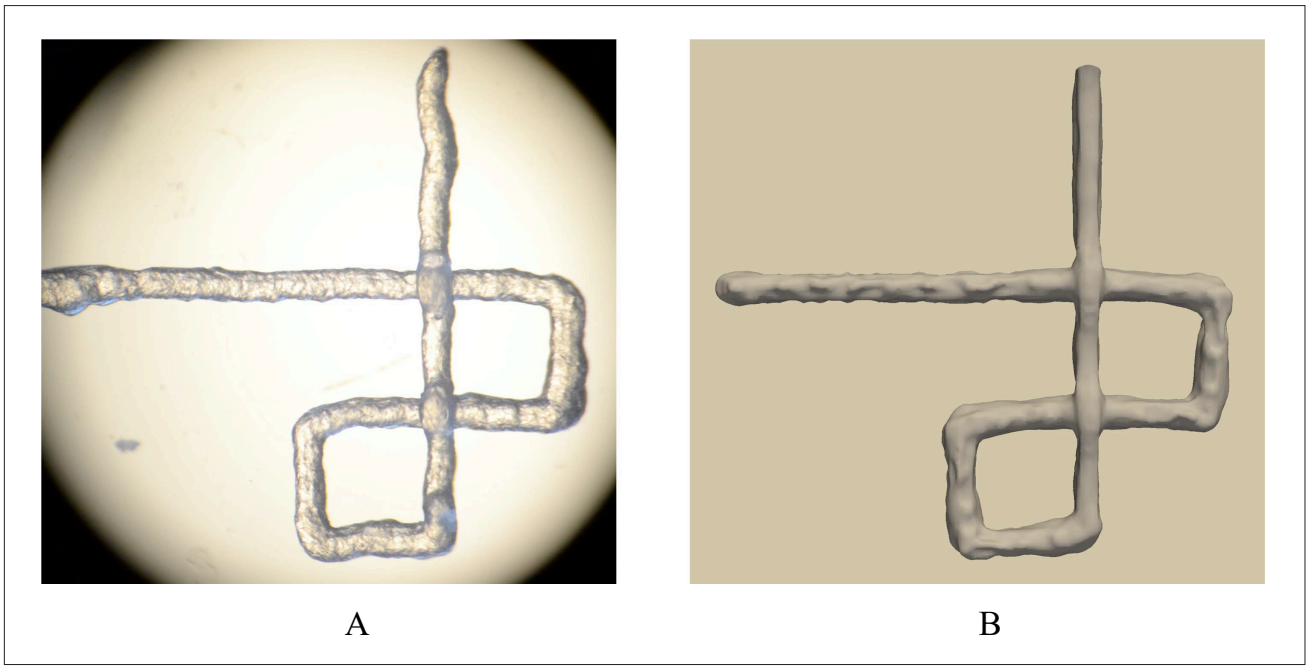

Figure 16. Comparison of (A) printed grid structure and (B) simulation result for printing of 4% cellulose nanofibril (CNF) ink. Reproduced with permission from ref.[112] Copyright © 2018 IOP Publishing.

role in the bioprinting process. Successful printing with good extrudability and filament fidelity requires a shear-thinning (thixotropic) bioink with a reasonable viscosity recovery rate. An increase in the elastic modulus of a viscoelastic bioink improves filament fidelity but reduces cell viability. Therefore, a successful bioprinting requires the careful preparation of bioink and rigorous selection of printing parameters, such as extrusion pressure, printing speed, and nozzle size. As an emerging aspect of extrusion bioprinting, multi-material bioprinting has garnered significant attention. Printing multi-material filaments with accurate control over their composition is key to addressing the challenge of printing heterogeneous constructs that mimic the zonal heterogeneity of native tissues. Although various multi-material printing methods have been developed and have achieved some success, printing a construct that can mimic the structure and cellular composition of natural tissue remains a significant challenge. This challenge is associated with several issues, including the printability and discrepancies between the printed construct and its CAD design, as well as difficulties in mixing and flow control that can affect the mechanical properties of the construct and potentially damage cells. Furthermore, reducing the transition length during the composition change can improve the resolution of multi-material bioprinting heads, especially when printing constructs with zonal heterogeneity.

A well-designed multi-material printing head can alleviate the negative effects of the shear and extensional stresses applied on the cell during extrusion. Simulations play a crucial role in the design of multi-material heads, as they provide detailed information about the stress field and concentration of precursors. This allows designers to understand the dynamics of the head and address potential operational issues before fabrication. The primary challenge in CFD simulations of the bioprinting process is accurately representating the rheological behavior of bioinks due to their time-dependent and viscoelastic natures. It becomes more challenging or worse for multi-material heads, where the viscoelastic properties of bioinks change during mixing, thereby requiring more complex constitutive equations for modeling the viscoelastic behavior of their mixtures. Finding suitable viscoelastic models for various bioinks and using CFD to simulate bioink flow during extrusion and deposition on the stage can provide much reliable information on the process-induced forces, fiber diameter, and printability of the bioink. Such information would be difficult, if not impossible, to capture through experiments alone. Developing composition-dependent constitutive equations that can model the behavior of miscible viscoelastic fluids as they are being mixed remains a significant challenge in this field, highlighting a critical area for future research.

Acknowledgments

The authors would like to thank the University of Saskatchewan and the Natural Sciences and Engineering Research Council (NSERC) for their financial support.

Funding

This research was financially supported by the University of Saskatchewan Dean's Scholarship and the Devolved Scholarship from the Department of Mechanical Engineering for the first author, and by the Natural Sciences and Engineering Research Council (NSERC) funds for the co-authors. Grant numbers: RGPIN 06396-2019, RGPIN 04981-2022

Conflict of interest

Xiongbiao Chen serves as the Editorial Board Member of the journal, but did not in any way involve in the editorial and peer-review process conducted for this paper, directly or indirectly. Other authors declare they have no competing interests.

Author contributions

Conceptualization: Reza Gharraei, Donald J. Bergstrom, Xiongbiao Chen
Supervision: Xiongbiao Chen, Donald J. Bergstrom
Writing – original draft: Reza Gharraei
Writing – review & editing: Donald J. Bergstrom, Xiongbiao Chen, Reza Gharraei

Ethics approval and consent to participate

Not applicable.

Consent for publication

Not applicable.

Availability of data

Not applicable.

References

1. Derakhshanfar S, Mbeleck R, Xu K, Zhang X, Zhong W, Xing M. 3D bioprinting for biomedical devices and tissue engineering: a review of recent trends and advances. *Bioact Mater*. 2018;3(2):144-156. doi: 10.1016/j.bioactmat.2017.11.008
2. DeSimone E, Schacht K, Jungst T, Groll J, Scheibel T. Biofabrication of 3D constructs: fabrication technologies and spider silk proteins as bioinks. *Pure Appl Chem*. 2015;87(8):737-749. doi: 10.1515/pac-2015-0106

3. Gao W, Zhang Y, Ramanujan D, et al. The status, challenges, and future of additive manufacturing in engineering. *Computer-Aided Design*. 2015;69:65-89. doi: 10.1016/j.cad.2015.04.001

4. Ozbolat IT, Yin Yu. Bioprinting toward organ fabrication: challenges and future trends. *IEEE Trans Biomed Eng*. 2013;60(3):691-699. doi: 10.1109/TBME.2013.2243912

5. Farzin A, Miri AK, Sharifi F, et al. 3D-printed sugar-based stents facilitating vascular anastomosis. *Adv Healthc Mater*. 2018;7(24):1800702. doi: 10.1002/adhm.201800702

6. Do AV, Khorsand B, Geary SM, Salem AK. 3D printing of scaffolds for tissue regeneration applications. *Adv Healthc Mater*. 2015;4(12):1742-1762. doi: 10.1002/adhm.201500168

7. Faramarzi N, Yazdi IK, Nabavinia M, et al. Patient-specific bioinks for 3D bioprinting of tissue engineering scaffolds. *Adv Healthc Mater*. 2018;7(11):1701347. doi: 10.1002/adhm.201701347

8. Ozbolat IT, Hospodiuk M. Current advances and future perspectives in extrusion-based bioprinting. *Biomaterials*. 2016;76:321-343. doi: 10.1016/j.biomaterials.2015.10.076

9. Bakarich SE, Gorkin R, Gately R, Naficy S, in het Panhuis M, Spinks GM. 3D printing of tough hydrogel composites with spatially varying materials properties. *Addit Manuf*. 2017;14:24-30. doi: 10.1016/j.addma.2016.12.003

10. Kirchmajer DM, Gorkin R, In Het Panhuis M. An overview of the suitability of hydrogel-forming polymers for extrusion-based 3D-printing. *J Mater Chem B*. 2015;3: 4105-4117. doi: 10.1039/c5tb00393h

11. Tavafoghi M, Darabi MA, Mahmoodi M, et al. Multimaterial bioprinting and combination of processing techniques towards the fabrication of biomimetic tissues and organs. *Biofabrication*. 2021;13(4):042002. doi: 10.1088/1758-5090/ac0b9a

12. Schwab A, Levato R, D'Este M, Piluso S, Eglin D, Malda J. Printability and shape fidelity of bioinks in 3D bioprinting. *Chem Rev*. 2020;120(19):11028-11055. doi: 10.1021/acs.chemrev.0c00084

13. Richard C, Neild A, Cadarso VJ. The emerging role of microfluidics in multi-material 3D bioprinting. *Lab Chip*. 2020;20(12):2044-2056. doi: 10.1039/c9lc01184f

14. Askari M, Afzali Naniz M, Kouhi M, Saberi A, Zolfagharian A, Bodaghi M. Recent progress in extrusion 3D bioprinting of hydrogel biomaterials for tissue regeneration: a comprehensive review with focus on advanced fabrication techniques. *Biomater Sci*. 2021;9(3):535-573. doi: 10.1039/d0bm00973c

15. Zhang J, Allardyce BJ, Rajkhowa R, et al. 3D printing of silk particle-reinforced chitosan hydrogel structures and their properties. *ACS Biomater Sci Eng*. 2018;4(8):3036-3046. doi: 10.1021/acsbiomaterials.8b00804

16. Aydogdu MO, Oner ET, Ekren N, et al. Comparative characterization of the hydrogel added PLA/β-TCP scaffolds produced by 3D bioprinting. *Bioprinting*. 2019; 13:e00046. doi: 10.1016/j.bprint.2019.e00046

17. Yan J, Wang Y, Zhang X, et al. Snakegourd root/Astragalus polysaccharide hydrogel preparation and application in 3D printing. *Int J Biol Macromol*. 2019;121:309-316. doi: 10.1016/j.ijbiomac.2018.10.008

18. Yazdanpanah Z, Johnston JD, Cooper DML, Chen X. 3D bioprinted scaffolds for bone tissue engineering: state-of-the-art and emerging technologies. *Front Bioeng Biotechnol*. 2022;10(April):824156. doi: 10.3389/fbioe.2022.824156

19. Ratner BD, Bryant SJ. Biomaterials: where we have been and where we are going. *Annu Rev Biomed Eng*. 2004;6:41-75. doi: 10.1146/annurev.bioeng.6.040803.140027

20. Caló E, Khutoryanskiy VV. Biomedical applications of hydrogels: a review of patents and commercial products. *Eur Polym J*. 2015;65:252-267. doi: 10.1016/j.eurpolymj.2014.11.024

21. Roehm KD, Madihally SV. Bioprinted chitosan-gelatin thermosensitive hydrogels using an inexpensive 3D printer. *Biofabrication*. 2018;10(1):015002. doi: 10.1088/1758-5090/aa96dd

22. Mora-Boza A, Włodarczyk-Biegun MK, Del Campo A, Vázquez-Lasa B, Román JS. Glycerylphytate as an ionic crosslinker for 3D printing of multi-layered scaffolds with improved shape fidelity and biological features. *Biomater Sci*. 2019;8(1):506-516. doi: 10.1039/c9bm01271k

23. Chen XB, Fazel Anvari-Yazdi A, Duan X, et al. Biomaterials / bioinks and extrusion bioprinting. *Bioact Mater*. 2023;28:511-536. doi: 10.1016/j.bioactmat.2023.06.006

24. Akkineni AR, Ahlfeld T, Lode A, Gelinsky M. A versatile method for combining different biopolymers in a core/ shell fashion by 3D plotting to achieve mechanically robust constructs. *Biofabrication*. 2016;8(4):045001. doi: 10.1088/1758-5090/8/4/045001

25. Liu X, Zhao K, Gong T, et al. Delivery of growth factors using a smart porous nanocomposite scaffold to repair a mandibular bone defect. *Biomacromolecules*. 2014;15(3):1019-1030. doi: 10.1021/bm401911p

26. Augst AD, Kong HJ, Mooney DJ. Alginate hydrogels as biomaterials. *Macromol Biosci*. 2006;6(8):623-633. doi: 10.1002/mabi.200600069

27. Izadifar Z, Chang T, Kulyk W, Chen X, Eames BF. Analyzing biological performance of 3D-printed, cell-impregnated hybrid constructs for cartilage tissue engineering. *Tissue Eng Part C Methods*. 2016;22:173-188. doi: 10.1089/ten.tec.2015.0307

28. Naghieh S, Sarker M, Izadifar M, Chen X. Dispensing-based bioprinting of mechanically-functional hybrid scaffolds with vessel-like channels for tissue engineering applications – a brief review. *J Mech Behav Biomed Mater*. 2018;78:298-314. doi: 10.1016/j.jmbbm.2017.11.037

29. Kiyotake EA, Douglas AW, Thomas EE, Nimmo SL, Detamore MS. Development and quantitative characterization of the precursor rheology of hyaluronic acid hydrogels for bioprinting. *Acta Biomater*. 2019;95:176-187. doi: 10.1016/j.actbio.2019.01.041

30. Hölzl K, Lin S, Tytgat L, Van Vlierberghe S, Gu L, Ovsianikov A. Bioink properties before, during and after 3D bioprinting. *Biofabrication*. 2016;8(3):032002. doi: 10.1088/1758-5090/8/3/032002

31. Monika Hospodiuk KKMMDITO. *Extrusion-Based Biofabrication in Tissue Engineering and Regenerative Medicine*. 1st ed. Springer; 2018.

32. Khalil S, Nam J, Sun W. Multi-nozzle deposition for construction of 3D biopolymer tissue scaffolds. *Rapid Prototyp J*. 2005;11(1):9-17. doi: 10.1108/13552540510573347

33. Boularaoui S, Al Hussein G, Khan KA, Christoforou N, Stefanini C. An overview of extrusion-based bioprinting with a focus on induced shear stress and its effect on cell viability. *Bioprinting*. 2020;20(August):e00093. doi: 10.1016/j.bprint.2020.e00093

34. Ning L, Yang B, Mohabatpour F, et al. Process-induced cell damage: pneumatic versus screw-driven bioprinting. *Biofabrication*. 2020;12(2):025011. doi: 10.1088/1758-5090/ab5f53

35. Murphy SV, Atala A. 3D bioprinting of tissues and organs. *Nat Biotechnol*. 2014;32(8):773-785. doi: 10.1038/nbt.2958

36. Daniel X. B. Chen. *Extrusion Bioprinting of Scaffolds for Tissue Engineering Applications*. 1st ed. Springer Nature; 2019.

37. Malekpour A, Chen X. Printability and cell viability in extrusion-based bioprinting from experimental, computational, and machine learning views. *J Funct Biomater*. 2022;13(2):40. doi: 10.3390/jfb13020040

38. Fu Z, Naghieh S, Xu C, Wang C, Sun W, Chen X. Printability in extrusion bioprinting. *Biofabrication*. 2021;13(3):033001. doi: 10.1088/1758-5090/abe7ab

39. Gillispie G, Prim P, Copus J, et al. Assessment methodologies for extrusion-based bioink printability. *Biofabrication*. 2020;12(2):22003. doi: 10.1088/1758-5090/ab6f0d

40. Xu X, Jagota A, Peng S, Luo D, Wu M, Hui CY. Gravity and surface tension effects on the shape change of soft materials. *Langmuir*. 2013;29(27):8665-8674. doi: 10.1021/la400921h

41. Hospodiuk M, Dey M, Sosnoski D, Ozbolat IT. The bioink: a comprehensive review on bioprintable materials. *Biotechnol Adv*. 2017;35(2):217-239. doi: 10.1016/j.biotechadv.2016.12.006

42. Petta D, Grijpma DW, Alini M, Eglin D, D'Este M. Three-dimensional printing of a tyramine hyaluronan derivative with double gelation mechanism for independent tuning of shear thinning and postprinting curing. *ACS Biomater Sci Eng*. 2018;4(8):3088-3098. doi: 10.1021/acsbiomaterials.8b00416

43. Gao T, Gillispie GJ, Copus JS, et al. Optimization of gelatin–alginate composite bioink printability using rheological parameters: a systematic approach. *Biofabrication*. 2018;10(3):034106. doi: 10.1088/1758-5090/aacdc7

44. Saha D, Bhattacharya S. Hydrocolloids as thickening and gelling agents in food: a critical review. *J Food Sci Technol*. 2010;47(6):587-597. doi: 10.1007/s13197-010-0162-6

45. He Y, Yang F, Zhao H, Gao Q, Xia B, Fu J. Research on the printability of hydrogels in 3D bioprinting. *Sci Rep*. 2016;6(1):29977. doi: 10.1038/srep29977

46. Soltan N, Ning L, Mohabatpour F, Papagerakis P, Chen X. Printability and cell viability in bioprinting alginate dialdehyde-gelatin scaffolds. *ACS Biomater Sci Eng*. 2019;5(6):2976-2987. doi: 10.1021/acsbiomaterials.9b00167

47. Lee JM, Ng WL, Yeong WY. Resolution and shape in bioprinting: strategizing towards complex tissue and organ printing. *Appl Phys Rev*. 2019;6(1):011307. doi: 10.1063/1.5053909

48. Ribeiro A, Blokzijl MM, Levato R, et al. Assessing bioink shape fidelity to aid material development in 3D bioprinting. *Biofabrication*. 2017;10(1):014102. doi: 10.1088/1758-5090/aa90e2

49. Ouyang L, Yao R, Zhao Y, Sun W. Effect of bioink properties on printability and cell viability for 3D bioplotting of embryonic stem cells. *Biofabrication*. 2016;8(3):035020. doi: 10.1088/1758-5090/8/3/035020

50. Herrada-Manchón H, Fernández MA, Aguilar E. Essential guide to hydrogel rheology in extrusion 3D printing: how to measure it and why it matters? *Gels*. 2023;9(7):517. doi: 10.3390/gels9070517

51. Cooke ME, Rosenzweig DH. The rheology of direct and suspended extrusion bioprinting. *APL Bioeng*. 2021;5(1):011502. doi: 10.1063/5.0031475

52. Clasen C, Entov V, Bico J, McKinley GH. `Gobbling Drops´: the jetting / dripping transition in flows of polymeric liquids. *J Fluid Mech*. 2009;636:5-40. doi: 10.1017/S0022112009008143

53. Clanet C, Lasheras JC. Transition from dripping to jetting. *J Fluid Mech*. 1999;383:307-326. doi: 10.1017/S0022112098004066

54. Philip M. Gerhart, Andrew L. Gerhart, John I. Hochstein. *Fundamentals of Fluid Mechanics*. 8th ed. Wiley; 2018.

55. Liliang Ouyang. 3D bioprinting of thermal-sensitive bioink. In: Study on Microextrusion-Based 3D Bioprinting and Bioink Crosslinking Mechanisms. Springer; 2019.

56. Savart F. M'emoire sur la constitution des veines liquides lanc'ees par des ori ces circulaires en mince paroi. *Ann Chim (Paris)*. 1833;53:337-386.

57. Plateau J. Statique Expe'rimentale et The'orique des Liquides. In: Gauthier-Villars et Cie; 1873.

58. Lord R. Investigations in capillarity: the size of drops. - The liberation of gas from supersaturated solutions. - Colliding jets. - The tension of contaminated water-surfaces. Curious observation. *Philos Magaz J Sci*. 1899;48(293):321-337.

59. Chen XB, Ke H. Effects of fluid properties on dispensing processes for electronics packaging. *IEEE Trans Electron Pack Manuf*. 2006;29(2):75-82. doi: 10.1109/TEPM.2006.874964

60. De Maria C, Vozzi G, Moroni L. Multimaterial, heterogeneous, and multicellular three-dimensional bioprinting. *MRS Bull*. 2017;42(8):578-584. doi: 10.1557/mrs.2017.165

61. You F, Wu X, Zhu N, Lei M, Eames BF, Chen X. 3D printing of porous cell-laden hydrogel constructs for potential applications in cartilage tissue engineering. *ACS Biomater Sci Eng*. 2016;2(7). doi: 10.1021/acsbiomaterials.6b00258

62. Ning L, Sun H, Lelong T, et al. 3D bioprinting of scaffolds with living Schwann cells for potential nerve tissue engineering applications. *Biofabrication*. 2018;10(3):035014. doi: 10.1088/1758-5090/aacd30

63. Ning L, Betancourt N, Schreyer DJ, Chen X. Characterization of cell damage and proliferative ability during and after bioprinting. *ACS Biomater Sci Eng*. 2018;4(11):3906-3918. doi: 10.1021/acsbiomaterials.8b00714

64. Xu HQ, Liu JC, Zhang ZY, Xu CX. A review on cell damage, viability, and functionality during 3D bioprinting. *Mil Med Res*. 2022;9(1):1-15. doi: 10.1186/s40779-022-00429-5

65. Fakhruddin K, Hamzah MSA, Razak SIA. Effects of extrusion pressure and printing speed of 3D bioprinted construct on the fibroblast cells viability. *IOP Conf Ser Mater Sci Eng*. 2018;440(1):012042. doi: 10.1088/1757-899X/440/1/012042

66. Ning L, Chen X. A brief review of extrusion-based tissue scaffold bio-printing. *Biotechnol J*. 2017;12(8):1200-1210. doi: 10.1002/biot.201600671

67. Bae YB, Jang HK, Shin TH, et al. Microfluidic assessment of mechanical cell damage by extensional stress. *Lab Chip*. 2016;16(1):96-103. doi: 10.1039/C5LC01006C

68. Aguado BA, Mulyasasmita W, Su J, Lampe KJ, Heilshorn SC. Improving viability of stem cells during syringe needle flow through the design of hydrogel cell carriers. *Tissue Eng Part A*. 2012;18(7-8):806-815. doi: 10.1089/ten.tea.2011.0391

69. Down LA, Papavassiliou DV, O'Rear EA. Significance of extensional stresses to red blood cell lysis in a shearing flow. *Ann Biomed Eng*. 2011;39(6):1632-1642. doi: 10.1007/s10439-011-0262-0

70. Byron Bird R, Stewart WE, Lightfoot EN. *Transport Phenomena*. 2nd ed. Wiley; 2009.

71. Cogswell FN. Measuring the extensional rheology of polymer melts. *Trans Soc Rheol*. 1972;16(3):383-403. doi: 10.1122/1.549257

72. Mitsoulis E, Hatzikiriakos SG, Christodoulou K, Vlassopoulos D. Sensitivity analysis of the Bagley correction to shear and extensional rheology. *Rheol Acta*. 1998;37(5):438-448. doi: 10.1007/s003970050131

73. Han S, Kim CM, Jin S, Kim TY. Study of the process-induced cell damage in forced extrusion bioprinting. *Biofabrication*. 2021;13(3):035048. doi: 10.1088/1758-5090/ac0415

74. Chirianni F, Vairo G, Marino M. Development of process design tools for extrusion-based bioprinting: From numerical simulations to nomograms through reduced-order modeling. *Comput Methods Appl Mech Eng*. 2024;419:116685. doi: 10.1016/j.cma.2023.116685

75. Li M, Tian X, Zhu N, Schreyer DJ, Chen X. Modeling process-induced cell damage in the biodispensing process. *Tissue Eng Part C Methods*. 2010;16(3):533-542. doi: 10.1089/ten.tec.2009.0178

76. Li M, Tian X, Schreyer DJ, Chen X. Effect of needle geometry on flow rate and cell damage in the dispensing-based biofabrication process. *Biotechnol Prog*. 2011;27(6):1777-1784. doi: 10.1002/btpr.679

77. Chhabra RP, Richardson JF. *Non-Newtonian Dlow and Applied Rheology*. Oxford, UK: Butterworth-Heinemann 2nd ed.; 2008. doi: 10.1016/B978-0-7506-8532-0.X0001-7

78. Byron Bird R, Robert C, Armstrong OH. *Dynamics of Polymeric Liquids*. 2nd ed. John Wiley & Sons; 1987. doi: 10.1002/aic.690340623

79. Cooke ME, Rosenzweig DH. The rheology of direct and suspended extrusion bioprinting. *APL Bioeng*. 2021;5(1):011502. doi: 10.1063/5.0031475

80. Ostwald W. Ueber die rechnerische Darstellung des Strukturgebietes der Viskosität. *Kolloid-Zeitschrift*. 1929;47(2):176-187. doi: 10.1007/BF01496959

81. de Waele A. Viscometry and plastometry. *J Oil and Colour Chemists' Assoc*. 1923;6(38):33-88.

82. Carreau PiJ. Rheological equations from molecular network theories. Trans Soc Rheol. 1972;16(1):99-127. doi: 10.1122/1.549276.

83. Yasuda K. *Investigation of the Analogies Berween Viscometric and Linear Viscoelastic Properties of Polystyrene Fluids*. Massachusetts Institute of Technology; 1979. http://hdl.handle.net/1721.1/16043

84. Cross MM. Rheology of non-Newtonian fluids: a new flow equation for pseudoplastic systems. *J Colloid Sci*. 1965;20(5):417-437. doi: 10.1016/0095-8522(65)90022-X

85. Herschel VWH, Bulkley R. Ronsistenzmessungen yon (ummi-BenzollGsungen). *Colloid Polym Sci*. 1926;39:291-300. doi: 10.1007/BF01432034

86. Nelson AZ, Schweizer KS, Rauzan BM, Nuzzo RG, Vermant J, Ewoldt RH. Designing and transforming yield-stress fluids. *Curr Opin Solid State Mater Sci*. 2019;23(5):100758. doi: 10.1016/j.cossms.2019.06.002

87. Pereira RF, Sousa A, Barrias CC, Bártolo PJ, Granja PL. A single-component hydrogel bioink for bioprinting of bioengineered 3D constructs for dermal tissue engineering. *Mater Horiz*. 2018;5(6):1100-1111. doi: 10.1039/C8MH00525G

88. Ramesh S, Harrysson OLA, Rao PK, et al. Extrusion bioprinting: Recent progress, challenges, and future opportunities. *Bioprinting*. 2021;21(November 2020): e00116. doi: 10.1016/j.bprint.2020.e00116

89. Nair K, Gandhi M, Khalil S, et al. Characterization of cell viability during bioprinting processes. *Biotechnol J*. 2009;4(8):1168-1177. doi: 10.1002/biot.200900004

90. Jiang Y, Zhou J, Feng C, Shi H, Zhao G, Bian Y. Rheological behavior, 3D printability and the formation of scaffolds with cellulose nanocrystals/gelatin hydrogels. *J Mater Sci*. 2020;55(33):15709-15725. doi: 10.1007/s10853-020-05128-x

91. Ouyang L, Armstrong JPK, Lin Y, et al. Expanding and optimizing 3D bioprinting capabilities using complementary network bioinks. *Sci Adv*. 2020;6(38):eabc5529. doi: 10.1126/sciadv.abc5529

92. Paxton N, Smolan W, Böck T, Melchels F, Groll J, Jungst T. Proposal to assess printability of bioinks for extrusion-based bioprinting and evaluation of rheological properties governing bioprintability. *Biofabrication*. 2017;9(4):044107. doi: 10.1088/1758-5090/aa8dd8

93. Tuladhar S, Nelson C, Habib A. Rheological study of highly thixotropic hydrogels for 3D bio-printing processes. In: Ghate A, Krishnaiyer K, Paynabar K, eds. *Proceedings of the 2021 IISE Annual Conference*; 2021.

94. Diañez I, Gallegos C, Brito-de la Fuente E, et al. 3D printing in situ gelification of κ-carrageenan solutions: effect of printing variables on the rheological response. *Food Hydrocoll*. 2019;87:321-330. doi: 10.1016/j.foodhyd.2018.08.010

95. Herrada-Manchón H, Celada L, Rodríguez-González D, Alejandro Fernández M, Aguilar E, Chiara MD. Three-dimensional bioprinted cancer models: A powerful platform for investigating tunneling nanotube-like cell structures in complex microenvironments. *Mater Sci Eng: C*. 2021;128:112357. doi: 10.1016/j.msec.2021.112357

96. Chen Y, Wang Y, Yang Q, et al. A novel thixotropic magnesium phosphate-based bioink with excellent printability for application in 3D printing. *J Mater Chem B*. 2018;6(27):4502-4513. doi: 10.1039/C8TB01196F

97. Jungst T, Smolan W, Schacht K, Scheibel T, Groll J. Strategies and molecular design criteria for 3D printable hydrogels. *Chem Rev*. 2016;116(3):1496-1539. doi: 10.1021/acs.chemrev.5b00303

98. Ma J, Lin Y, Chen X, Zhao B, Zhang J. Flow behavior, thixotropy and dynamical viscoelasticity of sodium alginate aqueous solutions. *Food Hydrocoll*. 2014;38:119-128. doi: 10.1016/j.foodhyd.2013.11.016

99. Cheng Y, Qin H, Acevedo NC, Jiang X, Shi X. 3D printing of extended-release tablets of theophylline using hydroxypropyl methylcellulose (HPMC) hydrogels. *Int J Pharm*. 2020;591:119983. doi: 10.1016/j.ijpharm.2020.119983

100. Sombatsompop N, Sergsiri S. Die swell ratio of polystyrene melt from an electro-magnetized capillary die in an extrusion rheometer: effects of barrel diameter, shear rate and die temperature. *Polym Adv Technol*. 2004;15(8):472-480. doi: 10.1002/pat.490

101. Michal Bathory. Modelling and analysis of flows of viscoelastic fluids Beyond the Navier–Stokes equations. *Res Outreach*. 2022;(132). doi: 10.32907/RO-132-3331282634

102. Boger DV, Binnington RJ. Experimental removal of the re-entrant corner singularity in tubular entry flows. *J Rheol*. 1994;38(2):333-349. doi: 10.1122/1.550517

103. Maklad O, Poole RJ. A review of the second normal-stress difference; its importance in various flows, measurement techniques, results for various complex fluids and theoretical predictions. *J Nonnewton Fluid Mech*. 2021;292:104522. doi: 10.1016/j.jnnfm.2021.104522

104. R J Poole. The Deborah and Weissenberg numbers. *Rheol Bull*. 2012;52(2):32-39.

105. Wu Q, Therriault D, Heuzey MC. Processing and properties of chitosan inks for 3D printing of hydrogel microstructures. *ACS Biomater Sci Eng*. 2018;4(7):2643-2652. doi: 10.1021/acsbiomaterials.8b00415

106. Vlachopoulos J, Polychronopoulos N. Basic concepts in polymer melt rheology and their importance in processing. In: Kontopoulou M, eds. *Applied Polymer Rheology*. John Wiley & Sons, Inc.; 2011:1-27. doi: 10.1002/9781118140611.ch1

107. Koopmans RJ. Die swell or extrudate swell. In: Karger-Kocsis J, ed. *Polypropylene: An A-Z Reference*. Kluwer Publishers; 1999.

108. Sodupe-Ortega E, Sanz-Garcia A, Pernia-Espinoza A, Escobedo-Lucea C. Accurate calibration in multi-material 3D bioprinting for tissue engineering. *Materials (Basel)*. 2018;11(8):1402. doi: 10.3390/ma11081402

109. Anna SL, Rogers C, McKinley GH. On controlling the kinematics of a filament stretching rheometer using a real-time active control mechanism. *J Nonnewton Fluid Mech*. 1999;87(2-3):307-335. doi: 10.1016/S0377-0257(99)00072-5

110. Ooi YW, Sridhar T. Extensional rheometry of fluid S1. *J Nonnewton Fluid Mech*. 1994;52(2):153-162. doi: 10.1016/0377-0257(94)80047-2

111. McKinley GH, Tripathi A, Yao M. Extensional rheometry of polymeric fluids and the uniaxial elongation of viscoelastic filaments. In: Kruijt PGM, Meijer HEH, van de Vosse FN, eds. *15th Annual Meeting of the International Polymer Processing Society*; 1999.

112. Göhl J, Markstedt K, Mark A, Håkansson K, Gatenholm P, Edelvik F. Simulations of 3D bioprinting: Predicting bioprintability of nanofibrillar inks. *Biofabrication*. 2018;10(3):34105. doi: 10.1088/1758-5090/aac872

113. Zaeri A, Zgeib R, Cao K, Zhang F, Chang RC. Numerical analysis on the effects of microfluidic-based bioprinting parameters on the microfiber geometrical outcomes. *Sci Rep*. 2022;12(1):3364. doi: 10.1038/s41598-022-07392-0

114. Hemasian Etefagh A, Razfar MR. Numerical study of the process parameters affecting the feature size of a microfiber fabricated by microfluidic-based bioprinting. *Proc Instit Mech Eng E: J Process Mech Eng*. 2024. doi: 10.1177/09544089241236265

115. Ma J, Lin Y, Chen X, Zhao B, Zhang J. Flow behavior, thixotropy and dynamical viscoelasticity of sodium alginate aqueous solutions. *Food Hydrocoll*. 2014;38:119-128. doi: 10.1016/j.foodhyd.2013.11.016

116. Talluri DJS, Nguyen HT, Avazmohammadi R, Miri AK. Ink rheology regulates stability of bioprinted strands. *J Biomech Eng*. 2022;144(7) 074503. doi: 10.1115/1.4053404

117. Gregory T, Benhal P, Scutte A, et al. Rheological characterization of cell-laden alginate-gelatin hydrogels for 3D biofabrication. *J Mech Behav Biomed Mater*. 2022;136:105474. doi: 10.1016/j.jmbbm.2022.105474

118. López-Marcial GR, Zeng AY, Osuna C, Dennis J, García JM, O'Connell GD. Agarose-based hydrogels as suitable bioprinting materials for tissue engineering. *ACS Biomater Sci Eng*. 2018;4(10):3610-3616. doi: 10.1021/acsbiomaterials.8b00903

119. Benchabane A, Bekkour K. Rheological properties of carboxymethyl cellulose (CMC) solutions. *Colloid Polym Sci*. 2008;286(10):1173-1180. doi: 10.1007/s00396-008-1882-2

120. Ramezani H, Mohammad Mirjamali S, He Y. Simulations of extrusion 3d printing of chitosan hydrogels. *Appl Sci*. 2022;12(15):7530. doi: 10.3390/app12157530

121. Rahimnejad M, Labonté-Dupuis T, Demarquette NR, Lerouge S. A rheological approach to assess the printability of thermosensitive chitosan-based biomaterial inks. *Biomed Mater*. 2021;16(1):015003. doi: 10.1088/1748-605X/abb2d8

122. Lan X, Adesida A, Boluk Y. Rheological and viscoelastic properties of collagens and their role in bioprinting by micro-extrusion. *Biomed Mater*. 2022;17(6):062005. doi: 10.1088/1748-605X/ac9b06

123. Andrade RD, Skurtys O, Osorio F, Zuluaga R, Gañán P, Castro C. Rheological and physical properties of gelatin suspensions containing cellulose nanofibers for potential coatings. *Food Sci Technol Int*. 2015;21(5):332-341. doi: 10.1177/1082013214535944

124. Kokol V, Pottathara YB, Mihelčič M, Perše LS. Rheological properties of gelatine hydrogels affected by flow- and horizontally-induced cooling rates during 3D cryo-printing. *Colloids Surf A Physicochem Eng Asp*. 2021;616:126356. doi: 10.1016/j.colsurfa.2021.126356

125. Tirella A, De Maria C, Criscenti G, Vozzi G, Ahluwalia A. The PAM 2 system: a multilevel approach for fabrication of complex three-dimensional microstructures. *Rapid Prototyp J*. 2012;18(4):299-307. doi: 10.1108/13552541211231725

126. Naghieh S, Karamooz-Ravari MR, Sarker M, Karki E, Chen X. Influence of crosslinking on the mechanical behavior of

3D printed alginate scaffolds: experimental and numerical approaches. *J Mech Behav Biomed Mater*. 2018;80:111-118. doi: 10.1016/j.jmbbm.2018.01.034

127. Sarker Md, Izadifar M, Schreyer D, Chen X. Influence of ionic crosslinkers (Ca 2+ /Ba 2+ /Zn 2+) on the mechanical and biological properties of 3D Bioplotted Hydrogel Scaffolds. *J Biomater Sci Polym Ed*. 2018;29(10):1126-1154. doi: 10.1080/09205063.2018.1433420

128. Pati F, Jang J, Ha DH, et al. Printing three-dimensional tissue analogues with decellularized extracellular matrix bioink. *Nat Commun*. 2014;5(1):3935. doi: 10.1038/ncomms4935

129. Chang R, Nam J, Sun W. Effects of dispensing pressure and nozzle diameter on cell survival from solid freeform fabrication-based direct cell writing. *Tissue Eng Part A*. 2008;14(1):41-48. doi: 10.1089/ten.a.2007.0004

130. Ashammakhi N, Ahadian S, Xu C, et al. Bioinks and bioprinting technologies to make heterogeneous and biomimetic tissue constructs. *Mater Today Bio*. 2019;1:100008. doi: 10.1016/j.mtbio.2019.100008

131. Ozbolat IT, Chen H, Yu Y. Development of "Multi-arm Bioprinter" for hybrid biofabrication of tissue engineering constructs. *Robot Comput Integr Manuf*. 2014;30(3):295-304. doi: 10.1016/j.rcim.2013.10.005

132. Hong S, Kim JS, Jung B, Won C, Hwang C. Coaxial bioprinting of cell-laden vascular constructs using a gelatin-tyramine bioink. *Biomater Sci*. 2019;7(11):4578-4587. doi: 10.1039/c8bm00618k

133. Gao G, Lee JH, Jang J, et al. Tissue Engineered Bio-Blood-Vessels Constructed Using a Tissue-Specific Bioink and 3D Coaxial Cell Printing Technique: A Novel Therapy for Ischemic Disease. *Adv Funct Mater*. 2017;27(33):1700798. doi: 10.1002/adfm.201700798

134. Shao L, Gao Q, Xie C, Fu J, Xiang M, He Y. Directly coaxial 3D bioprinting of large-scale vascularized tissue constructs. *Biofabrication*. 2020;12(3):035014. doi: 10.1088/1758-5090/ab7e76

135. Millik SC, Dostie AM, Karis DG, et al. 3D printed coaxial nozzles for the extrusion of hydrogel tubes toward modeling vascular endothelium. *Biofabrication*. 2019;11(4):45009. doi: 10.1088/1758-5090/ab2b4d

136. Gao Q, He Y, Fu JZ, Liu A, Ma L. Coaxial nozzle-assisted 3D bioprinting with built-in microchannels for nutrients delivery. *Biomaterials*. 2015;61:203-215. doi: 10.1016/j.biomaterials.2015.05.031

137. Mistry P, Aied A, Alexander M, Shakesheff K, Bennett A, Yang J. Bioprinting using mechanically robust core–shell cell-laden hydrogel strands. *Macromol Biosci*. 2017;17(6)1600472. doi: 10.1002/mabi.201600472

138. Tomasina C, Bodet T, Mota C, Moroni L, Camarero-Espinosa S. Bioprinting vasculature: materials, cells and emergent techniques. *Materials (Basel)*. 2019;12(17):2701. doi: 10.3390/ma12172701

139. Cameron T, Naseri E, MacCallum B, Ahmadi A. Development of a disposable single-nozzle printhead for 3D bioprinting of continuous multi-material constructs. *Micromachines (Basel)*. 2020;11(5):459. doi: 10.3390/mi11050459

140. Nelson C, Tuladhar S, Habib A. Designing an interchangeable multi-material nozzle system for the three-dimensional bioprinting process. *J Med Device*. 2023;17(2):1-8. doi: 10.1115/1.4055249

141. Puertas-Bartolomé M, Włodarczyk-Biegun MK, Del Campo A, Vázquez-Lasa B, Román JS. 3D printing of a reactive hydrogel bio-ink using a static mixing tool. *Polymers (Basel)*. 2020;12(9):1-17. doi: 10.3390/polym12091986

142. Rocca M, Fragasso A, Liu W, Heinrich MA, Zhang YS. Embedded multimaterial extrusion bioprinting. *SLAS Technol*. 2018;23(2):154-163. doi: 10.1177/2472630317742071

143. Liu W, Zhang YS, Heinrich MA, et al. Rapid continuous multimaterial extrusion bioprinting. *Adv Mater*. 2017;29(3):10.1002/adma.201604630. doi: 10.1002/adma.201604630

144. Puryear III JR, Yoon JK, Kim Y. Advanced fabrication techniques of microengineered physiological systems. *Micromachines (Basel)*. 2020;11(8):730. doi: 10.3390/mi11080730

145. Kantak C, Beyer S, Trau D. A novel microfluidic droplet manipulation method for fabrication of reverse-phase two layer layer-by-layer protein microcapsules. In: Zengerle R, eds. *17th Int. Conf. on Miniaturized Systems for Chemistry and Life Sciences (MicroTAS 2013)* ; 2013.

146. Shin SR, Kilic T, Zhang YS, et al. Label-free and regenerative electrochemical microfluidic biosensors for continual monitoring of cell secretomes. *Adv Sci*. 2017;4(5):1600522. doi: 10.1002/advs.201600522

147. Bsoul A, Pan S, Cretu E, Stoeber B, Walus K. Design, microfabrication, and characterization of a moulded PDMS/SU-8 inkjet dispenser for a Lab-on-a-Printer platform technology with disposable microfluidic chip. *Lab Chip*. 2016;16(17):3351-3361. doi: 10.1039/C6LC00636A

148. Davoodi E, Sarikhani E, Montazerian H, et al. Extrusion and microfluidic-based bioprinting to fabricate biomimetic tissues and organs. *Adv Mater Technol*. 2020;5(8):1901044. doi: 10.1002/admt.201901044

149. Hakimi N, Cheng R, Leng L, et al. Handheld skin printer: in situ formation of planar biomaterials and tissues. *Lab Chip*. 2018;18(10):1440-1451.

doi: 10.1039/c7lc01236e

150. Onoe H, Okitsu T, Itou A, et al. Metre-long cell-laden microfibres exhibit tissue morphologies and functions. *Nat Mater*. 2013;12(6):584-590. doi: 10.1038/nmat3606

151. Raja N, Yun H suk. A simultaneous 3D printing process for the fabrication of bioceramic and cell-laden hydrogel core/shell scaffolds with potential application in bone tissue regeneration. *J Mater Chem B*. 2016;4(27):4707-4716. doi: 10.1039/C6TB00849F

152. Angelozzi M, Miotto M, Penolazzi L, et al. Composite ECM-alginate microfibers produced by microfluidics as scaffolds with biomineralization potential. *Mater Sci Eng C*. 2015;56:141-153. doi: 10.1016/j.msec.2015.06.004

153. Lee C, Abelseth E, de la Vega L, Willerth SM. Bioprinting a novel glioblastoma tumor model using a fibrin-based bioink for drug screening. *Mater Today Chem*. 2019; 12:78-84. doi: 10.1016/j.mtchem.2018.12.005

154. Pati F, Jang J, Lee JW, and D.-W. Cho C. Extrusion Bioprinting. In: Atala A, Yoo JJ, eds. *Extrusion Bioprinting, in Essentials of 3D Biofabrication and Translation*. 1st ed. Academic Press; 2015.

155. Hardin JO, Ober TJ, Valentine AD, Lewis JA. Microfluidic printheads for multimaterial 3d printing of viscoelastic inks. *Adv Mater*. 2015;27(21):3279-3284. doi: 10.1002/adma.201500222

156. du Chatinier DN, Figler KP, Agrawal P, Liu W, Zhang YS. The potential of microfluidics-enhanced extrusion bioprinting. *Biomicrofluidics*. 2021;15(4):041304. doi: 10.1063/5.0033280

157. Utada AS, Fernandez-Nieves A, Stone HA, Weitz DA. Dripping to jetting transitions in coflowing liquid streams. *Phys Rev Lett*. 2007;99(9):094502. doi: 10.1103/PhysRevLett.99.094502

158. Derzsi L, Kasprzyk M, Plog JP, Garstecki P. Flow focusing with viscoelastic liquids. *Phys Fluids*. 2013;25(9):092001. doi: 10.1063/1.4817995

159. Ober TJ, Foresti D, Lewis JA. Active mixing of complex fluids at the microscale. *Proc Natl Acad Sci USA*. 2015;112(40):12293-12298. doi: 10.1073/pnas.1509224112

160. Hessel V, Löwe H, Schönfeld F. Micromixers—a review on passive and active mixing principles. *Chem Eng Sci*. 2005;60(8-9):2479-2501. doi: 10.1016/j.ces.2004.11.033

161. Grace HP. Dispersion phenomena in high viscosity immiscible fluid systems and application of static mixers as dispersion devices in such systems. *Chem Eng Commun*. 1982;14(3-6):225-277. doi: 10.1080/00986448208911047

162. Chávez-Madero C, De León-Derby MD, Samandari M, et al. Using chaotic advection for facile high-throughput fabrication of ordered multilayer micro-and nanostructures: continuous chaotic printing. *Biofabrication*. 2020;12(3): 035023. doi: 10.1088/1758-5090/ab84cc

163. Ober TJ, Foresti D, Lewis JA. Active mixing of complex fluids at the microscale. *Proc Natl Acad Sci USA*. 2015;112(40):12293-12298. doi: 10.1073/pnas.1509224112

164. Kuzucu M, Vera G, Beaumont M, et al. Extrusion-based 3D bioprinting of gradients of stiffness, cell density, and immobilized peptide using thermogelling hydrogels. *ACS Biomater Sci Eng*. 2021;7(6):2192-2197. doi: 10.1021/acsbiomaterials.1c00183

165. Giachini PAGS, Gupta SS, Wang W, et al. Additive manufacturing of cellulose-based materials with continuous, multidirectional stiffness gradients. *Sci Adv*. 2020;6(8):1-12. doi: 10.1126/sciadv.aay0929

166. Bracaglia LG, Smith BT, Watson E, Arumugasaamy N, Mikos AG, Fisher JP. 3D printing for the design and fabrication of polymer-based gradient scaffolds. *Acta Biomater*. 2017;56:3-13. doi: 10.1016/j.actbio.2017.03.030

167. Nadernezhad A, Khani N, Skvortsov GA, et al. Multifunctional 3D printing of heterogeneous hydrogel structures. *Sci Rep*. 2016;6(September):1-12. doi: 10.1038/srep33178

168. Samandari M, Alipanah F, Majidzadeh-A K, Alvarez MM, Trujillo-De Santiago G, Tamayol A. Controlling cellular organization in bioprinting through designed 3D microcompartmentalization. *Appl Phys Rev*. 2021;8(2): 021404. doi: 10.1063/5.0040732

169. Ceballos-González CF, Bolívar-Monsalve EJ, Quevedo-Moreno DA, et al. Plug-and-play multimaterial chaotic printing/bioprinting to produce radial and axial micropatterns in hydrogel filaments. *Adv Mater Technol*. 2023;8(17):2202208. doi: 10.1002/admt.202202208

170. Snyder J, Son AR, Hamid Q, Wu H, Sun W. Hetero-cellular prototyping by synchronized multi-material bioprinting for rotary cell culture system. *Biofabrication*. 2016;8(1):015002. doi: 10.1088/1758-5090/8/1/015002

171. Colosi C, Shin SR, Manoharan V, et al. Microfluidic bioprinting of heterogeneous 3D tissue constructs using low-viscosity bioink. *Adv Mater*. 2016;28(4):677-684. doi: 10.1002/adma.201503310

172. Stroock AD, Dertinger SKW, Ajdari A, Mezić I, Stone HA, Whitesides GM. Chaotic mixer for microchannels. *Science* (1979). 2002;295(5555):647-651. doi: 10.1126/science.1066238

173. Idaszek J, Costantini M, Karlsen TA, et al. 3D bioprinting of hydrogel constructs with cell and material gradients for the regeneration of full-thickness chondral defect using a microfluidic printing head. *Biofabrication*. 2019;11(4):044101. doi: 10.1088/1758-5090/ab2622

174. Li M, Tian X, Zhu N, Schreyer DJ, Chen X. Modeling process-induced cell damage in the biodispensing process. *Tissue Eng Part C Methods*. 2010;16(3):533-542. doi: 10.1089/ten.TEC.2009.0178

175. Metzner YC and AB. An analysis of apparent slip flow of polymer solutions. *Rheol Acta*. 1986;25:28-35.

176. Reid JA, Mollica PA, Johnson GD, Ogle RC, Bruno RD, Sachs PC. Accessible bioprinting: Adaptation of a low-cost 3D-printer for precise cell placement and stem cell differentiation. *Biofabrication*. 2016;8(2):025017. doi: 10.1088/1758-5090/8/2/025017

177. Li M, Tian X, Kozinski JA, Chen X, Hwang DK. Modeling mechanical cell damage in the bioprinting process employing a conical needle. *J Mech Med Biol*. 2015;15(05):1550073. doi: 10.1142/S0219519415500736

178. Martanto W, Baisch SM, Costner EA, Prausnitz MR, Smith MK. Fluid dynamics in conically tapered microneedles. *AIChE J*. 2005;51(6):1599-1607. doi: 10.1002/aic.10424

179. Leppiniemi J, Lahtinen P, Paajanen A, et al. 3D-printable bioactivated nanocellulose-alginate hydrogels. *ACS Appl Mater Interfaces*. 2017;9(26):21959-21970. doi: 10.1021/acsami.7b02756

180. Liravi F, Darleux R, Toyserkani E. Additive manufacturing of 3D structures with non-Newtonian highly viscous fluids: finite element modeling and experimental validation. *Addit Manuf*. 2017;13:113-123. doi: 10.1016/j.addma.2016.10.008

181. Billiet T, Gevaert E, De Schryver T, Cornelissen M, Dubruel P. The 3D printing of gelatin methacrylamide cell-laden tissue-engineered constructs with high cell viability. *Biomaterials*. 2014;35(1):49-62. doi: 10.1016/j.biomaterials.2013.09.078

182. Lee KY, Kong HJ, Larson RG, Mooney DJ. Hydrogel formation via cell crosslinking. *Adv Mater*. 2003;15(21):1828-1832. doi: 10.1002/adma.200305406

183. Park H, Kang SW, Kim BS, Mooney DJ, Lee KY. Shear-reversibly crosslinked alginate hydrogels for tissue engineering. *Macromol Biosci*. 2009;9(9):895-901. doi: 10.1002/mabi.200800376

184. Das S, Chowdhury AR, Datta P. Modelling cell deformations in bioprinting process using a multicompartment-smooth particle hydrodynamics approach. *Proc Inst Mech Eng H*. 2022;236(6):867-881. doi: 10.1177/09544119221089720

185. Müller M, Öztürk E, Arlov Ø, Gatenholm P, Zenobi-Wong M. Alginate sulfate–nanocellulose bioinks for cartilage bioprinting applications. *Ann Biomed Eng*. 2017;45(1):210-223. doi: 10.1007/s10439-016-1704-5

186. Ates G, Bartolo P. Computational fluid dynamics for the optimization of internal bioprinting parameters and mixing conditions. *Int J Bioprint*. 2023;9(6):0219. doi: 10.36922/ijb.0219

187. Chand R, Muhire BS, Vijayavenkataraman S. Computational fluid dynamics assessment of the effect of bioprinting parameters in extrusion bioprinting. *Int J Bioprint*. 2022;8(2):45-60. doi: 10.18063/ijb.v8i2.545

188. Magalhães IP, de Oliveira PM, Dernowsek J, Casas EB Las, Casas MS Las. Investigation of the effect of nozzle design on rheological bioprinting properties using computational fluid dynamics. *Revista Materia*. 2019;24(3):12401. doi: 10.1590/s1517-707620190003.0714

189. Li Y, Liu Y, Jiang C, Li S, Liang G, Hu Q. A reactor-like spinneret used in 3D printing alginate hollow fiber: a numerical study of morphological evolution. *Soft Matter*. 2016;12(8):2392-2399. doi: 10.1039/c5sm02733k

190. Li S, Liu Y, Li Y, Zhang Y, Hu Q. Computational and experimental investigations of the mechanisms used by coaxial fluids to fabricate hollow hydrogel fibers. *Chem Eng Process. Process Intensif*. 2015;95:98-104. doi: 10.1016/j.cep.2015.05.018

191. Nyande BW, Thomas MK, Lakerveld R. CFD analysis of a kenics static mixer with a low pressure drop under laminar flow conditions. *Ind Eng Chem Res*. 2021;60(14):5264-5277. doi: 10.1021/acs.iecr.1c00135

192. Ates G, Bartolo P. Numerical simulation of multimaterial polymer mixing for bioprinting applications. *J Addit Manuf Technol*. 2021;1:12–14. doi: 10.18416/JAMTECH.2111606

193. Blaeser A, Duarte Campos DF, Puster U, Richtering W, Stevens MM, Fischer H. Controlling shear stress in 3D bioprinting is a key factor to balance printing resolution and stem cell integrity. *Adv Healthc Mater*. 2016;5(3):326-333. doi: 10.1002/adhm.201500677

194. Mammoli AA, Brebbia CA, eds. Computational Methods in Multiphase Flow. Vol III. WIT; 2005.

195. Ramezani H, Mohammad Mirjamali S, He Y. Simulations of extrusion 3D printing of chitosan hydrogels. *Appl Sci*. 2022;12(15):7530. doi: 10.3390/app12157530

196. Emmermacher J, Spura D, Cziommer J, et al. Engineering considerations on extrusion-based bioprinting: interactions of material behavior, mechanical forces and cells in the printing needle. *Biofabrication*. 2020;12(2):025022. doi: 10.1088/1758-5090/ab7553

197. Phan-Thien N. A nonlinear network viscoelastic model. *J Rheol*. 1978;22(3):259-283.
doi: 10.1122/1.549481

198. Thien NP, Tanner RI. A new constitutive equation derived from network theory. *J Nonnewton Fluid Mech*. 1977;2(4):353-365.
doi: 10.1016/0377-0257(77)80021-9

199. Brackbill JU, Kothe DB, Zemach C. A continuum method for modeling surface tension. *J Comput Phys*. 1992;100(2):335-354.
doi: 10.1016/0021-9991(92)90240-Y

200. On the formulation of rheological equations of state. *Proc R Soc Lond A Math Phys Sci*. 1950;200(1063):523-541.
doi: 10.1098/rspa.1950.0035

201. Phan-Thien N, Mai-Duy N. *Understanding Viscoelasticity*. Springer International Publishing; 2017.
doi: 10.1007/978-3-319-62000-8

202. Mustapha SMFDS, Phillips TN. A dynamic nonlinear regression method for the determination of the discrete relaxation spectrum. *J Phys D Appl Phys*. 2000;33(10):1219-1229.
doi: 10.1088/0022-3727/33/10/313

ACCSCIENCE PUBLISHING

International Journal of Bioprinting

REVIEW ARTICLE

Comprehensive insight into 3D bioprinting technology for brain tumor modeling

Ayoung Kim[1,2†], Kyumin Mo[1,2†], Soohyun Choe[1,2†], Miyoung Shin[3], and Hyunho Yoon[1,2*]

[1]Department of Medical and Biological Sciences, The Catholic University of Korea, Bucheon, Gyeonggi, South Korea

[2]Department of Biotechnology, The Catholic University of Korea, Bucheon, Gyeonggi, South Korea

[3]Department of Pathology, Yale University School of Medicine, New Haven, Connecticut, United States of America

Abstract

Glioblastoma is one of the most common primary malignant brain tumors with a poor prognosis and high mortality rate. Since only small lipophilic molecules can penetrate the blood–brain barrier, chemotherapy and immunotherapy are limited in their ability to effectively treat brain tumors. 3D bioprinting has the potential to directly model the 3D environment of human pathology and diseases. In many cancers, 3D bioprinting technology closely mimics the tumor microenvironment, making it a promising tool for drug screening and uncovering the mechanisms of cancer initiation and progression. Recent 3D bioprinting technologies have been developed to recreate the dynamic interactions between the tumor and endothelial cells. Brain tumor models using 3D bioprinting technology can reconstruct the biophysical heterogeneity and immune interactions in the brain. These advanced models regulate the organization of tumor structures for preclinical drug testing and reveal the immunological pathways involved in brain tumors. Here, we highlight 3D bioprinting technologies that can replace conventional *in vitro* models for brain tumor treatment.

Keywords: 3D Bioprinting; Blood–brain barrier; Glioblastoma; Glioblastoma-on-a-chip; Tumor microenvironment

1. Introduction

Brain tumors remain one of the most complicated tumors, accounting for 85–90% of primary central nervous system (CNS) tumors.[1] Although brain tumors have various subtypes according to cell origin, their characteristics and prognosis are distinguished. Some types of brain tumors, such as glioblastoma (GBM) and diffuse intrinsic pontine glioma (DIPG), have a 5-year survival rate of only 30% following diagnosis.[2] GBM is the most common and aggressive malignant primary brain tumor in adults, increasing after the age of 40 years and peaking at 75–84 years.[3] Despite the struggles for new therapeutic strategies, including radiotherapy, chemotherapy, and surgery, GBM remains highly resistant to treatment, with poor survival rates. The most frequently used treatment for GBM is the Stupp regimen, which is a combination

†These authors contributed equally to this work.

***Corresponding author:**
Hyunho Yoon
(hyoon@catholic.ac.kr)

Citation: Kim A, Mo K, Choe S, Shin M, Yoon H. Comprehensive insight into 3D bioprinting technology for brain tumor modeling. *Int J Bioprint*. 2024;10(6):4166. doi: 10.36922/ijb.4166

Received: July 8, 2024
1st revised: August 8, 2024
2nd revised: August 21, 2024
Accepted: August 22, 2024
Published Online: August 27, 2024

Copyright: © 2024 Author(s). This is an Open Access article distributed under the terms of the Creative Commons Attribution License, permitting distribution, and reproduction in any medium, provided the original work is properly cited.

Publisher's Note: AccScience Publishing remains neutral with regard to jurisdictional claims in published maps and institutional affiliations.

of temozolomide (TMZ) and radiotherapy, resulting in an overall survival rate of 14.6 months for patients with GBM.[4] The combination of bevacizumab, an anti-angiogenic drug approved by the United States (US) Food and Drug Administration (FDA), with chemoradiotherapy markedly increased progression-free survival in patients with GBM in a phase 3 trial.[5] However, it often recurs due to tumor heterogeneity, immune evasion, glioma stem cells, and drug efflux pumps.[6] In particular, recent clinical studies have estimated the efficacy of some approaches to avoid the blood–brain barrier (BBB) and accomplish efficient delivery in patients with recurrent GBM.[5,7] Therefore, more patient-specific therapeutic approaches are required to improve the overall survival of patients with GBM.

For decades, general *in vitro* models for cancer research, including 2D cancer and animal models, have been used to elucidate cancer mechanisms. 2D monolayer cancer cell lines offer a hypothetical cancer environment that imitates tumor characteristics, such as protein expression, cell signaling, and cell viability.[8] However, the 2D culture model still has limitations in that it cannot perfectly reflect the actual tumor microenvironment (TME) owing to the absence of an extracellular matrix (ECM). As animal models have immunological similarities to humans, these models are conducive to studying drug responses, tumorigenicity, and immune responses.[9] Animal models also have limitations in demonstrating the complexity of human cancer, owing to issues, such as high cost, poor controllability, and immunodeficiency, in some species.[10]

Advanced 3D bioprinting technology helps overcome these limitations and enhances our understanding of the complexity of cancer. 3D bioprinting is an emerging technology that can be used to construct the biological organization of cancer using living cells, ECM components, and biochemical factors.[11] Furthermore, 3D bioprinting can resolve challenges, such as drug delivery and functional organ replacement. 3D tumor models have been developed using various strategies, including inkjet-based bioprinting, micro-extrusion, and laser-assisted bioprinting.[12] 3D cancer models have various applications based on modeling parameters such as extrusion pressure, nozzle diameter, and temperature.[8] By modifying these printing parameters, cell viability can be optimized after printing. Computational simulation programs provide a better understanding of optimized printing parameters for post-printing environments.[13] Moreover, co-printing bioink technology can provide different cell types, ECM, and biomolecules for the construction and complexity of the TME.[12] In particular, these techniques contribute to the study of tumors in complex organs, such as the brain.[4] As mentioned previously, the poor approach and complexity of multi-component interactions among various cell types limit the scope of brain tumor studies. 3D-bioprinted neural systems, including neurons, microglia, and astrocytes, can resolve previous limitations of neuronal tumor study.[14] Biomimetic GBM models with microfluidic chips recapitulate complex biological networks, including brain tumors, the BBB, and neurotransmission; thus, they can be more useful than conventional models.[15,16] Using gelatin methacrylate (GelMA) and glycidyl methacrylate-hyaluronic acid (GMHA) hydrogels, digital light processing (DLP)-based 3D bioprinting models with GBM ECM can mimic transcriptional profiles and immune cell composition with high quality.[9]

3D tumor models, including spheroids, organoids, biopolymer scaffolds, and tumor-on-a-chip models, are more indicative of human tumor properties, involving hypoxic regions and a gradient distribution of chemical/biological factors.[17] The TME has implications for immune interactions in GBM progression and intercellular crosstalk.[18] Furthermore, by integrating GBM stem cells (GSCs), the relation among GSCs, anticancer drug resistance, and vascularization can be identified.[19] A vascularized GBM-on-a-chip was designed to recapitulate the pathophysiological states of tumors and the adjacent vascular microenvironments.[20] It also interconnects with the porous membrane, which permits biochemical and mechanical interactions, resulting in the generation of a dynamic GBM environment. In this review, we describe advanced 3D biomimetic models of brain tumors, especially GBMs, and their therapeutic implications (Figure 1).

2. Biomaterials and methods of 3D bioprinting

2.1. Biomaterials

Recently, 3D bioprinting technologies that utilize various biomaterials and bioprinting methods have been developed, opening the possibility of reconstructing individual components of the TME (Table 1). In particular, neuronal microenvironments can be accurately constructed using bioink and 3D printing methods.[21] Given the various biocompatibilities and biodegradabilities of hydrogels, the selection of a proper hydrogel is pivotal prior to designing the TME of neural tissues and sustaining its viability.[4] Natural and synthetic substances are typically utilized as bioinks, owing to their lack of toxicity and biocompatibility.[22] In particular, gelatin- and fibrin-based bioinks can strengthen cell functions because they are natural polymers with intrinsic binding sites.[22] For example, collagen-derived gelatin has been widely used clinically because of its excellent safety and functionality.[23]

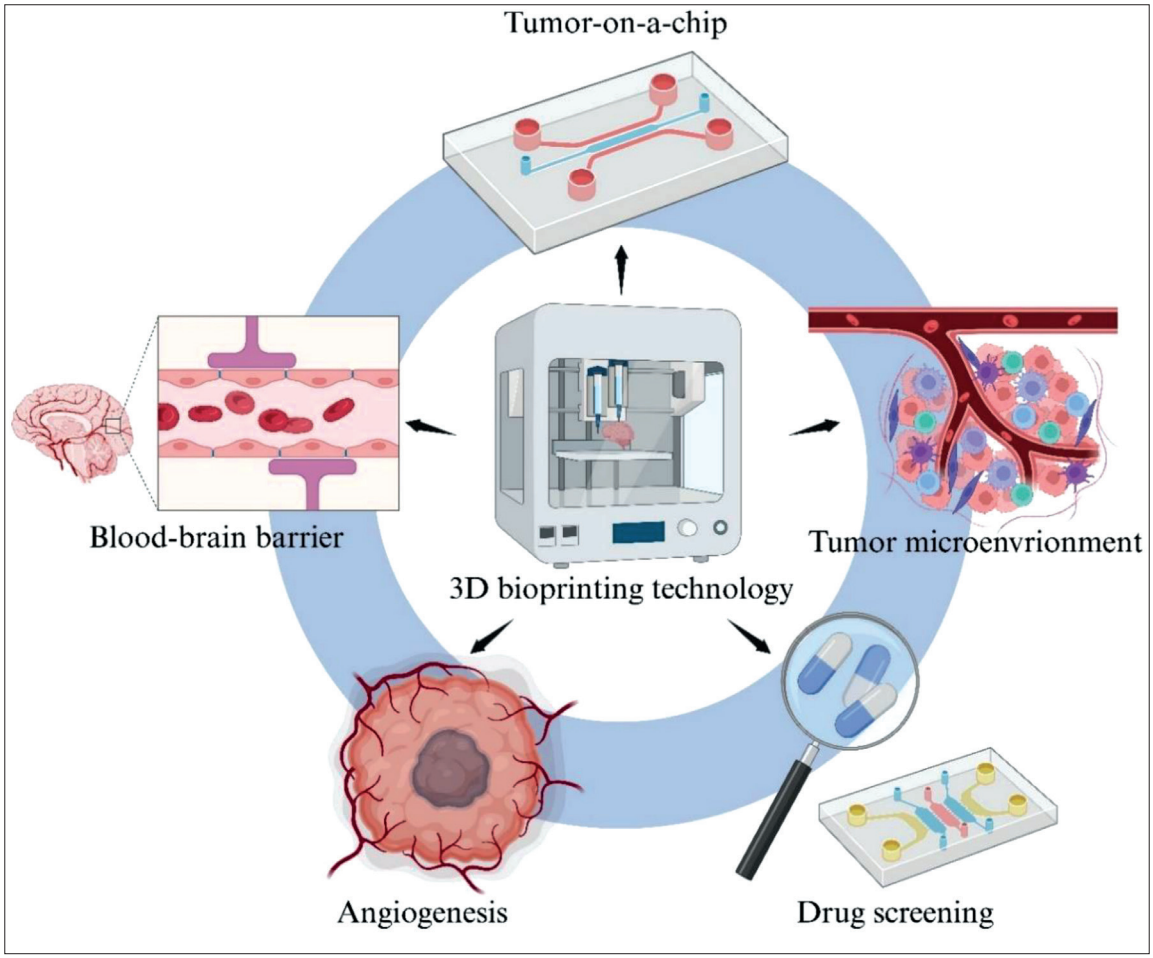

Figure 1. Schematic overview of 3D bioprinting applications for glioblastoma research. 3D bioprinting technology can be utilized as tumor-on-a-chip, drug screening, and tools for studying angiogenesis mechanisms, blood–brain barrier (BBB), and tumor microenvironment (TME).

When combined with other polymers, alginate can enhance mechanical durability, leading to increased cell viability by providing sufficient nutrients and oxygen through the pores.[19] Furthermore, GBM cells can be co-cultured with endothelial cells in a fibrin hydrogel matrix containing growth factors, allowing the observation of neural stem cell development and migration.[24]

Hyaluronic acid (HA), a natural bioink, is widely used to establish brain tumor models.[24] HA modulates cellular behaviors and functions with remarkable indispensability and biocompatibility.[25] Hydrogels produced from synthetic polymers can crosslink cells with the ECM, thereby providing better cell reproducibility than natural materials.[26] Polyethylene glycol (PEG), which exhibits remarkable biocompatibility and adjustability, is associated with cell proliferation and adhesion.[27] It is capable of producing stable and durable structures at low cost.[28] Interestingly, GelMA, a semi-synthetic substance made from gelatin with methacrylamide and methacrylate, displays a significant permeability resemblance to neural tissues.[26] Although synthetic materials alone exhibit insufficient biological activities, they can be combined with natural materials to enhance their biocompatibility.

2.2. Bioprinting methods

Extrusion-based bioprinting that incorporates microfluidic platforms is a common technique for building scaffolds. This method constructs a 3D shape layer-by-layer via a consecutively distributed stream of cells with a bioink through a nozzle.[50] However, the shear stress on cells during this process can affect cell viability.[23] Thus, it is necessary to utilize appropriate biomaterials to enhance cell viability. In contrast, inkjet bioprinting is a contactless technique that allows for the fabrication of 3D structures from hydrogels.[28] The viscosity of the bioink must be considered in the inkjet method due to limitations on continuous flow; however,

Table 1. Bioinks and printed TME components in brain tumors

Component		Bioink	Method	Properties of 3D-printed model	Experimental design	Reference
Glioma cell (U118)	-	GAF, transglutaminase	Extrusion	Expresses stability, upregulated EMT, stemness, chemoresistance, and tumorigenicity	*In vitro* and *in vivo*	[29,30]
	GSC (GSC23)	SA, gelatin	Extrusion	Exhibits proliferation and angiogenesis	*In vitro* and *in vivo*	[31,32]
	GSC (GSC23)	SA	Extrusion	Higher drug resistance	*In vitro*	[33,34]
Glioblastoma cell (U87)	GSC (SU3)	GAF	Extrusion	Enhanced drug resistance and cell viability	In vitro	[35,36]
	HUVECs, LFs	GAF	N/A	Distinct angiogenesis and EMT	*In vitro*	[37–38]
	GFP-expressing U87, hCMEC/D3	MRCSs	TPL	Constructs the complex BBB system	*In vitro*	[40]
	Patient-derived GBM, HUVECs	BdECM or collagen	GBM-on-a-chip	Incorporates heterogeneous TME; demonstrates patient-specific therapy resistance	*In vitro*	[39,41]
	-	Matrigel	MEW	Facilitates cell growth, migration, and drug screening	*In vitro*	[42,43]
	Astrocytes	Fibrinogen, alginate,genipin	Extrusion	Feasible to test cell viability against drug	*In vitro*	[4,44,45]
GSC (GSC23)	-	GAF	Extrusion	Alters cell morphology; promotes vasculogenesis and stemness	*In vitro*	[46,47]
	MSCs	GAF	Extrusion	High cell viability; sufficient cell–cell interaction	*In vitro*	[47]
	Macrophages, astrocytes, NPCs	GMHA, GelMA	DLP	Upregulated GBM tissue-specific genes; activates ECM and invasiveness	*In vitro* and *in vivo*	[9,2]
	GASCs, microglia	HA, RGD-alginate	Extrusion	Higher drug sensitivity in TMZ and cisplatin; maintains pluripotency	*In vitro*	[48,49]

Abbreviations: BBB, blood–brain barrier; BdECM, brain decellularized extracellular matrix; DLP, digital light processing; ECM, extracellular matrix; EMT, epithelial-mesenchymal transition; GAF, gelatin, alginate, fibrinogen; GASCs, glioma associated stromal cells; GBM, glioblastoma; GelMA, gelatin methacrylate; GFP, green fluorescent protein; GMHA: glycidyl methacrylate-hyaluronic acid; GSC, glioblastoma stem cell; HA, hyaluronic acid; hCMEC/D3, human cerebral microvascular endothelial cell line; HUVECs, human vascular endothelial cells; LFs, lung fibroblasts; MEW, melt electrowriting; MRCSs, magnetically responsive cage-like scaffolds; MSCs, mesenchymal stem cells; NPCs, neural precursor cells; RGD-alginate, alginate modified by Arg-Gly-Asp peptide sequence; SA, sodium alginate; TME, tumor microenvironment; TMZ, temozolomide; TPL, two-photon lithography.

the rapid printing speed is a significant advantage.[23] Similarly, laser-assisted printing can dispense formulated cells drop-by-drop using a pulsed laser.[51] It is highly efficient compared to other methods because nozzles are unnecessary; therefore, it can deliver a higher viscosity and density of cells with better viability.[23] DLP and two-photon polymerization-based bioprinting are light-assisted bioprinting techniques that can be used for sensitive cell types.[24] Overall, selecting the right bioprinting method and bioink has a critical impact on establishing an appropriate 3D model for brain tumor modeling.

3. Mimicking the brain TME using 3D bioprinting

The brain TME plays a pivotal role in tumor progression, metabolism, and metastasis. Optimized physiological conditions for tumor development are formed by communication between various cell types, including GSCs, glioma cells, microglia, astrocytes, neurons, mesenchymal stem cells, and tumor-associated microglia.[24] Tumor-associated microglia with an M2 pro-tumor phenotype create an immunosuppressive TME and promote tumor growth.57 When extracellular

vesicles and efflux transporters recruit astrocytes, the invasion of GSCs and the secretion of anti-inflammatory cytokines are promoted,[53] creating an immunosuppressive GBM microenvironment. Mesenchymal stem cells also play a major role in promoting mesenchymal-related transcription and mediating tumor proliferation via interleukin-6 and exosome-encapsulating miRNA-1587.[54] These studies suggest that TME cells activated by cell-to-cell interactions influence the development of treatment strategies for GBM. According to the type of cellular components and applications, various printing methods are applied, including inkjet-based, extrusion-based, and light-assisted bioprinting.[55] Although inkjet-based bioprinting has a wide range of biological applications, it is not appropriate for TME modeling due to limited cell density.[55] The 3D biomimetic models that reflect the TME of GBM can be constructed by extrusion-based and DLP-based 3D bioprinting.

3.1. Bioprinted TME models of brain tumors

3D bioprinting technology has emerged as a potential tool for recapitulating the heterogeneous TME in various cancer types, including brain tumors. 3D-bioprinted brain tumor models have been developed by optimizing the biomaterials and cell types according to their applications.[9] As neural cell cultures require a complex microenvironment to retain the function of neurons and glial cells, biomaterials with good biocompatibility and mechanical properties are necessary to support their function in 3D culture for brain tumor research.[3] For instance, while GelMA is used for culturing macrophages and astrocytes, which are essential cellular components of GBM; microglia and human umbilical vein endothelial cells are cultured using collagen[10,11] (Figure 2). Moreover, the critical properties of the cellular constituents vary depending on the biomaterials used.[12] 3D co-culture systems using GelMA and GMHA include various cellular compositions of GBM, such as astrocytes, GSCs,

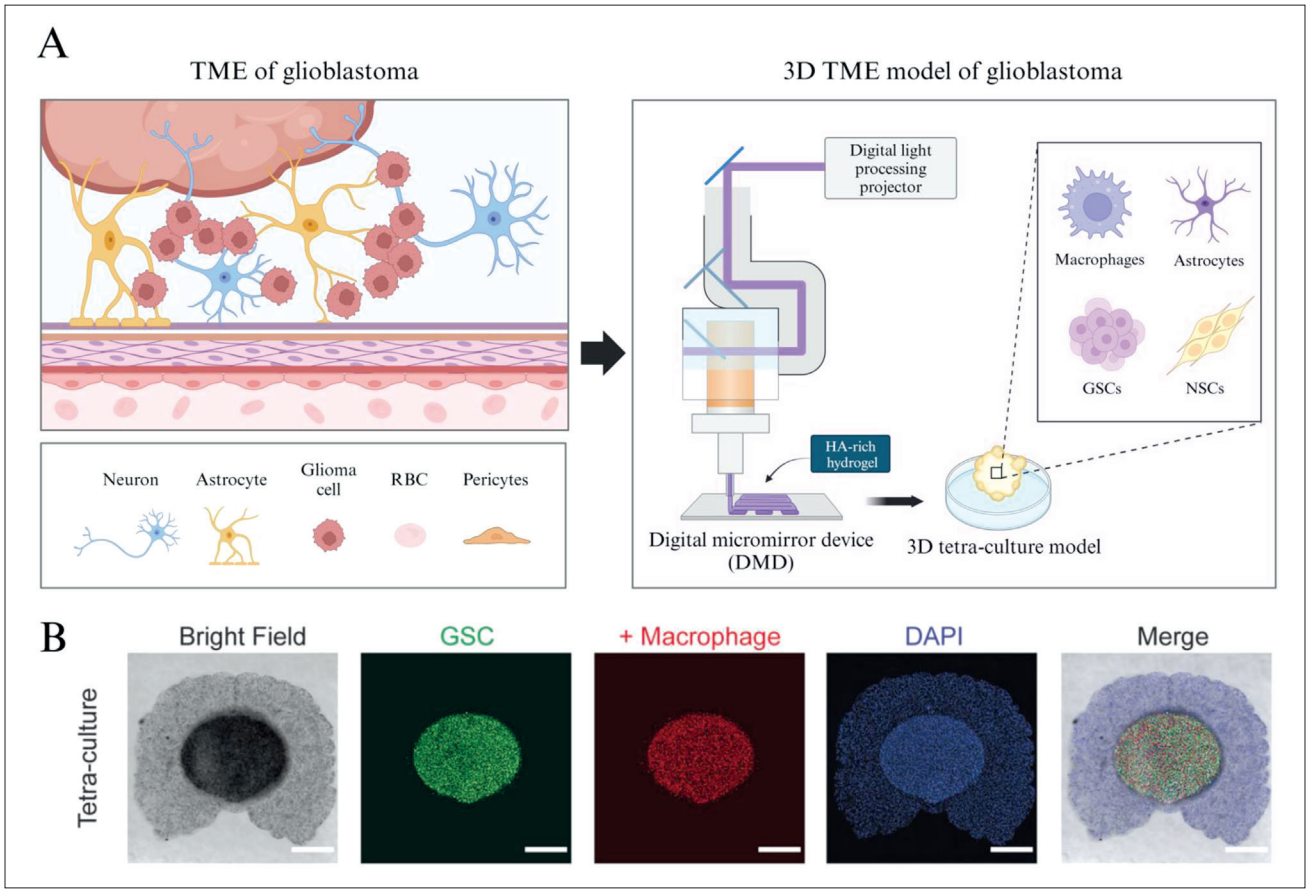

Figure 2. The cellular composition of glioblastoma tumor microenvironment (TME) with the 3D TME model. (A) It was constructed using a digital micromirror device (DMD) with hyaluronic acid (HA)-rich hydrogels (gelatin methacrylate [GelMA] and glycidyl methacrylate-HA [GMHA]).[56] This model recapitulates the TME of glioblastoma, containing cellular compositions such as macrophages, astrocytes, glioblastoma stem cells (GSCs), and neural stem cells (NSCs). (B) Immunofluorescence images of tetra-culture 3D glioblastoma models. Nuclei were labeled with DAPI. GSCs were labeled with green fluorescent protein (GFP), while macrophages were stained with mCherry. The cells were printed into two prearranged regions. These separated regions of both cells provide more physiologically relevant features to the *in vivo* TME. Abbreviation: RBC, red blood cell. Adapted with permission from ref.[56]

macrophages, and neural stem cells.[13] Due to its good biocompatibility, GelMA functions as an efficient stiffness modulator in devices without physiological intervention.[4] GMHA is a major component of the ECM and serves as a promoter of GBM progression.[14] A brain-shaped 3D GBM model was printed using a digital micromirror device chip controlled by light projection.[11] The 3D tetra-culture model, which included mixed proportions of M2 macrophages and GSCs, effectively recapitulated the immune cell-infiltrated tumor mass.[11] As the immune response is critical for GBM development, the use of a biomimetic 3D cancer microenvironment with immune cells is advantageous.[15]

A 3D brain model that mimics medulloblastoma, the most complicated type of brain tumor in children, was created using human fetal brain tissue and the medulloblastoma cell line, UW228-3.[16,17] In this model, both cell types were co-cultured and retained their 3D spheroid structures and cell viability. By labeling both cell populations separately, the differential effects of drugs on the TME cellular components could be distinguished.[16] When the model was treated with etoposide, a representative cancer management medication, several cell types, including stem cells, tumor cells, and apoptotic cells, were observed individually.[16,18] This 3D co-culture system for medulloblastoma is a promising tool for drug screening in brain tumors.

The 3D-bioprinted mini-brains composed of glioma cells and macrophages are also promising tools for understanding cell–cell interactions and examining the therapeutic efficacy of existing chemotherapy. This is a two-step bioprinting process: (i) a large brain model printed with a mouse macrophage cell line (RAW264.7) and (ii) an empty cavity filled with mouse GBM cells (GL261).[57,58] These cells were then encapsulated in a bioink composed of GelMA and gelatin. This model revealed that GBM cells highly express vimentin, nestin, and N-cadherin through interaction with macrophages, indicating increased aggressiveness.[58–62,31] Transcriptomic analysis demonstrated that the upregulated genes (such as *FGF2*, *MMP2*, *PP1*, *CCL2*, *CHI3L1*, and *MMP9*) are enhanced in the mini-brain model,[60–62] which are markers of poor prognosis in patients with GBM, suggesting that this 3D co-culture system closely mimics *in vivo* properties, including interactions between glioma cells and macrophages.

3.2. Bioprinted BBB models for brain tumor research

The BBB is an important component of the nervous system that protects the CNS and maintains homeostasis in the brain.[63] Astrocytes, neurons, microglia, pericytes, and brain microvascular endothelial cells (BMECs) are the major components of the BBB and form the neurovascular units of the CNS.[64,65] The selective permeability of the BBB is determined by BBB-specific influx/efflux transporters and BMECs, which maintain continuous tight junctions and limit transcytosis of BMECs.[66] In addition, the coverage or deficiency of pericytes and neuronal activity influences BBB permeability.[67] Astrocytes regulate the BBB diffusion barrier and repair it by synthesizing BBB-specific proteins.[63,68] In drug delivery for patients with GBM, the selective permeability of the BBB has limited efficient drug delivery to the CNS.[69] Therefore, *in vitro* models have been developed to mimic the BBB during GBM treatment.[70] Previous *in vitro* BBB models were transwell cultures based on the co-culture of multiple neurovascular cells; however, these models still struggle to recapitulate the actual metabolism and cell–cell interactions.[55,71]

By fabricating complex 3D structures using living cells and biomaterials, 3D bioprinting technologies can materialize the BBB with significant properties, such as selective permeability, transport mechanisms, tightness, and integrity.[72,73] The dynamic 3D biohybrid BBB model with a size of approximately 10 μm in diameter recapitulates the functional structure of microvessels in the brain.[74] Two-photon lithography can actualize BBB composition, including connections between endothelial cells via tight junctions in advanced 3D microfabrication models.[74] Biohybrid BBB models are encased by a liquid flow that mimics components of brain microcapillaries, which have circular pores that allow mass transport toward the external environment.[74] This advanced biohybrid 3D BBB model is envisioned as a 3D-fabricated model of nanostructured scaffolds using high-resolution photolithography techniques, providing a research platform for drug delivery in brain tumors.

4. Bioprinted models of brain tumor angiogenesis

Angiogenesis, the formation of new blood vessels, is a necessary and complex process for the development of cancer but is disrupted in many diseases.[75] Angiogenesis is controlled by numerous pro-angiogenic and inhibitory signals.[76] Angiogenesis arises from the concurrent upregulation of pro-angiogenic factors and downregulation of inhibitory factors.[77] Vascular endothelial growth factor (VEGF), released by tumor cells, plays a role in tumor vascular permeability, invasion, metastasis, and recurrence of treated cancers. It induces angiogenesis by binding to VEGF receptors,[78,79] making it a prevalent target for the inhibition of angiogenesis. Several drugs, including bevacizumab and pegaptanib, were approved in 2004 for cancer and neovascular ophthalmic diseases, respectively.[80] Resistance to anti-angiogenic drugs remains a problem in the treatment of tumors.[81]

3D-bioprinted scaffolds have also been used in tumor vascularization research. The 3D-bioprinted tumor model, mimicking the *in vivo* TME, has contributed to the search for 3D-bioprinted glioma stem cells in tumor angiogenesis. A hydrogel scaffold containing glioma stem cells (GSC23) was constructed using a bioprinter.[82] Traditional 2D suspension-cultured cells proliferated dramatically but decreased after 5 days. Meanwhile, 3D-bioprinted scaffold cells grew steadily over 10 days and consistently increased the secretion of VEGFA, a major stimulator of tumor angiogenesis, after 9 days.[83,84] QThe mRNA levels of CD31, VEGFR2, HIF-1α, and CD133, i.e., endothelial-specific makers of growth, metastasis, and angiogenesis, are higher in 3D-cultured cells than in the suspension culture.[85] Regarding the stemness of GSC23, the proportion of CD133+ cells in 3D-bioprinted scaffolds was remarkably higher than that in the 2D suspension culture.

The 3D monoculture GBM model mimics the angiogenic process of GBM and has been used to study antiangiogenic therapy with bevacizumab. Although antiangiogenic therapy delays the recurrence of GBM, the effects are transient due to drug resistance in many patients.[86] In general, a 3D GBM model for GBM research is structured as a monoculture of GBM cell lines, including U118 (a human glioma cell line) or GSC23 cells (a human glioma stem cell line). To closely mimic the neovascularization of GBM, both cell types formed a GBM cell morphology during monoculture encapsulated in a gelatin-alginate-fibrinogen hydrogel using a multi-nozzle extrusion-based bioprinter.[87] 3D-GSC23 and 3D-U118 cells exhibit neovascularization ability and secrete VEGFA proteins that promote angiogenesis and induce vascular permeability.[87,88] Moreover, tubule-like structures are formed by 3D-GSC23, indicating their ability to promote neovascularization by transdifferentiating into endothelial cells.[87] Xenograft models derived from 3D-GSC23 and 3D-U118 cells displayed abundant blood vessels on the surface of tumors and secreted VEGFA *in vitro*.[87]

5. Tumor-on-a-chip model with 3D bioprinting

3D bioprinting technology has also been utilized for the development of tumor-on-a-chip. Organs-on-a-chip is a well-established microfluidics-based technology that offers features that closely mimic the mechanical and/or chemical *in vivo* conditions of vasculature-like structures.[89,90] By using organ-on-a-chip, the functional units of human tissues and organs can be reconstructed *ex vivo* on microscopic cell and tissue culture platforms.[91] These platforms incorporate essential components such as multicellular structures, ECM, and physicochemical microenvironmental factors.[4,92] However, the main fabrication systems for organ-on-a-chip have limitations in creating tissue structures with a complicated 3D organization. The integration of 3D bioprinting with a chip has a synergistic effect on transforming *in vitro* models by incorporating physiological compositions into a controlled extracellular environment.[93] For example, 3D-bioprinted vessels-on-chips are superior to cell-seeded structures and can be manipulated mechanically to evoke a physiological response.[56]

Microfluidic organ-on-a-chip models control the organ microenvironment using living cells to simulate organ-level functions *in vitro*, including the lungs, liver, kidneys, and heart.[94] Moreover, a mini-brain tumor-on-a-chip was developed to mimic the *in vivo* TME. These chips are useful tools for brain tumor research because they recapitulate the essential properties of a complicated neural environment. The GBM-on-a-chip models are commonly based on microfluidic technology.[95] The major polymeric material used to manufacture microfluidic chips is polydimethylsiloxane, which has advantages such as transparency, biocompatibility, flexibility, and resolution.[96] Although *in vivo* analyses are widely conducted to study brain tumors, several crucial factors diminish precision and reproducibility, such as species differences in physiological mechanisms.[97] The integration of 3D bioprinting and on-a-chip microfluidic platforms facilitates rapid assessment of the effects of mechanical forces, drug components, and drug concentrations on cell growth and development through dynamic stress loading, growth factors, and drug stimulation.[41]

5.1. BBB-on-a-chip model

The BBB-on-a-chip model (BBBoC) system is an important device for developing high-quality BBB models (Figure 3). The BBBoC is based on a microfluidic platform composed of three layers: lid, chamber, and perfusion layers.[98] BMECs and astrocytes were co-cultured between the chamber and perfusion layers; this structure included silicon sheets and porous membranes.[98] This device uses BMECs derived from human-induced pluripotent stem cells to achieve barrier tightness. Fluorescent images from immunostaining displayed high-level tight junction proteins (claudin-5 and ZO-1),[99,100] suggesting that barrier integrity was well-established and maintained in microfluidic BBBoCs based on induced pluripotent stem cells.[98,101] BBB permeability was assessed using three small-molecule drugs: caffeine, cimetidine, and doxorubicin.[102] The chip exhibited differential permeability to the aforementioned molecules, similar to *in vivo* conditions.[98] The ability to closely reproduce permeability similar to the *in vivo* permeability of the BBB allows BBBoCs to be used in small-molecule drug screening.

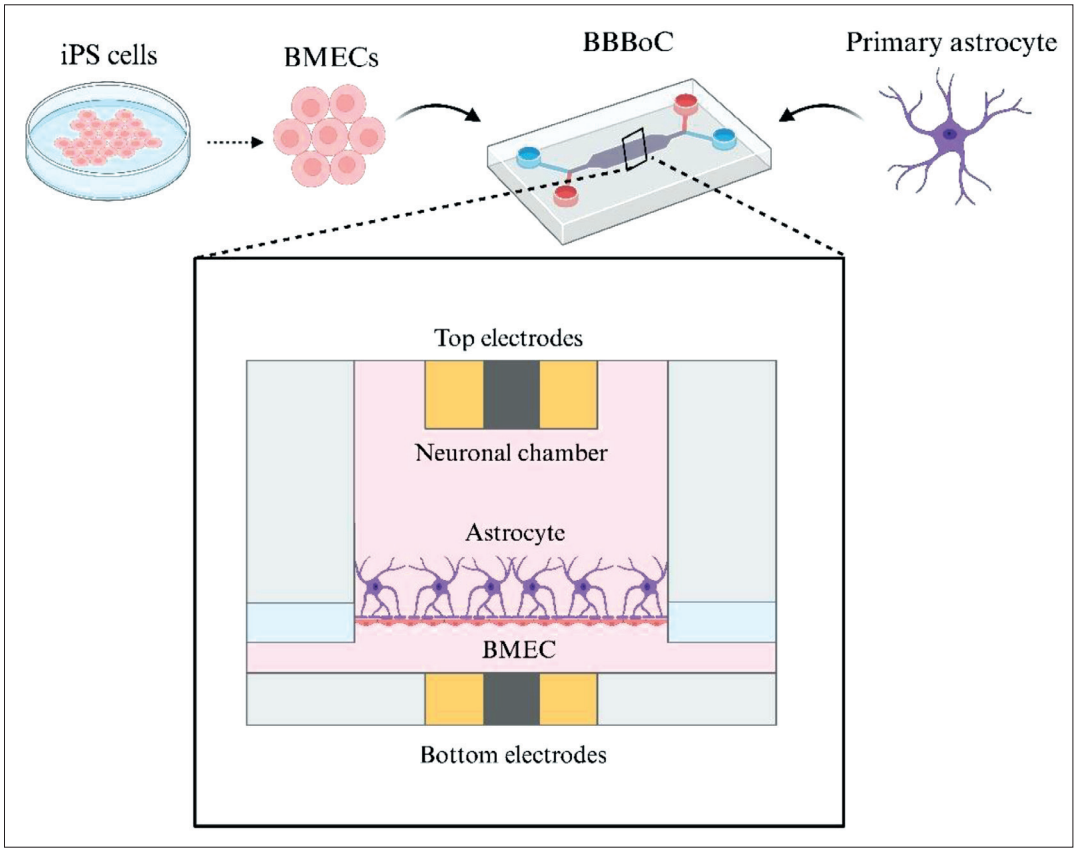

Figure 3. Illustration of the blood–brain barrier (BBB)-on-a-chip (BBBoC) composed of brain microvascular endothelial cells (BMECs) and astrocytes. While providing the same desired flow rate, both cell types were inserted between the porous polycarbonate membranes of the chip. This system mimics the permeability of *in vivo* BBB conditions. Abbreviation: iPS cells, induced pluripotent cells.

5.2. Brain tumor-on-a-chip for drug treatment response

Microfluidic-based cancer models enable precise biophysical manipulation by simulating the oxygen gradient and replicating localized interactions between cancer and associated cells, such as angiogenesis[103,104] (Figure 4). A patient-specific GBM chip was established by printing GBM-211 cells isolated from aggressively invasive GBM into the environment.[105] The GBM-on-a-chip displayed distinct drug sensitivities depending on the type of bioink used. GBM-211 cells printed with BdECM bioink were less reactive to cisplatin than collagen bioink-printed cells, whereas they were more sensitive to tissue inhibitors of metalloproteinases-1, an anti-invasion agent, accompanied by obvious morphological changes.[106] The GBM-on-a-chip can reproduce the differences in concurrent chemoradiation (CCRT) with TMZ, the current standard of care for GBM, and the treatment resistance of patients with GBM.[107] The survival rate of GBM-on-chips printed with primary GBM cells from patients following CCRT with TMZ was distinct, depending on the resistance to both treatments.[108] GBM-on-chips with extremely aggressive tumor progression after CCRT reported higher survival rates than those with low-to-moderate treatment resistance.[17,109] The decrease in the survival rate of the GBM-on-a-chip is positively correlated with patient overall survival, suggesting that the GBM-on-a-chip is a feasible model for representing treatment resistance in patients.[20,110]

In addition, the effects of DNA repair inhibition were evaluated on a GBM-on-a-chip using two DNA repair mechanism inhibitors, O^6-benzylguanine (O^6BG) and methoxyamine (MX), with CCRT. O^6BG is a pseudosubstrate of O^6BG-methylguanine-DNA methyltransferase, and MX is a base excision repair pathway inhibitor.[111–114] Both O^6BG and MX diminished the survival percentages of GBM-28- and GBM-37-on-chips, which were obtained during brain tumor removal surgery before receiving CCRT and from tumors following CCRT, respectively. In particular, the GBM-28-on-a-chip displayed higher sensitivity to these drugs. Among the two drugs and their combinations,

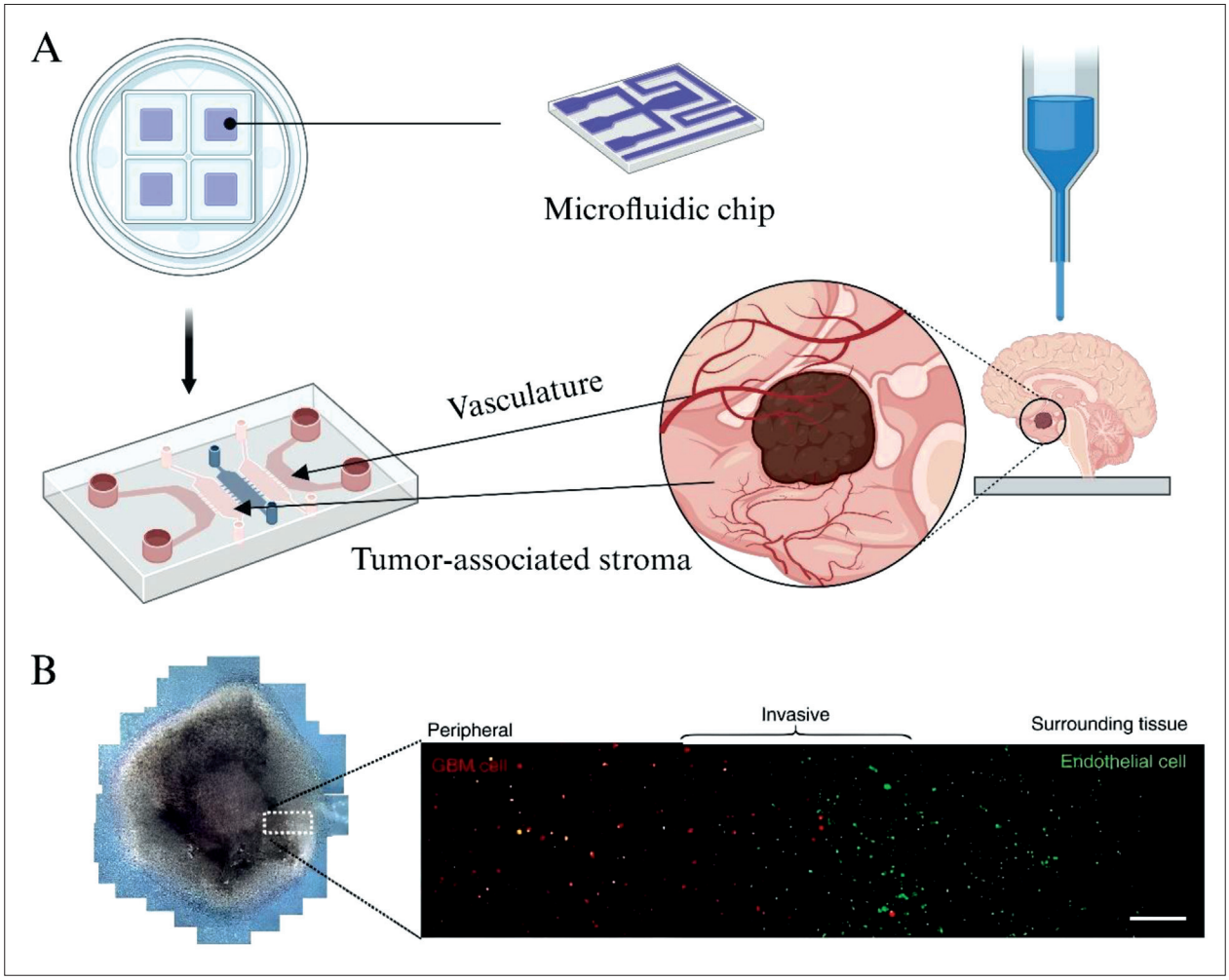

Figure 4. Construction and microscopic images of glioblastoma (GBM)-on-a-chip. (A) The microfluidic chip used in the GBM-on-a-chip contains chambers that control the flow of nutrients, oxygen, and culture media, which are necessary for reproducing the *in vivo* tumor environment. The bioink includes GBM cells and extracellular matrix components, deposited into the microfluidic chip using a 3D bioprinter. This system leads to the creation of intricate tumor structures within the chip. The integration of vasculature and tumor-associated stroma closely resembles the interaction between the tumor and surrounding tissues in the brain. (B) Representative phase-contrast optical image (left) and fluorescence microscopy image (right) of bioprinted GBM-on-a-chip cells distinguish between glioblastoma cells (red) and endothelial cells (green). Adapted with permission from ref.[105]

O^{6}BG suppressed the GBM-on-chips most effectively. In addition, the combination of cisplatin, KU60019 (a specific ATM kinase inhibitor for cancer combination therapy),[115] and *O*^{6}BG with radiation was notably effective on GBM-28-on-a-chip. In contrast, GBM-37-on-a-chip exhibited high resistance to the drugs involved in the DNA repair response,[105] suggesting that the *ex vivo* GBM model has the potential to identify optimal treatments.

5.3. Vascularized GBM-on-a-chip

A 3D microfluidic bioprinting model of a vascularized GBM-on-a-chip growing as a dense sphere revealed morphologically distinct regions within the brain TME.[116] Polydimethylsiloxane, based on a customized microfluidic network, was fabricated by casting it in a photolithographically created mold[117,118] (Figure 5). An open tissue compartment composed of concentrated GBM cells and surrounding brain endothelial cells was created to enable direct 3D bioprinting of the tumor construct.[119] The outer channels were designed for media perfusion, drug testing, and the introduction of other cell types, including astrocytes, to mimic a heterogeneous brain tumor environment.[116,9] The vascularized GBM-on-a-chip can represent the synergy of microfluidics and bioprinting by simultaneously recapitulating the significant physiological functions of *in vivo* GBMs, offering a more biomimetic and realistic strategy to simulate GBM tumors with flexibility.[120–123]

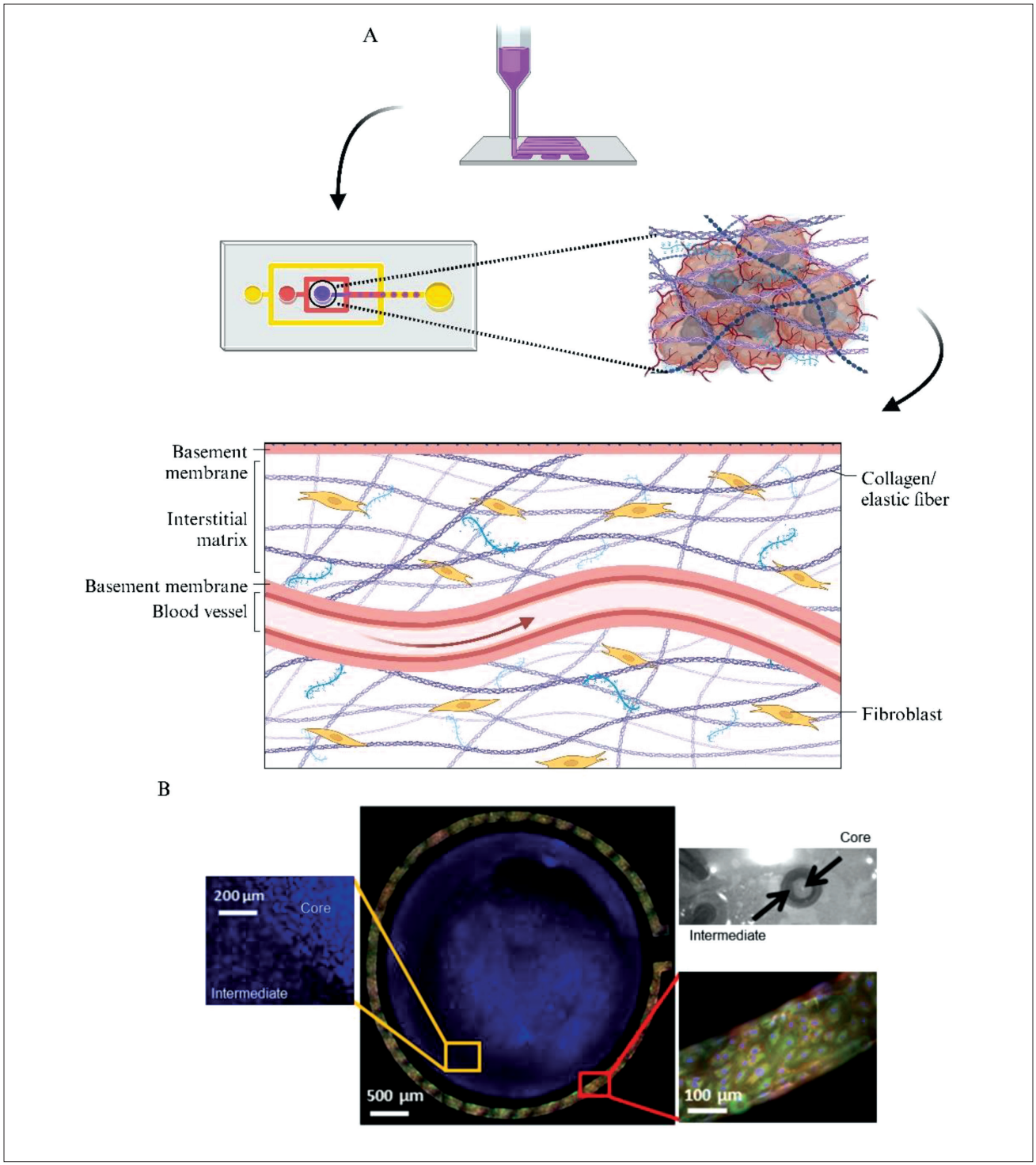

Figure 5. Characteristics and microscopic images of vascularized glioblastoma (GBM)-on-a-chip. (A) Bioink is loaded into a 3D bioprinter, which prints the cellular structures onto a microfluidic chip platform. The magnified view of the vascularized environment includes critical components such as the basement membrane, interstitial matrix, collagen/elastic fibers, fibroblasts, and blood vessels. The presence of blood vessels is essential for mimicking the supply of nutrients and the removal of waste products, closely replicating in vivo conditions. (B) The microscopic images of the bioprinted vascularized GBM model display different regions, including the core and intermediate zones. The left image illustrates that the gelatin methacrylate (GelMA) fibrin bioink loaded with brain endothelial cells was bioprinted in intermediate cells (black ring shape) and the GelMA-alginate bioink loaded with GBM cells was bioprinted in the core region (blue region). The fluorescence image visualizes a macro-scale dimension of the complete vascularized GBM-on-a-chip, reconstructing the entire system such as vascular vessels in the 3D tumor microenvironment, with scale bars (200, 500, and 100 μm). Adapted from ref.[117]

6. Bioprinted patient-derived tissues for clinical drug responses

Most *in vitro* studies are performed in 2D cell systems, and many drug candidates fail because 2D imaging does not reflect the complexity of our bodies.[124,125] More than 95% of cases fail during clinical trials despite continuous research.[126] Despite the availability of many effective drug candidates, non-physiological systems hinder further research and optimization.[127] However, bioprinting facilitates the evaluation of drug responses in terms of safety, efficacy, and personalized medicine before progressing to animal models (Table 2).[128,129]

Patient-specific bioinks were developed by mixing a prepolymer solution with a single-cell suspension. A bioink composed of GelMA and HA methacrylate was loaded into the bioprinter and polymerized to produce patient-derived tissues (PDTs).[136] Lobaplatin, a platinum-based compound with antitumor activity in multiple solid tumors, displays an average tumor inhibition rate of over 50% in PDT models.[149,150] Interestingly, drug testing using PDTs demonstrated that most patients with tumor recurrence did not respond to TMZ treatment. Lomustine (CCNU), an alkylating agent of the nitrosourea family, exhibits higher efficacy in suppressing tumor cells in PDTs, specifically in patients with recurrent GBM.[151,152]

GlioML, a machine learning system that incorporates nine different algorithms, effectively differentiates between World Health Organization grade III and IV gliomas, indicating varying drug responses at different stages of the disease.[153] Integrated 3D-bioprinted models and GlioML facilitated the prediction and evaluation of drug responses in individual patients (Figure 6). Three GlioML compounds (RSL, dasatinib, and lovastatin) were

Table 2. Results of drug response test in glioblastoma (GBM) 3D models

Drug	Related pathway	Combination therapy	Drug response	FDA approval	Reference
Temozolomide (TMZ)	Nrf2/HO-1 pathway, Wnt/β-catenin signaling, ferroptosis	CCRT	Different responses depend on treatment resistance in GBM-on-chips	Yes	[105,46,131]
O^6-benzylguanine (O^6BG)	Damaged DNA repair mechanism	CCRT	Represses the survival rates of GBM-on-chips	No	[105,132,133]
Methoxyamine (MX)	NAD+ salvage pathway			No	
Cisplatin	AXL/PI3K/Akt/NF-κB signaling	KU60019	Different responses are exhibited by GBM-on-chips obtained during surgery before and from tumors after treatment	Yes	[105,133–135]
		O^6BG			
		Radiation			
Lobaplatin	FUBP1/AA metabolic pathway, caspase-dependent pathway	N/A	Induces >50% tumor inhibition in PDT models	Yes	[136–139]
Lomustine (CCNU)	NER/FA pathway, programmed cell death pathway	N/A	Inhibits tumor cell progression in PDTs model with high efficiency, particularly in recurrent glioblastoma	Yes	[136,140–142]
1S,3R-RSL-3 (RSL)	Ferroptosis, UPR pathway	TMZ	Notably diminishes tumor viability in treated PDTs	No	[136,142–148]
Dasatinib	Src pathway, STAT3 signaling, AKT/ERK signaling			Yes	
Lovastatin	NF-κB pathway, MAPK signaling, Akt/mTOR signaling			Yes	

Abbreviations: AA, Arachidonic acid; AKT, protein kinase B; CCRT, concurrent chemotherapy; ERK, extracellular signal-regulated kinase; FA, Fanconi anemia; FUBP1, Far upstream element-binding protein 1; MAPK, mitogen-activated protein kinase; mTOR, mammalian target of rapamycin; NAD+, Nicotinamide adenine dinucleotide; NER, nucleotide excision repair; NF-κB, Nuclear factor kappa B; Nrf2/HO-1, nuclear factor erythroid-2-related factor 2/heme oxygenase 1; PDT, patient-derived tissue; PI3K, Phosphatidylinositol 3-kinase; STAT3, signal transducer and activator of transcription 3; Src, proto-oncogene tyrosine-protein kinase; UPR, unfolded protein response.

subjected to PDTs with TMZ. The median viability of these compounds was 5.8%, 4.2%, and 50%, respectively.[153] RSL, dasatinib, lovastatin, and TMZ were identified in three distinct clusters according to the overall GlioML predictions for all patient samples. Based on the efficacy of RSL and dasatinib, this cluster is a promising candidate for the treatment of GBM. In addition, PDTs treated with CCNU, cisplatin, lobaplatin, dasatinib, lovastatin, and RSL demonstrated remarkably reduced tumor viability compared with that of non-treated cells. As PDTs align

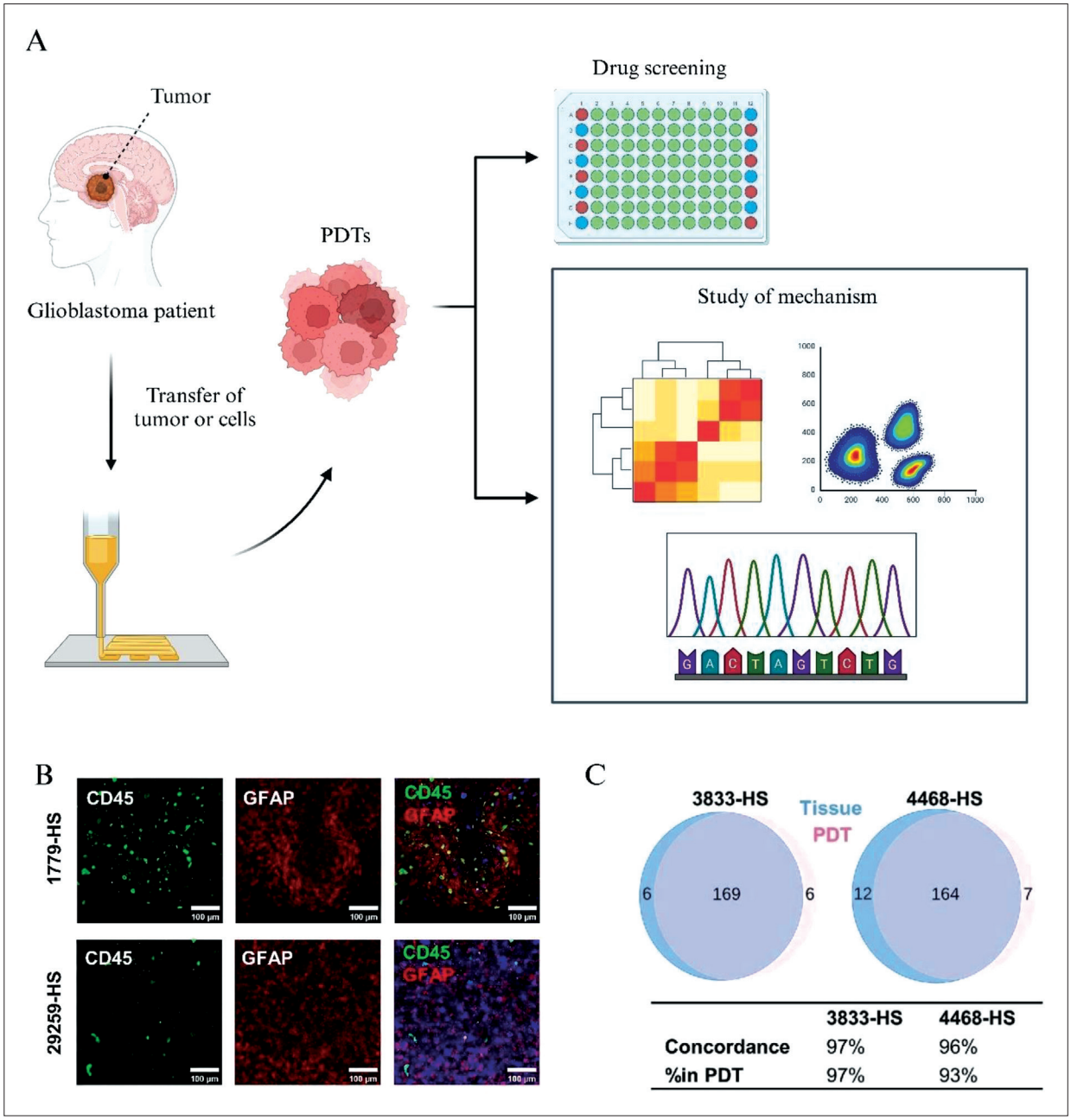

Figure 6. Application and characterization of patient-derived tissues (PDTs). (A) Schematic overview of PDT generation. The PDT model facilitates drug screening and mechanistic studies via RNA sequencing, whole exome sequencing, and flow cytometry. (B) Representative immunofluorescent staining of PDTs displays CD45 (green), a marker for immune cells, and GFAP (red), a marker for glial cells, in two different patient samples (1779-HS and 29259-HS). (C) Venn diagrams indicate the genomic concordance between two patient tissue samples and their PDTs. The concordance ratio for each comparison exceeded over 90%, indicating high similarity. Adapted from ref.[153]

with clinical responses to several drugs, the surpassing antitumor effectiveness of GlioML-identified compounds in PDTs has clinical potential for GBM treatment.

7. Challenges and future perspectives

3D-bioprinted models can reproduce the treatment responses of patients, providing environmental information that compels pathological cancer progression.[154] In particular, 3D bioprinting of human-based models can capture the *in vivo* TME better than 2D models and simplifies the separation of components compared to animal models.[155] Nevertheless, it remains challenging to practically mimic the membrane barrier, which limits the reconstruction of the BBB.[156] Consequently, advanced 3D bioprinting technology using revolutionary biomaterials and bioprinting methods is required to overcome the unsatisfactory recapitulation of the BBB. Furthermore, the development of *in vitro* modeling is ongoing and extends beyond 3D conditions. Some of this modeling involves 4D printing, which utilizes smart materials, such as shape memory polymers, alloys, and smart nanocomposites, along with additional functional processes.[157] Machine learning applications are also utilized in 3D technology, allowing the rapid production and prediction of the resemblance between the 3D model and the original patient.[121] Machine learning and 4D printing provide high-throughput processing systems for drug screening of GBM models. Although the present 3D models exhibit limitations in completely replacing the *in vivo* requirements and imitating GBM itself, further investigation is in progress to strengthen the bioprinting system.[158–165] Thus, it is anticipated that advanced GBM models will unveil unknown mechanisms of disease and benefit anticancer strategies in the future.

8. Conclusion

3D bioprinting technology has the potential to construct various functional models for cancer research. It provides a more realistic and dynamic approach for simulating GBM characteristics, including the TME, BBB, and angiogenesis. Several 3D bioprinting applications have been demonstrated to play a critical role in cell-to-cell interactions, drug screening, the establishment of a tumor-on-a-chip, and basic knowledge of GBM. However, the current 3D bioprinting technology remains challenging. It is difficult to obtain precise and complex tissues using bioprinting. Although some progress has been made in arranging cellular and ECM components, there are several obstacles to accurately mimicking a complicated and reliable TME. The convergence of organ-on-a-chip with bioprinting is still at an early stage, and few studies have described the enhancement of such biological models in brain cancer research. Additionally, the brain is an inaccessible organ; therefore, clinical data on GBM are lacking. Nevertheless, 3D bioprinting has contributed to the development of personalized tumor models, precision medicine, and immunotherapy. In this context, 3D-bioprinted cancer models can accelerate the discovery of therapeutic targets, relieve dependence on animal tests, and reduce the cost of cancer treatment research. Further studies should focus on the proper utilization of feasible models and optimization of preclinical research platforms.

Acknowledgments

The authors created the schematics of all Figures using images provided by BioRender (https://biorender.com/).

Funding

The authors wish to acknowledge Brain Korea 21 (BK21; grant number M2022B002600003) and the Ministry of Food and Drug Safety in Korea (grant number 22213MFDS421).

Conflict of interest

The authors declare they have no competing interests.

Author contributions

Conceptualization: Ayoung Kim, Kyumin Mo, Hyunho Yoon
Investigation: Ayoung Kim, Kyumin Mo, Soohyun Choe, Hyunho Yoon
Visualization: Ayoung Kim, Kyumin Mo, Soohyun Choe, Hyunho Yoon
Writing – original draft: Ayoung Kim, Kyumin Mo, Soohyun Choe, Hyunho Yoon
Writing – review & editing: Miyoung Shin, Soohyun Choe, Hyunho Yoon

Ethics approval and consent to participate

Not applicable.

Consent for publication

Not applicable.

Availability of data

None.

References

1. Tang M, Jiang S, Huang X, et al. Integration of 3D bioprinting and multi-algorithm machine learning identified glioma susceptibilities and microenvironment characteristics. *Cell Discov*. 2024;10(1):39.
doi: 10.1038/s41421-024-00650-7

2. Yi HG, Jeong YH, Kim Y, et al. A bioprinted human-glioblastoma-on-a-chip for the identification of patient-specific responses to chemoradiotherapy. *Nat Biomed Eng*. 2019;3(7):509-519.
doi: 10.1038/s41551-019-0363-x

3. Wang YI, Abaci HE, Shuler ML. Microfluidic blood-brain barrier model provides in vivo-like barrier properties for drug permeability screening. *Biotechnol Bioeng*. 2017;114(1):184-194.
doi: 10.1002/bit.26045

4. Tang M, Xie Q, Gimple RC, et al. Three-dimensional bioprinted glioblastoma microenvironments model cellular dependencies and immune interactions. *Cell Res*. 2020;30(10):833-853.
doi: 10.1038/s41422-020-0338-1

5. Silvani G, Basirun C, Wu H, et al. A 3D-bioprinted vascularized glioblastoma-on-a-chip for studying the impact of simulated microgravity as a novel pre-clinical approach in brain tumor therapy. Adv Ther. 2021;4(11):2100106.
doi: 10.1002/adtp.202100106

6. Colopi A, Fuda S, Santi S, et al. Impact of age and gender on glioblastoma onset, progression, and management. *Mech Ageing Dev*. 2023;211:111801.
doi: 10.1016/j.mad.2023.111801

7. Lauko A, Lo A, Ahluwalia MS, Lathia JD. Cancer cell heterogeneity & plasticity in glioblastoma and brain tumors. *Semin Cancer Biol*. 2022;82:162-175.
doi: 10.1016/j.semcancer.2021.02.014

8. Schaff LR, Mellinghoff IK. Glioblastoma and other primary brain malignancies in adults: a review. *JAMA*. 2023;329(7):574-587.
doi: 10.1001/jama.2023.0023

9. Xie Z, Chen M, Lian J, Wang H, Ma J. Glioblastoma-on-a-chip construction and therapeutic applications. *Front Oncol*. 2023;13:1183059.
doi: 10.3389/fonc.2023.1183059

10. Angom RS, Nakka NMR, Bhattacharya S. Advances in glioblastoma therapy: an update on current approaches. *Brain Sci*. 2023;13(11):1536.
doi: 10.3390/brainsci13111536

11. Sharma P, Aaroe A, Liang J, Puduvalli VK. Tumor microenvironment in glioblastoma: current and emerging concepts. *Neurooncol Adv*. 2023;5(1):vdad009.
doi: 10.1093/noajnl/vdad009

12. Pineda E, Domenech M, Hernandez A, Comas S, Balana C. Recurrent glioblastoma: ongoing clinical challenges and future prospects. *Onco Targets Ther*. 2023;16:71-86.
doi: 10.2147/OTT.S366371

13. Knowlton S, Onal S, Yu CH, Zhao JJ, Tasoglu S. Bioprinting for cancer research. *Trends Biotechnol*. 2015;33(9):504-513.
doi: 10.1016/j.tibtech.2015.06.007

14. Van Norman GA. Limitations of animal studies for predicting toxicity in clinical trials: is it time to rethink our current approach? *JACC Basic Transl Sci*. 2019;4(7):845-854.
doi: 10.1016/j.jacbts.2020.03.010

15. Kang Y, Datta P, Shanmughapriya S, Ozbolat IT. 3D bioprinting of tumor models for cancer research. *ACS Appl Bio Mater*. 2020;3(9):5552-5573.
doi: 10.1021/acsabm.0c00791

16. Gungor-Ozkerim PS, Inci I, Zhang YS, Khademhosseini A, Dokmeci MR. Bioinks for 3D bioprinting: an overview. *Biomater Sci*. 2018;6(5):915-946.
doi: 10.1039/c7bm00765e

17. Prendergast ME, Burdick JA. Computational modeling and experimental characterization of extrusion printing into suspension baths. *Adv Healthc Mater*. 2022;11(7):e2101679.
doi: 10.1002/adhm.202101679

18. Ozbek II, Saybasili H, Ulgen KO. Applications of 3D bioprinting technology to brain cells and brain tumor models: special emphasis to glioblastoma. *ACS Biomater Sci Eng*. 2024;10(5):2616-2635.
doi: 10.1021/acsbiomaterials.3c01569

19. Qiu B, Bessler N, Figler K, et al. Bioprinting neural systems to model central nervous system diseases. *Adv Funct Mater*. 2020;30(44):1910250.
doi: 10.1002/adfm.201910250

20. DePalma TJ, Sivakumar H, Skardal A. Strategies for developing complex multi-component in vitro tumor models: highlights in glioblastoma. *Adv Drug Deliv Rev*. 2022;180:114067.
doi: 10.1016/j.addr.2021.114067

21. Jiao W, Shan J, Gong X, et al. GelMA hydrogel: a game-changer in 3D tumor modeling. *Mater Today Chem*. 2024;38:102111.
doi: 10.1002/adfm.201910250

22. Jung M, Ghamrawi S, Du EY, Gooding JJ, Kavallaris M. Advances in 3D bioprinting for cancer biology and precision medicine: from matrix design to application. *Adv Healthc Mater*. 2022;11(24):e2200690.
doi: 10.1002/adhm.202200690

23. Crivii C-B, Boșca AB, Melincovici CS, et al. Glioblastoma microenvironment and cellular interactions. *Cancers*. 2022;14(4):1092.
doi: 10.1002/adfm.201910250

24. Thenuwara G, Javed B, Singh B, Tian F. Biosensor-enhanced organ-on-a-chip models for investigating glioblastoma tumor microenvironment dynamics. *Sensors*. 2024;24(9):2865.
doi: 10.3390/s24092865

25. Parra-Cantu C, Li W, Quiñones-Hinojosa A, Zhang YS. 3D bioprinting of glioblastoma model. *J 3D Print Med*. 2020;4(2):113-125.
doi: 10.2217/3dp-2019-0027

26. Cadena M, Ning L, King A, et al. 3D bioprinting of neural tissues. *Adv Healthc Mater*. 2021;10(15):e2001600. doi: 10.1002/adhm.202001600

27. Khoeini R, Nosrati H, Akbarzadeh A, et al. Natural and synthetic bioinks for 3D bioprinting. *Adv NanoBiomed Res*. 2021;1(8):2000097. doi: 10.1002/anbr.202000097

28. Leong SW, Tan SC, Norhayati MN, Monif M, Lee S-Y. Effectiveness of bioinks and the clinical value of 3d bioprinted glioblastoma models: a systematic review. *Cancers*. 2022;14(9):2149. doi: 10.3390/cancers14092149

29. Tang M, Rich JN, Chen S. Biomaterials and 3D bioprinting strategies to model glioblastoma and the blood-brain barrier. *Adv Mater*. 2021;33(5):2004776. doi: 10.1002/adma.202004776v

30. Ma L, Li Y, Wu Y, et al. 3D bioprinted hyaluronic acid-based cell-laden scaffold for brain microenvironment simulation. *Bio-Design Manuf*. 2020;3:164-174. doi: 10.1007/s42242-020-00076-6

31. de la Vega L, Lee C, Sharma R, Amereh M, Willerth SM. 3D bioprinting models of neural tissues: the current state of the field and future directions. *Brain Res Bull*. 2019;150:240-249. doi: 10.1016/j.brainresbull.2019.06.007

32. Kumar SL, Sureka P, Sowmitha A, Sentisenla J, Swathy M. Recent advancements of hydroxyapatite and polyethylene glycol (PEG) composites for tissue engineering applications—a comprehensive review. *Eur Polym J*. 2024;215(9):113226. doi: 10.1016/j.eurpolymj.2024.113226

33. Shi L, Zhang J, Zhao M, et al. Effects of polyethylene glycol on the surface of nanoparticles for targeted drug delivery. *Nanoscale*. 2021;13(24):10748-10764. doi: 10.1039/D1NR02065J

34. Walus K, Beyer S, Willerth SM. Three-dimensional bioprinting healthy and diseased models of the brain tissue using stem cells. *Curr Opin Biomed Eng*. 2020;14:25-33. doi: 10.1016/j.cobme.2020.03.002

35. Lee SJ, Esworthy T, Stake S, et al. Advances in 3D bioprinting for neural tissue engineering. *Adv Biosyst*. 2018;2(4): 1700213. doi: 10.1002/adbi.201700213

36. Esworthy TJ, Miao S, Lee S-J, et al. Advanced 4D-bioprinting technologies for brain tissue modeling and study. *Int J Smart Nano Mater*. 2019;10(3):177-204. doi: 10.1080/19475411.2019.1631899

37. Wang X, Dai X, Zhang X, et al. 3D bioprinted glioma cell-laden scaffolds enriching glioma stem cells via epithelial–mesenchymal transition. *J Biomed Mater Res A*. 2019;107(2):383-391. doi: 10.1002/jbm.a.36549

38. Sánchez-Salazar MG, Álvarez MM, Trujillo-de Santiago G. Advances in 3D bioprinting for the biofabrication of tumor models. *Bioprinting*. 2021;21:e00120. doi: 10.1016/j.bprint.2020.e00120

39. Wang X, Li X, Ding J, et al. 3D bioprinted glioma microenvironment for glioma vascularization. *J Biomed Mater Res A*. 2021;109(6):915-925. doi: 10.1002/jbm.a.37082

40. Graber P, Dolman MEM, Jung M, Kavallaris M. Ex vivo modeling of the tumor microenvironment to develop therapeutic strategies for gliomas. *Adv Ther.* 2024:2300442. doi: 10.1002/adtp.202300442

41. Wang X, Li X, Dai X, et al. Coaxial extrusion bioprinted shell-core hydrogel microfibers mimic glioma microenvironment and enhance the drug resistance of cancer cells. *Colloids Surf B Biointerfaces*. 2018;171:291-299. doi: 10.1016/j.colsurfb.2018.07.042

42. Suresh P. Saponins-uptake and targeting issues for brain-specific delivery for enhanced cell death induction in glioblastoma. *Lett Drug Des Discov*. 2022;19(6): 473-480. doi: 10.2174/1570180819666220121145332

43. Dai X, Ma C, Lan Q, Xu T. 3D bioprinted glioma stem cells for brain tumor model and applications of drug susceptibility. *Biofabrication*. 2016;8(4):045005. doi: 10.1088/1758-5090/8/4/045005

44. Ahmed T. Biomaterial-based in vitro 3D modeling of glioblastoma multiforme. *Cancer Pathog Ther*. 2023;1(3):177-194. doi: 10.1016/j.cpt.2023.01.002

45. Han S, Kim S, Chen Z, et al. 3D bioprinted vascularized tumour for drug testing. *Int J Mol Sci*. 2020;21(8):2993. doi: 10.3390/ijms21082993

46. Kim EH, Song HS, Yoo SH, Yoon M. Tumor treating fields inhibit glioblastoma cell migration, invasion and angiogenesis. *Oncotarget*. 2016;7(40):65125-65136. doi: 10.18632/oncotarget.11372

47. Tricinci O, De Pasquale D, Marino A, Battaglini M, Pucci C, Ciofani G. A 3D biohybrid real-scale model of the brain cancer microenvironment for advanced in vitro testing. *Adv Mater Technol*. 2020;5(10):2000540. doi: 10.1002/admt.202000540

48. Bakirci E, Schaefer N, Dahri O, et al. Melt electrowritten in vitro radial device to study cell growth and migration. *Adv Biosyst*. 2020;4(10):2000077. doi: 10.1002/adbi.202000077

49. Huang W, Ding X, Ye H, Wang J, Shao J, Huang T. Hypoxia enhances the migration and invasion of human glioblastoma U87 cells through PI3K/Akt/mTOR/HIF-1α pathway. *Neuroreport*. 2018;29(18):1578-1585. doi: 10.1097/WNR.0000000000001156

50. Smits IP, Blaschuk OW, Willerth SM. Novel N-cadherin antagonist causes glioblastoma cell death in a 3D bioprinted co-culture model. *Biochem Biophys Res Commun*. 2020;529(2):162-168.
doi: 10.1016/j.bbrc.2020.06.001

51. Wang X, Li X, Dai X, et al. Bioprinting of glioma stem cells improves their endotheliogenic potential. *Colloids Surf B Biointerfaces*. 2018;171:629-637.
doi: 10.1016/j.colsurfb.2018.08.006

52. Böttcher B, Pflieger A, Schumacher J, Jungnickel B, Feller K-H. 3d bioprinting of prevascularized full-thickness gelatin-alginate structures with embedded co-cultures. *Bioengineering*. 2022;9(6):242.
doi: 10.3390/bioengineering9060242

53. Dai X, Liu L, Ouyang J, et al. Coaxial 3D bioprinting of self-assembled multicellular heterogeneous tumor fibers. *Sci Rep*. 2017;7(1):1457.
doi: 10.1038/s41598-017-01581-y

54. Zhang Z, Chen X, Gao S, Fang X, Ren S. 3D bioprinted tumor model: a prompt and convenient platform for overcoming immunotherapy resistance by recapitulating the tumor microenvironment. *Cell Oncol (Dordr)*. 2024;47:1113-1126.
doi: 10.1007/s13402-024-00935-9

55. Hermida MA, Kumar JD, Schwarz D, et al. Three dimensional in vitro models of cancer: Bioprinting multilineage glioblastoma models. *Adv Biol Regul*. 2020;75:100658.
doi: 10.1016/j.jbior.2019.100658

56. Jamee R, Araf Y, Naser IB, Promon SK. The promising rise of bioprinting in revolutionalizing medical science: advances and possibilities. *Regen Ther*. 2021;18:133-145.
doi: 10.1016/j.reth.2021.05.006

57. Schiffer D, Annovazzi L, Casalone C, Corona C, Mellai M. Glioblastoma: microenvironment and niche concept. *Cancers*. 2018;11(1):5.
doi: 10.3390/cancers11010005

58. Nieland L, Morsett LM, Broekman MLD, Breakefield XO, Abels ER. Extracellular vesicle-mediated bilateral communication between glioblastoma and astrocytes. *Trends Neurosci*. 2021;44(3):215-226.
doi: 10.1016/j.tins.2020.10.014

59. Figueroa J, Phillips LM, Shahar T, et al. Exosomes from glioma-associated mesenchymal stem cells increase the tumorigenicity of glioma stem-like cells via transfer of miR-1587. *Cancer Res*. 2017;77(21):5808-5819.
doi: 10.1158/0008-5472.can-16-2524

60. Parak A, Pradeep P, du Toit LC, Kumar P, Choonara YE, Pillay V. Functionalizing bioinks for 3D bioprinting applications. *Drug Discov Today*. 2019;24(1):198-205.
doi: 10.1016/j.drudis.2018.09.012

61. Heinrich MA, Bansal R, Lammers T, Zhang YS, Michel Schiffelers R, Prakash J. 3D-bioprinted mini-brain: a glioblastoma model to study cellular interactions and therapeutics. *Adv Mater*. 2019;31(14):1806590.
doi: 10.1002/adma.201806590

62. Wang L, Wang C, Wu S, Fan Y, Li X. Influence of the mechanical properties of biomaterials on degradability, cell behaviors and signaling pathways: current progress and challenges. *Biomater Sci*. 2020;8(10):2714-2733.
doi: 10.1039/D0BM00269K

63. Tang M, Tiwari SK, Agrawal K, et al. Rapid 3D bioprinting of glioblastoma model mimicking native biophysical heterogeneity. *Small*. 2021;17(15):2006050.
doi: 10.1002/smll.202006050

64. Yue K, Trujillo-de Santiago G, Alvarez MM, Tamayol A, Annabi N, Khademhosseini A. Synthesis, properties, and biomedical applications of gelatin methacryloyl (GelMA) hydrogels. *Biomaterials*. 2015;73:254-271.
doi: 10.1016/j.biomaterials.2015.08.045

65. Tavsanli B, Okay O. Mechanically strong hyaluronic acid hydrogels with an interpenetrating network structure. *Eur Polym J*. 2017;94:185-195.
doi: 10.1016/j.eurpolymj.2017.07.009

66. Stanković T, Ranđelović T, Dragoj M, et al. In vitro biomimetic models for glioblastoma-a promising tool for drug response studies. *Drug Resiste Updates*. 2021;55:100753.
doi: 10.1016/j.drup.2021.100753

67. Ivanov DP, Parker TL, Walker DA, et al. In vitro co-culture model of medulloblastoma and human neural stem cells for drug delivery assessment. *J Biotechnol*. 2015;205:3-13.
doi: 10.1016/j.jbiotec.2015.01.002

68. Northcott PA, Robinson GW, Kratz CP, et al. Medulloblastoma. *Nat Rev Dis Primers*. 2019;5(1):11.
doi: 10.1038/s41572-019-0063-6

69. Reyhanoglu G, Tadi P. Etoposide; 2020.

70. Iwadate Y. Epithelial-mesenchymal transition in glioblastoma progression. *Oncol Lett*. 2016;11(3):1615-1620.
doi: 10.3892/ol.2016.4113

71. Nowicki MO, Hayes JL, Chiocca EA, Lawler SE. Proteomic analysis implicates vimentin in glioblastoma cell migration. *Cancers*. 2019;11(4):466.
doi: 10.3390/cancers11040466

72. Huleihel L, Dziki JL, Bartolacci JG, et al. Macrophage phenotype in response to ECM bioscaffolds. *Semin Immunol*. 2017;29:2-13.
doi: 10.1016/j.smim.2017.04.004

73. Im JH, Buzzelli JN, Jones K, et al. FGF2 alters macrophage polarization, tumour immunity and growth and can be targeted during radiotherapy. *Nat Commun*. 2020;11(1):4064.
doi: 10.1038/s41467-020-17914-x

74. Chen Z, Feng X, Herting CJ, et al. Cellular and molecular identity of tumor-associated macrophages in glioblastoma. *Cancer Res*. 2017;77(9):2266-2278.
doi: 10.1158/0008-5472.CAN-16-2310

75. Sweeney MD, Zhao Z, Montagne A, Nelson AR, Zlokovic BV. Blood-brain barrier: from physiology to disease and back. *Physiol Rev*. 2018;99(1):21-78. doi: 10.1152/physrev.00050.2017

76. Alahmari A. Blood-brain barrier overview: structural and functional correlation. *Neural Plast*. 2021;2021:1-10. doi: 10.1155/2021/6564585

77. Aday S, Cecchelli R, Hallier-Vanuxeem D, Dehouck MP, Ferreira L. Stem cell-based human blood-brain barrier models for drug discovery and delivery. *Trends Biotechnol*. 2016;34(5):382-393. doi: 10.1016/j.tibtech.2016.01.001

78. Gastfriend BD, Palecek SP, Shusta EV. Modeling the blood-brain barrier: Beyond the endothelial cells. *Curr Opin Biomed Eng*. Mar 2018;5:6-12. doi: 10.1016/j.cobme.2017.11.002

79. Brown LS, Foster CG, Courtney JM, King NE, Howells DW, Sutherland BA. Pericytes and neurovascular function in the healthy and diseased brain. *Front Cell Neurosci*. 2019; 13:282. doi: 10.3389/fncel.2019.00282

80. Heithoff BP, George KK, Phares AN, Zuidhoek IA, Munoz-Ballester C, Robel S. Astrocytes are necessary for blood–brain barrier maintenance in the adult mouse brain. *Glia*. 2021;69(2):436-472. doi: 10.1002/glia.23908

81. Luo H, Shusta EV. Blood-brain barrier modulation to improve glioma drug delivery. *Pharmaceutics*. 2020;12(11):1085. doi: 10.3390/pharmaceutics12111085

82. Chaulagain B, Gothwal A, Lamptey RNL, et al. Experimental models of in vitro blood–brain barrier for CNS drug delivery: an evolutionary perspective. *Int J Mol Sci*. 2023; 24(3):2710. doi: 10.3390/ijms24032710

83. Sivandzade F, Cucullo L. In-vitro blood-brain barrier modeling: A review of modern and fast-advancing technologies. *J Cereb Blood Flow Metab*. 2018;38(10):1667-1681. doi: 10.1177/0271678X18788769

84. Risau W, Wolburg H. Development of the blood-brain barrier. *Trends Neurosci*. 1990;13(5):174-178. doi: 10.1016/0166-2236(90)90043-a

85. Ventura RD. An overview of laser-assisted bioprinting (LAB) in tissue engineering applications. *Med Lasers* 2021;10(2):76-81. doi: 10.25289/ML.2021.10.2.76

86. Marino A, Tricinci O, Battaglini M, et al. A 3D real-scale, biomimetic, and biohybrid model of the blood-brain barrier fabricated through two-photon lithography. *Small*. 2018;14(6):1702959. doi: 10.1002/smll.201702959

87. Liu Z-L, Chen H-H, Zheng L-L, Sun L-P, Shi L. Angiogenic signaling pathways and anti-angiogenic therapy for cancer. *Signal Trans Targeted Ther*. 2023;8(1):198. doi: 10.1038/s41392-023-01460-1

88. Akbarian M, Bertassoni LE, Tayebi L. Biological aspects in controlling angiogenesis: current progress. *Cell Mol Life Sci*. 2022;79(7):349. doi: 10.1007/s00018-022-04348-5

89. Ansari MJ, Bokov D, Markov A, et al. Cancer combination therapies by angiogenesis inhibitors; a comprehensive review. *Cell Commun Signal*. 2022;20(1):49. doi: 10.1186/s12964-022-00838-y

90. Cao Y, Langer R, Ferrara N. Targeting angiogenesis in oncology, ophthalmology and beyond. *Nat Rev Drug Discov*. 2023;22(6):476-495. doi: 10.1038/s41573-023-00671-z

91. Yang Y, Cao Y. The impact of VEGF on cancer metastasis and systemic disease. *Semin Cancer Biol*. 2022;86(Pt 3):251-261. doi: 10.1016/j.semcancer.2022.03.011

92. Ahmad A, Nawaz MI. Molecular mechanism of VEGF and its role in pathological angiogenesis. *J Cell Biochem*. 2022;123(12):1938-1965. doi: 10.1002/jcb.30344

93. Xu D, Luo Y, Wang P, et al. Clinical progress of anti-angiogenic targeted therapy and combination therapy for gastric cancer. *Front Oncol*. 2023;13:1148131. doi: 10.3389/fonc.2023.1148131

94. Zou G, Zhang X, Wang L, et al. Herb-sourced emodin inhibits angiogenesis of breast cancer by targeting VEGFA transcription. *Theranostics*. 2020;10(15):6839-6853. doi: 10.7150/thno.43622

95. Majewska A, Wilkus K, Brodaczewska K, Kieda C. Endothelial cells as tools to model tissue microenvironment in hypoxia-dependent pathologies. *Int J Mol Sci*. 2021;22(2):520. doi: 10.3390/ijms22020520

96. Lizarraga-Verdugo E, Avendano-Felix M, Bermudez M, Ramos-Payan R, Perez-Plasencia C, Aguilar-Medina M. Cancer stem cells and its role in angiogenesis and vasculogenic mimicry in gastrointestinal cancers. *Front Oncol*. 2020;10:413. doi: 10.3389/fonc.2020.00413

97. Schulte JD, Aghi MK, Taylor JW. Anti-angiogenic therapies in the management of glioblastoma. *Chin Clin Oncol*. 2021;10(4):37. doi: 10.21037/cco.2020.03.06

98. Claesson-Welsh L, Welsh M. VEGFA and tumour angiogenesis. *J Intern Med*. 2013;273(2):114-27. doi: 10.1111/joim.12019

99. Mandrycky CJ, Howard CC, Rayner SG, Shin YJ, Zheng Y. Organ-on-a-chip systems for vascular biology. *J Mol Cell Cardiol*. 2021;159:1-13.

doi: 10.1016/j.yjmcc.2021.06.002

100. Pollet A, den Toonder JMJ. Recapitulating the vasculature using organ-on-chip technology. *Bioengineering (Basel)*. 2020;7(1):17.
doi: 10.3390/bioengineering7010017

101. Farhang Doost N, Srivastava SK. A comprehensive review of organ-on-a-chip technology and its applications. *Biosensors*. 2024;14(5):225.
doi: 10.3390/bios14050225

102. Kumar V, Varghese S. Ex vivo tumor-on-a-chip platforms to study intercellular interactions within the tumor microenvironment. *Adv Healthc Mater*. 2019;8(4): 1801198.
doi: 10.1002/adhm.201801198

103. Fetah K, Tebon P, Goudie MJ, et al. The emergence of 3D bioprinting in organ-on-chip systems. *Prog Biomed Eng*. 2019;1(1):012001.
doi: 10.1088/2516-1091/ab23df

104. Gao Q, Liu Z, Lin Z, et al. 3D bioprinting of vessel-like structures with multilevel fluidic channels. *ACS Biomater Sci Eng*. 2017;3(3):399-408.
doi: 10.1021/acsbiomaterials.6b00643

105. Samadian H, Jafari S, Sepand M, et al. 3D bioprinting technology to mimic the tumor microenvironment: tumor-on-a-chip concept. *Mater Today Adv*. 2021;12:100160.
doi: 10.1016/j.mtadv.2021.100160

106. Alves AH, Nucci MP, Mamani JB, et al. The advances in glioblastoma on-a-chip for therapy approaches. *Cancers*. 2022;14(4):869.
doi: 10.3390/cancers14040869

107. Song Q, Sun J, Mu Y, Xu Y, Zhu Q, Jin Q. A new method for polydimethylsiloxane (PDMS) microfluidic chips to maintain vacuum-driven power using Parylene C. *Sens Actuators B: Chem*. 2018;256:1122-1130.
doi: 10.1016/j.snb.2017.10.006

108. Tabatabaei Rezaei N, Kumar H, Liu H, Lee SS, Park SS, Kim K. Recent advances in organ-on-chips integrated with bioprinting technologies for drug screening. *Adv Healthc Mater*. 2023;12(20):e2203172.
doi: 10.1002/adhm.202203172

109. Nie J, Gao Q, Fu J, He Y. Grafting of 3D bioprinting to in vitro drug screening: a review. *Adv Healthc Mater*. 2020;9(7):e1901773.
doi: 10.1002/adhm.201901773

110. Radhakrishnan J, Varadaraj S, Dash SK, Sharma A, Verma RS. Organotypic cancer tissue models for drug screening: 3D constructs, bioprinting and microfluidic chips. *Drug Discov Today*. 2020;25(5):879-890.
doi: 10.1016/j.drudis.2020.03.002

111. Yang Z, Wu S, Fontana F, et al. The tight junction protein Claudin-5 limits endothelial cell motility. *J Cell Sci*. 2021;134(1):jcs248237.
doi: 10.1242/jcs.248237

112. Greene C, Campbell M. Tight junction modulation of the blood brain barrier: CNS delivery of small molecules. *Tissue Barriers*. 2016;4(1):e1138017.
doi: 10.1080/21688370.2015.1138017

113. Yang JY, Shin D-S, Jeong M, et al. Evaluation of drug blood-brain-barrier permeability using a microfluidic chip. *Pharmaceutics*. 2024;16(5):574.
doi: 10.3390/pharmaceutics16050574

114. Chittiboyina S, Rahimi R, Atrian F, Ochoa M, Ziaie B, Lelievre SA. Gradient-on-a-chip with reactive oxygen species reveals thresholds in the nucleus response of cancer cells depending on the matrix environment. *ACS Biomater Sci Eng*. 2018;4(2):432-445.
doi: 10.1021/acsbiomaterials.7b00087

115. Sontheimer-Phelps A, Hassell BA, Ingber DE. Modelling cancer in microfluidic human organs-on-chips. *Nat Rev Cancer*. 2019;19(2):65-81.
doi: 10.1038/s41568-018-0104-6

116. Malik A, Pal R, Gupta SK. EGF-mediated reduced miR-92a-1-5p controls HTR-8/SVneo cell invasion through activation of MAPK8 and FAS which in turn increase MMP-2/-9 expression. *Sci Rep*. 2020;10(1):12274.
doi: 10.1038/s41598-020-68966-4

117. Liu D, Yang T, Ma W, Wang Y. Clinical strategies to manage adult glioblastoma patients without MGMT hypermethylation. *J Cancer*. 2022;13(1):354.
doi: 10.7150/jca.63595

118. Qu S, Qi S, Zhang H, et al. Albumin-bound paclitaxel augment temozolomide treatment sensitivity of glioblastoma cells by disrupting DNA damage repair and promoting ferroptosis. *J Exp Clin Cancer Res*. 2023;42(1):285.
doi: 10.1186/s13046-023-02843-6

119. Tsai C-Y, Ko H-J, Huang C-YF, et al. Ionizing radiation induces resistant glioblastoma stem-like cells by promoting autophagy via the Wnt/β-catenin pathway. *Life*. 2021;11(5):451.
doi: 10.3390/life11050451

120. Yu W, Zhang L, Wei Q, Shao A. O6-methylguanine-DNA methyltransferase (MGMT): challenges and new opportunities in glioma chemotherapy. *Front Oncol*. 2020;9:1547.
doi: 10.3389/fonc.2019.01547

121. Kohutova A, Munzova D, Pesl M, Rotrekl V. alpha(1)-Adrenoceptor agonist methoxamine inhibits base excision repair via inhibition of apurinic/apyrimidinic endonuclease 1 (APE1). *Acta Pharm*. 2023;73(2):281-291.
doi: 10.2478/acph-2023-0012

122. Burman P, Lamb L, McCormack A. Temozolomide therapy for aggressive pituitary tumours–current understanding and future perspectives. *Rev Endocr Metab Disord*. 2020;21:263-276.

doi: 10.1007/s11154-020-09551-y

123. Erasimus H, Gobin M, Niclou S, Van Dyck E. DNA repair mechanisms and their clinical impact in glioblastoma. *Mutat Res Rev Mutat Res*. 2016;769:19-35. doi: 10.1016/j.mrrev.2016.05.005

124. Shu J, Wang X, Yang X, Zhao G. Author correction: ATM inhibitor KU60019 synergistically sensitizes lung cancer cells to topoisomerase II poisons by multiple mechanisms. *Sci Rep*. 2024;14(1):8785. doi: 10.1038/s41598-024-59332-9

125. Wang C, Li J, Sinha S, Peterson A, Grant GA, Yang F. Mimicking brain tumor-vasculature microanatomical architecture via co-culture of brain tumor and endothelial cells in 3D hydrogels. *Biomaterials*. 2019;202:35-44. doi: 10.1016/j.biomaterials.2019.02.024

126. Nguyen T, Sarkar T, Tran T, Moinuddin SM, Saha D, Ahsan F. Multilayer soft photolithography fabrication of microfluidic devices using a custom-built wafer-scale PDMS slab aligner and cost-efficient equipment. *Micromachines (Basel)*. 2022;13(8):1357. doi: 10.3390/mi13081357

127. Neufeld L, Yeini E, Reisman N, et al. Microengineered perfusable 3D-bioprinted glioblastoma model for in vivo mimicry of tumor microenvironment. *Sci Adv*. 2021;7(34):eabi9119. doi: 10.1126/sciadv.abi9119

128. Schober AL, Wicki-Stordeur LE, Murai KK, Swayne LA. Foundations and implications of astrocyte heterogeneity during brain development and disease. *Trends Neurosci*. 2022;45(9):692-703. doi: 10.1016/j.tins.2022.06.009

129. Slika H, Karimov Z, Alimonti P, et al. Preclinical models and technologies in glioblastoma research: evolution, current state, and future avenues. *Int J Mol Sci*. 2023;24(22):16316. doi: 10.3390/ijms242216316

130. Jung S, Jo H, Hyung S, Jeon NL. Advances in 3D vascularized tumor-on-a-Chip technology. *Adv Exp Med Biol*.2022;1379:231-256. doi: 10.1007/978-3-031-04039-9_9

131. Li W, Zhou Z, Zhou X, et al. 3D biomimetic models to reconstitute tumor microenvironment in vitro: spheroids, organoids, and tumor-on-a-chip. *Adv Healthc Mater*. 2023;12(18):2202609. doi: 10.1002/adhm.202202609

132. Langhans SA. Three-dimensional in vitro cell culture models in drug discovery and drug repositioning. *Front Pharmacol*. 2018;9:6. doi: 10.3389/fphar.2018.00006

133. Joseph JS, Malindisa ST, Ntwasa M. Two-dimensional (2D) and three-dimensional (3D) cell culturing in drug discovery. *Cell Cult*. 2018;2:1-22. doi: 10.5772/intechopen.81552

134. Hagenbuchner J, Nothdurfter D, Ausserlechner MJ. 3D bioprinting: novel approaches for engineering complex human tissue equivalents and drug testing. *Essays Biochem*. 2021;65(3):417-427. doi: 10.1042/EBC20200153

135. Sunildutt N, Parihar P, Chethikkattuveli Salih AR, Lee SH, Choi KH. Revolutionizing drug development: harnessing the potential of organ-on-chip technology for disease modeling and drug discovery. *Front Pharmacol*. 2023;14:1139229. doi: 10.3389/fphar.2023.1139229

136. Peng W, Datta P, Ayan B, Ozbolat V, Sosnoski D, Ozbolat IT. 3D bioprinting for drug discovery and development in pharmaceutics. *Acta Biomater*. 2017;57:26-46. doi: 10.1016/j.actbio.2017.05.025

137. Satpathy A, Datta P, Wu Y, Ayan B, Bayram E, Ozbolat IT. Developments with 3D bioprinting for novel drug discovery. *Expert Opin Drug Discov*. 2018;13(12):1115-1129. doi: 10.1080/17460441.2018.1542427

138. Yun EJ, Kim S, Hsieh JT, Baek ST. Wnt/beta-catenin signaling pathway induces autophagy-mediated temozolomide-resistance in human glioblastoma. *Cell Death Dis*. 2020;11(9):771. doi: 10.1038/s41419-020-02988-8

139. Song Q, Peng S, Sun Z, Heng X, Zhu X. Temozolomide drives ferroptosis via a DMT1-dependent pathway in glioblastoma cells. *Yonsei Med J*. 2021;62(9):843-849. doi: 10.3349/ymj.2021.62.9.843

140. Karve AS, Desai JM, Gadgil SN, et al. A review of approaches to potentiate the activity of temozolomide against glioblastoma to overcome resistance. *Int J Mol Sci*. 2024;25(6):3217. doi: 10.3390/ijms25063217

141. Ibarra LE, Vilchez ML, Caverzan MD, Milla Sanabria LN. Understanding the glioblastoma tumor biology to optimize photodynamic therapy: From molecular to cellular events. *J Neurosci Res*. 2021;99(4):1024-1047. doi: 10.1002/jnr.24776

142. Reed MR, Maddukuri L, Ketkar A, et al. Inhibition of tryptophan 2,3-dioxygenase impairs DNA damage tolerance and repair in glioma cells. *NAR Cancer*. 2021;3(2):zcab014. doi: 10.1093/narcan/zcab014

143. Cirri D, Chiaverini L, Pratesi A, Marzo T. Is the next cisplatin already in our laboratory? *Comm Inorganic Chem*. 2023;43(6):465-478. doi: 10.1080/02603594.2022.2152016

144. Luo H, Yi T, Huang D, et al. circ_PTN contributes to-cisplatin resistance in glioblastoma via PI3K/AKT signaling through the miR-542-3p/PIK3R3 pathway. *Mol Ther Nucleic Acids*. 2021;26:1255-1269. doi: 10.1016/j.omtn.2021.08.034

145. Lee SH, Kang MS, Jeon S, et al. 3D bioprinting of human mesenchymal stem cells-laden hydrogels incorporating MXene for spontaneous osteodifferentiation. *Heliyon*. 2023;9(3):e14490.
doi: 10.1016/j.heliyon.2023.e14490

146. Vignesh A, Binoy A, Thurakkal L, Bhuvanesh NS, Sadhukhan S, Porel M. Pyrene aroylhydrazone-based Pd (II) complexes for DNA/protein binding, cellular imaging and in vitro anticancer activity via ROS production. *J Mol Struct*. 2024;1295:136693.
doi: 10.1016/j.molstruc.2023.136693

147. Ma Q, Sun J, Wang H, et al. Far upstream element-binding protein 1 confers lobaplatin resistance by transcriptionally activating PTGES and facilitating the arachidonic acid metabolic pathway in osteosarcoma. *Med Comm (2020)*. 2023;4(3):e257.
doi: 10.1002/mco2.257

148. Du L, Fei Z, Song S, Wei N. Antitumor activity of Lobaplatin against esophageal squamous cell carcinoma through caspase-dependent apoptosis and increasing the Bax/Bcl-2 ratio. *Biomed Pharmacother*. 2017;95:447-452.
doi: 10.1016/j.biopha.2017.08.119

149. Vaz-Salgado MA, Villamayor M, Albarran V, et al. Recurrent glioblastoma: a review of the treatment options. *Cancers (Basel)*. 2023;15(17):4279.
doi: 10.3390/cancers15174279

150. Yamamuro S, Takahashi M, Satomi K, et al. Lomustine and nimustine exert efficient antitumor effects against glioblastoma models with acquired temozolomide resistance. *Cancer Sci*. 2021;112(11):4736-4747.
doi: 10.1111/cas.15141

151. Schneider M, Potthoff AL, Evert BO, et al. Inhibition of Intercellular Cytosolic Traffic via Gap Junctions Reinforces Lomustine-Induced Toxicity in Glioblastoma Independent of MGMT Promoter Methylation Status. *Pharmaceuticals (Basel)*. 2021;14(3):195.
doi: 10.3390/ph14030195

152. Amrein PC. Low-dose dasatinib: when less can be more. *Lancet Haematol*. 2021;8(12):e867-e868.
doi: 10.1016/S2352-3026(21)00342-2

153. Owusu A, Bonnaire K, Hailemeskel B. Lovastatin use in transplant: a review and survey. *Int J Pharm Res Allied Sci*. 2024;13(1):83-90.
doi: 10.51847/LJ2kXhjbtG

154. Alhalabi OT, Fletcher MNC, Hielscher T, et al. A novel patient stratification strategy to enhance the therapeutic efficacy of dasatinib in glioblastoma. *Neuro Oncol*. 2022;24(1): 39-51.
doi: 10.1093/neuonc/noab158

155. Ryu KY, Lee HJ, Woo H, et al. Dasatinib regulates LPS-induced microglial and astrocytic neuroinflammatory responses by inhibiting AKT/STAT3 signaling. *J Neuroinflammation*. 2019;16(1):190.
doi: 10.1186/s12974-019-1561-x

156. Liu PC, Lu G, Deng Y, et al. Inhibition of NF-kappaB pathway and modulation of MAPK signaling pathways in glioblastoma and implications for lovastatin and tumor necrosis factor-related apoptosis inducing ligand (TRAIL) combination therapy. *PLoS One*. 2017;12(1):e0171157.
doi: 10.1371/journal.pone.0171157

157. Zhu Z, Zhang P, Li N, et al. Lovastatin enhances cytotoxicity of temozolomide via impairing autophagic flux in glioblastoma cells. *Biomed Res Int*. 2019;2019:2710693.
doi: 10.1155/2019/2710693

158. Wu Q, Zhu C, Zhang S, Zhou Y, Zhong Y. Hematological toxicities of concurrent chemoradiotherapies in head and neck cancers: comparison among cisplatin, nedaplatin, lobaplatin, and nimotuzumab. *Front Oncol*. 2021;11:762366.
doi: 10.3389/fonc.2021.762366

159. Hua S, Kong X, Chen B, et al. Anticancer mechanism of lobaplatin as monotherapy and in combination with paclitaxel in human gastric cancer. *Curr Mol Pharmacol*. 2018;11(4):316-325.
doi: 10.2174/1874467211666180813095050

160. Weller M, Le Rhun E. How did lomustine become standard of care in recurrent glioblastoma? *Cancer Treat Rev*. 2020;87:102029.
doi: 10.1016/j.ctrv.2020.102029

161. Mekala JR, Adusumilli K, Chamarthy S, Angirekula HSR. Novel sights on therapeutic, prognostic, and diagnostics aspects of non-coding RNAs in glioblastoma multiforme. *Metabolic Brain Dis*. 2023;38(6):1801-1829.
doi: 10.1007/s11011-023-01234-2

162. Wang X, Luo Y, Ma Y, Wang P, Yao R. Converging bioprinting and organoids to better recapitulate the tumor microenvironment. *Trends Biotechnol*. 2024;42(5):648-663.
doi: 10.1016/j.tibtech.2023.11.006

163. Li Y, Liu J, Xu S, Wang J. 3D bioprinting: an important tool for tumor microenvironment research. *Int J Nanomed*. 2023:18;8039-8057.
doi: 10.2147/IJN.S435845

164. Shah B, Dong X. Current status of in vitro models of the blood-brain barrier. *Curr Drug Deliv*. 2022;
doi: 10.2174/1567201819666220303102614

165. Yigci D, Sarabi MR, Ustun M, et al. 3D bioprinted glioma models. *Prog Biomed Eng*. 2022;4(4):042001.
doi: 10.1088/2516-1091/ac7833

ACCSCIENCE PUBLISHING

International Journal of Bioprinting

RESEARCH ARTICLE

Electrospun polylactic acid-glycolic acid composite hydrogel scaffold loaded with 3D extracellular vesicles for nasal septal cartilage defect repair

Jie Yang[1,2†], Haolei Hu[2†], Qiang Guo[3†], Xiaolei Chen[1], Shuo Li[1], Gang Yin[2], Wei Yue[2], Yi Zhang[5], Boxun Liu[5], Jianwei Chen[4*], Tao Xu[4*], and Yi Li[2*]

[1]Department of Clinical, Faculty of Graduate Student, Xinxiang Medical University, Xinxiang City, 453003, Henan Province, China

[2]Department of Otolaryngology, The 988th Hospital of the Joint Support Force of the Chinese People's Liberation Army, Zhengzhou City, 450042, Henan Province, China

[3]Department of Urology, The Sixth Affiliated Hospital, Sun Yat-sen University, No 26 Yuancun Erheng Road, Guangzhou, 540655, Guangdong, China

[4]Bio-intelligent Manufacturing and Living Matter Bioprinting Center, Research Institute of Tsinghua University in Shenzhen, Tsinghua University, Shenzhen, 518053, Guangdong, China

[5]Department of Research and Development, Huaqing Zhimei (Shenzhen) Biotechnology Co., Ltd., Shenzhen 518107, Guangdong, China

(This article belongs to the Special Issue: *Bioprinting of Tissues and Organs: Materials, Technologies and Perspectives for Regenerative Medicine*)

Abstract

The nasal septum plays an important role in the growth and support of the human nose, and defects can cause nasal deformities. Extracellular vesicles (EVs) have demonstrated great potential in tissue repair. Stem cell EVs are widely used in the repair of articular cartilage defects, but their use for nasal septal cartilage defects has not been reported. Due to the low yield and loss of EVs during *in situ* injection, improved preparation methods and better carriers are needed for the effective sustained release of EVs in wounds. In this study, swelling and degradation experiments were initially conducted on the scaffold, along with mechanical performance testing, including observation of the scaffold morphology using scanning electron microscopy (SEM). Subsequently, *in vitro* cell experiments were conducted to evaluate the ability of 3D EVs to promote chondrocyte proliferation, migration, and extracellular matrix formation. Finally, the EV-laden gelatin methacrylic acid-polylactic acid-glycolic acid (Gel-PLGA) composite scaffold was implanted into the nasal septum defect site of rabbits *in vivo* to observe its repair effect on the defect. *In vitro* experiments demonstrated that the biological scaffold exhibited good biocompatibility and could effectively promote the proliferation and migration of chondrocytes. *In vivo*, the EV-laden composite biological scaffold was implanted into the nasal septum defect of rabbits, and the tissues were tested at 6 and 12 weeks after surgery. The results indicate that the composite scaffolds effectively facilitated the repair of defect sites. Taken together, 3D EVs facilitate tissue repair and healing, offering a novel approach to treating nasal septal defects.

Keywords: 3D printing; Electrospinning; Hydrogel; Extracellular vesicles; Nasal septal defect

[†]These authors contributed equally to this work.

Affiliations 1 and 2 are the co-first institutions

***Corresponding authors:**
Jianwei Chen (chenjw@tsinghua-sz.org)

Tao Xu (taoxu@mail.tsinghua.edu.cn)

Yi Li (liyi153@aliyun.com)

Citation: Yang J, Hu H, Guo Q, et al. Electrospun polylactic acid-glycolic acid composite hydrogel scaffold loaded with 3D extracellular vesicles for nasal septal cartilage defect repair. *Int J Bioprint.* 2024;10(6):4118. doi: 10.36922/ijb.4118

Received: July 2, 2024
Revised: August 11, 2024
Accepted: August 19, 2024
Published Online: August 20, 2024

Copyright: © 2024 Author(s). This is an Open Access article distributed under the terms of the Creative Commons Attribution License, permitting distribution, and reproduction in any medium, provided the original work is properly cited.

Publisher's Note: AccScience Publishing remains neutral with regard to jurisdictional claims in published maps and institutional affiliations.

1. Introduction

Nasal septal cartilage is hyaline cartilage, a specialized connective tissue that is devoid of blood vessels, nerves, and lymphatics.[1] Nasal septal cartilage is composed of approximately 1% chondrocytes and 99% extracellular matrix,[2] which imparts specific mechanical properties.[3] Nasal deformities caused by congenital nasal septal defects are rare. Most common nasal septal defects are caused by tumor resection and trauma.[4] These defects are often accompanied by facial deformities, which can significantly impact the patient's quality of life and psychological well-being.[5] Due to the poor self-repair ability of septal cartilage, it is difficult for the defected cartilage to rely on surrounding normal chondrocytes for repair. As a result, the defect often leads to varying degrees of nose deformity and dysfunction.[6] Currently, the most commonly used methods for repairing nasal septal defects include prosthesis implantation or autologous rib cartilage and ear cartilage.[7] However, using these materials for defect repair can easily compress the lower part of the nose and lead to poor ventilation.[8] Additionally, the use of autologous cartilage as graft material for repair poses challenges such as secondary damage, difficult shaping, easy deformation, and easy absorption after implantation. In contrast, the use of allogeneic cartilage for repair may be affected by immune rejection and the risk of related disease,[2] causing significant concerns for both doctors and patients. Although artificial materials are easy to shape and resistant to absorption, their implantation *in vivo* can induce rejection reactions and secondary infections, and their stability in the human body remains inadequate.[9,10]

The use of extracellular vesicles (EVs) for filling is a potential treatment for cartilage defects. These tiny vesicles, typically measuring 30–150 nm in diameter, are primarily produced by mesenchymal stem cell (MSC)-derived paracrine and have demonstrated promise in treating cartilage damage.[11] EVs are primarily composed of lipid molecular layers that encapsulate various nucleic acids, proteins, and molecules, promoting cell communication. Due to their nano-sized structure, EVs can be easily taken up by cells, allowing them to release their contents within the cell and play a role in promoting cell communication, as well as tissue regeneration and repair.[12] EVs have been utilized in the treatment of various clinical diseases, particularly cardiovascular diseases[13] and skin wound repair.[14,15] Studies have demonstrated that EVs can effectively enhance the proliferation and migration of chondrocytes, as well as the deposition of cartilage extracellular matrix, thereby facilitating the repair of cartilage defects.[16] This indicates the significant potential for using EVs in repairing nasal septal defects, though none has been reported to date.

Extracellular vesicles (EVs) are conventionally obtained via 2D extraction, which entails the monolayer culture of stem cells. However, studies have indicated that the growth environment of MSCs in 2D conditions differs significantly from that of natural stem cells *in vivo*,[17] resulting in limited stemness and functionality of the EVs secreted by MSCs.[18] In recent years, numerous studies have demonstrated that EVs secreted by MSCs cultured in a 3D environment exhibit significantly enhanced abilities to promote cell proliferation and cell communication.[19] For instance, Chen *et al.*[20] designed a method to culture MSCs in hollow alginate hydrogel microfibers using coaxial printing technology, significantly enhancing the enrichment efficiency and stemness of extracted EVs. Thus, this method can provide an ample supply of raw materials for regenerative EV treatment.

Injecting EVs into the damaged area often leads to significant loss, resulting in short residence time and low utilization of the target site. Therefore, there is a need for a tool that can retain EVs at the damaged site for a longer period.[21] Additionally, an ideal biological scaffold should maintain its shape and size,[22] which is why we focused on tissue-engineered biomaterials. Gelatin methacrylic acid (GelMA) is a widely used biomaterial in soft tissue repair due to its good biocompatibility, degradability, tunable mechanical properties, and drug-loading capabilities, thereby promoting cartilage repair and serving as an excellent carrier for sustained release of EVs.[23]. However, GelMA alone has relatively poor mechanical properties, making it difficult to simulate the mechanical modulus of the nasal septum.[24] Furthermore, due to the small number of cells in the nasal septal cartilage, achieving rapid defect healing is challenging, even with the support of EVs.[25] Therefore, we utilized polylactic acid-glycolic acid (PLGA) in combination with electrospinning technology to fabricate biological scaffolds for promoting chondrocyte adhesion and proliferation at the defect site. The PLGA electrospun membrane, when combined with hydrogel, offers mechanical support to better mimic the mechanical properties of nasal septal cartilage. Research has indicated that the 3D arrangement of electrospun fibers closely resembles natural collagen fibers in the extracellular matrix, effectively promoting chondrocyte adhesion, proliferation, and migration.[26] PLGA is a synthetic biomaterial with excellent biocompatibility and mechanical properties, which helps maintain the functional morphology of cartilage and promotes the synthesis of cartilage extracellular matrix.[27]

Currently, there is no effective engineering method for repairing nasal septal defects. In this study, we developed a composite PLGA-electrospun scaffold hydrogel for the sustained release of 3D EVs to promote nasal septum repair. The composite hydrogel scaffold serves as

temporary support, with PLGA nanofilaments arranged in an extracellular matrix fiber-like pattern to provide directional cell adhesion and growth sites. This composite hydrogel scaffold addresses the issue of EV injection loss by enabling slow release over an extended period, enhancing repair efficacy. After comparing the effects of 2D and 3D EVs on chondrocyte function, we investigate the effect of different concentrations of 3D EVs on chondrocyte proliferation, migration, and extracellular matrix production. Additionally, we constructed an *in vivo* model of nasal septal defect in rabbits and implanted biological scaffolds with or without EVs into the rabbits to explore the potential of EVs for tissue repair. The comprehensive experimental procedure is illustrated in Figure 1.

2. Materials and methods

2.1. Material preparation

Rabbit nasal septal chondrocytes were purchased from CMBIO (China); GelMA hydrogels were purchased from Engineering For Life (China). The PLGA-electrospun biofilm was synthesized as previously reported.[28] Briefly, 2 g PLGA (75:25) particles (Xinmiao, China) were combined at 14.5 wt% dissolved in hexafluoroisopropanol (Aladdin, China) and stirred at room temperature for 2 h. The solution was then added to the electrospinning equipment after the particles had completely dissolved. The high-voltage power supply was connected to the positive point of the discharge port; the receiver was connected to the negative point of the high-voltage power supply; the voltage was set to 16 kV; the distance between the discharge port and the receiver was set to 17.5 cm; and the discharge flow rate of the solution was set to 15 μL/ min. The biofilm was collected after electrospinning for 2 h using a 5 mL syringe with an 18-G needle, and the biofilm was incubated in a 37°C drying oven overnight to obtain the materials required for the experiment.

The composite scaffold is mainly composed of a combination of GelMA hydrogel and PLGA scaffold. Based on previous studies, a 10% hydrogel solution was used in this experiment.[29] Briefly, solid GelMA was dissolved in a photoinitiator solution at a 1:10 ratio in the dark, and the hydrogel solution was obtained by heating and shaking at 37°C using a dry bath (Thermo Scientific, China) for 40 min. The PLGA biofilm was cut into appropriate sizes and placed in molds. The prepared GelMA solution was added to the mold, and the hydrogel was light-cured into a gel using an ultraviolet (UV) light source (EFL, China) to obtain the desired composite scaffold. To ensure the accuracy of the experiment, we uniformly used a 3 W UV light source for 30 s for the light-curing process.

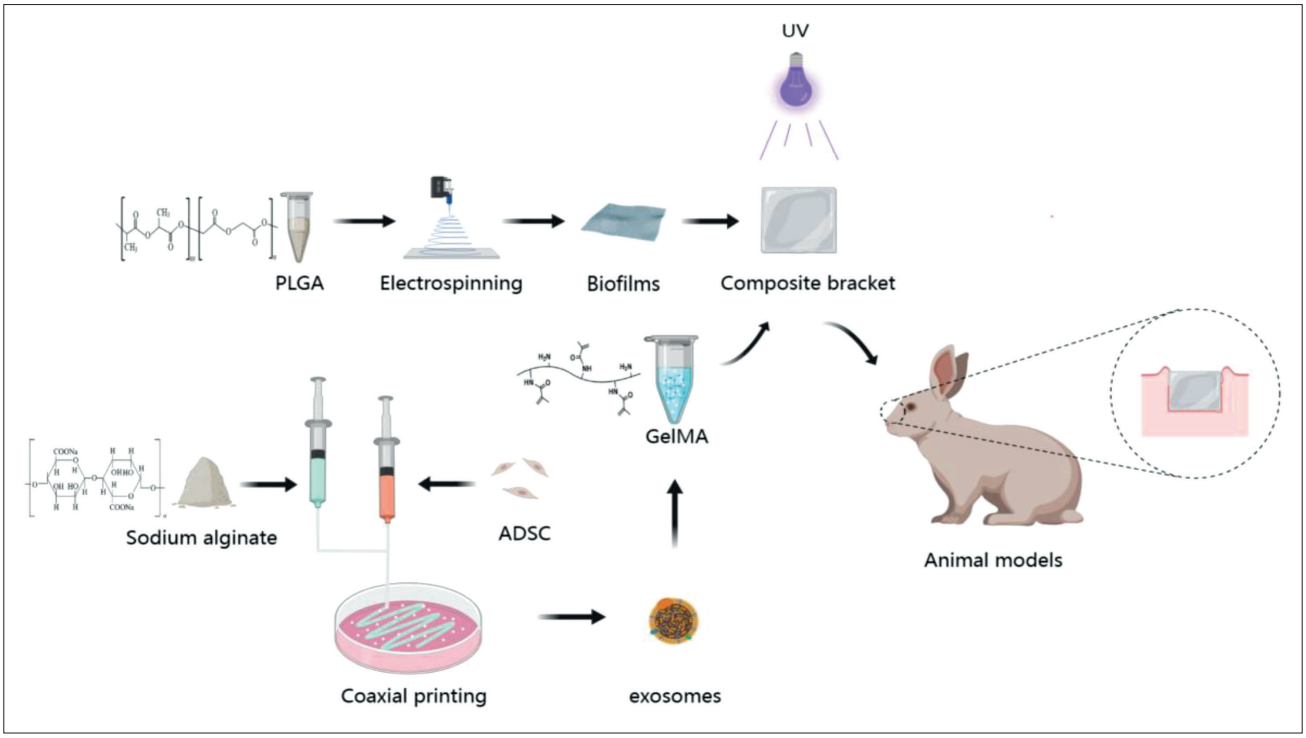

Figure 1. Schematic diagram of extracellular vesicle (EV)-loaded GelMA-PLGA composite scaffold implanted at the nasal septal defect site in rabbits. Abbreviations: PLGA: Polylactic acid-glycolic acid; ADSC: Adipose-derived stem cell; GELMA Gelatin methacrylic acid; UV: Ultraviolet light.

2.2. Isolation, identification, and staining of EVs from adipose-derived stem cells (ADSCs)

2.2.1. Isolation of EVs

The acquisition of 3D EVs is based on the findings of Chen *et al.*,[20] which involved the use of coaxial printing to obtain 3D adipose-derived stem cell (ADSC)-derived EVs. In this study, 1.5% alginate solution was used for shell flow at 20 mL/h; ADSC suspension (ScinencellTM Laboratories, USA) was used for core flow at 5 mL/h.; 3% $CaCl_2$ solution was used as the receiving medium. The alginate solution in the shell flow rapidly gelled in the $CaCl_2$ solution, forming microfibers that encapsulated the cells within approximately 10 min. The microfibers were then rinsed with a 0.9% NaCl solution for 5 min, before being transferred to a 150 mm Petri dish (Zhennuo, China) containing 25 mL MSC complete medium (NC0103; Yocon, China). The dish was then placed in a 5% CO_2 incubator at a temperature of 37°C. The cell culture medium was collected every 24 h and replaced promptly, and the collected medium was frozen at −80°C for storage.

Cell culture media uses continuous centrifugation and filtration for EV collection. Briefly, the cells were precipitated at 300 ×g for 10 min at 4°C using an Overspeed Centrifuge (Himac Japan) and subsequently at 2000 ×g for 30 min to remove dead cells. The remaining purified medium was centrifuged at 10000 ×g for 30 min, and the supernatant was filtered through a 0.22 μm filter (Sartorius, Germany) to remove excess protein. Next, the supernatant was centrifuged at 100000 ×g for 70 min; the sediment was washed with phosphate-buffered saline (PBS) (zqxzbio, China); and the solution was transferred to a new tube and centrifuged again at 100000 ×g for 70 min to obtain the 3D-cultured EVs.

The 2D EVs were synthesized according to the traditional preparation method.[30] ADSCs (passage [P]3–6) were cultured in serum-free stem cell medium (Corning, United States of America [USA]) for 48 h; the supernatant was collected and purified via ultracentrifugation; and the 2D-cultured EVs were obtained.

2.2.2. Transmission electron microscopy

The EVs were loaded onto Formvar carbon-coated EM copper mesh (HEAD, China), stained with PKH26 kit (Sigma-Aldrich, USA), air-dried, and observed using transmission electron microscopy (TEM; Hitachi, Japan).

2.2.3. Nanoparticle tracking analysis

The EV suspension was diluted to 1 mL with stock solution and transferred to a 1 mL syringe. The particle size distribution of EVs was detected using nanoparticle tracking analysis (NTA; Malvern Panalytical, Netherlands).

2.2.4. Western blot

The protein concentration of EVs was measured using a BCA kit (Bvant, China) according to the manufacturer's method, and the number of EVs in each sample was calculated based on the assay results. Sodium dodecyl sulfate (SDS) buffer (Servicebio, China) was added to the sample and mixed by vortexing. The proteins were then denatured in water at 95°C before electrophoresis. After electrophoresis, the gels were separated, and the positive EVs protein markers, CD63 and TSG101 (Abcam, England), and the negative protein marker calnexin were transferred to a polyvinylidene fluoride (PVDF) membrane (Millipore, Germany). After blocking with a 3% bovine serum albumin (BSA) blocking solution (Solarbio, China), the membrane was incubated with primary and secondary antibodies and visualized accordingly thereafter (Chemiscope, China).

2.2.5. Cell uptake

To validate the uptake of 3D-derived EVs by nasal septal chondrocytes, EVs were stained with PKH26 red fluorescent dye (Uimbio Shanghai, China) for 15 min at 37°C, and 3D-EV-loaded chondrocytes were treated for 24 h after centrifugation to remove excess dye. After incubation, the cells were fixed with 4% paraformaldehyde (Biosharp, China) for 15 min, washed three times with PBS, and permeabilized with Triton-100 (Coolaber, China) for 10 min. The membranes were stained using fluorescein isothiocyanate (FITC; Aladdin, China) and washed with PBS before staining the nuclei using DAPI. The images were captured under an inverted fluorescence microscope (Nikon, Japan).

2.3. Characterization of molecular structure and microstructure

Scanning electron microscopy (SEM) was used to characterize the electrospun biofilm and the microstructure of the composite scaffold; the fiber diameter of the scaffold was calculated using Origin 2021 (OriginLab, United States). Briefly, a biological scaffold of suitable size was prepared and its surface was evenly covered with chondrocyte suspension and Dulbecco's Modified Eagle Medium (DMEM; Gibco, China) supplemented with 10% FBS for 2 days. After complete cell adhesion and growth, the scaffold was washed with PBS. The biofilm of the loaded cells and the composite scaffold were freeze-dried, and the composite scaffold was treated with liquid nitrogen embrittlement to expose the cross-section. The surface of the scaffold was sprayed with gold at 18 mA using an ion sputter coater (Technol, China) for 60 s. SEM was used to observe the surface morphology of the scaffold; the fiber diameter of the scaffold was calculated accordingly.

2.4. Mechanical test

The tensile and compressive properties of composite stents were tested using a universal mechanical testing machine (Sunstest, China) at a tensile and compressive velocity of 10 mm/min. The stress–strain curves were plotted using Origin 2021.

2.5. EV release test

The obtained EVs were incorporated into the composite scaffold to assess the release of EVs from the scaffold. Briefly, the EV-doped composite scaffold was placed in a dialysis bag and incubated in PBS solution at 37°C. PBS samples were collected on days 1, 2, 3, 4, 7, and 10. After each EV collection, fresh PBS was added at the same volume. The EV concentration in the solution was detected using a BCA kit, and an EV-release curve was plotted.

2.6. *In vitro* degradation and swelling test

The swelling and degradation properties of composite scaffolds were evaluated based on previous reports.[29] Briefly, after lyophilizing the stent samples for 24 h, the initial weight W_0 was weighed. The samples were placed in PBS at 0.04 g/mL, and the samples were freeze-dried on days 5, 10, 15, 20, 25, and 30, respectively. The corresponding mass W_t was weighed, and scaffold degradation is calculated as follows:

$$\text{Degradation rate (\%)} = \frac{W_0 - W_t}{W_0} \times 100\% \quad \text{(I)}$$

Swelling of the stent also employed a similar method.[29] The weight of the freeze-dried stent is W_0, and the stent was soaked in PBS. The PBS on the surface of the stent was absorbed every 15 min using filter paper, and the weight W_t was recorded. The swelling weight of the stent was obtained after 24 h, and stent swelling was calculated based on the following:

$$\text{Swelling ratio (\%)} = \frac{W_t - W_0}{W_0} \times 100\% \quad \text{(II)}$$

2.7. Fourier-transform infrared spectroscopy

Fourier-transform infrared spectroscopy (FTIR) was employed to investigate the effect of EVs on the GelMA chemical functional groups. Freeze-dried GelMA hydrogel was ground into a powdered sample and completely mixed with potassium bromide. The processed samples were subsequently analyzed using FTIR at room temperature.

2.8. Biocompatibility assessment

As previously described, the biocompatibility of nasal septal chondrocytes and composite scaffolds was evaluated using live/dead cell staining and cell counting kit 8 (CCK-8) cytotoxicity assays.

For live/dead staining, 1×10^6 cells were seeded on a 2×2 cm composite scaffold and co-cultured with the composite scaffold for 1, 3, and 7 days. The staining solutions (calcein AM and propidium iodide [PI]; Keygen, China) were added to the cell-laden composite scaffold at 0.5 μL/ml each using PBS solution until the working solution submerged the sample. The samples were incubated at 37°C for 30 min and subsequently observed using an inverted fluorescence microscope (Nikon, Japan).

For CCK-8 cytotoxicity experiments, the GelMA hydrogel was soaked in DMEM for 24 h at room temperature in advance to obtain a solution containing the hydrogel extract. PLGA-electrospun membranes of the same size were cut and placed at the bottom of the 96-well plate. They were seeded on the biofilm with the standard 2000 cells per well, and 100 μL of complete medium containing the hydrogel extract was added. Cell viability was evaluated by measuring the absorbance at 450 nm using a microplate reader (Agilent, USA) with CCK-8 solution (Beyotime, China) on days 1, 3, and 5.

2.9. Cell proliferation and migration experiments

2.9.1. CCK-8 proliferation experiment

Chondrocytes (P3–5) were seeded into 96-well plates at 2000 cells per well. After overnight cell culture, 100 μL DMEM was added to the EVs/mL (5×10^8, 10×10^8, and 20×10^8 EVs/mL) and control groups, respectively. After days 1, 3, and 5, 10 μL of CCK-8 reagent was added to each well according to the manufacturer's instructions and incubated for 2 h in the cell culture incubator. Finally, the absorbance (optical density [OD]) of the samples at 450 nm was measured using a microplate reader to assess cell proliferation.

2.9.2. Wound-healing

Cell scratch assay was performed to evaluate the effect of different EV concentrations on the migration of nasal septal chondrocytes. Briefly, 5×10^6 cells/mL were seeded in a six-well plate, and the medium was aspirated after cell adhesion. A 200 μL pipette tip was used to create three marks in the well plate to simulate a wound. Each group of cells (EV: 5×10^8, 10×10^8, and 20×10^8 EVs/mL; and control) was photographed at 0, 12, 24, and 48 h, respectively. The migration area was quantified using ImageJ, and statistical analysis of the migration area was performed using Prism 9.5.

2.9.3. Transwell assay

An 8-μm transwell room was purchased from NEST (China). A 24-well plate was grouped according to EV concentrations of 5×10^8, 10×10^8, and 20×10^8 EVs/mL

and a control group. A total of 100 μL serum-free medium, containing 5×10^4 cells, was added to the transwell chamber and cultured at 37°C for 24 h. The chamber was washed with PBS, and 4% paraformaldehyde (Bbiosharp, China) was added for fixation. After wiping the upper chamber, cells at the bottom of the chamber were stained with 0.1% crystal violet dye solution (Solarbio, Germany) and placed under the microscope for cell migration observations.

2.9.4. Cell proliferation assay

Chondrocytes (P3) were seeded into 24-well plates, and the medium was replaced every two days with DMEM, containing 2D EVs, 3D EVs, or blank. Cells were incubated with EdU working solution (Beyotime, China) for 3 h; the medium was discarded; cells were fixed with 4% paraformaldehyde for 15 min and permeabilized with Triton X-100 (Beyotime, China) for 30 min; cells were washed again; and EdU reaction solution was added to the cells for 30 min at room temperature. Cell proliferation was observed using an inverted fluorescence microscope (Nikon, Japan).

2.10. Immunofluorescence

After seeding 1×10^6 chondrocytes into confocal cell culture dishes (WHB, China), EV (5×10^8, 10×10^8, and 20×10^8 EVs/mL) and control groups were set up and incubated for two days in the incubator. Thereafter, 4% paraformaldehyde was added for fixation for 15 min, and a blocking solution, containing FBS (Beyotime, China), was added at room temperature for 3 min. The primary antibody Col II was diluted according to the manufacturer's instructions (Proteintech, China) and incubated with the cells at 4°C overnight. After washing off the primary antibody, fluorescent secondary antibodies (goat anti-mouse fluorescent secondary antibody) (Proteintech, China)

(Proteintech, China) were diluted according to the manufacturer's instructions and incubated with the cells for 1 h at room temperature in the dark. The secondary antibodies were washed off before staining with DAPI for 10 min in the dark. An inverted fluorescence microscope (Eclipse-Ti2; Nikon, Japan) was then used to observe the cells.

2.11. Reverse transcription-quantitative polymerase chain reaction (qRT-PCR)

Chondrogenic genes ACAN, Col II, and SOX9 were detected using reverse transcription-quantitative polymerase chain reaction (qRT-PCR). Chondrocytes were harvested according to the manufacturer's instructions. RNA extraction kit (Karroten, China) was used to extract total RNA from cells treated with different concentrations of EVs. RNA concentration and purity were measured using an ultra-microvolume ultraviolet spectrophotometer (KAIAO, China). Reverse transcription to complementary DNA (cDNA) was performed according to the manufacturer's protocol for the reverse transcription kit (Vazyme, China). The synthesized cDNA was subjected to qRT-PCR using a real-time PCR detection system (3 107B-1612; Roche, Switzerland). Gene expression was normalized using glyceraldehyde-3-phosphate dehydrogenase, and the results were calculated using the $2^{-\triangle\triangle ct}$ method. All primer sequences are listed in Table 1.

2.12. Protein expression analysis

The expression of chondrocyte-specific proteins was examined after three days of treatment with different EV concentrations. RIPA Lysis Buffer (BLT, China) and PMSF (Beyotime, China) were added to cells at a ratio of 99:1. After 10 min of lysis on ice, the cells were scraped into 1.5 mL EP tubes (Corning, USA) and centrifuged to obtain supernatant. A spectrophotometer (KAIAO, China) was used to measure and calculate the protein concentration. Gel electrophoresis was performed with 12.5% SDS-PAGE (Epizyme, China), and the gel was transferred to a PVDF membrane. The sample was blocked with 5% skim milk for 1 h, rinsed with TBST (Servicebio, China) three times, and incubated with primary antibodies (anti-col II [Aifang, China], anti-ACAN [Aifang, China], and anti-SOX 9 [Aifang, China]) at 4°C. After washing off the primary antibody with TBST the next day, the goat anti-mouse fluorescent secondary antibody (Abcam, China) were incubated with the samples for 1 h at room temperature, and the images were visualized using a chemiluminescent solution (Advantage Biological, China). GAPDH (Aifang, China) was used as a reference for normalization.

2.13. *In vivo* animal experiments

The use of animals was approved by the 988 Hospital of the People's Liberation Army. Twenty-four adult

Table 1. Sequences of primers used in reverse transcription-quantitative polymerase chain reaction.

Gene	Primers	Sequences (5'–3')
Col2a1	Forward	TTCTCCTTTCTGCCCCTTTGGT
	Reverse	TCTGTGAAGACACCAAGGACTG
ACAN	Forward	CAGCCGGACAACTTCTTT
	Reverse	GTGAAGGGTAGGTGGTAATTG
SOX9	Forward	CTCCGACACCGAGAATACA
	Reverse	CCTCTTCGCTCTCCTTCTT
GAPDH	Forward	GTCGGAGTGAACGGATTTG
	Reverse	GTAGACCATGTAGTGGAGGT

New Zealand white rabbits were randomly divided into four groups: sham group, control group, Gel-PLGA group, and EVs-Gel-PLGA group (2.0–2.5 kg; The rabbits were divided equally into the 6-week group and the 12-week group,n = 3 in each group) . After weighing the rabbit before surgery, 2% sodium pentobarbital was injected into the rabbit's ear margin intravenously at a dose of 2 mL/kg of anesthesia. Next, an incision about 4 cm long was exposed in the center of the nasal bone of the rabbit, and a grinding drill was used to create a gap (2 × 1 cm) at the nasal bone in the center of the incision to ensure nasal septal cartilage exposure. Defects (length: 5 mm; depth: 5 mm; width: 1 mm) were made on the septal cartilage using ophthalmic scissors and a ruler, ensuring the same defect size for all experimental animals. Electrospun biofilm of the same size was cut and fitted to the defect site. The surrounding area was filled with 10% GelMA solution and light-cured to fix the scaffold. An adequate amount of EVs was mixed with GelMA in the EVs-Gel-PLGA group, before injecting the hydrogel. Light-curing was performed in all groups for 30 s. The rabbits were continuously injected with penicillin for three days after surgery. Thereafter, the rabbits were over-anesthetized at week 6 and euthanized at week 12. The nasal septum samples were collected accordingly.

2.14. Histomorphology evaluation

After fixation, decalcification, dehydration, and paraffin embedding of the nasal septum, the sample was sectioned at 3 μm using a cryomicrotome. Sections were stained with hematoxylin and eosin (H&E; Beyotime, China) and toluidine blue (Solarbio, China) according to the manufacturer's instructions. Immunohistochemical evaluation was performed using Col II according to the results of previous studies.[24]

2.15. Statistical analysis

Data was statistically analyzed using Prism 9.5 software (GraphPad, USA) and ImageJ, and all experiments were repeated at least three times. Data is presented as mean ± standard deviation. For multiple comparisons, one-way analysis of variance (ANOVA) was performed with Tukey's post-hoc test, and p-values < 0.05 were considered statistically significant.

3. Results

3.1. Characterization of ADSCs-EVs

Coaxially printed ADSC-derived EVs were characterized using particle size analysis, TEM, and western blotting. The particle size analysis revealed that the diameter of EVs ranged from approximately 120–150 nm (Figure 2B), and TEM observation indicated that the EVs exhibited a circular or oval membrane structure (Figure 2A). Furthermore, western blotting confirmed the presence of EV-specific markers CD63 and TSG101 on the surface of the extracted EVs (Figure 2C). Subsequent cell uptake experiments demonstrated the successful internalization of EVs by nasal septal chondrocytes, with fluorescence microscopy revealing endocytic entry into the cytoplasm and enrichment outside the nucleus (Figure 2E). These findings collectively demonstrate the successful generation of 3D EVs using coaxial printing techniques.

3.2. Physicochemical properties of composite scaffolds

Observation of electrospun biofilms and GelMA-PLGA composite scaffolds by SEM (Figure 3A) revealed that most fibers in the electrospun biofilms had a diameter of approximately 1 μm (Figure 3B). The GelMA-PLGA composite scaffold exhibited significant mechanical strength, as evidenced by the test results for tensile modulus (Figure 3E) and compression modulus (Figure 3F). Calculations indicated that the tensile modulus of the Gel-PLGA composite scaffold was 5.4249 MPa; 3.4271 MPa for the PLGA scaffold; and much lower for the GelMA hydrogel at only 0.00154 MPa. Additionally, the compression modulus of the PLGA scaffold was measured at 0.1661 MPa, but with the incorporation of hydrogel, this value decreased to 0.08995 MPa for the Gel-PLGA composite scaffold. The compression modulus of GelMA is 0.001497 MPa. The swelling experiment (Figure 3C) revealed that the swelling rate of the composite stent reached 750%. To prevent nasal cavity blockage from the high swelling rates post-implantation, we opted for the composite stent with non-freeze-dried treatment for defect implantation. The degradation experiment (Figure 3D) demonstrated that the composite scaffold can undergo continuous and stable degradation in PBS at 37°C, with hydrogel experiencing partial degradation over approximately 30 days, while the electrospinning biofilm exhibited a slower degradation rate. The PLGA component in the composite bracket was largely retained at day 30, with approximately 7% of its total weight remaining.

The extended-release EVs experiment (Figure 2D) demonstrated that the EV release rate was faster in the first three days of the experiment; from the fourth day onwards, the EV release rate began to slow down; by day 14, the total number of EVs released was close to 65%. The experimental results suggest that the composite scaffold could effectively achieve the sustained release of EVs. The FTIR spectra(Figure 3G) indicated that the functional groups of the GelMA hydrogel did not change after loading the EVs.

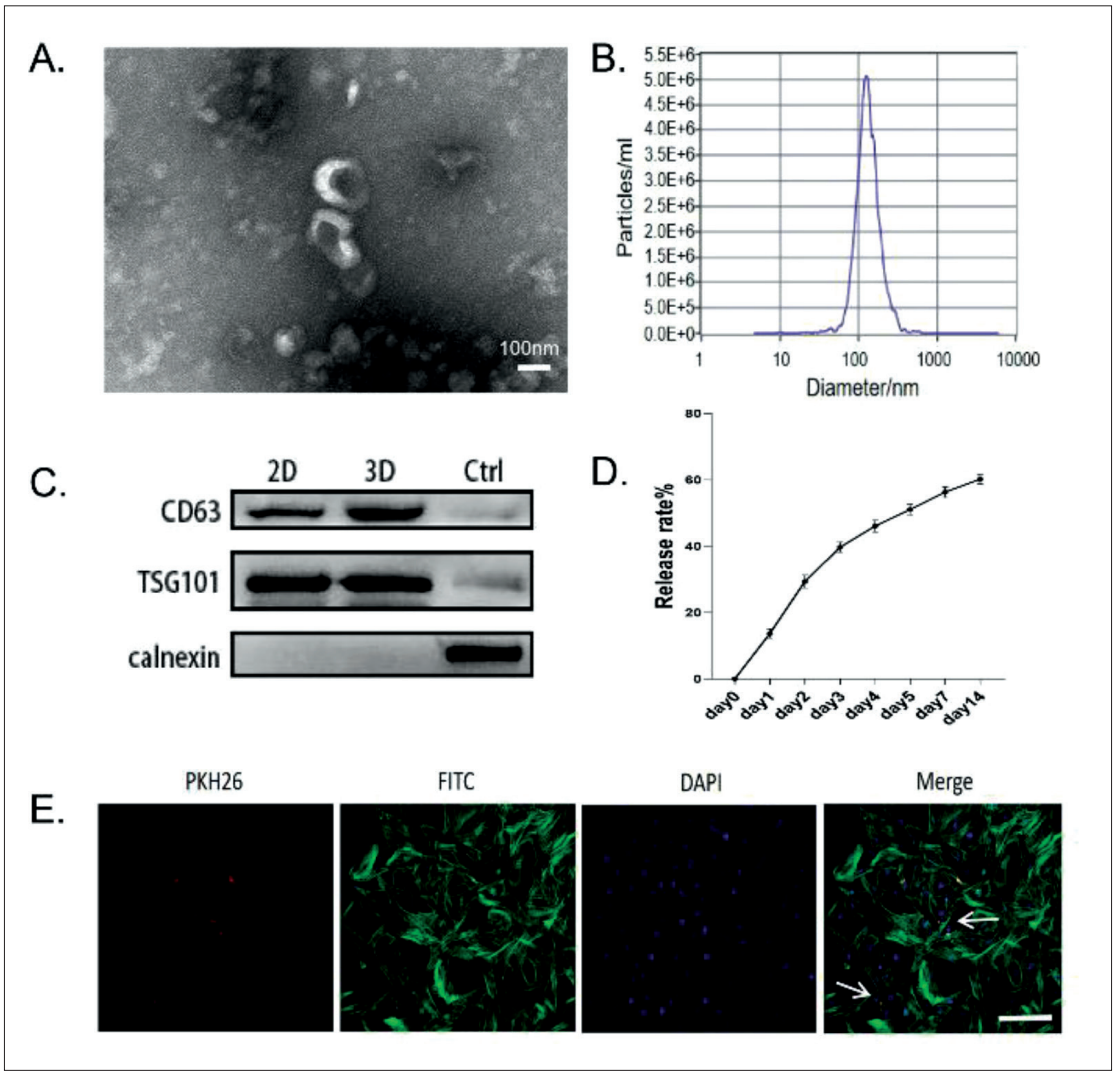

Figure 2. Characterization of adipose-derived stem cell (ADSC)-derived extracellular vesicles (EVs). (A) Observation of EV morphology under transmission electron microscope (TEM). (B) Nanoparticle tracking analysis (NTA) of the EV particle size. (C) Western blot results for detecting EV-specific markers. (D) Sustained EV release effect of composite scaffolds. (E) Cell uptake experiments. Scale bars: 100 nm (A); 50 μm (E). Abbreviations: Ctrl: Control; FITC: Fluorescein isothiocyanate.

3.3. Biocompatibility of composite scaffolds and sustained release of EVs

The biocompatibility of stents is crucial in determining their suitability for implantation in the body. In this study, the scaffold's biocompatibility was assessed using a cell viability staining kit to measure cell viability on days 1, 3, and 7. The results from fluorescence microscopy (Figure 3H) revealed an increase in the number of cells within the composite scaffold over time, with a significant rise in cell density after day 7 of culture compared to day 1. Furthermore, the Gel-PLGA composite scaffold demonstrated an ability to mimic the microstructure of cartilage *in vitro*. Microscopic analysis indicated that cells seeded within the scaffold transitioned from a 2D environment to a round-like structure more closely resembling a 3D environment *in vivo*, consistent with previous studies.[35] While some dead cells were detected through red fluorescence, most cells remained viable, underscoring the excellent biocompatibility of the composite scaffold.

We conducted a digitized cytotoxicity analysis of the scaffold using CCK-8 (Figure 3I). Cells were cultured for 1, 3, and 5 days using extracts from hydrogels, biofilms, and composite scaffolds, respectively. The cytotoxicity of the scaffold was assessed by measuring the absorbance of the liquid with a microplate reader. The results indicated that there was no significant difference in the OD value of

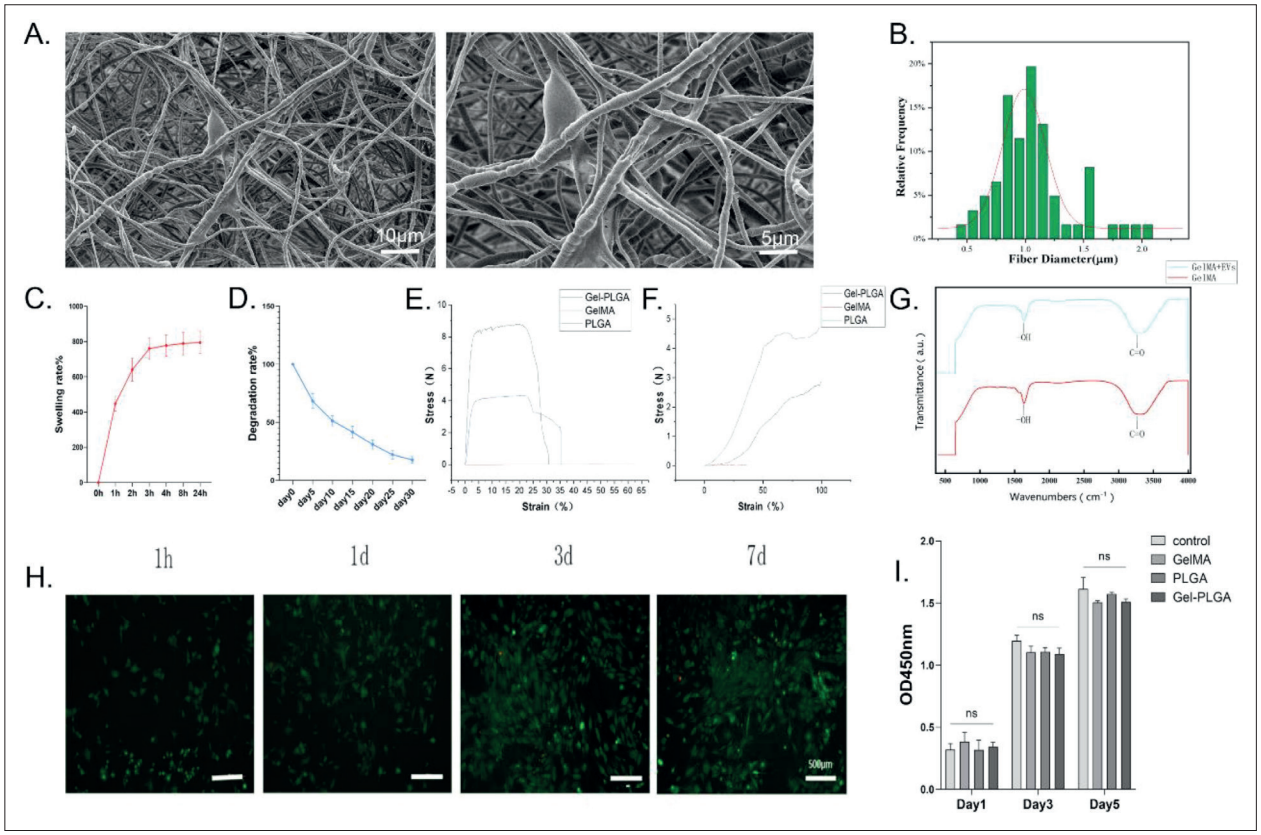

Figure 3. Physicochemical properties and biocompatibility of scaffolds. (A) Scanning electron microscopy (SEM) images of a polylactic acid-glycolic acid (PLGA) scaffold loaded with chondrocytes. (B) Fiber diameter analysis of PLGA scaffolds. (C and D) Swelling (C) and degradation (D) properties of composite scaffolds. (E and F) Tensile stress–strain curves (E) and compressive stress–strain curves (F) of composite scaffolds. (G) Fourier-transform infrared spectroscopy (FTIR) spectra of the gelatin methacrylic acid (GelMA) hydrogel with or without loaded EVs. (H) Cell viability staining of scaffolds after 1 h and days 1, 3, and 7. (I) Cytotoxicity assays of scaffolds. Scale bars: 10 μm (A, left); 5 μm (A, right); 500 μm (H). Abbreviation: ns: Non-significant.

the composite scaffold compared to normal cultured cells. Additionally, the OD value increased with time, further demonstrating that the Gel-PLGA composite scaffold exhibited good biocompatibility.

3.4. Comparison of chondrocyte function in 2D and 3D EVs

A growing body of literature suggests that the function and properties of EVs change with processing and culture conditions. Therefore, we compared the cellular function between EVs derived from 2D and 3D cultures. In each experiment, we used the same dose of 2D and 3D EVs. Cytological experiments on chondrocytes revealed that 3D EVs exhibited more significant chondrocyte proliferation and migration compared to conventional 2D EVs. CCK-8 and EdU cell proliferation experiments (Figure 4A–C) demonstrated that the OD value of 3D EVs was significantly higher than that of 2D EVs. Additionally, cell scratch experiments (Figure 4D and E) and transwell assays (Figure 4F and G) revealed that 3D EVs were more effective in promoting chondrocyte migration. Hence, based on these findings, we utilized 3D EVs for subsequent experiments.

3.5. Effect of different 3D EV concentrations on chondrocyte proliferation and migration

To assess how extracted EVs impact nasal septal chondrocyte proliferation and migration, we investigated their effects on chondrocyte function across concentration gradients of complete medium with particle counts of 5×10^8, 10×10^8, and 20×10^8 EVs/mL, respectively.

The CCK-8 cell proliferation experiment (Figure 5C) was performed for five days.

The effect of EVs on cell proliferation was evident on day 1. In addition, EVs still maintain a dominant effect on cell proliferation for the rest of the time. Interestingly, we found that the 20×10^8 EVs/mL group exhibited decreased cell proliferation rates compared to the other two groups,

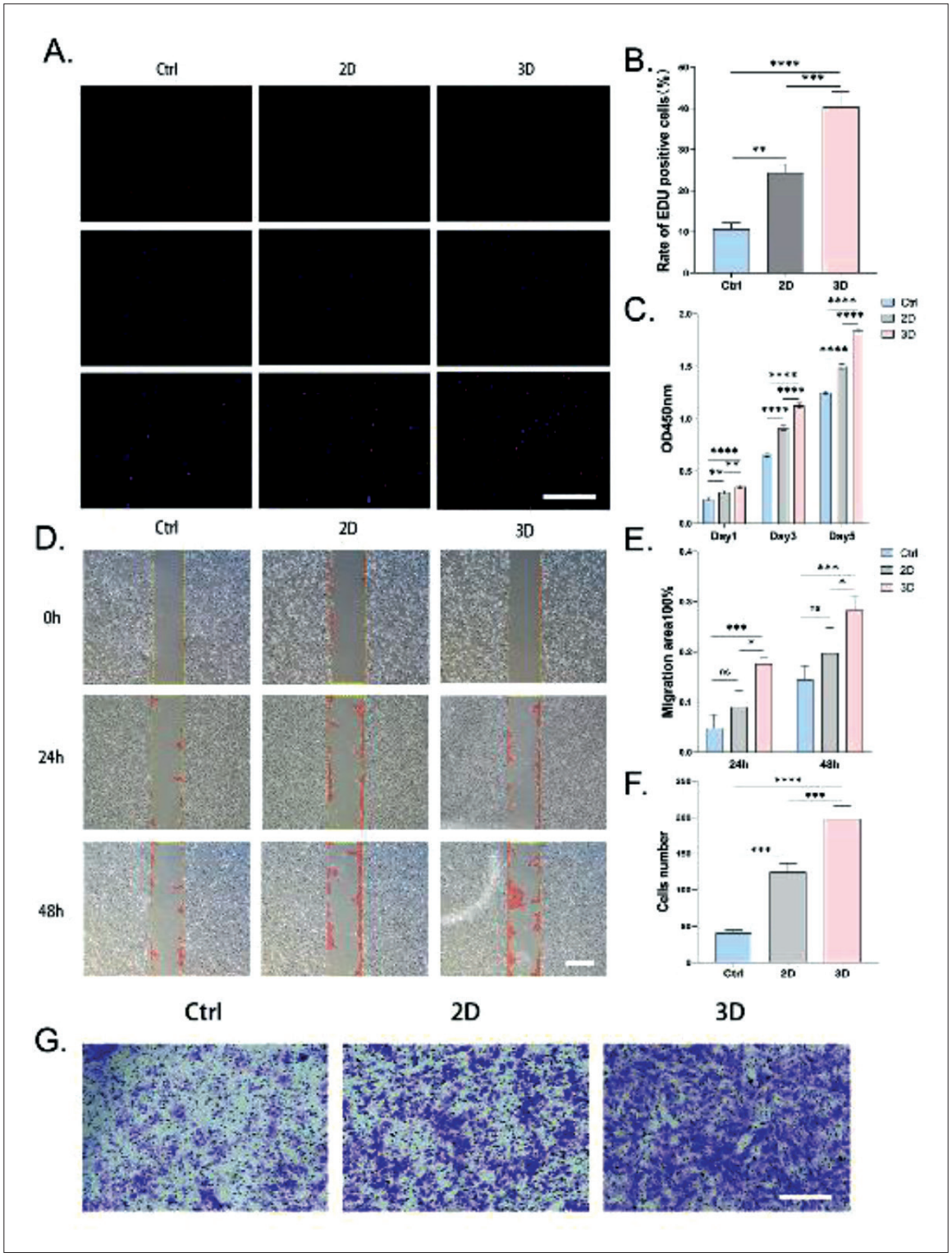

Figure 4. Comparison of chondrocyte proliferation and migration in 2D and 3D extracellular vesicles (EVs). (A–C) EdU (A and B) and cell-counting kit 8 (CCK-8) (C) experiments examined the effect of 2D and 3D EVs on cell proliferation. (D–G) Cell scratch (D) and transwell cell migration (E) assays evaluate the effect of 2D and 3D EVs on chondrocyte migration, as well as cell density (F and G). *$p < 0.05$, **$p < 0.01$, ***$p < 0.001$, ****$p < 0.0001$. Scale bars:100 μm (A, D, and F). Abbreviations: Ctrl: Control; ns: Non-significant.

contrary to previous findings that suggested higher EV concentrations would increase cell proliferation rates.[37]

We performed cell migration experiments to further explore cell function. The results of the scratch assay (Figure 5A and B) revealed significantly increased chondrocyte migration area in the EV groups. There was not much difference between the control and EV groups at 12 h, but cell migration in the EV groups gradually became apparent over time. Similarly, we observed that the 20 × 10^8 EVs/mL group exhibited a reduced migration area compared to the 10 × 10^8 EVs/mL group. To validate these findings, we performed a transwell migration experiment (Figure 5D and E), which revealed similar results. Collectively, a high concentration of EVs exerts an inhibitory effect on cell migration.

3.6. Immunofluorescence, qPCR, and western blot

To investigate the impact of EVs on the expression of chondrogenic-related genes, we examined the expression of ACAN, Col II, and SOX9 using qPCR and western blotting. Additionally, we performed immunofluorescence detection of Col II.

Col II is a crucial component in the cartilage extracellular matrix. Fluorescence microscopy revealed that the addition of EVs promoted Col II expression (Figure 6A and B). However, higher concentrations of EVs

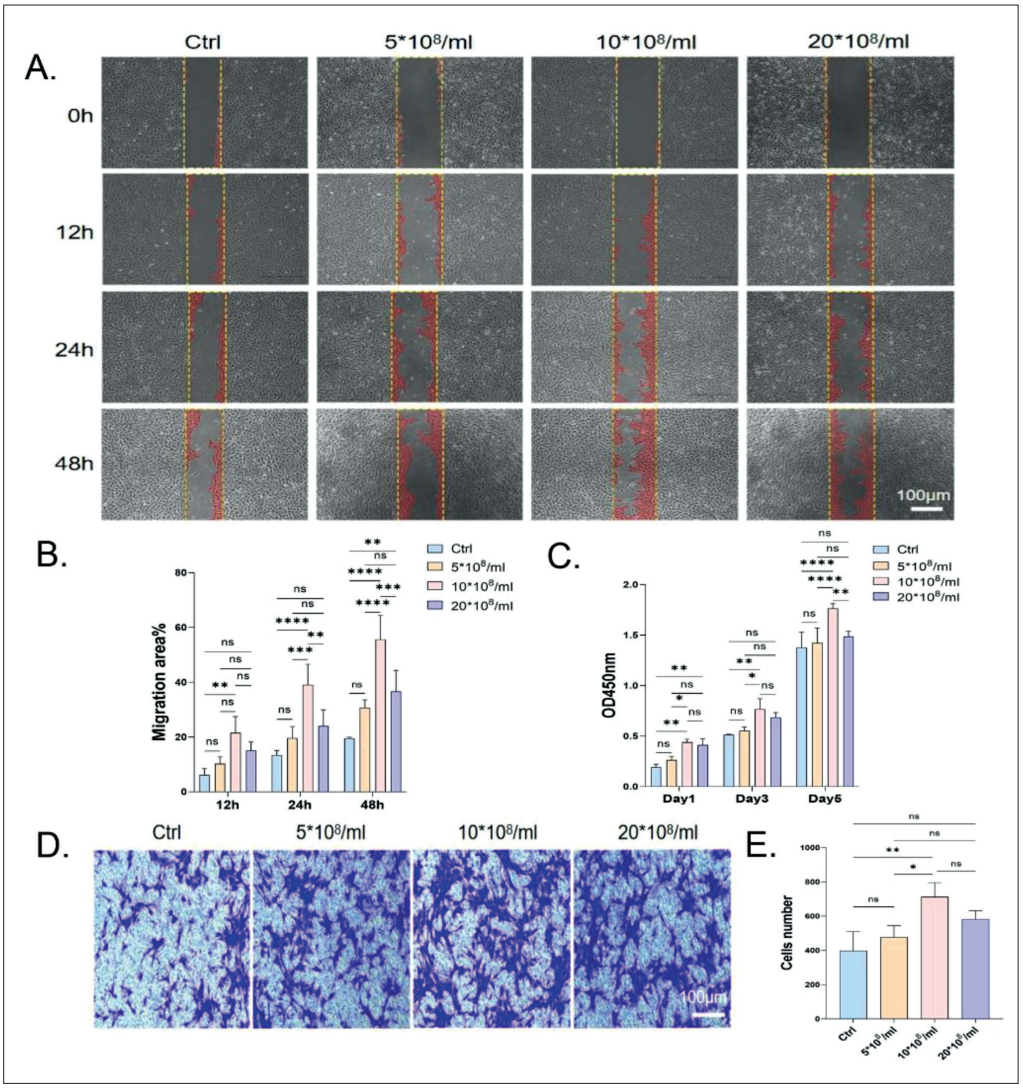

Figure 5. *In vitro* evaluation of the effects of different 3D EV concentrations on chondrocytes. (A and B) Effect of different 3D EV concentrations on chondrocyte migration area (A) and its analysis (B). (C) Effect of different 3D EV concentrations on chondrocyte proliferation. (D and E) Transwell experiments (D) and the number of migrating cells (E) at different 3D EV concentrations. Scale bars: 500 μm (A); 100 μm (D). *$p < 0.05$, **$p < 0.01$, ***$p < 0.001$, ****$p < 0.0001$. Abbreviations: ns: Non-significant; Con: Control.

did not enhance the expression of Col II and displayed similar fluorescence intensity to the control group. To further explore this phenomenon, we conducted qPCR and western blotting for genes related to chondrogenesis (Figure 6F). ACAN (Figure 6D and G) is also an important component of the cartilage extracellular matrix, while SOX9 (Figure 6E and H) primarily regulates chondrocyte formation. The results of qPCR and western blotting indicated that the 5×10^8 EVs/mL group upregulated these three genes, but was not statistically different relative to the control group. Interestingly, the three chondrogenesis genes in the 10×10^8 EVs/mL group were significantly upregulated relative to the other groups, corroborating our immunofluorescence results. In contrast, the 20×10^8 EVs/mL group displayed downregulated gene expressions compared to the other two EV groups, particularly for Col II (Figure 6C and I). Based on the above results, we speculate that the ability of chondrocytes to secrete the relevant matrix is inhibited in an environment with high concentrations of EVs.

3.7. EV composite scaffolds repair cartilage defects *in vivo*

A 5 × 5 mm defect was created in the nasal septum of rabbits; samples and tissues were examined at 6 and 12 weeks post-stent implantation. We previously tested the swelling properties of the composite stent, which rapidly absorbs blood and body fluids around the tissue upon implantation, causing it to swell. There were no adverse reactions in all experimental animal groups after surgery, with good survival rates.

We established a sham group, a control group, a Gel-PLGA scaffold group, and an EV-loaded composite scaffold group. The staining results of the sections are presented in Figures 7–9. H&E (Figure 7D) and toluidine blue (Figure 8A) staining revealed that the scaffold group exhibited some healing compared to the control

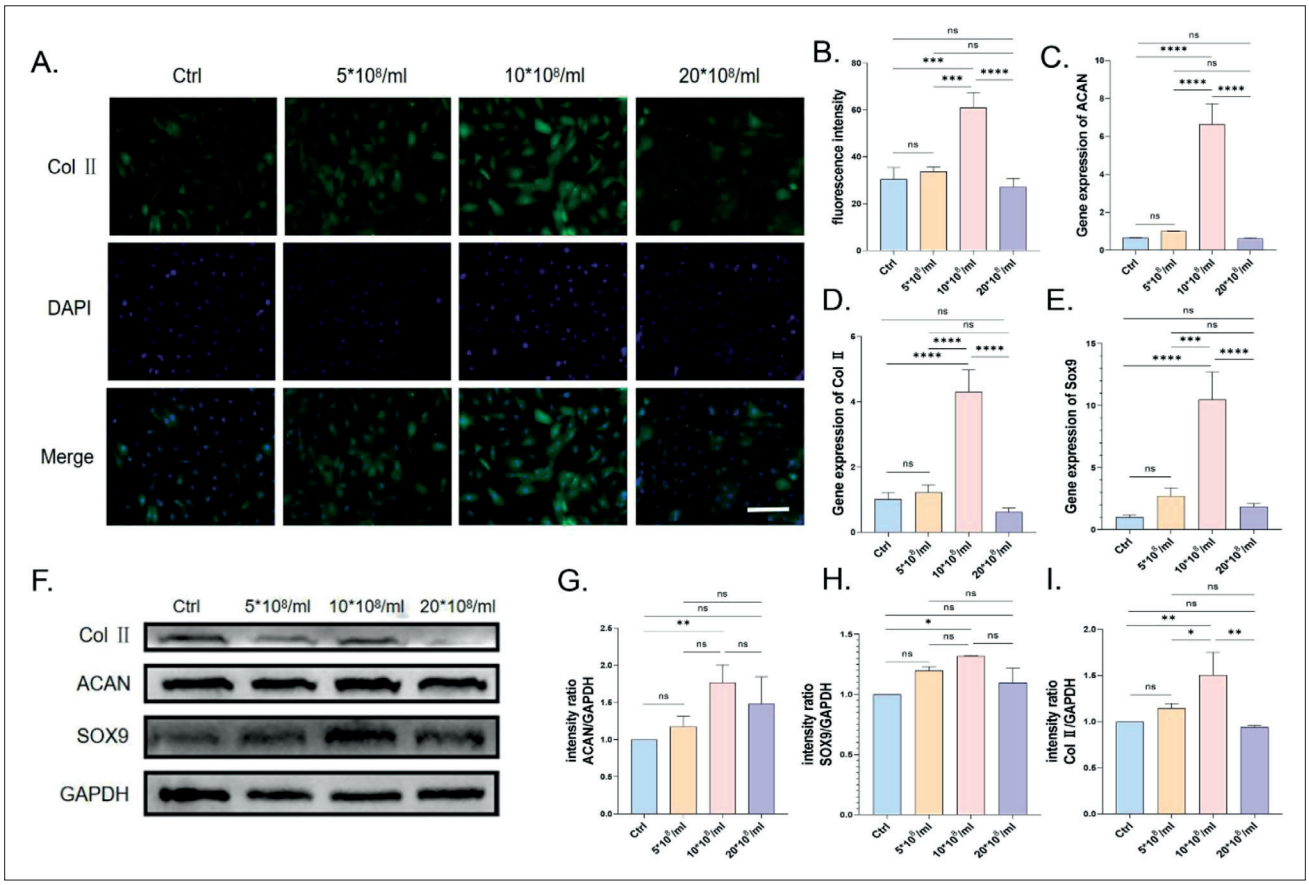

Figure 6. Expression of genes and proteins related to chondrogenesis. (A and B) Cellular immunofluorescence experiments of 3D extracellular vesicles (EVs) at different concentrations (A) and fluorescence intensity analysis of each group (B). (C–E) Quantitative polymerase chain reaction (qPCR) results for Col II (C), ACAN (D), and Sox9 (E). (F–I) Western blotting results (F) and normalized analyses of ACAN (G), Sox9 (H), and Col II (I). $^*p < 0.05$, $^{**}p < 0.01$, $^{***}p < 0.001$, $^{****}p < 0.0001$. Scale bar:100 μm (A). Abbreviation: Ctrl: Control.

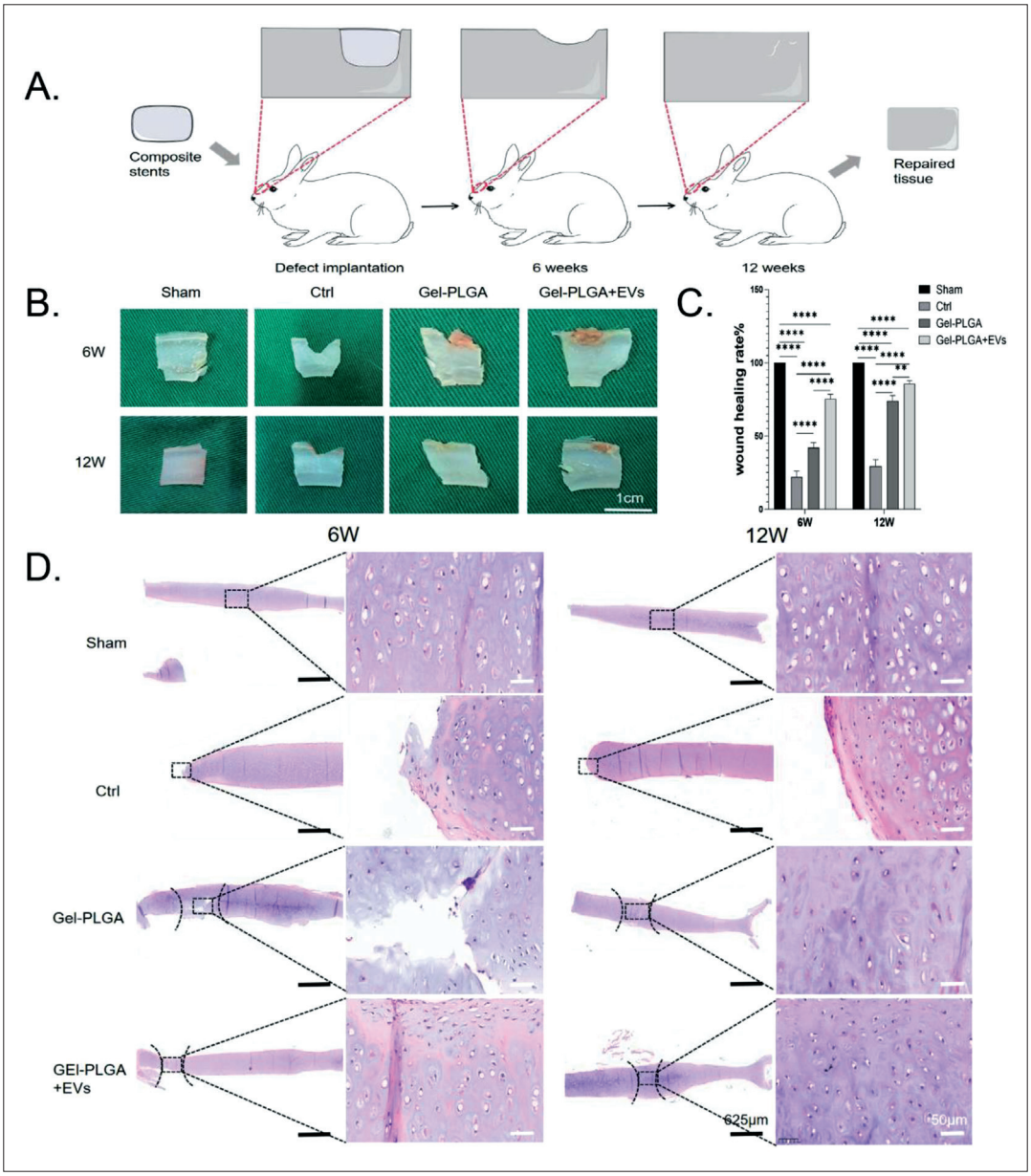

Figure 7. Animal models with nasal septal defects. (A) Schematic diagram of animal experiments. (B) Repaired cartilages obtained from different treatment groups. (C) Defect healing rates at different time points. (D) Hematoxylin and eosin (H&E) staining at the defect site. Scale bars: 1 cm (B); 50 μm (D, white); 625 μm (D, black). $^{**}p < 0.01$, $^{****}p < 0.0001$. Abbreviations: Ctrl: Control; W: Weeks; PLGA: Polylactic acid-glycolic acid; Gel: Gelatin; EVs: Extracellular vesicles.

group, particularly in the EV-loaded group, where new chondrocytes were generated at the defect site. However, cell arrangement in the scaffold group still differed from that of the sham group. By week 12, the defect site in the stent group was filled with fibrous tissue and had produced a small number of chondrocytes. Toluidine blue staining indicated inflammation at this site, leading to chondrocyte hypertrophy. A similar phenomenon was observed in the EV group. By week 12, the Gel-PLGA+EVs group had successfully repaired the defect site, leading to a significant increase in newly generated chondrocytes at the defect site. The excellent anti-inflammatory ability of EVs prevented cell hypertrophy, resulting in an overall cell and chondrocyte extracellular matrix arrangement that closely resembles that of the sham group. In contrast, due to the large defect size and inadequate cellular support

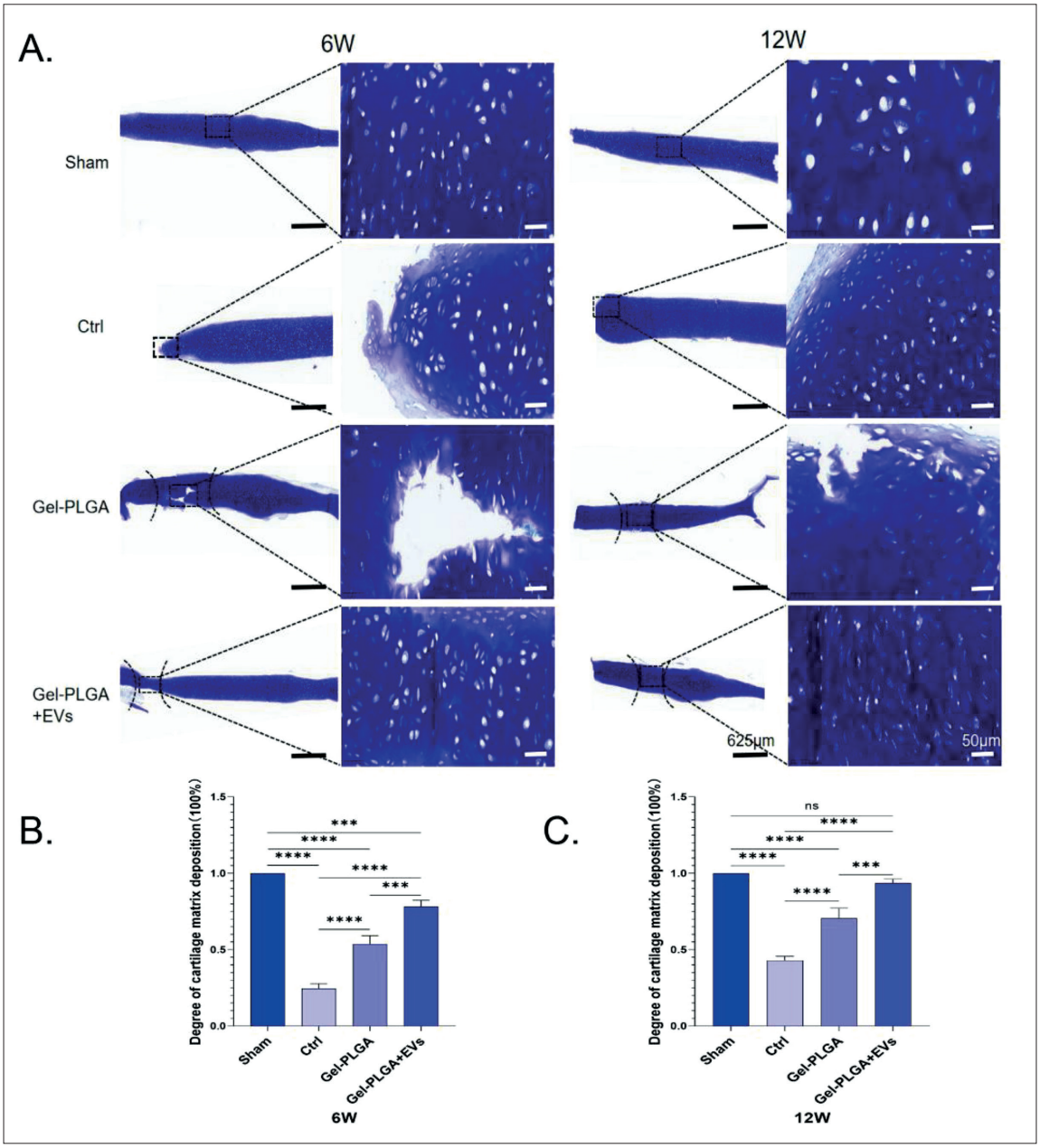

Figure 8. Toluidine blue staining of rabbit nasal septal cartilage after 6 and 12 weeks of repair. (A) Toluidine blue-stained tissues. (B and C) Normalized analysis of the extent of cartilage matrix deposition in the repaired tissues at week 6 (B) and 12 (C). ***$p < 0.001$, ****$p < 0.0001$. Scale bars: 50 μm (A, white); 625 μm (A, black). Abbreviations: Ctrl: Control; ns: Non-significant; Gel: Gelatin; PLGA: Polylactic acid-glycolic acid; EVs: Extracellular vesicles.

for proliferation and migration, the control group did not effectively repair the defect.

Toluidine blue staining (Figure 8A) indicates the presence of a cartilage matrix in newly formed tissue. The stained tissues were normalized (Figure 8B and C), and the results revealed that the EV-treated group exhibited a higher level of cartilage matrix deposition compared to the scaffold group. Although some cartilage matrix deposition was observed in the scaffold group, there were noticeable differences when compared to the EV-treated group.

Immunohistochemical staining of Col II was performed on the defect site (Figure 9) and revealed that the EV-treated group at weeks 6 and 12 displayed more Type 2 collagen expression than the control and Gel-PLGA groups. Additionally, only some nascent mast chondrocytes in the Gel-PLGA group exhibited positive

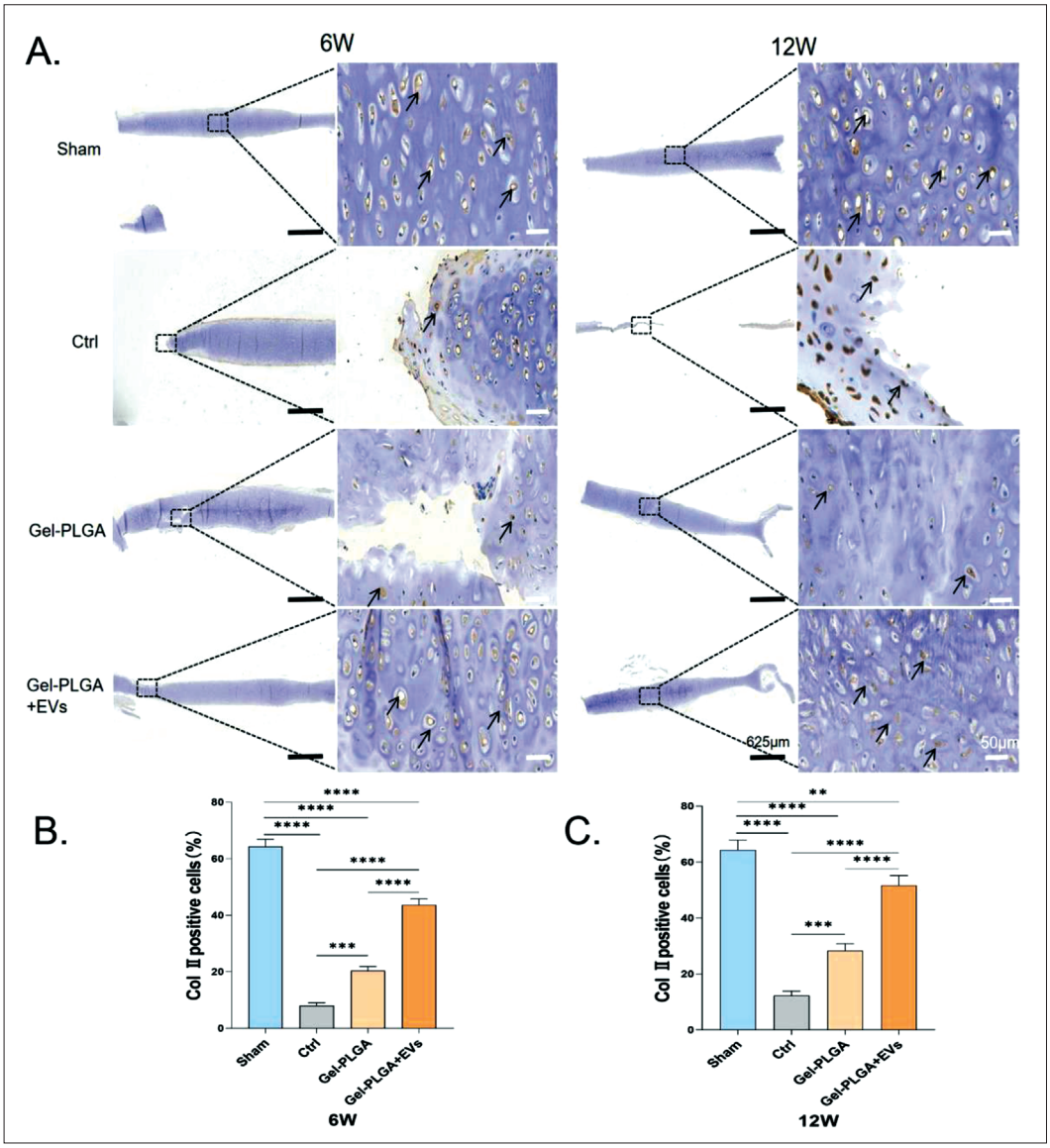

Figure 9. Immunohistochemical staining of Col II in rabbit nasal septal cartilage after 6 and 12 weeks (W) of repair. (A) Col II staining of the tissues. Arrows denote deposited Col II. (B and C) Normalized analysis of Col II expression in the repaired tissues. $^{**}p < 0.01$, $^{***}p < 0.001$, $^{****}p < 0.0001$. Scale bars: 625 μm (A, black); 50 μm (A, white). Abbreviations: Ctrl: Control; Gel: Gelatin; PLGA: Polylactic acid-glycolic acid; EVs: Extracellular vesicles.

features, though collagen deposition in the tissues increased over time. These results indicate that defects treated with Gel-PLGA+EVs exhibit enhanced healing and collagen deposition.

4. Discussion

In recent years, EVs have become prominent due to their crucial role in tissue repair and regulation of organ function.[13] In our study, we combined 3D-printed EVs with tissue-engineered biological scaffolds for the first time to repair nasal septum defects. Traditionally, tissue repair is often achieved by injecting stem cells into the defect site.[38] While stem cell therapy is effective, its safety and ethical aspects remain subjects of debate.[16] Moreover, an increasing number of studies have demonstrated that stem cells function *in vivo* through EVs as intermediaries.[39,40] In this study, we developed a cell-free therapy for repairing tissue defects by loading EVs into composite scaffolds and implanting them at the defect site. Composite scaffolds, composed of GelMA hydrogel and PLGA-electrospun biofilm, can provide the necessary microenvironment and structure.[41] Additionally, GelMA and PLGA have demonstrated good biocompatibility without damaging the cells. The PLGA-electrospun scaffold had an

approximate diameter of 1 μm, consistent with previous reports.[31] Chondrocytes can be observed attaching to fibers and displaying a similar round-like structure *in vivo* under SEM.[32] This observation confirms that the PLGA scaffold effectively mimics the extracellular matrix of chondrocytes, thereby facilitating chondrocyte growth and proliferation.[33] The porous surface and hydrophilic properties of GelMA hydrogel promote chondrocyte adhesion, while its extracellular matrix components support cartilage formation and deposition. Additionally, swelling experiments demonstrated that the scaffold efficiently absorbs blood and other body fluids.[34] The sustained-release ability is crucial for evaluating stent suitability. GelMA hydrogel, due to its capacity for sustained release at defect sites and strong self-decomposition of EVs, is a commonly used biomaterial in cartilage tissue repair. Our experimental findings indicate that composite scaffolds slowly release EVs over 14 days. Furthermore, the literature suggests that high concentrations of EVs exert high osmotic pressure, which enhances their diffusion in the medium.[29] As EV concentrations decrease, their release rate also slows down.

Due to their abundant protein and nucleic acid content, EVs are widely used in the repair of various tissues and organs. Most studies indicate that researchers still use traditional EV preparation methods, typically involving extraction from a 2D environment, i.e., by collecting the medium of adherent cells in a petri dish for ultracentrifugation.[42] This method of extracting EVs is time-consuming and tedious, and the final yield is often low.[36] Based on the results of previous studies, we used stem cell EVs cultured in a 3D environment to conduct the present study.[43] Coaxial printing was utilized for the encapsulation of EVs in hydrogels to mimic the 3D cellular environment both *in vivo* and *in vitro*. EVs collected within a 3D environment demonstrate higher productivity and lower cost consumption compared to those collected from a 2D setting. Additionally, proteomic analysis[20] and other studies have demonstrated that 3D EVs exhibit superior effects compared to traditional 2D EVs.[44,45] In this study, we conducted a simple functional comparison of chondrocytes using 2D and 3D EVs. Our preliminary findings indicate that 3D EVs are more effective at promoting cell proliferation and migration. Hence, we have selected 3D EVs as the primary focus for subsequent experiments.

Although the cartilage in the nasal septum does not bear the same load as knee or vertebral articular cartilage, its collapse can significantly impact a patient's appearance.[4] Therefore, any implanted material must possess specific mechanical properties to adequately support the defect.[46] In this experiment, the tensile and compressive modulus of the composite scaffold were measured. The results demonstrated that the composite scaffold exhibited strong tensile ductility and high compressive modulus, indicating sufficient mechanical strength to effectively support the defected part. The stable structure of the composite stent facilitated effective filling of the defect site without compromising nasal ventilation, i.e., no impairment of ventilation was observed in the rabbits. Cartilage defect repair is closely linked to chondrocytes. Like other hyaline cartilage, the nasal septal cartilage has a lower cell content and weaker repair ability. During cartilage repair, the formation of essential extracellular matrix components, such as Col II and ACAN, is primarily dependent on chondrocytes. Therefore, promoting the generation of chondrocytes in the defect tissue becomes essential for successful repair. Our study demonstrated that EVs can effectively enhance chondrocyte proliferation and migration. Likewise, the addition of EVs improves the ability of chondrocytes to secrete the extracellular matrix. Additionally, we found that chondrocytes secrete Col II in response to EV stimulation, and ACAN expression was gradually enhanced. *In vivo* Col II immunohistochemistry revealed that the addition of EVs promoted collagen deposition, further accelerating tissue repair.

In this experiment, we utilized 3D EVs with varying concentrations to investigate the functional roles of EVs in cells. Our previous study revealed that lower concentrations of 3D EVs had a positive promotes proliferation, migration, and extracellular matrix production on cells. However, we observed that high concentrations of EVs inhibited cell proliferation, migration, and the expression of related genes. These findings are novel[47] and have been rarely reported. EVs are small molecules that facilitate intercellular communication, regulating cell behavior within organisms. However, the effectiveness of EVs in organisms does not necessarily increase with higher doses. When the concentration of EVs exceeds a threshold, it may induce an inhibitory effect on the relevant cellular functions. This phenomenon helps explain certain observations from previous experiments, though further exploration is warranted to fully understand the specific causes of inhibition.[48] Previous studies have indicated that 3D EVs are more effective than 2D EVs in promoting skin defect healing and treating burns.[48,49] The present study builds on previous research findings where 3D EVs facilitate the treatment of nasal septum injury. However, the enhancement mechanism of 3D EVs remains unclear, and this will be the focus of our subsequent research. It is known that EVs derived from different tissue cells exhibit specific effects, allowing for targeted treatment of diseases. Additionally, recipient cells may exhibit varying sensitivity to stem cell-derived EVs. Therefore, leveraging our

expertise in 3D coaxial printing combined with different tissue cells to produce disease-specific 3D EVs is essential for optimizing treatment outcomes.

In this experiment, we investigated the impact of EVs derived from 3D coaxial printing on the repair of nasal septal cartilage defects in rabbits. Our findings demonstrate the significant potential of EVs in regenerative medicine. Additionally, our combination of GelMA and PLGA with 3D EVs achieved successful repair within the body. Future research should focus on identifying suitable biological materials for different anatomical locations to develop customized tissue repair therapies.

5. Conclusion

In this experiment, we have innovatively developed a composite biological scaffold by combining GelMA hydrogel and PLGA nanofiber. We have also successfully prepared 3D EVs using 3D coaxial printing technology and obtained a Gel-PLGA+EVs biological scaffold that enables sustained release of EVs. The composite scaffold has demonstrated potential in accelerating cartilage defect healing and promoting collagen deposition at the site. These findings indicate that the Gel-PLGA+EVs composite scaffold holds great promise for clinical applications in cartilage defect treatment.

Acknowledgments

The authors would like to thank all laboratory personnel at Huaqing Zhimei Technology Co., Ltd. for their assistance with the study.

Funding

This study was researched by the Joint Construction of Scientific and Technological Research Grant (No. LHGJ20220916) and the Natural Science Foundation (No. 242300420125) of the Henan province, the 988th Hospital selects scientific research projects for key disciplines (No. YNZX2024007), the Shenzhen Science and Technology Major Project of Shenzhen Science and Technology Innovation Bureau (No. KJZD20230923114302006), and the Guangdong Province key areas research and development plan (No. 2023B0909020003).

Conflict of interest

The authors have no competing interests.

Author contributions

Conceptualization: Jianwei Chen, Tao Xu, Yi Li
Formal analysis: Jie Yang
Investigation: Jie Yang, Haolei Hu, Qiang Guo, Xiaolei Chen, Shuo Li, Gang Yin, Wei Yue
Methodology: Haolei Hu
Resources: Yi Zhang, Boxun Liu
Writing - Original Draft: Jie Yang
Writing - Review & Editing: All authors

Ethics approval and consent to participate

The experimental animal ethics of this study have been reviewed by the Ethics Committee of the 988th Hospital of the Joint Logistics Support Force of the Chinese People's Liberation Army (approval no. 988YY20230007LLSP; approved project name: "Mechanism Study on Constructing MiR-920/BMSCs Biomimetic Stents for Repairing Rabbit Nasal Septal Cartilage Defects"). All animal experiments (male rabbits) comply with the ARRIVE guideline and EU animal experimentation directives.

Consent for publication

Not applicable

Availability of data

All relevant data are presented in the article. Other data is available upon reasonable request from the corresponding authors.

References

1. Samibut P, Meevassana J, Suwajo P, et al. The anatomical study of the nasal septal cartilage with its clinical implications. *Aesthetic Plast Surg*. 2021;45:1705-1711. doi: 10.1007/s00266-020-02116-z
2. Chiesa-Estomba CM, Aiastui A, González-Fernández I, et al. Three-dimensional bioprinting scaffolding for nasal cartilage defects: a systematic review. *Tissue Eng Regen Med*. 2021;18:343-53. doi: 10.1007/s13770-021-00331-6
3. Setton LA, Elliott DM, Mow VC. Altered mechanics of cartilage with osteoarthritis: human osteoarthritis and an experimental model of joint degeneration. *Osteoarthritis Cartilage*. 1999;7:2-14. doi: 10.1053/joca.1998.0170
4. Günebakan Ç, Kuzu S. Congenital deficiency of alar cartilage. *J Craniofac Surg*. 2021;32:e137-8. doi: 10.1097/SCS.0000000000006858
5. Lavernia L, Brown WE, Wong BJF, Hu JC, Athanasiou KA. Toward tissue-engineering of nasal cartilages. *Acta Biomater*. 2019;88:42-56. doi: 10.1016/j.actbio.2019.02.025
6. Bagher Z, Asgari N, Bozorgmehr P, Kamrava SK, Alizadeh R, Seifalian A. Will tissue-engineering strategies bring

new hope for the reconstruction of nasal septal cartilage? *Curr Stem Cell Res Ther*. 2020;15:144-54.
doi: 10.2174/1574888X14666191212160757

7. Rajzer I, Stręk P, Wiatr M, et al. Biomaterials in the reconstruction of nasal septum perforation. *Ann Otol Rhinol Laryngol*. 2021;130:731-7.
doi: 10.1177/0003489420970589

8. Wu N, Liu J, Ma W, et al. Degradable calcium deficient hydroxyapatite/poly(lactic-glycolic acid copolymer) bilayer scaffold through integral molding 3D printing for bone defect repair. *Biofabrication*. 2021;13(2).
doi: 10.1088/1758-5090/abcb48

9. Cao Y, Sang S, An Y, Xiang C, Li Y, Zhen Y. Progress of 3D printing techniques for nasal cartilage regeneration. *Aesthetic Plast Surg*. 2022;46:947-64.
doi: 10.1007/s00266-021-02472-4

10. Acevedo Rua L, Mumme M, Manferdini C, et al. Engineered nasal cartilage for the repair of osteoarthritic knee cartilage defects. *Sci Transl Med*. 2021;13:eaaz4499.
doi: 10.1126/scitranslmed.aaz4499

11. He L, He T, Xing J, et al. Bone marrow mesenchymal stem cell-derived exosomes protect cartilage damage and relieve knee osteoarthritis pain in a rat model of osteoarthritis. *Stem Cell Res Ther*. 2020;11:276.
doi: 10.1186/s13287-020-01781-w

12. Xu H, Xu B. BMSC-derived exosomes ameliorate osteoarthritis by inhibiting pyroptosis of cartilage via delivering miR-326 targeting HDAC3 and STAT1//NF-κB p65 to chondrocytes. In: Yokota S, ed. *Mediators Inflamm*. 2021:1-26.
doi: 10.1155/2021/9972805

13. Ha DH, Kim H-K, Lee J, et al. Mesenchymal stem/stromal cell-derived exosomes for immunomodulatory therapeutics and skin regeneration. *Cells*. 2020;9:1157.
doi: 10.3390/cells9051157

14. Tienda-Vázquez MA, Hanel JM, Márquez-Arteaga EM, et al. Exosomes: a promising strategy for repair, regeneration and treatment of skin disorders. *Cells*. 2023;12:1625.
doi: 10.3390/cells12121625

15. Zhao H, Zhao Z, Li D, Wang X, Dai D, Fu H. Effect study of exosomes derived from platelet-rich plasma in the treatment of knee cartilage defects in rats. *J Orthop Surg Res*. 2023;18:160.
doi: 10.1186/s13018-023-03576-0

16. Yan Z, Yin H, Wu J, et al. Engineering exosomes by three-dimensional porous scaffold culture of human umbilical cord mesenchymal stem cells promote osteochondral repair. *Materials Today Bio*. 2023;19:100549.
doi: 10.1016/j.mtbio.2023.100549

17. Chen J, Huang T, Liu R, Wang C, Jiang H, Sun H. Congenital microtia patients: the genetically engineered exosomes released from porous gelatin methacryloyl hydrogel for downstream small RNA profiling, functional modulation of microtia chondrocytes and tissue-engineered ear cartilage regeneration. *J Nanobiotechnol*. 2022;20:164.
doi: 10.1186/s12951-022-01352-6

18. Han B, Fang W, Yang Z, et al. Enhancement of chondrogenic markers by exosomes derived from cultured human synovial fluid-derived cells: a comparative analysis of 2D and 3D conditions. *Biomedicines*. 2023;11:3145.
doi: 10.3390/biomedicines11123145

19. Li Q, Yu H, Zhao F, et al. 3D printing of microenvironment-specific bioinspired and exosome-reinforced hydrogel scaffolds for efficient cartilage and subchondral bone regeneration. *Adv Sci (Weinh)*. 2023;10:e2303650.
doi: 10.1002/advs.202303650

20. Chen J, Zhou D, Nie Z, et al. A scalable coaxial bioprinting technology for mesenchymal stem cell microfiber fabrication and high extracellular vesicle yield. *Biofabrication*. 2021;14(1).
doi: 10.1088/1758-5090/ac3b90

21. Xu F, Dawson C, Lamb M, et al. Hydrogels for tissue engineering: addressing key design needs toward clinical translation. *Front Bioeng Biotechnol*. 2022;10:849831.
doi: 10.3389/fbioe.2022.849831

22. Xing H, Zhang Z, Mao Q, et al. Injectable exosome-functionalized extracellular matrix hydrogel for metabolism balance and pyroptosis regulation in intervertebral disc degeneration. *J Nanobiotechnol*. 2021;19:264.
doi: 10.1186/s12951-021-00991-5

23. Gao F, Xu Z, Liang Q, et al. Osteochondral regeneration with 3D-printed biodegradable high-strength supramolecular polymer reinforced-gelatin hydrogel scaffolds. *Adv Sci (Weinh)*. 2019;6:1900867.
doi: 10.1002/advs.201900867

24. Zhang Y, Li D, Liu Y, et al. 3D-bioprinted anisotropic bicellular living hydrogels boost osteochondral regeneration via reconstruction of cartilage-bone interface. *Innovation (Camb)*. 2024;5:100542.
doi: 10.1016/j.xinn.2023.100542

25. Gnatowski P, Gwizdała K, Kurdyn A, Skorek A, Augustin E, Kucińska-Lipka J. Investigation on filaments for 3D printing of nasal septum cartilage implant. *Materials (Basel)*. 2023;16:3534.
doi: 10.3390/ma16093534

26. Göttel B, Lucas H, Syrowatka F, et al. *In situ* gelling amphotericin B nanofibers: a new option for the treatment of Keratomycosis. *Front Bioeng Biotechnol*. 2020; 8:600384.
doi: 10.3389/fbioe.2020.600384

27. Niu L, Feng C, Shen C, Wang B, Zhang X. PLGA/PLCA casting and PLGA/PDPA electrospinning bilayer film for prevention of postoperative adhesion. *J Biomed Mater Res*. 2019;107:2030-2039.
doi: 10.1002/jbm.b.34294

28. Kalluri L, Satpathy M, Duan Y. Effect of electrospinning parameters on the fiber diameter and morphology of PLGA nanofibers. *Dent Oral Biol Craniofacial Res*. 2021;4(2): 103-107.
doi: 10.31487/j.dobcr.2021.02.04

29. Zhang D, Su Y, Sun P, et al. A TGF-loading hydrogel scaffold capable of promoting chondrogenic differentiation for repairing rabbit nasal septum cartilage defect. *Front Bioeng Biotechnol*. 2022;10:1057904.
doi: 10.3389/fbioe.2022.1057904

30. Shen K, Duan A, Cheng J, et al. Exosomes derived from hypoxia preconditioned mesenchymal stem cells laden in a silk hydrogel promote cartilage regeneration via the miR-205-5p/PTEN/AKT pathway. *Acta Biomaterialia*. 2022;143:173-88.
doi: 10.1016/j.actbio.2022.02.026. Erratum in: Acta Biomater. 2022 Oct 1;151:662-663.
doi: 10.1016/j.actbio.2022.09.005

31. Hu J, Ai B, Zhu S, Wang Z, Xia H, Jia W. Electrospun PLGA and PLGA/gelatin scaffolds for tubularized urethral replacement: Studies *in vitro* and *in vivo*. *J Biomater Appl*. 2022;36(6):956-964.
doi: 10.1177/08853282211030904.

Epub 2021 Jul 13. *Erratum in*: *J Biomater Appl*. 2023;29:8853282231217938.
doi: 10.1177/08853282211030904

32. Franco RA, Nguyen TH, Lee BT. Preparation and characterization of electrospun PCL/PLGA membranes and chitosan/gelatin hydrogels for skin bioengineering applications. *J Mater Sci: Mater Med*. 2011;22: 2207-18.
doi: 10.1007/s10856-011-4402-8

33. Wang XS, Yang JM, Ding RJ, et al. Fabrication of a polylactide-glycolide/poly-ε-caprolactone/dextran/plastrum testudinis extract composite anti-inflammation nanofiber membrane via electrospinning for annulus fibrosus regeneration. *J Biomed Nanotechnol*. 2021;17:873-88.
doi: 10.1166/jbn.2021.3070

34. Cao H, Chen M, Cui X, et al. Cell-free osteoarthritis treatment with sustained-release of chondrocyte-targeting exosomes from umbilical cord-derived mesenchymal stem cells to rejuvenate aging chondrocytes. *ACS Nano*. 2023;17:13358-76.
doi: 10.1021/acsnano.3c01612

35. Stüdle C, Vallmajó-Martín Q, Haumer A, et al. Spatially confined induction of endochondral ossification by functionalized hydrogels for ectopic engineering of osteochondral tissues. *Biomaterials*. 2018;171: 219-29.
doi: 10.1016/j.biomaterials.2018.04.025

36. Patel DB, Gray KM, Santharam Y, Lamichhane TN, Stroka KM, Jay SM. Impact of cell culture parameters on production and vascularization bioactivity of mesenchymal stem cell-derived extracellular vesicles. *Bioeng Transl Med*. 2017;2(2):170-179.
doi: 10.1002/btm2.10065

37. Mao G, Xu Y, Long D, et al. Exosome-transported circRNA_0001236 enhances chondrogenesis and suppress cartilage degradation via the miR-3677-3p/Sox9 axis. *Stem Cell Res Ther*. 2021;12:389.
doi: 10.1186/s13287-021-02431-5

38. Xiang XN, Zhu SY, He HC, Yu X, Xu Y, He CQ. Mesenchymal stromal cell-based therapy for cartilage regeneration in knee osteoarthritis. *Stem Cell Res Ther*. 2022;13:14.
doi: 10.1186/s13287-021-02689-9

39. Wu J, Kuang L, Chen C, et al. miR-100-5p-abundant exosomes derived from infrapatellar fat pad MSCs protect articular cartilage and ameliorate gait abnormalities via inhibition of mTOR in osteoarthritis. *Biomaterials*. 2019;206:87-100.
doi: 10.1016/j.biomaterials.2019.03.022

40. Hu H, Dong L, Bu Z, et al. miR-23a-3p-abundant small extracellular vesicles released from Gelma/nanoclay hydrogel for cartilage regeneration. *J Extracell Vesicle*. 2020;9:1778883.
doi: 10.1080/20013078.2020.1778883

41. Liu J, Tang C, Huang J, et al. Nanofiber composite microchannel-containing injectable hydrogels for cartilage tissue regeneration. *Adv Healthc Mater*. 2023;12: 2302293.
doi: 10.1002/adhm.202302293

42. Rahmati S, Khazaei M, Nadi A, Alizadeh M, Rezakhani L. Exosome-loaded scaffolds for regenerative medicine in hard tissues. *Tissue Cell*. 2023;82:102102.
doi: 10.1016/j.tice.2023.102102

43. Xavier J, Jerome W, Zaslav K, Grande D. Exosome-laden scaffolds for treatment of post-traumatic cartilage injury and osteoarthritis of the knee: a systematic review. *IJMS*. 2023;24:15178.
doi: 10.3390/ijms242015178

44. Kronstadt SM, Patel DB, Born LJ, et al. Mesenchymal stem cell culture within perfusion bioreactors incorporating 3D-printed scaffolds enables improved extracellular vesicle yield with preserved bioactivity. *Adv Healthc Mater*. 2023;12:e2300584.
doi: 10.1002/adhm.202300584

45. Kong X, Zhu D, Hu Y, et al. Melt electrowriting (MEW)-PCL composite three-dimensional exosome hydrogel scaffold for wound healing. *Materials Design*. 2024;238: 112717.
doi: 10.1016/j.matdes.2024.112717

46. Chiu YH, Chen IC, Lin TH, Young TH, Fang HW. Effects of chitosan on chondrocytes derived from human nasal septal cartilage. *In Vivo*. 2023;37:2001-5.
doi: 10.21873/invivo.13297

47. Yang YH, Wen CS, Kuo YL, et al. GuiLu-ErXian Glue extract promotes mesenchymal stem cells (MSC)-Induced chondrogenesis via exosomes release and delays aging in the MSC senescence process. *J Ethnopharmacol*. 2023;317:116784.
doi: 10.1016/j.jep.2023.116784

48. Guo K, Liu Y, Peng J, Qi W, Liu H. Chlorination of antiviral drug ribavirin: Kinetics, nontargeted identification, and concomitant toxicity evolution. *J Hazard Mater*. 2024;467:133478.
doi: 10.1016/j.jhazmat.2024.133478

49. Zhu D, Hu Y, Kong X, et al. Enhanced burn wound healing by controlled-release 3D ADMSC-derived exosome-loaded hyaluronan hydrogel. *Regen Biomater*. 2024;11:rbae035.
doi: 10.1093/rb/rbae035

ACCSCIENCE PUBLISHING

International Journal of Bioprinting

RESEARCH ARTICLE

Effect of graphene and graphene oxide addition on crosslinking and mechanical properties of photocurable resins for stereolithography

Sara Lopez de Armentia[1]*, Raquel Giménez[2], Juan Carlos del Real[1], Berna Serrano[2], Juan Carlos Cabanelas[2], and Eva Paz[1]

[1]Institute for Research in Technology/Mechanical Engineering Department, Universidad Pontificia Comillas, Madrid, Spain

[2]Department of Materials Science and Engineering and Chemical Engineering, Instituto Tecnológico de Química y Materiales Álvaro Alonso Barba, University Carlos III of Madrid, Leganés, Spain

Abstract

The mechanical properties of the resins used in stereolithography are often inadequate, prompting studies on their enhancement with nanofillers such as graphene-based nanomaterials (GBNs). GBNs hold promise for enhancing the mechanical performance of photocurable resins, yet their incorporation often leads to unexpected alterations that impact the final nanocomposite. The full spectrum of GBN effects on these resins remains incompletely understood, with many studies reporting suboptimal improvements. This study aims to elucidate the influence of graphene (G) and graphene oxide (GO) on the mechanical properties and polymer structure of an acrylic photocurable resin used in stereolithography. The novelty of this research lies in examining how GBNs affect the polymer structure during polymerization and the degree of crosslinking—parameters that have not been sufficiently explored—and correlating these effects with photopolymerization outcomes. Stereolithography is particularly valuable in biomedicine thanks to not only its exceptional precision in creating patient-specific models, functional parts, implant devices or scaffolds for tissue engineering, but also various other innovative uses across different industries. Through comprehensive tensile tests, dynamic mechanical thermal analysis, differential scanning calorimetry, Fourier-transformed infrared spectroscopy, and microscopy analyses, it was found that GO enhances tensile strength but reduces the crosslinking degree, thus hindering overall improvements. These findings highlight the critical roles of nanomaterial dispersion, matrix-polymer interaction, and reinforcement in affecting proper crosslinking. Future studies should investigate the impact of varying nanoparticle sizes on crosslinking to further validate these hypotheses.

Keywords: Graphene-based nanomaterials; Photocurable resin; Stereolithography; Dynamic mechanical thermal analysis; Crosslinking

***Corresponding author:**
Sara Lopez de Armentia
(sara.lopez@comillas.edu)

Citation: Lopez de Armentia S, Giménez R, del Real JC, Serrano B, Cabanelas JC, Paz E. Effect of graphene and graphene oxide addition on crosslinking and mechanical properties of photocurable resins for stereolithography. *Int J Bioprint*. 2024;10(6):4075. doi: 10.36922/ijb.4075

Received: June 28, 2024
Revised: August 13, 2024
Accepted: August 14, 2024
Published Online: August 15, 2024

Copyright: © 2024 Author(s). This is an Open Access article distributed under the terms of the Creative Commons Attribution License, permitting distribution, and reproduction in any medium, provided the original work is properly cited.

Publisher's Note: AccScience Publishing remains neutral with regard to jurisdictional claims in published maps and institutional affiliations.

1. Introduction

Additive manufacturing (AM) technologies have revolutionized the field of materials science by enabling the fabrication of complex geometries with high precision

and reducing waste. Among various AM techniques, vat polymerization technologies, based on the use of photocurable resins such as stereolithography (SLA), have gained significant attention due to their ability to produce high-resolution parts with excellent surface finish.[1]

One of the most promising examples of the use of photocurable resins is in the biomedical field, where their application has gained significant popularity in recent years.[2,3] This growth is driven by the development and commercialization of resins certified for biomedical applications. As a result, there has been a proliferation of applications, including the creation of patient-specific models and functional parts, implantable devices, particularly in dentistry, and short-term implantable devices. The ability to produce highly accurate and customized medical components has made vat polymerization techniques indispensable in modern medical practice. While the biomedical field represents a key area of application, photocurable resins are also being explored for various other innovative uses across different industries.[4]

The incorporation of graphene-based nanomaterials (GBN), such as graphene (G) and graphene oxide (GO), into ultraviolet (UV)-curable resins has opened up new avenues for enhancing the mechanical and functional properties of materials fabricated through vat polymerization technologies.[5] The unique two-dimensional structure of G, characterized by a single layer of carbon atoms arranged in a hexagonal lattice, imparts exceptional mechanical strength, electrical conductivity, and thermal stability.[6] GO, a derivative of G, offers additional functional groups that can facilitate dispersibility and bonding within the polymer matrix.

One of the most promising aspects of GBN-reinforced resins is the potential improvement in mechanical properties. Studies have shown that even a minor incorporation of G or GO can yield substantial increases in tensile strength, Young's modulus, and fracture toughness.[7–9] Beyond mechanical enhancements, GBNs have also demonstrated the capacity to improve thermal and electrical conductivity in photocurable resins. Consequently, this advancement has promoted the development of UV-curable resins with multifunctional properties, suitable for applications that range from structural designs to electronics and thermal management.[5,10]

It has been demonstrated that achieving proper dispersion of GBN within the polymeric matrix is crucial for unlocking the full potential of these nanomaterials in enhancing composite properties.[11] Various techniques, including ultrasonication, functionalization of GBNs, and the use of surfactants, have been employed to ensure the uniform distribution of these nanomaterials within UV-curable resins.[7,12,13] It is interesting to highlight that the chemical functionalization of GO is easier than G thanks to its oxygen-containing functional groups.[14]

Nevertheless, integrating G and GO into photocurable resins for three-dimensional (3D) printing poses unique challenges, like the low content of printable G and GO, high cost, and uncured photosensitive resins. Contrary to expectations, several studies have found that the addition of these nanomaterials does not consistently enhance the mechanical properties of these resins, even with adequate dispersion.[13,15,16] The most significant challenges include insufficient curing of the resin due to nanoparticle absorption of UV light, the induction of anisotropy in composites caused by the inherent alignment of G sheets, increased internal stresses from resin shrinkage, and compromised adhesion between layers. However, the precise nature and extent of these effects remain incompletely understood, necessitating further research to comprehensively discern their mechanisms and conditions, thereby facilitating the optimization of the development of these materials.

In the context of layer adhesion and internal stresses, it has been observed that the presence of GBN can either enhance or hinder these properties. This variation largely depends on their interaction with the polymer matrix, distribution, and dispersibility. On one hand, GBNs, due to their rigid structure, could potentially mitigate these stresses by providing a reinforcing network. Conversely, non-uniform dispersion or aggregation of GBNs can intensify internal stresses, counteracting their potential reinforcing benefits.

In relation to the challenge of achieving an adequate degree of polymerization, a significant issue arises with the use of GBN in photocurable 3D printing materials. G strongly absorbs light, especially at the critical photopolymerization wavelength of around 405 nm, impeding sufficient light penetration to the polymer resin.[17] This often results in under-polymerization of the polymer matrix, leading to a notable decrease in stiffness and strength when compared to the base polymer without G.[17] Several researchers have concentrated their efforts on enhancing the mechanical properties of SLA 3D-printed samples by employing various post-treatment methods aimed at ensuring complete resin curing. These investigations have demonstrated that post-treatment highly affects the properties of the final material.[18,19] Despite these efforts, it appears that these approaches do not fully resolve the issue, indicating that the problem of achieving optimal mechanical properties in SLA-G-printed materials extends beyond merely ensuring complete curing of the resins.

Finally, the anisotropic effect in the GBN-reinforced photocurable resins is an intriguing phenomenon that has been attributed to the self-selection of naturally aligned graphene (SNAG) effect.[10,12,20,21] SNAG is a proposed process caused by the light-blocking properties of G due to their strong absorbance of photopolymerizing light. This reduction in light transmission creates a shadowing effect, preventing sufficient laser light from reaching the photosensitive resin behind the G for polymerization and solidification. In the SNAG effect, horizontally oriented G platelets are particularly effective in blocking laser light and preventing polymerization. As a result of this selective alignment of G platelets, the composite material presents enhanced stiffness and strength of the polymer in the direction of the G alignment. However, while this SNAG effect can be advantageous in terms of improving material properties, it also poses challenges in achieving consistent and predictable 3D printing outcomes with G-reinforced photocurable resins.

In summary, while GBNs have the potential to significantly improve the mechanical properties of 3D-printed objects, their actual impact can be complicated by various factors inherent to the additive manufacturing process. Understanding and controlling these factors are essential for optimizing the reinforcing effect of GBNs in UV-curable resins used in vat polymerization technologies. Although several of these complex factors have already been studied, much work remains to be done to fully understand their global effects, particularly in crosslinking, which has not been thoroughly explored. Given these complexities, the aim of this work is to explore the influence of adding G and GO on the polymeric structure and crosslinking. We hypothesize that these nanomaterials can significantly alter the polymeric structure by affecting the curing of the resin, and therefore, mechanical properties of photocurable resins can be affected. Previous research has not thoroughly examined this aspect, and our study seeks to fill this gap, contributing to the optimization of these advanced materials.

2. Materials and methods

2.1. Materials

Commercially available photocurable Clear resin V4 with the following composition was obtained from Formlabs (Somerville, MA, USA): 55–75% urethane dimethacrylate, 15–25% methacrylate monomer(s), and <0.9% diphenyl(2,4,6-trimethylbenzoyl)phosphine oxide (TPO) photoinitiator.

The Clear resin was reinforced with two different GBNs: graphene (G) and graphene oxide (GO). G powder was composed of one to two layers of G sheets with an average lateral size of 2–4 μm supplied by Avanzare Nanotechnology (La Rioja, Spain), and GO powder had a thickness of 0.7–1.2 μm and average lateral size of 4–8 μm supplied by NanoInnova Technologies (Toledo, Spain). Micrographs taken with a scanning electron microscope (SEM) TENEO-LoVac (Eindhoven, the Netherlands) are shown in Figure 1. From those micrographs, the lateral size was measured, being 7.1 ± 1.9 μm and 11.9 ± 2.7 μm for G and GO, respectively. The measured size is larger than the value given by the manufacturer due to the natural agglomeration of these nanofillers.

2.2. Experimental methodology

2.2.1. Sample preparation

Dispersion of nanomaterials inside the matrix is a crucial factor in achieving improvements in mechanical properties. Due to the high viscosity of Clear resin, methyl methacrylate (MMA) supplied by Sigma Aldrich (St. Louis, MO, USA) was used to disperse the nanomaterials powders by ultrasonication following the procedure

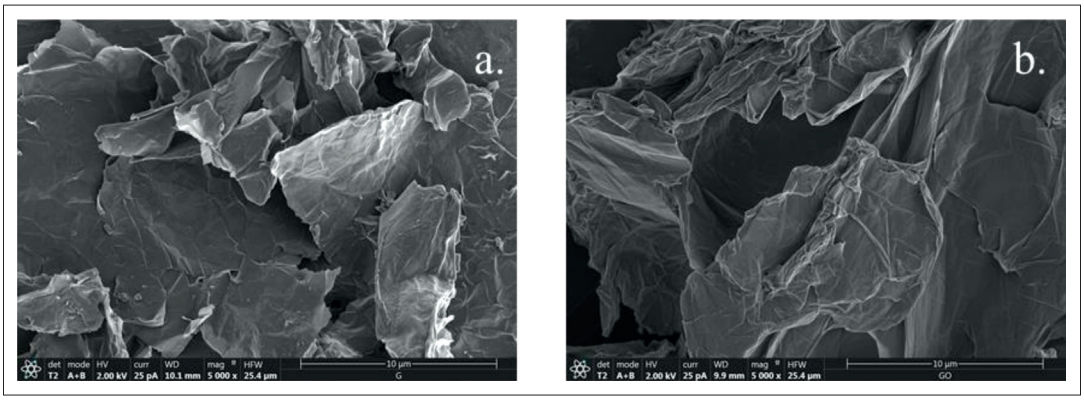

Figure 1. Scanning electron microscope (SEM) images of graphene (a) and graphene oxide (b).

explained in a previous study.[17] In short, G and GO were sonicated with MMA, and resin was gradually added with sonication steps. The resin:MMA ratio was 300:10 v/v. The frequency range applied was 1985–2050 kHz at a 50% amplitude for 10 ± 0.5 min—pulses of 10 ± 0.5 s on and 20 ± 0.5 s off. This process was followed by degassing to avoid the presence of microbubbles that could affect mechanical properties. Samples of as-received Clear resin and resin reinforced with 0.05 wt.% of G (R+G) and GO (R+GO) were prepared.

The printed samples were obtained by stereolithography with SLA printer Form2 (Formlabs, Somerville, MA, USA). Layer thickness was set at 100 μm and the wavelength used was 405 nm. Exposure time was set by the manufacturer specifications, but it was adapted in the case of R+G samples since these had shown printability issues,[13] then it was increased by an 8.9% to achieve enough polymerization degree to obtain parts. The other parameters were already set by the manufacturer. The samples were cleaned for 3 min with isopropyl alcohol in FormWash (Formlabs) equipment. Post-curing was realized in FormCure chamber (Formlabs). During this process, samples were subjected to UV and heat. Parameters used were 405 nm of wavelength, a temperature of 80°C, and a duration of 90 min. Samples without post-curing (as-printed) and with post-curing treatment (post) were studied in order to determine the effect of the post-curing treatment in the resin properties.

2.2.2. Differential scanning calorimetry

The differential scanning calorimetry (DSC) measurements were performed using DSC882e differential scanning calorimetery, (Mettler-Toledo, Greifensee, Switzerland). Dynamic scans from 20 to 250°C at 20°C/min were carried out, and STARe software (Mettler Toledo) was used to analyze the curves. Samples (5–10 mg) were placed into aluminum crucibles with a capacity of 40 μL and 50 μm hole in the lid. Nitrogen was the purge gas and was delivered at a rate of 80 mL/min. Two scans were carried out. In the first scan, the area of the curing peak was measured to determine if the polymer was completely cured and it could be completely polymerized by the application of heat, while in the second scan, glass transition temperature (T_g) was determined as the midpoint of the step of the baseline through the endothermal direction. At least, three samples per condition were tested and averaged.

2.2.3. Fourier-transformed infrared spectroscopy (FTIR)

Infrared spectra were obtained with an IRT-5200 FTIR spectrometer from Jasco (Jasco Analitica Spain, Madrid, Spain), with attenuated total reflectance (ATR) technique. DuraSample Diamond accessory formed by a diamond, with a diameter of 0.5 mm, embedded in a ZnSe crystal was used. The ratio signal-to-noise is better than 8000:1 (5.4×10^{-5} noise absorbance). Spectra were recorded with a resolution of 4 cm^{-1} from 4000 to 400 cm^{-1} by taking 32 scans.

Double bond conversion (DBC) was studied following the peaks corresponding to carbonyl groups (C=O) at 1728 cm^{-1} and the peak corresponding to acrylate double bond (C=C) located at 810 cm^{-1}.[22] As reference, liquid resin with or without GBN was used,[23] using Equation I.

$$DBC = \left[1 - \frac{I_{(C=C)}}{I_{liquid(C=C)}} \times \frac{I_{liquid(C=O)}}{I_{(C=O)}}\right] \times 100 \quad \text{(I)}$$

2.2.4. Tensile tests

To carry out tensile tests, dog bone samples were obtained following ISO 527-2:2012 standard (sample 1BA).[24] Printed layers formed 85° with the applied load direction. Tests were conducted using a Universal Testing Machine IBTH/500 (Ibertest, Madrid, Spain) with a load cell of 5 kN, operating at an elongation rate of 3 mm/min. The tensile strength, Young's modulus, and elongation at break were calculated using the load and elongation data.

2.2.5. Dynamic mechanical thermal analysis

Dynamic mechanical thermal analysis (DMTA) of post-cured samples was performed using DMTA Q800 (TA instrument, DE, USA) with printed rectangular specimens ($15.3 \times 5.0 \times 1.4$ mm^3) in tension mode in a temperature range of 30–225°C, at a single frequency of 1 Hz and a heating rate of 2°C/min. As in tensile tests, layers were printed with an angle of 85° with the applied load.

With the data obtained from DMTA, it was possible to calculate the molecular weight between crosslinks in a thermosetting resin. Firstly, storage modulus had to be measured within the rubbery plateau region ($E'_{rubbery}$) and, from that value and applying Equation II, molecular weight between crosslinks (M_c) could be calculated[25]:

$$M_c = \frac{3 \cdot R \cdot T \cdot \rho}{E'_{rubbery}} \quad \text{(II)}$$

where R is the universal gas constant, T is the absolute temperature at which the modulus was calculated (448 K), and ρ is the density of the polymer. Density was obtained by applying Archimedes' principle with a Density Kit (Mettler Toledo, Greifensee, Switzerland).

Besides, crosslinking density per unit volume was calculated using Equation III[26]:

Table 1. Area and temperature of polymerization peak, and Tg of as-printed and post-cured samples of R, R+G, and R+GO

	Polymerization peak				Glass transition temperature	
	As-printed		Post-cured		As-printed	Post
	Area (J/g)	*T* (°C)	Area (J/g)	*T* (°C)	T_g (°C)	T_g (°C)
R	16 ± 4	165 ± 3	-	-	109 ± 3	117 ± 3
R+G	14 ± 3	175 ± 3	-	-	104 ± 6	110 ± 4
R+GO	13 ± 5	173 ± 4	-	-	103 ± 4	110 ± 2

Notes: Results are presented as average ± S.D. "-" indicates that no polymerization peak was observed.

Abbreviations: G, graphene; GO, graphene oxide; R, resin; T, temperature; T_g, glass transition temperature.

$$d = \frac{E'_{rubbery}}{3 \cdot R \cdot (T_g + 40)} \quad \text{(III)}$$

where T_g is the glass transition temperature (K).

2.2.6. Scanning electron microscopy

Field emission scanning electron microscopy (FE-SEM) was carried out in TENEO-LoVac (Eindhoven, the Netherlands). Images were obtained from cryogenic fracturing and sputter-coating with gold.

2.2.7. Statistical analysis

The results were further analyzed for statistical significance using a one-way analysis of variance (ANOVA) test with a post hoc Scheffe's test. SPSS 28.0 was utilized for statistical analysis (for Windows; IBM SPSS, USA). A *p*-value of less than 0.05 was considered statistically significant.

3. Results

3.1. DSC results

DSC thermograms were analyzed to determine the presence of unpolymerized resin and the T_g of each sample. From the first scan, it was possible to ascertain whether polymerization was completed with the application of heat to the printed sample. Polymerization process appears as an exothermal peak in DSC thermogram; therefore, the presence of any exothermal peak in this first scan may indicate that the polymerization has not been fully complete. The results of the first scan for each material, as-printed and after post-curing treatment (post) are shown in Table 1. Values were calculated as the average ± standard deviation of the three performed experiments.

The results of the first scan showed a similar polymerization heat for all the as-printed samples (around 15 J/g), with the differences lying in the precision of the measurements. However, GBN-loaded resins (R+G and R+GO) showed a significantly higher peak temperature, which means that GBN showed a retardation effect in the polymerization reaction.[27]

Post-cured samples did not exhibit a peak, suggesting that the post-curing process may have achieved complete polymerization in all cases. It is important to consider that DSC primarily determines thermal curing; the absence of a peak might indicate that further curing through heat application is no longer feasible. However, a clear distinction was observed between the post-cured and non-post-cured samples.

The T_g calculated from the second scan is also shown in Table 1. It was found that during the printing process, R+G and R+GO showed lower T_g. When samples were post-cured, T_g increased in every case, this can be attributed to an increase in the crosslinking degree of samples because the application of UV light together with heat.[18]

3.2. FTIR results

It is well-known that a problem that UV-photocurable acrylic resins present is that the percentage of carbon-carbon double bond that are converted into single bonds to obtain a polymer is low, resulting in deficient mechanical properties.[28] DBC was calculated for every sample, and results are shown in Table 2.

Analyzing the DBC results of as-printed samples revealed that the addition of GBN (G and GO) produced a slight reduction of DBC during the printing process, compared to R. When the post-treatment was carried out, we found a slight increase in DBC conversion, although

Table 2. Double bond conversion of samples with the studied post-treatment

	As-printed	*Post-cured*
R	48.6	51.6
R+G	46.0	48.6
R+GO	46.3	50.4

Abbreviations: G, graphene; GO, graphene oxide; R, resin.

this increase was less notable for G resin. In all cases, the degree of conversion was around 50% with similar values reported in other studies.[29] The residual unreacted double bonds could exist either as free unreacted monomer or as pendant groups within the polymer network.

3.3. Tensile tests results

Besides tensile strength, tensile tests also provided information about the stiffness of samples and its elasticity through Young's modulus and elongation at break. The three parameters obtained are shown in Table 3, and a representative curve for each sample is shown in Figure 2.

The tensile strength of as-printed samples was significantly lower when both GBN types were added, with this reduction being particularly notable in the case of G. The reduction was about 18% in the case of R+GO and 38% in R+G. This decrease in mechanical properties was accompanied by a decrease in Young's modulus, which also was more pronounced for R+G. Regarding the elongation at break, a slight increase was observed only in the R+GO.

In all cases, post-curing enhanced the tensile strength and rigidity of the samples while reducing their elongation at break compared to the as-printed samples. This improvement may be attributable to increased polymerization and crosslinking, resulting in lower chains mobility. After post-curing, R+GO samples exhibited significantly higher tensile strength than R (5% higher), whereas R+G samples continued to show lower strength.

Table 3. Tensile strength, Young's modulus, and elongation at break of R, R+G, and R+GO samples with the studied post-treatments

		R	R+G	R+GO
As-printed	Tensile strength (MPa)	34.49 ± 0.52	21.27 ± 1.52*	28.41 ± 3.87*
	Young's modulus (GPa)	1.29 ± 0.06	0.87 ± 0.34*	1.06 ± 0.13*
	Elongation at break (%)	29.49 ± 8.56	28.66 ± 4.39	34.80 ± 3.87
Post-cured	Tensile strength (MPa)	73.79 ± 1.28	70.06 ± 4.23	77.55 ± 1.06*
	Young's modulus (GPa)	2.50 ± 0.13	2.72 ± 0.28	1.88 ± 0.39*
	Elongation at break (%)	6.68 ± 1.52	4.80 ± 1.11*	5.25 ± 0.49

Note: Results are presented as average ± S.D. *Significantly different than R ($p < 0.05$).
Abbreviations: G, graphene; GO, graphene oxide; R, resin.

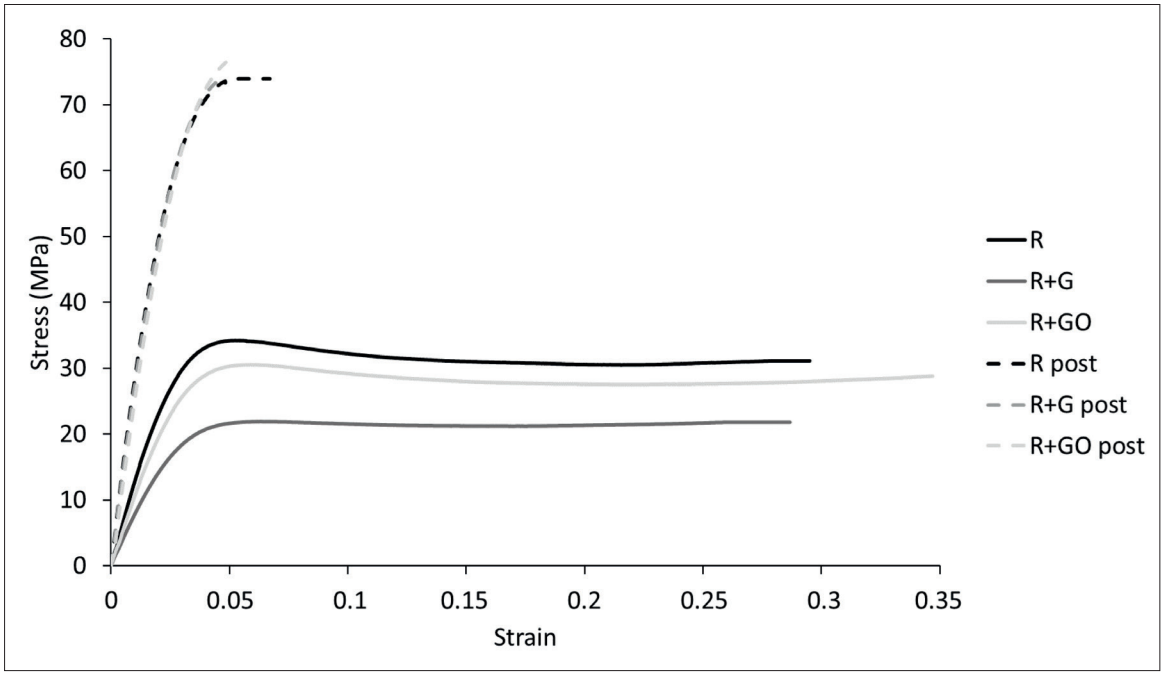

Figure 2. Stress–strain curves obtained from tensile tests. Abbreviations: G, graphene; GO, graphene oxide; post, post-cured; R, resin.

Interestingly, R+GO still showed a lower Young's modulus compared to R and R+G.

Considering that as-printed R+G and R+GO samples showed similar DBC values, the observed differences in mechanical properties do not seem proportional to the DBC reduction. This suggests that the differences are not solely due to low polymerization caused by GBN presence. This deduction is further supported by the post-cured mechanical results, where the lack of correlation between DBC and mechanical properties persists. While post-curing does enhance mechanical properties, this improvement may originate not only from increased polymerization but also from enhanced crosslinking within the polymeric matrix.

Furthermore, the reduction in Young's modulus for both, as-printed and post-cured samples, aligns with the observed decrease in T_g upon GBN addition. This correlation suggests that variations in mechanical properties are related to the crosslinking and changes in molecular structure of each composite.

3.4. FE-SEM analysis

The aspect and roughness of fracture surfaces provide insightful information about materials behavior, such as brittleness or ductility, and the crack deviation mechanism. This crack deviation typically manifests as shift in the crack growth plane because micro-cracks encounter stiff GBN and bypass them.[30] SEM micrographs in Figure 3 show the differences in post-cured R, R+G, and R+GO samples. In post-cured R and R+G samples, the surfaces were smooth, lacking any noticeable undulations, indicative of brittle fracture characteristics. This observation suggests that the addition of G does not significantly alter the crack path, likely due to inadequate adhesion or interaction with the resin matrix (see Figure 3b). In contrast, post-cured R+GO (Figure 3c) corresponds to a more ductile fracture pattern, showing homogeneously distributed undulations (shown with red arrows), which indicated a reasonably uniform dispersion of GO and a ductile fracture. Surface undulations often signal an increased fracture toughness, primarily because they absorb more fracture energy, thereby improving the matrix capacity to withstand damage.[31,32] This more ductile behavior observed in the fracture of R+GO samples should be reflected in the mechanical properties, while post-curing enhanced tensile strength in R+GO, the transition from the brittle fracture of R to the more ductile nature of R+GO is more pronounced than the observed increase in tensile strength values. This significant observation will be further discussed in the Section 4.

3.5. DMTA results

The DMTA tests were exclusively conducted on post-cured samples, as the as-printed specimens exhibited a sticky consistency that could damage the testing equipment. Furthermore, the focus on post-cured samples aligns with their relevance to the final application, with as-printed samples being studied just for comparative purposes to understand the impact of post-curing on the properties of resins. The storage modulus (Figure 4a), loss modulus (Figure 4b), and tan δ (T_α) (Figure 4c) parameters were obtained from these tests for each material: R, R+G, and R+GO.

The initial zone of the obtained curves, at lower temperatures, corresponds to the glassy state of the polymer/nanocomposite. In this zone, it was found that both storage (E') and loss modulus (E'') exhibited high values. As the temperature rises, free polymeric segments started to move and the excess of energy was dissipated as heat. Subsequently, this results in a noticeable decrease in both E' and E'' values, marking glass transition phase. After glass transition, E', E'', and T_α decreased because the material passes the rubbery state. Curves showed that only one transition occurred during the heating. This suggests that all the samples analyzed were completely polymerized

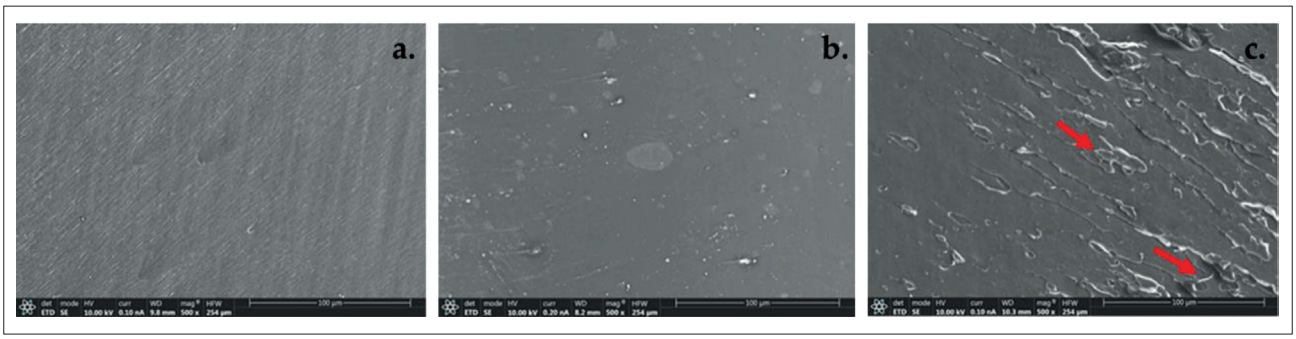

Figure 3. Scanning electron microscope (SEM) micrographs of the fracture surface of post-cured R (a), R+G (b), and R+GO (c). Abbreviations: G, graphene; GO, graphene oxide; R, resin.

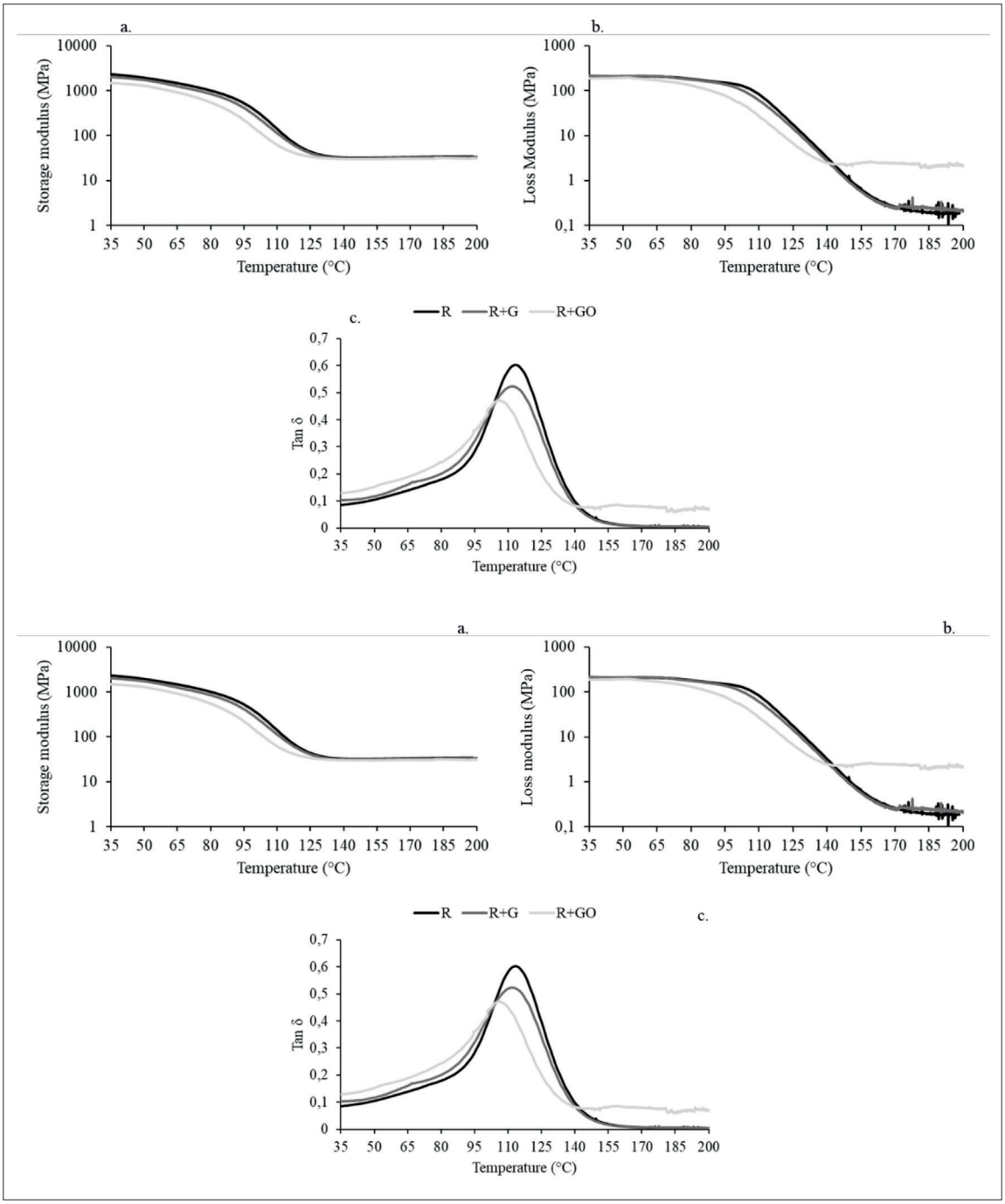

Figure 4. DMTA curves. (a) Storage modulus (E'), (b) loss modulus (E"), and (c) tan δ of post-cured R, R+G, and R+GO samples. Abbreviations: G, graphene; GO, graphene oxide; R, resin.

and only a physical transition could be observed, corresponding to the glass transition.[18]

The temperature of the peak on T_α corresponds to the glass transition temperature. It was found that DSC and DMTA detected similar temperatures, and the minor differences could be due to the heating rate used to perform the DSC scans. However, they also presented a small shoulder (T_α') before the glass transition, which could be attributed to a sub-T_g.[33] This reflects that there are segments of the polymerized network that relax more

Table 4. Summary of DMTA results

	E'_{glass} (GPa)	$E'_{rubbery}$ (MPa)	E''_{glass} (GPa)	T_α (°C)	T_α' (°C)	ΔT_α (°C)
R post-cured	2.26	31.5	0.19	115	75	33.9
R+G post-cured	2	32.7	0.2	112	68	38.0
R+GO post-cured	1.47	28.6	0.19	106	53	52.9

Abbreviations: *E*', storage modulus; E", loss modulus; G, graphene; GO, graphene oxide; R, resin.; T_α, glass transition temperature; T_α', sub-glass transition temperature; ΔT_α, ull width at half height

quickly, at lower temperatures, and therefore exhibit greater mobility. To facilitate the analysis of the results, all the data explained in this paragraph are summarized in Table 4.

The results showed that the modulus of R and R+G are very similar, while GO produced a reduction in *E*' and T_α peak. This suggests that GO interacted with the polymer chains, probably inhibiting the crosslinking. It could also be observed by the full width at half height (ΔT_α), which is higher for R+GO sample, as can be seen in Figure 4c and Table 4. The higher ΔT_α also suggested that a less homogeneous network was formed.[18] The printing process and the post-treatment resulted in different networks, with different crosslinking degrees and linearity, which was demonstrated in the different T_gs found.

The interaction of the acrylic resin with GO should be better than with G, which is more apolar and lacks oxygenated functionalities. Therefore, if the interfacial interaction is greater, the stiffness of the interface would also be higher, without lowering the T_α.[34] However, this is precisely what happened: with both reinforcements, the T_α of the bulk decreased. This could be explained by a lower degree of curing due to the presence of G.[17] Moreover, the rise in T_α was more gradual, especially in R+GO (as seen by a broadening in the transition). A possible explanation is that there was an interfacial subregion with increased mobility due to the disruption of the polymerized network, which was more pronounced in GO because it has a larger interface area due to better dispersion. In densely crosslinked polymers, this interface may act as a free surface where the chains exhibit greater mobility and faster relaxation.[35]

R and R+G showed similar temperatures for final T_α maximum, as well as the rubbery modulus, suggesting that the same final structure was obtained.[36] However, the addition of GO changed these values, resulting in a different final structure. It has been found from kinetics curves that a different polymerization rate is shown by R+GO samples.[17]

The polymer structure was analyzed by calculating molecular weight between crosslinks (M_c); the obtained results are presented in Table 5. It can be observed that the M_c for R+GO is higher compared to R and R+G, indicating a less crosslinked structure in the polymer after post-curing. Conversely, the M_c value for R+G was very similar to that for R, suggesting that the presence of G did not significantly impact the crosslinking density in the final polymer structure. These conclusions are confirmed through the analysis of crosslinking density values.

3.6. Adhesion between layers

Due to the inherent nature of 3D-printed specimens, which are created layer by layer rather than presenting as a purely continuous material, a decrease in the quality of layer adhesion or overall printing quality can negatively affect the final mechanical properties of the resulting material. For this reason, the samples were analyzed by optical microscopy to determine the layer adhesion and the surface quality. The detail of the interface between the layers is visible in Figure 5. The impact of different GBN on the superficial aspect and the interface between layers could explain the variations found in mechanical properties. GO had the smallest effect on printing quality, with only some marks being visible due to the presence of the nanofiller. In the case of G, the surface was not smooth, displaying many imperfections, which could potentially affect mechanical performance at the macroscale.

Table 5. Density, molecular weight between crosslinks and crosslinking density of post-cured samples

	ρ (g/cm^3)	M_c (g/mol)	d (mol/m^3)
R post-cured	1.185	400.0	2.95×10^{-3}
R+G post-cured	1.181	401.4	3.08×10^{-3}
R+GO post-cured	1.182	437.3	2.74×10^{-3}

Abbreviations: *d*, crosslinking density; G, graphene; GO, graphene oxide; M_c, molecular weight between crosslinks; R, resin; ρ, density.

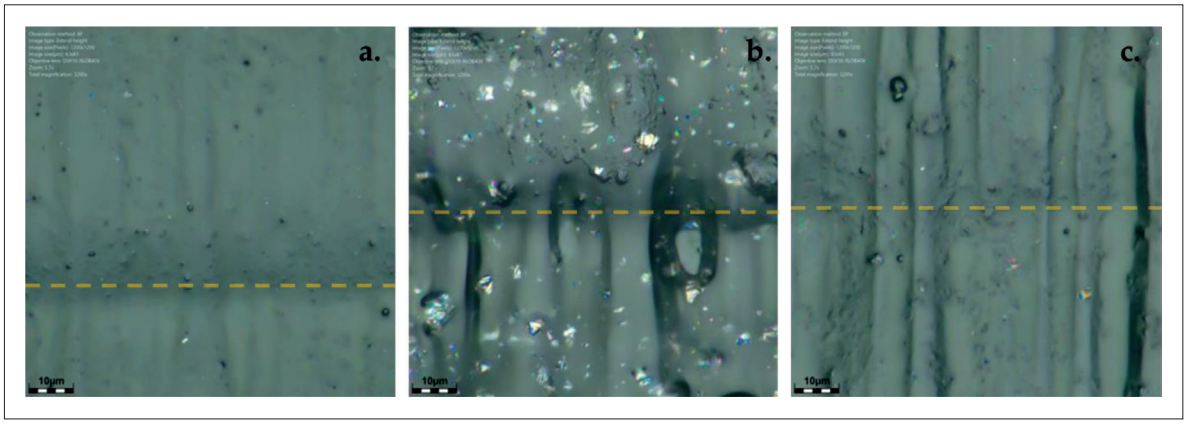

Figure 5. Surface analysis of printed samples of post-cured R (a), R+G (b), and R+GO samples (c). The interface between printed layers was marked with the yellow line. Abbreviations: G, graphene; GO, graphene oxide; R, resin.

4. Discussion

The aim of this study is to explore the factors that can affect the success of GBN as reinforcement agents in photocurable acrylic resins. The peculiar polymerization process of these resins makes it difficult to determine the factors that may influence the final polymer structure and performance.

Previous research has already identified some of the factors that could affect the performance of nanocomposites, including the dispersion quality of the nanofiller,[37,38] chemical interaction between the reinforcement and the matrix,[39,40] and the impact of nanomaterials on the curing degree.[17,41] However, other effects have gone unnoticed, such as the effect of the nanofiller on the final 3D structure of the polymer chains. This structure is known to directly influence the polymer properties; for example, changing crosslinking degree in thermosetting polymers directly correlates with mechanical strength.[42,43] While nanoparticles are known to enhance mechanical properties through different mechanisms, acting as crack stoppers and deflectors,[44] if their presence leads to a decrease in other polymer properties such as curing degree or crosslinking, the expected improvements may not be observed. This is evidenced in this study by adding G and GO to a photocurable acrylic resin for use in stereolithography 3D printing.

To understand whether G and GO affect the curing degree, DSC and FTIR tests were conducted. Previous studies indicated that G and GO in these photocurable acrylic resins affect the polymerization kinetics and mechanism,[17,45] potentially impacting mechanical properties. The results showed that the curing degree is not significantly affected by GO, especially after post-curing, although a slight decrease is detected in the case of G. This aligns with previous studies[46] demonstrating that G can hinder light from reaching the photoinitiator, thus affecting curing. However, this effect is less pronounced with the addition of GO.

Figure 6 presents a schematic representation of this effect. When UV light reaches the uncured resin, a portion of the light is absorbed by G, preventing it from reaching the photoinitiator and thus inhibiting the initiation of the polymerization process. In contrast, GO does not absorb UV light; instead, it acts as a radical scavenger. GO combines with the activated photoinitiator, which prevents effective crosslinking and results in a less crosslinked polymer network. This demonstrates the differing impacts of G and GO on the polymerization process and the final polymer structure.

Even without nanofillers, it has been found that UV-polymerized acrylic resins typically exhibit low carbon-carbon DBC. It is related with a low polymerization and crosslinking degree. Post-curing slightly improves this conversion, which remains around 50% for all samples. However, DSC analysis indicates complete curing in post-cured samples, suggesting that residual double bonds are probably pendant in the polymer network.

While the polymerization degree appears unaffected, differences are observed in T_g and mechanical properties, which decrease with the presence of GBNs. This suggests that nanofillers may adversely affects mechanical properties due to poor dispersion or interaction with the matrix, and/or alteration of the molecular structure of the resulting polymer.[38,47]

Besides previous considerations, additive manufacturing present a new parameter to consider when studying the mechanical performance of parts obtained by this technology. The observed decrease or lack of expected improvement in mechanical properties could result from

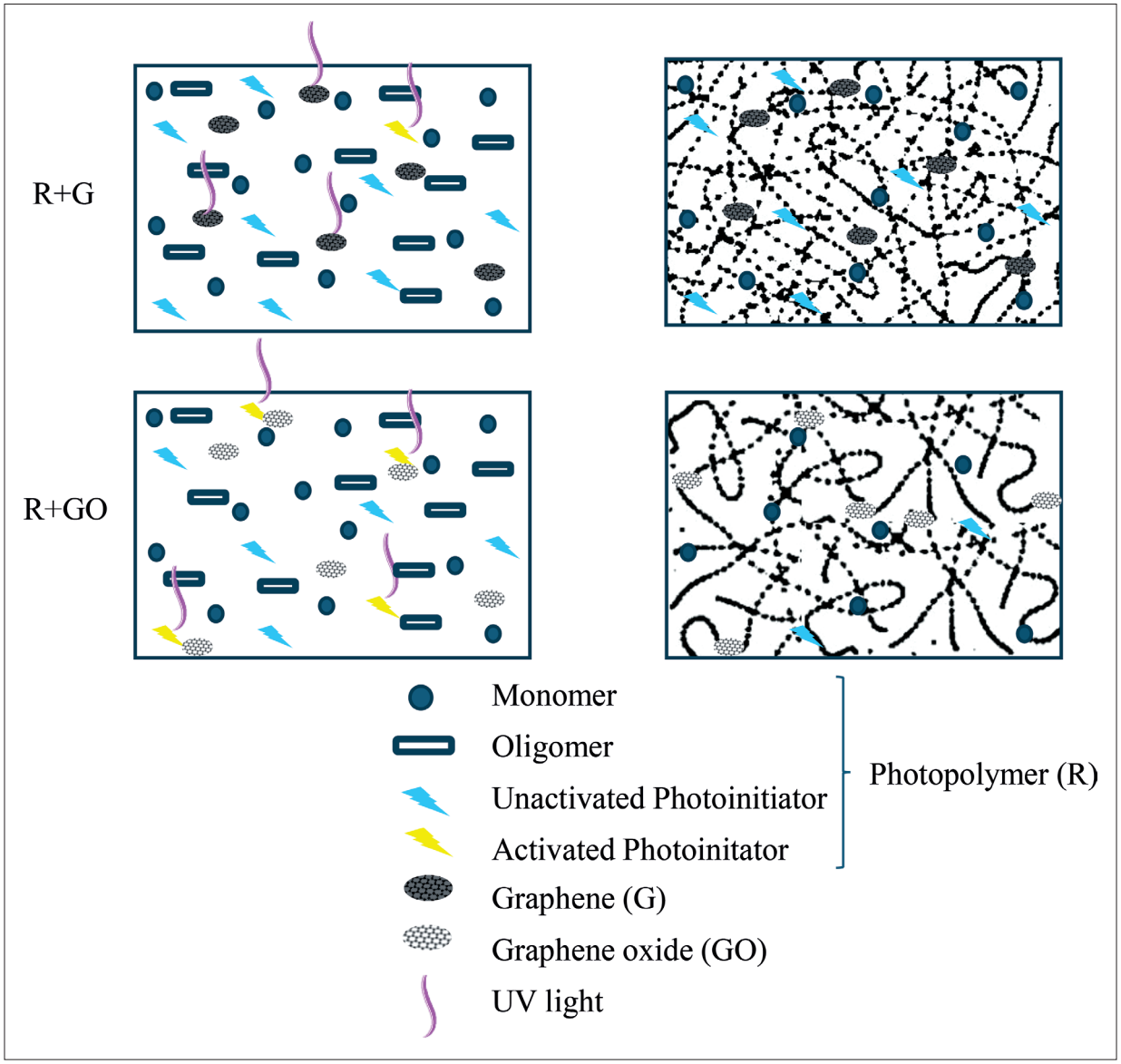

Figure 6. Schematic representation of the effects of graphene and graphene oxide on the photopolymerization process of the resin.

reduced interlayer adhesion due to the presence of GBN. Microscopic analysis does not reveal poor interlayer adhesion but indicates lower print quality with G, likely due to increased imperfections and defects, which contribute to the negative effect on mechanical properties. In relation to the effect of printing parameters on the mechanical properties of printed parts, it is worth mentioning that other studies have also reported correlations between mechanical properties, printing process peculiarities, and crosslinking of the polymeric structure. For example, previous research has found that the frequency of UV curing and the resulting crosslinking density play crucial roles. These studies demonstrated that as layer thickness decreases from 200 to 50 μm, higher crosslinking density is induced, increasing Young's modulus due to more densely spaced crosslinked layers. However, when the layer thickness is reduced to 25 μm, an unexpected decrease in Young's modulus is observed.[48] This decrease is attributed to insufficient inter-layer crosslinking, as there are not enough monomers available between each crosslinked layer to ensure efficient stress transfer, resulting in a lower modulus. Throughout our study, the layer thickness had been kept constant in all samples, but this mechanism is similar to the effect observed with the addition of GO, when it acts as radical scavenger.

The SEM images (**Figure 3**) provide crucial insights into the dispersion of GBN and its correlation with the fracture behavior of the material. The R+GO sample, following the applied dispersion protocols, exhibits an optimal degree of dispersion. The GO is uniformly distributed and shows strong interaction with the polymer matrix, being well-integrated within it. This homogeneity results in an irregular fracture surface, indicating enhanced toughness. In contrast, the dispersion of G is markedly inferior, characterized by the presence of distinct clusters (**Figure 3b**). Consequently, the fracture surface is smooth, corroborating the poor interaction with the polymer matrix.

These findings align well with the observed mechanical properties. In the post-cured R+G sample, there was an increase in Young's modulus and a decrease in elongation, attributed to the rigidity effect of the introduced G. However, this effect was less pronounced due to poor nanoparticle dispersion. In contrast, the GO sample exhibited a decrease in Young's modulus compared to G and an increase in elongation. This can be explained by reduced crosslinking, which leads to significant disruption of the polymer network, resulting in greater deformability and a lower modulus. In the R+GO sample, the reinforcing effect of GO was present but was offset and surpassed by the antagonistic effect of reduced crosslinking. The impact of GO on the crosslinking of the polymer network could be mitigated through surface modifications, such as silanization, as previously demonstrated by Uysal et al.[49] In their study, it was shown that silanization of the surface of nanomaterials can significantly enhance the physical and chemical properties of the polymer network.

It is noteworthy that R+GO fracture surface exhibited significantly higher ductility, showing uniformly dispersed undulations. This suggests that GO nanoparticles may effectively provide obstacles to the crack propagation.[8,50] This observation indicates that the lack of expected improvements may be the result of a change in the polymer structure, particularly from a crosslinking perspective.

The polymer crosslinking degree is evident in the calculated M_c after post-curing. Results indicated that R+GO exhibited a less crosslinked polymer structure. This could be attributed to the larger size of GO, which impedes proper formation of the reticulated network structure, resulting in a less crosslinked matrix and consequently weaker mechanical performance. Conversely, while G appears to have no significant impact on the crosslinking of the final polymer matrix, possibly due to its smaller size and lower chemical reactivity compared to GO, the observed poor mechanical properties may result from inadequate dispersion, incomplete curing, or poor G integration into the matrix. This conclusion is supported by the observation of the fracture surface, where a ductile behavior is not found.

5. Conclusion

The present study aimed to investigate factors influencing the effectiveness of GBNs in photocurable acrylic resins for stereolithography. While previous research identified several factors affecting nanocomposite performance, including nanofiller dispersion and chemical interactions, this study revealed that GBN may also produce effects on polymer chain structure.

The presence of G and GO nanoparticles in acrylic resins for 3D printing did not significantly affect polymerization degree but impacted mechanical properties and glass transition temperature. Differences in mechanical properties between samples indicate that GBNs may have different effects in the resin. Particularly, GO produced a slight increase in tensile strength (5%), but it was found that it led to a less crosslinked matrix, potentially due to its larger size. In the case of G, it showed poor mechanical properties possibly due to inadequate dispersion or integration, without affecting crosslinking degree. Therefore, the observed differences between the various nanocomposites are due to changes induced in the resin structure by the presence of the nanofillers, rather than the effect of the nanofillers themselves.

Acknowledgments

None.

Funding

This work was supported by Comillas Pontifical University (grant number PP2020_08).

Conflict of interest

The authors declare they have no competing interests.

Author contributions

Conceptualization: S. Lopez de Armentia, E. Paz
Formal analysis: S. Lopez de Armentia, R. Gimenez, J.C. del Real, B. Serrano, J.C. Cabanelas, E. Paz
Investigation: S. Lopez de Armentia, R. Gimenez, B. Serrano, E. Paz
Methodology: J.C. del Real, J.C. Cabanelas
Writing–original draft: S. Lopez de Armentia, E. Paz
Writing–review & editing: R. Gimenez, J.C. del Real, B. Serrano, J.C. Cabanelas

Ethics approval and consent to participate

Not applicable.

Consent for publication

Not applicable.

Availability of data

Data are available from the corresponding author upon reasonable request.

References

1. Pazhamannil RV, Govindan P. Current state and future scope of additive manufacturing technologies via vat photopolymerization. *Mater Today Proc*. 2021;43:130-136. doi: 10.1016/j.matpr.2020.11.225
2. Alifui-Segbaya F. Biomedical photopolymers in 3D printing. *RPJ*. 2019;26:437-444. doi: 10.1108/RPJ-10-2018-0268
3. Melchels FPW, Feijen J, Grijpma DW. A review on stereolithography and its applications in biomedical engineering. *Biomaterials*. 2010;31:6121-6130. doi: 10.1016/j.biomaterials.2010.04.050
4. Al Rashid A, Ahmed W, Khalid MY, Koç M. Vat photopolymerization of polymers and polymer composites: processes and applications. *Addit Manuf*. 2021; 47:102279. doi: 10.1016/j.addma.2021.102279
5. Shebeeb CM, Afif MB, Jacob L, Choi D, Butt H. Vat photopolymerisation 3D printing of graphene-based materials. *Virt Phys Prototyping*. 2013;18:e2276250. doi: 10.1080/17452759.2023.2276250
6. Al Rashid A, Khan SA, Al-Ghamdi SG, Koç M. Additive manufacturing of polymer nanocomposites: needs and challenges in materials, processes, and applications. *J Mater Res Technol*. 2021;14:910-941. doi: 10.1016/j.jmrt.2021.07.016
7. Alsaadi M, Hinchy EP, McCarthy CT, Moritz VF, Portela A, Devine DM. 3D printing of photocurable resin reinforced by functionalised graphene nanoplatelets. *Mater Proc*. 2023;14:20. doi: 10.3390/IOCN2023-14540
8. Paz E, Forriol F, del Real JC, Dunne N. Graphene oxide versus graphene for optimisation of PMMA bone cement for orthopaedic applications. *Mater Sci Eng C*. 2017;77:1003-1011. doi: 10.1016/j.msec.2017.03.269
9. He S, Petkovich ND, Liu K, Qian Y, Macosko CW, Stein A. Unsaturated polyester resin toughening with very low loadings of GO derivatives. *Polymer*. 2017;110:149-157. doi: 10.1016/j.polymer.2016.12.057
10. Zhang G, Song D, Jiang J, et al. Electrically assisted continuous vat photopolymerization 3D printing for fabricating high-performance ordered graphene/polymer composites. *Compos B Eng*. 2023;250:110449. doi: 10.1016/j.compositesb.2022.110449
11. Liang A, Jiang X, Hong X, Jiang Y, Shao Z, Zhu D. Recent developments concerning the dispersion methods and mechanisms of graphene. *Coatings*. 2018;8:33. doi: 10.3390/coatings8010033
12. Markandan K, Lai CQ. Enhanced mechanical properties of 3D printed graphene-polymer composite lattices at very low graphene concentrations. *Compos A: Appl Sci Manuf*. 2020;129:105726. doi: 10.1016/j.compositesa.2019.105726
13. de Armentia SL, Fernández-Villamarín S, Ballesteros Y, Del Real JC, Dunne N, Paz E. 3D printing of a graphene-modified photopolymer using stereolithography for biomedical applications: a study of the polymerization reaction. *Int J Bioprint*. 2022;8:503. doi: 10.18063/ijb.v8i1.503
14. Holt BD, Wright ZM, Arnold AM, Sydlik SA. Graphene oxide as a scaffold for bone regeneration. *WIREs Nanomed Nanobiotechnol*. 2017;9:e1437. doi: 10.1002/wnan.1437
15. Salgado H, Fialho J, Marques M, Vaz M, Figueiral MH, Mesquita P. Mechanical and surface properties of a 3D-printed dental resin reinforced with graphene. *J Rpemd*. 2023;64:12-19. doi: 10.24873/j.rpemd.2023.03.1050
16. Hanon MM, Ghaly A, Zsidai L, Szakál Z, Szabó I, Kátai L. Investigations of the mechanical properties of DLP 3D printed graphene/resin composites. *Acta Polytech Hung*. 2021;18(8):143-161. doi: 10.12700/APH.18.8.2021.8.8
17. Lopez De Armentia S, Abenojar J, Ballesteros Y, Del Real JC, Dunne N, Paz E. Polymerization kinetics of acrylic photopolymer loaded with graphene-based nanomaterials for additive manufacturing. *Nanomaterials*. 2022;12:4498. doi: 10.3390/nano12244498
18. Mendes-Felipe C, Patrocinio D, Laza JM, Ruiz-Rubio L, Vilas-Vilela JL. Evaluation of postcuring process on the thermal and mechanical properties of the Clear02™ resin used in stereolithography. *Polymer Test*. 2018;72:115-121. doi: 10.1016/j.polymertesting.2018.10.018
19. Cingesar IK, Marković M-P, Vrsaljko D. Effect of post-processing conditions on polyacrylate materials used in stereolithography. *Addit Manuf*. 2022;55:102813. doi: 10.1016/j.addma.2022.102813
20. Markandan K, Seetoh IP, Lai CQ. Mechanical anisotropy of graphene nanocomposites induced by graphene alignment during stereolithography 3D printing. *J Mater Res*. 2021;36:4262-4274. doi: 10.1557/s43578-021-00400-5

21. Lai CQ, Markandan K, Luo B, Lam YC, Chung WC, Chidambaram A. Viscoelastic and high strain rate response of anisotropic graphene-polymer nanocomposites fabricated with stereolithographic 3D printing. *Addit Manuf*. 2021;37:101721.
doi: 10.1016/j.addma.2020.101721

22. Jančovičová V, Mikula M, Havlínová B, Jakubíková Z. Influence of UV-curing conditions on polymerization kinetics and gloss of urethane acrylate coatings. *Prog Organic Coat*. 2013;76:432-438.
doi: 10.1016/j.porgcoat.2012.10.010

23. Arias-Ferreiro G, Ares-Pernas A, Lasagabáster-Latorre A, et al. Printability study of a conductive polyaniline/acrylic formulation for 3D printing. *Polymers*. 2021;13:2068.
doi: 10.3390/polym13132068

24. ISO 527-2:2012. Plastics – Determination of Tensile Properties – Part 2: Test Conditions for Moulding and Extrusion Plastics.

25. Quantifying Polymer Crosslinking Density Using Rheology and DMA – TA Instruments. Available at: https://www.tainstruments.com/applications-notes/quantifying-polymer-crosslinking-density-using-rheology-and-dma/ (accessed March 26, 2024).

26. Zheng J, Png ZM, Ng SH, et al. Vitrimers: Current research trends and their emerging applications. *Mater Today*. 2021;51:586-625.
doi: 10.1016/j.mattod.2021.07.003

27. Ryu SH, Sin JH, Shanmugharaj AM. Study on the effect of hexamethylene diamine functionalized graphene oxide on the curing kinetics of epoxy nanocomposites. *Eur Polymer J*. 2014;52:88-97.
doi: 10.1016/j.eurpolymj.2013.12.014

28. Berlanga Duarte ML, Reyna Medina LA, Torres Reyes P, Esparza González SC, Herrera González AM. Dental restorative composites containing methacrylic spiroorthocarbonate monomers as antishrinking matrixes. *J Appl Polym Sci*. 2019;136:47114.
doi: 10.1002/app.47114

29. Alifui-Segbaya F, Bowman J, White AR, George R, Fidan I. Characterization of the double bond conversion of acrylic resins for 3D printing of dental prostheses. *Compend Contin Educ Dent*. 2019;40:e7-e11.

30. Ahmadi-Moghadam B, Sharafimasooleh M, Shadlou S, Taheri F. Effect of functionalization of graphene nanoplatelets on the mechanical response of graphene/epoxy composites. *Mater Design (1980-2015)*. 2015;66:142-149.
doi: 10.1016/j.matdes.2014.10.047

31. Hawkins DA, Haque A. Fracture toughness of carbon-graphene/epoxy hybrid nanocomposites. *Procedia Eng*. 2014;90:176-181.
doi: 10.1016/j.proeng.2014.11.833

32. Guo W, Yang Y, Liu C, et al. 3D printed TPMS structural PLA/GO scaffold: process parameter optimization, porous structure, mechanical and biological properties. *J Mech Behav Biomed Mater*. 2023;142:105848.
doi: 10.1016/j.jmbbm.2023.105848

33. Sharma A, Pan X, Bjuggren JM, et al. Probing the relationship between molecular structures, thermal transitions, and morphology in polymer semiconductors using a woven glass-mesh-based DMTA technique. *Chem Mater*. 2019;31:6740-6749.
doi: 10.1021/acs.chemmater.9b01213

34. Jiménez-Suárez A, Moriche R, Prolongo SG, Sánchez M, Ureña A. GNPs reinforced epoxy nanocomposites used as thermal interface materials. *JNanoR*. 2016;38:18-25.
doi: 10.4028/www.scientific.net/JNanoR.38.18

35. Putz KW, Palmeri MJ, Cohn RB, Andrews R, Brinson LC. Effect of cross-link density on interphase creation in polymer nanocomposites. *Macromolecules*. 2008;41:6752-6756.
doi: 10.1021/ma800830p

36. Vilas JL, Laza JM, Garay MT, Rodríguez M, León LM. Unsaturated polyester resins cure: kinetic, rheologic, and mechanical dynamical analysis. II. The glass transition in the mechanical dynamical spectrum of polyester networks. *J Polym Sci B: Polym Phys*. 2001;39:146-152.
doi: 10.1002/1099-0488(20010101)39:1<146::AID-POLB130>3.0.CO;2-A

37. La LBT, Nguyen H, Tran LC, et al. Exfoliation and dispersion of graphene nanoplatelets for epoxy nanocomposites. *Adv Nanocompos*. 2024;1:39-51.
doi: 10.1016/j.adna.2023.10.001

38. Tang L-C, Wan Y-J, Yan D, et al. The effect of graphene dispersion on the mechanical properties of graphene/epoxy composites. *Carbon*. 2013;60:16-27.
doi: 10.1016/j.carbon.2013.03.050

39. Paz E, Ballesteros Y, Abenojar J, Dunne N, del Real JC. Advanced G-MPS-PMMA bone cements: influence of graphene silanisation on fatigue performance, thermal properties and biocompatibility. *Nanomaterials*. 2021;11:139.
doi: 10.3390/nano11010139

40. Hu K, Kulkarni DD, Choi I, Tsukruk VV. Graphene-polymer nanocomposites for structural and functional applications. *Prog Polym Sci*. 2014;39:1934-1972.
doi: 10.1016/j.progpolymsci.2014.03.001

41. Surnova A, Balkaev D, Musin D, Amirov R, Dimiev AM. Fully exfoliated graphene oxide accelerates epoxy resin curing, and results in dramatic improvement of the polymer mechanical properties. *Compos B: Eng*. 2019;162:685-691.
doi: 10.1016/j.compositesb.2019.01.020

42. Nielsen LE. Cross-linking–effect on physical properties of polymers. *J Macromol Sci C*. 1969;3:69-103.
doi: 10.1080/15583726908545897

43. Shokuhfar A, Arab B. The effect of cross linking density on the mechanical properties and structure of the epoxy polymers: molecular dynamics simulation. *J Mol Model*. 2013;19:3719-3731.
doi: 10.1007/s00894-013-1906-9

44. Gao C, Liu T, Shuai C, Peng S. Enhancement mechanisms of graphene in nano-58S bioactive glass scaffold: mechanical and biological performance. *Sci Rep*. 2014; 4:4712.
doi: 10.1038/srep04712

45. Sharif M, Pourabbas B, Sangermano M, et al. The effect of graphene oxide on UV curing kinetics and properties of SU8 nanocomposites. *Polym Int*. 2017;66: 405-417.
doi: 10.1002/pi.5271

46. Moriche R, Artigas J, Reigosa L, Sánchez M, Prolongo SG, Ureña A. Modifications induced in photocuring of Bis-GMA/TEGDMA by the addition of graphene nanoplatelets for 3D printable electrically conductive nanocomposites. *Compos Sci Technol*. 2019;184:107876.
doi: 10.1016/j.compscitech.2019.107876

47. Wan Y-J, Tang L-C, Yan D, et al. Improved dispersion and interface in the graphene/epoxy composites via a facile surfactant-assisted process. *Compos Sci Technol*. 2013;82:60-68.
doi: 10.1016/j.compscitech.2013.04.009

48. Borella PS, Alvares LAS, Ribeiro MTH, et al. Das neves, physical and mechanical properties of four 3D-printed resins at two different thick layers: an in vitro comparative study. *Dental Mater*. 2023;39:686-692.
doi: 10.1016/j.dental.2023.06.002

49. Uysal E, Çakir M, Ekici B. Graphene oxide/epoxy acrylate nanocomposite production via SLA and importance of graphene oxide surface modification for mechanical properties. *Rapid Prototyping J*. 2021;27:682-691.
doi: 10.1108/RPJ-06-2020-0114

50. Alexopoulos ND, Paragkamian Z, Poulin P, Kourkoulis SK. Fracture related mechanical properties of low and high graphene reinforcement of epoxy nanocomposites. *Compos Sci Technol*. 2017;150:194-204.
doi: 10.1016/j.compscitech.2017.07.030

ACCSCIENCE PUBLISHING

International Journal of Bioprinting

RESEARCH ARTICLE

Application of 3D-printed individualized porous tantalum buttress in shelf acetabuloplasty for developmental dysplasia of the hip

Yang Peng[1,2,3†], Xin Chen[1,2,3†], Juncai Xu[1,2,3], Ran Xiong[1,2,3], Chengjun Huang[1,2,3], Liu Yang[1,2,3*], and Guangxing Chen[1,2,3*]

[1]Center for Joint Surgery, The First Hospital Affiliated to Army Medical University, Chongqing, China

[2]Chongqing Municipal Science and Technology Bureau Key Laboratory of Precision Medicine in Joint Surgery, Chongqing, China

[3]Chongqing Municipal Education Commission Key Laboratory of Joint Biology, Chongqing, China

(This article belongs to the Special Issue: *Novel Materials and Processing for Medical 3D Printing and Bioprinting-Series 2*)

Abstract

Shelf acetabuloplasty is a viable treatment for developmental dysplasia of the hip (DDH), yet autologous bone grafts have faced challenges such as morphological mismatch, imprecise placement, and long-term graft resorption. The rapid advancement of 3D printing technology in orthopedics has enabled the acquisition of digital image correlation method (DICM) data from patient pelvic to bilateral femoral proximal regions through computed tomography (CT) scans. These data are then utilized by software to create 3D models and design individualized metal implants. Using tantalum-based type I (TA1) spherical powder as the raw material, a porous tantalum buttress with a pore size of 600 microns and a porosity of 75% was fabricated employing the selective electron beam melting (SEBM) technology. Our Center has applied this 3D-printed individualized porous tantalum buttress in shelf acetabuloplasty for 21 DDH patients (25 hips), including 6 males and 15 females, with a mean age of 21.38 ± 7.39 years. The follow-up period ranged from 12 to 47 months, averaging 22.64 ± 10.86 months. At the final follow-up, patient-reported outcomes (PROs) were used to assess the patient's subjective feelings. Significant improvements were observed in the Non-Arthritic Hip Score (NAHS), modified Harris Hip Score (mHHS), Hip Outcome Score-Sports Subscale (HOS-SSS), International Hip Outcome Tool-12 (iHOT-12), and Visual Analog Scale (VAS) compared with preoperative levels ($p < 0.01$). Radiographic assessments indicated that the postoperative lateral center-edge (LCE) angle, Tonnis angle, acetabular angle (Sharp's angle), and femoral head coverage all trended towards normal, with statistically significant differences ($p < 0.01$). There was no implant displacement or bone resorption in any case, and no progression in Tonnis grading for hip osteoarthritis (OA) was noted postoperatively, with an 84% patient satisfaction rate. The early follow-up results of 3D-printed individualized porous tantalum buttress in shelf acetabuloplasty are satisfactory, indicating a reliable application prospect for the treatment of DDH patients.

Keywords: 3D printing; Metal materials; Augmentation buttress; Hip; Shelf acetabuloplasty

†These authors contributed equally to this work.

***Corresponding authors:**
Liu Yang
(yangliu@tmmu.edu.cn)

Guangxing Chen
(cgx7676@tmmu.edu.cn)

Citation: Peng Y, Chen X, Xu J, et al. Application of 3D-printed individualized porous tantalum buttress in shelf acetabuloplasty for developmental dysplasia of the hip. *Int J Bioprint*. 2024;10(6):4074. doi: 10.36922/ijb.4074

Received: June 28, 2024
Revised: August 8, 2024
Accepted: August 19, 2024
Published Online: August 20, 2024

Copyright: © 2024 Author(s). This is an Open Access article distributed under the terms of the Creative Commons Attribution License, permitting distribution, and reproduction in any medium, provided the original work is properly cited.

Publisher's Note: AccScience Publishing remains neutral with regard to jurisdictional claims in published maps and institutional affiliations.

1. Introduction

Developmental dysplasia of the hip (DDH) includes a wide variety of hip joint abnormalities, characterized by incomplete acetabulum coverage of the femoral head. This often leads to excessive concentration of stress on the articular cartilage and labrum, resulting in damage to cartilage and labral structures, and eventually osteoarthritis (OA).[1] Therefore, addressing the pathological changes of hip dysplasia involves increasing the coverage area of the acetabulum to the femoral head and restoring the concentricity of the hip joint, which can effectively prevent cartilage and labrum damage and slow OA progression.

For adolescent and adult patients with DDH, various surgical techniques have been introduced to increase acetabular coverage of the femoral head, including periacetabular osteotomy (PAO) and shelf acetabuloplasty. PAO is time-consuming, highly invasive, and carries a high risk of injury to critical blood vessels and nerves; postoperative issues, such as unstable reduction and late-onset nonunion, are common complications.[2] In contrast, shelf acetabuloplasty is a simple and less invasive procedure that does not worsen the natural progression of OA and has a much lower risk of serious complications than PAO. However, despite its widespread clinical application, shelf acetabuloplasty still presents several technical limitations.

In this study, we utilized cutting-edge advancements in 3D printing technology and the promising properties of tantalum as an ideal bone substitute material. Individualized porous tantalum implants were designed and manufactured using 3D preoperative planning with a precise fit and optimal positioning, making them a viable alternative to traditional bone grafts in shelf acetabuloplasty. This approach aims to address the challenges associated with conventional bone implants, such as difficult implantation, potential positional deviation, inadequate coverage, and possible long-term resorption of the graft.[3] Moreover, tantalum's porous structure, adequate strength, and elastic modulus provide sustained mechanical support while facilitating healing and the transformation into fibrocartilaginous structures in different tissue regions. This improves the accuracy and efficacy of shelf acetabuloplasty, offering a safer and more effective treatment option for DDH.

2. Materials and methods

2.1. Materials

2.1.1. Tantalum powder

The 3D-printed porous tantalum buttress was fabricated using type I tantalum (Ta1) powder as raw material, sourced from the Northwest Institute for Nonferrous Metal Research in China. The primary element in its chemical composition is Ta, with impurity elements at mass fractions (%): O: 0.030, C: 0.010, N: 0.010, H: 0.0020, Nb: 0.050, Fe: 0.010, Ti: 0.005, W: 0.010, Mo: 0.010, Si: 0.005, and Ni: 0.010. The Ta1 powder is spherical and exhibits the following physical properties: particle size: 45–105 μm, apparent density ≥9.2 g/cm^3, tapped density ≥9.8 g/cm^3, and flowability ≤10 s/50 g.

2.1.2. Patients

Patients with DDH who underwent shelf acetabuloplasty using a 3D-printed porous tantalum buttress in our Center from November 2018 to January 2022 were selected. The inclusion criteria were: (i) diagnosis of symptomatic DDH with a lateral center-edge (LCE) angle <20°; (ii) symptoms lasting for more than 3 months and refractory to conservative treatment; (iii) Crowe type I and II; (iv) Tonnis OA grade 0–1; (v) patients voluntarily chose 3D-printed porous tantalum buttress in shelf acetabuloplasty. The exclusion criteria were: (i) patients with a history of previous hip surgery; (ii) patients with immature bones; (iii) patients with hip joint infection or active infection at other sites; (iv) patients with other serious diseases or intolerance to surgery on systemic evaluation; (v) patients who were allergic to metal implants; and (vi) postoperative follow-up for less than 12 months.

Finally, a total of 21 DDH patients (25 hips, encompassing 18 hips of Crowe type I and 7 hips of Crowe type II) were enrolled, including 6 males and 15 females, aged 13–39 years, with an average age of 21.38 ± 7.39 years. The average body mass index (BMI) was 21.69 ± 4.23 kg/m^2, and the duration of symptoms was 37.56 ± 30.99 months. All patients complained of hip pain after standing for a long time or walking long distances and limited motor functions (e.g., squatting, running, and jumping); three patients had claudication. All patients received conservative treatment for more than 3 months, but their symptoms did not improve, affecting their daily life and work.

This study was approved by the Ethics Committee of our hospital (No. KY201908), and all patients signed the informed consent form.

2.2. Design and fabrication of 3D-printed individualized porous tantalum buttress

2.2.1. Establishment of computer-aided design models for DDH

Bilateral hip joints were scanned using the SOMATOM Definition CT scanning equipment (SIEMENS, Germany), with slice thickness and spacing set at 1.0 mm. The scanning range included the entire pelvis and the proximal 15 cm of both femurs, with a resolution of 512 × 512 pixels. The 2D

computed tomography (CT) images were converted into digital image correlation method (DICM) format using INFINITT software (Infinitt, China). Patient CT data were imported into Mimics Research 19.0 software (Materialise, Belgium). Threshold-based and dynamic segmentations were conducted to extract masks for the pelvis, sacrum, and proximal ends of both femurs, converting them into 3D models. These models were then exported in STL format and reverse-engineered using Geomagic Studio software (Geomagic, United States of America [USA]) to generate STP format data. Deviation analysis was performed on the STP data before and after reverse engineering to provide foundational digital models and design references for the structural design of components for patients with DDH.

2.2.2. Design of the 3D-printed porous tantalum buttress

The STP file was imported into UG software (Unigraphics NX, USA), establishing a coordinate system in a normal standing position, and adjusting the 3D spatial position of the pelvis to ensure it was fully placed in a neutral position. The design of the porous tantalum buttress followed these principles:

(i) The bone healing surface of the tantalum buttress matched the anatomical morphology of the outer table of the pelvis and the outer rim of the acetabulum with high precision. The curvature of the bottom surface (capsular healing surface) paralleled the spherical surface of the femoral head, achieving concentric support.

(ii) After implantation, the LCE angle should be within the range of 30–35° and the anterior center-edge (ACE) angle within 25–30°.

(iii) The tantalum buttress must completely cover the lateral superior defect area of DDH, including the area from the anterior 3 o'clock position to the posterior 9 o'clock, ensuring that the non-coverage area of the femoral head in anteroposterior view was approximately 1/5 of the diameter of the femoral head.

(iv) Three screw holes with a diameter of 5.0 mm were designed on the tantalum buttress, capable of accommodating three screws for double-row fixation (Figure 1).

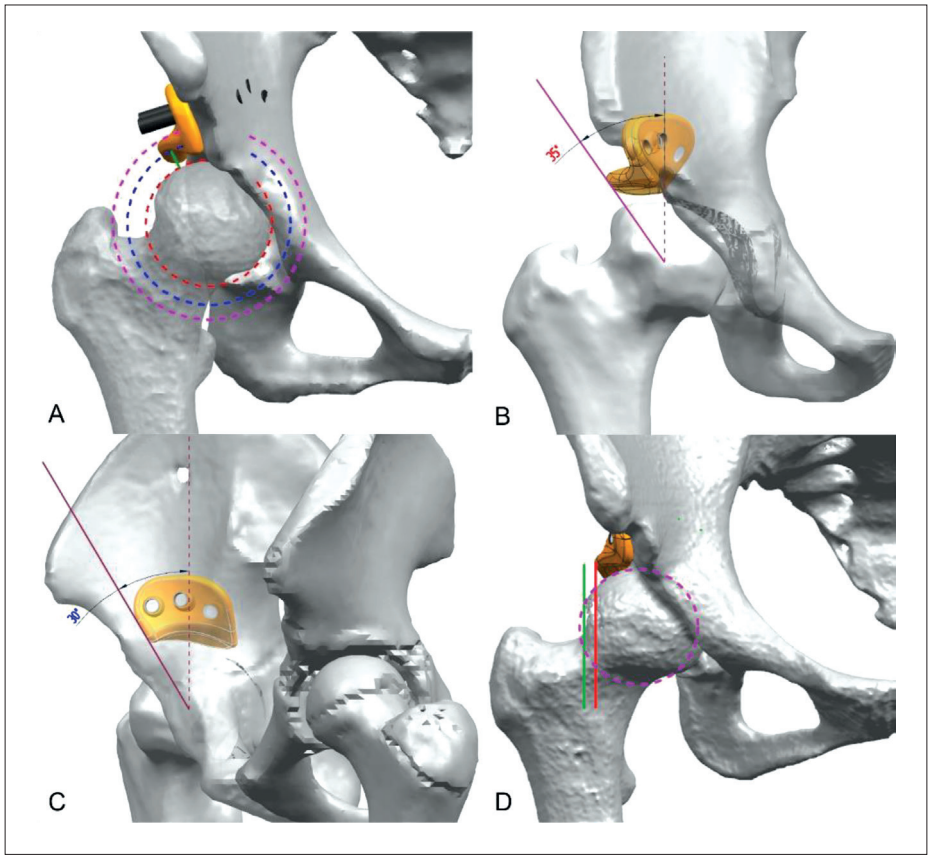

Figure 1. Design of the 3D-printed porous tantalum buttress. (A) The curvature of the bottom surface of the buttress parallels the spherical surface of the femoral head, achieving concentric support. (B) The lateral center-edge (LCE) angle is designed to be 35°. (C) The anterior center-edge (ACE) angle is designed to be 30°. (D) The non-coverage area of the femoral head is approximately 1/5 of its diameter.

The porous structure of the tantalum buttress was designed using 3-matic software (Materialise, Belgium), utilizing a rhombic dodecahedron as the basic unit structure, with a filament diameter of 0.35 mm, pore size of 600 μm, and porosity of 75%. Finally, three sizes of porous tantalum buttresses at 95%, 100%, and 105% were designed, and the STL format data were exported for 3D printing and subsequent application (Figure 2A).

2.2.3. Precision verification of the 3D-printed porous tantalum buttress

Based on STL format data, 3D-printed life-size models of the acetabulum, acetabular buttress, and femoral head were fabricated using polylactic acid (PLA). After assembling these components, a surgical simulation was conducted to verify the fit between each component and the coverage of the femoral head by the acetabulum. If the verification results were unsatisfactory, the design was refined, and surgical simulation was re-conducted until the fit was ideal.

2.2.4. Finite element analysis of 3D-printed porous tantalum buttress

The STP files of the generated and assembled acetabular model, femoral head model, buttress model, as well as screw models, were imported into ANSYS Workbench software (R19.0, ANSYS, USA). Material properties, contact settings, meshing, and boundary conditions were defined for all models. The parameters of elastic modulus and Poisson's ratio of each component material are displayed in Table 1. A mesh element size of 1.5 mm was used for this analysis. Constraint contacts were set between the buttress and screws, screws and bone, and cortical bone and cancellous bone. Frictional contacts with a coefficient of friction of 0.98 were defined between the buttress and cortical bone, and between the buttress and the joint capsule. To simulate the stresses on the hip joint during daily activities, the sacroiliac joints and pubic symphysis were fully fixed and constrained, and a vertical upward force was applied to the distal end of the femoral shaft. According to literature, peak hip joint stresses equivalent to approximately 3–4 times body weight would meet the demands of most daily activities.[4] Taking a patient weighing 75 kg as an example, the finite element simulation loading is set to be 3000 N. After the implantation of the buttress, the stress distribution in the ilium, acetabulum, and proximal femur decreased and became more uniform compared with before surgery. The maximum equivalent

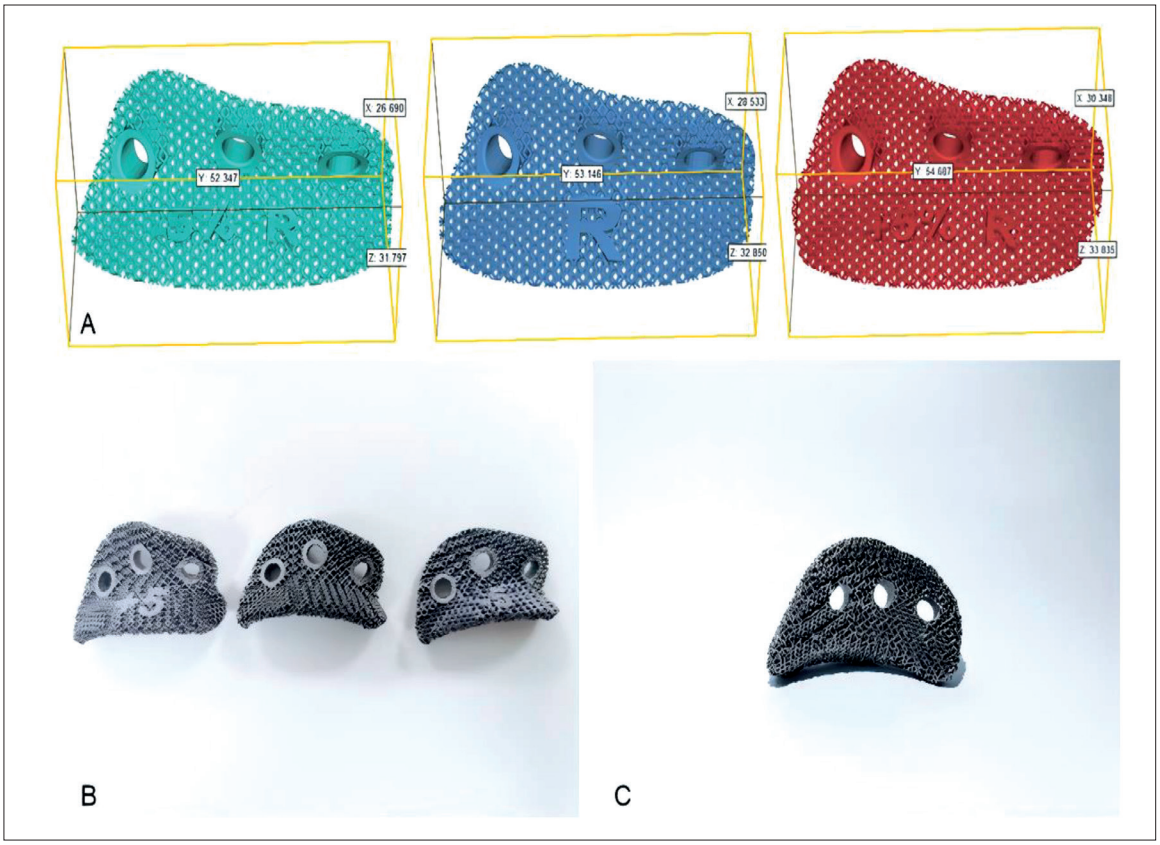

Figure 2. Fabrication of the 3D-printed tantalum buttress. (A) 3D digital files of porous tantalum buttresses in three sizes: 95% (green), 100% (blue), and 105% (red). (B) Appearances of the actual porous tantalum buttresses in the three sizes. (C) Appearance of the ilium contact surface.

Table 1. Modulus of elasticity and Poisson's ratio parameters for each component material

Component	Material	Modulus of elasticity (GPa)	Poisson's ratio
Buttress	Tantalum (porous)	4	0.35
	Tantalum (solid)	186	0.35
Cancellous bone	Cancellous bone	8	0.2
Cortical bone	Cortical bone	8	0.29
Screws	Titanium alloy	110	0.30
Joint capsule	Joint capsule	0.0105	0.45

stress in both the buttress and screws was lower than the corresponding yield strengths of their materials. Finite element mechanical analysis confirmed that the material had sufficient load-bearing capacity during use (Figure 3).

2.2.5. Fabrication of 3D-printed porous tantalum buttress

The 3D printing data of the buttress was imported into the Sailong Y150 powder bed electron beam equipment (Xi'an Sailong, China). In a vacuum environment, the baseplate was evenly preheated. The powder spreading device evenly laid down and preheated a layer of tantalum powder on the baseplate to over 600°C using an electron beam, causing sintering between the powders and ensuring the stability of the powder bed. This device's electron beam had a maximum power of 3000 W, capable of melting tantalum metal at 2996°C for shaping. The slicing software selectively melted the tantalum powder based on the characteristics of the buttress data, while the unmelted powder in other areas descended with the build chamber. The powder-spreading device then laid down a new layer of powder, initiating work on the next layer. Through layer-by-layer printing and stacking, the porous tantalum buttress was printed. This 3D-printed porous tantalum buttress was then slowly cooled to room temperature in a vacuum environment before being removed from the chamber. Compressed air and the impact of same-metal powder particles were used to remove any unmelted tantalum powder from the surface and interior of the porous tantalum buttress. Thereafter, using pure water as a medium, the porous tantalum buttress was placed in an ultrasonic cleaner for multiple rounds of oscillation cleaning. After drying, the porous tantalum buttress was fabricated (Figure 2B and C).

2.3. Surgical techniques

All surgeries were performed by the same senior associate chief surgeon specializing in joint surgery. Under combined spinal-epidural anesthesia, patients were positioned on their healthy side. A surgical dislocation approach was employed to minimize the impact on the blood supply of the hip joint. A skin incision approximately 10 cm long was made, sequentially cutting through the skin, subcutaneous tissue, and superficial and deep fascia. An oblique lateral osteotomy was performed from proximal to distal along the lateral posterior side of the top of the gluteus medius insertion on the greater trochanter. After the surgical dislocation of the hip, the greater trochanter, to which the gluteus medius and vastus lateralis muscles were attached, was pushed anteriorly. The gluteus minimus was completely stripped off the capsule surface at the 12 o'clock position of the acetabulum, both anteriorly and posteriorly, fully exposing the joint capsule, the outer rim of the acetabulum, and the outer table of the ilium 4 cm above the acetabulum rim between the 9 o'clock and 3 o'clock positions of the acetabulum. The cortical bone in this area was ground using a burr to achieve pinpoint bleeding. According to the preoperative design, the front side of the buttress reached the 3 o'clock position, the rear side extended to the 9 o'clock position, the medial side snugly adhered to the bone surface, and the bottom side closely contacted the capsule. The friction interface between the buttress and the femoral head was a capsulolabral complex and not in direct contact with the cartilage of the femoral head (Figure 4). Three 4.5-mm cortical screws were inserted along the planned screw holes and screw paths to fix the implant. The gluteus minimus was sutured *in situ*, the greater trochanter was relocated, and two double-headed compression screws were used to fix the greater trochanter in its original position. After repeated irrigation with saline, a drain was placed, and the incision was closed layer by layer.

2.4. Postoperative rehabilitation

Immediately upon recovery from anesthesia, ankle pump exercises and static contractions of the quadriceps for the affected limb were initiated; straight leg raises were conducted on the first postoperative day to strengthen the iliopsoas and lower limb muscles. Within 6 weeks post-surgery, partial weight-bearing activities on the affected limb could be conducted with the aid of crutches. By the seventh week post-surgery, the affected limb could bear full weight while walking, and strengthening exercises for the hip abductor muscles were intensified.

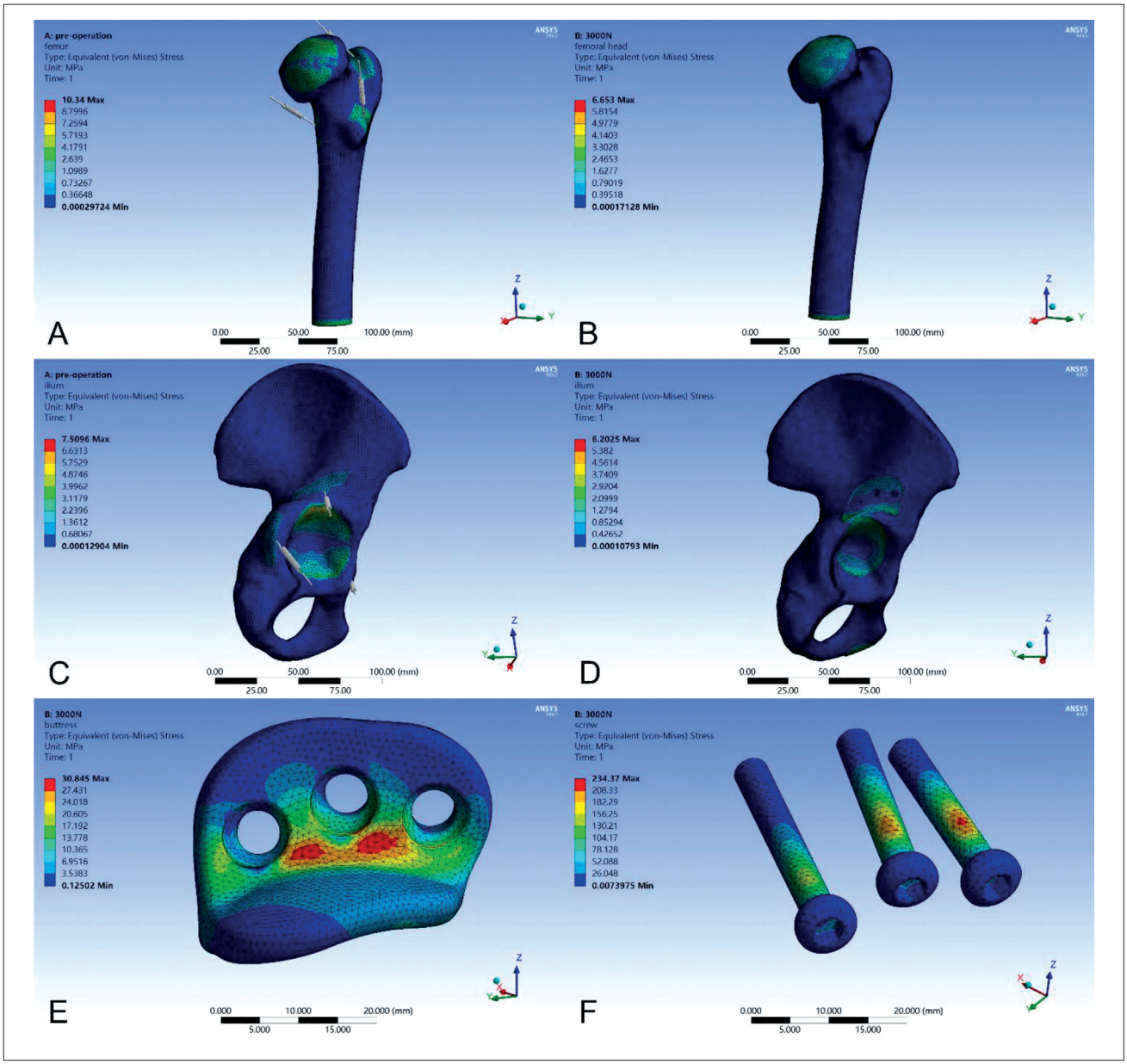

Figure 3. Finite element analysis of 3D-printed porous tantalum buttress. (A) Stress distribution of the proximal femur before buttress implantation. (B) Stress distribution of the proximal femur after buttress implantation. (C) Stress distribution of the acetabulum and ilium before buttress implantation. (D) Stress distribution of the acetabulum and ilium after buttress implantation. (E) Stress distribution after buttress implantation. (F) Stress distribution of the screws after buttress implantation.

2.5. Follow-ups and efficacy evaluation

2.5.1. Intraoperative data and follow-ups

The duration of the surgery, the amount of intraoperative bleeding, and any occurrences of complications were recorded. On the first postoperative day, a pelvic radiograph was taken to observe the position of the porous tantalum buttress and its fit with the acetabulum and femoral head. Patients were followed in the outpatient clinic at week 6, months 3, 6, and 12, and annually thereafter.

2.5.2. Subjective evaluation indicators

Patient-reported outcomes (PROs) were used to assess the patient's subjective feelings. Preoperative and final follow-up scores, such as the Non-Arthritic Hip Score (NAHS), the modified Harris Hip Score (mHHS), the Hip Outcome Score-Sports Subscale (HOS-SSS), the International Hip Outcome Tool-12 (iHOT-12), and the Visual Analog Scale (VAS) for pain were recorded. The patient's satisfaction score at the final follow-up (on a scale of 0–10) was documented, where 0–2 indicated very unsatisfied, 3–4

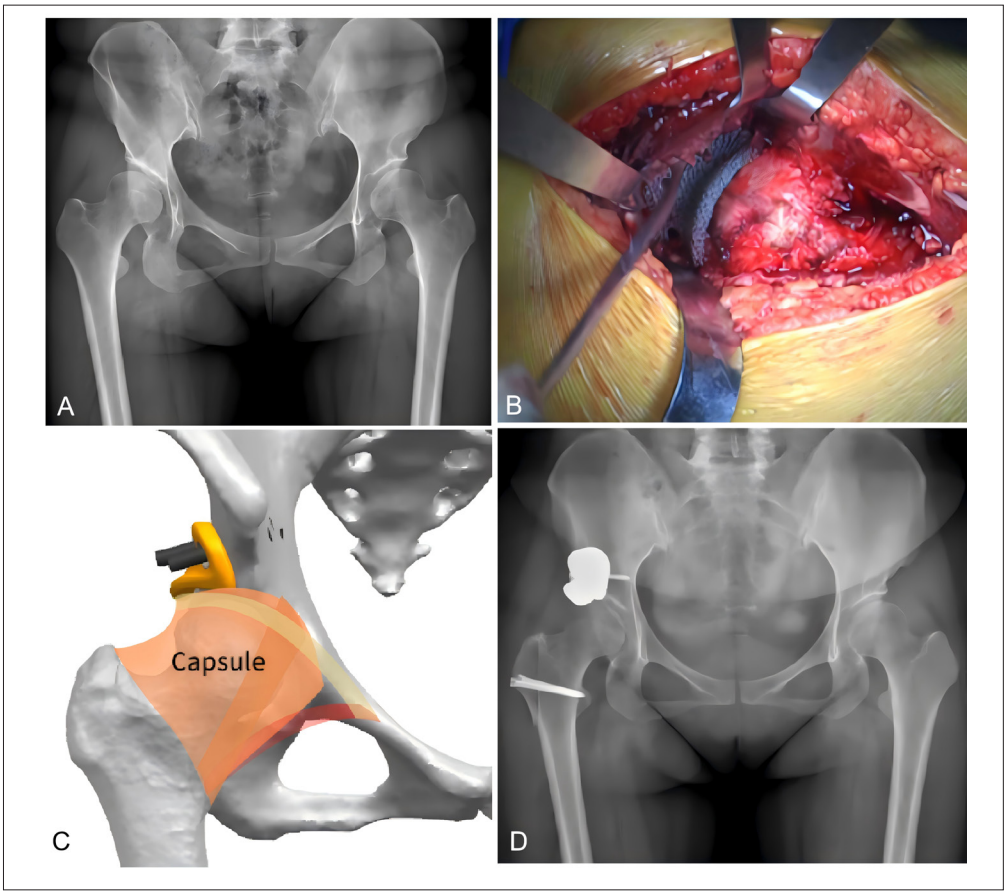

Figure 4. Surgical procedure and images. (A) Preoperative pelvic radiograph. (B) Implant placement outside the joint capsule. (C) Schematic illustration of the position of the buttress and the joint capsule. (D) Postoperative radiograph after implantation.

unsatisfied, 5–6 neutral, 7–8 satisfied, and 9–10 very satisfied. The satisfaction rate was calculated as:

$$\text{Satisfaction rate} = \frac{(\text{number of satisfied} + \text{number of very satisfied})}{\text{total number of cases}} \times 100\% \quad \text{(I)}$$

2.5.3. Objective evaluation indicators

Objective evaluation of the surgical outcome was conducted through radiographic measurements and observations. The LCE angle, Tonnis angle, Sharp's angle, and femoral head coverage at preoperative and the final follow-up were recorded (Figure 5).

2.5.4. Postoperative stability of the porous tantalum buttress and progression of hip osteoarthritis

At the final follow-up, imaging assessments were conducted to evaluate bone ingrowth into the buttress, checking for any lucency lines between the buttress and the ilium; radiological indicators, such as the LCE angle, Tonnis angle, and Sharp's angle at the immediate postoperative and the final follow-up, were also compared to determine if there had been any displacement, loosening, or screw fracture of the buttress. The progression of hip OA was assessed using the Tonnis grading system.

2.5.5. Correlation analysis between the placement of the porous tantalum buttress and clinical efficacy

The immediate postoperative pelvic radiographs were used to match the preoperative 3D model design in UG software to determine whether there were any displacements of high–low, forward–backward, and pronation–supination between the actual implantation and the preoperative design (Figure 6). Displacement parameters in these six directions were then correlated with the NAHS, mHHS, HOS-SSS, iHOT-12, and patient satisfaction scores to analyze whether the displacement deviation is an influencing factor on surgical efficacy.

2.6. Statistical analysis

Statistical analysis was performed using SPSS 20.0 statistical software (SPSS Inc., USA). PROs and radiographic indicators passed the normality tests and were represented

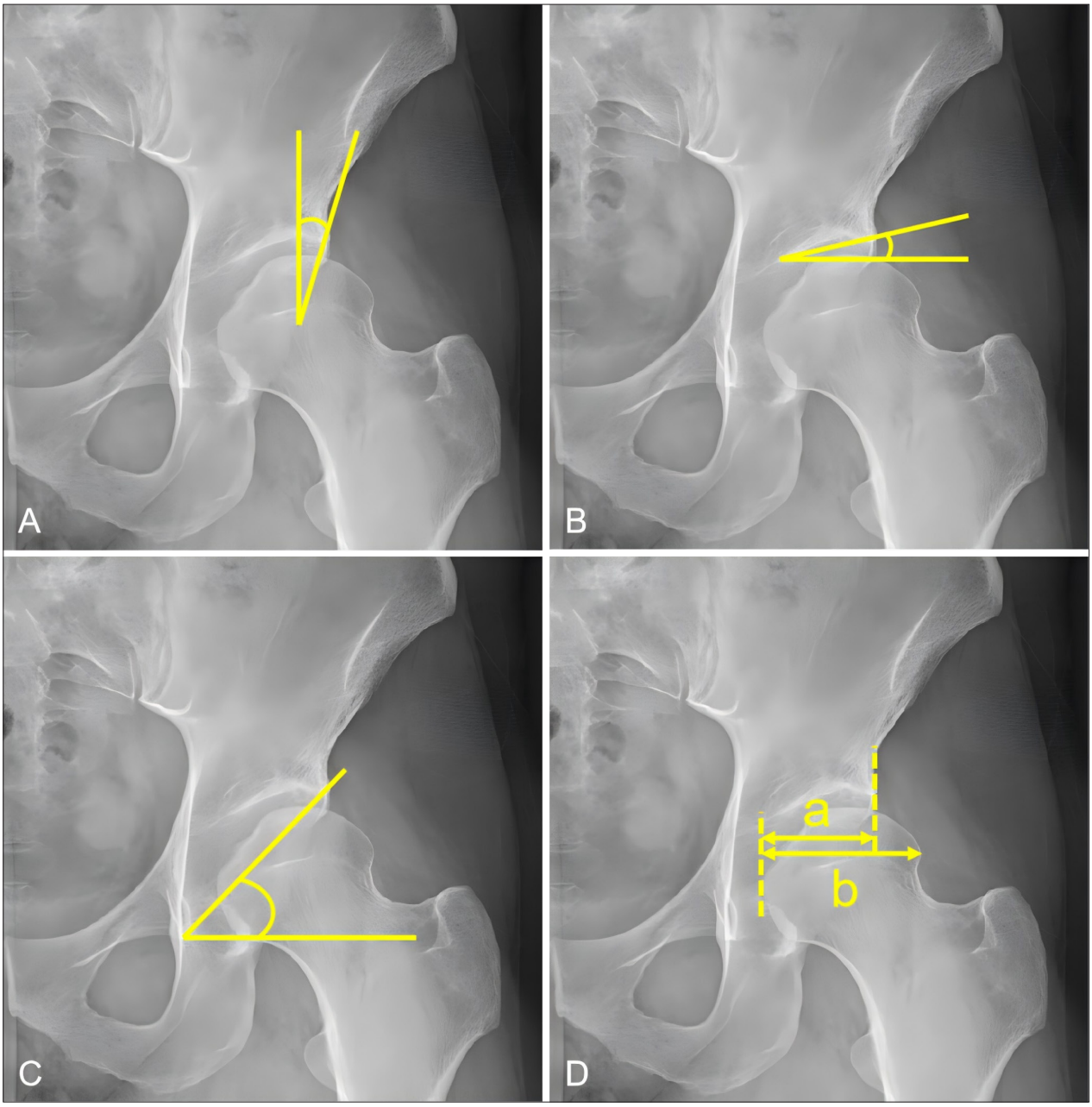

Figure 5. Radiographic indicators. (A) The lateral center-edge (LCE) angle. (B) The Tonnis angle. (C) The Sharp's angle. (D) The coverage of femoral head (a/b).

as mean ± standard deviation. Paired *t*-tests were used for comparisons between pre- and post-surgery data, with a significance level α set at 0.05 (two-tailed). Pearson correlation coefficients were used to analyze correlations between the implantation deviation parameters and NAHS, mHHS, HOS-SSS, iHOT-12, and patient satisfaction scores, respectively, with $p < 0.05$ indicating statistically significant differences.

3. Results

3.1. Perioperative data

All 21 patients (25 hips) underwent successful surgeries without any major vascular or nerve injuries. The surgical time per hip ranged from 1.08 to 2 h, with an average of 1.64 ± 0.27 h; the intraoperative blood loss ranged from 50 to 150 mL, averaging 88.60 ± 25.20 mL. All patients'

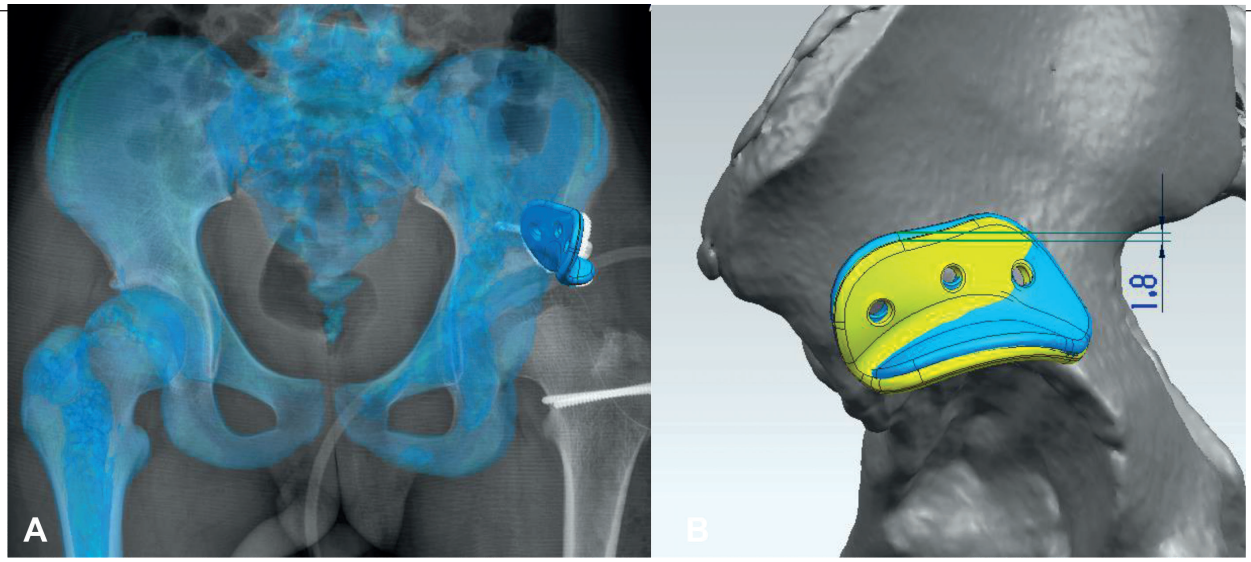

Figure 6. Displacement analysis between the implanted buttress position and the preoperative design. (A) Immediate postoperative pelvic radiograph is taken to match the preoperative designed 3D model. (B) Deviation in the placement of the porous tantalum buttress. Yellow represents the preoperative design position; blue represents the actual implanted position; in this case, the implanted buttress is 1.8 mm higher than the preoperative design.

surgical incisions healed excellently, and no complications, such as infection or thrombosis, occurred.

3.2. Patient-reported outcomes

Patients were followed for 12–47 months, with an average of 22.64 ± 10.86 months. All patients experienced significant relief from hip joint pain, and their hip joint function gradually improved, stabilizing between half a year to a year postoperatively. The preoperative NAHS score was 71.04 ± 12.14 points, significantly increasing to 86.92 ± 5.17 points at the final follow-up ($p < 0.01$); the preoperative mHHS score was 70.56 ± 9.53 points,

Table 2. Comparison of patient-reported outcomes and imaging measurement indicators at the final follow-up with preoperative data

Item	Preoperative	Final follow-up	*t*	*p*
NAHS	71.04 ± 12.14	86.92 ± 5.17	−6.311	<0.01
mHHS	70.56 ± 9.53	87.20 ± 4.06	−8.133	<0.01
HOS-SSS	62.52 ± 13.53	83.84 ± 4.98	−7.49	<0.01
iHOT-12	51.60 ± 14.01	85.32 ± 5.51	−12.519	<0.01
VAS	4.56 ± 0.92	1.08 ± 1.08	12.273	<0.01
LCE angle (°)	7.97 ± 9.48	35.75 ± 5.40	−15.454	<0.01
Sharp's angle (°)	49.85 ± 5.68	41.92 ± 4.45	7.98	<0.01
Tonnis angle (°)	26.83 ± 7.98	16.79 ± 4.89	7.568	<0.01
Femoral coverage (%)	59.59 ± 10.64	95.95 ± 8.68	−19.902	<0.01

Note: Data are presented as mean ± standard deviation. Abbreviations: HOS-SSS, Hip Outcome Score-Sports Subscale; iHOT-12, International Hip Outcome Tool-12; LCE, Lateral center-edge; mHHS, modified Harris Hip Score; NAHS, Non-Arthritic Hip Score; VAS, Visual Analog Scale.

Table 3. Comparison of imaging measurement indicators at the final follow-up with immediate postoperative data

Imaging measurement indicators	Immediate postoperative	Final follow-up	*t*	*p*
LCE angle (°)	36.80 ± 4.51	35.75 ± 5.40	1.14	0.265
Sharp's angle (°)	41.72 ± 4.31	41.92 ± 4.45	−0.541	0.593
Tonnis angle (°)	16.28 ± 4.50	16.79 ± 4.89	−0.879	0.388

Note: Data are presented as the mean ± standard deviation. Abbreviation: LCE, lateral center edge.

Table 4. Correlation analysis between the placement deviation of the porous tantalum buttress and patient-reported outcomes (PROs)

PROs	Statistical metric	Pronation	Supination	High	Low	Forward	Backward
NAHS	*r*	−0.019	−0.273	0.004	−0.042	−0.173	−0.026
	p	0.953	0.366	0.985	0.973	0.572	0.933
mHHS	*r*	−0.034	0.038	−0.15	0.708	−0.007	−0.053
	p	0.917	0.903	0.505	0.499	0.982	0.863
HOS-SSS	*r*	−0.464	−0.181	−0.322	−0.979	−0.01	−0.47
	p	0.129	0.554	0.144	0.13	0.973	0.105
iHOT-12	*r*	−0.667	−0.462	−0.145	−0.856	−0.24	−0.634
	p	0.018*	0.112	0.519	0.347	0.43	0.02*
Patient satisfaction	*r*	−0.58	−0.305	−0.257	−0.829	0.009	−0.554
	p	0.047*	0.312	0.249	0.378	0.976	0.049*

Abbreviations: HOS-SSS, Hip Outcome Score-Sports Subscale; iHOT-12, International Hip Outcome Tool-12; mHHS, modified Harris Hip Score; NAHS, Non-Arthritic Hip score; VAS, Visual Analog scale.
*Denotes statistical significance ($p < 0.05$).

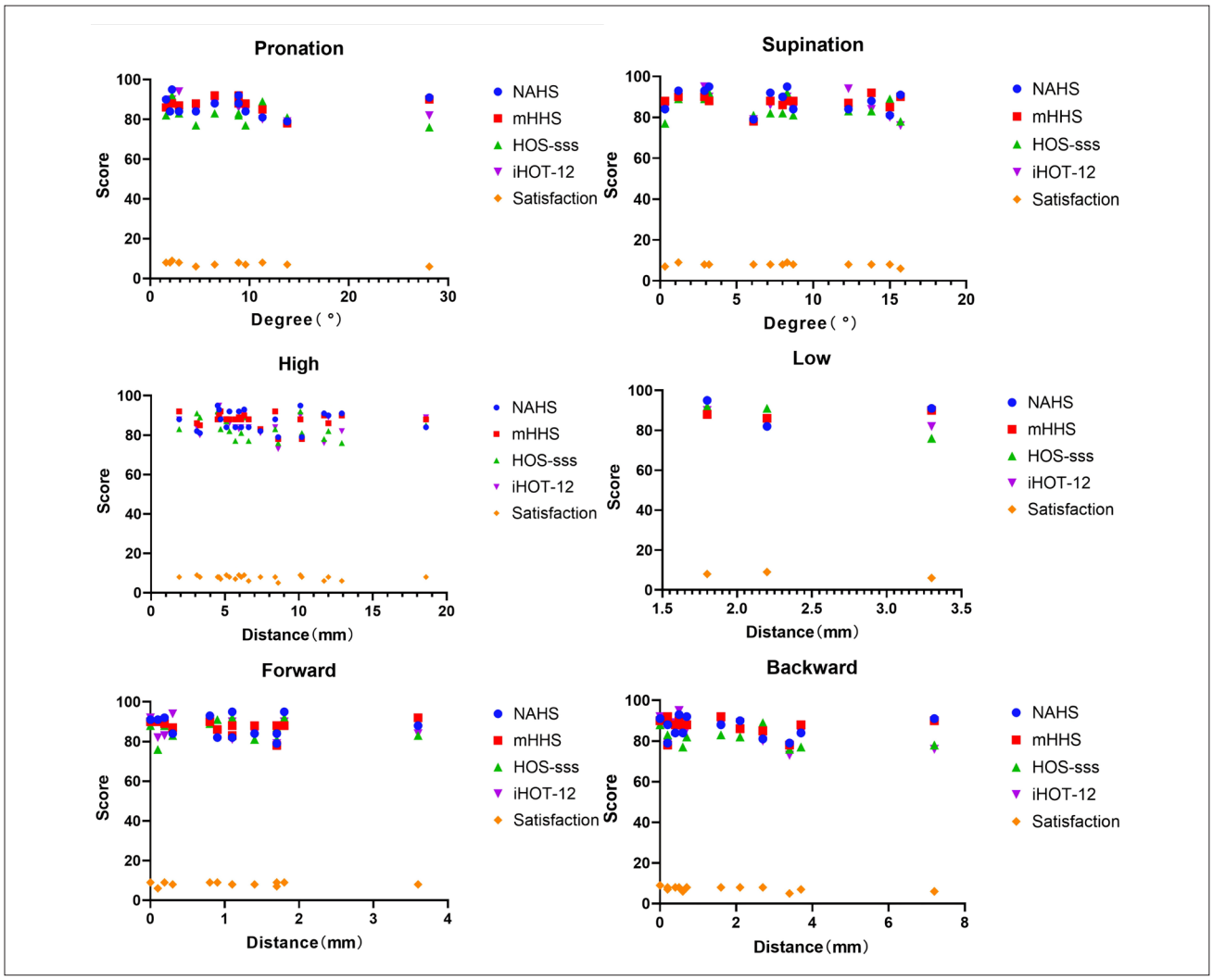

Figure 7. Scatter plot illustrating the correlation between the deviation in placement of the porous tantalum buttress and patient-reported outcomes.

increasing to 87.20 ± 4.06 points at the final follow-up ($p < 0.01$); the preoperative HOS-SSS score was 62.52 ± 13.53 points, increasing to 83.84 ± 4.98 points at the final follow-up ($p < 0.01$); the preoperative iHOT-12 score was 51.60 ± 14.01 points, increasing to 85.32 ± 5.51 points at the final follow-up ($p < 0.01$); the preoperative VAS pain score was 4.56 ± 0.92 points, decreasing to 1.08 ± 1.08 points at the final follow-up ($p < 0.01$) (Table 1). Patient satisfaction scores at the final follow-up: 0–2 points in zero hips, 3–4 points in zero hips, 5–6 points in four hips, 7–8 points in 15 hips, and 9–10 points in six hips, with an overall patient satisfaction rate of 84%.

3.3. Objective evaluation indicators

Preoperatively, the LCE angle was 7.97 ± 9.48°, which significantly increased to 35.75 ± 5.40° at the final follow-up ($p < 0.01$); the preoperative Sharp's angle was 49.85 ± 5.68°, decreasing to 41.92 ± 4.45° at the final follow-up ($p < 0.01$); the preoperative Tonnis angle was 26.83 ± 7.98°, reducing to 16.79 ± 4.89° at the final follow-up ($p < 0.01$); the preoperative femoral head coverage was 59.59 ± 10.64%, increasing to 95.95 ± 8.68% at the final follow-up ($p < 0.01$) (Table 2).

3.4. Evaluation of postoperative stability of the porous tantalum buttress and progression of hip osteoarthritis

At the final follow-up, radiographs indicated satisfactory bone ingrowth into the porous tantalum buttress, with no lucency lines observed between the implant and the ilium. Comparing the radiological indicators between the immediate postoperative image with the ones at the final follow-up, no cases displayed displacement or bone resorption, and the differences were not statistically significant ($p > 0.05$) (Table 3). At the final follow-up, the Tonnis grade of hip OA did not progress compared with the preoperative state for all cases.

3.5 Correlation analysis results between the placement of the porous tantalum buttress and PROs

The placement of the porous tantalum buttress was analyzed for displacement in six directions: high–low, forward–backward, and pronation–supination. Pronation displayed a moderate negative correlation with the iHOT-12 score ($r = -0.67$, $p = 0.018$), and a moderate negative correlation with patient satisfaction ($r = -0.58$, $p = 0.047$); while it did not exhibit any correlation with the NAHS score, mHHS score, or HOS-SSS score ($p > 0.05$). Placement in the backward direction demonstrated a moderate negative correlation with the iHOT-12 score ($r = -0.63$, $p = 0.020$), and a moderate negative correlation with patient satisfaction ($r = -0.55$, $p = 0.049$); with no correlation with the NAHS score, mHHS score, or HOS-SSS score ($p > 0.05$). Placement in supination, high, low, or forward directions displayed no correlation with the NAHS score, mHHS score, HOS-SSS score, iHOT-12 score, or patient satisfaction ($p > 0.05$) (Table 4; Figure 7).

4. Discussion

Developmental dysplasia of the hip (DDH) is a common condition causing hip pain in adolescents and young adults, serving as a primary cause of secondary OA.[5] DDH typically involves defects in two areas: acetabular dysplasia and abnormalities in the femoral side, with the former being more critical in diagnosis and treatment.[6] The etiology of acetabular dysplasia can be broadly categorized into developmental factors and secondary causes. Developmental factors generally refer to the progressive abnormalities of the hip joint due to developmental issues after birth, leading to a smaller and shallower acetabulum with insufficient coverage of the femoral head. Patients with these developmental issues have a single rotational center for the acetabulum that coincides with the rotational center of the femoral head. Of course, developmental factors do not always result in this outcome; some cases may progress to DDH, particularly if not effectively managed at the early stage. In such instances, the rotational centers of the femoral head and acetabulum may separate, leading to non-concentric development. The treatment aim for DDH is to increase femoral head coverage, and restore and maintain the concentricity between the acetabulum and femoral head.[5] Swiss physician Ganz et al.,[7] following his study on the anatomy and vascular distribution around the acetabulum, introduced the Bernese PAO for treating acetabular dysplasia. This technique carefully considers the preservation of blood supply to the acetabular osteotomy site, employing a medial pelvis approach for exposure and osteotomy, which, compared with other osteotomies, reduces the incidence of related complications to a certain extent and has gained widespread application. A systematic review incorporating 24 studies reported survival rates of 75.9% at 10 years and 36.5% at 20 years using this technique.[8] However, PAO still carries risks, including instability after repositioning, unsatisfactory femoral head coverage, as well as nonunion.[9] For acetabular dysplasia that is not developing concentrically, simply rotating the acetabulum could not restore the concentricity between the acetabulum and the femoral head, which may fail to achieve satisfactory bony coverage and does not alleviate the load on the acetabular labrum, potentially accelerating hip OA.[10] Moreover, Matsui et al.[11] reported that the efficacy of PAO was uncertain because the loss of acetabulum and femoral head cartilage might also hasten the progression of OA.

The concept of acetabuloplasty was initially proposed and refined by pioneers such as Konig, Spitzy, and Wiberg in the late 19th and early 20th centuries.[12] Due to limited understanding, early results of acetabuloplasty did not significantly surpass those of alternative treatments. As knowledge about acetabular dysplasia and acetabuloplasty advanced, Nishimatsu et al. continuously improved the surgical technique, achieving favorable outcomes in long-term follow-up: 87% of hips had no OA or in early OA over an average follow-up of 23.8 years.[13] Thus, this technique regained attention in recent years. However, previous studies have also indicated that approximately 22% of autograft bone used in acetabuloplasty experienced bone resorption,[14] which would compromise the supporting function of the acetabulum. Due to the relatively irregular bone morphology of the upper surface of the acetabular rim, the mismatch between the shape of the bone graft and the outer edge of the acetabulum and the femoral head often influences the optimal placement of the bone graft. Consequently, the placement of the graft can easily deviate during the procedure, particularly when placed too high, leading to weakened support, reduced stress distribution, and ultimately, bone resorption.[15] Issues with autograft bone also include adequate coverage only in the lateral superior region of the acetabulum, while failing to cover the anterior and posterior aspects. Furthermore, the smooth and dense surface of cortical bone is not conducive to the final attachment of the joint capsule to the bone graft and the transformation into fibrocartilaginous structures. Therefore, in this study, the design of the buttress required the curvature of the bottom surface of the buttress to parallel the spherical surface of the femoral head. This is aimed at restoring the concentricity of the hip joint while achieving an LCE angle of 30–35° and an ACE angle of 25–30°, ensuring coverage of both the lateral and anterior aspects of the acetabulum.

The 3D printing technology represents a rapid prototyping method that fabricates objects layer by layer based on digital model files. It integrates the latest advancements from modern digital capture techniques, software programming, numerical control, laser or electron beam technologies, and material science.[16] Developing precise and efficient surgical strategies is crucial for the success of bone defect surgeries, necessitating the preservation of host bone volume and achieving a good match between the graft and the bone defect's anatomical structure.[17] Previous preoperative planning predominantly relied on 2D images, lacking the precision offered by 3D representations of bone defect anatomy. The widespread application of 3D reconstruction and 3D printing technologies in medicine has made individualized and precise preoperative planning a reality. With advancements in 3D printing, individualized preoperative design and life-size printing enable the graft's shape to perfectly match the defect area, allowing for ideal placement during surgery. This approach effectively avoids time-consuming adjustments, difficulties in implantation, and unsatisfactory positioning, simplifying the surgical process, ensuring therapeutic efficacy and safety, and reducing perioperative complications. Additionally, 3D printing facilitates the creation of porous structures that promote bone tissue growth and allows for precise adjustment of the implant's mechanical strength to avoid stress shielding.[18,19] Therefore, 3D printing is emerging as an effective method for manufacturing implants in the field of orthopedics.

Currently, titanium and its alloys are the most widely used bone filler materials. Due to their structure that closely resembles bone tissue, high-load resistance, and excellent biocompatibility, 3D-printed titanium alloy materials have been widely utilized in orthopedics, particularly in the functional reconstruction of severe bone defects, significantly reducing the complexity and enhancing the accuracy of reconstruction. Borland et al.[20] reported that the prosthesis survival rate for complex acetabular bone defects reconstructed with titanium metal augments was 95.8% (23/24) over a median follow-up of 5 (range: 3–7) years. However, titanium alloys lack sufficient corrosion resistance and osseointegration capability, often requiring surface coatings to enhance their bioactivity and corrosion resistance.[21,22] Porous tantalum metal, characterized by its innovative porous structure, exhibits excellent biocompatibility, ideal elastic modulus, structural strength, corrosion resistance, and even antimicrobial properties.[23] Many clinical and animal studies have confirmed that porous tantalum metal serves as a promising substitute for bone grafts in reconstructive surgeries.[24–26] Porous tantalum has superior bio-inductive properties, promoting cell adhesion, growth, differentiation, and the formation of an abundant extracellular matrix, thereby accelerating bone ingrowth on the implant surface and early biological fixation, which is notably superior to materials like titanium alloys.[27] Thus, tantalum metal achieves favorable reconstructive outcomes even under conditions of severe bone defects and poor host bone quality. Compared with other porous metallic materials, porous tantalum has a higher porosity (75–85%), enhancing tissue permeability and nutrient exchange within the scaffold, which confers greater potential for osseointegration.[28,29] Balla et al.[30] first reported the additive manufacturing of porous tantalum in 2010, successfully fabricating a porous tantalum structure with a total porosity of 27–55% using Laser Engineered Net Shaping (LENS™). The mechanical properties of these structures were similar to those of human cortical bone; *in vitro* studies have also demonstrated that laser-treated

porous tantalum offers better human fetal osteoblast (hFOB) cell adhesion, growth, death, and differentiation compared with porous titanium, enhancing early bioactivity, and can be widely used in metal implants. Fan et al.[31] confirmed that 3D-printed porous tantalum exhibited superior biomechanical and microstructural properties compared with porous titanium, with more evident osseointegration 4–6 weeks postoperatively. Tantalum's compressive strength is closer to that of pig bone scaffolds, making it easier to integrate with host bone and prevent stress shielding and implant loosening. Macheras et al.[32] used porous tantalum for acetabular components in primary total hip arthroplasty, with an average follow-up of 18.1 years (range: 17.5–19 years) for 140 patients. The survival rate, with any reoperation for any reason as the endpoint, was 92.8%, and the survival rate with aseptic loosening as the endpoint was 100%. This study innovatively employed 3D-printed individualized porous tantalum buttress in shelf acetabuloplasty for patients with DDH. Both subjective functional scores and objective radiological indicators demonstrated significant improvements at the final follow-up compared with preoperative ones ($p < 0.01$), with an overall patient satisfaction rate reaching 84%. No complications, such as graft rejection, infection, or loosening, were observed among all patients. However, correlation analysis between the deviation in porous tantalum buttress placement and iHOT-12 score, as well as patient satisfaction, revealed moderate negative results when placed in pronation or backward. This may be due to pronation leading to flexion impingement, while backward placement results in insufficient coverage of the anterior acetabulum. Therefore, the implantation position of the porous tantalum buttress must be individually designed preoperatively and accurately placed intraoperatively to ensure the recovery of hip joint function and mobility.

This study also has limitations: (i) a control group was not established, lacking a large-scale control study on the clinical efficacy of the 3D-printed individualized porous tantalum buttress; (ii) some cases had a follow-up period of only 1 year, which was insufficient for any implant loosening or displacement to occur. Further validation of our findings requires additional cases and long-term follow-up studies.

5. Conclusion

The application of 3D-printed individualized porous tantalum buttress in shelf acetabuloplasty for patients with DDH offers advantages such as minimal surgical trauma, simple operation, and no donor site complications. More importantly, the buttress achieves a good fit with the acetabulum and femoral head, effectively compensating for inadequate coverage laterally and anteriorly, thus restoring the concentricity of the hip joint and providing sustained mechanical support. Postoperatively, patients experience pain relief and restoration of hip joint function, with satisfactory clinical efficacies in early follow-ups and no occurrence of serious complications. This method holds promising clinical application prospects in shelf acetabuloplasty for treating DDH.

Acknowledgments

None.

Funding

This study was supported by the General Program of the National Natural Science Foundation of China (No. 82372365).

Conflict of interest

The authors declare they have no competing interests.

Author contributions

Conceptualization: Guangxing Chen, Liu Yang
Formal analysis: Juncai Xu, Xin Chen
Investigation: Yang Peng, Ran Xiong, Chengjun Huang, Guangxing Chen, Liu Yang
Writing – original draft: Yang Peng, Xin Chen
Writing – review & editing: Guangxing Chen, Liu Yang

Ethics approval and consent to participate

This study was approved by the Ethics Committee of the Southwest Hospital (No. KY201908).

Consent for publication

All patients signed the informed consent form.

Availability of data

The raw data used to reproduce these findings are available from the corresponding author upon reasonable request.

References

1. Vaquero-Picado A, González-Morán G, Garay EG, Moraleda L. Developmental dysplasia of the hip: update of management. *EFORT Open Rev*. 2019;4(9):548-556. doi: 10.1302/2058-5241.4.180019
2. Tønning LU, O'Brien M, Semciw A, Stewart C, Kemp JL, Mechlenburg I. Periacetabular osteotomy to treat hip dysplasia: a systematic review of harms and benefits. *Arch Orthop Trauma Surg*. 2023;143(6):3637-3648. doi: 10.1007/s00402-022-04627-7

3. Holm AG, Reikerås O, Terjesen T. Long-term results of a modified Spitzy shelf operation for residual hip dysplasia and subluxation. A fifty year follow-up study of fifty six children and young adults. *Int Orthop*. 2017;41(2):415-421. doi: 10.1007/s00264-016-3286-0
4. Christen P, Ito K, Galis F, van Rietbergen B. Determination of hip-joint loading patterns of living and extinct mammals using an inverse Wolff's law approach. *Biomech Model Mechanobiol*. 2015;14(2):427-432. doi: 10.1007/s10237-014-0602-8
5. Yang S, Zusman N, Lieberman E, Goldstein RY. Developmental dysplasia of the hip. *Pediatrics*. 2019;143(1):e20181147. doi: 10.1542/peds.2018-1147
6. Schmitz MR, Murtha AS, Clohisy JC; ANCHOR Study Group. Developmental dysplasia of the hip in adolescents and young adults. *J Am Acad Orthop Surg*. 2020;28(3):91-101. doi: 10.5435/JAAOS-D-18-00533
7. Ganz R, Klaue K, Vinh TS, Mast JW. A new periacetabular osteotomy for the treatment of hip dysplasias. Technique and preliminary results. *Clin Orthop Relat Res*. 1988;(232):26-36.
8. Tan JHI, Tan SHS, Rajoo MS, Lim AKS, Hui JH. Hip survivorship following the Bernese periacetabular osteotomy for the treatment of acetabular dysplasia: a systematic review and meta-analysis. *Orthop Traumatol Surg Res*. 2022;108(4):103283. doi: 10.1016/j.otsr.2022.103283
9. Suzuki M, Kinoshita K, Sakamoto T, Seo H, Yoshimura I, Yamamoto T. Short-term outcomes of curved periacetabular osteotomy and factors influencing patient dissatisfaction. *J Hip Preserv Surg*. 2023;10(1):17-23. doi: 10.1093/jhps/hnac054
10. Abraham CL, Knight SJ, Peters CL, Weiss JA, Anderson AE. Patient-specific chondrolabral contact mechanics in patients with acetabular dysplasia following treatment with peri-acetabular osteotomy. *Osteoarthritis Cartilage*. 2017;25(5):676-684. doi: 10.1016/j.joca.2016.11.016
11. Matsui M, Masuhara K, Nakata K, Nishii T, Sugano N, Ochi T. Early deterioration after modified rotational acetabular osteotomy for the dysplastic hip. *J Bone Joint Surg Br*. 1997;79(2):220-224. doi: 10.1302/0301-620x.79b2.7202
12. Fawzy E, Mandellos G, De Steiger R, McLardy-Smith P, Benson MK, Murray D. Is there a place for shelf acetabuloplasty in the management of adult acetabular dysplasia? A survivorship study. *J Bone Joint Surg Br*. 2005;87(9):1197-1202. doi: 10.1302/0301-620X.87B9.15884
13. Nishimatsu H, Iida H, Kawanabe K, Tamura J, Nakamura T. The modified Spitzy shelf operation for patients with dysplasia of the hip. A 24-year follow-up study. *J Bone Joint Surg Br*. 2002;84(5):647-652. doi: 10.1302/0301-620x.84b5.12732
14. Summers BN, Turner A, Wynn-Jones CH. The shelf operation in the management of late presentation of congenital hip dysplasia. *J Bone Joint Surg Br*. 1988;70(1):63-68. doi: 10.1302/0301-620X.70B1.3276702
15. Ramdhan Ibrahim MA, Kamegaya M, Morita M, Saisu T, Kakizaki J, Oikawa Y. Radiological results of Shelf acetabuloplasty in adolescent hip dysplasia with aspherical femoral head: how to get an ideal placement of the Shelf graft. *J Pediatr Orthop B*. 2020;29(3):261-267. doi: 10.1097/BPB.0000000000000681
16. Okolie O, Stachurek I, Kandasubramanian B, Njuguna J. 3D printing for hip implant applications: a review. *Polymers (Basel)*. 2020;12(11):2682. doi: 10.3390/polym12112682
17. Jing Z, Zhang T, Xiu P, et al. Functionalization of 3D-printed titanium alloy orthopedic implants: a literature review. *Biomed Mater*. 2020;15(5):052003. doi: 10.1088/1748-605X/ab9078
18. Kumar A, Nune KC, Misra RDK. Design and biological functionality of a novel hybrid Ti-6Al-4V/hydrogel system for reconstruction of bone defects. *J Tissue Eng Regen Med*. 2018;12(4):1133-1144. doi: 10.1002/term.2614
19. Barui S, Chatterjee S, Mandal S, Kumar A, Basu B. Microstructure and compression properties of 3D powder printed Ti-6Al-4V scaffolds with designed porosity: Experimental and computational analysis. *Mater Sci Eng C Mater Biol Appl*. 2017;70(Pt 1):812-823. doi: 10.1016/j.msec.2016.09.040
20. Borland WS, Bhattacharya R, Holland JP, Brewster NT. Use of porous trabecular metal augments with impaction bone grafting in management of acetabular bone loss. *Acta Orthop*. 2012;83(4):347-352. doi: 10.3109/17453674.2012.718518
21. Han Y, Chen D, Sun J, Zhang Y, Xu K. UV-enhanced bioactivity and cell response of micro-arc oxidized titania coatings. *Acta Biomater*. 2008;4(5):1518-1529. doi: 10.1016/j.actbio.2008.03.005
22. Huang T, Wang H, Zhang Z, Feng K, Xiang L. Incorporation of inorganic elements onto titanium-based implant surfaces by one-step plasma electrolytic oxidation: an efficient method to enhance osteogenesis. *Biomater Sci*. 2022;10(23):6656-6674. doi: 10.1039/d2bm00818a
23. Levine B, Della Valle CJ, Jacobs JJ. Applications of porous tantalum in total hip arthroplasty. *J Am Acad Orthop Surg*. 2006;14(12):646-655. doi: 10.5435/00124635-200611000-00008
24. Carraro F, Bagno A. Tantalum as trabecular metal for endosseous implantable applications. *Biomimetics (Basel)*. 2023;8(1):49.

doi: 10.3390/biomimetics8010049

25. Brüggemann A, Mallmin H, Bengtsson M, Hailer NP. Safety of use of tantalum in total hip arthroplasty. *J Bone Joint Surg Am*. 2020;102(5):368-374.
doi: 10.2106/JBJS.19.00366

26. Ao Y, Guo L, Chen H, et al. Application of three-dimensional-printed porous tantalum cones in total knee arthroplasty revision to reconstruct bone defects. *Front Bioeng Biotechnol*. 2022;10:925339.
doi: 10.3389/fbioe.2022.925339

27. Rambani R, Nayak M, Aziz MS, Almeida K. Tantalum versus titanium acetabular cups in primary total hip arthroplasty: current concept and a review of the current literature. *Arch Bone Jt Surg*. 2022;10(5):385-394.
doi: 10.22038/ABJS.2021.55255.2750

28. Wieding J, Wolf A, Bader R. Numerical optimization of open-porous bone scaffold structures to match the elastic properties of human cortical bone. *J Mech Behav Biomed Mater*. 2014;37:56-68.
doi: 10.1016/j.jmbbm.2014.05.002

29. Wei X, Zhao D, Wang B, et al. Tantalum coating of porous carbon scaffold supplemented with autologous bone marrow stromal stem cells for bone regeneration in vitro and in vivo. *Exp Biol Med (Maywood)*. 2016;241(6):592-602.
doi: 10.1177/1535370216629578

30. Balla VK, Bodhak S, Bose S, Bandyopadhyay A. Porous tantalum structures for bone implants: fabrication, mechanical and in vitro biological properties. *Acta Biomater*. 2010;6(8):3349-3359.
doi: 10.1016/j.actbio.2010.01.046

31. Fan H, Deng S, Tang W, et al. Highly porous 3D printed tantalum scaffolds have better biomechanical and microstructural properties than titanium scaffolds. *Biomed Res Int*. 2021;2021:2899043.
doi: 10.1155/2021/2899043

32. Macheras GA, Lepetsos P, Leonidou AO, Anastasopoulos PP, Galanakos SP, Poultsides LA. Survivorship of a porous tantalum monoblock acetabular component in primary hip arthroplasty with a mean follow-up of 18 years. *J Arthroplasty*. 2017;32(12):3680-3684.
doi: 10.1016/j.arth.2017.06.049

ACCSCIENCE PUBLISHING

International Journal of Bioprinting

RESEARCH ARTICLE

Direct ink writing of biomimetic hydroxyapatite scaffolds with tailored concave porosity

Laura del-Mazo-Barbara[1,2,3], Anna Diez-Escudero[1,2,3,4], Irene Lodoso-Torrecilla[1,2,3], Morteza Aramesh[5,6], Cecilia Persson[5,6], and Maria-Pau Ginebra[1,2,4,6,7]*

[1]Biomaterials, Biomechanics and Tissue Engineering Group, Department of Materials Science and Engineering and Research Centre for Biomedical Engineering, Universitat Politècnica de Catalunya, Barcelona, Spain

[2]Barcelona Research Centre in Multiscale Science and Engineering, Universitat Politècnica de Catalunya, Barcelona, Spain

[3]Institut de Recerca Sant Joan de Déu, Barcelona, Spain

[4]Centro de Investigación Biomédica en Red—Bioingeniería, Biomedicina y Nanomedicina (CIBER-BBN), Carlos III Health Institute, Madrid, Spain

[5]Division of Biomedical Engineering, Department of Materials Science and Engineering, Uppsala University, Uppsala, Sweden

[6]Additive Manufacturing for the Life Sciences Competence Centre (AM4Life), Uppsala University, Uppsala, Sweden

[7]Institute for Bioengineering of Catalonia (IBEC), Barcelona Institute of Science and Technology, Barcelona, Spain

***Corresponding author:**
Maria-Pau Ginebra
(maria.pau.ginebra@upc.edu)

Citation: del-Mazo-Barbara L, Diez-Escudero A, Lodoso-Torrecilla I, Aramesh M, Persson C, Ginebra MP. Direct ink writing of biomimetic hydroxyapatite scaffolds with tailored concave porosity. *Int J Bioprint*. 2024;10(6):3805. doi: 10.36922/ijb.3805

Received: May 31, 2024
Revised: July 5, 2024
Accepted: July 19, 2024
Published Online: July 25, 2024

Copyright: © 2024 Author(s). This is an Open Access article distributed under the terms of the Creative Commons Attribution License, permitting distribution, and reproduction in any medium, provided the original work is properly cited.

Publisher's Note: AccScience Publishing remains neutral with regard to jurisdictional claims in published maps and institutional affiliations.

(This article belongs to the *Special Issue: Advanced Biomaterials for 3D Printing and Healthcare Application*)

Abstract

Direct ink writing (DIW) is a promising technology for the fabrication of personalized bone grafts, as it enables the customization of their geometrical conformation with high reproducibility and is compatible with the use of self-setting calcium-deficient hydroxyapatite inks. However, the scaffolds obtained by DIW consist mostly of convex filaments, which is a limitation since concave surfaces are known to promote bone regeneration *in vivo*. In this work, we explore the use of triply periodic minimal surface (TPMS) designs in DIW of calcium phosphate self-hardening inks as a strategy to obtain scaffolds with controlled concave macropores. The limitations of the printing parameters with high ceramic-loaded inks using DIW resulted in only 20% nominal porosity for gyroid-, diamond-, and Schwarz-based structures. The inherent layered pores from TPMS geometries enabled concavities typically unattainable via DIW, bearing substantial implications for subsequent osteoinductive capabilities. Although the mechanical properties were lower in the TPMS-based scaffolds than in the orthogonal patterned ones, the blood permeability of TPMS-based structures was higher. The concave pore architecture enhanced the osteogenic potential of the biomimetic ceramic, increasing SaOs-2 cell adhesion, proliferation, differentiation, and mineralization.

Keywords: Bone scaffold; Biomimetic hydroxyapatite; Direct ink writing; Biomorphic structures; Concavity; Pore architecture

1. Introduction

Additive manufacturing has emerged as a transformative technique, enabling the customization of designs and geometries with a profound impact on the development of bone scaffolds. The significant influence of such techniques stems from their ability to create reproducible macroporous structures and adjust the external shape of the scaffolds to the specific anatomy and the geometry of the bone defect, allowing for customized implant design. By integrating these design capabilities with the specific requirements for optimal bone scaffolds, it becomes possible to enhance, guide, and support the natural remodeling process of bone when compromised by large defects.[1,2]

The continuous ingrowth of new bone into a scaffold not only relies on the compositional properties and mechanical stability but also pore geometry and distribution. Pores should be open and highly interconnected,[3] which are difficult to achieve by conventional methods, such as foaming or sacrificial porogens.[4] Pore size plays a key role in bone extracellular matrix production and organization. Pore dimensions of at least 100 μm are needed for nutrient transport and waste removal. Enhanced bone formation and vascularization have been reported for scaffolds with pore sizes larger than 200–300 μm.[3,5,6] Though initial fast woven bone ingrowth can happen with pores as small as 1–10 μm.[7] Additionally, an *in vitro* study reported that pore geometry is also crucial, with concave surfaces accelerating and enhancing osteogenic differentiation.[8] The presence of concavities has been associated with favorable microenvironments capable of confining relevant ions and biological molecules that foster cell membrane contacts.[8] Notably, the presence of concavities in biomimetic apatite scaffolds was demonstrated to outperform the same scaffolds with convexities *in vivo*. Foamed apatite scaffolds, with interconnected concave pores, induced a significantly higher amount of new bone in a canine model compared to scaffolds with interconnected convex pores, and new bone formed preferentially in the concavities of the foamed apatite scaffold.[9,10] However, controlling the foaming process is challenging and has poor reproducibility in terms of pore interconnectivity, distribution, and size, and foams have lower mechanical strengths.[11]

Additive manufacturing techniques open up new possibilities for the fabrication of pore structures with controlled geometries, including designs inspired by nature. For instance, triply periodic minimal surfaces (TPMSs) have attracted great interest in bone regeneration due to the periodical nature-inspired models that resemble the trabecular bone structure[12] with a mean curvature close to zero.[13] In nature, these surfaces play an essential role in guiding chemical, biochemical, and cellular processes.[14] Three-dimensional (3D) structures can be obtained by thickening such surfaces,[15] creating unit cells whose periodic repetition results in scaffolds with complex porosity, numerous concave surfaces, and high interconnectivity. These scaffolds have reportedly enhanced cell growth, migration, and vascularization through improved body fluid permeability.[16–18]

Triply periodic minimal surface (TPMS) structures or their negative molds have been created by different additive manufacturing technologies: (i) extrusion-based methods like fused deposition melting (FDM),[16,19] (ii) multijet technology, where a piezoelectric printhead deposits either photocurable plastic resin or supporting material,[20,21] or (iii) selective laser\light curing\melting (SL).[14,22–25]

The high resolution required for TPMS printing makes SL the most common method. However, metallic SL is rather expensive, and polymeric SL is restricted to a few photo-curable materials, mainly based on resins,[17] which lacks the bioactivity and osteoinductive properties often achieved with ceramics. Recently, modified hydrogels, such as poly(ethylene glycol) diacrylate, have been proposed as biocompatible alternatives.[26] For bioceramic TPMS scaffolds, SL technology has been used in two ways: (i) generating sacrificial molds that can be easily impregnated with calcium phosphate (CaP) slurry,[27] or (ii) loading a photo-curable resin with CaP[28–32] or other bioceramic particles.[13,31,32] Both pathways require a sintering process to harden the green bodies and simultaneously eliminate the organic resin. The resulting TPMS CaP structures have displayed greater new bone formation *in vivo* in comparison to CaP granules[27] or inorganic bovine xenograft blocks.[29] Moreover, Montazerian et al.[16] and Deng et al.[30] incorporated porosity gradients in these geometries, more closely mimicking the highly anisotropic and heterogeneous structure of trabecular bone.[33]

Direct-ink writing (DIW) is another additive manufacturing technique, based on extruding a flowable paste through a nozzle and building a 3D part by stacking filaments.[34] One main advantage of DIW is its diversity of printable materials, including highly loaded ceramic pastes. It has been successfully applied for the fabrication of customized synthetic bone grafts.[35] Among the wide variety of materials that can be used, the development of reactive inks based on CaP bone cement that hardens at body temperature through a dissolution-precipitation reaction represents a breakthrough in the field.[36,37] A widely used and simple formulation consists of α-tricalcium phosphate particles (α-$Ca_3(PO_4)_2$, α-TCP) suspended in a Pluronic F127 hydrogel. This formulation transforms into calcium-deficient hydroxyapatite (CDHA) after hardening.[37–39] These inks have a shear-thinning behavior and adequate rheological properties for DIW, ensuring

excellent shape fidelity.[40] Unlike printed ceramic parts that require sintering, self-setting inks avoid shrinkage[32,39,41–45] and produce biomimetic apatites with a composition closely resembling the mineral phase of natural bone.[46] Previous studies have demonstrated that CDHA-based ceramic printed parts have excellent biocompatibility and bioactivity, supporting bone ingrowth and functioning as bone scaffolds.[39,47] This has led to interest in incorporating concavities into DIW CaP scaffolds. Various strategies have been explored, including modifying the nozzle geometry to obtain concave channels[40,48,49] or altering the ink formulation to introduce intra-strand porosity (e.g., by incorporating sacrificial particles[38,50] or using emulsified or foamed pastes[51]). However, the filament diameter often limits the size of the intra-strand pores, which can be insufficient.

Hitherto, the potential of TPMS, while widely explored in other 3D printing techniques, has not been exploited using DIW. In this study, we explore the use of TPMS models to create scaffolds with controlled concavities busing DIW, despite the challenge of filament convexity. The combination of concave confined spaces with high permeable geometries and the enhanced bioactive and osteogenic potential of reactive ceramics could produce promising bone regenerative grafts. We used a self-setting α-TCP ink to create CDHA scaffolds with complex architectures. Three TPMS structures were selected as printing patterns for DIW: gyroid (G), diamond (D; also known as diamond Schwarz), and Schwarz (S; also called Schwarz primitive). Cylindrical scaffolds with different porosities were designed using a MATLAB code from previous work,[19] and their printability was evaluated. The resulting CDHA scaffolds were then evaluated for the effects of pore architecture on physicochemical properties, blood permeability, mechanical behavior, and *in vitro* response of pre-osteoblastic (pre-OB) cells, compared to the typical orthogonal printing pattern with the same total porosity.

2. Materials and methods

2.1. Materials

Poloxamer 407 (Kolliphor® P 407), also known as Pluronic F127, was purchased from BASF Pharmaceuticals (Germany). Calcium phosphate dibasic (CaHPO4), calcium carbonate (CaCO3), Triton X-100, Alizarin red staining (AR-S), and cetyl pyridinium chloride powders were obtained from Sigma-Aldrich (United States of America [USA]). Disposable 3D printer cartridge (3cc Optimum® Syringe Barrels) and 250 μm tapered dispensing tips (Gauge 22 SmoothFlow Tapered Tips) from Nordson EFD (USA) were used for printing. McCoy's 5A media, fetal bovine serum (FBS), phosphate-buffered saline (PBS), penicillin/streptomycin (Pen/Strep), HEPES, sodium pyruvate, Presto Blue kit, and mammalian protein extraction reagent (M-PER) were purchased from Thermo Scientific-Gibco (USA). Lactate dehydrogenase (LDH) and alkaline phosphatase (ALP, SensoLyte® pNPP) kits were purchased from Roche (Switzerland) and Anaspec (USA), respectively. Immunocytochemistry reagents, TRIT-C conjugated phalloidin (Alexa Fluor 546), and 4′,6-diamidino-2-phenylindole (DAPI) were purchased from Invitrogen (USA) and Merck (USA), respectively. Paraformaldehyde was obtained from Aname-Instrumentación Científica (Spain). Glycine was purchased from Serva (Spain).

2.2. Scaffold design

Given the aforementioned advantages, slicer programs for 3D printing incorporate TPMS patterns, particularly the G type. However, these 3D models are generated by intersecting 2D wavy lines with a defined porosity. This is different from generating the 3D model in a mathematical program (e.g., MATLAB), where unit cell numbers, dimensions, and/or volumetric fractions can be customized. This allows us to obtain sufficient and representative porosities for each geometry type when slicing the coded geometry for DIW, taking into account the limitations of the printer.

Three different types of TPMS scaffolds were coded with MATLAB (MathWorks, USA), as in previous work.[19] G, D, and S lattice structures with a defined number of cells and volume fraction were generated by determining the isosurface ($U = 0$) using the following TPMS equations[22]:

$$U_G = \cos(K_x x)\cdot\sin(K_y y) + \cos(K_y y)\cdot\sin(K_z z) + \cos(K_z z)\cdot\sin(K_x x) - C_G \quad \text{(I)}$$

$$U_D = \sin(K_x x)\cdot\sin(K_y y)\cdot\sin(K_z z) + \sin(K_x x)\cdot\cos(K_y y)\cdot\cos(K_z z) + \cos(K_x x)\cdot\sin(K_y y)\cdot\cos(K_z z) + \cos(k_x x)\cdot\cos(K_y y)\cdot\sin(K_z z) - C_D \quad \text{(II)}$$

$$U_S = \cos(K_x x) + \cos(K_y y) + \cos(K_z z) - C_S \quad \text{(III)}$$

where the subscripts G, S and D refer to the type of geometry; parameters K and C represent the structure's periodicity and porosity, respectively. In each direction, K is defined as $\frac{2\pi n}{L}$, where n is the number of unit cells and L is the absolute size of the structure.

Cylindrical structures (2.8 × 2.8 × 4.2-unit cells; 6 mm diameter; 9 mm height) were designed with three different porosities (i.e., 20%, 35%, and 50%). The 3D models and their middle cross-sections are displayed in Figure 1. The selection of the number of unit cells per cm was based on balancing two factors: (i) ensuring sufficient pore density, and (ii) not exceeding the resolution limitations of a DIW printer. As a control, a dense cylindrical model with the same external dimensions was created using CAD (SolidWorks; Dassault Systems, France). For all structures, an STL file was generated. For the *in vitro* study, cylindrical structures (2.8 × 2.8 × 1-unit cells; 6 mm diameter; 2.14 mm height) with 20% nominal porosity were printed.

2.3. Ink preparation

An α-TCP solution was prepared according to a previously reported protocol.[52] Briefly, $CaHPO_4$ and $CaCO_3$ were mixed with a Ca:P molar ratio of 1.5 and sintered, followed by rapid quenching from 1400ºC to room temperature. The powder was then ball-milled (Pulverisette 6; Fritsch GmbB, Germany) in the following sequence: 450 rpm with 10 agate balls of 30 mm in diameter for 40 min; 500 rpm with the same balls for 60 min; and 500 rpm with 100 balls of 10 mm in diameter for 60 min. Fine powder with a 3.12 μm median particle size was obtained, which was subsequently sieved at 40 μm (Filtra, Spain) with the help of zirconia balls (Tosoh, Japan). The ink was obtained by mixing 70 wt.% of α-TCP powder with a Pluronic hydrogel solution, obtained by dissolving 30 wt% Pluronic pellets in water.[37] The mixing in the different stages of preparation was conducted at room temperature in a dual asymmetric centrifugal mixer (DAC 150; Speedmixer, USA).

2.4. Direct ink writing of the scaffolds

The TPMS models (in STL file format) were imported into 3D slicing software (Simplify3D, USA) to generate G-codes for the 3D printer. The main printing parameters for the TPMS geometries were: nozzle diameter of 250 μm; layer height of 0.2 mm (20% overlap in the Z-axis); and a rectangular printing pattern with a 100% infill. An orthogonal pattern (OP) was printed as a control, where the infill was defined according to the porosity selected for the TPMS geometries.

A disposable 3D printer cartridge filled with fresh ink was coupled with a tapered dispensing tip and installed in a customized 3D printer (Fundació CIM, Spain) for sample printing. The green bodies were hardened through the self-setting reaction triggered by the hydrolysis of α-TCP to CDHA.[37,38] For that purpose, the as-printed scaffolds were immediately placed in a vapor-saturated atmosphere at 37ºC for 24 h, followed by complete immersion in water at the same temperature for 6 days. After this process, pure ceramic scaffolds were obtained, as Pluronic is fully released in the water.[37,38]

2.5. Physicochemical characterization

Macroporosity (>3 μm) was analyzed using X-ray computed microtomography (micro-CT, Skyscan 1272 Microtomograph; Bruker, USA) using one sample for each printed geometry. The CT measurements were carried out at 90 kV voltage and 111 μA current; the generated beam was filtered with 0.5-mm-thick aluminum and 0.038-mm copper filters; and the projected images were collected every 0.02º over 180º with an exposure time of 3375 ms, obtaining an isotropic voxel size (voxel resolution) of 3 μm. NRecon software (Bruker, USA) was used for reconstructing the samples with alignment adjustments, beam hardening corrections, ring artifact filtering, and image smoothing. Porosity analysis was performed in CTAn software (Bruker, USA). Specifically, a volume of 5.70 cm diameter (2.66 units) by 4.29 cm height (2 units) was cut, smoothed with a Kuwahara filter, binary-segmented with a threshold of 40, and refined by removing white/black speckles (<30 voxels). Measurements were taken, and 3D reconstructions were rendered using CTvox software (Bruker, USA).

The microstructure was analyzed using scanning electron microscopy (SEM; Neon40 Crossbeam™ workstation; Carl Zeiss, Germany) after coating the samples with a carbon evaporated layer (K950X; EMITECH, France). The phase composition was evaluated by powder X-ray diffraction (XRD), using a D8 Advance diffractometer (Bruker, USA), a Bragg–Brentano geometry, and a Cu Kα radiation with the following conditions: 2θ scan range of 20–50°, scan step of 0.02°, counting time of 2 s per step at 40 kV, and 40 mA. Three samples per condition were ground to powder to ascertain representative compositions. The quantification of the proportions of α-TCP and CDHA phases was conducted through Rietveld refinement composition analyses using Profex software (version 4.0.3; https://www.profex-xrd.org/).

2.6. Blood permeability

Blood permeability of the scaffold was measured in a custom-made setup, manufactured by FDM using polylactic acid (Figure 2a and b). The design, based on a previous study of polymeric scaffolds,[19] was adapted for non-elastic pure ceramic scaffolds. A blood-mimicking fluid (BMF) simulating the rheological properties of blood at a normal hematocrit level (46%) at 37ºC was used.[53] The BMF composition is detailed in Figure 2c, and the BMF has a density (ρ) of 1.126 ± 0.002 g/mL. To confirm the rheological properties of the BMF, its viscosity as a

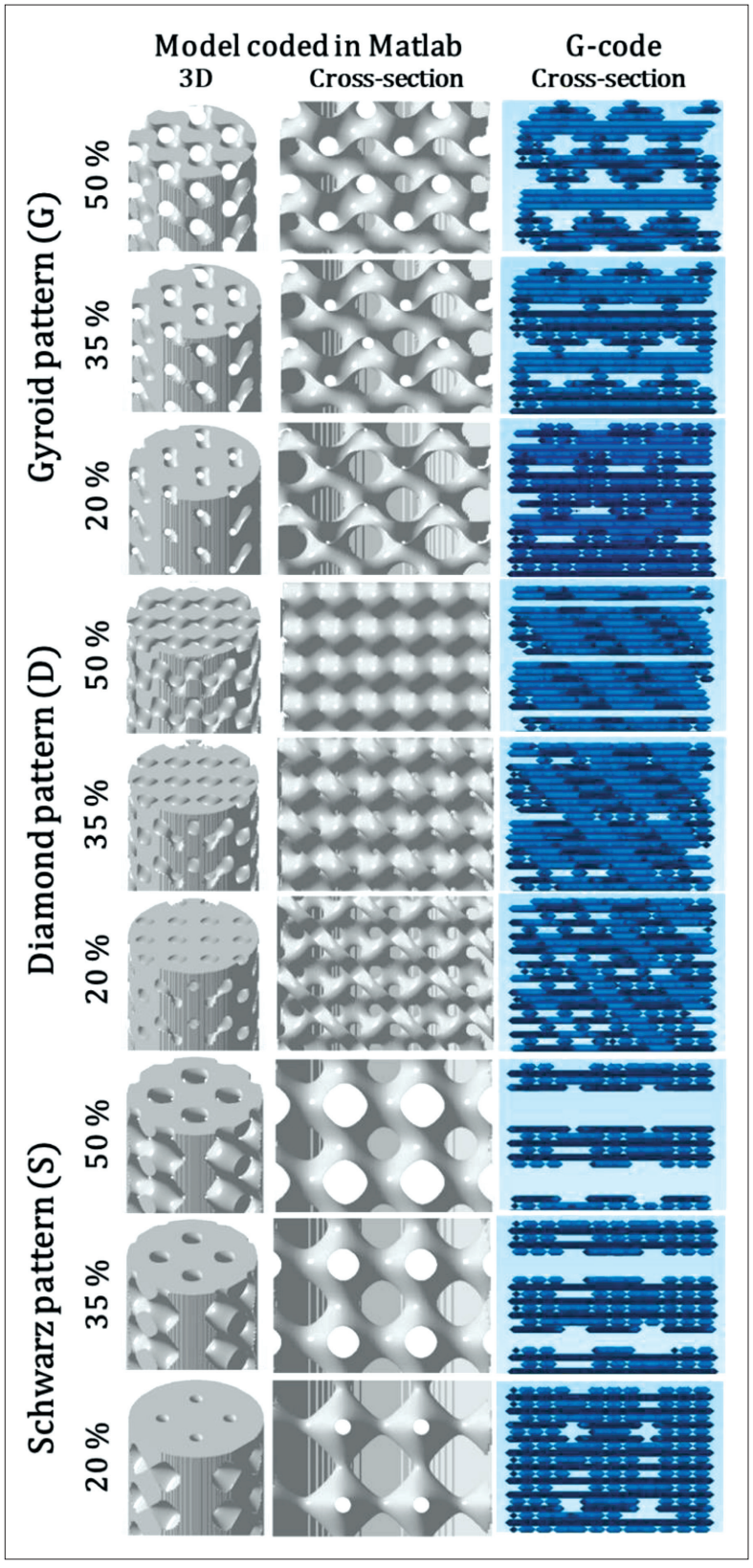

Figure 1. 3D-printed structures with different levels of porosity: 50%, 35%, and 20%. Designed 3D geometry (left column); 3D cross-section (middle column); and cross-section of the direct-ink writing (DIW) G-code simulation (right column).

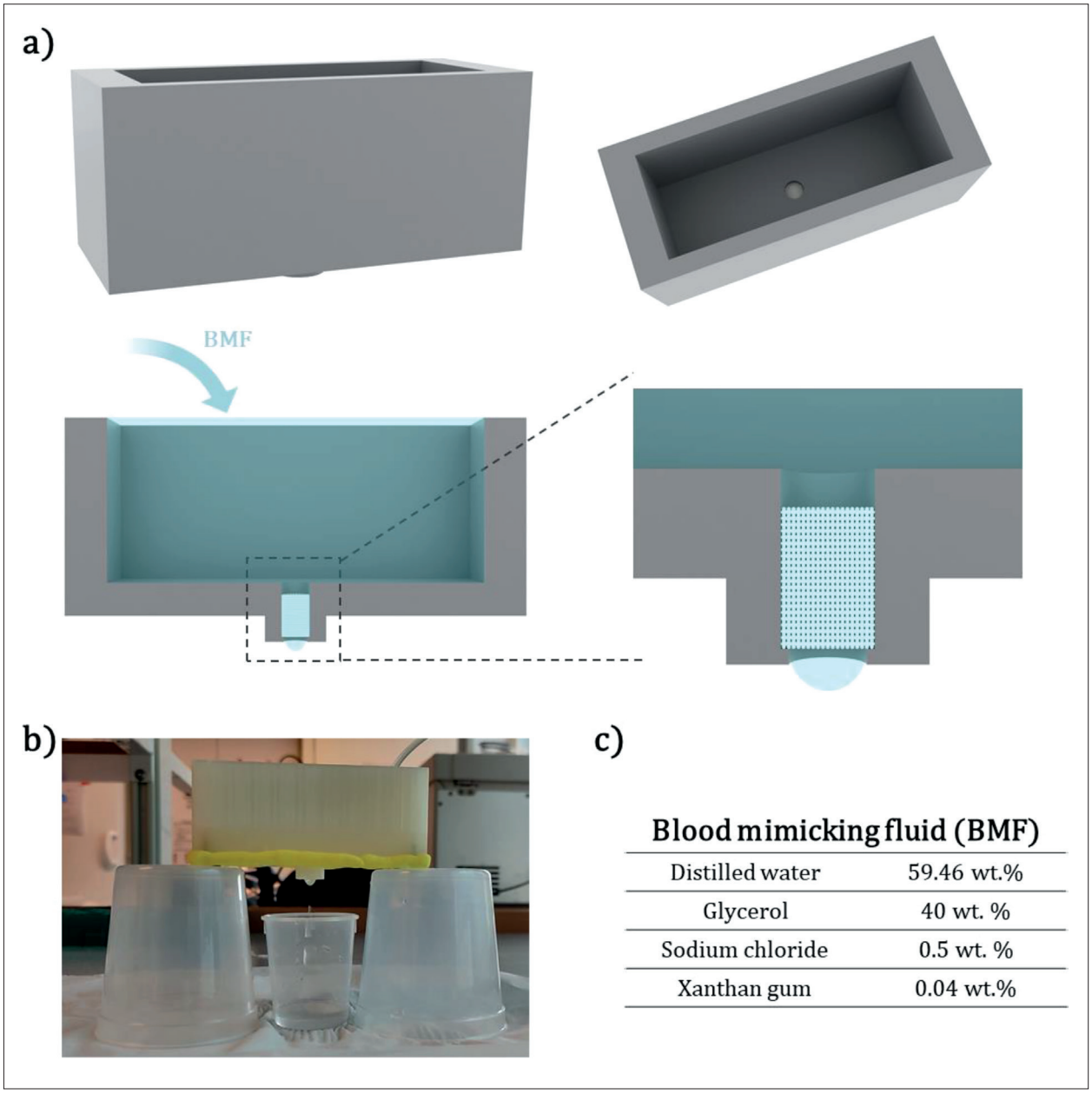

Figure 2. Blood permeability test. (a) Illustration of the custom-made setup, displaying the sample placement, the blood mimicking fluid with a constant column of liquid, and the outlet for recording the fluid flow rate. (b) Overview of the experimental setup. (c) Blood mimicking fluid composition.

function of shear rate was quantified at 25°C in a rotational rheometer (Discovery HR-2; TA Instrument, USA) with a parallel plate geometry (ø = 20 mm) at a flow sweep range of 1–100 s^{-1}.

The scaffolds were laterally sealed with Teflon tape and fitted exactly to the hole using play dough, as the ceramic parts are not flexible, to direct fluid flow longitudinally through the sample. The tank was then filled with BMF to a constant height (H) of 5 cm, and the fluid passing through the porous scaffold was collected every minute for a total of 10 min. All tests were performed at 25°C, and three specimens were measured per group. The BMF applied a pressure (ΔP) of 331.4 Pa on top of the scaffolds, as calculated from:

$$\Delta P = \rho \cdot 9.81 \cdot H \quad \text{(IV)}$$

To calculate the permeability of the porous scaffold, a simplified version of Darcy's law was used[17]:

$$K = \frac{\mu \cdot q \cdot L}{A \cdot \Delta P} \quad \text{(V)}$$

where K is the longitudinal permeability, μ the BMF viscosity, q the flow rate, L the scaffold's height in the longitudinal direction, A the scaffold's cross-sectional area, and ΔP the previously calculated applied pressure.

2.7. Mechanical properties in compression

The scaffolds were tested in uniaxial compression (10 samples per group) under wet conditions using a universal testing machine (BIONIX; MTS Systems Corporation, USA). A 0.5 mm/min cross-head speed was used, following the ISO 13175-3 standard. The strength was determined as the maximum stress; the elastic modulus as the slope in the elastic region; and the strain energy density (SED), i.e., the work of fracture normalized by the sample volume, as the area under the stress versus strain curve. Moreover, the Weibull modulus was calculated through the Weibull statistical analysis of the strength values:

$$\ln\left(\ln\left(\frac{1}{P_s}\right)\right) = m\left(\ln(S) - \ln(\sigma_0)\right) \quad \text{(VI)}$$

where P_s is the probability of survival, m is the Weibull modulus, σ is the stress, and σ_0 is a constant corresponding to the stress for which 37% of the samples survive.

2.8. *In vitro* study

2.8.1. Cell adhesion

The scaffolds were sterilized by immersion in 70% ethanol for 2 h, followed by rinsing in PBS three times, and incubated overnight with complete McCoy's 5A media (10% FBS, 1% Pen/Strep, 2% HEPES, and 1% sodium pyruvate). The next day, the scaffolds were dried using sterilized filter paper before seeding to optimize cell droplet sedimentation.

Approximately 50,000 SaOs-2 (ATCC® HTB85TM) pre-OB osteosarcoma cells were seeded per scaffold using a 10 µL droplet, and incubated for 1 h at 37°C and 5% CO_2. Thereafter, 2 mL of complete media were added, and cells were further incubated for 6 h. The scaffolds were then washed twice with warm PBS and transferred to new well plates. Subsequently, 500 µL of 10% Presto Blue diluted in complete media was added and incubated for 1 h. Cell adhesion was quantified by the fluorescence signal (excitation: 560 nm; emission: 590 nm). Quadruplicates were used for each sample type, and control samples, consisting of cells seeded directly in wells without scaffolds, were included. A calibration curve with a known cell number was used to calculate adhesion percentages. The number of adhered cells was normalized by the available area for each scaffold, as measured by micro-CT, and expressed as a percentage relative to the control samples.

2.8.2. Cell proliferation, differentiation, and mineralization

To assess the effect of geometry on cell behavior, both cell proliferation and differentiation were studied on days 1, 7, 14, and 21, while mineralization was quantified on days 14 and 21. Cells were seeded on the scaffolds at the same concentration used in the adhesion experiment for 1 h in the incubator and subsequently covered with complete media. At each time point, the scaffolds were transferred to new well plates, rinsed with warm PBS, and lysed using 500 µL M-PER. Cell lysates were stored at −80°C until measurement.

Cell proliferation was quantified using an LDH kit. Briefly, 100 µL of the cell lysates were added to the 96-well plates; 100 µL of the reaction mixture was added and incubated at room temperature for 15 min; 50 µL of stop solution was added; the absorbance at 490 nm was measured in a microplate reader (BioTek Instruments, USA). Cell proliferation was normalized by the area of each scaffold and expressed as a percentage of proliferation relative to the control sample on day 1. Cell differentiation was investigated by ALP quantification of the same cell lysates. Briefly, 50 µL of cell lysates were pipetted into 96-well plates; 100 µL of ALP buffer was added and incubated at room temperature for 15–20 min; 50 µL of stop solution was added; the absorbance was recorded at 405 nm. A calibration curve with known ALP concentrations was used for calculations, with ALP concentrations expressed as ng/mL. These values were normalized by the cell number (quantified by LDH) and expressed as ng/cell. Triplicate samples for each type of geometry were used.

Cell mineralization was investigated using AR-S and quantification after 14 and 21 days. The cell-laden scaffolds were fixed using 4% paraformaldehyde (Aname Instrumentación Científica, Spain) for 20 min at room temperature. Subsequently, the scaffolds were rinsed with PBS and stained with 40 mM Alizarin Red (AR) at pH 4.2 for 10 min at room temperature. The scaffolds were then rinsed under agitation in water and later with PBS to remove any unbound AR. The scaffolds were decolorized using 10% cetylpiridinium chloride in sodium hydrogen phosphate buffer at pH 7 for 20 min under agitation. The supernatant containing the dye was collected and measured in a microplate reader at 564 nm. Control

samples for each type of geometry without cells were included, maintained over the culture period, stained, and decolorized. The supernatant of the control group was measured and subtracted from the values with cells of each corresponding geometry type. A calibration curve with known AR concentrations was used to determine the AR values.

2.8.3. Cell morphology

Cell morphology was evaluated using SEM and laser scanning confocal microscopy (LSCM; Carl Zeiss LSM 800, Germany). Prior to imaging, the cell-laden scaffolds were rinsed with warm PBS and fixed with 4% paraformaldehyde at room temperature for 20 min. After fixation, the scaffolds were rinsed with PBS three times and stored at 4°C.

Immunocytochemistry was performed to stain and observe the actin filaments and cell nuclei after 1, 7, 14, and 21 days of cell culture. A solution of Alexa Fluor 546 (1:300) in 0.05% Triton X-100 was used to stain the actin filaments for 1 h in the dark. Thereafter, the scaffolds were washed three times with 1 mL PBS containing 20 mM glycine. Finally, DAPI (1:1000) in PBS containing glycine was used to stain cell nuclei for 2 min in the dark. Subsequently, the scaffolds were rinsed three times with 1 mL PBS containing 20 mM glycine and observed under LSCM using 5× and 10× magnification. A stitching covering 7 × 7 mm^2 was observed at 5× magnification to assess the cell coverage of the whole scaffold. One replica per sample type at each time point was used for imaging, in addition to a control group consisting of 5 mm diameter glass coverslips.

Cell morphology after 6 h of adhesion was investigated using SEM. The cells were fixed in 4% paraformaldehyde for 20 min at room temperature, rinsed in PBS three times, and dehydrated based on an ethanol gradient (10%, 30%, 50%, 70%, 90%, and 96%). After dehydration, the scaffolds were left to dry overnight, coated with a carbon-evaporated layer (K950X; EMITECH, France), and observed under the microscope (Neon40 Crossbeam™ Workstation; Carl Zeiss, Germany).

2.9. Statistical analysis

All data are represented as mean ± standard deviation (*SD*) or as a single value for porosity analysis and XRD. Statistical analysis was performed using SPSS Statistics 24.0 software (IBM, USA). For statistical differences ($p < 0.05$) between more than two groups of different geometries, one-way analysis of variance (ANOVA) with post-hoc Tukey or Tamhane (depending on the homogeneity of variances) was performed when normal distribution was observed; a Kruskal–Wallis test was conducted otherwise.

3. Results and discussion

3.1. Scaffolds printability

The three different types of TPMS (G, D, and S) designed using MATLAB R2021b with three different porosities (20%, 35%, and 50%) are displayed in Figure 1. The unit cell length was defined as 2.14 cm to fulfill two requirements: (i) to have more than one cell in the radial direction of a 3 mm radius scaffold; and (ii) to have sufficient resolution with a 250-μm nozzle in the radial direction of the G structure. These requirements limited the printability of some structures, as depicted in Figure 1. The resolution of a 250-μm nozzle was insufficient in the Z-direction for D-50%, S-50%, and S-35%, where some floating parts were generated without any material underneath, as one or more adjacent printing layers were completely empty (Figure 1). The layer height was set at 80% of the nozzle size as recommended for DIW inks loaded with ceramics, which was the main constrainer to exporting a feasible G-code.[54] This was more pronounced in the S structures and made printing unfeasible due to the lack of structural integrity. When the rest of the geometries with porosities of 50% or 35% (G-50%, G-35%, and D-35%) were printed, large overhangs caused filament yielding over gaps and partial pore filling. When the porosity was reduced to 20%, all TPMS patterns were successfully printed with clean pores, though the resolution was limited by the filament diameter. Hence, TPMS printing using DIW with a 250-μm nozzle was only possible at the lowest porosity (20%), which is much lower than the 65% or 75% porosities achieved using FDM[19] or SL,[28] respectively.

Different strategies can be explored in future studies to improve the poor resolution. The most obvious approach would be reducing the nozzle size. However, in highly loaded ceramic inks, such as the Pluronic/α-TCP slurry, the nozzle size cannot be arbitrarily reduced, as it is linked to the particle size in the ceramic slurry, and the nozzle diameter should be at least 10 times the largest particle size in the slurry.[55] Likewise, smaller nozzles entail a higher risk of clogging[56] and phase separation during printing. Another strategy would be reducing the layer height, as is usually practiced in FDM. For instance, Diez-Escudero et al. used a layer height of 60 μm with the same nozzle diameter of 250 μm.[19] The dimensional control of the extruded filaments is easier in FDM due to the melting of the ink when passing through the nozzle. For DIW, this should be adjusted by controlling the extrusion flow and/or increasing the printing speed, which minimizes excess material extrusion and stretches and tapers the filament. Additionally, reducing the ceramic load could result in a lower viscosity ink capable of resembling the fused filaments obtained via FDM approaches, but could result in lower mechanical

stability, as it is more difficult for the CDHA nanocrystals to interlock during the hardening process.

3.2. Physicochemical characterization of the scaffolds

Porosity analysis for a 5.70 cm diameter and 4.29 cm height region, corresponding to 2.66 × 2 unit cells in TPMS-based structures, is displayed in Figure 3. The printed OP structure has a total porosity of 20.17%, relatively close to the designed structure in the G-code (i.e., 20%). The total porosity was slightly increased in the TPMS-based structures: 24.51% for G, 26.28% for D, and 24.65% for S. Similar trends were observed for the closed porosity of the TPMS-based scaffolds: 2.63% for OP, 3.35% for G, 3.65%

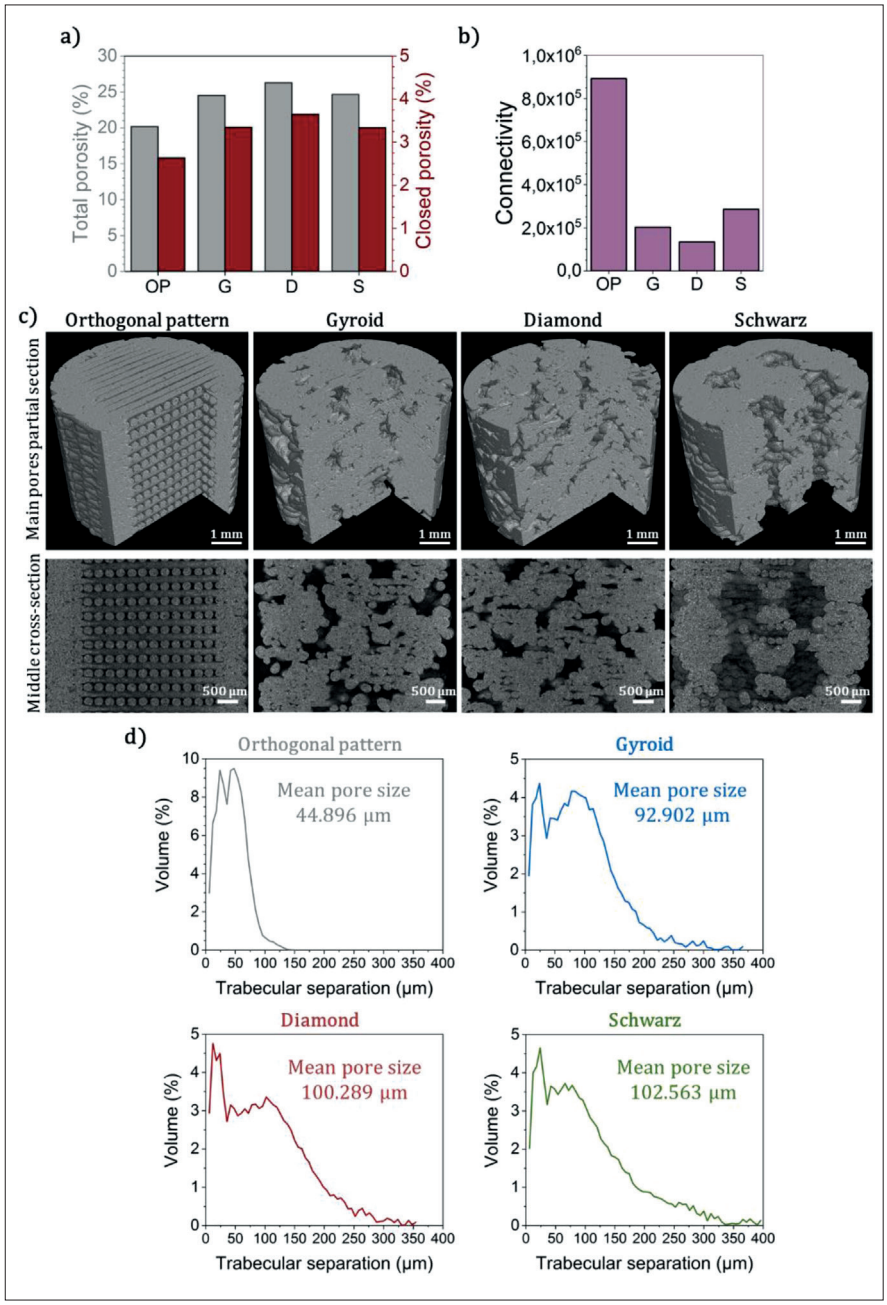

Figure 3. Porosity analysis by computed microtomography of the 3D-printed calcium-deficient hydroxyapatite (CDHA) scaffolds with either a typical orthogonal pattern (OP) or three triply periodic minimal surface (TPMS)-based structures (gyroid [G], diamond [D], and Schwarz [S]) printed with 20% nominal porosity: (a) total and closed porosity; (b) connectivity; (c) binary segmentation of different sections; and (d) trabecular separation distribution. Scale bars: 1 mm (c, top); 500 µm (c, bottom).

for D, and 3.34% for S. The discrepancy in total porosity across different TPMS patterns can be attributed to the difficulty of printing TPMS geometries with a 100% infill using DIW and the formation of some unwanted pores due to incomplete merging of adjacent filaments.

The connectivity of the pores (Figure 3b) measured using CTAn software was 8.93×10^5 for OP, 2.03×10^5 for G, 1.34×10^5 for D, and 2.86×10^5 for S. This is in agreement with the corresponding binary volumes (Figure 3c), where OP has more interconnected pores. However, the pore geometry was significantly different between the OP and TPMS-based structures. For the control, elongated pores, crossing the scaffold in orthogonal directions, with mostly convex surfaces and diameters of <100 μm were formed. In contrast, the TPMS-based patterns resulted in more tortuous porosity with more concave-like surfaces and without a constant diameter, forming significantly larger dimensions in some regions. This increase in pore size was reflected in the trabecular separation distribution (Figure 3d), which is an estimation of pore size distribution as the diameter of the largest sphere that can be fitted completely inside the pore.[57] All geometries had a peak under 40 μm, corresponding to the closed porosity within the ink filaments, generated during the hardening process (i.e., when the Pluronic hydrogel is released, as displayed in Figure 1 and described in previous works[38]) and small gaps between adjacent (not completely merged) filaments, especially in TPMS-based structures with 100% infill. Above this threshold, the trabecular separation for OP was in the range of 40–96 μm, consistent with the distance between filaments designed in the G-code (i.e., 62.5 μm). The second peak included mostly pores in the range of 40–192 μm for G, 40–210 μm for D, and 40–216 μm for S; the mean trabecular separation increased in the same order.

The composition and microstructure of the scaffolds are presented in Figure 4. As expected, according to the XRD analysis through Rietveld refinement (Figure 4a and b), α-TCP was completely hydrolyzed to CDHA after 7 days

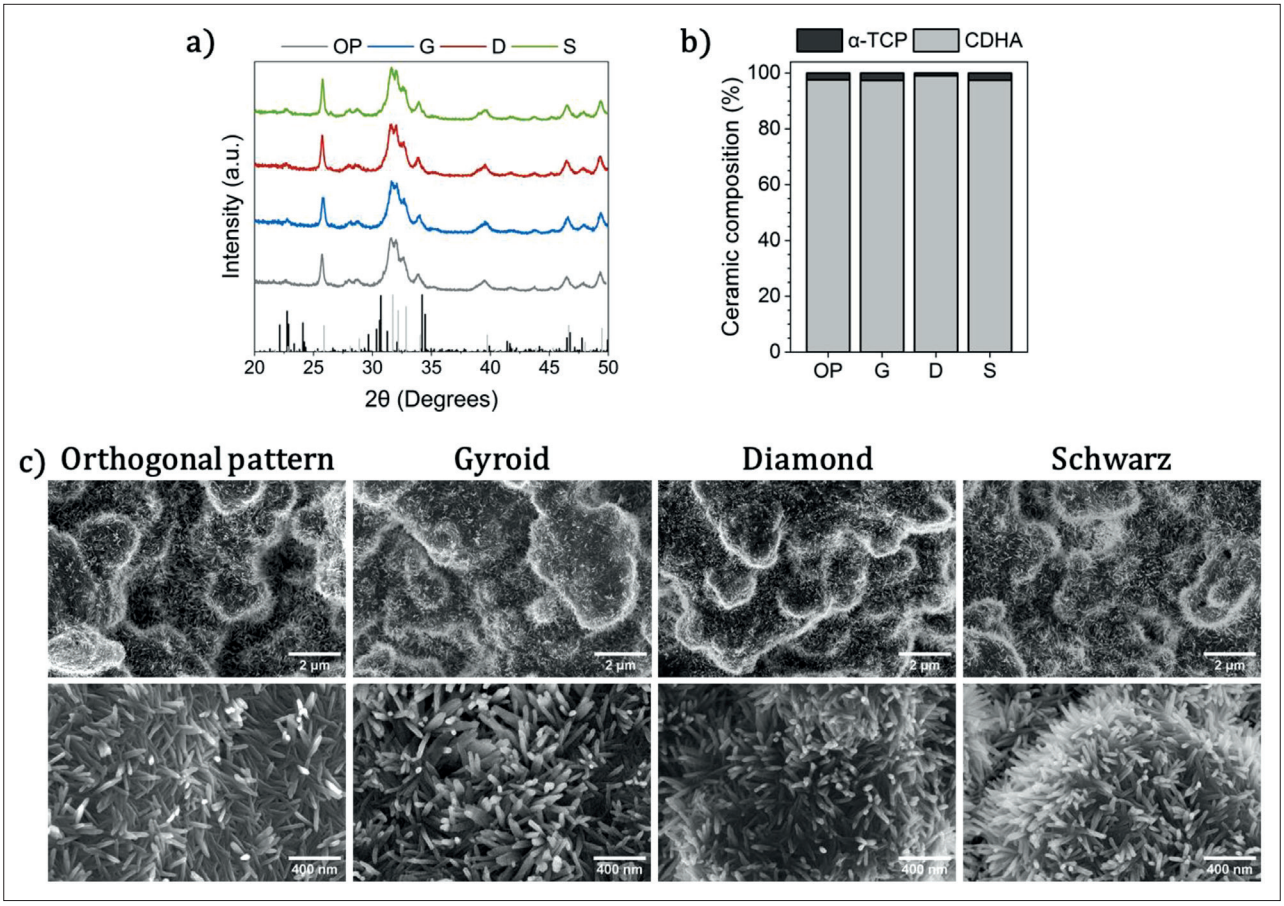

Figure 4. 3D-printed calcium-deficient hydroxyapatite (CDHA) scaffolds after the hardening treatment, with either orthogonal pattern (OP) or the three triply periodic minimal surface (TPMS)-based structures (gyroid [G], diamond [D], and Schwarz [S]): (a) X-ray diffraction patterns, including the theoretical patterns of hydroxyapatite (HA; light grey) and α-tricalcium phosphate (α-TCP; black) in the bottom row; (b) ceramic composition quantification using Profex software; and (c) scanning electron microscope images of the microstructures. Scale bars: 2 μm (c, top) and 400 nm (c, bottom).

of reaction, reaching conversion rates of 97.4–99.0%. Moreover, the SEM images (Figure 4c) implied that CDHA is in the form of an entangled network of needle-shape nanocrystals, as reported in previous works.[37,58,59] Nanocrystal formation was not influenced by the geometry of the 3D-printed scaffolds. Therefore, the excellent osteogenic properties found in previous *in vivo* studies are expected to be maintained in these scaffolds.[47,59]

3.3. Blood permeability

The BMF used for the permeability test exhibited shear-thinning behavior at 25°C, as determined from rheological evaluation (Figure 5a). The viscosity profile was similar to other BMFs consisting of xanthan gum and glycerol.[53,60,61] However, the viscosity of BMF used in this study was slightly higher than that of the standard human blood with a normal hematocrit level at 37°C, i.e., approximately 0.01 Pa·s at a shear rate of 10 s^{-1} versus 0.003 Pa·s at a shear rate of 100 s^{-1}.[61,62] Given the good correlation between the viscosity of the prepared BMF at 25°C and the human blood at 37°C.

The pore architecture of the scaffolds printed using TPMS patterns resulted in a significant increase in blood permeability through the longitudinal axis, in comparison with OP. A 5-, 22-, and 65-fold increase was reported for the D, G, and S structures, respectively (Figure 5b). These increases would facilitate the transport of nutrients and cells,

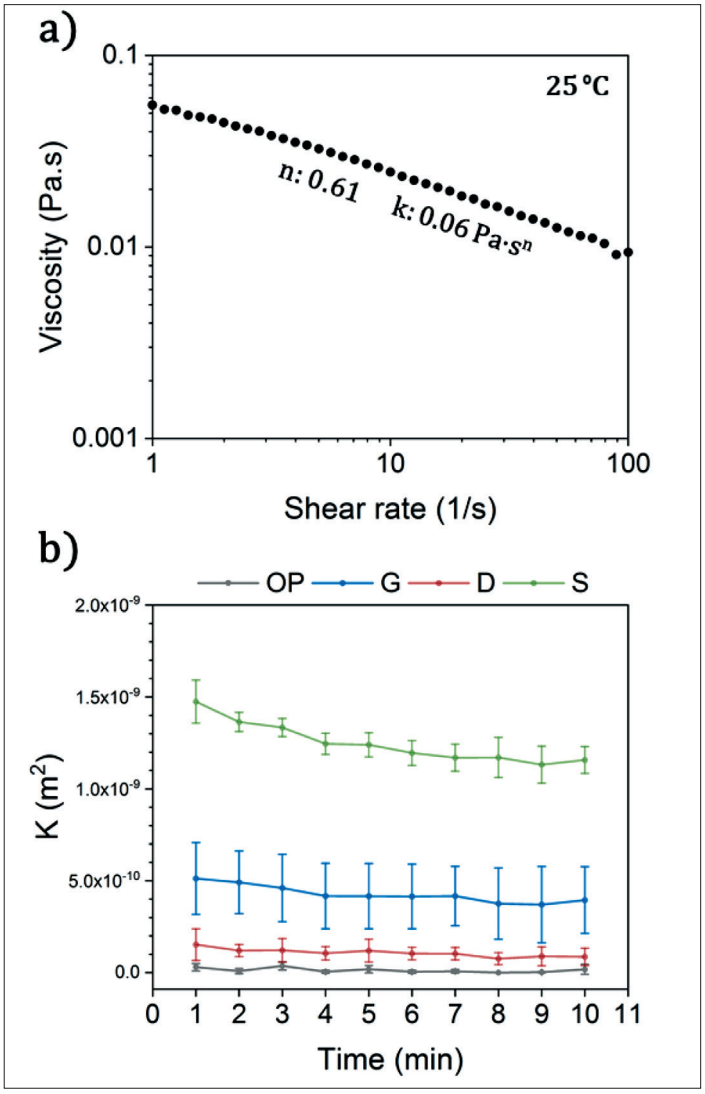

Figure 5. Blood permeability results. (a) Viscosity versus the shear rate of the blood mimicking fluid used for blood permeability study; (b) blood permeability (K) of 3D-printed calcium-deficient hydroxyapatite (CDHA) scaffolds with either a typical orthogonal pattern (OP) or three triply periodic minimal surface (TPMS)-based structures (gyroid [G], diamond [D], and Schwarz [S]) printed with a nominal porosity of 20%. Abbreviations: n, flow behaviour index; k, flow consistency parameter.

as well as waste removal. The pronounced increase in the S structure can be associated with the larger, vertical pores present in the structure. These results are in agreement with Blanquer et al., where the S structure exhibited the highest permeability among eight different TPMS structures.[14] Moreover, the three structures analyzed in this study—(G, D, and S -) displayed greater permeability than other geometries reported in the literature.[14] In contrast, Diez-Escudero et al. obtained the lowest permeability value for the S structure.[19] The direct comparison of our results to those in literature can be challenging due to the hydrophilic nature of CDHA compared to more hydrophobic surfaces, such as polylactic acid or other polymers. Additionally, other parameters, such as the flow rate applied in the permeability measurements, are also likely to contribute to the observed differences.[20]

3.4. Mechanical properties in compression

The results of the uniaxial compression test are presented in Figure 6. The compressive strength was lower for scaffolds printed with TPMS patterns compared to those printed with OP (Figure 6a and c(i)) despite having similar porosities, i.e., 14.22 ± 2.20 MPa for OP, 6.60 ± 1.03 MPa for G, 5.31 ± 0.66 MPa for D, and 9.60 ± 1.36 MPa for S. This could be attributed to the alignment of the OP structure, where the filament crossovers are piled up in load-supporting columns. In contrast, while vertical pores are also present in the S geometry, it has fewer pores with variably sized diameters along the longitudinal axis, resulting in a small load-bearing section when the pores reach their maximum diameter. Likewise, the pore structure observed in micro-CT is more complex for the G and D geometries. These pores have a helicoidal shape, with small connections between layers, resulting in significantly lower compressive strength. The D scaffold had the lowest strength, slightly lower than G, in consonance with its highest porosity. No statistically significant differences in elastic modulus were observed among OP (754.30 ± 270.65 MPa), G (475.91 ± 64.27 MPa), and S (658.69 ± 172.83 MPa) structures (Figure 6c2), whereas the D geometry exhibited a significantly lower elastic modulus of 371.63 ± 87.74 MPa.

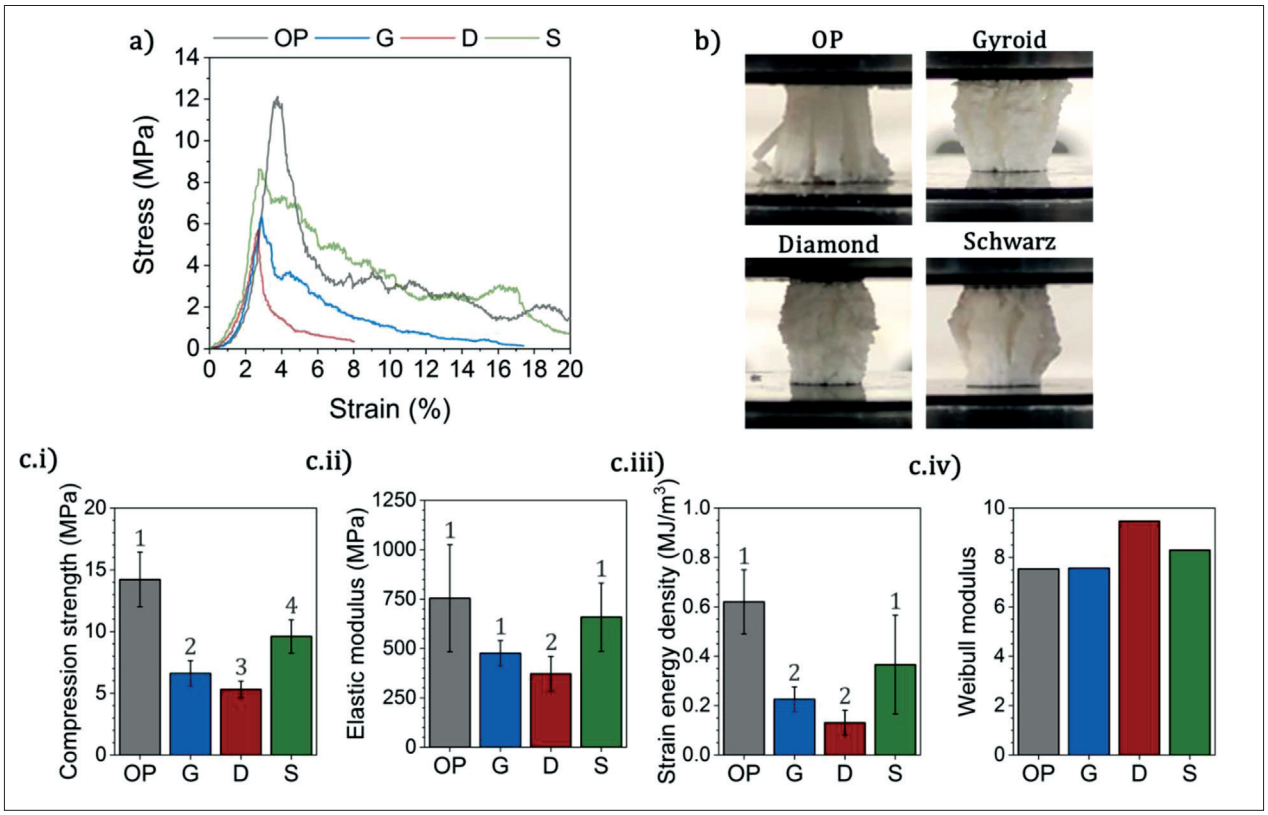

Figure 6. Compression testing of 3D-printed calcium-deficient hydroxyapatite (CDHA) scaffolds with a typical orthogonal pattern (OP) and the three triply periodic minimal surface (TPMS)-based structures (gyroid [G], diamond [D], and Schwarz [S]). (a) Stress versus strain curves. (b) Scaffold breaking process. (c) Compression parameters: (c1) strength, (c2) elastic modulus, (c3) strain energy density, and (c4) Weibull modulus. Different numbers indicate statistically significant differences between each scaffold geometry. *$p < 0.05$, **$p < 0.01$.

The strain energy density (SED) displayed in Figure 6c3 indicates the toughness of the scaffolds, i.e., the energy required for scaffold breakage normalized by the external scaffold volume. The OP scaffold reported the highest SED (0.62 ± 0.13 MJ/m^3), followed by the S geometry (0.37 ± 0.20 MJ/m^3), with no statistically significant difference between them. The OP scaffold was broken upon column splitting (Figure 6b), consistent with the critical fracture points identified from a finite element simulation study,[63] and the breakage was more abrupt than the progressive compaction observed for the S scaffolds. The SED for the G and D scaffolds was significantly lower at 0.23 ± 0.05 and 0.13 ± 0.05 MJ/m^3, respectively, similar to the trend observed for compressive strength, though no significant differences were observed between them. Moreover, their breaking mechanism was more similar to the S structure than to the OP, i.e., without any abrupt breakage. Finally, the Weibull modulus was not affected by pore architecture (Figure 6c (iv)).

Comparing our results with those of other studies is challenging due to the high dependence on material, porosity, and manufacturing process. For instance, utilizing a sintering process to harden the green body in CaP scaffolds results in significantly enhanced mechanical properties compared to scaffolds produced via a biomimetic route (similar to this study) due to microstructural differences.[37,64] However, two studies focusing on TPMS primarily composed of CaP materials can be compared to the present study. Sintered hydroxyapatite (HA) G structures with 10% åkermanite were manufactured by Shi et al. through SL technology, resulting in a slightly lower compressive strength (≈2 MPa) and elastic modulus (≈0.3 GPa) than the biomimetic G structures in the present study, despite having twice the porosity.[30] In addition, a twofold improvement in the mechanical properties was achieved by introducing radial porosity gradients from 50% to 80%, closely mimicking the natural anisotropy of bone. Likewise, Zhang et al. produced six different TPMS structures (including G, D, and S structures) of pure HA using SL technology coupled with a high-temperature sintering process.[28] Between the G, D, and S structures, the D structure exhibited the highest compressive strength (≈110 MPa), followed by the S (≈90 MPa), and G (≈25 MPa) structures. However, the results are inconclusive due to differing porosities, which resulted from unequal shrinkage during sintering, i.e., ≈35% for G, ≈45% for D, and ≈55% for S structures. Notably, the absolute values between these studies and our results cannot be directly compared as the layer height and resolution are also significantly different between SL and DIW printing. Nonetheless, the biomimetic approach adopted in the present study avoided scaffold shrinkage, which mitigated subsequent dimensional variations.[39]

3.5. *In vitro* study

The results of SaOs-2 cell adhesion on the different scaffolds are presented in Figure 7a. The seeding efficiency for all scaffolds is low, especially for the OP scaffold, which is typical of porous scaffolds.[65,66] In addition, CDHA is known to promote ionic exchange due to its high bioactivity, which reduces cell adhesion in static conditions.[67] Among the different TPMS-based scaffolds, significant differences were observed for G and D geometries compared to OP (Figure 7a). A similar trend was observed after a day of culture, and similar cell proliferation was reported for all the scaffolds on days 1, 7, and 14 (Figure 7b). Statistically significant differences were observed only on day 21, where cell proliferation was higher in the TPMS-based scaffolds compared to OP scaffolds.

Regarding cell differentiation, higher ALP activity was observed on day 1 for all TPMS-based structures compared to OP; the ALP activity for all TPMS-based structures was relatively similar to OP structure on day 7; the ALP activity for G and D structures was higher than the OP structure on day 14 (Figure 7c). At the end of the culture period (day 21), all TPMS-based scaffolds reported similar ALP levels, which were higher than the OP scaffold but lower than the control.

Mineralization was measured via AR quantification after 14 days (Figure 7d). Similarly, mineralization was highest for the G structure, followed by the D structure. No differences were observed between the S and OP structures, both of which were slightly higher than the control. After 21 days, G and D structures displayed similar values, with the S structure exhibiting a significant increase from its value on day 14. Notably, the high ALP levels in the control samples did not result in increased mineralization. The natural tendency of high ALP levels promoting mineralization may be affected by other factors. Topographical or compositional aspects could play a role, but further studies are warranted to clarify their effects on cell maturation. CaP is known to be more bioactive and cell-stimulating substrates compared to inert cover glass, providing biochemical and physical cues, including ionic fluctuations, absent in the glass substrate. For example, the measured intracellular ALP values do not directly translate to ALP release, as the concentrations of calcium and phosphate in the medium, mediated by a CaP scaffold, affect ALP release from SaOS-2 cells.[68] In contrast, differentiation in the control samples is confluent-induced, i.e., depending on the cell density, which can be more variable and slower.[69] Regardless of the presence of ALP protein, subsequent mineralization is assumed to be triggered by enzymatic hydrolysis, especially in *in vitro* environments.[70] Nevertheless, the presence of concavities

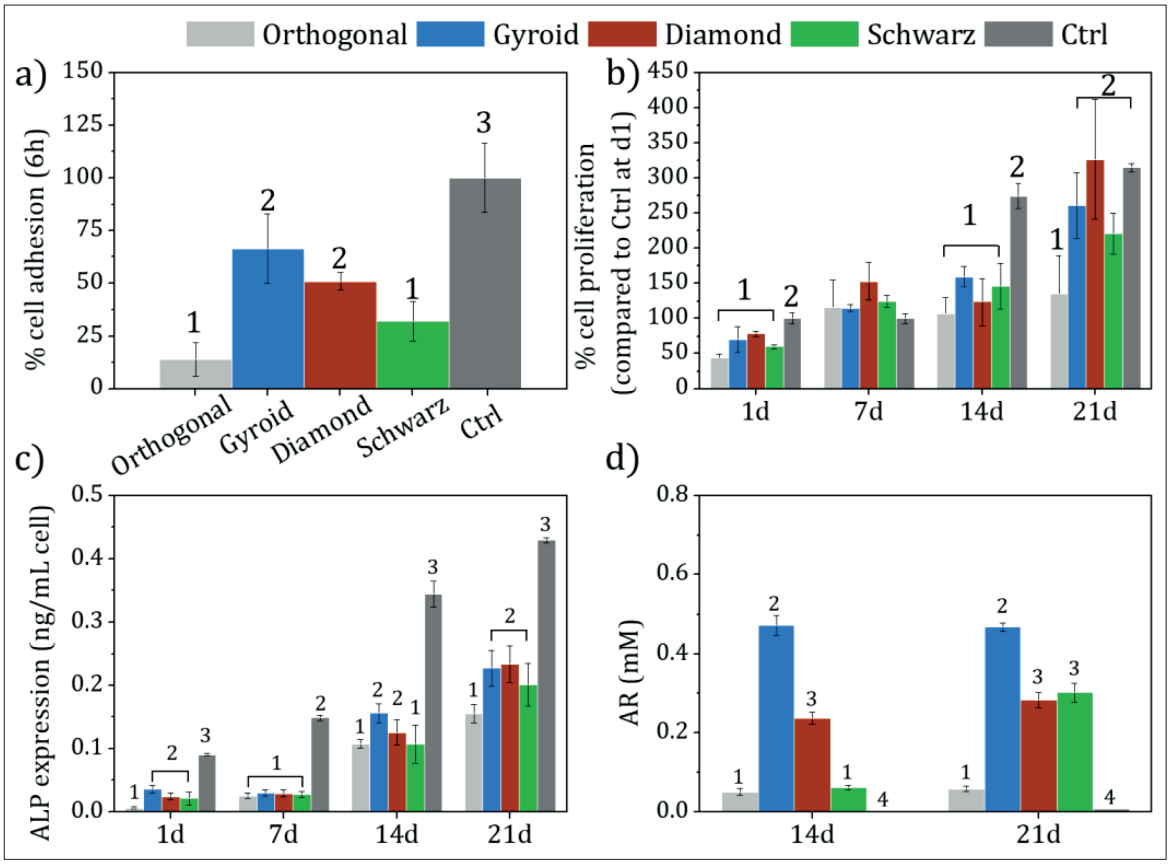

Figure 7. SaOs-2 pre-osteoblast cell cultures on the 3D-printed calcium-deficient hydroxyapatite (CDHA) scaffolds with either a typical orthogonal pattern (OP) or the three triply periodic minimal surface (TPMS)-based structures (gyroid [G], diamond [D], and Schwarz [S]), and the well plate as the control (Ctrl). (a) Percentage of cell adhesion after 6 h. (b) Percentage of cell proliferation at different time points compared to the control sample on day 1 (d1). (c) Cell differentiation, in terms of alkaline phosphatase (ALP) expression, over 21 days. (d) Mineralization quantified by Alizarin Red (AR) staining after 14 and 21 days. (Different numbers indicate statistically significant differences between the different geometries at each specific time point; $p < 0.05$). *$p < 0.05$, **$p < 0.01$.

derived from the TPMS-based pattern enhanced osteoblastic (OB) maturation, as observed from the ALP and AR measurements, compared to the conventional OP structure, achieving the main objective of our study.

Overall, all TPMS-based geometries outperformed OP scaffolds *in vitro*, consistent with Zhang et al., who reported enhanced cell adherence and retention, along with increased osteogenic marker expression, on sintered HA scaffolds with TPMS structures compared to OP structures.[28] Likewise, Bianchi et al.[71] and Urquia Edreira et al.[72] reported that bone mineralization on CaP disks preferentially begins within hemispherical concavities, as the pore concavities and layered structures present in the TPMS-based scaffolds favor cell retention during seeding, facilitating cell confinement, and creating a conducive microenvironment for cell differentiation and mineralization.[8]

The morphology of the attached cells after 6 h is displayed in Figure 8. In the OP structure, only a few cells were observed, indicating a low adhesion rate. In addition, most of these cells had an elongated morphology, bridging between adjacent filaments. Similar morphologies were observed by Graziano et al., where the cells were seeded on adjacent HA chips with convex surfaces and deep clefts between them, with cells bridging between granules and having minimal contact between the membrane and the surface.[8] Cell bridging in the OP structure is possible due to the short distance between filaments (~60 μm). The cells adopted a spread morphology only in the small concave-like regions created in the intersection between filaments in the OP scaffold. In contrast, greater cell spreading was observed in the TPMS-based geometries, more significantly in the concave regions.

To further investigate the cell coverage and density on the scaffolds, confocal microscopy was used. Stitching of the scaffolds at the different time points correlated with cell quantification (Figure 9). On day 1, full cell

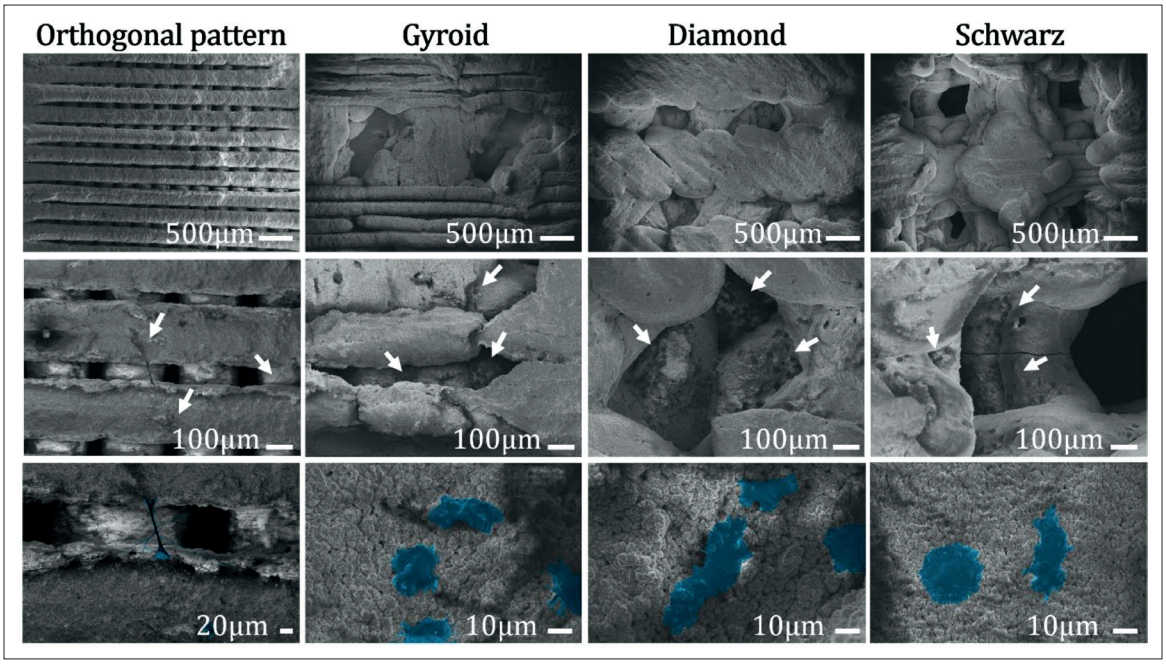

Figure 8. Scanning electron microscope images representing the adhesion of SaOs-2 pre-osteoblastic cells on the 3D-printed calcium-deficient hydroxyapatite (CDHA) scaffolds with different pore architectures after 6 h. Cells are colored in blue; white arrows indicate cell clusters found on the filaments.

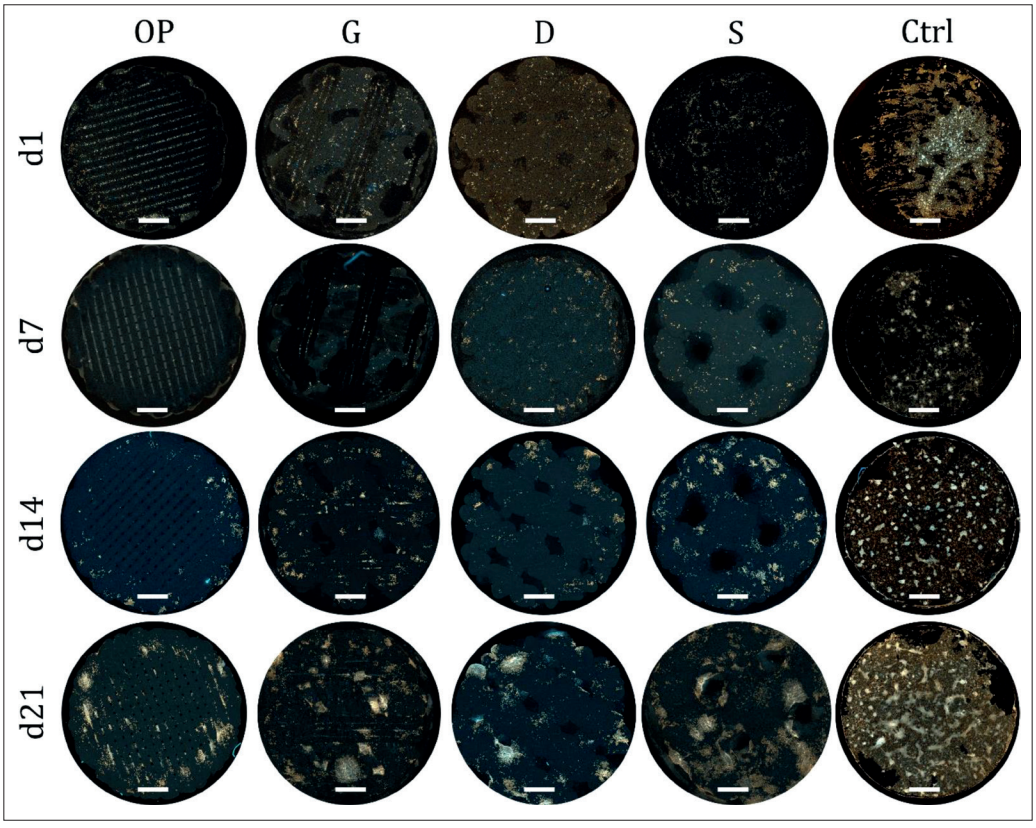

Figure 9. Confocal microscopy images of the full scaffold area (7 × 7 mm) at 5× magnification, displaying the cell density in the surface layer. Actin filaments appear in orange and cell nuclei in blue for each geometry on days 1, 7, 14, and 21. Scale bars: 1 mm. Abbreviations: Ctrl, Control; D, Diamond; G, Gyroid; OP, Orthogonal pattern; S, Schwarz.

coverage was observed of the surface of the glass cover slips used as control. In the OP structure, no cells were observed on the upper layer, but abundant cells were found in the underlying layer. In contrast, TPMS-based architectures displayed well-distributed cells over the scaffolds' surface. After 7 and 14 days, the cells started to aggregate, a common behavior of SaOs-2 cells, which was more prominent after day 14. After 14 days, OP samples displayed only a few cells, while the G and S structures featured more homogeneously distributed cells than the D structure. After 21 days, large areas of the scaffolds were covered with cells. Cell aggregates were abundant in the scaffolds' outer perimeter of the D scaffold. The center and perimeter of the G and S scaffolds displayed homogeneous cell coverage. Notably, one replicate was studied using laser scanning confocal microscopy (LSCM), which revealed that cell morphology correlates with cell quantification. Nonetheless, the formation of cell aggregates should be further studied.

Higher magnification images featuring cell morphology and spreading at all time points are displayed in Figures 10 and 11. On day 1, the cells had a round morphology on all printed scaffolds, and well-distributed actin filaments in highly spread cells were visible only on the control samples. Cell spreading increased over time, leading to full cell coverage after 14 days, especially on the concave surfaces of D and S scaffolds. At the end of the culture period, greater spreading was observed on the printed struts in the

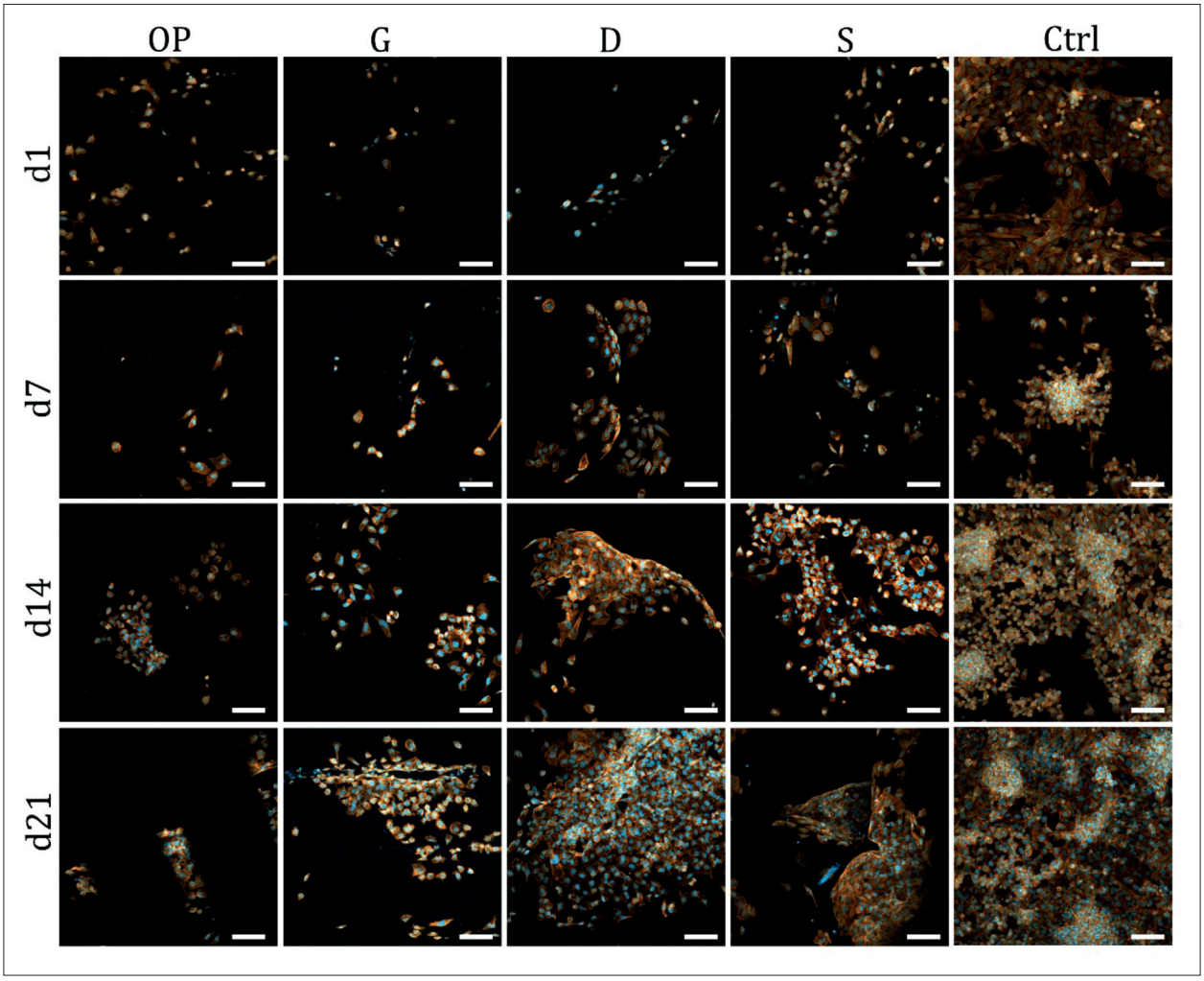

Figure 10. Confocal microscopy images obtained at 10× magnification, displaying the cell morphology and spreading. Actin filaments stained with phalloidin appear in orange and cell nuclei stained with DAPI in blue for each scaffold geometry on days 1, 7, 14, and 21. Scale bars: 100 μm. Abbreviations: Ctrl, Control; D, Diamond; G, Gyroid; OP, orthogonal pattern; S, Schwarz.

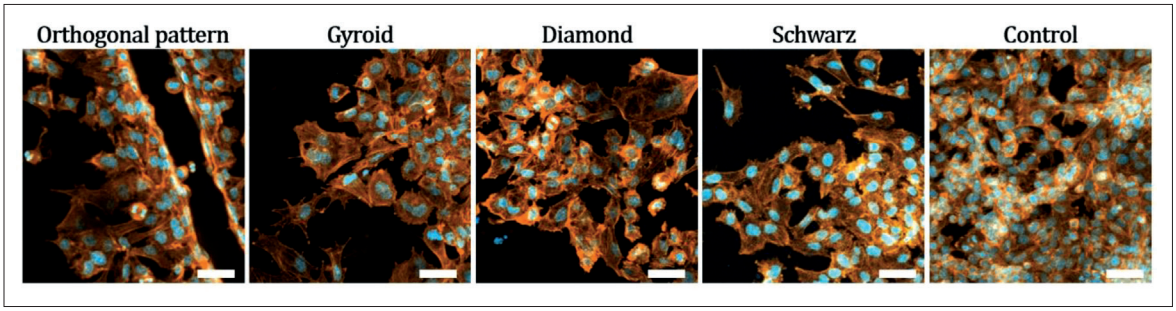

Figure 11. Confocal microscopy images depicting cell spreading, actin filaments in the cytoskeleton, and nuclei after 21 days of cell culture. Scale bars: 50 μm. Magnification: 25×.

TPMS-based structures, with cells displaying healthy cytoskeletons (Figure 11). Conversely, the OP scaffolds featured cells in the underlying filaments, with lesser spreading and density.

4. Conclusion

In this work, we developed and evaluated a new strategy to improve the biological performance of 3D-printed biomimetic HA scaffolds fabricated using DIW. Concave pores were formed on the scaffolds by printing TPMS patterns with a reactive self-hardening ink. Despite limitations in printing parameters, such as nozzle size, layer height, and printing speed, due to the rheology of highly loaded ceramic pastes and ceramic particle size, scaffolds with 20% porosity were successfully printed with G, D, and S patterns. Unlike the OP scaffold, TPMS scaffolds exhibited an interconnected porosity with mostly concave surfaces. Although the complexity of these structures reduced their mechanical properties (i.e., compressive strength), their corresponding blood permeability was enhanced (i.e., for cell colonization, nutrient supply, and waste removal). Moreover, the *in vitro* response of SaOs-2 pre-OB cells demonstrated cell sensitivity to pore geometry, as the presence of concavities promotes cell adhesion, proliferation, differentiation, and mineralization in comparison with the surface of OP structures. Despite these preliminary *in vitro* results suggesting enhanced cell performance with concave surfaces, further biological characterization should be conducted, including cell morphology and migration studies to elucidate the mechanism behind the enhanced bioactivity. While the tested porosity ranges demonstrated a positive effect on *in vitro* biological response, further improvements are required to incorporate higher porosities that can promote angiogenesis *in vivo*.

Acknowledgments

The authors are grateful to Judit Buxadera and Trifon Todorov for their technical assistance with the micro-CT and SEM, respectively.

Funding

This work was supported by the European Research Council (ERC; grant agreement number 101055053 [BAMBBI]), the Spanish Ministry of Science and Innovation (project PID2019-103892RB-I00/AEI/10.13039/501100011033 and FPU scholarship of L.d.M.B), and by AM4Life Competence Centre in Additive Manufacturing for the Life Sciences through Sweden's Innovation Agency VINNOVA (project number 2019-00029). This work is part of Maria de Maeztu Units of Excellence Programme CEX2023-001300-M / funded by MCIN/AEI / 10.13039/501100011033. A.D.E. acknowledges the Spanish Ministry of Universities for support through the Maria Zambrano fellowship and M.P.G the Generalitat de Catalunya for the ICREA Academia Award.

Conflict of interest

The authors declare no conflict of interest.

Author contributions

Conceptualization: Laura del-Mazo-Barbara, Morteza Aramesh, Cecilia Persson, Maria-Pau Ginebra

Formal analysis: Laura del-Mazo-Barbara, Anna Diez-Escudero

Funding: Cecilia Persson, Maria-Pau Ginebra

Investigation: Laura del-Mazo-Barbara, Anna Diez-Escudero, Irene Lodoso-Torrecilla

Methodology: Laura del-Mazo-Barbara, Anna Diez-Escudero
Writing - original draft: Laura del-Mazo-Barbara.
Writing - review & editing: Anna Diez-Escudero, Irene Lodoso-Torrecilla, Morteza Aramesh, Cecilia Persson, Maria-Pau Ginebra

Ethics approval and consent to participate

Not applicable

Consent for publication

Not applicable

Availability of data

All reported data are available upon reasonable request to the corresponding author.

Further disclosure

Part of this work was presented in the 2022 Young Ceramist Additive Manufacturing (yCAM) forum and the 33rd Annual Conference of the European Society for Biomaterials (ESB 2023).

References

1. Kalita SJ, Bose S, Hosick HL, Bandyopadhyay A. Development of controlled porosity polymer-ceramic composite scaffolds via fused deposition modeling. *Mater Sci Eng C*. 2003;23:611-620. doi: 10.1016/S0928-4931(03)00052-3
2. Bohner M, Galea L, Doebelin N. Calcium phosphate bone graft substitutes: failures and hopes. *J Eur Ceram Soc*. 2012;32:2663-2671. doi: 10.1016/j.jeurceramsoc.2012.02.028
3. Perez RA, Mestres G. Role of pore size and morphology in musculo-skeletal tissue regeneration. *Mater Sci Eng C*. 2016;61:922-939. doi: 10.1016/J.MSEC.2015.12.087
4. Habraken W, Habibovic P, Epple M, Bohner M. Calcium phosphates in biomedical applications: materials for the future? *Mater Today*. 2016;19:69-87. doi: 10.1016/J.MATTOD.2015.10.008
5. Bose S, Vahabzadeh S, Bandyopadhyay A. Bone tissue engineering using 3D printing. *Mater Today*. 2013;16:496-504. doi: 10.1016/J.MATTOD.2013.11.017
6. Thavornyutikarn B, Chantarapanich N, Sitthiseripratip K, Thouas GA, Chen Q. Bone tissue engineering scaffolding: computer-aided scaffolding techniques. *Prog Biomater*. 2014;3:61-102. doi: 10.1007/s40204-014-0026-7
7. Bohner M, Baroud G, Bernstein A, et al. Characterization and distribution of mechanically competent mineralized tissue in micropores of β-tricalcium phosphate bone substitutes. *Mater Today*. 2017;20:106-115. doi: 10.1016/j.mattod.2017.02.002
8. Graziano A, D'Aquino R, Angelis MGC-D, et al. Scaffold's surface geometry significantly affects human stem cell bone tissue engineering. *J Cell Physiol*. 2008;214:166-172. doi: 10.1002/jcp.21175
9. Barba A, Diez-Escudero A, Maazouz Y, et al. Osteoinduction by foamed and 3D-printed calcium phosphate scaffolds: effect of nanostructure and pore architecture. *ACS Appl Mater Interfaces*. 2017;9:41722-41736. doi: 10.1021/acsami.7b14175
10. Barba A, Diez-Escudero Y, Espanol M, et al. Impact of biomimicry in the design of osteoinductive bone substitutes: nanoscale matters. *ACS Appl Mater Interfaces*. 2019; 11:8818–8830. doi: 10.1021/acsami.8b20749
11. Ginebra MP, Espanol M, Montufar EB, Perez RA, Mestres G. New processing approaches in calcium phosphate cements and their applications in regenerative medicine. *Acta Biomater*. 2010;6:2863-2873. doi: 10.1016/J.ACTBIO.2010.01.036
12. Jinnai H, Watashiba H, Kajihara T, Nishikawa Y, Takahashi M, Ito M. Surface curvatures of trabecular bone microarchitecture. *Bone*. 2002;30:191-194. doi: 10.1016/S8756-3282(01)00672-X
13. Shen M, Li Y, Lu F, et al. Bioceramic scaffolds with triply periodic minimal surface architectures guide early-stage bone regeneration. *Bioact Mater*. 2023;25:374-386. doi: 10.1016/j.bioactmat.2023.02.012
14. Blanquer SBG, Werner M, Hannula M, et al. Surface curvature in triply-periodic minimal surface architectures as a distinct design parameter in preparing advanced tissue engineering scaffolds. *Biofabrication*. 2017;9:025001. doi: 10.1088/1758-5090/aa6553
15. Restrepo S, Ocampo S, Ramirez JA, Paucar C, Garcia C. Mechanical properties of ceramic structures based on Triply Periodic Minimal Surface (TPMS) processed by 3D printing. *J Phys Conf Ser*. 2017;935:0-6.v doi: 10.1088/1742-6596/935/1/012036
16. Montazerian H, Mohamed MGA, Montazeri MM, et al. Permeability and mechanical properties of gradient porous PDMS scaffolds fabricated by 3D-printed sacrificial templates designed with minimal surfaces. *Acta Biomater*. 2019;96:149-160. doi: 10.1016/j.actbio.2019.06.040
17. Montazerian H, Zhianmanesh M, Davoodi E, Milani AS, Hoorfar M. Longitudinal and radial permeability analysis of additively manufactured porous scaffolds: effect of pore shape and porosity. *Mater Des*. 2017;122:146-156. doi: 10.1016/j.matdes.2017.03.006

18. Ali D, Ozalp M, Blanquer SBG, Onel S. Permeability and fluid flow-induced wall shear stress in bone scaffolds with TPMS and lattice architectures: a CFD analysis. *Eur J Mech B/Fluids*. 2020;79:376-385. doi: 10.1016/j.euromechflu.2019.09.015

19. Diez-Escudero A, Harlin H, Isaksson P, Persson C. Porous polylactic acid scaffolds for bone regeneration: a study of additively manufactured triply periodic minimal surfaces and their osteogenic potential. *J Tissue Eng*. 2020;11:2041731420956541. doi: 10.1177/2041731420956541

20. Castro APG, Pires T, Santos JE, Gouveia BP, Fernandes PR. Permeability versus design in TPMS scaffolds. *Materials (Basel)*. 2019;12:1313. doi: 10.3390/ma12081313

21. Castro APG, Ruben RB, Gonçalves SB, Pinheiro J, Guedes JM, Fernandes PR. Numerical and experimental evaluation of TPMS Gyroid scaffolds for bone tissue engineering. *Comput Methods Biomech Biomed Engin*. 2019;22: 567-573. doi: 10.1080/10255842.2019.1569638

22. Maskery I, Sturm L, Aremu AO, et al. Insights into the mechanical properties of several triply periodic minimal surface lattice structures made by polymer additive manufacturing. *Polymer (Guildf)*. 2018; 152:62–71. doi: 10.1016/j.polymer.2017.11.049

23. Yan C, Hao L, Hussein A, Young P. Ti-6Al-4V triply periodic minimal surface structures for bone implants fabricated via selective laser melting. *J Mech Behav Biomed Mater*. 2015;51:61-73. doi: 10.1016/j.jmbbm.2015.06.024

24. Bobbert FSL, Lietaert K, Eftekhari AA, et al. Additively manufactured metallic porous biomaterials based on minimal surfaces: a unique combination of topological, mechanical, and mass transport properties. *Acta Biomater*. 2017;53:572-584. doi: 10.1016/j.actbio.2017.02.024

25. Kleger N, Fehlmann S, Lee SS, et al. Light-based printing of leachable salt molds for facile shaping of complex structures. *Adv Mater*. 2022;34(32):e2203878. doi: 10.1002/adma.202203878

26. Tikhonov A, Evdokimov P, Klimashina E, et al. Putlayev, stereolithographic fabrication of three-dimensional permeable scaffolds from CaP/PEGDA hydrogel biocomposites for use as bone grafts. *J Mech Behav Biomed Mater*. 2020;110:103922. doi: 10.1016/j.jmbbm.2020.103922

27. Paré A, Charbonnier B, Tournier P, et al. Tailored three-dimensionally printed triply periodic calcium phosphate implants: a preclinical study for craniofacial bone repair. *ACS Biomater Sci Eng*. 2020;6:553-563. doi: 10.1021/acsbiomaterials.9b01241

28. Zhang Q, Ma L, Ji X, et al. High-strength hydroxyapatite scaffolds with minimal surface macrostructures for load-bearing bone regeneration. *Adv Funct Mater*. 2022;32:1-12. doi: 10.1002/adfm.202204182

29. Bouakaz I, Drouet C, Grossin D, Cobraiville E, Nolesn G. Hydroxyapatite 3D-printed scaffolds with Gyroid-TPMS porous structure: fabrication and in vivo pilot study in sheep. *Acta Biomater*. 2023;170:580-595. doi: 10.1016/j.actbio.2023.08.041

30. Deng ZL, Pan MZ, Bin Hua S, Wu JM, Zhang XY, Shi YS. Mechanical and degradation properties of triply periodic minimal surface (TPMS) hydroxyapatite & akermanite scaffolds with functional gradient structure. *Ceram Int*. 2023;49:20808–20816. doi: 10.1016/j.ceramint.2023.03.213

31. Roohani I, Entezari A, Zreiqat H. Liquid crystal display technique (LCD) for high resolution 3D printing of triply periodic minimal surface lattices bioceramics. *Addit Manuf*. 2023;74:103720. doi: 10.1016/j.addma.2023.103720

32. Bin Hua S, Yuan X, Wu JM, et al. Digital light processing porous TPMS structural HA & akermanite bioceramics with optimized performance for cancellous bone repair. *Ceram Int*. 2022;48:3020-3029. doi: 10.1016/j.ceramint.2021.10.003

33. Oftadeh R, Perez-Viloria M, Villa-Camacho JC, Vaziri A, Nazarian A. Biomechanics and mechanobiology of trabecular bone: a review. *J Biomech Eng*. 2015;137:1–15. doi: 10.1115/1.4029176

34. del-Mazo-Barbara L, Ginebra MP. Rheological characterisation of ceramic inks for 3D direct ink writing: a review. *J Eur Ceram Soc*. 2021;41:18-33. doi: 10.1016/J.JEURCERAMSOC.2021.08.031

35. Raymond Y, Johansson L, Thorel E, Ginebra MP. Translation of three-dimensional printing of ceramics in bone tissue engineering and drug delivery. *MRS Bull*. 2022;47:59-69. doi: 10.1557/s43577-021-00259-1

36. Maazouz Y, Montufar EB, Guillem-Marti J, et al. Robocasting of biomimetic hydroxyapatite scaffolds using self-setting inks. *J Mater Chem B*. 2014;2:5378-5386. doi: 10.1039/C4TB00438H

37. Raymond S, Maazouz Y, Montufar EB, et al. Accelerated hardening of nanotextured 3D-plotted self-setting calcium phosphate inks. *Acta Biomater*. 2018;75:451-462. doi: 10.1016/j.actbio.2018.05.042

38. Konka J, Buxadera-Palomero J, Espanol M, Ginebra MP. 3D printing of hierarchical porous biomimetic hydroxyapatite scaffolds: adding concavities to the convex filaments. *Acta Biomater*. 2021;134:744-759. doi: 10.1016/j.actbio.2021.07.071

39. Raymond Y, Bonany M, Lehmann C, et al. Hydrothermal processing of 3D-printed calcium phosphate scaffolds

enhances bone formation in vivo: a comparison with biomimetic treatment. *Acta Biomater*. 20221; 135:671-688.
doi: 10.1016/j.actbio.2021.09.001

40. Raymond Y, Thorel E, Liversain M, Riveiro A, Pou J, Ginebra MP. 3D printing non-cylindrical strands: morphological and structural implications. *Addit Manuf*. 2021;46: 102129.
doi: 10.1016/j.addma.2021.102129

41. Moreno Madrid AP, Vrech SM, Sanchez MA, Rodriguez AP. Advances in additive manufacturing for bone tissue engineering scaffolds. *Mater Sci Eng C*. 2019;100: 631-644.
doi: 10.1016/j.msec.2019.03.037

42. Roopavath UK, Malferrari S, Van Haver A, Verstreken SM, Rath SN, Kalaskar DM. Optimization of extrusion based ceramic 3D printing process for complex bony designs. *Mater Des*. 2019;162:263-270.
doi: 10.1016/j.matdes.2018.11.054

43. Shao H, He J, Lin T, Zhang Z, Zhang Y, Liu S. 3D gel-printing of hydroxyapatite scaffold for bone tissue engineering. *Ceram Int*. 2019;45:1163-1170.
doi: 10.1016/j.ceramint.2018.09.300

44. Wang Y, Chen S, Liang H, Liu Y, Bai J, Wang M. Digital light processing (DLP) of nano biphasic calcium phosphate bioceramic for making bone tissue engineering scaffolds. *Ceram Int*. 2022;48:27681-27692.
doi: 10.1016/j.ceramint.2022.06.067

45. Navarrete-Segado P, Tourbin M, Frances C, Grossin D. Masked stereolithography of hydroxyapatite bioceramic scaffolds: from powder tailoring to evaluation of 3D printed parts properties. *Open Ceram*. 2022;9:100235.
doi: 10.1016/j.oceram.2022.100235

46. Ginebra M-P, Espanol M, Maazouz Y, Bergez V, Pastorino D. Bioceramics and bone healing. *EFORT Open Rev*. 2018;3:173-183.
doi: 10.1302/2058-5241.3.170056

47. Vidal L, Kampleitner C, Krissian S, et al. Regeneration of segmental defects in metatarsus of sheep with vascularized and customized 3D-printed calcium phosphate scaffolds. *Sci Rep*. 2020;10:7068.
doi: 10.1038/s41598-020-63742-w

48. Feng C, Zhang W, Deng C, et al. 3D printing of lotus root-like biomimetic materials for cell delivery and tissue regeneration. *Adv Sci (Weinh)*. 2017;4(12):1700401.
doi: 10.1002/advs.201700401

49. Raymond Y, Lehmann C, Thorel E, et al. 3D printing with star-shaped strands: a new approach to enhance in vivo bone regeneration. *Biomater Adv*. 2022;137:12807.
doi: 10.1016/j.bioadv.2022.212807

50 Moon YW, Choi IJ, Koh YH, Kim C. Porous alumina ceramic scaffolds with biomimetic macro/micro-porous structure using three-dimensional (3-D) ceramic/camphene-based extrusion. *Ceram Int*. 2015;41:12371-12377.
doi: 10.1016/j.ceramint.2015.06.069

51. Minas C, Carnelli D, Tervoort E, Studart AR. 3D printing of emulsions and foams into hierarchical porous ceramics. *Adv Mater*. 2016;28:9993-9999.
doi: 10.1002/adma.201603390

52. Ginebra MP, Fernández E, De Maeyer, et al. Setting reaction and hardening of an apatitic calcium phosphate cement. *J Dent Res*. 1997;76:905-912.
doi: 10.1177/00220345970760041201

53. Brookshier KA, Tarbell JM. Evaluation of a transparent blood analog fluid: aqueous Xanthan gum/glycerin. *Biorheology*. 1993;30:107-116.
doi: 10.3233/BIR-1993-30202

54. Chan SSL, Sesso ML, Franks GV. Direct ink writing of hierarchical porous alumina-stabilized emulsions: rheology and printability. *J Am Ceram Soc*. 2020;103:5554-5566.
doi: 10.1111/jace.17305

55. Seoane-Viaño I, Januskaite P, Alvarez-Lorenzo C, Basit AW, Goyanes A. Semi-solid extrusion 3D printing in drug delivery and biomedicine: personalised solutions for healthcare challenges. *J Control Release*. 2021;332:367-389.
doi: 10.1016/j.jconrel.2021.02.027

56. Franco ESJ, Hunger P, Launey ME, Tomsia AP. Direct-write assembly of calcium phosphate scaffolds using a water-based hydrogel. *Acta Biomater*. 2010;6:218-228.
doi: 10.1016/j.actbio.2009.06.031.Direct-Write

57. Mys K, Varga P, Stockmans F, et al. Quantification of 3D microstructural parameters of trabecular bone is affected by the analysis software. *Bone*. 2021;142:115653.
doi: 10.1016/j.bone.2020.115653

58. Maazouz Y, Montufar EB, Malbert J, Espanol M, Ginebra MP. Self-hardening and thermoresponsive alpha tricalcium phosphate/pluronic pastes. *Acta Biomater*. 2017;49:563-574.
doi: 10.1016/j.actbio.2016.11.043

59. Barba A, Maazouz Y, Diez-Escudero A, et al. Osteogenesis by foamed and 3D-printed nanostructured calcium phosphate scaffolds: effect of pore architecture. *Acta Biomater*. 2018;79:135-147.
doi: 10.1016/j.actbio.2018.09.003

60. Anastasiou AD, Spyrogianni AS, Koskinas KC, Giannoglou GD, Paras SV. Experimental investigation of the flow of a blood analogue fluid in a replica of a bifurcated small artery. *Med Eng Phys*. 2012;34(2):211-218.
doi: 10.1016/j.medengphy.2011.07.012

61. Webb L. Mimicking blood rheology for more accurate modeling in benchtop research. *Pegasus Rev UCF Undergrad Res J*. 2020;12:28-34.
https://stars.library.ucf.edu/urj/vol12/iss1/6

62. Alves MM, Rocha C, Gonçalves MP. Study of the rheological behaviour of human blood using a controlled stress rheometer. *Clin Hemorheol Microcirc*. 2013;53:369-386.
doi: 10.3233/ch-121645

63. Entezari A, Liu NC, Roohani I, et al. On design for additive manufacturing (DAM) parameter and its effects on biomechanical properties of 3D printed ceramic scaffolds. *Mater Today Commun*. 2020;23:101065.
doi: 10.1016/j.mtcomm.2020.101065

64. Miranda P, Pajares A, Saiz E, Tomsia AP, Guiberteau F. Mechanical properties of calcium phosphate scaffolds fabricated by robocasting. *J Biomed Mater Res A*. 2008;85:218-227.
doi: 10.1002/jbm.a.31587

65. Charbonnier B, Manassero M, Bourguignon M, et al. Custom-made macroporous bioceramic implants based on triply-periodic minimal surfaces for bone defects in load-bearing sites. *Acta Biomater*. 2020;109:254-266.
doi: 10.1016/j.actbio.2020.03.016

66. Panzavolta S, Torricelli P, Sturba L, Bracci B, Giardino R, Bigi A. Setting properties and in vitro bioactivity of strontium-enriched gelatin-calcium phosphate bone cements. *J Biomed Mater Res A*. 2008;84:965-972.
doi: 10.1002/jbm.a.31412

67. Sadowska JM, Guillem-Marti J, Ginebra MP. The influence of physicochemical properties of biomimetic hydroxyapatite on the in vitro behavior of endothelial progenitor cells and their interaction with mesenchymal stem cells. *Adv Healthc Mater*. 2019;8(2):e1801138.
doi: 10.1002/adhm.201801138

68. Farley JR, Hall SL, Tanner MA, Wergedal JE. Specific activity of skeletal alkaline phosphatase in human osteoblast-line cells regulated by phosphate, phosphate esters, and phosphate analogs and release of alkaline phosphatase activity inversely regulated by calcium. *J Bone Miner Res*. 1994;9(4):497-508.
doi: 10.1002/jbmr.5650090409

69. Gao L, McBeath R, Chen CS. Stem cell shape regulates a chondrogenic versus myogenic fate through Rac1 and N-cadherin. *Stem Cells*. 2010;28(3):564-572.
doi: 10.1002/stem.308

70. Sugawara Y, Suzuki K, Koshikawa M, Ando M, Iida J. Necessity of enzymatic activity of alkaline phosphatase for mineralization of osteoblastic cells. *Jpn J Pharmacol*. 2002;88(3):262-269.
doi: 10.1254/jjp.88.262

71. Bianchi M, Urquia Edreira ER, Wolke JG, et al. Substrate geometry directs the in vitro mineralization of calcium phosphate ceramics. *Acta Biomater*. 2014;10(2):661-669.
doi: 10.1016/j.actbio.2013.10.026

72. Urquia Edreira ER, Wolke JG, Jansen JA, van den Beucken JJ. Influence of ceramic disk material, surface hemispheres, and SBF volume on in vitro mineralization. *J Biomed Mater Res A*. 2015;103(8):2740-2746.
doi: 10.1002/jbm.a.35406

ACCSCIENCE PUBLISHING

International Journal of Bioprinting

RESEARCH ARTICLE

3D-bioprinted *in vitro* skeletal muscle with pennate fiber architecture to enhance contractile function

Lin Gao [1,2]*, Liuhe Li [1,2], Wenze Wu [1,2], Junnan Feng [1,2], Ziwei Liu[1,2], Jiankang He [1,2], and Dichen Li [1,2]

[1] State Key Laboratory for Manufacturing System Engineering, School of Mechanical Engineering, Xi'an Jiaotong University, Xi'an, Shaanxi, China

[2] National Medical Products Administration (NMPA) Key Laboratory for Research and Evaluation of Additive Manufacturing Medical Devices, Xi'an Jiaotong University, Xi'an, Shaanxi, China

Abstract

Skeletal muscle tissue engineering (SMTE) has important research value and broad applicational prospects in areas such as muscle repair, disease modeling, drug testing, and biohybrid robotics. Despite advances in research on engineered skeletal muscles, it remains challenging to improve their functional performance, especially relatively large-sized muscles. Inspired by pennate muscles with a large force output capacity, a novel *in vitro* skeletal muscle tissue design mimicking the macro and microstructures of the gastrocnemius muscle in frogs was proposed and optimized through simulation. The cell-laden hydrogel was then 3D-bioprinted to fabricate tissues with fusiform geometry and induced microchannels with a pennate angle of 15°. The morphology, cell status, and contraction performance of 3D-bioprinted muscle tissues were evaluated after electrical stimulation, which induced the directional alignment of myotubes. The results indicated that our 3D-bioprinted pennate skeletal muscle tissues exhibited high cell viability (79.89%) and alignment of muscle fibers (51.93%), with a maximum contraction force of 443.085 μN, almost twice the force of 3D-printed parallel muscle tissues in our study. This work will support the exploration of design strategies and rapid manufacturing techniques for next-generation SMTEs with enhanced functional performance.

Keywords: Skeletal muscle; 3D bioprinting; Pennate muscle; Contraction performance

***Corresponding author:**
Lin Gao
(gaolin2013@xjtu.edu.cn)

Citation: Gao L, Li L, Wu W, et al. 3D-bioprinted *in vitro* skeletal muscle with pennate fiber architecture to enhance contractile function. *Int J Bioprint*. 2024;10(6):4371 . doi: 10.36922/ijb.4371

Received: July 29, 2024
Revised: August 22, 2024
Accepted: September 3, 2024
Published Online: September 3, 2024

Copyright: © 2024 Author(s). This is an Open Access article distributed under the terms of the Creative Commons Attribution License, permitting distribution, and reproduction in any medium, provided the original work is properly cited.

Publisher's Note: AccScience Publishing remains neutral with regard to jurisdictional claims in published maps and institutional affiliations.

1. Introduction

Skeletal muscle accounts for approximately 45% of the body's mass and is capable of generating contractile forces for movements of body parts, supporting internal organs, and facilitating vital functions, such as chewing and maintaining homeostasis.[1,2] Severe muscular defects, involving >20% loss of the original mass, invariably result in the loss of innate regenerative capabilities, thereby requiring reconstructive surgical procedures, such as autologous muscle transplantation.[3,4] However, the outcome of current surgical interventions is limited by inadequate innervation, muscle regeneration, and functional recovery, making the treatment of extensive muscle

defect injuries increasingly challenging.[5] Skeletal muscle tissue engineering (SMTE) and regenerative medicine, as significantly effective alternatives to current clinical strategies, have great research value and development potential[6] for replicating the structure and function of natural muscle *in vitro*.[7] To achieve these goals, functionalizing the myogenic capacity of natural muscles in artificial muscles is a primary research focus in this field, especially through the use of advanced materials such as nanomaterials.[8] Moreover, tissue-engineered skeletal muscle can play a role in disease modeling, drug testing, and bio-robotics.[7,9,10] Some examples include *in vitro* models for studying myogenesis and muscle pathology, and preclinical models for drug screening and toxicity testing.[11–13] Additionally, engineered skeletal muscles could also serve as advanced bio-actuators to microrobots due to their controllability and adaptability,[14–19] enabling biomimetic movements, such as crawling[20] and gripping,[21] and promoting the development of self-powered microrobots.[9]

3D bioprinting is a powerful approach to precisely deliver cells, biomaterials, and biological factors to targeted positions. It has great potential for fabricating 3D-customized skeletal muscle tissues with complex microscopic arrangements in a one-step process. For example, 3D bioprinting was applied to precisely deposit mouse myoblasts (C2C12) in a matrix on cantilevers with 85 μm resolution, >90% cell viability, and high reproducibility, and the myotubes became excitable after differentiation.[22] Biomimetic human skeletal muscle constructs were also 3D-bioprinted from mm^2 to cm^2 scale, consisting of tens to hundreds of densely packed long parallel myofiber bundles, thereby demonstrating that 3D-bioprinted skeletal muscle constructs can form multi-layered bundles with aligned myofibers.[23,24] Researchers also validated the feasibility of 3D-printed skeletal muscle tissues to treat critical-sized muscle defect injuries in a rodent model; however, the tissues did not fully support the structural and functional restoration of defected muscles.[22] Furthermore, researchers revealed that neural input into the bioprinted skeletal muscle construct could greatly improve myofiber formation, long-term survival, and neuromuscular junction formation *in vitro*, facilitating rapid innervation and maturation into organized muscle tissue in a rodent model.[25] However, despite significant progress in the development of 3D-engineered skeletal muscle tissues, the contractile forces generated by the engineered skeletal muscle tissues remain low compared to their natural counterparts. Thus, functional skeletal muscle tissue constructs have not yet been fabricated *in vitro*. Since the muscle fiber arrangement is highly relevant to contractile performance and 3D bioprinting is effective in controlling the microstructure of engineered muscle tissues, biofabrication of *in vitro* 3D skeletal muscle tissues with improved muscle fiber organization design have great potential to improve muscle function.

Unlike the arrangement of muscle fibers in parallel muscles, the contraction and extension of pennate gastrocnemius muscles in the hind limbs of frogs play a significant role in their explosive jumping capacity (with a horizontal jumping distance of ~30 times their body length) with a high mechanical power output in the jumping process (Figure 1A and B).[26] The pennate architecture in native skeletal muscles, characterized by the tilted contractile force direction of the muscle fibers, is widely recognized for producing greater force despite having less contraction displacement. This is due to the higher density of muscle fibers per unit volume compared to parallel muscles (Figure 1C).[27] In this regard, we proposed a basic process, including the design, fabrication, and evaluation of a novel *in vitro* skeletal muscle tissue design, that mimics the macro and microstructure of the gastrocnemius muscle in frogs (Figure 2). The design and modeling of muscle tissue, including its macro shape and microstructure, were optimized through simulation based on mechanical properties. Subsequently, a repeatable and customizable technique of multi-material 3D bioprinting technique was used to fabricate tissues with fusiform geometry and induced pennate myotube alignment for optimal force generation. Next, we stimulated the 3D-bioprinted muscle tissues using an electrical field to induce directional differentiation of myotubes. Finally, we validated the controllable contractile function of the tissues by modifying stimulation amplitudes and frequencies. This work would be useful for exploring design strategies and rapid fabrication techniques for the next generation of high-function *in vitro* skeletal muscle tissues.

2. Materials and methods

2.1. Design of engineered muscle tissue inspired by the gastrocnemius muscle

The design model was inspired by the gastrocnemius muscle in frogs, featuring a spindle shape that fits the leg. Therefore, the engineered muscle construct was designed with a shuttle shape in macro geometry, with interlaced strips and microchannels (Figure 3A). In the macrostructure, the diameter of the muscle belly was defined as the major diameter (R), and the diameter of the muscle tendon as the minor diameter (r). Measurement of the frog's gastrocnemius muscles revealed that the ratio of the long axis to minor diameter (L/r) was 6:1, while the ratio of the major diameter to minor diameter (R/r) was 3:1. To obtain macro and microstructure designs with better contractility, we adjusted the ratios and pennate angles

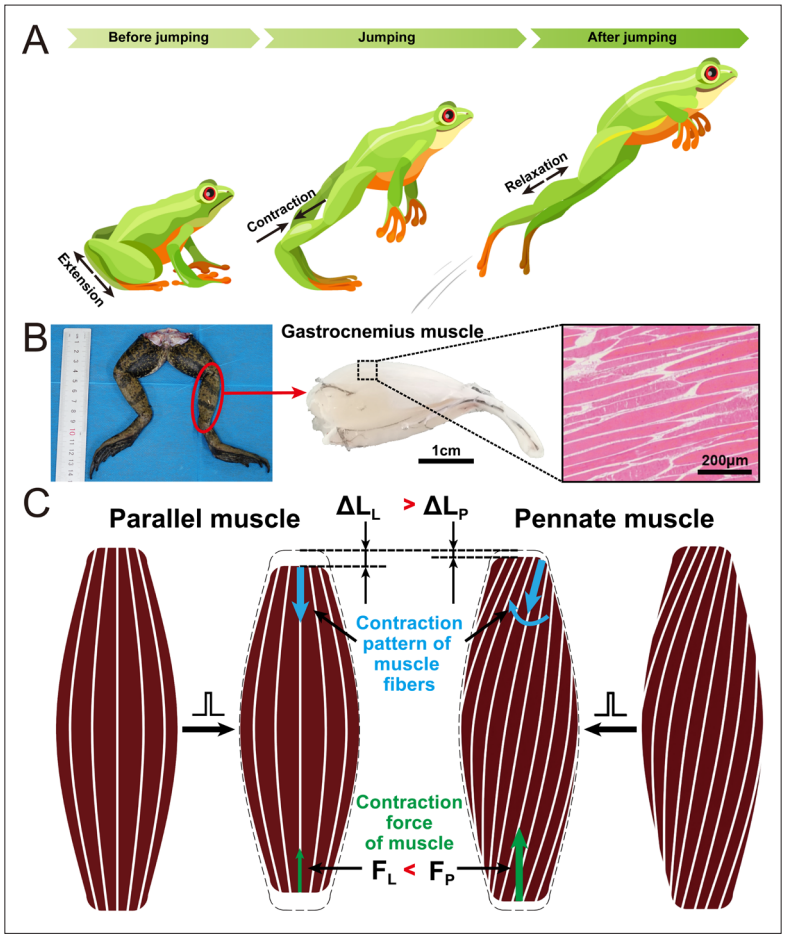

Figure 1. Biomimetic design and fabrication of *in vitro* skeletal muscle tissues with pennate architecture. (A) The jumping process of frogs is accompanied by the extension and contraction of the gastrocnemius muscle. (B) Anatomy of leg muscles in frogs, and the macro and microscopic structure of the gastrocnemius muscle of frogs. (C) Comparison of contractions between parallel and pennate muscles. Under the same stimulation, due to the contraction and rotation of muscle fibers, pennate muscles can provide a larger contraction force with less contraction displacement. Scale bars: 1 cm for gastrocnemius muscle and 200 μm for microstructure. Abbreviations: ΔL_L: contraction displacement of parallel muscle; ΔL_P: contraction displacement of pennate muscle; F_L: contraction force of parallel muscle; F_P: contraction force of pennate muscle.

within a certain range to change the shape of the tissues (Figures S1 and S2, Supporting Information). Furthermore, we conducted simulations to measure the deformation to obtain an optimal geometry for the engineered muscle tissue. Regarding the microstructure, the strips were designed to induce the directional differentiation of skeletal muscle cells, promoting the formation of myotubes that enable actuation. The gaps between the strips could also serve as microchannels for nutrient transport in tissues. We designed the strips as diamond-shaped with the advantage of self-support during the 3D bioprinting process. The maximum radius of the cross-sectional area of the strips was ~200 μm to ensure the long-term survival of the tissue, and the cross-sectional radius of the gaps was 482.8 μm to meet the requirements for nutrient transport in biological tissues. Finally, the optimized design, including both macro and microstructural parameters, was obtained (Figure 3B–D).

2.2. Mechanical simulation of engineered muscle tissue

Mechanical simulation analysis of the deformation of the contractile muscle model was conducted according to specific boundary conditions (displayed in Figure 4A) to optimize the structural design using ANSYS Workbench software. The Young's modulus was set to 12077 GPa, the Poisson's ratio was set to 0.117, and the mesh size was set to 0.1 mm using automatic grid partitioning. A simplified boundary condition was used with a fixed end, and a compression of 0.01 N was applied on the other end to simulate the contraction of the tissue.[21] The effect of the pennate angle between the muscle fibers and the

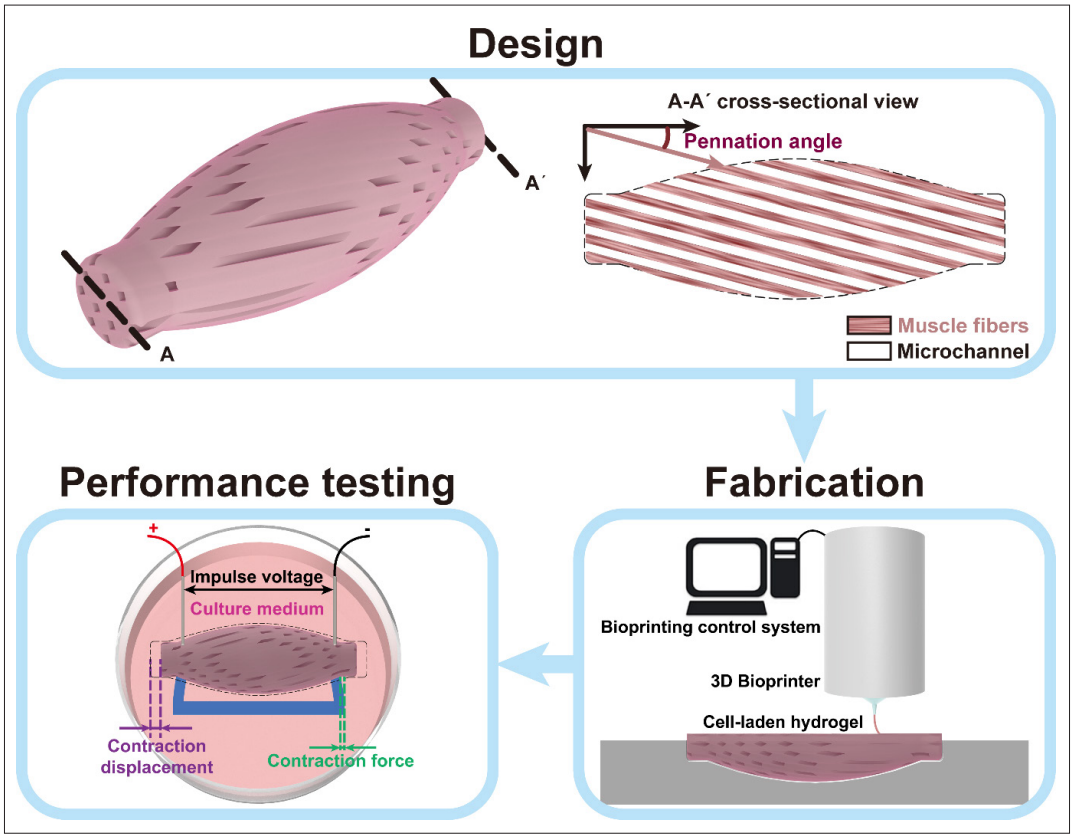

Figure 2. Fabrication process of muscle tissues, including biomimetic design of the macro and microstructures, extrusion 3D-printing fabrication, and contraction performance testing.

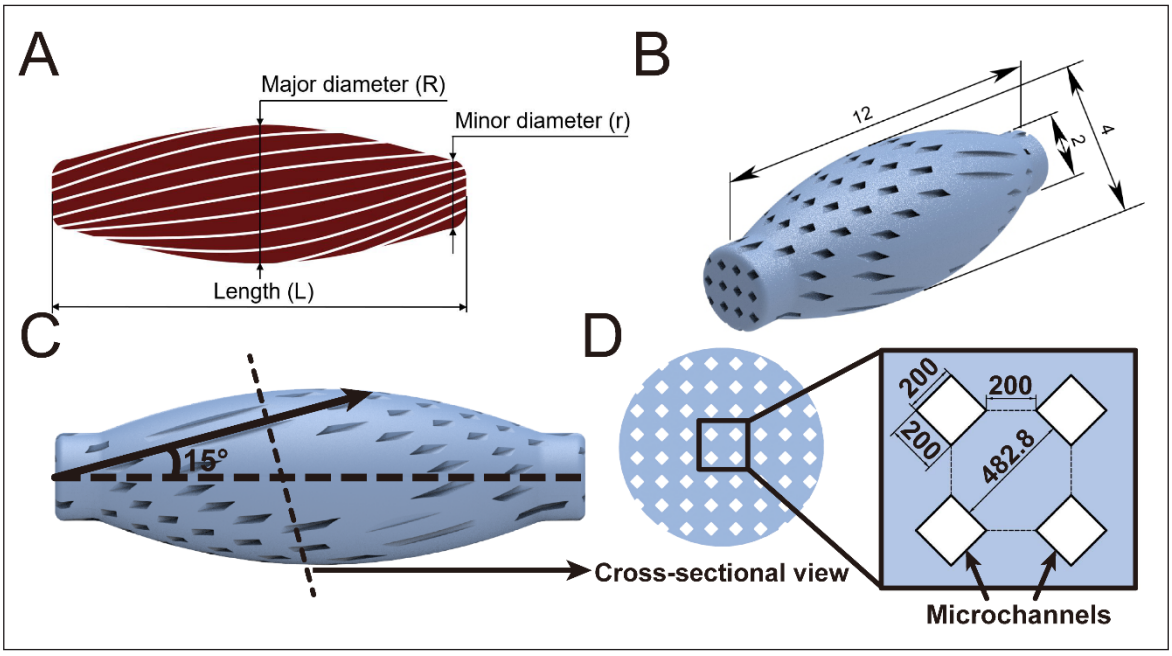

Figure 3. Design and modeling of the engineered tissues inspired by the gastrocnemius muscle. (A) Parameters of the macro and microstructure of the engineered muscle tissue. (B) Macro dimensions of pennate muscle model (unit: mm). (C) Pennation angle of pennate muscle model. (D) Size and shape of microchannels (unit: μm).

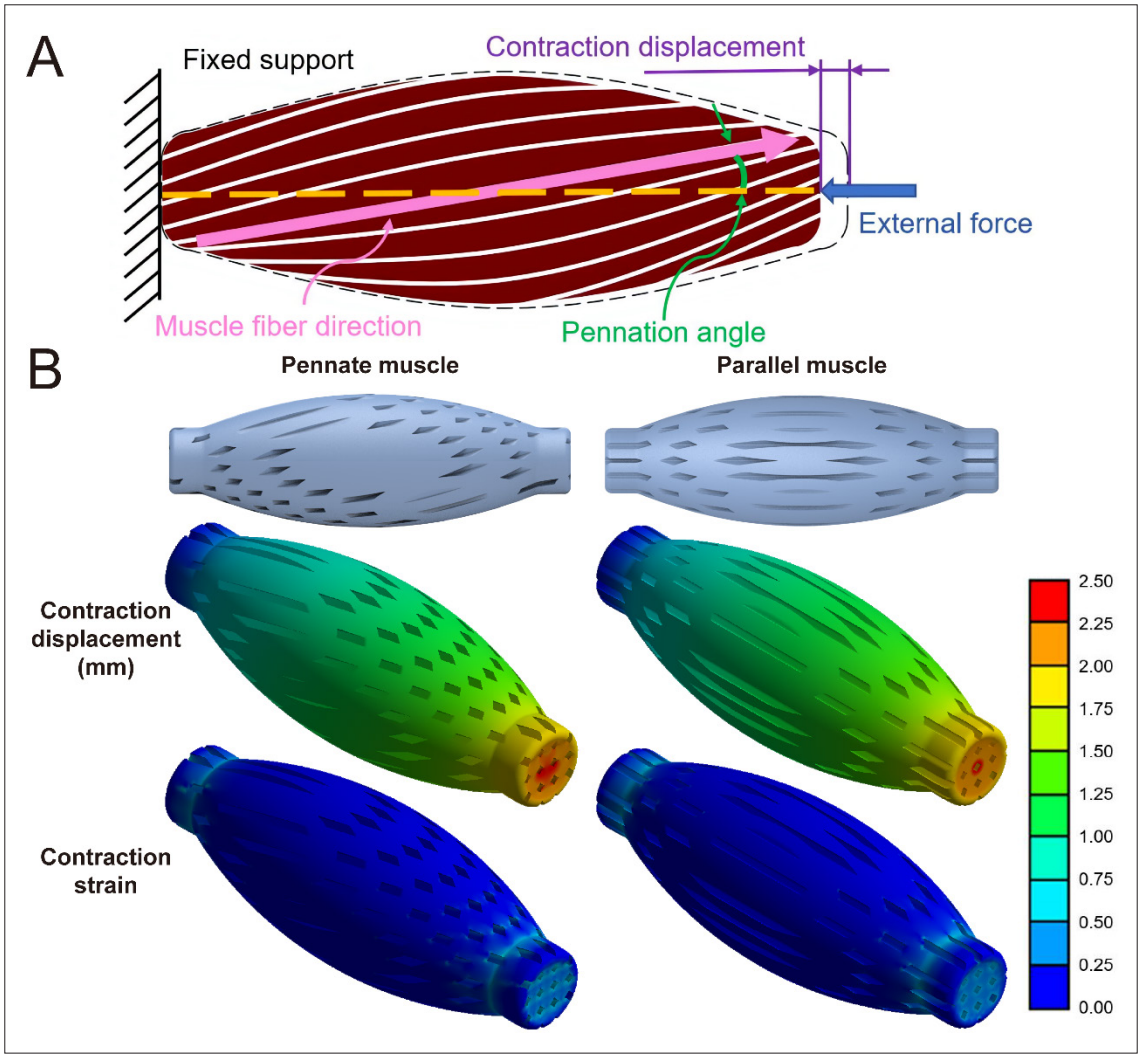

Figure 4. Contraction simulation of pennate and parallel muscle models. (A) Boundary condition settings for mechanical simulation. (B) Contraction displacement and strain of respective pennate and parallel muscle models.

long axis on total deformation was also investigated for microstructural design optimization. As a result, the compression force was applied along the direction of the pennate angle on the model to simulate the force output of the pennate myotubes. The total deformation and equivalent strain of the model were then calculated. Finally, the deformation performance of muscle models, including macro and microparameters, was evaluated based on the simulation results (Figure 4B).

2.3. Materials

C2C12 mouse skeletal myoblasts (CL-0044; Pricella, China) under five passages, gelatin methacryloyl (GelMA; GM-60; EFL, China), and lithium phenyl-2,4,6-trimethylbenzoylphosphinate (LAP; EFL, China) were employed as bioinks for 3D printing. Phosphate-buffered saline (PBS; Corning, United States of America [USA]) was utilized for washing cells and tissues. Growth medium (GM) was composed of 89% Dulbecco's modified Eagle's medium (DMEM, Corning, USA), 10% fetal bovine serum (FBS; FSP500; Excell, China), and 1% penicillin-streptomycin solution (PS; PB180120; Procell, China). Differentiation medium (DM) was composed of 89% DMEM, 10% horse serum (HS; SH30074.02; Cytiva, USA), 1% PS, 1 mg/mL 6-aminocaproic acid (ACA; A7824-25G; Sigma-Aldrich, USA), and 50 ng/mL insulin-like growth factor (IGF-1; I8830; Solarbio, China). Trypsin-EDTA (25200072; Gibco, USA) was applied to digest cells from petri dishes. The Live/Dead Viability/Cytotoxicity Kit (L3224; Invitrogen, USA), consisting of calcein AM and ethidium homodimer-1 (EthD-1), was exploited for

cell viability assessment. Immunol staining fix solution (P0098; Beyotime, China), Triton X-100 (T8200; Solarbio, China), Alexa Fluor 488-conjugated phalloidin (A12379; Invitrogen, USA) (affinity [Kd]: 20 nM), and 4′,6-diamidino-2-phenylindole staining solution (DAPI; C1006; Beyotime, China) were utilized for fluorescence staining. Polydimethylsiloxane (PDMS; Sylgard 184; Dow Corning, USA) was used to fabricate U-shape posts.

2.4. 3D printing and cultivation of skeletal muscle tissues

As displayed in Figure 5A, a 3D bioprinting platform independently developed by Xi'an Jiaotong University was used for the extrusion printing process. This printing platform is equipped with a cooling system for multi-extruders, which can achieve precise temperature control below room temperature, effectively improving bioink printability. The pressure was set to 3 kPa, and the cooler system was used to maintain the hydrogel temperature at 2°C.

Fabrication based on skeletal muscle cells requires selecting a biocompatible hydrogel that is suitable for cell survival, myotube formation and differentiation, and easy to deform under small contractile force. Furthermore, the bioink should fulfill specific rheological characteristics for reliable printability and shape fidelity. Here, bioink consisting of GelMA (at a 60% degree of substitution) and C2C12 myoblasts (under five passages) was selected for 3D bioprinting. The GelMA was dissolved at a concentration of 5% in PBS with 0.25% w/v LAP, and heated in a water bath at 60°C for 30 min. The mixture was then refrigerated at 4°C for 30 min and thawed at 37°C. The C2C12 cells were cultured in GM at 37°C and 5% CO_2 atmosphere and passaged at 80% confluency. For the 3D bioprinting experiments, the cells were digested with 0.25% trypsin-EDTA at about 80% confluency and mixed with GelMA solution at a concentration of 2×10^6 cells/mL. The printing fill pattern was aligned in a straight line with a distance of 0.23 mm and an angle consistent with the direction of the microchannel. Support molds matching the shape of the tissues were also designed and manufactured by stereolithography to provide external support during the printing process (Figure 5B and C). An extruder containing the cell-laden hydrogel was preserved in the cooling system for about 30 min. Nozzles with an inner diameter of 250 μm were used, and tissues were printed at a speed of 8 mm/s. Figure 5B illustrates the specific process of extrusion 3D printing. After loading the bioink, the extruder was connected to the nozzle and then placed in the cooling system to precisely regulate the state of

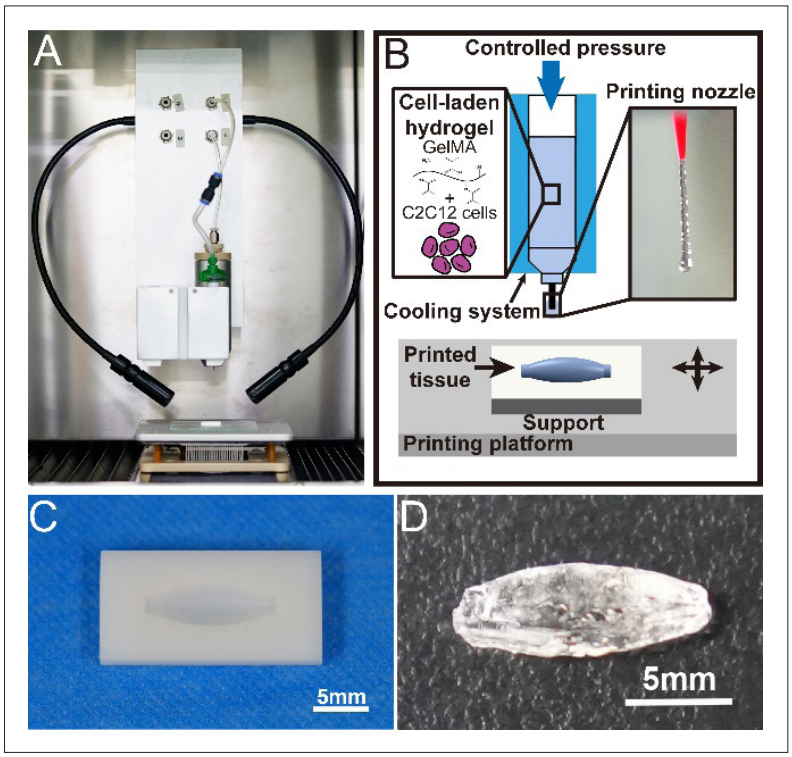

Figure 5. Fabrication and morphology analysis of the 3D-printed muscle tissues. (A) 3D-bioprinting platform with a cooling system. (B) Fabrication by means of extrusion 3D bioprinting with cell-laden hydrogel. (C) Supporting mold. (D) The engineered skeletal muscle tissue.

the bioink. The extruder was connected to an air pump, which extruded the bioink at the appropriate air pressure. Simultaneously, it followed the predetermined route in the slicing software, printing the muscle tissues layer-by-layer in the support mold (Figure 5C). After printing, the 3D-printed pieces were crosslinked under 405 nm light using a portable curing light source (LS-1601; EFL, China), and the supports were removed.

The quality of muscle tissue morphology includes macroscopic shape dimensions and microscopic structure dimensions. For macro dimensions, the length and major diameter of the tissue were measured using a micrometer and thickness gauge, respectively. For the microstructure dimensions, a layer containing microchannels from the sliced model of tissue was printed separately, and the width of the microchannels was then measured under a stereomicroscope (SMZ745; Nikon, Japan).

2.5. Cell viability evaluation

Cell viability was analyzed on days 1, 3, 5, and 7 after 3D printing using fluorescent labeling with molecular probes from the Live/Dead Viability/Cytotoxicity Kit. Since the printed muscles were not exposed to electrical stimulation to induce cell differentiation before cell viability evaluation, the cells retained their ability to proliferate. The culture medium was changed daily during cultivation to remove dead cells from the muscle. Molecular probes were used to characterize cell activity and observe cell growth in the 3D-printed muscle tissues. The staining solution was prepared under dark conditions by adding 1 mL PBS to an Eppendorf tube, followed by 2 μL EthD-1 and 0.5 μL calcein AM. The tissues were washed with PBS once and incubated in the mixed staining solution in the dark for 15 min. The tissues were washed with PBS three times and observed under an inverted fluorescence microscope (Ti-S; Nikon, Japan). Stained live cells emitted green fluorescence (Ex/Em = 488/500 nm) under blue light excitation, while dead cells emitted red fluorescence (Ex/Em = 560/600 nm) under green light excitation. ImageJ software was used to count the number of living and dead cells. The cell survival rate was calculated as the ratio of the number of living cells to the total number of cells.

2.6. Cell differentiation with electrical stimulation

The 3D-printed tissues were cultivated with 5 mL DM after incubating in GM for 3 days. After 24 h cultivation in DM, electrical field stimulation was generated by a signal stimulator (DG812; Rigol, China) as square waves (amplitude: 1.0 V/mm; pulse duration: 10 ms; frequency: 1 Hz) and transmitted to platinum electrodes fixed on both sides of the petri dish. After electrical field stimulation was performed on the tissues with the corresponding parameters for 10 h (every 1 h stimulation followed with 1 h rest), the tissues were incubated in DM for 7 days, during which the culture medium was changed daily.[28] We then studied the differentiation of myoblasts into myotubes using fluorescence staining of F-actin and nuclei and subsequently characterized the differentiation level of C2C12 cells via confocal laser scanning microscopy (CLSM).

2.7. Myotube alignment analysis in engineered tissues

Myotube alignment of skeletal muscle cells was analyzed using fluorescence staining and subsequent observation under a laser confocal microscope (A1; Nikon, Japan). After a seven-day culture, the 3D-printed pieces were cut into thin slices along the long axis, washed, fixed, and permeabilized. The samples were incubated in Alexa Fluor 488-conjugated phalloidin (1:200) at room temperature in the dark for 30 min and rinsed with PBS after incubation. The cell nuclei were then stained with a DAPI staining solution for 30 s (the detailed staining procedure is described in the Supporting Information). A laser confocal microscope was used for confocal imaging of skeletal muscle cell nuclei to assess myotube alignment. ImageJ software was used to identify the long-axis angle of each cell nucleus. Origin software was used to conduct a frequency distribution analysis of the angular orientation, calculating the frequency of cell orientations in each 20° interval from −95° to 85°. Cells with an angle <30° between the long axis of the nucleus and the orientation direction were assumed to be oriented cells.[29] Additionally, we investigated the effect of 3D printing parameters on cell orientation rate, and various printing speeds (6, 8, and 10 mm/s) and air pressure (2, 3, and 4 kPa) were considered in this study.

2.9. Contractility evaluation

Contraction displacement of tissues was measured without load under the electric field, while contraction force was measured when loaded with U-shape posts made of PDMS. Electrical stimuli were applied to induce contraction and displacement. The electrical signal generator was used to generate a pulse square wave with adjustable amplitude and frequency (1, 2, and 4 Hz). The signal generator was connected to a booster device to create an electric field between the two electrodes (1, 2, and 4 V/mm). A microscope thermo plate (TP-C-108; Mshot, China) was utilized to maintain the media at 37°C, providing an appropriate temperature for the muscle tissues. A stereomicroscope (SMZ745; Nikon, Japan) was used to observe the contraction process and record videos; the load-free contraction displacement was measured using Tracker software; the displacement of posts was measured to compute the force exerted against the posts after electrical stimulation using Euler-Bernoulli's beam bending equation:

$$F = \frac{3EI_z\gamma(a)}{a^3} \quad \text{(I)}$$

where F is the contraction force, E is the Young's modulus, I_Z is the second moment of area of the post around the z-axis, a is the height at which tissue is pulling from the post, and $\gamma(a)$ is the displacement of the post at that height.

2.10. Statistical analysis

All experimental results were processed and plotted using Origin software (OriginPro 2021; OriginLab Corporation, USA). The data are expressed as mean ± standard deviation. Statistical analysis was performed via one-way analysis of variance (ANOVA), and $p < 0.05$ was considered statistically significant ($^*p < 0.05$; $^{**}p < 0.01$; $^{***}p < 0.001$).

3. Results

3.1. Structural design of the engineered tissue after optimization

The *in vitro* skeletal muscle in our study should possess macro and microstructures similar to the gastrocnemius muscle of frogs. Based on our observations and measurements of the gastrocnemius muscle, as well as our production capability, specific tissue dimensions were selected (i.e., *L*: 12 mm, *R*: 4 mm, *r*: 2 mm, and pennate angle: 15°; Figure 3). Simultaneously, we conducted simulation experiments on models with different macro and microparameters, demonstrating the rationality of our parameter selection (Figures S1 and S2, Supporting Information). The simulation results on the deformation distribution of the model revealed that maximum deformation occurred at the end face, where the contractile force was exerted (Figure 4B). This phenomenon is consistent with the characteristics of compression deformation. However, in the actual contraction process of the muscle tissues, the deformation distribution should be more uniform than the simulation results, as the muscle fibers are evenly distributed inside.

Furthermore, simulations were conducted to compare the deformation performance of the designed pennate tissue model with that of the parallel muscle model, both with the same macro geometry. In Figure 4B, results indicate no significant difference in the deformation displacement between the two muscle configurations under the same contraction force. The simulation results displayed an average deformation strain of 0.1308 for the pennate muscle. In contrast, the average strain of the parallel muscle model was 0.1334. As a result, the pennate muscle model exhibited an average deformation that was 1.95% lower compared to the parallel muscle model. Based on the simulation results, it can be inferred that the pennate muscle model provides greater contraction force compared to the parallel muscle model under the same deformation, demonstrating the superior properties of the pennate muscle structure.

3.2. Morphology analysis of the engineered muscle tissues

The macroscopic shape of the 3D-printed muscle tissues is displayed in Figure 5D, and its dimension was measured and analyzed accordingly (Figure 5E); the long axis was 12.18 ± 0.06 mm, and the major diameter was 4.37 ± 0.03 mm ($n = 6$). Compared to the designed dimensions in Figure 4, the fabrication error of the long axis is about 1.52%, while that of the major diameter reaches 9.33%. To accurately measure the width of the microchannels in the engineered tissues, we printed a separate layer of microchannels from the layer-by-layer printing process. Figure 6A displays the microchannel size in the muscle tissues observed under an inverted microscope; the average measured width was 284.28 ± 14.40 μm ($n = 3$). There was no significant difference between the measured and designed values of the width of the printed microchannels (Figure 6B), indicating that they meet the requirements for nutrient transport and cell survival.

3.3. Cell status analysis

Live/dead staining was performed on sliced tissues on days 1, 3, 5, and 7 after printing. Figure 6C demonstrates a steady increase in cell viability over time, reaching 79.89% on day 7 after printing. Under electrical stimulation in DM, the skeletal muscle cells would differentiate into muscle fibers that are essential for the functionalization of muscle tissues. Myotube alignment was compared between the pennate and parallel muscle tissues under different printing parameters (printing speed: 6, 8, and 10 mm/s; air pressure: 2, 3, and 4 kPa). The differentiation status was observed via fluorescence staining of the cytoskeleton (Figure 6D), and the angle of the nucleus was calculated to assess the degree of cell alignment. Figure 6E displays the frequency distribution of cell nucleus angles (*S*: printing speed [mm/s]; *P*: air pressure [kPa]; cell orientation rate: S6P2: 44.74%, S8P2: 45.87%, S10P2: 51.93%, S6P3: 41.04%, S6P4: 45.22%). We noticed that the cell orientation rate increased with higher printing speed, while no significant correlation was established between air pressure and cell orientation rate. The highest orientation rate was 51.93%, obtained at a printing speed of 10 mm/s and an air pressure of 2 kPa.

3.4. Contraction performance of muscle tissues

Contraction performance was evaluated based on the contraction displacement and force. The test platform was constructed (Figure 7A), and the contraction displacement was first measured without any load. The configuration of

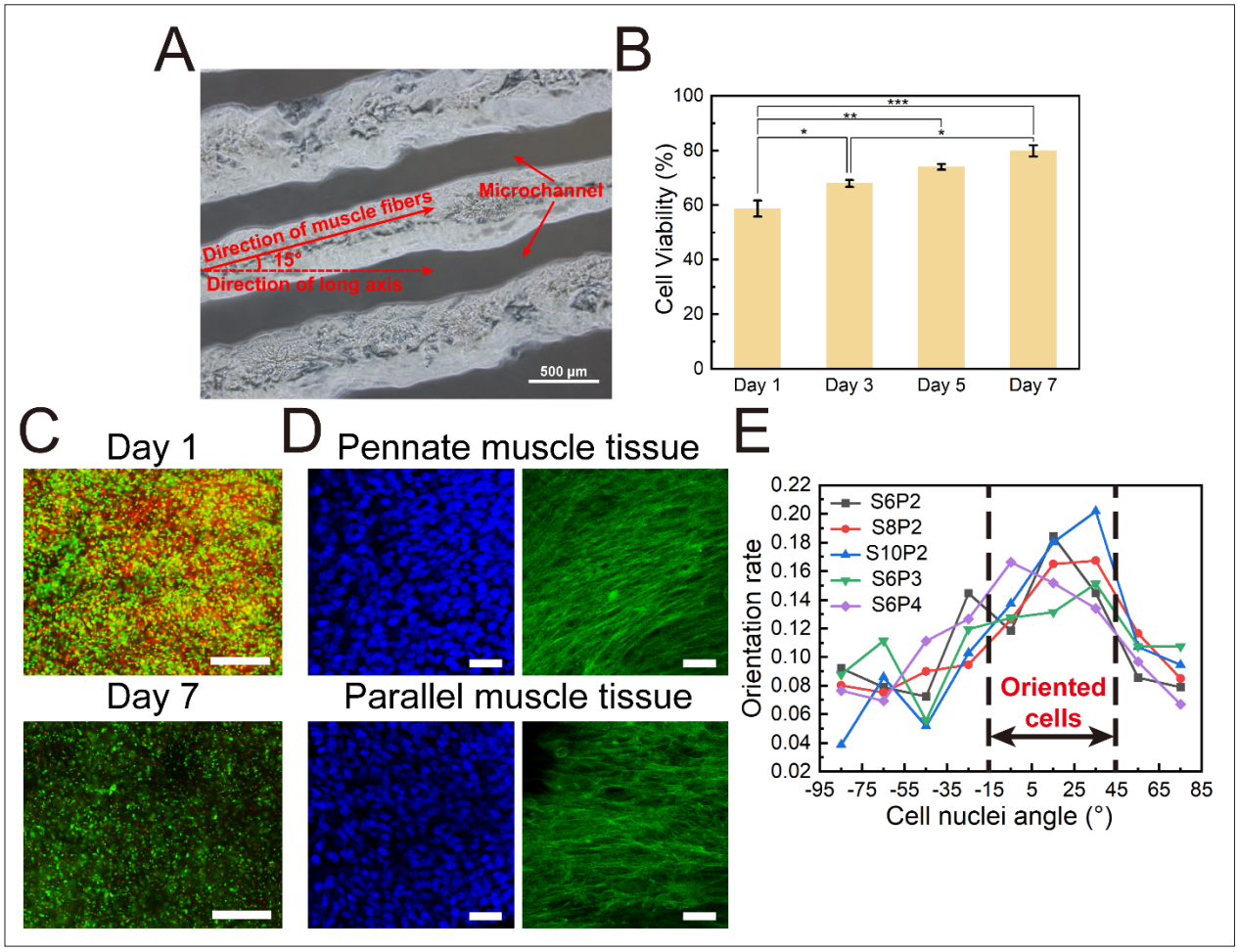

Figure 6. Microscopic characterization of muscle tissues, including microstructure and cell status. (A) The microchannels were printed separately for observation. (B) Cell viability at 1, 3, 5, and 7 days after printing (n = 3); *p < 0.05, **p < 0.01, ***p < 0.001. (C) Comparison of cell viability by live/dead viability/cytotoxicity fluorescence staining on days 1 and 7 after printing. (D) Fluorescence confocal imaging on day 7 after electrical stimulation. Blue represents the cell nucleus, and green indicates the distribution of the cytoskeleton. (E) Orientation rate of cells (S: printing speed, unit: mm/s; P: air pressure, unit: kPa). Scale bars: 500 μm (A), 500 μm (C); 100 μm (D).

contraction displacement evaluation is illustrated in Figure 7B. Two L-shaped platinum electrodes were attached to a petri dish and connected to an external power source, forming an impulse electrical field between the two electrodes. The contraction of the muscle tissue was recorded under a microscope and calculated in Tracker software (Figure 7C and D). Figure 7E and F illustrate the contraction displacement of pennate and parallel muscles under various electrical stimulation for comparison. The contraction displacement increased proportionally to the electric field intensity, reaching a maximum value of 24.64 ± 1.64 μm at an electrical field intensity of 4 V/mm for the pennate muscle tissues. As the stimulation frequency increased, the maximum contraction displacement displayed a decreasing trend to reduce the contraction amplitude, leading to more frequent contractions. Additionally, we observed that the contraction displacement of the parallel muscles was consistently higher than that of the pennate muscles (Figure 7E and F).

The contractile force of both parallel and pennate muscle tissues was also compared (Figure 8A). The tissue was placed on U-shaped posts, and the deformation of the posts under electrical stimulation from the platinum electrodes was measured (Figure 8B and C). Under an impulse electrical field of 1 V/mm and 1 Hz, the parallel muscle generated a contractile force of 239.662 ± 30.974 μN (n = 3), whereas the force of the pennate muscle reached 443.085 ± 33.521 μN (n = 3), about twice of that of parallel muscle (Figure 8D). Compared to previous studies on *in vitro* skeletal muscle tissues with C2C12 cells

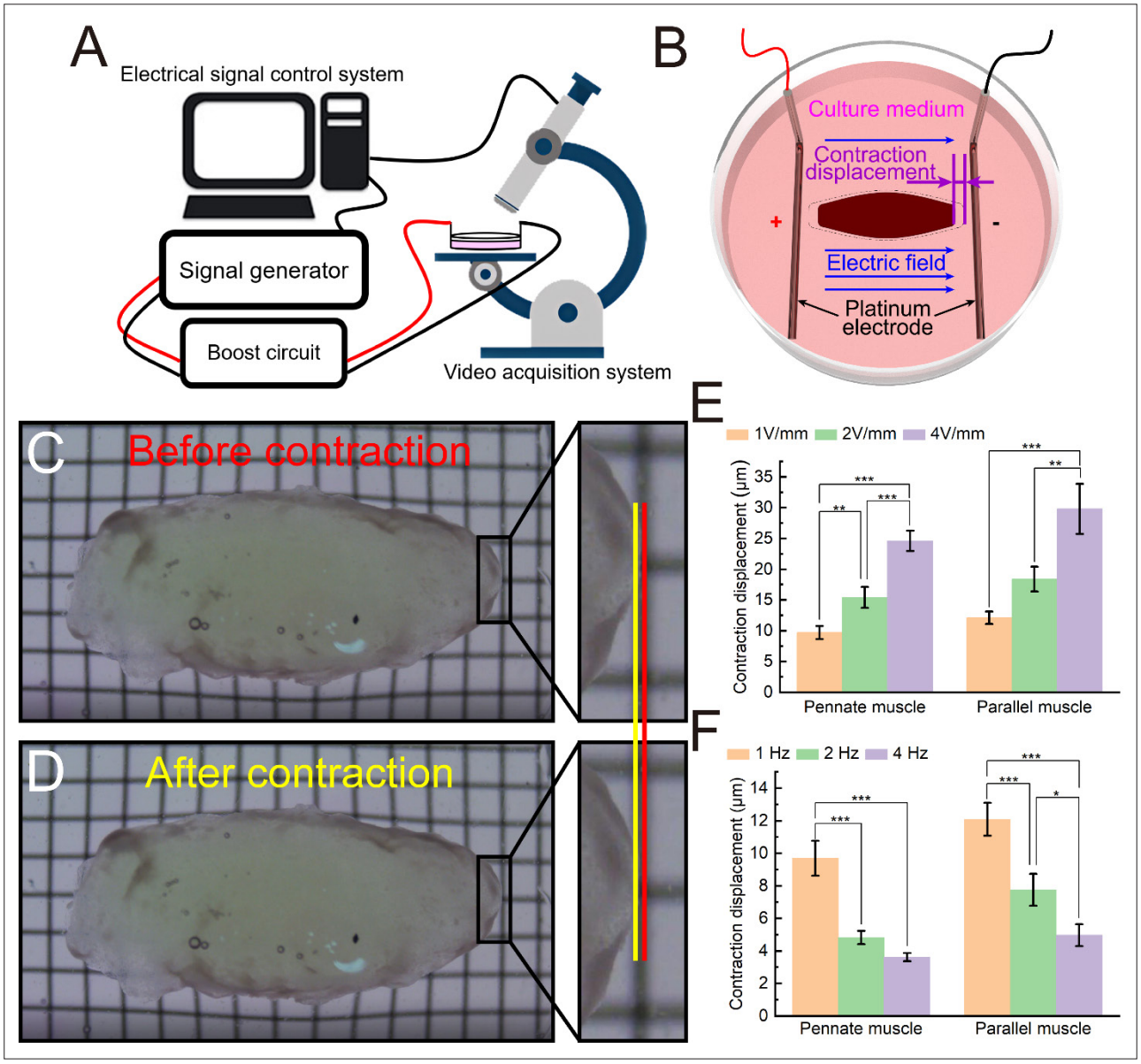

Figure 7. Evaluation of contraction displacement of muscle tissues. (A) Electrical stimulation platform. (B) Schematic diagram of the measurement method for contraction displacement of tissues. (C and D) Contraction of tissues under an impulse electric field formed between two electrodes and recorded by a microscope. Grid size: 1mm. (E and F) Contraction displacement of pennate and parallel muscle tissues under different (E) electrical fields and (F) frequencies (n = 3). *p < 0.05; **p < 0.01; ***p < 0.001.

(Figure 8E), our study demonstrates advantages in both volume and contraction force.

4. Discussion

In our study, we designed and manufactured engineered skeletal muscle tissues with a macroscopic shape simulating the gastrocnemius muscle, with an internal 15° pennate angle of muscle fiber arrangement, using 3D bioprinting technology. The manufacturing process could effectively achieve uniform distribution of cells within the tissue, as well as complex 3D microstructure, and the cells inside the tissues were induced to differentiate under the electrical field to attain high cell viability (79.89%) and alignment of muscle fibers (51.93%). The pennate tissues could achieve a maximum contraction displacement of 24.64 μm and a contractile force of 443.085 μN. The structural design and manufacturing scheme of the engineered muscle tissues that mimic the gastrocnemius muscle proposed in this study could provide new ideas and methods for establishing a modular and highly contractile muscle construct.

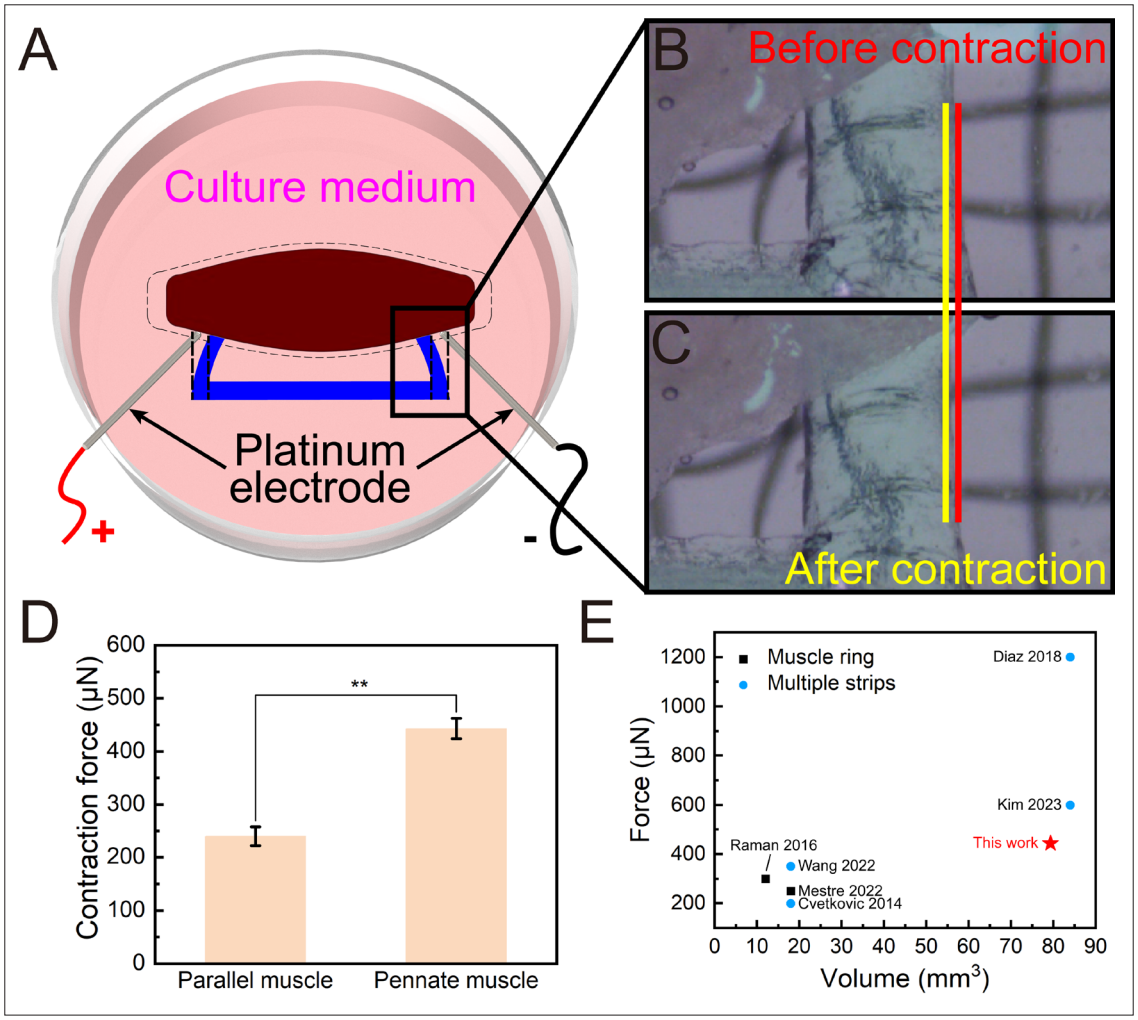

Figure 8. Evaluation of the contraction force of muscle tissues. (A) A schematic diagram of the measurement method for contraction force and the contraction of pennate and parallel muscle tissues, loaded with U-shaped posts under electrical stimulation, was recorded by a microscope using the same electrical stimulation platform displayed in **Figure 5A**. Grid size: 1mm. (B and C) Deformation of U-shaped posts was measured and computed to obtain (D) contraction force of pennate and parallel muscle tissues ($n = 3$) by using Euler-Bernoulli's beam bending equation. (E) Comparison of contractile force of *in vitro* skeletal muscle tissues based on C2C12 cells.[20,36–40] $^{**}p < 0.01$.

The contraction performance comparison between engineered pennate and parallel muscle tissues revealed that the pennate muscle exhibited superior performance in contractile force. The results are consistent with natural observations that the pennate muscle provides greater contraction force compared to the parallel muscle. This may be due to the pennate arrangement allowing for a higher density of muscle fibers within a certain volume, thereby generating a relatively larger force. In addition, during the contraction process of the pennate muscle, the fibers would shorten and rotate simultaneously, increasing the amount of muscle contraction to some extent.[30] Conversely, under different electrical stimulation parameters, the contraction displacement of the pennate muscle was consistently smaller than that of the parallel muscle. In biological organisms, the parallel fibers could transmit contractile forces in the same direction as the long axis, while the pennate fibers only transmit a portion of the force to generate smaller displacement. Thus, the orientation of parallel fibers aligning with the long axis could promote greater contraction displacement in contrast to pennate muscles.

Regarding 3D biofabrication quality, it was found that the forming accuracy in the horizontal direction is satisfactory compared to the forming direction, as revealed by the forming errors. The macro size error of the tissues was approximately 10% in the layer-by-layer forming direction, and the horizontal error was reduced to 1.82%, indicating that the current 3D bioprinting process with GelMA cell-

laden hydrogel has a good molding accuracy. This could be due to the use of molds as external support, which enhances the forming quality macroscopically, especially in the horizontal direction. During the fabricating process, the support had dimensional limitations on both horizontal ends of the print-outs, while in the height direction, it only restricted the bottom of the fabricated tissues. Therefore, the actual height of the print-outs is significantly higher than the theoretical value.

Regarding the microscale formation, we observed that the surface of the microchannels was relatively rough. Due to temperature changes during the printing process, there is solidification of the bioink from liquid to solid. During this process, the bioink is extruded from the extruder to the print piece. At this time, the hydrogel retains a certain liquid fluidity, and the surface tension may lead to the boundary of microchannels being rough, thus affecting the microscale forming quality. The microchannels were designed in a diamond shape with a self-supporting ability to ensure its shape integrity during manufacturing and cultivation processes. However, we also noticed that in subsequent cultivation, some microchannels fused under gravity. Other remaining microchannels could support the diffusion of nutrients for the long-term viability of artificial muscles. In contrast, GelMA, as a porous material, can also facilitate the permeation of culture medium into the *in vitro* muscle for nutrient transport. Considering the change in cell viability in the engineered tissues after biofabrication, we observe a trend consistent with previous results. However, overall cell viability is slightly lower compared to traditional fabrication techniques,[31–34] especially on the first day after printing. To ensure the printability of GelMA, the cell-laden bioink was preserved in the cooling system for about 30 min before printing. This step initially reduces the cell activity to some extent after fabrication. Thereafter, cell viability gradually increased with culture time and reached approximately 80% after 7 days, providing a basis for contraction performance evaluation.

We also investigated the influence of printing speed and air pressure on myotube alignment in the engineered tissues. The cell orientation rate would increase with higher printing speed, while there is no evident relationship between air pressure and cell orientation rate. As the printing speed increases, the nozzle moves faster during the extrusion printing process, causing the diameter of the formed hydrogel filaments to shrink and resulting in smaller microchannels. A previous study has demonstrated that reducing the size of cell culture substrate can improve the directional differentiation effect of cells.[35] Thus, increasing the printing speed can improve the directional effect of cell alignment. In contrast, an increase in air pressure would increase the accumulation of hydrogels at the same spatial location. The combined effect between printing speed and flow rate, particularly when there is a mismatch between them, would affect layer thickness during the printing process. This, in turn, affects the accuracy of microchannel formation and ultimately the orientation effect.

The contraction performance was also compared between our tissues and previously engineered muscle tissues cultured from C2C12 cells by traditional fabrication approaches. Some researchers developed skeletal muscle strips and rings with the aim of actuation in biohybrid robots,[20,36–40] which were fabricated by molding in 3D-printed strip/ring molds. The latter involves two muscle rings tightly integrated with the mechanical body during fabrication, thus generating a greater force during contraction. On one hand, the 3D printing process may cause damage to cell viability during extrusion, which can negatively affect cell differentiation and functionalization. On the other hand, decreased cell density observed in our study should also be considered a factor influencing functional performance. Although our study has room for improvement, its strength lies in the successful 3D bioprinting of large-sized *in vitro* tissues with a designed organization of pennate fibers, achieving relatively high viability and functionality.

Currently, there has been significant progress in the construction of 3D-bioprinted muscle tissue structure *in vitro*, with limited consideration of the functional properties, especially contraction performance.[31,33,41] In this paper, we developed a novel frog gastrocnemius muscle-inspired 3D-bioprinted muscle mimetic for the regeneration of damaged skeletal muscles and actuation of biohybrid robotics. Using 3D bioprinting, we created skeletal muscle tissues with a fusiform shape and pennate angle microchannels, displaying good cytocompatibility and fiber alignment. The engineered muscle tissues with biomimetic design exhibited much higher contraction forces compared to those of common parallel-printed muscle, suggesting the excellent potential of the developed muscle models. Thus, this paper presents a developed model aimed at achieving higher contraction performance, contributing to future advancements in SMTE applications.

5. Conclusion

In our study, we designed and 3D printed modular skeletal muscle tissues with customized shuttle micro shapes, pennate fiber arrangement, and microchannels for nutrient transport during culture. The engineered tissues could achieve a maximum contractile force of over 400 μN when subjected to electrical stimulation after functionalization. Our study proved that 3D printing could be used to effectively achieve uniform distribution of

muscle fibers and complex 3D microstructures. The design and fabrication approach for *in vitro* modular tissues could provide new ideas and techniques in the fields of skeletal muscle engineering, drug testing, and biohybrid robotics.

Acknowledgments

The authors express their gratitude to those who provide contribution and assistance to the experiment and manuscript writing. Editors of International Journal of Bioprinting are appreciated for their contribution to the format and content of this article.

Funding

This work is supported by the National Natural Science Foundation of China (grant number: 52175276) and the Program for Innovation Team of Shaanxi Province (2023-CX-TD-17).

Conflict of interest

Jiankang He serves as the Editorial Board Member of the journal, but was not in any way involved in the editorial and peer-review process conducted for this paper, directly or indirectly. Other authors declare they have no competing interests.

Author contributions

Conceptualization: Lin Gao
Funding Acquisition: Lin Gao
Investigation: Liuhe Li, Lin Gao, Wenze Wu
Methodology: Liuhe Li, Wenze Wu, Junnan Feng, Ziwei Liu
Project Administration: Lin Gao
Supervision: Lin Gao, Dichen Li, Jiankang He
Visualization: Liuhe Li
Writing – Original Draft: Liuhe Li, Lin Gao
Writing – Review & Editing: Lin Gao

Ethics approval and consent to participate

Not applicable.

Consent for publication

Not applicable.

Availability of data

The authors declare that all data supporting the findings in this study are available on request.

References

1. Samandari M, Quint J, Rodríguez-delaRosa A, Sinha I, Pourquié O, Tamayol A. Bioinks and bioprinting strategies for skeletal muscle tissue engineering. *Adv Mater.* 2022;34(12):2105883.
doi: 10.1002/adma.202105883

2. Derakhshanfar S, Mbeleck R, Xu K, Zhang X, Zhong W, Xing M. 3D bioprinting for biomedical devices and tissue engineering: a review of recent trends and advances. *Bioact Mater*. 2018;3(2):144-156.
doi: 10.1016/j.bioactmat.2017.11.008

3. Corona BT, Rivera JC, Owens JG, Wenke JC, Rathbone CR. Volumetric muscle loss leads to permanent disability following extremity trauma. *J Rehabil Res Dev.* 2015;52(7):785-792.
doi: 10.1682/jrrd.2014.07.0165

4. Liu J, Saul D, Böker KO, Ernst J, Lehman W, Schilling AF. Current methods for skeletal muscle tissue repair and regeneration. *Biomed Res Int*. 2018;11:1984879.
doi: 10.1155/2018/1984879

5. Zhuang P, An J, Chua CK, Tan LP. Bioprinting of 3D *in vitro* skeletal muscle models: a review. *Mater Des*. 2020;193:108794.
doi: 10.1016/j.matdes.2020.108794

6. Kwee BJ, Mooney DJ. Biomaterials for skeletal muscle tissue engineering. *Curr Opin Biotechnol.* 2017;47:16-22.
doi: 10.1016/j.copbio.2017.05.003

7. Gholobova D, Terrie L, Gerard M, Declercq H, Thorrez L. Vascularization of tissue-engineered skeletal muscle constructs. *Biomaterials*. 2020;235:119708.
doi: 10.1016/j.biomaterials.2019.119708

8. Kang MS, Yu Y, Park R, et al. Highly aligned ternary nanofiber matrices loaded with MXene expedite regeneration of volumetric muscle loss. *Nanomicro Lett*. 2024;16(1):73.
doi: 10.1007/s40820-023-01293-1

9. Ricotti L, Trimmer B, Feinberg AW, et al. Biohybrid actuators for robotics: a review of devices actuated by living cells. *Sci Robot.* 2017;2(12):eaaq0495.
doi: 10.1126/scirobotics.aaq0495

10. Ostrovidov S, Hosseini V, Ahadian S, et al. Skeletal muscle tissue engineering: methods to form skeletal myotubes and their applications. *Tissue Eng Part B Rev.* 2014;20(5):403-436.
doi: 10.1089/ten.teb.2013.0534

11. Rao LJ, Qian Y, Khodabukus A, Ribar T, Bursac N. Engineering human pluripotent stem cells into a functional skeletal muscle tissue. *Nat Commun*. 2018;9126.
doi: 10.1038/s41467-017-02636-4

12. Martin NRW, Turner MC, Farrington R, Player DJ, Lewis MP. Leucine elicits myotube hypertrophy and enhances maximal contractile force in tissue engineered skeletal muscle *in vitro*. *J Cell Physiol.* 2017;232(10):2788-2797.
doi: 10.1002/jcp.25960

13. Madden L, Juhas M, Kraus WE, Truskey GA, Bursac N. Bioengineered human myobundles mimic clinical responses of skeletal muscle to drugs. *Elife*. 2015;4:e04885.

doi: 10.7554/eLife.04885

14. Nagamine K, Kawashima T, Sekine S, Ido Y, Kanzaki M, Nishizawa M. Spatiotemporally controlled contraction of micropatterned skeletal muscle cells on a hydrogel sheet. *Lab Chip*. 2011;11(3):513-517. doi: 10.1039/c0lc00364f
15. Kamm RD, Bashir R. Creating living cellular machines. *Ann of Biome Eng*. 2013;42(2):445-459. doi: 10.1007/s10439-013-0902-7
16. Chan V, Asada HH, Bashir R. Utilization and control of bioactuators across multiple length scales. *Lab Chip*. 2014;14(4):653-670. doi: 10.1039/c3lc50989c
17. Ricotti L, Menciassi A. Bio-hybrid muscle cell-based actuators. *Biomed Microdevices*. 2012;14(6):987-998. doi: 10.1007/s10544-012-9697-9
18. Zupan M, Ashby MF, Fleck NA. Actuator classification and selection—the development of a database. *Adv Eng Mater*. 2002;4(12):933-940. doi: 10.1002/adem.200290009
19. Coyle S, Majidi C, LeDuc P, Hsia KJ. Bio-inspired soft robotics: material selection, actuation, and design. *Extreme Mech Lett*. 2018;22:51-59. doi: 10.1016/j.eml.2018.05.003
20. Kim Y, Yang Y, Zhang X, et al. Remote control of muscle-driven miniature robots with battery-free wireless optoelectronics. *Sci Robot*. 2023;8(74):eadd1053. doi: 10.1126/scirobotics.add1053
21. Morimoto Y, Onoe H, Takeuchi S. Biohybrid robot powered by an antagonistic pair of skeletal muscle tissues. *Sci Robot*. 2018;3(18):eaat4440. doi: 10.1126/scirobotics.aat4440
22. Gao GF, Cui XF. Three-dimensional bioprinting in tissue engineering and regenerative medicine. *Biotechnol Lett*. 2016;38(2):203-211. doi: 10.1007/s10529-015-1975-1
23. Kim JH, Seol YJ, Ko IK, et al. 3D bioprinted human skeletal muscle constructs for muscle function restoration. *Sci Rep*. 2018;8(1):12307. doi: 10.1038/s41598-018-29968-5
24. Kang HW, Lee SJ, Ko IK, Kengla C, Yoo JJ, Atala A. A 3D bioprinting system to produce human-scale tissue constructs with structural integrity. *Nat Biotechnol*. 2016;34(3):312-319. doi: 10.1038/nbt.3413
25. Kim JH, Kim I, Seol YJ, et al. Neural cell integration into 3D bioprinted skeletal muscle constructs accelerates restoration of muscle function. *Nat Commun*. 2020;11(1)1025. doi: 10.1038/s41467-020-14930-9
26. Bian WN, Liau B, Badie N, Bursac N. Mesoscopic hydrogel molding to control the 3D geometry of bioartificial muscle tissues. *Nat Protoc*. 2009;4(10):1522-1534. doi: 10.1038/nprot.2009.155
27. Tanaka Y, Noguchi Y, Yalikun Y, Kamamichi N. Earthworm muscle driven bio-micropump. *Sens Actuator B Chem*. 2017;242:1186-1192. doi: 10.1016/j.snb.2016.09.123
28. Liu L, Zhang C, Wang W, Xi N, Wang Y. Regulation of C2C12 differentiation and control of the beating dynamics of contractile cells for a muscle-driven biosyncretic crawler by electrical stimulation. *Soft Robot*. 2018;5(6):748-760. doi: 10.1089/soro.2018.0017
29. Mita H, Mizuno Y, Tanaka H, Fujie T. UV laser-processed microstructure for building biohybrid actuators with anisotropic movement. *Biofabrication*. 2024;16(2):025010. doi: 10.1088/1758-5090/ad2080
30. Roberts TJ, Eng CM, Sleboda DA, et al. The multi-scale, three-dimensional nature of skeletal muscle contraction. *Physiology (Bethesda)*. 2019;34(6):402-408. doi: 10.1152/physiol.00023.2019
31. Mestre R, Patiño T, Barceló X, Anand S, Pérez-Jiménez A, Sánchez S. Force modulation and adaptability of 3d-bioprinted biological actuators based on skeletal muscle tissue. *Adv Mater Technol*. 2018;4(2):1800631. doi: 10.1002/admt.201800631
32. Markstedt K, Mantas A, Tournier I, Martínez Ávila H, Hägg D, Gatenholm P. 3D bioprinting human chondrocytes with nanocellulose–alginate bioink for cartilage tissue engineering applications. *Biomacromolecules*. 2015;16(5):1489-1496. doi: 10.1021/acs.biomac.5b00188
33. Kolesky DB, Truby RL, Gladman AS, Busbee TA, Homan KA, Lewis JA. 3D bioprinting of vascularized, heterogeneous cell-laden tissue constructs. *Adv Mater*. 2014;26(19):3124-3130. doi: 10.1002/adma.201305506
34. Cernencu AI, Lungu A, Dragusin DM, et al. 3D bioprinting of biosynthetic nanocellulose-filled gelma inks highly reliable for soft tissue-oriented constructs. *Materials*. 2021;14(17):4891. doi: 10.3390/ma14174891
35. Mao M, He J, Li Z, Han K, Li D. Multi-directional cellular alignment in 3D guided by electrohydrodynamically-printed microlattices. *Acta Biomater*. 2020;101:141-151. doi: 10.1016/j.actbio.2019.10.028
36. Raman R, Cvetkovic C, Uzel SGM, et al. Optogenetic skeletal muscle-powered adaptive biological machines. *Proc Natl Acad Sci*. 2016;113(13):3497-3502. doi: 10.1073/pnas.1516139113
37. Mestre R, Fuentes J, Lefaix L, et al. Improved performance of biohybrid muscle-based bio-bots doped with piezoelectric boron nitride nanotubes. *Adv Mater Technol*. 2022;8(2):2200505. doi: 10.1002/admt.202200505

38. Cvetkovic C, Raman R, Chan V, et al. Three-dimensionally printed biological machines powered by skeletal muscle. *Proc Natl Acad Sci U S A*. 2014;111(28):10125-10130. doi: 10.1073/pnas.1401577111

39. Pagan-Diaz GJ, Zhang X, Grant L, et al. Simulation and fabrication of stronger, larger, and faster walking biohybrid machines. *Adv Funct Mater.* 2018;28(23):1801145. doi: 10.1002/adfm.201801145

40. Wang J, Wang Y, Kim Y, Yu T, Bashir R. Multi-actuator light-controlled biological robots. *APL Bioeng*. 2022;6(3):036103. doi: 10.1063/5.0091507

41. Choi YJ, Kim TG, Jeong J, et al. 3D cell printing of functional skeletal muscle constructs using skeletal muscle-derived bioink. *Adv Healthc Mater*. 2016;5(20):2636-2645. doi: 10.1002/adhm.201600483

ACCSCIENCE PUBLISHING

International Journal of Bioprinting

RESEARCH ARTICLE

Bioprinted keratinocyte and stem cell-laden constructs for skin tissue engineering

Eva Bettendorf[1†], Rafael Schmid[1†], Raymund E. Horch[1], Annika Kengelbach-Weigand[1], Yvonne Kulicke[1], Stefan Schrüfer[2], Dirk W. Schubert[2], Zan Lamberger[3], Philipp Stahlhut[3], Gregor Lang[3], and Celena A. Sörgel[1*]

[1]Department of Plastic and Hand Surgery and Laboratory for Tissue Engineering and Regenerative Medicine, University Hospital of Erlangen, Friedrich-Alexander University Erlangen-Nürnberg, Erlangen, Germany

[2]Department of Materials Science and Engineering, Institute of Polymer Materials, Friedrich-Alexander University Erlangen-Nürnberg, Erlangen, Germany

[3]Department for Functional Materials in Medicine and Dentistry, University Hospital of Würzburg, Julius-Maximilians University Würzburg, Würzburg, Germany

Abstract

Treating large-scale skin wounds remains a significant therapeutic challenge, often due to insufficient autologous material for complete coverage. Recent advances in biofabrication offer a solution with reproducible and precise large-scale production. Herein, this study aims to evaluate the feasibility of biofabrication and develop a customized three-dimensional (3D) bioprinted skin construct containing immortalized HaCaT keratinocytes and adipose-derived stem cells (ADSCs). Keratinocytes were cultured in various hydrogels (e.g., containing alginate [Alg], fibrin [Fib], collagen, gelatin [Gel], gelatin methacryloyl [GelMA], hyaluronic acid [HA], and a pre-fabricated collagen-elastin-matrix) for 7 days. The metabolic activity of cultured keratinocytes was then evaluated during the co-cultivation of HaCaT and ADSCs in a transwell model. The metabolic activity in all groups increased over the experimental period. Alg/HA/Gel and GelMA hydrogels demonstrated good printability and high diffusion rates. There was no significant difference in pore size between all hydrogels. Based on the results of printability and diffusion assays, as well as scanning electron microscopy (SEM) and rheological measurements, Alg/HA/Gel and GelMA hydrogels were selected for the bioprinted 3D model. Fib hydrogel was integrated into the biofabricated constructs for its excellent metabolic activity in the transwell model. Hydrogel stability, cell survival, and metabolic activity in bioprinted 3D models containing keratinocytes and ADSCs were evaluated over 14 days. On day 14, metabolic activity and live cell count within the bioprinted constructs of the co-cultured groups were significantly higher compared to day 1. The biofabricated GelMA constructs displayed higher cell viability than Alg/HA/Gel constructs. Additionally, to evaluate cell migration out of the constructs, the metabolic activity and viability of the cells on the well bottom were examined. After 14 days, an average of 50% of the well bottom was covered by HaCaT cells, which were initially printed in co-culture into the constructs. These findings indicate that GelMA constructs containing keratinocytes and ADSCs may offer a promising therapeutic option in the treatment of large chronic wounds.

[†]These authors contributed equally to this work.

***Corresponding author:**
Celena A. Sörgel
(celena.soergel@uk-erlangen.de)

Citation: Bettendorf E, Schmid R, Horch RE, et al. Bioprinted keratinocyte and stem cell-laden constructs for skin tissue engineering. *Int J Bioprint*. 2024;10(6):3925. doi: 10.36922/ijb.3925

Received: June 12, 2024
Revised: July 25, 2024
Accepted: August 6, 2024
Published Online: August 7, 2024

Copyright: © 2024 Author(s). This is an Open Access article distributed under the terms of the Creative Commons Attribution License, permitting distribution, and reproduction in any medium, provided the original work is properly cited.

Publisher's Note: AccScience Publishing remains neutral with regard to jurisdictional claims in published maps and institutional affiliations.

Keywords: Keratinocytes; Stem cells; Bioprinting; Skin substitution; Wound healing; Hydrogel

1. Introduction

The skin, the largest organ of the human body, plays a crucial role in our interaction with the environment and protection against pathogens. Extensive damage to the skin and tissue loss from trauma, infection, or surgical intervention are not only difficult to treat but also can be life-threatening,[1,2] especially for large-scale and deep tissue burns from thermal, electrical, or chemical injuries.[2] Their prognosis is determined by the affected skin surface area, the depth of the lesion, and the patient's age.[3] The primary goal in the treatment of large-scale burns is to provide rapid surgical intervention with necrosectomy combined with adequate temporary wound coverage to prevent excessive fluid loss and maintain optimal moisture levels.[1,4,5] This temporary wound coverage must prevent desiccation of the wound bed, function as a bacterial barrier, be semipermeable to allow gas exchange and drainage of wound exudate, and provide good adherence to the wound bed.[1,3,4] If uninjured skin areas suitable for skin grafting are available during treatment, the temporal wound coverage can be replaced with definitive autologous skin grafts.[3,4] In some cases, there may be insufficient uninjured tissue for complete autologous treatment.[2] Autograft treatment can be supported by skin tissue engineering. Many commercially available biological or synthetic skin substitutes have been developed over the past decades. For example, cultured epithelial autografts have been used in the treatment of burn injuries for almost four decades and have since become part of the standard treatment protocol.[4] Nevertheless, there are problems regarding graft stability and resilience. The use of tissue-engineered skin substitutes, such as cultured epithelial sheet grafts, remains limited due to insufficient dermal elasticity, inadequate regeneration of skin appendages, and long-term postoperative scarring.[6] Ideally, an exemplary skin graft substitute would enable sufficient nutrient diffusion into the graft, exhibit healing and revascularization rates equal to or better than those of full-thickness skin grafts, and cause minimal donor site morbidity. Bioprinted constructs for skin graft substitution provide an ideal framework for optimal cell ingrowth due to their 3D structure. Unlike sprayed hydrogels or prefabricated substitutes, they can be adapted to the shape and depth of the wound surface.[7] Hydrogels can mimic the extracellular matrix and allow the diffusion of nutrients, cytokines, and growth factors throughout the construct. Alg is commonly used in bioprinting due to its non-antigenicity and favorable polymerization properties.[8–10] It has a high absorption capacity, allowing it to resorb wound exudate while maintaining a physiologically moist environment that promotes healing.[11] Studies revealed that Alg promotes cell adhesion, proliferation, and vascularization.[8,12] HA plays a major role in skin regeneration by increasing keratinocyte migration and proliferation and facilitating the repair and remodeling of the extracellular matrix.[9,11] A previous study examined the influence of Alg/HA-based hydrogels on ADSCs and HaCaT cell cultures. Alg/HA-based hydrogel promoted gap closure in an *in vitro* scratch assay, and *in vivo* testing on a rat model revealed a promoting effect in wound healing.[11]

Gelatin (Gel) is a popular hydrogel component because of its low immunogenicity and good mechanical properties.[1] It contains integrin-binding motif (RGD) sequences, which improve cell adhesion and stimulate angiogenesis. Furthermore, it contains target sequences for matrix metallopeptidases (MMPs) that support wound healing.[13] Additionally, Gel has good printability, increases shape fidelity, and functions as a temperature-thickener. Nevertheless, a polymeric additive, like Alg, or chemical functionalization is necessary to attain suitable mechanical strength.[13–16] GelMA is a photo-crosslinkable Gel that is biodegradable and allows high cell viability.[13,17,18] Methacrylation of Gel allows the polymerization, improving its mechanical properties and slowing degradation.[13,19] Fib hydrogels possess excellent biocompatibility and biodegradation properties.[1,20] Previous studies demonstrated that the formation of the dermo-epidermal junction can be enhanced by the use of a Fib-glue matrix.[21,22] Other studies indicated the good attachment properties of keratinocytes in a Fib net for rapid healing of full-thickness skin defects.[23]

To adequately support skin healing, a dermal equivalent mimicking the skin's natural properties is needed. Ideally, the graft would provide sufficient nutrient diffusion combined with optimal cell ingrowth into a construct that is adapted to the depth and size of the wound surface.[1,9] The utilized biomaterials must be biologically compatible and not adversely impact wound healing. Therefore, natural or synthetic polymer-based hydrogels can be combined with skin cells.[1,6] Optimally, stem cells are incorporated into the graft to synergistically influence keratinocyte metabolic activity and proliferation. Given the above, we aim to develop a customized 3D bioprinted construct containing immortalized HaCaT keratinocytes and ADSCs. Keratinocytes were initially cultivated in and on various hydrogels (e.g., containing Alg, Fib, collagen, and HA), as well as a prefabricated collagen-elastin-matrix. Furthermore, the metabolic activity of keratinocytes was evaluated during the co-cultivation of keratinocytes in the upper chamber and ADSCs in the

lower chamber of a transwell model. A biphasic bioprinted construct, containing keratinocytes and ADSCs in various hydrogels, was then developed. Hydrogel stability and the cells' metabolic activity and survival were evaluated over 14 days. Based on the results of this study, potential new treatment options could include bioprinted constructs with keratinocytes and stem cells. These constructs may promote earlier wound healing and complete skin regeneration, helping to prevent acute and chronic sequelae resulting from large-scale burn injuries.[24]

2. Methods

2.1. Cell lines

The immortalized HaCaT cell line was purchased from Cell Lines Service GmbH (CLS, Germany) and cultivated up to passage 50. Immortalized ADSCs were obtained from Evercyte GmbH (Austria) and cultivated up to passage 24. HaCaT were cultivated in Dulbecco's modified eagle medium (DMEM) (Gibco; Thermo Fisher Scientific, USA), supplemented with 4500 mg/mL glucose, L-glutamine, sodium pyruvate, and sodium bicarbonate, 10% fetal calf serum (FCS) (Sigma-Aldrich, United States of America [USA]) and 1% penicillin-streptomycin (P/S) (Sigma-Aldrich, USA). ADSCs were grown in Endothelial Cell Basal Medium-2 (EBM®-2) (Clonetics®; Lonza Group AG, Switzerland) enriched with the supplement mix, 2% FCS superior (Sigma-Aldrich, USA), and 1% geneticin (Gibco; Thermo Fisher Scientific, USA). Both cell lines were incubated at 37°C with 5% CO_2.

2.2. HaCaT in co-culture with ADSC in a transwell model

2.2.1. Cell seeding

Adipose-derived stem cells (ADSCs) were seeded in a 24-well plate at a density of 5×10^4 cells/well in EMB®-2 and left to adhere for 4 h at 37°C. The medium was then changed to 1 mL DMEM with 10% FCS and 1% P/S (all from Sigma-Aldrich, USA). HaCaT keratinocytes were seeded in the hydrogel at a density of 2×10^5 cells/transwell according to the experimental groups presented in Table 1. For each experimental group, a control group without ADSCs was set up in parallel. Therefore, the well below the control group was left cell-free but filled with 1 mL DMEM, 10% FCS, and 1% P/S. For groups I, II, IV, V, and VI, hydrogels were prepared with a concentration of 1×10^6 cells/mL. In group III, 2×10^5 cells were seeded on each scaffold.

Table 1. Biomaterials used for 3D cell culture

Group	Biomaterial(s)
I	Alginate (0.5% [m/v]) and gelatin (0.5% [m/v])
II	Fibrin (1.1% [m/v])
III	Collagen-elastin template matrix
IV	Alginate (0.5% [m/v]), gelatin (0.5% [m/v]), collagen (0.05% [m/v]), and hyaluronic acid (3% [m/v])
V	Alginate (0.5% [m/v]), gelatin (3% [m/v]), and hyaluronic acid (0.1% [m/v])
VI	Gelatin methacryloyl (4% [m/v]) and lithium phenyl-2,4,6-trimethylbenzoyl phosphinate (LAP; 0.2% [m/v])

2.2.2. Biomaterial for 3D cell culture

The following groups of biomaterials were used for 3D cell culture within the transwell model: I: 0.5% (m/v) Alg (PH 176; JRS PHARMA GmbH & Co. KG, Germany) and 0.5% (m/v) Gel (Sigma-Aldrich, USA); II: 1.1% (m/v) fibrinogen and thrombin (Baxter Healthcare GmbH, Austria); III: collagen-elastin template matrix (MatriDerm®; Dr. Suwelack Skin and Health Care, Germany); IV: 0.5% (m/v) Alg, 0.5% (m/v) Gel, 0.05% (m/v) collagen (Sigma-Aldrich, USA), and 3% (m/v) HA (CarboSynth Ltd., UK); V: 0.5% (m/v) Alg, 3% (m/v) Gel, and 0.1% (m/v) HA; VI: 4% (m/v) gelatin methacryloyl (Biotechnologies Ltd., Canada) and 0.2% (m/v) lithium phenyl-2,4,6-trimethylbenzoyl phosphinate (LAP; Sigma-Aldrich, USA). All experimental groups were seeded as triplicates.

Hydrogel groups I, IV, V, and VI were synthesized by dissolving the respective composition (m/v) in phosphate-buffered saline (PBS) without Ca^{2+} and Mg^{2+} (Sigma-Aldrich, USA). The pH of the solution was adjusted to 7.4 with PBS (PBS Dulbecco's w/o Ca^{2+} and Mg^{2+}, Instamed 9.55 g/L; Biochrom GmbH, Germany) for groups IV, V, and VI. The hydrogels were mixed at 37°C until a homogenous state was reached. HaCaTs were re-suspended in the hydrogel using a positive displacement pipette, and 200 µL of each hydrogel was seeded into the upper chamber of the transwell with a pore size of 0.4 µm. The hydrogels of groups IV and V were chelated for 10 min in 100 mM calcium chloride ($CaCl_2$) solution (Sigma-Aldrich, USA) and then washed with PBS (Sigma-Aldrich, USA). The hydrogel of group VI was crosslinked using 405 nm light for 1 min.

For the preparation of Fib in group II, 9.1% (m/v) human fibrinogen and 500 IU/mL thrombin were each diluted with Hanks buffered saline solution (HBSS; Sigma-Aldrich, USA) in a 1:4 ratio. The cells were mixed into the fibrinogen component of the kit and re-suspended. Thereafter, 100 µL of the mixture was pipetted into the transwell, and the same amount of thrombin was added. For chelation, the two components were gently mixed with a positive displacement pipette.

The collagen-elastin template matrix is a commercially available dermal replacement scaffold available in sheets and was used as the control (group III). Under sterile

conditions, 6 mm diameter pieces were punched out, and each scaffold was seeded with 2×10^5 cells dissolved in 100 µL DMEM with 10% FCS and 1% P/S. HaCaTs were left to adhere on the scaffolds for 5 min and then transferred to the transwells.

After seeding, all transwells were transferred into the corresponding 24-well plate and covered with 200 µL DMEM with 10% FCS and 1% P/S (Figure 1). Samples were incubated at 37°C with 5% CO_2 for 7 days. The medium was changed every 48–72 h.

2.2.3. Cell viability

Live/dead staining of exemplary samples was performed for demonstration purposes on day 7 for all groups. The transwells were washed in HBSS for 15 min at room temperature. The staining solutions were produced by mixing each reagent, 2 µM calcein-acetoxymethyl (calcein-AM; Sigma-Aldrich, USA), and 1.5 µM propidium iodide (Sigma-Aldrich, USA), with the cell culture medium. Subsequently, the samples were incubated in calcein-AM suspension at 37°C and 5% CO_2 for 30 min, followed by incubation at room temperature in propidium iodide solution for 5 min. Samples were protected from light and washed twice with HBSS. Microscopic examination in 100× magnification was conducted using Olympus IX83 (CellSens software; Olympus, Japan).

The WST-8 Assay (PromoCell GmbH, Germany) was used for measuring the metabolic activity. On days 1, 4, and 7, three replicates of each group were examined. The reagent solution was prepared by mixing CCVK1 reagent with DMEM, supplemented with 10% FCS and 1% P/S, in a ratio of 1:11. The transwells were transferred into a new 24-well plate, containing 500 µL CCVK1 reagent suspension with DMEM, supplemented with 10% FCS and 1% P/S, and added with additional 200 µL reagent suspension. A blank sample without cells was also prepared. The samples were incubated at 37°C and 5% CO_2 for 4 h, protected from light. Approximately 50 µL of reagent solution from both the lower and upper chambers were merged in a 96-well plate. The absorbance of 100 µL solution was measured at 450 and 600 nm (background) in a 96-well plate using Multiscan Go and SkanIT RE for Multiscan Go 6.1 (Thermo Fisher Scientific, USA) in triplicates.

2.3. Material characterization of hydrogels

2.3.1. Printability assay

The printability of the different hydrogels (Table 2) was evaluated immediately after bioprinting.

Scaffolds (1 cm^2) were printed using a cylindrical needle with a 0.25 mm inner diameter at a speed of 5 mm/s. The printed scaffolds were placed under a light microscope for optical magnification. The diagonal length of five crossing points in the printed scaffold was measured (Figure 2). As the inner diameter is 250 µm, the ideal length of the intersection would be 353.55 µm. The diagonal crossing ratio (DCR) of each intersection was determined by dividing the ideal length by the mean real values of each crossing point.

2.3.2. Cryo-scanning electron microscopy

The samples were rapidly frozen in slushed nitrogen at −210°C after placing them between aluminum plates (diameter: 3 mm) with a 2 mm notch for sample fixation. Subsequent transfer steps were performed at −140°C with EM VCT100 cryo-shuttle (Leica Microsystems, Germany). To generate a freshly fractured hydrogel surface, one of the aluminum plates was knocked off and freeze-etched for 15

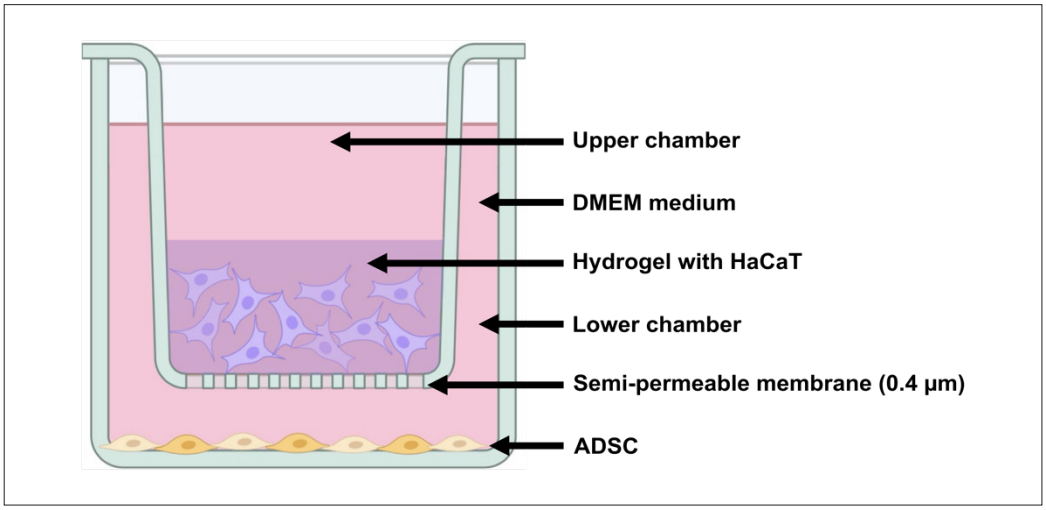

Figure 1. Schematic representation of HaCaT keratinocytes and adipose-derived stem cells (ADSCs) in co-culture in the transwell model. Abbreviation: DMEM, Dulbecco's modified eagle medium.

Table 2. Composition of hydrogels

Hydrogel	Biomaterial(s)
I	Alginate (0.5% [m/v]) and gelatin (0.5% [m/v])
II	Fibrin (1.1% [m/v])
III	Fibrinogen (1.8% [m/v]), alginate (1% [m/v]), and hyaluronic acid (1% [m/v])
IV	Alginate (0.5% [m/v]), gelatin (0.5% [m/v]), collagen (0.05% [m/v]), and hyaluronic acid (3% [m/v])
V	Alginate (0.5% [m/v]), gelatin (3% [m/v]), and hyaluronic acid (0.1% [m/v])
VI	Gelatin methacryloyl (4% [m/v]) and lithium phenyl-2,4,6-trimethyl benzoyl phosphinate (LAP) (0.2% [m/v])

min at −85°C under high vacuum (<1 × 10^3 mbar) in a Sputter Coater machine (ACE 400; Leica Microsystems, Germany). The samples were then sputtered with 3 nm platinum and transferred to the scanning electron microscope (SEM) chamber (Crossbeam 340; Zeiss, Germany). Images of the hydrogel surface morphology were taken at −160°C using an acceleration voltage of 8 kV.

2.3.3. Stiffness analysis

The stiffness of the cast hydrogels of the second phase of the study was analyzed for groups I–VI. Here, samples were measured on day 1 after overnight incubation in HBSS at 37°C. The stiffness of the biofabricated constructs of the third phase was analyzed for groups Ib (Alg/HA/Gel and Alg/HA/Fib with HaCaT and ADSCs) and IIb (GelMA and Alg/HA/Fib with HaCaT and ADSCs), as well as for comparative constructs without cells (Alg/HA/Gel and Alg/HA/Fib; GelMA and Alg/HA/Fib). The samples were cultured in cell culture media. Viscoelastic properties of the bioprinted constructs were measured using a DHR-3 rheometer (TA Instruments, USA), equipped with a 20-mm plate-plate geometry for the hydrogels and an 8-mm plate-plate geometry for the biofabricated constructs, and set to oscillating compression mode. The tests were performed at a constant rheometer temperature of 37°C. The storage modulus (E') and loss modulus (E'') were determined by increasing the frequency from 0.3 to 100 rad/s. The complex modulus was calculated using the following equation:

$$|E^*| = \sqrt{E'^2 + E''^2} \quad \text{(I)}$$

The mean and standard deviation of the samples were calculated for samples that fulfill the following criteria: (i) storage modulus and loss modulus were positive and recorded by the rheometer; (ii) no drastic alteration of the axial force was recorded during the measurement; (iii) the oscillation force was significantly higher than the predetermined lower limit given by the manufacturer; and (iv) raw data signals for recorded force and displacement resulted in a sinusoidal curve. The values are based on at least three technical replicates, except for GelMA (at 75.4 and 100 rad/s) in phase 1, where only two replicates met the above criteria.

2.3.4. Diffusion assay

To ensure that proteins expressed by encapsulated cells can diffuse through the hydrogels, we used HEK293 reporter cells, which have been reported to consistently express a fusion protein consisting of the extracellular domain of TNFR2, the human IgG1 Fc domain, and Gaussia princeps luciferase (GpL). The reporter cells were mixed with the hydrogels (Table 2) at a concentration of 1 × 10^6 cells/mL. A total of 100 µL of each hydrogel was cast into the wells of

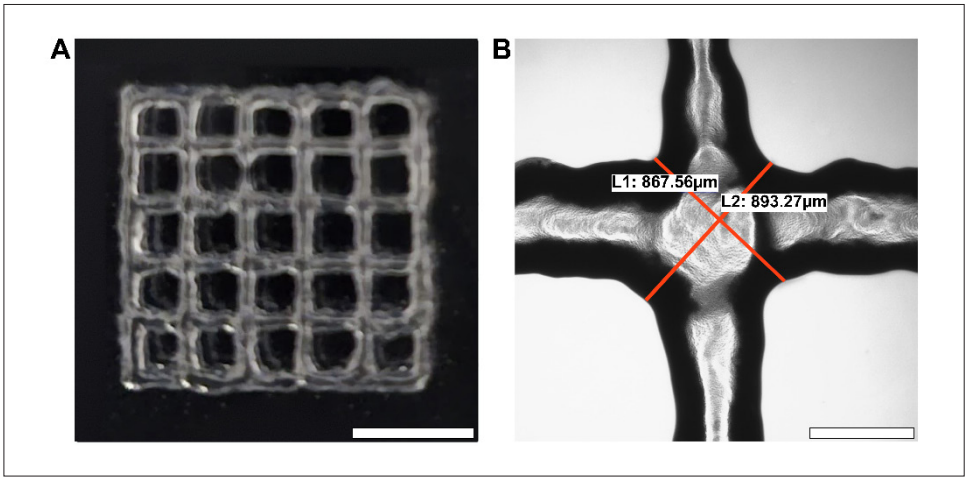

Figure 2. Printability assay. (A) Example of a printed scaffold with Alg/HA/Gel. (B) Exemplary measurement of a crossing point on the printed scaffold; L1: 867.56 µm; L2: 893.27 µm. Scale bars: 4 mm (A); 500 µm (B). Abbreviations: Alg, alginate; HA, hyaluronic acid; Gel, gelatin.

a 96-well plate and crosslinked as described above; 100 µL of RPMI40 medium (Sigma Aldrich, USA), supplemented with 10% FCS and 1% P/S, were added to each well. On days 1, 3, 5, and 7, the supernatant was removed and stored at −20°C. To measure the luciferase activity of the fusion protein, 5 µL supernatant was diluted with 45 µL RPMI40 medium, containing 0.5% FCS and 1% P/S, in a black 96-well plate (Greiner Bio-One, Austria). Directly before measurement, 25 µL of 1.5 µM coelenterazine solution (Carl Roth, Germany) was added to each well. The relative light units (RLU) were determined using a microplate reader (Promega, USA).

2.4. HaCaT in an ADSC-enriched 3D-bioprinted hydrogel model

2.4.1. Bioprinting

Owing to their higher long-term stability and better printing properties, Alg/HA/Gel (0.5% [m/v] Alg; 3% [m/v] Gel; and 0.1% [m/v] HA) and GelMA hydrogels were selected for bioprinting the 3D model. Additionally, the Alg/HA/Fib hydrogel was integrated into the biofabricated constructs.

The Alg/HA/Gel hydrogel was synthesized by dissolving Alg, Gel, and HA in PBS without Ca^{2+} and Mg^{2+}. The hydrogel was homogenized for 30 min at 37°C on a magnetic stirrer. To produce the bioink containing 4% (m/v) GelMA and 0.2% (m/v) LAP, solid GelMA (80% degree of substitution) was dissolved in PBS with constant stirring for 30 min at 37°C. Additionally, LAP was dissolved in PBS and added to the GelMA solution. To obtain a homogenized hydrogel, the solution was stirred for another 10–15 min at 37°C. In the experimental groups containing keratinocytes, HaCaTs were resuspended in the Alg/HA/Gel or GelMA hydrogel to a final concentration of 1×10^6 cells/mL.

To produce the Alg/HA/Fib bioink, 1.8% (m/v) fibrinogen was dissolved in HBSS on a magnetic stirrer at 25°C for 15 min. Thereafter, 1% (m/v) Alg and 1% (m/v) HA were added to the solution and homogenized by constant stirring for 10–15 min at 37°C. ADSCs cultured in EBM-2, supplemented with 2% FCS and 1% geneticin, were mixed into the Alg/HA/Fib hydrogel at 1×10^6 cells/mL.

The different hydrogels and cell lines were combined according to the experimental groups presented in Table 3. The bioinks were transferred into 3-mL cartridges using a displacement pipette and subsequently cooled in a 15°C water bath for 10 min to obtain the appropriate viscosity.

The pneumatic extrusion-based bioprinter Cellink Inkredible+ (Cellink, USA) was used for cell-printing. Two print heads were used during the printing process, i.e., for Alg/HA/Gel (or GelMA) and Alg/HA/Fib, respectively. The print heads were also cooled to 15°C to maintain structural integrity during fabrication. Three-layered constructs of 1 cm^2 were printed at a speed of 5 mm/s onto Petri dishes using conical nozzles (Vieweg GmbH, Germany) with an inner diameter of 0.41 mm. Each layer had a height of 0.6 mm; the total height of each construct was 1.8 mm. A pressure of 20–25 kPa was used for Alg/HA/Gel and GelMA, while Alg/HA/Fib was printed at 10–15 kPa. Each biofabricated Alg/HA/Gel or GelMA construct contained an average of 12×10^4 HaCaTs; each biofabricated Alg/HA/Fib construct contained 6×10^4 ADSCs. Figure 3 illustrates the biofabrication process.

The printed constructs were crosslinked with the respective crosslinking agent at room temperature. Groups Ia, Ib, and Ic were crosslinked with 50 IU/mL thrombin for 1 min and 100 mM $CaCl_2$ for 10 min immediately after bioprinting the entire construct. Groups IIa, IIb, and IIc were crosslinked with 405 nm light for 2 min and 50 IU/mL thrombin for 1 min; the crosslinking process was initiated before the printing process to ensure shape retention.

The firm constructs were transferred into 6-well plates coated with 3 mg/cm^2 rat-tail collagen type I (Sigma-Aldrich, USA), covered with DMEM (supplemented with 10% FCS and 1% P/S), and incubated at 37°C and 5% CO_2. The medium was changed every 2–3 days.

For all experiments containing the respective cell type, HaCaTs were seeded in either Alg/HA/Gel or GelMA,

Table 3. Biomaterials and cell lines used for 3D cell culture

Group	Hydrogel	Cell line
Ia	Alg/HA/Gel and Alg/HA/Fib	ADSCs
Ib		HaCaT and ADSCs
Ic		HaCaT
IIa	GelMA and Alg/HA/Fib	ADSCs
IIb		HaCaT and ADSCs
IIc		HaCaT

Abbreviations: ADSCs, adipose-derived stem cells; Alg, alginate; Fib, fibrin; Gel, gelatin; GelMA, gelatin methacryloyl; HA, hyaluronic acid.

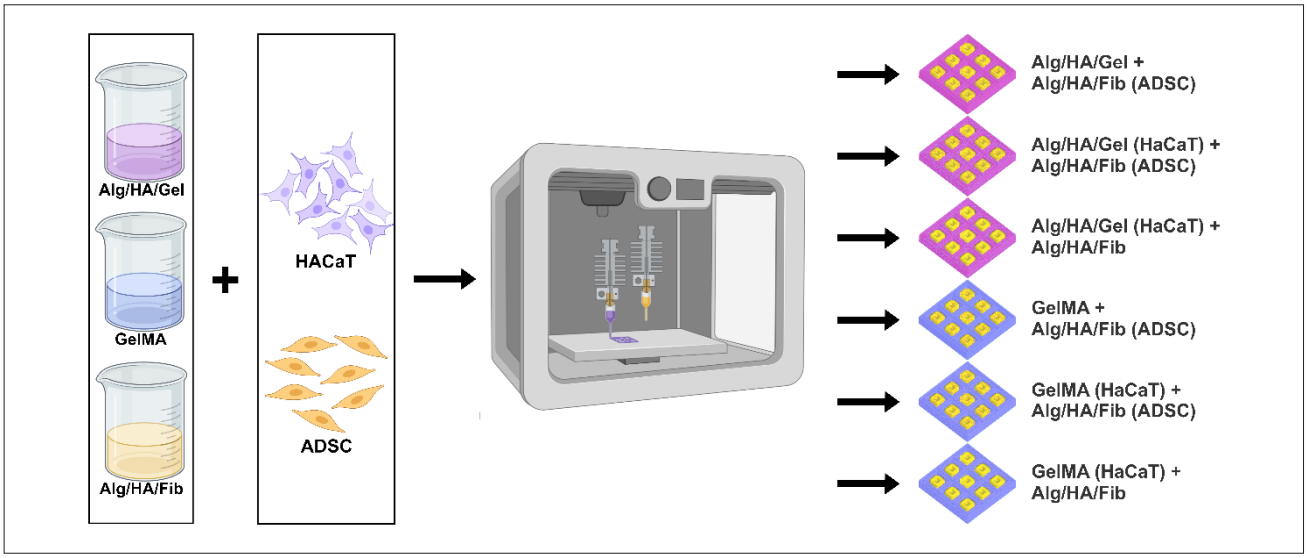

Figure 3. Schematic representation of the biofabrication process. The process begins with selecting the combination of either "Alg/HA/Gel and Alg/HA/Fib" or "GelMA and Alg/HA/Fib." Three different groups were printed: group I: Alg/HA/Fib bioink containing ADSCs; group II: either Alg/HA/Gel or GelMA bioink containing HaCaTs; and group III: Alg/HA/Fib bioink containing ADSCs and either Alg/HA/Gel or GelMA bioink containing HaCaTs. Abbreviations: ADSCs, adipose-derived stem cells; Alg, alginate; Fib, fibrin; Gel, gelatin; GelMA, gelatin methacryloyl; HA, hyaluronic acid.

while ADSCs were seeded into Alg/HA/Fib. Regardless of the cell type, every biofabricated construct consists of two hydrogels, Alg/HA/Gel or GelMA combined with Alg/HA/Fib, hereinafter referred to as Alg/HA/Gel or GelMA, respectively (Figure 3).

2.4.2. Degradation behavior

For degradation studies, biofabricated constructs (groups Ib and IIb) containing both cell types (HaCaTs and ADSCs) were produced alongside constructs without cells. The constructs were stored in sterile cell strainers (Corning, USA) in 6-well plates containing DMEM and incubated at 37°C and 5% CO_2. On days 1, 4, 7, and 14, the size (length [l] and width [w]) of the bioprinted constructs was analyzed. The area (A) was calculated using the following equation:

$$A = l \times w \quad \text{(II)}$$

2.4.3. WST-8 assay

The metabolic activity of cells within the hydrogel and those that had migrated out of the biofabricated constructs onto the well bottom was evaluated separately using a WST-8 Assay on days 1, 4, 7, and 14 after bioprinting. The reagent solution was prepared by mixing the CCVK1 reagent with DMEM in a ratio of 1:11. Three constructs were transferred into a 24-well plate containing 550 µL reagent solution per well. An additional blank sample (without cells) was prepared for each group. The medium within the former wells of the bioprinted constructs was replaced with 2.2 mL of reagent solution. The samples were incubated with the reagent solution at 37°C for 2 h, protected from light. The absorbance of 100 µL solution was measured at 450 and 600 nm (background) in a 96-well plate using Multiscan Go and SkanIT RE for Multiscan Go 6.1 (Thermo Fisher Scientific, USA) in triplicates.

2.4.4. Live/dead assay

A live/dead assay was performed to assess cell viability in the printed constructs and cells at the well bottom, i.e., using calcein-AM (stains living cells) and propidium iodide (stains dead cells). Three constructs were transferred to a 24-well plate. The biofabricated constructs and their former wells were incubated with the calcein-AM solution at 37°C. After 30 min, the calcein-AM solution was replaced by propidium iodide solution, and the samples were incubated at room temperature for 5 min. All samples were washed with HBSS and protected from light. Cell viability was examined using fluorescent microscopy (Olympus IX-83, cellSens Software V1.16; Olympus, Japan) on days 1, 4, 7, and 14. The stained constructs and cells at the well bottom were analyzed at 40× and 100× magnifications.

For the constructs, images were taken at three standardized positions in two different planes. Cell survival and proliferation inside the bioprinted constructs were assessed by counting live and dead cells on days 1, 4, 7, and 14 manually using FIJI (version 2.140.0/1.54f), a distribution of Image J. The amount of cell migration and distribution on the well bottom was evaluated by

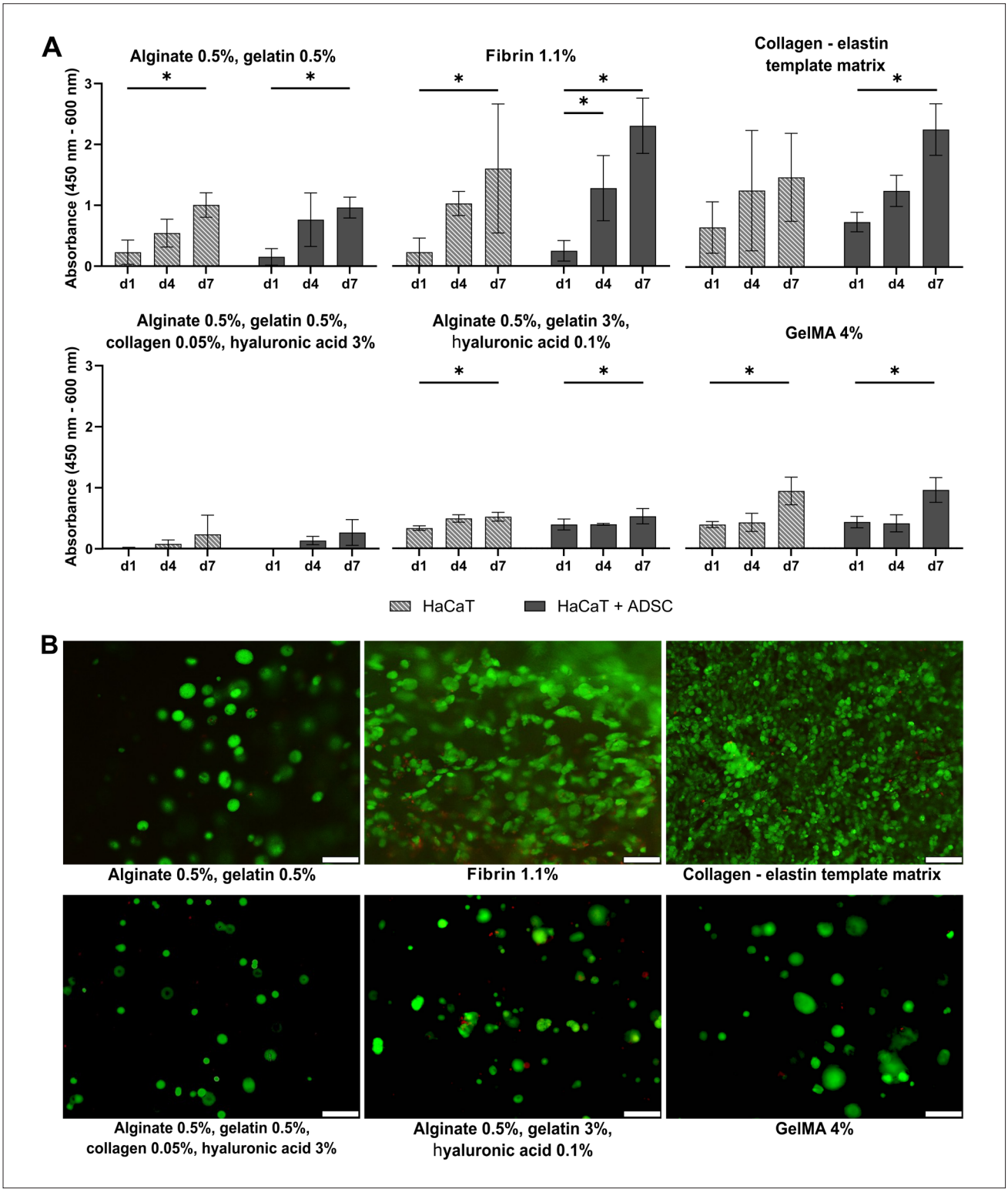

Figure 4. Metabolic activity and cell viability of HaCaT in the transwell model. (A) Metabolic activity of HaCaT cells within the hydrogels in the transwell model on days 1, 7, and 14 (n = 3). Data are represented as mean ± standard deviation; *p ≤ 0.05. (B) HaCaT cells within hydrogels in the transwell model with adipose-derived stem cells (ADSCs) in the lower chamber on days 1, 4, and 7. Green color denotes living cells; red color denotes dead cells. Scale bars: 100 μm. Abbreviation: GelMA, gelatin methacryloyl.

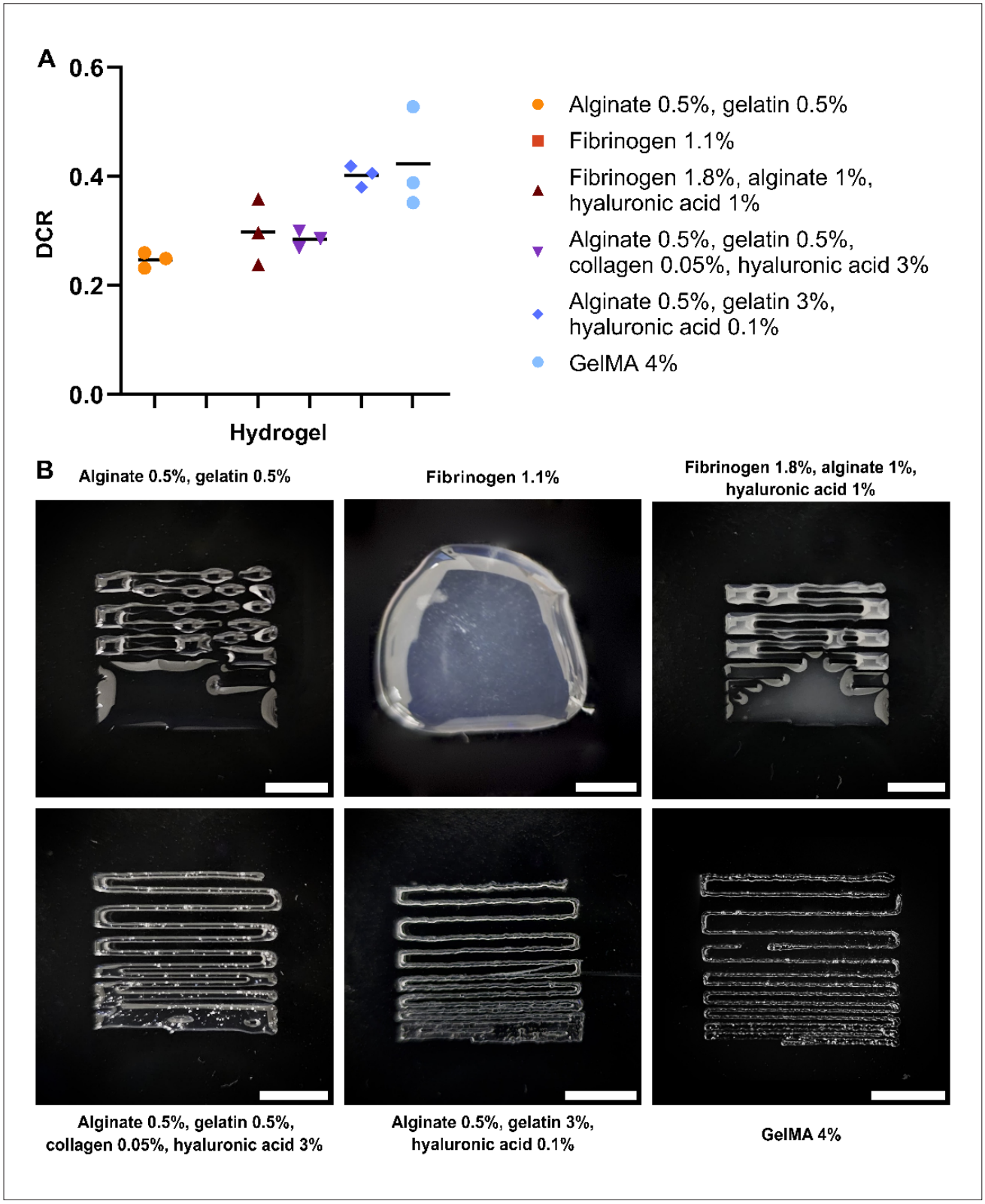

Figure 5. Printability of the different hydrogels (n = 3). (A) Diagonal crossing ratio (DCR) of each hydrogel. DCR for fibrinogen (1.1%) is not defined as the hydrogel had low shape-fidelity and could not be measured. (B) Exemplary images of each hydrogel printed in a meander shape. Scale bars: 10mm. Abbreviation: GelMA, gelatin methacryloyl.

calculating the area of the well bottom covered by living cells using Image J. HaCaTs and ADSCs were differentiated based on their morphology in the live/dead staining.

2.5. Statistical analysis

All experiments were performed in triplicate, and results were analyzed using Graph Pad Prism 10 (GraphPad Software Inc., USA). Data are presented as the mean ± standard deviation or box plots with whiskers. The *p*-value was set to ≤0.05 to define statistical significance. Differences between the groups were analyzed using a *t*-test and two-way analysis of variance (ANOVA) with Tukey's multiple comparisons for assessing cell viability and metabolic activity. For the transwell model, two-way ANOVA with Tukey's multiple comparisons and Fisher's Least significant difference (LSD) were used for analysis. The stiffness of the biofabricated constructs was analyzed with two-way ANOVA and three-way ANOVA with Fisher's LSD test. Three-way ANOVA with Fisher's LSD test was also used to analyze the degradation results. Figures 1 and 3 were created with biorender.

3. Results

3.1. Cell viability of HaCaT in co-culture with ADSCs in a transwell model

The metabolic activity of the cell cultures within the transwells was measured on days 1, 4, and 7. All samples (listed in Table 1) exhibited increased metabolic activity over 7 days (Figure 4A). Analysis of the metabolic rate suggests that time played a significant role for all groups, except group IV (Alg/Gel/collagen/HA).

Hydrogels I (Alg/Gel), II (Fib), and VI (GelMA) displayed significantly higher cell metabolic activity on day 7 compared with day 1 for the co-culture and control (without ADSCs) groups. Additionally, cells seeded within hydrogel II demonstrated a significant increase in metabolic activity from days 1 to 4 for the group containing HaCaT and ADSC co-culture. Although the difference in metabolic activity of hydrogel V between days 1 and 7 was less pronounced compared to the other bioinks, it was still statistically significant. The metabolic activity of cells within the collagen-elastin template matrix was significantly higher on day 7 compared with day 1 for the co-culture group. Samples containing HaCaT and ADSCs in hydrogels II (Fib) and III (collagen-elastin template matrix) exhibited increased metabolic activity in comparison to the groups without ADSCs. The weakest metabolic activity was observed for hydrogel IV (Alg/Gel/collagen/HA). Hydrogel II and the collagen-elastin template matrix reported the highest metabolic activity. Within these hydrogels, cells proliferated rapidly and formed multiple small colonies, i.e., visible in Figure 4B. The keratinocytes seeded into hydrogels I (Alg/Gel), V (Alg/Gel/HA), and VI (GelMA) formed fewer but larger colonies. The images of HaCaT within the different hydrogels indicate good cell survival, i.e., without any notable dead cells.

3.2. Material characterization of hydrogels

Characterizations of all hydrogels (listed in Table 2) are presented in this section.

3.2.1. Printability assay

As illustrated in Figure 5, hydrogels IV, V, and VI demonstrated good printability. The printability of hydrogel II was immeasurable as the hydrogel deliquesced right after extrusion from the printing nozzle. Therefore, fibrinogen was enriched with 1% (m/v) Alg and 1% (m/v) HA (i.e., hydrogen III), resulting in a DCR of 0.30. For hydrogels V and VI, the highest DCR was observed at 0.40 and 0.42, respectively. Hydrogels I and IV reported the lowest DCR of 0.24 and 0.29, respectively.

3.2.2. Microstructure and material properties

The hydrogels were analyzed on day 1 using cryo-SEM (Figure 6). No significant difference in pore size was observed when comparing hydrogels I–IV. Hydrogel VI exhibited smaller pores than the other samples. The pore sizes ranged from 0.21 (hydrogel VI) to 1.03 (hydrogel V). Hydrogel V has a less homogenous pore distribution compared with the other hydrogels (Figure 6A).

Measuring the mechanical properties of the hydrogels on day 1 revealed notable differences (Figure 7). All hydrogels, except for hydrogel IV (Alg/Gel/collagen/HA), primarily exhibit elastic properties, with a higher storage modulus than loss modulus. Hydrogel IV exhibited much higher viscous properties, resulting in a less stable hydrogel that could barely be transferred into the rheometer. Hydrogel VI (GelMA) was the softest hydrogel. The other hydrogels were in a similar range throughout the tested frequency range.

Hydrogels that could not be printed (I, II, and III) or unstable (IV) were not suitable for use as biofabricated constructs. However, hydrogel III, despite issues with shape fidelity, was still used in the pockets of the constructs due to its high cell compatibility.

3.2.3. Diffusion assay

A diffusion assay was performed to evaluate the diffusion characteristics of the hydrogels (Figure 8). For this assay, HEK-293 cells producing a 150 kDa protein with a luciferase domain were implanted into the hydrogels.

An increase in protein concentration was measured over 7 days in the supernatant for all hydrogels, suggesting HEK-293 proliferation and diffusion of the protein into the

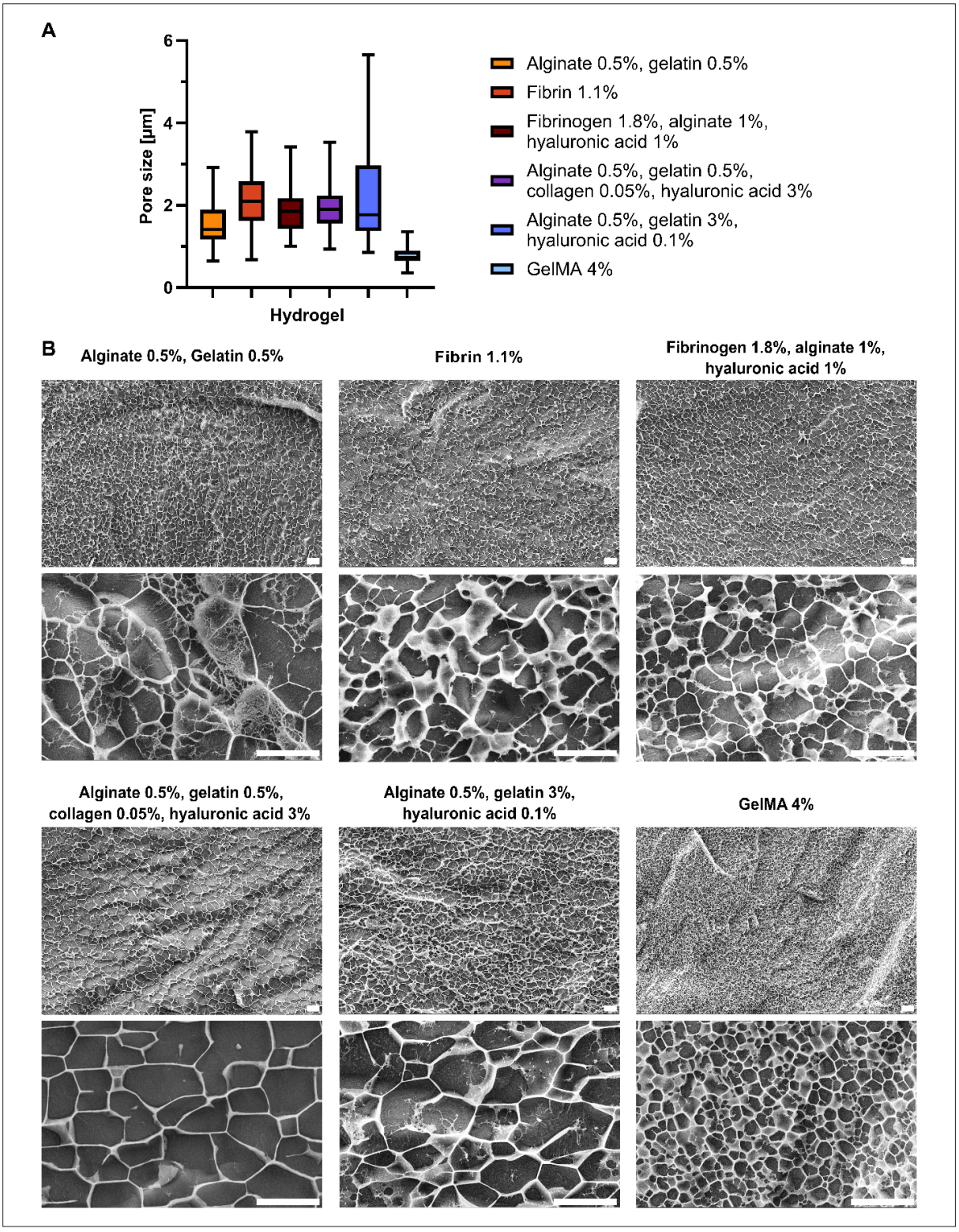

Figure 6. Scanning electron microscopy (SEM) of the different hydrogels ($n = 1$). (A) Pore sizes measured from the SEM images and displayed as box plots with whiskers. (B) Exemplary images of the hydrogels in two different magnifications. The magnification of the upper pictures is 1000× (top image) and 5000× (bottom image), the magnification of the lower picture is 5000-fold. Scale bars: 5 µm. Abbreviation: GelMA, gelatin methacryloyl.

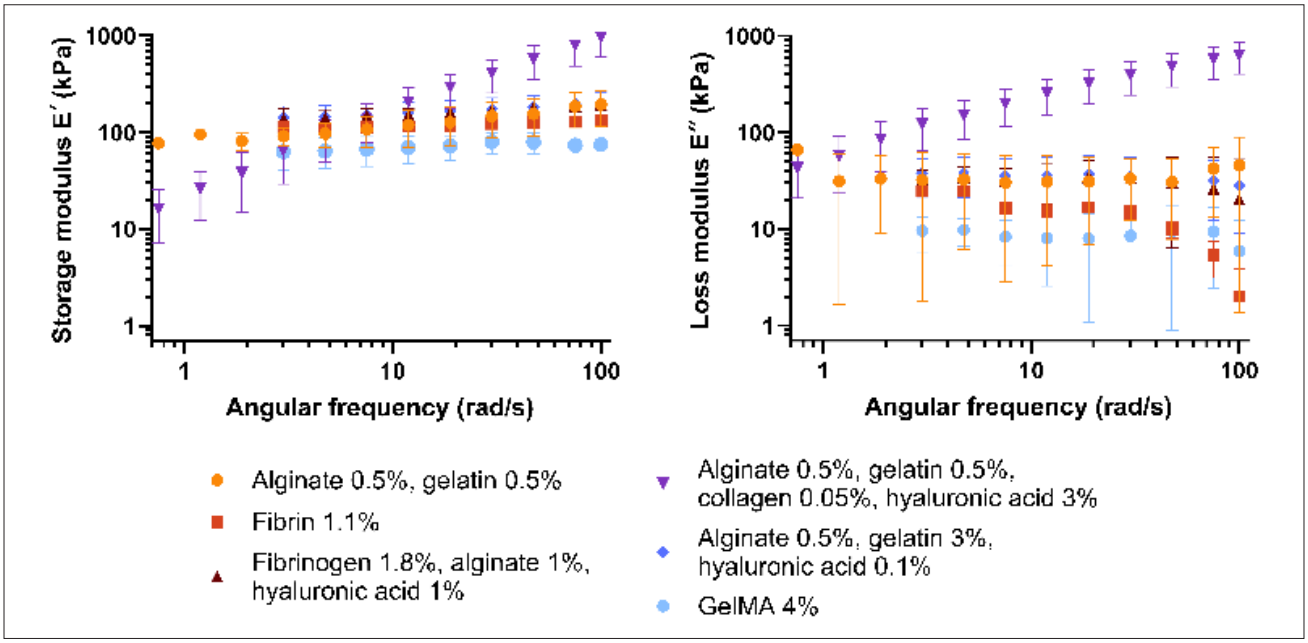

Figure 7. Material characteristics of the different hydrogels (n = 4). All groups, except for group IV (purple), primarily exhibited elastic properties. Abbreviation: GelMA, gelatin methacryloyl.

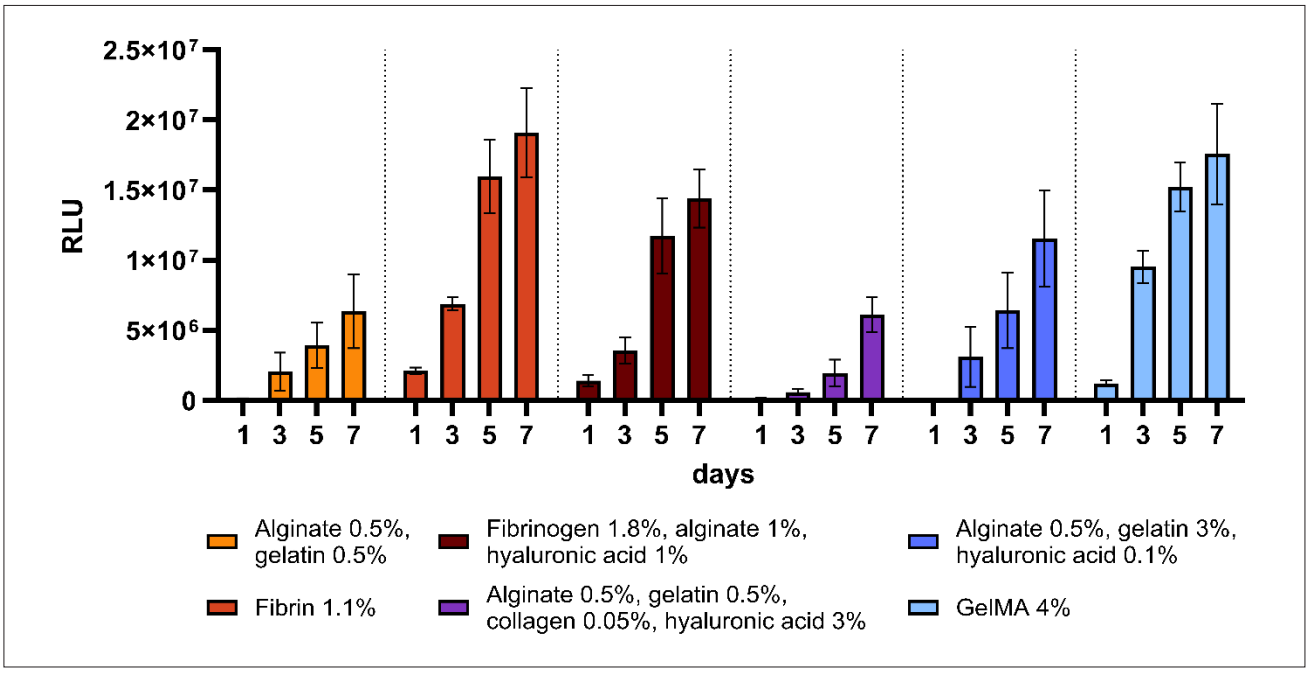

Figure 8. Luciferase assay of the hydrogels. All tested hydrogels allowed diffusion of a 150 kDa protein and displayed an increase in luciferase activity in the medium over 7 days (n = 5). Abbreviations: GelMA, gelatin methacryloyl; RLU, relative light units.

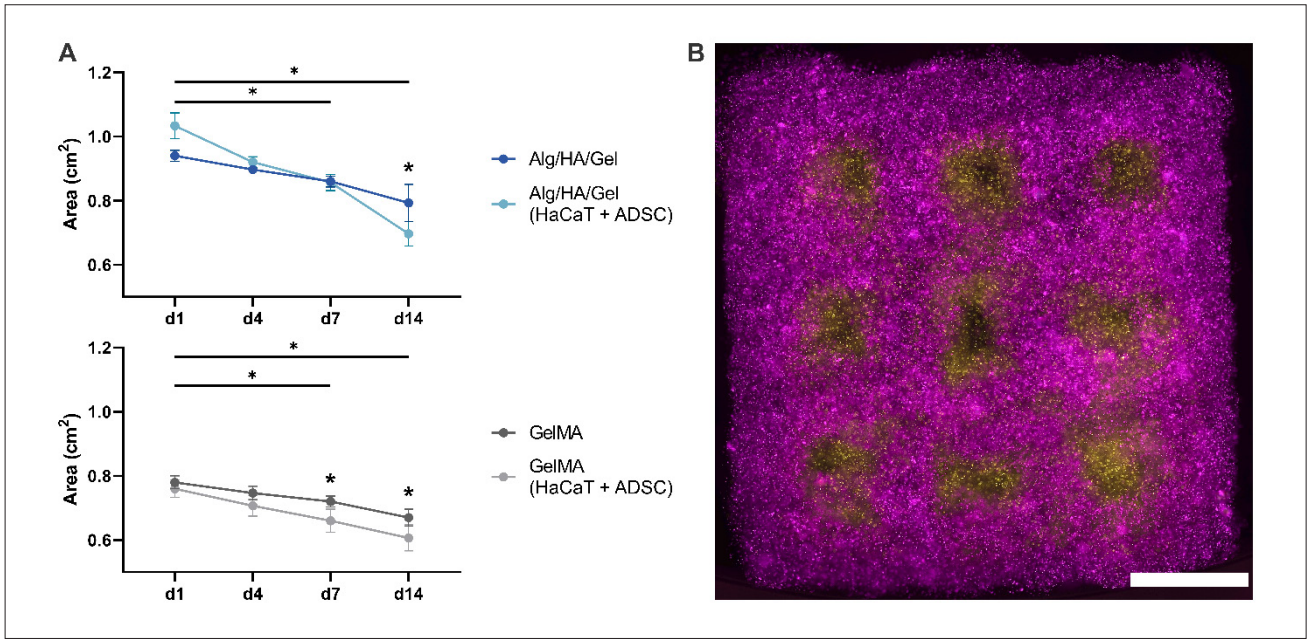

Figure 9. Size and cell distribution of the bioprinted constructs. (A) Area of biofabricated cell-laden and cell-free constructs composed of alginate (Alg)/hyaluronic acid (HA)/gelatin (Gel) or gelatin methacryloyl (GelMA). Data represented as mean ± standard deviation (n = 3); * $p \leq 0.05$. (B) HaCaTs and adipose-derived stem cells (ADSCs) bioprinted in Alg/HA/Gel and Alg/HA/fibrin (Fib); HaCaTs are stained with DiI (pink) and ADSCs are stained with Oregon green (yellow) before the printing process. Scale bar: 2 mm.

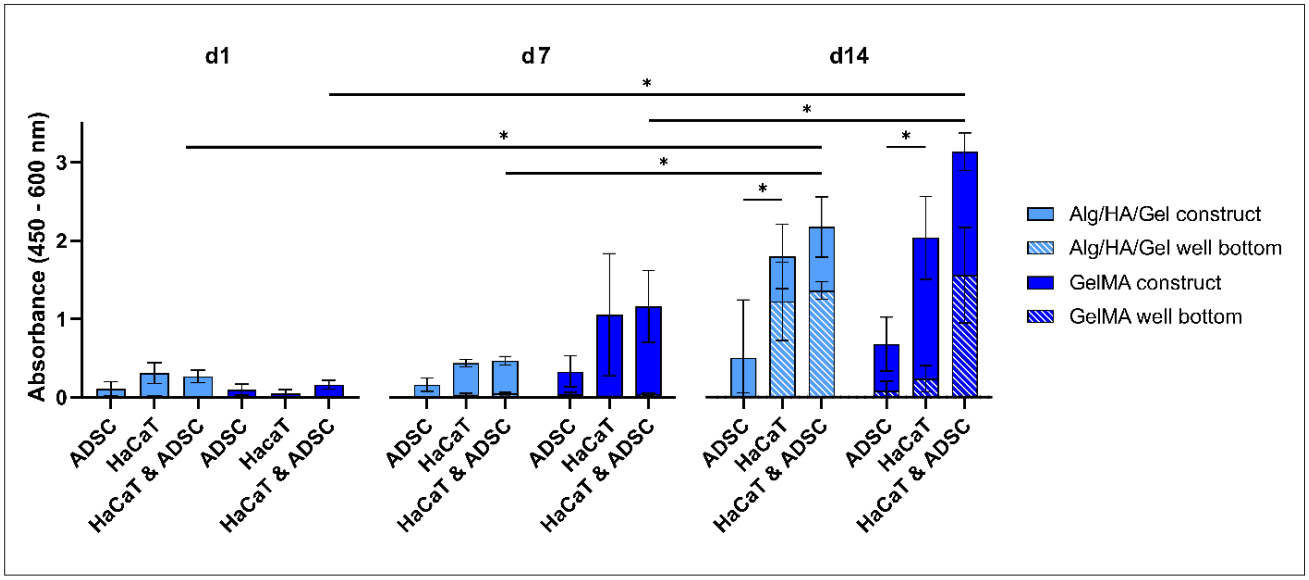

Figure 10. Combined metabolic activity of cells within the bioprinted constructs and at the well bottom on days 1, 7, and 14 ($n = 3$). Data are represented as mean ± standard deviation; *$p \leq 0.05$. Abbreviations: ADSC, adipose-derived stem cell; Alg, alginate; Gel, gelatin; GelMA, gelatin methacryloyl; HA, hyaluronic acid.

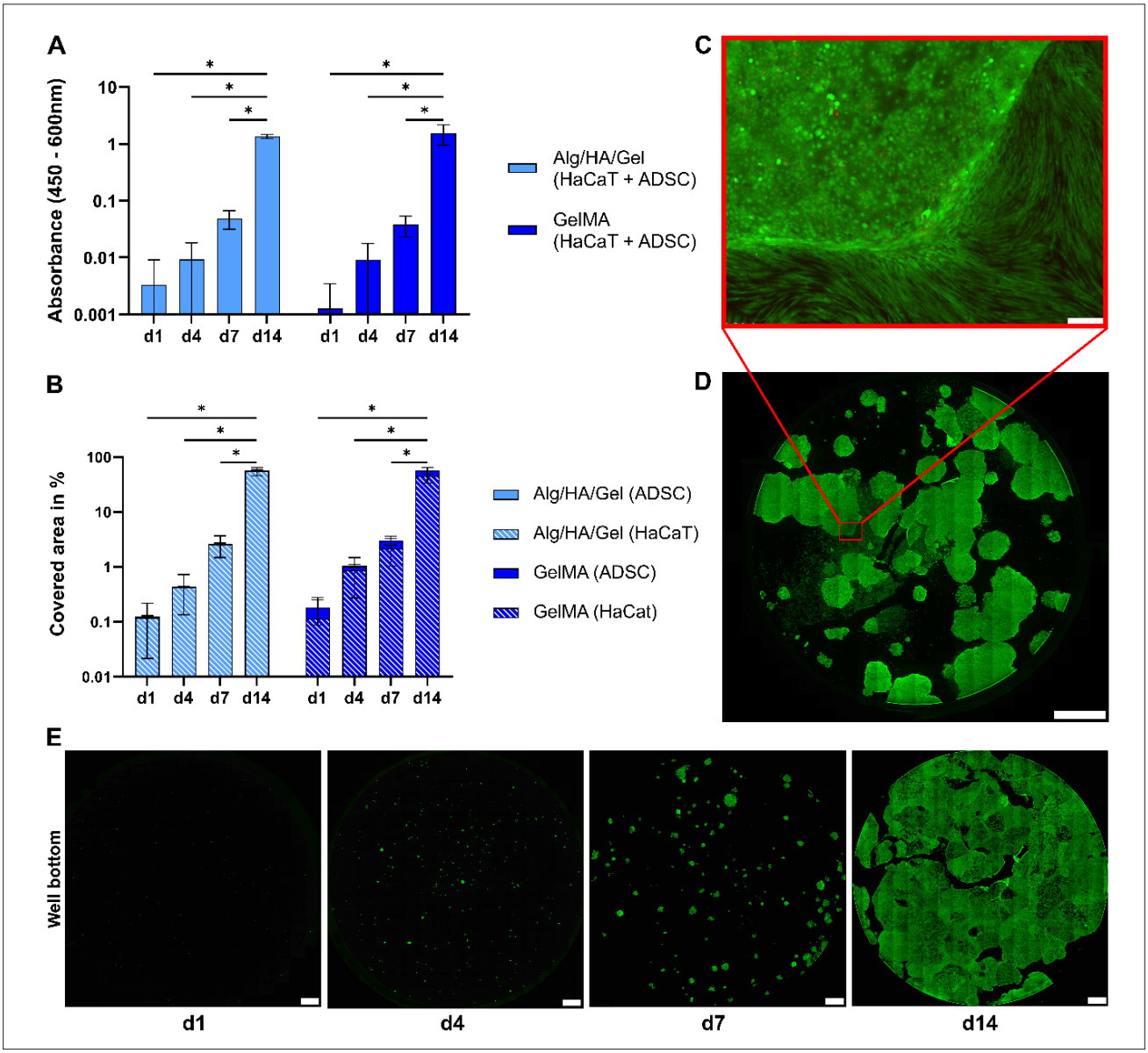

Figure 11. Cell viability of cells at the well bottom. (A) Metabolic activity of HaCaT and adipose-derived stem cells (ADSCs) at the well bottom on days (d) 1, 4, 7, and 14 (n = 3). (B) Living cells at the well bottom on days 1, 4, 7, and 14 (n = 3). (C–D) Cells at the well bottom from cell-laden Alg/HA/Gel constructs day 14: HaCaT (top left); ADSCs (bottom right). (E) Cells at the well from cell-laden Alg/HA/Gel constructs on days 1, 4, 7, and 14; magnification: 40×. Scale bars: 200 µm (C); 5 mm (D); and 2 mm (E). Green: living cells; red: dead cells. Data are represented as mean ± standard deviation (n = 3); *p ≤ 0.05. Abbreviations: Alg, alginate; Gel, gelatin; GelMA, gelatin methacryloyl; HA, hyaluronic acid.

medium. Hydrogels II (Fib), III (Fib/Alg/HA), V (Alg/Gel/HA), and VI (GelMA) reported relatively high measured relative light units (RLU).

3.3. HaCaTs in an ADSC-enriched 3D-bioprinted hydrogel model

3.3.1. Degradation behavior

The length and width of the bioprinted constructs were evaluated on days 1, 4, 7, and 14. The size of the constructs of all groups decreased over the experimental period of 14 days (Figure 9A). Statistical analysis revealed a significant difference in the size of the bioprinted constructs between Alg/HA/Gel and GelMA at all time points, regardless of cell presence. Cell-laden GelMA constructs were significantly smaller on day 7 than the comparative group without cells. In addition, for both hydrogel compositions, cell-laden constructs were significantly smaller on day 14 than those without cells.

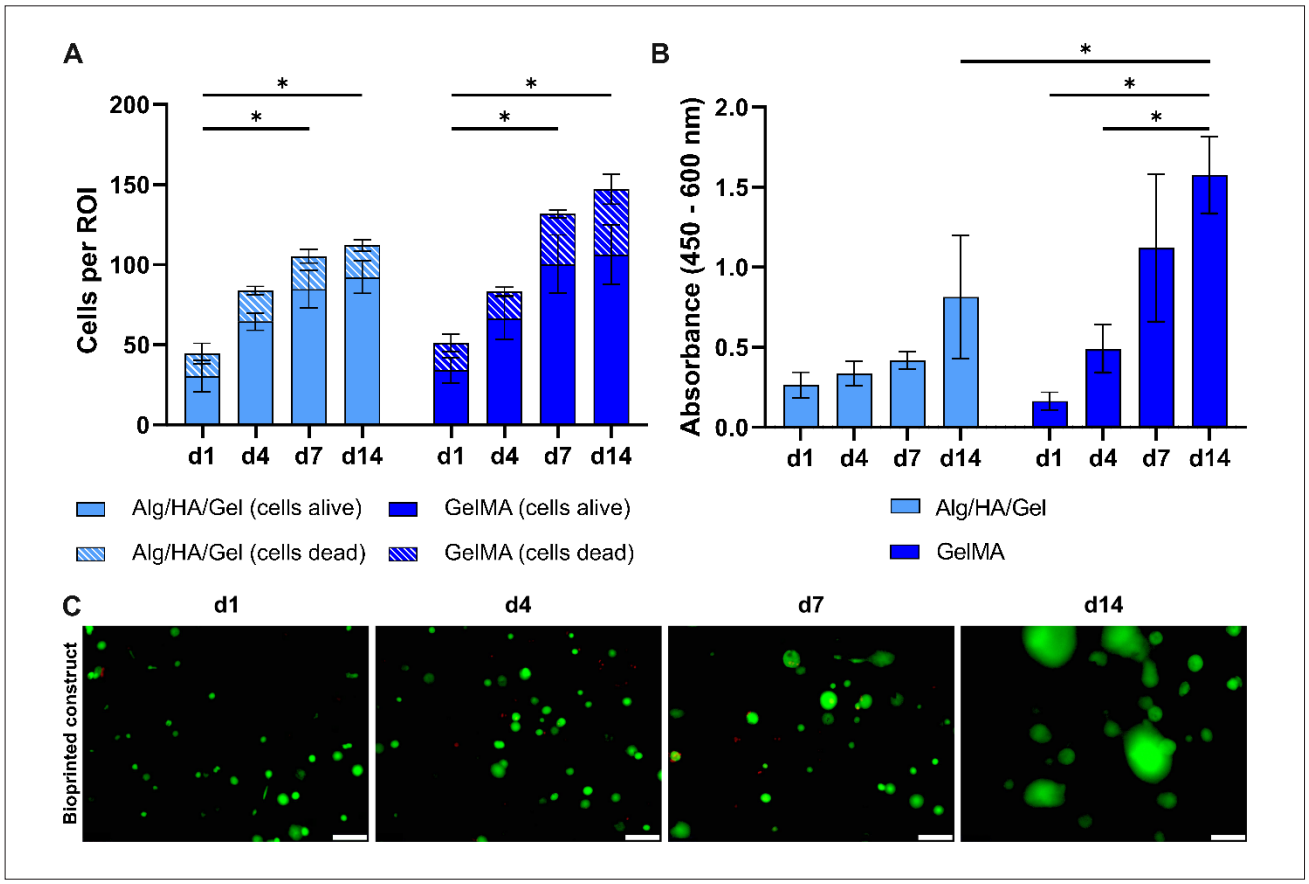

Figure 12. Viability and metabolic activity of co-cultured constructs. (A) Cell viability of biofabricated constructs containing HaCaT and ADSCs on days (d) 1, 4, 7, and 14 (n = 3). (B) Metabolic activity of HaCaT and ADSCs within printed constructs on days 1, 4, 7, and 14 (n = 3). (C) HaCaT and ADSCs in Alg/HA/Gel and Alg/HA/Fib on days 1, 4, 7, and 14. Scale bars: 100 μm. Green indicates living cells; red indicates dead cells. Data are represented as mean ± standard deviation; *p ≤ 0.05. Abbreviations: ADSC, adipose-derived stem cell; Alg, alginate; Fib, fibrin; Gel, gelatin; GelMA, gelatin methacryloyl; HA, hyaluronic acid; ROI, region of interest.

Time significantly impacts the degradation process. All constructs displayed a significantly higher area on day 1 compared with days 7 and 14, independent of hydrogel and cell composition. Furthermore, all experimental groups significantly decreased in size from day 4 to 14. Cell-laden constructs significantly degraded from day 1 to 4 and from day 7 to 14.

3.3.2. WST-8 assay

The metabolic activity of the bioprinted samples and cells at the well bottom was measured on days 1, 4, 7, and 14 (Figure 10).

All printed constructs displayed a steady increase in metabolic activity regardless of cell composition or choice of hydrogel over the experimental period. Likewise, the metabolic activity of cells at the well bottom increased for all experimental groups until day 14. On day 14, the metabolic activity of the constructs composed of Alg/HA/Fib with HaCaT and ADSC in co-culture accounted for 37% of the combined metabolic activity, compared to 50% for the GelMA control group. Analyzing the metabolic rate over the entire test period using two-way ANOVA and unpaired *t*-test revealed significant differences over time for cells within the biofabricated constructs and those at the well bottom.

Cells at the well bottom displayed a significant difference between day 14 and days 1, 4, and 7 for experimental groups Ib (Alg/HA/Gel and Alg/HA/Fib with HaCaT and ADSC), Ic (Alg/HA/Gel and Alg/HA/Fib with HaCaT), and IIb (GelMA and Alg/HA/Fib with HaCaT and ADSC). On day 14, the cells of group Ic (Alg/HA/Gel and Alg/HA/Fib with HaCaT) at the well bottom exhibited a significantly higher metabolic activity than those of group IIc (GelMA and Alg/HA/Fib with HaCaT) (Figure 11A).

Additionally, for the cells at the well bottom, Alg/HA/Gel displayed a significantly higher metabolic rate compared with GelMA on day 1. HaCaT and ADSCs at the well bottom were differentiated according to their

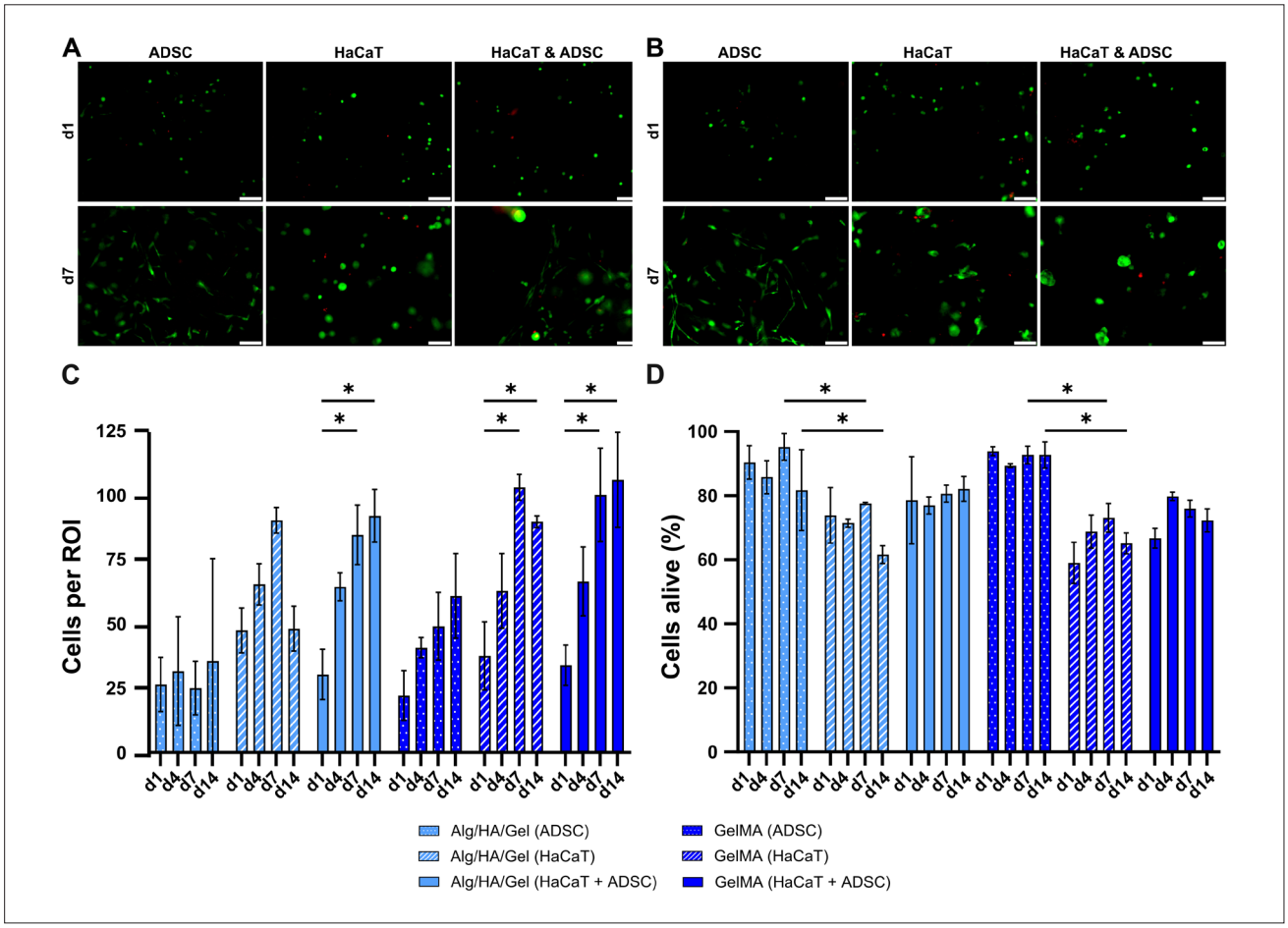

Figure 13. Cell viability of biofabricated constructs of all experimental groups. (A) Cells in Alg/HA/Gel and Alg/HA/Fib on days (d) 1 and 7. (B) Cells in GelMA and Alg/HA/Fib. Scale bars: 100 µm. Green indicates living cells; red indicates dead cells. (C) Living cells per ROI within the printed constructs of all experimental groups on days 1, 4, 7, and 14 (n = 3). (D) Ratio of living cells within the constructs of all experimental groups on days 1, 4, 7, and 14 (n = 3). Data are represented as mean ± standard deviation; *p ≤ 0.05. Abbreviations: ADSC, adipose-derived stem cell; Alg, alginate; Fib, fibrin; Gel, gelatin; GelMA, gelatin methacryloyl; HA, hyaluronic acid; ROI, region of interest.

morphology (Figure 11C). On days 4, 7, and 14 two-way ANOVA revealed a significantly higher metabolic activity of HaCaTs at the well bottom compared with that of ADSCs.

Cells within GelMA constructs (groups IIb and IIc) exhibited a significantly higher metabolic activity on day 14 compared with days 1 and 4. On days 7 and 14, the metabolic activity of the biofabricated GelMA constructs was significantly higher compared to Alg/HA/Gel samples. On day 14, group IIb (GelMA and Alg/HA/Fib with HaCaT and ADSC) constructs demonstrated a significantly higher metabolic activity compared with the respective constructs of group Ib (Alg/HA/Gel with HaCaT and ADSC) (Figure 12B). Furthermore, a significant difference was observed for constructs containing only HaCaT. The cells within group IIc (GelMA) displayed higher metabolic activity than the comparative group Ic (Alg/HA/Gel) on day 14.

3.3.3. Live/dead assay

To determine the viability of cells within the biofabricated constructs and those at the well bottom, a live/dead assay was performed on days 1, 4, 7, and 14.

A statistical significance for time could be determined using two-way ANOVA for cells at the well bottom. The area of the well bottom covered with living cells was significantly higher on day 14 compared to days 1, 4, and 7 for both hydrogels (Alg/HA/Gel and GelMA) containing only HaCaT. In comparison to days 1, 4, and 7, day 14 also correlates to significantly higher viability of cells at the well bottom for both hydrogels containing HaCaT and ADSCs in co-culture (Figure 12B). Moreover, cell type significantly influences the results. On days 4, 7, and 14, a significantly higher amount of HaCaT was detected at the well bottom compared to ADSCs. The area of the well bottom covered by

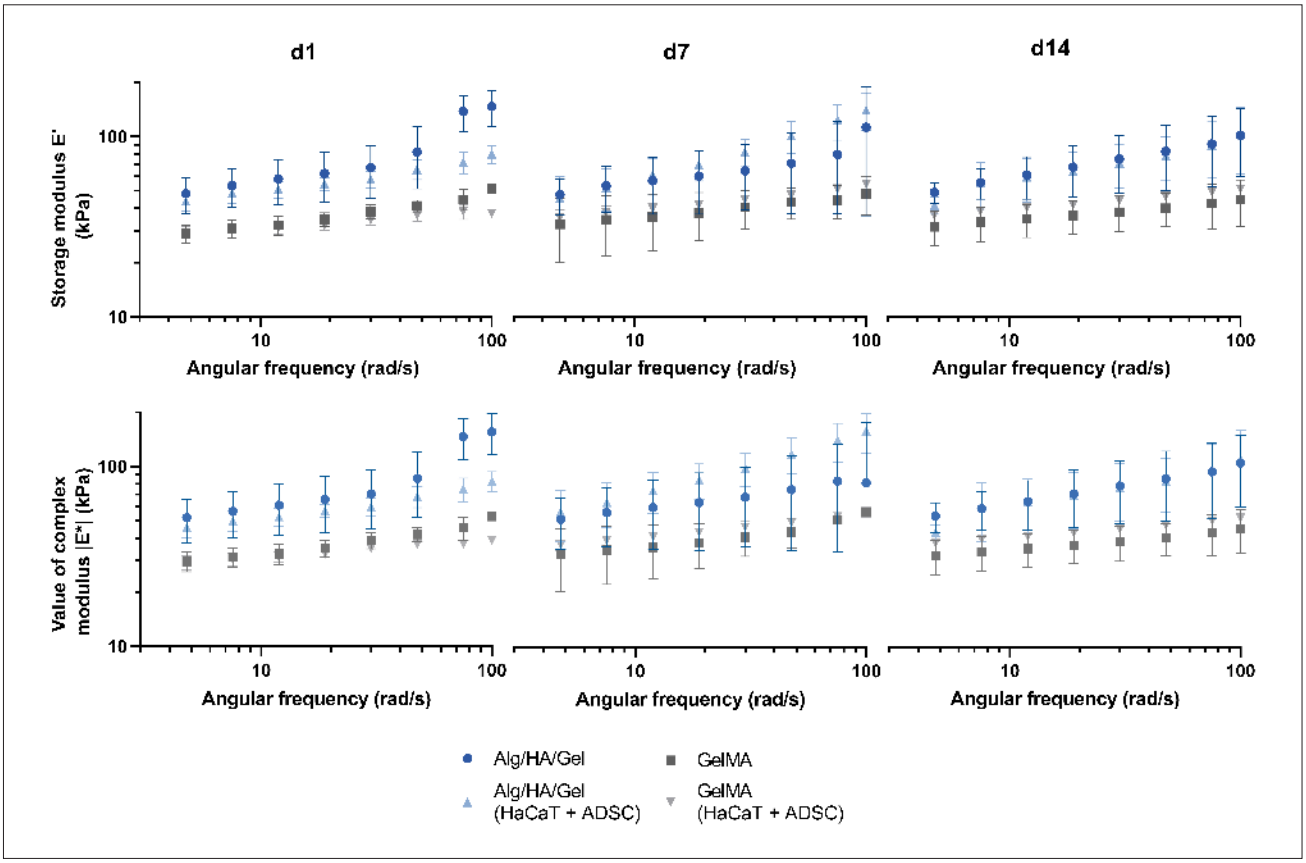

Figure 14. Storage modulus and complex modulus of printed constructs on days (d) 1, 7, and 14 at 37°C (n = 3). Data are represented as mean ± standard deviation. Abbreviations: ADSC, adipose-derived stem cell; Alg, alginate; Gel, gelatin; GelMA, gelatin methacryloyl; HA, hyaluronic acid.

living cells strongly correlated with the metabolic activity of cells at the well bottom (i.e., correlation coefficient of 1 for both hydrogels).

The bioprinted constructs containing HaCaT and ADSCs displayed a steady increase in living cells over the experimental period (Figure 12A). Experimental groups containing both HaCaT and ADSCs revealed significantly higher cell viability on days 7 and 14 compared to day 1. Figure 13 features the cell viability within the biofabricated constructs of all experimental groups. Within the constructs, two-way ANOVA revealed a significant role of time for the total number of cells and number of living cells per region of interest (ROI). Furthermore, on days 7 and 14, the total number of cells and number of living cells per ROI within GelMA constructs with HaCaT was significantly higher than that of day 1. On day 14, the total number of cells per ROI within the GelMA constructs with HaCaT was significantly higher compared with the respective Alg/HA/Gel constructs. In contrast to the constructs containing only HaCaT, constructs containing HaCaT and ADSC in co-culture displayed an increasing trend in live cell count over the 14 days.

Two-way ANOVA revealed a significant difference in cell viability between the hydrogels. The viability of cells within GelMA constructs was significantly higher compared to those in Alg/HA/Gel constructs on days 7 and 14. Moreover, the cell type significantly affected the results. The ratio of living cells within the constructs was higher for ADSCs compared to that of HaCaT. On days 1 and 4, the ratio of living cells within GelMA constructs was significantly higher for ADSCs than for HaCaT. On days 7 and 14, the survival of ADSCs was significantly higher than that of HaCaT for the constructs of both hydrogel types. Cell viability and metabolic activity of cells within the biofabricated constructs indicate a strong correlation for Alg/HA/Gel (correlation coefficient: 0.75) and GelMA (correlation coefficient: 0.98).

3.3.4. Stiffness analysis

The rheological behavior of the bioprinted constructs was measured on days (d) 1, 7, and 14. All biofabricated constructs had a higher storage modulus than loss modulus on all days, confirming the gel-like behavior of the hydrogels. Figure 14 features the viscoelastic properties of

the bioprinted constructs at a constant deformation of 1% (0.15 N pre-load) and an increasing frequency in the range of 0.3–100 rad/s on days 1, 7, and 14. By comparing the samples made of Alg/HA/Gel with those made of GelMA at a frequency of 7.5 rad/s, two-way ANOVA revealed a significant difference between the hydrogels. Alg/HA/Gel constructs had a significantly higher storage modulus and value of complex modulus than GelMA constructs.

On day 1, the biofabricated Alg/HA/Gel construct displayed significantly higher storage modulus and complex modulus compared to GelMA constructs, regardless of cell presence. Considering the storage modulus, this significant difference between the hydrogels was also observed on day 14 for the constructs without cells.

4. Discussion

The treatment of large-scale burn wounds and skin defects remains a major challenge in reconstructive surgery due to the limited availability of autologous skin grafts and the resulting donor-site morbidity.[1,2,8] Given the urgency of closing large burn wounds, biofabrication offers new possibilities by enabling automated and precise skin substitute production in large quantities. Bioengineered skin substitutes in combination with autologous stem cells could represent a promising therapeutic alternative to the transplantation of autologous tissue.[1,6,25] Within this study, the influence of ADSCs on the growth of HaCaT keratinocytes was evaluated in a transwell model, as well as in a bioprinted 3D model composed of two different hydrogel combinations. This study aimed to identify a bioink that facilitates optimal cell survival and elucidate the synergistic influence of ADSCs on HaCaT keratinocyte viability and growth.

In this study, we initially employed a transwell model to compare the cell metabolic activity of HaCaT keratinocytes within different hydrogels. The cells displayed a significant increase in metabolic activity from days 1 to 7 when seeded into or onto different hydrogels composed of Alg/Gel, Fib, collagen/elastin, Alg/HA/Gel, or GelMA. The keratinocytes within the Fib hydrogel demonstrated excellent metabolic activity with significantly increasing metabolic activity within 7 days, despite Fib hydrogels possessing weak shape fidelity (confirmed via bioprintability assay), which is consistent with other studies.[20] Hydrogels VI (GelMA) and V (Alg/HA/Gel) exhibited precise printing properties and shape fidelity. For GelMA, the highest DCR was observed at 0.42, consistent with the findings of Schulik et al.[26] There was no significant difference in pore size between hydrogels I and IV. GelMA (hydrogel VI) resulted in significantly smaller pores in SEM than the other samples.

Mechanical characterization of the hydrogels revealed that hydrogel IV (Alg/Gel/collagen/HA) had much higher viscous characteristics than the others (that exhibit elastic properties). Hence, hydrogel IV is less suitable for constructs that require long-term stability.

The reporter protein TNFR2-Fc-GpL expressed by encapsulated HEK293 cells was detected in the culture medium. Since TNFR2-Fc-GpL has a relatively high molecular weight (~150 kDa), the secreted proteins can diffuse through the hydrogels and stimulate the cells in co-culture. Alg/HA/Gel and GelMA demonstrated adequate protein diffusion into the medium.

Both Alg/HA/Gel and GelMA hydrogels were chosen for the bioprinted 3D model due to stable cell viability inside the hydrogels and good bioink printability. The excellent cell metabolic activity within the Fib hydrogel in the transwell model led us to integrate the hydrogel into the 3D model. Since printing the original Fib concentration from the transwell experiments proved unfeasible, as demonstrated by the printability assay, we opted to add 1% Alg and 1% HA to the hydrogel to enable bioprinting.

During the experimental period of the bioprinted 3D model, an increase in metabolic activity in all experimental groups was demonstrated. Within the constructs of both hydrogels, the metabolic activity was significantly higher on day 14 compared to days 1 and 4. The live/dead assay indicated an increasing cell count for the co-cultured groups over the experimental period. The biofabricated GelMA constructs demonstrated nine-fold higher cell viability on day 14 compared to day 1, consistent with the findings of Zhao et al., whereby GelMA hydrogels reportedly support the growth of HaCaT.[17] The Alg/Ha/Gel constructs also displayed a steady increase in cell viability and count. Alg- and HA-based bioinks are widely used in tissue engineering due to their good biocompatibility and biodegradability.[20] Several studies reported a high cell viability in Alg-, Gel-, or HA-containing hydrogels.[10,27–30]

In this study, we incorporated ADSCs into biofabricated constructs. It has been proposed that HA/Gel-based hydrogels enhance the cell differentiation and viability of ADSCs.[29] ADSCs play a major role in activating tissue regeneration via paracrine signaling and can differentiate into skin cells.[31–33] Seo et al. examined human ADSCs and human keratinocytes in a transwell model and demonstrated that, when co-cultured with keratinocytes, ADSCs express increased amounts of keratinocyte-specific markers and may differentiate into keratinocyte lineage.[33] Previous 2D and transwell studies described how HaCaT and ADSCs could positively influence each other.[33–36] Treating HaCaT keratinocytes with a 50% conditioned medium of ADSCs increased the proliferation of HaCaT

cells and enhanced *in vitro* wound healing.[34] These findings are consistent with the results of our 3D model. The bioprinted constructs containing HaCaT and ADSCs in co-culture revealed significantly higher cell viability on days 14 and 7 compared to day 1. In contrast, Alg/HA/Gel constructs containing only HaCaT did not exhibit a statistically significant increase in cell viability from days 1 to 14. Additionally, the live/dead assay indicated increasing live cell counts in constructs containing both HaCaT and ADSCs, whereas groups containing only HaCaT displayed increased live cell count only until day 7. Our study revealed a mean survival rate of 88% for ADSCs within Alg/HA/Gel constructs and 92% within GelMA constructs throughout the experimental period, consistent with the findings of Schmid et al., whereby Alg/HA/Gel bioinks resulted in good printability and ADSC survival, proliferation, and differentiation.[15] Moreover, Li et al. also demonstrated high ADSC proliferation and growth factor secretion after ADSC conjugation onto a GelMA hydrogel.[37]

Mechanical stress from passing through the printing nozzle can cause cell damage or death.[38] The shear-thinning behavior of bioinks reduces viscosity during printing but maintains high viscosity when at rest.[26,39] Thus, the hydrogel could be printed at much lower pressure, reducing the hydrodynamic stress on cells and improving cell viability. The high resting viscosity of hydrogels is essential for the printability, shape-fidelity, and mechanical stability of bioprinted constructs.[38] The overall survival rate of all cells during the entire test period was at least 75% with peak survival on day 7 at 82.5%, suggesting that cells regenerated from the printing process and faced less competitive pressure due to lower density in the bioprinted constructs. To reduce mechanical stress and cell damage or death, conical nozzles were used for bioprinting instead of cylindrical ones, as the latter requires higher pressure for printing at the same flow rate. Likewise, conical nozzles can induce higher shear stress on the cells at a greater area compared to cylindrical nozzles.[40]

The stiffness analysis confirmed the viscoelastic properties of the bioprinted constructs, whereby the hydrogels primarily exhibit elastic properties. The stiffness of the constructs was determined by the hydrogel composition, whereas cell type did not play a significant role. Biofabricated Alg/HA/Gel constructs reported a significantly higher elastic modulus compared to GelMA constructs, indicating that GelMA is softer than Alg/HA/Gel. However, the mechanical parameters of natural skin vary widely and are influenced by patient-related parameters, such as weight loss, body mass index (BMI), age, and the specific body site on which the skin was obtained. These parameters introduce a high degree of variability and inconsistency, making precise mechanical characterization challenging. According to Joodaki and Panzer, the skin exhibits Young's modulus of 1.1–210 kPa, depending on the skin site, as determined in indentation studies. The literature Young's modulus of the upper skin layer is 0.11 kPa, whereas Young's modulus of the reticular dermis is much higher at 160 kPa.[41] Furthermore, the dermal skin layer provides additional stability and significantly contributes to the stiffness of the skin. Since our 3D model lacks a dermal layer of fibroblasts, which would enhance the skin stiffness, our results are not comparable to those of natural skin but fall within the broad range aforementioned.

During the process of re-epithelialization, keratinocytes proliferate and migrate towards the center of the lesion until the wound surface is covered by a monolayer of keratinocytes.[1,42] To evaluate the re-epithelialization of the wound bed, the degree of cell migration out of the bioprinted constructs to the well bottom was analyzed. For experimental groups containing HaCaT and ADSC in co-culture, the metabolic activity and viability of the cells at the well bottom were significantly increased during the experimental period, independent of the selection of hydrogels. After 14 days, 55% of the well bottom was covered by HaCaTs, which were initially printed in co-culture into Alg/HA/Gel constructs. HaCaTs from co-cultured GelMA constructs covered 45% of the well bottom. In a wound situation, it can be assumed that keratinocytes can migrate from the bioprinted skin substitute onto the wound bed, potentially enhancing re-epithelialization. Several studies have reported the stimulatory effect of ADSC on the proliferation and migration of HaCaT cells. HaCaT proliferation and migration, under the influence of ADSCs, were examined *in vitro*, using vitality assays and scratch tests.[34,36,43] Likewise, an *in vivo* mouse wound healing model validated the positive effects of ADSCs on HaCaT cells and wound healing.[43]

In addition to the migrated HaCaT, a significantly smaller amount of ADSCs migrated to the well bottom. Seo et al. indicated that these migrated ADSCs could potentially differentiate into keratinocytes and further enhance re-epithelialization.[33]

The degradation assay displayed a significant decrease in the size of the biofabricated constructs throughout the experimental period. In addition, cell-laden constructs were significantly smaller on day 14 than the comparative cell-free group.

The degradation of Alg/HA/Gel and GelMA has been reported previously.[26,27] Consistent with these findings, our study revealed a higher degradation rate for Alg/HA/Gel constructs compared to GelMA constructs, particularly for cell-laden constructs. A degradation of 33% was observed

for cell-laden Alg/HA/Gel constructs over 14 days, while a degradation of 20% was observed for GelMA constructs, highlighting the importance of optimizing the degradation rate in accordance with the tissue repair rate.[27] Depending on the type of wound, the cutaneous healing time can last up to 8 weeks.[17] Crosslinking delays the degradation process.[16] For instance, photo-crosslinking of GelMA produces a stable construct with slow degradation rates, making GelMA suitable for long-term applications.[19] During long-term incubation, the rapid degradation rate of Alg/HA/Gel-based skin substitutes could limit its application, but this may be avoided by additional crosslinking of Alg/HA/Gel with microbial transglutaminase (mTG) to slow down degradation.[26]

5. Conclusion

Biofabricated potential skin substitutes made of GelMA demonstrated excellent survival and viability of bioprinted HaCaT keratinocytes, outperforming bioprinted constructs made of Alg/HA/Gel. Both hydrogels facilitated cell migration from the constructs to the well bottom. These findings indicate that GelMA-based constructs with keratinocytes and ADSCs may offer a promising therapeutic option in the treatment of large chronic wounds.

Acknowledgments

We would like to thank Stefan Fleischer for the excellent technical assistance during the study.

Funding

The work was funded by the Deutsche Forschungsgemeinschaft (DFG, German Research Foundation; project number 326998133, TRR 225; subprojects C03, A07, and C04).

Conflict of interest

The authors declare no conflict of interest.

Author contributions

Conceptualization: Rafael Schmid, Celena A. Sörgel
Formal analysis: Eva Bettendorf, Rafael Schmid
Investigation: Eva Bettendorf, Celena A. Sörgel, Yvonne Kulike
Methodology: Rafael Schmid, Celena A. Sörgel
Resources: Stefan Schrüfer, Dirk W. Schubert, Zan Lamberger, Philipp Stahlhut, Gregor Lang, Raymund E. Horch
Supervision: Raymund E. Horch, Celena A. Sörgel
Writing – original draft: Eva Bettendorf
Writing – review & editing: Eva Bettendorf, Annika Kengelbach-Weigand, Rafael Schmid, Celena A. Sörgel

Ethics approval and consent to participate

Not applicable.

Consent for publication

Not applicable.

Availability of data

Data are available on request from the authors.

References

1. Tottoli EM, Dorati R, Genta I, Chiesa E, Pisani S, Conti B. Skin wound healing process and new emerging technologies for skin wound care and regeneration. *Pharmaceutics*. 2020;12(8):735. doi: 10.3390/pharmaceutics12080735
2. Sörgel CA, Cai A, Schmid R, Horch RE. Perspectives on the current state of bioprinted skin substitutes for wound healing. Biomedicines. 2023;11(10):2678. doi: 10.3390/biomedicines11102678
3. Zuo KJ, Medina A, Tredget EE. Important developments in burn care. *Plast Reconstr Surg*. 2017;139(1):120e-138e. doi: 10.1097/prs.0000000000002908
4. Wang Y, Beekman J, Hew J, et al. Burn injury: challenges and advances in burn wound healing, infection, pain and scarring. *Adv Drug Deliv Rev*. 2018;123:3-17. doi: 10.1016/j.addr.2017.09.018
5. Jeschke MG, Shahrokhi S, Finnerty CC, Branski LK, Dibildox M. Wound coverage technologies in burn care: established techniques. *J Burn Care Res*. 2018;39(3):313-318. doi: 10.1097/BCR.0b013e3182920d29
6. Varkey M, Visscher DO, van Zuijlen PPM, Atala A, Yoo JJ. Skin bioprinting: the future of burn wound reconstruction? *Burns Trauma*. 2019;7:4. doi: 10.1186/s41038-019-0142-7
7. Sorgel CA, Schmid R, Kengelbach-Weigand A, Promny T, Horch RE. Air-pressure-supported application of cultured human keratinocytes in a fibrin sealant suspension as a potential clinical tool for large-scale wounds. *J Clin Med*. 2022;11(17):5032. doi: 10.3390/jcm11175032
8. Tan SH, Ngo ZH, Sci DB, Leavesley D, Liang K. Recent advances in the design of three-dimensional and bioprinted scaffolds for full-thickness wound healing. *Tissue Eng Part B Rev*. 2022;28(1):160-181. doi: 10.1089/ten.TEB.2020.0339
9. Weng T, Zhang W, Xia Y, et al. 3D bioprinting for skin tissue engineering: current status and perspectives. *J Tissue Eng*. 2021;12:20417314211028574. doi: 10.1177/20417314211028574
10. Park J, Lee SJ, Chung S, et al. Cell-laden 3D bioprinting hydrogel matrix depending on different compositions for

soft tissue engineering: characterization and evaluation. *Mater Sci Eng C*. 2017;71:678-684.

11. Catanzano O, D'Esposito V, Acierno S, et al. Alginate–hyaluronan composite hydrogels accelerate wound healing process. *Carbohydr Polym*. 2015;131:407-414. doi: 10.1016/j.carbpol.2015.05.081
12. Wang S, Xiong Y, Chen J, et al. Three dimensional printing bilayer membrane scaffold promotes wound healing. *Front Bioeng Biotechnol*. 2019;7:348. doi: 10.3389/fbioe.2019.00348
13. Yue K, Trujillo-de Santiago G, Alvarez MM, Tamayol A, Annabi N, Khademhosseini A. Synthesis, properties, and biomedical applications of gelatin methacryloyl (GelMA) hydrogels. *Biomaterials*. 2015;73:254-271. doi: 10.1016/j.biomaterials.2015.08.045
14. Cohen B, Pinkas O, Foox M, Zilberman M. Gelatin–alginate novel tissue adhesives and their formulation–strength effects. *Acta Biomater*. 2013;9(11):9004-9011. doi: 10.1016/j.actbio.2013.07.002
15. Schmid R, Schmidt SK, Detsch R, et al. A new printable alginate/hyaluronic acid/gelatin hydrogel suitable for biofabrication of in vitro and in vivo metastatic melanoma models. *Adv Funct Mater*. 2022;32(2):2107993. doi: 10.1002/adfm.202107993
16. Kim BS, Gao G, Kim JY, Cho D-W. 3D cell printing of perfusable vascularized human skin equivalent composed of epidermis, dermis, and hypodermis for better structural recapitulation of native skin. *Adv Healthc Mater*. 2019;8(7):1801019. doi: 10.1002/adhm.201801019
17. Zhao X, Lang Q, Yildirimer L, et al. Photocrosslinkable gelatin hydrogel for epidermal tissue engineering. *Adv Healthc Mater*. 2016;5(1):108-118. doi: 10.1002/adhm.201500005
18. Billiet T, Gevaert E, De Schryver T, Cornelissen M, Dubruel P. The 3D printing of gelatin methacrylamide cell-laden tissue-engineered constructs with high cell viability. *Biomaterials*. 2014;35(1):49-62. doi: 10.1016/j.biomaterials.2013.09.078
19. Heltmann-Meyer S, Steiner D, Müller C, et al. Gelatin methacryloyl is a slow degrading material allowing vascularization and long-term usein vivo. *Biomed Mater*. 2021;16(6). doi: 10.1088/1748-605X/ac1e9d
20. Gopinathan J, Noh I. Recent trends in bioinks for 3D printing. *Biomater Res*. 2018;22(1):11. doi: 10.1186/s40824-018-0122-1
21. Horch RE, Bannasch H, Kopp J, Andree C, Stark GB. Single-cell suspensions of cultured human keratinocytes in fibrin–glue reconstitute the epidermis. *Cell Transplant*. 1998;7(3):309-317. doi: 10.1177/096368979800700309
22. Bannasch H, Unterberg T, Föhn M, Weyand B, Horch RE, Stark GB. Cultured keratinocytes in fibrin with decellularised dermis close porcine full-thickness wounds in a single step. *Burns*. 2008;34(7):1015-1021. doi: 10.1016/j.burns.2007.12.009
23. Hunyadi J, Farkas B, Bertényi C, Oláh J, Dobozy A. Keratinocyte grafting: a new means of transplantation for full-thickness wounds. *J Dermatol Surg Oncol*. 1988;14(1):75-78. doi: 10.1111/j.1524-4725.1988.tb03343.x
24. Thamm OC, Theodorou P, Stuermer E, et al. Adipose-derived stem cells and keratinocytes in a chronic wound cell culture model: the role of hydroxyectoine. *Int Wound J*. 2015;12(4):387-396. doi: 10.1111/iwj.12120
25. Jorgensen AM, Varkey M, Gorkun A, et al. Bioprinted skin recapitulates normal collagen remodeling in full-thickness wounds. *Tissue Eng Part A*. 2020;26(9-10):512-526. doi: 10.1089/ten.TEA.2019.0319
26. Schulik J, Salehi S, Boccaccini AR, et al. Comparison of the behavior of 3D-printed endothelial cells in different bioinks. *Bioengineering (Basel)*. 2023;10(7):751. doi: 10.3390/bioengineering10070751
27. Safikhani MM, Asefnejad A, Aghdam RM, Rahmati S. Fabrication, and characterization of crosslinked sodium alginate/hyaluronic acid/gelatin 3Dprinted heparin-loaded scaffold. *J Polym Res*. 2024;31(4):121. doi: 10.1007/s10965-024-03942-4
28. Christensen K, Xu C, Chai W, Zhang Z, Fu J, Huang Y. Freeform inkjet printing of cellular structures with bifurcations. *Biotechnol Bioeng*. 2015;112(5):1047-1055.
29. Sakai S, Ohi H, Hotta T, Kamei H, Taya M. Differentiation potential of human adipose stem cells bioprinted with hyaluronic acid/gelatin-based bioink through microextrusion and visible light-initiated crosslinking. *Biopolymers*. 2018;109(2). doi: 10.1002/bip.23080
30. Law N, Doney B, Glover H, et al. Characterisation of hyaluronic acid methylcellulose hydrogels for 3D bioprinting. *J Mech Behav Biomed Mater*. 2018;77:389-399. doi: 10.1016/j.jmbbm.2017.09.031
31. Marfia G, Navone SE, Di Vito C, et al. Mesenchymal stem cells: potential for therapy and treatment of chronic non-healing skin wounds. *Organogenesis*. 2015;11(4):183-206. doi: 10.1080/15476278.2015.1126018
32. Mazini L, Rochette L, Admou B, Amal S, Malka G. Hopes and limits of adipose-derived stem cells (ADSCs) and mesenchymal stem cells (MSCs) in wound healing. *Int J Mol Sci*. 2020;21(4):1306. doi: 10.3390/ijms21041306
33. Seo BF, Kim KJ, Kim MK, Rhie JW. The effects of human keratinocyte coculture on human adipose-derived stem cells. *Int Wound J*. 2016;13(5):630-635. doi: 10.1111/iwj.12335

34. Lee SH, Jin SY, Song JS, Seo KK, Cho KH. Paracrine effects of adipose-derived stem cells on keratinocytes and dermal fibroblasts. *Ann Dermatol*. 2012;24(2):136-143. doi: 10.5021/ad.2012.24.2.136

35. Hermann M, Peddi A, Gerhards A, et al. Secretome of adipose-derived stem cells cultured in platelet lysate improves migration and viability of keratinocytes. *Int J Mol Sci*. 2023;24(4):3522. doi: 10.3390/ijms24043522

36. Ong HT, Redmond SL, Marano RJ, et al. Paracrine activity from adipose-derived stem cells on in vitro wound healing in human tympanic membrane keratinocytes. *Stem Cells Dev*. 2017;26(6):405-418. doi: 10.1089/scd.2016.0204

37. Li S, Sun J, Yang J, et al. Gelatin methacryloyl (GelMA) loaded with concentrated hypoxic pretreated adipose-derived mesenchymal stem cells(ADSCs) conditioned medium promotes wound healing and vascular regeneration in aged skin. *Biomater Res*. 2023;27(1):11. doi: 10.1186/s40824-023-00352-3

38. Müller SJ, Fabry B, Gekle S. Predicting cell stress and strain during extrusion bioprinting. *Phys Rev Appl*. 2023;19(6):064061. doi: 10.1103/PhysRevApplied.19.064061

39. Schmid R, Schmidt SK, Schrüfer S, et al. A vascularized in vivo melanoma model suitable for metastasis research of different tumor stages using fundamentally different bioinks. *Mater Today Bio*. 2024;26:101071. doi: 10.1016/j.mtbio.2024.101071

40. Chand R, Muhire BS, Vijayavenkataraman S. Computational fluid dynamics assessment of the effect of bioprinting parameters in extrusion bioprinting. *Int J Bioprint*. 2022;8(2):545. doi: 10.18063/ijb.v8i2.545

41. Joodaki H, Panzer MB. Skin mechanical properties and modeling: a review. *Proc Inst Mech Eng H*. 2018;232(4):323-343. doi: 10.1177/0954411918759801

42. Martin P. Wound healing--aiming for perfect skin regeneration. *Science*. 1997;276(5309):75-81. doi: 10.1126/science.276.5309.75

43. Zhang Y, Han F, Gu L, et al. Adipose mesenchymal stem cell exosomes promote wound healing through accelerated keratinocyte migration and proliferation by activating the AKT/HIF-1α axis. *J Mol Histol*. 2020;51(4):375-383. doi: 10.1007/s10735-020-09887-4

ACCSCIENCE PUBLISHING

International Journal of Bioprinting

RESEARCH ARTICLE

3D-printed zinc/magnesium-doped hydroxyapatite-polycaprolactone composite scaffolds for angiogenesis and osteogenesis

Lei Qiang[1,2,3,4], Hao Huang[2], Jing Shan[5], Guanlu Shen[6], Quan Zhang[6], Weize Kong[4], Ya Fang[6], Yiwei Zhang[4], Jinwu Wang[4], Yihao Liu[4]*, Chengwei Wang[4]*, Pengfei Zheng[3,6]*, and Jie Weng[1,2]*

[1]Institute of Biomedical Engineering, College of Medicine, Southwest Jiaotong University, Chengdu, Sichuan, China

[2]Key Laboratory of Advanced Technologies of Materials (MOE), School of Materials Science and Engineering, College of Medicine, Southwest Jiaotong University, Chengdu, Sichuan, China

[3]Department of Orthopaedic Surgery, Children's Hospital of Nanjing Medical University, Nanjing, Jiangsu, China

[4]Shanghai Key Laboratory of Orthopedic Implant, Department of Orthopedic Surgery Shanghai Ninth People's Hospital, Shanghai Jiao Tong University School of Medicine, Shanghai, China

[5]Faculty of Medicine and Health, School of Pharmacy, The University of Sydney, Sydney, Australia

[6]Jiangsu Key Laboratory of Marine Bioresources and Environment, Co-Innovation Center of Jiangsu Marine Bio-industry Technology, Jiangsu Key Laboratory of Marine Pharmaceutical Compound Screening, Jiangsu Ocean University, Lianyungang, Jiangsu, China

(This article belongs to the Special Issue: *Advances in Bioprinting and Organ-on-a-chip and Applications for Precision Medicine*)

Abstract

Critical-sized bone defect repair remains a major clinical challenge that requires scaffolds with angiogenesis and osteogenesis potential. Herein, we synthesized zinc (Zn)-doped and zinc/magnesium (Zn/Mg)-co-doped hydroxyapatite (HA) via the hydrothermal method and subsequently mixed them with polycaprolactone (PCL) as ink to fabricate composite scaffolds through 3D printing. We explored the potential of composite scaffolds in promoting angiogenesis and osteogenesis. *In vitro* experiments demonstrated that Zn/Mg-co-doped composite scaffolds can promote angiogenesis. In addition, Zn/Mg-co-doped scaffolds could promote osteogenesis and were superior to Zn-doped composite scaffolds. Furthermore, *in vivo* studies using a rat femoral defect model confirmed that the Zn/Mg-co-doped scaffolds repaired bone defects. Thus, the Zn/Mg-co-doped composite scaffolds developed in this study were effective in promoting angiogenesis and bone defect repairs, providing an excellent solution for the design and development of clinical materials.

***Keywords*:** Zinc/magnesium-doped hydroxyapatite-polycaprolactone scaffolds; 3D printing; Angiogenesis; Osteogenesis; Bone regeneration

1. Introduction

Critical-sized bone defects, caused by trauma, bone tumors, infections, and other diseases, cannot be self-repaired and require external intervention. Presently, the treatments for critical-sized bone defects repair primarily include autologous bone

***Corresponding authors:**
Jie Weng
(jweng@swjtu.edu.cn)

Pengfei Zheng
(zhengpengfei@njmu.edu.cn)

Chengwei Wang
(wangcw_1222@163.com)

Yihao Liu
(lyh19950227sjtu@sjtu.edu.cn)

Citation: Qiang L, Huang H, Shan J, et al. 3D-printed zinc/magnesium-doped hydroxyapatite-polycaprolactone composite scaffolds for angiogenesis and osteogenesis. *Int J Bioprint*. 2024;10(6):4243. doi: 10.36922/ijb.4243

Received: July 15, 2024
Revised: August 27, 2024
Accepted: September 3, 2024
Published Online: September 4, 2024

Copyright: © 2024 Author(s). This is an Open Access article distributed under the terms of the Creative Commons Attribution License, permitting distribution, and reproduction in any medium, provided the original work is properly cited.

Publisher's Note: AccScience Publishing remains neutral with regard to jurisdictional claims in published maps and institutional affiliations.

grafting, allogeneic bone transplantation, and artificial bone substitutes.[1] Autologous bone grafting, renowned for its high osteoinductivity and osteoconductivity, is regarded as the "gold standard" for bone repair. However, its applicability is limited due to the scarcity of resources and the difficulty in precisely matching the size and shape of the defect.[2] Allograft bone transplantation carries risks of immune rejection and even disease transmission, limiting its clinical use.[3] Consequently, artificial bone grafts, owing to their wide sourcing and low immunogenicity, have emerged as a focal point among researchers in bone defect repair. Diverse biomaterials have been engineered for bone defect repair, including bioactive glasses,[4,5] porous ceramic scaffolds,[6,7] metals,[8] hydrogels,[9] polymers,[1,10] and their composites.

Calcium phosphate (CaP) bioceramics, such as hydroxyapatite (HA), are extensively used for mending skeletal defects across the body due to their chemical similarity to mammalian bones and teeth, as well as their excellent bioadaptability (commonly utilized for filling hard tissue defects and coating implant surfaces).[11,12] Among them, HA, the primary inorganic constituent of human hard tissues, theoretically appears to be one of the most suitable materials for human bone tissue repair.[13] With its outstanding osteoconductive and osteoinductive properties, HA not only provides a spatial and supportive framework for vascular and new bone ingrowth but also induces mesenchymal stem cells to differentiate into osteoblasts; thereby expediting bone reconstruction and enhancing osteogenic efficiency and the effect of bone integration.[14,15] Natural bone HA comprises mixed phases deviating from the ideal chemical composition (Ca/P = 1.67) and doped with trace elements. Therefore, synthesizing HA with the ideal chemical composition is simplistic and inadequate to meet clinical demands, necessitating diverse methods to modify HA to impart requisite biological functions. Currently, trace element doping stands as one of the most common HA modification techniques, broadly classified into cation and anion doping.[16] These trace elements exhibit serval unique biological functions. For instance, boron ions could upregulate the expression of osteogenic differentiation markers (BMP, etc.) in MC3T3-E1 cells and induce osteogenic differentiation of bone marrow mesenchymal stem cells (BMSCs).[17] Copper ions could stimulate stem cells to secrete VEGF, promoting angiogenesis.[18] Additionally, in a rat cranial defect model, the Cu-containing group displayed a significant improvement in bone regeneration, compared to the control.[19] Silicon ions could regulate the coupling of osteogenesis and angiogenesis and create a beneficial immune microenvironment at the site of bone defects to achieve vascularized bone regeneration.[20] Doping with divalent or multivalent ions (e.g., Zn^{2+}- or Si^{4+}-doped HA nanoparticles) improves composite material biocompatibility[21] and fosters osteogenic differentiation[20] and tissue-material interface stable bonding.[22] Moreover, HA doping ions (e.g., Sr^{2+} or Mg^{2+}) induce BMSCs to synthesize and secrete VEGF and other angiogenic factors,[23] thereby further expediting the induction of vascular regeneration *in vitro* or *in vivo*.[24]

Notably, magnesium, an essential human element, boasts numerous beneficial biological effects and plays a pivotal role in bone metabolism.[25] Mg deficiency is highly associated with osteoporosis.[26] Additionally, Mg deficiency upregulates tumor necrosis factor-alpha (TNF-α), interleukin-1 beta (IL-1β), and receptor activator of nuclear factor kappa-B ligand (RANKL) expression and downregulates osteoprotegerin (OPG) expression, hastening bone resorption, and inducing osteoporosis.[27] Moreover, Mg could enhance angiogenesis through the CGRP-mediated CGRP-FAK-VEGF signaling pathway to repair critical-sized bone defects.[1] Zinc, also abundant in bones, is a crucial element in bone metabolism. It heightens alkaline phosphatase (ALP) activity in BMSCs to further induce osteogenic differentiation and stimulate bone development and mineralization.[28] Zinc can inhibit osteoclasts and accelerate bone healing to some extent.[29] Additionally, zinc exerts antibacterial effects, particularly against *Staphylococcus aureus*, *Lactobacillus*, and Gram-positive bacteria,[30] which positively correlates with the Zn doping molar fraction. Compared to single-element (Mg and Zn ions)-doped HA, research on Mg/Zn-co-doped HA is relatively scarce. Moreover, some prevalent co-doped HA studies mainly investigated physical properties, such as lattice and crystal size post-doping,[31] but they are limited in studying the effects on the biological domain (cells, e.g., osteogenic-related cells). Hence, further research is warranted to delineate the synergistic effects of Mg/Zn-co-doping on angiogenesis and osteogenesis.

Furthermore, the biocompatibility, degradation rate, and mechanical properties of bone repair scaffolds must match those of natural bone tissue. Traditional HA scaffolds are often brittle and lack sufficient mechanical strength, which may result in fractures under load, particularly in areas with significant bone defects. Additionally, their surface characteristics, such as porosity and pore size, are often inadequate, which can impact nutrient exchange and waste removal.[32] The optimal pore size for bone repair scaffolds ranges from 200 to 350 μm.[33] 3D printing technology allows for the precise control of mechanical properties and the adjustment of pore size and porosity to better suit bone repair requirements.[34] Polycaprolactone (PCL) offers

excellent mechanical properties and processability and is a United States (US) Food and Drug Administration (FDA)-approved synthetic polymer widely used in bone tissue repair.[35]

As displayed in Figure 1, this study initially synthesized Zn-doped HA and Zn/Mg-co-doped HA via hydrothermal synthesis. Subsequently, 3D printing technology was employed to fabricate element-doped HA-PCL composite scaffolds for *in vitro* and *in vivo* angiogenesis and osteogenesis studies. The angiogenic and osteogenic potential of co-doped HA-PCLs was confirmed via human umbilical vein endothelial cells (HUVECs) and rat BMSCs (RBMSCs) activity assays *in vitro*. Meanwhile, the osteogenic efficacy of co-doped HA-PCLs was validated using a rat femoral defect model.

2. Materials and methods

2.1. Materials

Calcium nitrate tetrahydrate ($Ca(NO_3)_2{\cdot}4H_2O$, analytical reagent [AR]), magnesium nitrate hexahydrate ($Mg(NO_3)_2{\cdot}6H_2O$, AR), zinc nitrate tetrahydrate ($Zn(NO_3)_2{\cdot}4H_2O$, AR), phosphoric acid dodecahydrate disodium hydrogen ($Na_2HPO_4{\cdot}12H_2O$, AR), nitric acid (HNO_3, AR), glutaraldehyde ($C_5H_8O_2$, AR), urea (CH_4N_2O, AR), and absolute ethanol (AR) were purchased from Chengdu Kelong Chemical Reagent Factory (China).

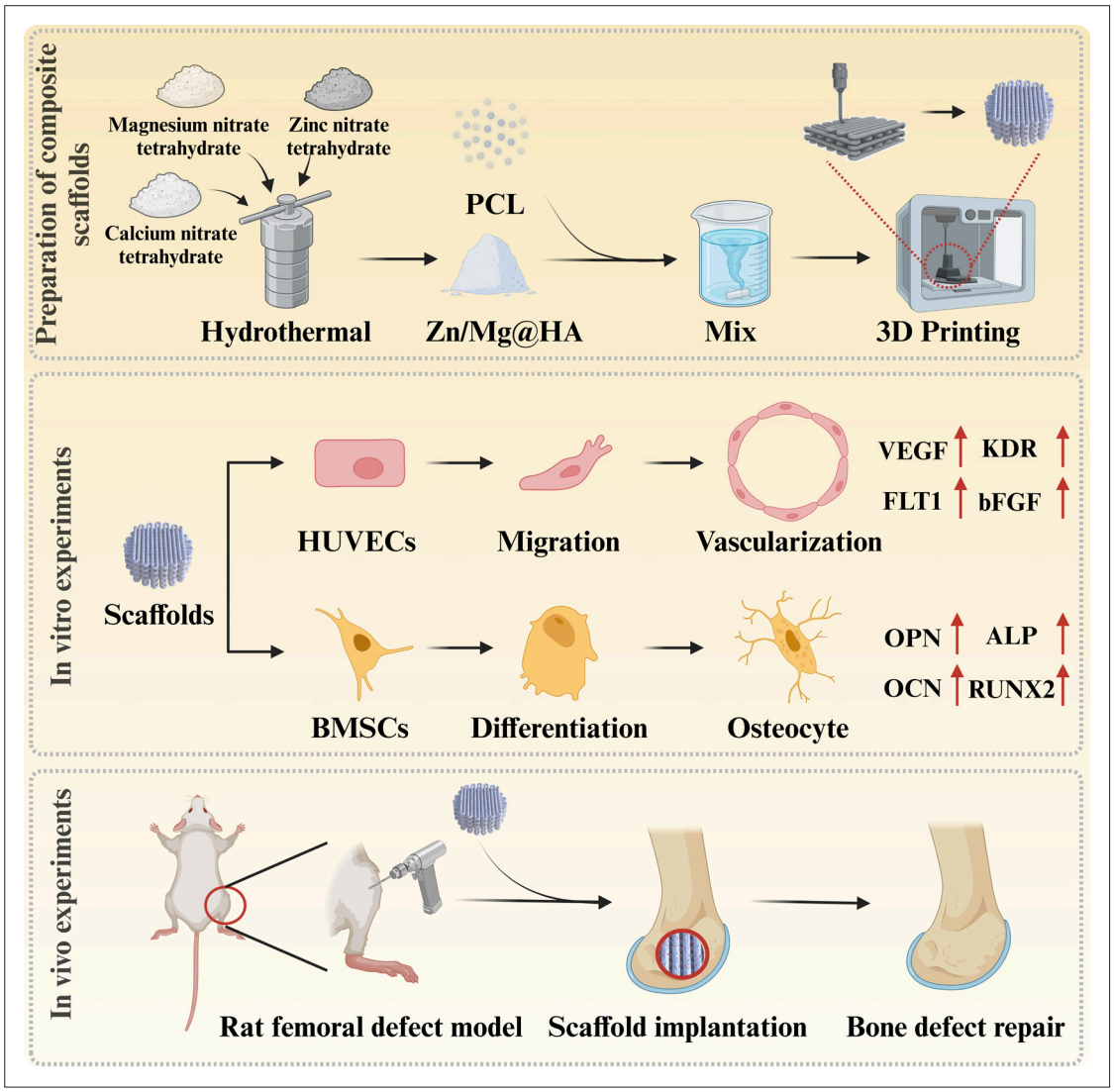

Figure 1. Schematic diagram of the preparation and function of Zn/Mg@HA and Zn/Mg@HA-PCL in angiogenesis and osteogenesis. The figure was created using BioRender (biorender.com). Abbreviations: BMSCs, bone marrow mesenchymal stem cells; HA, hydroxyapatite; HUVECs, human umbilical vein endothelial cells; PCL, polycaprolactone.

1,2,3,4,5,6-Cyclohexanehexacarboxylic acid monohydrate (H_6L; $C_{12}H_{12}O_{12}·H_2O$; molecular weight [M_W] = 366.24, AR) was purchased from TCI (Shanghai) Development Co., Ltd. (China). Dichloromethane (M_W = 84.93) was provided by Zhiyuan Chemical Reagent Co., Ltd. (China). PCL (M_W = 45,000) was purchased from Macklin Biochemical Technology Co., Ltd. (China). All reagents were used without further purification unless specifically mentioned.

2.2. Fabrication and evaluation of element-doped hydroxyapatite and composite scaffolds

2.2.1. Synthesis of hydroxyapatite and element-doped hydroxyapatite

Several HA powders in this study were prepared by hydrothermal methods, as previously reported.[36] Briefly, to prepare Zn-doped HA with designed Zn/(Zn + Ca) molar ratios of 10% (denoted as 10Zn@HA), $Ca(NO_3)_2$, $Zn(NO_3)_2$, and Na_2HPO_4 were sequentially added into 150 mL of deionized water, while the molar ratio of (Ca + Zn)/P in the solution was 1.67. To prepare Zn/Mg-doped HA with a designed molar ratio of 10% Zn/(Zn + Mg + Ca) with 5%/10%/15% Mg/(Zn + Mg + Ca) (denoted as 5Mg10Zn@HA, 10Mg10Zn@HA, and 15Mg10Zn@HA, respectively), $Ca(NO_3)_2$, $Zn(NO_3)_2$, $Mg(NO_3)_3$, and Na_2HPO_4 were sequentially added into 150 mL of deionized water, while the molar ratio of (Ca + Zn + Mg)/P in the solution was 1.67. The prepared solutions were all magnetically stirred, and the Ca^{2+} was determined as 0.1 M. Then, the pH of the mixture was adjusted to 2.3 with HNO_3 (10.83 M), followed by the addition of H_6L (1 mM). After the H_6L was dissolved completely, urea (0.56 M) was added until it was completely dissolved. The prepared solutions were then transferred to six-station Teflon autoclaves (Xataikang, China) for reaction at 200°C for 12 h. The precipitates were collected after the reactions were completed. The obtained precipitates were rinsed by centrifugation at 4000 rpm for 3 min, followed by repeated cleaning with deionized water and absolute ethanol until the pH value reached neutral; the precipitates were then dried in an oven at 65°C for 48 h. The un-doped HA was fabricated using the same method.

2.2.2. Characterization of element-doped hydroxyapatite

The morphology, elements, and phase compositions of the samples were examined using scanning electron microscopy (SEM; VEGA3; TESCAN, Czech Republic) equipped with energy dispersive X-ray spectroscopy (EDS) and X-ray diffraction (XRD; D8 ADVANCE Da Vinci, Cu, 40 mA, 40 kV; Bruker, Germany), respectively. The chemical structure was examined using Fourier transform infrared spectroscopy (FTIR, 500–3500 cm^{-1}, Thermo Nicolet 6700; Thermo Fisher Scientific, USA). The quantity of the doping element in the samples was determined by inductively coupled plasma atomic emission spectra (ICP-AES; Avio 500; PerkinElmer, Singapore). The actual doping efficiency, theoretical doping efficiency, and relative doping efficiency of the element were calculated according to Equations I–VI, as follows:

Actual doping of Zn ($\mathcal{X}_{a-Zn}$)

$$= \frac{n(Zn)_{actual}}{n(Ca)_{actual}+n(Zn)_{actual}+n(Mg)_{actual}} \times 100\% \quad (I)$$

Actual doping of Mg ($\mathcal{X}_{a-Mg}$)

$$= \frac{n(Zn)_{actual}}{n(Ca)_{actual}+n(Zn)_{actual}+n(Mg)_{actual}} \times 100\% \quad (II)$$

Theoretical doping of Zn ($\mathcal{X}_{t-Zn}$)

$$= \frac{n(Zn)_{theoretical}}{n(Ca)_{theoretical}+n(Zn)_{theoretical}+n(Mg)_{theoretical}} \times 100\% \quad (III)$$

Theoretical doping of Mg ($\mathcal{X}_{t-Mg}$)

$$= \frac{n(Zn)_{theoretical}}{n(Ca)_{theoretical}+n(Zn)_{theoretical}+n(Mg)_{theoretical}} \times 100\% \quad (IV)$$

$$\text{Relative doping of Zn } (R_{Zn}) = \frac{\chi_{t-Zn}}{\chi_{a-Zn}} \times 100\% \quad (V)$$

$$\text{Relative doping of Mg } (R_{Mg}) = \frac{\chi_{t-Mg}}{\chi_{a-Mg}} \times 100\% \quad (VI)$$

where $n(Ca)_{actual}$, $n(Zn)_{actual}$, and $n(Mg)_{actual}$ represent the actual contents of Ca, Zn, and Mg in the element-doped HA, respectively; $n(Ca)_{theoretical}$, $n(Zn)_{theoretical}$, and $n(Mg)_{theoretical}$ represent the theoretical contents of Ca, Zn, and Mg in the element-doped HA, respectively.

2.2.3. Preparation of 3D-printed composite scaffolds

Several porous 3D composite scaffolds were fabricated by 3D printing (Biobulid-S, China) as reported previously.[37] Before printing, 0.5 g of HA, 10Zn@HA, 5Mg10Zn@HA, 10Mg10Zn@HA, and 15Mg10Zn@HA powders were dispersed in 40 mL of dichloromethane and stirred to form uniform dispersion, respectively. Then, the dispersion was added into a PCL solution (4.5 g of PCL in a certain amount of dichloromethane) and fully stirred for 3 h to form a uniform ink. The printing procedure is illustrated in

Figure 1A. Briefly, the prepared ink was extruded through a conical plastic nozzle (23 G, 0.33 mm) at a speed of 5 mm/s and pressure of 0.2 MPa to obtain a porous 3D scaffold. Finally, the 3D-printed HA-PCLs, 10Zn@HA-PCLs, 5Mg10Zn@HA-PCLs, 10Mg10Zn@HA-PCLs, and 15Mg10Zn@HA-PCLs were freeze-dried for 24 h to remove the organic solvent.

2.2.4. Characterization of composite scaffolds

The morphology and elements of the scaffolds were examined using SEM (VEGA3; TESCAN, Czech Republic) equipped with EDS, respectively. A microcomputer-controlled electronic universal testing machine (WDW-5; Bairoe, China) was used for compression testing, and the stress and strain curves were monitored to calculate the compression modulus. A scaffold with a size ($H \times \Phi$) of 5 × 6 mm was compressed to 60% strain at a speed of 60 mm/min. The compression modulus was determined by drawing a compressive stress–strain curve for each scaffold ($n = 4$).

2.2.5. In vitro ion release of HA-PCLs, Zn@HA-PCLs, and Zn/Mg@HA-PCLs

A total of 40 mg of the scaffolds were dispersed into 40 mL phosphate-buffered saline (PBS; Servicebio®, China) at 10 mg/mL. The solutions were kept in a constant temperature oscillation chamber (SHZ-82A; Aohua Instrument, China) at 37℃ and 90 rpm for 1, 2, 3, 7, and 14 days. At each time point, 10 mL of supernatant was collected and replaced with 10 mL of fresh PBS before continuing the shaking process until the end of the release process.

2.3. *In vitro* cell experiments of composite scaffolds

2.3.1. Cell isolation, source, and cultivation

The RBMSCs were extracted from the femur and cranial bone of male Sprague-Dawley rats (4 weeks old; Shengchang Biotech, China). HUVECs were provided by the American Type Culture Collection (ATCC, United States of America [USA]). They were all used to study the effects of Zn^{2+} and Mg^{2+} on cell proliferation, viability, osteogenesis, and angiogenesis. The RBMSCs and HUVECs were cultured in cell culture dishes with Alpha Minimum Essential Medium (α-MEM; Gibco, USA) and Dulbecco's Modified Eagle Medium (DMEM; Gibco, USA) supplemented with 10% fetal bovine serum (FBS; Gibco, USA) and 1 % penicillin-streptomycin (PS; Biosharp, China) at 37℃ in 5% CO_2.

2.3.2. Preparation of composite scaffold extracts

The composite scaffolds were immersed in 75% ethanol solution for 30 min, followed by washing with sterile PBS three times, each for 10 min. Subsequently, they were added to α-MEM and DMEM culture media at a concentration of 10 mg/mL and incubated at 37°C in a sterile environment for real-time extraction. Fresh complete culture media were replenished every other day to generate real-time extracts of the composite scaffolds.

2.3.3. Cell proliferation and cytotoxicity

Cell proliferation of BMSCs and HUVECs was evaluated using the Cell Counting Kit-8 (CCK-8; Bimake, China). BMSCs and HUVECs were seeded at a density of 1×10^3 cells/well in a 96-well plate and incubated with α-MEM and DMEM complete culture media until cell attachment. After discarding the original culture media, cells were washed with PBS and then treated with the extracts prepared in **Section 2.3.2**, with fresh extracts replaced every 48 h. Cell proliferation was assessed on days 1, 3, and 7 and 12, 24, and 48 h using a microplate reader (BioTek, USA) at a wavelength of 450 nm according to the manufacturer's instructions. The experiments were repeated four times and statistically analyzed.

Cell cytotoxicity of the composite scaffolds was assessed using the Live/Dead Cell Staining Kit (YEASEN, China). After co-culturing the scaffolds with BMSCs and HUVECs for 72 h, the cells were stained with 600 mL of Live/Dead staining working solution for 30 min, followed by observation of live and dead cells under a fluorescence microscope and image capture.

2.3.4. In vitro angiogenic capacity assessment

For the wound healing assay, HUVECs were cultured in a six-well plate using DMEM complete culture media until reaching 90% confluence. A scratch was made directly with a 1 mL pipette tip, and suspended cells were washed with PBS. The culture media were then replaced with the extracts of the composite scaffolds, and images of migrated cells were captured after 12 and 24 h using an optical microscope (Olympus, Japan) and subjected to statistical analysis.

Quantitative reverse transcription polymerase chain reaction (RT-qPCR) was performed to evaluate the expression of angiogenesis-related genes, including VEGF, FLT1 (VEGFR1), KDR (VEGFR2), bFGF, and GAPDH. Briefly, after co-culturing sterile composite scaffolds with HUVECs for 24 h, the total RNA was extracted from the cells using TRIzol (Sangon Biotech, China). Complementary DNA (cDNA) synthesis was performed using the PrimeScript RT kit (Takara, DaLian, China), followed by amplification using the SYBR Green RT-PCR kit (Bimake, China) and real-time PCR equipment (CFX Connect™ Optics Module; Bio-Rad, USA). Each step was performed in accordance with the manufacturer's instructions. The sequences of the primers are summarized in Table S1, Supporting Information. The experiments were repeated four times.

2.3.5. In vitro osteogenic differentiation potential evaluation

Composite scaffolds and BMSCs were co-cultured in a 24-well plate at 1×10^4 cells/well. After cell attachment to the bottom of the plate, the culture media was replaced with the composite scaffold extracts. After 7 and 14 days of culture, cells were stained using the ALP kit (YEASEN, China), and the optical density (OD) value at 405 nm was determined using the enzyme marker method on day 7 of culture for semi-quantitative analysis.

Mineralized nodules on BMSCs after co-culture were observed using Alizarin Red S (ARS) staining. Briefly, after 21 days of co-culture, cells were stained using ARS staining solution (C0138; Beyotime, China) and imaged using an optical microscope (Olympus, Japan). Subsequently, 10% cetylpyridinium chloride solution was added for decolorization for 15 min. The OD value at 562 nm was determined using an enzyme marker at 562 nm for semi-quantitative analysis.

The RT-qPCR was performed to evaluate the expression of osteogenic-related genes, including OPN, OCN, ALP, RUNX2, and β-actin. Briefly, after co-culturing sterile composite scaffolds with BMSCs for 7 days, cDNA synthesis and amplification were performed as described in **Section 2.3.4**. The sequences of the primers are summarized in Table S1, Supporting Information. The experiments were repeated four times.

2.3.6. Western blot

Both HUVECs and BMSCs were cultured for 24 h and 14 days in composite scaffold extracts, respectively. The cells were then lysed on ice for 30 min in 200 μL of RIPA lysis buffer. After that, the samples were centrifuged at 14,000 × *g* at 4℃ for 15 min. The supernatants were collected and the protein concentrations were measured using a BCA protein assay kit (Beyotime, China). The samples were separated using a Precast Protein Plus Gel (36250ES10; YEASEN, China) and were then transferred onto a polyvinylidene difluoride (PVDF) membrane. The membranes were blocked in TBST solution with 5% bovine serum albumin (BSA; Beyotime, China). The membranes for HUVECs were incubated overnight with anti-CD31 (1:2000; Proteintech, China), anti-VEGF (1:1000; Proteintech, China), and anti-GAPDH (1:1000; Proteintech, China) antibodies. The membranes for BMSCs were incubated overnight with anti-COL1 (1:500; Proteintech, China), anti-OPN (1:1000; Proteintech, China), anti-OCN (1:500; ABclonal, China), and anti-GAPDH (1:1000; Proteintech, China) antibodies. Thereafter, the membranes were incubated with an HRP-conjugated secondary antibody. The band signals were detected using a chemiluminescence imaging system (Tanon, China).

2.4. *In vivo* experiments

2.4.1. Surgical procedure of animal studies in vivo

In vivo bone repair was detected using a rat femoral defect model. Forty-eight Sprague-Dawley rats (250 g; six weeks old; male) were divided into six groups: control, HA-PCLs, 10Zn@HA-PCLs, 5Mg10Zn@HA-PCLs, 10Mg10Zn@HA-PCLs, and 15Mg10Zn@HA-PCLs; the control group had femoral defect without a scaffold. After anesthesia was induced with an intraperitoneal injection of 4% pentobarbital sodium (0.9 mL/100 g), a hole with a depth of 3 mm and a diameter of 3 mm was drilled into the lateral epicondyle using a hand drill. Utilizing 4-0 silk sutures, the skin incision was stitched shut. The experiment followed the recommendations of the Institutional Animal Care and Use Committee (IACUC) of Shanghai Jiao Tong University (animal protocol number: O_A2023001).

2.4.2. Histological evaluation and immunohistochemistry

The animals were divided into six groups, every group had eight animals. At week 6, half of every group was euthanized. At week 12, the remaining animals were euthanized.

The femora were removed and fixed in 4% paraformaldehyde for 7 days (replaced twice with tissue fixative). The tissue samples were subsequently decalcified with 10% EDTA for approximately 30 days, in preparation for the histopathological analysis. According to the steps specified by the manufacturer, hematoxylin and eosin (H&E), Masson's trichrome staining, and α-SMA, CD31, and COL I immunohistochemical staining were performed. The sections were examined on a pathological tissue section scanner (Pannoramic MIDI II; 3DHIDTECH®, Hungary).

2.5. Statistical analysis

All data are presented as the mean ± standard deviation. Differences between the groups were examined by using Tukey's post hoc test and one-way analysis of variance (ANOVA). Statistical analysis was performed using GraphPad Prism software. A p-value < 0.05 (*p < 0.05, **p < 0.01, ***p < 0.001) was considered statistically significant.

3. Results and discussion

3.1. Preparation and characterization of element-doped HA

In this study, HA and element-doped HA were synthesized using elements Zn and Mg, as well as the H6L small molecular template agent, via the hydrothermal synthesis method. The SEM results (Figure 2A) indicated that all HA groups exhibit spherical shapes with diameters ranging from 5 to 10 μm. Compared with HA synthesized without H_6L,[37] the addition of H_6L resulted in the uniformly spherical HA with regular morphology. The sphericality

and particle size of the element-doped HA were consistent with HA, indicating that element doping had no significant effect on the morphology of HA with H_6L. Additionally, EDS (Figure 2A) displayed that all groups contained elements such as Ca and P. The 10Zn@HA, 5Mg10Zn@HA, 10Mg10Zn@HA, and 15Mg10Zn@HA groups contained Zn; the 5Mg10Zn@HA, 10Mg10Zn@HA, and 15Mg10Zn@HA groups contained Mg; the 10Zn@HA group did not contain Mg. All elements were uniformly distributed on the surface of HA, indicating successful synthesis of Zn- and Mg-doped HA.

X-ray diffraction (XRD) analysis was conducted to investigate the crystal structure of element-doped HA

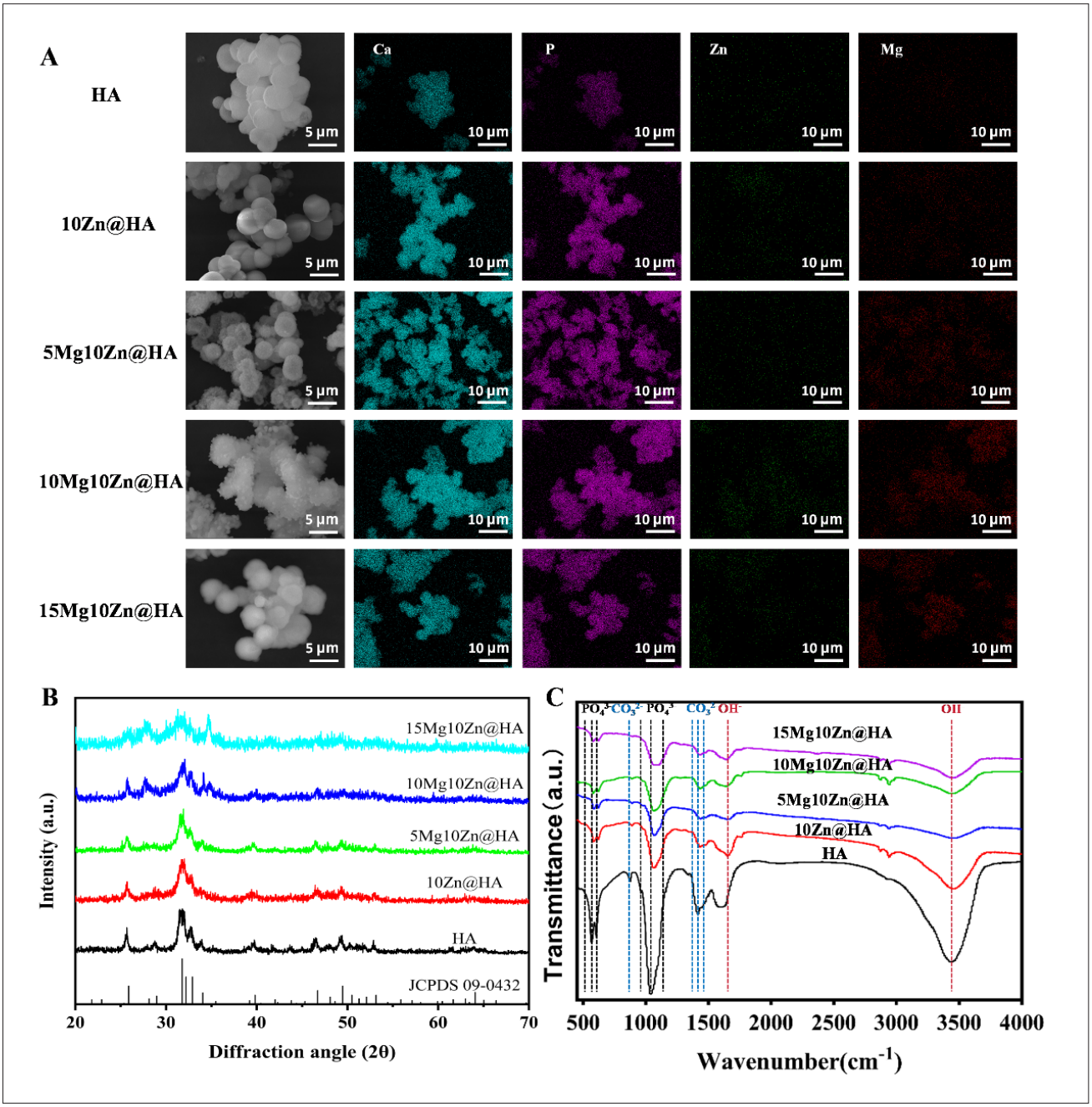

Figure 2. Characterization of hydroxyapatite (HA), 10Zn@HA, 5Mg10Zn@HA, 10Mg10Zn@HA, and 15Mg10Zn@HA. (A) Scanning electron microscope (SEM) images and element mapping. (B) X-ray diffraction (XRD) patterns. (C) Fourier transform infrared (FTIR) spectra. Scale bars: 5 μm.

(Figure 2B) and discuss the effects of element doping on the crystallinity and lattice parameters, such as crystal growth direction, of HA. The results indicated that all samples exhibited characteristic peaks of HA, without the presence of other phase impurity peaks, demonstrating that the main phase structure of synthesized HA and element-doped HA remained as HA, as compared to the standard card of HA (JCPDS09-0432).[38] Moreover, the $I_{(300)}/I_{(211)}$ ratio of pure HA (42%) was lower than that of the standard card (60%), contrary to the pure HA result that we previously synthesized without H_6L.[37] This indicates that the addition of H_6L slows down the growth rate of HA crystals on the *a*-axis and weakens the trend of preferred growth on the *c*-axis. The HA crystals tended to grow isotropically and form globular structures, which is consistent with the SEM results. After doping with 10% Zn, the $I_{(300)}/I_{(211)}$ ratio (73%) increased, and the $I_{(002)}/I_{(300)}$ ratio (57%) also increased compared to pure HA (48%), indicating a weakening trend of crystal growth in all directions and a tendency to form irregular spherical structures, consistent with the SEM results. Conversely, the addition of 5% Mg led to a decrease in the $I_{(300)}/I_{(211)}$ ratio (43%) and a further increase in the $I_{(002)}/I_{(300)}$ ratio (68%), indicating a slowdown in the growth rate of HA crystals on the *a*-axis and a weakening trend of preferential growth on the *c*-axis, tending towards spherical structures. With an increase in Mg concentration, the trend gradually weakened, and the HA exhibited irregular spherical shapes, consistent with the SEM results. Therefore, the morphology of HA can be controlled by adding the small molecular template agent H_6L and adjusting the amount of element doping.

Fourier transform infrared (FTIR) spectroscopy was used to analyze the functional groups of element-doped HA (Figure 2C). The results displayed that all HA groups exhibited characteristic peaks of HA functional groups. The broad peak on the right (3700–2500 cm^{-1}) represents the stretching vibration peak of H–O in free H_2O molecules adsorbed on the material surface. The bending vibration peak of H–O in free H_2O molecules adsorbed on the material surface was located at 1639 cm^{-1}. The bending and stretching vibration peaks of P–O in PO_4^{3-} were located at 564 and 602 cm^{-1} and 958, 1034, and 1108 cm^{-1},[36] respectively. Additionally, the C–O bond in CO_3^{2-} was also present in the synthesized HA and element-doped HA. The characteristic peaks of C–O at 872, 1416, and 1453 cm^{-1} represent the A- and B-type CO_3^{2-} substitutions occurring at PO_4^{3-} and OH^-,[39] respectively, indicating that the synthesized HA and element-doped HA were carbonated apatite with a small amount of carbonate substitution. Moreover, the characteristic peaks of O–H in OH^- were not obvious in the FTIR spectra of modified HA, indicating that HA underwent A- and B-type carbonate substitutions. Carbonated apatite is also present in human bone tissue and exhibits better biocompatibility than pure HA,[40] thus the synthesized HA and element-doped HA are not affected by the presence of carbonate substitution, which affects their biological efficacy.

The ICP-AES was used to determine the actual doping amount of elements in each group of element-doped HA and calculate the relative doping efficiency of Mg and Zn elements (Table S2, Supporting Information). The results indicated that the overall doping efficiency of Zn was high (>89%), and with an increase in the doping amount of Mg, there was a slight decrease in the doping efficiency of Zn. Additionally, the doping efficiency of Mg decreased with an increase in Mg^{2+} doping amount, indicating that the theoretical doping amount does not represent the actual doping amount, and there is a certain amount of loss in element doping.

3.2. Characterization of 3D-printed composite scaffolds

Polycaprolactone (PCL), as a material with a slow degradation rate and the ability to maintain its shape and mechanical properties after implantation at the defect site, is an excellent material for constructing 3D scaffolds. When combined with HA, it can improve the low physicochemical interaction between PCL and surface cells due to the hydrophobicity of PCL. For example, Kundu et al.[41] combined PCL with montmorillonite nanoclay (MMT-Clay) and nano-HA-clay (HAP MMT-Clay) to prepare polymer composite fiber scaffolds for bone tissue engineering, significantly enhancing the cell activity and osteogenic differentiation ability of BMSCs. Therefore, in this study, the PCL was combined with element-doped HA to manufacture composite scaffolds for bone tissue engineering. The surface morphology of HA-PCLs, 10Zn@HA-PCLs, 5Mg10Zn@HA-PCLs, 10Mg10Zn@HA-PCLs, and 15Mg10Zn@HA-PCLs scaffolds is displayed in Figure 3A. All composite scaffolds exhibited a uniform and interconnected 3D porous structure with pore sizes of approximately 300 μm, which facilitates cell migration and nutrient transport and enhances capillary formation and new bone formation.[42] Additionally, the cross-section of 15Mg10Zn@HA-PCLs was circular and regular with a diameter of approximately 400 μm. EDS results demonstrate that Ca, P, Zn, and Mg were uniformly distributed within the scaffolds, indicating uniform mixing of synthesized HA and PCL (Figure 3B).

We evaluated the mechanical strength of each group of scaffolds (Figure 3C). The results indicated that there was no significant difference in the elastic modulus of each group of scaffolds (Figure 3D), while the ultimate compressive modulus of 10Zn@HA-PCLs and 15Mg10Zn@HA-PCLs

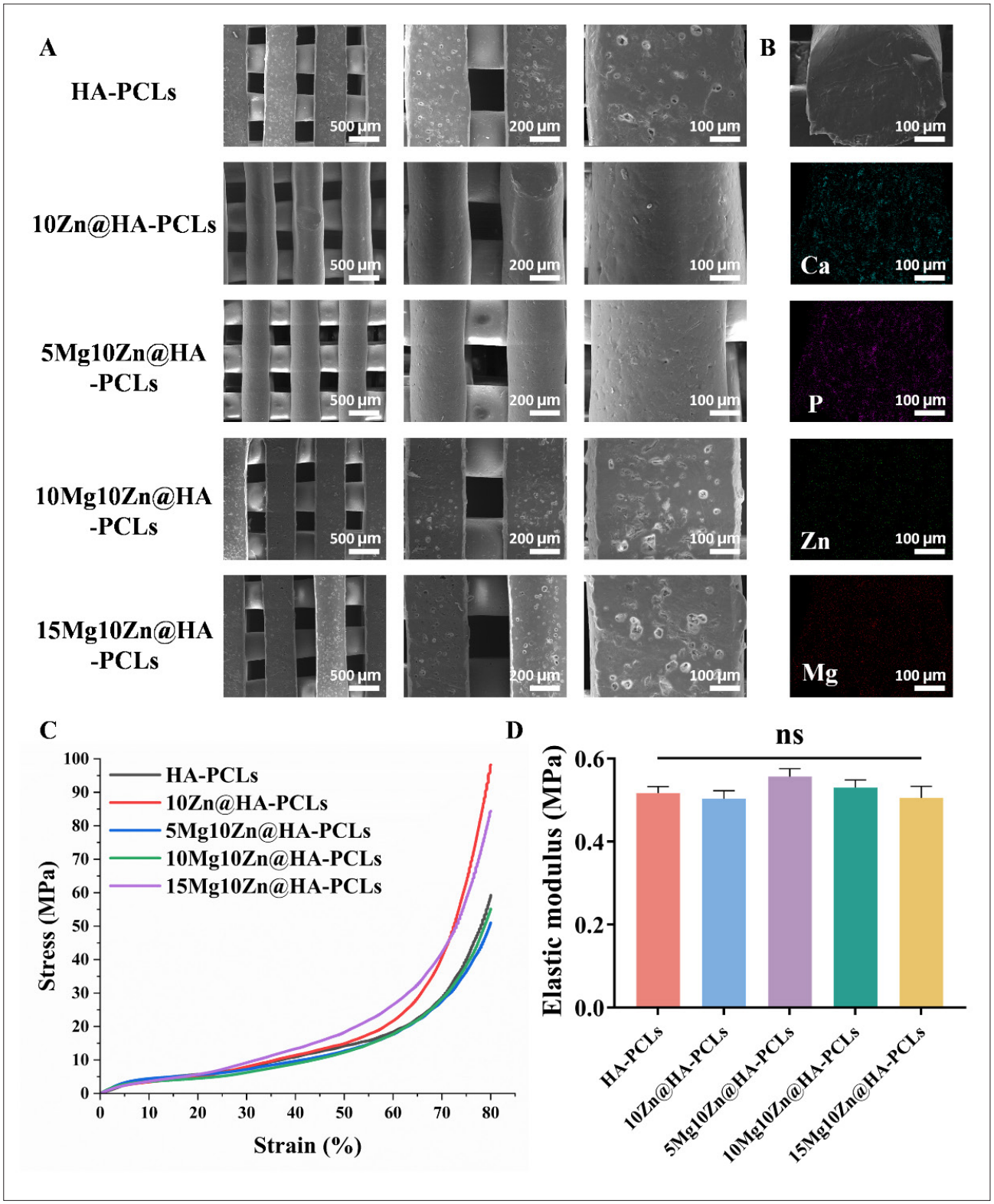

Figure 3. Characterization of HA-PCLs, 10Zn@HA-PCLs, 5Mg10Zn@HA-PCLs, 10Mg10Zn@HA-PCLs, and 15Mg10Zn@HA-PCLs. (A) Scanning electron microscope (SEM) images. (B) Element mapping of the cross-section of 15Mg10Zn@HA-PCLs. (C) Stress-strain curve. (D) Elastic modulus (n = 3). Scale bars: 500, 200, and 100 μm in SEM images and 100 μm in element mapping. Abbreviations: HA, hydroxyapatite; ns, non-significant; PCL, polycaprolactone.

scaffolds was significantly higher than that of HA-PCLs, 5Mg10Zn@HA-PCLs, and 10Mg10Zn@HA-PCLs groups (Figure S1, Supporting Information), which may be related to the morphology of HA in each group. In the XRD results of 10Zn@HA and 15Mg10Zn@HA, the $I_{(300)}/I_{(211)}$ and $I_{(002)}/I_{(300)}$ ratios were closer, indicating irregular spherical shapes, which may enhance the mechanical performance of the composite scaffolds.

Furthermore, we evaluated the cumulative release of Zn and Mg from the composite scaffolds in simulated *in vitro* environments (Figure S2, Supporting Information). All groups demonstrated stability and sustained release effects over 14 days. With the addition of Mg ions, the concentration of Zn ions also decreased with increasing concentration of Mg ions. Further comparison of Zn and Mg ion release revealed that Zn^{2+} was less released than Mg^{2+}, probably due to more stable doping of Zn^{2+} (fixed in the crystal lattice).

3.3. Evaluation of the angiogenic ability of 3D-printed composite scaffolds *in vitro*

We performed CCK-8 experiments to assess the proliferation of HUVECs on the composite scaffolds (Figure 4A). With the increase in culture time, the number of HUVECs increased, with the Mg/Zn double-doped group displaying the best cell proliferation effect. Meanwhile, with the increase in Mg^{2+} concentration, its effect on promoting cell proliferation also increased, and at 72 h of culture, the proliferation rate of the 15Mg10Zn@HA-PCLs group was significantly higher than the 5Mg10Zn@HA-PCLs group. Additionally, after co-culture for 72 h, the live/dead staining indicated that almost all HUVECs remained viable (green fluorescence), with few dead cells (red fluorescence), and the double-element-doped group had more cells than the other three groups, consistent with the CCK-8 results, indicating that all scaffolds had good cell compatibility (Figure 4C).

We assessed the effect of composite scaffolds on HUVEC migration using a wound healing assay, calculating the effect of the composite scaffolds on wound healing based on the difference in the area between 0 and 12/24 h (Figure 4D). Statistical results (Figure 4B) demonstrated that although all groups could promote wound healing, the 10Zn@HA-PCLs group had the worst effect compared to other groups. However, with the addition of Mg, the trend of the 10Zn@HA-PCLs group was reversed, and the effects of the various groups containing Mg were enhanced with increasing culture time; the 10Mg10Zn@HA-PCLs and 15Mg10Zn@HA-PCLs groups being the best.

Meanwhile, we investigated the expression of angiogenesis-related genes VEGF, VEGFR1 (FLT1), VEGFR2 (KDR), and bFGF (Figure 5E). The expression of these genes in the groups containing Mg^{2+} was higher than that in the other three groups, with the highest expression observed in the 10Mg10Zn@HA-PCLs and 15Mg10Zn@HA-PCLs groups, consistent with the results of the wound healing assay. Western blot (Figure S3, Supporting Information) analysis confirmed that the Mg-doped group exhibited stronger expressions of CD31 and VEGF compared to the pure Zn-doped group, and the expression levels increased with the concentration of Mg^{2+}, consistent with the qPCR results. These findings suggest that Mg^{2+} can promote the proliferation and migration of HUVECs.

3.4. Evaluation of the osteogenic differentiation potential of 3D-printed composite scaffolds *in vitro*

We investigated the effects of scaffolds on the cytotoxicity and proliferation of BMSCs. First, we performed CCK-8 experiments to assess how composite scaffolds affected cell proliferation. Results after co-culturing composite scaffold extracts with BMSCs for 1, 3, and 5 days indicated no significant difference in relative cell viability between each group and the control group on the first day, and all groups exhibited a trend of promoting the proliferation of BMSCs with longer culture time; the trend was more pronounced in the Mg/Zn element-doped groups (Figure 5A). Additionally, after co-culturing with composite scaffolds for 72 h, the live/dead staining results indicated that all samples had no obvious dead cells (Figure 5B).

To study the effect of composite scaffolds on osteogenic differentiation, we co-cultured BMSCs with composite scaffolds for 7 and 14 days and performed ALP staining to determine the early bone regeneration ability of the composite scaffolds (Figure 6A). The results indicated that the ALP staining area of the element-doped groups was larger than that of the control group and HA-PCLs group. Moreover, the ALP staining area of the Mg/Zn double-doped group was greater than that of the single Zn-doped group, and the staining area also increased with increasing Mg^{2+} concentration; there was no significant difference between the 10Mg10Zn@HA-PCLs and 15Mg10Zn@HA-PCLs groups, consistent with the quantitative analysis results of ALP activity (Figure 6C). After 21 days of induction *in vitro*, ARS staining was performed to evaluate the late-stage mineralization ability of BMSCs on the composite scaffolds. The results indicated that the mineralization nodule formation of the Mg/Zn double-doped group was greater than that of the other three groups, and the formation of mineralization nodules also increased with increasing Mg ion doping concentration, (Figure 6B). The quantitative results (Figure 6D) indicated that the 15Mg10Zn@HA-PCLs group had the highest

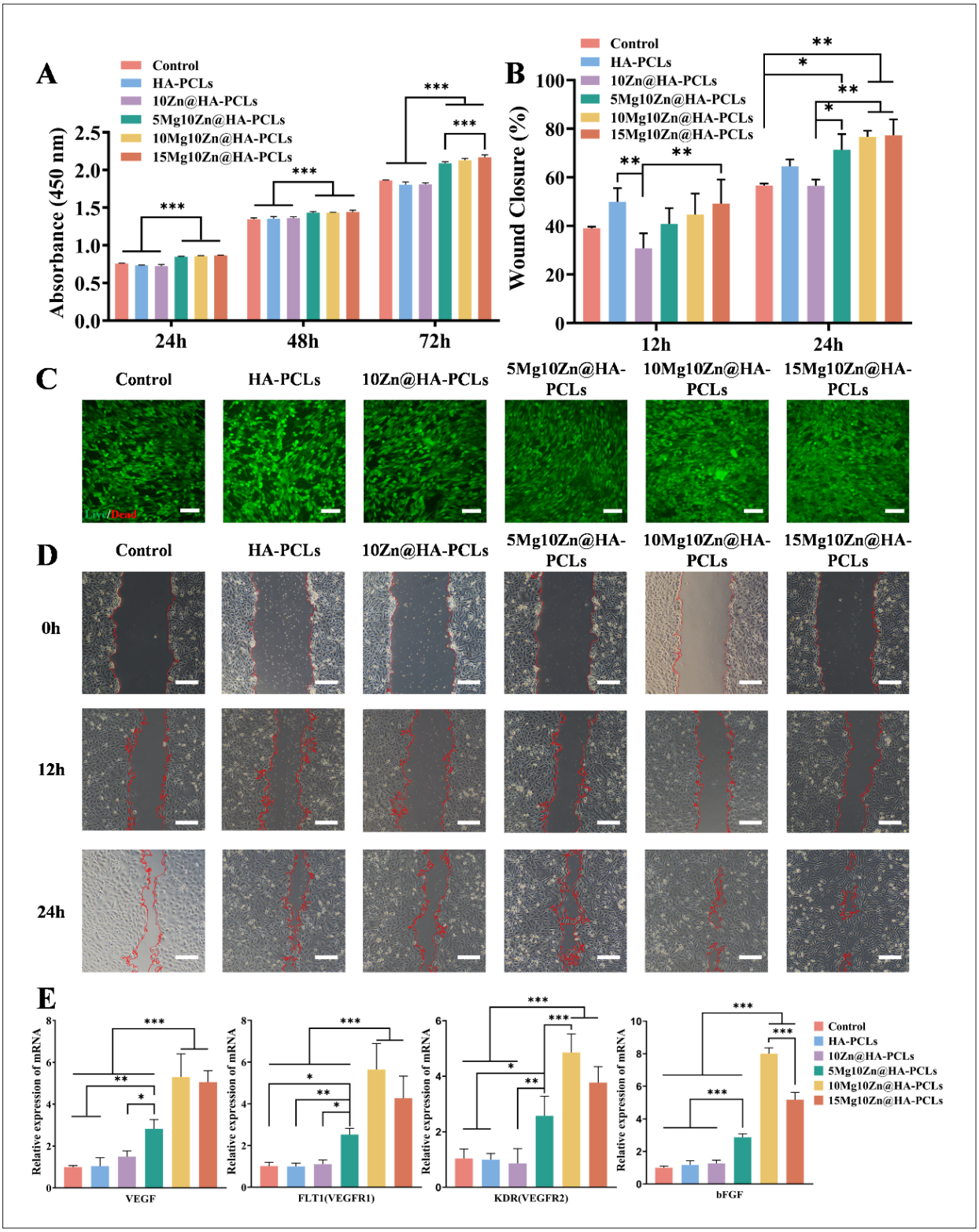

Figure 4. Evaluation of the angiogenic ability of HA-PCLs, 10Zn@HA-PCLs, 5Mg10Zn@HA-PCLs, 10Mg10Zn@HA-PCLs, and 15Mg10Zn@HA-PCLs *in vitro*. (A) Proliferative activity of HUVECs in each group of scaffolds after 24, 48, and 72 h of culture. (B) Statistical results of wound healing. (C) Live/dead staining images of each group of scaffolds. (D) Wound healing assay of HUVECs in the presence of each group of scaffolds (scale bars = 400 μm). (E) The angiogenesis-related gene expression of each group of scaffolds (VEGF, FLT1, KDR, and bFGF). *$p < 0.05$, ** $p < 0.01$, *** $p < 0.001$; $n = 4$. Scale bars: 500 μm (C); 100 μm (D). Abbreviations: HA, hydroxyapatite; HUVECs, human umbilical vein endothelial cells; PCL, polycaprolactone.

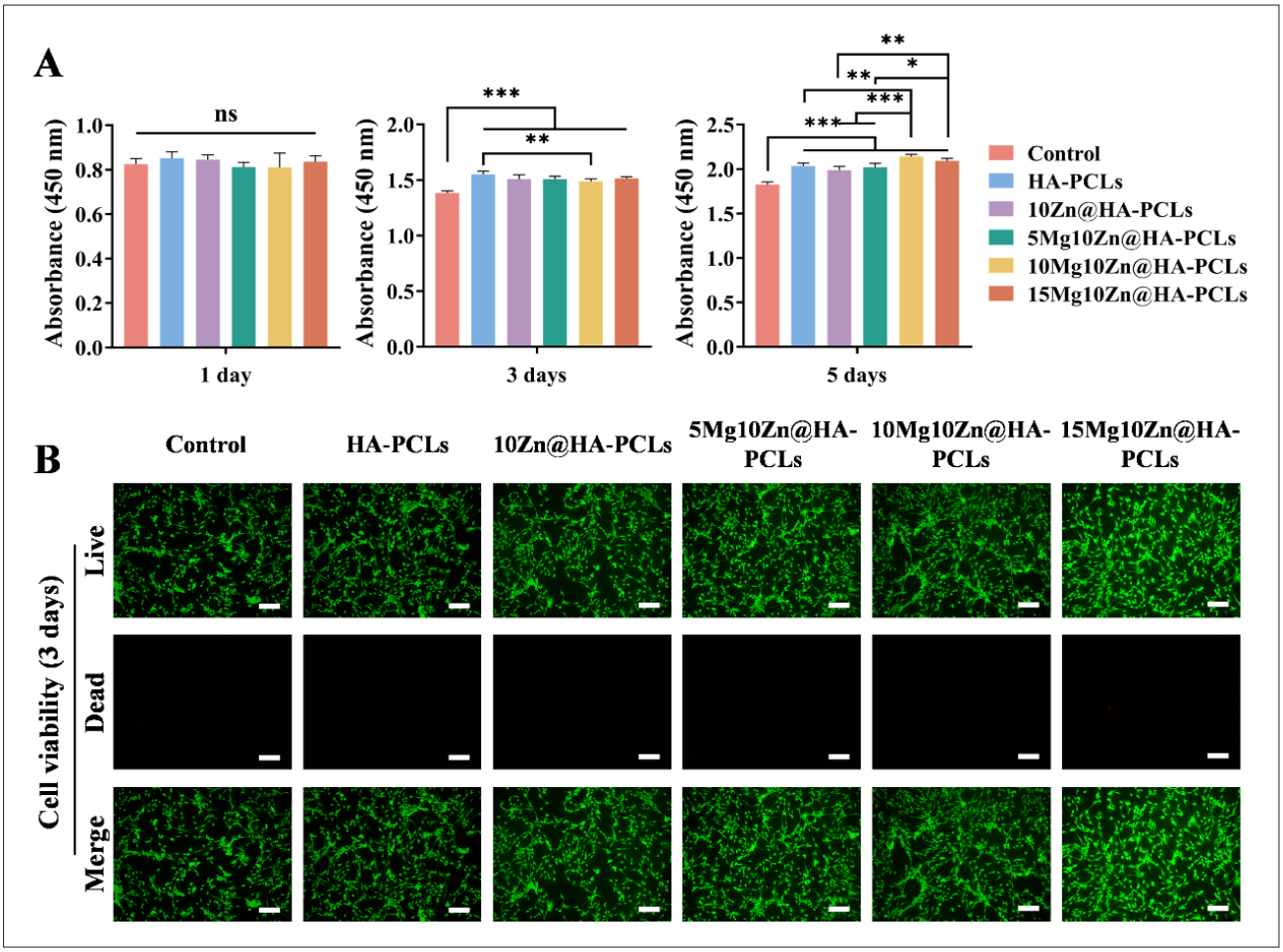

Figure 5. Cell viability and proliferation activity of rat bone marrow mesenchymal stem cells (RBMSCs) in each group of scaffolds. (A) Proliferative activity of RBMSCs after 1, 3, and 5 days of culture (*$p < 0.05$, **$p < 0.01$, ***$p < 0.001$; $n = 4$). (B) Live/dead staining images of each group of scaffolds. Scale bars: 500 μm. Abbreviations: HA, hydroxyapatite; ns: non-significant; PCL, polycaprolactone;.

mineral deposition, consistent with the ARS staining results. These results indicated that Mg/Zn double-doped composite scaffolds promote osteogenic differentiation of BMSCs and that the differentiation effect improves with increasing Mg ion doping concentration.

To elucidate the effect of Mg/Zn double-doped composite scaffolds on osteogenic differentiation, we quantitatively and qualitatively studied the expression of osteogenic-related genes and proteins in BMSCs co-cultured with composite scaffolds for 7 and 14 days, respectively. The qPCR results (Figure 6E) indicated that the expression of OPN, OCN, ALP, and RUNX2 in the Mg/Zn double-doped group was higher than that in the control group and positively correlated with the Mg doping concentration, with the 15Mg10Zn@HA-PCLs group exhibiting the highest expression, consistent with the ALP and ARS staining and quantitative results. Western blot results (Figure S4, Supporting Information) demonstrated that the expression of OPN, OCN, and COL1 in the Mg/Zn double-doped group was higher than that in the control group, consistent with the qPCR results.

3.5. Evaluation of the osteogenic differentiation potential of 3D-printed composite scaffolds *in vivo*

Using a rat femoral defect model, the ability of the composite scaffolds to promote bone repair was evaluated. H&E and Masson staining were used to evaluate bone regeneration following treatment with composite scaffolds after 1 and 3 months (Figures 7 and S6, Supporting Information). The H&E results displayed new bone formation in all groups. However, the Zn-doped and Zn/Mg-co-doped groups exhibited more prominent new bone formation than the control and HA groups. New bone formed around the scaffold (the blank area was the scaffold), and its formation was enhanced with increasing Mg doping.

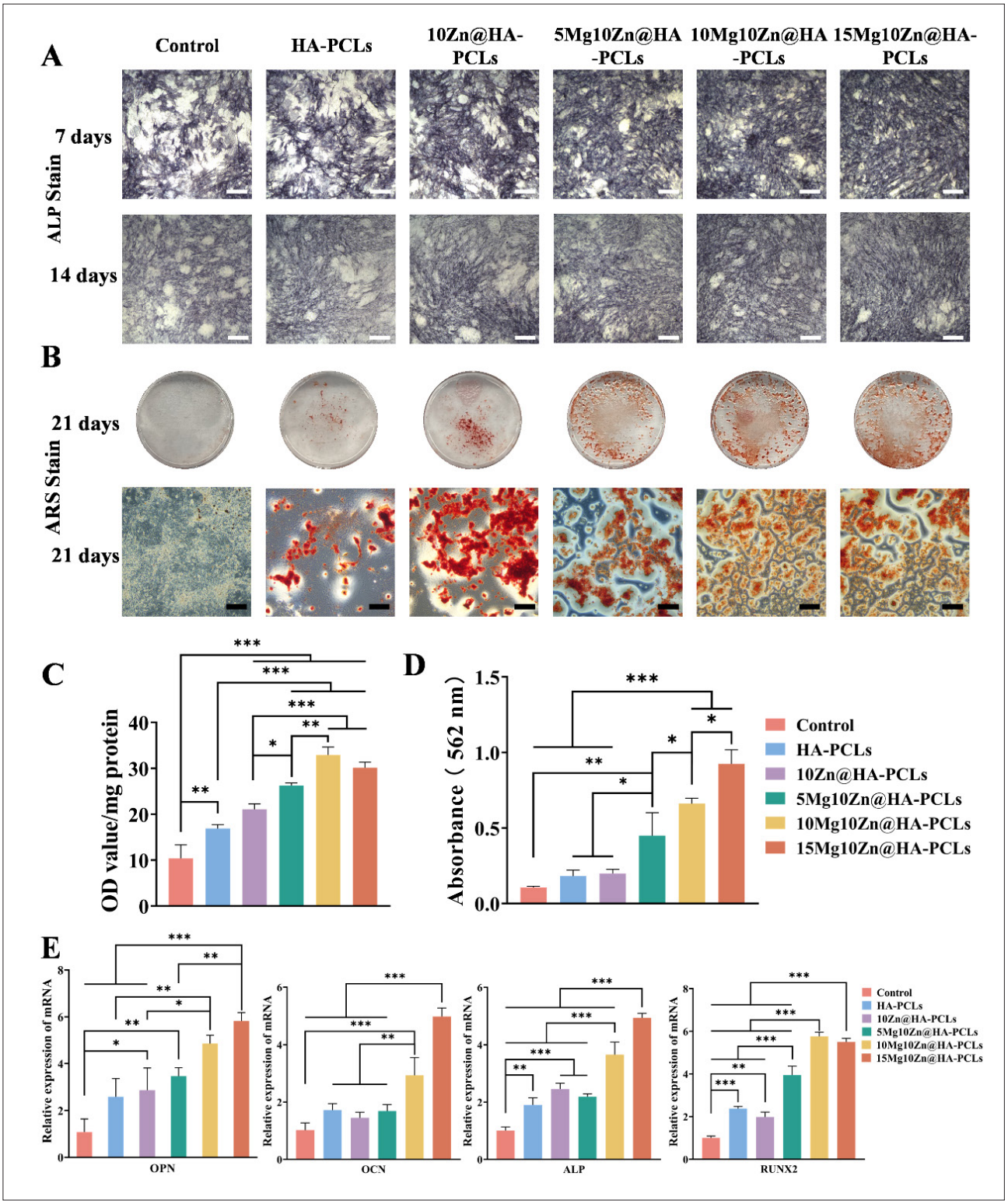

Figure 6. Evaluation of the osteogenic ability of HA-PCLs, 10Zn@HA-PCLs, 5Mg10Zn@HA-PCLs, 10Mg10Zn@HA-PCLs, and 15Mg10Zn@HA-PCLs *in vitro*. (A) Cells that have been in culture for 7 and 14 days using alkaline phosphatase (ALP) staining. (B) On day 21, cells were stained with alizarin red S (ARS). (C) ALP activity of cells cultured for 7 days. (D) Quantification of cell mineralization on day 21. (E) The osteogenic-related gene expression of each group of scaffolds (OPN, OCN, ALP, and RUNX2). $^{*}p < 0.05$, $^{**}p < 0.01$, $^{***}p < 0.001$; $n = 4$. Scale bars: 200 μm (A); 500 μm (B). Abbreviations: HA, hydroxyapatite; PCL, polycaprolactone.

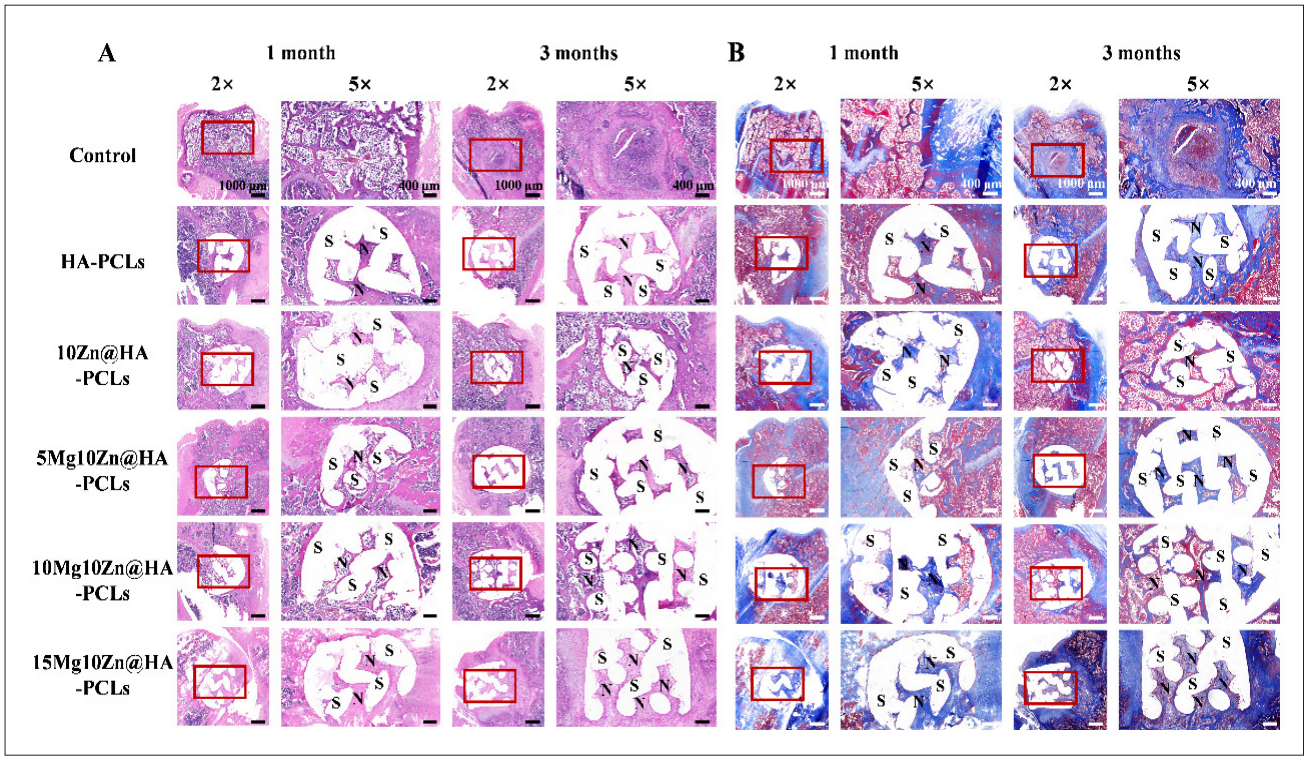

Figure 7. (A) Hematoxylin and eosin (H&E) and (B) Masson staining of bone formation after composite scaffold implantation for 1 and 3 months. Scale bars: 1000 μm (2×); 400 μm (5×). Abbreviations: HA, hydroxyapatite; N, new bone; PCL, polycaprolactone; S, scaffold.

Meanwhile, Masson staining analysis further validated enhanced new bone formation with Zn/Mg-co-doping. The 10Mg10Zn@HA-PCLs and the 15Mg10Zn@HA-PCLs groups demonstrated the deepest and broadest staining area (the blue and red colors represent collagen synthesis and new bone formation, respectively), indicating more calcification and bone maturity.

To further verify the angiogenic and osteogenic properties of the composite scaffolds, we conducted α-SMA and CD31 immunohistochemical staining to assess their angiogenic performance (Figures 8 and S7, Supporting Information). The α-SMA and CD31 results demonstrated a significant increase in the number of blood vessels in the new bone areas of the Mg-doped group. During the early repair process (1 month), the number of vessels increased at higher levels of Mg ion doping, indicating that Mg ions have a pro-angiogenic effect. Additionally, we performed COL1A1 immunohistochemical staining to evaluate the osteogenic performance (Figures 8 and S7, Supporting Information). All groups exhibited varying degrees of osteogenesis. In the early stages of bone formation, Mg ion doping accelerated the process. After 3 months, there were no significant differences between the scaffold groups, and the collagen type I content in the newly formed bone was comparable, suggesting that Mg/Zn-co-doping has a synergistic effect in promoting bone regeneration.

Relevant studies have demonstrated that Zn^{2+} exhibits both osteogenic and antibacterial activity.[43] However, excessive concentrations of Zn may induce toxicity *in vivo*, which is a potential safety hazard.[44] High doses and concentrations of Zn ions are harmful, as their accumulation within cells can lead to mitochondrial damage and disruption of cellular Zn homeostasis.[45] Hence, the controlled release of Zn ions not only reduces their cytotoxicity but also harnesses their potential to promote osteogenic differentiation of stem cells. Additionally, Mg ions have been reported to promote angiogenesis[46] and bone repair.[1,47] Therefore, co-doping of HA with Zn and Mg not only achieves slow and safe release of Zn ions but also synergistically enhances angiogenesis to facilitate bone repair. Therefore, this study employed a continuous sustained release of Zn^{2+} to ensure its safe release *in vivo*. Likewise, the addition of Mg^{2+} can synergistically promote vascular growth and new bone generation.

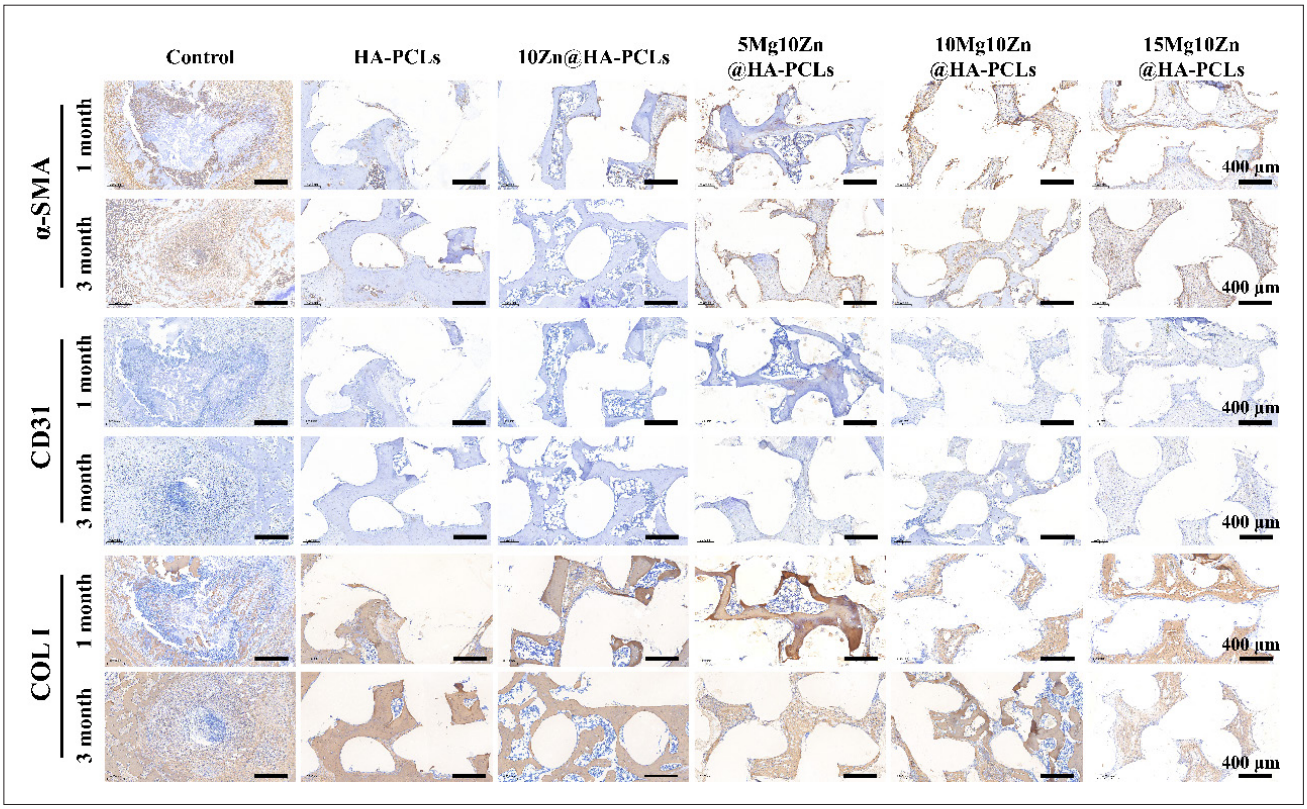

Figure 8. Staining of α-SMA, CD31, and COL I during bone formation after composite scaffold implantation for 1 and 3 months. Scale bar: 400 μm. Abbreviations: HA, hydroxyapatite; PCL, polycaprolactone.

4. Conclusion

In this study, HA, Zn-doped HA, and Mg/Zn-co-doped HA were successfully synthesized via hydrothermal synthesis. After compounding with PCL, porous scaffolds were fabricated via 3D printing. Experimental results demonstrated excellent mechanical properties, making them suitable for repairing load-bearing bone defects. *In vitro* experiments confirmed good biocompatibility of all scaffold groups. Moreover, the Mg/Zn-co-doped group promoted angiogenesis and bone defect repair, with a more pronounced effect observed when increasing Mg doping. Compared to the Zn-doped group, the co-doped group exhibited significant advantages. Furthermore, all scaffold groups exhibited favorable bone repair outcomes *in vivo*, with the 10Mg10Zn and 15Mg10Zn groups demonstrating particularly promising results. Taken together with the *in vitro* evaluations, the 10Mg10Zn group may be a potential candidate for bone defect repair.

Acknowledgments

The authors would like to acknowledge the creation of Graphical abstract and Figure 1 using BioRender (biorender.com).

Funding

This work was supported by the National Key Research and Development Program of China (2023YFC2411300); National Natural Science Foundation of China (82072412/92048205/ 52071277); Biomaterials and Regenerative Medicine Institute Cooperative Research Project by Shanghai Jiao Tong University School of Medicine (2022LHB08); Project of Shanghai Science and Technology Commission (22015820100); China Postdoctoral Science Foundation (2022M721685/2022M722121); and the China Postdoctoral Science Foundation Special Grant Program (2023T160331).

Conflict of interest

The authors declare that they have no known competing financial interests or personal relationships that could have appeared to influence the work reported in this paper.

Author contributions

Conceptualization: Jie Weng, Pengfei Zheng, Jinwu Wang
Formal analysis: Hao Huang, Lei Qiang, Yiwei Zhang
Investigation: Lei Qiang, Guanlu Shen, Quan Zhang
Methodology: Hao Huang, Lei Qiang, Ya Fang, Weize Kong
Writing – original draft: Lei Qiang
Writing – review & editing: Jing Shan, Yihao Liu, Chengwei Wang

Ethics approval and consent to participate

The animal surgical procedures involved in this study followed the recommendations of the Institutional Animal Care and Use Committee (IACUC) of Shanghai Jiao Tong University (animal protocol number: O_A2023001).

Consent for publication

Not applicable.

Availability of data

Data is available from the corresponding author upon reasonable request.

References

1. Li Y, Xu JK, Mi J, et al. Biodegradable magnesium combined with distraction osteogenesis synergistically stimulates bone tissue regeneration via CGRP-FAK-VEGF signaling axis. *Biomaterials.* 2021;275:120984. doi: 10.1016/j.biomaterials.2021.120984
2. Wang Q, Xia QQ, Wu Y, et al. 3D-printed atsttrin-incorporated alginate/hydroxyapatite scaffold promotes bone defect regeneration with TNF/TNFR signaling involvement. *Adv Healthc Mater.* 2015;4:1701-1708. doi: 10.1002/adhm.201500211
3. Hasani-Sadrabadi MM, Sarrion P, Pouraghaei S, et al. An engineered cell-laden adhesive hydrogel promotes craniofacial bone tissue regeneration in rats. *Sci Transl Med.* 2020;12:eaay6853. doi: 10.1126/scitranslmed.aay6853
4. Possolli NM, Raupp-Pereira F, Montedo ORK, et al. LZS bioactive glass-ceramic scaffolds: colloidal processing, foam replication technique and mechanical properties to bone tissue engineering. *Open Ceram.* 2022;9:100219. doi: 10.1016/j.oceram.2022.100219
5. Ren Y, Kong WQ, Liu YH, et al. Photocurable 3D-printed PMBG/TCP scaffold coordinated with PTH (1-34) bidirectionally regulates bone homeostasis to accelerate bone regeneration. *Adv Healthc Mater.* 2023;12:e202300292. doi: 10.1002/adhm.202300292
6. Wu YG, Xing ZY, Zhao R, et al. Engineered cell-laden armor unit-mimicking bioceramic granules for bone regeneration. *Adv Funct Mater.* 2024;34:10331. doi: 10.1002/adfm.202310331
7. Zhao R, Chen SY, Zhao WL, et al. A bioceramic scaffold composed of strontium-doped three-dimensional hydroxyapatite whiskers for enhanced bone regeneration in osteoporotic defects. *Theranostics.* 2020;10: 1572-1589. doi: 10.7150/thno.40103
8. Xu JK, Hu PJ, Zhang XT, et al. Magnesium implantation or supplementation ameliorates bone disorder in CFTR-mutant mice through an ATF4-dependent Wnt/β-catenin signaling. *Bioact Mater.* 2022;8:95-108. doi: 10.1016/j.bioactmat.2021.06.034
9. Li WT, Miao WQ, Liu YH, et al. Bioprinted constructs that mimic the ossification center microenvironment for targeted innervation in bone regeneration. *Adv Funct Mater.* 2022;32:2109871. doi: 10.1002/adfm.202109871
10. Gu JN, Zhang QQ, Geng MR, et al. Construction of nanofibrous scaffolds with interconnected perfusable microchannel networks for engineering of vascularized bone tissue. *Bioact Mater.* 2021;6:3254-3268. doi: 10.1016/j.bioactmat.2021.02.033
11. Dorozhkin SV. Multiphasic calcium orthophosphate (CaPO) bioceramics and their biomedical applications. *Ceram Int.* 2016;42:6529-6554. doi: 10.1016/j.ceramint.2016.01.062
12. Thompson JB, Kindt JH, Drake B, et al. Bone indentation recovery time correlates with bond reforming time. *Nature.* 2001;414:773-776. doi: 10.1038/414773a
13. Lim KT, Patel DK, Dutta SD, et al. Human teeth-derived bioceramics for improved bone regeneration. *Nanomaterials Basel.* 2020;10:2396. doi: 10.3390/nano10122396
14. Zhang H, Huang HF, Hao GR, et al. 3D printing hydrogel scaffolds with nanohydroxyapatite gradient to effectively repair osteochondral defects in rats. *Adv Funct Mater.* 2021;31:2006697. doi: 10.1002/adfm.202006697
15. Huang H, Yang AC, Li JS, et al. Preparation of multigradient hydroxyapatite scaffolds and evaluation of their osteoinduction properties. *Regen Biomater.* 2022;9:001. doi: 10.1093/rb/rbac001
16. Supova M. Substituted hydroxyapatites for biomedical applications: a review. *Ceram Int.* 2015;41:9203-9231. doi: 10.1016/j.ceramint.2015.03.316

17. Lakhkar NJ, Lee IH, Kim HW, et al. Bone formation controlled by biologically relevant inorganic ions: role and controlled delivery from phosphate-based glasses. *Adv Drug Deliver Rev.* 2013;65:405-420.
doi: 10.1016/j.addr.2012.05.015

18. Li SJ, Zhang LY, Liu CY, et al. Spontaneous immunomodulation and regulation of angiogenesis and osteogenesis by Sr/Cu-borosilicate glass (BSG) bone cement to repair critical bone defects. *Bioact Mater.* 2023;23:101-117.
doi: 10.1016/j.bioactmat.2022.10.021

19. D'Mello S, Elangovan S, Hong L, et al. Incorporation of copper into chitosan scaffolds promotes bone regeneration in rat calvarial defects. *J Biomed Mater Res B.* 2015;103: 1044-1049.
doi: 10.1002/jbm.b.33290

20. Wang Y, Wang XY, Pang YY, et al. Ion-engineered microcryogels via osteogenesis-angiogenesis coupling and inflammation reversing augment vascularized bone regeneration. *Adv Funct Mater.* 2024;34(34):2400745.
doi: 10.1002/adfm.202400745

21. Ghorbani FM, Kaffashi B, Shokrollahi P, et al. PCL/chitosan/Zn-doped nHA electrospun nanocomposite scaffold promotes adipose derived stem cells adhesion and proliferation. *Carbohyd Polym.* 2015;118:133-142.
doi: 10.1016/j.carbpol.2014.10.071

22. Kulanthaivel S, Mishra U, Agarwal T, et al. Improving the osteogenic and angiogenic properties of synthetic hydroxyapatite by dual doping of bivalent cobalt and magnesium ion. *Ceram Int.* 2015;41:11323-11333.
doi: 10.1016/j.ceramint.2015.05.090

23. Xiao DQ, Yang F, Zhao Q, et al. Fabrication of a Cu/Zn co-incorporated calcium phosphate scaffold-derived GDF-5 sustained release system with enhanced angiogenesis and osteogenesis properties. *RSC Adv.* 2018;8:29526-29534.
doi: 10.1039/c8ra05441j

24. Elrayah A, Zhi W, Feng S, et al. Preparation of micro/nano-structure copper-substituted hydroxyapatite scaffolds with improved angiogenesis capacity for bone regeneration. *Materials.* 2018;11:1516.
doi: 10.3390/ma11091516

25. Shoaib M, Bahadur A, Iqbal S, et al. Magnesium doped mesoporous bioactive glass nanoparticles: a promising material for apatite formation and mitomycin c delivery to the MG-63 cancer cells. *J Alloy Compd.* 2021;866:159013.
doi: 10.1016/j.jallcom.2021.159013

26. Castiglioni S, Cazzaniga A, Albisetti W, et al. Magnesium and osteoporosis: current state of knowledge and future research directions. *Nutrients.* 2013;5:3022-3033.
doi: 10.3390/nu5083022

27. Rude RK, Singer FR, and Gruber HE. Skeletal and hormonal effects of magnesium deficiency. *J Am Coll Nutr.* 2009;28:131-141.
doi: 10.1080/07315724.2009.10719764

28. Shrestha S, Lee SY, Shrestha D, et al. Micro/nanometer-sized porous structure of zinc phosphate incorporated Ti (HPO4) hydrate bioceramic induces osteogenic gene expression and enhances osteoporotic bone regeneration. *Chem Eng J.* 2022;450:138360.
doi: 10.1016/j.cej.2022.138360

29. Yin S, Lin SH, Xu JY, et al. Dominoes with interlocking consequences triggered by zinc: involvement of microelement-stimulated MSC-derived exosomes in senile osteogenesis and osteoclast dialogue. *J Nanobiotechnol.* 2023;21:346.
doi: 10.1186/s12951-023-02085-w

30. Shahed CA, Ahmad F, Günister E, et al. Antibacterial mechanism with consequent cytotoxicity of different reinforcements in biodegradable magnesium and zinc alloys: a review. *J Magnes Alloy.* 2023;11:3038-3058.
doi: 10.1016/j.jma.2023.08.018

31. Matsunaga K. First-principles study of substitutional magnesium and zinc in hydroxyapatite and octacalcium phosphate. *J Chem Phys.* 2008;128:245101.
doi: 10.1063/1.2940337

32. Naing MW, Chua CK, Leong KF, et al. Fabrication of customised scaffolds using computer-aided design and rapid prototyping techniques. *Rapid Prototyping J.* 2005;11(4):249-259.
doi: 10.1108/13552540510612938

33. Chua CK, Leong KF, Cheah CM, et al. Development of a tissue engineering scaffold structure library for rapid prototyping. part 1: investigation and classification. *Int J Adv Manuf Technol.* 2003;21:291-301.
doi: 10.1007/s001700300034

34. Chua CK, Leong KF, Cheah CM, et al. Development of a tissue engineering scaffold structure library for rapid prototyping. Part 2: Parametric library and assembly program. *Int J Adv Manuf Technol.* 2003;21:302-312.
doi: 10.1007/s001700300035

35. Dong C, Wei H, Zhang XN, et al. 3D printed hydrogel/wesselsite-PCL composite scaffold with structural change from core/shell fibers to microchannels for enhanced bone regeneration. *Compos B: Eng.* 2022;246:110264.
doi: 10.1016/j.compositesb.2022.110264

36. Xiao DQ, Tan Z, Fu YK, et al. Hydrothermal synthesis of hollow hydroxyapatite microspheres with nano-structured surface assisted by inositol hexakisphosphate. *Ceram Int.* 2014;40:10183-10188.
doi: 10.1016/j.ceramint.2014.02.057

37. Huang H, Qiang L, Fan MJ, et al. 3D-printed tri-element-doped hydroxyapatite/ polycaprolactone composite scaffolds with antibacterial potential for osteosarcoma therapy and bone regeneration. *Bioact Mater.* 2024;31:18-37.
doi: 10.1016/j.bioactmat.2023.07.004

38. Kim H, Mondal S, Bharathiraja S, et al. Optimized Zn-doped hydroxyapatite/doxorubicin bioceramics system for efficient

drug delivery and tissue engineering application. *Ceram Int.* 2018;44:6062-6071.
doi: 10.1016/j.ceramint.2017.12.235

39. Fleet ME, Liu X. Coupled substitution of type A and B carbonate in sodium-bearing apatite. *Biomaterials.* 2007;28:916-926.
doi: 10.1016/j.biomaterials.2006.11.003

40. Karunakaran G, Kumar GS, Cho EB, et al. Microwave-assisted hydrothermal synthesis of mesoporous carbonated hydroxyapatite with tunable nanoscale characteristics for biomedical applications. *Ceram Int.* 2019;45:970-977.
doi: 10.1016/j.ceramint.2018.09.273

41. Kundu K, Afshar A, Katti DR, et al. Composite nanoclay-hydroxyapatite-polymer fiber scaffolds for bone tissue engineering manufactured using pressurized gyration. *Compos Sci Technol.* 2021;202:108598.
doi: 10.1016/j.compscitech.2020.108598

42. Karageorgiou V, Kaplan D. Porosity of 3D biomaterial scaffolds and osteogenesis. *Biomaterials.* 2005;26:5474-5491.
doi: 10.1016/j.biomaterials.2005.02.002

43. Zhao FL, Gao A, Liao Q, et al. Balancing the anti-bacterial and pro-osteogenic properties of Ti-based implants by partial conversion of ZNO nanorods into hybrid zinc phosphate nanostructures. *Adv Funct Mater.* 2024;34:2311812.
doi: 10.1002/adfm.202311812

44. Li Y, Xiong W, Zhang CC, et al. Enhanced osseointegration and antibacterial action of zinc-loaded titania-nanotube-coated titanium substrates: and studies. *J Biomed Mater Res A.* 2014;102:3939-3950.
doi: 10.1002/jbm.a.35060

45. Rasmussen JW, Martinez E, Louka P, et al. Zinc oxide nanoparticles for selective destruction of tumor cells and potential for drug delivery applications. *Expert Opin Drug Del.* 2010;7:1063-1077.
doi: 10.1517/17425247.2010.502560

46. Xu L, Willumeit-Römer R, Luthringer-Feyerabend BJC. Effect of magnesium-degradation products and hypoxia on the angiogenesis of human umbilical vein endothelial cells. *Acta Biomater.* 2019;98:269-283.
doi: 10.1016/j.actbio.2019.02.018

47. Hung CC, Chaya A, Liu K, et al. The role of magnesium ions in bone regeneration involves the canonical Wnt signaling pathway. *Acta Biomater.* 2019;98:246-255.
doi: 10.1016/j.actbio.2019.06.001

ACCSCIENCE PUBLISHING

International Journal of Bioprinting

RESEARCH ARTICLE

Development and *in vitro* evaluation of bioprinted plasma-infused biocarriers for mesenchymal stromal cell delivery in musculoskeletal disorder treatment

Cristina Del Amo[1,2†], Miguel Perez Garrastachu[3†], Inés Jaúregui[2], Francisco J. Alvarez[1,4], and Isabel Andia[1,4*]

[1]Regenerative Therapies Unit, Biobizkaia Health Research Institute, Barakaldo, Bizkaia, Spain

[2]3D Printing and Bioprinting Lab, Biobizkaia Health Research Institute, Barakaldo, Bizkaia, Spain

[3]Department of Cell Biology and Histology, Faculty of Medicine and Nursing, University of the Basque Country (UPV/EHU), Leioa, Biscay, Spain

[4]Cruces University Hospital, Osakidetza-Basque Health Service and Biobizkaia Health Research Institute, Barakaldo, Bizkaia, Spain

(This article belongs to the Special Issue: *Bioprinting of nanomaterials for biomedical applications*)

Abstract

A meta-analysis revealed no advantage of surgical over non-surgical treatments, emphasizing the need for non-invasive methods, particularly for prevalent osteoarticular diseases like knee osteoarthritis. To enhance therapeutic efficacy, we developed a plasma-infused gelatin methacryloyl (GelMA) biocarrier loaded with bone marrow-derived mesenchymal stromal cells (BMSCs). These constructs were evaluated *in vitro* for their properties and paracrine interactions in non-inflamed and inflamed environments. GelMA infused with platelet-rich plasma (PRP) and fresh frozen plasma (FFP; platelet-poor) were compared. Pristine GelMA was used as a control. Both PRP and FFP enhanced the proliferation and viability of BMSCs in biocarriers, promoting cell survival pathways while inhibiting necrotic and apoptotic events. Proteomic analysis displayed no differences in BMSC behavior between PRP and FFP in the absence of inflammation ($p = 0.550$). However, both plasmas significantly modified cell behavior under inflammatory conditions ($p = 0.001$). Both PRP- and FFP-infused biocarriers activated 10 key signaling pathways, including HIF-1α, neuroinflammation, and extracellular matrix turnover. PRP-specific pathways included IL-17, IL-6, and several growth factor signaling pathways. No significant differences in angiogenesis were linked to platelet dose ($p = 0.079$), but both PRP and FFP significantly enhanced angiogenesis compared to GelMA alone ($p < 0.001$ for PRP; $p = 0.002$ for FFP). FFP displayed stronger angiogenesis than PRP under IL-1β treatment ($p = 0.042$). Plasma-infused biocarriers altered BMSC behavior in response to inflammatory cytokines compared to GelMA ($p = 0.001$). PRP specifically activated TGF-β signaling under IL-1β ($Z = 2.308$; $p = 1.02E-35$), which was not observed under TNF-α exposure. These findings suggest that PRP- and FFP-infused biocarriers may offer promising improvements in regenerative therapies for inflammatory osteoarticular conditions like knee osteoarthritis.

Keywords: Extrusion bioprinting; Mesenchymal stromal cells; Platelet-rich plasma; Biocarrier; Musculoskeletal conditions; Osteoarticular pathology

†These authors contributed equally to this work

***Corresponding author:**
Isabel Andia
(sabel.andiaortiz@osakidetza.eus)

Citation: Del Amo C, Perez Garrastachu M, Jaúregui I, J Alvarez F, Andia I. Development and *in vitro* evaluation of bioprinted plasma-infused biocarriers for mesenchymal stromal cell delivery in musculoskeletal disorder treatment. *Int J Bioprint*. 2024;10(6):4426. doi: 10.36922/ijb.4426

Received: August 2, 2024
Revised: September 10, 2024
Accepted: September 24, 2024
Published Online: September 24, 2024

Copyright: © 2024 Author(s). This is an Open Access article distributed under the terms of the Creative Commons Attribution License, permitting distribution, and reproduction in any medium, provided the original work is properly cited.

Publisher's Note: AccScience Publishing remains neutral with regard to jurisdictional claims in published maps and institutional affiliations.

1. Introduction

In 2020, musculoskeletal (MSK) disorders affected 494 million people worldwide. These disorders can be categorized into three groups: inflammatory conditions (e.g., rheumatoid arthritis), conditions involving MSK pain (e.g., osteoarthritis [OA] and back pain), and osteoporosis with fragility fractures. Since 2010, the economic burden of MSK disorders has increased by 20%,[1] and the global forecast estimates an increase from 494 million in 2020 to 1060 million in 2050.[2] The global prevalence is higher in females than in males.[2] To mitigate this burden, both surgical and non-invasive approaches are currently being developed.

A systematic review and meta-analysis comparing surgical and non-surgical interventions for MSK conditions, including prevalent osteoarticular pathologies, found no support for recommending surgery over non-surgical alternatives.[3] This highlights the need for developing non-invasive treatments based on orthobiologics and 3D bioprinting technologies.

Orthobiologic products under investigation include blood-derived products and cell-based therapies.[4–6] Cell-based therapies can be divided into two types. The first type, commonly used in clinical practice, involves minimally manipulated products from adipose tissue (e.g., stromal vascular fraction, micro-fragmented adipose tissue) and bone marrow (e.g., bone marrow concentrate, bone marrow aspirate).[7] These products' therapeutic effects are due to mesenchymal stem cells (MSCs) and other bioactive effectors within the niche.[8]

The second category involves advanced MSC therapies, which include laboratory expansion of MSCs to obtain purified cell preparations (expanded-MSCs).[9,10] Achieving a therapeutic quantity of 20–50 million cells requires multiple passages and adherence to good manufacturing practice standards, resulting in an injectable advanced therapy.[11] However, clinical data indicate that these cells rarely engraft in host tissues. Recent studies revealed that MSCs, when isolated and cultured *in vitro*, lose their ability to integrate into host tissues due to alterations during expansion, shifting their therapeutic potential to their trophic and paracrine actions.[12,13]

Bone marrow-derived MSCs (BMSCs) can be delivered through extrusion bioprinting, using gelatin methacryloyl (GelMA) as a carrier and combined with bioactive molecules. As recently reviewed by Namidi et al.,[14] GelMA is a versatile hydrogel that serves as an optimal cell carrier, making it highly suitable for developing tailored strategies in bioprinting various MSK tissue substitutes. To mimic the composition and mechanical properties of tissues, GelMA can be combined with inorganic compounds like hydroxyapatite or polymers, such as polycaprolactone (PCL) and poly(ethylene glycol) diacrylate (PEGDA). Additionally, incorporating silver (Ag^{+}) or gold ions (Au^{3+}) can endow GelMA with antibacterial properties against pathogens like *Escherichia coli and Staphylococcus aureus*. GelMA can also be used to fill 3D-printed titanium (Ti6Al4V) hip structures customized to patient anatomies, thereby enhancing osseointegration. Further enhancements to GelMA's functionalities can be achieved by incorporating extracellular vesicles (EVs) containing nucleic acids, proteins, and other bioactive compounds. Growth factors (GFs), such as PDGF, BMPs, TGF-β, and VEGF, have also been investigated for their potential to promote osteoinduction and osteogenesis, as they regulate cell migration, proliferation, adhesion, and angiogenesis. However, there are significant challenges associated with the use of these molecules, including safety concerns during manufacturing and determining the most effective concentrations.

In this study, we address these challenges by using a combination of autologous GFs and cytokines, maintaining their natural balance of concentrations. Given the complexity of this molecular pool, bioinformatics tools are essential to predict the functionalities these molecules confer to GelMA hydrogels and, consequently, to the bioprinted scaffolds.

Autologous blood-derived products are extensively used in clinical settings and represent a key advancement in personalized medicine. By utilizing a patient's peripheral blood, various formulations can be created with differing concentrations of platelets and/or leukocytes, such as pure platelet-rich plasma (PRP) and leukocyte-rich PRP (L-PRP).[15] Incorporating these products into medical engineering enhances their potential, improving other medical-grade biomaterials. For instance, combining L-PRP with hyaluronic acid (HA) results in interpenetrating polymer networks that, when loaded with adipose-derived MSCs, form advanced constructs for regenerative medicine applications.[16]

To bridge the gap between classical cell-based injections and surgical implantation of tissue-engineered scaffolds, we developed a cell-instructive scaffold (biocarrier) based on plasma-infused GelMA loaded with BMSCs. This approach leverages the synergy between bioprinting, the trophic actions of MSCs, and blood-derived cytokine delivery. Multifunctional bioactive constructs were formulated by combining GelMA, plasma, and BMSCs, followed by *in vitro* evaluation.[17,18]

To explore the paracrine interactions initiated by biocarriers, we examined the biocarrier secretome

collected after 96 h in a non-inflamed environment *in vitro*. Understanding how inflammatory molecules influence MSC activities is crucial, given that MSCs frequently encounter an inflammatory milieu within host tissues. Without a suitable delivery vehicle, making therapeutic projections is challenging due to uncertainties regarding cell survival in the joint. Therefore, we created reproducible BMSC biocarriers through bioprinting and examined their main properties and trophic actions *in vitro*.

2. Methods

2.1. Preparation of plasma products

Whole blood anticoagulated with citrate phosphate dextrose (CPD) was collected from six healthy donors via apheresis and processed by the Basque Biobank. Leuko-reduced PRP and fresh frozen plasma (FFP) were generated using the REVEOS Automated Blood Processing System (TERUMO BCT, Japan). PRP samples were diluted 1:5 in FFP to standardize platelet counts. Due to limited blood availability at the Basque Blood Biobank, platelet donors were not matched with FFP donors. Supernatants were prepared by adding 10% $CaCl_2$, incubating at 37°C for 1 h, then centrifuging, filtering, aliquoting, and storing at −80°C.

2.2. Preparation of functionalized GelMA

To prepare the GelMA stock solution, sterile lyophilized GelMA (CellInk PhotoGel® 50% DS; CellInk, Sweden) was combined with sterile-filtered Dulbecco's Modified Eagle Medium/Nutrient Mixture F12 (DMEM-F12; ThermoFisher Scientific Inc., USA), supplemented with 0.5% (w/v) lithium phenyl-2,4,6-trimethylbenzoylphosphinate (LAP) to achieve a final concentration of 10%. The solution was kept at 37°C overnight, with gentle agitation and protection from light, allowing it to fully dissolve without trapping air bubbles. Once completely dissolved, the GelMA stock was stored in the dark at 4°C and used within 1 month.

For bioink preparation, the GelMA stock was heated in a culture oven at 37°C for at least 30 min until liquefied. It was then diluted to a 5% final concentration by mixing equal volumes of either preheated DMEM-F12 or the extruded supernatant from PRP clots, all kept at 37°C.[19]

2.3. Bioprinting of MSC biocarriers

Biocarriers were fabricated using a CellInk BioX bioprinter (CellInk, Sweden). To prepare the bioink, 10% GelMA stock was mixed with the appropriate supplement (DMEM or PRP-derived secretome) and a cell concentrate (3×10^6 MSCs/mL) in a 50:40:10 ratio. All components were pre-warmed to 37°C before mixing. The prepared bioinks were then loaded into 3 mL pneumatic syringes and briefly placed in a freezer for 2 min to accelerate gelation and prevent cell precipitation. After gelation, the syringes were transferred to a bioprinter head maintained at 22°C for at least 5 min to ensure uniform temperature throughout the cartridge. The BioX printer was operated under the following conditions: an extrusion pressure of 30–50 kPa, a 20G plastic conical tip, a cartridge maintained at 22°C, a pre-flow of −300 ms, a head movement speed of 5 mm/s, and a bed temperature of 10°C. Following bioprinting, each structure was photocured using the BioX 405 photocuring module at 100% power, 4 cm height, for 60 s.

2.4. MSC viability within bioprinted biocarriers

The viability of MSCs was assessed using the CyQUANT TN XTT Cell Viability Assay (Invitrogen, Thermo Fisher, USA). GelMA bioinks mixed with an MSC suspension were photocrosslinked and incubated. After adding the XTT working solution and further incubation, absorbances at 660 and 450 nm were measured to calculate the specific absorbance. Experiments were conducted in triplicate.

2.5. *In vitro* evaluation of biocarrier biology with/without inflammation

The GelMA biocarriers enriched with PRP or FFP and loaded with BMSCs were evaluated in non-inflamed and inflamed environments (50 ng/mL IL-1β or 50 ng/mL TNF-α). The conditioned medium was collected after 96 h and centrifuged, and the supernatants were stored at −80°C for further analysis.

2.6. Antibody-based protein arrays

Protein release from BMSCs in various hydrogel formulations was evaluated using the Human Cytokine Array Q1000 Kit (126QAH-CAA-1000-1; RayBiotech Inc., USA). Array experiments were conducted as per the manufacturer's instructions, with results quantified relative to positive controls. Plasma samples from six donors were pooled to address biological variability.

2.7. Bioinformatic analyses

2.7.1. STRING database

We used the STRING database (version 11.5; string-db.org, accessed on February 2024) to explore known protein interactions and enriched biological functions. Proteins overexpressed more than two-fold in PRP biocarriers compared to nude biocarriers were selected, with a high edge confidence of 0.9. Figure 1A and B illustrates robust networks with edges representing physical and functional associations, excluding disconnected nodes. The main network was clustered into four groups using *k*-means. Enriched functions are presented against –LOG10 (FDR), where FDR represents the false discovery rate.

2.7.2. Ingenuity pathway analysis

Proteins secreted by MSCs were categorized based on Gene Ontology (GO) functions. We compared PRP biocarriers

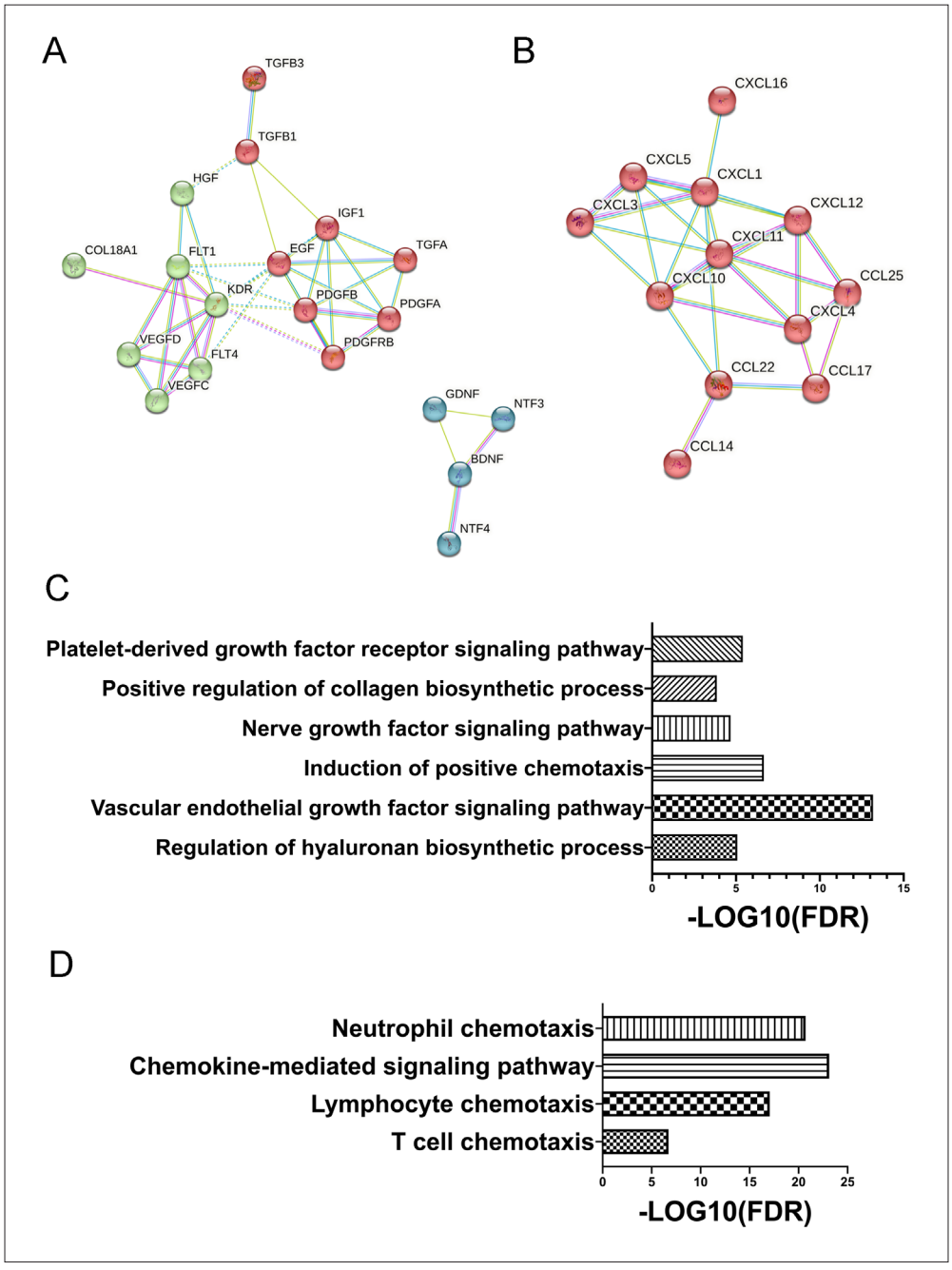

Figure 1. Protein–protein interactions and biological functions of growth factors and chemokines used in PRP biocarrier functionalization. (A) Key growth factors (GFs) and cytokines used for biocarrier functionalization using platelet-rich plasma (PRP), highlighting protein–protein interactions and three molecular clusters. (B) Principal chemokines utilized to dope the PRP biocarrier and their interactions. (C) Enriched biological processes involving molecules described in (A). (D) Main biological functions associated with the chemokine cluster. False Discovery Rate (FDR) indicates the significance of biological enrichment, with *p*-values corrected for multiple testing using the Benjamini–Hochberg procedure.

and inflamed PRP biocarriers against nude biocarriers or inflamed nude biocarriers, calculating fold changes in protein expression.

Data from the multiplexing platform were analyzed using Ingenuity Pathway Analysis Software (IPA®; QIAGEN Inc., https://digitalinsights.qiagen.com/IPA, accessed on May 2024; Qiagen, Germany), which incorporates nearly 5 million curated findings from experimental settings and third-party databases. IPA® algorithms predicted signaling pathways and canonical pathways, with the core analysis

module identifying pathway activation or inhibition based on the *Z*-score algorithm. The comparison analysis module was used to compare different experimental conditions

2.8. Matrigel assays

Angiogenesis assays were performed using a 15-well chambered coverslip with Matrigel (356231; Corning, USA). Human umbilical vein endothelial cells (HUVECs) were added to the Matrigel bed, and conditioned media from cell-loaded biocarriers was added. Cells were stained with CellMask™ Plasma Membrane Green Stain (C37608; Thermo Fisher, USA) and counterstained with Hoechst 33342 (PureBlu™ Nuclear Staining Dye; BioRad, USA). A Zeiss microscope (Axio Observer.Z1 Apotome 2.0, Axiocam 503M camera, Plan Neofluor 20×, 40×; Zeiss, Germany) was used for capturing live cell fluorescence images. Angiogenesis was evaluated using AngioTool software.

2.9. Statistical analysis

Differences in the distribution of *Z*-scores among biocarriers were compared using the Kruskal–Wallis test, followed by the Bonferroni adjustment. The data were analyzed using the statistical program SPSS (version 18.0; IBM Corp., USA)

3. Results

3.1. Characteristics of the plasma products used for biocarrier functionalization

The soluble blood-derived product was obtained by coagulating PRP, which contained twice the platelet concentration of peripheral blood. Additionally, for experimental validation, we prepared a soluble blood-derived product by coagulating plasma with a platelet count three times lower than that of peripheral blood, named FFP. PRP, the primary tested product, had a platelet concentration of 400,000 platelets/μL (twice that of peripheral blood), while the platelet-poor plasma (FFP) had a platelet concentration of 65,000 platelets/μL. In the identification of key signaling proteins within the primary tested PRP, we classified 130 proteins that were at least two times more concentrated in serum-converted PRP compared to serum-converted FFP. Employing STRING to unravel protein–protein interactions (with a minimum required interaction score of the highest confidence level at 0.9) and functions, Markov Cluster Algorithm (MCL) clustering methodology revealed distinct clusters of functional proteins.

As displayed in Figure 1, we identified two main groups: (i) GFs, including neurotrophins (Figure 1A); and (ii) a molecular cluster of chemokines (Figure 1B), particularly involved in leukocyte chemotaxis (Figure 1D). The GF cluster primarily (but not exclusively) engages in PDGF, VEGF, and NGF signaling pathways. Additionally, these factors participate in regulating collagen and hyaluronan biosynthetic processes (Figure 1C).

3.2. BMSC viability and adhesion within biocarriers

We aimed to evaluate the effect of biocarriers on the viability of BMSCs (Figure 2). We conducted live/dead assays on bioprinted constructs after 96 h in culture (Figure 2A). Fluorescence microscopy of live cells revealed that GelMa-based hydrogels are cytocompatible, indicated by the high proportion of live cells after 96 h in culture. Doping the biocarriers with sera (FFP and PRP) consistently improved viability and proliferation rates, as evidenced by direct counts on the whole geometry of the hydrogels after bioprinting (Figure 2B). Additionally, cell morphology in the serum-doped hydrogels qualitatively displayed a more vital cell phenotype and increased cell-to-cell contact (Figure 2A).

The sera also promoted cell metabolism, as evidenced by absorbance readings in XTT-type proliferation assays (Figure 2C), exhibiting approximately twice the intensity compared to bare hydrogels. More importantly, comparing the readings at 24 and 96 h reveals higher readings at 96 h in the presence of sera. In their absence, cell metabolism tends to decrease over time, suggesting hibernation of cells in bare hydrogels. Additionally, IL-1β-mediated inflammation did not alter proliferation rates. Overall, these findings indicate that blood products, both FFP and PRP, enhance the proliferation and viability of BMSCs within hydrogels.

Bioinformatic analysis of the secretome of cells cultured in biocarriers doped with hemoderivatives (Table 1) provides further depth to the previous results. The predictions made by IPA® revealed that hemoderivatives promote signaling pathways involved in cell survival and viability and inhibit those related to necrotic and apoptotic events. Notably, these stimulatory effects are maintained in the secretome regardless of whether the culture was performed under inflammatory conditions (IL-1β).

To further investigate cell adhesion in the different hydrogel types, we seeded cells directly onto acellular hydrogels. Figure 3 displays representative fields of BMSCs cultured on these hydrogels. After 96 h, the cells exhibit uniform growth on the hydrogels under both normal (control) and inflammatory (IL-1β) conditions. However, there are minor qualitative differences between the three types of hydrogels. Without serum in the formulation, cells tend to grow without agglomeration or strong interactions. In contrast, hydrogels doped with hemoderivatives display the formation of nodules connected by large bridging cells,

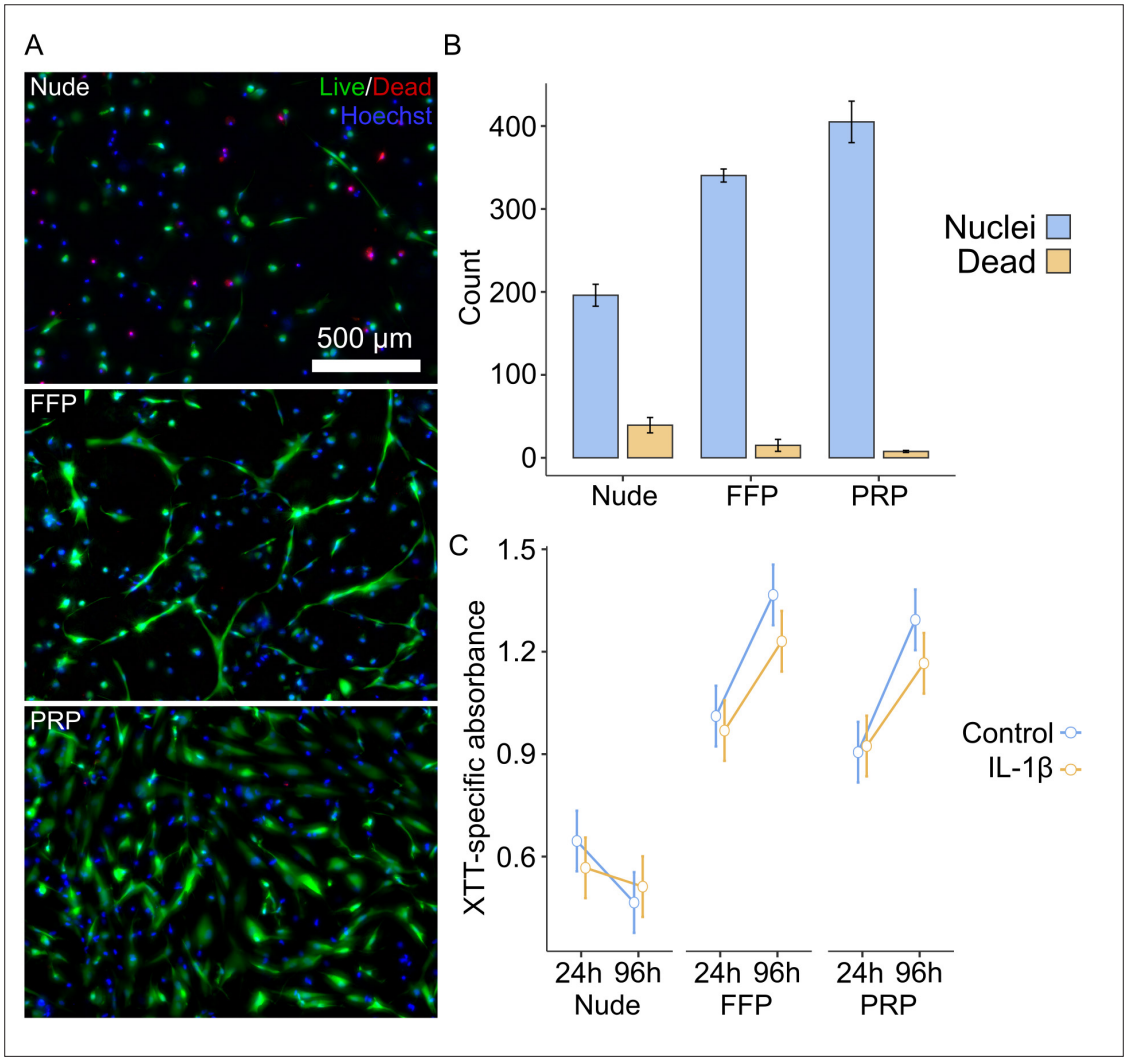

Figure 2. Morphology and viability of bone marrow-derived mesenchymal stem cells (BMSCs) cultured in biocarriers for 96 h. (A) Z-stacks of live/dead-type microscopy images, with cells counterstained with Hoechst 33342. (B) Total nuclei and dead cell count in random fields of live/dead microscopy images are shown for the three hydrogels after 96 h of culture. (C) XTT-specific absorbance readings of BMSCs cultured in biocarriers at 24 and 96 h under normal or pro-inflammatory (IL-1β) conditions. Scale bar: 500 µm. Abbreviations: FFP, fresh frozen plasma; PRP, platelet-rich plasma.

Table 1. Z-scores and *p*-values of non-inflamed and IL-1β-inflamed biocarriers obtained from Ingenuity Pathway Analysis Software (IPA®) predictions for different relevant biological settings

Function	Plasma-infused biocarriers	Z-score (*p*-value)	
		Non-inflamed	IL-1β-inflamed
Cell survival	PRP-biocarrier	4.439 (3.58E-71)	3.854 (2.13E-69)
	FFP-biocarrier	4.315 (3.58E-71)	3.556 (2.13E-69)
Cell viability	PRP-biocarrier	4.545 (7.50E-70)	4.108 (5.43E-68)
	FFP-biocarrier	4.613 (7.50E-70)	3.821 (5.43E-68)
Necrosis	PRP-biocarrier	−0.319 (9.02E-90)	0.091 (1.55E-89)
	FFP-biocarrier	−0.547 (9.02E-90)	−0.893 (1.55E-89)
Apoptosis	PRP-biocarrier	−1.960 (5.37E-81)	−1.979 (5.71E-81)
	FFP-biocarrier	−2.814 (5.37E-81)	−2.445 (5.71E-81)

Abbreviations: FFP, fresh frozen plasma; PRP, platelet-rich plasma.

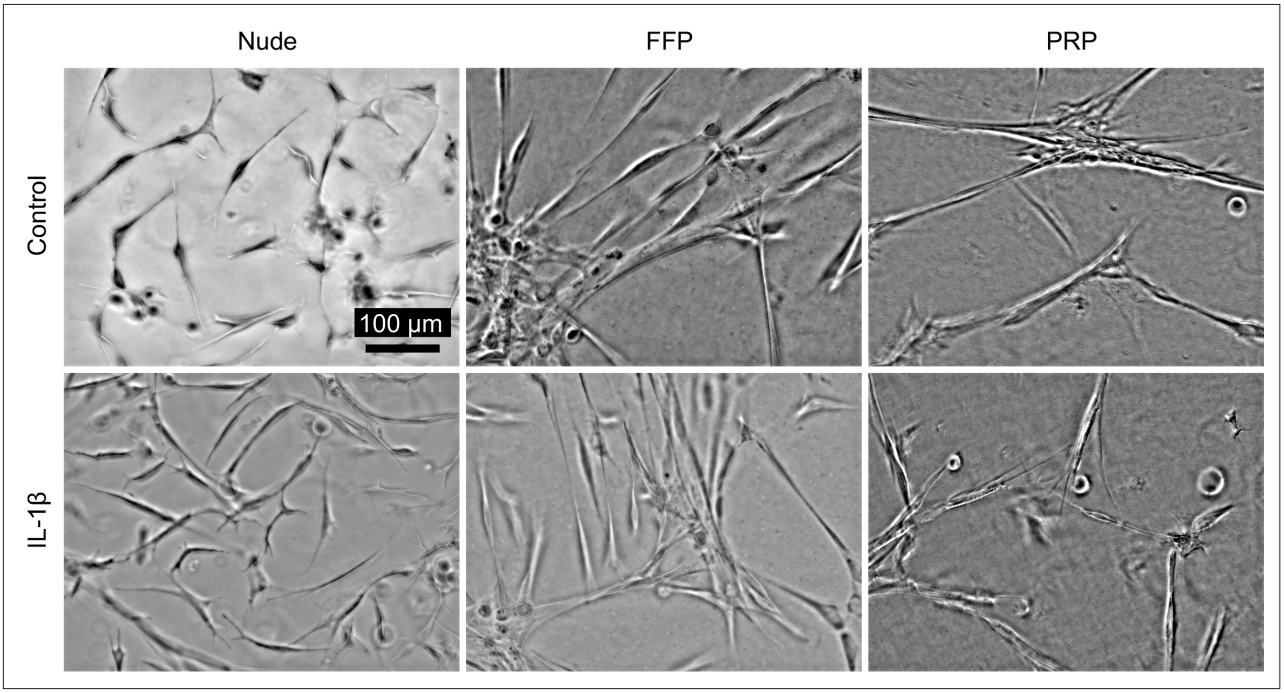

Figure 3. Differential interference contrast micrographs of bone marrow-derived mesenchymal stem cells (BMSCs) seeded on nude or biocarrier-doped (fresh frozen [FFP] or platelet-rich plasma [PRP]) hydrogels for 96 h. As observed, cells grow randomly on the bare gels. In contrast, they tend to aggregate and orient between clusters in the presence of biocarriers. No qualitative differences in adhesion were observed between normal and inflammatory (IL-1β) culture conditions. Scale bar: 100 µm.

and the surface area occupied by each cell appears larger compared to bare hydrogels. IL-1β-mediated inflammation does not significantly affect cell adhesion properties.

3.3. Functionality of plasma-infused biocarriers

To gain deeper insights into which inflammatory pathways could be favored when implanting these biocarriers in a non-inflamed environment, we analyzed the quantitative proteomes secreted by the two biocarriers with different platelet concentrations, normalizing them against nude biocarriers. In the absence of inflammation, there were no differences between BMSCs encapsulated in either PRP or FFP ($p = 0.550$). However, both plasmas modified cell behavior compared to BMSCs encapsulated in nude GelMA and exposed to inflammation ($p = 0.001$).

The association of PRP with BMSCs can be described as a buffered system, activating both inflammatory and anti-inflammatory pathways (Figure 4A). The inflammatory pathways include alarmin signaling (S100 and HMGB1), neuroinflammation, leukocyte extravasation, Toll-like receptor cascades, and NF-kB signaling. The anti-inflammatory pathways involve IL-4 and IL-13 signaling, which promote the "alternative activation" of macrophages, inducing an anti-inflammatory phenotype via IL4R alpha and STAT6-dependent signaling (Reactome, 10.3180/R-HSA-6785807.1). Additionally, IL-10, a pleiotropic cytokine crucial for modulating inflammation and maintaining cell homeostasis, is activated.

Both PRP- and FFP-infused biocarriers activate 10 significant canonical pathways, including HIF-1a signaling, neuroinflammation, IL-8, IL-33, S100 signaling, toll-like receptor cascades, and two pathways related to extracellular matrix (ECM) turnover, including collagen fibril assembly and ECM degradation. Differentially activated pathways in PRP-infused biocarriers included IL-17, IL-6 family signaling, IL-10, IL-4, and IL-13 signaling, leukocyte extravasation, and macrophage classical activation. Additionally, differential activation of GF signaling was observed in PRP-infused but not in FFP-infused biocarriers, including TGF-β1, VEGF, PDGF, EGFR, neurotrophin/TRK, and BMP signaling (Figure 4).

3.4. Behavior of biocarriers in inflammatory environments

To gain a deeper understanding of how these biocarriers function when placed in an inflammatory setting, we subjected the biocarriers to IL-1β exposure for 96 h *in vitro*. Using IPA®, we scrutinized the secreted proteomes across all conditions, normalizing them against secretomes without any infused plasma (nude biocarriers).

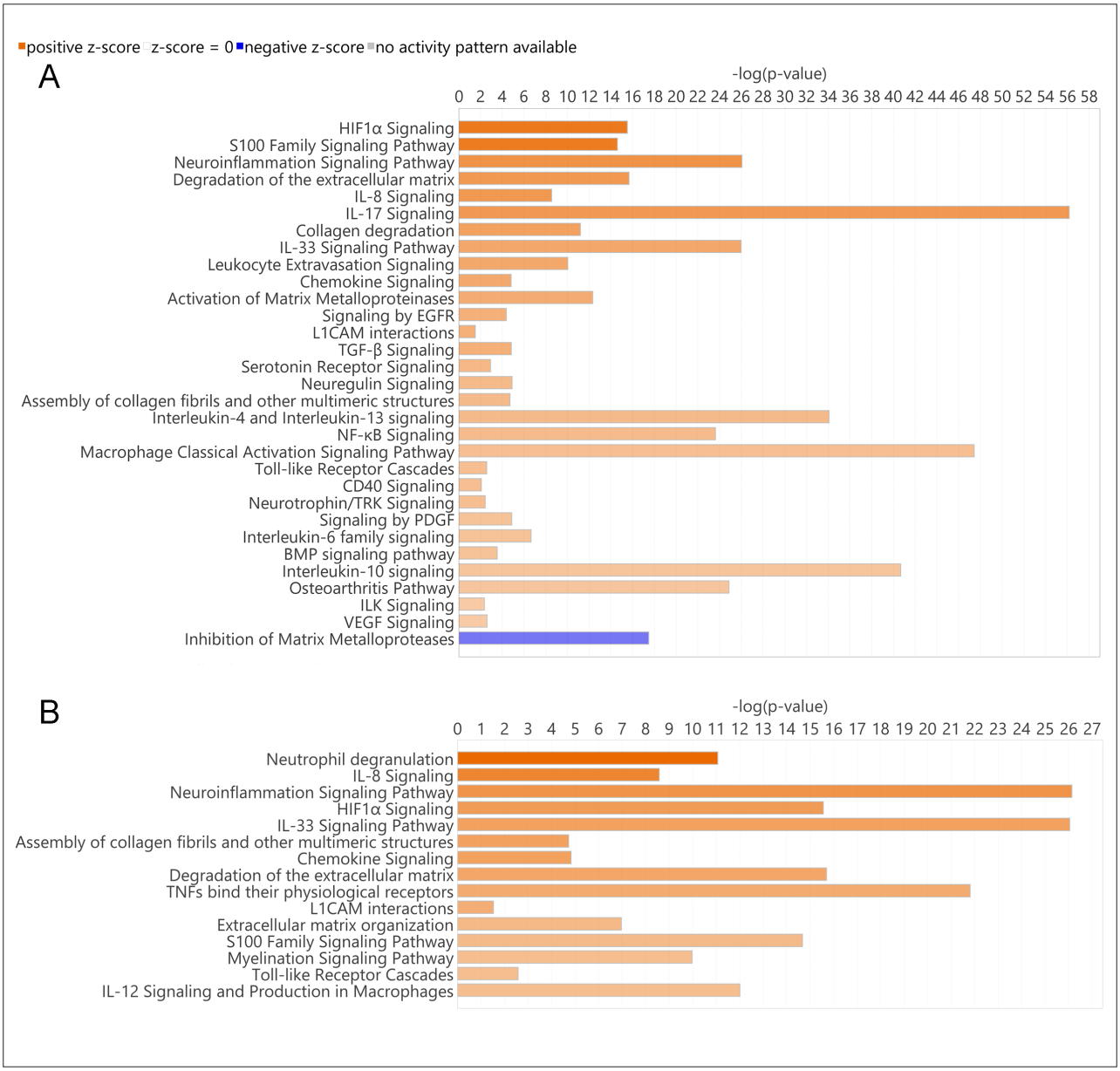

Figure 4. Canonical pathways significantly activated by the secretome (Z-score > 2) of PRP- (A) and FFP-infused biocarriers (B). Abbreviations: FFP, fresh frozen plasma; PRP, platelet-rich plasma.

3.4.1. Paracrine angiogenic activities of BMSCs under inflammatory conditions

Using IPA®, we predicted and identified differences in angiogenesis between groups. Table 2 presents *Z*-scores for angiogenesis across all experimental conditions. A Kruskal–Wallis test, followed by Bonferroni adjustment, revealed no significant differences in angiogenesis *Z*-scores concerning platelet dose ($p = 0.079$).

However, significant differences were noted in the angiogenic behavior of cells within scaffolds infused with any type of plasma compared to those encapsulated solely in GelMA ($p < 0.001$ for PRP biocarriers; $p = 0.002$ for FFP biocarriers).

3.4.2. Matrigel assays

To examine how inflammation, i.e., IL-1β exposure, influenced angiogenesis, we performed Matrigel assays to examine the impact of the secretome released from PRP biocarriers on the angiogenic potential of HUVECs after exposure to conditioned media collected under inflammatory conditions (IL-1β, 50 ng/mL).

Table 2. *Z*-scores of common diseases and biofunctions for each experimental condition in an inflammatory environment (IL-1β)

Disease/biofunction	Z-score		
	GelMA	PRP	FFP
Activation of endothelial cells	0.749	5.562	1.122
Adhesion of endothelial cells	0.045	5.446	2.339
Angiogenesis	−0.836	4.542	2.587
Cell movement of endothelial cells	−0.031	3.939	4.295
Growth of vessel	1.192	2.818	2.023
Migration of endothelial cells	−0.395	2.557	3.793
Migration of vascular cells	−0.541	2.466	1.491
Migration of vascular endothelial cells	−1.505	2.466	1.46
Proliferation of vascular cells	0.102	2.252	2.105
Proliferation of vascular smooth muscle cells	2.488	2.244	2.216
Tubulation of endothelial cells	0.676	2.049	2.389
Tubulation of vascular endothelial cells	0.719	2.044	2.042
Adhesion of vascular endothelial cells	0.071	4.676	1.66

Abbreviations: FFP, fresh frozen plasma; GelMA, gelatin methacryloyl; PRP, platelet-rich plasma.

Figure 5 depicts differences in junction density (junction/mm^2) for each experimental condition: cellular nude-biocarriers, cellular FFP-biocarriers, and cellular PRP-biocarriers. Although not conclusive, HUVECs exposed to media conditioned by FFP-infused carriers treated with IL-1β displayed a higher number of junctions between skeletal branches, indicating a stronger induction of angiogenesis.

3.5. Comparative analyses of plasma-infused biocarriers exposed to TNF-α versus IL-1β environment

To evaluate the effects of different inflammatory cytokines in the milieu, we generated heat maps based on proteomic analyses of the biocarriers' paracrine functions, using a *p*-value cutoff of 1.3 LOG10. We categorized the canonical pathways into two groups: one related to inflammation modulation (chemokine signaling) and neuroinflammation (Figure 6A and B), and the other associated with GF signaling and ECM turnover (Figure 7), both under TNF-α or IL-1β exposure.

Protein analysis of the secretomes from all BMSC biocarriers subjected to inflammatory environments (TNF-α or IL-1β) displayed clustering based on their compositions. BMSCs within nude GelMA biocarriers clustered together under either IL-1β or TNF-α exposure. In contrast, plasma-infused biocarriers showed distinct clustering patterns when exposed to IL-1β or TNF-α, regardless of plasma composition (i.e., B3 vs. B4 and B5 vs. B6). Plasma-infused biocarriers altered cell behavior in response to IL-1β or TNF-α compared to BMSCs in nude GelMA ($p = 0.001$). Furthermore, in plasma-infused biocarriers, we observed a significant difference in BMSC behavior when exposed to IL-1β compared to TNF-α ($p = 0.050$).

Regarding plasma composition, cells within PRP or FFP biocarriers exhibited a similar inflammatory phenotype ($p = 0.874$), characterized by three distinct clusters of canonical pathways. The first cluster highlights differences in four interleukin signaling pathways: IL-27, IL-20, IL-10, and IL 1. The second cluster features differences in "Macrophage Classical Activation Signaling Pathways" along with alarmin signaling (S100 and HMGB1), IL-8, and IL-33, among others. The third cluster indicates differences in "Macrophage Alternative Activation Signaling Pathways," including NF-kB, Th1 and Th2 pathways, and the TNFR2 non-canonical NF-kB pathway.

Several canonical pathways regulating the response to both stress and pain were predicted to be differentially activated or inhibited among biocarriers. These pathways included neuroinflammation, neurotransmitter signaling (adrenergic and serotoninergic), and neurotrophin/TRK signaling (Figure 6B).

Regarding GF signaling/ECM turnover (Figure 7), BMSC-nude biocarriers displayed no discrepancies in response to TNF-α or IL-1β exposure. Both FFP and PRP biocarriers differed from nude biocarriers in IL-1β exposure, with *p*-values of 0.001 and <0.001, respectively. Comparative analyses reveal differences related to the

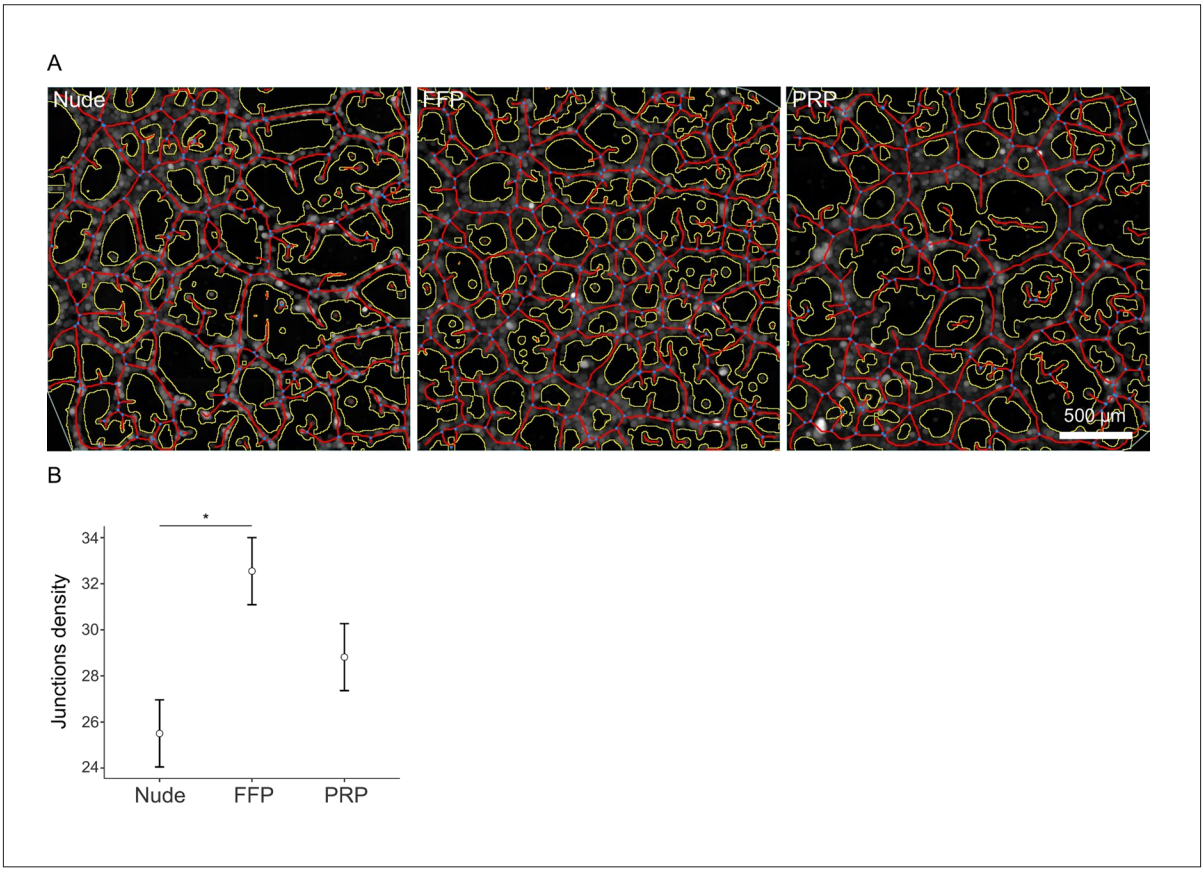

Figure 5. Evaluation of angiogenesis by human umbilical vein endothelial cell (HUVEC) tube formation assay. (A) Images of the network of vessels (red) formed by HUVECs when grown on a Matrigel bed and exposed to medium conditioned by the three bone marrow-derived mesenchymal stem cell (BMSC)-loaded biocarriers (nude, fresh frozen plasma [FFP]-infused, and platelet-rich plasma [PRP]-infused) cultured under pro-inflammatory conditions. The junctions between the skeletal branches are illustrated in blue. (B) The graph illustrates the density of junctions (blue dots in [A]) per mm^2 detected in HUVEC vessel networks; * $p = 0.042$; $n = 3$.

signaling of various GFs and ECM degradation/remodeling. The results indicated by the upper dendrogram distribute the samples according to (i) the different types of biocarrier (nude vs. plasma-infused), and (ii) the inflammatory molecule added (IL-1β or TNF-α).

Notably, the type of inflammatory molecule in the microenvironment influences TGF-β signaling. When IL-1β is present, PRP-infused biocarriers activated TGF-β signaling, encompassing 51 molecules ($Z = 2.308$; $p = 1.02E-35$), with 27 of the 51 proteins exhibiting a measurement direction consistent with TGF-β1 activation. Conversely, TNF-α did not trigger activation of the TGF-β signaling pathway.

Based on bioinformatic results, we hypothesize that TGF-β may drive interactions between PRP-infused biocarriers and the environment post-transplantation, distinguishing them from FFP-infused biocarriers. Figure 8 illustrates the predicted TGF-β1 network with BMSCs in PRP-infused biocarriers.

4. Discussion

Leveraging the complementary aspects of emerging medical technologies suitable for bioink formulation, including MSCs and PRP therapies, is crucial for advancing bioprinting and addressing health challenges like MSK disorders.[20–22] In this context, it is crucial to advance bioink formulations and translational strategies for medical applications simultaneously; in particular, extrusion-based bioprinters can be easily integrated with minimally invasive surgical tools,[23–25] allowing for *in situ* delivery of biocarriers tailored to specific medical conditions.

Bioprinting technology was employed in this study to achieve precise cell and blood-derived material placement within the GelMA biocarriers, ensuring consistent distribution and reproducibility, which is difficult to obtain

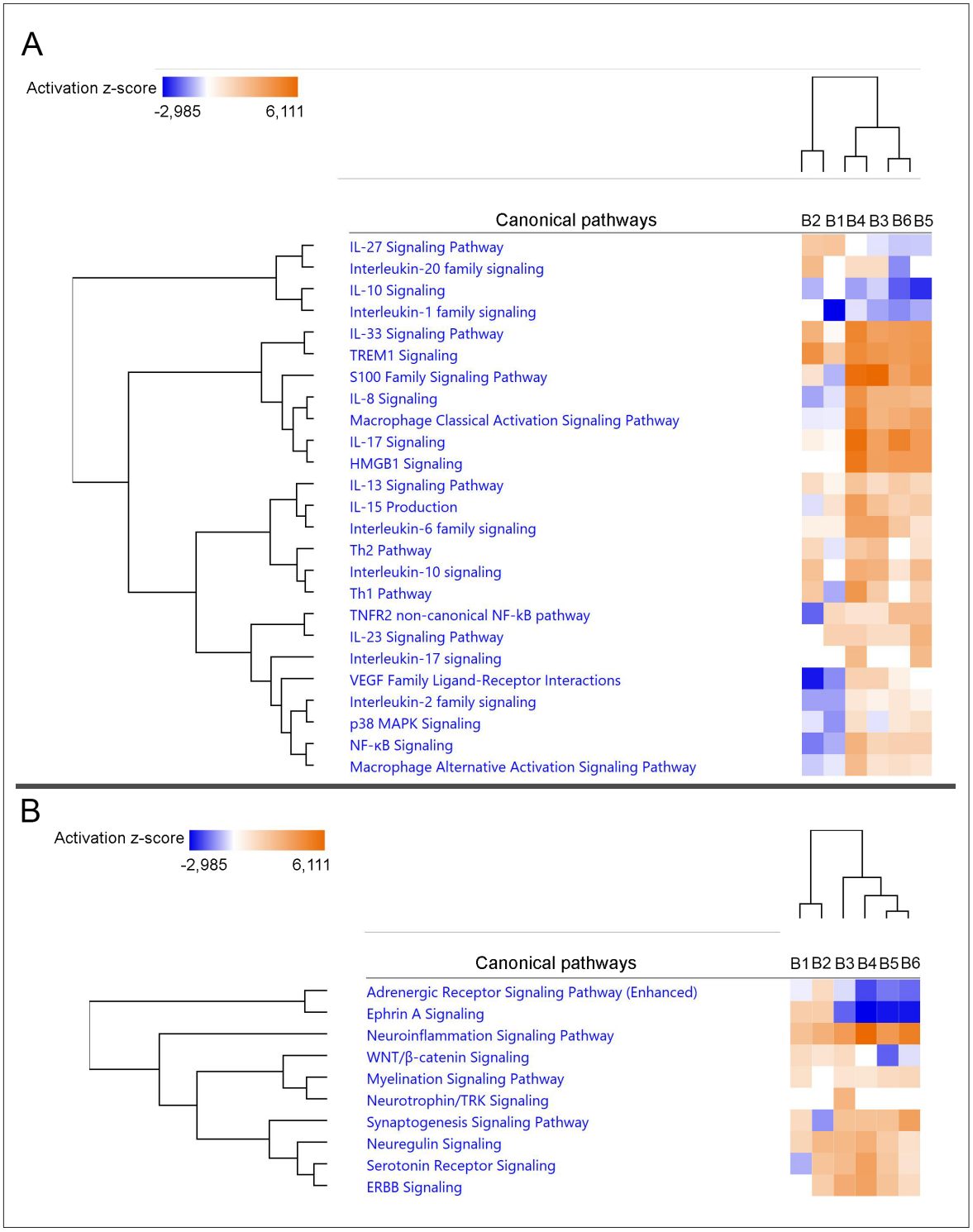

Figure 6. Heat maps comparing the bone marrow-derived mesenchymal stem cell (BMSC) secretome in the presence of IL-1β versus TNF-α. (A) Canonical pathways associated with inflammation. (B) Canonical pathways associated with nervous system signaling and pain. The dendrograms at the top of the heatmap illustrate biocarrier clustering based on their differing compositions (i.e., nude, fresh frozen plasma [FFP]-infused, or platelet-rich plasma [PRP]-infused) and the differences between exposure to either IL-1β or TNF-α. The dendrogram on the left displays three differentiated groups of canonical pathways activated by inflammatory cytokines. Abbreviations: B1, nude biocarrier exposed to TNF-α; B2, nude biocarrier exposed to IL-1β; B3, FFP-infused biocarrier exposed to IL-1β; B4, PRP-infused biocarrier exposed to IL-1β; B5, FFP-infused biocarrier exposed to TNF-α; B6, PRP-infused biocarrier exposed to TNF-α; FFP, fresh frozen plasma; PRP, platelet-rich plasma.

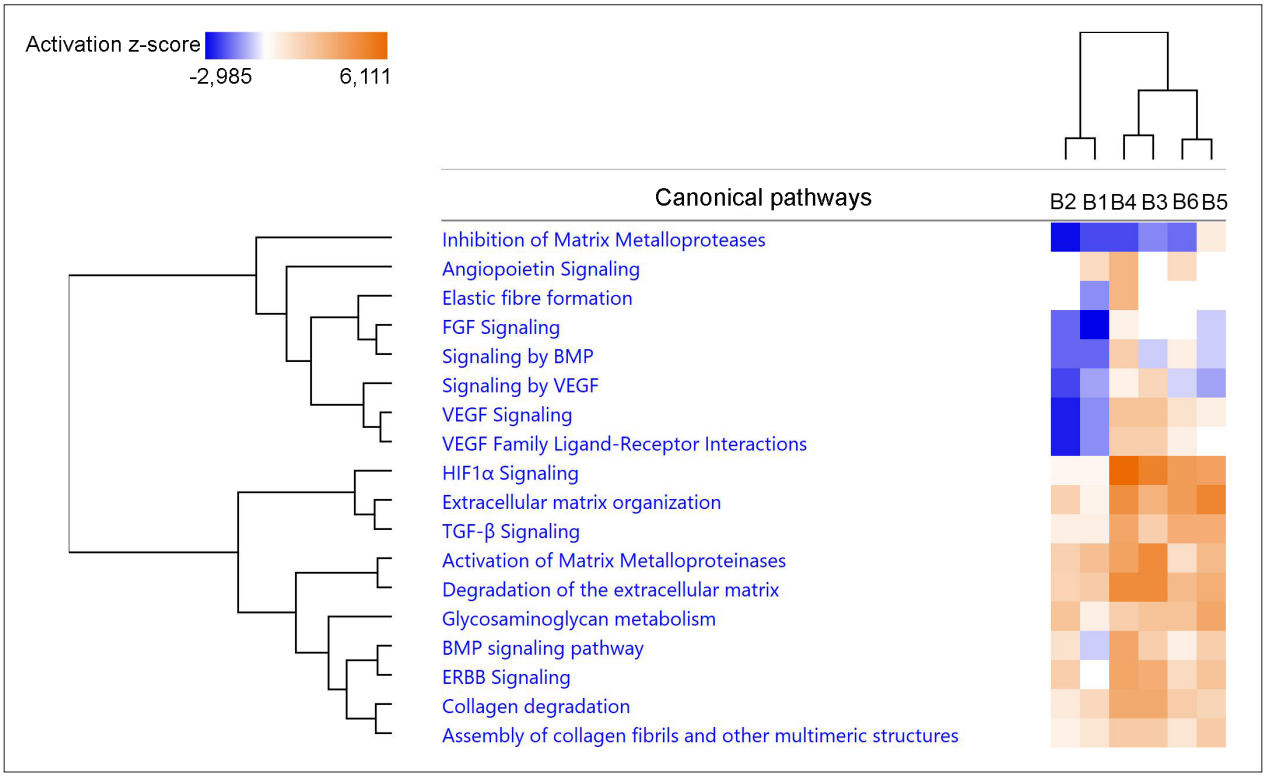

Figure 7. Representation of differential activation of canonical pathways related to signaling of different growth factors (GFs) and extracellular matrix degradation/remodeling. Abbreviations: B1, nude biocarrier exposed to TNF-α; B2, nude biocarrier exposed to IL-1β; B3, FFP-infused biocarrier exposed to IL-1β; B4, PRP-infused biocarrier exposed to IL-1β; B5, FFP-infused biocarrier exposed to TNF-α; B6, PRP-infused biocarrier exposed to TNF-α; FFP, fresh frozen plasma; PRP, platelet-rich plasma.

with traditional methods. Moreover, bioprinting facilitates scalability and customization of constructs, aligning with personalized medicine principles. Additionally, this technology optimizes cell–matrix interactions, crucial for improving cell viability, adhesion, and paracrine activity, thus enhancing the overall therapeutic efficacy of the biocarriers.

Blood-derived products, particularly PRP, should be considered a biological system rather than a drug. This distinction is important because the biological effects of PRP cannot be attributed to a single active ingredient, given the presence of hundreds of molecules within these biomaterials. By using pure PRP instead of L-PRP, we can conduct dosing experiments, as FFP (platelet-poor plasma) and PRP differ in the concentration of the molecular pool released by platelets.

The therapeutic potential of MSCs is well-recognized due to their trophic actions and ability to modulate inflammation in the environment in which they are implanted.[26,27] BMSCs are the most commonly used source in clinical applications.[28] In contrast, PRP has emerged as a promising infiltrative therapy for multiple clinical conditions across multiple medical fields.[29] The therapeutic potential of PRP is primarily attributed to the α-granules in platelets, which house essential signaling molecules for tissue repair, released during plasma coagulation.[30] By integrating BMSCs and PRP, we have manufactured a biocarrier, which releases a pool of proteins, including those derived from serum-converted PRP, as well as *de novo* synthesized proteins by the MSCs embedded within the hydrogel. In the clinics, the synergic combination of BMSCs and PRP is being researched for treating disc degeneration, and knee and hip osteoarthritis, among other MSK conditions.[31]

Research focused on the integration of bioprinting, cell therapies, and drug delivery has been recently reviewed.[32] To understand the potentiality of the biocarrier under investigation, the first challenge was to describe the complex pool of signaling proteins, followed by the biological processes triggered upon *in vivo* implantation. To address the former, we used arrays to quantify up to

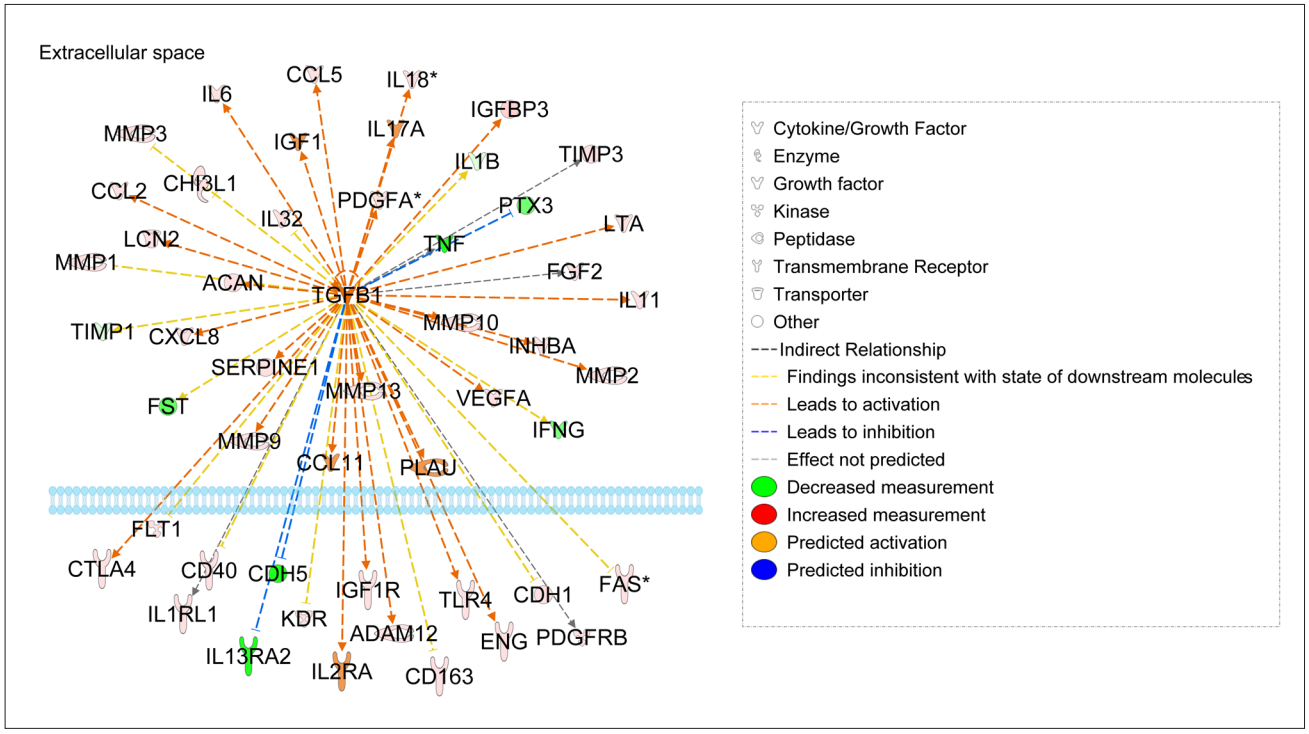

Figure 8. Predicted TGF-β1 network in platelet-rich plasma (PRP)-infused biocarriers. Lines depict molecular relationships, with details provided in the legend on the right. These lines indicate interactions where molecules bind or act upon one another. All molecular relationships are derived from scientific data in the IPA® knowledgebase.

430 proteins in the conditioned media obtained from the biocarrier cultured *in vitro* for 96 h, and we also applied bioinformatics to predict the activation of canonical pathways. Similarly, approaches using proteomic studies have helped characterize complex molecular matrices,[33] and the integration of bioinformatics has helped in predicting adipose derived mesenchymal stem cell (Ad-MSC) performance in the presence of PRP molecules, resulting in enhanced exosome secretion and upregulation of multiple proteins involved in tissue repair and immune regulation.[10]

As previously reported, plasma-infused GelMA is suitable for cell viability, survival, and supporting cell functions.[34–36] We demonstrated that PRP-infused GelMA provides optimal 3D conditions for BMSC proliferation, thus less cell density is required for optimal delivery, e.g., cell density is commonly 1×10^7 cells/mL[32] versus 3×10^6 cells/mL, thereby reducing the time of 2D expansion prior to bioprinting. Other studies have reported the advantages of 3D-GelMA for induced pluripotent stem cell (iPSC)-derived MSC proliferation when bioreactors are used concurrently.[37] Compared to monolayer cultures, 3D conditions and biomechanical stimulation can enhance MSC functionality.[38]

It is reported that GelMA serves as a scaffold for MSC adhesion and functions, while also acting as a biodegradable and immune-compatible vehicle for delivering cytokines and GFs.[35,39] These biocarriers enhance the bioactivity and therapeutic potential of encapsulated cells, promoting tissue regeneration and repair across various biomedical applications.[25,27] Other researchers have demonstrated the proof-of-concept by implanting GelMA/adipose stromal cell (ASC)/PRP into osteochondral defects in the patellar groove of rabbits' joints, resulting in higher histological, macroscopic, and mechanical scores, highlighting the synergistic effects of this combination.[39]

However, untangling the intricacies of tissue repair, which involves a myriad of molecules and multicellular cross-talks, demands advanced technologies to identify driver molecules, and establish plausible hypotheses. Our proteomic analysis of plasma biomaterials revealed two interconnected groups of proteins with significant roles in regenerative medicine. Given the higher expression levels of these molecules in PRP compared to FFP, we chose to dope the hydrogel with both blood derivatives to explore the primary functions of PRP. The first group comprised GFs and neurotrophins, while the second, less-studied

group consisted of chemokines. Chemokine profiling has been proposed to predict leukocyte recruitment and immunomodulatory mechanisms of BMSCs.[40] In addition, we demonstrated that serum-converted PRP provides additional chemokines to reinforce the actions of BMSCs. Thus, following biocarrier delivery and the establishment of chemokine gradients, we can anticipate the infiltration of both myeloid and lymphoid cells, thereby organizing the immune response.

The number of platelets in plasma preparations, i.e., platelet doses, is a debated topic in clinical PRP therapies. In our study, we employed two outdated allogeneic plasma products[41] obtained from our local blood bank. Firstly, PRP had a twofold increase in platelet concentration relative to peripheral blood; conversely, FFP had a significantly reduced platelet concentration (threefold below peripheral blood). Both variants were utilized for hydrogel doping and bioink formulations. Our data revealed differences between serum-converted PRP or FFP and their interactions with MSCs, thereby modifying the secretome of the biocarriers and providing a model to investigate the influence of platelet concentration. PRP biocarriers can activate canonical GF signaling pathways (TGF-β, PDGF, VEGF, EGFR, and BMP), whereas FFP-biocarriers do not significantly affect these mechanisms. Since GFs are primary components of platelet α-granules, these differences highlight the variability of plasma biomaterials.

A common line of research is improving the efficacy of MSC therapies by preconditioning them with pro-inflammatory mediators, also known as cell priming or licensing. Priming can be done with pro-inflammatory cytokines, such as IFN-γ and IL-17.[42] Other methods include priming with hypoxia, biomaterials, or 3D culture systems. As demonstrated here, PRP-converted serum contains inflammatory cytokines that could prime BMSCs alongside the hypoxic conditions in our 3D culture model.

In cell transplantation, the aim of carriers is to mitigate environmental fluctuations in host tissues that could diminish cell survival and therapeutic efficacy.[43] The most common carriers include alginate, hyaluronan, chitosan, and gelatin-based hydrogels. We selected gelatin as the vehicle due to its immunocompatibility and biodegradability (non-toxic degradation by-products).[44] Additionally, gelatin is thermosensitive, printable at various concentrations, and allows chemical modification with methacrylate groups for UV-crosslinking after extrusion. In our biocarriers, GelMA encapsulates BMSCs and plasma secretomes, placing interleukins, chemokines, and GFs in close contact with BMSCs. To investigate how these carriers behave in a harsh environment, we exposed them to IL-1β or TNF-α, which are commonly present in MSK conditions. Principal component analyses grouped nude carriers and plasma-licensed carriers into separate categories. Additionally, carriers activate various interleukin signaling pathways differently, highlighting key interactions between adaptive and immune cells.

A similar pattern of carrier grouping was observed when comparing canonical pathways related to neuroinflammation and pain signaling. Notably, FFP carriers exposed to IL-1β differed from other plasma carriers exposed to IL-1β or TNF-α, with the main differentially activated pathway being neurotrophin/TRK signaling. In the context of GF signaling, canonical pathways were clustered into two main groups: one associated with angiogenesis and the other with ECM turnover. These comparative analyses generate further hypotheses to establish tailored tissue delivery for optimal therapeutic benefits.

A significant achievement of bioinformatics analyses is the creation of theoretical frameworks and well-supported hypotheses. Our thorough analysis of biocarriers' proteomes led us to hypothesize that TGF-β1 could be a crucial component in plasma biomaterials, greatly affecting BMSC activation. However, additional research is necessary to elucidate the molecular mechanisms through which TGF-β1 facilitates tissue repair.

This study has several limitations. Firstly, we utilized a commercial GelMA (CellInk) but did not report its rheological properties. Another limitation is the absence of detailed spectral analysis, including X-ray diffraction (XRD), nuclear magnetic resonance (NMR), and Fourier transform infrared (FTIR) spectra, for both the initial and final materials. While the core findings remain robust, the inclusion of these spectra would have facilitated a more comprehensive understanding and comparison of the compositional changes during material processing. Future studies should aim to incorporate these analyses to provide a deeper insight into the structural and chemical transformations involved.

Our bioprinted carriers were intended to enhance the paracrine effects of BMSCs rather than support cell differentiation, leading us to maintain the constructs in cell media without supplements. The preliminary study involved short cell culture times (96 h), but considering the constructs' interaction with immune cells, *in vivo* experiments to evaluate inflammatory cell infiltration and angiogenic capabilities are crucial for advancing these biocarriers toward clinical use. Another limitation of this study is the lack of experimental validation of MSC differentiation, particularly osteogenesis, which would strengthen the bioinformatics findings.

Furthermore, functionalizing hydrogels with molecular pools adds complexity to preclinical studies, making omics and bioinformatics essential for understanding the biological processes they affect. *In vitro* evaluations face challenges such as reduced model complexity, the lack of immune or inflammatory responses, and the inability to replicate complex post-implantation events.

5. Conclusion

The study demonstrates that both PRP and FFP effectively enhance the proliferation and viability of BMSCs within the GelMA biocarrier. In non-inflammatory conditions, no significant differences in BMSC behavior were observed between PRP and FFP (p = 0.550). However, under inflammatory conditions, both plasma types significantly altered cell behavior (p = 0.001). PRP and FFP both activated 10 key signaling pathways, including those related to cell survival, neuroinflammation, and ECM turnover. PRP uniquely activated additional pathways, such as IL-17, IL-6, and several GF signaling pathways.

Both plasma types significantly promoted angiogenesis compared to the GelMA control ($p < 0.001$ for PRP; p = 0.002 for FFP), with FFP exhibiting a particularly strong effect under IL-1β treatment (p = 0.042). PRP specifically activated TGF-β signaling in response to IL-1β (Z = 2.308; p = 1.02E-35), but a response was not observed with TNF-α exposure.

These findings underscore the potential of plasma-infused biocarriers in enhancing therapeutic efficacy, particularly in inflammatory environments, with PRP offering specific advantages in modulating certain inflammatory responses.

Acknowledgments

The authors would like to thank Javier Diez-Garcia and Maria Dolores Garcia-Vazquez from Microscopy and Cell Culture Facilities at the Biobizkaia Health Research Institute, Spain.

Funding

This work was supported by a collaborative fundamental research grant from the Basque Government, Elkartek Program (grant no. BIO4CURE kk-2022-000). Cristina Del Amo and Inés Jaúregui are funded by PT20/00185 from ISCIII, and Miguel Perez-Garrastachu is funded by the post-doctoral fellowship Margarita Salas.

Conflict of interest

The authors declare they have no competing interests.

Author contributions

Conceptualization: Cristina Del Amo, Isabel Andia, Miguel Perez Garrastachu
Formal analysis: Cristina del Amo, Ines Jaúregui, Isabel Andia
Investigation: Miguel Perez Garrastachu, Cristina Del Amo
Methodology: Miguel Perez Garrastachu, Cristina Del Amo
Writing – original draft: Isabel Andia, Cristina Del Amo
Writing – review & editing: Isabel Andia, Cristina Del Amo, Francisco J. Alvarez, Miguel Perez Gasrrastachu
Funding Acquisition: Francisco J. Alvarez, Isabel Andia

Ethics approval and consent to participate

This study was conducted according to the guidelines of the Declaration of Helsinki and approved by the Institutional Review Board of Galdakao Hospital, Bizkaia, Spain (CEIC no. CES-BIOEF 201907). Informed consent was obtained from all subjects involved in this study.

Consent for publication

Not applicable.

Availability of data

The data presented in this study are available on request from the corresponding author.

References

1. Chen N, Fong DYT, Wong JYH. Health and economic outcomes associated with musculoskeletal disorders attributable to high body mass index in 192 countries and territories in 2019. *JAMA Netw Open.* 2023;6:E2250674. doi: 10.1001/jamanetworkopen.2022.50674

2. Ferrari AJ, Santomauro DF, Aali A, et al. Global incidence, prevalence, years lived with disability (YLDs), disability-adjusted life-years (DALYs), and healthy life expectancy (HALE) for 371 diseases and injuries in 204 countries and territories and 811 subnational locations, 1990-2021: a systematic analysis for the Global Burden of Disease Study 2021. *Lancet.* 2024;403(10440):2133-2161. doi: 10.1016/S0140-6736(24)00757-8

3. Skou ST, Poulsen E, Bricca A, et al. Benefits and harms of interventions with surgery compared to interventions without surgery for musculoskeletal conditions: a systematic review with meta-analysis. *J Orthop Sports Phys Ther.* 2022;52:312-344. doi: 10.2519/jospt.2022.11075

4. Yin P, Jiang Y, Fang X, et al. Cell-based therapies for degenerative musculoskeletal diseases. *Adv Sci (Weinh).* 2023; 10(21):e2207050. doi: 10.1002/advs.202207050

5. Belk JW, Lim JJ, Keeter C, et al. Patients with knee osteoarthritis who receive platelet-rich plasma or bone marrow aspirate concentrate injections have better outcomes than patients who receive hyaluronic acid: systematic review and meta-analysis. *Arthroscopy.* 2023;39:1714-1734. doi: 10.1016/j.arthro.2023.03.001

6. Anz AW, Plummer HA, Cohen A, Everts PA, Andrews JR, Hackel JG. Bone marrow aspirate concentrate is equivalent to platelet-rich plasma for the treatment of knee osteoarthritis at 2 years: a prospective randomized trial. *Am J Sports Med.* 2022;50:618-629. doi: 10.1177/03635465211072554

7. Zhang Y, Yang H, He F, Zhu X. Intra-articular injection choice for osteoarthritis: making sense of cell source-an updated systematic review and dual network meta-analysis. *Arthritis Res Ther.* 2022;24:260. doi: 10.1186/s13075-022-02953-0

8. Brunet A, Goodell MA, Rando TA. Ageing and rejuvenation of tissue stem cells and their niches. *Nat Rev Mol Cell Biol.* 2023;24(1):45-62. doi: 10.1038/S41580-022-00510-w

9. Kim SH, Djaja YP, Park YB, Park JG, Ko YB, Ha CW. Intra-articular injection of culture-expanded mesenchymal stem cells without adjuvant surgery in knee osteoarthritis: a systematic review and meta-analysis. *Am J Sports Med.* 2020;48:2839-2849. doi: 10.1177/0363546519892278

10. Dai P, Wu Y, Gao Y, et al. Multiomics analysis of platelet-rich plasma promoting biological performance of mesenchymal stem cells. *BMC Genomics.* 2024;25(1):564. doi: 10.1186/s12864-024-10329-8

11. Álvarez Hernández P, de la Mata Llord J. Expanded mesenchymal stromal cells in knee osteoarthritis: a systematic literature review. *Reumatol Clin (Engl Ed).* 2022;18(1):49-55. doi: 10.1016/j.reumae.2020.10.001

12. de Morree A, Rando TA. Regulation of adult stem cell quiescence and its functions in the maintenance of tissue integrity. *Nat Rev Mol Cell Biol.* 2023;24:334. doi: 10.1038/S41580-022-00568-6

13. Zohora FT, Aliyu M, Saboor-Yaraghi AA. Secretome-based acellular therapy of bone marrow-derived mesenchymal stem cells in degenerative and immunological disorders: a narrative review. *Heliyon.* 2023;9(7):e18120. doi: 10.1016/j.heliyon.2023.e18120

14. Mamidi N, Ijadi F, Norahan MH. Leveraging the recent advancements in GelMA scaffolds for bone tissue engineering: an assessment of challenges and opportunities. *Biomacromolecules.* 2024;25(4):2075-2113. doi: 10.1021/acs.biomac.3c00279

15. Harrison P. Subcommittee on platelet physiology. The use of platelets in regenerative medicine and proposal for a new classification system: guidance from the SSC of the ISTH. *J Thromb Haemost.* 2018;16(9):1895-1900. doi: 10.1111/jth.14223

16. de Melo BAG, França CG, Dávila JL, et al. Hyaluronic acid and fibrin from L-PRP form semi-IPNs with tunable properties suitable for use in regenerative medicine. *Mater Sci Eng C Mater Biol Appl.* 2020;109:110547. doi: 10.1016/j.msec.2019.110547

17. Daly AC, Prendergast ME, Hughes AJ, Burdick JA. Bioprinting for the biologist. *Cell.* 2021;184(1):18-32. doi: 10.1016/j.cell.2020.12.002

18. Del Amo C, Andia I. Blood-derived biomaterials for tissue graft biofabrication by solvent-based extrusion bioprinting. *Int J Bioprinting.* 2023;9:762. doi: 10.18063/ijb.762

19. Del Amo C, Perez-Garrastachu M, Jauregui I, Llama-Pino X, Andia I. Assessing bioprinted functionalized grafts for biological tendon augmentation in vitro. *Int J Mol Sci.* 2024;25(9):4752. doi: 10.3390/ijms25094752

20. IRIS Home. Available at: https://iris.who.int/?locale-attribute=en& (accessed on Jul 23, 2024)

21. Potyondy T, Uquillas JA, Tebon PJ, et al. Recent advances in 3D bioprinting of musculoskeletal tissues. *Biofabrication.* 2021;13(2):10.1088/1758-5090/abc8de. doi: 10.1088/1758-5090/abc8de

22. Singh S, Choudhury D, Yu F, Mironov V, Naing MW. In situ bioprinting - bioprinting from benchside to bedside? *Acta Biomater.* 2020;101:14-25. doi: 10.1016/j.actbio.2019.08.045

23. Adib AA, Sheikhi A, Shahhosseini M, et al. Direct-write 3D printing and characterization of a GelMA-based biomaterial for intracorporeal tissue. *Biofabrication.* 2020;12(4):045006. doi: 10.1088/1758-5090/ab97a1

24. Samandari M, Mostafavi A, Quint J, Memić A, Tamayol A. In situ bioprinting: intraoperative implementation of regenerative medicine. *Trends Biotechnol.* 2022;40:1229-1247. doi: 10.1016/j.tibtech.2022.03.009

25. Andia I, Iturregi A, Jauregi I, et al. Intracorporeal extruder device for bio-ink application in laparoscopic surgery. Spanish patent 232528ES. 2023.

26. Jovic D, Yu Y, Wang D, et al. A brief overview of global trends in MSC-based cell therapy. *Stem cell Rev Rep.* 2022;18:1525-1545. doi: 10.1007/S12015-022-10369-1

27. Gupta PK, Maheshwari S, Cherian JJ, et al. Efficacy and safety of stempeucel in osteoarthritis of the knee: a phase 3 randomized, double-blind, multicenter, placebo-controlled study. *Am J Sports Med.* 2023;51:2254-2266. doi: 10.1177/03635465231180323

28. Jeyaraman M, Muthu S, Ganie PA. Does the source of mesenchymal stem cell have an effect in themanagement of osteoarthritis of the knee? Meta-analysis of randomized controlled trials. *Cartilage.* 2021;13:1532S. doi: 10.1177/1947603520951623

29. Hurley ET, Sherman SL, Stokes DJ, et al. Experts achieve consensus on a majority of statements regarding platelet-rich plasma treatments for treatment of musculoskeletal pathology. *Arthroscopy.* 2024;40:470-477.e1. doi: 10.1016/j.arthro.2023.08.020

30. Nurden AT. Platelets, inflammation and tissue regeneration. Thromb *Haemost.* 2011;105(Suppl 1):S13-33. doi: 10.1160/THS10-11-0720

31. Schol J, Tamagawa S, Volleman TNE, Ishijima M, Sakai D. A comprehensive review of cell transplantation and platelet-rich plasma therapy for the treatment of disc degeneration-related back and neck pain: a systematic evidence-based analysis. *JOR Spine.* 2024;7(2):e1348. doi: 10.1002/JSP2.1348

32. Abbadessa A, Ronca A, Salerno A. Integrating bioprinting, cell therapies and drug delivery towards in vivo regeneration of cartilage, bone and osteochondral tissue. *Drug Deliv Transl Res.* 2024;14:858-894. doi: 10.1007/s13346-023-01437-1

33. Acebes-Huerta A, Martínez-Botía P, Carbajo-Argüelles G, et al. Characterization of the molecular composition and in vitro regenerative capacity of platelet-based bioproducts and related subfractions. *Acta Biomater.* 2024;177(3):132-147. doi: 10.1016/j.actbio.2024.01.029

34. Piao Y, You H, Xu T, et al. Biomedical applications of gelatin methacryloyl hydrogels. *Eng Regen.* 2021;2:47-56. doi: 10.1016/j.engreg.2021.03.002

35. Kurian AG, Singh RK, Patel KD, Lee JH, Kim HW. Multifunctional GelMA platforms with nanomaterials for advanced tissue therapeutics. *Bioact Mater.* 2022;8:267-295. doi: 10.1016/j.bioactmat.2021.06.027

36. Gu Y, Miao F, Liu K, et al. Fabrication of gelatin methacryloyl/graphene oxide conductive hydrogel for bone repair. *J* Biomater *Sci Polym Ed.* 2023;34:2076-2090. doi: 10.1080/09205063.2023.2217063

37. Haskell A, White BP, Rogers RE, et al. Scalable manufacture of therapeutic mesenchymal stromal cell products on customizable microcarriers in vertical wheel bioreactors that improve direct visualization, product harvest, and cost. *Cytotherapy.* 2024;26(4):372-382. doi: 10.1016/j.jcyt.2024.01.009

38. Kusuma GD, Carthew J, Lim R, Frith JE. Effect of the microenvironment on mesenchymal stem cell paracrine signaling: opportunities to engineer the therapeutic effect. *Stem Cells Dev.* 2017;26:617-631. doi: 10.1089/scd.2016.0349

39. Iseki T, Rothrauff BB, Kihara S, et al. Enhanced osteochondral repair by leukocyte-depleted platelet-rich plasma in combination with adipose-derived mesenchymal stromal cells encapsulated in a three-dimensional photocrosslinked injectable hydrogel in a rabbit model. *Stem Cell Res. Ther.* 2024;15(1):159. doi: 10.1186/S13287-024-03750-z

40. Cuesta-Gomez N, Graham GJ, Campbell JDM. Chemokines and their receptors: predictors of the therapeutic potential of mesenchymal stromal cells. *J Transl Med.* 2021; 19(1):1-10. doi: 10.1186/s12967-021-02822-5

41. Burnouf T, Chou ML, Lundy DJ, Chuang EY, Tseng CL, Goubran H. Expanding applications of allogeneic platelets, platelet lysates, and platelet extracellular vesicles in cell therapy, regenerative medicine, and targeted drug delivery. *J Biomed Sci.* 2023;30:79. doi: 10.1186/S12929-023-00972-w

42. Noronha NDC, Mizukami A, Caliári-Oliveira C, et al. Correction to: priming approaches to improve the efficacy of mesenchymal stromal cell-based therapies. *Stem Cell Res Ther.* 2019;10(1):132. doi: 10.1186/S13287-019-1259-0

43. Lu P, Ruan D, Huang M, et al. Harnessing the potential of hydrogels for advanced therapeutic applications: current achievements and future directions. *Signal Transduct Target Ther.* 2024;9(1):166. doi: 10.1038/s41392-024-01852-x

44. Cruz EM, Machado LS, Zamproni LN, et al. A gelatin methacrylate-based hydrogel as a potential bioink for 3d bioprinting and neuronal differentiation. *Pharmaceutics.* 2023;15(2):627. doi: 10.3390/pharmaceutics15020627

ACCSCIENCE PUBLISHING

International Journal of Bioprinting

RESEARCH ARTICLE

3D-printed poly(*p*-dioxanone)/graphene oxide composite bioresorbable stents for congenital heart disease treatment

Enrong Chen[1†], Xiji Qin[1†], Zhihui Xiong[2*], Xiaorong Cai[3], Xuejun Jin[2], Kun Sun[1,4*], and Jing Sun[1,4*]

[1]Department of Pediatric Cardiology, Xinhua Hospital, School of Medicine, Shanghai Jiao Tong University, Shanghai, China

[2]Institute of Medical Robotics, School of Biomedical Engineering, Shanghai Jiao Tong University, Shanghai, China

[3]State Key Lab of Metal Matrix Composite, School of Materials Science and Engineering, Shanghai Jiao Tong University, Shanghai, China

[4]Engineering Research Center of Techniques and Instruments for Diagnosis and Treatment of Congenital Heart Disease, Ministry of Education, Shanghai, China

[†]These authors contributed equally to this work.

***Corresponding authors:**
Jing Sun
(sunjing02@xinhuamed.com.cn)

Kun Sun
(sunkun@xinhuamed.com.cn)

Zhihui Xiong
(xiongzhihui@sjtu.edu.cn)

Citation: Chen E, Qin X, Xiong Z, et al. 3D-printed poly(*p*-dioxanone)/graphene oxide composite bioresorbable stents for congenital heart disease treatment. *Int J Bioprint.* 2024;10(6):4530. doi: 10.36922/ijb.4530

Received: August 15, 2024
Revised: September 17, 2024
Accepted: September 30, 2024
Published Online: September 30, 2024

Copyright: © 2024 Author(s). This is an Open Access article distributed under the terms of the Creative Commons Attribution License, permitting distribution, and reproduction in any medium, provided the original work is properly cited.

Publisher's Note: AccScience Publishing remains neutral with regard to jurisdictional claims in published maps and institutional affiliations.

Abstract

Bioresorbable stents (BRSs) offer significant advantages in treating congenital heart disease (CHD)-related vascular stenoses, especially for pediatric patients. However, the insufficient mechanical performance of polymeric BRSs remains a critical challenge. In this study, poly(*p*-dioxanone) (PPDO) was incorporated with graphene oxide (GO) for the first time to improve both mechanical properties and biocompatibility. PPDO/GO composites with varying GO content were fabricated via solution mixing and solvent casting, and tensile tests revealed that lower GO content levels (0.2% and 0.5%) significantly improved Young's modulus, tensile strength, and elongation at break of PPDO due to hydrogen bonding and increased degree of crystallinity. 3D-printed PPDO/GO sliding-lock stents with optimal GO contents were fabricated by fused deposition modeling and demonstrated superior compression force compared to pristine PPDO stents. *In vitro* hemocompatibility and cytocompatibility assessments indicated that 3D-printed PPDO/GO stents exhibited a low hemolysis rate, reduced platelet adhesion, and enhanced adhesion and proliferation of endothelial cells. *In vivo* evaluation further demonstrated improved endothelialization in rat abdominal aortas implanted with 3D-printed PPDO/GO filaments for four weeks. Overall, PPDO/0.5%GO exhibited superior performance in compression force, hemocompatibility, cytocompatibility, and *in vivo* endothelialization. This study, for the first time, combines PPDO with GO and elucidates the mechanism behind the enhanced mechanical properties of PPDO/GO composite material. Using 3D printing, PPDO/GO BRSs with improved compression performance and biocompatibility were developed, highlighting their potential for treating pediatric patients with CHD-related vascular stenoses.

Keywords: 3D printing; Bioresorbable stents; Poly(*p*-dioxanone); Graphene oxide; Congenital heart disease

1. Introduction

Congenital heart disease (CHD) is the most common birth defect, with 13.3 million patients worldwide in 2019, and the leading cause of morbidity and mortality in newborns.[1] CHD-related vascular stenoses account for approximately 12% of all CHDs,[2] including pulmonary artery or vein stenosis,[3,4] coarctation of the aorta and its branches,[5,6] and postoperative stenosis.[7] In recent years, intravascular stent implantation has become the preferred treatment due to its efficacy.[8] Bioresorbable stents (BRSs) have been developed to overcome the drawbacks of permanent metal stents that are currently used in clinical practice. BRSs can provide short- to mid-term radial support to prevent stenotic vessel recoil and are gradually resorbed by the body afterward.[9] This reduces the risks of in-stent restenosis, stent thrombosis, and chronic inflammation.[10,11] Most critically for pediatric patients, BRSs are adapted to the vascular growth of infants and children, eliminating the need for secondary interventions, as the implanted segments can perform luminal remodeling without stenosis formation. Therefore, BRSs exhibit significant advantages in the treatment of CHD-related vascular stenoses. Notably, there are currently no pediatric BRS products available worldwide. Many researchers have attempted to develop BRSs for pediatric patients. Various bioresorbable materials have been studied, including poly-L-lactic acid (PLLA), poly(lactic-co-glycolic acid) (PLGA), zinc alloy, and nitride iron.[12–15] However, the degradation times of all the above-mentioned materials are over 1 year,[16] mismatching the constructive remodeling period of vessels (3–6 months).[17] Prolonged degradation triggers inflammatory response and delayed vascular growth. Another key issue is that, compared to stainless steel and CoCr alloy used in permanent metal stents, these bioresorbable materials exhibit inferior mechanical properties, leading to poor radial strength of the stent.[18] Radial strength is defined as the maximum force that a stent can withstand before collapsing and is the most critical mechanical property of a stent.[19,20] Low radial strength results in vascular recoil and flow disruptions, which can lead to worse conditions, including stent restenosis and stent migration.[10,21] Therefore, it is crucial to develop a BRS with sufficient radial strength and moderate degradation time for CHD pediatric patients.

Poly(*p*-dioxanone) (PPDO) is a semi-crystalline aliphatic polyester with good bioresorbability and biocompatibility.[22] Research has demonstrated that the degradation time of PPDO is 6 months,[23] and a braided PPDO BRS can maintain radial support for at least 3 months during *in vitro* degradation,[24] which is ideal for CHD pediatric patients. Recently, PPDO has been explored for application in vascular stents.[25] Traditional fabrication methods for vascular BRSs, such as laser cutting and braiding,[26] present respective challenges. Overheating during the laser cutting process can significantly impair the mechanical properties of the stent.[27] Similarly, braided stents tend to exhibit relatively low radial force.[25,28] 3D printing has become a research focus in the development of medical implants. This technique offers advantages such as speed, cost-efficiency, flexibility in the manufacturing location, and material conservation.[29] It enables the personalized customization of products with high precision and geometrical complexity, which is well-suited for BRSs. Common 3D printing technologies used for polymeric BRSs include stereolithography (SLA), selective laser sintering (SLS), fused deposition modeling (FDM), etc.[30] During SLA, photosensitive resins are polymerized and cured under ultraviolet (UV) light, but photoinitiators and photoabsorbers may be toxic.[31,32] SLS uses a laser to partially melt powder materials and bond the particles together, resulting in a rough surface and requiring post-processing.[33] FDM is a cost-effective and user-friendly method that involves melting and extruding materials, which is suitable for printing thermoplastic polymers.[34–37] Lu et al.[38] developed a PPDO/stabaxol-1 stent using FDM to treat cerebrovascular disease.

However, the inadequate mechanical performance of PPDO stents, as noted in our previous study,[39] remains an issue due to their low modulus and strength. The incorporation of nanofillers has been considered effective in improving the mechanical properties of polymers. Some studies have reported PPDO nanocomposites reinforced with carbon nanotubes, chitin nanocrystals, and hydroxyapatite nanoparticles.[40–42] Graphene oxide (GO) is a 2D carbon nanomaterial with high modulus and strength.[43,44] Its high specific surface area provides a larger contact area with the composite matrix. Its rich oxygen-containing functional groups (hydroxyl, carboxyl, epoxy groups) on the surface enhance the interfacial interaction with the polymer matrix through covalent bonds, hydrogen bonds, π–π interactions, etc., facilitating stress transfer and improving the mechanical performance of the composite.[45,46] The hydrophilicity and surface negative charge of GO are conducive to protein adsorption via electrostatic interaction, hydrogen bonding, and hydrophobic interaction, which promotes cell adhesion and proliferation.[47,48] Stent implantation inevitably damages the endothelium, leading to thrombosis and intimal hyperplasia, thereby causing restenosis. It is essential to promote endothelial cell adhesion, migration, and proliferation to accelerate endothelialization.[49] Studies have reported that GO facilitates the adhesion, proliferation, and migration of human umbilical vein endothelial cells (HUVECs),[50,51] demonstrating good hemocompatibility

by reducing hemolysis rate and platelet adhesion.[52,53] Therefore, GO is considered a potential nanofiller for the PPDO matrix in vascular stent applications.

In this study, we employed solution mixing and solvent casting to fabricate PPDO/GO composite with varying GO content for the first time to enhance the mechanical properties and biocompatibility of PPDO. Physical and chemical properties of PPDO/GO materials were analyzed by Raman spectroscopy, Fourier transform infrared (FT-IR) spectroscopy, X-ray diffraction (XRD) analysis, and X-ray photoelectron spectroscopy (XPS). Thermal and electrical properties were investigated by differential scanning calorimetry (DSC) and the direct current (DC) polarization method, respectively. Surface morphology and hydrophilicity of PPDO/GO materials were characterized by scanning electron microscopy (SEM) and static water contact angle test, respectively. The influence of GO content on the mechanical properties of PPDO/GO materials was studied by uniaxial tensile test to derive the optimum GO content. Bioresorbable PPDO/GO sliding-lock stents with optimum GO content were fabricated by FDM, and the compression performance was evaluated by a parallel plate compression test. The cytocompatibility and hemocompatibility of PPDO/GO stents were also analyzed. PPDO/GO filaments were also 3D printed and implanted into the abdominal aortas of Sprague–Dawley (SD) rats to evaluate *in vivo* endothelialization. This study is the first to integrate PPDO with GO, elucidating the mechanism behind the enhanced mechanical properties of PPDO/GO composite material. Through 3D printing, we developed PPDO/GO BRSs with superior compressive force and biocompatibility, underscoring its promising application for treating pediatric patients with CHD-related vascular stenoses.

2. Materials and methods

2.1. Materials

Poly(*p*-dioxanone) (PPDO) monofilament with a diameter of 0.6 mm was purchased from META® BIOMED (Korea); GO (multi-walled; purity ≥98%) was purchased from Yuanye Biotech (China); 1,1,1,3,3,3-fluoro-2-propanol (HFIP; purity ≥99.8%) was purchased from Aladdin Reagent (China).

2.2. Preparation of PPDO/GO films

Briefly, PPDO/GO films were prepared by solution mixing and solvent casting (Figure 1), where 1.0 g of PPDO monofilament was cut into small pieces and then dissolved in 15 mL of HFIP. GO (0–5 wt% with respect to the weight of PPDO) was ultrasonic-dispersed in HFIP at 25°C for 1 h and mixed with the PPDO-HFIP solution by stirring for 5 min and subjected to ultrasonic vibration for 15 min. PPDO/GO-HFIP solution was poured into a flat polytetrafluoroethylene mold and dried in a vacuum oven at 45°C for 10 h to evaporate the solvent.

2.3. Physical and chemical characterizations of PPDO/GO materials

The surface morphology of PPDO/GO films was observed using an optical microscope (ZEISS Axio Image A1m microscope; ZEISS, Germany) and SEM (RISE-MAGNA; TESCAN, Czech Republic) with an accelerating voltage of 5 kV. Surfaces of PPDO/GO films were sprayed with gold before SEM observation.

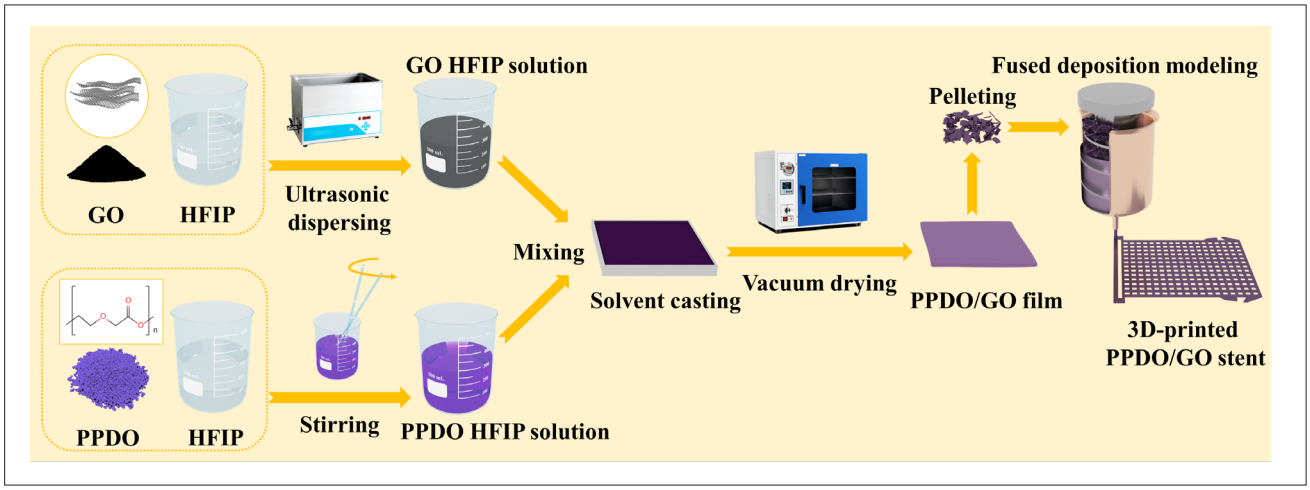

Figure 1. A schematic illustration of the preparation of PPDO/GO materials and stents. Abbreviations: GO, graphene oxide; HFIP, 1,1,1,3,3,3-fluoro-2-propanol; PPDO, poly(*p*-dioxanone).

Raman spectra of PPDO/GO films were analyzed using Renishaw inVia Qontor (Renishaw, United Kingdom [UK]) with laser wavelengths of 532 and 785 nm, to characterize the chemical composition of PPDO/GO.

The FT-IR spectra of PPDO/GO films over a spectral range of 650–4000 cm^{-1} were analyzed by Spectrum 100 (Perkin Elmer, United States of America [USA]) with attenuated total reflectance mode to characterize the functional groups of PPDO/GO materials.

The XRD analysis was performed using D8 DISCOVER (Bruker AXS GmbH, Germany) with Cu Kα radiation (λ = 0.15406 nm) at a 2θ range of 10°–50° at 35 kV to characterize the crystal structure of PPDO/GO materials.

Thermal properties of PPDO/GO materials were characterized by DSC using DSC8500 (PerkinElmer, USA). The temperature scan was performed from 30 to 140°C, with a heating rate of 10°C/min under a helium atmosphere. The degree of crystallinity (X_c) was calculated by the following equation:

$$X_c = \frac{\Delta H_m}{\Delta H_m^0 \left(1 - m_f\right)} \times 100\% \quad \text{(I)}$$

where ΔH_m is the enthalpy of fusion of PPDO/GO materials, ΔH_m^0 is the enthalpy of fusion of PPDO with 100% crystallinity, which is 141.18 J/g, and m_f is the mass fraction of GO.

The electrical conductivity of PPDO/GO materials was determined by the DC polarization method. PPDO/GO films were subject to an Au-ion sputtering instrument (2 mA ion current, SBC-12; KYKY Technology Co. Ltd., China) for 300 s for each surface, and then stamped into an Au|Sample|Au disc with a diameter of 8 mm. A bias voltage of 1 V was applied on the Au|Sample|Au disc, and the current was measured using a potentiostat (Biologic VMP3; Biologic, France). The average current of the last 100 s was used to calculate the electrical conductivity according to the following equation:

$$\sigma = \frac{4IL}{U\pi d^2} \quad \text{(II)}$$

where σ is the electrical conductivity of PPDO/GO materials, I is the average current, L is the thickness of PPDO/GO film, U is the bias voltage, and is the diameter of the PPDO/GO film.

Mechanical properties of PPDO/GO materials were measured using a microcomputer-controlled electronic universal testing machine (Labsans Testing Machine Co. Ltd., China) with a 5 kN load cell at 25°C, according to ISO 527-2:2012. PPDO/GO films were cut into dog-bone Type 1BB specimens (Figure S1). Tensile tests were carried out with an extension rate of 5 mm/min until failure.

X-ray photoelectron spectroscopy (XPS) was performed using Thermo Scientific K-Alpha (Thermo Fisher Scientific, USA) with an Al Kα X-ray source (1486.6 eV) to analyze the chemical states of carbon and oxygen in PPDO/GO materials. The binding energy of C1s and O1s scans was calibrated by the C1s peak of adventitious carbon (284.8 eV). Data analysis was conducted using Avantage software (Thermo Fisher Scientific, USA).

The static water contact angle of PPDO/GO films was measured by DSA100 (KRÜSS, Germany) with 5 μL water droplet at 20°C to evaluate the hydrophilicity of PPDO/GO materials.

Rheological measurements were conducted using a rheometer (MCR 302; Anton Paar, Austria) with a 25 mm parallel plate and a shear rate range of 0.1–100 s^{-1}. The melt viscosity of PPDO/GO materials was tested at different temperatures (130, 140, and 150°C) to analyze the printability of PPDO/GO materials at different nozzle temperatures.

2.4. Fabrication of PPDO/GO sliding-lock stents and PPDO/GO filaments

The structural design of PPDO/GO sliding-lock stents was based on our previous work.[54] The stents were 3D-printed using Bio-Architect® SR (Regenovo, China), with a nozzle diameter of 0.2 mm, layer thickness of 0.2 mm, and printing speed of 5 mm/s. The influence of nozzle temperature on the compression force of 3D-printed PPDO sliding-lock stents was investigated. Compression force was reportedly increased with the nozzle temperature (Figure S2). This may result from improved mechanical properties of PPDO due to stronger interfacial adhesion.[55] The compression force at the nozzle temperature of 150°C was significantly higher than other lower temperatures; hence, 150°C was selected to fabricate PPDO and PPDO/GO sliding-lock stents. 3D-printed PPDO/GO filaments with a diameter of 0.1 mm were also prepared for *in vivo* evaluation.

2.5. Mechanical properties of PPDO/GO sliding-lock stents

The compression performance of PPDO/GO sliding-lock stents was assessed by parallel plate compression tests using an Electroforce 3200 universal testing machine (TA Instruments, USA), according to ISO 25539-2. Stents were compressed to 50% of the original outer diameter at a compression speed of 0.05 mm/s. Compression force was recorded and normalized by the length of the corresponding stent.

2.6. Surface morphology analysis of PPDO/GO films and sliding-lock stents

The surface morphology of PPDO/GO films and sliding-lock stents was analyzed by SEM using a RISE-MAGNA system (TESCAN, Czech Republic) at an accelerating voltage of 5 kV. The surfaces were sputtered with gold before observation.

2.7. *In vitro* evaluation of hemocompatibility

2.7.1. Hemolysis test

Fresh Sprague–Dawley (SD) rats blood was collected in heparinized test tubes. Red blood cells (RBCs) were obtained by centrifuging the anticoagulated blood at 4000 r/min for 5 min and then removing the supernatant plasma. The 2% RBC solution was prepared by dispersing the RBCs in normal saline. PPDO/GO stents were cut into small pieces and incubated with 2 mL of the 2% RBC solution at 37°C for 2 h. After the removal of stents, the suspension was centrifuged at 4000 r/min for 5 min. For positive and negative controls, the 2% RBC solution was incubated with deionized water and normal saline, respectively. The absorbance of the supernatant was measured at 545 nm using a microplate reader. The hemolysis rate was calculated using the following equation:

$$Hemolysis\,(\%) = \frac{OD_s - OD_n}{OD_p - OD_n} \times 100\% \qquad \text{(III)}$$

where OD_s is the absorbance of the sample, OD_n is the absorbance of the negative control, and OD_p is the absorbance of the positive control.

2.7.2. Platelet adhesion test

Platelet-rich plasma was prepared by centrifuging the anticoagulated fresh rat blood at 1000 r/min for 10 min. PPDO/GO stents were cut into small pieces and incubated with 1 mL platelet-rich plasma for 2 h at 37°C. The samples were rinsed with phosphate-buffered saline (PBS; BasalMedia, China) three times and immersed in 2.5% glutaraldehyde solution (Solarbio, China) for at least 6 h to fix the adhered platelets. The samples were then dehydrated by gradient ethanol solutions (50%, 60%, 70%, 80%, 90%, and 100%) and dried at room temperature. Thereafter, the samples were sprayed with gold and observed by SEM.

2.8. *In vitro* evaluation of cell compatibility

2.8.1. Cell culture

Human umbilical vein endothelial cells (HUVECs) were sourced from the Type Culture Collection of the Chinese Academy of Sciences (China) and cultured in Dulbecco's Modified Eagle Medium (DMEM; Gibco, USA), supplemented with 1% penicillin-streptomycin (HyClone, USA) and 10% fetal bovine serum (Gibco, USA), before incubation in a humidified incubator with 5% CO_2 at 37°C. The culture medium was refreshed every two days. PPDO/GO stents were cut into small pieces (1 × 1 cm), washed with 75% ethanol solution and deionized water, and sterilized by ultraviolet radiation. After sterilization, the samples were placed into 12-well culture plates, immersed in DMEM, and incubated for 2 h.

2.8.2. Cell adhesion and proliferation

The HUVECs were seeded on the samples in 12-well culture plates at a density of 2×10^4 cells/mL and incubated in the culture medium. After incubation for 1, 3, 5, and 7 days, cell viability and proliferation were evaluated by a Cell Counting Kit-8 (CCK-8) assay according to the manufacturer's protocol. The culture medium was removed, and the samples were washed with PBS. The samples were then transferred to a 12-well plate, and CCK-8 reagent (Beyotime, China) was added to each well and incubated for 2 h at 37°C. The absorbance of the supernatant was measured using a microplate reader at 450 nm.

2.8.3. Cell morphology

The HUVECs were seeded on the samples in 12-well culture plates at a density of 2×10^4 cells/mL and incubated in the culture medium. After incubation for 1, 3, 5, and 7 days, the samples were washed with PBS, and the adhered HUVECs were fixed with 4% paraformaldehyde (Beyotime, China). The HUVECs were permeabilized using 0.1% Triton X-100 (Beyotime, China). Actin filaments were stained with rhodamine-conjugated phalloidin (Solarbio, China), and cell nuclei were stained by 4,6-diamidino-2-phenylindole (DAPI; Vector Laboratories, USA). Afterwards, the samples were observed using laser confocal scanning microscopy (LCSM; Leica, Germany) to evaluate the cell morphology on the PPDO/GO stents.

2.9. *In vivo* evaluation

All procedures were approved by the Animal Ethics Committee and performed in strict accordance with their regulations. 3D-printed PPDO/GO filaments with a length of 15 mm and a diameter of 0.1 mm were implanted in the abdominal aortas of SD rats to evaluate the effect of PPDO/GO materials on *in vivo* endothelialization. After implantation for 2 weeks, the vessels containing embedded filaments were harvested and cut longitudinally to expose the tissue on the surface of the filaments. The samples were fixed by 2.5% glutaraldehyde solution (Solarbio, China) for at least 6 h and dehydrated using gradient ethanol solutions (50%, 60%, 70%, 80%, 90%, and 100%). After drying at room temperature, the samples were sprayed with gold on the surface and observed by SEM. After implantation for 4 weeks, the PPDO and PPDO/GO filaments, along with

the surrounding artery tissues, were isolated to prepare paraffin sections. The paraffin sections were stained with hematoxylin and eosin (H&E) and anti-CD31 antibody (Servicebio, China).

2.10. Statistical analysis

Statistical analysis was carried out using SPSS Statistics 26.0 (IBM, USA). Statistics were expressed as mean ± standard deviation. At least three specimens were tested for each experiment in this research. Statistical significance was analyzed by one-way analysis of variance (ANOVA) with Tukey's multiple comparison test. A p-value <0.05 was considered to be statistically significant: * $p < 0.05$, ** $p < 0.01$, *** $p < 0.001$.

3. Results and discussion

The surface morphology of PPDO/GO films was characterized by SEM (Figure 2a–f). Films fabricated by solvent casting display a surface morphology consisting of densely packed, bubble-like polygonal elements, similar to the surface topography of polyhydroxyoctanoate reported by Sofińska et al.[56] After the incorporation of GO, the color of PPDO/GO films darkens (Figure 2g–l). With increasing GO content, aggregates begin to appear on the surface and at the junctions of the polygonal elements. For GO contents ≤0.5%, almost no aggregates are observed. However, for GO contents >0.5%, the number and size of aggregates start to increase, and a large number of aggregates can be observed in PPDO/5%GO. This phenomenon may be caused by the aggregation of GO at higher content levels, resulting from hydrogen bonding and strong interlayer π–π stacking interactions.[57,58]

Raman spectroscopy is a fast and non-destructive technique to recognize carbon nanomaterials and characterize their structures in composites with high resolution.[59] Raman spectra of PPDO/GO materials are presented in Figure 3a. Using a 785-nm laser, the characteristic peaks of PPDO at 1735 and 874 cm^{-1} are observed, corresponding to the C=O symmetric stretching vibration of the ester carbonyl group and C–O–C symmetric stretching vibration, respectively. Peaks at 1458 and 1050 cm^{-1} are attributed to -CH_2- bending vibration and the stretching vibration of C–C of the aliphatic chains, respectively.[60] However, the Raman spectrum of PPDO exhibits a relatively flat curve under a 532-nm laser, suggesting no interaction of PPDO with the laser at such a wavelength. However, the characteristic peaks of GO are detected in PPDO/GO materials. The D band at ~1345 cm^{-1} and the G band at ~1600 cm^{-1} correspond to defects and disorders in the carbon lattice and C–C stretching of sp^2-bonded carbon, respectively.[61] In the case of PPDO/1%GO, no typical peaks of GO are observed due to the low GO content. However, the peaks are more distinct as the GO content increases. Results of Raman spectra suggest that PPDO/GO composite material is successfully prepared.

The FT-IR spectra characterize the chemical groups of PPDO, GO, and PPDO/GO materials (Figure 3b and c). For pristine PPDO, the sharp and narrow peak at 1732 cm^{-1} corresponds to the C=O stretching vibration. Peaks at 1200, 1122, and 1050 cm^{-1} correspond to the stretching vibration of C–O. Peaks at 1429 cm^{-1} and in the range of 2957–2880 cm^{-1} are attributed to the bending and stretching vibrations of -CH_2-.[62] For GO, peaks at 1723, 1385, and 1065 cm^{-1} correspond to C=O stretching vibration, C–O–C asymmetric stretching vibration, and C–O stretching vibration, respectively.[63] The peak at 1620 cm^{-1} is ascribed to the aromatic C=C in GO.[64] Figure 3c displays the FT-IR spectra of PPDO/GO materials with the wavenumber ranging from 3450 to 3000 cm^{-1}. The broad peak at ~3300 cm^{-1} is attributed to the stretching vibration of hydroxyl groups.[64] With the incorporation of GO, the peaks become stronger due to the introduction of rich hydroxyl groups from GO and shift to lower wavenumbers as the GO content increases. In the detailed spectra ranging from 1800 to 1650 cm^{-1} (Figure S3), the peak intensity of carbonyl groups of PPDO is enhanced with the elevation of GO content. This indicates the formation of hydrogen bonds between the hydroxyl groups of GO and the carbonyl groups of PPDO.

The XRD results (Figure 3d) display the characteristic peaks of PPDO at 21.9° and 23.8° in all PPDO/GO materials.[65] Both PPDO and PPDO/GO materials exhibit similar XRD patterns regardless of the increase of GO content, indicating that the incorporation of GO does not affect the crystal structure of PPDO. DSC results (Figure 3e) demonstrate an increase in the degree of crystallinity of PPDO/GO materials with the increase of GO content. GO acts as a nucleating agent, promoting the heterogeneous nucleation of PPDO.[66] Some studies have also reported an increase in the degree of crystallinity caused by hydrogen bonds.[67,68]

As presented in Figure 3f, both PPDO and PPDO/GO materials exhibit electrical conductivities at the same order of magnitude due to the insulative nature of PPDO. At lower levels of GO content, no significant change in the electrical conductivity of PPDO/GO materials is observed compared to pristine PPDO. This may be attributed to the uniform dispersion of GO at a low content. With the elevation of GO content, the electrical conductivity of PPDO/GO materials increases, as the aggregation of conductive GO leads to the formation of a local conductive

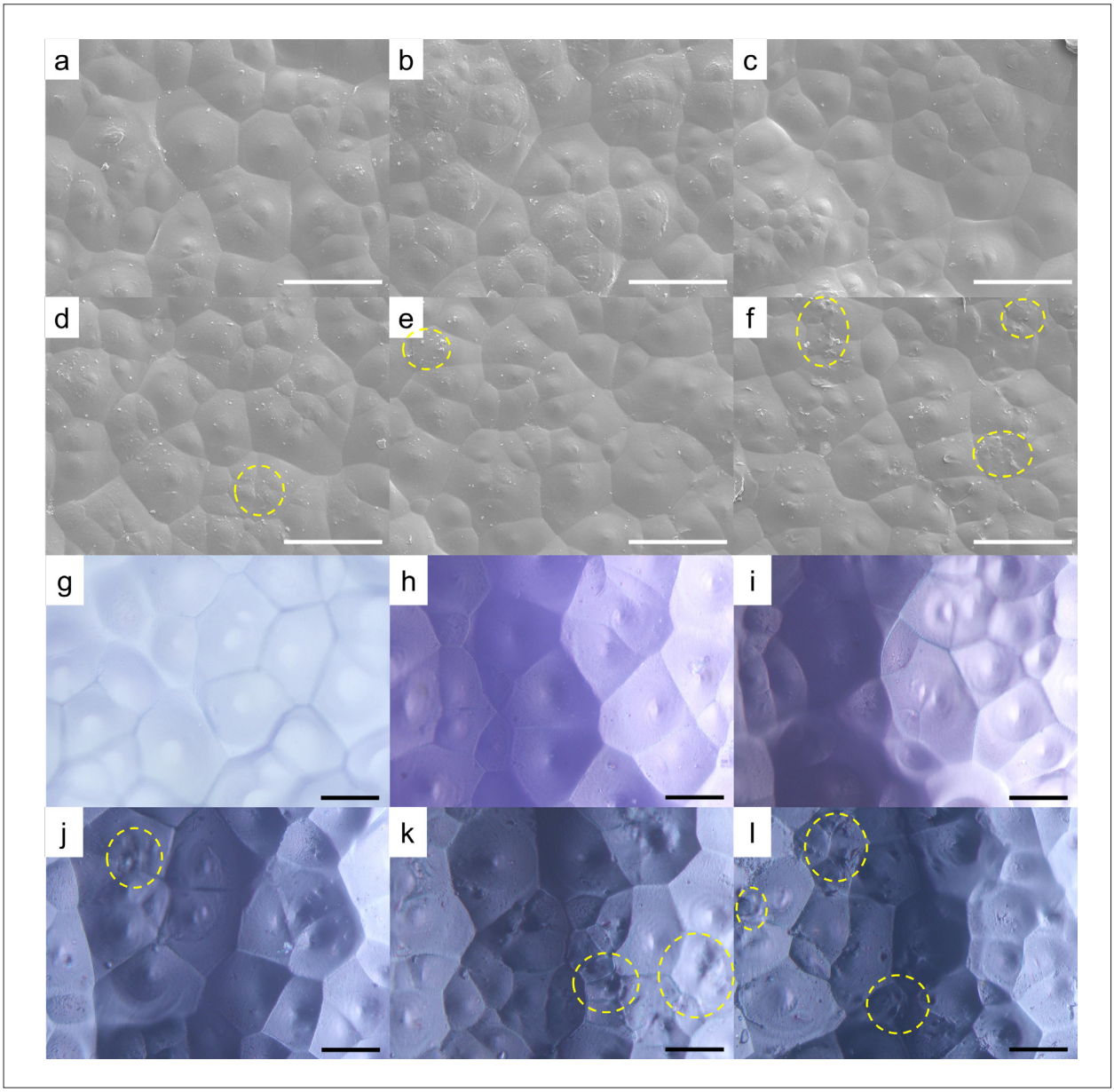

Figure 2. Surface morphology of PPDO/GO and PPDO films. (a–f) SEM images of different samples: (a) PPDO; (b) PPDO/0.2%GO; (c) PPDO/0.5%GO; (d) PPDO/1%GO; (e) PPDO/2%GO; and (f) PPDO/5%GO. The scale bar is 50 μm. (g–l) Optical microscopy images of different samples: (g) PPDO; (h) PPDO/0.2%GO; (i) PPDO/0.5%GO; (j) PPDO/1%GO; (k) PPDO/2%GO; and (l) PPDO/5%GO. GO aggregates are indicated by yellow dashed circles. Scale bars: 20 μm. Abbreviations: GO, graphene oxide; PPDO, poly(*p*-dioxanone); SEM, scanning electron microscopy.

pathway. Consistent with the findings from other studies on polymer/GO composites,[69,70] the inclusion of GO improves the electrical conductivity of the PPDO matrix.

The mechanical performance of PPDO/GO materials was evaluated by uniaxial tensile tests (Figure 3g–i). The Young's modulus, tensile strength, and elongation at break of pristine PPDO are 107.89 ± 16.15 MPa, 12.56 ± 2.10 MPa, and 1.026 ± 0.268, respectively. Incorporating GO results in an enhancement of Young's modulus of PPDO/GO materials. Initially, the tensile strength and elongation at break of PPDO/GO materials increase with increasing GO content but then decrease. PPDO/0.2%GO displays an increment of 44.18% in Young's modulus (155.56 ± 10.81 MPa), 48.21% in tensile strength (18.63 ± 0.63 MPa), and 60.84% in elongation at break (1.650 ± 0.453). PPDO/0.5%GO displays an increment of 53.44% in Young's modulus (165.54 ± 2.07 MPa), 52.82% in tensile

strength (19.21 ± 0.41 MPa), and 16.96% in elongation at break (1.120 ± 0.207). At higher GO content (i.e., reaching 5%), the elongation at break drastically decreases by 88.01% compared to that of pristine PPDO. The abundant functional groups of GO promote uniform dispersion in the PPDO matrix, fostering increased intermolecular interactions with the PPDO matrix. Hydrogen bonding enhances the mechanical properties of materials, including Young's modulus, tensile strength, and elongation at break.[71–74] It facilitates polymer chain crosslinking and impedes chain movement, thus improving the stiffness of PPDO.[75] The elevation in the degree of crystallinity also contributes to the improvement of Young's modulus. GO has an intrinsically high modulus and acts as a reinforcement in the PPDO matrix. As displayed in Figure 3g, at 5% GO content, Young's modulus reaches its peak at 179.46 ± 2.76 MPa. Many studies have revealed that as GO content increases, Young's modulus of the composite material increases as well.[76–78] Wan and Chen[79] reported that at higher GO content, Young's modulus of the composite material gradually increases despite poor dispersion. GO reinforces the PPDO matrix due to its intrinsic high strength and enables more effective load transfer from the matrix to the nanofiller through hydrogen bonding,[80] enhancing the tensile strength of PPDO/GO materials. At a higher level of GO content, the aggregation of GO impairs load transfer efficiency and results in poor reinforcement. Under external load, micro-cracking is formed at the matrix–GO interface during crack propagation and absorbs plenty of fracture energy. Besides, GO nanosheets can prevent crack propagation by crack deflection and crack pinning,[81–83] thereby enhancing the toughness of PPDO/GO materials. However, the high degree of crystallinity of PPDO leads to a decrease of elongation at break at higher GO contents. According to the results of the mechanical characterization of PPDO/GO composites, the mechanical properties of PPDO are enhanced when GO contents are at 0.2% and 0.5%. Therefore, PPDO/0.2%GO and PPDO/0.5%GO are selected for stent fabrication and subsequent biocompatibility evaluation.

The XPS analysis characterizes the surface element composition and the chemical states of carbon and oxygen in PPDO/GO materials. The wide scan spectra (Figure 4a) indicate that PPDO/GO materials are composed of carbon and oxygen, and no fluorine is detected, implying the complete removal of the HFIP solvent. The high-resolution spectra of C1s and O1s core levels of PPDO/GO materials are displayed in Figure 4b and c. The C1s peaks are deconvoluted into three components with binding energies of 284.8 eV, 286.6 ± 0.2 eV, and 288.9 ± 0.2 eV, corresponding to C–C, C–O, and C=O, respectively.[84,85] For GO, another component with a binding energy of 284.4 eV is deconvoluted, which is attributed to sp^2 carbon. The O1s peaks are deconvoluted into four components with binding energies of 531.5 ± 0.2 eV, 532.2 ± 0.2 eV, 533.1 ± 0.2 eV, and 534.1 ± 0.2 eV, corresponding to O–C=O, C=O, C–OH, and C–O–C, respectively.[85] By calculating the area percentage of the deconvoluted O1s spectra, it is found that the C–OH percentage of PPDO/GO materials exhibits an increasing trend as the GO content rises (Figure 4d). This can be attributed to the abundant hydroxyl groups present in GO, and the finding is consistent with the FT-IR results.

Figure 4e features the water contact angle of PPDO/GO materials. As the GO content increases, the water contact angle of PPDO/GO materials gradually decreases from 76.2° ± 1.0° of PPDO to 69.0° ± 0.8° of PPDO/5%GO, indicating enhanced wettability. The presence of abundant hydrophilic groups in GO, such as carboxyl and hydroxyl (as observed in the FT-IR and XPS results), improves the hydrophilicity of PPDO. The enhanced hydrophilicity may facilitate HUVEC adhesion and proliferation.[86,87]

The melt viscosity of the material is crucial for FDM. The material needs to have sufficiently low viscosity to ensure continuous extrusion through the nozzle, while also exhibiting shear thinning behavior, where melt viscosity sharply increases when the shear rate decreases. This helps the material maintain its shape after extrusion under gravity and the stress from the deposition of subsequent layers[88,89]. As displayed in Figure S4, both PPDO and PPDO/GO materials exhibit shear thinning behavior, and the melt viscosity decreases as the temperature increases. The incorporation of GO enhances the melt viscosity of the PPDO matrix, which is also observed in polyamide 6/GO composite.[90] This may be due to the improved interaction between PPDO and GO under hydrogen bonding.

The design of sliding-lock stents is inspired by cable ties. Stents with a series of diameters can be fabricated by adjusting the lateral dimension. Figure 5a features the 3D-printed PPDO/GO sliding-lock stents. FDM can accomplish personalized customization of vascular stents with intricate structures and is suitable for printing thermoplastic polymers (PPDO, PLLA, PLGA, etc.), exhibiting the advantages of convenience, speed, and cost-effectiveness.[91] The thickness of PPDO, PPDO/0.2%GO, and PPDO/0.5%GO sliding-lock stents is measured as 257.20 ± 5.73, 263.20 ± 6.35, and 256.69 ± 2.86 mm, respectively. Figure 5b and c demonstrate the front and top views of PPDO/GO sliding-lock stents (diameter: 9 mm), respectively. Compression performance is one of the primary properties of vascular stents. Results of parallel plate compression tests (Figure 5d) reveal that incorporating GO significantly enhances PPDO sliding-lock stents' compression performance. The compression

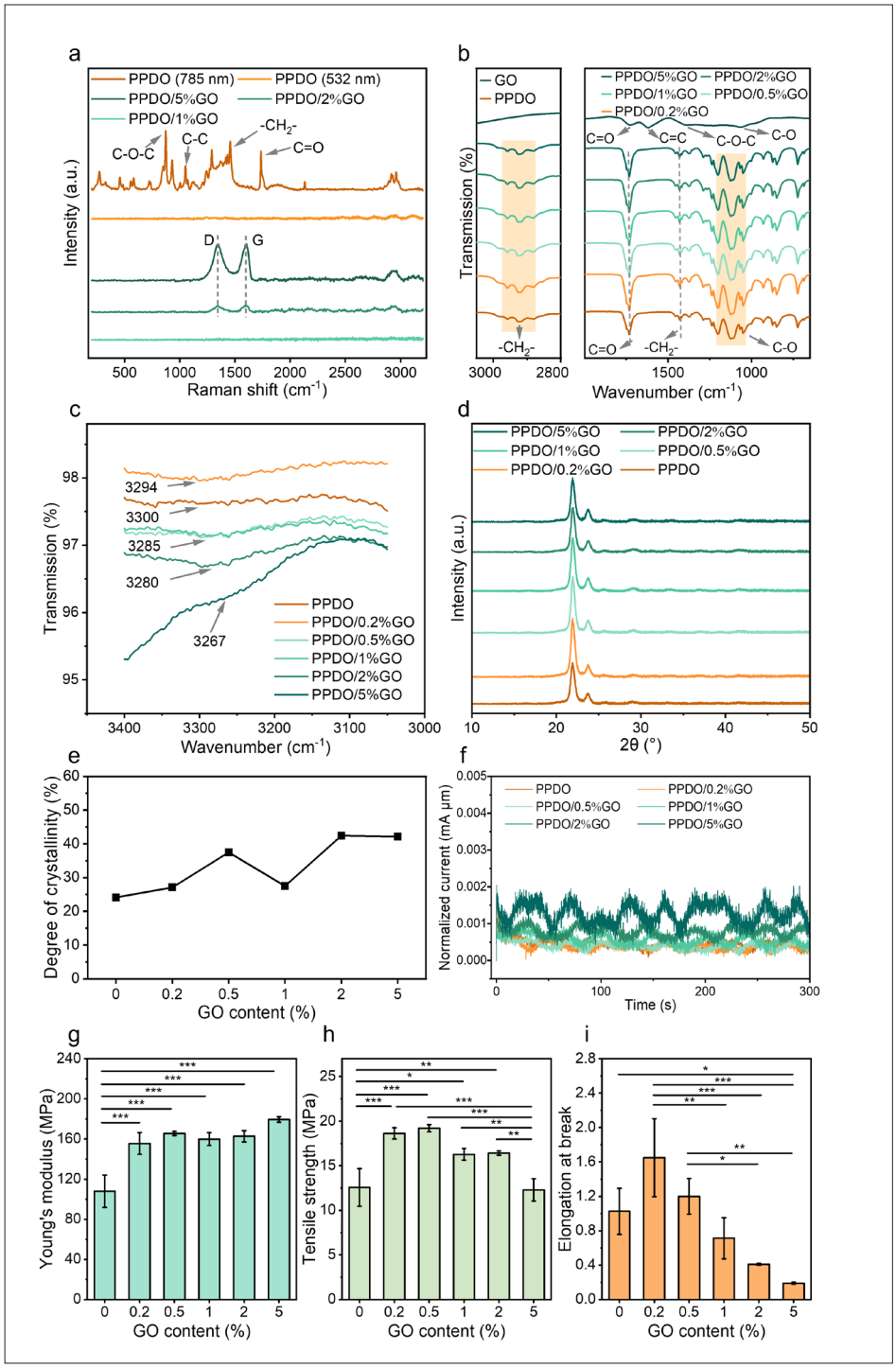

Figure 3. Characterizations of PPDO/GO films. (a) Raman spectra of PPDO/GO and PPDO films. FT-IR spectra of PPDO/GO, PPDO films, and GO powder with wavenumber from (b) 650–2000 cm^{-1}, and 2800–3050 cm^{-1}, and (c) 3050–3400 cm^{-1}. (d) XRD patterns of PPDO/GO and PPDO films. (f) DC polarization curves of PPDO/GO and PPDO films, with the corresponding electrical conductivity listed in the upper right corner. (g–i) Mechanical properties of PPDO/GO and PPDO films: (g) Young's modulus; (h) tensile strength; and (i) elongation at break. * $p < 0.05$, ** $p < 0.01$, *** $p < 0.001$. Abbreviations: DC, direct current; FT-IR, Fourier transform infrared; GO, graphene oxide; PPDO, poly(*p*-dioxanone); XRD, X-ray diffraction.

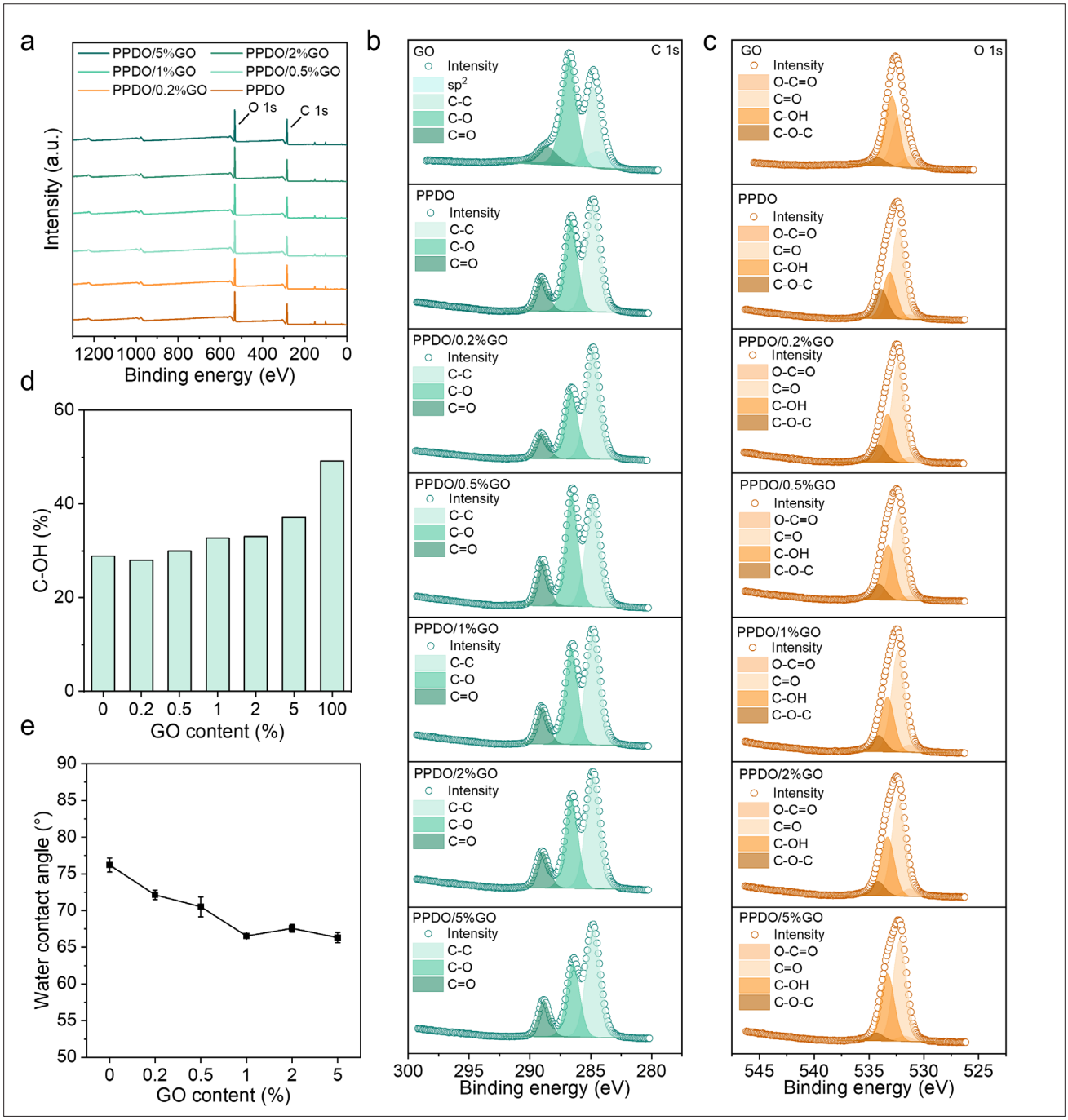

Figure 4. Hydroxyl groups content analysis of PPDO/GO and PPDO films. (a) XPS wide scan spectra of PPDO/GO and PPDO films. (b and c) High-resolution XPS binding energy spectra of (b) C1s, and (c) O1s. (d) Percentage of C–OH group in PPDO/GO, PPDO films, and GO powder. (e) The water contact angle of PPDO/GO and PPDO films (n = 3). Abbreviations: GO, graphene oxide; PPDO: poly(p-dioxanone); XPS, X-ray photoelectron spectroscopy.

force of PPDO/0.2%GO sliding-lock stents is 0.155 ± 0.018 N/mm (p = 0.0008), and 0.177 ± 0.023 N/mm for PPDO/0.5%GO sliding-lock stents (p = 0.0001), indicating a statistically significant difference compared to PPDO stents (0.084 ± 0.010 N/mm). This enhancement may result from the reinforcement of the mechanical properties of PPDO by GO. Figure 5e–g presents the surface morphology of PPDO/GO sliding-lock stents. All surfaces appear flat and contain some small pores, and the number and size of the pores increase with the increase of GO content.

Vascular stents are one of the medical devices that are directly in contact with blood; hence, the hemocompatibility of PPDO/GO stents needs to be evaluated to avoid hemolysis and thrombosis. During hemolysis, RBCs rupture; free hemoglobin, intracellular components, and pro-thrombotic substances are released into the plasma, activating the coagulation cascade and leading to thrombosis.[92] According to the ISO 10993-4 standard, a hemolysis rate lower than 5% is acceptable for blood-contacting biomaterials. Results of the hemolysis test (Figure 6a and b) revealed that the hemolysis rates of all samples are below 1%, indicating that PPDO/GO stents are acceptable and do not cause hemolysis.

After adherence to the stent surface, platelets can be activated and aggregate, causing thrombosis, inflammation, and even restenosis.[93,94] Therefore, it is essential to evaluate the level of platelet adhesion of PPDO/GO stents. With the incorporation of GO, the quantity of adhered platelets decreases. According to Figure 6c, the number of adhered platelets per unit area for PPDO/0.2%GO and PPDO/0.5%GO are 6853.25 ± 1237.32 and 4405.66 ± 1207.06 mm^{-2}, respectively, and are significantly lower than that of pristine PPDO (12346.72 ± 1225.30 mm^{-2}). Additionally, there is a significant statistical difference between the PPDO/0.2% and PPDO/0.5% groups. The SEM images (Figure 6d–f) also demonstrate the trend of a smaller quantity of adhered platelets with the increase of GO content. The adhered platelets in all groups demonstrate a round shape without protruded pseudopodia, suggesting a non-activated state. GO introduces a large number of hydrophilic groups, which conduce albumin adsorption and competitively inhibit fibrinogen adsorption. This forms a protective layer on the surface of the material to prevent the direct contact of platelets, thus reducing the adhesion and activation of platelets.[95]

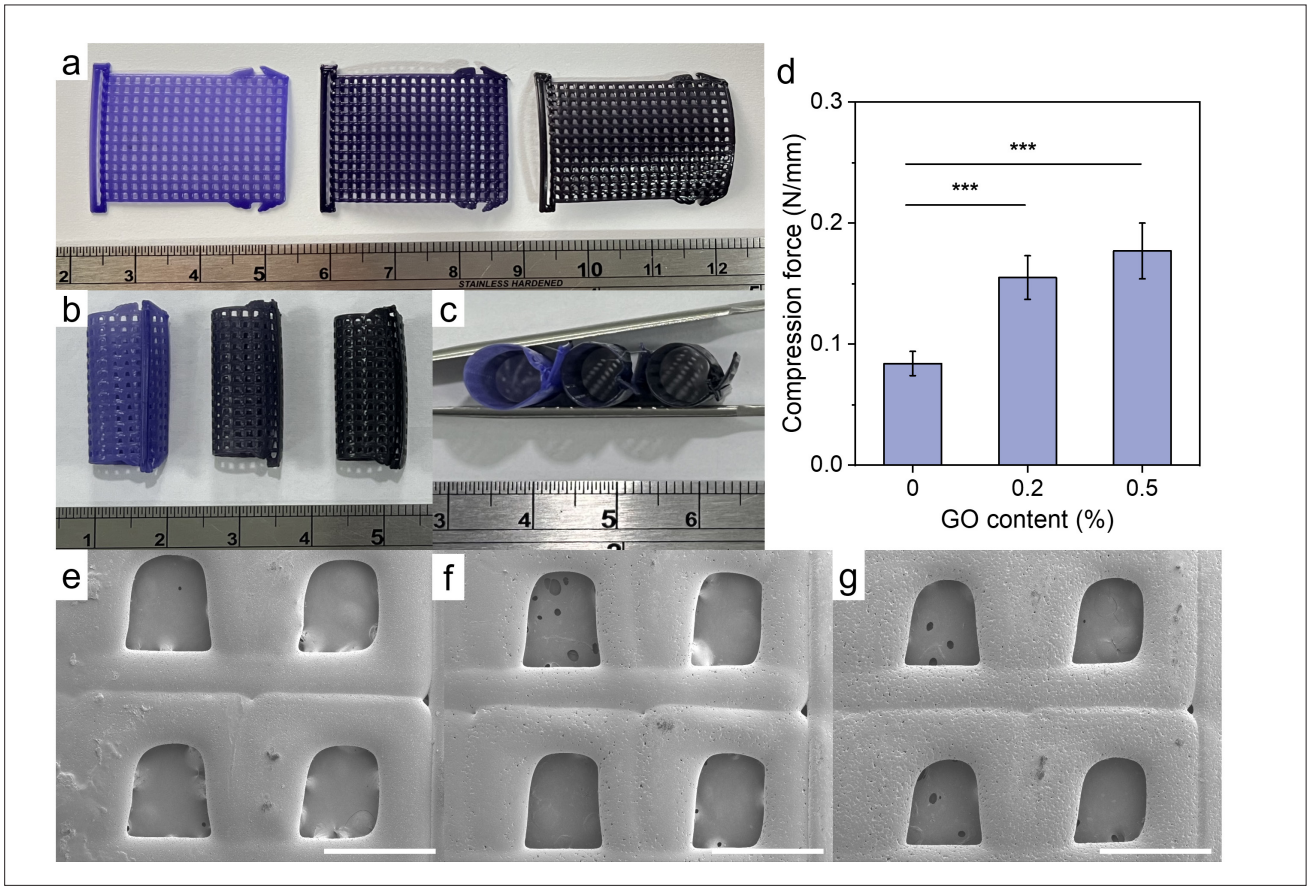

Figure 5. Photos of 3D-printed PPDO/GO and PPDO sliding-lock stents and corresponding compression performance. (a) 3D-printed PPDO/GO and PPDO sliding-lock stents in the initial expanding state. (b and c) Front view (b) and top view (c) of PPDO/GO and PPDO sliding-lock stents in the locked state. From left to right: PPDO, PPDO/0.2%GO, and PPDO/0.5%GO stents, respectively. (d) Compression force of PPDO/GO and PPDO sliding-lock stents measured by parallel plate compression test. ***$p < 0.001$. (e–g) SEM images of the surface morphology of 3D-printed PPDO/GO and PPDO sliding-lock stents: (e) PPDO; (f) PPDO/0.2%GO; and (g) PPDO/0.5%GO. Scale bars: 1 mm. Abbreviations: GO, graphene oxide; PPDO, poly(*p*-dioxanone); SEM, scanning electron microscopy.

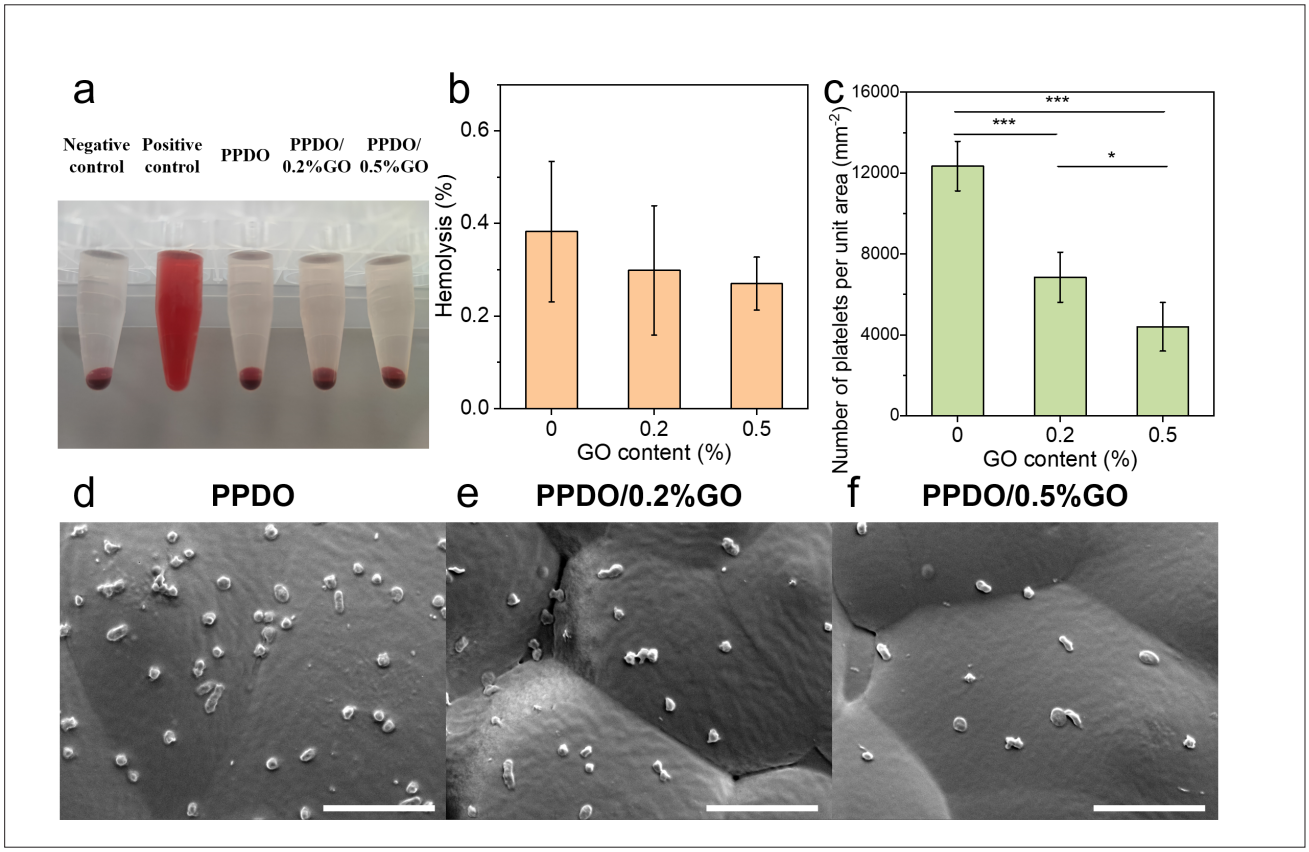

Figure 6. *In vitro* hemocompatibility of PPDO/GO stents. (a) Photograph of hemolysis test. (b) Hemolysis rate of different samples. (c) Number of adhered platelets per unit area on the surface of the stents. *p <0.05, ***p < 0.001. (d–f) SEM images of platelets adhered to the surface of the stents: (d) PPDO; (e) PPDO/0.2%GO; and (f) PPDO/0.5%GO. Scale bars: 20 μm. Abbreviations: GO, graphene oxide; PPDO, poly(p-dioxanone); SEM, scanning electron microscopy.

Stent implantation inevitably damages the endothelium, a physical barrier between blood and vascular tissues that is composed of endothelial cells (ECs). ECs secrete a series of substances, including anticoagulation molecules, nitric oxide, etc., to prevent thrombosis, inflammation, and in-stent restenosis, and to restore vasomotion.[96,97] In order to realize endothelialization, ECs have to adhere and proliferate on the surface of stents. Here, the endothelial cytocompatibility of PPDO/GO stents is evaluated by CCK-8 assay and immunofluorescence staining. After 1, 3, 5, and 7 days of culture with HUVECs, all stents support the adhesion and growth of HUVECs, and the number of cells increases with time (Figure 7a). The HUVECs on all stents display a typical cobblestone morphology with large nuclei and normal cytoskeleton organization (Figure 7b). According to the quantitative results of the CCK-8 assay and fluorescence images (Figure 7a–c), there is a significant statistical difference in the number of HUVECs after 1, 3, 5, and 7 days of culture between PPDO/GO and pristine PPDO groups. An increased proliferation rate is also observed in PPDO/GO groups. After 7 days of culture, HUVECs form a confluent layer in PPDO/GO groups (Figure 7b). These results indicate that PPDO/GO stents are not cytotoxic to HUVECs and enhance their adhesion and proliferation. The π-electron cloud of graphene interacts with the hydrophobic cores of proteins, while the high-density oxygen-containing groups of GO bind with serum proteins through electrostatic interactions.[98] Serum proteins, including fibronectin and insulin, directly mediate cell adhesion and morphology.[99] Additionally, the incorporation of GO increases hydrophilicity, which may also contribute to protein loading, thereby enhancing cell adhesion and proliferation. Results of cell count of fluorescence images (Figure 7c) indicate that the number of HUVECs in the PPDO/0.5%GO group is significantly greater than that of the PPDO/0.2%GO group after 3, 5, and 7 days of culture. The proliferation rate of HUVECs also demonstrates a similar trend. This dosage-dependency of GO on cell adhesion and proliferation in a relatively low range of GO content has also been reported in other

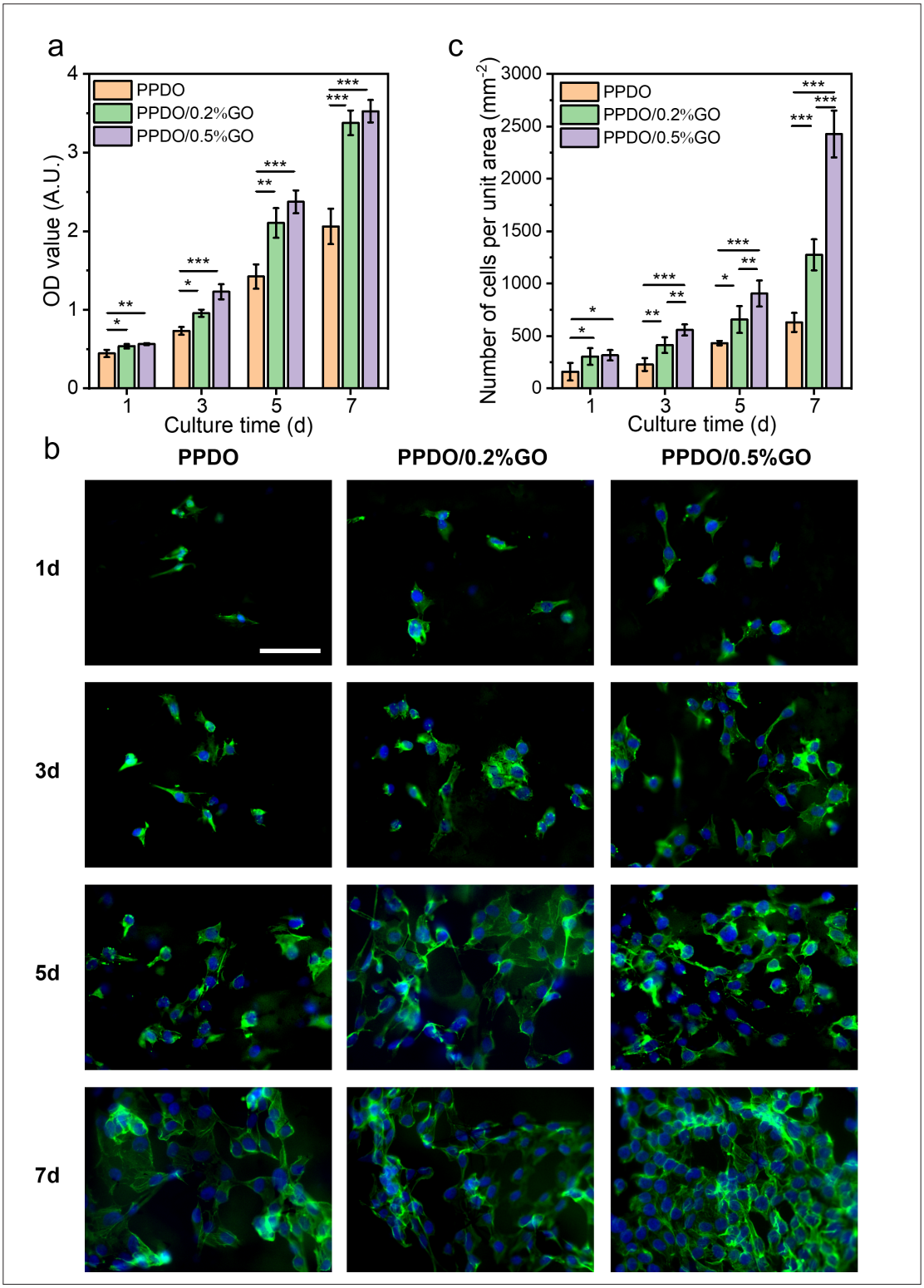

Figure 7. *In vitro* cell viability, proliferation, and morphology of HUVECs cultured on PPDO/GO stents for 1, 3, 5, and 7 days (d). (a) OD value of CCK-8 test. (b) Immunofluorescence images of HUVECs on the surface of PPDO/GO and PPDO stents. Green: actin filaments; blue: nuclei. Scale bar: 75 μm. (c) Number of HUVECs per unit area adhered to the surface of the stents, calculated from the immunofluorescence images. $^{*}p < 0.05$, $^{**}p < 0.01$, $^{***}p < 0.001$. Abbreviations: GO, graphene oxide; HUVEC, human umbilical vein endothelial cells; OD, optical density; PPDO, poly(*p*-dioxanone).

studies,[51,100] one of which discovered that 0.5% GO-incorporated thermoplastic polyurethane presented higher HUVEC attachment and proliferation.[100]

To further evaluate the *in vivo* endothelialization of PPDO/GO materials, 3D-printed PPDO/GO and PPDO filaments were implanted into the abdominal aortas of SD rats. As displayed in Figure 8, the surfaces of all filaments are covered with ECs after 2 weeks of implantation. ECs grew on the surface of the PPDO filament and formed a relatively thin and smooth layer, while the layers of ECs on PPDO/GO filaments are thicker with a morphology of undulating ridges and valleys. This morphology is more significant in the PPDO/0.5%GO group, similar to that of normal endothelium. The H&E staining (Figure 9a–c) revealed that, after implantation in the abdominal aortas of SD rats for 4 weeks, intimal hyperplasia was observed in the surrounding vascular tissues in both PPDO and PPDO/0.5%GO groups. Compared to the PPDO group, there is a larger quantity of CD31-positive cells on the surface of the PPDO/0.5%GO filament (Figure 9d–f), indicating a higher level of endothelialization. These results indicate that PPDO/GO stents can improve endothelialization, especially PPDO/0.5%GO, which can be ascribed to enhanced adhesion and proliferation of HUVECs.

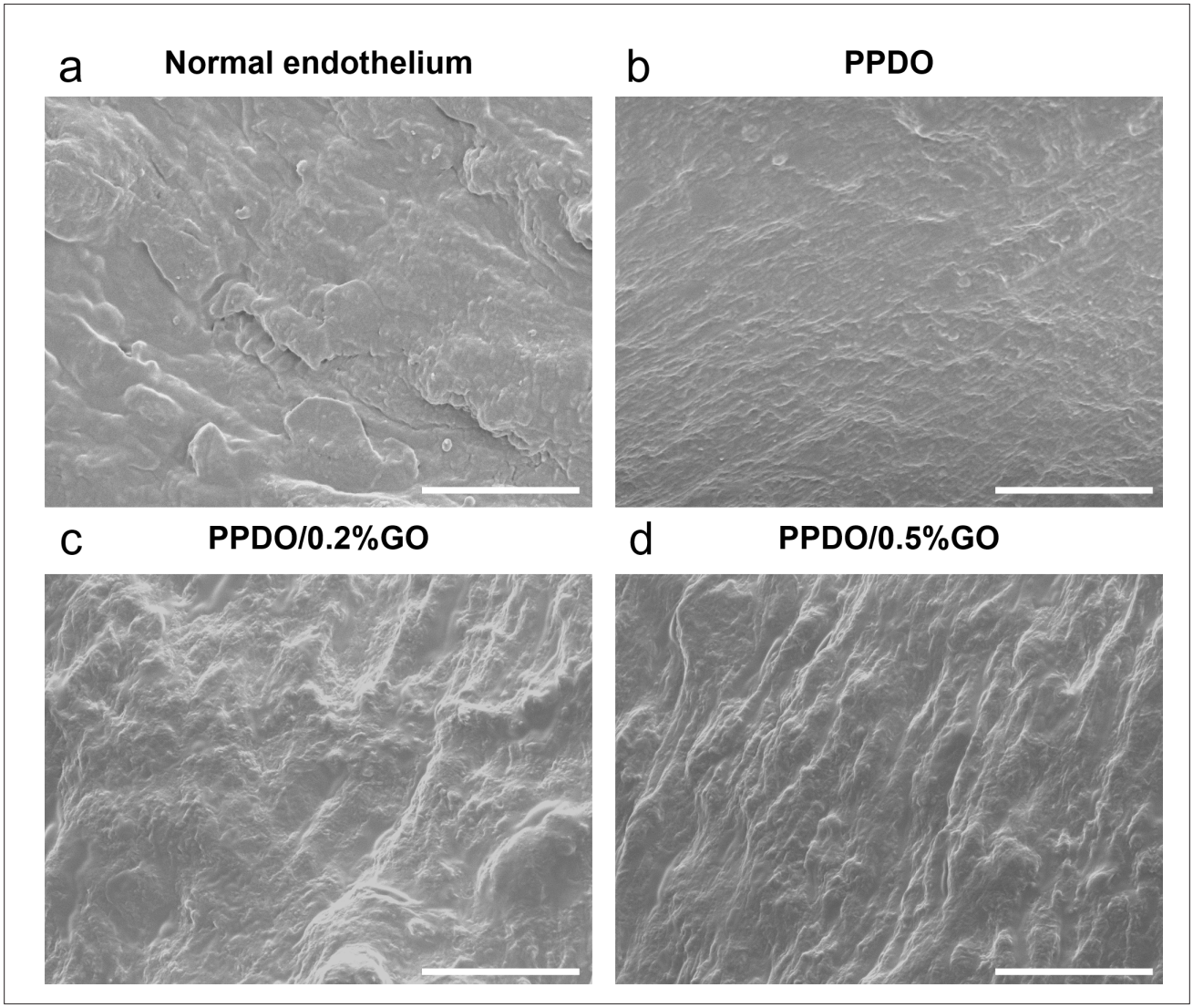

Figure 8. *In vivo* endothelialization evaluation of PPDO/GO stents. (a–d) SEM images of the surface of 3D-printed PPDO/GO and PPDO filaments after 2 weeks of implantation: (a) normal endothelium; (b) PPDO; (c) PPDO/0.2%GO; and (d) PPDO/0.5%GO. Scale bars: 20 μm. Abbreviations: GO, graphene oxide; PPDO, poly(*p*-dioxanone); SEM, Scanning electron microscopy.

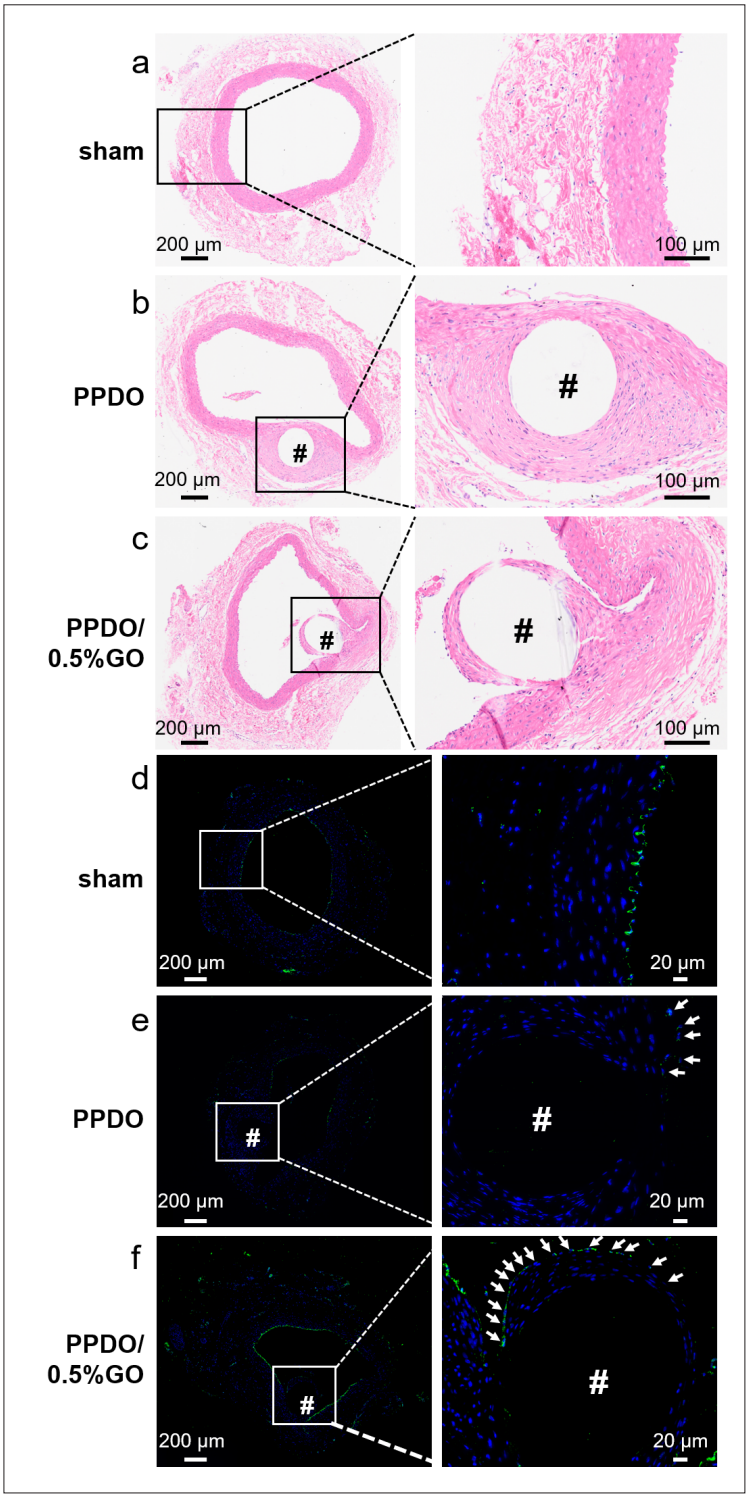

Figure 9. Staining images of the endothelialization evaluation of PPDO/GO stents. (a–c) H&E and (d–f) CD31 staining of the vascular tissues surrounding (b, e) PPDO and (c, f) PPDO/0.5%GO filaments implanted in the abdominal aortas of SD rats for 4 weeks. (a and c) Native abdominal aorta served as the sham group. # represents the implantation location; arrows represent CD31-positive endothelial cells in the neointima. Scale bars: 200 μm (a–c, left; d–f, left); 100 μm (a–c, right); 20 μm (d–f, right). Abbreviations: GO, graphene oxide; H&E, Hematoxylin and eosin; PPDO, poly(p-dioxanone); SD, Sprague–Dawley.

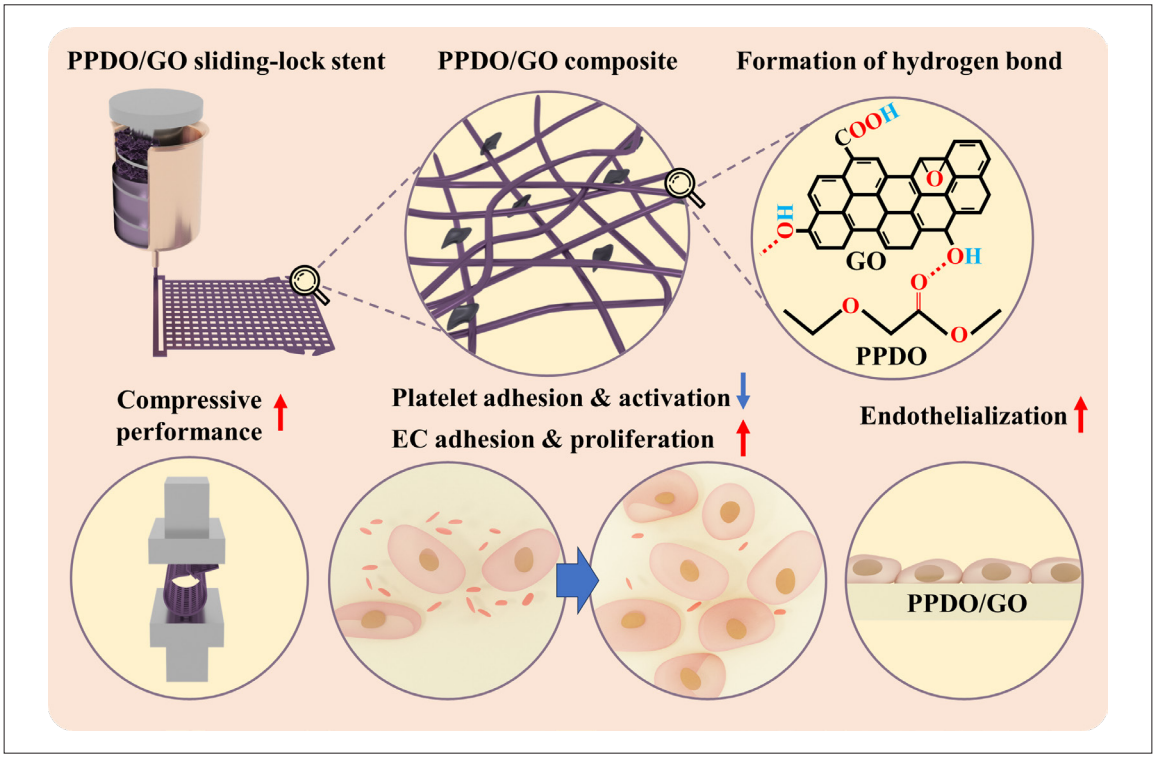

Figure 10. A schematic illustration of the mechanisms of improved PPDO/GO stent performance with GO incorporation. Abbreviations: EC, endothelial cell; GO, graphene oxide; PPDO, poly(p-dioxanone).

3.1. Staining images of the endothelialization evaluation of PPDO/GO stents.

Based on the *in vitro* and *in vivo* results, the possible mechanisms of enhanced PPDO/GO stent performance with GO incorporation are summarized in Figure 10. Incorporating GO introduced a large number of oxygen-containing groups, and the hydroxyl groups of GO formed hydrogen bonds with the carbonyl groups of PPDO, facilitating effective stress transfer from the PPDO matrix to the GO filler. This improved the mechanical properties of PPDO/GO materials, and subsequently enhanced the compressive performance of PPDO/GO sliding-lock stents. These oxygenated hydrophilic groups allow albumin to adsorb onto the surface of the material, forming a protective layer that reduces platelet adhesion and activation.[95] Likewise, these groups bind with serum proteins,[98] promoting HUVEC adhesion and proliferation, thereby enhancing the *in vivo* endothelialization of PPDO/GO materials.

4. Conclusion

This work, for the first time, prepared PPDO/GO composite material and investigated the effect of GO incorporation on the physical, chemical, surface, and mechanical properties of PPDO. 3D-printed PPDO/GO sliding-lock stents displayed improved compression performance and good biocompatibility. PPDO/0.5%GO stent exhibited higher compression force, lower hemolysis rate, reduced platelet adhesion, and enhanced adhesion and proliferation of HUVECs. 3D-printed filament implantation results indicate that PPDO/0.5%GO facilitated *in vivo* endothelialization. Therefore, PPDO/0.5%GO demonstrated the potential for application in BRSs. This study provides an effective approach to improving the mechanical properties and biocompatibility of polymeric BRSs, playing an important role in the treatment of CHD-related vascular stenoses. However, this study has several limitations: the profile of PPDO/GO sliding-lock stents is larger than that of benchmark metallic stents, and the long-term *in vivo* safety and efficacy of PPDO/GO stents remain to be evaluated. Future research will focus on the structural optimization of PPDO/GO sliding-lock stents to reduce the profile, as well as the long-term *in vivo* safety and effects of PPDO/GO sliding-lock stents implanted in rabbits or porcines.

Acknowledgments

None.

Funding

This work was funded by the National Natural Science Foundation of China (grant number 82300344), Shanghai Shenkang Hospital Development Center Program (grant number SHDC22021209), and Xinhua Hospital Affiliated to Shanghai Jiao Tong University School of Medicine-Shanghai Jiao Tong University Institute of Medical Robotics Joint Program (grant number 21XJMR01).

Conflict of interest

The authors declared no conflict of interest.

Author contributions

Conceptualization: Enrong Chen, Xiji Qin, Jing Sun, Kun Sun
Formal analysis: Enrong Chen, Xiji Qin
Funding acquisition: Xuejun Jin, Kun Sun
Investigation: Enrong Chen, Xiji Qin, Zhihui Xiong,
Methodology: Enrong Chen, Xiji Qin, Xiaorong Cai, Zhihui Xiong, Jing Sun
Resources: Xuejun Jin, Jing Sun, Kun Sun
Supervision: Zhihui Xiong, Jing Sun, Kun Sun
Writing – original graft: Enrong Chen, Xiji Qin
Writing – review & editing: Enrong Chen, Xiji Qin, Xiaorong Cai, Zhihui Xiong, Jing Sun

Ethics approval and consent to participate

The animal experiments in this study were approved by the Animal Ethics Committee of Xinhua Hospital Affiliated to Shanghai Jiao Tong University School of Medicine (XHEC-F-2024-079), and all procedures were performed in strict accordance with the regulations of the Animal Ethics Committee of Xinhua Hospital Affiliated to Shanghai Jiao Tong University School of Medicine.

Consent for publication

Not applicable.

Availability of data

Data is available from the corresponding authors upon reasonable request.

References

1. Su Z, Zou Z, Hay SI, et al. Global, regional, and national time trends in mortality for congenital heart disease, 1990–2019: an age-period-cohort analysis for the Global Burden of Disease 2019 study. *eClinicalMedicine.* 2022;43:101249. doi: 10.1016/j.eclinm.2021.101249
2. Liu Y, Chen S, Zühlke L, et al. Global birth prevalence of congenital heart defects 1970–2017: updated systematic review and meta-analysis of 260 studies. *Int J Epidemiol.* 2019;48(2):455-463. doi: 10.1093/ije/dyz009
3. Baerlocher L, Kretschmar O, Harpes P, Arbenz U, Berger F, Knirsch W. Stent implantation and balloon angioplasty for treatment of branch pulmonary artery stenosis in children. *Clin Res Cardiol.* 2008;97(5):310-317. doi: 10.1007/s00392-007-0631-8
4. Balasubramanian S, Marshall AC, Gauvreau K, et al. Outcomes after stent implantation for the treatment of congenital and postoperative pulmonary vein stenosis in children. *Circ Cardiovasc Interv.* 2012;5(1):109-117. doi: 10.1161/CIRCINTERVENTIONS.111.964189
5. Forbes TJ, Kim DW, Du W, et al. Comparison of surgical, stent, and balloon angioplasty treatment of native coarctation of the aorta. *J Am Coll Cardiol.* 2011;58(25):2664-2674. doi: 10.1016/j.jacc.2011.08.053
6. Lezo JSd, Romero M, Pan M, et al. Stent repair for complex coarctation of aorta. *J Am Coll Cardiol Intv.* 2015;8(10): 1368-1379. doi: 10.1016/j.jcin.2015.05.018
7. Moore JW, Spicer RL, Perry JC, et al. Percutaneous use of stents to correct pulmonary artery stenosis in young children after cavopulmonary anastomosis. *Am Heart J.* 1995;130(6):1245-1249. doi: 10.1016/0002-8703(95)90149-3
8. Ing F. Stents: what's available to the pediatric interventional cardiologist? *Catheter Cardiovasc Interv.* 2002;57(3): 374-386. doi: 10.1002/ccd.10342
9. Wiebe J, Nef HM, Hamm CW. Current status of bioresorbable scaffolds in the treatment of coronary artery disease. *J Am Coll Cardiol.* 2014;64(23):2541-2551. doi: 10.1016/j.jacc.2014.09.041
10. McMahon S, Bertollo N, Cearbhaill EDO, et al. Bio-resorbable polymer stents: a review of material progress and prospects. *Prog Polymer Sci.* 2018;83:79-96. doi: 10.1016/j.progpolymsci.2018.05.002
11. Sotomi Y, Onuma Y, Collet C, et al. Bioresorbable scaffold. *Circ Res.* 2017;120(8):1341-1352. doi: 10.1161/CIRCRESAHA.117.310275
12. Shibbani K, De Lima e Silva Bagno L, Poulin M-F, et al. Preclinical comparative assessment of a dedicated pediatric poly-L-lactic-acid-based bioresorbable scaffold with a low-profile bare metal stent. *Catheter Cardiovasc Interv.* 2020;96(4):878-888. doi: 10.1002/ccd.28893
13. Wright J, Nguyen A, D'Souza N, et al. Bioresorbable stent to manage congenital heart defects in children. *Materialia.* 2021;16:101078. doi: 10.1016/j.mtla.2021.101078
14. Bowen PK, Guillory RJ, Shearier ER, et al. Metallic zinc exhibits optimal biocompatibility for bioabsorbable

endovascular stents. *Mater Sci Eng C Mater Biol Appl.* 2015;56:467-472.
doi: 10.1016/j.msec.2015.07.022

15. Sun L, Li J-j, Xu Y-k, Xie Y-m, Wang S-s, Zhang Z-w. Initial status and 3-month results relating to the use of biodegradable nitride iron stents in children and the evaluation of right ventricular function. *Front Cardiovasc Med.* 2022;9:914370.
doi: 10.3389/fcvm.2022.914370

16. Veeram Reddy SR, Welch TR, Nugent AW. Biodegradable stent use for congenital heart disease. *Prog Pediatr Cardiol.* 2021;61:101349.
doi: 10.1016/j.ppedcard.2021.101349

17. Ormiston JA, Serruys PWS. Bioabsorbable coronary stents. *Circ Cardiovasc Intervent.* 2009;2(3):255-260.
doi: 10.1161/CIRCINTERVENTIONS.109.859173

18. Ang HY, Huang YY, Lim ST, Wong P, Joner M, Foin N. Mechanical behavior of polymer-based vs. metallic-based bioresorbable stents. *J Thorac Dis.* 2017;9(Suppl 9):s923-s934.
doi: 10.21037/jtd.2017.06.30

19. Sousa AM, Amaro AM, Piedade AP. 3D printing of polymeric bioresorbable stents: a strategy to improve both cellular compatibility and mechanical properties. *Polymers (Basel).* 2022;14(6):1099.
doi: 10.3390/polym14061099.

20. Bratincsak A, Moore JW, Gulker B, Choules B, Koren L, El-Said HG. Breaking the limit: mechanical characterization of overexpanded balloon expandable stents used in congenital heart disease. *Congenit Heart Dis.* 2015;10(1):51-63.
doi: 10.1111/chd.12175

21. Yasmin F, Vafadar A, Tolouei-Rad M. Application of additive manufacturing in the development of polymeric bioresorbable cardiovascular stents: a review. *Adv Mater Technol.* 2024;2400210.
doi: 10.1002/admt.202400210

22. Martins JA, Lach AA, Morris HL, Carr AJ, Mouthuy P-A. Polydioxanone implants: a systematic review on safety and performance in patients. *J Biomater Appl.* 2020;34(7):902-916.
doi: 10.1177/0885328219888841

23. Zamiri P, Kuang Y, Sharma U, et al. The biocompatibility of rapidly degrading polymeric stents in porcine carotid arteries. *Biomaterials.* 2010;31(31):7847-7855.
doi: 10.1016/j.biomaterials.2010.06.057

24. Zhao F, Xue W, Wang F, et al. Braided bioresorbable cardiovascular stents mechanically reinforced by axial runners. *J Mech Behav Biomed Mater.* 2019;89:19-32.
doi: 10.1016/j.jmbbm.2018.09.003

25. Sun J, Sun K, Bai K, et al. Oversized composite braided biodegradable stents with post-dilatation for pediatric applications: mid-term results of a porcine study. *Biomater Sci.* 2020;8(18):5183-5195.
doi: 10.1039/d0bm00567c

26. Vahabli E, Mann J, Heidari BS, et al. The technological advancement to engineer next-generation stent-grafts: design, material, and fabrication techniques. *Adv Healthc Mater.* 2022;11(13):2200271.
doi: 10.1002/adhm.202200271

27. Wang L, Jiao L, Pang S, Yan P, Wang X, Qiu T. The development of design and manufacture techniques for bioresorbable coronary artery stents. *Micromachines.* 2021;12(8):990.
doi: 10.3390/mi12080990

28. Rebelo R, Vila N, Fangueiro R, Carvalho S, Rana S. Influence of design parameters on the mechanical behavior and porosity of braided fibrous stents. *Mater Design.* 2015;86:237-247.
doi: 10.1016/j.matdes.2015.07.051

29. Khalaj R, Tabriz AG, Okereke MI, Douroumis D. 3D printing advances in the development of stents. *Int J Pharm.* 2021;609:121153.
doi: 10.1016/j.ijpharm.2021.121153

30. Ng WL, An J, Chua CK. Process, material, and regulatory considerations for 3D printed medical devices and tissue constructs. *Engineering.* 2024;36:146-166.
doi: 10.1016/j.eng.2024.01.028

31. van Lith R, Baker E, Ware H, et al. 3D-printing strong high-resolution antioxidant bioresorbable vascular stents. *Adv Mater Technol.* 2016;1(9):1600138.
doi: 10.1002/admt.201600138

32. Ware HOT, Farsheed AC, Van Lith R, Baker E, Ameer G, Sun C. Process development for high-resolution 3D-printing of bioresorbable vascular stents. Paper presented at: Conference on Advanced Fabrication Technologies for Micro/Nano Optics and Photonics X; Jan 29-Feb 01, 2017; San Francisco, CA.
doi: 10.1117/12.2252856

33. Flege C, Vogt F, Höges S, et al. Development and characterization of a coronary polylactic acid stent prototype generated by selective laser melting. *J Mater Sci Mater Med.* 2013;24(1):241-255.
doi: 10.1007/s10856-012-4779-z

34. Li JF, Ye WY, Fan ZY, Lu ZQ. Stereocomplex poly(lactic acid) vascular stents by 3D-printing with long chain branching structures: toward desirable crystallization properties and mechanical performance. *Polym Adv Technol.* 2021;32(1): 97-110.
doi: 10.1002/pat.5064

35. Misra SK, Ostadhossein F, Babu R, et al. 3D-printed multidrug-eluting stent from graphene-nanoplatelet-doped biodegradable polymer composite. *Adv Healthc Mater.* 2017;6(11).
doi: 10.1002/adhm.201700008

36. Guerra A, Roca A, de Ciurana J. A novel 3D additive manufacturing machine to biodegradable stents. Paper presented at: 7th Manufacturing-Engineering-Society International Conference (MESIC); Jun 28-30, 2017; Vigo, Spain.

37. Kim TH, Lee JH, Ahn CB, Hong JH, Son KH, Lee JW. Development of a 3D-printed drug-eluting stent for treating obstructive salivary gland disease. *ACS Biomater Sci Eng.* 2019;5(7):3572-3581.
doi: 10.1021/acsbiomaterials.9b00636

38. Lu J, Hu X, Yuan T, et al. 3D-printed poly (P-Dioxanone) stent for endovascular application: in vitro evaluations. *Polymers.* 2022;14(9):1755.
doi: 10.3390/polym14091755

39. Feng Q, Jiang W, Sun K, et al. Mechanical properties and in vivo performance of a novel sliding-lock bioabsorbable poly-p-dioxanone stent. *J Mater Sci: Mater Med.* 2011;22(10):2319.
doi: 10.1007/s10856-011-4407-3

40. Wu S, Qi Y, Shi W, Kuss M, Chen S, Duan B. Electrospun conductive nanofiber yarns for accelerating mesenchymal stem cells differentiation and maturation into Schwann cell-like cells under a combination of electrical stimulation and chemical induction. *Acta Biomater.* 2022;139:91-104.
doi: 10.1016/j.actbio.2020.11.042

41. Zhu L, Liang K, Ji Y. Prominent reinforcing effect of chitin nanocrystals on electrospun polydioxanone nanocomposite fiber mats. *J Mech Behav Biomed Mater.* 2015;44:35-42.
doi: 10.1016/j.jmbbm.2014.12.019

42. Shiroud Heidari B, Lopez EM, Chen P, et al. Silane-modified hydroxyapatite nanoparticles incorporated into polydioxanone/poly(lactide-co-caprolactone) creates a novel toughened nanocomposite with improved material properties and in vivo inflammatory responses. *Mater Today Bio.* 2023;22:100778.
doi: 10.1016/j.mtbio.2023.100778

43. Suk JW, Piner RD, An J, Ruoff RS. Mechanical properties of monolayer graphene oxide. *ACS Nano.* 2010;4(11):6557-6564.
doi: 10.1021/nn101781v

44. Cao C, Daly M, Singh CV, Sun Y, Filleter T. High strength measurement of monolayer graphene oxide. *Carbon.* 2015;81:497-504.
doi: 10.1016/j.carbon.2014.09.082

45. Fu X, Lin J, Liang Z, et al. Graphene oxide as a promising nanofiller for polymer composite. *Surf Interfaces.* 2023;37:102747.
doi: 10.1016/j.surfin.2023.102747

46. Shuai C, Peng B, Feng P, Yu L, Lai R, Min A. In situ synthesis of hydroxyapatite nanorods on graphene oxide nanosheets and their reinforcement in biopolymer scaffold. *J Adv Res.* 2022;35:13-24.
doi: 10.1016/j.jare.2021.03.009

47. Raslan A, Saenz del Burgo L, Ciriza J, Pedraz JL. Graphene oxide and reduced graphene oxide-based scaffolds in regenerative medicine. *Int J Pharma.* 2020;580:119226.
doi: 10.1016/j.ijpharm.2020.119226

48. Sahafnejad-Mohammadi I, Rahmati S, Najmoddin N, Bodaghi M. Biomimetic polycaprolactone-graphene oxide composites for 3D printing bone scaffolds. *Macromol Mater Eng.* 2023;308(5):2200558.
doi: 10.1002/mame.202200558

49. Jana S. Endothelialization of cardiovascular devices. *Acta Biomater.* 2019;99:53-71.
doi: 10.1016/j.actbio.2019.08.042

50. Wang W, Lin S, Ye Z, et al. Electrospun egg white protein/polyvinyl alcohol/graphene oxide fibrous wound dressing: Fabrication, antibacterial, cytocompatibility and wound healing assay. *Colloids Surf A: Physicochem Eng Aspects.* 2023;658:130658.
doi: 10.1016/j.colsurfa.2022.130658

51. Wang Y, Wu Y, Zhang Y, et al. Graphene oxide coated three-dimensional printed biphasic calcium phosphate scaffold for angiogenic and osteogenic synergy in repairing critical-size bone defect. *J Mater Sci Technol.* 2023;145:25-39.
doi: 10.1016/j.jmst.2022.10.016

52. Henriques PC, Pereira AT, Pires AL, Pereira AM, Magalhães FD, Gonçalves IC. Graphene surfaces interaction with proteins, bacteria, mammalian cells, and blood constituents: the impact of graphene platelet oxidation and thickness. *ACS Appl Mater Interf.* 2020;12(18):21020-21035.
doi: 10.1021/acsami.9b21841

53. Zhao Z, Zong L, Liu C, et al. Dual strengthened corrosion control of biodegradable coating on magnesium alloy for vascular stent application. *Prog Organic Coat.* 2023;174:107297.
doi: 10.1016/j.porgcoat.2022.107297

54. Chen E, Xiong Z, Cai X, et al. Bioresorbable PPDO sliding-lock stents with optimized FDM parameters for congenital heart disease treatment. *J Mech Behav Biomed Mater.* 2023;138:105609.
doi: 10.1016/j.jmbbm.2022.105609

55. Davis CS, Hillgartner KE, Han SH, Seppala JE. Mechanical strength of welding zones produced by polymer extrusion additive manufacturing. *Addit Manuf.* 2017;16:162-166.
doi: 10.1016/j.addma.2017.06.006

56. Sofińska K, Barbasz J, Witko T, et al. Structural, topographical, and mechanical characteristics of purified polyhydroxyoctanoate polymer. *J Appl Polymer Sci.* 2019;136(4):47192.
doi: 10.1002/app.47192

57. Niu R, Gong J, Xu D, Tang T, Sun Z-Y. Influence of molecular weight of polymer matrix on the structure and rheological properties of graphene oxide/polydimethylsiloxane composites. *Polymer.* 2014;55(21):5445-5453.
doi: 10.1016/j.polymer.2014.08.056

58. Yang W, Zhong Y, He C, et al. Electrostatic self-assembly of pFe3O4 nanoparticles on graphene oxide: a co-dispersed nanosystem reinforces PLLA scaffolds. *J Adv Res.* 2020;24:191-203.
doi: 10.1016/j.jare.2020.04.009

59. Li Z, Deng L, Kinloch IA, Young RJ. Raman spectroscopy of carbon materials and their composites:

graphene, nanotubes and fibres. *Prog Mater Sci.* 2023; 135:101089.
doi: 10.1016/j.pmatsci.2023.101089

60. Loskot J, Jezbera D, Bezrouk A, et al. Raman spectroscopy as a novel method for the characterization of polydioxanone medical stents biodegradation. *Materials* (Basel). 2021;14(18):5462.
doi: 10.3390/ma14185462

61. Zainy M, Huang NM, Vijay Kumar S, Lim HN, Chia CH, Harrison I. Simple and scalable preparation of reduced graphene oxide–silver nanocomposites via rapid thermal treatment. *Mater Lett.* 2012;89:180-183.
doi: 10.1016/j.matlet.2012.08.101

62. Zheng Y, Zhou J, Du F, et al. Formation of mesomorphic polymorph, thermal-induced phase transition, and crystalline structure-dependent degradable and mechanical properties of poly(p-dioxanone). *Crystal Growth Design.* 2019;19(1):166-176.
doi: 10.1021/acs.cgd.8b01246

63. Ren P-G, Yan D-X, Ji X, Chen T, Li Z-M. Temperature dependence of graphene oxide reduced by hydrazine hydrate. *Nanotechnology.* 2011;22(5):055705.
doi: 10.1088/0957-4484/22/5/055705

64. Joy A, Unnikrishnan G, Megha M, et al. Hybrid gold/graphene oxide reinforced polycaprolactone nanocomposite for biomedical applications. *Surf Interfaces.* 2023;40:103000.
doi: 10.1016/j.surfin.2023.103000

65. Du Y, Xing L, Hou P, et al. Dual stimulus response mechanical properties tunable biodegradable and biocompatible PLCL/PPDO based shape memory composites. *Colloids Surf A: Physicochem Eng Aspects.* 2022;648:129244.
doi: 10.1016/j.colsurfa.2022.129244

66. Qian Y, Li C, Qi Y, Zhong J. 3D printing of graphene oxide composites with well controlled alignment. *Carbon.* 2021;171:777-784.
doi: 10.1016/j.carbon.2020.08.077

67. Zheng Y, Ashizawa M, Zhang S, et al. Tuning the mechanical properties of a polymer semiconductor by modulating hydrogen bonding interactions. *Chem Mater.* 2020;32(13):5700-5714.
doi: 10.1021/acs.chemmater.0c01437

68. Wang R, Xu H, Cheng S, et al. Ultrahigh-energy-density dielectric materials from ferroelectric polymer/glucose all-organic composites with a cross-linking network of hydrogen bonds. *Energy Storage Mater.* 2022;49:339-347.
doi: 10.1016/j.ensm.2022.04.028

69. Cheng X, Kumar V, Yokozeki T, et al. Highly conductive graphene oxide/polyaniline hybrid polymer nanocomposites with simultaneously improved mechanical properties. *Compos Part A: Appl Sci Manuf.* 2016;82:100-107.
doi: 10.1016/j.compositesa.2015.12.006

70. Zhong J, Gao S, Xue G, Wang B. Study on enhancement mechanism of conductivity induced by graphene oxide for polypyrrole nanocomposites. *Macromolecules.* 2015;48(5):1592-1597.
doi: 10.1021/ma502449k

71. Huang X, Nakagawa S, Houjou H, Yoshie N. Insights into the role of hydrogen bonds on the mechanical properties of polymer networks. *Macromolecules.* 2021;54(9):4070-4080.
doi: 10.1021/acs.macromol.1c00120

72. Chen Q, Mangadlao JD, Wallat J, De Leon A, Pokorski JK, Advincula RC. 3D printing biocompatible polyurethane/poly(lactic acid)/graphene oxide nanocomposites: anisotropic properties. *ACS Appl Mater Interfaces.* 2017;9(4):4015-4023.
doi: 10.1021/acsami.6b11793

73. Sun N, Di M, Liu Y. Lignin-containing polyurethane elastomers with enhanced mechanical properties via hydrogen bond interactions. *Int J Biol Macromol.* 2021;184:1-8.
doi: 10.1016/j.ijbiomac.2021.06.038

74. Wang F, Yang Z, Li J, Zhang C, Sun P. Bioinspired polyurethane using multifunctional block modules with synergistic dynamic bonds. *ACS Macro Lett.* 2021;10(5): 510-517.
doi: 10.1021/acsmacrolett.1c00054

75. Peng H, Du X, Cheng X, Wang H, Du Z. Room-temperature self-healable and stretchable waterborne polyurethane film fabricated via multiple hydrogen bonds. *Prog Organic Coat.* 2021;151:106081.
doi: 10.1016/j.porgcoat.2020.106081

76. Abdullah SI, Ansari MNM. Mechanical properties of graphene oxide (GO)/epoxy composites. *HBRC J.* 2015;11(2):151-156.
doi: 10.1016/j.hbrcj.2014.06.001

77. Forati T, Atai M, Rashidi AM, Imani M, Behnamghader A. Physical and mechanical properties of graphene oxide/polyethersulfone nanocomposites. *Polym Adv Technol.* 2014;25(3):322-328.
doi: 10.1002/pat.3243

78. Mianehrow H, Lo Re G, Carosio F, et al. Strong reinforcement effects in 2D cellulose nanofibril-graphene oxide (CNF-GO) nanocomposites due to GO-induced CNF ordering. *J Mater Chem A.* 2020;8(34):17608-17620.
doi: 10.1039/d0ta04406g

79. Wan CY, Chen BQ. Reinforcement and interphase of polymer/graphene oxide nanocomposites. *J Mater Chem.* 2012;22(8):3637-3646.
doi: 10.1039/c2jm15062j

80. Wang H, Li Z, Zuo M, et al. Stretchable, freezing-tolerant conductive hydrogel for wearable electronics reinforced by cellulose nanocrystals toward multiple hydrogen bonding. *Carbohydr Polym.* 2022;280:119018.

doi: 10.1016/j.carbpol.2021.119018

81. Wang J, Jin X, Li C, Wang W, Wu H, Guo S. Graphene and graphene derivatives toughening polymers: toward high toughness and strength. *Chem Eng J.* 2019;370:831-854. doi: 10.1016/j.cej.2019.03.229

82. Quaresimin M, Schulte K, Zappalorto M, Chandrasekaran S. Toughening mechanisms in polymer nanocomposites: from experiments to modelling. *Compos Sci Technol.* 2016;123:187-204. doi: 10.1016/j.compscitech.2015.11.027

83. Yang F, Lin Y, Shen S, Gu Y, Shuai C, Feng P. Polydopamine chelating strontium on graphene oxide enhances the mechanical and osteogenic induction properties of PLLA/PGA bone scaffold. *IJB.* 2024;10(3):1829. doi: 10.36922/ijb.1829

84. Singh G, Divakar Botcha V, Sutar DS, Talwar SS, Srinivasa RS, Major SS. Graphite mediated reduction of graphene oxide monolayer sheets. *Carbon.* 2015;95:843-851. doi: 10.1016/j.carbon.2015.08.067

85. Ortiz M, Rosales-Ibáñez R, Pozos-Guillén A, et al. DPSC colonization of functionalized 3D textiles. *J Biomed Mater Res B: Appl Biomater.* 2017;105(4):785-794. doi: 10.1002/jbm.b.33609

86. Zhu Y, Gao C, Liu X, Shen J. Surface modification of polycaprolactone membrane via aminolysis and biomacromolecule immobilization for promoting cytocompatibility of human endothelial cells. *Biomacromolecules.* 2002;3(6):1312-1319. doi: 10.1021/bm020074y

87. An N, Schedle A, Wieland M, Andrukhov O, Matejka M, Rausch-Fan X. Proliferation, behavior, and cytokine gene expression of human umbilical vascular endothelial cells in response to different titanium surfaces. *J Biomed Mater Res A.* 2010;93A(1):364-372. doi: 10.1002/jbm.a.32539

88. Arrigo R, Frache A. FDM printability of PLA based-materials: the key role of the rheological behavior. *Polymers (Basel).* 2022;14(9):1754. doi: 10.3390/polym14091754

89. Tabriz AG, Scoutaris N, Gong Y, Hui H-W, Kumar S, Douroumis D. Investigation on hot melt extrusion and prediction on 3D printability of pharmaceutical grade polymers. *Int J Pharma.* 2021;604:120755. doi: 10.1016/j.ijpharm.2021.120755

90. Scaffaro R, Maio A. Optimization of two-step techniques engineered for the preparation of polyamide 6 graphene oxide nanocomposites. *Compos B: Eng.* 2019;165:55-64. doi: 10.1016/j.compositesb.2018.11.107

91. Garcia-Villen F, López-Zárraga F, Viseras C, et al. Three-dimensional printing as a cutting-edge, versatile and personalizable vascular stent manufacturing procedure: Toward tailor-made medical devices. *Int J Bioprint.* 2023;9(2):664. doi: 10.18063/ijb.v9i2.664

92. Meng X, Cheng Y, Wang P, et al. Enhanced hemocompatibility of a direct chemical vapor deposition-derived graphene film. *ACS Appl Mater Interfaces.* 2021;13(4):4835-4843. doi: 10.1021/acsami.0c19790

93. Jaffer IH, Fredenburgh JC, Hirsh J, Weitz JI. Medical device-induced thrombosis: what causes it and how can we prevent it? *J Thromb Haemost.* 2015;13(S1):S72-S81. doi: 10.1111/jth.12961

94. Breton HL, Plow EF, Topol EJ. Role of platelets in restenosis after percutaneous coronary revascularization. *J Am Coll Cardiol.* 1996;28(7):1643-1651. doi: 10.1016/S0735-1097(96)00417-2

95. Pan C, Xu R, Chen J, Zhang Q, Deng L, Hong Q. A CO-releasing coating based on carboxymethyl chitosan-functionalized graphene oxide for improving the anticorrosion and biocompatibility of magnesium alloy stent materials. *Int J Biol Macromol.* 2024;271:132487. doi: 10.1016/j.ijbiomac.2024.132487

96. Liu W, Wang XY, Feng YK. Restoring endothelial function: shedding light on cardiovascular stent development. *Biomater Sci.* 2023;11(12):4132-4150. doi: 10.1039/d3bm00390f

97. Wang X, Fang F, Ni Y, et al. The combined contribution of vascular endothelial cell migration and adhesion to stent re-endothelialization. *Front Cell Dev Biol.* 2021;9:641382. doi: 10.3389/fcell.2021.641382

98. Yoon HH, Bhang SH, Kim T, Yu T, Hyeon T, Kim B-S. Dual roles of graphene oxide in chondrogenic differentiation of adult stem cells: cell-adhesion substrate and growth factor-delivery carrier. *Adv Funct Mater.* 2014;24(41):6455-6464. doi: 10.1002/adfm.201400793

99. Lee WC, Lim CHYX, Shi H, et al. Origin of enhanced stem cell growth and differentiation on graphene and graphene oxide. *ACS Nano.* 2011;5(9):7334-7341. doi: 10.1021/nn202190c

100. Jing X, Mi H-Y, Salick MR, Cordie TM, Peng X-F, Turng L-S. Electrospinning thermoplastic polyurethane/graphene oxide scaffolds for small diameter vascular graft applications. *Mater Sci Eng C.* 2015;49:40-50. doi: 10.1016/j.msec.2014.12.060

ACCSCIENCE PUBLISHING

International Journal of Bioprinting

RESEARCH ARTICLE

3D-printed scaffold of dopamine methacrylate oligomer grafted on PEGDMA incorporated with collagen hydrolysate for engineering cartilage tissue

Kitipong Pasanaphong[1], Acharee Suksuwan[2], Narongrit Srikaew[3], Ruedee Hemstapat[4], Tulyapruek Tawonsawatruk[5], Sutee Wangtueai[6], Nanthaphong Khamthong[7], Sani Boonyagul[1], Phavit Wongsirichot[8], and Nuttapol Tanadchangsaeng[1]*

[1]College of Biomedical Engineering, Rangsit University, Pathum Thani, Thailand

[2]The Halal Science Center, Chulalongkorn University, Bangkok, Thailand

[3]Research Center, Faculty of Medicine Ramathibodi Hospital, Mahidol University, Bangkok, Thailand

[4]Department of Pharmacology, Faculty of Science, Mahidol University, Bangkok, Thailand

[5]Department of Orthopaedics, Faculty of Medicine Ramathibodi Hospital, Mahidol University, Bangkok, Thailand

[6]School of Agro-Industry, Faculty of Agro-Industry, Chiang Mai University, Chiang Mai, Thailand

[7]College of Oriental Medicine, Rangsit University, Pathum Thani, Thailand

[8]Department of Chemical Engineering, The University of Manchester, Manchester, United Kingdom

***Corresponding author:**
Nuttapol Tanadchangsaeng
(nuttapol.t@rsu.ac.th)

Citation: Pasanaphong K, Suksuwan A, Srikaew N, et al. 3D-printed scaffold of dopamine methacrylate oligomer grafted on PEGDMA incorporated with collagen hydrolysate for engineering cartilage tissue. *Int J Bioprint.* 2024;10(6):4385. doi: 10.36922/ijb.4385

Received: July 30, 2024
Revised: August 27, 2024
Accepted: September 5, 2024
Published Online: September 5, 2024

Copyright: © 2024 Author(s). This is an Open Access article distributed under the terms of the Creative Commons Attribution License, permitting distribution, and reproduction in any medium, provided the original work is properly cited.

Publisher's Note: AccScience Publishing remains neutral with regard to jurisdictional claims in published maps and institutional affiliations.

Abstract

This study demonstrated the synthesis and characterization of dopamine methacrylate (DMA), oligomers of dopamine methacrylate (ODMA), and their integration with polyethylene glycol dimethacrylate (PEGDMA) to enhance 3D-printing scaffold fabrication for tissue engineering, using digital light processing (DLP) technology. The results confirm the successful synthesis of DMA, as evidenced by nuclear magnetic resonance (NMR) and Fourier transform infrared spectroscopy (FTIR) analysis and its subsequent conversion to ODMA. The obtained ODMA was then combined with PEGDMA (1.25–10% w/v ODMA) to optimize scaffold printability. The morphological characteristics of the ODMA/PEGDMA scaffolds were assessed via scanning electron microscopy (SEM). Furthermore, using FTIR and differential scanning calorimetry (DSC), the chemical stability and biological compatibility of collagen hydrolysate (CH) derived from tuna tendon were studied and compared after sterilization. An *in vitro* fibroblast viability test was conducted using 3-(4,5-dimethylthiazol-2-yl)-2,5-diphenyltetrazolium bromide (MTT) assay to assess the biocompatibility of CH with cells. Sterilization did not adversely affect the chemical composition of CH, maintaining its compatibility with fibroblast cells. Subsequently, ODMA/PEGDMA/CH composite scaffolds were fabricated using a DLP 3D printer, and their efficacy in supporting chondrocyte viability and proliferation were examined at 24, 48, and 72 h using PrestoBlue® assay. Mixing ODMA with PEGDMA significantly enhanced the printability of the scaffolds. Our tri-component 3D-printed scaffolds significantly enhanced human cartilage stem/progenitor cell (CSPC) viability and proliferation compared to a 24-well culture plate. These

scaffolds excel in both mechanical properties, crucial for bearing physiological loads, and biological properties that promote cell growth and proliferation. This dual enhancement underscores their superior performance and positions them as frontrunners in the development of advanced solutions for cartilage engineering, potentially revolutionizing medical treatments.

Keywords: 3D-printed scaffold; Dopamine methacrylate oligomer; Collagen hydrolysate; Digital light processing 3D printer; Cartilage tissue engineering

1. Introduction

Cartilage regeneration is of great importance in regenerative medicine because cartilage lacks blood vessels, nerves, and a lymphatic system, unlike other tissues in the body, resulting in a severely limited ability to repair itself when damaged.[1] Consequently, injuries to cartilage tissue heal slowly compared to other tissues, often leading to chronic pain and mobility issues for patients.[2] Conditions, like osteoarthritis, unintentional injuries, or aging-related wear and tear, frequently cause damage. Traditional treatments usually involve pain management or joint replacement arthroplasty,[3] which differs from cartilage restoration techniques that aim to restore the natural function of a joint by grafting or repairing damaged cartilage. Various treatment techniques have been developed for cartilage restoration, such as cartilage transplantation from another person (allograft)[4] and autologous cartilage transplantation (autograft),[5] microfracture,[6] autologous chondrocyte implantation (ACI),[7] and matrix-associated autologous chondrocyte implantation (MACI).[8] However, these cartilage treatment techniques are highly invasive and require a considerable amount of time for treatment. Furthermore, if the injured area cannot withstand the load applied during the healing process, this may result in additional or chronic injuries.[9] Therefore, tissue engineering approaches have been explored to develop various scaffolds suitable for cartilage regeneration.

Recent advances in the field of cartilage tissue engineering have focused on developing biomaterials that mimic the mechanical and biochemical environment of natural cartilage. This approach offers several advantages, including improved cell attachment, proliferation, and differentiation, as well as enhanced tissue formation and integration with surrounding tissues. Moreover, it provides better mechanical support and load-bearing capabilities, more closely resembling the function of native cartilage. This study introduces a novel composite scaffold composed of an oligomer of dopamine methacrylate (ODMA), polyethylene glycol dimethacrylate (PEGDMA), and collagen hydrolysate (CH) from tuna tendon, manufactured using digital light processing (DLP) printing technology. The combination of these materials was chosen based on their potential synergistic benefits for cartilage regeneration. ODMA contributes exceptional flexible mechanical and adhesive properties, ensuring stable cell attachment,[10] which is crucial for supporting chondrocyte growth and extracellular matrix production. PEGDMA enhances the scaffold's mechanical properties[11,12] and hydrophilicity,[13] providing a stable and biocompatible environment for cell proliferation and tissue formation. The incorporation of CH, rich in amino acids and peptides, closely resembles the natural extracellular matrix of cartilage,[14,15] promoting cellular activities essential for tissue regeneration. The DLP printing process enables the creation of complex and accurate 3D structures,[16–18] allowing for the simulation of the intricate architecture of cartilage tissue. This study stands out from previous research by combining these specific materials and utilizing DLP printing technology to create a scaffold that more accurately mimics the natural cartilage environment, potentially leading to improved cartilage regeneration outcomes. The thorough examination of the scaffold's physical, chemical, and biological properties, as well as its ability to support chondrocyte viability and proliferation, demonstrates this novel biomaterial's potential impact on cartilage tissue engineering. The results of this study will pave the way for further *in vivo* testing and clinical studies of this novel biomaterial composite, contributing to the advancement of regenerative medicine and offering new possibilities for the treatment of cartilage defects and injuries.

2. Materials and methods

2.1. Materials and equipment

Pure distilled water was obtained from MAY (Thailand). Sodium borate was supplied by KemAus (Australia). Sodium bicarbonate, dopamine hydrochloride, methacrylic anhydride, sodium hydroxide, methanol deuterate, tris-hydrochloric acid, polyethylene glycol dimethacrylate Mn 750 (PEGDMA), and lithium phenyl (2,4,6-trimethylbenzoyl) phosphinate (LAP) photoinitiator were all procured from Sigma-Aldrich (Germany).

Tetrahydrofuran, hydrochloric acid, ethyl acetate, hexane, acetonitrile, and trifluoroacetic acid were supplied by QReC (New Zealand). Biological materials, such as CH extracted from tuna tendon,[19] were sourced from Chiang Mai University. Sterilization equipment included an ethylene oxide (EtO) sterilizer from Namwiwat Company in Thailand, a gamma irradiation carrier type model JS 8900 IR-155 designed by Nordion International Inc. (Canada), and a beta radiation electron beam accelerator model MB 20-16 manufactured by Mevex Corporation Ltd. (Canada). Both radiation devices are located at the Thailand Institute of Nuclear Technology (TINT). The fibroblast cell lines (L929, CLS Cell Lines Service) were purchased from XL Biotec Co., Ltd. (Thailand). For cell culture, high glucose cell culture medium, fetal bovine serum (FBS), penicillin-streptomycin, L-glutamine, and trypsin were all acquired from Gibco (United States of America [USA]). The 3-(4,5-dimethylthiazol-2-yl)-2,5-diphenyltetrazolium bromide (MTT) and PrestoBlue® test kits were purchased from Invitrogen™ (USA). Formaldehyde and the live/dead cell dye for calcein and ethidium homodimer staining were supplied by QReC (New Zealand) and Invitrogen (USA), respectively. Non-chemical materials utilized included nitrogen gas, liquid nitrogen, and carbon dioxide gas. Additionally, phosphate-buffered saline (PBS) was obtained from Millipore (Germany) to ensure precise and reliable experimental conditions.

2.2. Synthesis of dopamine methacrylate

The ODMA hydrogel was fabricated via the steps displayed in Figure 1. Dopamine hydrochloride was dissolved in a sodium borate/sodium bicarbonate solution at a weight ratio of 5:2 in 200 mL of deionized water under nitrogen gas. Methacrylic anhydride tetrahydrofuran was added slowly to the top of the solution at 0.2 mL per 150 mL. Sodium hydroxide was added to maintain the pH above 8 during the reaction. Subsequently, 1 M hydrochloric acid was added to decrease the pH of the mixture to 2 when dopamine methacrylate (DMA) was precipitated. Next, ethyl acetate was used to extract the DMA, which was then recrystallized by adding hexane and dried using a lyophilizer. The entire process is depicted in Figure 2.

2.3. Characterization of dopamine methacrylate

To elucidate the chemical structure of DMA, both ^{1}H- and ^{13}C-nuclear magnetic resonance (NMR) spectroscopy techniques were employed. A 10% (w/v) solution of DMA in methanol-d4 (CD_3OD) was prepared and analyzed at room temperature. The NMR 500 MHz (JEOL, USA) was used for the characterization.

Fourier transform infrared spectroscopy (FTIR) analysis was employed to investigate the chemical composition of DMA. Briefly, 10 mg of DMA was analyzed using an FTIR spectrometer (Bruker, USA). The infrared spectral data were comprehensively acquired over a broad wavenumber range of 400–4000 cm^{-1}.

The thermal characteristics of DMA were determined through differential scanning calorimetry (DSC), utilizing a Rigaku differential scanning calorimeter (Japan). The DSC analysis was conducted over a temperature range of 25–250°C, with a consistent heating rate of 10°C/min.

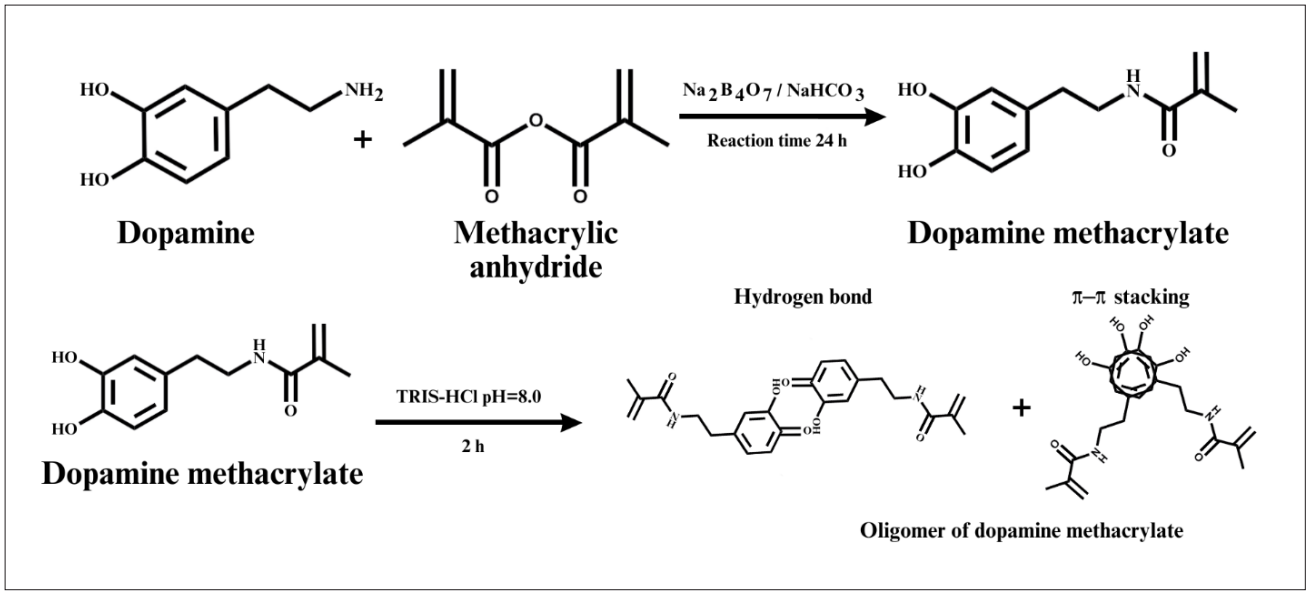

Figure 1. Schematic diagram of the synthesis of dopamine methacrylate and oligomers of dopamine methacrylate.

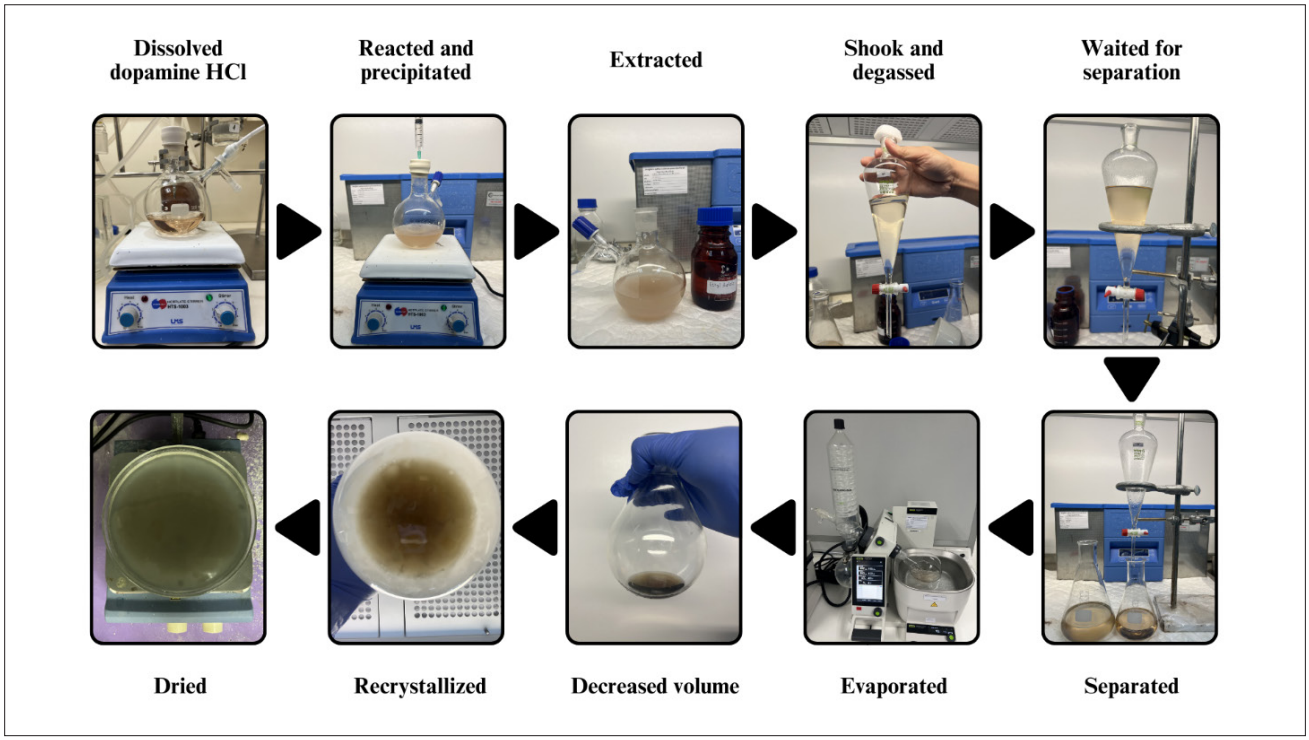

Figure 2. Illustration of the synthesis and extraction procedure of dopamine methacrylate (DMA).

2.4. Preparation of oligomer dopamine methacrylate-poly(ethylene glycol) dimethacrylate resin

Dopamine methacrylate (DMA) was initially dissolved in 4 mL of Tris-hydrochloric acid (Tris–HCl) at a pH of 8 and incubated for 2 h at 37°C. This process transformed the methacrylate into ODMA, which was subsequently mixed with PEGDMA at various concentrations, i.e., 0.625–10% (w/v) ODMA. The amount of the photoinitiator was standardized at 0.5% (w/v) LAP in each mixture to ensure consistent polymerization conditions across all samples. The mixture with optimal printability, containing 10% ODMA in ODMA/PEGDMA, was mixed with CH to form ODMA/PEGDMA/CH, which was subsequently tested with the chondrocyte cells.

2.5. Printability of resin using a digital light processing 3D printer

Printability was assessed by fabricating scaffolds from ODMA/PEGDMA resin at ODMA concentrations of 10%, 5%, 2.5%, 1.25%, and 0.625% (w/v). These scaffolds were designed as squares, measuring 6 × 6 mm with a thickness of 0.8 mm. The design process involved creating a simulation model using SolidWorks (USA) and preparing the slide files with CHITUBOX (China) before initiating the print job. Finally, the printing was conducted using Phrozen DLP 3D printer, Sonic Mighty 12K (CHITUBOX, China), as displayed in Figure 3. The printing accuracy (% accuracy) was determined by comparing the width and length of both the large and small squares of the printed scaffold and the designed scaffold using ImageJ software version 1.54j.

2.6. Morphology analysis of scaffolds using scanning electron microscopy

A sample of the ODMA/PEGDMA scaffold was fixed on stubs with carbon tape. To ensure the purity of the samples, a blower is employed to remove excess powder that could potentially contaminate the observations. Subsequently, the surface morphology of these scaffolds was investigated using scanning electron microscopy (SEM; FEI, USA), which was conducted at an acceleration voltage of 15 kV, utilizing magnifications of 70× and 400×.

2.7. Mechanical characterization of the ODMA/PEGDMA resin

The mechanical characterization of the ODMA–PEGDMA resin was conducted to assess the compressive modulus and deformation. The test specimens, in cylinders with 1.5 cm diameter and 1 cm height, were fabricated from both pure PEGDMA and copolymerized with 10% (w/v) of

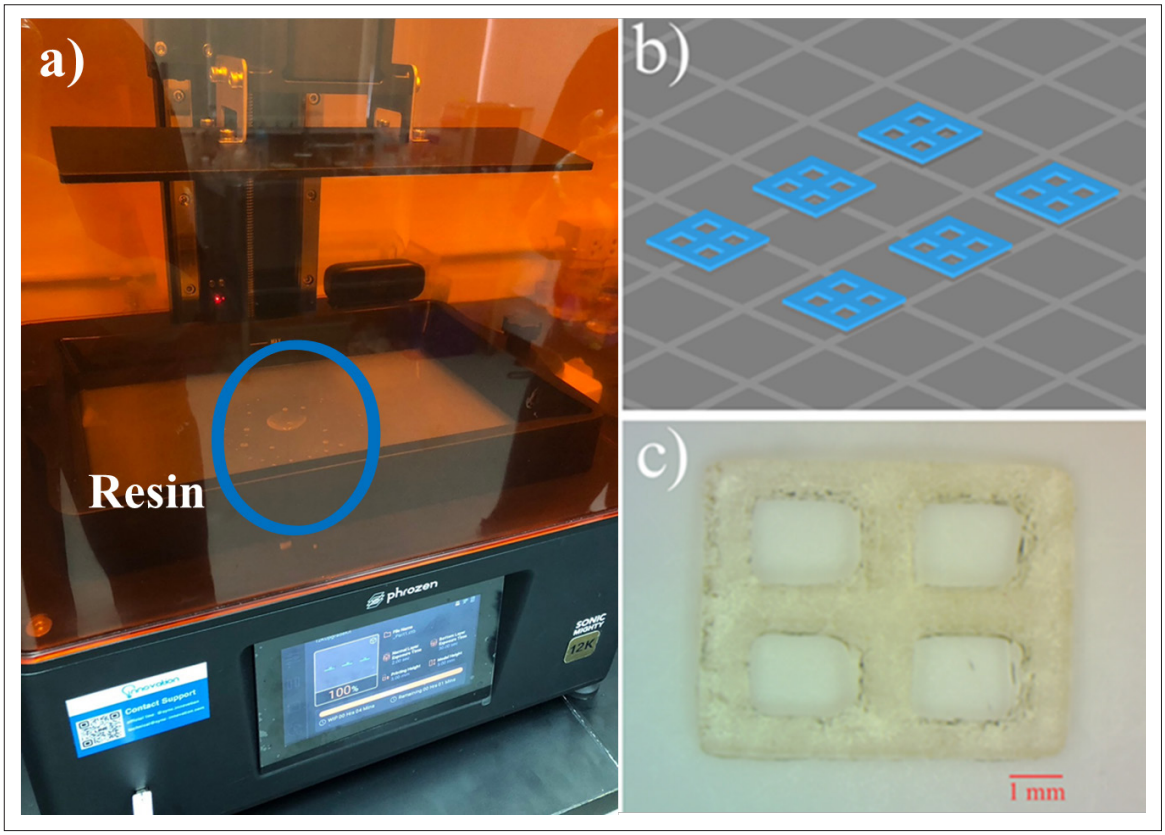

Figure 3. Illustration of the printing of ODMA/PEGDMA using a DLP 3D printer. (a) During printing, inside the blue circle is the ODMA/PEGDMA resin. (b) The scaffold model before printing in the CHITUBOX program. (c) The scaffold after it has been printed. Abbreviations: DLP, digital light processing; ODMA, oligomer of dopamine methacrylate; PEGDMA, polyethylene glycol dimethacrylate.

ODMA (10% ODMA/PEGDMA). The compression tests were performed using a dynamic mechanical analyzer (TAXT plus Stable Micro Systems, United Kingdom [UK]). A preload force of 0.001 N was applied to standardize the interface between the top plate and the sample surface to ensure contact uniformity. These tests proceeded at a consistent compression rate of 1 mm/min at ambient room temperature. The compressive modulus was calculated from the initial linear zone of the stress–strain curve, which represents the material's response from 0% to 50% strain.

2.8. Sterilization of collagen hydrolysate

2.8.1. Ethylene oxide sterilization

This sterilization process was conducted in accordance with EN ISO 11135 standards, utilizing EtO for its effective antimicrobial performance. CH was first securely packaged in sterile bags to maintain purity. The samples were then exposed to an EtO gas atmosphere at a concentration of 700 mg/L with 70% relative humidity for 8 h at a controlled temperature of 55°C. Following this, a detoxification process was employed, wherein CH was subjected to a stream of warm air at approximately 46°C under atmospheric pressure for 48 h. This crucial step ensures the complete removal of any residual EtO, thereby eliminating potential toxicity and ensuring the safety and sterility of CH for medical and nutritional applications.

2.8.2. Beta radiation sterilization

Collagen hydrolysate (CH) was first securely enclosed in a sealed medicinal pouch and placed inside an opaque sealed box for protection against light and external contamination. The samples underwent beta radiation treatment, ensuring thorough sterilization with a minimum radiation dose of 17.5 kGy.

2.8.3. Gamma radiation sterilization

Collagen hydrolysate (CH) was meticulously packaged within a hermetically sealed medicinal pouch for its purity and integrity. This pouch was placed inside an opaque, sealed box to protect against light and external contamination. The packaged CH underwent sterilization through exposure to gamma radiation at a minimum radiation dose of 17.5 kGy.

2.8.4. Analysis of changes in collagen hydrolysate chemical composition post-sterilization using FTIR

The FTIR technique, performed with a Bruker spectrometer (Billerica, USA), was employed to characterize chemical composition changes in CH post-sterilization. A sample amounting to 10 mg was analyzed, and its infrared spectrum was recorded across a broad wavenumber spectrum spanning from 400 to 4000 cm^{-1}, providing a detailed chemical fingerprint of CH.

2.9. *In vitro* experiments

2.9.1. Ethics statement

Human cartilage stem/progenitor cells (CSPCs) were harvested from the articular cartilage of knee joints of a patient with osteoarthritis who had undergone knee joint replacement procedures. The study protocol (COA. NO. MURA2022/469) was approved by the Human Research Ethics Committee, Faculty of Medicine Ramathibodi Hospital, Mahidol University. A written informed consent document was signed by the enrolled participant prior to the initiation of the study. This experimental protocol was carried out in accordance with relevant guidelines and regulations.

2.9.2. Preparation and isolation of human cartilage stem/progenitor cells

The isolated articular cartilage tissues were washed and rinsed with Dulbecco's phosphate-buffered saline (DPBS; SH2002803; Hyclone, USA) containing 1% penicillin/streptomycin (SV30010; Hyclone, USA) and incubated at room temperature for 1–2 h. The tissues were minced into approximately 0.5 mm^3 pieces and washed twice with DPBS. The minced tissues were enzymatically digested using 0.1% collagenase type II (17101-015; Gibco, USA) and incubated at 37°C for 12 h in a shaking water bath. Following incubation, the digested tissue solution was centrifuged at 400 × *g* for 10 min; the supernatant was carefully removed; the centrifugation process was repeated twice. The cell pellets were resuspended in DPBS, filtered through a Falcon™ 40 µm cell strainer (352340; Corning, USA), and centrifuged again. The cells pellets were then resuspended in DMEM complete medium containing high glucose (SH3024302; Hyclone, USA), 10% FBS (Gibco, USA), 1% penicillin/streptomycin (15140122; Gibco, USA), 1% of 200 mM L-glutamine (SH3003401; Hyclone, USA), and 0.1% amphotericin-B (SV30078.01; Hyclone, USA). Subsequently, the cells were plated at a density of 5 × 10^3 cells/cm^2 in a T-25 flask (Nunc, Denmark) and cultured in DMEM complete medium at 37°C in a humidified atmosphere of 95% O_2 and 5% CO_2. The culture medium was replaced every 3–4 days until reaching the third passage.

2.9.3. Assessment of human cartilage stem/progenitor cell differentiation potential

The CSPCs in the third passage were trypsinized and used for phenotype analysis and differentiation potential assays. CSPCs were plated at a density of 5 × 10^3 cells/cm^2 in a T-25 flask and induced to differentiate into adipogenic, osteogenic, and chondrogenic lineages using established differentiation protocols.[20] To induce adipogenic differentiation, CSPCs were cultured in DMEM complete medium supplemented with 0.035% indomethacin (I7378; Sigma-Aldrich, USA), 0.03% 3-isobutyl-1-methylxanthine (I5879; Sigma-Aldrich, USA), 0.01% dexamethasone (D4902; Sigma-Aldrich, USA), and 0.005% human insulin solution (I9278; Sigma-Aldrich, USA). To induce osteogenic differentiation, CSPCs were cultured in DMEM complete medium supplemented with L-ascorbic acid (A92902; Sigma-Aldrich, USA), B-glycerophosphate (154804-51-0; Sigma-Aldrich, USA), and 0.001% dexamethasone (Sigma-Aldrich, USA). To induce chondrogenesis differentiation, CSPCs were cultured in StemMACS™ ChondroDiff Medium (130-091-679; Miltenyi Biotec, USA). After 3 weeks in culture, CSPC differentiation potentials were confirmed using histological staining techniques. Adipogenic-induced CSPCs were evaluated by Oil Red O (O0625; Sigma-Aldrich, USA), osteogenic-induced CSPCs were stained with Alizarin Red S (A5533; Sigma-Aldrich, USA), and chondrogenic-induced CSPCs were stained with Alcian Blue solution (A5268; Sigma-Aldrich, USA).

2.9.4. Human cartilage stem/progenitor cell immunophenotype analysis

Immunotypic mesenchymal cell surface markers on CSPCs were characterized using flow cytometry. At the third passage, CSPCs were trypsinized using 0.25% trypsin (3004201; Hyclone, USA), washed, and resuspended in DPBS at a density of 2 × 10^5 cells/tube, followed by centrifugation at 400 × *g* for 10 min. After centrifugation, the cells were resuspended in 100 µL DPBS and incubated with fluorochrome-conjugated antibodies targeting human CD11b, CD34, CD45, CD73, CD90, and CD105 (Biolegend, USA) at 4°C for 30 min in the dark according to the manufacturer's instructions. Following centrifugation at 400 × *g* for 5 min, cells were washed twice with PBS, resuspended in 500 µL PBS, and analyzed using a flow cytometer (Beckman Coulter, USA).

2.9.5. Cell viability analysis of human cartilage stem/progenitor cells on resin scaffolds

Cell viability and cell proliferation of CSPCs on a series of 3D-printed scaffolds (diameter: 15.60 mm), including PEGDMA, ODMA/PEGDMA, and ODMA/PEGDMA/CH were assessed using PrestoBlue® (A13261; Thermo

Fisher, USA) according to the manufacturer's instructions. In brief, CSPCs were seeded on each scaffold at a density of 5×10^4 cells/scaffold and cultured in a 24-well plate containing DMEM complete medium at 37°C and in 5% CO_2 for 24, 48, and 72 h, respectively. After reaching each incubation period, each scaffold was then transferred to a new well and incubated in a fresh culture medium containing 0.1% PrestoBlue® in the dark for 1.5 h to assess cell metabolic activity. The medium containing PrestoBlue® was then transferred into a 96-well plate in triplicate (100 µL/well/sample). The absorbance was measured using a microplate reader (Infinite 200 Pro; Tecan, Switzerland) at a wavelength of 570 nm to evaluate cell viability.

2.9.6. Cell viability analysis of collagen hydrolysate

The mouse fibroblast cell lines (L929, CLS Cell Lines Service), purchased from XL Biotec Co., Ltd. (Thailand), were used in the cell viability assessment of CH. Fibroblasts were seeded in a 24-well plate (Corning, USA) at approximately 5×10^4 cells/well. Cells were cultured in high-glucose completed medium (Gibco, USA) containing 10% FBS (Gibco, USA) and 1% penicillin/streptomycin (Gibco, USA) at 37°C in a humidified atmosphere of 95% O_2 and 5% CO_2 overnight. The next day, the old medium was removed and replaced with the medium containing 20% (w/v) CH, which underwent different sterilization methods, including 0.22 µm sterile filter, EtO, beta, and gamma radiation sterilization, and incubated for 24 h. The CH cell viability protocol used in this study was based on a previous study.[21] After incubation, cell viability was determined by the MTT assay according to the manufacturer's protocol. The optical density was measured at a wavelength of 570 nm using a microplate reader (Infinite 200 Pro; Tecan, Switzerland).

2.9.7. Live/dead cell viability assay on various scaffolds using fluorescence staining

Live/dead staining was performed 72 h after the cells had initially adhered to and proliferated on the scaffold. This method is used to visually confirm the viability of CSPCs on a series of 3D-printed scaffolds. In brief, each scaffold was carefully transferred to a new well and rinsed in triplicate with DPBS to eliminate any remaining esterase activity. The live and dead CPSCs on each scaffold were assessed by staining with fluorometric detection reagents, including calcein (206700; 1:1000; Sigma-Aldrich, USA) and ethidium homodimer (ab145323; 1:500; Abcam, USA). The live cells were stained fluorescent green (calcein), while dead cells were stained fluorescent red (ethidium homodimer). The morphology of CSPCs and their distribution on the surface of each scaffold was examined using an inverted fluorescence microscope (Carl Zeiss, Germany).

2.10. Statistical analysis

Statistical analyses were performed using GraphPad Prism version 9.0.0 (GraphPad Software, USA). Data are expressed as mean ± standard deviation. The cell viability (%) assays of fibroblasts treated with CH and human CSPCs cultured on different scaffolds were analyzed using one-way analysis of variance (ANOVA) and two-way analysis of variance (two-way ANOVA), followed by the post hoc Tukey's for multiple comparison tests, respectively. The statistical significance criterion was $p < 0.05$.

3. Results and discussion

3.1. Synthesis and characterization of dopamine methacrylate

The chemical structure of DMA produced was analyzed using ^1H and ^{13}C NMR spectroscopy techniques. The ^1H NMR spectrum revealed distinct resonance signals, including the amide group at 7.9 ppm, phenyl protons at 6.7 and 6.5 ppm, methylene protons at 3.4 and 2.6 ppm, and alkenyl hydrogens at 5.7 and 5.3 ppm. Similarly, the ^{13}C NMR spectrum displayed a prominent signal corresponding to the resonance of 12 carbon atoms, aligning with DMA's molecular formula $C_{12}H_{15}NO_3$. These findings are consistent with the characteristics of the DMA chemical structure as established in previous studies.[10,22] The data demonstrate the successful grafting of the methacrylamide group onto the dopamine structure, as illustrated in Figure 4.

Several critical transmission peaks were identified when analyzing the chemical composition of DMA using FTIR. These peaks include a significant transmission peak at 3354 cm^{-1}, attributed to the stretching vibration of the amide (N–H) group; and peaks at 2964 and 2932 cm^{-1}, resulting from the stretching vibration of the carbon–hydrogen bond (C–H), which are also present in dopamine. Additionally, the transmission peaks at 1650, 1540, and 1240 cm^{-1} correspond to amide I (ν, C=O), amide II (ν, N–H), and amide III (ν, C–N), respectively. Notably, these specific peaks are absent in the FTIR spectrum of dopamine alone. This pattern of peaks in the FTIR spectrum confirms the presence of an amide bond in DMA. Comparing these peaks with prior research[10,22] verifies that they align with the characteristics of the DMA chemical composition, as depicted in Figure 5.

The thermal properties of DMA analyzed using DSC revealed a notable heat absorption peak between 90 and 130°C (Figure 6). Specifically, the thermal absorption peak of DMA occurs at 118°C, indicating its melting point. The thermogram obtained is similar to a previous study, i.e., a higher heat absorption range of 120–160°C and a maximum heat absorption value of 143°C.[22] The lower heat

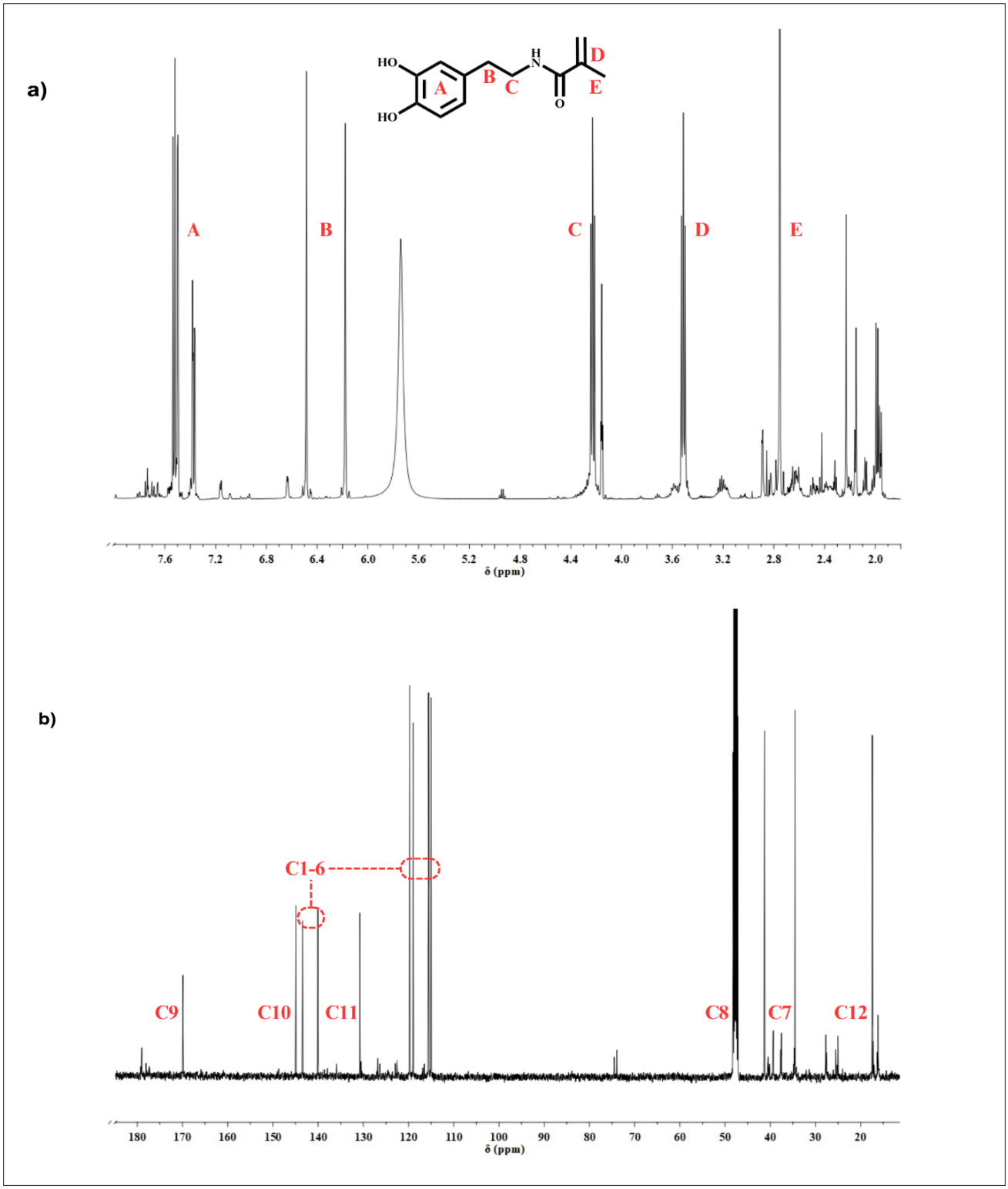

Figure 4. The spectral results of using nuclear magnetic resonance (NMR) techniques to examine the chemical structure of dopamine methacrylate (DMA). (a) ^{1}H NMR. (b) ^{13}C NMR.

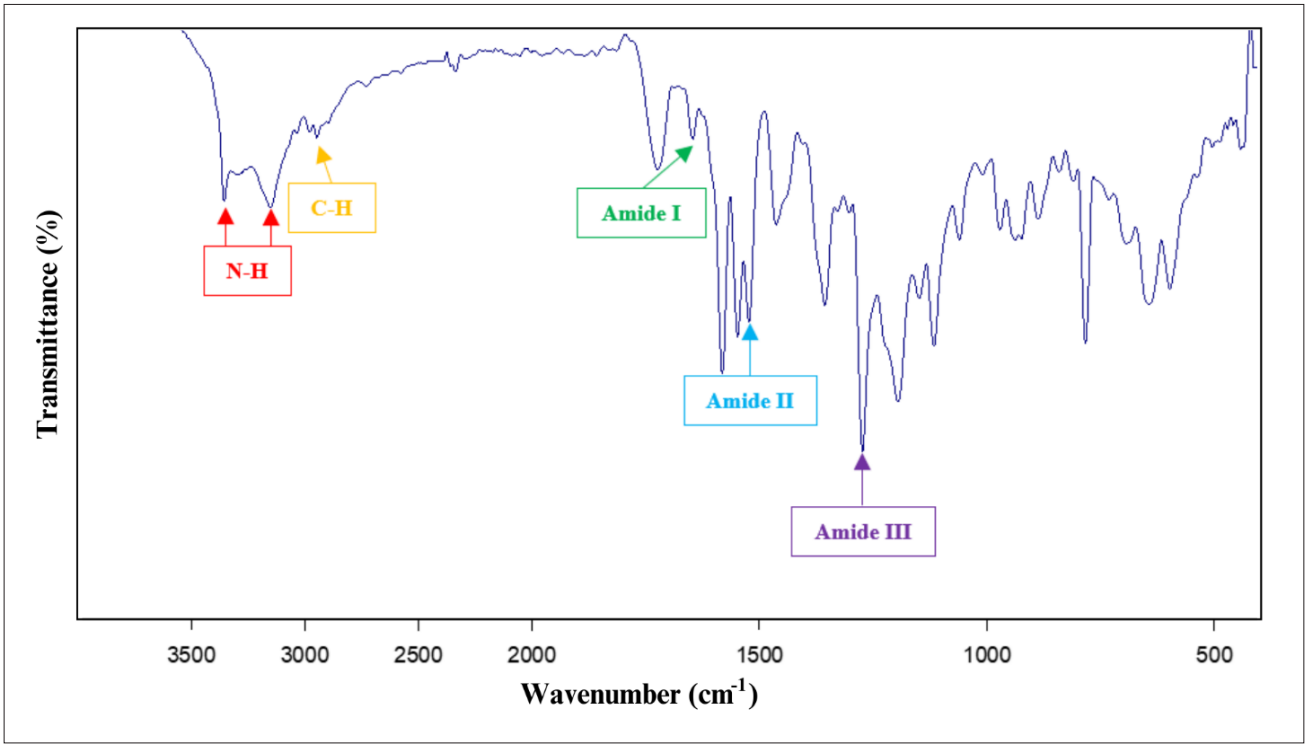

Figure 5. Fourier transform infrared (FTIR) spectrum of the chemical composition of dopamine methacrylate (DMA).

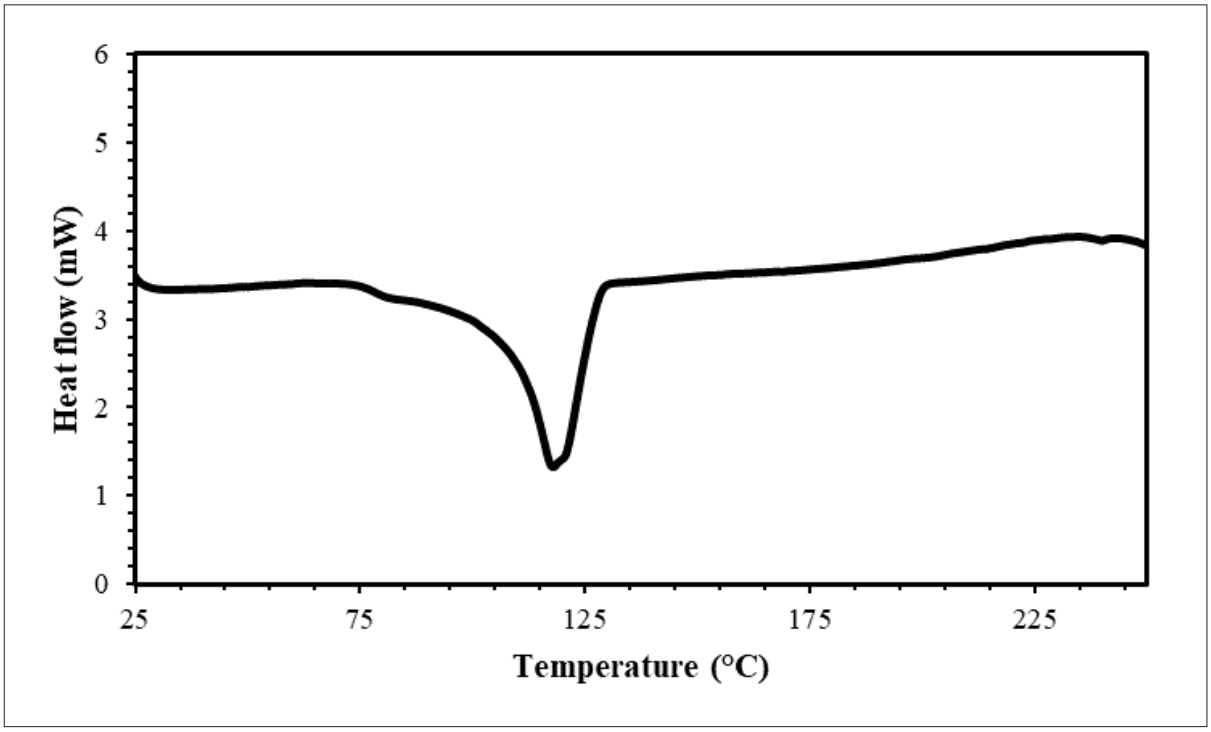

Figure 6. Differential scanning calorimetry (DSC) thermogram from examining the thermal properties of dopamine methacrylate (DMA).

absorption value (relative to previous research) is likely due to the synthesis and crystallization processes, which affect the glass transition temperature (T_g). Typically, crystalline polymers have a higher T_g than the same polymer in an amorphous state because crystals have a more ordered structure. Therefore, this study may have achieved less ordered crystallization than previous work, with more amorphous polymers of the same type. This would result in a lower melting temperature, making the material easier to prepare before use. This result also demonstrates the need for high energy to break the material's structure, and the maximum heat absorption value demonstrates the material's durability. This characteristic becomes even more significant when considering its application in the body, as cartilage repair or replacement methods often involve long-term implantation of materials.

3.2. Printability of ODMA–PEGDMA resin with DLP printer and morphology of the scaffold

The 3D-printed scaffolds using PEGDMA resin mixed with various concentrations of ODMA (0.625%, 1.25%, 2.5%, 5%, and 10% w/v) revealed that the resin with 0.625% ODMA exhibited the least formability, achieving only 75% printing accuracy (Figure 7). In contrast, resins with higher ODMA concentrations demonstrated equally effective printability (approximately 90%) when using DLP 3D printing techniques.

Scanning electron microscopy (SEM) analysis of the surface morphology of ODMA/PEGDMA scaffolds at various magnifications revealed different textures among the printed samples at 70× magnification. Scaffolds composed of the PEGDMA resin with 0.625% ODMA exhibited square pores and a rough surface, which may affect cell adhesion and cause damage due to high surface roughness. In contrast, samples with higher ODMA concentrations displayed a smoother surface finish, consistent with the printability results from DLP 3D printer testing. Further examination at 400× magnification displayed a consistent pattern across all concentrations, similar to previous research using SEM techniques to examine the morphology of PEGDMA as a scaffold material.[12] However, the compactness of the pattern was influenced by the ODMA concentration, with higher concentrations resulting in denser patterns. These findings are detailed in Figure 8 and demonstrate the impact of ODMA concentration on the surface texture and microstructure of ODMA/PEGDMA scaffolds.

3.3. Compression testing of the ODMA/PEGDMA scaffold

Figure 9 presents the stress–strain analysis comparing pure PEGDMA with a composite material containing 10% ODMA within a PEGDMA matrix, highlighting the distinct mechanical responses of the two materials under compressive stress. Pure PEGDMA exhibits a linear increase in strain, reaching up to approximately 20%, indicating elastic behavior before undergoing plastic deformation as the curve steepens. In contrast, the ODMA/PEGDMA composite demonstrates significantly better compression resistance throughout the stress test period, with a consistent slope indicating increased hardness. The composite's initial strength is superior to pure PEGDMA and exhibits higher compression stress compared to previous research using pure GelMA and ODMA-GelMA as cell scaffolds, which reported compression stresses of approximately 0.5 and 2.375 MPa, respectively.[10] However, the ODMA–PEGDMA composite has a lower strain value due to the hard but brittle nature of PEGDMA, causing easier deformation. The incorporation of ODMA effectively strengthens the matrix, making ODMA/PEGDMA an ideal material for applications with high structural demands, such as the development of scaffolds that must withstand physiological stress. The observed mechanical properties suggest that the addition of ODMA enhances the rigidity of the PEGDMA structure, potentially increasing the concentration of intermolecular connections and the crosslinking density upon copolymerization, which is crucial for durable mechanical stability.[23,24] This enhanced mechanical stability is particularly important for tissue engineering applications, as stable scaffolds can better withstand the stresses and strains encountered *in vivo* and maintain their shape and function over extended periods.

3.4. Characterization and cytotoxicity of collagen hydrolysate after sterilization by various methods

Investigations into the effects of various sterilization methods on CH revealed distinct changes. Sterilization with EtO transformed the hydrolysate from a light brown powder to a burnt brown and sticky lump, which affected its solubility in distilled water. In contrast, beta and gamma radiation did not alter its physical characteristics.

The FTIR spectroscopic analysis of CH post-sterilization revealed key chemical structure insights. The amide A band appeared at 3281 cm^{-1}, indicating N—H stretch vibrations, which suggests hydrogen bonding within the peptide.[25] The amide B band was identified at 2961 cm^{-1}, corresponding to the asymmetric stretching vibrations of the CH_2 groups and the presence of the alkyl chain.[26] The characteristic frequency of the amide I band at 1635 cm^{-1} was primarily related to the stretching vibrations of the carbonyl group along the polypeptide backbone.[27,28] Moreover, amide bands II and III, at 1536 and 1242 cm^{-1}, respectively, correspond to the flexural vibrations of N–H bonds coupled with the C–N stretching vibrations.[27,28]

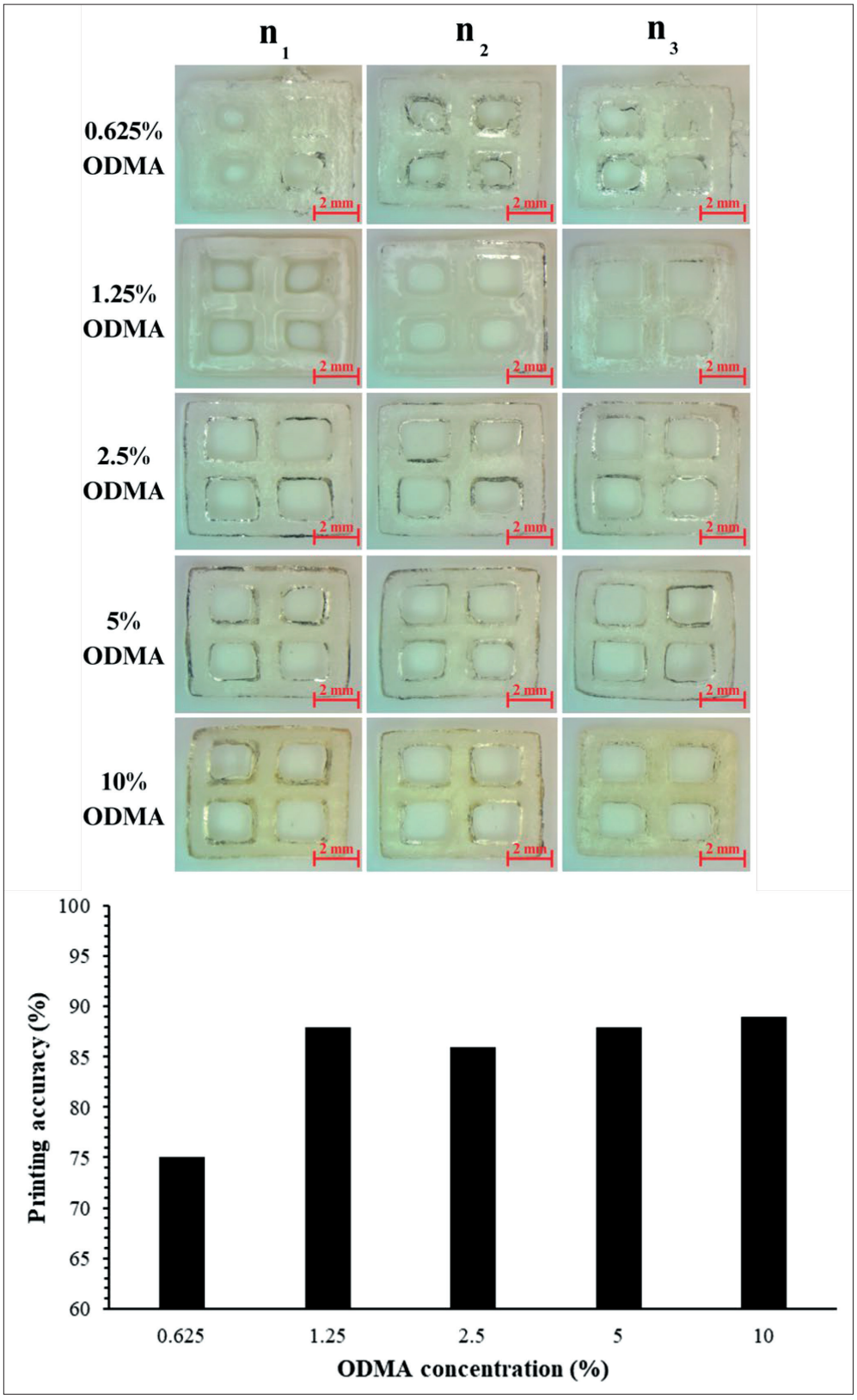

Figure 7. The physical appearance image (above) and the printing accuracy (below) of the digital light processing (DLP)-printed oligomers of dopamine methacrylate/polyethylene glycol dimethacrylate (ODMA/PEGDMA) resin at various concentrations of ODMA. Scale bars: 2 mm. Abbreviations: n_1: first printing specimen; n_2: second printing specimen; n_3: third printing specimen.

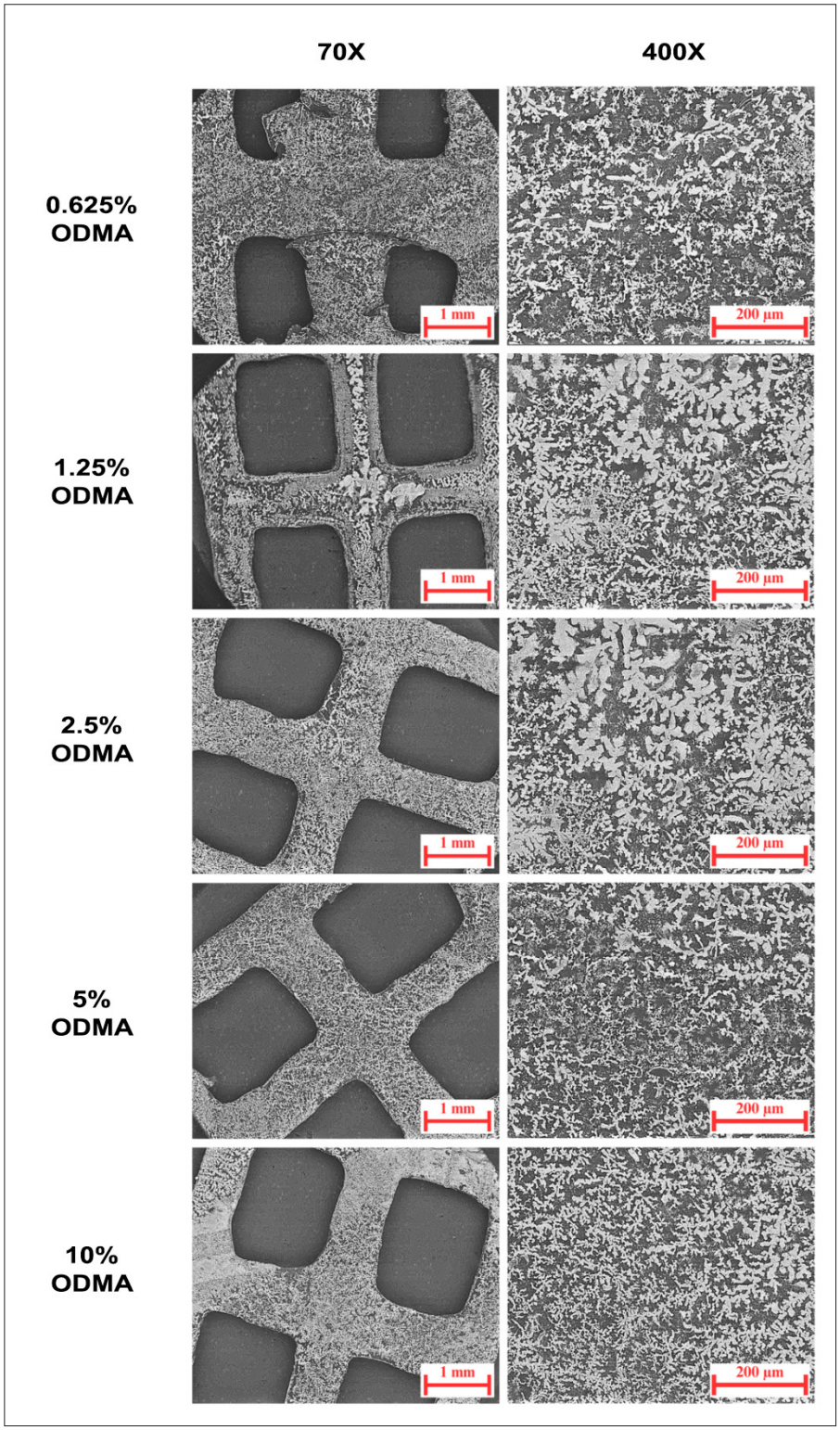

Figure 8. Scanning electron microscopy (SEM) images of surface morphology of oligomers of dopamine methacrylate/polyethylene glycol dimethacrylate (ODMA/PEGDMA) scaffolds at various concentrations of ODMA. Scale bars: 1 mm (70×) and 200 µm (400×).

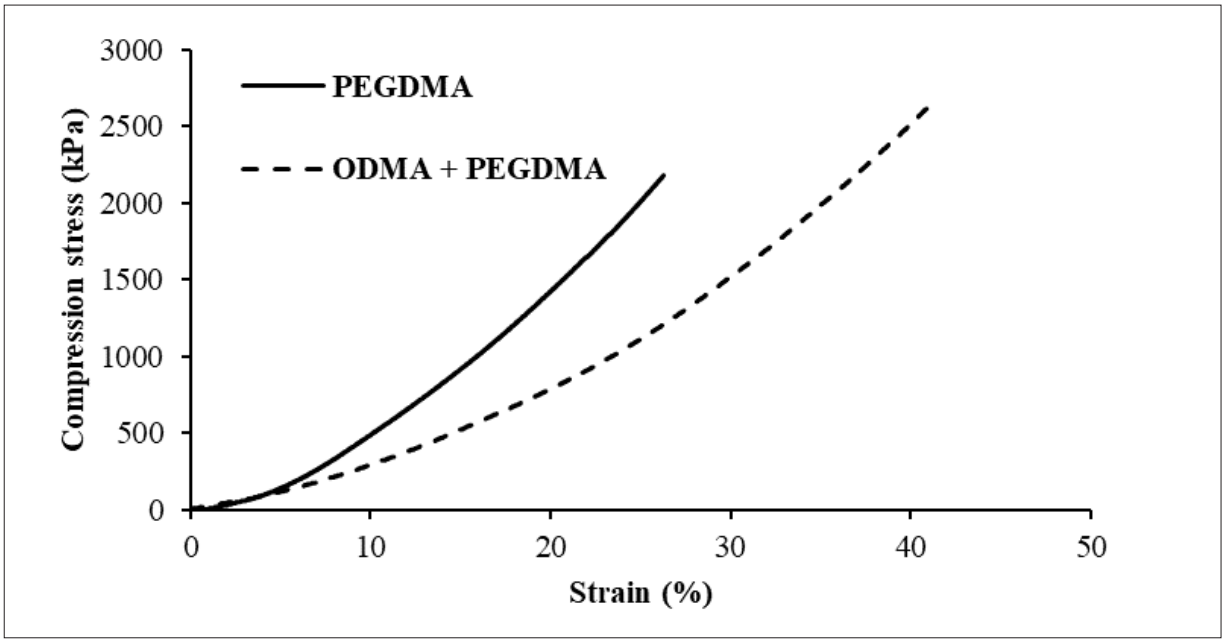

Figure 9. Stress–strain behaviors of polyethylene glycol dimethacrylate (PEGDMA) compared to PEGDMA with 10% oligomers of dopamine methacrylate (ODMA) (i.e., ODMA–PEGDMA).

A comparison of the CH FTIR spectra before and after sterilization exhibited no shift in the position of these amide bands, indicating that the sterilization methods did not influence the secondary structure of CH. This finding is consistent with previous research that examined the chemical composition of CH,[29,30] as illustrated in Figure 10.

The viability of fibroblast cells when tested with CH using the MTT assay over 24 h compared to a control group (without CH) yielded insightful results. The fibroblast cells cultured in a medium containing 20% w/v CH and post-sterilized by filtration, EtO, beta radiation, and gamma radiation demonstrated survival rates of 112.46%, 122.90%, 117.40%, and 118.95%, respectively. These results are illustrated in Figure 11. Furthermore, when the cells were stained with fluorescent markers to assess viability within the CH-containing culture medium after various sterilization methods, the cells exhibited a prominent green fluorescence from the calcein staining of fibroblast cells, which indicates a high number of live cells. In contrast, the red stains of ethidium staining revealed only a minimal presence of dead cells, consistent across all samples (Figure 12). These consistent results suggest that the sterilization methods did not detrimentally affect cell viability, aligning with previous research on the cell toxicity of CH subjected to different sterilization methods.[31–33]

3.5. Viability of human cartilage stem/progenitor cells on 3D-printed scaffolds

The common characteristics of CSPCs were accessed after being cultured *in vitro*. The CSPCs adhered to the culture plates as observed under the inverted microscope. Morphologically, CSPCs displayed a fibroblastic phenotype (spindle-shaped cells) (Figure 13), similar to a previous report.[34]

Flow cytometry analysis for CSPCs surface markers (Figure 14) demonstrated that CSPCs were positive for stem cells-associated surface markers (i.e., CD73, CD90, and CD105), whereas hematopoietic stem cell-associated markers (i.e., CD34, CD45, and CD11b) were expressed at low levels. Tri-lineage differentiation was also assessed to confirm the characteristics of CSPCs, as demonstrated by Oil Red O (adipogenic-induced CSPCs; indicated by lipid droplets), Alizarin Red (osteogenic-induced CSPCs; indicated by calcium deposits), and Alcian Blue (chondrogenic-induced CSPCs; indicated by blue staining for glycosaminoglycans) staining (Figure 15).

The viability of human CSPCs cultured on various scaffolds at 24, 48, and 72 h intervals was compared to the control (culture plate) group (Figure 16). For PEGDMA scaffolds, the survival rates were 72.89%, 56.60%, and 119.70% at the respective time points. When ODMA was incorporated into the PEGDMA scaffold, the survival rates

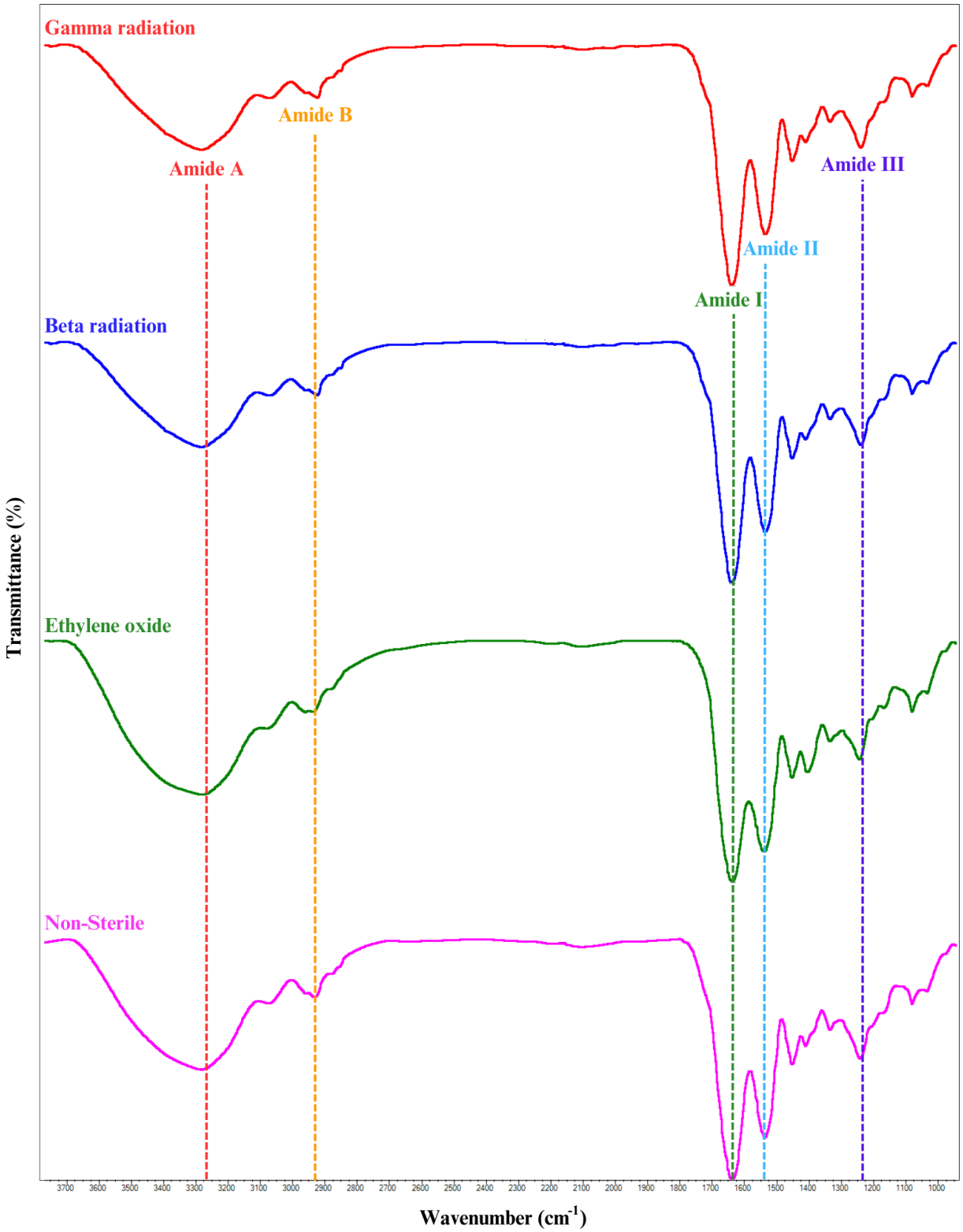

Figure 10. Fourier transform infrared (FTIR) spectra of the chemical composition of collagen hydrolysate (CH) before and after sterilization by different methods. The *X*-axis is wave number (cm^{-1}) and the *Y*-axis is transmittance (%*T*).

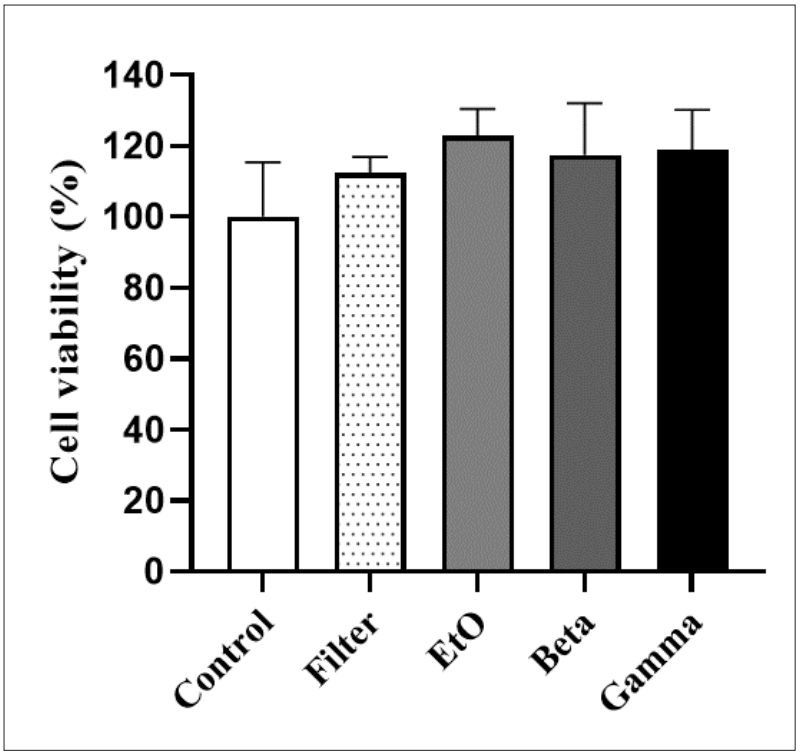

Figure 11. A bar graph displaying the percentage survival of fibroblasts cultured with medium containing collagen hydrolysate (CH) subjected to various sterilization techniques, i.e., filtration (filter), ethylene oxide (EtO), beta radiation (beta), and gamma radiation (gamma), for 24 h ($n = 3$).

improved to 102.71%, 139.62%, and 163.34%, respectively. The inclusion of CH into the ODMA/PEGDMA scaffold further enhanced cell viability to 138.85%, 148.67%, and 190.64% at 24, 48, and 72 h, respectively (Figure 16). Additionally, fluorescent staining to visualize cell survival on the scaffolds confirmed these findings. Human CSPCs displayed a bright green fluorescence after calcein staining at 72 h, indicating a high number of living cells. Conversely, ethidium homodimer revealed a small number of dead cells. This pattern was consistent across all scaffold compositions, as illustrated in Figure 17. Compared to previous research using polyglycolide/polylactic acid cellular cartilage matrix/gelatin and ODMA/gelatin methacrylate as scaffolds to regenerate cartilage tissue,[10,35] our findings indicated a similarly high potential for the scaffolds used in the current study. The observed cell viability in our experiments had significant implications for the future development and improvement of materials for cartilage regeneration. These results suggest that our scaffolds provided a suitable microenvironment for chondrocyte survival and proliferation, which is crucial for successful tissue engineering. The high cell viability we observed not only validated the biocompatibility of our scaffolds but also implied their potential to support long-term cartilage tissue formation. This finding opens up new avenues for refining scaffold compositions and structures to further enhance cell attachment, proliferation, and extracellular matrix production. Our result is consistent with a previous finding, which demonstrated that CH could enhance cell viability and proliferation of human articular chondrocytes *in vitro* via downregulated mRNA levels of several enzymes, including aggrecanases, matrix metalloproteinases, and serine proteases such as Htra1. This may have beneficial effects by delaying the degradation of the extracellular matrix.[36] Moreover, the promising cell viability results warrant further investigation into the scaffolds' ability to maintain chondrocyte phenotype and promote the synthesis of cartilage-specific components. However, further studies are required to further validate the potential of scaffolds for cartilage repair by analyzing the expression levels of chondrocyte phenotypes and cartilage synthesis-related genes. Ultimately, these advancements could lead to more effective cartilage defect treatments.

Additionally, we hypothesized that it is possible to develop and improve the ODMA/PEGDMA/CH scaffold in hydrogel form. This hypothesis is based on previous studies demonstrating the ability of each component to form hydrogels individually.[10] We anticipate that

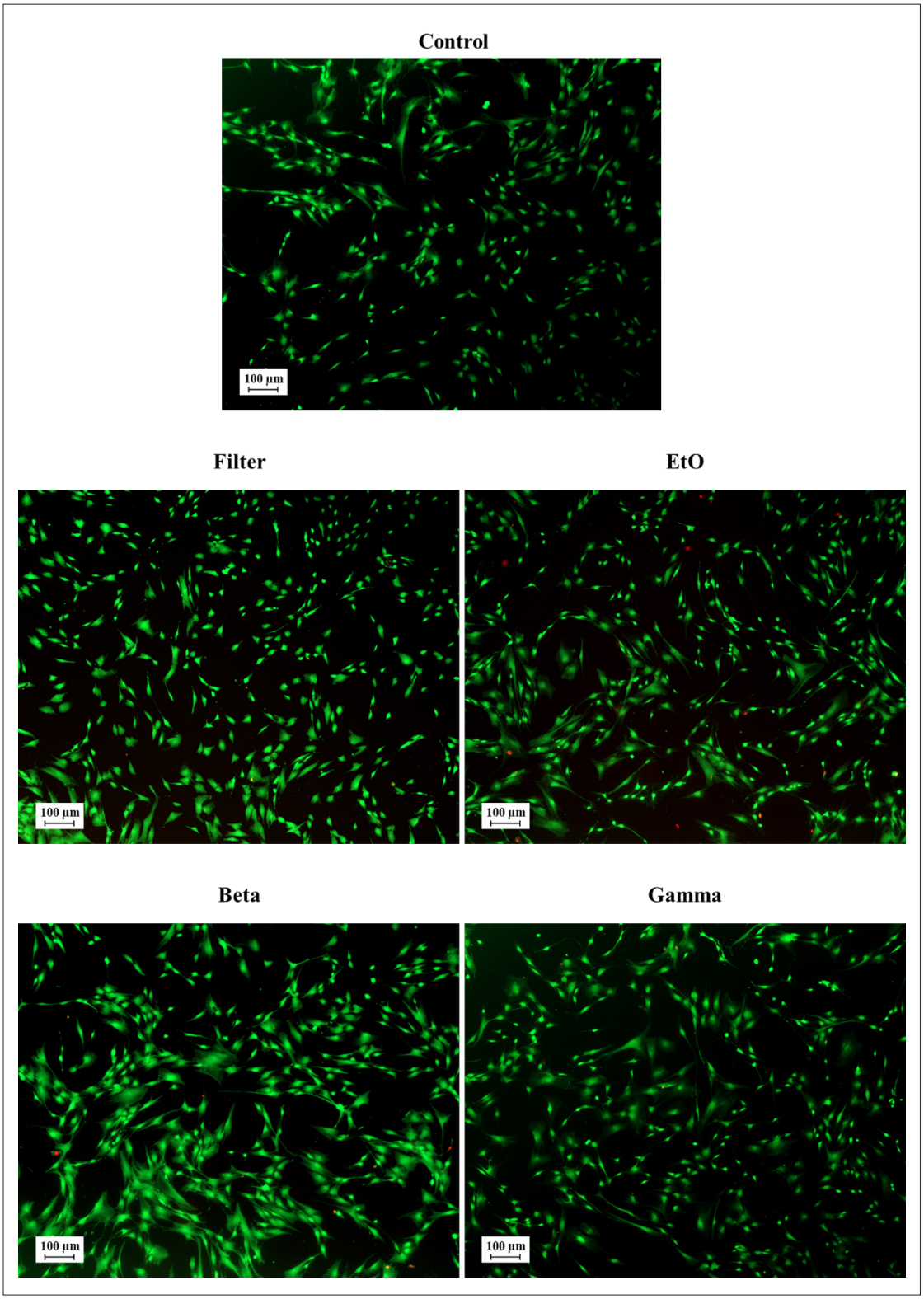

Figure 12. Live/dead fluorescence staining images at 5× magnification of fibroblast cells cultured with a medium containing collagen hydrolysate (CH) from various sterilization methods, i.e., filtration (filter), ethylene oxide (EtO), beta radiation (beta), and gamma radiation (gamma), over 24 h. Scale bars: 100 µm.

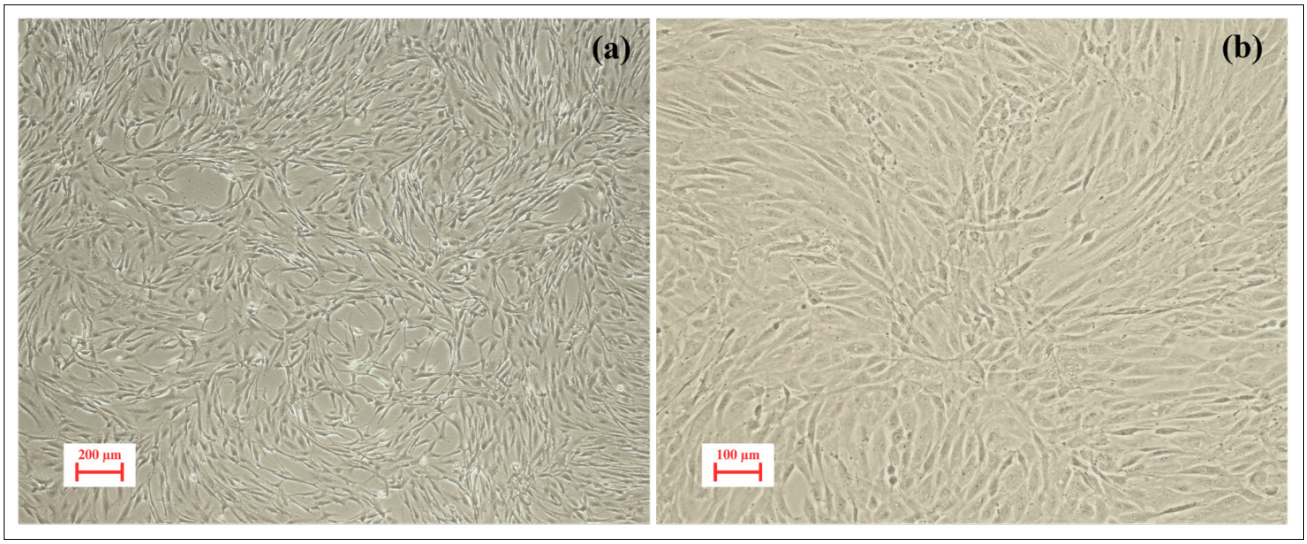

Figure 13. Cell morphology of human cartilage stem/progenitor cells (CSPCs) on day 7 of culture at (a) 4× and (b) 10× magnifications. Scale bars: 200 µm (A); 100 µm (B).

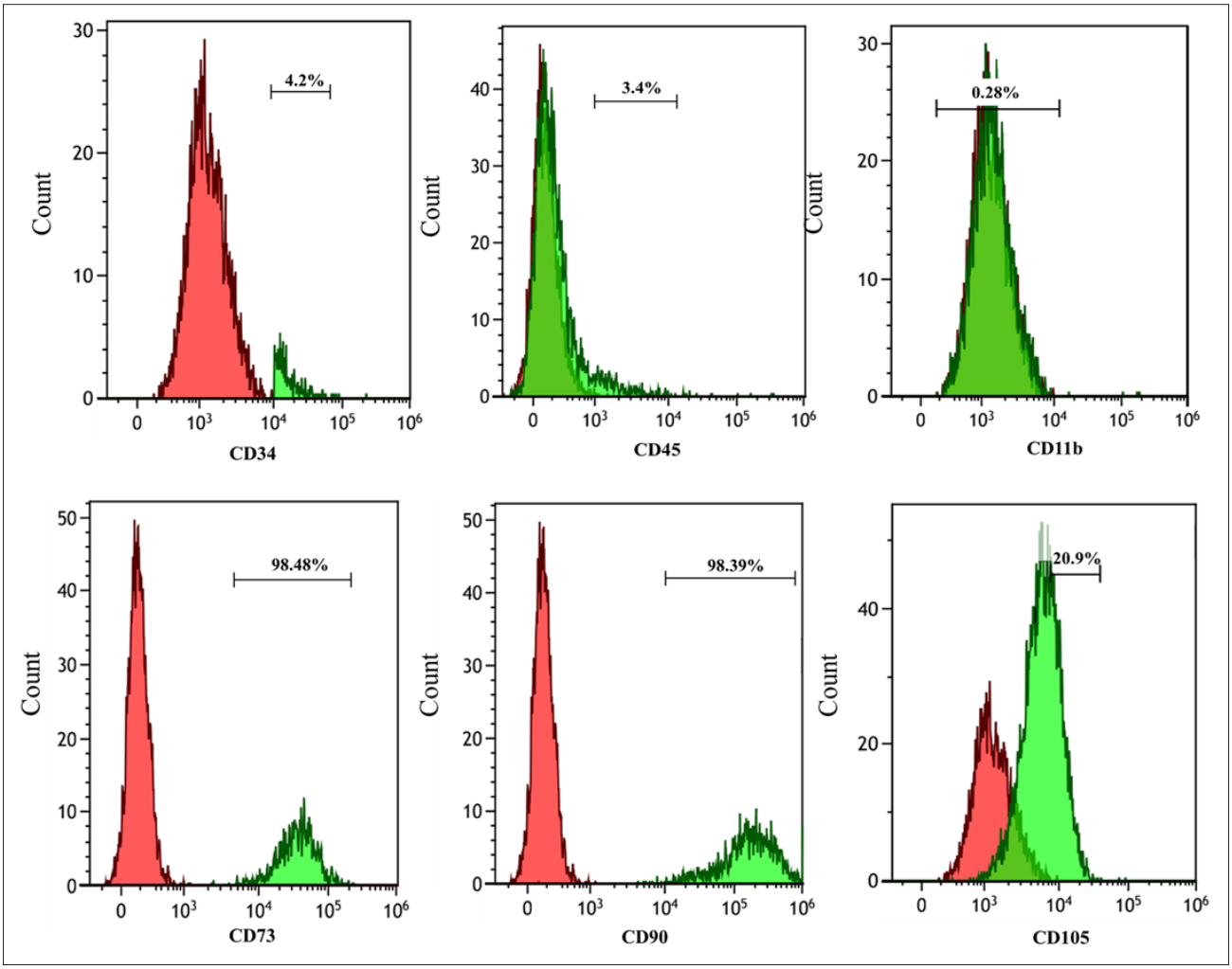

Figure 14. Flow cytometric analysis of human cartilage stem/progenitor cells (CSPCs) indicates high expressions of stem cell-associated surface markers (i.e., CD73, CD90, and CD105) and low expressions of hematopoietic stem cell-associated markers (i.e., CD34, CD45, and CD11b).

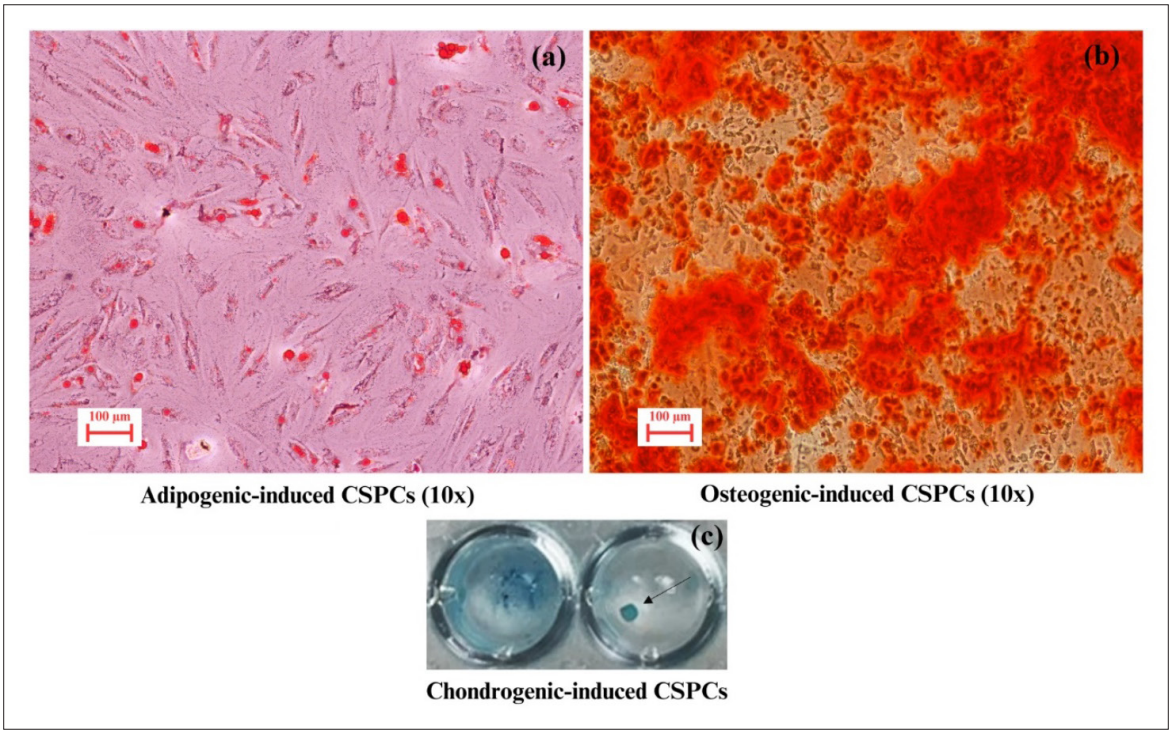

Figure 15. Representative images of human cartilage stem/progenitor cells (CSPCs) differentiated into (A) adipocytes, (B) osteoblasts, and (C) chondrocytes at day 21 of culture, following staining with (A) Oil Red-O, (B) Alizarin Red, and (C) Alcian Blue. The black arrow indicates the differentiation of CSPCs into a 3D cartilage construct. Scale bars: 100 µm (A and B).

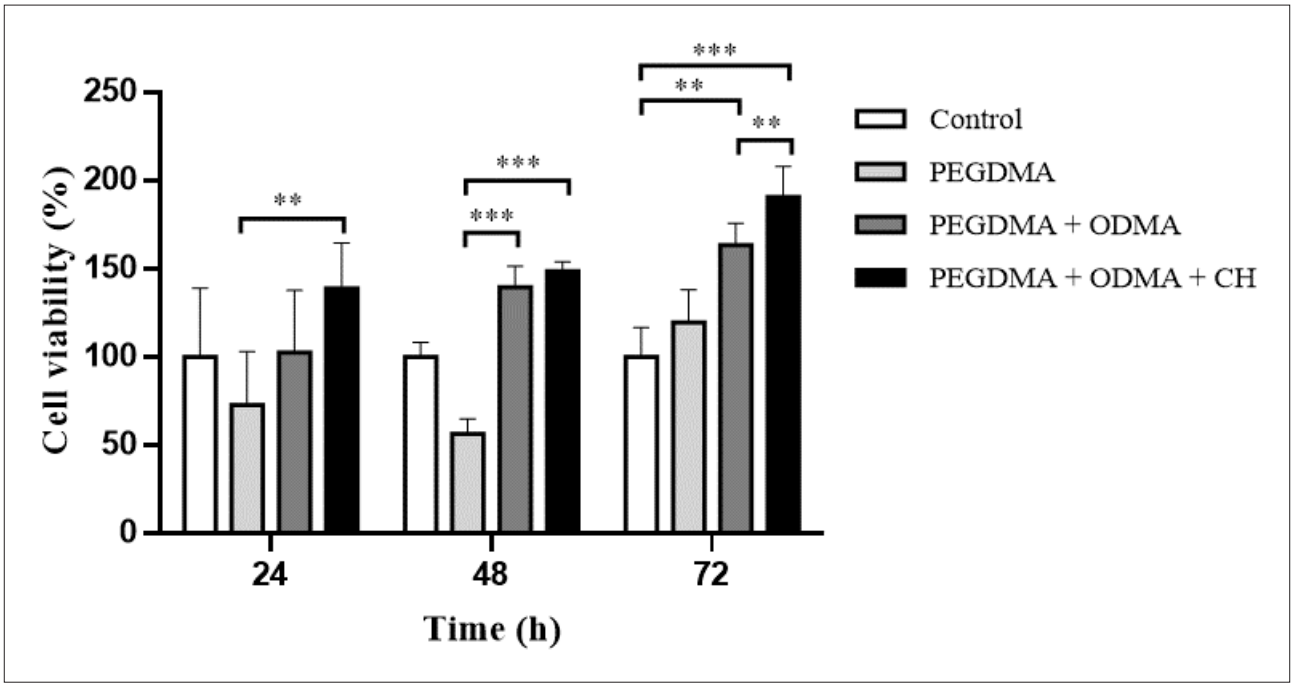

Figure 16. The percentage survival of chondrocytes on scaffolds with different compositions (PEGDMA; PEGDMA/ODMA; PEGDMA/ODMA/CH) at 24, 48, and 72 h (n = 3). Abbreviations: CH, collagen hydrolysate; ODMA, oligomers of dopamine methacrylate; PEGDMA, polyethylene glycol dimethacrylate. $^{**}p < 0.01$ and $^{***}p < 0.001$ were regarded as significant.

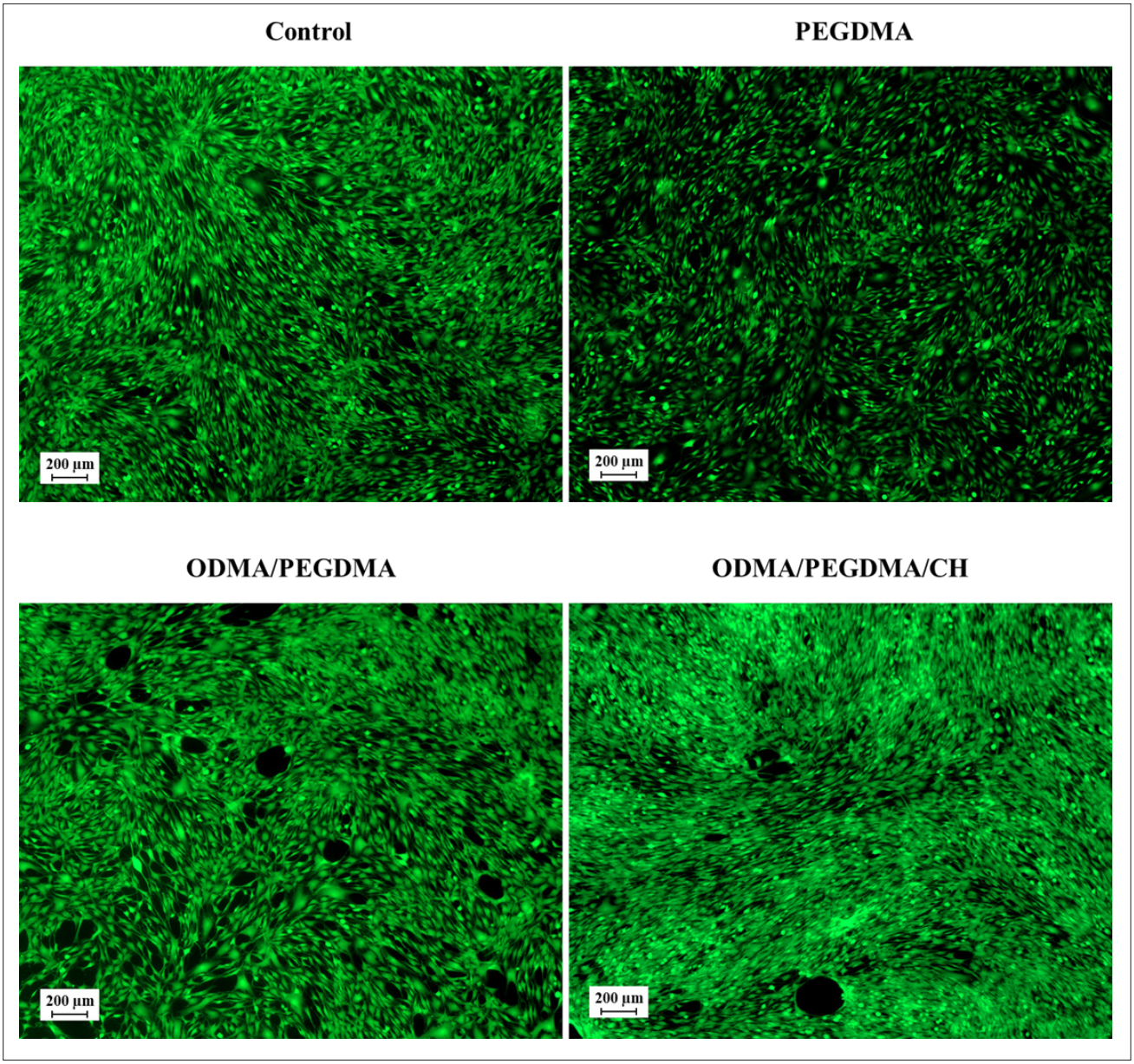

Figure 17. Live/dead fluorescence staining images of chondrocytes on scaffolds with different compositions over 72 h at 5× magnification. Abbreviations: CH, collagen hydrolysate; ODMA, oligomers of dopamine methacrylate; PEGDMA, polyethylene glycol dimethacrylate. Scale bars: 200 µm.

combining these components will enhance their mechanical properties and cell encapsulation capabilities, making it feasible to create hybrid scaffolds with durable parts to withstand applied forces and weaker parts that can serve as hydrogels to encapsulate cells, growth factors, or drugs within the material. This facilitates the growth and differentiation of chondrocyte cells, allowing for faster cartilage regeneration compared to scaffolds made from conventional thermoplastic materials, such as polycaprolactone (PCL), poly(glycolic acid) (PGA), or polylactide (PLA), which cannot form hydrogels and accommodate cells, growth factors, or drugs within. In addition, the scaffold can be precisely replicated using DLP bioprinting techniques.

4. Conclusion

We successfully synthesized DMA and verified its chemical structure and composition using NMR and FTIR, respectively. These analyses confirmed that the structure of DMA aligned with previous studies. Additionally, DSC analysis of DMA's thermal properties identified a melting point at 118°C. Further exploration

of the properties of ODMA resin mixed with PEGDMA at varying concentrations revealed its compatibility with DLP 3D printing, except for the lowest concentration (0.625% w/v), which exhibited reduced formability. SEM analysis of the cell scaffolds fabricated from this resin highlighted differences in surface morphology, with the 0.625% concentration exhibiting a rough and irregular surface compared to the smoother surfaces obtained at higher concentrations. For the mechanical property test, it was found that PEGDMA with 10% ODMA, the highest compared to 0.625%, 1.25%, 2.5%, and 5.0% concentration studied here, had the maximum strain and stress values compared to the other concentrations. Cytotoxicity tests on fibroblast cells in media containing CH post-sterilization reported promising results; fluorescent staining revealed a high number of viable fibroblasts in all samples. Chondrocyte cell viability on scaffolds displayed varying survival rates across different scaffold compositions, with ODMA/PEGDMA and ODMA/PEGDMA/CH composites exhibiting significantly higher viability compared to PEGDMA alone. These findings demonstrate the potential of these materials for biomedical applications, particularly in cartilage tissue engineering, where scaffold biocompatibility and mechanical properties are crucial.

Acknowledgments

The authors are thankful to Anuchan Panaksri for proofreading and editing this manuscript.

Funding

The present study was supported by the National Research Council of Thailand (NRCT) via the Invention to Business (I-2B) Program (contract number: N82A670613). This research was also supported by Rangsit University. This research project was funded by Fundamental Fund 2023, Chiang Mai University.

Author contributions

Conceptualization: K. Pasanaphong, A. Suksuwan, R. Hemstapat, T. Tawonsawatruk, S. Boonyagul, N. Tanadchangsaeng

Data curation: K. Pasanaphong, N. Srikaew, R. Hemstapat, P. Wongsirichot, N. Tanadchangsaeng

Formal analysis: K. Pasanaphong, A. Suksuwan, N. Srikaew, R. Hemstapat, N. Khamthong, S. Boonyagul, P. Wongsirichot, N. Tanadchangsaeng

Funding acquisition: S. Wangtueai, N. Tanadchangsaeng

Investigation: K. Pasanaphong, A. Suksuwan, N. Srikaew, N. Khamthong, S. Boonyagul, N. Tanadchangsaeng

Methodology: K. Pasanaphong, A. Suksuwan, R. Hemstapat, T. Tawonsawatruk, S. Boonyagul, N. Tanadchangsaeng

Resources: K. Pasanaphong, N. Srikaew, T. Tawonsawatruk, S. Wangtueai, N. Tanadchangsaeng

Software: A. Suksuwan, R. Hemstapat, T. Tawonsawatruk, S. Wangtueai, N. Tanadchangsaeng

Supervision: A. Suksuwan, R. Hemstapat, T. Tawonsawatruk, S. Boonyagul, N. Tanadchangsaeng

Project administration: N. Tanadchangsaeng

Validation: All authors

Visualization: K. Pasanaphong, A. Suksuwan, N. Srikaew

Writing – original draft: K. Pasanaphong, A. Suksuwan, N. Srikaew, R. Hemstapat, S. Boonyagul, P. Wongsirichot, N. Tanadchangsaeng

Writing – review & editing: K. Pasanaphong, A. Suksuwan, N. Srikaew, R. Hemstapat, S. Boonyagul, P. Wongsirichot, N. Tanadchangsaeng

Conflict of interest

The authors declare no competing interests.

Ethics approval and consent to participate

All human samples used in this study were approved by the Human Research Ethics Committee of the Faculty of Medicine Ramathibodi Hospital, Mahidol University (COA. MURA2022/469). A written informed consent document was signed by the enrolled participant prior to the initiation of the study. The demographic data of patients cannot be tracked to their profiles. We confirm that all methods and experimental protocols were carried out in accordance with relevant guidelines and regulations.

Consent for publication

Not applicable.

Availability of data

The datasets used and/or analyzed in the study are available from the corresponding author upon reasonable request.

References

1. Sophia Fox AJ, Bedi A, Rodeo SA. The basic science of articular cartilage: structure, composition, and function. *Sports Health*. 2009; 1:461-468. doi: 10.1177/1941738109350438

2. Wojcieszek A, Kurowska A, Majda A, Liszka H, Gądek A. The impact of chronic pain, stiffness and difficulties in

performing daily activities on the quality of life of older patients with knee osteoarthritis. *Int J Environ Res Public Health*. 2022;19(24):16815.
doi: 10.3390/ijerph192416815

3. Putti V. Arthroplasty. *J Orthop Surg*. 1921;3(9):421-430.

4. Bugbee WD, Pallante-Kichura AL, Görtz S, Amiel D, Sah R. Osteochondral allograft transplantation in cartilage repair: graft storage paradigm, translational models, and clinical applications. *J Orthop Res*. 2016;34:31-38.
doi: 10.1002/jor.22998

5. Redondo ML, Beer AJ, Yanke AB. Cartilage restoration: microfracture and osteochondral autograft transplantation. *J Knee Surg*. 2018;31:231-238.
doi: 10.1055/s-0037-1618592

6. Mithoefer K, McAdams T, Williams RJ, Kreuz PC, Mandelbaum BR. Clinical efficacy of the microfracture technique for articular cartilage repair in the knee: an evidence-based systematic analysis. *Am J Sports Med*. 2009;37:2053-2063.
doi: 10.1177/0363546508328414

7. Davies RL, Kuiper NJ. Regenerative medicine: a review of the evolution of autologous chondrocyte implantation (ACI) therapy. *Bioengineering*. 2019;6:22.
doi: 10.3390/bioengineering6010022

8. Gille J, Behrens P, Schulz AP, Oheim R, Kienast B. Matrix-associated autologous chondrocyte implantation: a clinical follow-up at 15 years. *Cartilage*. 2016;7(4): 309-315.
doi: 10.1177/1947603516638901

9. Chang LR, Marston G, Martin A. Anatomy, cartilage. In: *StatPearls [Internet]*. StatPearls Publishing; 2024.
doi: 10.1177/1947603516638901

10. Gan D, Xu T, Xing W, et al. Mussel-inspired dopamine oligomer intercalated tough and resilient gelatin methacryloyl (GelMA) hydrogels for cartilage regeneration. *J Mater Chem B*. 2019;7(10):1716-1725.
doi: 10.1039/C8TB01664J

11. Killion JA, Geever LM, Devine DM, Kennedy JE, Higginbotham CL. Mechanical properties and thermal behaviour of PEGDMA hydrogels for potential bone regeneration application. *J Mech Behav Biomed Mater*. 2011;4:1219-1227.
doi: 10.1016/j.jmbbm.2011.04.004

12. Burke G, Barron V, Geever T, Geever L, Devine DM, Higginbotham CL. Evaluation of the materials properties, stability and cell response of a range of PEGDMA hydrogels for tissue engineering applications. *J Mech Behav Biomed Mater*. 2019;99:1-10.
doi: 10.1016/j.jmbbm.2019.07.003

13. Husár B, Hatzenbichler M, Mironov V, Liska R, Stampfl J, Ovsianikov A. Photopolymerization-based additive manufacturing for the development of 3D porous scaffolds. In: Dubruel P, Van Vlierberghe S (eds.) *Biomaterials for Bone Regeneration*. Woodhead Publishing; 2014.
doi: 10.1533/9780857098104.2.149

14. Liu H, Yang Y, Liu Y, Cui L, Fu L, Li B. Various bioactive peptides in collagen hydrolysate from salmo salar skin and the combined inhibitory effects on atherosclerosis in vitro and in vivo. *Food Res Int*. 2022;157:111281.
doi: 10.1016/j.foodres.2022.111281

15. Larder CE, Iskandar MM, Kubow S. Collagen hydrolysates: a source of bioactive peptides derived from food sources for the treatment of osteoarthritis. *Medicines*. 2023;10:50.
doi: 10.3390/medicines10090050

16. Li H, Dai J, Wang Z, et al. Digital light processing (DLP)-based (bio)printing strategies for tissue modeling and regeneration. *Aggregate*. 2023;4:e270.
doi: 10.1002/agt2.270

17. Zhang J, Hu Q, Wang S, Tao J, Gou M. Digital light processing based three-dimensional printing for medical applications. *Int J Bioprint*. 2020;6:242.

18. Sultan MT, Lee OJ, Lee JS, Park CH. Three-dimensional digital light-processing bioprinting using silk fibroin-based bio-ink: recent advancements in biomedical applications. *Biomedicines*. 2022;10:3224.
doi: 10.3390/biomedicines10123224

19. Chanmangkang S, Maneerote J, Surayot U, Panya A, You S, Wangtueai S. Physicochemical and biological properties of collagens obtained from tuna tendon by using the ultrasound-assisted extraction. *J Agric Food Res*. 2024;15:100984.
doi: 10.1016/j.jafr.2024.100984

20. Tangchitphisut P, Srikaew N, Numhom S, Liao M, et al. Infrapatellar fat pad: an alternative source of adipose-derived mesenchymal stem cells. *Arthritis*. 2016; 2016: 4019873.
doi: 10.1155/2016/4019873

21. Ritian J, Teng X, Liao M, et al. Release of dipeptidyl peptidase IV inhibitory peptides from salmon (Salmo salar) skin collagen based on digestion–intestinal absorption in vitro. *Int J Food Sci Technol*. 2021;56:3507-3518.
doi: 10.1111/ijfs.14977

22. Xiong X, Qu SX, Liu YM. Synthesis and characterization of dopamine graft compound N-methacryloyl 3,4-dihydroxyl-phenylamine. *J Phys Conf Series*. 2013;419:2047.
doi: 10.1088/1742-6596/419/1/012047

23. Hu H, Wang L, Xu B, et al. Construction of a composite hydrogel of silk sericin via horseradish peroxidase-catalyzed graft polymerization of poly-PEGDMA. *J Biomed Mater Res B Appl Biomater*. 2020; 108(6):2643-2655.
doi: 10.1002/jbm.b.34596

24. Lin X, Zhao X, Xu C, Wang L, Xia Y. Progress in the mechanical enhancement of hydrogels: Fabrication strategies and underlying mechanisms. *J Polym Sci*. 2022;60: 2525-2542.

doi: 10.1002/pol.20220154

25. Sai KP, Babu M. Studies on Rana tigerina skin collagen. *Comp Biochem Physiol B Biochem Mol Biol*. 2001; 128:81-90.
doi: 10.1016/s1096-4959(00)00301-8

26. Hsu B-L, Weng Y-M, Liao Y-H, Chen W. Structural investigation of edible zein films/coatings and directly determining their thickness by FT-Raman spectroscopy. *J Agric Food Chem*. 2005;53:5089-5095.
doi: 10.1021/jf0501490

27. Kittiphattanabawon P, Benjakul S, Sinthusamran S, Kishimura H. Gelatin from clown featherback skin: Extraction conditions. *LWT Food Sci Technol*. 2016;66:186-192.
doi: 10.1016/j.lwt.2015.10.029

28. Payne KJ, Veis A. Fourier transform ir spectroscopy of collagen and gelatin solutions: Deconvolution of the amide I band for conformational studies. *Biopolymers*. 1988;27:1749-1760.
doi: 10.1002/bip.360271105

29. Zhang Y, Chen Z, Liu X, Shi J, Chen H, Gong Y. SEM, FTIR and DSC investigation of collagen hydrolysate treated degraded leather. *J Cult Herit*. 2021;48:205-210.
doi: 10.1016/j.culher.2020.11.007

30. Schmidt MM, Fontoura AMd, Vidal AR, et al. Characterization of hydrolysates of collagen from mechanically separated chicken meat residue. *Food Sci Technol*. 2020;40:355-362.
doi: 10.1590/fst.14819

31. Monaco G, Cholas R, Salvatore L, Madaghiele M, Sannino A. Sterilization of collagen scaffolds designed for peripheral nerve regeneration: Effect on microstructure, degradation and cellular colonization. *Mater Sci Eng C Mater Biol Appl*. 2017;71:335-344.
doi: 10.1016/j.msec.2016.10.030

32. Pasanaphong K, Jittrontrum P, Srikaew N, et al. Effect of sterilization methods on collagen hydrolysate obtained from tuna tendon. *Appl Sci*. 2024;14:6201.
doi: 10.3390/app14146201

33. Grandis RAD, Miotto LN, Genaro LE, et al. In vitro evaluation of acellular collagen matrices derived from porcine pericardium: influence of the sterilization method on its biological properties. *Materials*. 2021; 14:6255.
doi: 10.3390/ma14216255

34. Wang H-C, Lin T-H, Hsu C-C, Yeh M-L. Restoring osteochondral defects through the differentiation potential of cartilage stem/progenitor cells cultivated on porous scaffolds. *Cells*. 2021;10:3536.
doi: 10.3390/cells10123536

35. Jia L, Zhang P, Ci Z, et al. Immune-inflammatory responses of an acellular cartilage matrix biomimetic scaffold in a xenotransplantation goat model for cartilage tissue engineering. *Front Bioeng Biotechnol*. 2021; 9:667161.
doi: 10.3389/fbioe.2021.667161

36. Bourdon B, Cassé F, Gruchy N, et al. Marine collagen hydrolysates promote collagen synthesis, viability and proliferation while downregulating the synthesis of pro-catabolic markers in human articular chondrocytes. *Int J Mol Sci*. 2021;22:3693.
doi: 10.3390/ijms22073693

ACCSCIENCE PUBLISHING

International Journal of Bioprinting

RESEARCH ARTICLE

Development and applications of an *in vitro* non-alcoholic fatty liver disease model based on 3D-printed liver tissue

Kun Du[1], Wei Peng[2], Ying Zhao[2], Tianma He[2], Tao Ding[2], Feifei Pu[3], Zibei Ming[2], Renquan Ruan[4], and Jing Liu[2]*

[1] Department of Medical Equipment, Wuhan No. 1 Hospital, Wuhan, Hubei, China

[2] Department of Biological Engineering, School of Biology, Food and Environment, Hefei University, Hefei, Anhui, China

[3] Department of Orthopedics, Wuhan No.1 Hospital, Wuhan, Hubei, China

[4] Shenzhen Mellgen Biotechnology Co. Ltd., Shenzhen, Guangdong, China

Abstract

Non-alcoholic fatty liver disease (NAFLD) is a prevalent chronic disease worldwide, but its underlying etiology and molecular mechanisms are complex, and there are currently no effective clinical treatments. Animal models for studying NAFLD have limitations, necessitating the development of novel *in vitro* models. In this study, a bioink was first optimized for the cultivation of liver tissue. Subsequently, 3D bioprinting technology was utilized to construct large-scale liver tissue with a vascular-like function *in vitro* using the optimized bioink. Thereafter, the printed HepaRG cells were induced to form liver organoids. Compared with traditional liver tissue models, 3D-printed liver tissue has superior hepatic functions and greater cell viability. Moreover, glycogen storage and the formation of bile canaliculi-like structures were observed within it. Subsequently, 3D-printed liver tissue was induced to establish an NAFLD model, which was confirmed by lipid droplet analysis, liver function assays, and cell viability assessments. Additionally, this NAFLD model was used for drug testing and analysis. Our study successfully constructed a functional NAFLD model, which contributes to a deeper understanding of the mechanisms underlying NAFLD, facilitates the development of related pharmaceuticals, and promotes the development of new therapeutic strategies.

Keywords: Non-alcoholic fatty liver disease; 3D bioprinting; Large-scale liver tissue; *In vitro* model; Drug testing

***Corresponding author:**
Jing Liu (liujing@hfuu.edu.cn)

Citation: Du K, Peng W, Zhao Y, et al. Development and applications of an *in vitro* non-alcoholic fatty liver disease model based on 3D-printed liver tissue. *Int J Bioprint*. 2024;10(6):4312. doi: 10.36922/ijb.4312

Received: July 23, 2024
Revised: September 2, 2024
Accepted: September 18, 2024
Published Online: September 18, 2024

Copyright: © 2024 Author(s). This is an Open Access article distributed under the terms of the Creative Commons Attribution License, permitting distribution, and reproduction in any medium, provided the original work is properly cited.

Publisher's Note: AccScience Publishing remains neutral with regard to jurisdictional claims in published maps and institutional affiliations.

1. Introduction

Non-alcoholic fatty liver disease (NAFLD) is currently one of the most prevalent chronic diseases worldwide and is significantly associated with obesity and metabolic disorders. The global prevalence of NAFLD is estimated to be approximately 25% of the population, with an increasing trend observed annually.[1] Early-stage NAFLD is generally asymptomatic and does not affect patient survival; however, if left untreated, it can

progress to non-alcoholic steatohepatitis (NASH).[2] NASH is a more severe form of NFALD that can lead to liver fibrosis, cirrhosis, and hepatocellular carcinoma.[1,3] Despite the high prevalence and potential severity of NAFLD, the underlying etiology and molecular mechanisms are extremely complex and not fully understood,[4,5] posing significant challenges for drug development. Currently, no effective clinical treatments are available for NAFLD.[6,7] To address these challenges, it is crucial to select appropriate models for studying NAFLD. Presently, research predominantly relies on animal models, which are commonly developed through high-fat diet induction,[8,9] genetic modification,[10] and chemical induction.[11] These animal models are invaluable for simulating the multifaceted physiological and pathological processes of NAFLD, including lipid accumulation, inflammation, and fibrosis,[12] thereby facilitating comprehensive and systematic investigations of the disease. However, animal models have several limitations, including species differences, strain variability, high costs, long durations, limited capacity for high-throughput studies, and ethical concerns.[6,13,14] These limitations necessitate the development of novel, effective *in vitro* models of NAFLD.

In recent decades, *in vitro* NAFLD models have advanced rapidly and are categorized primarily into three types based on their cultivation methods: 2D models, 3D models, and liver-on-a-chip models. 2D cell culture is the simplest and most commonly used *in vitro* model for NAFLD research. Various cell lines, such as HL-7702, HepaRG, and HepG2, have been used to generate these NAFLD models and investigate physiological pathology and drug mechanisms.[15-17] Despite their simplicity, 2D NAFLD models have significant limitations, including the loss of liver cell-specific functions during cultivation, nonbiomimetic cell arrangement, and the inability to sustain long-term culture, thus restricting their application in disease research and drug screening. To overcome these limitations, 3D NAFLD models, including cell spheroids,[14] organoids,[6,18] and extracellular matrix-based 3D culture methods,[19] have been developed. These 3D models provide a more accurate simulation of the *in vivo* environment and are used to study the pathogenesis, drug treatment, development mechanisms, genetic factors, and inflammatory responses of NAFLD.[14,18,20,21] While 3D cell cultures offer improved biomimicry over 2D models, most existing 3D models are limited to cell spheroids, which suffer from mass transfer efficiency issues, preventing the preparation of large-scale *in vitro* models. The advent of microfabrication and microfluidics technologies has led to the emergence of organ-on-a-chip models with complex microstructures and precisely controllable physicochemical microenvironments.[22] Liver-on-a-chip NAFLD models incorporating various designs such as liver sinusoid structures, high-throughput systems, and vascularized chips, have been developed.[23-25] These models more closely replicate the *in vivo* progression of NAFLD than traditional 3D models do[26] and have been used to study disease progression mechanisms, inflammatory responses, and drug efficacy.[24,27,28] However, current microfluidic chips are often limited to microscale dimensions, constraining the size of cultured tissues and making it difficult to detect certain key cellular metabolites. Large-scale organs necessitate an effective nutrient supply system to deliver oxygen and nutrients while removing waste products. However, replicating a functional vascular supply system in an *in vitro* environment poses significant challenges. Consequently, the construction of large-scale liver tissue models remains a formidable task in tissue engineering research. 3D bioprinting technology, which can create complex 3D structures, holds great potential and advantages in creating highly biomimetic human tissue models. However, there are still few reports on the use of 3D-printed liver tissues to construct NAFLD models.

In this study, we first optimized a bioink suitable for the cultivation of liver tissue. By leveraging 3D bioprinting technology, we subsequently generated large-scale liver tissue *in vitro* with vascular-like function and induced HepaRG cells to form liver organoids. Compared with traditional liver tissue models, 3D-printed liver tissue exhibited superior hepatic functions and greater cell viability; additionally, glycogen storage and the formation of bile canaliculi-like structures were observed. Next, we used 3D-printed liver tissue to establish an NAFLD model. The successful establishment of the NAFLD model was confirmed through lipid droplet analysis, liver function assays, and cell viability assessments. We subsequently utilized this NAFLD model for drug testing and analysis. In summary, our study successfully constructed a functional NAFLD model, which contributes to a deeper understanding of the mechanisms underlying NAFLD, facilitates the development of related pharmaceuticals, and promotes the development of new therapeutic strategies.

2. Materials and methods

2.1. Materials

Alginate, gelatin, fibrinogen, and 5(6)-carboxy-2',7'-dichlorofluorescein diacetate (CDFDA) were purchased from Sigma-Aldrich (United States of America [USA]). Dulbecco's modified Eagle's medium (DMEM), penicillin-streptomycin, and glutamine were obtained from Gibco-Invitrogen (USA). HepaRG cells were acquired from the Bena Culture Collection (China). Insulin, hydrocortisone

hemisuccinate, Nile red, and calcein-AM were obtained from Shanghai Aladdin Biochemical Technology Co., Ltd. (China). Fetal bovine serum was sourced from Lonsera (Uruguay). Trypsin-EDTA, PAS staining solution, and FAA fixative were obtained from Wuhan Servicebio Technology Co., Ltd. (China). Anhydrous calcium chloride, DAPI staining solution, propidium iodide (PI), Triton X-100, xylene, absolute ethanol, palmitic acid, oleic acid, and bovine serum albumin (BSA) were obtained from Sangon Biotech (Shanghai) Co., Ltd. (China). Albumin and CYP3A4 primary antibodies were purchased from Proteintech Co., Ltd. (China). Secondary antibodies Alexa Fluor 488 and 594 were from Invitrogen (USA). Commercial Tissue/Cell RNA Rapid Extraction Kits, cDNA Synthesis Kits, and SYBR Green were obtained from Mei5 Biotechnology, Co., Ltd. (China).

2.2. Cell culture

HepaRG cells were cultured in DMEM supplemented with 1% penicillin-streptomycin, 5 μg/mL insulin, 2 mM glutamine, 50 μM hydrocortisone hemisuccinate, and 10% fetal bovine serum. The cultures were maintained at 37°C in a humidified incubator with 5% CO_2. When the cells reached 90% confluence, they were passaged with 0.25% trypsin-EDTA. The culture medium was changed every 2–3 days.

2.3. Design of the printing model

The design of the liver tissue printing model was developed via BIOCAD software (provided with the REGENHU/R-GEN 200). To ensure adequate nutrient supply and timely removal of metabolic waste, the printing model was designed in a grid pattern. The overall structure is a 10 × 10 mm square, printed with a 0.33 mm inner diameter needle and divided into four layers. The printing method is extrusion-based, with a line spacing of 1 mm (**Figures 1A** and **S1A, Supporting Information**). The printing direction of the first and third layers is horizontal, whereas the second and fourth layers are printed vertically. This alternating printing direction forms a grid-like structure.

2.4. Preparation of the bioink

Based on our previous experience,[29] we further optimized the bioink formulation to enhance its printability, mechanical properties, and biocompatibility, making it more suitable for liver tissue printing. A precise amount of gelatin and alginate powder was weighed and sterilized by ultraviolet (UV) lamp irradiation for 1 h before use. The powders were then dissolved in the culture medium and incubated in a water bath at 60°C for 1 h. To ensure thorough pasteurization, the solution was removed every hour and cooled for 30 min, and this process was repeated three times. After complete dissolution and cooling to approximately 37°C, the solution was mixed with the cell suspension to prepare cell-laden bioinks with varying concentrations. The gelatin concentrations were set at 3, 5, and 7%, and the alginate concentrations were set at 0.5, 1, 1.5, and 2% (w/v) for subsequent experiments. Next, the fibrinogen and laminin powders were weighed and dissolved in phosphate-buffered saline (PBS) to prepare stock solutions with concentrations of 10 mg/mL for fibrinogen and 100 μg/mL for laminin. Different concentrations of fibrinogen (0.5, 1, 3, and 5 mg/mL) and laminin (10, 30, 50, and 70 μg/mL) were then added to the optimized gelatin/alginate bioinks to create optimized bioinks suitable for liver tissue culture.

2.5. Printing and culturing of liver tissue

A HepaRG cell suspension with a density of 4×10^6 cells/mL was prepared and thoroughly mixed with bioink at a 1:1 ratio to produce the cell-laden bioink. The cell-laden bioink was injected into a sterile printing syringe and loaded into the temperature-controlled printhead of the 3D bioprinter. The syringe temperature was set to 5°C, and the ambient temperature was maintained at 25°C. The liver tissue was printed in a layered square grid structure at an extrusion pressure of 0.178 kPa and a speed of 5 mm/s. Upon completion of printing, the liver tissue was immediately transferred to a 2% $CaCl_2$ solution for 5 min to induce crosslinking. After crosslinking, the tissue was rinsed with PBS and then cultured. HepaRG is a human hepatic progenitor cell line that requires induction to differentiate into functional hepatocytes and biliary epithelial cells. In this study, we used the conventional method of adding 2% dimethyl sulfoxide (DMSO) to the culture medium for differentiation.[19]

2.6. Cell viability

Calcein-AM can permeate the cell membrane, where intracellular esterases hydrolyze it to calcein, which remains inside the cells and emits green fluorescence, thereby labeling live cells. PI is an ethidium bromide analog that binds to double-stranded DNA, producing red fluorescence under UV excitation. PI can only enter cells and stain the nucleus when the cells are dead and their membranes are compromised. In the experiment, the working concentration of PI was 10 μg/mL, and the working concentration of calcein-AM was 5 μM. After the cultured liver tissue was harvested, it was incubated with the calcein-AM/PI working solution at 37°C for 30 min. Imaging was then performed via a laser light source dual spinning disk confocal high-content analysis system (CQ1; YOKOGAWA, Japan). To ensure the accuracy and reliability of calcein-AM/PI staining, we conducted three replicate stains for each experimental condition.

2.7. CDFDA staining

Bile canaliculi formation was evaluated via the use of 5(6)-carboxy-2',7'-dichlorofluorescein diacetate.[27] The CDFDA stock solution was diluted with PBS to create a 5 μM working solution for staining. The samples were washed with PBS before being exposed to the CDFDA working solution at 37°C for 20–30 min. Subsequently, 10 μg/mL DAPI was added, and the samples were incubated for 10 min. After the staining solution was removed, the samples were washed with another round of PBS. Finally, the samples were analyzed via the CQ1 system to visualize CDF accumulation (green) and capture images.

2.8. Immunofluorescence analysis

Following a similar protocol,[30] liver tissue samples were fixed with 50% FAA fixative for 60 min and then permeabilized with 0.2% Triton X-100 in PBS for 15 min. Subsequently, the samples were blocked with 2% BSA in PBS for 60 min, followed by overnight incubation with primary antibodies (albumin and CYP3A4) at 4°C. The cells were then incubated with the corresponding secondary antibodies Alexa Fluor 488 or 594 at room temperature for 40 min, and the nuclei were stained with DAPI (10 μg/mL) at room temperature for 20 min. Each step was followed by three washes with PBS. Finally, the samples were imaged via the CQ1 system.

2.9. Hepatic gene expression analysis

Quantitative reverse transcription polymerase chain reaction (qRT-PCR) was conducted to compare gene expression levels among the experimental groups. Total RNA was extracted from the experimental groups via a Tissue/Cell RNA Rapid Extraction Kit according to the manufacturer's instructions. The RNA quantity and purity were assessed via a microvolume spectrometer (LB 915; Colibri, Germany). Complementary DNA (cDNA) was synthesized via a commercial cDNA synthesis kit. qRT-PCR was performed to compare gene expression levels using SYBR Green on a LightCycler 96 system (Roche Life Science, Switzerland). The primers used were previously described,[19] and their sequences are listed in Table 1. Gene expression levels were normalized to those of glyceraldehyde-3-phosphate dehydrogenase (GAPDH) via the $2^{-\Delta\Delta Ct}$ method.

2.10. Induction of NAFLD

To induce NAFLD, we used a commonly employed induction method and fatty acid ratios, creating a lipid culture medium composed of a base medium supplemented with 5.5 mM glucose and a mixture of free fatty acids (FFAs) at 300, 600, or 900 μM.[27,31] The FFAs used in our model were a combination of palmitic acid and oleic acid at a 1:2 ratio. The FFA stock solution was prepared by dissolving palmitic acid (1 M) and oleic acid (2 M) in DMSO. This stock solution was then diluted in a culture medium supplemented with 1% BSA and incubated at 37°C for 2 h. The lipogenic medium was introduced on day 4 to the 3D-printed liver model to induce NAFLD through simple incubation. In this work, both 3D and 2D NAFLD models were developed via the experimental methods described above.

2.11. Lipid droplet staining and quantification

Nile red was used to detect intracellular lipid accumulation. The samples were fixed with FAA for 2 h at room temperature and then washed three times with PBS. The samples were subsequently incubated in PBS containing 2 μM Nile red and 10 μg/mL DAPI in the dark for 2 h, followed by three washes with PBS. Next, images were taken via microscopy, with a focus on the middle section of the sample. Lipid droplets were quantified by calculating the fluorescence intensity of Nile red normalized to the cell area (images were processed with ImageJ). The results for the control group were normalized, and those for the other experimental groups were expressed as relative multiples.

2.12. Drug treatments

Both preventive and reversible effects of drugs on NAFLD were assessed using elafibranor (ELA), a peroxisome proliferator-activated receptor α/δ agonist known for its ability to improve lipid metabolism and reduce inflammation.[32] The concentrations tested (10 and 30 μM) were selected based on prior NAFLD-related literature.[27] To evaluate the preventive effects, lipogenic medium (containing 5.5 mM glucose and 900 μM FFAs) with or

Table 1. List of Primers for qRT-PCR.

Gene	Sequence	
	Forward	Reverse
ALB	AGCATGGGCAGTAGCTCGCCT	AGGTCCGCCCTGTCATCAGCA
CYP3A4	CAGGAGGAAATTGATGCAGTTTT	GTCAAGATACTCCATCTGTAGCACAGT
CYP1A2	GCCTTCATCCTGGAGACCTT	AGCGTTGTGTCCCTTGTTG
β-actin	GAGCTGCGTGTGGCTCCC	CCAGAGGCGTACAGGGATAGCA

without ELA was introduced into the NAFLD model from days 4 to 7. Lipid accumulation and liver function were assessed on day 7. To assess the reversible effects, the lipogenic medium was added to the culture medium from days 4 to 6, followed by the culture medium with or without ELA introduced for 24 h. Lipid accumulation and liver function were evaluated on day 7.

2.13. Statistical analysis

The data are presented as the mean ± standard deviation of at least three samples per test. The *p*-values were calculated via two-tailed Student's *t*-test for comparisons between two groups, or one-way analysis of variance (ANOVA) for multiple group comparisons. Significance levels are indicated as follows: $*p < 0.05$; $**p < 0.01$; $***p < 0.001$; and N.S.: no significant difference.

3. Results and discussion

3.1. Optimization of the bioink formulation

To prepare bioink for liver tissue printing with good printability and biocompatibility, 12 different ratios of gelatin and sodium alginate were tested, and the optimal concentrations of fibrinogen and laminin were explored. The experimental results demonstrated that when the concentrations of gelatin and sodium alginate were too low, the bioink remained in droplet form at 5°C, making extrusion printing impossible. Conversely, when the concentrations were too high, the bioink formed a hard gel at 5°C, which was difficult to extrude. Only at appropriate ratios could the bioink be extruded into suitable filaments for printing (Figures 1A and S1D, Supporting Information). It was statistically determined (Figure 1B) that the printable concentration range for gelatin at 5°C is 3–5%. When the gelatin concentration reached 7%, the bioink became too hard for extrusion printing. For sodium alginate, the printable concentration range was 0.5–2%. Below 0.5%, crosslinking with $CaCl_2$ was difficult, and above 2%, the bioink was too viscous for printing. Therefore, the suitable gelatin/alginate ratios for extrusion printing were 3/0.5, 3/1, 3/1.5, 3/2, 5/0.5, and 5%/1%, respectively. Further analysis of cell viability under these six ratios revealed (Figure 1C) that the highest cell viability was achieved with 5% gelatin/0.5% alginate and 5% gelatin/1% alginate. The bioink with 3% gelatin resulted in lower overall cell viability, possibly due to its lower hardness, leading to structural collapse and slow degradation during the cultivation process, which negatively affected cell viability. Sodium alginate at 0.5% also tended to degrade during the later stages of cultivation. Based on these results, 5% gelatin and 1% alginate were selected for further experiments. Fibrinogen and laminin were added to the gelatin/alginate bioink to support cell adhesion and fixation within the 3D structure, promoting cell growth and migration. The results (Figure 1D) indicated that cell viability increased with increasing concentrations of fibrinogen and laminin, both on days 1 and 7 of cultivation. However, cell viability did not further improve when fibrinogen and laminin concentrations exceeded 1 mg/mL and 30 μg/mL, respectively. Considering the experimental costs, 1 mg/mL fibrinogen and 30 μg/mL laminin were selected as the optimal concentrations. The optimal bioink formulation for liver tissue printing was determined to be gelatin (5%), sodium alginate (1%), fibrinogen (1 mg/mL), and laminin (30 μg/mL). To evaluate the effects of the optimized bioink on liver cell function, we measured the gene expression levels of liver-specific proteins (CYP1A2, CYP3A4, and ALB). The results (Figure 1E) demonstrate that after 7 days of cultivation, liver tissues grown with bioink enriched with fibrinogen and laminin presented significantly higher expression levels of liver-specific proteins than those cultured with bioink containing only Gelatin Methacryloyl (GelMA) and alginate. This result is consistent with the literature,[30] indicating that the addition of fibrinogen and laminin can effectively enhance liver cell function. This formulation ensures good printability and significantly improves cell viability, providing a solid foundation for future liver tissue engineering applications.

3.2. Evaluation of 3D-printed liver tissues

To evaluate the growth status of 3D-printed liver tissue, the viability of hepatocytes was first analyzed. The results (Figure 2A and B) revealed that on days 1, 3, 5, and 7 of culture, high cell viability was maintained (i.e., >90%), with most areas exhibiting green fluorescence and no significant necrosis. To further validate the advantages of 3D-printed liver tissue, a comparison was made between the 3D-printed liver tissue model (bioprinting) and the hepatocyte gel-spheroid model constructed via suspension droplet technology (microsphere). The results (Figures 2C, D, and S1E, Supporting Information) indicated that after 1 day of culture, no significant difference in cell diameter was observed between the bioprinting and microsphere groups, with an average diameter of approximately 12 μm. However, by day 7 of culture, hepatocytes in the bioprinting group had proliferated to form organoid-like cell clusters, which were significantly larger (50.2 ± 6.4 μm) than those in the microsphere group (25 ± 1.2 μm). This was primarily due to the large scale (millimeter scale) of the gel spheroids in the microsphere group, where mass transfer limitations led to insufficient diffusion of nutrients and oxygen to the center, resulting in nutrient and oxygen deficiency in the central cells, thus hindering cell proliferation and growth (Figure S1F, Supporting Information). In contrast, a grid-like structure was provided by the bioprinting group, which mimicked the vascular channels in the liver, offering a similar

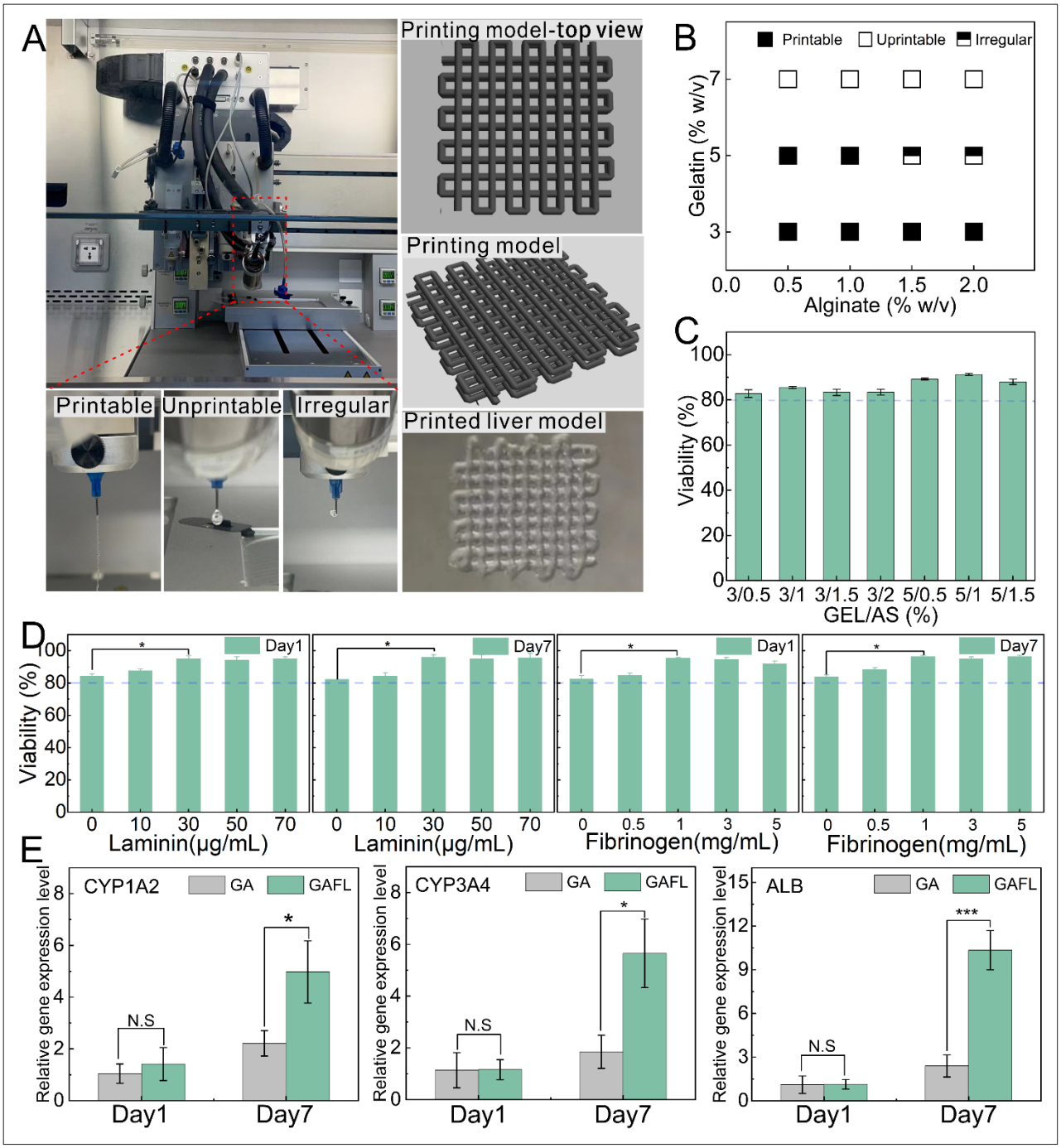

Figure 1. Optimization of the bioink formulation for liver tissue printing. (A) 3D bioprinting system and printing model of liver tissue. (B) Printability assessment of the bioink. (C) Biocompatibility assessment of the bioink. (D) Optimization of laminin and fibrinogen concentrations in the bioink. (E) Effects of optimized bioink on liver function. GA Refers to Bioink Containing only GelMA and Alginate, whereas GAFL Refers to Optimized Bioink Containing GelMA, Alginate, Laminin, and Fibrinogen.

culture environment for all cell regions. This structure facilitated uniform diffusion and transport of nutrients and oxygen, assisted in the removal of metabolic waste, and allowed for continuous cell proliferation, as illustrated in Figure S1B and C, Supporting Information. After 7 days of culture, central necrosis occurred in the microsphere group, indicating that the supply of oxygen and nutrients in the center was lacking. In contrast, the cells in the bioprinting group survived well. The glycogen storage capacity is directly related to the metabolic ability of hepatocytes. Therefore,

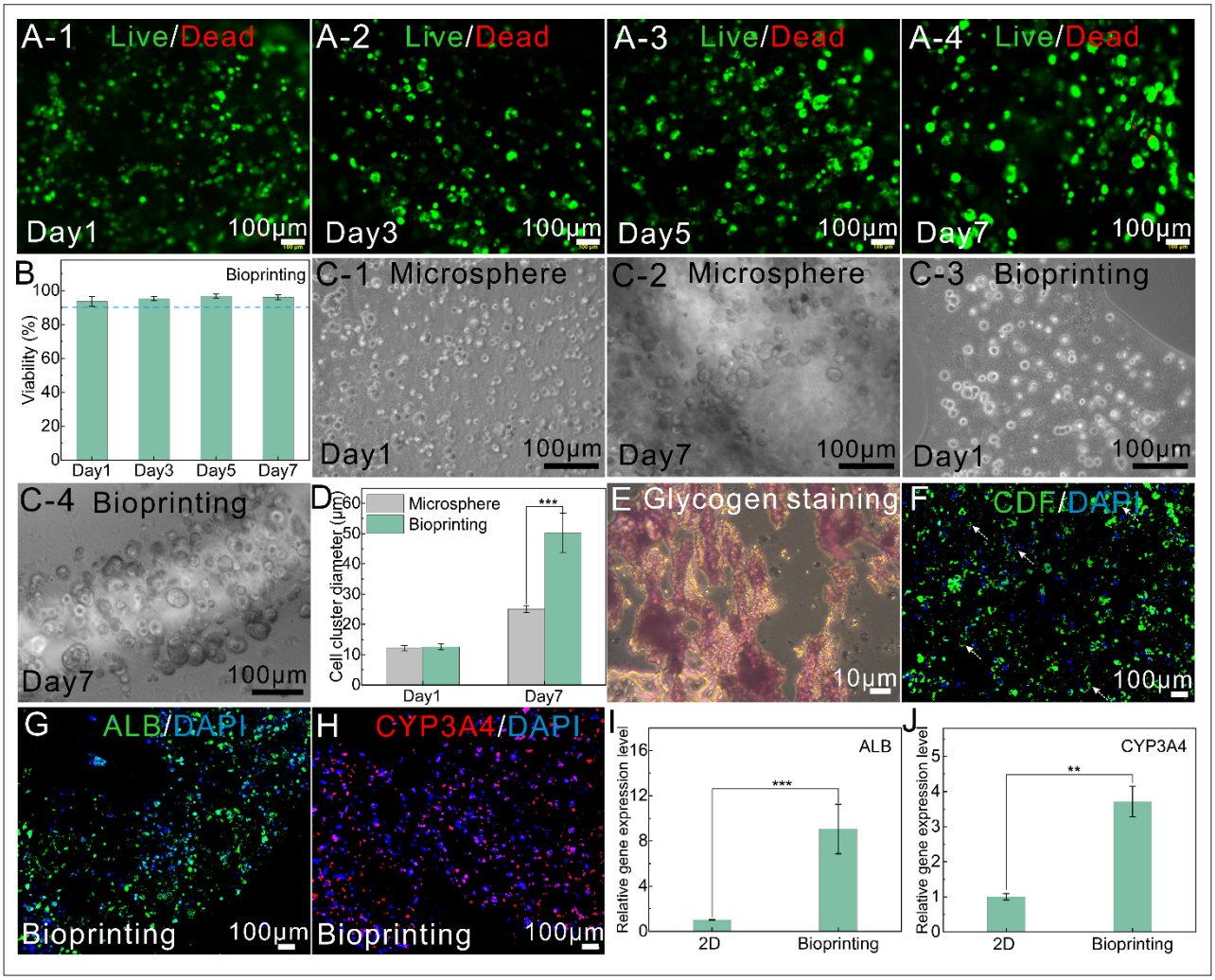

Figure 2. *In vitro* functional validation of 3D-printed liver tissue models. (A) Viability staining images of 3D-printed liver tissue on days 1 (A-1), 3 (A-2), 5 (A-3), and 7 (A-4). (B) Viability statistics of 3D-printed liver tissue. (C) Images of hepatocyte clusters in microspheres (C-1 and C-2) and 3D-printed liver tissue (C-3 and C-4) at different time points. (D) Size analysis of hepatocyte clusters in microspheres and 3D-printed liver tissue at different time points. (E) Image of glycogen-stained 3D-printed liver tissue. (F) Bile duct staining image. (G and H) Immunofluorescence image of hepatic-specific protein expression in 3D-printed liver tissue: ALB (G) and CYP3A4 (H). (I and J) Analysis of hepatic-specific protein-encoding gene expression levels in 3D-printed liver tissue: ALB (I) and CYP3A4 (J). Scale bar: 100 and 10 μm (E). $^{**}p < 0.01$; $^{***}p < 0.001$.

PAS staining was used to analyze the glycogen storage capacity of the 3D-printed liver tissue. The stain turned glycogen in the cells red, with deeper red indicating higher glycogen content. In Figure 2E, extensive deep red areas were observed within the liver tissue, indicating significant glycogen accumulation. Bile canaliculi are important structures in liver tissue, formed by local invaginations of the cell membranes of adjacent hepatocytes. On day 7, CDFDA staining was used to observe the formation of bile canaliculi in the 3D-printed liver tissue. CDFDA, a nonfluorescent, nonpolar ester compound, enters hepatocytes and is hydrolyzed by intracellular esterases into fluorescent CDF. CDF is transported to the bile canaliculi by relevant transport proteins, making it useful for detecting the formation and function of bile canaliculi. Figure 2F reveals that after 7 days of culture, CDF was released into the bile canaliculi-like structures between cells in the liver tissue model. According to the literature,[39] bile canaliculi can form *in vitro* in human hepatocytes after 6–10 days of culture. In this study, evaluation on day 7 revealed that bile canaliculi formed in the model, which is consistent with the literature. To evaluate the hepatic function of 3D-printed liver tissues, immunofluorescence (IF) was employed to qualitatively analyze the expression of albumin (ALB) and cytochrome P450 3A4 (CYP3A4). Additionally, qRT-PCR was used to quantitatively assess the gene expression

levels of these two proteins. The immunofluorescence results (Figure 2G and 2H) demonstrated that both ALB and CYP3A4 were normally expressed in 3D-printed liver tissues, and a uniform distribution was observed. The qRT-PCR quantitative analysis revealed that the gene expression levels of ALB and CYP3A4 in 3D-printed liver tissues were significantly greater than those in traditional 2D cultured hepatocytes (Figure 2I and 2J). Overall, 3D-printed liver tissues were found to be superior to conventional 2D and 3D hepatocyte models in both structure and function. The 3D-printed liver tissues not only closely resembled the morphology of *in vivo* liver tissues but also exhibited significantly enhanced expression of functional proteins. These advantages are attributed to the 3D microenvironment provided by 3D printing technology, which better simulates the tissue structure and function of the *in vivo* liver, particularly its vascular-like functionality, thereby promoting cell-cell interactions and nutrient transfer and consequently enhancing hepatic function. Therefore, the significant structural and functional advantages of 3D-printed liver tissues highlight their broad application potential in liver disease modeling and drug testing.

3.3. Establishment of a 3D-printed NAFLD model

An NAFLD model was established based on the 3D-printed liver tissues. Notably, research reports on 3D-printed NAFLD *in vitro* models are relatively limited. To investigate the time required to induce NAFLD, preliminary experiments were conducted to determine the optimal induction period. The results (Figure S2, Supporting Information) indicated that the lipid droplet content in 3D-printed liver tissues rapidly increased during the first 3 days of culture in the induction medium containing 600 or 900 μM FFAs and then gradually stabilized. Therefore, further studies were conducted 3 days post-induction. The accumulation of intracellular lipid droplets in the 3D-printed liver tissue model was studied after 3 days of induction with NAFLD medium to evaluate the effect of NAFLD induction medium on lipid droplet accumulation. The experimental procedure is illustrated in Figure 3A. The cells were cultured in an ordinary medium for the first 4 days and then transferred to the NAFLD induction medium on the fourth day. The experimental results (Figure 3B and C) demonstrated that the control group exhibited only minimal lipid droplets, whereas significant lipid droplet accumulation was observed in

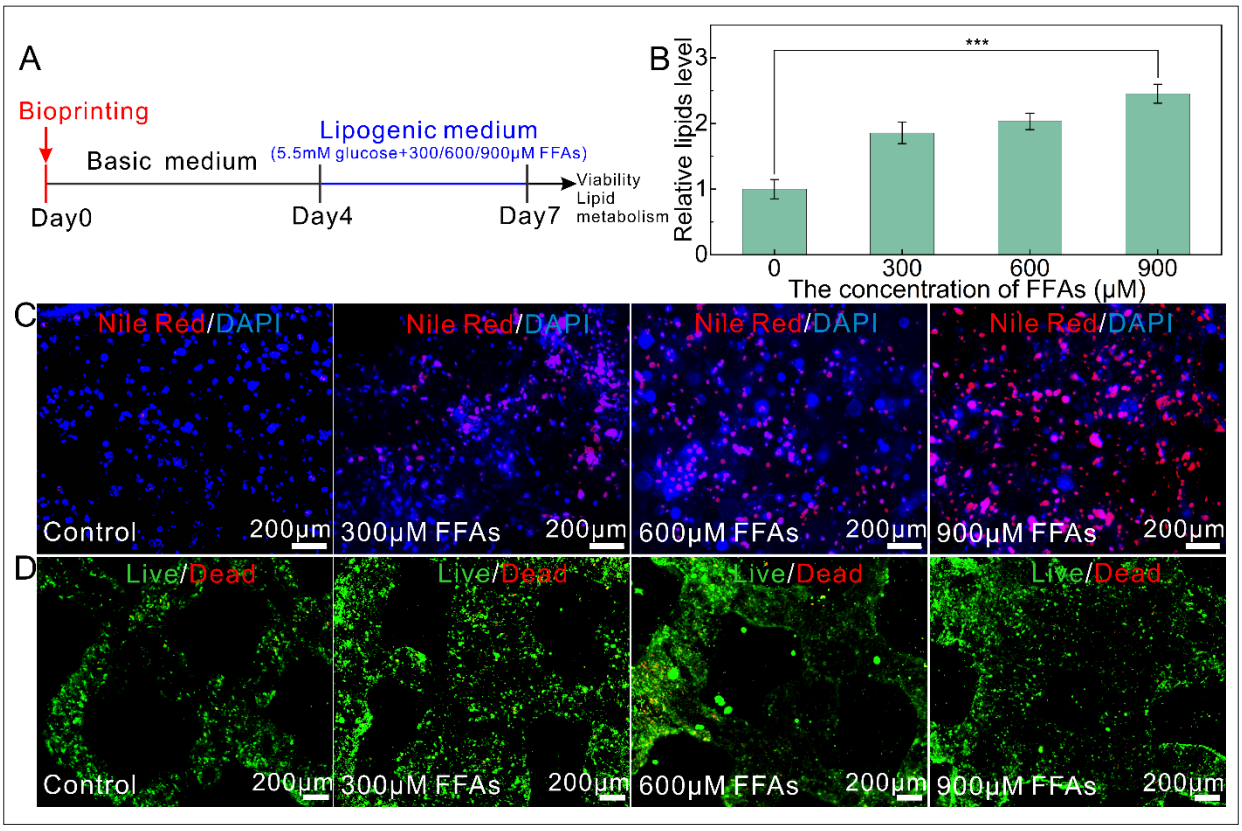

Figure 3. Construction of the non-alcoholic fatty liver disease (NAFLD) model. (A) Experimental procedure for constructing the NAFLD model. (B) Analysis of lipid droplet accumulation in NAFLD models; ***$p < 0.001$. (C) Images of lipid droplet accumulation in the NAFLD model. (D) Impact of different free fatty acid (FFA) concentrations on hepatocyte viability. Scale bar: 200 μm.

the 3D-printed model treated with NAFLD induction medium. Furthermore, as the concentration of FFAs in the NAFLD induction medium increased, the accumulation of intracellular lipid droplets also increased, indicating more effective induction. To assess the cytotoxicity of the NAFLD induction medium, cell viability analysis was performed on the induced liver tissue model. The results (Figure 3D) indicated that cell viability remained above 90% in NAFLD induction medium containing 300, 600, and 900 μM FFAs, with no significant difference compared with the control group (cultured in ordinary medium). These findings demonstrated that the NAFLD medium used in the present study did not affect cell viability and did not exhibit noticeable toxicity. These findings are consistent with the characteristics of NAFLD in humans, which are characterized by lipid droplet accumulation without cell apoptosis.[32] The experimental results demonstrated that significant lipid droplet accumulation could be achieved in 3D-printed liver tissue after 3 days of induction with NAFLD induction medium. Additionally, a higher concentration of FFAs in the induction medium resulted in a greater degree of lipid droplet accumulation. Moreover, the NAFLD induction medium had no significant effect on cell viability, suggesting its suitability for NAFLD model construction. Based on these findings, subsequent experiments used the NAFLD induction medium containing 900 μM FFAs for further research.

3.4. Evaluation of the 3D-printed NAFLD model

To evaluate the hepatic function of the NAFLD model, immunofluorescence qualitative analysis was used to assess the expression of albumin (ALB) and cytochrome P450 (CYP), and qRT-PCR was used to analyze the gene expression levels of ALB and CYP enzymes (CYP3A4 and CYP1A2). The immunofluorescence results revealed the expression of both key proteins ALB and CYP3A4 in the NAFLD model (Figure 4A). Compared with the control group (non-induced liver tissue model), ALB exhibited intense positive expression, indicating ongoing albumin synthesis. However, the protein expression level of CYP3A4 was significantly reduced, further emphasizing the similarity in CYP3A4 expression between the developed NAFLD model and NAFLD patients.[33] The qRT-PCR results revealed no significant difference in ALB expression between the NAFLD model group and the control group (Figure 4B), suggesting that the induced NAFLD model retained basic liver function and the potential for albumin synthesis. Some studies have suggested that albumin synthesis in NAFLD patients is unaffected by the disease,[26] which is consistent with the cellular albumin synthesis observed in the NAFLD model in this study. Compared with that in the control group, the activity of CYP3A4 or CYP1A2 in the NAFLD model group was significantly lower (Figure 4B). This may be due to NAFLD affecting liver function, resulting in reduced activity of the CYP450 enzyme and thereby

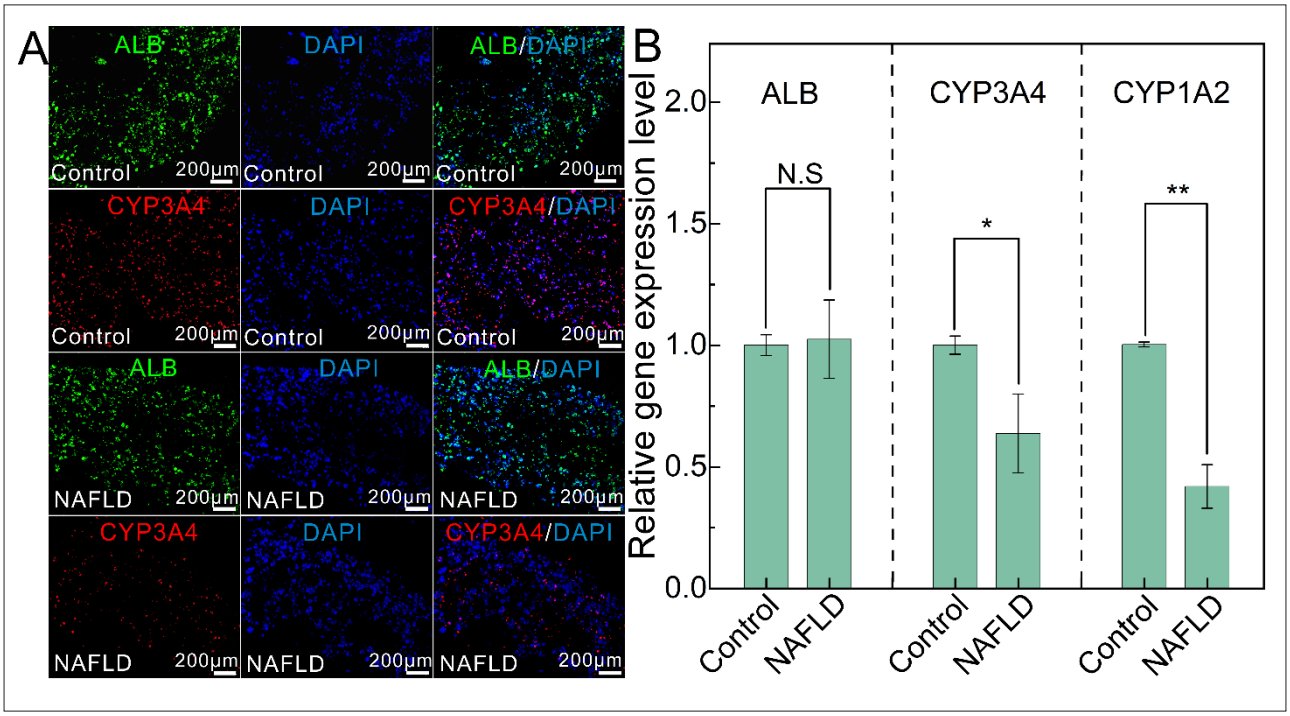

Figure 4. Functional analysis of the liver in the non-alcoholic fatty liver disease (NAFLD) model. (A) Immunofluorescence images of hepatic-specific proteins. (B) Analysis of hepatic-specific protein-encoding gene expression levels. Scale bar: 200 μm. *$p < 0.05$; **$p < 0.01$. Abbreviation: N.S.: No significant difference.

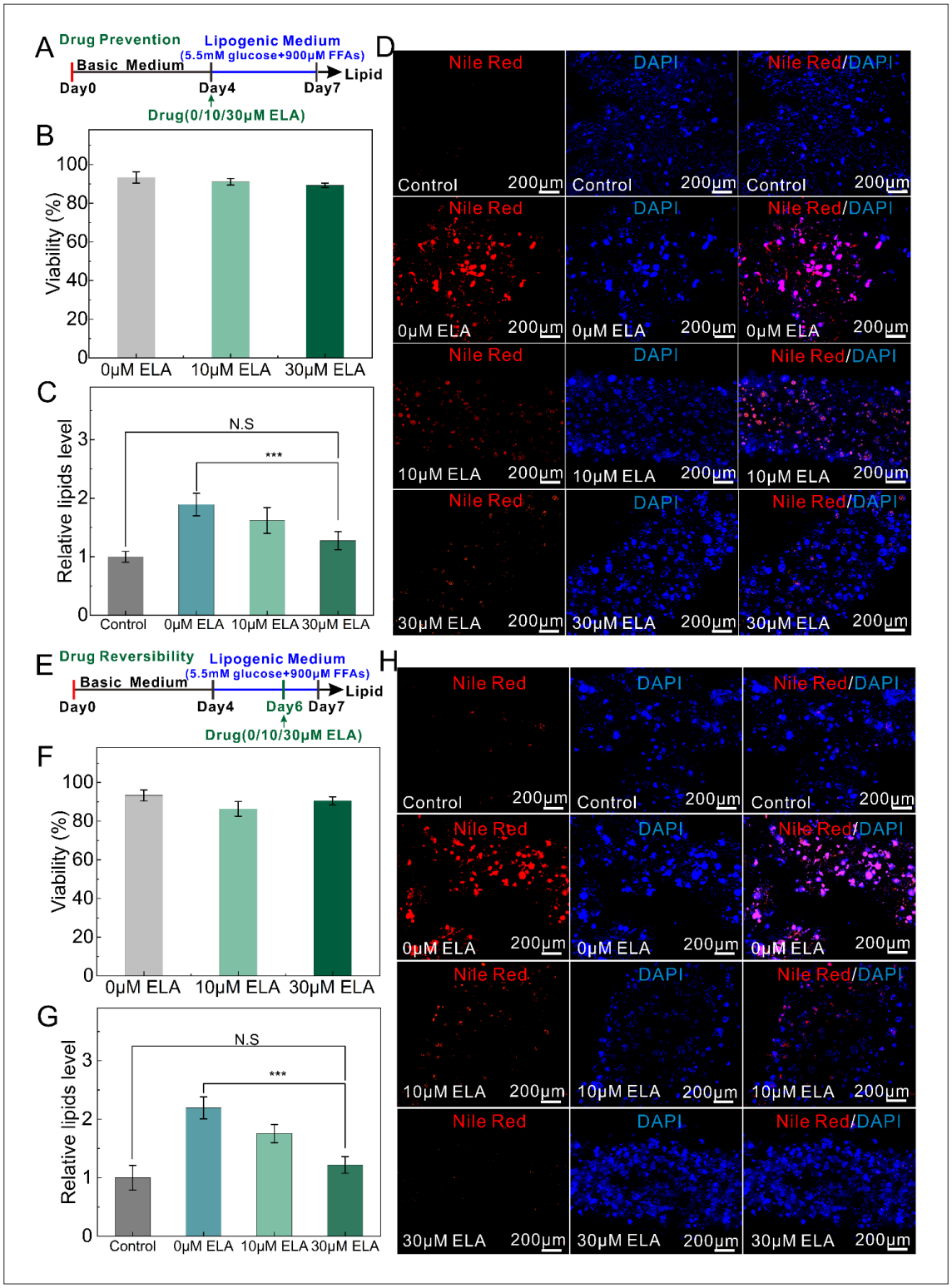

Figure 5. Study of the bioprinted non-alcoholic fatty liver disease (NAFLD) model for NAFLD prevention and reversal. (A–D) Investigation on NAFLD prevention. (A) Experimental procedure for drug prevention. (B) Analysis of cell viability under different drug concentrations. (C) Analysis of lipid accumulation under different drug concentrations. (D) Fluorescence images of lipid accumulation under different drug concentrations. (E–H) Investigation on NAFLD reversibility. (E) Experimental procedure for drug reversibility. (F) Analysis of cell viability under different drug concentrations. (G) Analysis of lipid accumulation under different drug concentrations. (H) Fluorescence images of lipid accumulation under different drug concentrations. Scale bar: 200 μm. ***$p < 0.001$. Abbreviations: FFAs: Free fatty acids; ELA: Elafibranor; N.S.: No significant difference.

impacting hepatic detoxification capacity. The experimental findings align with most of the literature reporting decreased secretion of CYP450 enzymes in NAFLD patients, affecting drug metabolism and excretion.[34]

3.5. 3D-printed NAFLD model application: Prevention and reversibility

The 3D-printed NAFLD model was used for drug testing, and ELA (a PPARα and PPARδ agonist) was selected due to its positive efficacy in both animal studies and *in vitro* cell experiments.[35,36] The therapeutic effects of ELA for the prevention and reversal of NAFLD were studied in 3D-printed NAFLD models. For NAFLD prevention, ELA and lipogenic medium were added simultaneously (Figure 5A). ELA (10 or 30 μM) was used to prevent NAFLD, and both ELA dosages had no significant effect on the cell survival rate (Figure 5B), whereas 30 μM ELA prevented intracellular lipid accumulation (lipid accumulation was close to that of the control group) (Figure 5C and D). For NAFLD reversal, lipogenic medium was added to induce NAFLD, which was then replaced with medium containing 10 or 30 μM ELA to reverse NAFLD (Figure 5E). Moreover, 10 and 30 μM ELA did not affect the cell survival rate (Figure 5F), whereas 30 μM ELA reversed intracellular lipid accumulation (the lipid accumulation was close to that of the control group) (Figure 5G and H). Notably, ELA is a PPARα and PPARδ agonist that has beneficial effects on lipid metabolism according to the literature.[37,38] In this study, ELA was used as an example to verify the feasibility of this platform for studying NAFLD drugs, suggesting that both prevention and reversal of NAFLD could be replicated on the platform. Owing to the highly biomimetic 3D-printed liver tissue, physiologically similar physical and chemical microenvironments, and more accurate NAFLD modeling, the NAFLD model proposed in this study can be used as a promising platform for *in vitro* drug screening and liver disease mechanism research.

4. Conclusion

In this study, a functional NAFLD model was successfully constructed via 3D bioprinting technology. Large-scale liver tissue with vascular-like functions was created *in vitro* through bioink optimization and the induction of HepaRG cells to form liver organoids. Compared with traditional models, 3D-printed liver tissue exhibited superior hepatic functions and greater cell viability; glycogen storage and the formation of bile canaliculi-like structures were also observed within it. The induced NAFLD model displayed significant lipid droplet accumulation in the NAFLD induction medium, and the concentration of FFAs influenced this accumulation. Importantly, the induction medium had no significant effect on cell viability. Overall, this study provides a promising platform for *in vitro* drug screening and research on liver disease mechanisms, which contributes to a deeper understanding of NAFLD and facilitates the development of related pharmaceuticals and therapeutic strategies. Furthermore, in future studies, liver sinusoidal endothelial cells, stellate cells, and Kupffer cells can be used to gain a more comprehensive understanding of NAFLD.

Acknowledgments

None.

Funding

This research was funded by the Natural Science Foundation of Hubei Province (grant number 2023AFB411) and the Knowledge Innovation Project of Wuhan Science and Technology Bureau (grant number 2023020201020532).

Conflict of interest

The authors declare no conflicts of interest.

Author contributions

Conceptualization: Jing Liu
Formal analysis: Tao Ding, Tianma He
Investigation: Kun Du, Wei Peng, Zibei Ming
Methodology: Feifei Pu, Ying Zhao, Renquan Ruan
Writing – original draft: Kun Du, Wei Peng
Writing – review & editing: Jing Liu

Ethics approval and consent participate

Not applicable.

Consent for publication

Not applicable.

Availability of data

Data is available from the corresponding author upon reasonable request.

References

1. Lazarus JV, Mark HE, Villota-Rivas M, et al. The global NAFLD policy review and preparedness index: are countries ready to address this silent public health challenge? *J Hepatol*. 2022;76(4):771-780.
doi: 10.1016/j.jhep.2021.10.025

2. Sozen E, Demirel-Yalciner T, Sari D, Ozer NK. Cholesterol accumulation in hepatocytes mediates IRE1/p38 branch of endoplasmic reticulum stress to promote nonalcoholic steatohepatitis. *Free Radic Biol Med*. 2022;191:1-7.
doi: 10.1016/j.freeradbiomed.2022.08.024

3. Parola M, Pinzani M. Liver fibrosis in NAFLD/NASH: from pathophysiology towards diagnostic and therapeutic strategies. *Mol Aspects Med*. 2024;95:101231. doi: 10.1016/j.mam.2023.101231

4. Rosso C, Kazankov K, Younes R, et al. Crosstalk between adipose tissue insulin resistance and liver macrophages in non-alcoholic fatty liver disease. *J Hepatol*. 2019;71(5):1012-1021. doi: 10.1016/j.jhep.2019.06.031

5. Canfora EE, Meex RCR, Venema K, Blaak EE. Gut microbial metabolites in obesity, NAFLD and T2DM. *Nat Rev Endocrinol*. 2019;15(5):261-273. doi: 10.1038/s41574-019-0156-z

6. Hendriks D, Brouwers JF, Hamer K, et al. Engineered human hepatocyte organoids enable CRISPR-based target discovery and drug screening for steatosis. *Nat Biotechnol*. 2023;41(11):1567-1581. doi: 10.1038/s41587-023-01680-4

7. Zhu C, Huai Q, Zhang X, Dai H, Li X, Wang H. Insights into the roles and pathomechanisms of ceramide and sphigosine-1-phosphate in nonalcoholic fatty liver disease. *Int J Biol Sci*. 2023;19(1):311. doi: 10.7150/ijbs.78525

8. Im YR, Hunter H, de Gracia Hahn D, et al. A systematic review of animal models of NAFLD finds high-fat, high-fructose diets most closely resemble human NAFLD. *Hepatology*. 2021;74(4):1884-1901. doi: 10.1002/hep.31897

9. Smati S, Polizzi A, Fougerat A, et al. Integrative study of diet-induced mouse models of NAFLD identifies PPARalpha as a sexually dimorphic drug target. *Gut*. 2022;71(4):807-821. doi: 10.1136/gutjnl-2020-323323

10. Trépo E, Valenti L. Update on NAFLD genetics: from new variants to the clinic. *J Hepatol*. 2020;72(6): 1196-1209. doi: 10.1016/j.jhep.2020.02.020

11. Tsuchida T, Lee YA, Fujiwara N, et al. A simple diet- and chemical-induced murine NASH model with rapid progression of steatohepatitis, fibrosis and liver cancer. *J Hepatol*. 2018;69(2):385-395. doi: 10.1016/j.jhep.2018.03.011

12. Nevzorova YA, Boyer-Diaz Z, Cubero FJ, Gracia-Sancho J. Animal models for liver disease – a practical approach for translational research. *J Hepatol*. 2020;73(2):423-440. doi: 10.1016/j.jhep.2020.04.011

13. Ma L, Wu Y, Li Y, et al. Current advances on 3D-bioprinted liver tissue models. *Adv Healthc Mater*. 2020;9(24):2001517. doi: 10.1002/adhm.202001517

14. Suurmond CE, Lasli S, van den Dolder FW, et al. *In vitro* human liver model of nonalcoholic steatohepatitis by coculturing hepatocytes, endothelial cells, and Kupffer cells. *Adv Healthc Mater*. 2019;8(24):e1901379. doi: 10.1002/adhm.201901379

15. Cheng S, Yang Y, Zhou Y, Xiang W, Yao H, Ma L. Influence of different concentrations of uric acid on oxidative stress in steatosis hepatocytes. *Exp Ther Med*. 2018;15(4):3659-3665. doi: 10.3892/etm.2018.5855

16. Michaut A, Le Guillou D, Moreau C, et al. A cellular model to study drug-induced liver injury in nonalcoholic fatty liver disease: application to acetaminophen. *Toxicol Appl Pharmacol*. 2016;292:40-55. doi: 10.1016/j.taap.2015.12.020

17. Luckert C, Braeuning A, de Sousa G, et al. Adverse outcome pathway-driven analysis of liver steatosis *in vitro*: a case study with cyproconazole. *Chem Res Toxicol*. 2018;31(8): 784-798. doi: 10.1021/acs.chemrestox.8b00112

18. Kimura M, Iguchi T, Iwasawa K, et al. En masse organoid phenotyping informs metabolic-associated genetic susceptibility to NASH. *Cell*. 2022;185(22):4216-4232 e16. doi: 10.1016/j.cell.2022.09.031

19. Yang H, Sun L, Pang Y, et al. Three-dimensional bioprinted hepatorganoids prolong survival of mice with liver failure. *Gut*. 2021;70(3):567-574. doi: 10.1136/gutjnl-2019-319960

20. Ryu JS, Lee M, Mun SJ, et al. Targeting CYP4A attenuates hepatic steatosis in a novel multicellular organotypic liver model. *J Biol Eng*. 2019;13:69. doi: 10.1186/s13036-019-0198-8

21. Leite SB, Roosens T, El Taghdouini A, et al. Novel human hepatic organoid model enables testing of drug-induced liver fibrosis *in vitro*. *Biomaterials*. 2016;78:1-10. doi: 10.1016/j.biomaterials.2015.11.026

22. Zhang B, Korolj A, Lai BFL, Radisic M. Advances in organ-on-a-chip engineering. *Nat Rev Mater*. 2018;3(8):257-278. doi: 10.1038/ s41578-018-0034-7

23. Feaver RE, Cole BK, Lawson MJ, et al. Development of an *in vitro* human liver system for interrogating nonalcoholic steatohepatitis. *JCI Insight*. 2016;1(20):e90954. doi: 10.1172/jci.insight.90954

24. Bulutoglu B, Rey-Bedón C, Kang YBA, Mert S, Yarmush ML, Usta OB. A microfluidic patterned model of non-alcoholic fatty liver disease: applications to disease progression and zonation. *Lab Chip*. 2019;19(18):3022-3031. doi: 10.1039/c9lc00354a

25. Lasli S, Kim HJ, Lee K, et al. A human liver-on-a-chip platform for modeling nonalcoholic fatty liver disease. *Adv Biosyst*. 2019;3(8):e1900104. doi: 10.1002/adbi.201900104

26. Gori M, Simonelli MC, Giannitelli SM, Businaro L, Trombetta M, Rainer A. Investigating nonalcoholic fatty liver disease in a liver-on-a-chip microfluidic device. *PLoS One*. 2016;11(7):e0159729. doi: 10.1371/journal.pone.0159729

27. Du K, Li S, Li C, et al. Modeling nonalcoholic fatty liver disease on a liver lobule chip with dual blood supply. *Acta Biomater*. 2021;134:228-239. doi: 10.1016/j.actbio.2021.07.013

28. Kostrzewski T, Maraver P, Ouro-Gnao L, et al. A microphysiological system for studying nonalcoholic steatohepatitis. *Hepatol Commun*. 2020;4(1):77-91. doi: 10.1002/hep4.1450

29. Liu J, Zhou Z, Zhang M, Song F, Feng C, Liu H. Simple and robust 3D bioprinting of full-thickness human skin tissue. *Bioengineered*. 2022;13(4):10087-10097. doi: 10.1080/21655979.2022.2063651

30. Li R, Liu J, Ma J, et al. Fibrinogen improves liver function via promoting cell aggregation and fibronectin assembly in hepatic spheroids. *Biomaterials*. 2022;280:121266. doi: 10.1016/j.biomaterials.2021.121266

31. Lee JB, Park JS, Shin YM, et al. Implantable vascularized liver chip for cross-validation of disease treatment with animal model. *Adv Funct Mater*. 2019;29(23): 1900075. doi: 10.1002/adfm.201900075

32. Mahjoubin-Tehran M, De Vincentis A, Mikhailidis DP, et al. Non-alcoholic fatty liver disease and steatohepatitis: state of the art on effective therapeutics based on the gold standard method for diagnosis. *Mol Metab*. 2021;50:101049. doi: 10.1016/j.molmet.2020.101049

33. Jamwal R, Barlock BJJP. Nonalcoholic fatty liver disease (NAFLD) and hepatic cytochrome P450 (CYP) enzymes. *Pharmaceuticals (Basel)*. 2020;13(9):222. doi: 10.3390/ph13090222

34. Fierbinteanu-Braticevici C, Baicus C, Tribus L, Papacocea R. Predictive factors for nonalcoholic steatohepatitis (NASH) in patients with nonalcoholic fatty liver disease (NAFLD). *J Gastrointestin Liver Dis*. 2011;20(2):153-159. doi: 10.15403/jgld.2011.1121.202

35. Roth JD, Veidal SS, Fensholdt LKD, et al. Combined obeticholic acid and elafibranor treatment promotes additive liver histological improvements in a diet-induced ob/ob mouse model of biopsy-confirmed NASH. *Sci Rep*. 2019;9(1):9046. doi: 10.1038/s41598-019-45178-z

36. Boeckmans J, Natale A, Rombaut M, et al. Human hepatic *in vitro* models reveal distinct anti-NASH potencies of PPAR agonists. *Cell Biol Toxicol*. 2021;37:293-311. doi: 10.1007/s10565-020-09544-2

37. Pingitore P, Sasidharan K, Ekstrand M, Prill S, Lindén D, Romeo S. Human multilineage 3D spheroids as a model of liver steatosis and fibrosis. *Int J Mol Sci*. 2019;20(7):1629. doi: 10.3390/ijms20071629

38. Boeckmans J, Buyl K, Natale A, et al. Elafibranor restricts lipogenic and inflammatory responses in a human skin stem cell-derived model of NASH. *Pharmacol Res*. 2019;144:377-389.

39. Banaeiyan AA, Theobald J, Paukštyte J, Wölfl S, Adiels CB, Goksör MJB. Design and fabrication of a scalable liver-lobule-on-a-chip microphysiological platform. 2017;9(1):015014. doi:10.1088/1758-5090/9/1/015014. doi: 10.1016/j.phrs.2019.04.016

ACCSCIENCE PUBLISHING

International Journal of Bioprinting

RESEARCH ARTICLE

ChocOmega-3: Innovative manufacturing of ω-3-enriched chocolate

Esra Pilavci[1,2], Dilruba Baykara[1,2], Kubra Ozkan[3], Ayşegul Tiryaki[1,2], Melih Musa Ayran[1,2], Gozde Enguven[1,2], Tufan Arslan Tut[1,2], Mehmet Murat Bozdag[1,2], Osman Sagdic[3], Oguzhan Gunduz[1,2], Roger J. Narayan[4]*, and Canan Dogan[1,2]*

[1]Center for Nanotechnology and Biomaterials Application & Research (NBUAM), Marmara University, Istanbul, Turkey

[2]Department of Metallurgical and Materials Engineering, Faculty of Technology, Marmara University, Istanbul, Turkey

[3]Department of Food Engineering, Faculty of Chemical and Metallurgical Engineering, Yildiz Technical University, Istanbul, Turkey

[4]Department of Materials Science and Engineering, North Carolina State University, Raleigh, North Carolina, United States of America

Abstract

3D printing technology allows food to be shaped into unique and complex forms. Chocolate is frequently used in food printing due to its extrusion melting capacity and attractiveness. In this study, chocolates enriched with ω-3 were produced with 3D printing technology. By using electrospraying, ω-3 was encapsulated within sodium alginate (SA) microparticles, which were then used to coat 3D-printed chocolates. The ω-3 blend and ω-3-SA coated chocolates were compared. Before printing, the rheological properties of the chocolates were analyzed. In addition to their characteristics, the printed chocolates were evaluated for total phenolic content (TPC) and antioxidant capacity, *in vitro* gastrointestinal digestion, and ω-3 release profile. Fourier transform infrared (FTIR) spectroscopy indicated that ω-3 was successfully incorporated into the SA particles. According to mechanical testing, the chocolate structures coated with ω-3-SA exhibited higher compressive strength than structures mixed with ω-3. The results revealed that the incorporation of alginate into pure chocolate scaffolds through the coating process increased their compressive strength. The TPC and antioxidant capacities of ω-3-SA microparticles (MP)-coated and ω-3-mixed chocolate samples were also significantly increased compared to those of pure chocolate after *in vitro* digestion. The ω-3-SA MP-coated chocolate reported a lower quality release profile. The faster release of encapsulated ω-3 at a pH value of 7 may be attributed to the fact that SA particles dissolve faster in high pH environments. This study revealed that 3D printing technology could be actively leveraged to create food-based products with the necessary ingredients to meet consumer demand.

Keywords: 3D printing; Food technology; ω-3; Electrospraying; Rheology; Bioaccessibility

***Corresponding authors:**
Roger Narayan
(roger_narayan@ncsu.edu)

Canan Dogan
(canan.dogan@marmara.edu.tr)

Citation: Ozkan K, Baykara D, Pilavci E, et al. ChocOmega-3: Innovative manufacturing of ω-3-enriched chocolate. *Int J Bioprint*. 2024;10(6):3969. doi: 10.36922/ijb.3969

Received: June 17, 2024
1st revised: July 20, 2024
2nd revised: August 15, 2024
Accepted: August 23, 2024
Published Online: August 23, 2024

Copyright: © 2024 Author(s). This is an Open Access article distributed under the terms of the Creative Commons Attribution License, permitting distribution, and reproduction in any medium, provided the original work is properly cited.

Publisher's Note: AccScience Publishing remains neutral with regard to jurisdictional claims in published maps and institutional affiliations.

1. Introduction

3D printing, also referred to as additive manufacturing, for food applications is growing in popularity in terms of fundamental research and commercial efforts. It has been favored for industrial and biomedical applications due to its unique ability to create 3D objects with geometries based on a digital design in a layer-by-layer manner. In terms of fabrication efforts, it is possible to separate raw materials into printable and non-printable foods; alternative resources, such as microorganisms, can serve as raw materials. Figure 1 summarizes the 3D printing approach that is typically used in basic food printing applications. With improvements in 3D printing technologies, it is even possible to assemble multilayer cake-like food structures that are made up of both printable and non-printable layers. Nowadays, food printing applications are an emerging branch of food engineering, with an estimated value of 400 million USD.[1] Moreover, new types of 3D printing technologies are emerging; low-cost materials and printers facilitate the daily use of 3D printing technology.[1] Designing meals to fulfill the needs of specific market segments, such as newborns, adults, and older people, has become necessary due to the need to innovate food manufacturing with specialized structural and chemical properties, as well as longer shelf life.[2] If the machine parts in contact with the food are thoroughly cleaned, 3D-printed food can exhibit a longer shelf life than conventionally prepared food.[3] Numerous 3D-printed foods have been created, ranging from savory dishes to sugary sweets; simple shapes and intricate designs have been demonstrated. Biodegradable cups with 3D-printed poly-capsules of energy drink ingredients; plant-based meats that mimic the nutritional properties, texture, taste, and appearance of animal-based meat products; cereal-based snacks that are enriched with edible insects; 3D food structures made out of sugars with a variety of flavors, such as chocolate, watermelon, cherry, sour apple, mint, and vanilla; and biometric 3D-printed sushi that uses biometric data (e.g., the DNA of customers) to address specific nutritional requirements are some examples of 3D food printing.[1]

Chocolate is one of the materials that is frequently utilized in food printing due to its capability to melt and extrude, as well as its appeal in the high-end food industry.[2] Owing to its varying thermodynamic stability, chocolate can take the form of tempered chocolate, which has desirable properties in terms of melting point, hardness, attractive color, and shine.[4] Due to its propensity to maintain its shape after being deposited on the print surface and its inclination to promote flow through extrusion while under pressure, the shear-thinning

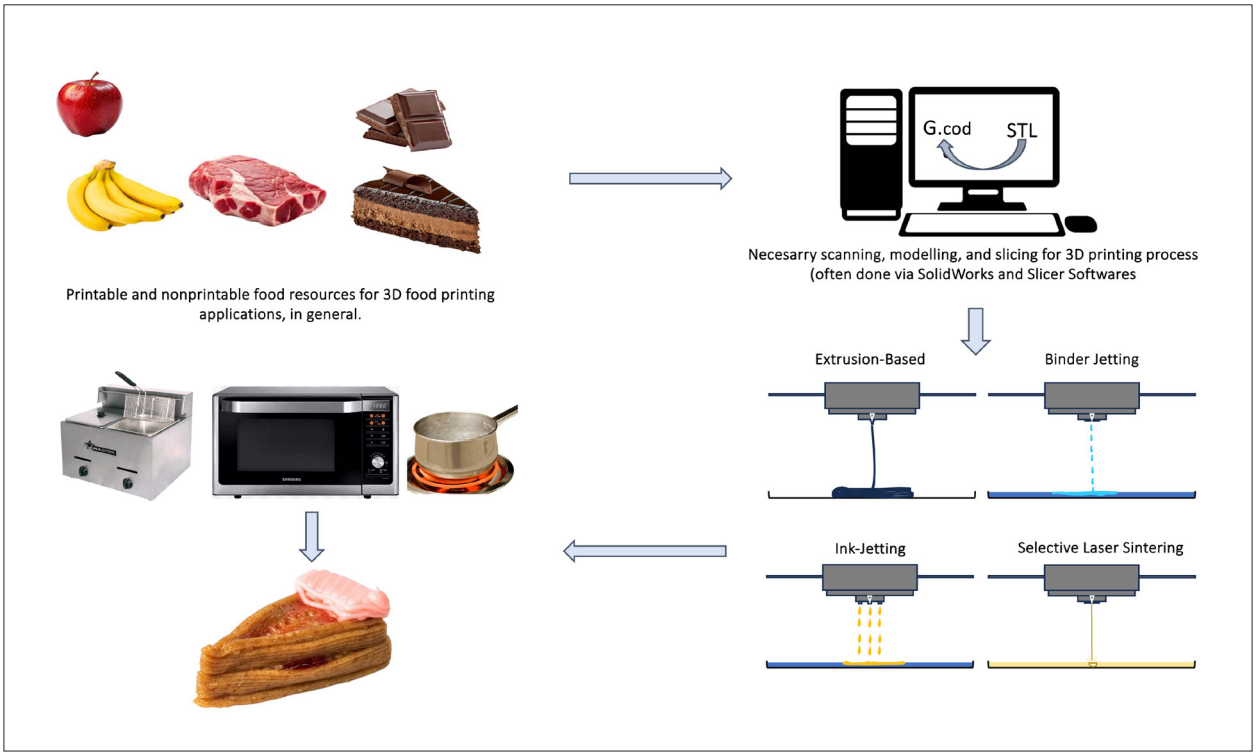

Figure 1. Schematic overview of 3D printing for food applications.

behavior of chocolate is regarded as a favorable attribute for melt extrusion 3D printing.[5] Lanaro et al.[4] stated that, despite differences between brands, most chocolates are based on cocoa, fat, and various triglycerides; they noted that conditions in which these triglyceride structures are thermally stable should be adjusted to achieve efficient printing. Mantihal et al.[5] reported that accurate temperature control and optimization of chocolate particle size could boost printing efficiency. Another crucial parameter is that grating chocolate before melting could reduce its particle size and prevent blockages during printing. Karavasili et al.[6] produced ibuprofen or paracetamol-loaded 3D-printed chocolate to obtain high and rapid release from pediatric-friendly chocolates. Several studies have utilized 3D printing for the preparation of complex structures using chocolate.[5–8] This approach was aimed at obtaining nutritionally fortified foods by adding active substances, such as vitamins, proteins, and probiotics, to foods.[9–11] Moreover, dosage forms with controlled release characteristics can be produced using 3D printing.[12] Due to characteristics such as solubility, drug release patterns, and diffusivity, nano-scale drug delivery provides considerable advantages that can increase the effectiveness of drug delivery systems.[13] Nanoparticles have been created using electrospray technology.[14] Electrospraying, a process of atomizing liquid through electrical forces,[15] enhances chemical stability and enables prolonged release *in vivo* by utilizing nanoencapsulation; this approach was recently applied for encapsulating and stabilizing dietary bioactive compounds, such as curcumin, folic acid, lycopene, and epigallocatechin gallate, as well as live cells (e.g., *Lactobacillus acidophilus*).[16] The ω-3 polyunsaturated fatty acids are widely utilized as functional components in food and medicine due to their high biological activity.[17] Some ω-3 polyunsaturated fatty acids, such as eicosapentaenoic acid (EPA) and docosahexaenoic acid (DHA), are found in aquatic organisms, particularly in oily fish (e.g., mackerel, salmon, and menhaden) and in the oils of marine mammals (e.g., seals and whales). ω-3 polyunsaturated fatty acids also occur naturally in the livers of lean white fish (e.g., halibut and cod). The human body is unable to produce ω-3 on its own.[18] In a study performed by Pacifico et al.,[19] DHA supplements were given to children with nonalcoholic fatty liver disease for 6 months, resulting in significant reductions of liver fat, epicardial adipose tissues, and visceral adipose tissues; in addition, fasting insulin and triglyceride values were improved in the treated children. De Goede et al.[20] studied 21342 participants between the ages of 20 and 65 and demonstrated that fatal coronary heart disease and fatal myocardial infarction rates were reduced in EPA and DHA-consuming individuals in a dose-responsive manner. Therefore, ω-3 fatty acids should be a part of our diets as they support health and physical performance; moreover, they may lower the risk of developing several diseases.[21] Gómez-Mascaraque et al.[22] determined that electrospraying processes produce ω-3 capsules with a greater encapsulation rate.[19] Compared to neat oil, microencapsulated oil is more bioaccessible; controlled release may be obtained depending on the characteristics of the emulsifying and encapsulating agents.[23]

A linear polymer derived from sea algae, sodium alginate (SA), has a molecular weight ranging from thousands to hundreds of thousands.[24] SA exhibits several advantageous qualities, including low toxicity, low cost, water-retaining functionality, and degradability.[25] SA is frequently utilized in the chemical, food, and biomedical industries; for example, SA microcapsules have been used to encapsulate tissues and cells. Bioactive molecules can be encapsulated in SA microcapsules; this approach can facilitate the controlled release of the bioactive molecules and shield the bioactive molecules from enzymolysis in the gastrointestinal system.[24]

To our knowledge, there is no existing research on the 3D printing of chocolate and subsequent coating with ω-3 particles. Therefore, we aim to: (i) produce 3D-printed chocolates enriched with ω-3; (ii) encapsulate ω-3 into SA biopolymeric particles using electrospraying; (iii) compare the *in vitro* release profiles of chocolates directly mixed with polymeric ω-3 and chocolates coated with ω-3 particles; (iv) extend the ω-3 release time to achieve a controlled release; (v) evaluate the rheological, chemical bonding (via Fourier transform infrared [FTIR] analysis), color, thermal, and mechanical properties of chocolates; and (vi) examine the retention of bioactive compounds from chocolates during simulated *in vitro* digestion.

2. Materials and methods

2.1. Materials

Couverture dark chocolate (Ulker Biscuits Industry Inc., Turkey) and ω-3 (TASA, PERU) were purchased from a neighborhood market. SA (molecular weight [M_w] = 216000 g/mol), all reagents, solvents, α-amylase (1500 U/mL; A1031), pancreatin (800 U/mL; P7545), lipase (2000 U/mL; L3126), bile salts (160 mM; B8631), and pepsin (25000 U/mL; P7012) were acquired from Sigma-Aldrich Ltd. (Germany). The foods produced in this study pose no risks to human health, as all ingredients are of natural origin.

2.2. Rheological analysis

A rotational rheometer, the Lamy RM 200 from Lamy Rheology Instruments (France), was employed to conduct rheological assessments using the method of

Izgordu et al.[26] The rheometer contained an MK-PP25 measuring system and a laboratory thermostat. Measurements were performed at two specific temperatures: 25°C, which represents ambient temperature, and 37°C, which corresponds to the temperature of normal human skin. The flow and viscosity curves were generated under controlled shear conditions, over the range of 1–1000 s^{-1} and over a time period of 150 s. Subsequently, both graphical and mathematical analyses were performed on the collected data using Rheotex software.

2.3. 3D printing of chocolate

Couverture dark chocolate was melted in water vapor, and 0.3 g of ω-3 was added to 10 mL of chocolate. Using a metal spatula, the chocolate/ω-3 blend was mixed gently to obtain a homogenous mixture without aggregation. The chocolate scaffolds were designed using SolidWorks software. The scaffold exhibited a square shape with dimensions of 3 × 3 cm. The designed shape was saved in .stl format and then transferred to RepetierHost software, which is compatible with the 3D printer (AXO-A3; Axolotl Biosystems, Turkey). After preparing the design, the chocolate/ω-3 mixture was loaded into an empty syringe that was specifically arranged for the AXO-A3 system, and the syringe was connected to the pressure tubes through a nozzle in order to obtain the necessary extrusion force.

2.4. Fabrication of ω-3 microparticles using electrospraying

Microparticles were fabricated using the method described by Ulag et al.[27] Briefly, 0.1 g of SA was dissolved in distilled water with a magnetic stirrer. After dissolving, 0.3 g of Tween 80 was added to the solution, serving as a surfactant; 0.3 g of ω-3 was added. Electrospraying parameters were optimized at 0.18 mL/h flow rate, 12 cm distance between the needle tip and the 3D printed chocolates, and 25.5 kV applied voltage. All chocolate scaffolds were coated for 1 h with ω-3-loaded particles. After the coating process, the samples were stored at −18°C. A schematic representation of the production process is displayed in Figure 2. Pure chocolate, ω-3-mixed chocolate, and ω-3-SA MP-coated chocolate sample images, obtained using a light microscope (Zeiss, Germany), are presented in Figure 3. The

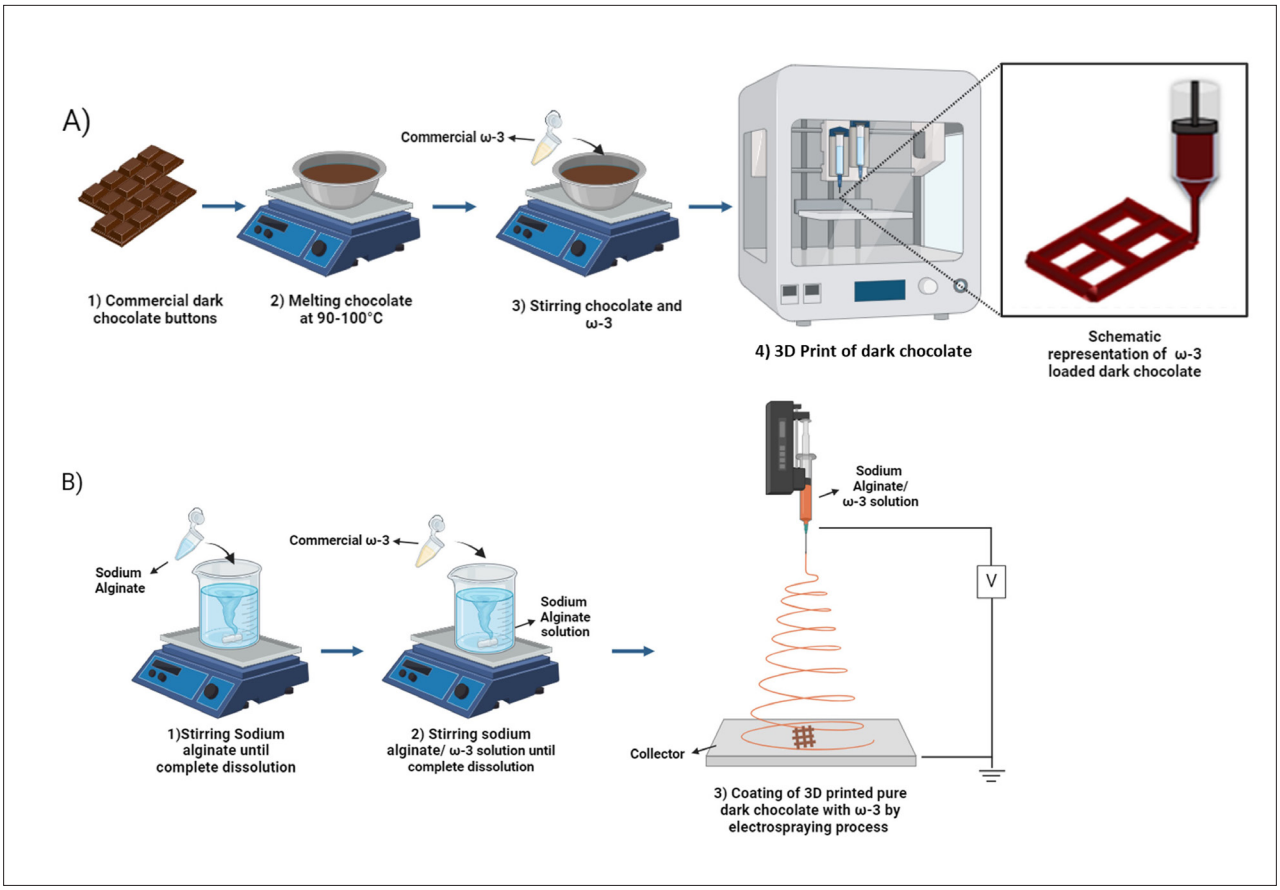

Figure 2. Schematic illustration of (A) the 3D printing process of ω-3-loaded dark chocolate and (B) the coating process of pure 3D-printed dark chocolate with ω-3 by electrospraying.

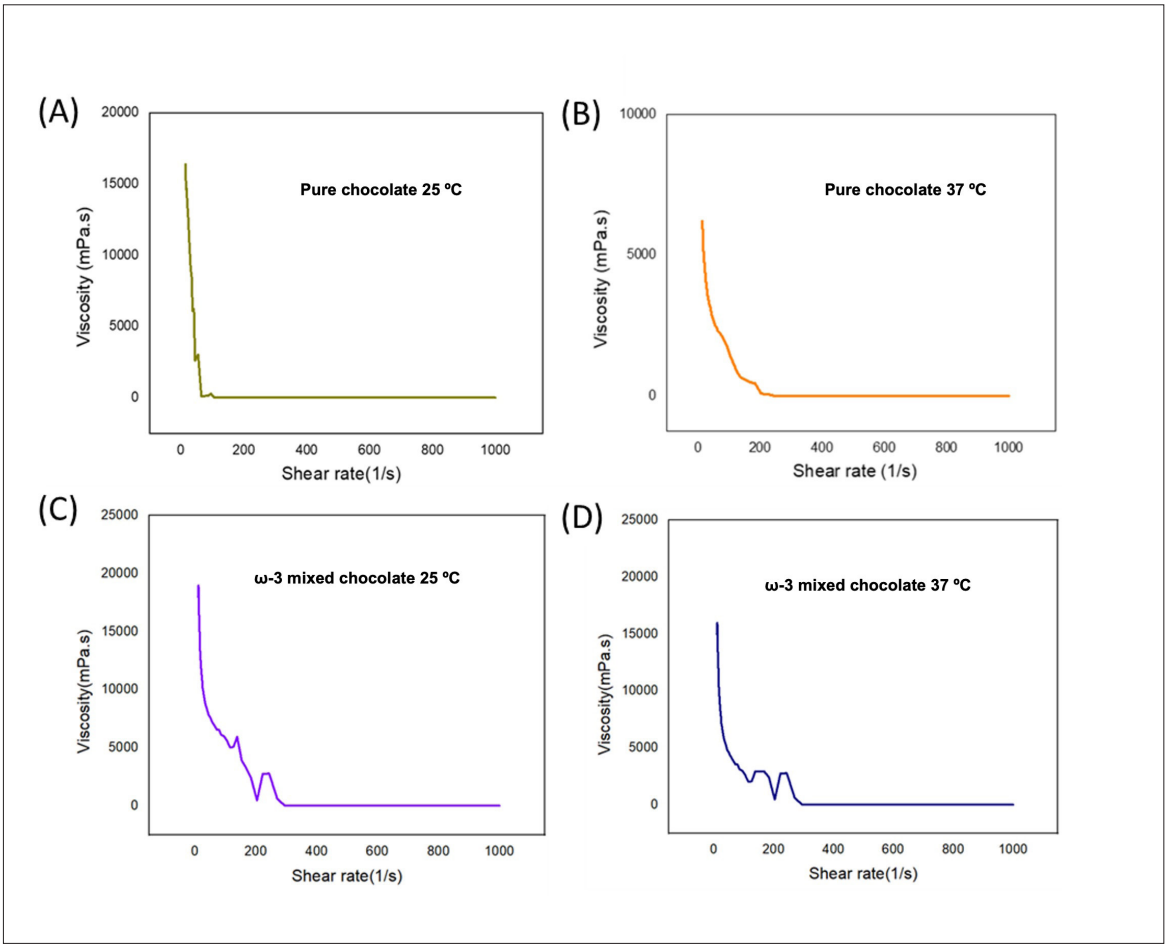

Figure 3. The shear rate-viscosity relationship in pure (A and B) and ω-3-mixed (C and D) chocolate at various temperatures, i.e., 25°C (A and C) and 37°C (B and D).

electrospraying method does not allow pure ω-3 particles to be produced; the material requires encapsulation within a polymer. For this reason, we created three experimental groups to facilitate comparisons.

2.5. Light microscopy and scanning electron microscopy (SEM)

SEM (EVO LS 10, Zeiss) was used to examine the surface morphologies of microparticles. First, microparticles were coated with a layer of gold and palladium for 120 s with a spray coating machine (Quorum SC7620, USA). Chocolate samples were viewed under light microscopy.

2.6. Fourier transform infrared analysis

The functional groups in the chocolates were identified using FTIR, as described by Baykara et al.[28] A Jasco FT/IR-ATR 4700 instrument (Jasco, United States of America [USA]) was used to collect spectra from 400 to 4000 cm^{-1}; a resolution of 4 cm^{-1} was utilized for analysis.

2.7. Moisture content and water activity

The moisture content of the chocolate samples was evaluated using 1 g of sample with a ventilated oven, which was set at 105 ± 2°C until constant weight. The water activity (aw) of the chocolate samples was assessed with a Novasina LabMaster instrument (Novasina AG Ltd., Switzerland) at 25°C.

2.8. Color analysis

The color of chocolate samples was examined using a chromameter (Konica Minolta CR-400, USA) and expressed as a* (redness/greenness), L* (lightness), and b* (yellowness/blueness) values. The colorimeter was calibrated using a white calibration plate (CR-A44 Konica Minolta Sensing Inc., Japan) prior to testing.

2.9. Mechanical property analysis

A compression test was conducted to observe changes in the material upon applying a force to the samples. Using a

compression testing machine (EZ-LX; Shimadzu, Japan), the mechanical strength of the 3D-printed chocolates was determined.

2.10. Differential scanning calorimetry

Differential scanning calorimetry (DSC) was performed using DSC-6O Plus (Shimadzu, Japan) to examine the thermal properties of the chocolates (as described by Aydin et al.[29]); a heating rate of 10°C/min over a temperature range of 25–350°C in an N_2 stream was used in the study. The parameters representing the melting profile associated with the samples, i.e., onset temperature (T_{onset}; the temperature at which the samples begin to melt), peak temperature (T_{peak}; the temperature at which the highest melting rate was noted), end temperature (T_{end}; the temperature at which the samples completely melted), and ΔH (the energy that is required for complete sample melting) were determined from thermograms obtained from the measurements.

2.11. Determination of total polyphenol content

The chocolate samples were defatted prior to phenolic extraction using the approach described by Hu et al.[30] with some modifications. Briefly, the samples were sliced into small pieces; 0.5 g of each piece was extracted using 2.5 mL of n-hexane twice via shaking for 45 min at 25 ± 0.03°C at 150 ×g. After each extraction step, the mixtures were centrifuged at 2000 ×g for 10 min; the supernatant was subsequently discarded. After the second extraction step, the samples were dried in a hot-air dryer for 24 h at 25°C. The defatted samples were subsequently weighed; the phenolics were extracted using 5 mL of 0.1% HCl and 80% aqueous methanol from the defatted samples. After vortexing for 2 min, the solution was sonicated for 20 min.[31] Next, the solution was centrifuged for 10 min at 2000 ×g. The supernatant was subsequently recovered, filtered through a 0.45 μm filter, and then stored at −20°C until further extraction. The total phenolic content (TPC) was finally measured.[32] The TPC results are presented as mg gallic acid equivalent (GAE)/100 g dw (dw: dry weight).

2.12. Antioxidant capacity assessment

The 2,2-Diphenyl-1-picrylhydrazylradical (DPPH) radical scavenging activity, 2,2-azino-*bis*-3-ethylbenzothiazoline-6-sulphonic acid (ABTS) radical scavenging activity, and copper-reducing antioxidant capacity (CUPRAC)[32] were measured accordingly. To conduct the DPPH assay, 0.1 mL of the extract was mixed with 4.9 mL of DPPH solution (0.1 mM in methanol). The mixture was subsequently incubated at room temperature in the dark for 20 min. The absorbance was then measured at 517 nm using a spectrophotometer. To conduct the ABTS assay, 0.1 mL of the extract was mixed with 2 mL of diluted ABTS solution; the absorbance values were measured at 734 nm using a spectrophotometer 6 min after initial mixing. To conduct the CUPRAC assay, 1 mL portions of $CuCl_2$ (0.01 M), ammonium acetate buffer (1 M, pH 7.0), and neocuproine (7.5 mM) were mixed. After adding 0.1 mL of the extract and 1 mL of distilled water, the mixture was incubated at room temperature for 1 h in the dark. Absorbance measurements were obtained at 450 nm using a spectrophotometer. The results are expressed as μmol Trolox equivalent (TE)/g dw.

2.13. *In vitro* simulation of gastrointestinal digestion

In vitro simulated digestion studies were performed as described by Tolve et al.[31] and Ozkan et al.[32] Briefly, 1 g of chocolate samples was mixed with 0.7 mL of simulated salivary fluid (SSF), 5 μL of 3 M $CaCl_2$, 195 μL of water, and 0.1 mL of α-amylase. After 3 min, 1.5 mL of simulated gastric fluid (SGF), 139 μL of water, 1 μL of 0.3 M $CaCl_2$, and 0.32 mL of pepsin were added. The pH of the solution was subsequently adjusted to 3.0 with 40 μL of HCl (1 M); the sample was incubated at 37°C for 2 h. After 2 h of incubation at 37°C, 1.3 mL of simulated intestinal fluid (SIF), 1 mL of lipase, 1 mL of pancreatin, 0.5 mL of bile salts, 8 μL of 0.3 M $CaCl_2$, and 162 μL of water were added. The pH was adjusted to a pH value of 7 in this phase using 30 μL of NaOH (1 M). The sample was incubated at 37°C for 3 h. The aliquots collected at the end of the salivary, gastric, and intestinal phases were added to 9 mL of methanol/HCl/water (79.9:0.1:20, v/v/v) and brought to −20°C in order to inhibit the enzyme activity prior to polyphenol determination. A blank test tube without a chocolate sample but with all digestion fluids was also analyzed. The bioaccessibility index (BI) value was determined as follows:

$$BI\ (\%) = \frac{A}{B} \times 100\% \quad \text{(I)}$$

where *A* is the TPC in the intestinal phase after *in vitro* digestion and *B* is the TPC in the samples before *in vitro* digestion.

2.14. *In vitro* ω-3 release study

Standard ω-3 solutions were prepared using an ultraviolet (UV) spectrometer (Shimadzu UV-3600; Shimadzu, Japan) as described by Baykara et al.[33] A calibration graph (0.2, 0.4, 0.6, 0.8, and 1 μL/mL) was plotted accordingly. *In vitro* release studies of ω-3-mixed chocolate and ω-3-SA MP-coated chocolates were performed. Briefly, 5 mg of chocolate samples were placed in Eppendorf tubes; 1 mL of phosphate-buffered saline (PBS; pH 4 and 7.4) was added to each sample. The release of ω-3 was determined in PBS in a shaking incubator (37°C; 1.5 ×g). Thereafter, 1 mL of the solution was removed from the tubes at the specified intervals, and a UV-visible (Vis) spectrophotometer

was utilized to measure the amount of drug release. The original volume of the Eppendorf tubes was then restored by adding an equivalent volume (1 mL) of fresh PBS. Every experiment was performed three times.

2.15. Statistical analysis

All experiments were performed in triplicate; the data are expressed as the mean ± standard deviation. Statistical analysis was performed using SPSS Statistics Software (IBM version 20, USA). One-way analysis of variance (ANOVA) and Tukey's post-hoc test were used to assess differences among the chocolate samples.

3. Results and discussion

3.1. Rheological analysis

The rheological properties of chocolate are essential for predicting its printability since the chocolate ink must exhibit the appropriate flowability and viscosity reduction. A better understanding of the flow behavior of chocolate at low viscosity can ensure the stability of the printed design and enable smooth dispensing through the nozzles.[34] Representative plots of viscosity versus the shear rate of chocolate and ω-3-containing chocolate at various temperatures, including room temperature and human skin temperature, were prepared; the results are provided in Figure 3A–D. This test assessed the behavior of chocolate under ambient conditions, typically ranging from 20 to 25°C. However, upon contact with the human oral environment, i.e., approximately 37°C, chocolate undergoes a transformation, mimicking its natural melting process facilitated by the warmth of the mouth and the enzymatic action of saliva.[35] A study investigating the correlation between temperature and the properties of chocolate revealed that its apparent viscosity remains relatively consistent at 32–40°C, indicating that melted chocolate exhibits favorable printability characteristics.[36] The rheological data demonstrated that the apparent viscosity of the chocolate is time-dependent, exhibiting a thixotropic characteristic, as evidenced by the decreasing viscosity values with increasing shear rate. These variables play crucial roles in determining how effectively a material can be printed. Some of these properties are directly linked to printability and can be assessed prior to extrusion. In addition to examining processing parameters, investigating rheological properties and printability variables offers valuable insights into the behavior of materials throughout the printing process.[37] Our results are in agreement with those of Mantihal et al.[6] The literature indicates that the viscosity of chocolate plateaus at shear rates above 50 s^{-1}.[38] Our results corroborate this finding, demonstrating that the viscosity of pure chocolate at room temperature reaches a plateau after approximately 50–70 s^{-1}. However, as the temperature increases, the viscosity of pure chocolate plateaus at higher shear rates (approximately 180–200 s^{-1}). Our results also agree with those of a previous study,[39] which found that chocolate viscosity reduced in a significant manner as the shear rate was increased from 2 to 110 s^{-1}. This shear-induced viscosity reduction benefits chocolate printing, allowing the chocolate to flow smoothly through the printer nozzle. Furthermore, the maximum viscosity of pure chocolate at room temperature is approximately 15000 mPa·s, while that of ω-3-mixed chocolate is approximately 18000 mPa·s. As the temperature increased to 37°C, the maximum viscosity of pure chocolate and ω-3-mixed chocolate decreased to around 6300 and 16000 mPa·s, respectively. This decline suggests a decrease in the plastic viscosity and thixotropy of the chocolate masses. Our results also agree with those of Quispe-Chambilla et al.,[40] who reported that the viscosity values of different dark chocolate samples changed with increasing temperature. In the present study, adding ω-3 to chocolate further increases the shear rate at which the viscosity plateaus to approximately 300 s^{-1}. These findings suggest that ω-3 improves the rheological properties of pure chocolate, resulting in higher viscosity values.

3.2. Light microscopy and scanning electron microscopy imaging

Figure 4A presents the film structure on the surface of the pure chocolate chips. Figure 4B features ω-3 mixed chocolate chips, with no particles observed. In Figure 4C,

Figure 4. Light microscopy images of (A) pure chocolate, (B) ω-3-mixed chocolate, and (C) ω-3-sodium alginate (SA) microparticle (MP)-coated chocolate. Magnification: 20 X. Scale bars: 200 pixel.

particle formation is observed on the surface of the ω-3-SA-coated chocolate. These results indicate that the mixing and coating processes were successfully achieved. Scanning electron microscopy (SEM) images of ω-3-loaded SA microparticles (Figure 5) revealed that microparticles were successfully produced; particle sizes of 0.5 μm were noted. The chocolate samples could not be imaged using SEM because of they were melting under electron gun.

3.3. Analysis of physicochemical properties

Fourier transform infrared (FTIR) analysis is a chemical characterization method that provides information on the functional groups within a material, which involves the assessment of molecular vibrations generated in response to the absorption of infrared radiation.[41] It is important to note that each bond in a molecule has a distinct natural vibrational frequency, meaning that certain infrared radiation frequencies are absorbed by certain bonds inside the molecule. When materials containing an electric dipole interact with infrared radiation, the molecule absorbs energy and causes the bonds to oscillate. As a result, the oscillation modifies the net dipole moment of the molecule for absorbing infrared energy.[41,42] Figure 6 displays the FTIR spectra of ω-3-mixed chocolate, ω-3-SA microparticles, ω-3-SA MP-coated chocolate, pure chocolate, SA, and commercial ω-3 itself. Characteristic peaks of commercial ω-3 were observed at 1743 cm^{-1} (carbonyl stretching, C=O) and 2852 cm^{-1} (symmetric C–H stretching). As noted in the FTIR spectra, all groups containing commercial ω-3 exhibited these characteristic peaks, suggesting the successful incorporation of ω-3 into the chocolate.[43] For SA, the broad spectral bands in the range of 1600–1610 cm^{-1} were indicative of the asymmetric stretching of O–C–O carboxylate groups; the bands between 1400 and 1428 cm^{-1} were attributed to the deformation vibration of C–OH, possibly involving the symmetric stretching vibration of O–C–O.[44] Additionally, in the ω-3-SA microparticles group, the characteristic peak of SA at 1597 cm^{-1} shifted to 1652 cm^{-1} (Figure 6). This shift might be attributed to the interaction between SA and ω-3. However, these characteristic peaks of SA were not observed in the ω-3-SA MP-coated chocolate group, possibly due to the lower level of SA MP-coating. Quispe-Chambilla et al. also reported that the regions associated with the peaks 2924 and 2853 cm^{-1} can be assigned to the functional group $-CH_2$ in the vibrational mode of symmetric and asymmetric stretching.[40] Lipids and carbohydrates in dark chocolate would be linked to this finding.[45] A band was noted around 3009 cm^{-1} (Figure 6), which can be assigned to the stretching vibration of cis-olefinic double bonds (=C–H) of polyunsaturated fatty acids (PUFA)[40,46]; a greater intensity was noted for the ω-3-mixed and ω-3-SA-coated chocolate samples due to the presence of polyunsaturated acids.

3.4. Moisture content and water activity

Moisture content is an important characteristic that affects the texture, rheological properties, crystallization, and shelf life of a chocolate product.[47] The ω-3-coated and mixed chocolate samples were characterized by significantly higher levels of moisture compared to the pure chocolate sample; the moisture content of the samples was 2.25 ± 0.06% (pure chocolate), 3.17 ± 0.08% (coated chocolate), and 5.56 ± 0.60% (mixed chocolate). Erunsal et al.[47] reported that the moisture content of chocolate samples increased proportionally with the ratio of carob extract.

Water activity (aw) values of chocolate samples ranged from 0.43 to 0.59 (Table 1); this value is within the acceptable limit (< 1%). It should be noted that the presented results

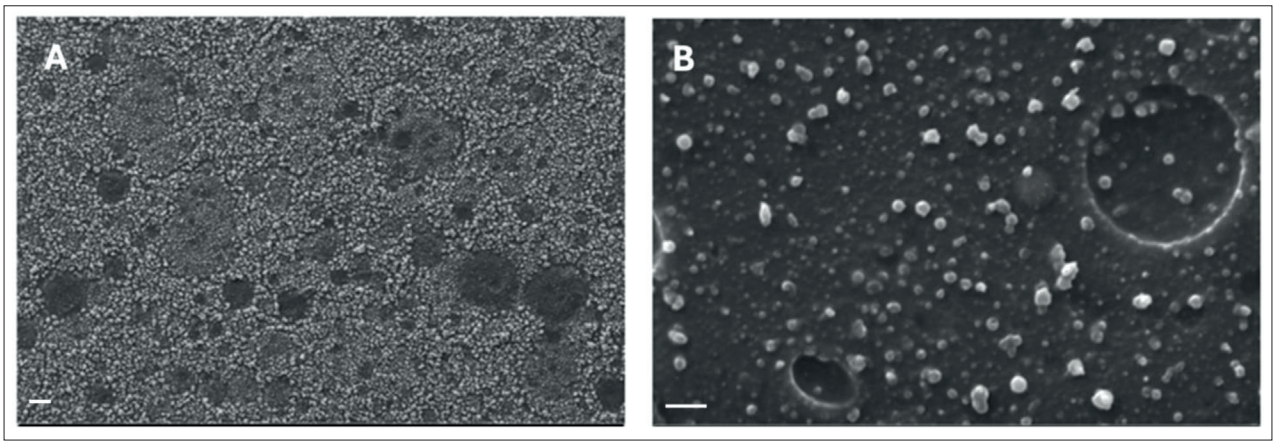

Figure 5. Scanning electron microscopy (SEM) images of ω-3 loaded sodium alginate (SA) microparticles. (A) Magnification: 500 X Scale bar: 20 μm (B) Magnification:10 KX, Scale bar: 2 μm.

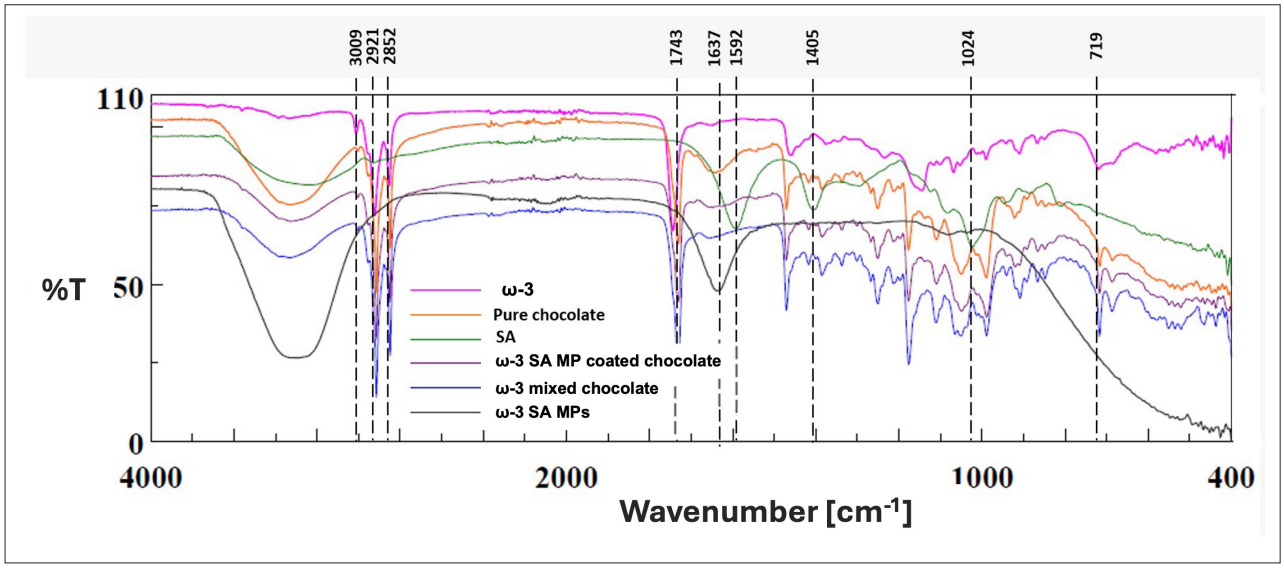

Figure 6. Fourier transform infrared (FTIR) spectrum of commercial ω-3, pure chocolate, sodium alginate (SA), ω-3-SA microparticle (MP)-coated chocolate, and ω-3-mixed chocolate. Abbreviation: % T: Transmittance.

agree with those of previous studies[48,49] for microbial growth as defined by aw. This parameter has a significant impact on the sensory qualities, texture, processing, shelf life, safety, and quality of confectionery items.[49] Various factors, such as the surface area of the materials, the raw materials used, as well as the humidity and temperature associated with refining and conching, might affect this parameter.[50] The results suggest that utilizing various kinds of ω-3 source components affects aw. Overall, the aw level of the samples was noted to be acceptable.

3.5. Color analysis

As a perceptual phenomenon, color depends on the observer and the environment in which it is perceived. It is a characteristic of light interaction that is obtained through wavelength and intensity measurements.[51] The results in Table 1 indicate significant differences ($p < 0.05$) in the color parameters. The L* (lightness) values of the chocolate samples were noted to be 39.89–44.92. The lower values for L* (brightness) are associated with a darker appearance. These results agree with previous studies by Konar et al. and Toker et al.[49,52] The L* value of dark chocolate samples that were enriched with EPA and DHA fatty acids varied from 32.16 to 33.37.[52] Differences in color characteristics occur during the manufacture of chocolate due to variations in the chocolate surface, composition, and processing parameters.[53] The a* values indicated changes from 4.24 to 4.51. The control provided the highest value; no significant difference was noted when compared to other chocolate samples. Furthermore, all samples exhibited no significant

Table 1. Physicochemical properties of chocolate samples.

Chocolate sample	Color properties			Moisture (%)	aw
	L*	a*	b*		
Pure chocolate	44.92 ± 1.52[a]	4.51 ± 0.42[a]	2.38 ± 0.25[b]	2.25 ± 0.06[c]	0.43 ± 0.01[c]
ω-3-mixed chocolate	40.88 ± 3.03[ab]	4.41 ± 0.64[a]	2.84 ± 0.37[b]	5.26 ± 0.18[a]	0.59 ± 0.04[a]
ω-3-SA NP-coated chocolate	39.89 ± 1.99[b]	4.24 ± 0.09[a]	2.52 ± 0.29[b]	3.17 ± 0.08[b]	0.48 ± 0.02[b]

Note: Data are expressed as the mean ± standard deviation of triplicate measurement; The color of chocolate samples are expressed as a* (redness/greenness), L* (lightness), and b* (yellowness/blueness) values; Means with different letters (superscripts[a,b,c]) in the same column are significantly different (p< 0.05). Abbreviations: aw: Water activity; MP: microparticle; SA: Sodium alginate.

Data are expressed as the mean ± standard deviation of triplicate measurement; The color of chocolate samples are expressed as a* (redness/greenness), L* (lightness), and b* (yellowness/blueness) values; Means with different letters (superscripts[a,b,c]) in the same column are significantly different (p< 0.05). Abbreviations: aw: Water activity; MP: microparticle; SA: Sodium alginate.

differences in the b* value. According to these findings, the L* value was associated as a color indicator since the a* and b* values did not give any distinction among the chocolate samples ($p > 0.05$). Similar results were obtained by Erunsal et al.[47]

3.6. Mechanical analysis

Products, such as biscuits, cakes, and cookies are characterized by flavor and texture when consumed; fat is one of the factors that affects texture.[54] The texture of the samples was evaluated by conducting a compression test.

The influence of different loading types (mixing and coating processes) of ω-3 on chocolates in relation to their mechanical properties is described in Table 2. A compressive strength value of 0.65 MPa was obtained for the pure chocolate, along with a strain value of 81.73%. In contrast, the incorporation of SA/ω-3 solution into the 3D-printed pure chocolate scaffolds led to an increase in the compressive strength to 0.82 MPa, with a decrease in the strain value to 61.08%. Keshavarz et al. indicated that the mechanical properties of 3D structures improved after coating with alginate.[55] As noted in the compression test, the incorporation of alginate into pure chocolate scaffolds via coating was associated with an increase in compressive strength. The addition of ω-3 to the melted chocolate solution resulted in a reduction in both compressive strength (0.60 MPa) and strain value (75.98%). The results suggest that different types of loading, such as ω-3-mixed chocolate and ω-3-SA MP, could decrease strain values compared to pure chocolate scaffolds.

3.7. Analysis of thermal properties

Differential scanning calorimetry (DSC) was used to examine the melting temperatures (T_m) of three different chocolate groups that were evaluated in this study. Figure 7 displays the DSC thermogram values of pure chocolate, ω-3-mixed chocolate, and ω-3-SA MP-coated chocolate. The T_{onset} and T_{endset} values of the chocolate samples were found to be between 25.26–28.88°C and 36.07–42.19°C, respectively. The ΔH values varied between

Table 2. Compressive testing results for pure, ω-3-mixed, and ω-3-sodium alginate (SA) microparticle (MP)-coated chocolate scaffolds.

Scaffold	Compressive strength (MPa)	Strain (%)
Pure chocolate	$0.65^{a} \pm 0.025$	$81.73^{c} \pm 3.377$
ω-3-mixed chocolate	$0.60^{a} \pm 0.003$	$75.98^{c} \pm 7.445$
ω-3-SA MP coated chocolate	$0.82^{b} \pm 0.064$	$61.08^{b} \pm 8.496$

Note: Data are expressed as the mean ± standard deviation of triplicate measurements. Means with different letters in the same column are significantly different ($p < 0.05$).

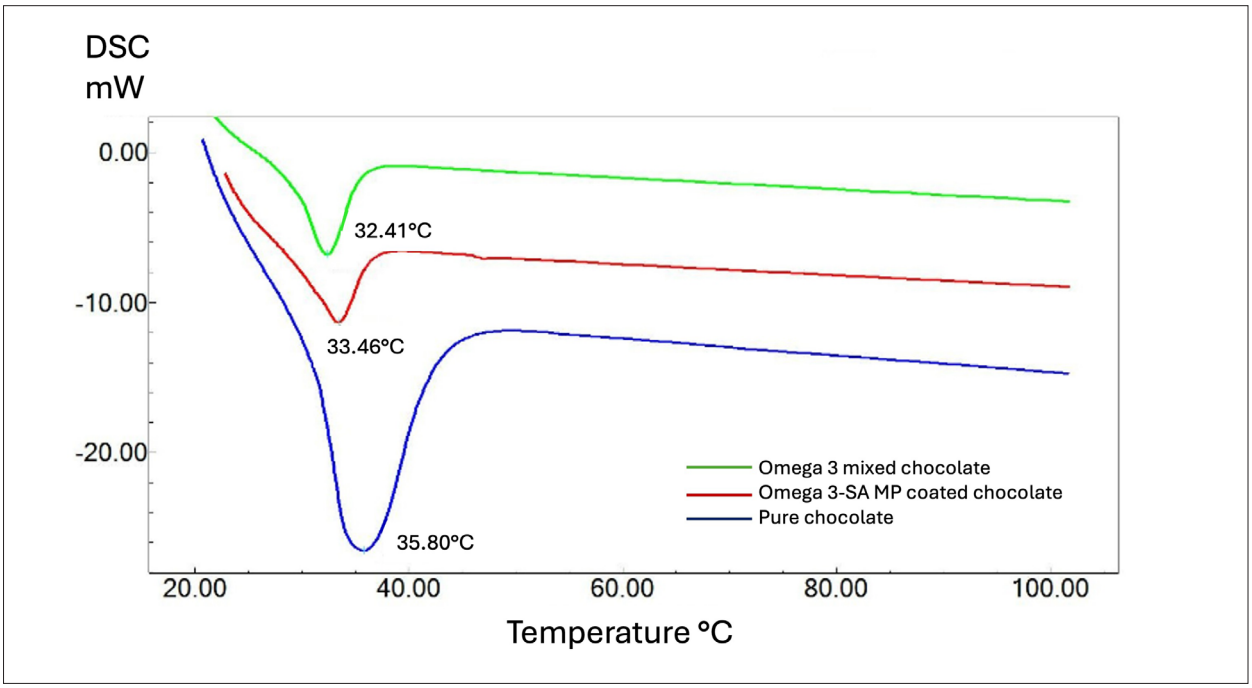

Figure 7. Differential scanning calorimetric (DSC) graph of pure chocolate, ω-3-mixed chocolate, and ω-3-sodium alginate (SA) microparticle (MP)-coated chocolate.

131.33 and 242.93 J/g; the ΔH values of dark chocolate samples increased with the addition of ω-3 and ω-3-SA (Table 3). The T_m of pure chocolate used in this study was 35.80°C. The T_m values for chocolate mixed with ω-3 and chocolate coated with ω-3 were measured as 32.41 and 33.46°C, respectively. Similar results were noted for the T_m of pure chocolate, as noted in the literature.[56] Another study reported that crystalline chocolate exhibits a T_m range of 33.8–35°C[57]; this value is similar to our finding, i.e., approximately 35.8°C. The increased melting behavior of chocolate after extrusion can be attributed to continuous crystallization into the more stable beta form.[6]

The addition of ω-3 reduced the T_m of chocolate. Studies have demonstrated that T_m decreases when ω-3 is added to chocolate. No significant change was observed in the chocolate coated with SA compared to pure chocolate. This finding was due to the lower amount of ω-3 in the coated chocolate compared to the mix and the coating of the ω-3 with SA. The decrease in T_m is likely caused by the changes in the thermal properties of the ω-3 oil. In studies where particles were added to chocolate, no significant change in the T_m of chocolate was noted.[48,58] Similarly, adding ω-3 into chocolate did not significantly change its thermal properties.

3.8. Total phenolic content and antioxidant capacity of chocolate samples

The changes in the TPC and antioxidant capacity of chocolate samples are provided in Figure 8. The initial TPC of pure chocolate, ω-3-coated, and ω-3-mixed chocolate samples were 602.82 ± 4.68, 727.27 ± 5.68, and 692.50 ± 3.16 mg GAE/100 g dw, respectively; the TPC of the ω-3-coated and mixed chocolate samples were also significantly

Table 3. Melting characteristics of chocolate samples.

Chocolate sample	T_{onset} (°C)	T_{peak} (°C)	T_{end} (°C)	ΔH (J/g)
Pure chocolate	28.88	35.80	42.19	131.33
ω-3-mixed chocolate	26.72	32.41	35.15	242.93
ω-3-SA MP-coated chocolate	25.26	33.46	36.07	239.76

Abbreviations: T_{onset}: Onset temperature; T_{peak}: Peak temperature; T_{end}: End of melting temperature ΔH: Energy required for the complete melting of the samples; SA: Sodium alginate; MP: microparticle.

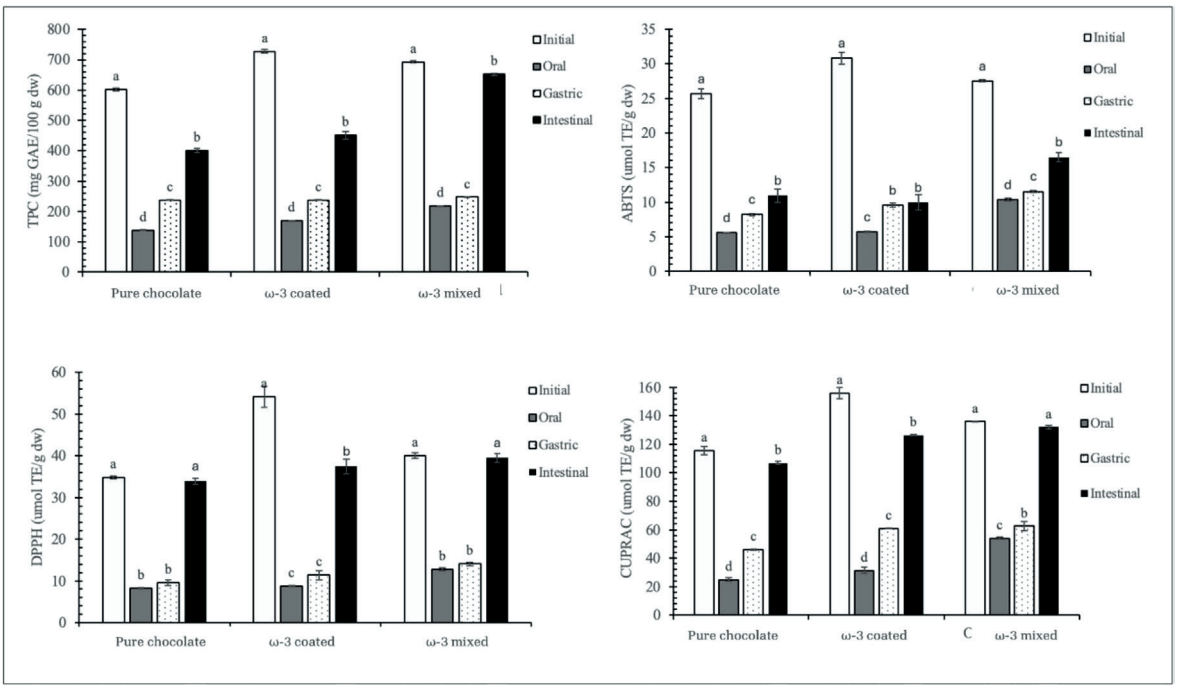

Figure 8. Changes in total phenolic content (TPC) and antioxidant capacity during *in vitro* gastrointestinal digestion. Vertical bars represent the standard deviation of each data point (n = 3). Different letters (a–d) above the bars for each chocolate sample indicate significant differences ($p < 0.05$) among the digestion phases. Abbreviations: TE: Trolox equivalent; GAE: Gallic acid equivalent; ABTS: 2,2′-azino-bis (3-ethylbenzothiazoline6- sulphonic acid); DPPH: 2,2-diphenyl-1-picrylhydrazyl radical scavenging activity; CUPRAC: Copper-reducing antioxidant capacity.

increased ($p < 0.05$) compared to the control sample. Tolve et al.[31] reported that the highest polyphenol concentration was observed in the control (spreadable chocolate: 369 mg GAE/100 g); spreadable chocolate enriched with 11.6 g/kg Mg-$CaCO_3$ nanoparticles and 166 µg/kg vitamin D exhibited the lowest value (272 mg GAE/100 g). Caponio et al.[59] noted that the TPC values of artisanal (Choco-A) and industrial (Choco-I) dark chocolate were 20.66 and 21.53 mg GAE/g, respectively.

Similarly, the antioxidant capacities of ω-3-coated and mixed chocolate samples were also significantly increased ($p < 0.05$) compared to the control sample. The DPPH values of chocolate samples ranged from 34.85 to 40.11 µmol TE/g dw; the ABTS values of chocolate samples ranged from 25.67 to 30.80 µmol TE/g dw. As indicated by the antioxidant capacity results, differences among DPPH, ABTS, and CUPRAC assays were observed; higher values were observed using the CUPRAC method. These variations could be related to the variety of reaction conditions used in the study, such as the wavelength and reaction time at which the measurements were obtained. In the present study, the CUPRAC values of all chocolate extracts were higher than the values obtained using the DPPH and ABTS methods. The Cu^{2+} ion takes part in forming free radicals; the reduction of the cupric ion indicates a mechanism other than that associated with the DPPH and ABTS methods, which reflects the antioxidant potential. This observation can be associated with the fact that the CUPRAC assay may measure the hydrophilic and lipophilic antioxidant capacities of the extracts, as the reagent is soluble in organic and aqueous solvents.[32,60] Caponio et al.[59] demonstrated that the ABTS and DPPH values of artisanal chocolate (Choco-A) were 98.39 and 79.81 µmol TE/g, respectively; the ABTS and DPPH values of industrial (Choco-I) dark chocolate were 88.99 and 68.65 µmol TE/g, respectively.

3.9. *In vitro* digestion test

The changes in TPC and antioxidant capacity values during *in vitro* gastrointestinal digestion (oral, gastric, and intestinal phases) are provided in Figure 8. For all chocolate samples, an increase was noted from the oral phase to the intestinal phase. Compared to the initial amount, the lower values of TPC and antioxidant capacity in the oral phase (Figure 8) may be justified by the low solubility of the compounds in salivary fluid and the short period (3 min). The TPC of chocolate samples in the oral phase was noted to vary between 137.65 mg GAE/100 g dw and 217.29 mg GAE/100 g dw. During the *in vitro* simulation of GI digestion, an increase was noted in the total antioxidant capacity of the chocolate samples from the oral phase to the gastric phase. Similar results have been described by Martini et al., who examined dark chocolate.[61] After the intestinal phase, a significant increase ($p < 0.05$) was observed in the TPC and antioxidant capacity of all the chocolate samples (Figure 8). These increases could be due to enhanced extractability of phenolics and flavonoids, influenced by factors such as pH, enzymes, organic solvent dependency, bile concentration, and incubation (3 h) during the intestinal phase.[32,62] In a study by Tolve et al.,[31] the bioaccessibility of polyphenols in chocolate hazelnut spreads was examined after simulated *in vitro* digestion; the authors reported that the same trend may occur for all the samples, in which there is a high polyphenol concentration in the simulated salivary phase, followed by a reduction in the simulated gastric phase, and a subsequent increase in the simulated intestinal phase. The TPC and antioxidant capacities of ω-3-coated and mixed chocolate samples were also significantly increased ($p < 0.05$) compared to the pure chocolate sample after *in vitro* digestion. Ingredients of the ω-3-coated and mixed chocolate samples may influence the structure and degradation of the matrix when exposed to digestion. Particle size, amount, distribution of fat, emulsifier type, quantity, and solid particles all affect the chocolate microstructure.[63] In the present study, the highest TPC and antioxidant capacity were noted in chocolate coated with ω-3-SA MP before *in vitro* digestion. In contrast, the highest TPC and antioxidant capacity were found in ω-3-mixed chocolate samples after *in vitro* digestion. Despite the high initial TPC and antioxidant capacity in the chocolate coated with ω-3-SA MP, the BI value was not the highest among the chocolate samples (Figure 8). The BI values of the TPC were 67%, 62%, and 94% in pure chocolate, ω-3-coated, and ω-3 mixed, respectively, while the BI values of DPPH, ABTS, and CUPRAC ranged between 69–98%, 32–60%, and 81–97%, respectively.

3.10. *In vitro* release study

Encapsulation techniques are used for the controlled release of bioactive compounds and to increase bioavailability.[64] To compare the controlled release characteristics, *in vitro* ω-3 release studies were conducted using chocolates coated with ω-3-SA MP and mixed with ω-3. To mimic gastrointestinal fluids, ω-3 release profiles of chocolates were performed in PBS (pH 4 and 7) at 37°C; the results are displayed in Figure 10. The UV spectra for the 0.2–1 µg/mL ω-3 concentration range are displayed in Figure 10A. The released ω-3 was identified at an absorbance of 214 nm. Figure 10C and D demonstrate the cumulative release of ω-3 from ω-3-SA-coated chocolate and ω-3-mixed chocolates at pH 4 and 7. As observed in Figure 10C, 59% burst release was observed in the first 15 min from SA-ω-3-coated chocolates at pH 7, and the release was completed in 1 h. A burst release of 27% was observed in the first 1 h from SA-ω-3-coated

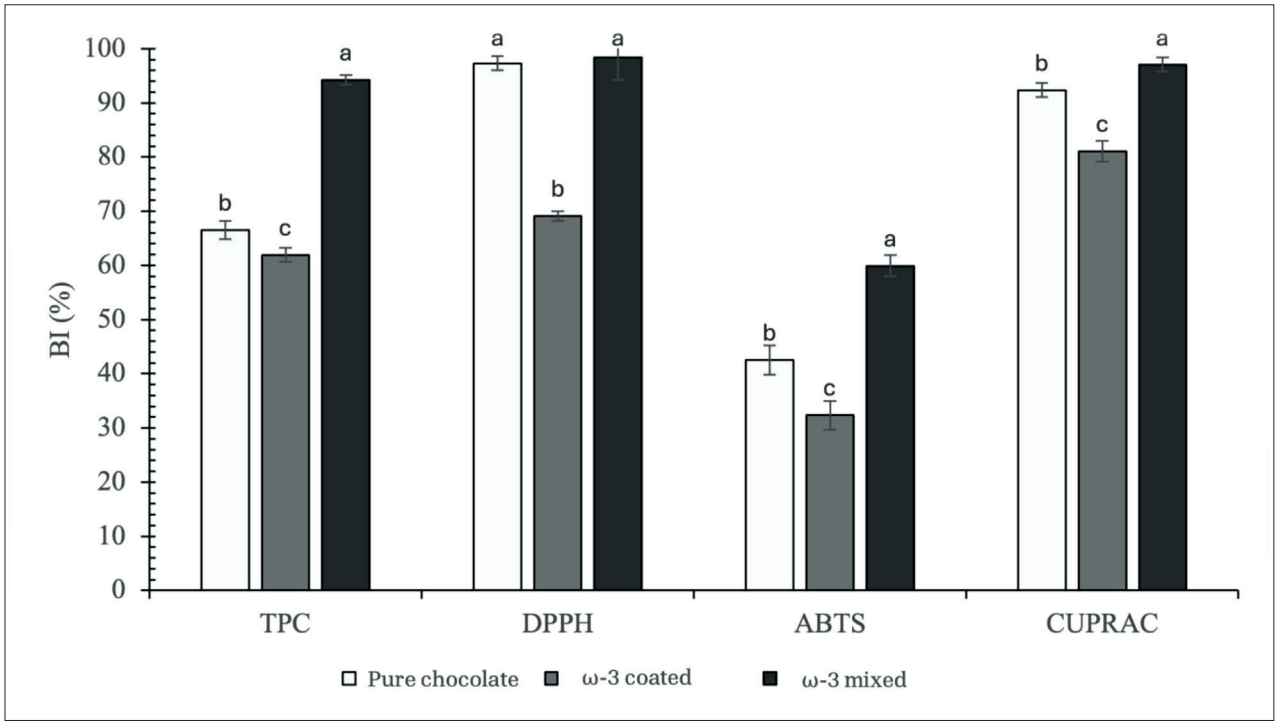

Figure 9. The bioaccessibility index (BI) of chocolate samples. Different letters (a–c) above the bars for each chocolate sample indicate significant differences ($p < 0.05$; $n = 3$). Abbreviations: TPC: Total phenolic content; ABTS: 2,2′-azino-bis (3-ethylbenzothiazoline6- sulphonic acid); DPPH: 2,2-diphenyl-1-picrylhydrazyl radical scavenging activity; CUPRAC: Copper-reducing antioxidant capacity.

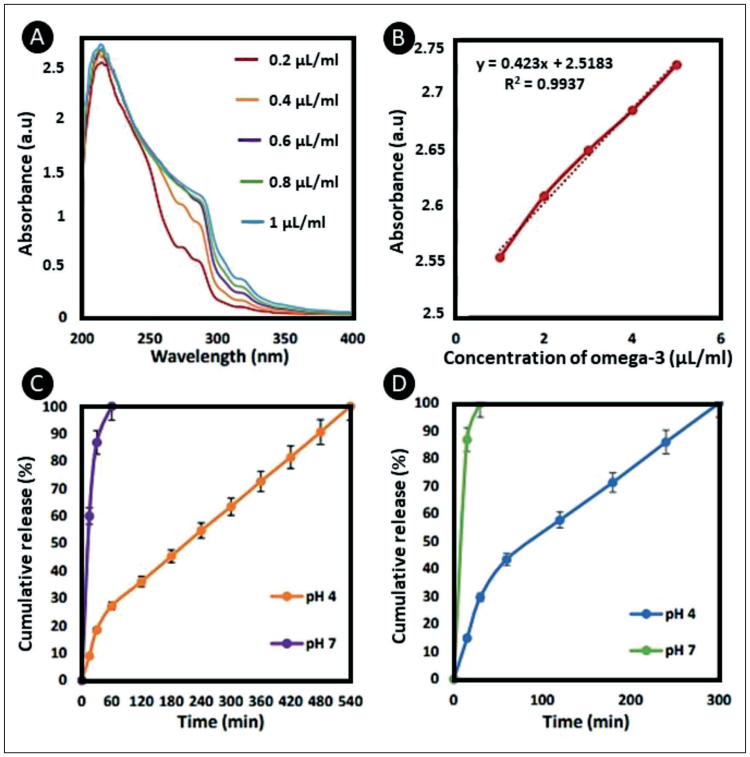

Figure 10. *In vitro* release profile of ω-3-sodium alginate (SA)-coated chocolate and ω-3-mixed chocolate. (A) Absorption spectra of ω-3 at different conditions. (B) Calibration curve of ω-3. (C and D) Release profile of ω-3 from ω-3-SA microparticle (MP)-coated chocolate (C) and ω-3-mixed chocolate (D). All the values were calculated based on the averages of three experiments ($n = 3$), and the errors were less than 5%).

chocolate at pH 4, and the release was completed in 9 h. Figure 10D indicates that the burst release in the first 15 min involved the release of over 86% of ω-3 from ω-3-mixed chocolate at pH 7. At pH 4, while 43% of ω-3 release from ω-3-mixed chocolate was released in 60 min; the release was completed in 5 h. Small diameter particles offer a larger specific surface area, thus increasing the release profile associated with the bioactive compound.[65] In this study, the release profile of ω-3 encapsulated with particles was higher than ω-3-mixed in chocolate. Encapsulating the oil using encapsulation techniques leads to the oil being protected from degradation by stomach enzymes and prolonged release under intestinal conditions.[66] The rapid release of ω-3 from the encapsulated particles is attributed to the hydrophilic property of SA.[67] In addition, carboxylic acid groups in the structure of SA make the polymer pH-sensitive. In an environment above pH 4.4, the carboxylic acid groups in the SA structure are ionized. As a result, electrostatic repulsion of the negative charge occurs, the polymer chain expands, and the matrix swells. This effect is more significant when the pH value is 7.4. When the pH value is below 3.4, the polymer can become challenging to dissolve as the carboxylic groups do not ionize.[68] This result may explain the faster release of encapsulated ω-3 at a pH value of 7, as SA particles dissolve faster in high pH environments, such as those found in the oral and intestinal regions.

Chang et al.[66] found that microencapsulation of fish oil with TMFCC (thiol-modified β-lactoglobulin fibrils/chitosan complex) led to lower levels of fish oil release under simulated gastric (< 25%) and intestinal (< 65%) conditions. According to these findings, TMFCC serves as an encapsulation agent that can protect the structure in gastric conditions and provide a sustainable release of encapsulated fish oil in intestinal conditions. Razavizadeh and Yeganehzad described the release of chia seed oil from microspheres (the solutions mixed in three ratios of alginate to soy protein isolate: 5:1, 5:3, and 5:5) in SGF and SIF environments; for microspheres exposed to SGF conditions for 2 h, the release range was approximately 42–39%. Exposure to a sequential SGF-SIF medium (cumulative SGF + SIF) for 6 h resulted in an oil release range of 96.30–98.73%.[69] In another study, Bannikova et al.[70] encapsulated fish oil in an alginate polymer to develop a structure targeting a specific part of the human digestive system. It was observed that the encapsulated oils exhibited little release in the stomach stage; the release was increased in the intestinal stage. The findings confirmed the controlled release of the encapsulated ω-3 under *in vitro* simulated gastrointestinal conditions, facilitating efficient absorption and utilization by the body.

4. Conclusion

This study introduced the fabrication of 3D-printed dark chocolate structures supported with ω-3 via bulk mixing and electrospray methods. The electrospraying method was used for ω-3 encapsulation into biopolymeric particles made from SA; an AXO-A3 3D printer was utilized for the fabrication of dark chocolate-based structures. To observe the ω-3 release profiles associated with both techniques, *in vitro* release profiles of ω-3-mixed chocolate and ω-3-SA MP-coated chocolate were compared to prolong the ω-3 release duration. From these results, it is suggested that the ω-3-SA MP-coated chocolate has a better release profile than the ω-3-mixed chocolate due to the protection of the biopolymeric particles. *In vitro* bioaccessibility and antioxidant capacity analysis reported increased TPC in ω-3-SA MP-coated chocolate and ω-3-mixed chocolate compared to pure chocolate. Similarly, *in vitro* digestion analysis displayed increased antioxidant capacity and TPC for all chocolate samples from oral to intestinal phases. Mechanical testing also indicated that ω-3-SA-coated chocolate structures exhibited an increase in compressive strength compared to the ω-3-mixed structures. Thus, it can be concluded that additive manufacturing and 3D printing systems can be actively used to fabricate optimized food-based products with required additives based on nutritional demands.

Acknowledgments

None.

Funding

None.

Conflict of interest

Roger J. Narayan serves as the Editorial Board Member of the journal but was not in any way involved in the editorial and peer-review process conducted for this paper, directly or indirectly. Other authors declare they have no competing interests

Author contributions

Conceptualization: Canan Dogan, Oguzhan Gunduz
Formal analysis: Esra Pilavci, Dilruba Baykara, Kubra Ozkan, Aysegul Tiryaki, Melih Musa Ayran, Gozde Enguven, Tufan Arslan Tut, Mehmet Murat Bozdag
Investigation: Canan Dogan, Oguzhan Gunduz, Osman Sagdıc, Roger J. Narayan
Methodology: Canan Dogan, Oguzhan Gunduz, Osman Sagdıc, Esra Pilavci, Dilruba Baykara, Kubra Ozkan,

Aysegul Tiryaki, Melih Musa Ayran, Gozde Enguven, Tufan Arslan Tut, Mehmet Murat Bozdag

Supervision: Canan Dogan, Oguzhan Gunduz, Roger J. Narayan

Validation: Canan Dogan, Oguzhan Gunduz, Roger J. Narayan

Writing – original draft: Esra Pilavci, Dilruba Baykara, Kubra Ozkan, Aysegul Tiryaki, Melih Musa Ayran, Gozde Enguven, Tufan Arslan Tut, Mehmet Murat Bozdag

Writing – review & editing: Osman Sagdıc, Roger J. Narayan, Canan Dogan, Oguzhan Gunduz

Ethics approval and consent to participate

Not applicable.

Consent for publication

Not applicable.

Availability of data

Not applicable.

References

1. Taneja A, Sharma R, Ayush K, et al. Innovations and applications of 3-D printing in food sector. *Int J Food Sci Technol.* 2022;57(6):3326-3332. doi: 10.1111/ijfs.15691
2. Athira VA, Udayarajan CT, Goksen G, Brennan CS, Nisha P. A brief review on 3D printing of chocolate. *Int J Food Sci Technol*. 2023;58(6):2811-2828. doi: 10.1111/ijfs.16415
3. Singhal S, Rasane P, Kaur S, et al. 3D food printing: paving way towards novel foods. *An Acad Bras Cienc.* 2020:92(3):e20180737. doi: 10.1590/0001-3765202020180737
4. Lanaro M, Forrestal DP, Scheurer S, et al. 3D printing complex chocolate objects: platform design, optimization and evaluation. *J Food Eng.* 2017;215:13-22. doi: 10.1016/j.jfoodeng.2017.06.029
5. Mantihal S, Prakash S, Godoi FC, Bhandari B. Optimization of chocolate 3D printing by correlating thermal and flow properties with 3D structure modeling. *Innov Food Sci Emerg Technol.* 2017;44:21-29. doi: 10.1016/j.ifset.2017.09.012
6. Karavasili C, Gkaragkounis A, Moschakis T, Ritzoulis C, Fatouros DG. Pediatric-friendly chocolate-based dosage forms for the oral administration of both hydrophilic and lipophilic drugs fabricated with extrusion-based 3D printing. *Eur J Pharm Sci* 2020;147:105291. doi: 10.1016/j.ejps.2020.105291
7. Turner BN, Strong R, Gold SA. A review of melt extrusion additive manufacturing processes: I. process design and modeling. *Rapid Prototyp J*. 2014;20:192-204. doi: 10.1108/RPJ-01-2013-0012
8. You S, Huang Q, Lu X. Development of fat-reduced 3D printed chocolate by substituting cocoa butter with water-in-oil emulsions. *Food Hydrocoll.* 2023;135:108114. doi: 10.1016/j.foodhyd.2022.108114
9. Lille M, Nurmela A, Nordlund E, Metsä-Kortelainen S, Sozer N. Applicability of protein and fiber-rich food materials in extrusion-based 3D printing. *J Food Eng.* 2018;220:20–27. doi: 10.1016/J.JFOODENG.2017.04.034
10. Rezaei S, Valipouri A, Hosseini Ravandi SA, Kouhi M, Ghasemi Mobarakeh L. Fabrication, characterization, and drug release study of Vitamin C–loaded alginate/polyethylene oxide nanofibers for the treatment of a skin disorder. *Polym Adv Technol.* 2019;30(9):2447-2457. doi: 10.1002/pat.4692
11. Yilmaz MT, Taylan O, Karakas CY, Dertli E. An alternative way to encapsulate probiotics within electrospun alginate nanofibers as monitored under simulated gastrointestinal conditions and in kefir. *Carbohydr Polym.* 2020;244:116447. doi: 10.1016/j.carbpol.2020.116447
12. Seoane-Viaño I, Januskaite P, Alvarez-Lorenzo C, Basit AW, Goyanes A. Semi-solid extrusion 3D printing in drug delivery and biomedicine: personalised solutions for healthcare challenges. *J Control Release*. 2021;332:367-389. doi: 10.1016/j.jconrel.2021.02.027
13. Mutlu ME, Ulag S, Sengor M, Daglılar S, Narayan R, Gunduz O. Electrosprayed collagen/gentamicin nanoparticles coated microneedle patches for skin treatment. *Mater Lett.* 2021;305:130844. doi: 10.1016/j.matlet.2021.130844
14. Asadi M, Salami M, Hajikhani M, Emam-Djomeh Z, Aghakhani A, Ghasemi A. Electrospray production of curcumin-walnut protein nanoparticles. *Food Biophys.* 2021;16(1):15-26. doi: 10.1007/s11483-020-09637-9
15. Raval D, Kabariya J, Hazra T, Ramani V. A review on electrospraying technique for encapsulation of nutraceuticals. *Int J Chem Stud.* 2019;51(5), 227-240. doi: 10.20546/ijcmas.2019.807.334
16. Bhushani JA, Kurrey NK, Anandharamakrishnan C. Nanoencapsulation of green tea catechins by electrospraying technique and its effect on controlled release and *in-vitro* permeability. *J Food Eng.* 2017;199:82-92. doi: 10.1016/j.jfoodeng.2016.12.010
17. Du Q, Zhou L, Li M, Lyu F, Liu J, Ding Y. Omega-3 polyunsaturated fatty acid encapsulation system: physical and oxidative stability, and medical applications. *Food Frontiers*. 2022;3(2):239-255. doi: 10.1002/fft2.134

18. Shahidi F, Ambigaipalan P. Omega-3 polyunsaturated fatty acids and their health benefits. *Annu Rev Food Sci Technol.* 2018;9:345–381.
doi: 10.1146/annurev-food-111317-095850

19. Pacifico L, Bonci E, Di Martino M, et al. A double-blind, placebo-controlled randomized trial to evaluate the efficacy of docosahexaenoic acid supplementation on hepatic fat and associated cardiovascular risk factors in overweight children with nonalcoholic fatty liver disease. *Nutr Metab Cardiovasc Dis.* 2015;25(8):734-741.
doi: 10.1016/j.numecd.2015.04.003

20. de Goede J, Geleijnse JM, Boer JMA, Kromhout D, Verschuren WMM. Marine (n-3) fatty acids, fish consumption, and the 10-year risk of fatal and nonfatal coronary heart disease in a large population of dutch adults with low fish intake. *J Nutr.* 2010;140(5):1023-1028.
doi: 10.3945/jn.109.119271

21. Rittenhouse MA, Barringer ND, Jaffe DA, et al. Omega-3 index improves after increased intake of foods with omega-3 polyunsaturated fatty acids among US service academy cadets. *Nutrition Research.* 2023;117:30-37.
doi: 10.1016/j.nutres.2023.06.005

22. Gómez-Mascaraque LG, López-Rubio A. Protein-based emulsion electrosprayed micro- and submicroparticles for the encapsulation and stabilization of thermosensitive hydrophobic bioactives. *J Colloid Interface Sci.* 2016;465:259-270.
doi: 10.1016/j.jcis.2015.11.061

23. Rahmani-Manglano NE, Guadix EM, Jacobsen C, García-Moreno PJ. Comparative study on the oxidative stability of encapsulated fish oil by monoaxial or coaxial electrospraying and spray-drying. *Antioxidants.* 2023;12(2):266.
doi: 10.3390/antiox12020266

24. Zhou X, Guan C, Ma Q, et al. Elaboration and characterization of ε-polylysine-sodium alginate nanoparticles for sustained antimicrobial activity. *Int J Biol Macromol.* 2023;251:126329.
doi: 10.1016/j.ijbiomac.2023.126329

25. Wu X, Zhang Q, Wang Z, et al. Investigation of construction and characterization of carboxymethyl chitosan – sodium alginate nanoparticles to stabilize pickering emulsion hydrogels for curcumin encapsulation and accelerating wound healing. *Int J Biol Macromol.* 2022;209:1837-1847.
doi: 10.1016/j.ijbiomac.2022.04.157

26. Izgordu MS, Ayran M, Ulag S, et al. Fabrication of gentamicin sulfate-loaded 3D-printed polyvinyl alcohol/sodium alginate/gelatin-methacryloyl hybrid scaffolds for skin tissue replacement. *Macromol Mater Eng.* 2023;308(12): 2300151.
doi: 10.1002/mame.202300151

27. Ulag S, Celik SE, Sengor M, Gunduz O. Fabrication of amphotericin-B-loaded sodium alginate nanoparticles for biomedical applications. *Bionanoscience.* 2022;12(4): 1230–1237.
doi: 10.1007/s12668-022-01018-5

28. Baykara D, Bedir T, Ilhan E, et al. Fabrication and optimization of 3D printed gelatin methacryloyl microneedle arrays based on vat photopolymerization. *Front Bioeng Biotechnol.* 2023;11:1157541.
doi: 10.3389/fbioe.2023.1157541

29. Aydin A, Ulag S, Sahin A, et al. Biocompatible polyvinyl alcohol nanofibers loaded with amoxicillin and salicylic acid to prevent wound infections. *Biomedical Materials (Bristol).* 2023;18(5):055029.
doi: 10.1088/1748-605X/acf25c

30. Hu Y, Pan ZJ, Liao W, et al. Determination of antioxidant capacity and phenolic content of chocolate by attenuated total reflectance-Fourier transformed-infrared spectroscopy. *Food Chem.* 2016;202:254-261.
doi: 10.1016/j.foodchem.2016.01.130

31. Tolve R, Tchuenbou-Magaia FL, Verderese D, et al. Physico-chemical and sensory acceptability of no added sugar chocolate spreads fortified with multiple micronutrients. *Food Chem.* 2021;364:130386.
doi: 10.1016/j.foodchem.2021.130386

32. Ozkan K, Karadag A, Sagdic O. The effects of different drying methods on the *in vitro* bioaccessibility of phenolics, antioxidant capacity, minerals and morphology of black 'Isabel' grape. *LWT.* 2022;158:113185.
doi: 10.1016/j.lwt.2022.113185

33. Baykara D, Pilavci E, Cesur S, et al. Controlled release of gentamicin from electrospun poly(vinyl alcohol)/gelatin nanofibers: the effect of crosslinking time using glutaraldehyde vapor. *ChemistrySelect.* 2023;8(5):e202203681.
doi: 10.1002/slct.202203681

34. Zhong Y, Wang B, Lv W, Wu Y, Lv Y, Sheng S. Recent research and applications in lipid-based food and lipid-incorporated bioink for 3D printing. *Food Chem.* 2024;458: 140294.
doi: 10.1016/J.FOODCHEM.2024.140294

35. Karyappa R, Hashimoto M. Chocolate-based ink three-dimensional printing (Ci3DP). *Sci Rep.* 2019;9(1):14178.
doi: 10.1038/s41598-019-50583-5

36. Lanaro M, Forrestal DP, Scheurer S, et al. 3D printing complex chocolate objects: platform design, optimization and evaluation. *J Food Eng.* 2017;215:13-22.
doi: 10.1016/J.JFOODENG.2017.06.029

37. Maldonado-Rosas R, Tejada-Ortigoza V, Cuan-Urquizo E, et al. Evaluation of rheology and printability of 3D printing nutritious food with complex formulations. *Addit Manuf.* 2022;58:103030.
doi: 10.1016/j.addma.2022.103030

38. Karnjanolarn R, Mccarthy KL. Rheology of different formulations of milk chocolate and the effect on coating thickness. *J Texture Stud.* 2006;37(6):668-680.
doi: 10.1111/j.1745-4603.2006.00077.x

39. Biswas N, Cheow YL, Tan CP, Siow LF. Physical, rheological and sensorial properties, and bloom formation of dark

chocolate made with cocoa butter substitute (CBS). *LWT.* 2017;82:420-428.
doi: 10.1016/j.lwt.2017.04.039

40. Quispe-Chambilla L, Pumacahua-Ramos A, Choque-Quispe D, et al. Rheological and functional properties of dark chocolate with partial substitution of peanuts and sacha inchi. *Foods.* 2022;11(8):1142.
doi: 10.3390/foods11081142

41. Khan SA, Khan SB, Khan LU, Farooq A, Akhtar K, Asiri AM. Fourier transform infrared spectroscopy: fundamentals and application in functional groups and nanomaterials characterization. In: *Handbook of Materials Characterization*. Cham:Springer. 2018.
doi: 10.1007/978-3-319-92955-2_9

42. Sherban-Kline M. *Infrared Spectroscopy: A Key to Organic Structure*. Yale-New Haven Teachers Institute. Volume V: How Do You Know? The Experimental Basis of Chemical Knowledge. 1999.

43. Lopes TIB, Pereira ES, dos Freitas DS, Oliveira SL, Alcantara GB. Spectral profiles of commercial omega-3 supplements: an exploratory analysis by ATR-FTIR and 1H NMR. *J Food Sci Technol.* 2020;57(4):1251-1257.
doi: 10.1007/s13197-019-04157-y

44. Sellimi S, Younes I, Ben AH, et al. Structural, physicochemical and antioxidant properties of sodium alginate isolated from a Tunisian brown seaweed. *Int J Biol Macromol.* 2015;72:1358-1367.
doi: 10.1016/j.ijbiomac.2014.10.016

45 Gómez-Fernández AR, Faccinetto-Beltrán P, Orozco-Sánchez NE, et al. Sugar-free milk chocolate as a carrier of omega-3 polyunsaturated fatty acids and probiotics: a potential functional food for the diabetic population. *Foods.* 2021;10(8):1866.
doi: 10.3390/foods10081866

46. Karunathilaka SR, Kia ARF, Srigley C, Chung JK, Mossoba MM. Nontargeted, rapid screening of extra virgin olive oil products for authenticity using near-infrared spectroscopy in combination with conformity index and multivariate statistical analyses. *J Food Sci.* 2016;81(10):C2390-C2397.
doi: 10.1111/1750-3841.13432

47. Cikrikci Erunsal S, Basturk ZS, Canturkoglu I, Ozturk HI. Development of 3D printed dark chocolate sweetened with carob extract. *Int J Gastron Food Sci.* 2023; 34:100794.
doi: 10.1016/j.ijgfs.2023.100794

48. Faccinetto-Beltrán P, Gómez-Fernández AR, Orozco-Sánchez NE, et al. Physicochemical properties and sensory acceptability of a next-generation functional chocolate added with omega-3 polyunsaturated fatty acids and probiotics. *Foods.* 2021;10(2):333.
doi: 10.3390/foods10020333

49. Konar N, Toker OS, Rasouli Pirouzian H, et al. Enrichment of milk chocolate by using EPA and DHA originated from various origins: effects on product quality. *Sugar Tech.* 2018;20(6):745–755.
doi: 10.1007/s12355-018-0611-5

50. Toker OS, Konar N, Pirouzian HR, et al. Developing functional white chocolate by incorporating different forms of EPA and DHA – effects on product quality. *LWT.* 2018;87:177-185.
doi: 10.1016/j.lwt.2017.08.087

51. Sharma G. Colour fundamentals for digital imaging. In: *Digital Color Imaging Handbook.* Boca Raton, FL: CRC Press; 2017.
doi: 10.1201/9781420041484

52. Toker OS, Konar N, Palabiyik I, et al. Formulation of dark chocolate as a carrier to deliver eicosapentaenoic and docosahexaenoic acids: effects on product quality. *Food Chem.* 2018;254:224-231.
doi: 10.1016/j.foodchem.2018.02.019

53. Aidoo RP, Afoakwa EO, Dewettinck K. Optimization of inulin and polydextrose mixtures as sucrose replacers during sugar-free chocolate manufacture – rheological, microstructure and physical quality characteristics. *J Food Eng.* 2014;126:35-42.
doi: 10.1016/j.jfoodeng.2013.10.036

54. Garvey EC, O'Sullivan MG, Kerry JP, Kilcawley KN. Factors influencing the sensory perception of reformulated baked confectionary products. *Crit Rev Food Sci Nutr.* 2020;60(7):1160-1188.
doi: 10.1080/10408398.2018.1562419

55. Keshavarz M, Alizadeh P. On the role of alginate coating on the mechanical and biological properties of 58S bioactive glass scaffolds. *Int J Biol Macromol.* 2021;167: 947-961.
doi: 10.1016/J.IJBIOMAC.2020.11.051

56. Razavizadeh BM, Tabrizi P. Characterization of fortified compound milk chocolate with microcapsulated chia seed oil. *LWT.* 2021;150(June):111993.
doi: 10.1016/j.lwt.2021.111993

57. Mantihal S, Prakash S, Godoi FC, Bhandari B. Optimization of chocolate 3D printing by correlating thermal and flow properties with 3D structure modeling. *Innov Food Sci Emerg Technol.* 2017;44:21-29.
doi: 10.1016/J.IFSET.2017.09.012

58. Tan J, Kerr WL. Determination of chocolate melting properties by capacitance based thermal analysis (CTA). *J Food Measure Character.* 2018;12(1):641-649.
doi: 10.1007/s11694-017-9677-0

59. Caponio GR, Lorusso MP, Sorrenti GT, et al. Chemical characterization, gastrointestinal motility and sensory evaluation of dark chocolate: a nutraceutical boosting consumers' health. *Nutrients.* 2020;12(4):939.
doi: 10.3390/nu12040939

60. Capanoglu E, Kamiloglu S, Ozkan G, Apak R. Evaluation of antioxidant activity/ capacity measurement methods

for food products. In: *John Wiley & Sons, Ltd eBooks*. 2017;273-286.
doi: 10.1002/9781119135388.ch13

61. Martini S, Conte A, Tagliazucchi D. Bioaccessibility, bioactivity and cell metabolism of dark chocolate phenolic compounds after *in vitro* gastro-intestinal digestion. *J Funct Foods*. 2018;49:424-436.
doi: 10.1016/j.jff.2018.09.005

62. Ozkan K, Karadag A, Sagdic O. The effects of drying and fermentation on the bioaccessibility of phenolics and antioxidant capacity of thymus vulgaris leaves. *Acta Aliment*. 2022;51(2):155-165.
doi: 10.1556/066.2021.00140

63. Paz-Yépez C, Peinado I, Heredia A, Andrés A. Lipids digestibility and polyphenols release under *in vitro* digestion of dark, milk and white chocolate. *J Funct Foods*. 2019;52: 196-203.
doi: 10.1016/j.jff.2018.10.028

64. Torres-Giner S, Martinez-Abad A, Ocio MJ, Lagaron JM. Stabilization of a nutraceutical omega-3 fatty acid by encapsulation in ultrathin electrosprayed zein prolamine. *J Food Sci*. 2010;75(6):N69-79.
doi: 10.1111/j.1750-3841.2010.01678.x

65. García-Moreno PJ, Pelayo A, Yu S, et al. Physicochemical characterization and oxidative stability of fish oil-loaded electrosprayed capsules: combined use of whey protein and carbohydrates as wall materials. *J Food Eng*. 2018;231:42-53.
doi: 10.1016/j.jfoodeng.2018.03.005

66. Chang HW, Tan TB, Tan PY, et al. Microencapsulation of fish oil using thiol-modified β-lactoglobulin fibrils/chitosan complex: a study on the storage stability and *in vitro* release. *Food Hydrocoll*. 2018;80:186-194.
doi: 10.1016/j.foodhyd.2018.02.002

67. Jadach B, Świetlik W, Froelich A. Sodium alginate as a pharmaceutical excipient: novel applications of a well-known polymer. *J Pharm Sci*. 2022;111(5):1250-1261.
doi: 10.1016/j.xphs.2021.12.024

68. Chaturvedi K, Ganguly K, More UA, et al. Sodium Alginate in Drug Delivery and Biomedical Areas. In *Elsevier eBooks*. 2019;59-100.
doi: 10.1016/B978-0-12-817055-7.00003-0

69. Razavizadeh BM, Yeganehzad S. Alginate/soy protein isolavte microspheres for fortifying dark chocolate: an innovative approach for enriching with omega-3. *J Food Measure Character* 2024;18(7):1-11.
doi: 10.1007/s11694-024-02570-2

70. Bannikova A, Evteev A, Pankin K, Evdokimov I, Kasapis S. Microencapsulation of fish oil with alginate: *in-vitro* evaluation and controlled release. *LWT*. 2018;90:310-315.
doi: 10.1016/j.lwt.2017.12.045

ACCSCIENCE PUBLISHING

International Journal of Bioprinting

RESEARCH ARTICLE

3D-printed polycaprolactone-magnetic nanoparticles composite multifunctional scaffolds for bone tissue regeneration and hyperthermia treatment

Susheem Kanwar[1,2] and Sanjairaj Vijayavenkataraman[1,2*]

[1]The Vijay Lab, Division of Engineering, New York University Abu Dhabi, Abu Dhabi, United Arab Emirates

[2]Department of Mechanical and Aerospace Engineering, Tandon School of Engineering, New York University, Brooklyn, New York, United States of America

Abstract

Cancer management after tumor resection is characterized by two critical needs: (i) rehabilitation of the resected tissue and (ii) preventing post-surgical tumor recurrence by destroying any residual tumors. The state-of-the-art in literature is limited because it tackles these two major priorities individually: achieving tissue regeneration via autologous grafting and preventing tumor recurrence through chemotherapy. In this paper, extrusion 3D printing has been employed to manufacture composite multi-functional scaffolds with polycaprolactone (PCL) as a polymeric matrix and magnetic nanoparticles (MNPs) in a 0–50 wt% ratio, which would aid in bone regeneration and cancer management via magnetic hyperthermia treatment. The fabricated scaffolds were evaluated for their mechanical, magnetic, and thermal characteristics. The Young's modulus of the scaffolds increased multi-fold with increasing concentration of MNPs added to PCL (i.e., 26.88 ± 9.02 MPa for pure PCL to 229.06 ± 37.05 MPa for PCL/50 wt% MNP scaffolds). PCL/MNP scaffolds displayed a directly proportional correlation between MNP concentration and saturation magnetization. While the *in vitro* tests demonstrated a statistically significant cell growth of human mesenchymal stem cells (hMSCs) over 7 days for all MNP concentrations, only the 50% MNP scaffold exhibited an increase in temperature over 41°C when subjected to an alternating magnetic field, making it suitable for the hyperthermia treatment. On application of alternating magnetic fields to PCL and PCL/50 wt% MNP scaffolds, there was an increase in hMSCs proliferation and a decrease in bone cancer cell proliferation, thus validating the potential of the multi-functional scaffold for post-surgical bone cancer management.

***Keywords*:** Cancer; Hyperthermia; Magnetic nanoparticles; Polycaprolactone; 3D printing; Scaffolds

***Corresponding author:**
Sanjairaj Vijayavenkataraman (vs89@nyu.edu)

Citation: Kanwar S, Vijayavenkataraman S. 3D-printed polycaprolactone-magnetic nanoparticles composite multifunctional scaffolds for bone tissue regeneration and hyperthermia treatment. *Int J Bioprint*. 2024;10(6):4538. doi: 10.36922/ijb.4538

Received: August 15, 2024
Revised: September 6, 2024
Accepted: September 18, 2024
Published Online: September 18, 2024

Copyright: © 2024 Author(s). This is an Open Access article distributed under the terms of the Creative Commons Attribution License, permitting distribution, and reproduction in any medium, provided the original work is properly cited.

Publisher's Note: AccScience Publishing remains neutral with regard to jurisdictional claims in published maps and institutional affiliations.

1. Introduction

Porous biocompatible scaffolds have long been used as an alternative to autografts or allografts to promote tissue regeneration.[1] Their performance is typically improved by

incorporating growth factors, which enhance cell viability but come at the cost of limited shelf-life.[2,3] In addition to tissue regeneration, these scaffolds also serve as delivery platforms for drugs and other therapeutic agents to treat diseases such as cancer via hypothermia treatment.[4] The 3D microenvironment provided by these scaffolds seeks to mimic the native tissue microenvironment, which subsequently facilitates cell proliferation and tissue in-growth and is ideal for localized delivery of drugs at the target site.[5]

One particular class of bioactive agents that has caught the attention of researchers and is increasingly being investigated is magnetic nanoparticles (MNPs). These particles can be placed in an alternating magnetic field (AMF) to promote hyperthermia treatment and aid bone regeneration.[6,7] Hence, MNPs provide an excellent basis for the creation of multi-functional scaffolds. While several different kinds of MNPs exist, such as iron oxide nanoparticles (IONPs), magnesioferrite nanoparticles, copper IONPs, manganese-based nanoparticles, and cobalt-based nanoparticles,[8,9] the vast majority of the research deals specifically with magnetic IONPs. This is due to the beneficial biological properties of iron oxide, such as its biocompatibility and low toxicity, in addition to the fact that it is the only metal-based nanoparticle cleared for clinical use by the United States (US) Food and Drug Administration (FDA).[10] While several researchers have utilized modified magnetic IONPs to achieve their goals, the base material remains iron oxide. Diaz et al.[11] doped their MNPs with nanohydroxyapatite to enhance osteoblast adhesion, proliferation, and differentiation. Cojocaru et al.[12] fabricated a novel magnetic scaffold by combining biopolymers, like chitosan and gelatin, with MNPs to enhance cell adhesion, migration, and osteoconductivity *in vivo*. Li et al.[13] used magnetic graphene oxide in composite polymeric scaffolds to exploit their thermal attributes for effective tumor treatment.[14] Despite their advantageous biological and mechanical properties, it is their magnetic attributes that have attracted the attention of researchers for use in drug delivery systems and non-invasive tumor management.[15] MNPs can possess diamagnetic, paramagnetic, and ferromagnetic properties depending on their susceptibility to the application of an AMF. When these nanoparticles are placed in an AMF, it creates a dipole moment, which is aligned in the direction of the field for paramagnetic particles and opposite to the field in the case of diamagnetic particles.[16] When the particle size of these nanoparticles is below 30 nm, they exhibit a superparamagnetic effect, which essentially allows each particle to possess its respective local magnetic field, driving interaction at the cell-scaffold interface.[17]

Other than their use in non-invasive cancer management, they are increasingly being employed for enhancing bone tissue regrowth. There is evidence to suggest that a magnetic field stimulus aids the bone tissue regeneration process as a result of its osteoinductive properties.[18,19] This works by using the magnetic field to activate specific cell receptors and corresponding signaling pathways, which increases overall cell activity and serves as a modulator for tissue regeneration in the body.[20–23] Magnetic field stimulation for tissue engineering can be utilized for both soft and hard tissues, including cartilage, muscle tissues, and bone tissues.[24] Paun et al.[25] observed that upon the application of a static magnetic field, mesenchymal stem cells (MSCs) proliferated and were influenced to differentiate into osteogenic-type cells. Jia et al.[26] demonstrated that mesoporous silica-coated MNPs (M-MSNs) enhance bone tissue regrowth in a rat model, suggesting their use for clinical purposes. They validated their findings through a series of tests, including imaging, histological, and immunohistochemical examination. Wu et al.[27] found that low doses of Fe_3O_4 nanoparticles, in conjunction with a magnetic field, led to osteogenesis enhancement induced by stem cell exosomes. Jasemi et al.[28] fabricated composite calcium and zirconium scaffolds with 5–15 wt% MNPs; they observed a positive correlation with respect to the scaffold modulus and the growth of an apatite layer on the scaffold. Zhao et al.[29] produced chitosan and collagen composite scaffolds, incorporated with nano-hydroxyapatite and Fe_3O_4 nanoparticles, and implanted them *in vivo* using a rat skull model. They found that these composite scaffolds displayed greater tissue compatibility and bone regrowth compared to the control set.

Despite the growing interest in MNPs, targeting them at the critically sized defect in the bone and/or using them as agents of drug delivery remains a challenge. Hence, 3D-printed platforms are utilized to better achieve these objectives. Zhang et al.[30] fabricated an additively manufactured composite scaffold made from bioactive glass, polycaprolactone (PCL), and MNPs. The PCL provided a biocompatible matrix and was also responsible for providing an adequate surface for cell adhesion and growth. The 3D-printed scaffold was found to satisfy the dual goal of sustained drug release and exhibiting greater osteogenic activity. Dankova et al.[31] used the electrospinning technique to create PCL and MNP nanofibrous scaffolds. These composite scaffolds were biocompatible and also supported MSC proliferation and osteogenic differentiation. De Santis et al.[32] 3D printed a PCL and iron-doped hydroxyapatite nanoparticle scaffold and tested them *in vitro* and *in vivo*. While the *in vitro* analysis reported enhanced cell growth, the *in vivo* rabbit model displayed excellent bone growth within just 4 weeks.

While all these studies proved the effectiveness of PCL and MNP scaffolds in bone tissue regrowth (i.e., due to their biocompatibility and the regulatory approval of MNPs from the FDA for clinical use), they still were limited in other ways. Apart from adequate cell viability and proliferation, the scaffolds failed to have sufficient mechanical strength that matches that of the native bone.[30] This study addressed this challenge by fabricating scaffolds with concentrations as high as 50% to explore the possibility of these additional MNPs seeping into the polymer matrix and increasing the mechanical strength closer to that of the trabecular bone.

In addition to boosting the mechanical strength to match the native bone, the incorporation of a higher amount of MNPs still maintains the cell viability of the scaffolds, thereby preserving their biocompatibility. Moreover, a greater amount of MNPs is directly correlated to increased heating capacity upon the application of a magnetic field; the scaffold would reach hyperthermic temperatures much earlier. Furthermore, the use of a PCL-MNP solution in an extrusion printhead allowed for the printing of relatively complex structures with high resolution compared to using a die-cast.[33] While several different additive manufacturing processes exist for fabricating these scaffolds, each with its own set of advantages and limitations, extrusion 3D printing allows us to achieve the desired shape with relative simplicity.[24,34]

Cancer management after tumor resection is characterized by two critical needs: (i) rehabilitation of the resected tissue and its reconstruction, and (ii) preventing the recurrence of tumors post-surgery by destroying any residual tumors. The state-of-the-art in literature is limited because it tackles these two major priorities individually: achieving tissue resection via autologous grafting and preventing tumor recurrence through chemotherapy. In this study, we 3D printed a custom PCL-MNP scaffold with MNP concentrations ranging from 0% to 50%, achieving our four primary objectives: (i) demonstrating the ease of 3D printing for patient-specific customization of the scaffold according to the critical size defect; (ii) providing adequate mechanical strength under physiological loads; (iii) aiding in bone tissue regeneration by enhancing hMSC functionality; and (iv) inducing cancer cell death due to the hyperthermia effect caused by the application of an external AMF.

2. Methods

2.1. Magnetic nanoparticle characterization

The chemical composition of the nanoparticles (Luoyang Tongrun Info Technology Co. Ltd., China) is $MgFe_2O_4$ as determined by X-ray diffraction (XRD) analysis (Empyrean 3; Malvern Panalytical Pvt. Ltd., United Kingdom [UK]). The sample was scanned at 10°–80° with a 0.05° step size. $MgFe_2O_4$ nanoparticles were found to be less susceptible to oxidation compared to Fe_3O_4; therefore, they are more effective as hyperthermia agents due to their large heating capacity.[35] The average particle size is 20 nm, as verified by transmission electron microscopy (TEM; Talos F200X; Thermo Fisher Scientific, USA). The stability of the MNP solution was determined using a Malvern zetasizer (Malvern Panalytical Pvt. Ltd., UK).

2.2. 3D printing

Briefly, 2 g of PCL pellets (molecular weight [Mw]: 80,000 kDa; Sigma-Aldrich, United States of America [USA]) were dissolved in 5 mL acetic acid solution to obtain a 40% (w/v) PCL solution, which was then ultrasonicated for 3 h to fully dissolve the pellets. Thereafter, MNPs were weighed using a balance and added to the solution at 2.5%, 5%, 7.5%, 10%, 30%, and 50% (w/v). The resulting solution was then ultrasonicated for 5 h until a uniform mixture of MNPs was obtained; if ultrasonication was not performed properly, the MNPs would coagulate. Once uniformly dissolved, the mixture was filled in a syringe and extruded using the extrusion printhead of the bioprinter (RegenHU 3D Discovery, Switzerland) with a nozzle of diameter 0.41 mm at a pressure of 0.06 MPa. The printed scaffolds had a grid-like structure with dimensions 2 × 2 cm.

2.3. Scaffold characterization

The 3D-printed scaffolds were imaged using scanning electron microscopy (SEM; Quanta™ 450 FEG, FEI company, USA) after sectioning the scaffolds and coating the cross-section with gold. The scaffolds were characterized using Fourier-transform infrared spectroscopy (FTIR; Invenio S; Bruker, USA) in a frequency range of 400–4500 cm^{-1} to determine the constituent chemical groups. Uniaxial tensile tests were carried out using an Instron machine (Universal Testing System-5960 series; Instron, USA), with a cross-head speed of 1 mm/min and a 5 kN load cell. The load versus displacement data obtained from the tensile test allowed us to determine the stress versus strain curve along with the modulus of the individual samples.

Thermal degradation properties were assessed using a thermal gravimetric analyzer (TGA; TG209 F1 Libra; Netzsch, Germany). The samples were heated from 25 to 500°C, with a 10°C/min step size. A differential scanning calorimeter (DSC; Q2000 V24; TA Instruments, USA) was used to evaluate samples in the range of –90 to 120°C, with a 10°C/min step size. After reaching 120°C, the samples are cooled at 10°C/min and heated again at the same rate.

Magnetic hysteresis loops were measured using a physical property measurement system (PPMS; DynaCool

9T, Quantum Design, USA) outfitted with a vibrating-sample magnetometer (VSM). The machine operated at a temperature of 310 K, with a magnetic field strength range of −15,000 to 15,000 Oe.

2.4. Temperature profile test

A Magnetherm (NanoTherics, United Kingdom [UK]) was used to measure the increase in temperature exhibited by the scaffold reinforced with MNPs. Pure PCL and PCL-MNP scaffolds (MNP concentration: 2.5–50%) were placed in a 2 mL vial. These vials were gently lowered into the Magnetherm, while a temperature probe measured the increase in temperature. The apparatus was set at 30 V (the maximum allowed by the system), and the increase in temperature over 15 min was measured.

2.5. *In vitro* analysis

2.5.1. Degradation test

All fabricated scaffolds, from pure PCL to PCL with 50% MNP concentration, were submerged in 5 mL of phosphate-buffered saline (PBS) at 37°C in glass vials. The scaffolds were taken out of the glass vials at every time point and then dried to remove any excess weight due to PBS on their surface. Once dried, the weight of the scaffolds was measured. They were then placed back in the glass vial, and a fresh supply of PBS was provided. The degradation was measured using the following formula:

$$\text{Wt\%} = \frac{(Final\ weight - Initial\ weight)}{Initial\ weight} \times 100 \qquad \text{(I)}$$

2.5.2. Cell viability assay

The Alamar Blue (AB) reagent (Invitrogen, USA) was utilized for determining the cell growth of the human mesenchymal stem cells (hMSCs) on PCL-MNP samples. By using the AB assay, we can quantitatively measure cell viability *in vitro*. The scaffolds were sterilized first by submerging them in ethanol for 1 h and subsequently washing them with PBS. The samples were then kept under ultraviolet (UV) irradiation for 1 h. The samples were placed in a 24-well plate, along with the respective 2D and 3D controls and blanks consisting of just media. The AB reagent was added at each time point and incubated for 4 h. Thereafter, 200 µL of the solution was collected into a 96-well plate from each well of the 24-well plate. A Biotek Synergy H1 microplate reader (Agilent, USA) was used to determine the absorbance at wavelengths of 570 and 600 nm. To minimize biological variability in the results, experiments were performed in triplicates.

The Live/Dead staining kit (Thermofisher Scientific, USA) was used to qualitatively determine the number of live and dead cells at a given time point. Cell culture media was drained out, and the scaffolds were submerged in 500 µL of staining media (calcein and ethidium homodimer) and incubated for 15 min. After incubation, the well plate containing the stained scaffolds was taken out, and the scaffolds were imaged under a microscope. Image analysis was carried out using ImageJ for cell viability using the equation:

$$Cell\ viability = \frac{Live\ cells}{Live\ cells + Dead\ cells} \times 100 \qquad \text{(II)}$$

2.5.3. Hyperthermia test

The hMSCs (immortalized human bone marrow mesenchymal stromal cells, hTERT iMSC3, Catalogue No. T0529; Applied Biological Materials Inc., Canada) and HOS bone cancer cells (Catalogue No. 300449; Cytion, Germany) were seeded on all concentrations of PCL-MNP samples, followed by incubation at 37°C for 24 h. Thereafter, AB reagent was supplied to these scaffolds, and the supernatant was collected after 4 h for performing the assay. The media in the vials with cell-laden scaffolds was replaced with fresh media. These glass vials were then placed in the Magnetherm (NanoTherics, UK) and subjected to an external magnetic field for 2 h each. The vials were taken out, supplied with AB reagent, and collected after 4 h of incubation. Finally, cell viability was measured for each scaffold using a Biotek Synergy H1 microplate reader (Agilent Technologies Inc., USA).

2.6. Statistical analysis

All experiments were performed in triplicates. To determine whether cell growth was statistically significant in the seeded scaffolds, a two-tailed t-test was utilized. Results with $p < 0.05$ were determined to be statistically significant. Data are presented as mean ± standard deviation. For cell viability percentage calculated from Live/Dead images, one-tailed student t-test was used and $p<0.1$ was determined to be statistically significant."

3. Results

3.1. Characterization of magnetic nanoparticles

The average particle size of the MNPs was determined by TEM. Figure 1A and B presents the TEM images of magnesioferrite nanoparticles at 100 and 50 nm magnifications, respectively. The average particle size was determined to be approximately 20 nm (Figure 1C). In addition to the particle size, the MNPs were also characterized using XRD (Figure 1D) and FTIR

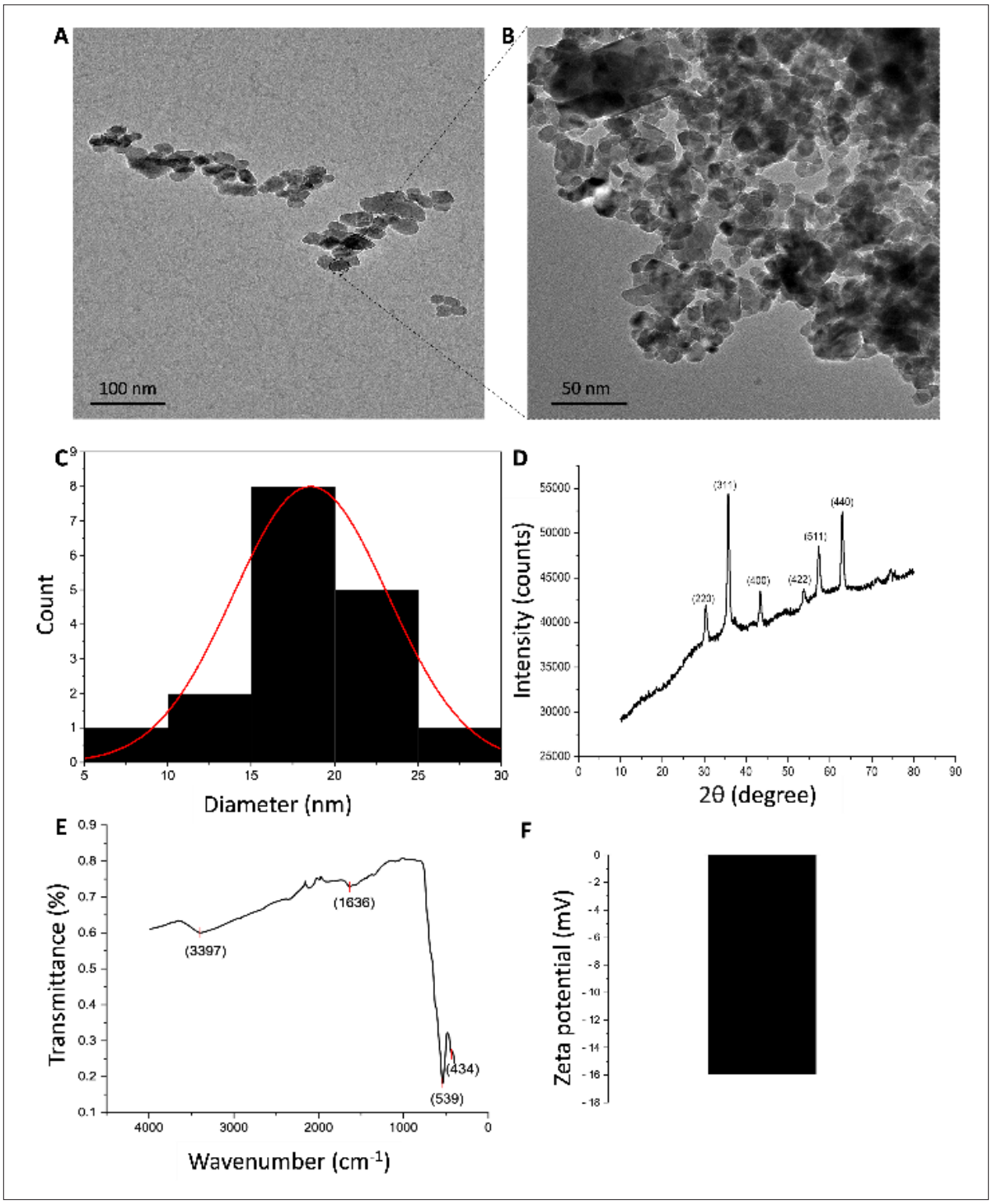

Figure 1. Characterization of magnetic nanoparticles (MNPs). (A and B) Transmission electron microscopy (TEM) image of MNPs taken at a magnification of 100 nm (A) and 50 nm (B), respectively. (C) Average particle diameter of the MNPs. (D) X-ray diffraction (XRD) peaks corresponding to the chemical compound magnesioferrite. (E) Fourier-transform infrared (FTIR) spectra of the MNP powder. (F) Zeta potential of MNPs. Scale bars: 100 nm (A); 50 nm (B).

(Figure 1E). The XRD analysis allowed us to determine the concentration of different elements in the sample. Figure 1D displays peaks at 2Θ = 31, 36, 43, 54, 57, and 63. XRD analysis was conducted through the Execute Search and Match tool, and a match with magnesioferrite was observed. The FTIR spectra in Figure 1E revealed the chemical bonds in the MNPs. A sharp peak was observed around 540 cm^{-1}, indicative of the Fe-O bond in the materials, thus pointing towards iron oxide nanoparticles. Figure 1F displays the zeta potential of MNPs in the suspension. The zeta potential determines the suspension stability. Nanoparticles with a zeta potential in the range of −30 to +30 mV display great potential for agglomeration; therefore, they are characterized as having low stability. Particle stability is directly proportional to their charge. At a zeta potential higher than +30 mV or lower than −30 mV, good stability is achieved, signified by a lack of agglomerates. The MNP suspension that was tested exhibited an average zeta potential of −15.9 mV.

3.2. Characterization of 3D-printed PCL-MNP scaffolds

Once the MNPs were characterized, scaffold preparation was carried out. A 40% (w/v) solution of PCL was used as the base material. To this solution, 0–2.5 g MNPs were added to obtain 0–50% (w/v) PCL-MNP solutions (0%, 2.5%, 5%, 10%, 20%, 30%, and 50%). The printing process is represented in Figure 2A. It can be observed from the printed scaffold that the extrusion 3D printing process was successful in fabricating a scaffold of desired dimensions (2 × 2 cm), comprising a uniform mixture of PCL and MNPs, with high resolution and relative ease. From Figure 2B, we observe that pure PCL is unaffected when an external magnet is applied, while the scaffold with MNPs is attracted to it, validating the magnetic characteristic of the MNP scaffold.

Three representative PCL-MNP scaffolds and their scanning electron microscopy (SEM) images are displayed in Figure 2C–E. The SEM images were obtained at resolutions of 100 and 500 µm after cutting the scaffolds and coating the cross-section with gold. While the pure PCL scaffold cross-section has relatively larger pores, the 10% and 50% scaffolds displayed a more filled internal structure due to the magnesioferrite nanoparticles settling within the polymer matrix. The scaffolds with MNPs were

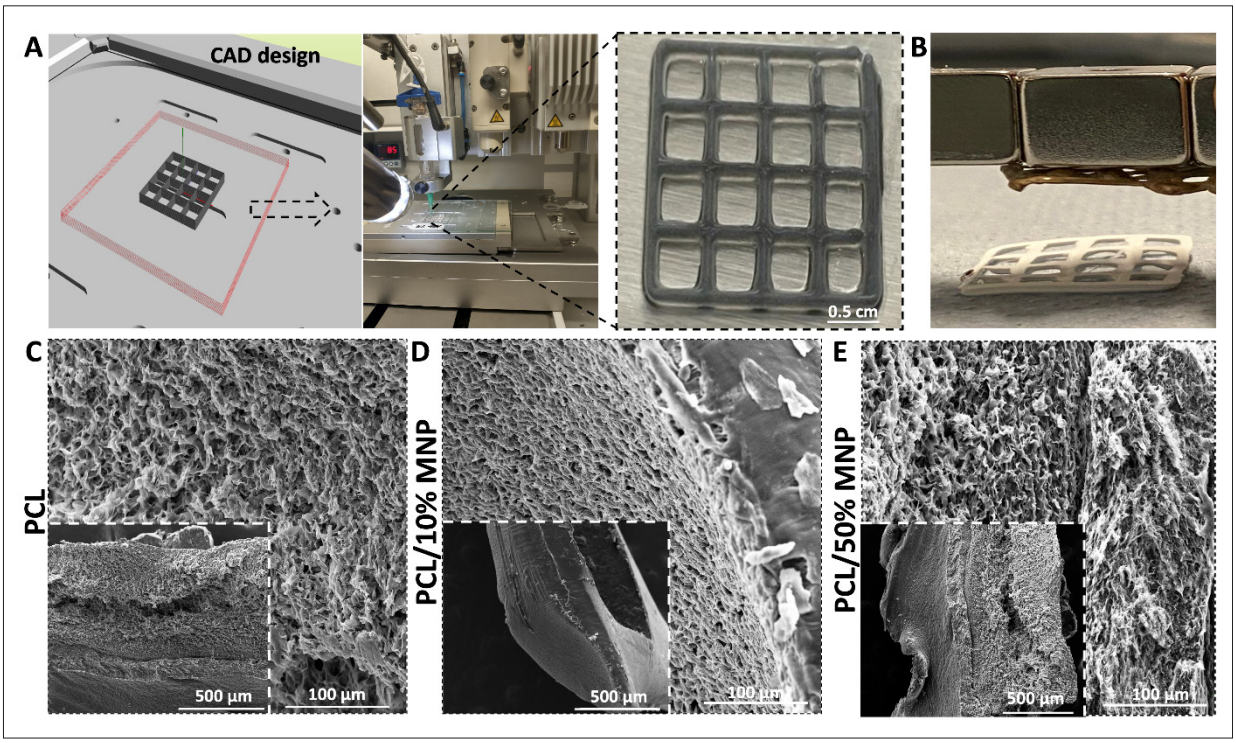

Figure 2. Extrusion 3D printing of PCL and PCL-MNP scaffolds. (A) Printing process of PCL-MNP scaffolds using the RegenHU bioprinter. **(B)** Effect of magnet on pure PCL and PCL-MNP scaffolds. (C–E) Scanning electron microscopy (SEM) images of three representative scaffolds: pure PCL (C), PCL with 10% MNP (D), and PCL with 50% MNP (E). Scale bars: 0.5 cm (A); 100 µm (C–E); 500 µm (C–E, inset). Abbreviations: CAD, computer-aided design; MNP, magnetic nanoparticle; PCL, polycaprolactone.

printed after a long ultrasonication cycle to prevent MNP agglomeration.

The thermal characteristics of PCL-MNP scaffolds were examined using the TGA and DSC tests. The DSC graph (Figure 3A) displays an endothermal peak at around 60°C, consistent with the melting temperature of PCL.[36] The pure PCL scaffold started deteriorating the earliest since its heating capacity was the lowest. The melting point did not significantly vary upon the incorporation of MNPs, indicating that the presence of MNPs does not significantly change the thermal degradation of the scaffolds.

The decomposition temperature of the PCL-MNP composite scaffolds was obtained through TGA (Figure 3B). As observed, the scaffold without MNPs started degrading last since it had the lowest heating capacity, whereas the other scaffolds, with higher heating capacities due to the presence of MNPs, started degrading earlier. Furthermore, degradation time is inversely proportional to MNP concentration in the scaffolds, with the 50% MNP scaffolds taking the least time to start degrading. This phenomenon is in line with results found in the literature.[37] The difference is notable as the scaffold with 50% MNP started degrading at around 300°C, whereas the pure PCL scaffold started degrading at 400°C. The temperature range over which weight loss occurs is roughly 300–450°C. From Figure 3B, we can glean information about the degradation time of the scaffolds and their residual weights. All samples have a residual weight approximately corresponding to the MNP concentration in the scaffold. While the pure PCL scaffold degrades completely by the time it reaches 500°C, the residual weight of the other samples at 500°C is 1.57%, 4.09%, 6.47%, 9.09%, 23.164%, and 36.69%, respectively, in ascending order of MNP concentration.

Tensile tests were carried out on all scaffolds with different concentrations of MNPs. Figure 3C features the representative stress–strain curves, clearly ascertaining the fact that the modulus of the scaffolds with MNPs is generally higher than pure PCL, which has the lowest modulus of all the scaffolds. Figure 3D displays the tensile modulus of PCL and PCL-MNP scaffolds. The average modulus for the pure PCL scaffold is 26.88 ± 9.02 MPa, while the modulus for that of PCL with 50% MNP is 229.06 ± 37.05 MPa. The modulus of the remaining scaffolds follows the expected trend, exhibiting an increase with increasing MNP concentrations. The only exception is the scaffold with 30% MNP, which has a modulus similar to the scaffold with 10% MNP. This is because, despite the entire scaffold having a 30% MNP concentration, the non-uniform distribution of nanoparticles leads to variations in the expected modulus. The degradation test results are presented in Figure 3E. The fabricated scaffolds exhibited good stability even after 20 days. PCL is known to be relatively resistant to degradation over such short time scales.[38] The sharp drop over the 20-day period is caused by sections of the main scaffold breaking off, which has more to do with the fabricated scaffold itself than any degradation.

The fabricated PCL-MNP scaffolds were analyzed using FTIR to identify the peaks corresponding to their constituent chemical structures (Figure 3F). Prominent vibrational peaks are observed around 2900 and 1720 cm^{-1}, corresponding to the C–H and C–O bonds, respectively. Fe–O bond vibration is observed at around 580 cm^{-1} and behaves in a directly proportional manner to the increasing MNP concentration.

3.3. *In vitro* analysis

The PCL-MNP composite scaffolds were seeded with hMSCs (1.5×10^4 cells/well). The viability of hMSCs on PCL-MNP composite scaffolds was examined via the AB colorimetric assay. Cell growth was evaluated qualitatively, as displayed in Figure 4A via live/dead imaging. Representative images of two different concentrations of PCL-MNP scaffolds (10% and 50% [w/v]), pure PCL, and 2D controls are featured. Similarly, quantitative analysis of cell growth (Figure 4C) revealed that all scaffolds exhibited statistically significant cell proliferation over 7 days. The calculated cell viabilities presented in Figure 4B were ≥90% for all samples on day 7. There was no significant difference between the cell viability of the 10% and 50% scaffold compared to pure PCL at either day 1 or 7. While Figure 4B is indicative of the cell viability for the portion of the scaffold under focus during the live/dead test, AB analysis of the overall cell viability suggests the suitability of the various scaffolds for cell proliferation.

3.4. Magnetization properties of PCL-MNP scaffolds and hyperthermia application

The magnetic properties of the PCL-MNP scaffolds were examined using a VSM, which provided the hysteresis curve for the PCL-MNP scaffolds (Figure 5C). In Figure 5C, it is observed that when the samples were placed in a magnetic field between −15,000 and +15,000 Oe, scaffolds without MNPs displayed no response to the magnet, while scaffolds with concentrations of 2.5–50% MNPs resulted in a hysteresis loop, thus validating their magnetic behavior. The magnetization observed under the test conditions of the VSM increased with the concentration of MNPs in the scaffolds. This proportional increase in magnetization values with MNP concentration is consistent with other results found in the literature.[39] The saturation magnetization increased from about 0.68 emu/g in scaffolds with 2.5% MNPs to about 16.87 emu/g in scaffolds with 50% MNPs.

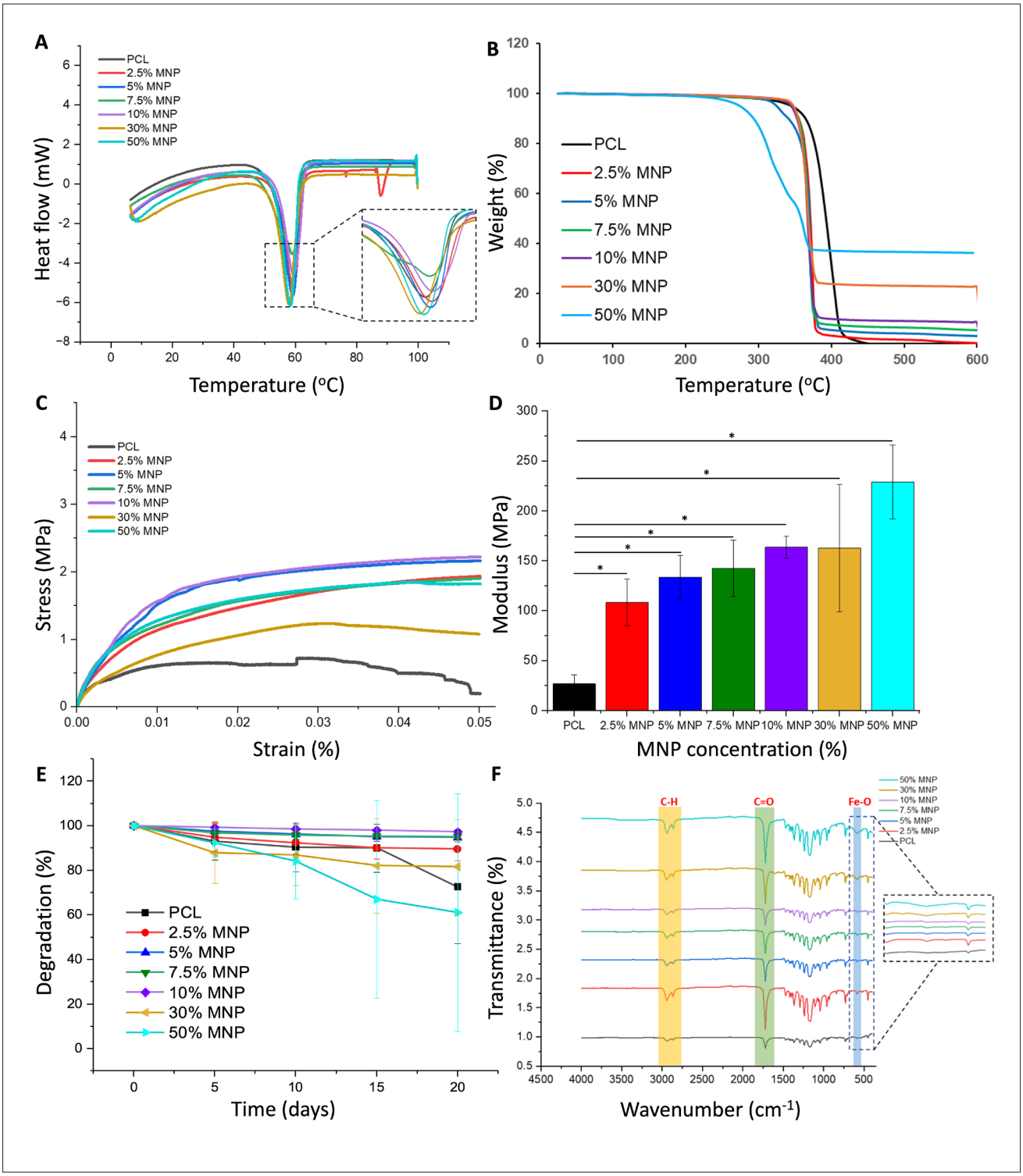

Figure 3. Characterization of 3D-printed PCL and PCL-MNP scaffolds. (A) Differential scanning calorimetric (DSC) curves. (B) Thermograms obtained from thermal gravimetric analysis (TGA). (C) Representative stress versus strain curves. (D) Young's modulus. (E) Degradation test. (F) Fourier-transform infrared (FTIR) spectra of each fabricated scaffold. *$p < 0.05$; $n = 3$. Abbreviations: MNP, magnetic nanoparticles; PCL, polycaprolactone.

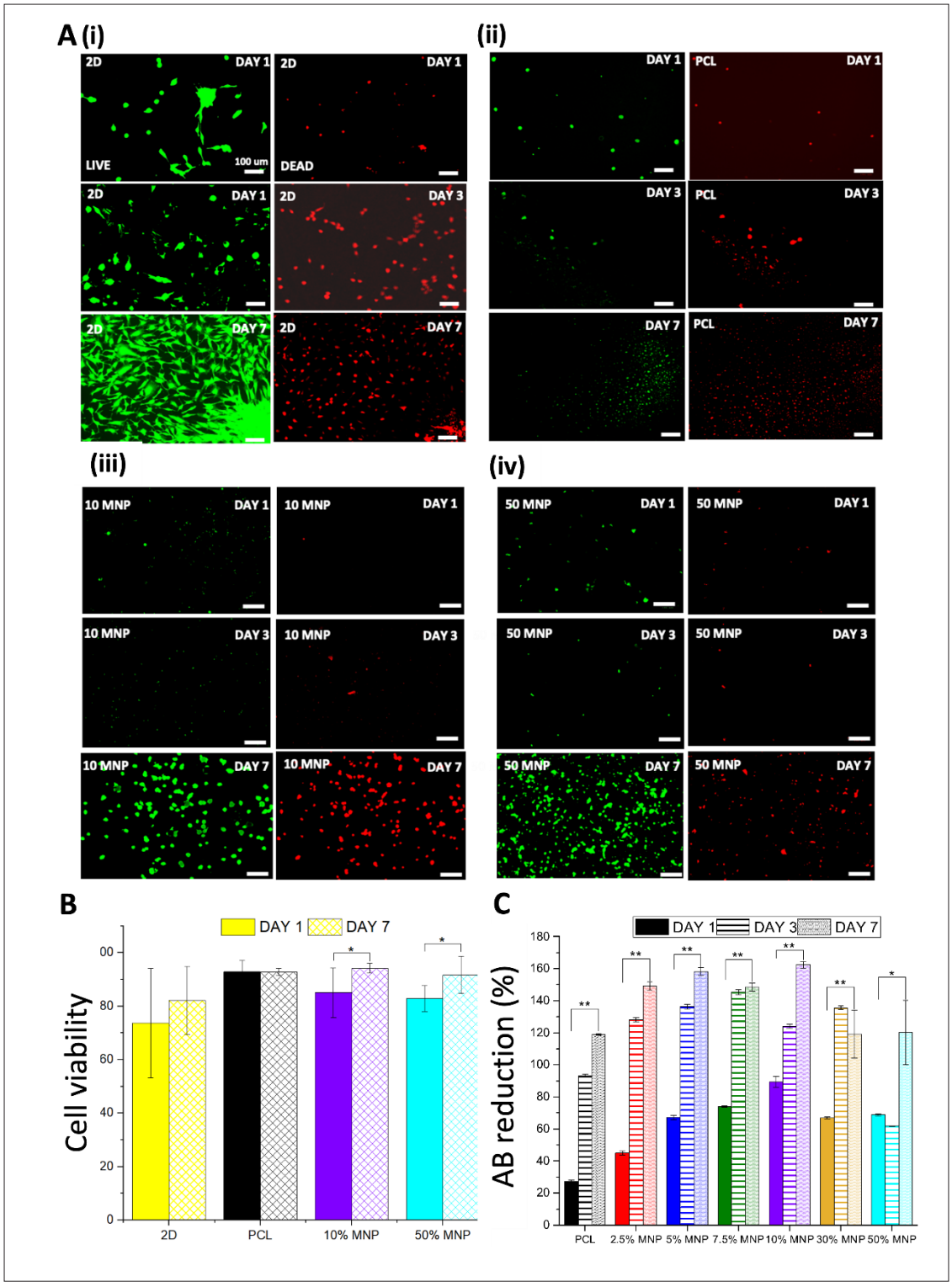

Figure 4. Cytocompatibility studies of PCL and PCL-MNP scaffolds. (A) Live (green)/dead (red) images at days 1, 3, and 7 for 2D cell culture (A, i), pure PCL scaffold (A, ii), PCL with 10% MNP scaffold (A, iii), and PCL with 50% MNP scaffold (A, iv). Scale bars: 100 µm. (B) Average cell viability calculated by analyzing the live/dead images using ImageJ software. (C) Results of cell viability assay using Alamar Blue, displaying statistically significant growth in cells over 7 days. *$p < 0.1$, **$p < 0.05$; $n = 3$. Abbreviations:; AB, Alamar Blue; MNP, magnetic nanoparticle; PCL, polycaprolactone.

When developing our PCL-MNP scaffolds, we aimed to (i) fabricate a biocompatible scaffold that aids in bone tissue regeneration by providing the necessary mechanical support under physiological load and activating the correct signaling pathways, and (ii) target cancerous tumors via hyperthermia treatment. The hyperthermia capability of the scaffolds is evaluated by measuring the temperature rise when placed in an AMF (Figure 5A). Figure 5B presents the temperature versus time graph for all MNP concentrations in the PCL-MNP scaffolds. The peak temperature increases with increasing concentration of MNPs. For scaffolds with 50% MNPs, the average peak temperature reached was more than 46°C.

For the scaffold with 50% MNPs, the temperature stabilized around 46°C, which is higher than the hypothermia threshold temperature required; hence, the scaffold with 50% MNPs was used for subsequent hyperthermia experiments. Pure PCL and PCL with 50% MNP scaffolds were seeded with hMSCs and bone cancer cells in respective glass vials. These scaffolds were then cultured for 24 h in an incubator at 37°C. After 24 h, the cell viability of the scaffolds was measured. After the supernatant was collected in a 96-well plate and fresh media replaced, the scaffolds were then placed in an AMF for 2 h each, as depicted in the schematic in Figure 6A. After 2 h, these glass vials were taken out and supplied with AB to identify changes in viability after subjecting the seeded scaffolds to an AMF. From Figure 6B, a statistically significant decrease is observed in the proliferation of cancer cells after 2 h, indicating that the increase in temperature caused by the 50% MNP scaffold helped kill the cancer cells. Conversely, the hMSCs exhibited increased proliferation for the 50% MNP scaffold.

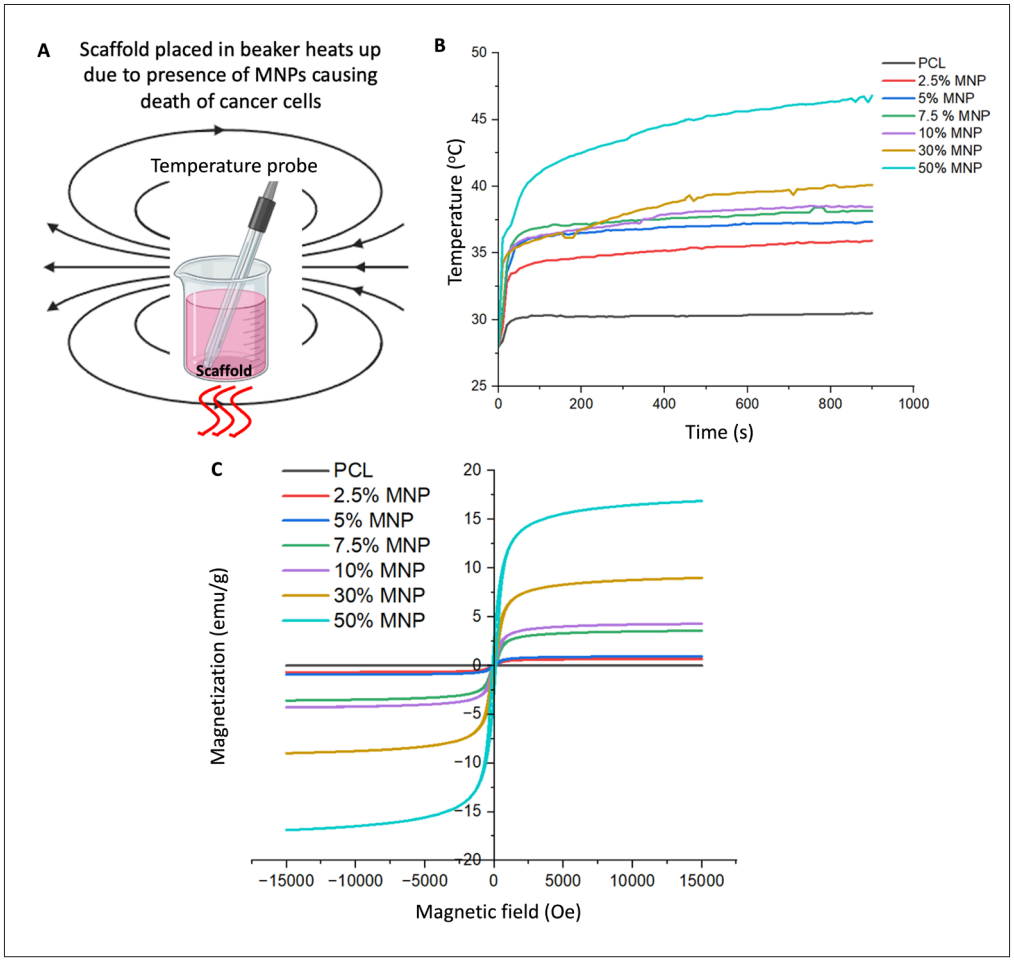

Figure 5. Magnetization and hyperthermic measurements of PCL and PCL-MNP scaffolds. (A) Schematic of the process of a scaffold being placed in an alternating magnetic field, while the temperature is measured using a probe. (B) Temperature versus time graph. (C) Magnetization curves. Abbreviations: MNP, magnetic nanoparticle; PCL, polycaprolactone.

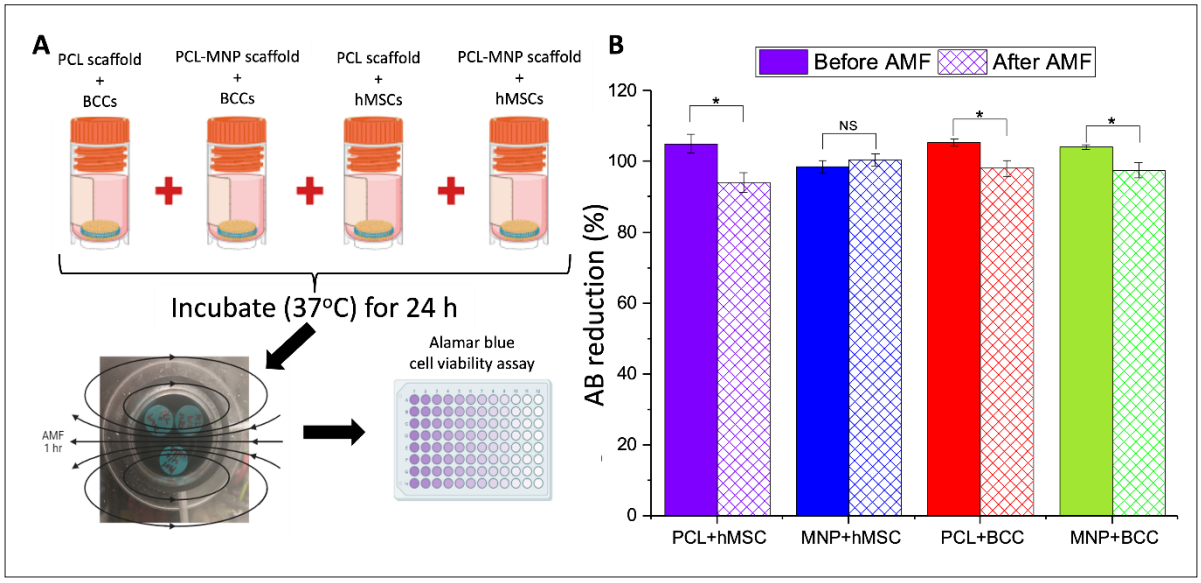

Figure 6. Cell-laden scaffolds in AMF. (A) Schematic of seeding human mesenchymal stem cells (hMSCs) and bone cancer cells (BCCs) in pure polycaprolactone (PCL) and PCL with 50% magnetic nanoparticles (MNPs) scaffolds placed in an alternating magnetic field (AMF). (B) Alamar Blue analysis of hMSCs and BCCs after being placed in an AMF. *$p < 0.05$. Abbreviation: NS, non-significant.

4. Discussion

The dual needs of cancer management necessitate the fabrication of a material that will not only aid bone regeneration and provide adequate mechanical support *in vivo* but also target tumors and kill them via hyperthermia treatment and prevent their recurrence. This study investigates the possibility of using a composite polymeric scaffold, made by combining biocompatible PCL with magnesioferrite nanoparticles. Earlier studies have indicated that the PCL and IONP scaffolds support cell adhesion and proliferation and are thus biocompatible; the incorporation of IONPs in the polymer matrix also enhances the mechanical and wettability characteristics of the scaffold.[40,41] However, even after the substantial improvement in mechanical characteristics achieved by using the IONPs, their mechanical strength falls short of that possessed by the native bone,[30] limiting their use as bone scaffold implants.

In order to overcome these challenges and to make the scaffold more suitable for cancer management, this study focuses on replacing the typically used IONPs with magnesioferrite nanoparticles. In comparison to IONPs, these particles are less susceptible to oxidation and display a greater heating capacity, which makes them more attractive alternatives for hyperthermia treatment.[42] While other studies only fabricated scaffolds with MNP concentrations of less than 15%,[17,30] this study enhanced the mechanical strength of the scaffold by using MNP concentrations as high as 50%. The scaffolds fabricated with 50% MNPs helped achieve strength close to the native trabecular bone, with a modulus of 229.06 ± 37.05 MPa, while still maintaining their biocompatibility.

The critically sized defect of the bone is often irregularly shaped. In such cases, being able to fabricate a high-resolution, customizable, and patient-specific 3D implant is important for overcoming this barrier.[40] The design features of the critically sized defect can typically be extracted using CT scans, and 3D printing can then be used to mimic a patient-customized bone scaffold.[41] Figure 2 demonstrates the extrusion 3D printing process to fabricate a composite scaffold of desired dimensions and pore size. While the pores of the grid-like structures printed were about 5 × 5 mm, they only serve as a proof-of-concept. The extrusion process using a RegenHU 3D printer enabled us to print scaffolds with smaller pore diameters as well. In addition to achieving the desired pore size, our composite samples revealed that the pores were quite interconnected, which is a necessary condition for bone tissue regeneration.[43] Furthermore, while the extrusion 3D printing process is indeed relatively easy to use and implement, it is still limited by its inability to form highly complex structural configurations.[44,45] Other additive manufacturing processes, such as fused deposition modeling (FDM), can be explored in the future with PCL-MNP composite filaments.

For successful bone tissue regrowth and overall scaffold success, the scaffold must possess certain desirable properties. The printed PCL-MNP composite scaffolds were validated using a series of thermal, magnetic, and mechanical tests to benchmark their performance against existing scaffolds. Firstly, the chemical composition of the scaffold is evaluated using FTIR. The peaks on the spectrum are within the expected range and accurately depict the C–H bond vibration.[42] However, the presence of magnesioferrite MNPs is validated through the Fe–O bond vibration. As the concentration of the MNPs increases, so does the peak sharpness.[33] The magnetization curves also reflect the concentration of MNPs present in the scaffold. With an increase in the MNP concentration, the hysteresis curve of magnetization increases under the application of an external magnetic field. The magnetization property of the scaffold is important because it determines the ability of the scaffolds to efficiently target cancer tumors and prevent their recurrence. In contrast to isolated cancer therapies, the side effects are decreased when tumors are properly targeted. Thermal analysis in the form of TGA and DSC enables us to determine the condition of the scaffold implant under hyperthermia temperatures. Since the DSC of the scaffolds reports that the melting point of PCL is above 50°C, it confirms that the PCL-based scaffolds are suitable for hyperthermia treatment. As the temperature increases, the thermogram displays a sharp decrease above a certain temperature until a saturation point is reached. Since the PCL chains present in the scaffold degrade into components like CO and CO_2, the remaining weight at saturation is entirely due to the presence of residual MNPs. These MNPs, while ideally directly proportional to MNP concentration in the scaffold, sometimes display anomalous results due to uneven distribution of the nanoparticles in the scaffold matrix. Finally, the scaffold matrix was reinforced with an MNP concentration as high as 50%, which is a step up from other works in the literature that typically fabricated scaffolds with an MNP concentration of less than 15%.

While the success of the composite scaffold is dependent upon its thermal, magnetic, and mechanical properties, ultimately it needs to be suitable for biological applications. In order to evaluate the cell viability of these scaffolds, they were seeded with hMSCs, and their growth was observed using AB cell viability analysis. The analysis revealed statistically significant cell proliferation observed for all concentrations of the scaffolds. This is in concordance with other results in the literature that report MNPs imparting superior cell proliferation and differentiation characteristics to the scaffolds.[46] While the 50% MNP scaffolds had less viability in comparison to the 10% MNP scaffolds, the results were still satisfactory for biological applications. Moreover, these scaffolds were tested for their ability in cancer management via hyperthermia treatment. Indeed, one of the key needs for postoperative tumor resection is to prevent tumor recurrence by eliminating any residual tumor cells. This has led to a demand for a minimally invasive and targeted implant that can keep the tumors at bay by killing them *in vivo* upon the application of an AMF. Figure 6B features the AB cell viability results for scaffolds seeded with hMSCs and bone cancer cells at two different time points, i.e., before applying the AMF and after applying the external magnetic field. The temperature increase in the 50% MNP scaffold due to the magnetic field stimulus led to a statistically significant decrease in the viability of bone cancer cells. Furthermore, even the pure PCL scaffold demonstrated a decrease in cancer cell proliferation, which can be attributed to the heat conduction between the adjacent vials, leading to a lack of perfect insulation. These results are in line with the existing literature.[47]

Prevention of recurring tumors is a challenging problem. Thus, using MNPs that are uniformly dispersed throughout the polymer matrix led to a more uniform heating effect under an AMF. This leads to a more effective hyperthermia effect, as uniform heating requires a lower hyperthermia temperature and reduces the significance of scaffold orientation compared to scaffolds with a non-uniform distribution of heating elements.[47] While the heating effect is proportional to the strength of the magnetic field,[48] it is also affected by the size and shape of the MNPs.[49] Numerous *in vitro* and *in vivo* tests have displayed cell death between 41 and 47°C.[50,51] High fever is known to reach temperatures similar to mild hyperthermia, but the difference is that hyperthermia locally targets the tumor without affecting the surrounding cells and tissues, while high fever triggers the body's immune response and ends up protecting the tumor along with the rest of the body.[52] Thus, PCL scaffolds reinforced with 50% MNPs display a temperature rise above 41°C under the magnetic field stimulus, which is ideal for hyperthermia, as the temperature facilitates cell death, but remains below the melting point of PCL.[53] Furthermore, these advantageous properties, coupled with the degradation rates of the PCL-MNP scaffolds, allow for multiple instances of hyperthermia treatment.

While this work is a promising indicator in the fabrication of multi-functional scaffolds, it still has some limitations. MNPs tend to agglomerate, making it difficult to achieve a uniform mixture in the solution. This lack of uniformity can lead to wide variations in the results, resulting in high standard deviations. Lack of insulation in

the Magnetherm can cause undue heating, even in the glass vial with the pure PCL scaffold, negatively affecting bone cancer cells. The multi-functional PCL-MNP composite scaffolds still require a significant amount of fine-tuning to consistently achieve the necessary properties. While the results of this study are positive, the efficacy of the PCL-MNP composite scaffolds in achieving its objectives can be further strengthened by testing their suitability for stem cell differentiation and residual cancer cell death in animal models in future studies.

5. Conclusion

In this work, we have examined the suitability of 3D-printed PCL-MNP composite scaffolds in fulfilling both objectives of cancer management, i.e., resected tissue restoration and tumor recurrence prevention, thus displaying their prospect. The multi-functional scaffolds were evaluated for their magnetic, thermal, and mechanical properties, as well as their biocompatibility. The mechanical strength and saturation magnetization of the scaffolds increased with increasing MNP concentration, indicating enhanced performance compared to pure PCL scaffolds. All scaffolds were then tested for their biological viability and exhibited statistically significant cell growth with increased cell proliferation commensurate with the concentration of MNPs. This indicates that the PCL-MNP scaffolds are suitable for bone TE. While all scaffolds were suitable for cell proliferation, only the scaffold with 50% MNP displayed temperatures necessary for hyperthermia treatment when placed under an AMF. When the PCL-50% MNP scaffolds were subjected to an external magnetic field, a significant decrease in cancerous cells was observed after 2 h. In conclusion, this work demonstrates the fabrication of multi-functional bone scaffolds that satisfied four objectives: (i) patient-specific customization through 3D printing, (ii) augmented mechanical strength matching that of the native bone, (iii) enhanced stem cell proliferation, and (iv) cancer cell necrosis under an external magnetic field.

Acknowledgments

This research was partially carried out using the Core Technology Platforms (CTP) resources at New York University Abu Dhabi (NYUAD). The authors would like to thank Dr. Qiang Zhang (CTP, NYUAD) for his help with the PPMS machine; Dr. Yao He (CTP, NYUAD) for his help with TGA; Dr. James Weston (CTP, NYAD) for his help with XRD; as well as Sharon Lee and the Trabolsi Lab (NYUAD) for their help with using the Magnetherm. The authors would also like to extend their heartiest appreciation to Dr. Gopinathan and Dr. Kamil for their support.

Funding

Sanjairaj Vijayavenkataraman was supported by the start-up funds from NYUAD. Susheem Kanwar acknowledges the NYUAD Global PhD Fellowship received to pursue his graduate education.

Conflict of interest

Sanjairaj Vijayavenkataraman serves as the Editorial Board Member of the journal but was not in any way involved in the editorial and peer-review process conducted for this paper, directly or indirectly. Susheem Kanwar declares no known competing financial interests or conflicts of interest.

Author contribution

Conceptualization: Susheem Kanwar, Sanjairaj Vijayavenkataraman
Data curation: Susheem Kanwar
Formal analysis: Susheem Kanwar
Funding acquisition: Sanjairaj Vijayavenkataraman
Investigation: Susheem Kanwar
Methodology: Susheem Kanwar, Sanjairaj Vijayavenkataraman
Project administration: Sanjairaj Vijayavenkataraman
Resources: Sanjairaj Vijayavenkataraman
Software: Susheem Kanwar
Supervision: Sanjairaj Vijayavenkataraman
Validation: Susheem Kanwar, Sanjairaj Vijayavenkataraman
Visualization: Susheem Kanwar, Sanjairaj Vijayavenkataraman
Writing – original draft: Susheem Kanwar
Writing – review & editing: Sanjairaj Vijayavenkataraman

Ethics approval and consent to participate

Not applicable

Consent for publication

Not applicable

Data availability

The authors confirm that all data supporting the findings of this study are available within the article.

References

1. Kanwar S, Al-Ketan O, Vijayavenkataraman S. A novel method to design biomimetic, 3D printable stochastic scaffolds with controlled porosity for bone tissue engineering. *Mater Design*. 2022;220:110857. doi: 10.1016/j.matdes.2022.110857
2. Liu JMH, Zhang J, Zhang X, et al. Transforming growth factor-beta 1 delivery from microporous scaffolds decreases

inflammation post-implant and enhances function of transplanted islets. *Biomaterials*. 2016;80:11-19. doi: 10.1016/j.biomaterials.2015.11.065

3. Llopis-Hernández V, Cantini M, González-García C, et al. Material-driven fibronectin assembly for high-efficiency presentation of growth factors. *Sci Adv*. 2016;2(8):e1600188. doi: 10.1126/sciadv.1600188

4. Wan T, Stylios GK, Giannoudi M, Giannoudis PV. Investigating a new drug delivery nano composite membrane system based on PVA/PCL and PVA/HA(PEG) for the controlled release of biopharmaceuticals for bone infections. *Injury*. 2015;46:S39-S43. doi: 10.1016/s0020-1383(15)30053-x

5. Chocholata P, Kulda V, Babuska V. Fabrication of scaffolds for bone-tissue regeneration. *Materials*. 2019;12(4):568. doi: 10.3390/jfb14070343

6. Dong S, Chen Y, Yu L, Lin K, Wang X. Magnetic hyperthermia–synergistic H2O2 self-sufficient catalytic suppression of osteosarcoma with enhanced bone-regeneration bioactivity by 3D-printing composite scaffolds. *Adv Funct Mater*. 2020;30(4):1907071. doi: 10.1002/adfm.201907071

7. Gu J, Liu X, Cui P, Yi X. Multifunctional bioactive glasses with spontaneous degradation for simultaneous osteosarcoma therapy and bone regeneration. *Biomater Adv*. 2023;154:213626. doi: 10.1016/j.bioadv.2023.213626

8. Kiumarsi N, Najmoddin N. Systematically engineered GO with magnetic CuFe2O4 to enhance bone regeneration on 3D printed PCL scaffold. *Surf Interf*. 2023;39:102973. doi: 10.1016/j.surfin.2023.102973

9. Giustini AJ, Petryk AA, Cassim SM, Tate JA, Baker I, Hoopes PJ. Magnetic nanoparticle hyperthermia in cancer treatment. *Nano Life*. 2010;1(1n02):10.1142/S1793984410000067. doi: 10.1142/S1793984410000067

10. Sadeghzadeh H, Dianat-Moghadam H, Del Bakhshayesh AR, Mohammadnejad D, Mehdipour A. A review on the effect of nanocomposite scaffolds reinforced with magnetic nanoparticles in osteogenesis and healing of bone injuries. *Stem Cell Res Ther*. 2023;14(1):194. doi: 10.1186/s13287-023-03426-0

11. Díaz E, Valle MB, Barandiarán JM. Magnetic composite scaffolds of polycaprolactone/nFeHA, for bone-tissue engineering. *Int J Polym Mater Polym Biomater*. 2016;65(12):593-600. doi: 10.1080/00914037.2016.1149848

12. Cojocaru FD, Balan V, Popa MI, et al. Biopolymers - calcium phosphates composites with inclusions of magnetic nanoparticles for bone tissue engineering. *Int J Biol Macromol*. 2019;125:612-620. doi: 10.1016/j.ijbiomac.2018.12.083

13. Li Y, Huang L, Tai G, et al. Graphene oxide-loaded magnetic nanoparticles within 3D hydrogel form high-performance scaffolds for bone regeneration and tumour treatment. *Compos A: Appl Sci Manuf*. 2022;152:106672. doi: 10.1016/j.compositesa.2021.106672

14. Zhang Y, Zhang Y, Yang Z, et al. Cytotoxicity effect of iron oxide (Fe3O4)/graphene oxide (GO) nanosheets in cultured HBE cells. *Front Chem*. 2022;10:888033. doi: 10.3389/fchem.2022.888033

15. Ali A, Shah T, Ullah R, et al. Review on recent progress in magnetic nanoparticles: synthesis, characterization, and diverse applications. *Front Chem*. 2021;9:629054. doi: 10.3389/fchem.2021.629054

16. Obisesan OS, Ajiboye TO, Mhlanga SD, Mufhandu HT. Biomedical applications of biodegradable polycaprolactone-functionalized magnetic iron oxides nanoparticles and their polymer nanocomposites. *Colloids Surf B Biointerfaces*. 2023;227:113342. doi: 10.1016/j.colsurfb.2023.113342

17. Shuai C, Yang W, He C, et al. A magnetic micro-environment in scaffolds for stimulating bone regeneration. *Mater Design*. 2020;185:108275. doi: 10.1016/j.matdes.2019.108275

18. Ortolani A, Bianchi M, Mosca M, et al. The prospective opportunities offered by magnetic scaffolds for bone tissue engineering: a review. *Joints*. 2017;4(4):228-235. doi: 10.11138/jts/2016.4.4.228

19. Gujjalapudi M, Anam C, Mamidi P, Chiluka R, Kumar AG, Bibinagar R. Effect of magnetic field on bone healing around endosseous implants - an in-vivo study. *J Clin Diagn Res*. 2016;10(10):ZF01-ZF4. doi: 10.7860/JCDR/2016/21509.8666

20. Zhu Y, Yang Q, Yang M, et al. Protein corona of magnetic hydroxyapatite scaffold improves cell proliferation via activation of mitogen-activated protein kinase signaling pathway. *ACS Nano*. 2017;11(4):3690-3704. doi: 10.1021/acsnano.6b08193

21. Wójcik-Piotrowicz K, Kaszuba-Zwoińska J, Rokita E, Thor P. Cell viability modulation through changes of Ca(2+)-dependent signalling pathways. *Prog Biophys Mol Biol*. 2016;121(1):45-53. doi: 10.1016/j.pbiomolbio.2016.01.004

22. Wang Q, Chen B, Cao M, et al. Response of MAPK pathway to iron oxide nanoparticles in vitro treatment promotes osteogenic differentiation of hBMSCs. *Biomaterials*. 2016;86:11-20. doi: 10.1016/j.biomaterials.2016.02.004

23. Hu S, Zhou Y, Zhao Y, et al. Enhanced bone regeneration and visual monitoring via superparamagnetic iron oxide nanoparticle scaffold in rats. *J Tissue Eng Regen Med*. 2018;12(4):e2085-e98. doi: 10.1002/term.2641

24. Duarte A, Paola S-A, João CS, Frederico CF. 3D (bio)printing of magnetic hydrogels: formulation and applications in tissue engineering. *Int J Bioprinting*. 2024;10(1):0965.

doi: 10.36922/ijb.0965

25. Paun IA, Popescu RC, Calin BS, Mustaciosu CC, Dinescu M, Luculescu CR. 3D biomimetic magnetic structures for static magnetic field stimulation of osteogenesis. *Int J Mol Sci*. 2018;19(2):495.
doi: 10.3390/ijms19020495

26. Jia Y, Zhang P, Sun Y, et al. Regeneration of large bone defects using mesoporous silica coated magnetic nanoparticles during distraction osteogenesis. *Nanomedicine*. 2019;21:102040.
doi: 10.1016/j.nano.2019.102040

27. Wu D, Chang X, Tian J, et al. Bone mesenchymal stem cells stimulation by magnetic nanoparticles and a static magnetic field: release of exosomal miR-1260a improves osteogenesis and angiogenesis. *J Nanobiotechnol*. 2021;19(1):209.
doi: 10.1186/s12951-021-00958-6

28. Jasemi A, Kamyab Moghadas B, Khandan A, Saber-Samandari S. A porous calcium-zirconia scaffolds composed of magnetic nanoparticles for bone cancer treatment: fabrication, characterization and FEM analysis. *Ceram Int*. 2022;48(1):1314-1325.
doi: 10.1016/j.ceramint.2021.09.216

29. Zhao Y, Fan T, Chen J, et al. Magnetic bioinspired micro/nanostructured composite scaffold for bone regeneration. *Colloids Surf B Biointerfaces*. 2019;174:70-79.
doi: 10.1016/j.colsurfb.2018.11.003

30. Zhang J, Zhao S, Zhu M, et al. 3D-printed magnetic Fe3O4/MBG/PCL composite scaffolds with multifunctionality of bone regeneration, local anticancer drug delivery and hyperthermia. *J Mater Chem B*. 2014;2(43):7583-7595.
doi: 10.1039/C4TB01063A

31. Daňková J, Buzgo M, Vejpravová J, et al. Highly efficient mesenchymal stem cell proliferation on poly-ε-caprolactone nanofibers with embedded magnetic nanoparticles. *Int J Nanomed*. 2015;7(10):7307-7317.
doi: 10.2147/ijn.s93670

32. De Santis R, Russo A, Gloria A, et al. Towards the design of 3D fiber-deposited poly(-caprolactone)/iron-doped hydroxyapatite nanocomposite magnetic scaffolds for bone regeneration. *J Biomed Nanotechnol*. 2015;11(7):1236-1246.
doi: 10.1166/jbn.2015.2065

33. Rezaei V, Mirzaei E, Taghizadeh S-M, Berenjian A, Ebrahiminezhad A. Nano iron oxide-PCL composite as an improved soft tissue scaffold. *Processes*. 2021;9(9):1559.
doi: 10.3390/pr9091559

34. Cheah C, Chua C, Leong K, et al. Development of a tissue engineering scaffold structure library for rapid prototyping. Part 1: investigation and classification. *Int J Adv Manuf Technol*. 2003;21:291-301.
doi: 10.1007/s001700300034

35. Sato K, Watanabe Y, Horiuchi A, et al. Feasibility of new heating method of hepatic parenchyma using a sintered MgFe2O4 needle under an alternating magnetic field. *J Surg Res*. 2008;146(1):110-116.
doi: 10.1016/j.jss.2007.05.022

36. Newman D, Laredo E, Bello A, Grillo A, Feijoo JL, Müller AJ. Molecular mobilities in biodegradable poly(dl-lactide)/poly(ε-caprolactone) blends. *Macromolecules*. 2009;42(14):5219-5525.
doi: 10.1021/ma9007303

37. Galarreta-Rodriguez I, Lopez-Ortega A, Garayo E, et al. Magnetically activated 3D printable polylactic acid/polycaprolactone/magnetite composites for magnetic induction heating generation. *Adv Compos Hybrid Mater*. 2023;6:102.
doi: 10.1007/s42114-023-00687-4

38. Atanasova N, Paunova-Krasteva T, Stoitsova S, et al. Degradation of poly(ε-caprolactone) by a thermophilic community and *Brevibacillus thermoruber* Strain 7 isolated from Bulgarian hot spring. *Biomolecules*. 2021;11(10):1488.
doi: 10.3390/biom11101488

39. Bin S, Wang A, Guo W, Yu L, Feng P. Micro magnetic field produced by Fe3O4 nanoparticles in bone scaffold for enhancing cellular activity. *Polymers (Basel)*. 2020;12(9):2045.
doi: 10.3390/polym12092045

40. Mirkhalaf M, Men Y, Wang R, No Y, Zreiqat H. Personalized 3D printed bone scaffolds: a review. *Acta Biomater*. 2023;156:110-124.
doi: 10.1016/j.actbio.2022.04.014

41. Kanwar S, Vijayavenkataraman S. 3D printable bone-mimicking functionally gradient stochastic scaffolds for tissue engineering and bone implant applications. *Mater Design*. 2022;223:111199.
doi: 10.1016/j.matdes.2022.111199

42. Meenarathi B, Siva P, Palanikumar S, Kannammal L, Anbarasan R. Synthesis, characterization and drug release activity of poly(ε-caprolactone)/Fe3O4–alizarinred nanocomposites. *Nanocomposites*. 2016;2(2):98-107.
doi: 10.1080/20550324.2016.1207009

43. Saeed M, Beigi-Boroujeni S, Rajabi S, Ashteiani GR, Dolatfarahi M, Özcan M. A simple, green chemistry technology for fabrication of tissue-engineered scaffolds based on mussel-inspired 3D centrifugal spun. *Mater Sci Eng C*. 2021;121:111849.
doi: 10.1016/j.msec.2020.111849

44. Zeng X, Meng Z, Qiu Z, He J, Fan J, Li D. Melt-based embedded printing for freeform fabrication of overhanging and flexible polycaprolactone scaffolds. *Virtual Phys Prototype*. 2023;18(1):e2209778.
doi: 10.1080/17452759.2023.2209778

45. Haag H, Dalton PD, Bloemen V. The synergy of biomimetic design strategies for tissue constructs. *Adv Funct Mater*. 2022;32:2201414.
doi: 10.1002/adfm.202201414

46. Bakhtiary N, Pezeshki-Modaress M, Najmoddin N. Wet-electrospinning of nanofibrous magnetic composite 3-D scaffolds for enhanced stem cells neural differentiation. *Chem Eng Sci*. 2022;264:118144. doi: 10.1016/j.ces.2022.118144

47. Lam T, Moy A, Lee HR, Shao Q, Bischof JC, Azarin SM. Iron oxide-loaded polymer scaffolds for non-invasive hyperthermic treatment of infiltrated cells. *AIChE J*. 2020;66(12):e17001. doi: 10.1002/aic.17001

48. Shah RR, Davis TP, Glover AL, Nikles DE, Brazel CS. Impact of magnetic field parameters and iron oxide nanoparticle properties on heat generation for use in magnetic hyperthermia. *J Magn Magn Mater*. 2015;387:96-106. doi: 10.1016/j.jmmm.2015.03.085

49. Xie W, Guo Z, Gao F, et al. Shape-, size- and structure-controlled synthesis and biocompatibility of iron oxide nanoparticles for magnetic theranostics. *Theranostics*. 2018;8(12):3284-3307. doi: 10.7150/thno.25220

50. Urano M, Kuroda M, Nishimura Y. For the clinical application of thermochemotherapy given at mild temperatures. *Int J Hyperthermia*. 1999;15(2):79-107. doi: 10.1080/026567399285765

51. Hildebrandt B, Wust P, Ahlers O, et al. The cellular and molecular basis of hyperthermia. *Crit Rev Oncol Hematol*. 2002;43(1):33-56. doi: 10.1016/S1040-8428(01)00179-2

52. Freeman C, Halperin EC, Brady LW, David EW. *Perez and Brady's Principles and Practice of Radiation Oncology*. Philadelphia: Wolters Kluwer Health/Lippincott Williams & Wilkins; 2008: 637-644. ISBN 978-0-7817-6369-1.

53. Chew SA, Danti S. Biomaterial-based implantable devices for cancer therapy. *Adv Healthc Mater*. 2017;6(2):1600766. doi: 10.1002/adhm.201600766

ACCSCIENCE PUBLISHING

International Journal of Bioprinting

RESEARCH ARTICLE

3D-bioprinted respiratory disease model: Exploring the importance of culture conditions and controlled release in modeling infection

Amanda Zimmerling[1,2*], Lauren Aubrey[2], Kathryn Avery[1], Xavier Tabil [1], Jim Boire[1,3], Xiongbiao Chen[1*], and Yan Zhou[2*]

[1]Division of Biomedical Engineering, College of Engineering, University of Saskatchewan, Saskatoon, Canada

[2]Vaccine and Infectious Disease Organization (VIDO), University of Saskatchewan, Saskatoon, Canada

[3]RMD Engineering Inc., Saskatoon, Canada

(This article belongs to the *Special Issue: Bioprinting for Tissue Engineering and Modeling*)

***Corresponding authors:**
Amanda Zimmerling
(asz694@usask.ca)

Xiongbiao Chen
(xbc719@usask.ca)

Yan Zhou
(yan.zhou@usask.ca)

Citation: Zimmerling A, Aubrey L, Avery K, et al. 3D-bioprinted respiratory disease model: Exploring the importance of culture conditions and controlled release in modeling infection. *Int J Bioprint*. 2024;10(6):3895. doi: 10.36922/ijb.3895

Received: June 8, 2024
1st revised: August 28, 2024
2nd revised: September 10, 2024
Accepted: September 12, 2024
Published Online: September 12, 2024

Copyright: © 2024 Author(s). This is an Open Access article distributed under the terms of the Creative Commons Attribution License, permitting distribution, and reproduction in any medium, provided the original work is properly cited.

Publisher's Note: AccScience Publishing remains neutral with regard to jurisdictional claims in published maps and institutional affiliations.

Abstract

The burden of respiratory illnesses is substantial, significantly impacting healthcare systems worldwide. As researchers work to better understand chronic diseases, as well as newly emerging respiratory viruses, the need for improved respiratory models has become evident. While 3D bioprinting has been illustrated as a feasible method to create complex cellularized constructs or respiratory models, it remains to be determined whether incorporating relevant biomechanical stimuli and/or relevant growth factors significantly impacts the response of these models to infection. In this study, an alginate/gelatin/collagen solution was synthesized and characterized in terms of rheology, printability, degradation, mechanical properties, and biocompatibility. The bioink, which incorporated primary human pulmonary fibroblasts and THP-1 cells, was bioprinted to form hierarchical 3D constructs and subsequently seeded with primary human bronchial epithelial cells to form the respiratory tissue model. To explore the importance of growth factors and culture conditions in modeling infection, we strategically developed a hepatocyte-growth-factor-loaded nanoparticle system and incorporated them into the bioink for bioprinting the respiratory tissue model, followed by culturing under dynamic conditions in a breath-mimicking bioreactor. The effect of incorporating growth factors and dynamic culture conditions was examined over 28 days, followed by the infection of these constructs with the influenza A virus. It was determined that these constructs support infection, demonstrating a more clinically relevant infection pattern than 2D models. It was further determined that the inclusion of hepatocyte growth factor aids in epithelial cell growth, while the inclusion of biomechanical stimulus increases cellular metabolism and has a moderating effect on response to infection.

Keywords: Bioprinting; Respiratory tissue model; Influenza; Disease model

1. Introduction

It is well-known and documented that respiratory diseases have a significant impact on healthcare systems globally. Aside from pandemics, chronic respiratory diseases, including chronic obstructive pulmonary disease (COPD), pulmonary cystic fibrosis, and asthma, are the third leading cause of death worldwide.[1,2] Further, there are approximately one billion influenza A cases per year, with 3–5 million resulting in severe illness, along with many other viral respiratory infections.[3,4] The influenza A virus (IAV), which can be further classified into subtypes based on their viral surface proteins (H1N1, H3N2, etc.), is the most common type of virus that infects humans. It preferentially infects the respiratory epithelium through α2,6-linked sialic acid receptors found on the nasal epithelium to the respiratory bronchioles.[5-8] Tight junctions between epithelial cells, apical polarity, and antimicrobial and mucosal excretions, all act as a first line of defense against infection; however, if the virus crosses these barriers and bonds to a sialic acid receptor, it is internalized via receptor-mediated endocytosis where conformational changes induce the release of viral RNA and proteins into the cytoplasm.[9,10] These viral proteins then enter the nucleus and utilize the host's machinery to initiate viral replication.[5,6,9] During this process, pattern recognition receptors recognize the relevant pathogen-associated molecular patterns (PAMPs), triggering various signaling pathways to initiate a stronger immune response.[5,6,9]

As part of the immune response to infection, various cytokines/chemokines are released, including interleukins (IL)-8, 29, and 1β along with interferon gamma-induced protein 10 (IP-10).[11-13] IL-8, also known as chemokine C-X-C motif ligand 8, is produced by epithelial cells and macrophages, and it induces chemotaxis in target cells to facilitate the migration of neutrophils or other granulocytes to the site of infection, further stimulating phagocytosis.[14,15] IL-29 is a type III interferon, primarily produced by epithelial cells.[16] Upon viral infection, IL-29 is released and exhibits antiviral responses aiming to stimulate the production of antiviral proteins and upregulate the expression of major histocompatibility complex I molecules.[16,17] IL-1β is a cytokine that is cleaved by cytosolic caspase 1 to form mature IL-1β.[18] Produced by activated macrophages and monocytes, IL-1β plays a role in mediating the inflammatory response and apoptosis.[18,19] IP-10 is a small cytokine secreted by monocytes and fibroblasts, and it acts as a chemoattractant for immune cells among other functions.[20,21] Collectively, along with various other signaling molecules and pathways, these chemokines can be used to demonstrate the extent of a cellular immune response to infection.

Tissue engineering focuses on integrating engineering design principles with molecular biology to create functional tissues, including skin, liver, kidney, and bone, among others. While various branches of tissue engineering focus on regenerative medicine applications, such as organ/tissue transplants or grafts, a significant segment of respiratory tissue engineering (RTE) is focused on expanding the respiratory modeling capacity to allow researchers and medical professionals to gain a better understanding of both pre-existing and emerging diseases, as well as expanding pre-clinical options for screening therapeutics.[22-24] Currently, 2D *in vitro* and animal models are used in pre-clinical research for respiratory diseases; however, there is still a lack of understanding of various pathogens and conditions, with many promising therapeutics from these trials failing at the clinical stage.[25-27] As 2D *in vitro* models often lack relevance due to their simplicity, and animal models may not accurately reflect human physiology, there is a knowledge gap that could be addressed by developing complex humanized 3D tissue constructs.

Bioprinting is a promising approach to developing such 3D humanized constructs.[28] By depositing human cell-laden biomaterials in a layer-by-layer manner, bioprinting allows for the recapitulation of hierarchical structures, such as the respiratory epithelium.[22,29,30] Biocompatible materials, including alginate, gelatin, and collagen, are commonly utilized in tissue engineering as they exhibit a combination of printability/compatibility with ionic or thermal crosslinking, cell binding motifs, and post-printing mechanical stability.[31-33] While 3D hierarchical constructs improve upon the relevance and complexity of 2D models, methods of further increasing the relevance of these constructs include the use of bioreactors during culture to mimic the biomechanical stimulus that native tissues experience, as well as incorporating biochemical stimuli such as growth factors to guide cellular growth and differentiation.[33-36] Respiratory tissue is subjected to constant expansion and relaxation, shear forces imposed by airflow, and pressure changes. It was previously found that including these stimuli on bioprinted respiratory tissue stimulates cellular proliferation.[34,37,38] Controlled release of growth factors through the use of growth factor-incorporating nanoparticles was also reported to promote epithelialization.[33]

The current state of the field is promising, with various models developed, including 3D-printed models focused on creating an *in vitro* air-blood barrier,[39,40] as well as others that have demonstrated the feasibility of infecting 3D-bioprinted respiratory constructs with IAV[39,41] and their use in bacterial and inhibitor studies.[42] These studies have identified 3D bioprinting as a promising avenue

for engineering lung tissues that exhibit a greater degree of physiological relevance in comparison to 2D systems through the utilization of co-cultures consisting of epithelial cells, pulmonary fibroblasts, endothelial cells, and in some instances, immune cells. However, these studies lack the inclusion of one important factor in the behavior of lung tissues, the biomechanical stimulus of breathing. As biomechanical stimulus has previously been identified to have a drastic impact on cellular behavior in various tissues, the inclusion of this stimulus is considered an important addition to respiratory models, especially when studying host-pathogen interactions and responses to viral infections.[34,37,38] Further, these bioprinted respiratory construct infection studies, to date, have not included growth factors or other chemical signaling molecules commonly present in the respiratory system.

This paper presents a study on incorporating both biomechanical and biochemical stimuli within bioprinted constructs to explore the importance and effects of including these stimuli on the constructs in disease modeling applications. Alginate/gelatin/collagen constructs were bioprinted, incorporating primary human pulmonary fibroblasts (HPFs) and THP-1 cells, and further seeded with primary human bronchial epithelial cells (HBEpCs). These constructs were then used as a respiratory disease model through infection with IAV A/Puerto Rico/8/34 (PR8) H1N1. The immune response, measured through chemokine/cytokine mRNA expression, was used to determine the effects of biomechanical stimuli (via a specialized breath-mimicking bioreactor) and biochemical stimuli (through a growth factor-containing nanoparticle system) on the response of the engineered construct to infection. It was found that incorporating biomechanical stimuli resulted in an increase in cellular metabolism, which was further increased with growth factor-loaded nanoparticles, in agreement with previous studies.[33,34] It was hypothesized that the greater cellular proliferation and activity caused by the biomechanical stimulus may enhance the overall immune response, while the increased epithelialization resulting from the inclusion of hepatocyte growth factor (HGF) may lead to a stronger epithelial response. While the system containing both nanoparticles and dynamic stimulus displayed the greatest immune response 6 h post-infection, constructs without nanoparticles cultured in the bioreactor demonstrated the least immune response at this timepoint. However, at later timepoints, the inclusion of biomechanical stimulus with or without the further addition of nanoparticles demonstrated a more moderate immune response in comparison to the control condition.

2. Materials and methods

2.1. Cells and virus

Primary human pulmonary fibroblasts (HPFs; cryopreserved, C12360, LOT #446Z031; PromoCell, Germany) were cultured in Human Fibroblast Growth Medium 2 (C-21020; PromoCell, Germany) supplemented with Growth Medium 2 Supplemental Mix (C-39325; PromoCell, Germany) and 1× Anti-Anti (antibiotic-antimycotic, 15240-062; Gibco, United States of America [USA]). Primary bronchial epithelial cells (HBEpCs; cryopreserved, C12640, LOT#468Z003; PromoCell, Germany) were cultured in Airway Epithelial Cell Growth Medium (C-21060; PromoCell, Germany) supplemented with Growth Medium Supplement Mix (C-39165; PromoCell, Germany) and 1× Anti-Anti. Undifferentiated THP-1 cells were cultured in RPMI 1640 media (Lot 1967664; Gibco, USA) supplemented with 5% fetal bovine serum (FBS; Cat: 12103C, Lot 21G129, SAFC; St. Louis, USA), 0.2 mg/mL GlutaMAX (35050-061, Lot 1897177; Gibco, USA), 50 mM 2-mercapotoethanol (21985-023; Gibco, USA), 20 mM HEPES (15630-080; Gibco, USA), and 1× Anti-Anti. All cells were incubated in a standard incubator at 37°C with 5% CO_2 until the required number of cells was reached.

Influenza A/Puerto Rico/8/34 (H1N1) (PR8) was propagated in 11-day-old embryonated chicken eggs, and titrated in MDCK cells, as described previously.[43]

2.2. Nanoparticle preparation

Hepatocyte growth factor (HGF)-loaded chitosan-coated alginate nanoparticles were produced using an emulsion synthesis technique, as previously described.[33] HGF was selected as it is documented to play a role in lung healing, aiding in the formation of an epithelial barrier layer by promoting cell proliferation and differentiation toward epithelial cell lineages.[44] Briefly, a 5% low-viscosity alginate (A1112; Sigma Aldrich, USA) solution was created through the dissolution of alginate in ultrapure water via magnetic stirring. 0.18% (wt.) HGF (recombinant human HGF protein, ab259401, Lot GR3453764-1; Abcam, United Kingdom [UK]) was added to this solution and stirred for 2 h before 300 µL of solution was added dropwise to an oil phase consisting of 1 mL paraffin oil (18512; Sigma-Aldrich, USA) and 100 µL Span 80 (viscosity 1000–2000 mPa·s, 85548; Sigma-Aldrich, USA) with magnetic stirring at 1200 rpm. After 1 h, 150 µL 0.68 M $CaCl_2$ (223506, Lot MKCG9612; Sigma-Aldrich, USA) was added to the solution to crosslink the formed alginate particles. The solution was stirred for another hour before 200 µL isopropanol was added to harden the alginate spheres. The solution was then centrifuged and washed with isopropanol three times, followed by a wash with ultrapure water. The

collected nanoparticles were then freeze-dried for 24 h. To coat the nanoparticles, 0.1% chitosan (448877; Sigma-Aldrich, USA) was dissolved in 2% acetic acid and adjusted to pH 5 with NaOH (BP359, Lot 217634; Fisher Reagents, USA). Thereafter, 200 µL chitosan solution and 100 µL 5 mM $CaCl_2$ were added to the collected alginate particles, mixed for 1 h, centrifuged, washed with ultrapure water three times, and freeze-dried. As previously characterized, these nanoparticles were spherical with an average size of just under 1000 nm.[33]

2.3. Bioink development

A bioink solution, consisting of 6.25% (w/v) medium-viscosity sodium alginate (180947; Sigma-Aldrich, USA), 6.25% (w/v) porcine gelatin (G1890; Sigma-Aldrich, USA), and 0.05% collagen, was formed by magnetically stirring the alginate and gelatin with 50% HPF culture media and 50% HBEpC culture media at 60°C. The composition of the bioink solution was designed based on the complementary properties of alginate, collagen, and gelatin. Specifically, alginate is a favorable material for bioprinting but lacks cell-binding motifs, which reduces biocompatibility.[45] The addition of a low concentration of collagen, which lacks printability in liquid form, increases biocompatibility and cell proliferation within an alginate-based bioink. Including gelatin further enhances the biocompatibility of alginate-based bioinks through the addition of cell-binding motifs, while allowing for temperature-based tuning of printing parameters due to gelatin's thermally sensitive nature.[45] The formed solution was stored in the refrigerator until the day of printing. Directly before printing, the ink was reheated to 50°C while magnetically stirred. Printing batches were done with 5 mL of ink each. To create 5 mL of complete bioink, 4 mL of the alginate/gelatin solution was collected in a syringe. HPFs and THP-1s were collected at a density of 2.5×10^7 and 2×10^6 cells/mL of bioink, respectively; these were then combined and resuspended in 200 µL HPF media. The cell suspension was collected in a syringe along with 800 µL collagen (Collagen 1, Rat Tail, A10483, Lot 963787; Gibco, USA), creating a final bioink with 5% alginate, 5% gelatin, and 0.05% collagen, containing both HPFs and THP-1 cells. To incorporate nanoparticles into the bioink, 4 µg/mL of nanoparticles was mixed into the alginate/gelatin solution before being collected in a syringe for the addition of collagen and cells. This concentration of nanoparticles was designed and selected as per a recent study that demonstrated increasing the concentration of nanoparticles beyond 4 µg/mL negatively affected printability.[33] Air was removed from both syringes before they were connected and plunged back and forth to mix the components. Mixing was considered complete when the material appeared homogeneous. HBEpCs were not added directly to the bioink and were instead seeded onto the printed constructs seven days post-printing at a density of 50,000 cells/construct.

2.4. Rheology

The rheological behavior of the cell-containing bioink was tested and characterized using a TA Instruments HR20 Discovery Series Rheometer fitted with a 60 mm parallel plate geometry. Constant shear stress sweeps ($n = 3$) were carried out as temperature was increased from 20 to 40°C at a rate of 1°C/ min to determine the temperature dependence of rheological properties, such as viscosity. To model temperature dependence, viscosity data was fitted with a modified Arrhenius equation (**Equation I**):

$$\mu = Ae^{\frac{B}{T}} \quad \text{(I)}$$

where A is the Arrhenius viscosity coefficient (Pa·s), B is the Arrhenius temperature coefficient (K), and T is the temperature (K). The modified equation describes viscosity as a function of temperature. The obtained results were then used to determine whether printing the bioink at physiologically relevant temperatures would be feasible while balancing process-induced forces and their influence on cell viability with printability. Rheological results were also used to strategically inform initial printing parameters, followed by a trial-and-error approach described in previous studies.[33,45]

2.5. Bioprinting

A cylindrical structure, 6 mm in diameter, was designed with the bottom four layers consisting of a 90° lattice structure with 1 mm strand spacing. The fifth layer was designed to be printed as a solid layer with a strand spacing of 0.27 mm. On top of this solid surface, a ring structure was printed with six layers, forming an enclosed pool. The rationale behind the construct design was that the base lattice structure would facilitate the mobility of nutrients and waste throughout the construct, while the solid layer would provide a surface for seeding epithelial cells to form an epithelial barrier layer. Further, creating the enclosed ring structure to form a pool on the surface layer facilitates the easy creation of an air-liquid interface and allows for physiologically relevant infection, as the infectious agent can be deposited within the pool in contact with the epithelial surface, rather than the underlying fibroblasts and immune cells. In this way, the infection can progress from the epithelial surface into the depths of the construct, similar to an inhaled pathogen crossing the respiratory epithelial barrier.

Briefly, 24-well plates were prepared for printing by adding 1 mL 0.1% polyethyleneimine (PEI; molecular weight [Mw]: 60,000, 50% [w/w] aqueous solution, J61270.22; Thermo Scientific, USA) and incubating overnight in an incubator at 37°C. The 0.1% PEI solution was then removed and replaced with 0.5 mL 50 mM $CaCl_2$ with 0.1% PEI as the crosslinking solution. Using a GeSiM mbH BioScaffolder 3.2 (GeSiM, Germany) outfitted with a 27-gauge needle (inner diameter: 200 μm), the synthesized bioink was pneumatically extruded at 37°C into the prepared 24-well plates. Constructs remained submersed in the crosslinking solution for 10 min before the crosslinking solution was replaced with 3D culture media (50% HPF media, 50% HBEpC media, 20 mM $CaCl_2$). Notably, the use of PEI in bioprinting has toxic effects on the incorporated cells, and high concentrations of $CaCl_2$ can also negatively impact cell viability. Therefore, scaffolds were printed into the crosslinking solution (50 mM $CaCl_2$ + 0.1% PEI) and immersed for only 10 min, allowing for appropriate crosslinking and limited toxicity. The inclusion of the lower concentration of 20 mM $CaCl_2$ in the culture media allowed for further crosslinking throughout the culture period, thus maintaining the structural integrity without negatively impacting cell viability.

Each construct was bioprinted with approximately 1.3 × 10^6 HPFs and 1 × 10^5 THP-1s for subsequent biological studies. Specifically, the constructs underwent a 7-day standard submerged culture period post-printing and then were seeded, with each construct receiving 5 × 10^4 HBEpCs on its pool surface. At 24 h post-seeding, air-liquid interface (ALI) conditions were created through the reduction of media levels below that of the pool surface, exposing the epithelial cell-seeded surface. The start of ALI culture was considered day 1 for all biological experiments. It should be noted that constructs used in studies on printability, degradation, and mechanical properties (as discussed below) did not incorporate cells for simplicity and cost-effectiveness. As suggested by previous studies,[33,34,45] the involvement of cells has a limited effect on the construct's printability, degradation, and mechanical properties over the timeframes of interest.

2.6. Incubation

Incubation in dynamic conditions was carried out in a customized incubator, as previously described.[34] Briefly, the bioreactor induces cyclic pressure changes in the incubation chamber, mimicking both the pressure and air-flow changes that occur in the lung. Instead of directly imposing mechanical stretch on the 3D-bioprinted constructs, the incubator mimics the ventilation conditions of the breathing cycle as seen in the bronchi/bronchioles. These ventilation conditions induce both shear and hydrostatic forces on the cells, acting as a relevant biomechanical stimulus. It has been recently illustrated that the incubation of constructs in such dynamic conditions affects cell proliferation, with variations observed during light, normal, and heavy breathing conditions, compared to static culture conditions.[34]

2.7. Printability

Printability was assessed by printing the bottom two layers of the cylindrical scaffold design and characterizing them by measuring the strand diameter, maximum and minimum diameter, and pore size, as well as an assessment of scaffold repeatability using ImageJ software (n = 72). The printed scaffolds were submerged in the crosslinking solution for 10 min and then imaged on a BioTek Lionheart LX automated fluorescence microscope at 4× magnification. Printability analysis was carried out for scaffolds both with and without nanoparticles and with varying printing parameters, including temperature, pressure, and print head speed, for each test, as these factors have been reported to affect printability.[46,47] To minimize uncertainties in the assessment, printing parameters were selected to ensure consistent and repeatable strand printing while creating the designed scaffolds, instead of primarily basing selection on meeting a specific strand dimension.

2.8. Degradation

Degradation studies were carried out using cell-free scaffolds in both static and dynamic culture conditions to determine the material loss over a 28-day culture period. Briefly, 3D-printed constructs were transferred to 3D culture media (50% HPF media, 50% HBEpC media, 20 mM $CaCl_2$) after being immersed in the 50 mM $CaCl_2$ crosslinker for 10 min. The plates were then moved into a standard or ventilated incubator for culturing at 37°C. In the dynamic condition, the incubation chamber was ventilated in a cycle that mimicked normal breathing conditions with biomechanical stimuli, including airflow and pressure changes, as previously described.[34] At the timepoints of 1, 7, 14, and 28 days, scaffolds were removed (n = 12), freeze-dried for 24 h, and weighed for determination of mass loss over time, with day 1 used as the control.

2.9. Compressive testing on scaffold materials

Cell-free bulk material specimens were created and used for compression testing to determine the bulk material compressive modulus. Briefly, the prepared solution was poured into cylindrical molds before being immersed in 100 mM $CaCl_2$. The molds remained immersed for 48 h at 25°C to ensure complete crosslinking through the cross-section of the samples. The higher concentration of

crosslinker and extended crosslinking time were selected to avoid concerns regarding toxic effects on cells, as the use of molds and bulk material requires a longer time for the crosslinking solution to permeate the entire structure. The samples were then removed from the molds and sectioned into discs with a diameter of 10 mm and a height of 5 mm. These discs were then placed in 3D culture media and incubated in static or dynamic conditions over a 28-day period. At timepoints of 1, 7, 14, and 28 days, specimens (n = 12) were loaded onto the stage of a BOSE BioDynamic 5010 Mechanical Tester and compressed at a rate of 0.01 mm/s to a total deformation of 2 mm at 25°C. The force and displacement recorded were then used to evaluate the compressive modulus of the bulk material. The linear viscoelastic region was determined using linear fitting in Excel. Visually, the expected linear zone was identified, and a linear fit was plotted. The fit linear viscoelastic region was then extended through the data in both directions separately until the R-value of the fit decreased below 0.95.

2.10. Tensile testing of bioprinted scaffolds

Cell-free scaffolds for tensile testing were printed as cylindrical shapes (3 mm height and 9 mm diameter) with 1 mm lattice spacing, except the top two layers that were printed as solid layers with a strand spacing of 0.27 mm. During testing, the tensile force pulls the structures apart along the z-axis, causing failure in the lattice region within the scaffold. Due to this, as long as the lattice design remained the same between scaffolds, the properties measured remained consistent. Therefore, the scaffold design used for tensile testing was slightly adjusted from that of all other studies to allow for the greatest compatibility with the tensile testing apparatus, while also being representative of all the scaffolds utilized in this study. After being immersed in the crosslinking solution for 10 min, the media was replaced with 3D culture media, and the constructs were incubated in static or dynamic conditions over a 28-day period. At the set timepoints of 1, 7, 14, and 28 days, constructs (n = 6), still adhered to the bottom of the plate they were printed in, were tensile-tested at a rate of 50 μm/s until failure or a maximum displacement of 5 mm to determine the tensile strength of the lattice structure. This crosshead speed was selected based on previous tests that determined this setting resulted in the most consistent results. The measured load and displacement were then used to determine the Young's modulus and ultimate tensile strength (UTS) of the printed constructs. Cross-sectional area was calculated as per **Equation II**:

$$Cross\text{-}sectional\ area = 60 \times \left(\left(measured\ average\ strand\ diameter \times 2 \right) + \left(\frac{\pi * 9mm}{2} \right) \right)$$

This assumption was reasonable to account for the spreading of printed strands over the bottom layer while also taking design factors into account.

2.11. Live/dead assay

A Live/Dead Cell Viability Assay Kit (ab287858, Lot 1021052604; Abcam, UK) was used to determine cellular viability throughout 28 days of culture in both static and dynamic conditions, and later during the two-day infection period. Briefly, samples (n = 3) were washed once with Hanks buffered salt solution (HBSS; 14025-076, Lot 2537086; Gibco, USA), before 0.5 mL of 0.1% dead stain and 0.2% live stain buffer solution was added to each sample. Samples were incubated for 15 min before imaging with a BioTek Lionheart LX automated fluorescence microscope.

2.12. XTT assay

A CyQuant XTT Cell Viability assay kit (X12223; Invitrogen, USA) was used for the determination of cellular metabolism throughout both the 28-day culture period and the two-day infection period. Briefly, the XTT reagents were thawed at 37°C in a water bath; 0.2 mL XTT reagent A/well was combined with 0.014 mL electron coupling reagent/well and mixed. In each well of interest, culture media was removed and replaced with 0.8 mL of fresh culture media before 200 μL of the XTT reagent mixture was added. The samples (n = 3) were then incubated for 4 h before 200 μL of the media was removed and plated in a 96-well plate. Standard solutions of XTT reagent mixture with culture media were also plated in the 96-well plate as blanks. An xMark microplate spectrophotometer was then used to measure absorbance at both 450 and 660 nm, with final measurements being calculated as:

$$\text{Absorbance} = \begin{matrix}(450\text{ nm test reading}-450 \\ \text{nm blank reading})-660\text{ nm} \\ \text{test reading}\end{matrix} \quad \text{(II)}$$

2.13. Infection

2D infection experiments on A549s, HBEpCs, and HPFs were carried out to generate a baseline of data for the infectivity of primary cell types and their cytokine response. Briefly, each cell type was seeded into a 6-well plate and cultured in standard culture conditions until confluent (24 h). Cells were infected at a multiplicity of infection (MOI) of 5 with PR8 wild-type IAV. Briefly, the required

concentration of PR8 was mixed with basal Dulbecco's Modified Eagle's Medium-high glucose (DMEM; D5796, Lot RNBJ5275; Sigma-Aldrich, USA). Basal DMEM (bDMEM) was used to wash each well before 200 µL of the viral solution was added. Mock infections were carried out as a control using 200 µL bDMEM. After incubating for 1 h, the viral inoculum was carefully removed with a pipette before being replaced with 2.5 mL of a bDMEM, containing 0.2% bovine serum albumin (BSA; A8806, Lot SLBZ3340), and 1 µg/mL L-[(toluene-4-sulphonamido)-2-phenyl] ethyl chloromethyl ketone (TPCK)-Trypsin. Cells were further incubated for 5 h before being harvested for RNA extraction, i.e., a total of 6 h post-infection (HPI).

Following the completion of bioink characterization, specimens were prepared for a 3D infection experiment for comparison of viral progression and cellular response in three different conditions: standard incubation without nanoparticles (static), bioreactor incubation without nanoparticles (dynamic), and bioreactor incubation with nanoparticles (dynamic with nanoparticles).

Briefly, 3D-bioprinted constructs were cultured in 3D media for 1 week before being seeded with 50000 HBEpCs on the top solid surface within the pool. Constructs were then cultured on an ALI for 2 weeks before being used for infection studies (day 1 of infection corresponds to day 14 of biological experiments in non-infected constructs). Constructs were infected at an MOI of 1 with each construct estimated to contain 4×10^5 cells. Similar to the 2D infection experiment, the required concentration of PR8 was mixed with bDMEM, and 20 µL of the viral inoculum was added to the air-exposed pool of each construct. Mock infections were carried out as a control using 20 µL bDMEM. After incubating for 1 h, the viral inoculum was carefully removed with a pipette before being replaced with 20 µL bDMEM containing BSA TPCK-Trypsin. After 1 h of incubation, all liquid was removed from the pool, leaving it air-exposed. The surrounding culture media was replaced with bDMEM containing BSA, TPCK-Trypsin, and 20 mM $CaCl_2$, with adjustments made to the culture media levels to prevent the construct from drying out, while maintaining the ALI. Samples were collected for analysis at 6, 24, and 48 HPI.

2.14. Reverse transcription-quantitative real-time polymerase chain reaction

Reverse transcription-quantitative real-time polymerase chain reaction (RT-qPCR) was carried out for each timepoint of the infection studies to characterize the resulting immune response. RNA was extracted from each sample using a Zymo Research Quick-RNA miniprep kit (#R1054; Zymo Research, USA).

For 2D infections, cell media was removed from each sample (n = 3) and replaced with 600 µL RNA lysis buffer. The bottom of each well was gently scraped to remove any remaining cells before the lysis buffer was transferred into a yellow "Spin-Away" filter column and placed in a collection tube. After spinning down, the flow through was saved and 600 µL of 100% ethanol was added and mixed. The solution was then transferred to a green "Zymo-Spin IIICG" filter column in a collection tube and spun down. The flow-through was discarded and 400 µL RNA prep buffer was added to the column before spinning down again. Flow through was discarded and the process was repeated with 700 µL RNA wash buffer, followed by 400 µL RNA wash buffer. After centrifuging for 2 min, the filter was transferred to a new collection tube, and 52 µL of elution buffer (Lot 00165805; Thermo Scientific, USA) was added. After centrifuging once again, the collected RNA concentration was measured using a Thermo Scientific Nanodrop 2000. Collected RNA was stored in a -80°C freezer until it was used for RT-qPCR.

The procedure for RNA extraction from the 3D-printed constructs (n = 3) was slightly modified at the lysis stage to dissolve the construct. Briefly, 500 µL lysis buffer and 100 µL 100 mM ethylenediaminetetraacetic acid (EDTA; E6511, Lot SLCH11239; Sigma-Aldrich, USA) were added to each construct and incubated for 10 min before being gently pipetted up and down using a 1 mL pipette until partially dissolved. The solution was then transferred to an Eppendorf tube along with the construct remnants and vortexed until fully dissolved. The tube was then centrifuged before the liquid was collected, transferred to a yellow "Spin-Away" filter column, and placed in a collection tube. Subsequent procedures remain the same as described above for 2D infections.

For RT, approximately 5 ng of RNA for each sample was collected into a tube strip. Thereafter, 1 µL OligodT (Oligo dT [20] Primer, 18418020, Lot 2577004; Invitrogen, USA) and 1 µL dNTP Mix (10 mM dNTP Mix, 1912584; Invitrogen, USA) were added to each tube before topping up each tube to 20 µL with the corresponding amount of nuclease-free water (AM9937, Lot 1511277; ThermoFisher, USA). The tube strip was incubated at 65°C for 5 min, cooled on ice, and spun down. Next, 4 µL first strand buffer (5× First Strand Buffer, Y02321, Lot 2417931; Invitrogen, USA) and 1 µL each of 0.1 M DTT (Y00147, Lot 2385398; Invitrogen, USA), Ribonuclease Inhibitor (RNAse Out; 10777-019, Lot 2475863; Invitrogen, USA), and Superscript III (Reverse Transcriptase, 18080-044, Lot

2378584; Invitrogen, USA) was added to each tube before incubation at 50°C for 1 h, followed by incubation at 70°C for 15 min. During this time, 1:10 dilutions of forward and backward primers for GAPDH, IL-29, IL-1β, IL-8, and IP-10 (Table 1) were created by diluting in nuclease-free water to reach 10 μM.

For qPCR, a master solution was then created for each primer by combining 10 μL SYBR Green (PowerSYBR Green PCR Master Mix, 4367659, Lot 2305638; Applied Biosystems, USA), 1 μL forward primer, and 1 μL backward primer, multiplied by the number of samples for each primer. After incubation of the tube strip was complete, the prepared complementary DNA (cDNA) was diluted by a factor of 1:10. A 96-well plate was then prepared for PCR by adding 18 μL of the corresponding primer master solution and 2 μL of the diluted cDNA to each well. PCR was then carried out using a StepOnePlus Real-Time PCR System (Applied Biosystems, USA). The temperature was originally raised to 95°C for 10 min. Following that, 50 cycles were carried out starting at 95°C, dropping to 55°C for 15 s, before increasing to 72°C for 20 s, followed by a melt-curve stepping at 0.3°C/min. Relative mRNA expression was normalized to mRNA levels of the housekeeping gene GAPDH and expressed using the ΔΔCt method relative to the mock infection.

2.15. Plaque assays

Standard plaque assays were carried out to determine the viral titer throughout the 3D infection period. Briefly, Madin-Darby Canine Kidney (MDCK) cells, cultured in Minimum Essential Medium Eagle (MEM; M4655, Lot RNBL9920; Sigma-Aldrich, USA) with 10% FBS and 1× gentamicin sulfate (Lot J721R0K; Biowest, USA) were plated in 6-well plates and incubated overnight before being observed for confluency. Serial dilutions of the viral supernatant (n = 3) were created by diluting in MEM. Media was removed from the MDCK cells with a pipette, and the cells were washed with basal media. The diluted viral supernatant was added to each well in duplicate. After incubating for 1 h, the viral inoculum was removed and virus-growing media containing 0.8% agarose was added to the cells. The plates were incubated for 72 h. The agarose overlay was then removed, and 2 mL Coomassie Blue was added to each well and let stain for 5 min. The stain was then removed, and the plaques were counted for calculating viral titer.

Table 1. Primer sequences used in polymerase chain reaction (PCR).

Gene	Primer direction	Primer sequence
GAPDH	Forward	CCTGGCACCCTATGGACACG
	Backward	CAAAGTTGTCATGGATGACC
IL-8	Forward	TCTGCAGCTCTGTGTGAAGG
	Backward	CAACCCTCTGCACCCAGTTT
IL-29	Forward	GACGCCTTGGAAGAGTCACT
	Backward	TGGTCTAGGACGTCCTCCAG
IL-1β	Forward	CGGCATCCAGCTACGAATCT
	Backward	TCGTGCACATAAGCCTCGTT
IP-10	Forward	CCTGCTTCAAATATTTCCCT
	Backward	CCTTCCTGTATGTGTTTGGA

2.16. Statistical analysis

All statistical analysis was carried out using Statistical Product and Service Solutions analysis software (SPSS 28). General linear modeling with univariate analysis of variance (ANOVA) was used for analysis, with $p < 0.05$ considered significant. For studies with n = 3, non-parametric Kruskal–Wallis tests with pairwise comparisons were used for analysis.

3. Results

3.1. Rheology

Rheological analysis of the alginate/gelatin/collagen solution demonstrated a relatively consistent decrease in viscosity as temperature was increased from 20 to 40°C (Figure 1). From this data, the modified Arrhenius model is given as (**Equation III**):

$$\mu(T) = 0.091\ Pa \cdot s \times e^{\left(\frac{2036.19K}{T}\right)} \quad \text{(III)}$$

As gelatin is temperature-sensitive and exists generally as a liquid at physiological temperatures, this decrease in viscosity with increasing temperature is likely due to the melting of gelatin.

It is known that being able to print at physiological temperatures aids in maintaining cell viability by creating more favorable biological conditions and that printing with materials with lesser viscosity reduces printing-induced mechanical forces, which may damage cells during the printing process.[28] The results displayed in Figure 1 suggest that heating the solution to physiological temperatures (37°C) for printing decreases the printing pressure, thus reducing shear forces imposed on cells within the bioink. In addition, the comparison of our rheological data in Figure 1 to previous studies indicates that this solution has a higher viscosity than alginate/collagen solutions of similar concentrations but without the addition of gelatin, suggesting better printability at elevated temperatures.[33]

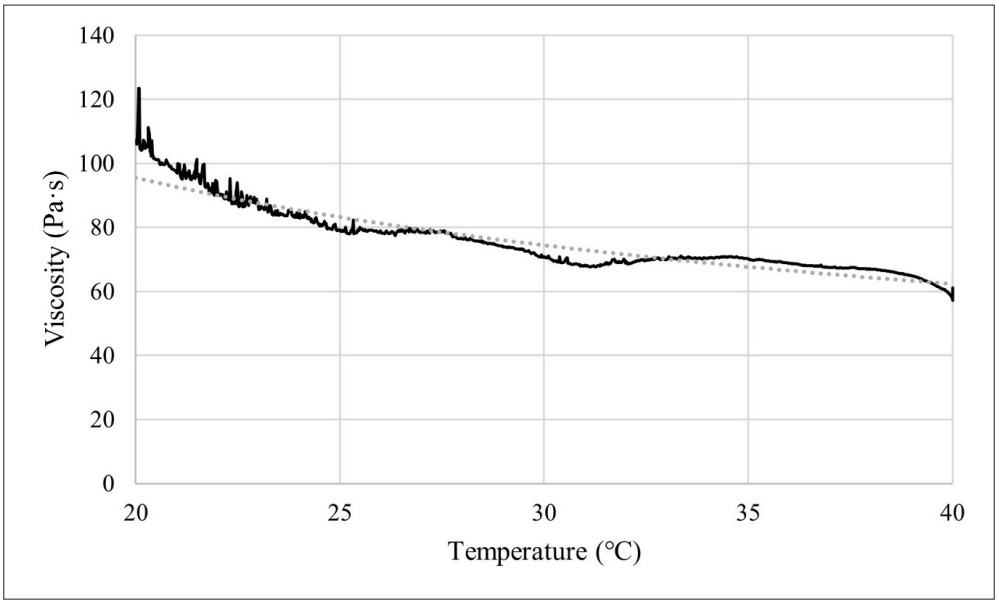

Figure 1. Temperature dependence of viscosity of the 5% alginate/5% gelatin/0.05% collagen solution undergoing constant shear stress sweeps as the temperature was increased from 20 to 40°C at a rate of 1°C/min.

3.2. Printability

Based on the rheological results, an initial printing temperature of 37°C was selected to balance the trade-off of printability, process-induced mechanical forces, and cell viability. Printability was tested and characterized with and without the presence of nanoparticles to confirm that the addition of 4 μg/mL nanoparticles would not have a significant impact. It should be noted that in bioprinting, nanoparticles with diameters less than 1000 nm are generally preferred to allow for smooth extrusion through printing needles (often around 200 μm in diameter), as the use of smaller particles helps to avoid clogging even if some particle aggregates form.

The optimal printing parameters that allowed for repetitive printing of structures with consistent strand diameters and pore sizing were determined to be 25 kPa and 10 mm/s (Figure 2). As observed in Tables 2 and 3, a decrease in pressure resulted in smaller average strand diameters, lesser strand adhesion, and higher strand discontinuities (Figure 3). Increased pressures and speeds resulted in larger pore sizes with increased amounts of strand swelling. Average strand dimensions using these parameters were found to be 555 ± 78 μm for solutions without nanoparticles and 544 ± 56 μm for solutions containing 4 μg/mL nanoparticles. Similarly, the average pore sizes for these parameters were 577 μm ± 218 μm without nanoparticles and 578 μm ± 214 μm with nanoparticles. The large standard deviation for pore spacing was due to the design of the scaffold, which has larger pores on the outer edges. These statistically insignificant differences, i.e., $p = 0.737$ for strand diameter and $p = 0.991$ for pore size (determined via ANOVA and pair-wise analysis), demonstrate the consistency in printability between inks with and without nanoparticles, as reported in previous studies.[33] The influence of printing temperature was examined at the optimized printing pressure and speed to determine if the altered temperature would significantly influence printability. Lowering the printing temperature was found to have inconsistent results on strand diameter, and it was determined that printing at physiological conditions (37°C) was most favorable. Some bubbles trapped during the mixing and printing process can be seen in Figure 2A and B.

3.3. Scaffold degradation and mass loss

Degradation studies, carried out in both static and dynamic conditions, were used to test if the inclusion of 20 mM $CaCl_2$ crosslinker in the 3D media was sufficient to maintain the constructs' stability over an extended culture period. As observed in Figure 4, up to 20% mass loss was still seen over 28 days, but there was never a significant difference in mass loss between static and dynamic culture conditions. More rapid mass loss appears to occur in the seven-day period between days 7 and 14 in comparison to the 14-day period between days 14 and 28. This suggests that the decrease in mass is primarily driven by the loss of gelatin and collagen from the matrix that was not fully contained by the crosslinked alginate polymeric network.

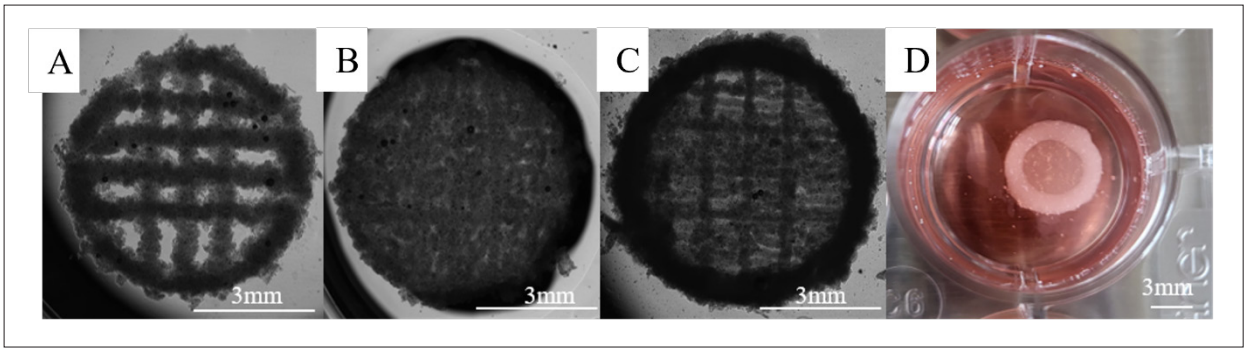

Figure 2. Images of the different section designs and fully printed scaffold for printability analysis: (A) 1 mm strand spacing lattice, (B) solid surface layer, (C) brightfield fully printed 11-layer scaffold, and (D) colored photo of the immersed scaffold. Scale bars: 3 mm.

Table 2. Printability results for scaffolds without nanoparticles.

Printing parameters			Average strand diameter (μm)	Pore size (μm)	Comments
Temperature (°C)	Pressure (kPa)	Speed (mm/s)			
37	22	6	638 ± 69	463 ± 284	Strand swelling
37	22	10	489 ± 87	753 ± 358	Small amount of material accumulation
37	22	14	540 ± 68	561 ± 246	Material accumulation
37	25	6	580 ± 34	505 ± 407	Inconsistent printing; material accumulation
37	25	10	555 ± 78	577 ± 218	Consistent pore sizing
37	25	14	505 ± 75	735 ± 376	Small amount of strand discontinuities
37	28	6	481 ± 26	658 ± 227	Small amount of strand discontinuities
37	28	10	425 ± 45	679 ± 250	Strand discontinuities
37	28	14	300 ± 8	901 ± 338	Needle clogging; missing strands
27	25	10	704 ± 100	503 ± 411	Strand swelling; material accumulation
32	25	10	525 ± 45	617 ± 193	Small amount of swelling

Table 3. Printability results for scaffolds with nanoparticles.

Printing parameters			Average strand diameter (μm)	Pore size (μm)	Comments
Temperature (°C)	Pressure (kPa)	Speed (mm/s)			
37	22	6	435 ± 87	766 ± 360	Inconsistent printing
37	22	10	436 ± 166	824 ± 338	Strand discontinuities
37	22	14	485 ± 38	666 ± 248	Strand discontinuities
37	25	6	609 ± 71	579 ± 419	Strand swelling; material accumulation
37	25	10	544 ± 56	578 ± 214	Small amount of swelling; consistent pore sizing
37	25	14	443 ± 42	716 ± 363	Dragging of strands
37	28	6	676 ± 86	544 ± 352	Large amount of strand swelling; material accumulation
37	28	10	616 ± 85	653 ± 415	Large amount of strand swelling; material accumulation
37	28	14	731 ± 92	N/A	Large amount of swelling; strand discontinuities; minimal pore spacing
27	25	10	342 ± 115	855 ± 398	Strand discontinuities
32	25	10	281 ± 60	928 ± 376	Strand discontinuities

Abbreviation: N/A: Not available.

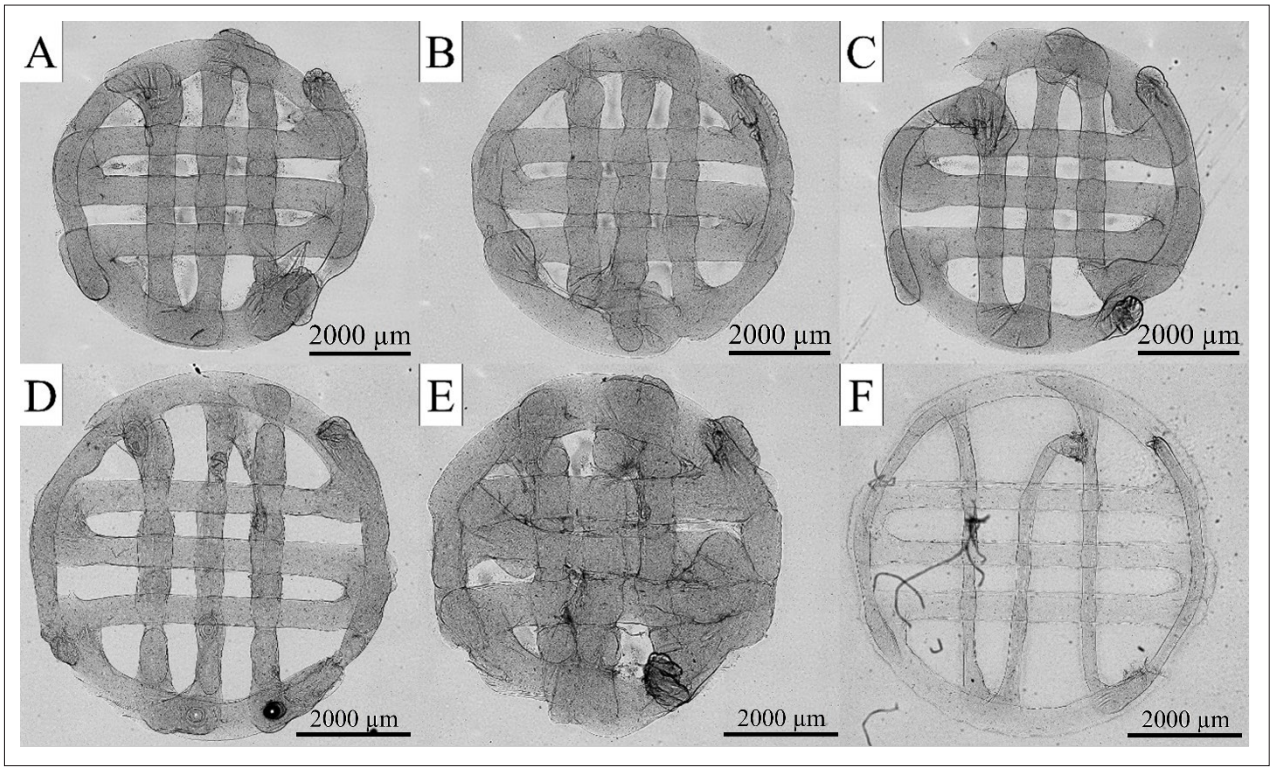

Figure 3. Representative scaffolds used for printability analysis. The top row (A, B, and C) represents scaffolds printed without nanoparticles, while the bottom row (D, E, and F) represents scaffolds printed with nanoparticles. Optimized parameters: 37°C, 25 kPa, and 10 mm/s (A and D); 37°C, 22 kPa, and 6 mm/s (B); 27°C, 25 kPa, and 10 mm/s (C); 37°C, 28 kPa, and 14 mm/s (E); 32°C, 25 kPa, and 10 mm/s (F). Scale bars: 2000 µm.

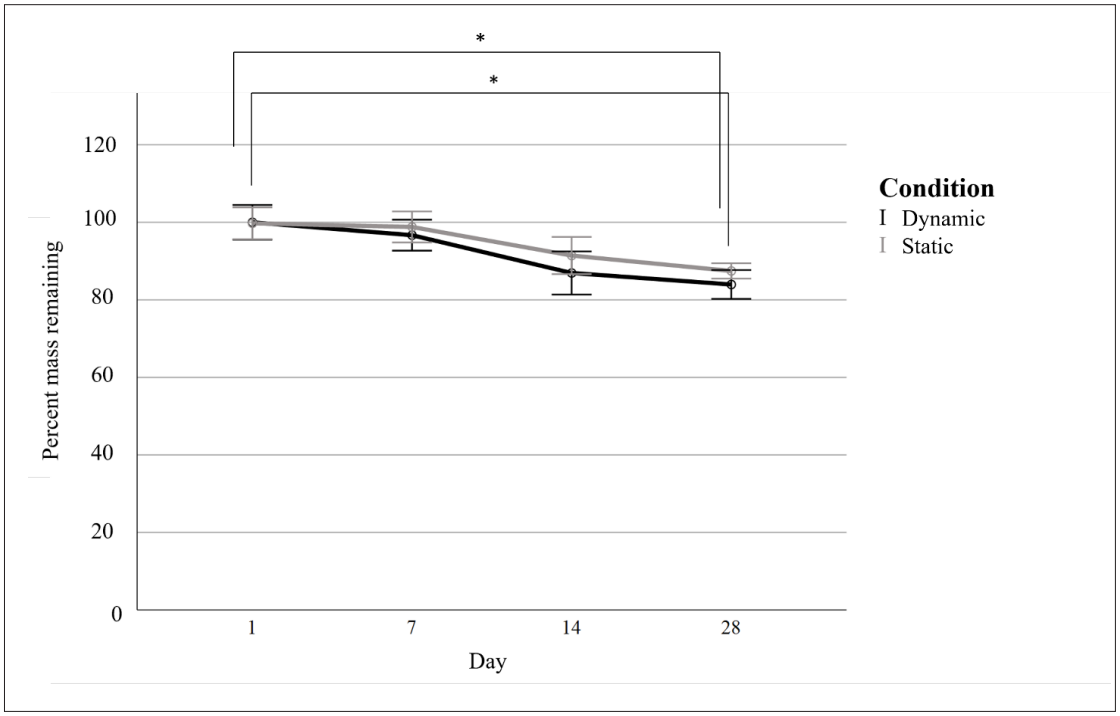

Figure 4. Percent mass remaining over a 28-day culture period in dynamic and static culture conditions. Error bars: ± 1 standard deviation. *$p < 0.05$; $n = 12$.

3.4. Compressive testing of bulk materials

Compressive testing (n = 12) was used to analyze the mechanical properties of the bulk alginate/gelatin/collagen material. As displayed in Figure 5, there was no significant difference in the compressive modulus of constructs cultured in static or dynamic conditions. Although statistically insignificant, a downward trend in compressive modulus can be seen, corresponding to the decrease in mass observed in the degradation studies. As these bulk scaffolds have a reduced surface-area-to-volume ratio in comparison to 3D-printed structures, the effect of degradation and the corresponding decrease in mechanical properties may be underrepresented in these results; however, the demonstrated trend would be expected to remain the same.

3.5. Tensile testing of printed scaffolds

Tensile testing was carried out on 3D-printed structures with the same lattice spacing used for the biological studies to allow for the determination of how Young's modulus and UTS would vary over a 28-day culture period in both static and dynamic conditions for the alginate/gelatin/collagen solution. As observed in Figure 6, no significant difference was found in either property between static and dynamic conditions; however, a statistically significant decrease in Young's modulus between day 1 and days 14 and 28 was seen in both static and dynamic conditions, while a significant decrease in UTS between days 1 and 28 was only seen in the static condition.

3.6. Live/Dead staining of printed scaffolds

Live/dead staining was carried out starting on day 1 post-seeding. Images were taken on days 1, 7, 14, and 28 for constructs cultured in both static and dynamic conditions. Figure 7 provides representative images for days 1 and 28 for both static and dynamic conditions.

Cells were highly viable post-printing with a high degree of live cells visible throughout the printed strands; however, cells generally exhibited a more rounded shape instead of the extended morphology that would be expected of fibroblasts. While this is relatively common when encapsulating cells in bioinks, this suggests that the encapsulation of cells within the biomaterial is limiting their ability to behave in a physiologically relevant fashion. Background emission from the bioink within the green channel is due to the inclusion of collagen within the bioink. Image processing included background removal of this autofluorescence; however, not all background emissions could be removed without losing the ability to identify cells through the depth of a strand. This is especially visible as cell density increases (Figure 7C and D).

Live/dead staining of infected constructs was carried out 6, 24, and 48 h post-infection. Figure 8 provides representative montage images of infected constructs at the 6-, 24- and 48-h timepoints.

As observed in Figure 8, constructs remained highly viable throughout the infection period; however, an increasing number of clusters of dead cells can be seen from the 6 to 48-h timepoint, especially on the epithelial surface and construct edge. The green and red outlines of the well plate seen in Figure 8A and B are due to the reflectivity of the well plate during fluorescence imaging.

3.7. XTT metabolic assay on printed scaffolds

Cellular metabolism was tracked over time using an XTT Assay. As observed in Figure 9, constructs for all conditions started with a similar number of cells; however, by day 14, significant differences in cell metabolism were seen between constructs cultures in static conditions and those cultured in dynamic conditions containing nanoparticles. By day 28, all constructs cultured in dynamic conditions were demonstrating significantly higher cellular metabolism than those cultured in static conditions. Cellular metabolism was also tracked over a two-day infection period (Figure 10). A slight decrease in cellular metabolism can be observed over the 48-h period, while the mock conditions resulted in a steady rate of cellular metabolism. No significant differences in cellular metabolism were observed between the different culture and nanoparticle conditions.

3.8. RT-qPCR for determination of immune response

Reverse transcription-quantitative real-time polymerase chain reaction (RT-qPCR) was used to measure the mRNA levels of various cytokines of interest, including IL-1β, IL-29, IL-8, and IP-10, with GAPDH used as an internal control. Mock infections were carried out as a negative control and used to identify a baseline (fold change of 1) for each cell type, cytokine, and condition. In the 2D culture, HPFs and HBEpCs were plated separately in 6-well plates to determine their cytokine mRNA profile. A549 cells were included for comparison and validation of the experimental procedures, as their behavior under influenza infection has been well-reported in the literature (Figure 11).[48-50]

As can be observed in Figure 11, each cytokine mRNA was upregulated to a significant extent by at least one of the cell types tested. IL-1β mRNA was upregulated by both epithelial cell types (A549s and HBEpCs) as was IL-29. IL-8 mRNA was upregulated by both primary cell types (HPFs and HBEpCs), though HBEpCs upregulated IL-8 mRNA to a much greater extent. IP-10 mRNA was upregulated to the greatest extent by A549s; however, HBEpCs and HPFs

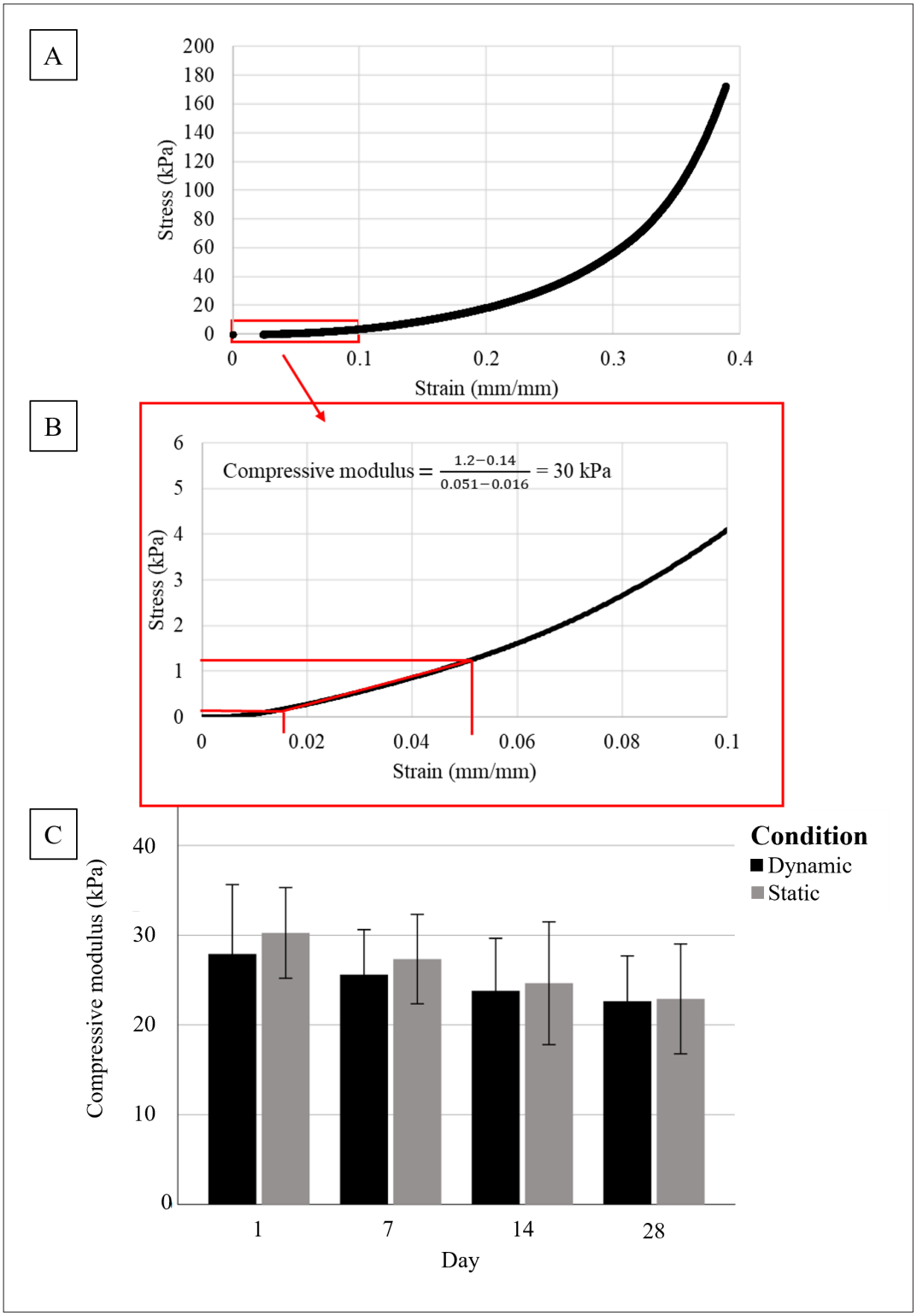

Figure 5. Compressive testing data: (A) Full representative stress–strain curve acquired during testing up to 2 mm of deformation; (B) Stress–strain curve of the elastic region; and (C) Summary of the compressive moduli of bulk material cultured in static or dynamic conditions obtained over a 28-day period. $n = 12$; error bars: ± 1 standard deviation.

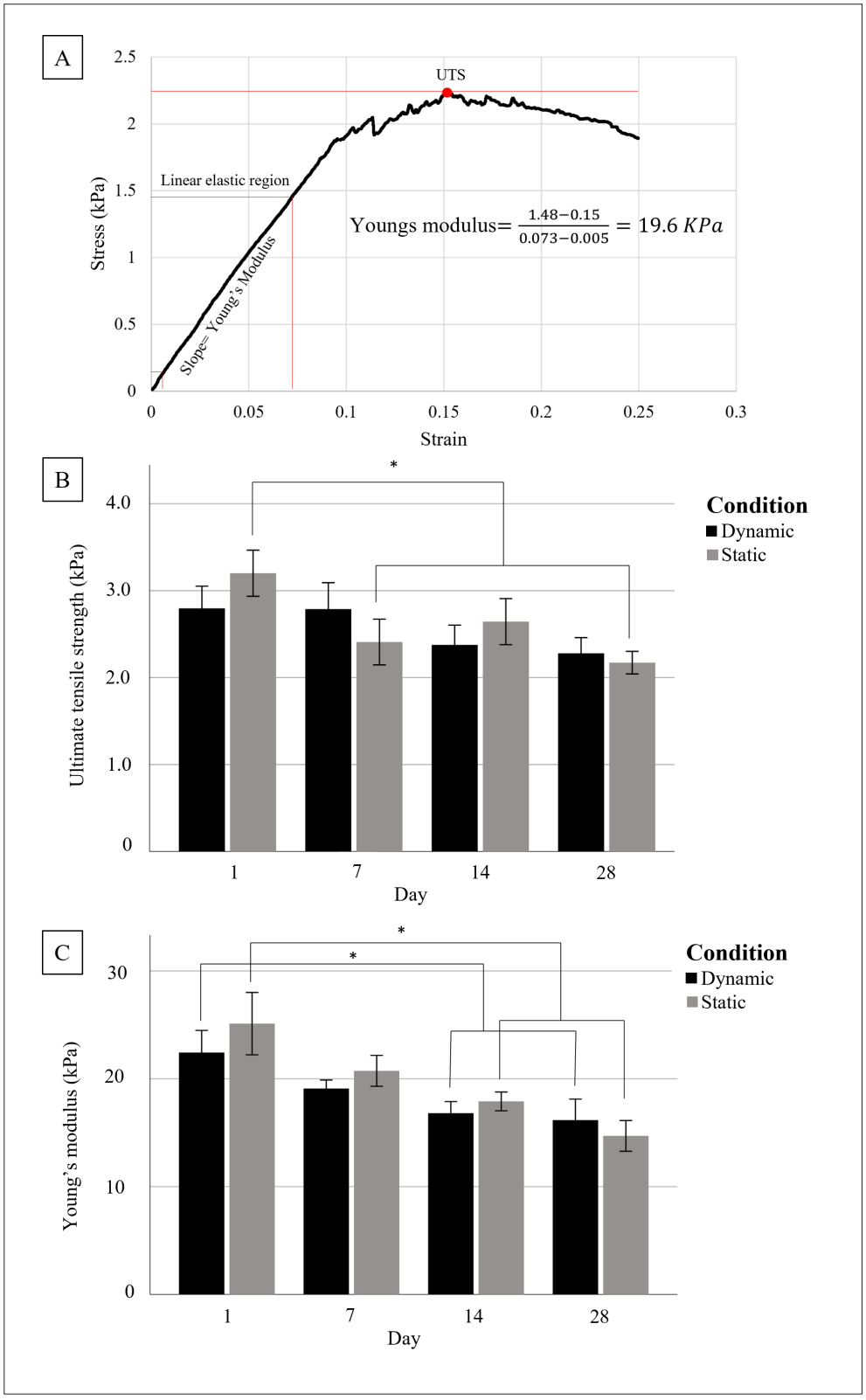

Figure 6. Tensile testing data: (A) Representative stress–strain curve acquired, and the determination of Young's Modulus and ultimate tensile strength (UTS); (B) UTS over a 28-day culture period in dynamic and static conditions; and (C) Young's modulus over 28 days of culture in static or dynamic conditions. $n = 6$; $^*p < 0.05$; error bars: ± 1 standard deviation.

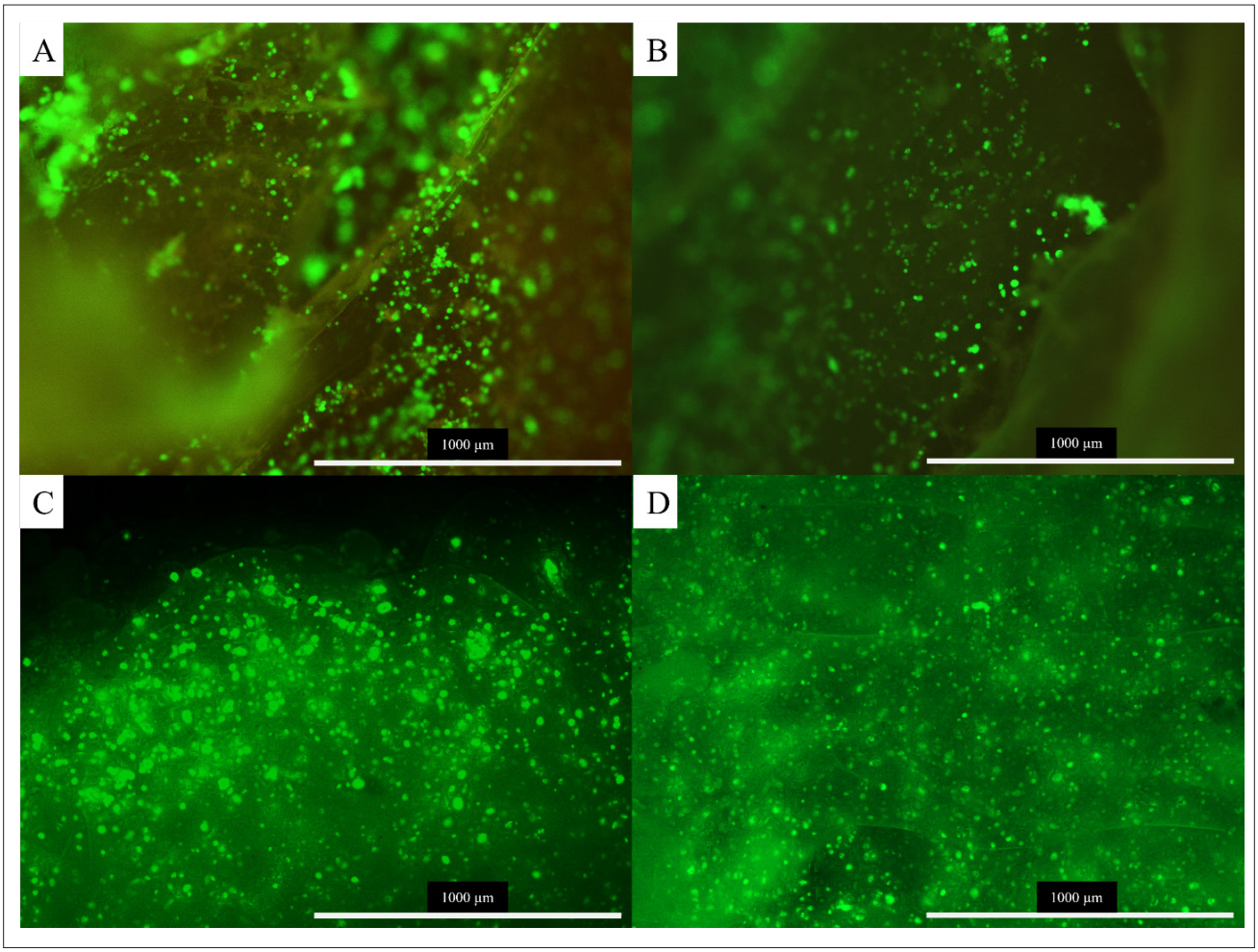

Figure 7. Live/dead staining of constructs: (A) day 1, static conditions; (B) day 1, dynamic conditions; (C) day 28, static conditions; and (D) day 28, dynamic conditions. Scale bars: 1000 µm.

both significantly upregulated IP-10 mRNA as well. IL-29 mRNA was upregulated to the greatest extent by HBEpCs, followed by IL-8, while HPFs upregulated IP-10 to the greatest extent.

Similarly, Figure 12 demonstrates that the upregulation of these cytokines in the infected constructs was determined over the 48-h infection period for the three different culture conditions with a mock infection used to normalize the results for each condition (fold change of 1).

At 6 h post-infection, the highest cytokine mRNA fold change is exhibited by IL-29, with a fold change of around 49 in the dynamic condition with nanoparticles. IL-29 mRNA is maintained as the cytokine that undergoes the greatest increase; by 24 hours, the static condition exhibits the highest average mRNA fold change of IL-29, reaching 120; however, its fold change is less significant than that of both dynamic conditions. Cytokine mRNA production appears to have stabilized at the 24-h mark, as there are no significant changes in cytokine release between 24 and 48 h. Generally, at 24 and 48 h, all cytokine mRNAs of interest are upregulated in the static condition; however, Il-1β and IL-8 mRNAs are not significantly upregulated in the dynamic condition with nanoparticles.

3.9. Plaque assays for viral titre

Plaque assays were used to determine the viral titer in each condition at 6, 24, and 48 HPI (Figure 13). From the original diluted supernatant, the viral titer increased from ~8×10^5 at 6 HPI to ~1.1×10^7 PFU/mL by 24 HPI; the viral titer then decreased slightly by the 48-h timepoint.

4. Discussion

Mechanical characterization, consisting of rheological analysis, printability analysis, compression testing, and tensile testing, all demonstrated that the synthesized

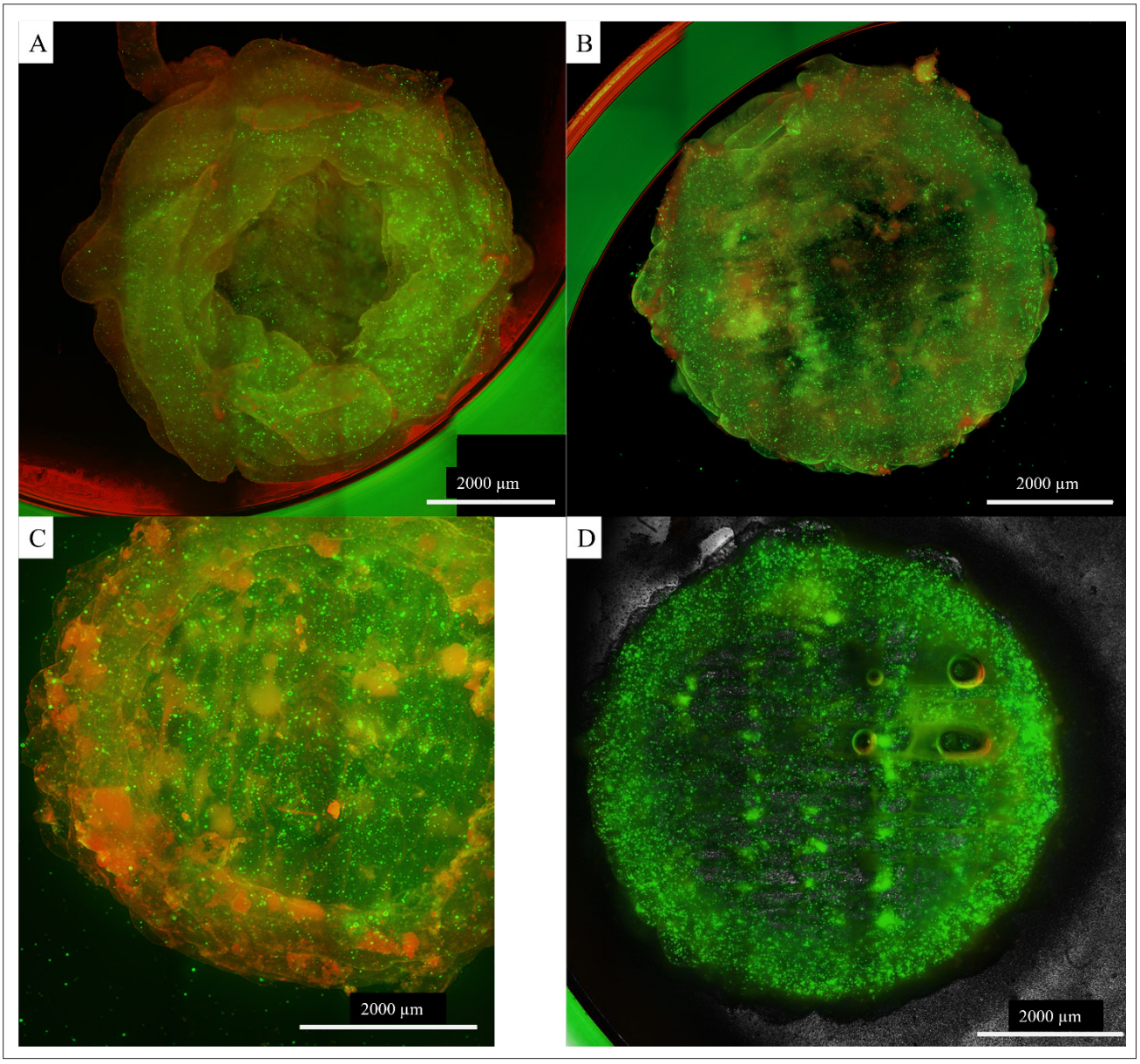

Figure 8. Live/dead stained montage images of infected 3D constructs and a mock infection cultured in dynamic conditions: (A) 6 HPI, (B) 24 HPI, (C) 48 HPI, and (D) mock 48 HPI.

alginate/gelatin/collagen solution was highly compatible with 3D printing for tissue engineering applications. While the viscosity of the solution containing a relatively high percentage of alginate (5%) and gelatin (5%) was increased over previous studies utilizing alginate/collagen inks,[33,34] the thermal responsiveness of gelatin and shear-thinning behavior of alginate allowed for printing at reasonable pressures, resulting in high cell viability post-printing. While low, the addition of collagen has previously been identified as having a positive impact on the biocompatibility of alginate-based bioinks, making it a useful addition even in low concentrations.[45] As the ink was able to be printed before crosslinking in an ionic crosslinking bath, a high degree of printability was maintained, regardless of whether the ink contained 4 µg/mL of nanoparticles, consistent with previously reported results.[33] As the culture media used consisted of 20 mM $CaCl_2$, which acts as the ionic crosslinking, mechanical stability was generally maintained. However, as 20% of mass loss still occurred over the 28-day period, it is hypothesized

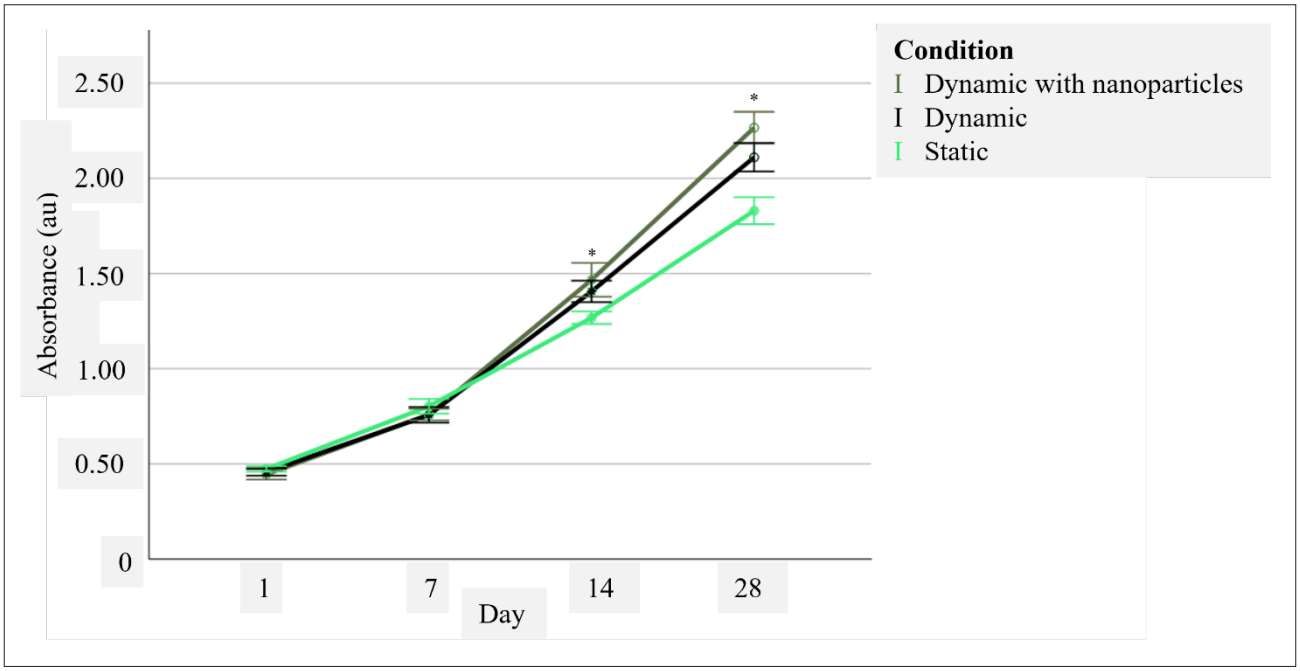

Figure 9. Cellular metabolism of constructs cultured in static or dynamic conditions, with or without nanoparticles, for 28 days as calculated using EQ II. *denotes significance ($p < 0.05$) between culture conditions at the same timepoint. Error bars: ± standard deviation.

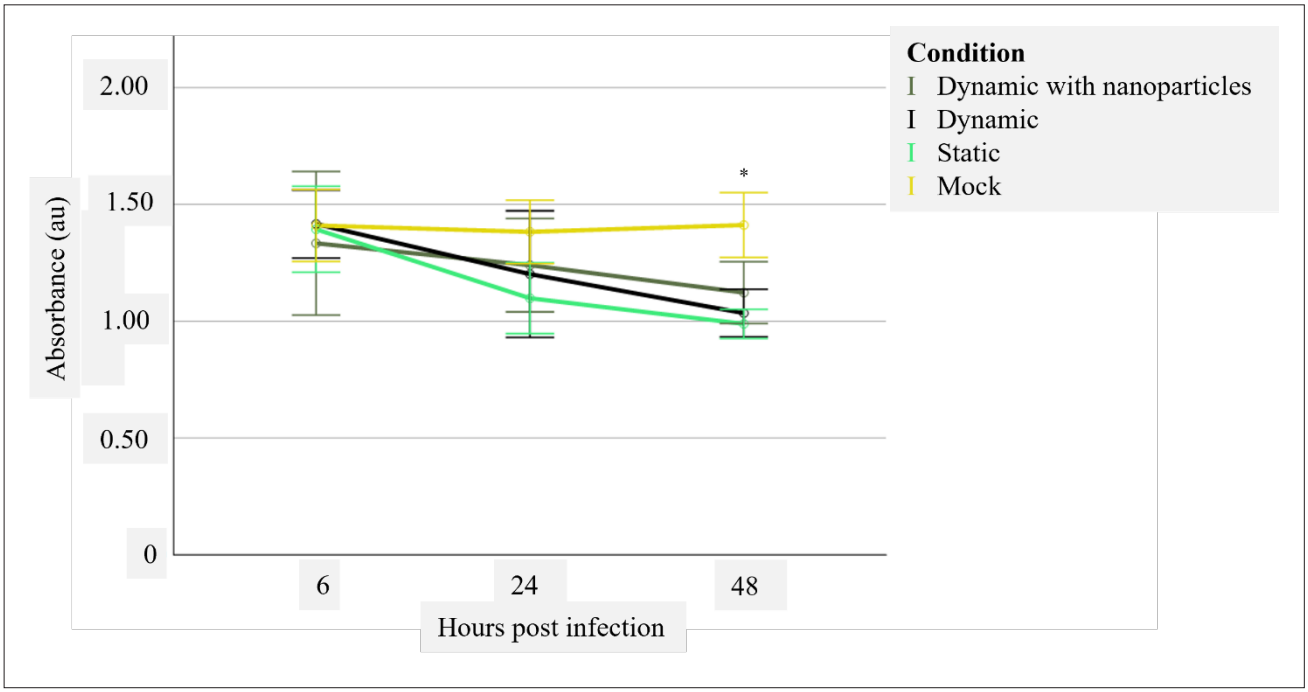

Figure 10. Cellular metabolism of infected constructs cultured in static or dynamic conditions, with or without nanoparticles. * denotes significance ($p < 0.05$) between culture conditions at the same timepoint. Error bars: ± standard deviation.

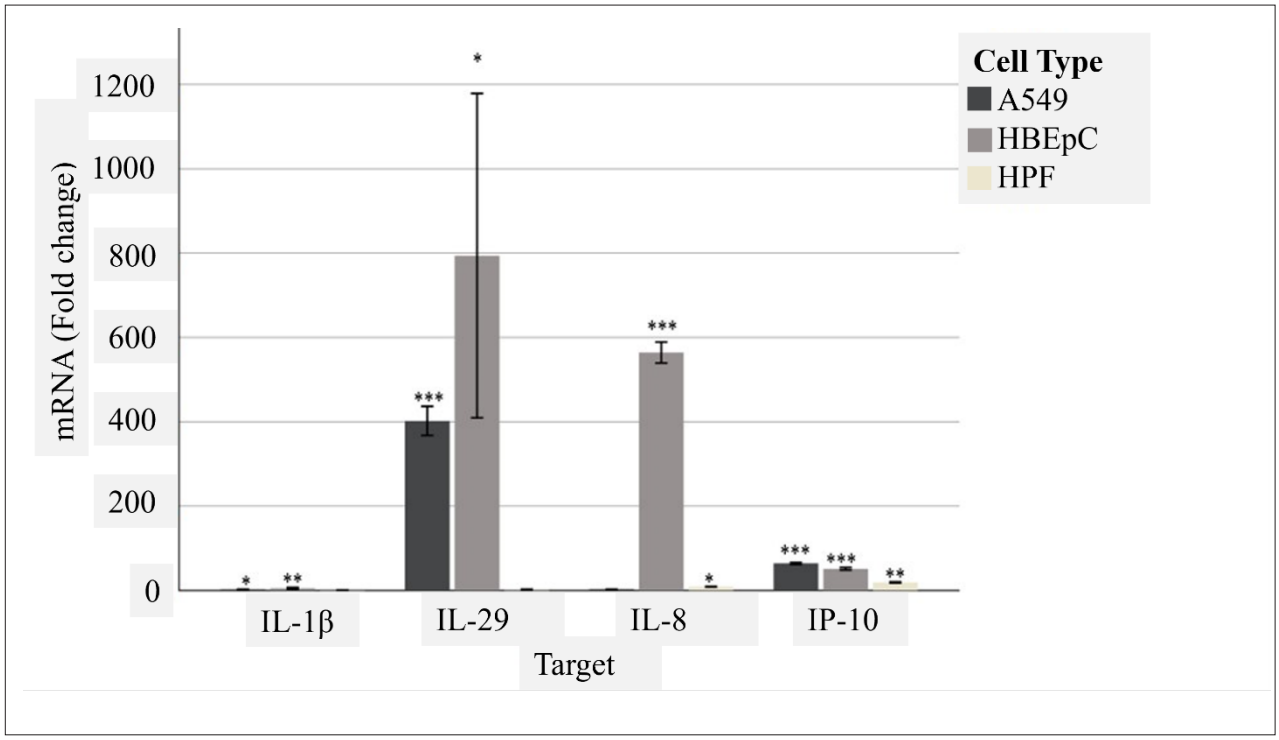

Figure 11. Fold change of cytokine mRNA of interest released from A549s, HPFs, and HBEpCs. Significant increase fold changes are indicated as $*p < 0.05$, $**p < 0.01$, or $***p < 0.001$. Error bars: ± standard deviation.

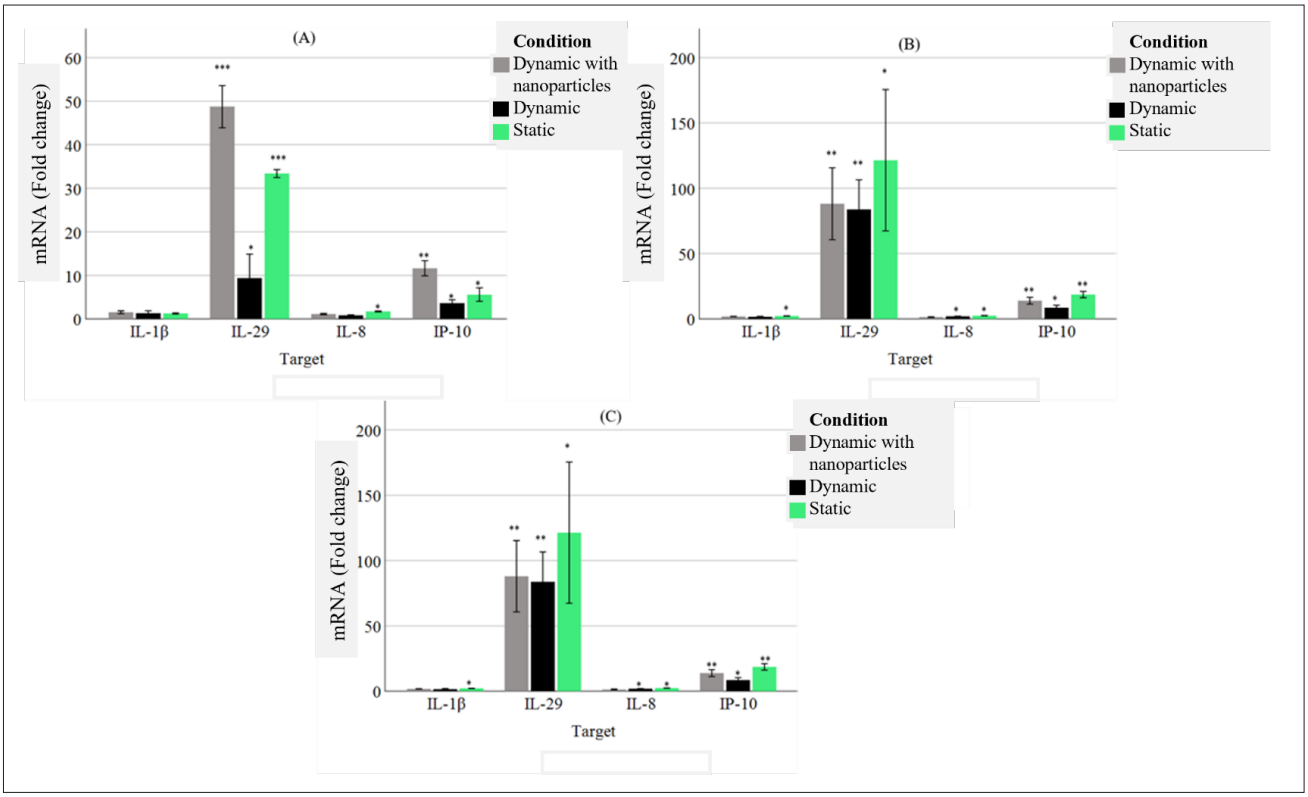

Figure 12. Cytokine mRNA release from 3D constructs cultured in different conditions at (A) 6 HPI, (B) 24 HPI, and (C) 48 HPI. Significant increase fold changes are indicated as $*p < 0.05$, $**p < 0.01$, and $***p < 0.001$. Error bars: ± standard deviation.

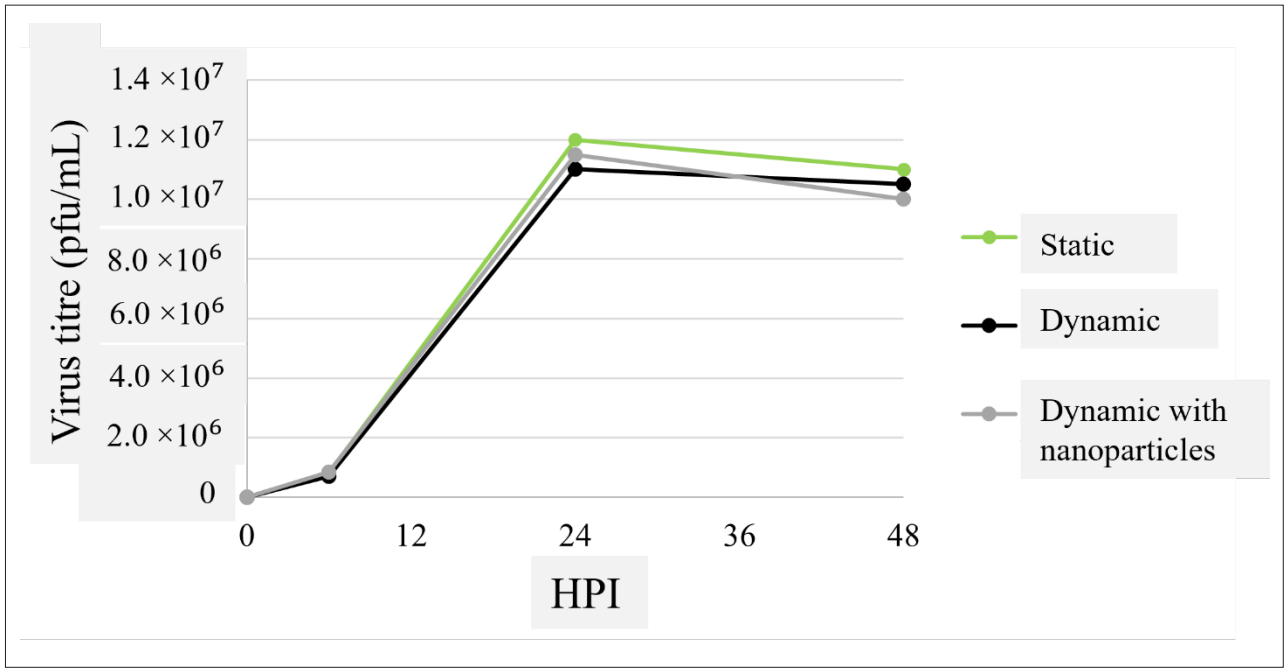

Figure 13. Viral growth curve of influenza A virus (IAV) determined by plaque assay for static, dynamic, and dynamic with nanoparticle culture conditions.

that some of the collagen and gelatin materials may have leached out of the crosslinked alginate material due to the extended period spent at elevated temperatures (37°C) during culture, resulting in the mass loss and downward trend in mechanical properties. This may be reduced by crosslinking at a higher concentration for a greater length of time to form a tighter polymeric mesh; however, this would have to be balanced with the possible decrease in cell viability post-printing. While the Young's modulus of the printed lattice structure sat between 15 and 25 kPa, it is within the range of that measured for native lung tissue throughout the 28-day culture period. In contrast, the compressive modulus of the bulk material and UTS are higher than those of native lung tissue.[51] Although these mechanical studies were carried out in cell-free scaffolds, previous studies demonstrated that very similar values were found between cell-free and cell-containing scaffolds over a 14-day period. This similarity likely results from cell remodeling, which balances material degradation caused by cells with the deposition of cellular matrix materials, but it cannot fully compensate for general material degradation.[34]

Biological characterization of the bioink further demonstrates its ability to be used in RTE applications, as cellular metabolism of printed HPFs and seeded HBEpCs measured through the XTT assays was seen to steadily increase over the 28-day period. This highlights the bioink's ability to co-culture primary cells for an extended time with high viability. Other studies reported in the literature, utilizing slightly different materials and A549 cells instead of primary respiratory epithelial cells, have also demonstrated that the use of 3D-bioprinted co-culture can extend cell culture life beyond 28 days.[41,42] Along with the use of primary respiratory cells in the form of HPFs and HBEpCs for increased physiological relevance of the model, the incorporation of other methods for increasing relevance, including the culture of the bioprinted constructs in a bioreactor mimicking the biomechanical stimulus of the lung increased cellular proliferation/metabolism. Additionally, the incorporation of HGF-loaded nanoparticles also resulted in a further (though insignificant) increase in cellular metabolism at the 28-day timepoint, building on the results of previous studies.[33,34] While live/dead imaging helped confirm the presence of a high density of viable cells, the background autofluorescence of collagen within the green "live" channel created noise in the images that was challenging to fully remove without significant image manipulation. Therefore, an improved process for imaging may be required for future studies. While live/dead imaging did qualitatively confirm the increased cell density indicated by the quantitative cellular metabolism studies, it also demonstrated that the incorporated cells did not take on physiologically relevant morphology. This may be due to the encapsulating bioink being challenging to remodel,

limiting the mobility and communication of incorporated cells. The addition of low concentrations of components that may aid in cellular remodeling and dissolution of the matrix material, such as sodium citrate, may be considered; however, this would have to be balanced with maintaining the structural integrity of the constructs to limit degradation for long-term use.

The 3D-bioprinted constructs are designed in a way to create an epithelial surface layer within a contained pool. Infection begins with the HBEpC barrier layer, followed by the virus progressing into the bulk of the material. Infection of the 3D constructs caused a slight decrease in cellular metabolism, with clusters of dead cells visible in live/dead imaging, demonstrating a clustered infection pattern similar to that observed in clinical infections and previous studies.[41] The 2D and 3D PCR results displayed consistent trends, with the 3D infection results demonstrating lower mRNA fold changes overall. However, IL-29 mRNA was upregulated to the greatest extent in both conditions, with IP-10 mRNA also significantly upregulated in all conditions. One notable difference between the 2D and 3D experiments is the extent of IL-8 mRNA upregulation, as the 2D studies demonstrated a ~550-fold increase in IL-8 mRNA that was not evident at any stage of the 3D infection study, though slight upregulation of IL-8 mRNA in the dynamic and static condition was recorded. When comparing differences in cytokine release between static, dynamic, and dynamic with nanoparticle conditions, the differences are greatest at the 6-h timepoint, with the nanoparticle-containing constructs upregulating IL-29 mRNA and IP-10 mRNA to a greater extent early in the infection period. As nanoparticles are incorporated before printing and infection experiments are not conducted until 14 days of culture (7 days pre-seeding; 7 days post-seeding), it is likely that the influence of incorporating nanoparticles is limited to increasing epithelial cell proliferation during culture, leading to an increased number of epithelial cells. This would cause a greater upregulation in cytokine release early in the infection before the virus has penetrated the underlying fibroblast cells in the construct. By the 24 HPI, most differences fall within standard deviation; however, there is a general trend of the static condition, resulting in greater up-regulation of cytokine mRNAs, such as IL-29 and IP-10, in comparison to both dynamic conditions. This demonstrates that the inclusion of a biomechanical stimulus may influence viral infection.

The three-layer design of the present model shares similarities to other models reported in the literature, as many aim to form a surface epithelial barrier layer overlaying fibroblasts, with alveolar models reported in the literature often also incorporating endothelial cells as the bottom layer.[41,42,52] These multi-layer designs have been reported to provide good physiological relevance, thus increasing the applicability of these engineered models. Similar trends can be observed when comparing the results obtained in this study to previous literature on respiratory disease models; though it should be noted that different cell sources and biomaterials have been used across studies, resulting in some variance. The viral titer obtained can be compared with viral mRNA and viral titers tracked in other respiratory model studies with the same trend, i.e., a significant increase at 24 HPI before remaining relatively steady to slightly decreasing by 48 h.[39,41] The XTT results were also quite similar, with cellular metabolism slightly decreasing over the infection period. The upregulation of mRNAs related to IL-29, IL-8, and IL-1β is also similar to the literature, though a direct comparison cannot be made due to different methods of measurement.[42]

Overall, the cumulation of results indicates that the alginate/gelatin/collagen biomaterial is a favorable material for bioprinting and long-term culture of respiratory tissue constructs. The inclusion of a biomechanical stimulus in the form of a bioreactor mimicking the airflow and pressure conditions of breathing increases cellular metabolism. This can be further increased through the inclusion of hepatocyte growth factor-loaded nanoparticles to generate a highly viable cellular construct. Infection of these 3D-bioprinted constructs designed to have a contained, air-exposed epithelial barrier layer can easily be carried out through the addition of the infectious agent to the pool to mimic biological infection pathways; the results obtained were similar to that of the 2D experiments. It is indicated that the inclusion of biomechanical stimulus when culturing infected constructs affects cytokine gene expression, while an increase in epithelial cell numbers caused by nanoparticle incorporation in the biomaterial may lead to increased cytokine gene expression at the early stages of infection.

The scope of this research was to determine whether the inclusion of a biomechanical stimulus and a controlled release system for growth factors is worth pursuing for the further development of respiratory tissue models in infection studies. While this study successfully demonstrates the importance of both factors, this scope did result in some limitations. For example, the microbiological characterization of cell behavior within this study was limited, and the use of undifferentiated THP-1 cells only functions as a monocytic immune component, which lacks relevance to alveolar and other relevant macrophages. Further work related to this should focus on enhancing the relevance of the immune component and conducting further characterizations on the differences in cell behavior, including flow cytometry and cell transcriptomes, in both dynamic and static conditions.

5. Conclusion

The development of more advanced respiratory models for use in disease modeling is a promising avenue of research to speed up and increase the efficiency of therapeutic development. This study aimed to characterize an alginate/gelatin/collagen solution, incorporate multiple cell types (including HPFs, THP-1 cells, and HBEpCs), and use 3D bioprinting to form a complex hierarchical respiratory tissue model. The influence of culturing the printed constructs in a breath-mimicking bioreactor was evaluated alongside the effect of incorporating a growth factor-loaded nanoparticle system, followed by testing the ability of this model to function as an infection model for IAV. The results demonstrated that the synthesized solution was highly printable and mechanically stable over a 28-day culture period while demonstrating a high degree of biocompatibility. Further, the incorporated primary cells were able to maintain high viability during long-term culture, with the bioreactor and controlled release system enhancing cellular metabolism. These constructs supported IAV infection, demonstrating a similar cytokine release profile as that of a 2D *in vitro* model while demonstrating a more clinically relevant clustered infection pattern. Overall, this study demonstrated the feasibility and benefits of using a 3D-bioprinted model in infection studies, with the possibility of expanding its application to therapeutic testing.

Acknowledgments

The authors would like the thank Nathalie Berube for her assistance and training on RNA extraction and RT-qPCR techniques. The authors would also like to thank the Kurreck lab (TU Berlin) for sharing their knowledge and "baby-pool" design, which was slightly modified for use in this study.

Funding

This study was supported by the University of Saskatchewan Dean's Scholarship to Amanda Zimmerling; the Natural Science and Engineering Research Council of Canada (NSERC) Canada Graduate Scholarship-Doctoral (CGS-D) to Amanda Zimmerling; and the Discovery Grants from NSERC to Yan Zhou and Xiongbiao Chen. VIDO receives operational funding from the Government of Saskatchewan through Innovation Saskatchewan and the Ministry of Agriculture and from the Canada Foundation for Innovation through the Major Science Initiatives. This work is published with the permission of the director of VIDO as manuscript series #1049.

Conflict of interest

Authors declare they have no competing interests. The funders had no role in the design of the study; in the collection, analyses, or interpretation of data; in the writing of the manuscript; or in the decision to publish the results.

Author contributions

Conceptualization: Amanda Zimmerling
Data curation: Amanda Zimmerling, Kathryn Avery, Xavier Tabil
Formal analysis: Amanda Zimmerling, Kathryn Avery, Xavier Tabil
Funding acquisition: Amanda Zimmerling, Yan Zhou, Xiongbiao Chen
Investigation: Amanda Zimmerling, Lauren Aubrey, Kathryn Avery, Xavier Tabil
Methodology: Amanda Zimmerling, Lauren Aubrey, Jim Boire
Resources: Jim Boire, Yan Zhou, Xiongbiao Chen
Supervision: Yan Zhou, Xiongbiao Chen
Validation: Amanda Zimmerling, Jim Boire
Writing - original draft: Amanda Zimmerling
Writing - review & editing: Amanda Zimmerling, Lauren Aubrey, Kathryn Avery, Xavier Tabil, Yan Zhou, Xiongbiao Chen

All authors have read and agreed to the published version of the manuscript.

Ethics approval and consent to participate

Not applicable.

Consent for publication

Not applicable.

Availability of data

All data collected and analyzed in this manuscript are available upon reasonable request from the corresponding author.

References

1. Naghavi M, Antony C, Brauer M, et al. GBD 2019 Chronic Respiratory Diseases Collaborators. Global burden of chronic respiratory diseases and risk factors, 1990–2019: an update from the global burden of disease study 2019. *eClinicalMedicine*. 2023;59:101936. doi: 10.1016/j.eclinm.2023.101936
2. Viegi G, Maoi S, Fasola S, Baldacci S. Global burden of chronic respiratory diseases. *J Aerosol Med Pulm Drug Deliv*. 2020;33(4):1-38. doi: 10.1089/jamp.2019.1576

3. Macias A, McElhaney J, Chaves S, et al. The disease burden of influenza beyond respiratory illness. *Vaccine*. 2021;39:A6-A14. doi: 10.1016/j.vaccine.2020.09.048

4. World Health Organization. Influenza (Seasonal). https://www.who.int/news-room/fact-sheets/detail/influenza-(seasonal). Accessed January 24, 2024

5. Yamauchi Y. Chapter one – influenza A virus uncoating. *Adv Virus Res*. 2020;106:1-38. doi: 10.1016/bs.aivir.2020.01.001

6. Suarez D. Influenza A virus. In: *Animal Influenza*. Ames, Iowa, USA:John Wiley & Sons, Inc.;2017:1-29. doi: 10.1002/9781118924341.ch1

7. Julkunen I, Melen K, Nyqvist M, Pirhonen J, Sareneva T, Matikainen S. Inflammatory responses in influenza A virus infection. *Vaccine*. 2000;19(1):S32-S37. doi: 10.1016/S0264-410X(00)00275-9

8. Borau M, Stertz S. Entry of influenza A virus into host cells – recent progress and remaining challenges. *Curr Opin Virol*. 2021;48:23-29. doi: 10.1016/j.coviro.2021.03.001

9. Zhang Y, Xu Z, Cao Y. Host-virus interaction: how host cells defend against influenza A virus infection. *Viruses*. 2020;12(4):376. doi: 10.3390/v12040376

10. Mifsud E, Kuba M, Barr I. Innate immune responses to influenza virus infections in the upper respiratory tract. *Viruses*. 2021;13(10):2090. doi: 10.3390/v13102090

11. Gu Y, Zuo X, Zhang S, et al. The mechanism behind influenza virus cytokine storm. *Viruses*. 2021;13(7):1362. doi: 10.3390/v13071362

12. Julkunen I, Sareneva T, Pirhonen J, Ronni T, Melen K, Matikainen S. Molecular pathogenesis of influenza A virus infection and virus-induced regulation of cytokine gene expression. *Cytokine Growth Factor Rev*. 2001;12(2-3):171-180. doi: 10.1016/S1359-6101(00)00026-5

13. Betakova T, Kostrabova A, Lachova V, Turianova L. Cytokines induced during influenza virus infection. *Curr Pharm Des*. 2017;23(18):2616-2622. doi: 10.2174/1381612823666170316123736

14. Matsushima K, Yang D, Oppenheim J. Interleukin-8: an evolving chemokine. *Cytokine*. 2022;153:155828. doi: 10.1016/j.cyto.2022.155828

15. Can F, Ozkurt Z, Ozturk N, Sezen S. Effect of IL-6, IL-8/CXCL8, IP-10/CXCL 10 levels on the severity in COVID 19 infection. *Int J Clin Pract*. 2021;75(12):e14970. doi: 10.1111/ijcp.14970

16. Wang J, Oberley-Deegan R, Wang S, et al. Differentiation human alveolar type II cells secrete antiviral IL-29 (IFN-λ1) in response to influenza A infection. *J Immunol*. 2012;188(5):1924-1932. doi: 10.4049/jimmunol.1101987

17. Vastani Z, Ahmadi A, Abounoori M, et al. Interleukin-29 profiles in COVID-19 patients: survival is associated with IL-29 levels. *Health Sci Rep*. 2022;5(2):e544. doi: 10.1002/hsr2.544

18. Niu J, Wu S, Chen M, et al. Hyperactivation of the NLRP3 inflammasome protects mice against influenza A virus infection via IL-1β mediated neutrophil recruitment. *Cytokine*. 2019;120:115-124. doi: 10.1016/j.cyto.2019.04.019

19. Robinson K, Choi S, McHugh K, et al. Influenza A exacerbates staphylococcus aureus pneumonia by attenuating IL-1β production in mice. *J Immunol*. 2013;191(10):5153-5159. doi: 10.4049/jimmunol.1301237

20. Wang W, Yang P, Zhong Y, et al. Monoclonal antibody against CXCL-10/IP-10 ameliorates influenza A (H1N1) virus induced acute lung injury. *Cell Res*. 2013;23:577-580. doi: 10.1038/cr.2013.25

21. Hayney M, Henrique K, Barnet J, et al. Serum IFN-γ-induced protein 10 (IP-10) as a biomarker for severity of acute respiratory infection in healthy adults. *J Clin Virol*. 2017;90:32-37. doi: 10.1016/j.jcv.2017.03.003

22. Zimmerling A, Zhou Y, Chen X. Bioprinted constructs for respiratory tissue engineering. *Bioprinting*. 2024;24:1-29. doi: 10.1016/j.bprint.2024.100135

23. O'Leary C, Gilbert J, O'Dea S, O'Brien F, Cryan S. Respiratory tissue engineering: current status and opportunities for the future. *Tissue Eng Part B Rev*. 2015;21(4):323-344. doi: 10.1089/ten.TEB.2014.0525

24. Shrestha J, Paudel K, Nazari H, et al. Advanced models for respiratory disease and drug studies. *Med Res Rev*. 2023;43(5):1470-1504. doi: 10.1002/med.21956

25. Baroon S, Saez J, Owens R. *In vitro* models for studying respiratory host–pathogen interactions. *Adv Biol*. 2021;5(6). doi: 10.1002/adbi.202000624

26. Bouvier N, Lowen A. Animal models for influenza virus pathogenesis and transmission. *Viruses*. 2010;2(8):1530-1563. doi: 10.3390/v20801530

27. Nguyen T, Rollon R, Choi Y. Animal models for influenza research: strengths and weaknesses. *Viruses*. 2021;13(6):1011. doi: 10.3390/v13061011

28. Chen X, Anvari-Yazdi A, Duan X, et al. Biomaterials/bioinks and extrusion bioprinting. *Bioact Mater*. 2023;28:511-536. doi: 10.1016/j.bioactmat.2023.06.006

29. Mahfouzi S, Tali S, Amoabediny G. 3D bioprinting for lung and tracheal tissue engineering: criteria, advances, challenges, and future directions. *Bioprinting*. 2021;21:e00124. doi: 10.1016/j.bprint.2020.e00124

30. Carpio M, Dabaghi M, Ungureanu J, Kolb M, Hirota J, Moran-Mirabal J. 3D bioprinting strategies, challenges, and opportunities to model the lung tissue microenvironment and its function. *Front Bioeng Biotechnol*. 2021;9:773511. doi: 10.3389/fbioe.2021.773511

31. Labowska M, Cierluk K, Jankowska A, Kulbacka J, Detyna J, Michalak I. A review on the adaption of alginate-gelatin hydrogels for 3D cultures and bioprinting. *Materials*. 2021;14(4):85. doi: 10.3390/ma14040858

32. Geevarghese R, Somasekharan L, Bhatt A, Kasoju N, Nair R. Development and evaluation of a multicomponent bioink consisting of alginate, gelatin, diethylaminoethyl cellulose and collagen peptide for 3D bioprinting of tissue construct for drug screening application. *Int J Biol Macromol*. 2022;207:278-288. doi: 10.1016/j.ijbiomac.2022.02.191

33. Zimmerling A, Sunil C, Zhou Y, Chen X. Development of a nanoparticle system for controlled release in bioprinted respiratory scaffolds. *J Funct Biomater*. 2024;15:20. doi: 10.3390/jfb15010020

34. Zimmerling A, Boire J, Zhou Y, Chen X. Influence of breath-mimicking ventilated incubation on 3D bioprinted respiratory tissue scaffolds. *ASME J Biomech Eng*. 2024;146(9):091004. doi: 10.1115/1.4065214

35. Butler D, Goldstein S, Guldberg R, et al. The impact of biomechanics in tissue engineering and regenerative medicine. *Tissue Eng Part B Rev*. 2009;15(4):477-484. doi: 10.1089/ten.teb.2009.0340

36. Gresham R, Bahney C, Leach J. Growth factor delivery using extracellular matrix-mimicking substrates for musculoskeletal tissue engineering and repair. *Bioact Mater*. 2021;6(7):1945-1956. doi: 10.1016/j.bioactmat.2020.12.012

37. Nossa R, Costa J, Cacaopardo L, Ahluwalia A. Breathing *in vitro*: designs and applications of engineered lung models. *J Tissue Eng*. 2021;12:20417314211008696. doi: 10.1177/20417314211008696

38. Huang D, Liu T, Liao J, et al. Reversed-engineered human alveolar lung-on-a-chip model. *Proc Natl Acad Sci USA*. 2021;118(19):e2016146118. doi: 10.1073/pnas.2016146118

39. Kang D, Park J, Kim W, et al. All-inkjet printed 3D alveolar barrier model with physiologically relevant microarchitecture. *Adv Sci*. 2021;8:2004990. doi: 10.1002/advs.202004990

40. Horvath L, Umehara Y, Jud C, Blank F, Petri-Fink A, Rothen-Rutishauser B. Engineering an *in vitro* air-blood barrier by 3D bioprinting. *Sci Rep*. 2015;5:7974. doi: 10.1038/srep07974

41. Berg J, Hiller T, Kissner M, et al. Optimization of cell-laden bioinks for 3D bioprinting and efficient infection with influenza A virus. *Sci Rep*. 2018;8:13877. doi: 10.1038/s41598-018-31880-x

42. Berg J, Weber Z, Fechler-Bitteti M, et al. Bioprinted multi-cell type lung model for the study of viral inhibitors. *Viruses*. 2021; 13:1590. doi: 10.3390/v13081590

43. Liu G, Park H, Pyo H, Liu Q, Zhou Y. Influenza A virus panhandle structure is directly involved in RIG-I activation and interferon induction. *J Virol*. 2015;89(11):6067-6079. doi: 10.1128/JVI.00232-15

44. Panganiban R, Day R. Hepatocyte growth factor in lung repair and pulmonary fibrosis. *Acta Pharmacol Sin*. 2010;32:12-20. doi: 10.1038/aps.2010.90

45. Zimmerling A, Zhou Y, Chen X. Synthesis of alginate/collagen bioinks for bioprinting respiratory tissue models. *J Funct Biomater*. 2024;15:90. doi: 10.3390/jfb15040090

46. Malekpour A, Chen X. Printability and cell viability in extrusion-based bioprinting from experimental, computational, and machine learning views, *J Funct Biomater.* 2022;13(2):40. doi: 10.3390/jfb13020040

47. Fu ZQ, Naghieh S, Xu CC, Wang CJ, Sun W, Chen XB. Printability in extrusion bioprinting. *Biofabrication.* 2021; 13(3):033001. doi: 10.1088/1758-5090/abe7ab

48. Sousa dos Santos K, Oliveira L, de Lima Fontes M. et al. Alginate-based 3D A549 cell culture model to study paracoccidioides infection. *J. Fungi.* 2023;9(6):634. doi: 10.3390/jof9060634

49. Zhang J, Zhang W, Ren L, et al. Astragaloside IV attenuates IL-1β secretion by enhancing autophagy in H1N1 infection. *Microbiol Letters.* 2020;367(4):fnaa007. doi: 10.1093/femsle/fnaa007

50. Gao J, Gao L, Li R, Lai Z, Zhang Z, Fan X. Integrated analysis of microRNA-nRNA expression in A549 cells infected with influenza A viruses (IAVs) from different host species. *Virus Res.* 2019;263:34-46. doi: 10.1016/j.virusres.2018.12.016

51. Mondrinos M, Lelkes P, Samadikuchaksaraei A, Mantalaris A, Polak J. Lungs. In: *Principles of Tissue Engineering (Fourth Edition)*. San Diego, USA: Academic Press/Elsevier;2014:1560-1577 doi: 10.1016/B978-0-12-398358-9.00074-4

52. Kim W, Lee Y, Kang D, Kwak T, Lee H, Jung S. 3D inkjet-bioprinted lung-on-a-chip. *ACS Biomater Sci Eng.* 2023;9:2806-2815. doi: 10.1021/acsbiomaterials.3c00089

ACCSCIENCE PUBLISHING

International Journal of Bioprinting

RESEARCH ARTICLE

Evaluation of 3D-bioprinted skin scaffolds in mice along with gold nanoparticle exposure

Yi Wang[1,2], Xin Ma[1,3], Xu Wu[4], Shuaideng Wang[1], Peng Peng[1,2], Guozhang Tang[1,3], Xinya Qin[5,6], Xinmeng Wang[7]*, Chenwei Wang[1]*, and Jiangning Zhou[5]

[1]School of Basic Medical Sciences, Anhui Medical University, Hefei, Anhui, China

[2]First School of Clinical Medicine, Anhui Medical University, Hefei, Anhui, China

[3]Second School of Clinical Medicine, Anhui Medical University, Hefei, Anhui, China

[4]Chinese Academy of Sciences Key Laboratory of Brain Function and Diseases, School of Life Sciences, University of Science and Technology of China, Hefei, Anhui, China

[5]Institute of Brain Science, The First Affiliated Hospital of Anhui Medical University, Hefei, Anhui, China

[6]Institute of Artificial Intelligence, Hefei Comprehensive National Science Center, Hefei, Anhui, China

[7]Department of Pharmacy, The First Affiliated Hospital of Anhui Medical University, Hefei, Anhui, China

Abstract

The progress in nanomedicine has sparked increasing concerns regarding its applications with biocompatible materials. Here, we assessed and optimized a three-dimensional (3D) bioprinting technique by testing various printing parameters with multiple cell types. Cell-laden scaffolds were designed, cultivated, imaged, and transplanted onto the dorsal skin of nude mice. The structure of bioprinted scaffolds retained its shape and dimensions with no cell migration between layers. Moreover, gold nanoparticles (GNPs) were intravenously administered to transplanted nude mice and aggregately deposited in the cell-laden scaffolds. Importantly, GNPs exhibited extensive accumulation in bioprinted scaffolds compared to natural skin and other organs *in vivo*. GNPs accumulated in the dermis of the transplanted scaffolds, while they stayed in the subcutaneous tissue of the natural skin with no permeation to the dermis, indicating a high absorption tendency of GNPs for artificial scaffolds. The results revealed a lack of similarity between the artificial skin scaffolds and natural skin, which may diminish their potential as artificial skin substitutes. Furthermore, the absorption property of 3D-bioprinted scaffolds suggests their potential as (i) a therapeutic method to absorb and excrete GNPs; and (ii) a strategy for targeted drug delivery of GNPs.

***Keywords*:** 3D bioprinting; Skin scaffolds; Gold nanoparticles; Biodistribution; *In vivo* transplant

***Corresponding authors:**
Chen-Wei Wang
(cwwang@ustc.edu.cn)

Xin-Meng Wang
(wxinmeng@ustc.edu.cn)

Citation: Wang Y, Ma X, Wu X, et al. Evaluation of 3D-bioprinted skin scaffolds in mice along with gold nanoparticle exposure. *Int J Bioprint*. 2024;10(6):4692. doi: 10.36922/ijb.4692

Received: August 29, 2024
Revised: September 24, 2024
Accepted: October 2, 2024
Published Online: October 2, 2024

Copyright: © 2024 Author(s). This is an Open Access article distributed under the terms of the Creative Commons Attribution License, permitting distribution, and reproduction in any medium, provided the original work is properly cited.

Publisher's Note: AccScience Publishing remains neutral with regard to jurisdictional claims in published maps and institutional affiliations.

1. Introduction

Within the last decade, research efforts in the field of tissue engineering continue to address the unmet need for artificial tissues and organs for transplantation.[1] Among these

studies, effective treatment is crucial to prevent morbidity or mortality in patients with skin injuries resulting from burns, infections, cancer surgery, and other genetic and somatic diseases.[2] To address these challenges, three-dimensional (3D) bioprinting, as an additive manufacturing technology to fabricate biological constructs with hierarchical architecture similar to their native counterparts, offers significant advantages in fabricating artificial skin substitutes.[3] 3D bioprinting has adopted various techniques, including inkjet-based bioprinting,[4] laser-assisted bioprinting,[5] extrusion-based bioprinting,[6] and stereolithography bioprinting,[7] to improve the viability of cells and biomaterials. Using a pneumatic micro-extrusion-based 3D freeform fabrication technology, artificial scaffolds can be fabricated by precisely positioning various types of matrix materials and cells in a layer-by-layer assembly, with appropriate structures and cell compositions in different sizes, high throughput, and reproducible fashion.[8] Artificial skin scaffolds are mainly fabricated using cell lines and stem cells with adequate structures and viability. Recently, organoid engineering holds significant promise for fabricating skin substitutes, leveraging the self-renewal and differentiation capabilities to create complex structures that mimic the morphology and function of native tissues.[9–11] Thus, with these significant improvements in the areas of bioinks, printing techniques, and various cell types, 3D bioprinting has become a reliable and promising approach to fabricating artificial tissue for skin transplantation.

Besides grafts, 3D-bioprinted scaffolds can also be used as implants for drug delivery, serving as physical protection for wounds and a depot to release therapeutic drugs.[12] Notably, nanoparticles, including gold nanoparticles (GNPs), are increasingly utilized as carriers for the delivery of drugs,[13] genetic materials,[14] and antigens.[15,16] For skin wound healing, GNPs have been widely used as delivery devices for drugs and antimicrobial agents.[17,18] Most studies employ GNPs for transdermal drug delivery.[19,20] In this regard, employing GNP delivery systems in artificial skin grafts raises concerns about potential risks.[21] However, the retention, deposition, and biodistribution of GNPs in the fabricated scaffold still require detailed investigation.

For this purpose, cell-laden scaffolds were bioprinted and transplanted on the dorsal back of nude mice for 11 days along with GNP exposure. Importantly, the retention and biodistribution of GNPs in skin scaffolds and other tissues were investigated in transplanted mice after tail-vein injection.

2. Methods

2.1. Development of a 3D bioprinter

A robotic bioprinting system utilizing pneumatic micro-extrusion-based 3D freeform fabrication technology was developed. The overall schematic of the 3D bioprinting hardware is displayed in Figure S1, Supplementary File. This system is capable of accurately positioning cells, extracellular matrix (ECM), and growth factors in any desired 3D configuration. Each dispenser operates independently with electromechanical valves and is mounted on a high-precision XYZ robotic stage with three axes. The liquid materials are dispensed using pneumatic pressure during the micro-valves' gate-opening phase. Moreover, the volume of the dispensed droplets (drop size) can be adjusted by controlling the valve opening time and air pressure. The non-contact dispensers can dispense cells in volumes of 769.5 nL, maintaining high cell viability. The dispensed volume is regulated by digitally controlling the pressure and pulse duration (3 ms). The system allows for continuous dispensing at an actuation frequency of 200 Hz, ensuring high-throughput printing. The minimum printing resolution varies with material viscosity: 400 μm for aqueous materials (e.g., water and cell culture media), and higher resolution for viscous substances (e.g., collagen and matrix proteins). The bioprinting resolution can be systematically adjusted by controlling the dispensed droplet volume. Both the syringe and building plate were maintained at 4°C.

2.2. Optimization of bioprinting parameters

Before cell-laden scaffold bioprinting, we conducted experiments on the optimization of bioprinting parameters with ultrapure water and different types of cells, such as human epidermal keratinocytes (HEK; 2110; ScienCell, United States of America [USA]) and human dermal fibroblasts (HDF; 2320; ScienCell, USA). Different air pressures (2, 4, 6, 8, 10, 12, 14, 16, 18, and 20 psi) and internal needle diameters (0.18, 0.23, 0.26, 0.3, 0.34, and 0.41 mm) were investigated with ultrapure water to test the performance and sensitivity of the machine. Furthermore, the required pulses of 1 mL ultrapure water were examined as a reference for comparison.

Cell viability was tested at different bioprinting air pressures, internal needle diameters, and cell suspension densities to determine the optimum conditions for each cell type. Combinations of various bioprinting air pressures (2, 4, 6, 8, and 10 psi), internal needle diameters (0.2, 0.25, 0.3, 0.35, and 0.4 mm), and cell suspension densities (0.5, 0.75, 1, 2, and 3×10^6 cells/mL for HDF; 0.5, 1, 2, 3, and 5×10^6 cells/mL for HEK) were tested. Various bioprinting air pressures were examined with 0.2 mm internal needle diameter and cell suspension densities of 2×10^6 cells/mL (Figure 1G and J). Additionally, various internal needle diameters were examined with an air pressure of 0.2 psi and cell suspension densities of 2 million cells/mL (Figure 1H and K), as cell suspension densities were examined with 0.2 mm internal needle diameter and an air pressure of 0.2 psi (Figure 1I and L).

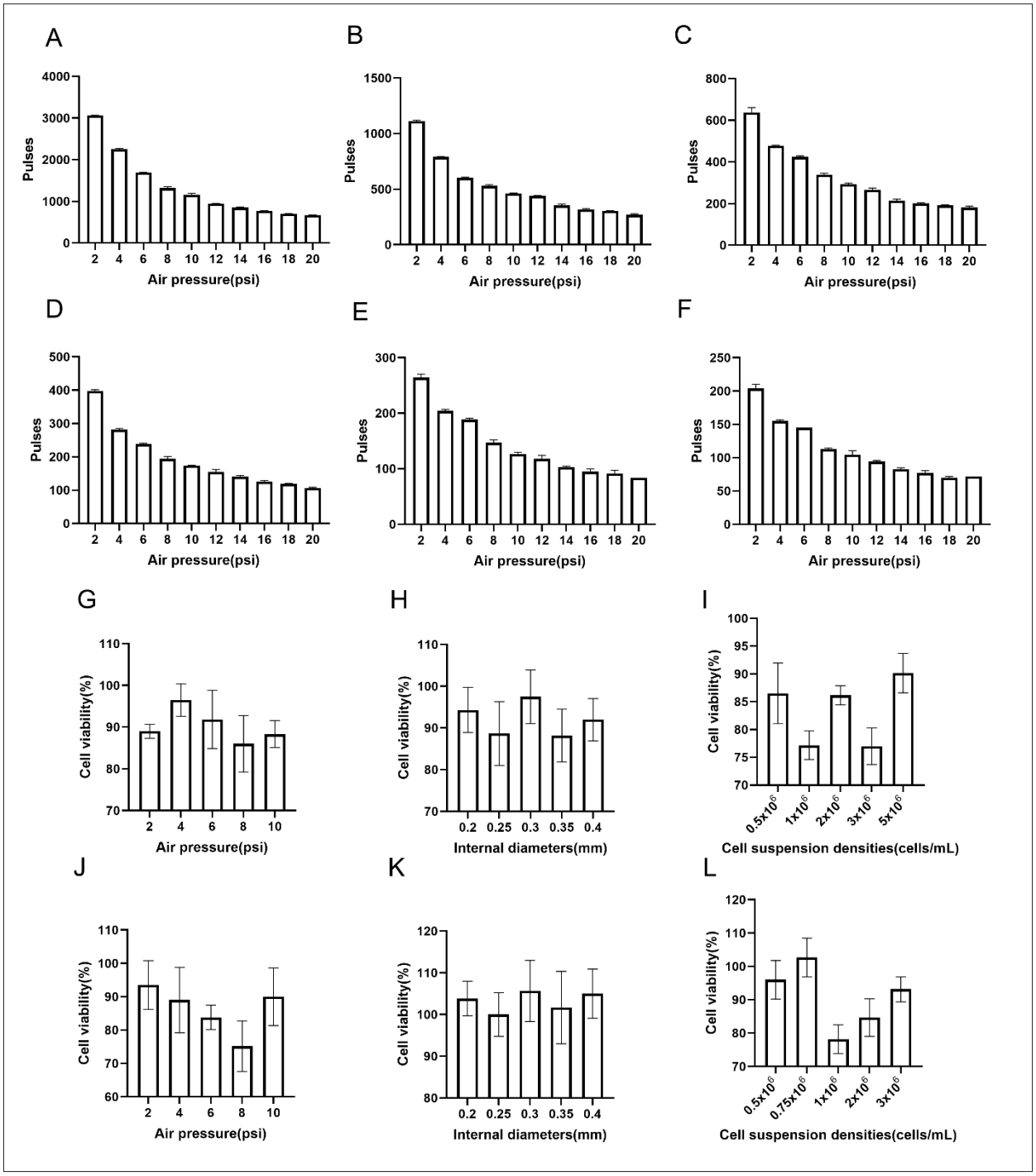

Figure 1. Numbers of pulses for the extrusion of 1 mL ultrapure water and MTT assay at different air pressures, internal diameters, and cell suspension densities. (A–F) Examination of the numbers of pulses at different air pressures (2–20 psi) with internal needle diameters of 0.41 (A), 0.34 (B), 0.3 (C), 0.26 (D), 0.23 (E), and 0.18 mm (F). (G–I) The cell viability of HEKs was examined at different air pressures (G), internal diameters (H), and different cell suspension densities (I). (J–L) The cell viability of HDFs was examined at different air pressures (J), internal diameters (K), and different cell suspension densities (L). The results are presented as the mean ± standard deviation; A–F, $n = 3$, and for G–L, $n = 6$. Abbreviations: HDFs, human dermal fibroblasts; HEKs, human epidermal keratinocytes.

The bioprinted cells were then placed in an incubator with culture media. Cell viability was determined by using a 3-(4,5-dimethylthiazol-2-yl)-2,5-diphenyltetrazolium bromide colorimetric (MTT) assay. Briefly, cells were seeded in 96-well plates and incubated, and cells were selected during the logarithmic phase and were subject to different treatment regimens. After the treatment, cells were washed with phosphate-buffered saline (PBS) and then incubated in MTT solution for 4 h. After dimethyl sulfoxide was added into each well, the absorbance was measured at 490 nm to determine the cell viability with a microplate reader. The acquired absorbance in each group was divided by the absorbance of the unprinted cells to indicate the viability of the printed cells. All the tests were operated through the MitoTracker® Deep Red FM (M22426; Life Technologies, USA).

Cell viability was also examined by live-dead staining at different internal needle diameters (0.2, 2.25, 0.3, 0.35, and 0.4 mm) to determine the optimum conditions for cell viability for each cell type. Cell viability was measured via confocal microscopy (Olympus BX53; Olympus, Japan) using Hoechst 33342 (E607302; Sangon Biotech, China) and propidium iodide (E607306; Sangon Biotech, China) staining at days 1, 4, and 7.

2.3. Cell transfection

Through liposome transfection, the plasmid PE-GFP-N1 was transfected into fibroblasts (HDF-1), whereas the plasmid pCMV DsRed-Express2 was transfected into keratinocytes (HEK). Thus, stable GFP-HEK and RFP-HDF cell lines were successfully obtained. After transfection, fibroblasts and keratinocytes were cultured with DMEM/F12 DMEM (1:1; Sigma-Aldrich, USA) supplied with 10% fetal bovine serum (GIBCO, USA) at 37°C in a 5% CO_2 humidified atmosphere.

2.4. Cell-laden scaffold composites

Bioprinted skin was achieved using a layer-by-layer fabrication approach, as described in Figure 2. For these presented skin scaffolds, the cells were trypsinized and centrifuged. The cells were then extruded at 1.75 psi and 0.25 mm diameter. For pattern 3, a pellet containing 50×10^6 GFP-HEK cells/cm^2 was resuspended in a mixture of 50 µL collagen (Collagen Type I, RatTail; BD Biosciences, USA), 10 µL 10× PBS, and 3 µL sodium hydroxide (0.1 M NaOH) for neutralization, whereas a pellet containing 10×10^6 RFP-HDF cells/cm^2 was resuspended in the same solution. The cell-laden scaffold structure with embedded cells was constructed on poly-D-lysine-coated glass-bottom Petri dishes (MatTek, USA). The cell-laden scaffold was fixed at 37°C for 30 min and then immersed in a complete medium overnight. We also tested the composites containing 60×10^6 GFP-HEK cells/cm^2 and 30×10^6 RFP-HDF cells/cm^2 for pattern 1, and 50×10^6 GFP-HEK cells/cm^2 and 15×10^6 RFP-HDF cells/cm^2 for pattern 2. For better vascularization, 10 ng/mL of vascular endothelium growth factor 165 (VEGF 165) was added into the GFP-HEK and RFP-HDF layers.

2.5. Bioprinted skin construction transplant

All animal experiments were evaluated and approved by the Institutional Animal Care and Use Committee of Anhui Medical University (LLSC20211388). Nude mice (BALB/cASlac-nu) were obtained from Shanghai SLAC Laboratory Animal Co. Ltd. (China). They received standardized food and water, living with a day-night cycle of 12 h each. Animals were used for the experiments when they were 6 weeks old. The nude mice were deeply anesthetized with pentobarbital sodium (80 mg/kg, i.p.); then, natural dorsal skin of 2.5 cm in diameter was carefully cut off and replaced by bioprinted skin at the same size. After 30 min, the wound was sealed with a Vaseline filter membrane and bandaged with three to four layers of medical gauze for 11 days. The transplanted skin was removed 11 days later and used for subsequent experiments. All animals survived the surgical intervention and dorsal implantation procedure well, exhibiting no signs of discomfort or changes in sleeping and feeding habits. The procedure is illustrated in Figure 3A.

2.6. Histology

The transplanted skin was removed after sacrifice and sliced with a cryotome (20 µm) on a cryostat (Leica CM1860; Leica Biosystems, Germany). Each slide was washed with PBS twice. Transplanted tissue sections were stained with hematoxylin and eosin (H&E) for histopathological assessment. For immunohistochemistry, the sections were incubated in 0.3% (v/v) Triton X-100 for 0.5 h, blocked with 5% normal goat serum for 30 min, and then incubated overnight at 4°C with primary antibodies against Mouse CD31 McAb (1:200, Cat. #66065-1-lg; Proteintech, USA). Following washing with PBS, sections were incubated for 1 h at 37°C with biotinylated horse anti-mouse IgG (1:200, BA-2000; Vector laboratories, USA). Sections were then washed and incubated with standard avidin-biotin complex (ABC; PK-4000; Vector laboratories, USA) for 1 h at 37°C. Antibody binding was revealed using H_2O_2 as a substrate and diaminobenzidine as chromogen. Counterstaining was performed with hematoxylin. All sections were analyzed by microscopy (Olympus BX53; Olympus, Japan).

2.7. Injection of gold nanoparticles

Gold nanoparticles (16 nm) functionalized by polyethylene glycol (PEG) were synthesized as previously described.[22] The actual intravenous administration concentration was about 253 mg Au/kg 5 days after the bioprinted skin

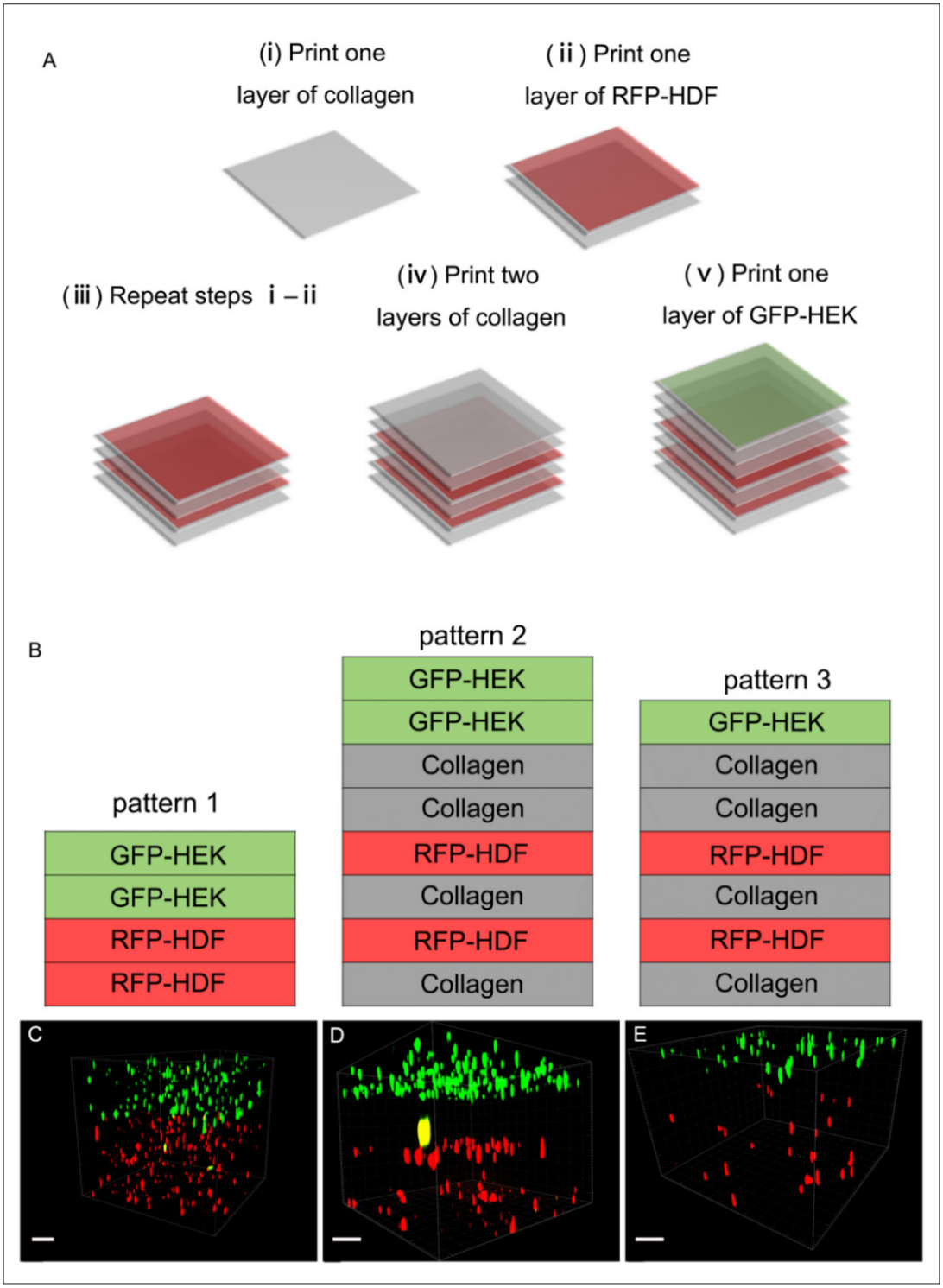

Figure 2. Construction of 3D-bioprinted scaffolds. (A) Collagen matrix and cells (RFP-HDFs, GFP-HEKs) were incorporated via layer-by-layer bioprinting to construct the dermal and epidermal compartments. (B) Schematics of all the tested patterns of the 3D-bioprinted tissue are presented in the cross-section view. (C–E) Before transplantation, 3D structures of three kinds of bioprinted patterns (pattern 1 [C], pattern 2 [D], and pattern 3 [E]) were imaged and reconstructed. GFP-HEKs exhibit green fluorescence; RFP-HDFs exhibit red fluorescence. The yellow marking in Figure 2D may be unusual aggregated cells. Scale bars: 200 μm (C–E). Abbreviations: HDFs, human dermal fibroblasts; HEKs, human epidermal keratinocytes.

transplant. The mice's skin was removed 6 days later and used for further experiments.

2.8. Inductively coupled plasma-optical emission spectrometry

Three mice were euthanized at 6 days post-injection. Transplanted skin and other organs were collected and weighed. A section of each part was minced into small pieces, digested, and dissolved in nitric acid and a small amount of hydrochloric acid. The amount of gold was determined using inductively coupled plasma-optical emission spectrometry (ICP-OES; Optima 7300 V ICP-OES; PerkinElmer, USA). Natural skin was obtained from the nearby site of the transplanted collagen scaffold in the same mouse.

2.9. Statistical analysis

Results are presented as mean ± standard deviation unless otherwise indicated. All of the data were analyzed using SPSS Statistics 17.0 (IBM, USA) and processed using GraphPad Prism 7 (GraphPad, USA). Differences between two groups were analyzed using a two-tailed unpaired *t*-test. Differences were considered significant at $p < 0.05$.

3. Results

3.1. Bioprinting parameters estimate

Prior to 3D cell-laden scaffold bioprinting, we examined the utility of the bioprinter by testing serial bioprinting conditions and cell viability. Firstly, different internal needle diameters and air pressures were used to assess the performance of the bioprinter. As anticipated, the number of pulses required to extrude 1 mL of ultrapure water decreased with the internal needle diameter and air pressures. However, little correlation was observed when the air pressures exceeded 12 psi (Figure 1A–F). These results indicated that the bioprinter functioned effectively over a broad range of internal needle diameters and air pressures.

In skin bioprinting, achieving a representative cell density within each layer (epidermis and dermis) is crucial for obtaining morphologically and functionally representative tissue. Various bioprinting air pressures and internal diameter of needles were examined with different types of cells (Figure 1G–L). Both sets of results displayed high cell viability across various pressures and diameters, indicating the stability of the bioprinter under different conditions. The viability of the bioprinted cells appeared to be equivalent to or slightly higher than that of the cells cultivated in the Petri dish. The cell density was optimized by controlling the key bioprinting parameters, such as cell suspension densities.

In addition, live-dead staining was conducted to examine the cell viability under selected conditions with skin cells (Figures S2 and S3, Supplementary File). The range of internal needle diameter had no significant influence on cell viability. As days progressed, the ratio of dead cells gradually increased, consistent with those cultivated directly *in vitro*.

3.2. Bioprinting of cell-laden hydrogel

Figure 2A illustrates the steps used for the bioprinting of the composite 3D skin tissue. To better imitate the spatial skin structure, we designed and investigated three different cell-laden scaffold composites (Figure 2B). After the bioprinting process, the skin tissue was immediately imaged by confocal microscopy and cultured in media under submerged conditions. Figure 2C–E features the uniformly distributed GFP-HEKs in the epidermis and RFP-HDFs in the dermis. The cells were sparsely but uniformly distributed in the collagen matrix in pattern 3, whereas in other patterns, the cells were too dense. The bioprinted cells maintained their shape and viability, and the boundary between layers was distinct, indicating no cell invasion across the dermal and epidermal layers.

3.3. *In vivo* transplant

Over an 11-day period (Figure 3A), the borders of the bioprinted skin construct tightly adhered to the surrounding mouse skin. As time progressed, the previously shining surface of the constructs became matte, yet the wounds gradually reduced in size (Figures 3B–M and S4A, Supplementary File). The healing of the wound injected with GNPs and normal saline was also analyzed on day 11 (Figure S4B, Supplementary File). No interruption of the epidermis could be observed at the junction between the skin scaffolds and the mouse skin (Figures 4, 5, and S5, Supplementary File). The structure of bioprinted scaffolds retained its shape and dimensions. The absence of color merging indicated no cell migration between layers (Figure 4). The HEK layers in patterns 1 and 2 were much thicker than those in pattern 3 (Figures 2C–E and 4), suggesting that the cell density in patterns 1 and 2 was too high for the optimal growth, proliferation, and differentiation of the HEKs.

3.4. Vascularization

Platelet endothelial cell adhesion molecule-1 (PECAM-1, CD31) is a member of the immunoglobulin gene superfamily of cell adhesion molecules. CD31 is a transmembrane glycoprotein that is highly expressed on the surface of the endothelium, making up a large portion of its intercellular junctions. Thus, CD31 can be used as a marker of vascular endothelial and a hint for endothelial formation, consequently aiding in tissue development. Here, the increased expressions of CD31 were found in

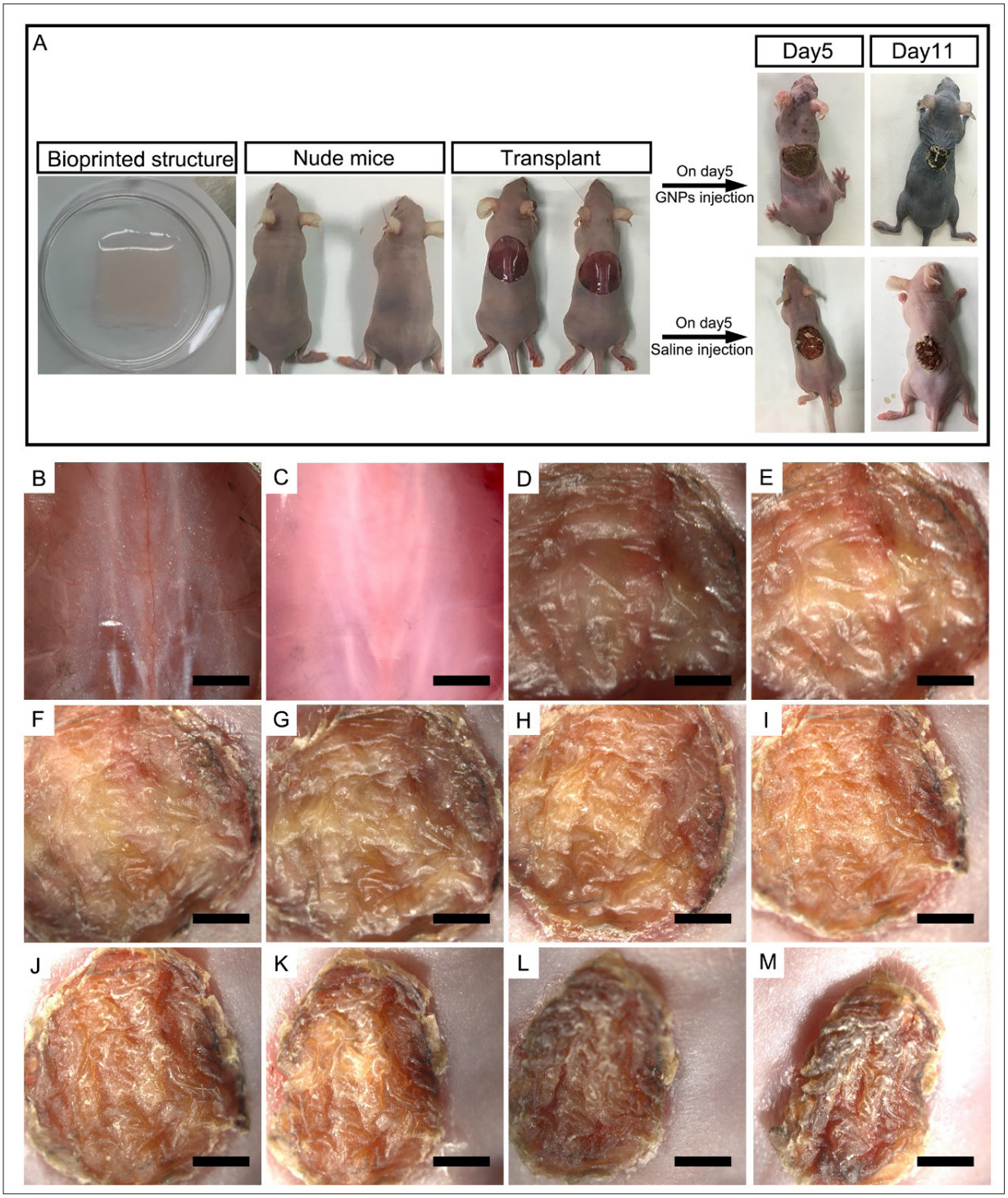

Figure 3. Transplantation on the dorsal skin of nude mice. (A) Illustration of the *in vivo* transplantation and administration processes. Layer-by-layer structures were fabricated using the bioprinter and substituted the dorsal skin of the nude mice. One group was injected with GNPs and another group was injected with saline. The entire bodies of mice from both groups were carefully monitored for 6 days before further experiments. (B–M) The recovery process was illustrated by pictures of a mouse injected with saline with a fresh wound (B) and a scaffold transplanted into the wound directly after implantation (C), as well as on days 1–10 (D–M). Scale bars: 200 μm. Abbreviations: GNP, gold nanoparticle.

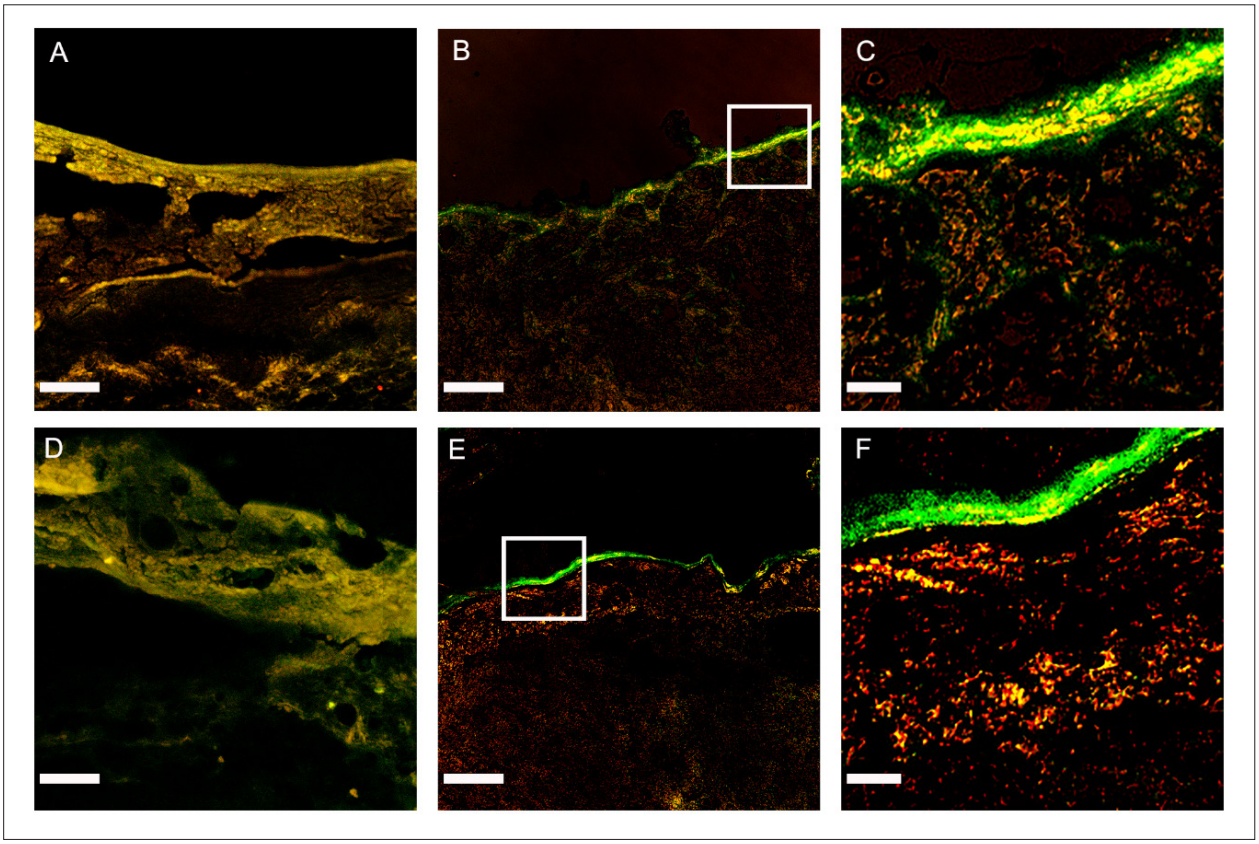

Figure 4. Fluorescence imaging of bioprinted scaffolds. Bioprinted constructs (A–C) and VEGF-added scaffolds (D–F) were captured by fluorescence microscopy 11 days after transplantation. The bioprinted structures of pattern 2 (A and D) and pattern 3 (B and E) were imaged. (C and F) Magnified view of the boxed regions in (B) and (E), respectively. Scale bars: 100 μm (A, B, D, and E); 20 μm (C and F).

the VEGF-added skin scaffolds, indicating the growth of primary vessels from the depth of the wound bed in the direction of the bioprinted cell layers and the enhanced vascularization of the skin scaffolds (Figure 5).

3.5. Gold nanoparticle exposure

To further investigate the biodistribution of GNPs in transplanted skin *in vivo*, nude mice were tail-vein injected 16-nm GNPs functionalized with the anti-fouling polymer-methoxy-terminated polyethylene glycol (mPEG) 5 days after transplantation and monitored for 6 days post-injection. The skin scaffolds were subsequently examined by H&E and CD31 immunohistochemistry staining. Compared with the natural skin, the dermis of the skin scaffolds was thicker and the seeded cells were dense and uniformly. The black dots observed represent clustered GNPs without staining as observed under the light microscope. Notably, the injected GNPs easily aggregated and deposited in the dermis of the skin scaffolds, whereas in natural skin tissue, GNPs accumulated and stayed in subcutaneous tissue with no permeation to the dermis (Figure 5C, D, G, H, K, and L). In addition, the ECM of the 3D-bioprinted skin scaffolds displayed little similarity with natural skin in H&E staining. Furthermore, the penetration appeared more severe in the VEGF-added group (Figure 5G and K). No GNPs were detected in the epidermis in either group.

The concentration of Au in the collagen scaffold and each organ was quantified by ICP-OES (Figure 6). The GNPs accumulated in the collagen scaffold (2.5 mg/g), spleen (1.606 mg/g), natural skin (1.070 mg/g), liver (0.915 mg/g), and kidneys (0.364 mg/g), suggesting that the collagen scaffold has stronger adsorption to GNPs. GNP accumulation in the collagen scaffold significantly exceeded that in other organs ($p = 0.0174$ [spleen], 0.0047 [natural skin], 0.0042 [liver], 0.0008 [kidney], 0.0005 [muscle], and 0.0004 [bone, heart, lung, and brain]). The concentration of GNPs accumulated in the collagen scaffold (2.5 mg/g) was 10.6 times that of the injected concentration (0.235 mg/g) and 2.3 times that of the concentration accumulated in the natural skin (1.070 mg/g).

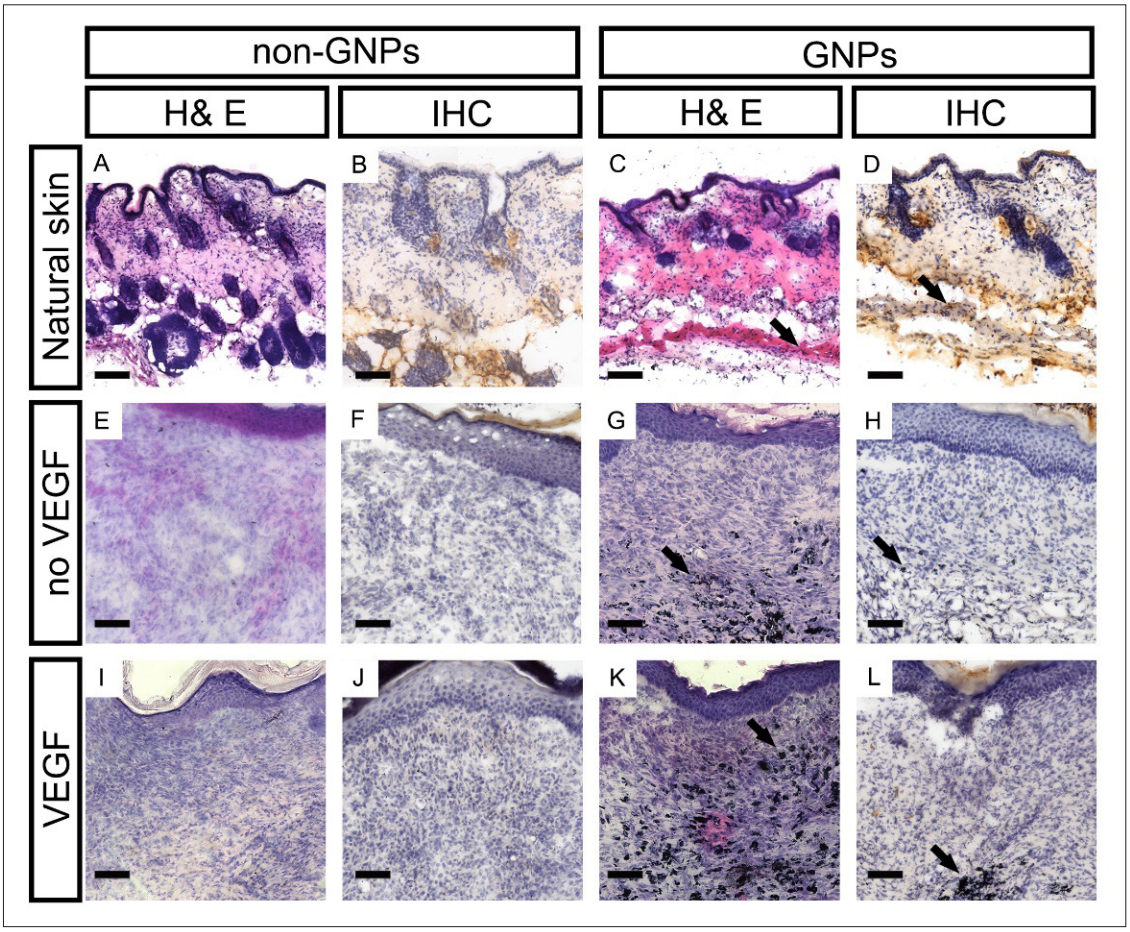

Figure 5. Hematoxylin and eosin (H&E) and immunohistochemistry (IHC) staining of the transplanted scaffolds 6 days after transplantation. Gold nanoparticles (GNPs) were detected in the subcutaneous tissue, but they did not penetrate the dermis of the natural mouse skin (C and D). However, GNPs can be detected in the dermis of the transplanted skin (G, H, K, and L). H&E staining of natural skin (A and C) and transplanted scaffolds without (E and G) or with VEGF (I and K) was illustrated. Vascularization of the skin was illustrated by anti-CD31 staining of natural skin (B and D) and transplanted scaffolds without (F and H) or with VEGF (J and L). The black dots represent clustered GNPs, observed without staining under a light microscope. Black arrows indicate GNP depositions. Scale bars: 100 μm (A, C, E, G, I, and K); 200 μm (B, D, F, H, J, and L).

4. Discussion

3D bioprinting is a promising technology to fabricate design-specific skin constructs that imitate natural skin, the largest organ in direct contact with the outside world and vulnerable to injury. In previous studies, skin substitutes were created using laser-assisted bioprinting and assessed *in vivo*.[12] Furthermore, stratified skin cellular structures were designed,[23] bioprinted, analyzed *in vivo*,[2] and observed on both planar and non-planar surfaces.[24] In our study, three patterns of 3D cell-laden bioprinted skin scaffolds were designed and evaluated. Histology and fluorescence imaging revealed that the essential factors for constructing a uniform skin scaffold were uniform distribution within each layer and adequate collagen spacing between layers. Besides, proper construction of the scaffolds, ensuring ordered stratification and keratinization, was crucial for minimizing the shrinking process and maintaining the original shape after transplantation. However, aspects of cell-level morphology, such as specific microcellular environment and cell–cell interactions, have not yet been effectively mimicked. Thus, improving the resolution of bioprinting to achieve cellular-level precision would be both interesting and valuable for biological and clinical applications.

As skin injuries raised the demand for artificial skin substitutes, local drug delivery strategies for wound healing gained interest.[25] 3D bioprinting has been employed for local drug delivery, using polymers with stimuli-responsive properties to actively release a drug when in contact with the target environment.[26] As chronic wounds

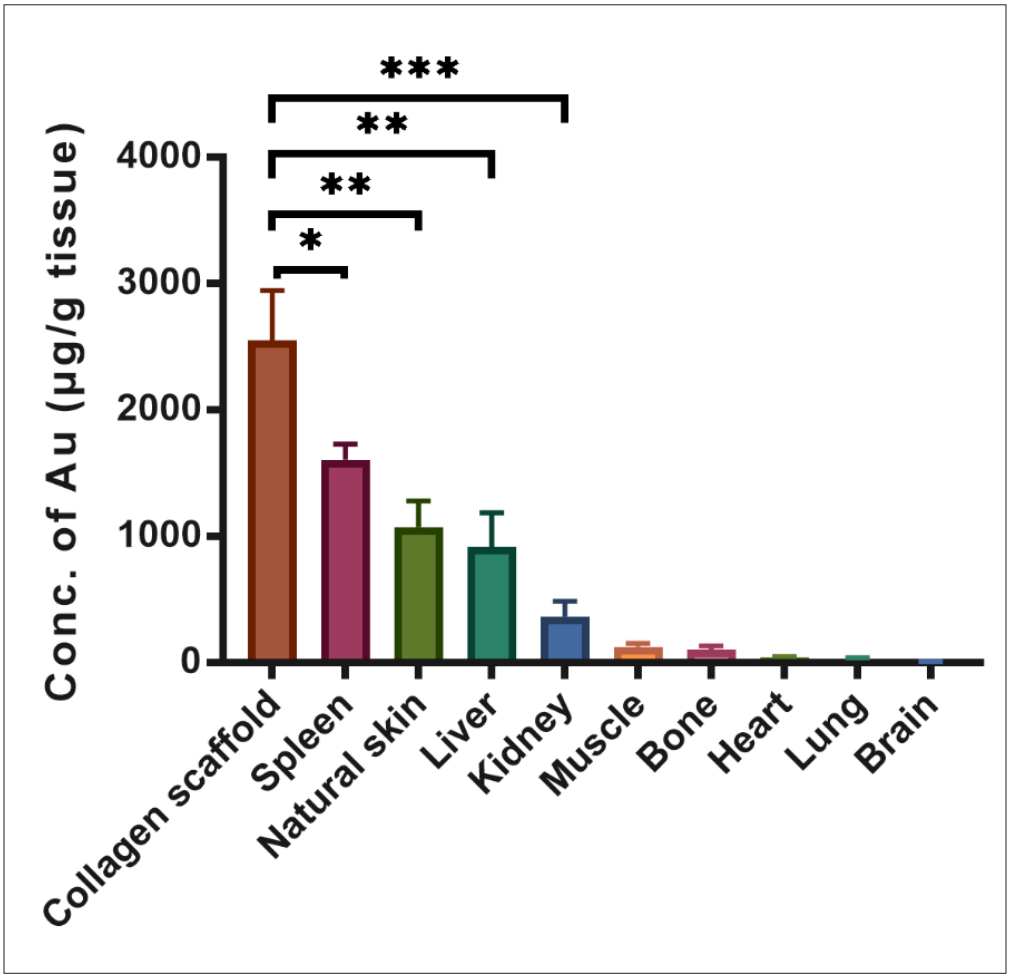

Figure 6. Biodistribution of Au in collagen scaffold and mice organs. Inductively coupled plasma-optical emission spectrometry (ICP-OES) analysis of Au concentration in the collagen scaffold and multiple organs of mice 6 days after injection with 16-nm GNPs-PEG. The results are presented as the mean ± standard deviation. *$p < 0.05$; **$p < 0.01$; ***$p < 0.005$; $n = 3$. Abbreviations: GNP, gold nanoparticle; PEG, polyethylene glycol.

and burns require painstakingly long-term treatment, drug-incorporated scaffolds have emerged as a promising therapeutic strategy.[21,27]

Collagen, the most abundant protein in the ECM and known for its properties in wound healing and tissue regeneration, is one of the most widely used biopolymers as a carrier matrix for controlled drug delivery systems.[28–30] The biodegradable and absorbable properties of collagen, along with its non-toxic and biocompatible nature, support cell attachment, migration, and proliferation.[8,31] The benefits of the ECM in acute wounds and burns have also been demonstrated in clinical studies.[32] In this study, the essential role of collagen in preventing cell migration between layers verified that collagen promotes the maintenance of cellular phenotypes.[33] Other ECM components, such as proteoglycans/glycosaminoglycans, elastin, fibronectin, laminins, and several other glycoproteins, also contribute to constructing a 3D macromolecular network. H&E staining results indicate a lack of similarity in ECM, such as deficiency in other acidophilic substances. We infer that appropriate collagen density and the addition of other ECM components are essential to imitate natural skin.

Gold nanoparticles (GNPs) are widely used in diagnostics and biosensing applications because of their exquisite intrinsic properties, such as ease of synthesis and surface functionalization, tunable size and shape, and favorable optical, electronic, and physicochemical features. Their diagnostic applications include biosensing, photoimaging, and bioimaging.[34–36] Additionally, GNPs offer slower extracellular drug release due to an adequate surface-to-volume ratio,[21] while PEG functionalization has been reported to improve the stability of GNPs in complex

media. This further prevents opsonization, making nanoconjugates more biocompatible and increasing their circulation time *in vivo*.[37] GNPs are widely used in the wound healing process for the delivery of drugs and antimicrobial agents.[18,38] Current studies mainly focus on GNP penetration and percutaneous delivery on natural skin.[39–42] Thus, GNP-conjugated drug delivery through 3D-bioprinted scaffolds is crucial in wound healing and warrants further exploration. Several studies have elucidated how GNPs, commonly used in molecular diagnostics and drug delivery applications,[13] interact with collagen.[43,44] In recent studies, the mechanical stability and diffusion characteristics of gel interconnection and hindrance of GNPs *in vitro* were investigated.[45] Further, the incorporation of GNPs into crosslinked scaffolds enhanced their stability against enzymatic degradation and increased the tensile strength, promoting the wound healing process.[46] In another study, increased concentration of GNPs enhanced the free radical inhibition effect of the skin substitutes.[47] However, these studies only focused on the inherent percutaneous penetration of GNPs from the scaffold. In our study, after systematic administration of GNPs, we noted GNP accumulation tendency in our scaffold *in vivo*, exceeding natural skin and other organs. As chronic wounds require a long recovery process, drugs with a short half-life may not adequately meet the treatment needs for single-use applications. However, frequent changes in the transplanted drug-incorporated scaffolds may cause further damage to the wounds. Thus, intermittent systematic administration of drugs with a short half-life may be a promising strategy. Future studies could focus on how GNP-delivered drugs can enhance the recovery process and ameliorate inflammatory response following cell-laden scaffold transplantation.

As the use of GNPs expands, concerns about toxicity and biosafety have gained significant attention.[48] Notably, the skin is an important site of nanoparticle accumulation following systemic administration.[49] Besides, *in vivo* skin penetration of quantum dot nanoparticles was reported.[50] However, the *in vivo* biodistribution of GNPs within collagen remains unclear. In this study, 3D-bioprinted skin scaffolds, despite being thick and abundant with seeded cells, exhibited higher GNP accumulation than natural skin and other organs after intravenous administration, indicating a strong tendency for cell-laden scaffolds to absorb GNPs. The differences in GNP accumulation and absorption may be due to the microstructure between natural skin and skin scaffolds. The dermis of natural skin appeared densely arranged and overlapping under scanning electron microscopy (SEM).[51] However, the microstructure of the collagen-based scaffold was porous under SEM.[52] The porous structure of collagen may induce the accumulation and retention of the GNPs. Furthermore, there were some other additional structures in the natural skin, such as elastic fibers and appendages, which may block the absorption of GNPs. Further studies could also focus on the dynamic behavior of different functional nanomaterials and the investigation of the long-term health effects.[37] Besides, adopting GNPs of certain sizes and observing GNP deposits at specific post-injection time points may be crucial for GNP accumulation. However, the exact binding position of the GNPs to the scaffold, as well as the aggregation and deposition mechanism of GNPs, is still unknown. Further studies may extend to evaluate the binding mechanism of GNPs to the scaffold at a subcellular level. Additionally, clinical applications of the cell-laden scaffold could be advanced by: (i) serving as a potential material to absorb and excrete toxic GNPs, and (ii) a targeted site to accumulate GNP-delivered drugs.

5. Conclusion

In the present study, 3D bioprinting was applied to fabricate cell-laden scaffold composites as skin substitutes. After intravenous administration, the accumulation of GNPs on the skin scaffolds exceeded that in natural skin and other organs, indicating the strong tendency of the skin scaffolds to absorb GNPs. Thus, 3D-bioprinted skin scaffolds could be utilized to enhance the understanding of nanoparticle biodistribution *in vivo*, reducing the need for animal skins. Furthermore, they can be employed as a potential method to absorb and excrete nanoparticles after systemic exposure and as a targeted site for the accumulation of GNP-delivered drugs.

Acknowledgments

None.

Funding

This work was supported by the STI2030-Major Projects (2022ZD0205202), the Anhui Province University Scientific Research Project (KJ2021A0212, 2022AH051169), the Anhui Medical University Research Funding (2021xkj008), the University Synergy Innovation Program of Anhui Province (GXXT-2022-030), and the College Students' Innovation and Entrepreneurship Training Program of Anhui Province (S202210366019).

Conflict of interest

The authors declare no conflict of interest.

Author contributions

Conceptualization: Chenwei Wang, Xinmeng Wang, Xinya Qin

Data curation: Yi Wang, Xin Ma
Funding acquisition: Chenwei Wang, Xinmeng Wang, Xinya Qin
Investigation: Yi Wang, Xin Ma, Shuaideng Wang, Xinmeng Wang
Methodology: Yi Wang, Xu Wu, Xinmeng Wang
Project administration: Chenwei Wang, Xinmeng Wang
Resources: Shuaideng Wang
Supervision: Chenwei Wang, Jiangning Zhou
Visualization: Yi Wang, Xinya Qin
Validation: Yi Wang, Peng Peng, Guozhang Tang
Writing – original draft: Yi Wang, Chenwei Wang
Writing – review & editing: Yi Wang, Xinmeng Wang, Chenwei Wang, Jiangning Zhou

Ethics approval and consent to participate

All animal experiments were evaluated and approved by the Institutional Animal Care and Use Committee of Anhui Medical University (LLSC20211388). No experiments involving human subjects were conducted in this study.

Consent for publication

Not applicable.

Availability of data

Data are available from the corresponding author upon reasonable request.

References

1. Matai I, Kaur G, Seyedsalehi A, McClinton A, Laurencin CT. Progress in 3D bioprinting technology for tissue/organ regenerative engineering. *Biomaterials*. 2020;226:119536.
doi: 10.1016/j.biomaterials.2019.119536

2. Cubo N, Garcia M, Del Canizo JF, Velasco D, Jorcano JL. 3D bioprinting of functional human skin: production and in vivo analysis. *Biofabrication*. 2016;9(1):015006.
doi: 10.1088/1758-5090/9/1/015006

3. Zhu W, Ma X, Gou M, Mei D, Zhang K, Chen S. 3D printing of functional biomaterials for tissue engineering. *Curr Opin Biotechnol*. 2016;40:103-112.
doi: 10.1016/j.copbio.2016.03.014

4. Li X, Liu B, Pei B, et al. Inkjet bioprinting of biomaterials. *Chem Rev*. 2020;120(19):10793-10833.
doi: 10.1021/acs.chemrev.0c00008

5. Douillet C, Nicodeme M, Hermant L, et al. From local to global matrix organization by fibroblasts: a 4D laser-assisted bioprinting approach. *Biofabrication*. 2022;14(2):025006.
doi: 10.1088/1758-5090/ac40ed

6. Rossi A, Pescara T, Gambelli AM, et al. Biomaterials for extrusion-based bioprinting and biomedical applications. *Front Bioeng Biotechnol*. 2024;12:1393641.
doi: 10.3389/fbioe.2024.1393641

7. Li W, Wang M, Ma H, Chapa-Villarreal FA, Lobo AO, Zhang YS. Stereolithography apparatus and digital light processing-based 3D bioprinting for tissue fabrication. *iScience*. 2023;26(2):106039.
doi: 10.1016/j.isci.2023.106039

8. Weng T, Zhang W, Xia Y, et al. 3D bioprinting for skin tissue engineering: Current status and perspectives. *J Tissue Eng*. 2021;12:20417314211028574.
doi: 10.1177/20417314211028574

9. Rossi G, Manfrin A, Lutolf MP. Progress and potential in organoid research. *Nat Rev Genet*. 2018;19(11):671-687.
doi: 10.1038/s41576-018-0051-9

10. Hong ZX, Zhu ST, Li H, et al. Bioengineered skin organoids: from development to applications. *Mil Med Res*. 2023;10(1):40.
doi: 10.1186/s40779-023-00475-7

11. Zhao H, Chen Y, Shao L, et al. Airflow-assisted 3D bioprinting of human heterogeneous microspheroidal organoids with microfluidic nozzle. *Small*. 2018;14(39):e1802630.
doi: 10.1002/smll.201802630

12. Michael S, Sorg H, Peck CT, et al. Tissue engineered skin substitutes created by laser-assisted bioprinting form skin-like structures in the dorsal skin fold chamber in mice. *PloS One*. 2013;8(3):e57741.
doi: 10.1371/journal.pone.0057741

13. Chen Y, Feng X. Gold nanoparticles for skin drug delivery. *Int J Pharm*. 2022;625:122122.
doi: 10.1016/j.ijpharm.2022.122122

14. Revia RA, Stephen ZR, Zhang M. Theranostic nanoparticles for RNA-based cancer treatment. *Acc Chem Res*. 2019;52(6):1496-1506.
doi: 10.1021/acs.accounts.9b00101

15. de Puig H, Bosch I, Salcedo N, Collins JJ, Hamad-Schifferli K, Gehrke L. Multiplexed rapid antigen tests developed using multicolored nanoparticles and cross-reactive antibody pairs: implications for pandemic preparedness. *Nano Today*. 2022;47:101669.
doi: 10.1016/j.nantod.2022.101669

16. Surendran SP, Moon MJ, Park R, Jeong YY. Bioactive nanoparticles for cancer immunotherapy. *Int J Mol Sci*. 2018;19(12):3877.
doi: 10.3390/ijms19123877

17. Yang X, Yang J, Wang L, et al. Pharmaceutical intermediate-modified gold nanoparticles: against multidrug-resistant bacteria and wound-healing application via an electrospun scaffold. *ACS Nano*. 2017;11(6):5737-5745.
doi: 10.1021/acsnano.7b01240

18. Randeria PS, Seeger MA, Wang XQ, et al. siRNA-based spherical nucleic acids reverse impaired wound healing in diabetic mice by ganglioside GM3 synthase knockdown. *Proc Natl Acad Sci U S A*. 2015;112(18):5573-5578. doi: 10.1073/pnas.1505951112

19. Koushki K, Varasteh AR, Shahbaz SK, et al. Dc-specific aptamer decorated gold nanoparticles: a new attractive insight into the nanocarriers for allergy epicutaneous immunotherapy. *Int J Pharm*. 2020;584:119403. doi: 10.1016/j.ijpharm.2020.119403

20. Niu J, Chu Y, Huang YF, et al. Transdermal gene delivery by functional peptide-conjugated cationic gold nanoparticle reverses the progression and metastasis of cutaneous melanoma. *ACS Appl Mater Interfaces*. 2017;9(11):9388-9401. doi: 10.1021/acsami.6b16378

21. Kim HS, Sun X, Lee JH, Kim HW, Fu X, Leong KW. Advanced drug delivery systems and artificial skin grafts for skin wound healing. *Adv Drug Deliv Rev*. 2019;146:209-239. doi: 10.1016/j.addr.2018.12.014

22. Wang XM, Wu XW, Zhao XY, Wang CW, Zhou JN. Exposure-time-dependent subcellular staging of gold nanoparticles deposition and vesicle destruction in mice livers. *Nanomedicine*. 2021;34:102393. doi: 10.1016/j.nano.2021.102393

23. Lee V, Singh G, Trasatti JP, et al. Design and fabrication of human skin by three-dimensional bioprinting. *Tissue Eng Part C Methods*. 2014;20(6):473-484. doi: 10.1089/ten.TEC.2013.0335

24. Lee W, Debasitis JC, Lee VK, et al. Multi-layered culture of human skin fibroblasts and keratinocytes through three-dimensional freeform fabrication. *Biomaterials*. 2009;30(8):1587-1595. doi: 10.1016/j.biomaterials.2008.12.009

25. Tiwari R, Pathak K. Local drug delivery strategies towards wound healing. *Pharmaceutics*. 2023;15(2):634. doi: 10.3390/pharmaceutics15020634

26. Osouli-Bostanabad K, Masalehdan T, Kapsa RMI, et al. Traction of 3D and 4D printing in the Healthcare Industry: from drug delivery and analysis to regenerative medicine. *ACS Biomater Sci Eng*. 2022;8(7):2764-2797. doi: 10.1021/acsbiomaterials.2c00094

27. Sufiyan M, Kushwaha P, Ahmad M, Mandal P, Vishwakarma KK. Scaffold-mediated drug delivery for enhanced wound healing: a review. *AAPS PharmSciTech*. 2024;25(5):137. doi: 10.1208/s12249-024-02855-1

28. Mbese Z, Alven S, Aderibigbe BA. Collagen-based nanofibers for skin regeneration and wound dressing applications. *Polymers (Basel)*. 2021;13(24):4368. doi: 10.3390/polym13244368

29. Liang Y, He J, Guo B. Functional hydrogels as wound dressing to enhance wound healing. *ACS Nano*. 2021;15(8):12687-12722. doi: 10.1021/acsnano.1c04206

30. An B, Lin YS, Brodsky B. Collagen interactions: drug design and delivery. *Adv Drug Deliv Rev*. 2016;97:69-84. doi: 10.1016/j.addr.2015.11.013

31. Yanez M, Rincon J, Dones A, De Maria C, Gonzales R, Boland T. In vivo assessment of printed microvasculature in a bilayer skin graft to treat full-thickness wounds. *Tissue Eng Part A*. 2015;21(1-2):224-233. doi: 10.1089/ten.TEA.2013.0561

32. Eweida AM, Marei MK. Naturally occurring extracellular matrix scaffolds for dermal regeneration: do they really need cells? *Biomed Res Int*. 2015;2015:839694. doi: 10.1155/2015/839694

33. Lee CH, Singla A, Lee Y. Biomedical applications of collagen. *Int J Pharm*. 2001;221(1-2):1-22. doi: 10.1016/s0378-5173(01)00691-3

34. Kang MS, Lee SY, Kim KS, Han DW. State of the art biocompatible gold nanoparticles for cancer theragnosis. *Pharmaceutics*. 2020;12(8):701. doi: 10.3390/pharmaceutics12080701

35. Akshaya K, Arthi C, Pavithra AJ, et al. Bioconjugated gold nanoparticles as an efficient colorimetric sensor for cancer diagnostics. *Photodiagnosis Photodyn Ther*. 2020;30:101699. doi: 10.1016/j.pdpdt.2020.101699

36. Hahn MA, Singh AK, Sharma P, Brown SC, Moudgil BM. Nanoparticles as contrast agents for in-vivo bioimaging: current status and future perspectives. *Anal Bioanal Chem*. 2011;399(1):3-27. doi: 10.1007/s00216-010-4207-5

37. Oliveira BB, Ferreira D, Fernandes AR, Baptista PV. Engineering gold nanoparticles for molecular diagnostics and biosensing. *Wiley Interdiscip Rev Nanomed Nanobiotechnol*. 2023;15(1):e1836. doi: 10.1002/wnan.1836

38. Comune M, Rai A, Chereddy KK, et al. Antimicrobial peptide-gold nanoscale therapeutic formulation with high skin regenerative potential. *J Control Release*. 2017;262:58-71. doi: 10.1016/j.jconrel.2017.07.007

39. Cao M, Li B, Guo M, et al. In vivo percutaneous permeation of gold nanomaterials in consumer cosmetics: implication in dermal safety assessment of consumer nanoproducts. *Nanotoxicology*. 2021;15(1):131-144. doi: 10.1080/17435390.2020.1860264

40. Huang Y, Yu F, Park YS, et al. Co-administration of protein drugs with gold nanoparticles to enable percutaneous delivery. *Biomaterials*. 2010;31(34):9086-9091. doi: 10.1016/j.biomaterials.2010.08.046

41. Mascarenhas-Melo F, Mathur A, Murugappan S, et al. Inorganic nanoparticles in dermopharmaceutical and cosmetic products: properties, formulation development, toxicity, and regulatory issues. *Eur J Pharm Biopharm*. 2023;192:25-40.

doi: 10.1016/j.ejpb.2023.09.011

42. Labouta HI, Liu DC, Lin LL, et al. Gold nanoparticle penetration and reduced metabolism in human skin by toluene. *Pharm Res*. 2011;28(11):2931-2944. doi: 10.1007/s11095-011-0561-z

43. Wilson CG, Sisco PN, Gadala-Maria FA, Murphy CJ, Goldsmith EC. Polyelectrolyte-coated gold nanorods and their interactions with type I collagen. *Biomaterials*. 2009;30(29):5639-5648. doi: 10.1016/j.biomaterials.2009.07.011

44. Slowinska K. Cross-linked collagen gels using gold nanoparticles. *Methods Mol Biol*. 2018;1798:203-212. doi: 10.1007/978-1-4939-7893-9_16

45. Schuetz T, Richmond N, Harmon ME, Schuetz J, Castaneda L, Slowinska K. The microstructure of collagen type I gel cross-linked with gold nanoparticles. *Colloids Surf B Biointerfaces*. 2013;101:118-125. doi: 10.1016/j.colsurfb.2012.06.006

46. Akturk O, Kismet K, Yasti AC, et al. Collagen/gold nanoparticle nanocomposites: a potential skin wound healing biomaterial. *J Biomater Appl*. 2016;31(2):283-301. doi: 10.1177/0885328216644536

47. Sasidharan S, Pottail L. Biodegradable polymers and gold nanoparticle-decorated skin substitutes: synthesis, characterization, and in vitro biological activities. *Appl Biochem Biotechnol*. 2021;193(10):3232-3252. doi: 10.1007/s12010-021-03600-1

48. Khlebtsov N, Dykman L. Biodistribution and toxicity of engineered gold nanoparticles: a review of in vitro and in vivo studies. *Chem Soc Rev*. 2011;40(3):1647-1671. doi: 10.1039/c0cs00018c

49. Sykes EA, Dai Q, Tsoi KM, Hwang DM, Chan WC. Nanoparticle exposure in animals can be visualized in the skin and analysed via skin biopsy. *Nat Commun*. 2014;5:3796. doi: 10.1038/ncomms4796

50. Mortensen LJ, Oberdörster G, Pentland AP, DeLouise LA. In vivo skin penetration of quantum dot nanoparticles in the murine model: the effect of UVR. *Nano Lett*. 2008;8(9):2779-2787. doi: 10.1021/nl801323y

51. Smith LT, Holbrook KA, Byers PH. Structure of the dermal matrix during development and in the adult. *J Invest Dermatol*. 1982;79(Suppl 1):93s-104s. doi: 10.1111/1523-1747.ep12545877

52. Zidek J, Vojtova L, Abdel-Mohsen AM, et al. Accurate micro-computed tomography imaging of pore spaces in collagen-based scaffold. *J Mater Sci Mater Med*. 2016;27(6):110. doi: 10.1007/s10856-016-5717-2

ACCSCIENCE PUBLISHING

International Journal of Bioprinting

RESEARCH ARTICLE

Development of multi-layered 3D-printed scaffold for sequential delivery of biomolecules

Jong-Eun Won[1], Hyun Kyung Moon[2], Hae-Won Kim[3,4]*, and Ji Suk Shim[1,5]*

[1] Institute of Clinical Dental Research, Korea University Guro Hospital, Seoul, South Korea

[2] Department of Medicine, Korea University Graduate School, Seoul, South Korea

[3] Institute of Tissue Regeneration Engineering (ITREN), Dankook University, Cheonan, South Korea

[4] Department of Nano-Biomedical Science & BK21 NBM Global Research Center for Regenerative Medicine, Dankook University, Cheonan, South Korea

[5] Department of Dentistry, Korea University Guro Hospital, Seoul, South Korea

Abstract

Spatiotemporal control of exogenous growth factors plays a crucial role in the sequential repair of damaged tissues. However, traditional therapeutic trials have mostly relied on the delivery of a single molecule due to limitations in rapid diffusion and the instability of biomolecules. In this study, we developed a novel strategy using a composite of gelatin and silica as an alternative for the stable and sequential release of biomolecules. Two biomolecules, basic fibroblast growth factor, and bone morphogenetic protein-2, were incorporated into two separate composites and sequentially layered onto the activated polymer surface. Each molecule was sequentially released from each layer of the scaffold, and the silica composite prevented rapid diffusion due to its nanoporous structure. The adhesion, proliferation, and osteogenic differentiation of rat bone marrow-derived mesenchymal stem cells were significantly enhanced in the double-layered group containing separately delivered dual molecules compared with the control or single groups. Our developed gelatin-silica composite was successfully incorporated in double layers on polymer scaffolds, and cellular responses were promoted in this manner. These results demonstrated that our scaffolding system has potential as a therapeutic strategy for the delivery of dual or multiple biomolecules in regenerative medicine.

Keywords: Dual delivery; Basic fibroblast growth factor; Bone morphogenic protein; 3D printing; Xerogel; Growth factor

***Corresponding authors:**
Hae-Won Kim
(kimhw@dku.edu)

Ji Suk Shim
(shoss@korea.ac.kr)

Citation: Won JE, Moon HK, Kim HW, Shim JS. Development of multi-layered 3D-printed scaffold for sequential delivery of biomolecules. *Int J Bioprint*. 2024;10(6):4638. doi: 10.36922/ijb.4638

Received: August 23, 2024
Revised: September 20, 2024
Accepted: September 24, 2024
Published Online: September 24, 2024

Copyright: © 2024 Author(s). This is an Open Access article distributed under the terms of the Creative Commons Attribution License, permitting distribution, and reproduction in any medium, provided the original work is properly cited.

Publisher's Note: AccScience Publishing remains neutral with regard to jurisdictional claims in published maps and institutional affiliations.

1. Introduction

To repair damaged tissue, endogenous signal molecules, including cytokines, chemokines, and growth factors (GFs), are required in dynamic cellular processes.[1,2] Among these, GFs, including fibroblast GFs (FGFs), platelet-derived GFs (PDGFs), vascular endothelial GFs (VEGFs), and bone morphogenetic proteins (BMPs), spatiotemporally modulate various cellular responses, such as adhesion, proliferation, migration, and differentiation. Cellular signaling affects tissue repair and healing processes to overcome

tissue damage from various diseases and accidents.[3-6] Therefore, researchers are interested in exploring exogenous GFs as a potential therapeutic approach for rapid repair and healing.[3,5,7-9] However, successful outcomes in typical trials frequently appeared in therapies that involved only a single GF administration.[10,11] Injected GFs diffuse rapidly into surrounding tissues and are degraded by enzymes in the body. However, such trials are limited to small-scale cohort and animal studies.[12] Furthermore, their ability to play a role as effective mediators in the body requires time-controlled signaling.[13] Therefore, the development of novel scaffolds should simultaneously address the need to be preserved in GFs to prevent rapid degradation and to release them at the desired time and location.[5,14-16]

Recently, 3D printing has received great global interest as a novel technology.[2,17,18] In bone tissue engineering, the application of 3D printing has been noted in the fabrication of successful patient-specific scaffolds.[19-21] Moreover, the controlled porosity, pore size, and interconnectivity in 3D-printed scaffolds have the potential to enhance the exchange of nutrients and wastes, tissue ingrowth, and angiogenesis. In particular, poly-ε-caprolactone (PCL) has been widely used in 3D printing systems due to its biodegradability, biocompatibility, and high ease of handling.[22-27] However, incorporating GFs into a polymer strut of the 3D-printed scaffolds is difficult, as the process requires a high temperature or organic solvent content for dissolving the synthetic polymers.

In this study, we fabricated 3D-printed scaffolds, which release spatiotemporally controlled GFs. The polymer scaffold was printed and coated with a gelatin-silica (GS) composite containing GFs on its surface. The scaffolds were double-layered and incorporated with basic fibroblast GF (bFGF) in the outer layer and BMP-2 in the inner layer to modulate the early and late processes of osteogenic differentiation of rat bone marrow-derived mesenchymal stem cells, respectively. We found the best conditions for fabricating double layers with the composite and observed the morphology. The release of GFs from the scaffold was investigated *in vitro*, and the cellular effects on the scaffold were assessed using stem cells.

2. Materials and methods

2.1. Fabrication of scaffolds and hybrid sol coating

A PCL (Sigma-Aldrich, United States of America [USA]) slurry was prepared by dissolving PCL in acetone (30% [w/v]) at 50°C. The scaffolds were designed in a square shape of 13 × 13 × 1 mm, with a pore size of 0.5 × 0.5 mm and strut size of 0.25 mm. The 3D scaffolds were fabricated using a computer-based robotic dispensing machine (Ez-ROBO3; Iwashita Engineering Inc., Japan). To solidify the polymer solution, the slurry was printed in a 70% ethanol bath as a fixative solution. To coat the surface of the scaffold, silica xerogel and composite solution were prepared in a 1:10 molar ratio of tetramethyl orthosilicate (Sigma-Aldrich, USA) to distilled water; subsequently, a gelatin (Sigma-Aldrich, USA) solution dissolved in distilled water was mixed with the silica solution according to the determined volume percentage (i.e., 5, 10, 15, and 20%), which indicates the volume percent of gelatin solution in the silica solution. The mixture was stirred for 2 h at 4°C. To obtain the bulk form, the solution was poured into a plastic column and dried. Cytochrome *c* (Cyt *c*; Sigma-Aldrich, USA) was used as a model protein. To improve the adhesion of the GS composite on the PCL scaffold, norepinephrine surface treatment was applied. This modification enhanced the hydrophilicity of the PCL surface, facilitating stronger bonding between the scaffold and the composite coating.[28] The scaffold was activated with 2 mg/mL norepinephrine solution dissolved in 10 mM Tris-HCl (pH 8.8) for 1 h at room temperature. The scaffold was washed with Tris-HCl and distilled water and dried to remove unreacted molecules. To envelope the GFs in the composite solution, lyophilized 100 μg/mL recombinant BMP-2 and 100 μg/mL recombinant bFGF (PeproTech EC Ltd., USA) were mixed in the composite solution for 30 min. The activated 3D scaffolds were immersed in this solution for 30 min. The scaffolds were then washed with phosphate-buffered saline (PBS; Welgene, Korea) and centrifuged at 1300 rpm for 1 min. After drying, the second layer was coated on the pre-coated surface. The procedure for 3D printing and the predicted release of GFs from the scaffolding system are illustrated in Figure 1.

2.2. Characterization of the composites and scaffolds

Chemical analyses of the hybrid coatings were performed using an attenuated total reflectance Fourier transform infrared (ATR FTIR) spectrometry. The morphologies of the scaffolds were observed using scanning electron microscopy (SEM; JSM-6510; JEOL, Japan). The degradation of bulk materials was assessed by weight measurements on predetermined dates for 24 days. The release of Cyt *c*, selected as a representative model protein for small, water-soluble proteins, from the bulk was measured by assessing absorbance at a specific wavelength of 409 nm. The Cyt *c* was eluted in PBS at 37°C with agitation at 150 rpm for 24 days. To visualize the bilayer distribution of the hybrid layers, PCL scaffolds were coated with fluorescein isothiocyanate (FITC) and rhodamine dye loaded into the composite solution. The first and second layers contained rhodamine and FITC dyes, respectively. The results were visualized using a confocal laser scanning microscope (CLSM; LSM700; Carl Zeiss, Germany).

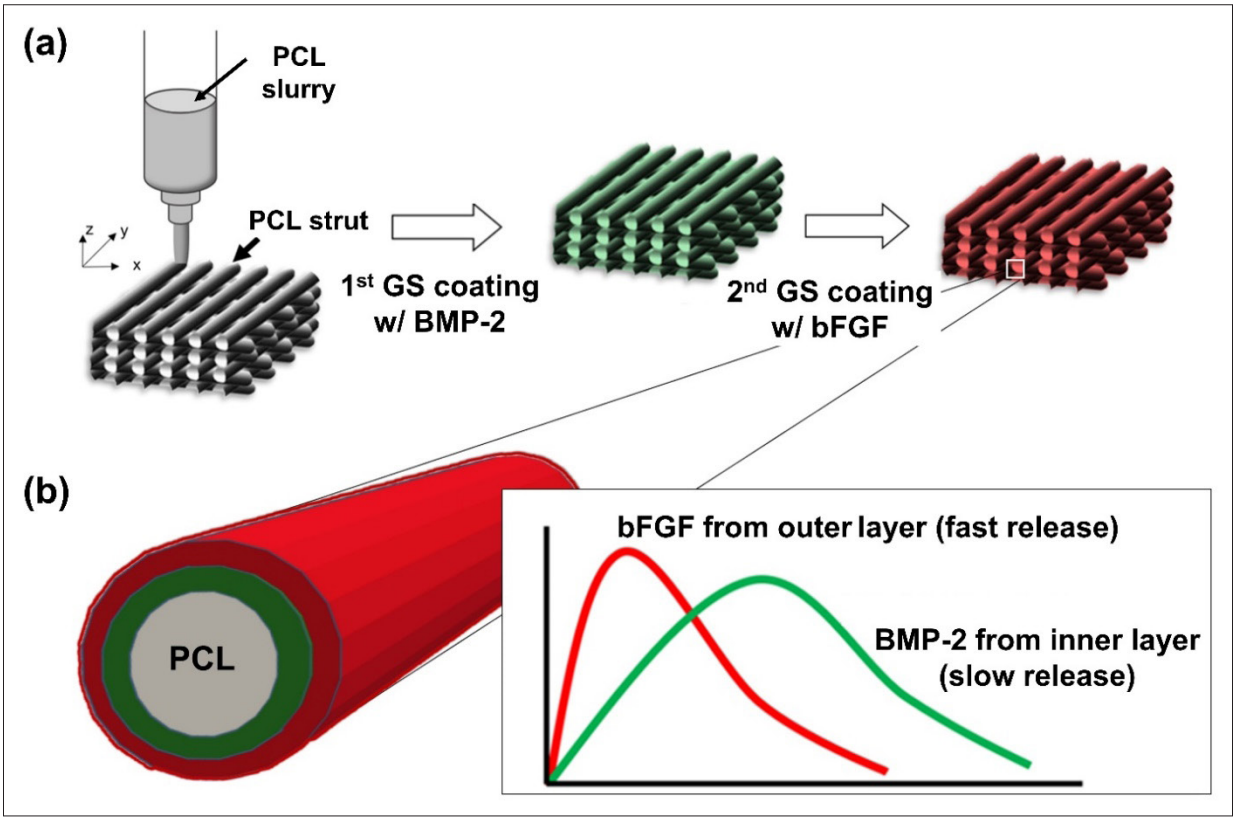

Figure 1. Experimental illustration of the 3D scaffold for the delivery of dual biomolecules. (a) The 3D printing and coating processes. (b) Expected release of growth factors from the double layers. Abbreviations: PCL: Poly-ε-caprolactone; GS: Gelatin-silica; bFGF: Basic fibroblast growth factor; BMP-2: Bone morphogenetic protein-2.

To release GFs, the scaffolds were soaked in 1 mL PBS and incubated at 37°C with shaking for 42 days. At a pre-determined time, the supernatant was collected and stored at −80°C until further use. The release profiles of bFGF and BMP-2 were assessed using an enzyme-linked immunosorbent assay (Quantikine ELISA kit; R&D Systems, USA) according to the manufacturer's instructions.

2.3. Cellular responses on the scaffolds

The rat bone marrow-derived mesenchymal stem cells were obtained as detailed in previous experiments. Briefly, the bone marrow was separated from the femora and tibia (age four weeks) with 2.5 mg/mL of type I collagenase (ThermoFisher Scientific, USA). Single cells were harvested from the cell suspension by centrifugation and sieved three times. The cells were cultured in total culture medium, which is α-Minimum Essential Medium (α-MEM; Welgene, Korea) supplemented with 10% fetal bovine serum and 1% penicillin/streptomycin (Gibco, USA) in a humidified atmosphere of 95% air and 5% CO_2 at 37°C. Nonadherent cells were removed by the medium exchange when the cells reached 70% confluence and formed a monolayer. Passages three and four were used for further evaluation. To confirm the biological effects of bFGF and BMP-2 released from the bilayers on the scaffolds, initial adhesion and viability in conditioned and osteogenic media were examined. The activated scaffolds were sterilized with 70% ethanol and ultraviolet light. For the adhesion assay, 1×10^5 cells were seeded onto the scaffolds and incubated for 2 h. The cell adhesion samples were fixed with 4% paraformaldehyde solution for 15 min and permeabilized in 0.1% Triton X-100 in PBS for 10 min. The cytoskeletons and nuclei were stained with phalloidin and Hoechst 33342, respectively, in PBS and were visualized using CLSM. Cell viability was measured in stem cells cultured on scaffolds for 14 days using a cell counting kit-8 (CCK; Dojindo Laboratories, Japan) according to the manufacturer's instructions.

To confirm the osteogenic ability of BMP-2 released from the scaffolds, cells were cultured for 24 days in osteogenic media consisting of conditioned media supplemented with ascorbic acid (50 μg/mL) and β-glutaraldehyde (10 mM). For alkaline phosphatase (ALP) activity measurement, cell lysates extracted from the samples cultured for seven

days were assessed using a colorimetric assay kit (ALP assay kit; Abcam, United Kingdom [UK]) according to the manufacturer's instructions. The absorbance was measured at 405 nm, and the results were converted using a standard curve of *p*-nitrophenyl phosphate. Calcium deposition derived from mineralization, characterized by late osteogenic differentiation, was measured using an Alizarin Red staining kit (ScienCell Research Laboratories, USA). The cells were cultured for 21 days and stained according to the manufacturer's instructions. The stained minerals on the scaffolds were extracted, and their optical density was assessed at a wavelength of 405 nm.

2.4. Statistical analysis

Prism version 9.5 (GraphPad Software, USA) was used for the statistical analyses. The data is expressed as the mean ± standard deviation. One-way analysis of variance followed by Tukey's post-hoc multiple comparison test was used.

3. Results and discussion

3.1. Characterization of the gelatin-silica composite

Silica xerogel is a suitable material for biomolecule delivery due to its nanoporous structure formed by processing at room temperature.[29-32] The fabrication of nanoporous structures processed at room temperature has the advantage of protecting biomolecules from rapid denaturation induced by the manufacturing process and biological environment.[30,33,34] However, the brittleness of silica xerogel and the bursting of biomolecules from silica xerogel has limited its utility as a delivery material for biomolecules.[35,36]

Gelatin has been used as a biomaterial to improve the biocompatibility and mechanical properties of composites, as well as to reduce the brittleness of composites containing ceramics.[37-39] The capacity of gelatin as a delivery and coating material was verified using the type of bulk material produced by the GS composite (Figure 2a). The hybrid became more opaque as the amount of gelatin increased (Figure 2b, top). Brittleness and shrinkage were reduced when the model protein (Cyt *c*) was mixed more in the hybrid bulk, and the stability of the xerogel was increased (Figure 2b, bottom). In contrast, pristine and 5 GS were broken readily in the dry state and were immediately smashed into pieces when soaked in PBS or distilled water (data not shown). Our results indicate that the xerogel composite was stabilized by hybridization with gelatin, and the bulks were crack-free when they were contained in gelatin at 10% or more. The addition of gelatin and proteins to silica xerogel increased its stability. Therefore, the GS composite xerogel was evaluated as a suitable material for the delivery of GFs, owing to its increased stability and reduced shrinkage rate in the silica xerogel.

The chemical bonding structures of xerogel, gelatin, and the composite were analyzed using ATR FTIR (Figure 2c). The spectrum of the silica xerogel displayed bands at approximately 3400 (–OH stretching), 1620 (molecular H_2O bending), 1250–1000 (Si-O-Si asymmetric stretching), 960–900 (Si-OH stretching), 790 (Si-O-Si symmetric stretching), and 500–450 cm^{-1} (Si-O-Si). Meanwhile, the gelatin bands were detected at 3443 (N-H stretching), 1640 (C=O stretching), and 670 cm^{-1} (N-H out-of-plane wagging). In the hybrid test, all characteristic bands of the xerogel and gelatin were observed, but no other bands were identified as byproducts. The presence of amino groups in gelatin is thought to enhance the chemical interactions between the hydroxyl groups on PCL and gelatin, as well as between silica and gelatin.

To measure the degradation rate of the bulk GS, the weight loss from the composite was determined for 24 days (Figure 2d). As the gelatin content increased, the rate of GS hybrid degradation increased. The release of Cyt *c* from the bulk-type composite also indicates that the release from the GS composite containing a high amount of gelatin was faster than that from the silica hybrid with a low dose of gelatin (Figure 2e). Overall, the release of Cyt *c*, a positively charged model protein, was well-controlled by the ratio of gelatin to silica solution.[40,41]

3.2. Morphologies of the gelatin-silica composite-coated PCL surface

Gelatin, silica, and their composites demonstrated enhanced bioactivity on the synthetic polymer.[42] Moreover, various coating strategies on the polymer scaffolds enabled the delivery of exogenous factors, such as GFs.[7,18] Therefore, the GS coating on the PCL surface was expected to regulate various biological functions induced by GF delivery, as well as increased bioactivity. To fabricate composite coating layers on the 3D scaffolds, 10, 15, and 20 GS were selected. After coating with the GS composite (Figure 3a), the surface morphology of the scaffolds was observed using SEM. Several cracks were observed on the surfaces with 10 and 15 GS, and the surface was readily detached from the PCL surface after drying (Figure S1, Supplementary File). In contrast, the 20 GS-coated surface was crack-free (Figure 3b and c). Notably, the morphologies of the hybrid surface were uniform regardless of the presence of cracks. To measure the thickness of the coating layers, the thickness of the mono- and bi-layers in the 20 GS groups were measured to be 1409.12 ± 162.8 and 2818.50 ± 325.8 μm, respectively (Figure 3d and e). The thickness of the double-coated layer was approximately twice that of the single layer. However, the results obtained from SEM imaging were not distinguishable in the other layers. The results indicate that an increased amount of gelatin

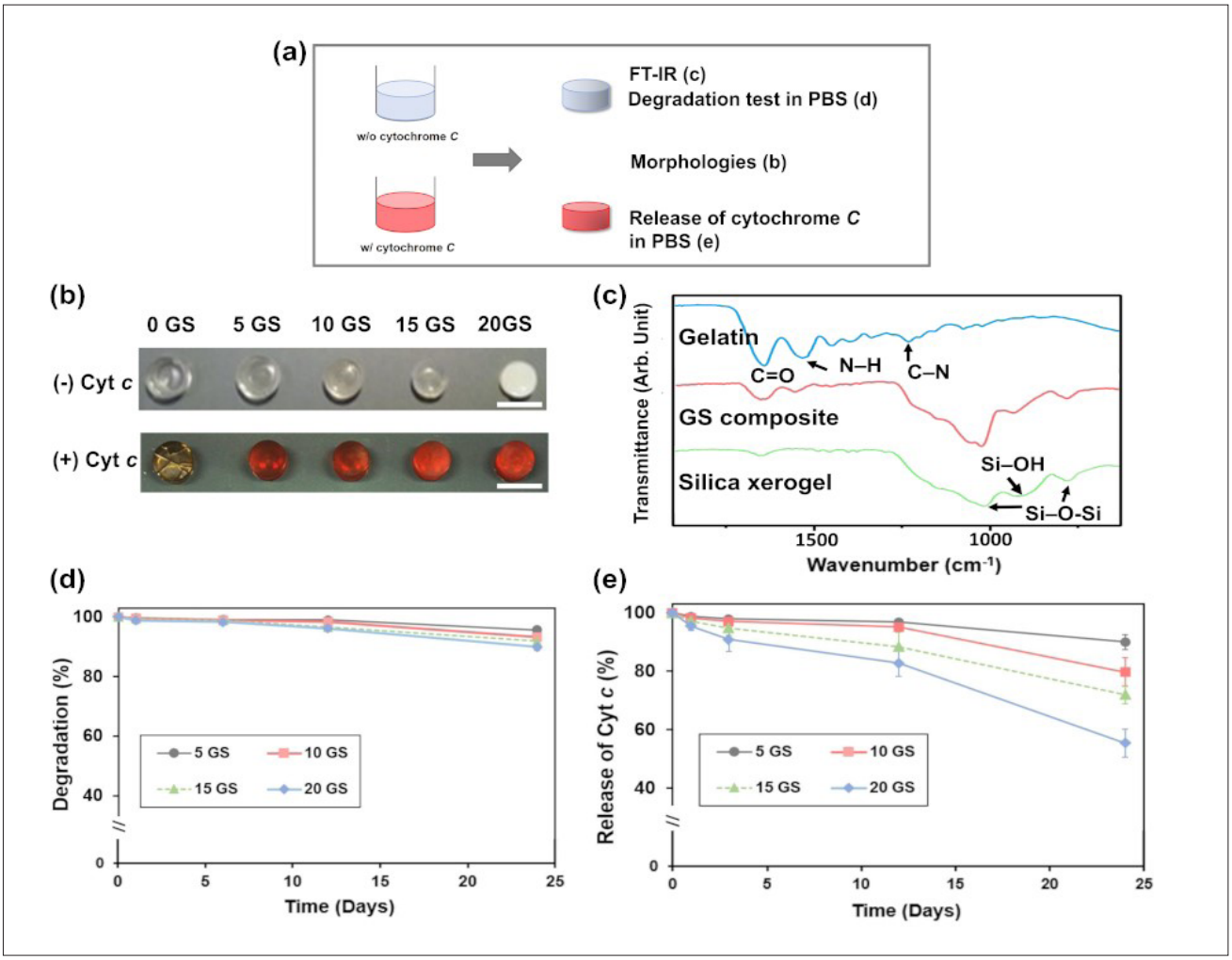

Figure 2. Characterization of the gelatin-silica (GS) composite xerogel bulk. (a) Illustration of the experimental procedure for characterizing the bulk-type xerogel. (b) optical images of the xerogel bulk produced by gelatin ratio without (upper) and with (bottom) 100 μg/mL of Cyt *c* as a model protein. Scale bars: 5 mm. (c) Attenuated total reflectance Fourier transform infrared (ATR FTIR) spectra display the differences in the interactions between specific molecules in silica xerogel, gelatin, and GS composite. (d and e) Degradation (d) and release of Cyt *c* (e) from xerogel bulk in phosphate-buffered saline (PBS) at 37°C for 24 days. All data (n = 8) are presented as the mean ± standard deviation.

during the hybrid process enhanced the physical stability due to an increase in strength and reduction in shrinkage. Some reports have suggested that organic and inorganic composites exhibit improved mechanical properties due to the inorganic networks formed in the organic matrix.[37,43]

To confirm whether each layer was mixed or separated, each component of the 20 GS was stained with fluorescence dyes FITC (first layer: later effect) and rhodamine (second layer: earlier effect) and then coated on the 3D scaffold. As featured in Figure 4a–e, the layers have separate colors. This indicates that the double layers were coated separately without mixing on the scaffold. The developed scaffolds were expected to maintain a controlled release with independently positioned GFs. The hybridization of GS was achieved by synthesis using the sol-gel method at room temperature. Low-temperature processing prevents protein denaturation and is useful for multilayer coatings with good physical stability. Fluorescence intensity measurements were conducted to evaluate the potential intermixing between the two layers during scaffold preparation (Table 1). The intensity profiles for the green channel (Ch1) and the red channel (Ch2) were recorded across the scaffold. The green signal (Ch1) exhibited an average intensity of approximately 1000–1500 units, while the red signal (Ch2) demonstrated a higher intensity range of 1000–4000 units. Notably, the two signals remained confined to their respective layers,

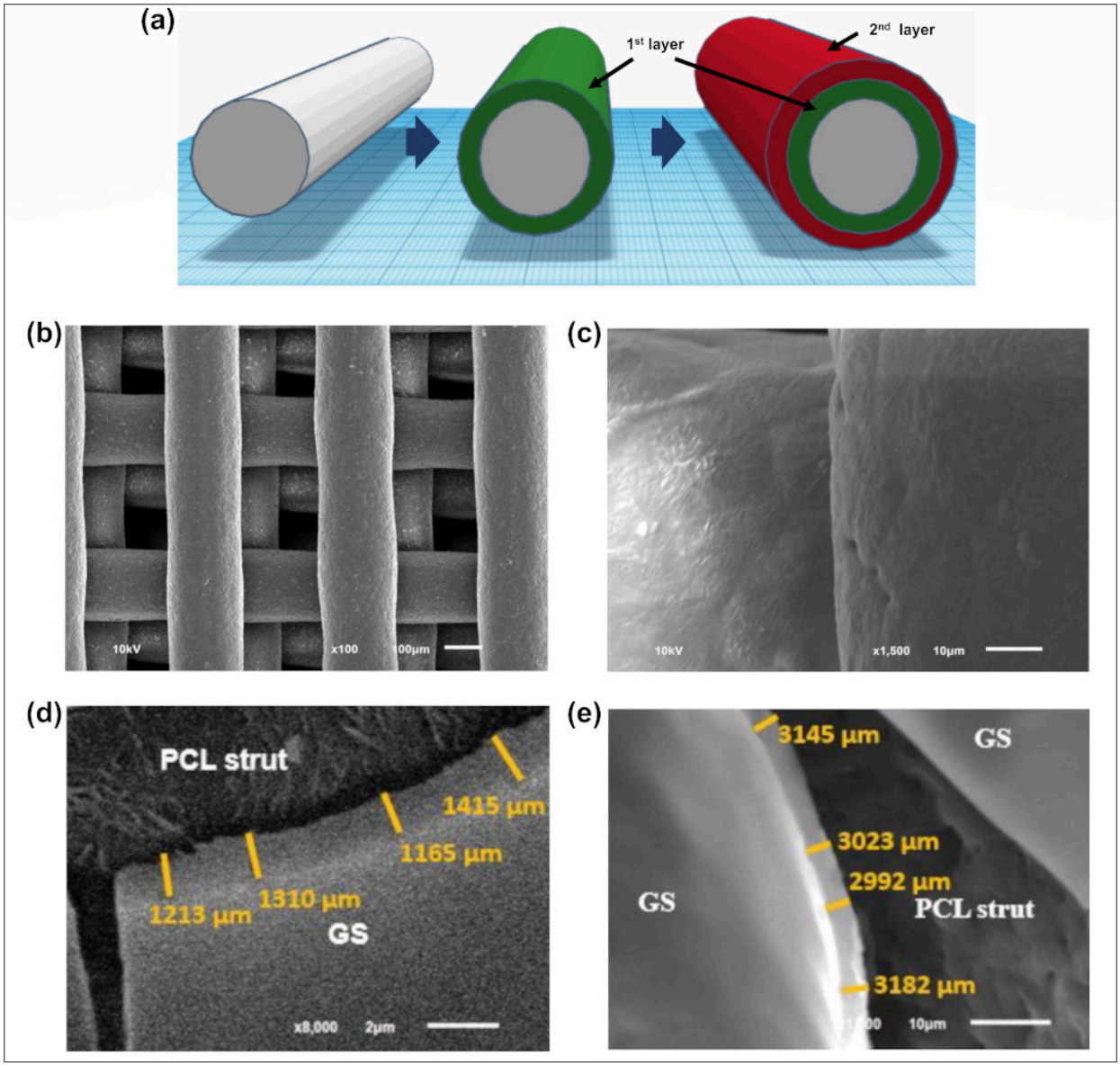

Figure 3. Double-layered 3D scaffolds. (a) Schematic of coating the 3D scaffold with the gelatin-silica (GS) composite; green denotes the first coating layer and red denotes the secondary coating layers. (b–d) Scanning electron microscopy (SEM) images in low (b) and high (c) magnification demonstrate that the poly-ε-caprolactone (PCL) struts are well-coated with the 20 GS composite xerogel. The image showing the thickness increased according to the number of coatings, once (d) and twice (e) with 20 GS composite xerogel. The yellow letters indicate the thickness of layers. Scale bars: 100 μm (b); 10 μm (c and e); 2 μm (d).

with minimal overlap, indicating limited intermixing. The measured distance between markers 1 and 2 was 174.54 μm. The reported intensity differences for Ch1 and Ch2 were −20 and 305 units, respectively. These values likely reflect the variability in fluorescence intensity rather than a direct difference between the markers. The low variability in Ch1 and the higher variability in Ch2 suggest that the separation between the two layers is maintained, with minimal disruption during the coating process. Thus, the fluorescence intensity data confirm that the integrity of the BMP-2-loaded layer was preserved during the second coating process, supporting the intended design for controlled, sequential release of biomolecules.

3.3. Growth factor release from the developed scaffold

The release of bFGF and BMP-2 was observed after 42 d. The rate of bFGF release from the second layer was higher than that of BMP-2 release from the first layer.

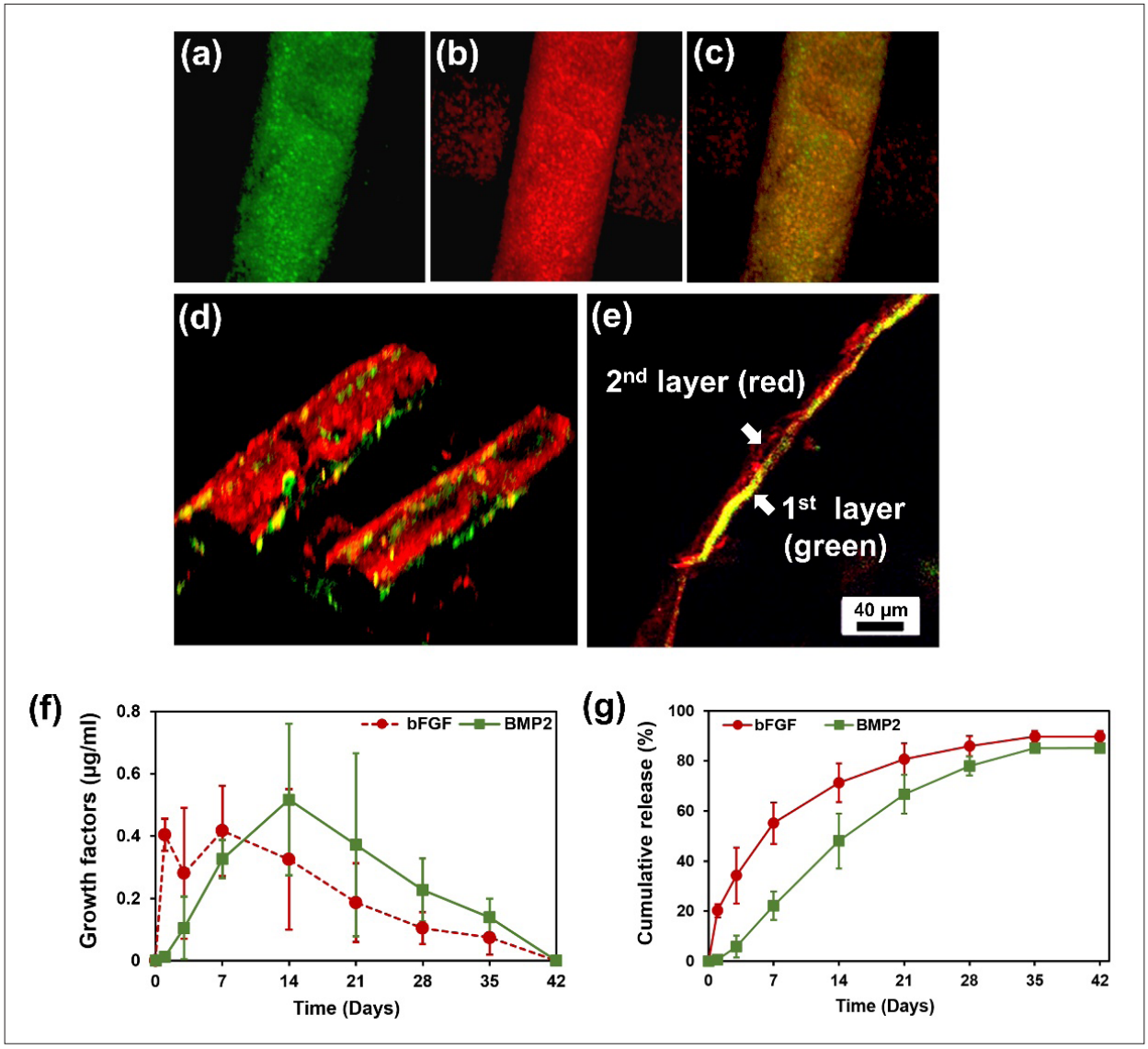

Figure 4. Confocal laser scanning microscope (CLSM) fluorescence images and the release of growth factors from bilayers. (a–e) Each layer was stained with FITC (green; a) and rhodamine (red; b) dye; merged image (c); image of the separated 3D bilayer (d); and side-view of the separated bilayer (e). (f and g) The amount of bFGF and BMP-2 released at different time points (f) and the ratio of cumulative release (g) from 20 GS composite xerogel layers on the 3D-printed scaffold. All data (n = 8) are presented as the mean ± standard deviation.

Table 1. Comparison of fluorescence intensity at two different points on a double-layered strut.

Parameter	Point	
	1	2
Distance (μm)	175.06	349.60
Intensity (units)		
Green channel, Ch1	903	883
Red channel, Ch2	1151	1456

Approximately 60% of bFGF was released after seven days, whereas BMP-2 was released twice as slowly (Figure 4f). Figure 4g reveals that GFs from the scaffolding were sequentially released from the second layer. We could not check the adsorptive GFs, but the pretreated proteins were almost completely released after 42 days. The amounts of BMP-2 and bFGF were indirectly estimated by summing the released quantities. The amounts of bFGF and BMP-2 were 1.792 ± 0.86 and 1.700 ± 0.87 μg/mL, respectively.

Previous studies have demonstrated how multilayer coatings reduce burst release and offer better control of GF release kinetics. Multilayered poly(lactic-co-glycolic acid) (PLGA) microparticle systems have been reported to significantly reduce the burst release of BMP-2, leading to better-controlled delivery profiles.[28] Similarly, electrospun nanofibrous scaffolds have been used to achieve biphasic release profiles, with an initial burst followed by sustained release, effectively maintaining the bioactivity of GFs.[44,45] In comparison to single-layer systems, the double-layer coating in our study provides enhanced control over the sequential release of bFGF and BMP-2, which is crucial for orchestrating different stages of tissue regeneration. Soaking the hybrid containing GFs onto the hydrolyzed scaffolds resulted in a coating layer, and the use of the scaffold facilitated the construction of multiple layers. The highly viscous hybrid was well-fixed on the hydrolyzed polymer surface, and the loading efficiency of the GFs was enhanced. In contrast to previous studies, coating with GS has the potential for GF delivery due to the decrease in initial burst release, increase in loading capacity, the possibility of dual-or multipronged delivery, and sustained release of GFs.

As demonstrated in our study, both the PCL scaffold and GS composite layers critically influence the release kinetics of BMP-2 and bFGF. The dual-layer coating enables sequential release, where BMP-2 is released from the inner layer and bFGF from the outer layer, with the release profile governed by diffusion barriers dependent on the thickness and density of the layers. This observation aligns with previous studies, such as Lee et al.,[36] which reported that thicker composite layers slow down release kinetics. Therefore, the thickness of the coating materials, in particular, plays a vital role in controlling the spatiotemporal release of biomolecules. Additionally, while the release profiles of bFGF and BMP-2 were stable over the 42-day period, any potential uneven release could be attributed to factors such as variations in coating thickness or localized differences in scaffold porosity. To mitigate these issues, the fabrication process was optimized to ensure uniform coating and consistent GF loading. Similar studies have demonstrated that adjusting the ratio of gelatin to silica can fine-tune the release rates.[46] In future research, we plan to investigate further the effects of coating thickness, bonding, and variability to address potential challenges associated with uneven release.

3.4. Cellular responses of rat bone marrow-derived mesenchymal cells on the scaffold

To observe the morphology of the initially adherent cells, fluorescent images of stem cells cultured for 2 h were captured using CLSM. The results in Figure 5a indicate that the adherent stem cells on the GS scaffolds enhanced the expansion and formation of filopodia compared to the cells on pristine PCL struts. The number of cells that initially adhered to the GS-coated scaffolds is presented in Figure 5b. The following *in vitro* experiments were performed using bilayer scaffolds divided into four groups: no GFs (control), bFGF only (w/o/bFGF), BMP2 only (BMP2/w/o), and both bFGF and BMP2 (BMP2/bFGF). The stem cells were cultured for 24 h, and mitochondrial metabolism was assessed using the CCK-8 assay. The optical density was converted into a standard curve, which was assessed using the cell number. A significant difference in the number of adherent cells was observed among the four groups. The groups containing bFGF reported higher cell adherence than the control and BMP2-only groups. Figure 5c indicates that cell proliferation significantly increased in cells on the scaffolds containing bFGF in the second layer after 14 days compared to that in the control or BMP-2-only samples. The osteogenic differentiation of stem cells induced on the scaffolds for seven days was established based on ALP activity. The ALP activity of the stem cells was higher in the bilayer containing both BMP-2 and bFGF (Figure 5d). Additionally, ALP activity was not significantly different in the BMP2-only groups, but a significant difference was observed in the other groups. The osteogenic capacity of the bilayer containing both BMP-2 and bFGF was observed through Alizarin Red S staining and an assay for the detection of mineral deposition (Figure 5e). Mineralization was significantly higher than in the other groups.

Biomimetic or functional matrices on the scaffold have been engineered to stimulate and modulate stem cell behaviors, such as cell adhesion, proliferation, migration, and differentiation.[2,17,26] In particular, the attachment of stem cells to the artificial surface is related to various biological processes associated with subsequent stages and influences intracellular signaling pathways, including phenotype, stemness, growth, and differentiation. Therefore, research on the initial adhesion and mechanisms of stem cells is of continuous interest in tissue engineering. Generally, physical and chemical strategies are employed for the surface modification of biomaterials. Notably, geometrical engineering strategies at the nano- or micro-scale, including specific patterns, height and width of pillars, size or shape of deposited particles, and roughness, have been induced to modulate stem cell behaviors. Mimicking extracellular matrices, such as fibronectin, laminin, poly-D, L-lysine, and collagen, has also been used for chemical surface modification. In a previous study, engineered bFGF was reportedly involved in cell adhesion, i.e., heparan sulfate proteoglycan-mediated adhesion and phosphorylation of focal adhesion kinase.

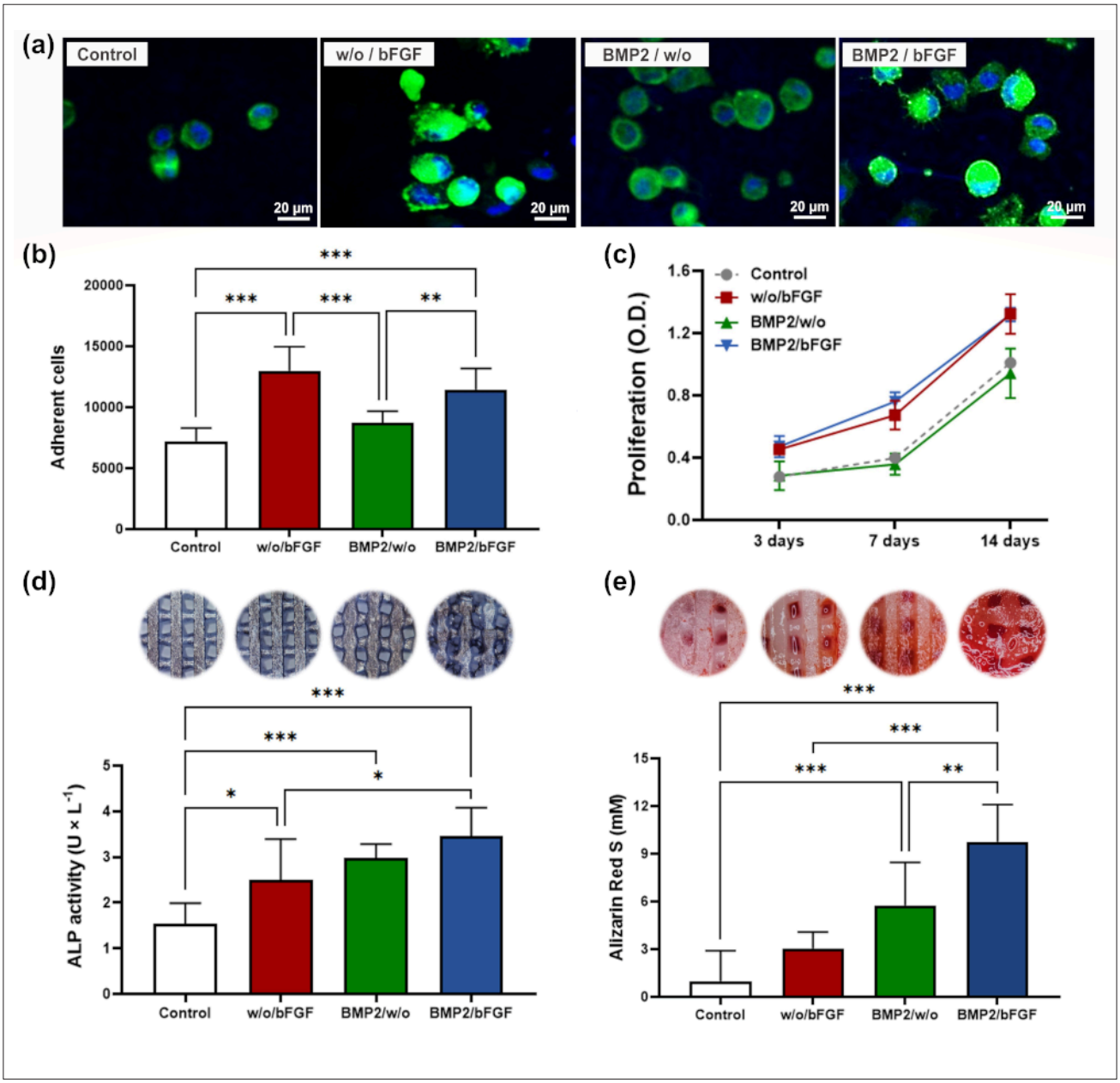

Figure 5. Cellular responses of the rat bone marrow-derived mesenchymal cells on the scaffolds. (a) Cell morphology images of cells adhered to the scaffold for 2 h. (b) Number of adherent cells cultured for 24 h. (c) Proliferation of cells cultured for 14 days. (d and e) Alkaline phosphatase (ALP; d) and Alizarin Red S (e) assays evaluating the osteogenic capacity of the scaffold. All data are presented as the mean ± standard deviation. The optical images represent the stained cells on the scaffold. Significant difference between groups is indicated as: $^{*}p < 0.05$, $^{**}p < 0.01$, and $^{***}p < 0.001$. Scale bars: 20 μm. Abbreviation: O.D.: Optical density.

The stem cells were represented in higher adhesion, and the stemness was controlled by modified bFGFs.[6,47] The bFGF supplementation increased proliferation with hepatocyte GF expression in mesenchymal stem cells.[47] Moreover, Rick et al. explained that bFGF increased osteogenic differentiation in mesenchymal stem cells and pre-osteoblasts, along with an increase in BMP-6.[48] In this study, bFGF plays role in a key factor in controlling cellular responses, including adhesion and proliferation. The initial release of bFGF from the second layer enhances cell attachment and proliferation. Simultaneously, bFGF had a synergistic effect in the BMP-2 release group in terms of stem cell osteogenesis. Various combinations of GFs have been used to modulate the stem cell fate in

tissue engineering. However, further studies are warranted to elucidate the sequential and spatiotemporal controls associated with the release of GFs and other biomolecules.

The 3D printing technology has rapidly advanced and is widely used to develop biomaterials as alternative implants in dentistry and orthopedics for medical therapy. Recently, the development of 3D printing has been further accelerated by the introduction and application of various tissue engineering methodologies, such as structural changes, surface modification, and biomolecule tethering. The 3D-printed scaffold is often modulated by structural alterations, such as the control of nano- or micro-sized pores and struts or by adjusting the roughness or morphology of the surface. Our previous study demonstrated that the nanoporous strut surface of a 3D-printed scaffold enhanced cell adhesion, and the increased surface area of the scaffold provided an adhesive interface for biomolecules or cells. In this study, a novel strategy to modify 3D-printed scaffolds was used as a delivery material for biomolecules, such as GFs, cytokines, nucleotides, and drugs. Tethering biomolecules onto the scaffold modulates cell-cell and cell-biomaterial interactions and stimulates cell behaviors, such as recruitment, adherence, and proliferation. Specific cellular modulation facilitates wound healing and regenerative processes in damaged tissues. Overall, the implementation of the biomimetic interface and the introduction of exogenous biomolecules into the 3D-printed scaffold are expected to ultimately contribute to the improved biocompatibility and regeneration of the target tissue. Recent studies have also reported that surface-modified 3D-printed PCL scaffolds can enhance cell adhesion and tissue regeneration, particularly when combined with bioactive coatings for controlled GF delivery.[49] In our results, it was confirmed that 20 GS released proteins without delamination in a bulk form for 24 days (Figure 2e), even under stirring conditions at 37°C, and sustained the release of GFs for a total of 42 days without any burst release due to surface delamination after surface erosion (Figure 4f and g). On day 21 of cell culture, continuous cell proliferation and differentiation were observed, and staining images after differentiation confirmed that cells were well-distributed on the scaffold surface (Figure 5d and e). This indirectly indicates that the GS coating surface remained stable, supporting continuous cell proliferation and differentiation without delamination. While our study has demonstrated that the thickness of both the PCL scaffold and GS gel layers plays an important role in drug release, further investigation is necessary to fully understand these dynamics. Future studies will explore variations in PCL scaffold thickness and surface modifications, such as using our previously developed porous scaffold,[2] as well as changes in the thickness of the coating materials to assess their impact on the release kinetics of BMP-2 and bFGF. Such investigations will provide a deeper understanding of how these factors can be optimized for enhanced therapeutic outcomes.

We constructed a GS composite xerogel to reduce its brittleness and control the release of GFs from it. The novel GS possibly promoted easy handling when the coating was applied to a 3D-structured scaffold. The double layers were physically stable and represented a sustained release of GFs. Moreover, the composite xerogel matrices on 3D-printed PCL scaffolds may control the spatiotemporal release of GFs and impart bioactivity to the PCL surfaces. GFs, which are included separately in a double-layer fashion, can be sequentially released and may promote biological responses. Previous studies have demonstrated that the incorporation of gelatin into silica xerogel can reduce the brittleness and enhance the flexibility of the composite, thereby improving its mechanical properties. While this modification is expected to increase the resilience of the composite and make it more suitable for bone tissue engineering applications, no specific mechanical testing was conducted in this study, resulting in limited findings in this regard. Therefore, a more detailed mechanical evaluation is required to comprehensively assess these properties. Future studies will focus on conducting in-depth tests of the GS composite's mechanical properties, such as compressive strength and elasticity, to provide a more thorough evaluation of its performance.

4. Conclusion

The matrix for GF delivery should have a large porous structure to transport GFs and possess properties to prevent burst release. In this study, GS controlled the release of GFs, and the hybrid matrix was well-coated on 3D synthetic polymer scaffolds. The use of the proposed coating method and the hybrid-coated 3D-printed scaffolds may contribute to regenerative applications.

Acknowledgments

None.

Funding

This research was supported by National Research Foundation of Korea (NRF) Grants funded by the Korean government (MEST) (grant nos. NRF-2023R1A2C2004600, RS-2023-00239273, 2016R1D1A1B03930163) and the Korea University Grant.

Conflict of interest

The authors have no competing interests to declare.

Author contributions

Conceptualization: Jong-Eun Won, Hae-Won Kim
Formal analysis: Jong-Eun Won, Hyun Kyung Moon
Investigation: Jong-Eun Won
Methodology: Jong-Eun Won
Writing – original draft: Jong-Eun Won, Ji Suk Shim
Writing – review & editing: Jong-Eun Won, Hae-Won Kim, Ji Suk Shim

Ethics approval and consent to participate

This work was approved by Animal Care and Use Committee of the Korea University (KOREA-2021-0004). All necessary ethical guidelines have been followed, and relevant documentation is available upon request.

Consent for publication

Not applicable.

Availability of data

Data is available from the corresponding author upon reasonable request.

References

1. Hussey GS, Dziki JL, Badylak SF. Extracellular matrix-based materials for regenerative medicine. *Nat Rev Mater*. 2018;3(7):159-173.
doi: 10.1038/s41578-018-0023-x

2. Won JE, Lee YS, Park JH, et al. Hierarchical microchanneled scaffolds modulate multiple tissue-regenerative processes of immune-responses, angiogenesis, and stem cell homing. *Biomaterials*. 2020;227:119548.
doi: 10.1016/j.biomaterials.2019.119548

3. Babensee JE, McIntire LV, Mikos AG. Growth factor delivery for tissue engineering. *Pharm Res*. 2000;17(5):497-504.
doi: 10.1023/a:1007502828372

4. Wang ZM, Wang ZF, Lu WW, Zhen WX, Yang DZ, Peng SL. Novel biomaterial strategies for controlled growth factor delivery for biomedical applications. *NPG Asia Mater*. 2017;9:e435-451.
doi: 10.1038/am.2017.171

5. Yun YR, Jang JH, Jeon E, et al. Administration of growth factors for bone regeneration. *Regen Med*. 2012;7(3): 369-385.
doi: 10.2217/rme.12.1

6. Kang J, Park HM, Kim YW, et al. Control of mesenchymal stem cell phenotype and differentiation depending on cell adhesion mechanism. *Eur Cell Mater*. 2014;28:387-403.
doi: 10.22203/ecm.v028a27

7. Shah NJ, Hyder MN, Quadir MA, et al. Adaptive growth factor delivery from a polyelectrolyte coating promotes synergistic bone tissue repair and reconstruction. *Proc Natl Acad Sci USA*. 2014;111(35):12847-12852.
doi: 10.1073/pnas.1408035111

8. Kuttappan S, Mathew D, Jo JI, et al. Dual release of growth factor from nanocomposite fibrous scaffold promotes vascularisation and bone regeneration in rat critical sized calvarial defect. *Acta Biomater*. 2018;78:36-47.
doi: 10.1016/j.actbio.2018.07.050

9. Barnes GL, Kostenuik PJ, Gerstenfeld LC, Einhorn TA. Growth factor regulation of fracture repair. *J Bone Miner Res*. 1999;14(11):1805-1815.
doi: 10.1359/jbmr.1999.14.11.1805

10. Termaat MF, Den Boer FC, Bakker FC, Patka P, Haarman HJ. Bone morphogenetic proteins. Development and clinical efficacy in the treatment of fractures and bone defects. *J Bone Joint Surg Am*. 2005;87(6):1367-1378.
doi: 10.2106/JBJS.D.02585

11. Cochran DL, Jones AA, Lilly LC, Fiorellini JP, Howell H. Evaluation of recombinant human bone morphogenetic protein-2 in oral applications including the use of endosseous implants: 3-year results of a pilot study in humans. *J Periodontol*. 2000;71(8):1241-1257.
doi: 10.1902/jop.2000.71.8.1241

12. Epstein SE, Fuchs S, Zhou YF, Baffour R, Kornowski R. Therapeutic interventions for enhancing collateral development by administration of growth factors: basic principles, early results and potential hazards. *Cardiovasc Res*. 2001;49(3):532-542.
doi: 10.1016/s0008-6363(00)00217-0

13. Freeman FE, Pitacco P, van Dommelen LHA, et al. 3D bioprinting spatiotemporally defined patterns of growth factors to tightly control tissue regeneration. *Sci Adv*. 2020;6(33):eabb5093.
doi: 10.1126/sciadv.abb5093

14. Oliveira ER, Nie L, Podstawczyk D, et al. Advances in growth factor delivery for bone tissue engineering. *Int J Mol Sci*. 2021;22(2):903-935.
doi: 10.3390/ijms22020903

15. Nyberg E, Holmes C, Witham T, Grayson WL. Growth factor-eluting technologies for bone tissue engineering. *Drug Deliv Transl Res*. 2016;6(2):184-194.
doi: 10.1007/s13346-015-0233-3

16. Keceli HG, Bayram C, Celik E, Ercan N, Demirbilek M, Nohutcu RM. Dual delivery of platelet-derived growth factor and bone morphogenetic factor-6 on titanium surface to enhance the early period of implant osseointegration. *J Periodontal Res*. 2020;55(5):694-704.
doi: 10.1111/jre.12756

17. Won JE, Yun YR, Jang JH, et al. Multifunctional and stable bone mimic proteinaceous matrix for bone tissue engineering. *Biomaterials*. 2015;56:46-57. doi: 10.1016/j.biomaterials.2015.03.022

18. Lee SJ, Won JE, Han C, et al. Development of a three-dimensionally printed scaffold grafted with bone forming peptide-1 for enhanced bone regeneration with *in vitro* and *in vivo* evaluations. *J Colloid Interface Sci*. 2019;539:468-480. doi: 10.1016/j.jcis.2018.12.097

19. Heller M, Bauer HK, Goetze E, et al. Applications of patient-specific 3D printing in medicine. *Int J Comput Dent*. 2016;19(4):323-339.

20. Laubach M, Suresh S, Herath B, et al. Clinical translation of a patient-specific scaffold-guided bone regeneration concept in four cases with large long bone defects. *J Orthop Translat*. 2022;34:73-84. doi: 10.1016/j.jot.2022.04.004

21. Han HH, Shim JH, Lee H, et al. Reconstruction of complex maxillary defects using patient-specific 3D-printed biodegradable scaffolds. *Plast Reconstr Surg Glob Open*. 2018;6(11):e1975. doi: 10.1097/GOX.0000000000001975

22. Hernandez I, Kumar A, Joddar B. A bioactive hydrogel and 3D printed polycaprolactone system for bone tissue engineering. *Gels*. 2017;3(3):26-38. doi: 10.3390/gels3030026

23. Yu HS, Park J, Lee HS, Park SA, Lee DW, Park K. Feasibility of polycaprolactone scaffolds fabricated by three-dimensional printing for tissue engineering of tunica albuginea. *World J Mens Health*. 2018;36(1):66-72. doi: 10.5534/wjmh.17025

24. Khandaker M, Riahinezhad S, Sultana F, Morris T, Wolf R, Vaughan M. Effect of collagen-polycaprolactone nanofibers matrix coating on the *in vitro* cytocompatibility and *in vivo* bone responses of titanium. *J Med Biol Eng*. 2018;38(2):197-210. doi: 10.1007/s40846-017-0312-7

25. Burton TP, Corcoran A, Callanan A. The effect of electrospun polycaprolactone scaffold morphology on human kidney epithelial cells. *Biomed Mater*. 2017;13(1):015006. doi: 10.1088/1748-605X/aa8dde

26. Won JE, Mateos-Timoneda MA, Castano O, et al. Fibronectin immobilization on to robotic-dispensed nanobioactive glass/polycaprolactone scaffolds for bone tissue engineering. *Biotechnol Lett*. 2015;37(4):935-942. doi: 10.1007/s10529-014-1745-5

27. Dorj B, Won JE, Purevdorj O, et al. A novel therapeutic design of microporous-structured biopolymer scaffolds for drug loading and delivery. *Acta Biomater*. 2014;10(3):1238-1250. doi: 10.1016/j.actbio.2013.11.002

28. Kirby GTS, White LJ, Rahman CV, et al. PLGA-based microparticles for the sustained release of BMP-2. *Polymers-Basel*. 2011;3(1):571-586. doi: 10.3390/polym3010571

29. Bryans TR, Brawner VL, Quitevis EL. Microstructure and porosity of silica xerogel monoliths prepared by the fast sol-gel method. *J Sol-Gel Sci Techn*. 2000;17(3):211-217. doi: 10.1023/A:1008711921746

30. Czarnobaj K. Preparation and characterization of silica xerogels as carriers for drugs. *Drug Deliv*. 2008;15(8):485-492. doi: 10.1080/10717540802321495

31. Kortesuo P, Ahola M, Karlsson S, Kangasniemi I, Yli-Urpo A, Kiesvaara J. Silica xerogel as an implantable carrier for controlled drug delivery – evaluation of drug distribution and tissue effects after implantation. *Biomaterials*. 2000;21(2):193-198. doi: 10.1016/S0142-9612(99)00148-9

32. Ahola M, Kortesuo P, Kangasniemi I, Kiesvaara J, Yli-Urpo A. Silica xerogel carrier material for controlled release of toremifene citrate. *Int J Pharm*. 2000;195(1-2):219-227. doi: 10.1016/s0378-5173(99)00403-2

33. Munusamy P, Seleem MN, Alqublan H, Tyler R, Sriranganathan N, Pickrell G. Targeted drug delivery using silica xerogel systems to treat diseases due to intracellular pathogens. *Mat Sci Eng C-Mater*. 2009;29(8):2313-2318. doi: 10.1016/j.msec.2009.05.020

34. Simovic S, Ghouchi-Eskandar N, Sinn AM, Losic D, Prestidge CA. Silica materials in drug delivery applications. *Curr Drug Discov Technol*. 2011;8(3):269-276. doi: 10.2174/157016311796799026

35. Xue JM, Tan CH, Lukito D. Biodegradable polymer-silica xerogel composite microspheres for controlled release of gentamicin. *J Biomed Mater Res B Appl Biomater*. 2006;78(2):417-422. doi: 10.1002/jbm.b.30503

36. Lee EJ, Shin DS, Kim HE, Kim HW, Koh YH, Jang JH. Membrane of hybrid chitosan-silica xerogel for guided bone regeneration. *Biomaterials*. 2009;30(5):743-750. doi: 10.1016/j.biomaterials.2008.10.025

37. Mahony O, Tsigkou O, Ionescu C, et al. Silica-gelatin hybrids with tailorable degradation and mechanical properties for tissue regeneration. *Adv Funct Mater*. 2010;20(22):3835-3845. doi: 10.1002/adfm.201000838

38. Kim HW, Knowles JC, Kim HE. Hydroxyapatite and gelatin composite foams processed via novel freeze-drying and crosslinking for use as temporary hard tissue scaffolds. *J Biomed Mater Res A*. 2005;72(2):136-145. doi: 10.1002/jbm.a.30168

39. Carpena NT, Min YK, Lee BT. Improved *in vitro* biocompatibility of surface-modified hydroxyapatite sponge scaffold with gelatin and BMP-2 in comparison against a commercial bone allograft. *ASAIO J*. 2015;61(1):78-86. doi: 10.1097/MAT.0000000000000155

40. Fu A, Tang R, Hardie J, Farkas ME, Rotello VM. Promises and pitfalls of intracellular delivery of proteins. *Bioconjug Chem*. 2014;25(9):1602-1608.
doi: 10.1021/bc500320j

41. Zhou X, Weng W, Chen B, et al. Mesoporous silica nanoparticles/gelatin porous composite scaffolds with localized and sustained release of vancomycin for treatment of infected bone defects. *J Mater Chem B*. 2018;6(5):740-752.
doi: 10.1039/c7tb01246b

42. Uskokovic V, Ghosh S, Wu VM. Antimicrobial hydroxyapatite-gelatin-silica composite pastes with tunable setting properties. *J Mater Chem B*. 2017;5(30):6065-6080.
doi: 10.1039/C7TB01794D

43. Song JH, Kim HE, Kim HW. Collagen-apatite nanocomposite membranes for guided bone regeneration. *J Biomed Mater Res B Appl Biomater*. 2007;83(1):248-257.
doi: 10.1002/jbm.b.30790

44. Liu C, Li X, Zhao Q, et al. Nanofibrous bicomponent scaffolds for the dual delivery of NGF and GDNF: controlled release of growth factors and their biological effects. *J Mater Sci Mater Med*. 2021;32(1):9.
doi: 10.1007/s10856-020-06479-2

45. Gaydhane MK, Sharma CS, Majumdar S. Electrospun nanofibres in drug delivery: advances in controlled release strategies. *RSC Adv*. 2023;13(11):7312-7328.
doi: 10.1039/d2ra06023j

46. Houaoui A, Szczodra A, Lallukka M, et al. New generation of hybrid materials based on gelatin and bioactive glass particles for bone tissue regeneration. *Biomolecules*. 2021;11(3):444.
doi: 10.3390/biom11030444

47. Fujimoto Y, Yokozeki T, Yokoyama A, Tabata Y. Basic fibroblast growth factor enhances proliferation and hepatocyte growth factor expression of feline mesenchymal stem cells. *Regen Ther*. 2020;15:10-17.
doi: 10.1016/j.reth.2020.03.013

48. Visser R, Arrabal PM, Santos-Ruiz L, Becerra J, Cifuentes M. Basic fibroblast growth factor enhances the osteogenic differentiation induced by bone morphogenetic protein-6 *in vitro* and *in vivo*. *Cytokine*. 2012;58(1):27-33.
doi: 10.1016/j.cyto.2011.12.020

49. Lee H, Won DS, Park S, et al. 3D-printed versatile biliary stents with nanoengineered surface for anti-hyperplasia and antibiofilm formation. *Bioact Mater*. 2024;37:172-190.
doi: 10.1016/j.bioactmat.2024.03.018

ACCSCIENCE PUBLISHING

International Journal of Bioprinting

RESEARCH ARTICLE

Deformation monitoring and stress distribution prediction of 3D-printed hydroxyapatite scaffolds

Danyu Yao[1], Luge Zhang[1], Hong Liu[1], Ming Liu[2], Ling Wang[1]*, and Mingen Xu[1]*

[1]School of Automation, Hangzhou Dianzi University, Hangzhou, Zhejiang, China

[2]Zhejiang Cancer Hospital, Hangzhou Institute of Medicine (HIM), Chinese Academy of Sciences, Hangzhou, Zhejiang, China

Abstract

Hydroxyapatite (HAP) scaffolds created through biological three-dimensional (3D) printing have been extensively utilized in bone tissue engineering. However, clinical outcomes remain unsatisfactory. Stress-induced fractures are a primary cause of failure in clinical bone implant repairs. Finite element analysis (FEA) can predict stress distribution within scaffolds under load, aiding in the identification of stress concentrations. Nevertheless, limitations in the printing fidelity of bioinks lead to discrepancies between the printed scaffold structure and the theoretical design, resulting in inaccurate predictions. This study introduced an effective approach for predicting the mechanical properties and internal stress distribution of printed scaffolds. HAP scaffolds with varying filling angles (90°, 60°, 45°) were constructed through 3D printing. These scaffolds were analyzed using a combination of optical coherence tomography (P-OCT) scanning and micro-computed tomography (micro-CT) imaging, integrated with FEA, to enhance the accuracy of stress distribution predictions. The findings demonstrated that the mechanical strength of scaffolds predicted by the reconstructed model was closer to experimental values compared to predictions made by commonly used theoretical models (improved from 55% to 78%). During actual testing, stress concentration sites predicted by the reconstructed model were the first to exhibit fragmentation, validating the accuracy of stress distribution predictions. Moreover, scaffolds printed at different infill angles displayed varying degrees of distortion. Scaffolds printed at a 90° angle displayed the highest fidelity with the fewest defects, and their stress distributions under different conditions were well-correlated. The method proposed in this study facilitates more accurate prediction and evaluation of scaffold performance early in development, enabling the selection of scaffolds with suitable mechanical properties, thereby reducing testing cycles and improving safety in bone defect repair.

Keywords: Deformation monitoring; Stress distribution prediction; Finite element analysis; 3D printed scaffold; Bone repair

***Corresponding authors:**
Ling Wang
(lingw@hdu.edu.cn)

Mingen Xu
(xumingen@hdu.edu.cn)

Citation: Yao D, Zhang L, Liu H, Liu M, Wang L, Xu M. Deformation monitoring and stress distribution prediction of 3D-printed hydroxyapatite scaffolds. *Int J Bioprint*. 2024;10(6):4460. doi: 10.36922/ijb.4460

Received: August 6, 2024
1st revised: September 3, 2024
2nd revised: September 18, 2024
Accepted: September 26, 2024
Published Online: September 26, 2024

Copyright: © 2024 Author(s). This is an Open Access article distributed under the terms of the Creative Commons Attribution License, permitting distribution, and reproduction in any medium, provided the original work is properly cited.

Publisher's Note: AccScience Publishing remains neutral with regard to jurisdictional claims in published maps and institutional affiliations.

1. Introduction

Bone defects, resulting from tumor resection, congenital malformations, sports injuries, or infections, often lead to significant loss of function.[1] The regeneration and reconstruction

of bone defects are pressing needs. Although organ transplantation is an effective treatment for bone repair,[2] the challenge of insufficient donor supply remains.[3,4] Bone tissue engineering offers hope for repairing bone defects and has garnered significant attention in the field of bone regeneration.[5,6] Bone tissue engineering scaffolds provide a temporary environment for cell adhesion, proliferation, and differentiation, gradually degrading as new bone tissue forms, ultimately facilitating bone tissue regeneration.[7] The mechanical properties of bone implants are crucial factors influencing implant stability and success. There is an urgent need to develop bone scaffolds that integrate both biological and mechanical properties.

In clinical settings, artificial bone scaffolds may fracture after a period of implantation, leading to repair failures or even bone necrosis. This issue is closely related to the mechanical strength and stress distribution of the implanted scaffolds.[8] When the elastic modulus of an implant significantly exceeds that of natural bone or when stress concentrations occur, the mechanical balance between the implant and the surrounding bone tissue can be disrupted, leading to implant loosening and premature fracture.[9] Additionally, localized stress within the scaffold that exceeds that of the surrounding material may result in stress-induced fractures. One of the urgent problems to be solved is how to optimize and accurately predict the mechanical properties of scaffolds during their construction process, avoiding stress concentration while ensuring their biocompatibility.

Hydroxyapatite (HAP), the main component of natural bone, is an ideal material for bone repair. It can be fabricated into bone repair scaffolds with different properties through techniques such as freeze-drying or biological 3D printing.[10–14] Among these, 3D printing technology allows for customized design for patients and precise control over the shape of the scaffolds,[15] thus widely used in bone tissue engineering.[16] Researchers have optimized the mechanical properties of scaffolds and regulated the stress distribution within scaffolds, by altering their macroscopic morphologies.[17,18] Controlling the surface morphology and pore geometry of scaffolds provides great potential for manipulating the mechanical behavior of 3D-printed scaffolds. Although a large amount of work has been reported in the biomedical field,[19–22] there is still a lack of understanding regarding how these structures affect the stress distribution within the scaffold under mechanical compressive loads.

Finite element analysis (FEA) can analyze the mechanical behavior of various complex structures by simulating their mechanical behavior under loading conditions, predicting mechanical properties such as modulus and strength, as well as stress distribution within the scaffold,[23–28] providing important references for the design and optimization of bone repair scaffolds. Currently, FEA often uses theoretically designed scaffold structures as models. However, there are deviations between the actual structure of the 3D printed scaffold and the design structure, leading to the distortion of the FEA model, low prediction accuracy, and lack of application value.[29–31]

To address these issues, this work proposes an effective method for predicting the mechanical properties and stress distribution within printed scaffolds, which is more accurate compared to traditional FEA. This study combined optical coherence tomography (P-OCT), micro-computed tomography (CT), and FEA to evaluate and monitor the deformation of HAP scaffolds in different states during the preparation process (after printing, sintering, and drying). It also investigated the impact of different states and micropore morphologies (90°, 60°, 45°) on the stress distribution within the HAP scaffolds. This method can effectively predict the stress distribution of the scaffold after sintering immediately after printing, shortening the experimental cycle and improving the success rate of clinical applications.

2. Methods

2.1. Printing ink preparation

The printing ink was prepared by mixing HAP powder with organics. Briefly, 5.2 mL of deionized water (Mingshan, China) was mixed with 0.16 g of ammonium polyacrylate powder (Mingshan, China) and 0.2 g of sodium alginate powder (Regenovo Biotechnology Co., Ltd., China). This mixture was subjected to agitation for 5 min in a mixer (Thinky, Japan). Subsequently, 7 g of HAP powder (Macklin, China) was added and stirred thoroughly. The final uniformly mixed ink was loaded into a printing cartridge, which was then sealed and stored in a refrigerator at 4°C for preservation.

2.2. Scaffold design and fabrication

After ink preparation, 3D printing was conducted using Bio-Architect-PX (Regenovo Biotechnology Co., Ltd., China). Three different printing angles (90°, 60°, 45°) of HAP scaffolds were designed in this study, with a porosity of 60% (Figure 1). A needle with an inner diameter of 0.41 mm was selected, with a printing speed of 8 mm/s and air pressure set at 0.2 MPa. The model parameters of the printing scaffolds are listed in Table 1. After printing, the scaffolds were crosslinked in a 5% (w/v) calcium chloride solution and then transferred to a −80°C ultralow temperature freezer overnight. Finally, the scaffolds were dried in a freeze-dryer (Christ, Germany). The dried scaffolds were sintered at 1100°C in a box-type resistance furnace to achieve the final state.

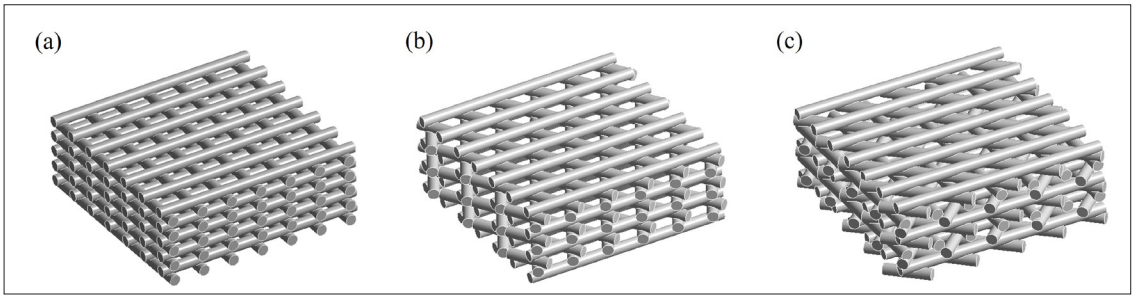

Figure 1. Schematic of the designed model: (a) 0°/90° scaffold; (b) 0°/60°/120° scaffold; and (c) 0°/45°/90°/135° scaffold. All scaffolds have a size of 8 × 8 × 3 mm^3, and a layer thickness of 0.3 mm.

Table 1. Scaffold model parameters

Rotation angle (°)	Size (mm^3)	Porosity (%)	Pore size (mm)
90	8 × 8 × 3	60	1.2
60	8 × 8 × 3	60	1.2
45	8 × 8 × 3	60	1.3

2.3. Mechanical properties

The mechanical properties of the HAP scaffolds were tested using an AI-700-S (GOTECH, China) compression testing machine. Loading was performed at a displacement rate of 5 mm/min, and scaffolds with different angles in different states were tested separately. According to the stress–strain curve, the compressive modulus (*E*) and compressive strength () of the scaffolds were calculated using **Equations I and II**, respectively.

$$E = \frac{F_1 - F_2}{D_1 - D_2} \quad \text{(I)}$$

$$\sigma = \frac{F_{max}}{S} \quad \text{(II)}$$

In these equations, F_1 and F_2 represent the stress corresponding to any two points in the linear variation stage of the stress–strain curve of the scaffold, respectively. D_1 and D_2 represent the strain corresponding to the above two points, respectively. F_{max} is the force corresponding to the fracture point of the scaffold, and *S* is the cross-sectional area of the scaffold, that is, the area under force.

2.4. Macroscopic morphology and porosity testing

The macroscopic structure of the HAP scaffolds was observed and recorded using a digital camera. The weight of the scaffolds was measured using an electronic balance, and the length, width, and height of the scaffolds were measured using a vernier caliper. The porosity test was conducted using the density method:

$$P = \left(1 - \frac{\rho_1}{\rho_2}\right) \times 100\% \quad \text{(III)}$$

where *P* is the desired porosity, ρ_1 is the density of the scaffold, i.e., the mass divided by the volume, and ρ_2 is the theoretical density of the HAP material.

2.5. Scaffold morphology acquisition and reconstruction

The Bio-Architect-PX device integrates optical coherence tomography (OCT) technology, which allows for non-destructive monitoring of the 3D structure of printed scaffolds during the additive manufacturing process and captures the 3D structural images of the entire printed scaffold after printing. Previous works of our team have reported on this technology and system, referring to it as P-OCT technology.[32,33] In this study, a swept-source OCT system with a lateral resolution of 15 μm and an axial resolution of 7.2 μm was used to scan the printed scaffold layer by layer during the printing process, and the P-OCT images of the entire printed scaffold were obtained using the software integrated within the Bio-Architect-PX device after printing. Micro-CT, a nondestructive 3D imaging technique, was used to perform non-destructive imaging of the scaffold, obtaining internal 2D cross-sectional images. In this study, a micro-CT (μCT-100; Scanco Medical AG, Switcerland) with a resolution of 15 μm was used to scan the scaffold after it was dried and sintered. The DICOM files of the P-OCT and micro-CT images were imported into Mimics software (Materialise, Belgium), selecting the threshold value range for image segmentation to generate the 3D reconstructed model.

2.6. Finite element analysis

Ansys Workbench 19.2 software was used to simulate the mechanical properties of both the theoretically designed scaffolds (Figure 1) and the reconstructed scaffolds (Figure 2). The properties of the HAP material were consistent with our previous work,[34] as presented in Table 2.

Regarding boundary conditions, to simulate actual compression mechanics testing experiments, two identical

Table 2. Properties of hydroxyapatite (HAP)

Parameter	Specification
Density (g/cm^3)	3.16
Elastic modulus (MPa)	300
Poisson's ratio	0.3
Tensor property	Anisotropy

rigid bodies were modeled at the upper and lower ends of the scaffold model, simulating the weights and steel plates used in compression experiments. The lower rigid body was fixed, and a downwards displacement boundary condition of 2.5 mm was applied to the upper rigid body. The displacement in other directions was set to 0 mm. The calculation time was set to 30 s and the compression speed to 5 mm/min. The contact between the scaffold and the rigid bodies was set as bonded contact.

For mesh partitioning, in the theoretical model, tetrahedra meshes with a size of 0.2 mm were selected. For the reconstructed model, after converting the surface mesh to a solid mesh following the method described below, tetrahedra meshes with a size of 0.2 mm were also selected (Figure 2). Briefly, automatic mesh partitioning was conducted on the 3D solid model in STL format using 3-matic software. After completing the surface mesh partitioning, quality inspection and adjustment were performed on the generated mesh. Following mesh repair, further manual mesh partitioning was performed on the model. By adjusting the mesh size, optimizing the surface mesh, and smoothing the model, it was ensured that no sharp structures would exist on the model's surface. Lastly, a quadratic tetrahedral mesh was created. The model, with a partitioned volume mesh, was exported as an STL file and saved for subsequent FEA.

The solver setup used artificial time-stepping control, with a termination time for solving set at 30 s, corresponding to the practical compression test at a speed of 5 mm/min, and the time step was set at 0.1 s, with 300 iterations. The equivalent stress of all scaffolds was evaluated.

2.7. Statistical analysis

The results were presented as mean ± standard deviation, and statistical analysis was performed using SPSS 22.0 software. Two-way analysis of variance (ANOVA) was used to evaluate the differences between groups. In statistics, * denotes $p < 0.05$, ** denotes $p < 0.01$, and *** denotes $p < 0.001$; $p < 0.05$ is considered statistically significant.

3. Results and discussion

3.1. Macroscopic deformation of 3D-printed hydroxyapatite scaffolds

The scaffold used for bone repair should accurately match the size and shape of the defect to ensure that it can effectively support and repair the damaged tissue. However, the scaffold will undergo significant deformations during the preparation process, especially during the drying and sintering stages. To ensure that the final porous scaffold could fit the defect site, we explored the shape characteristic changes of the scaffold during the preparation process.

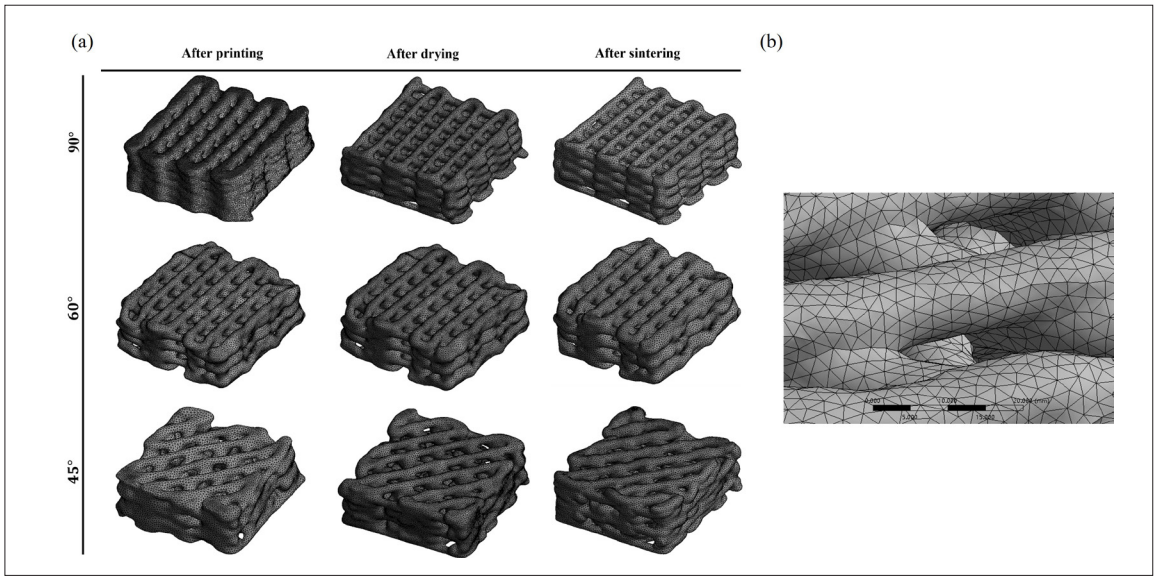

Figure 2. Reconstruction model mesh division and local mesh characteristic diagram. (a) Mesh division effect of the reconstructed models. (b) Local mesh distribution characteristics of the reconstructed scaffold model at 90° after sintering. Areas with irregular structures had denser meshes. Scale bar: The scale bar was divided into four sections, with a total length of 20 mm and each section representing 5 mm.

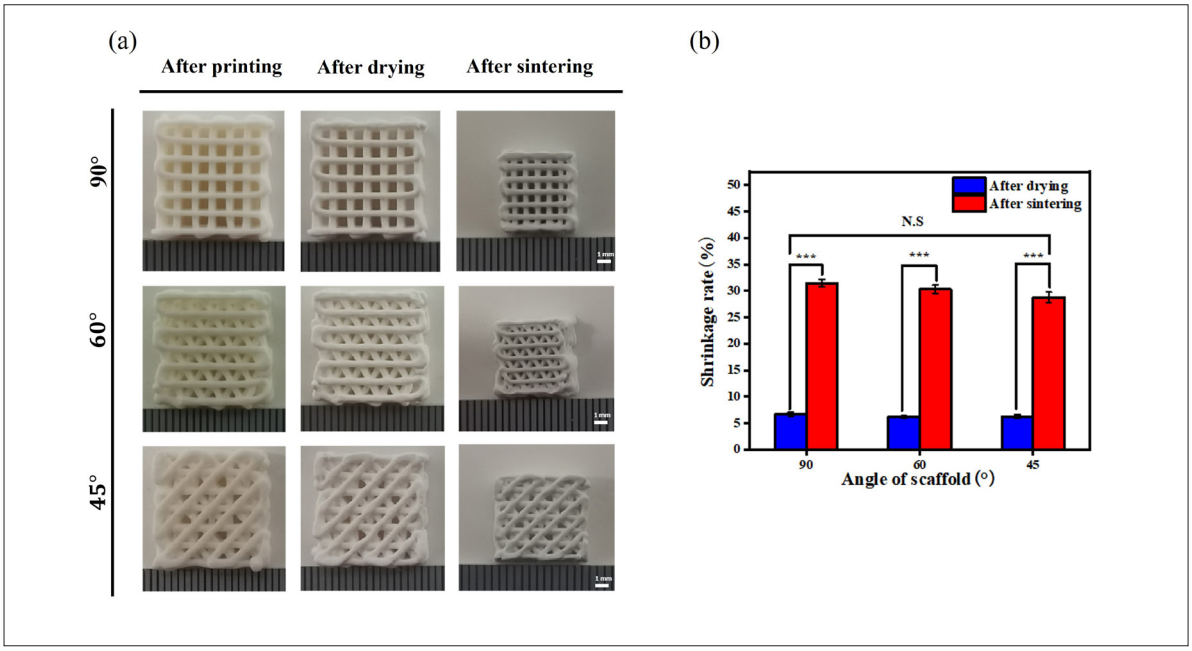

Figure 3. Macroscopic deformation of porous scaffolds. (a) Schematic diagram of the macroscopic morphology of scaffolds in three states; scale bars: 1 mm. (b) Shrinkage rate of scaffolds (n = 3); significant shrinkage observed in scaffold volume at different angles in both drying and sintering states, with a shrinkage rate of 30% after sintering. ***$p < 0.001$; N.S., not significant.

Porous scaffolds were fabricated using extrusion-based 3D printing, and their macroscopic morphological changes after drying and sintering were observed (Figure 3).

The printed scaffolds (Figure 3a) exhibited high similarity to the theoretically designed (Figure 1) morphology. There was no significant difference in macroscopic morphology between the printed and theoretically designed scaffolds. However, after drying and sintering, the scaffolds exhibited significant macroscopic morphological changes (Figure 3). After lyophilization, the scaffold volume shrank by nearly 7% compared to the printed state, mainly due to moisture evaporation from within the scaffold during drying. The printing angle had no significant effect on the scaffold shrinkage rate (Figure 3b). After sintering, the scaffolds underwent a volume contraction of approximately 30% compared to the post-printing state. During sintering, organic matters in the scaffolds were removed, leaving only HAP, which resulted in significant shrinkage. The shrinkage rate of scaffolds at the three printing angles decreased significantly after sintering, but the printing angle did not have a significant impact on the scaffold's shrinkage rate.

3.2. Monitoring of microscopic deformation of 3D-printed hydroxyapatite scaffold

We found that during the preparation process, the macroscopic morphology of the scaffolds underwent significant changes (Figure 3). These changes might lead to alterations in their surface or internal microstructures, such as variations in the stress contact surface, filament diameter, and scaffold porosity, which affect the stress distribution within the scaffolds. Scanning and reconstruction were performed on the scaffolds after printing, drying, and sintering (Figure 4). Unlike the theoretically designed structure, the actual printed scaffolds had uneven surfaces (Figure 4a). Scaffolds printed at three different angles exhibited varying degrees of distortion and printing defects. Among them, the 90° scaffold had a relatively regular shape and a smoother surface, while the 60° and 45° scaffolds displayed collapse and protrusion on the surface. After drying and sintering, the 90° scaffold exhibited more uniform shrinkage, while the 60° and 45° scaffolds experienced warping, with the originally protruded areas forming dense tips.

The pore size of the scaffold plays a crucial role in the rate of mass transfer and cell growth during bone repair, and it, together with porosity, influences cell adhesion, growth, migration, and differentiation within the scaffold. According to macroscopic images, the morphology of the "after printing" scaffold exhibited a high degree of similarity to the theoretically designed morphology (Figures 1 and 3). Statistical analysis of pore size revealed that the pore sizes of the "after printing" 90°, 60°, and 45° scaffolds were 90.97 ± 4.00%, 90.63 ± 1.45%, and 87.02 ± 4.42% of the designed dimensions, respectively. The pore sizes of all three scaffold

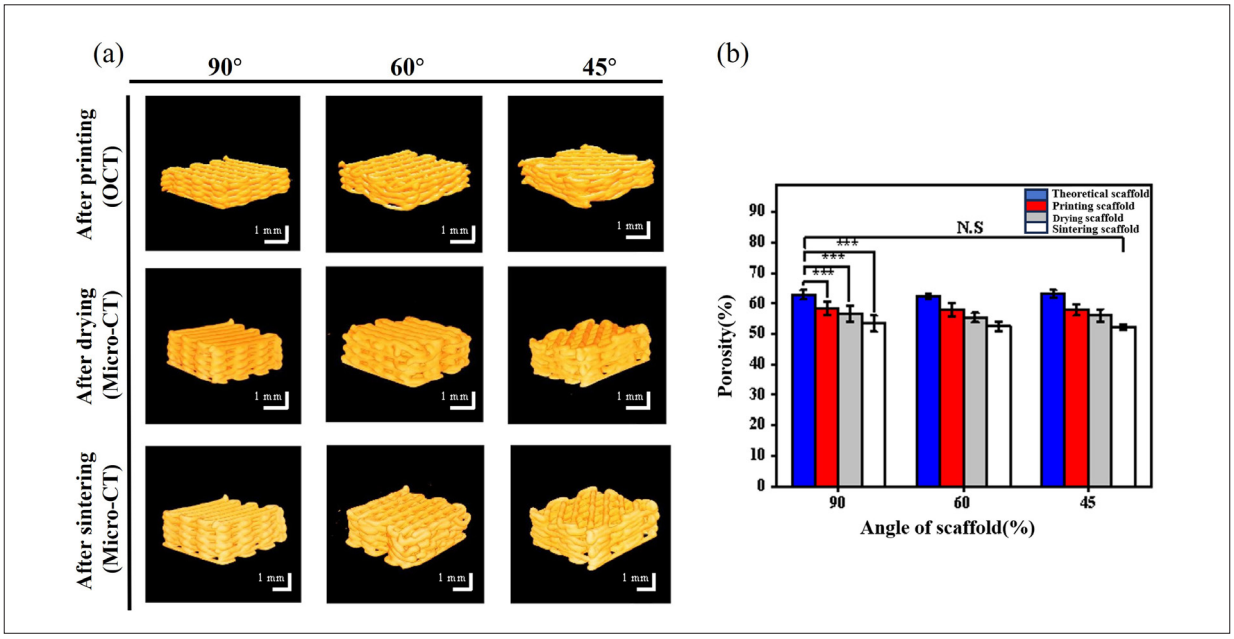

Figure 4. 3D reconstruction of scaffolds in different states and angles. (a) Macroscopic morphology of reconstructed scaffolds in three angles (left to right: 90°, 60°, and 45°) and states (top to bottom: printed, dried, and sintered), with protrusions or collapses present on the surface of 60° and 45° scaffolds during scaffold preparation. (b) Porosity of scaffolds (n = 3); the porosity decreased after drying and sintering, but there was no significant difference in porosity between scaffolds in the same state at different angles. ***$p < 0.001$; N.S., not significant. Scale bars: 1 mm.

groups were approximately 1 mm, which was similar to the pore size of bone trabeculae.[35]

In this study, the designed porosity of each scaffold was 60%. Porosity calculations of scaffolds (Figure 4b) demonstrated that after drying and sintering, the porosity of 90°, 60°, and 45° scaffolds decreased to 53.48 ± 2.64%, 52.49 ± 1.46%, and 52.23 ± 1.19%, respectively. All scaffolds displayed a decreasing trend in porosity with different printing angles, but no significant differences in porosity between different angles. The porosity of scaffolds after sintering remained above 50%. Cortical bone typically has a porosity of only 5–10%, while cancellous bone contains a porosity of 50–90%[27,36]; the porosity of the sintered scaffolds was within a reasonable range of the porosity of human trabecular bone.

As observed from the top view of the XY plane of the scaffolds (Figure 5a), the filament diameter of the 90° scaffold was relatively uniform, while the 60° and 45° scaffolds exhibited ink accumulation at the corners, resulting in larger fiber diameters at these points, especially for the 45° scaffold, where the accumulation was more pronounced. Quantitative analysis of the scaffold morphology (Figure 5b) revealed that the average measured filament diameters after actual printing were larger than the theoretical filament diameter (0.41 mm). Among them, the average filament diameter of the 90° scaffold was closest to the theoretical value, indicating its high fidelity. After drying and sintering, the filament diameter of the scaffold gradually decreased. The printing ink contained inorganic HAP particles, organic matter, and a large amount of water. After drying, the water in the scaffold was removed, leading to a decreasing trend in filament diameter. After sintering, the organic materials were removed, and the sintering temperature was much higher than the melting point of HAP, causing HAP particles to form dense agglomerates and further reducing the fiber diameter. These factors contributed to the microscopic deformation of the scaffold structure.

3.3. Mechanical properties of 3D-printed hydroxyapatite scaffold

The scaffold before sintering contained organics, which gave scaffolds a certain degree of toughness, and the presence of organics led to a lower mechanical strength. After sintering, only HAP remained. The stress-strain curves of the sintered scaffolds exhibited linear characteristics (Figure 6). The compressive strengths of the 90°, 60°, and 45° scaffolds were 7.65 ± 1.08, 4.81 ± 0.31, and 3.45 ± 0.28 MPa, respectively, indicating a decreasing trend with the decrease in angle. The trend of compressive modulus changes was consistent with compressive strength. The 90° scaffold significantly outperformed the 60° and 45° scaffolds in both compressive strength and compressive modulus.

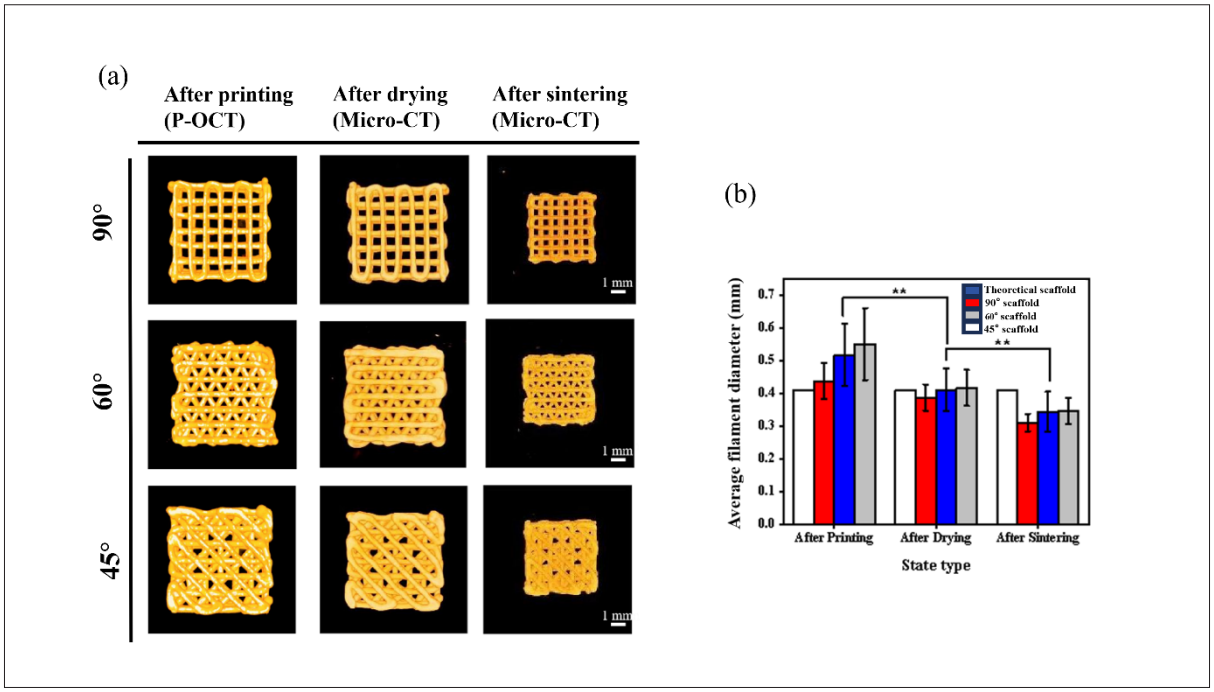

Figure 5. Reconstructed images of scaffolds at different states and angles on the XY plane. (a) Macroscopic morphology of reconstructed scaffolds in three states: printed scaffolds (left), dried scaffolds (middle), and sintered scaffolds (right). (b) Average filament diameter of reconstructed scaffolds (n = 3); filament diameter significantly decreased after drying and sintering. **$p < 0.01$.

This result was consistent with published research; the pore structure significantly affects the mechanical properties of the scaffold. Adjacent layers of ink deposition on scaffolds with different pore structures resulted in varying numbers of joints, with structures with more intersections exhibiting stronger mechanical properties.[37] The 90° scaffold had the maximum number of joints, whereas the 45° scaffold exhibited the fewest (Figure 3). The larger number of joints might strengthen the mechanical properties of the 90° scaffolds when it is compressed.

3.4. Establishment of finite element analysis prediction methods

3.4.1. Comparison of simulation and experimental data

In this study, FEA was employed to reveal the stress distribution within the scaffolds. Given the printing defects and morphological changes during the scaffold preparation, the scan-reconstructed model was adopted to simulate and analyze the mechanical behavior of the sintered HAP scaffold. The results were then compared with those obtained from a commonly used theoretical model. Both models predicted linear stress–strain curves for the sintered HAP scaffolds, consistent with the behavior of brittle materials (Figure 7b), matching the measured trend (Figure 7a). The prediction results of both models indicate that the compressive strength and modulus of compression of the 90° scaffolds were the highest, demonstrating its superior compressive ability, followed by the 60° and 45° scaffolds, indicating that the microporous structure of the scaffold had a significant impact on its mechanical properties. However, there was a significant difference in the numerical predictions between the two models. Taking the 90° scaffold as an example, the predicted compressive strength and compressive modulus of the reconstruction model were 6.54 ± 2.12 and 42.02 ± 3.74 MPa, respectively, while in the theoretical model, they were 14.02 ± 1.88 and 80.24 ± 9.88 MPa, respectively. Comparing the predicted results with the actual test results (compressive strength: 7.65 ± 1.08 MPa; compressive modulus: 45.96 ± 3.57 MPa), it was found that the accuracy of the reconstruction model prediction was over 85%, significantly better than that of the theoretical model (less than 60%). This deviation might be due to simplification during the modeling process and fluctuations in filament diameter during actual printing (Figure 5), which prevented the theoretical model from accurately reflecting the true structure and performance of the scaffold. Using theoretical models for analysis and prediction might overestimate the mechanical performance of scaffolds, leading to scaffold failure during clinical use. In contrast, the reconstruction model was

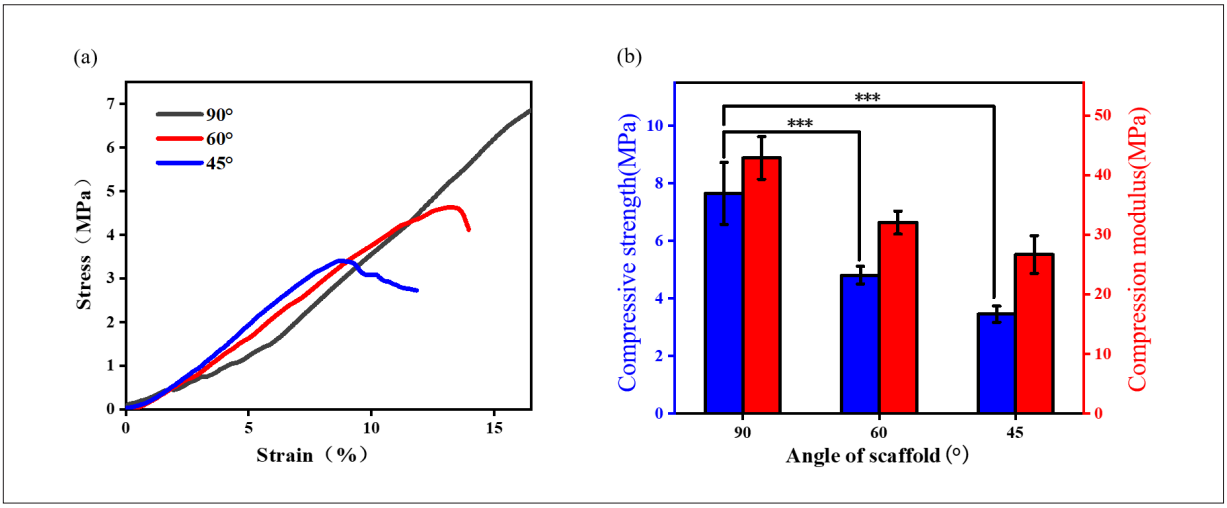

Figure 6. Mechanical properties of 3D-printed hydroxyapatite (HAP) scaffolds. (a) Stress–strain curve of sintered scaffolds, displaying a linear trend. (b) Mechanical properties of scaffolds at different angles ($n = 3$); blue color denotes compressive strength and red color denotes compression modulus. The 90° scaffold exhibits the highest compressive strength and compression modulus. ***$p < 0.001$.

based on scanning a printed scaffold, which could better reflect the true state of the scaffold.

3.4.2. Stress distribution predictions

Corresponding equivalent stress nephograms (Figure 8) were obtained from the FEA results of the theoretical model and reconstructed model. By comparing the results of the two analysis methods, it was found that there were significant differences in the stress distribution obtained by the reconstructed model compared to that of the design model.

According to the stress nephogram obtained from the theoretical model analysis (Figure 8a), the stress distribution within the scaffold was highly regular, with all stress concentrations occurring at the intersection points. This distribution characteristic can be attributed to the orderly structure of the design model and uniformity in the positions and sizes of the pillars, leading to even stress transfer and distribution. As the main factors supporting the scaffold and withstanding pressure, the number and alignment of the struts directly affect the mechanical properties of the scaffold, suggesting that more and better-aligned pillars can better withstand pressure and improve mechanical performance.

However, there were significant differences between the stress distribution obtained from the FEA using the reconstructed model and the results of the theoretical model (Figure 8b). The predictions of the reconstructed model revealed pronounced stress concentration areas, with the 90° scaffold mainly experiencing stress concentrations at the edges, while the 60° and 45° scaffolds exhibited more disordered concentration areas, primarily in the protruding regions of the scaffold. These results are related to the uneven surface of the printed scaffold due to material deposition during the printing process. The uneven surface of printed scaffolds, with areas around the 90° corners and edges higher than the central region, experienced greater stress, and stress was more concentrated at the edges. The 60° and 45° scaffolds had more printing defects, with stress concentrated at protruding parts.

Compression tests were conducted on the scaffolds to obtain the scaffold fracture state diagram (Figure 9). It was observed that the fracture points of the 90° scaffold were mainly distributed along the peripheral edges, while the 60° and 45° scaffolds fractured at the protruding vertices, consistent with the stress concentration areas predicted by the reconstruction model. This demonstrated that the reconstructed model can accurately reflect the stress concentration within the scaffolds, improving the accuracy of the analysis. It was noteworthy that when the edge of the scaffold fractured, its central region remained intact, which further proved the influence of stress concentration on scaffold failure.

3.5. Early prediction of stress distribution in hydroxyapatite scaffolds

Using the reconstructed model for FEA can effectively predict the internal stress distribution of the scaffold without additional costs. The preparation process of 3D-printed HAP scaffolds is cumbersome, requiring further drying and sintering after printing, which leads to a relatively long cycle. This paper analyzes the equivalent stress nephograms of scaffolds in different states

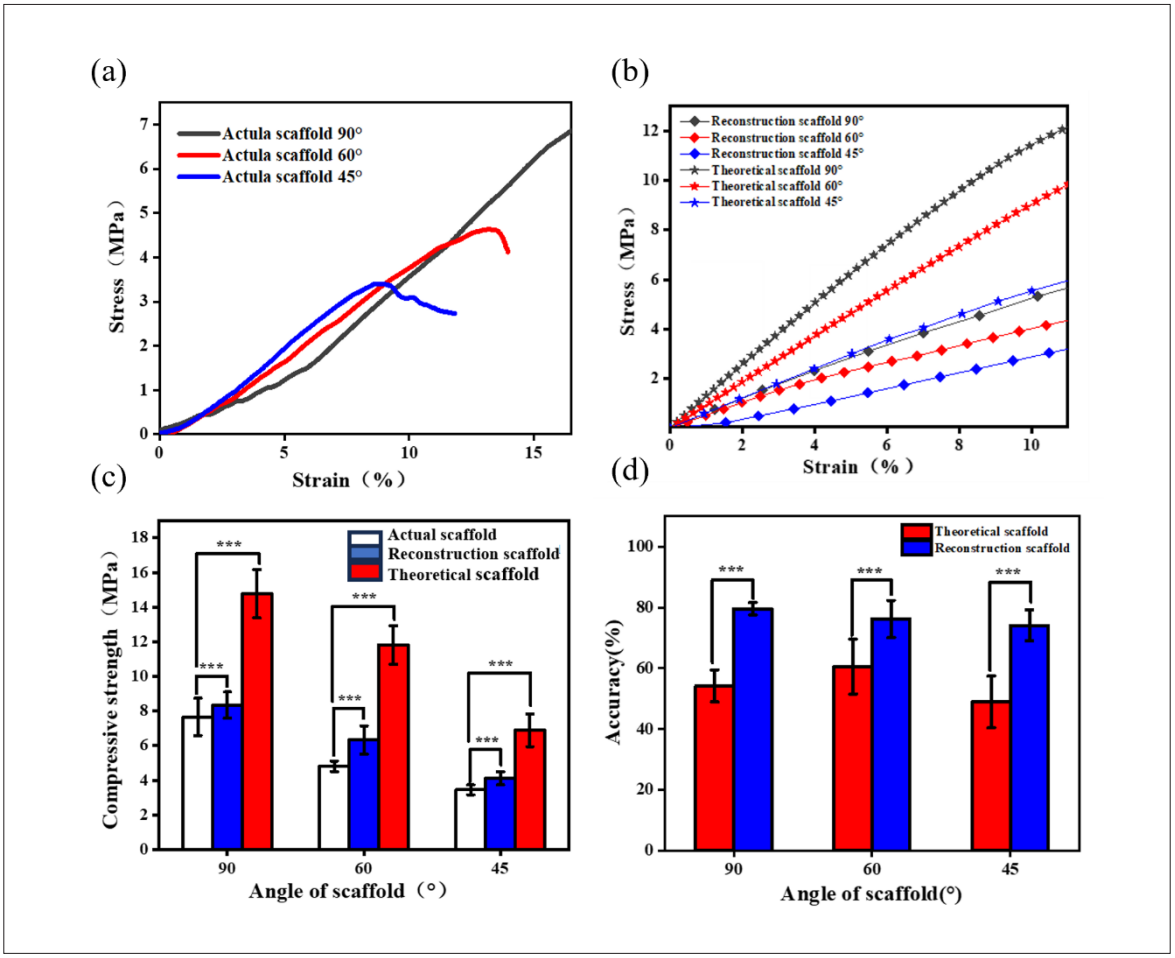

Figure 7. Mechanical data of sintered scaffolds at different angles. (a) Stress–strain curve of the actual scaffold. (b) Stress–strain curve of the simulated scaffold. (c) Mechanical performance of the simulated versus actual scaffolds ($n = 3$); the compressive strength of reconstructed and theoretical scaffolds was generally higher than that of the actual scaffold. (d) Accuracy of simulation versus experimental finite element analysis (FEA) data ($n = 3$); reconstructed scaffold FEA data exhibit higher accuracy; ***$p < 0.001$.

(Figure 10) to explore the changes in stress distribution during the preparation process of the same scaffold.

The states "after printing," "after drying," and "after sintering" correspond to the state of the same scaffold right after printing, after freeze-drying to remove moisture, and finally after sintering, respectively. We performed P-OCT/micro-CT scans on the scaffolds in these states, reconstructed the scaffold morphology based on the scan data, and then performed FEA analysis on the reconstructed images. If the scaffold structure did not change during the preparation process, the predicted FEA stress distribution of the model should be consistent in all states. If it couldn't correspond, it indicated that the structure of the scaffold had undergone non-uniform changes. According to the results of the equivalent stress nephograms of the scaffolds, there was a correspondence between the initial state (after printing) and the final state (after sintering) of the 90° scaffold in terms of stress distribution. Specifically, the stress of the scaffold in both states was mainly concentrated at the edges and corners. In contrast, the correspondence of stress distribution for the 60° scaffold in the three states was relatively low. For the 45° scaffold, there was only partial correspondence in stress distribution among the three states, and the distribution range of stress concentration points in the sintered scaffold was wider.

During the drying and sintering processes, significant morphological changes occurred, introducing uncertainties in the regulation of the scaffold's mechanical properties. The internal moisture and organics in the scaffold were gradually removed, leading to scaffold shrinkage and warping phenomena. These significant changes in the macroscopic morphology resulted in notable differences in its stress distribution compared to its post-printing state. The 60° and 45° scaffolds, due to their structural complexity, exhibited more printing defects

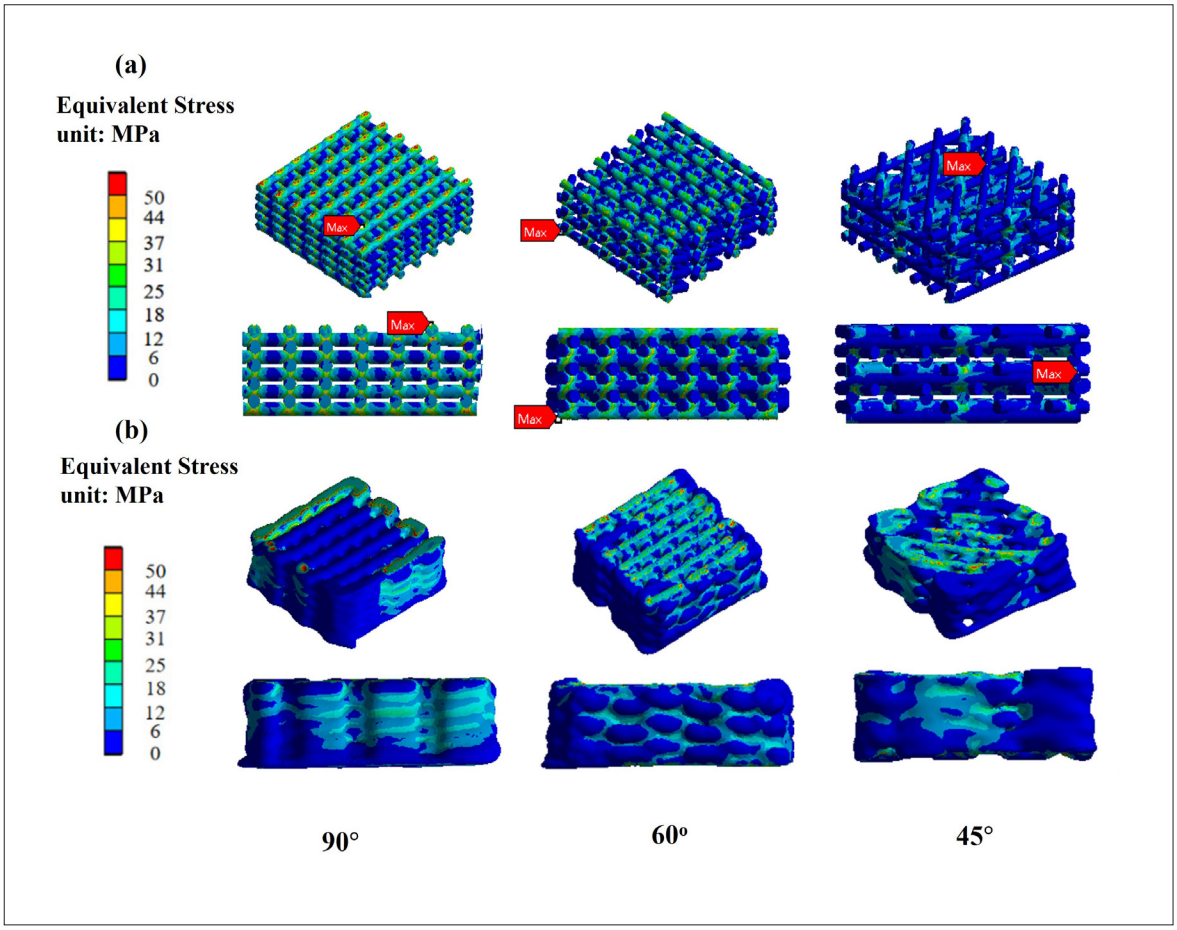

Figure 8. Finite element analysis stress distribution of design and reconstruction models: (a) design model; and (b) reconstruction model. A significant difference in stress distribution was observed between the design and reconstruction models. The design model displayed a regular stress distribution, while the reconstruction model exhibited noticeable stress concentration areas. The red mark indicated the location of the maximum equivalent stress distribution point.

such as ink accumulation, resulting in uneven and more uncontrollable deformations during drying and sintering, and led to significant differences in stress distribution across different states of these scaffolds.

Conversely, the 90° scaffolds exhibited higher fidelity in pore structure printing with fewer printing defects. The deformations, such as shrinkage, were relatively uniform and controllable, having a smaller impact on its stress distribution. Consequently, its mechanical properties were the most stable. When printing fidelity attained a high level with minimal printing defects present, the structure of the scaffold remained largely unchanged across different states, and the stress distribution pattern remained fundamentally consistent with the preceding state. As a result, the anticipated FEA stress concentration zone in the "after printing" scaffold model served as a reliable indicator of the stress concentration points of the "after sintering" scaffold.

However, CT scanning only captured the final morphology of "after drying" or "after sintering," and the simulation technique lacked exploration into the morphological changes of scaffolds during these processes. Advanced simulation technologies, such as the element birth and death technique, can effectively simulate local damage, addition, and other changes that occur in materials during drying or sintering. By dynamically adding or deleting elements within the finite element mesh, this technique can more accurately reflect complex phenomena and transformation processes in actual physical processes. In future work, we plan to employ such advanced simulation technologies to model the drying and sintering processes, thereby enabling a more precise assessment of stress states.

Stress concentration fracture is one of the main causes of clinical failure in bone implant repair.[8] Predicting the possible sites and extent of stress concentration before

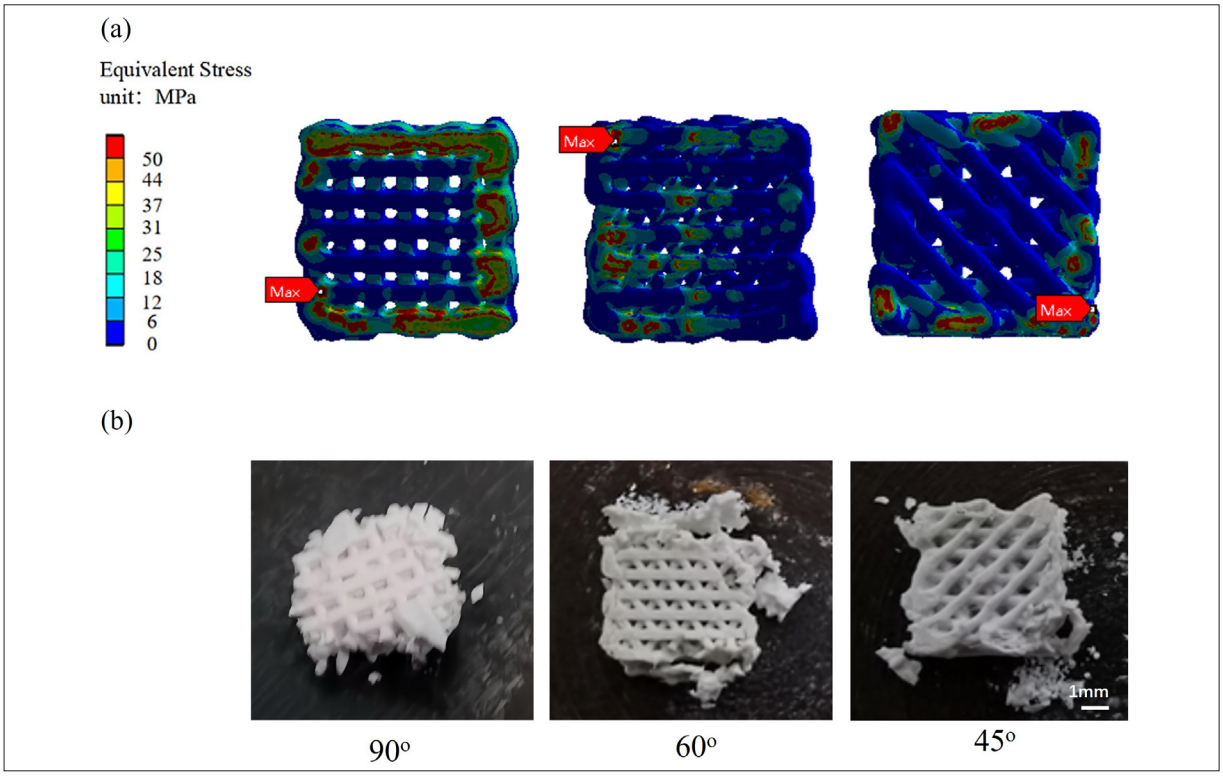

Figure 9. Model validation. (a) Stress distribution of reconstruction models at different angles, with noticeable differences among the three angles. The red mark indicated the location of the maximum equivalent stress distribution point. (b) Fracture conditions of scaffolds under compression testing, with the 90° scaffold fracturing around the edges and the 60° and 45° scaffolds fracturing at more protruding parts. Scale bar: 1 mm.

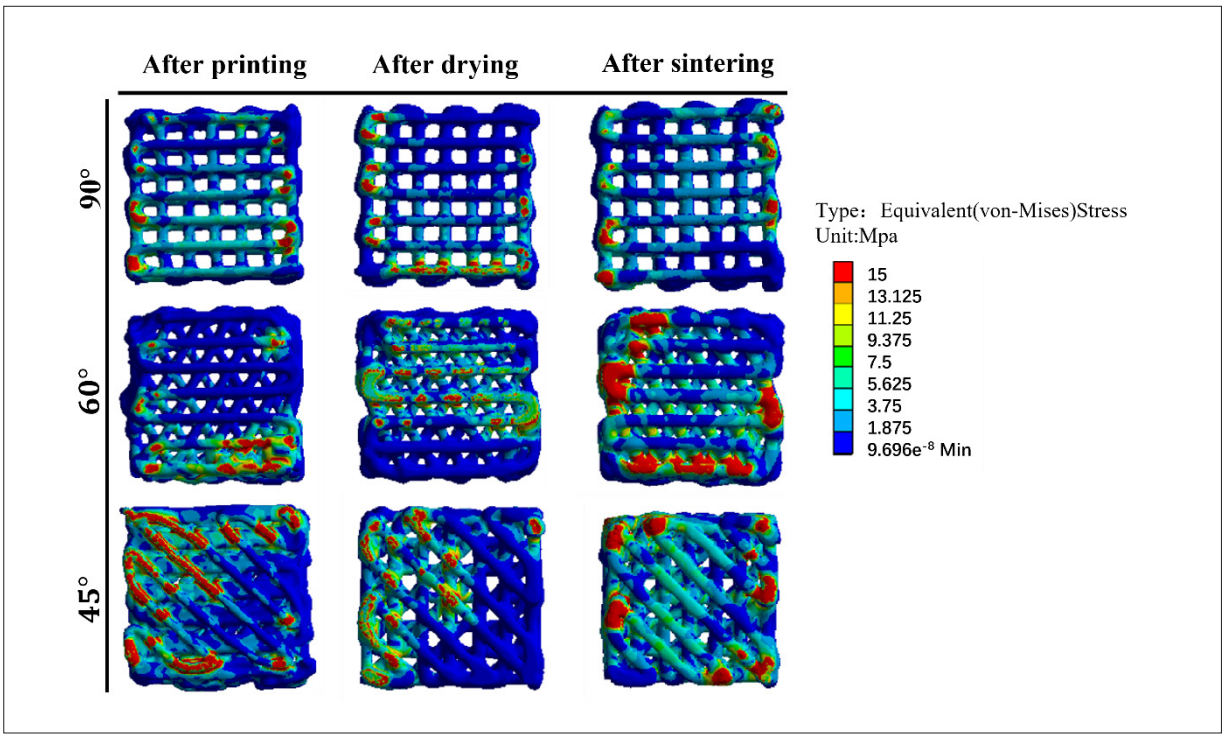

Figure 10. Stress distribution of scaffolds at different angles (top to bottom: 90°, 60°, and 45°) and states (left to right: post-printing, post-drying, and post-sintering). The stress distribution of the 90° scaffold corresponds relatively well across the three states.

implantation and taking preventive measures in advance are effective measures to avoid stress concentration fractures. Biological 3D printing scaffolds used for bone repair are mostly prepared by the extrusion method. The fidelity issue between the prepared scaffold structure and the designed structure is one of the problems to be solved in the field of biological 3D printing. Due to the inconsistency between the printed structure and the designed structure, it is difficult to obtain reliable results when evaluating the mechanical properties of the printed scaffold, especially its stress distribution. In this work, the accuracy of the proposed stress distribution prediction method was significantly improved compared with the traditional method, which was conducive to improving the clinical applicability of the scaffold. At the same time, for scaffolds with little printing distortion, the clinical applicability of the final scaffold can be predicted based on the morphological monitoring of the scaffold after printing, thereby reducing the test cycle.

4. Conclusion

This study combined 3D imaging (P-OCT, micro-CT) with FEA to monitor morphological changes during the fabrication of 3D-printed scaffolds, identified differences between design structures and actual prints, and assessed their impact on the overall strength of the scaffold and the internal stress distribution. The research found that both the macroscopic volume and microscopic filament diameter of the scaffold shrink after drying or sintering, leading to significant deformation, with no significant effect of scaffold angle on deformation. Printing defects had a significant impact on stress distribution. The 90° scaffolds exhibited the highest printing fidelity and the fewest defects, whereas the 60° and 45° scaffolds had more material accumulation defects, affecting the load-bearing contact surfaces and consequently influencing mechanical strength and stress distribution. The stress concentration areas of the 90° scaffold correspond well across different states. In subsequent research, the deformation process of the scaffold could be monitored to obtain the post-printing state of the scaffold. For scaffolds with few printing defects, the stress distribution of the final sintered scaffold can be predicted based on the post-printing state. This method may help shorten the experimental period and facilitate the clinical application of bone defect repair scaffolds.

For scaffolds with weak printing distortions (such as the 90° scaffold), the clinical applicability of the final scaffold can be predicted based on the monitoring of the scaffold's morphology after printing, thereby reducing the experimental cycle.

Acknowledgments

None

Funding

This research was funded by the National Key Research and Development Program of China (2022YFA1104600); the National Natural Science Foundation of China (319278 and 12002112); and the Zhejiang Provincial Natural Science Foundation of China (LY24A020006 and LZ22A020005).

Conflict of interest

The authors declare they have no competing interests.

Author contributions

Conceptualization: Ling Wang, Mingen Xu
Data Curation: Hong Liu, Luge Zhang
Formal analysis: Danyu Yao, Hong Liu, Luge Zhang
Investigation: Danyu Yao, Hong Liu, Luge Zhang
Methodology: Danyu Yao, Hong Liu
Writing – original draft: Danyu Yao
Writing – review & editing: Danyu Yao, Ling Wang, Luge Zhang, Ming Liu

Ethics approval and consent to participate

Not applicable.

Consent for publication

Not applicable.

Availability of data

Data is available from the corresponding author upon reasonable request.

References

1. Schemitsch EH. Size matters: defining critical in bone defect size! *J Orthop Trauma.* 2017;31(Suppl 5):S20-S22. doi: 10.1097/BOT.0000000000000978

2. Kang Y, Xu C, Meng LA, et al. Exosome-functionalized magnesium-organic framework-based scaffold with osteogenic, angiogenic and anti-inflammatory properties foraccelerated bone regeneration. *Bioact. Mater.* 2022; 18:26-41. doi: 10.1016/j.bioactmat.2022.02.012

3. Turnbull G, Clarke J, Picard F, et al. 3D bioactive composite scaffolds for bone tissue engineering. *Bioact Mater.* 2018;3(3):278-314. doi: 10.1016/j.bioactmat.2017.10.001

4. Anjum S, Rahman F, Pandey P, et al. Electrospun biomimetic nanofibrous scaffolds: a promising prospect for bone tissue engineering and regenerative medicine. *Int J Mol Sci.* 2022;23(16):9206.
doi: 10.3390/ijms23169206

5. Huang L, Zhang J, Liu X, et al. L-Arginine/nanofish bone nanocomplex enhances bone regeneration via antioxidant activities and osteoimmunomodulatory properties. *Chinese Chem Lett.* 2021;32(1):234-238.
doi: 10.1016/j.cclet.2020.11.046

6. Liu X, Ma PX. Polymeric scaffolds for bone tissue engineering. *Ann Biomed Eng.* 2004;32(3):9622-9629.
doi: 10.1023/b:abme.0000017544.36001.8e

7. Pareek A, Reardon PJ, Macalena JA, et al. Osteochondral autograft transfer versus microfracture in the knee: a meta-analysis of prospective comparative studies at midterm. *Arthroscopy.* 2016;32(10):2118-2130.
doi: 10.1016/j.arthro.2016.05.038

8. Zhou S, Jung S, Hwang J. Mechanical analysis of femoral stress-riser fractures. *Clin Biomech.* 2019;63:10-15.
doi: 10.1016/j.clinbiomech.2019.02.004

9. Huo J, Dérand P, Rnnar LE, et al. Failure location prediction by finite element analysis for an additive manufactured mandible implant. *Med Eng Phys.* 2015;37(9):862-869.
doi: 10.1016/j.medengphy.2015.06.001

10. Dong J, Li Y, Lin P, et al. Solvent-cast 3D printing of magnesium scaffolds. *Acta Biomater.* 2020;114:497-514.
doi: 10.1016/j.actbio.2020.08.002

11. Barbetta A, Costantini M. Gas *Foaming Technologies for 3D Scaffold Engineering*. Woodhead Publishing; 2018:127-149.
doi: 10.1016/b978-0-08-100979-6.00006-9

12. Kordjamshidi A, Saber-Samandari S, Nejad MG, Khandan A. Preparation of novel porous calcium silicate scaffold loaded by celecoxib drug using freeze drying technique: fabrication, characterization and simulation. *Ceram Int.* 2019;45(11):14126-14135.
doi: 10.1016/j.ceramint.2019.04.113

13. Dong Z, Cui H, Zhang H, et al. 3D printing of inherently nanoporous polymers via polymerization-induced phase separation. *Nat Commun.* 2021;12(1):247.
doi: 10.1038/s41467-020-20498-1

14. Maharjan B, Kaliaanagounder VK, Jang SR, et al. In-situ polymerized polypyrrole nanoparticles immobilized poly(ε-caprolactone) electrospun conductive scaffolds for bone tissue engineering. *Mater Sci Eng C Mater Biol Appl.* 2020;114:111056.
doi: 10.1016/j.msec.2020.111056

15. Shuai C, Yang W, Feng P, Peng S, Pan H. Accelerated degradation of HAP/PLLA bone scaffold by PGA blending facilitates bioactivity and osteoconductivity. *Bioact Mater.* 2021;6(2):490-502.
doi: 10.1016/j.bioactmat.2020.09.001

16. Su J, Hua S, Chen A, et al. Three-dimensional printing of gyroid-structured composite bioceramic scaffolds with tuneable degradability. *Biomater Adv.* 2021;133:112595.
doi: 10.1016/j.msec.2021.112595

17. Xiao J, Xue H, Qian Z, et al. Jumbo bionic trabecular metal acetabular cups improve cup stability during acetabular bone defect reconstruction:a finite element analysis study. *J Bionic Eng.* 2023;20(6):2814-2825.
doi: 10.1007/s42235-023-00413-2

18. Liu L, Liu C, Deng C, et al. Design and performance analysis of 3D-printed stiffness gradient femoral scaffold. *J Orthop Surg Res.* 2023;18(1):120.
doi: 10.1186/s13018-023-03612-z

19. Pang S, Wu D, Gurlo A, Kurreck J, Hanaor DAH. Additive manufacturing and performance of bioceramic scaffolds with different hollow strut geometries. *Biofabrication* 2023;15(2):025011.
doi: 10.1088/1758-5090/acb387

20. Hao YL, Li S-J, Yang R. Biomedical titanium alloys and their additive manufacturing. *Rare Metals.* 2016;35(009): 661-671.
doi: 10.1007/s12598-016-0793-5

21. Melenka GW, Schofield JS,Dawson MR, Carey JP. Evaluation of dimensional accuracy and material properties of the MakerBot 3D desktop printer. *Rapid Prototyping J.* 2015;21(5):618-627.
doi: 10.1108/rpj-09-2013-0093

22. Sharma R, Singh R, Penna R, Fraternali F. Investigations for mechanical properties of Hap, PVC and PP based 3D porous structures obtained through biocompatible FDM filaments. *Compos Part B-Eng.* 2018;132:237-243.
doi: 10.1016/j.compositesb.2017.08.021

23. Muhammad A, Ali MA, Shanono IH. Fatigue and harmonic analysis of a diesel engine crankshaft using ANSYS[C]// iMEC-APCOMS 2019: Proceedings of the 4th International Manufacturing Engineering Conference and The 5th Asia Pacific Conference on Manufacturing Systems. Springer Singapore; 2020:371-376.
doi: 10.1007/978-981-15-0950-6_56

24. Liu H, Ahlinder A, Yassin MA, et al. Computational and experimental characterization of 3D-printed PCL structures toward the design of soft biological tissue scaffolds. *Mater Design.* 2020;188:108488.
doi: 10.1016/j.matdes.2020.108488

25. Soufivand AA, Abolfathi N, Hashemi A, Lee SJ. Prediction of mechanical behavior of 3D bioprinted tissue-engineered scaffolds using finite element method (FEM) analysis. *Addit Manuf.* 2020;33(8):101181.
doi: 10.1016/j.addma.2020.101181

26. de Galarreta SR, Jeffers JRT, Ghouse S. A validated finite element analysis procedure for porous structures. *Mater Design.* 2020;189:108546.
doi: 10.1016/j.matdes.2020.108546

27. Zhou J, Huang H, Wang LJ, et al. Stable mechanical fixation in a bionic osteochondral scaffold considering bone growth. *Rare Metals.* 2022;41(8):2711-2718. doi: 10.1007/s12598-022-02000-6

28. Mohol SS, Kumar M, Sharma V. PLA-based nature-inspired architecture for bone scaffolds: a finite element analysis. *Comput Biol Med.* 2023;163:107163. doi: 10.1016/j.compbiomed.2023.107163

29. Scocozza F, Gravina GMD, Bari E, et al. Prediction of the mechanical response of a 3D (bio)printed hybrid scaffold for improving bone tissue regeneration by structural finite element analysis. *J Mech Behav Biomed Mater.* 2023;142:105822. doi: 10.1016/j.jmbbm.2023.105822

30. Zhang B, Guo L, Chen H, Ventikos Y, Narayan RJ, Huang J. Finite element evaluations of the mechanical properties of polycaprolactone/hydroxyapatite scaffolds by direct ink writing: effects of pore geometry. *J Mech Behav Biomed Mater.* 2020;104:103665. doi: 10.1016/j.jmbbm.2020.103665

31. Yunsheng D, Hui X, Jie W, et al. Sustained release silicon from 3D bioprinting scaffold using silk/gelatin inks to promote osteogenesis. *Int J Biol Macromol.* 2023;234:123659. doi: 10.1016/j.ijbiomac.2023.123659

32. Yang S, Wang L, Chen Q, Xu M. J. A. M. In situ process monitoring and automated multi-parameter evaluation using optical coherence tomography during extrusion-based bioprinting. *Addit Manuf.* 2021;47:102251. doi: 10.1016/j.addma.2021.102251

33. Yang S,Chen Q, Wang L, Xu M. In situ defect detection and feedback control with three-dimensional extrusion-based bioprinter-associated optical coherence tomography. *Int J Bioprint.* 2023;9(1):624. doi: 10.18063/ijb.v9i1.624

34. Suo H,Chen Y, Liu J, Wang L, Xu M. 3D printing of biphasic osteochondral scaffold with sintered hydroxyapatite and polycaprolactone. *J Mater Sci.* 2021;56:16623-16633. doi: 10.1007/s10853-021-06229-x

35. Keaveny TM, Morgan EF, Niebur GL, Yeh OC. Biomechanics of trabecular bone. *Annu Rev Biomed Eng.* 2001;3(1): 307-333. doi: 10.1146/annurev.bioeng.3.1.307

36. Collins MN, Ren G, Young K, et al. Scaffold fabrication technologies and structure/function properties in bone tissue engineering. *Adv Funct Mater.* 2021;31(21):2010609. doi: 10.1002/adfm.202010609

37. Lee JS, Cha HD, Shim JH, et al. Effect of pore architecture and stacking direction on mechanical properties of solid freeform fabrication-based scaffold for bone tissue engineering. *J Biomed Mater Res A.* 2012;100A(7): 1846-1853. doi: 10.1002/jbm.a.34149

ACCSCIENCE PUBLISHING

International Journal of Bioprinting

RESEARCH ARTICLE

Nanomaterial-modified bioinks for DLP-based bioprinting of bone constructs: Impact on mechanical properties and mesenchymal stem cell function

Julie Kühl[1], Sven Malte Krümpelmann[1], Larissa Hildebrandt[1], Malte Bruhn[2], Jan-Bernd Hövener[3], Ronald Seidel[3], Stanislav Gorb[4], Fabian Schütt[2], Rainer Adelung[2], Andreas Seekamp[1], Leonard Siebert[2], and Sabine Fuchs[1]*

[1]Experimental Trauma Surgery, Department of Orthopedics and Trauma Surgery, University Medical Center, Kiel, Germany

[2]Functional Nanomaterials Group, Department of Materials Science, Faculty of Engineering, Kiel University, Kiel, Germany

[3]Section for Biomedical Imaging (SBMI), Molecular Imaging North Competence Center (MOIN CC), Department of Radiology and Neuroradiology, University Medical Center Kiel, Kiel University, Kiel, Germany

[4]Department of Functional Morphology and Biomechanics, Faculty of Mathematics and Natural Sciences, Kiel University, Kiel, Germany

(This article belongs to the Special Issue: *Bioprinting for Tissue Engineering and Modeling*)

***Corresponding author:**
Sabine Fuchs
(sabine.fuchs@uksh.de)

Citation: Kühl J, Krümpelmann SM, Hildebrandt L, et al. Nanomaterial-modified bioinks for DLP-based bioprinting of bone constructs: Impact on mechanical properties and mesenchymal stem cell function. *Int J Bioprint*. 2024;10(6):4015. doi: 10.36922/ijb.4015

Received: June 21, 2024
Revised: July 27, 2024
Accepted: July 31, 2024
Published Online: August 1, 2024

Copyright: © 2024 Author(s). This is an Open Access article distributed under the terms of the Creative Commons Attribution License, permitting distribution, and reproduction in any medium, provided the original work is properly cited.

Publisher's Note: AccScience Publishing remains neutral with regard to jurisdictional claims in published maps and institutional affiliations.

Abstract

3D printing technologies offer tremendous potential to produce patient-specific implants and treat critical-sized bone defects, which vary in size, shape, and clinical requirements. Despite advancements in 3D printing of biomaterial-based bone constructs, they often lack biologically active material. For larger-sized bone implants, early biologization and vascularization are essential. In this context, bioprinting technologies enable the integration of vital cells or active growth factors into 3D-printed constructs, while the integration of nanomaterials enables material-mediated functionalization of the bioink. To date, such bioink modifications with nanomaterials have rarely been reported for digital light processing (DLP) bioprinting technology. Furthermore, there is a notable lack of direct comparative studies on the impact of nanomaterials on cellular processes. In this study, we assessed and compared graphene oxide (GO)- and calcium phosphate (CaP)-modified bioinks for DLP bioprinting of methacrylated gelatin (GelMa)-based bone constructs. After printing, the impact of bioinks on cell distribution, viability, cell proliferation, and differentiation, as well as the mechanical and structural properties of constructs, was evaluated. In comparison to commercial bioinks, cell viability was higher in the established GelMa bioinks. Morphological data and DNA quantification indicate the highest cell vitality and proliferation over time in basic GelMa bioink. CaP-modified GelMa bioink displayed the highest differentiation of human mesenchymal stem cells (hMSCs), in terms of osteogenic gene expression and calcium deposition. Conversely, GO increased the Young's modulus of the material, affecting cell morphology. Overall, the direct comparison of nanomaterials suggests diverse effects in functionalizing DLP-printed bone constructs containing living osteogenic cells.

Keywords: Hydrogel; Bone implant; Calcium phosphate; Graphene oxide; 3D printing; GelMa, Nanomaterials; Bioprinting

1. Introduction

Bone tissue has a high natural regeneration capacity. However, in cases of larger or more complex bone defects, as well as certain pathophysiological conditions, surgical intervention is often needed to ensure adequate reconstitution of bone stability and a proper healing process.[1–6] In this context, 3D printing technologies offer a tremendous potential to produce patient-specific implants that vary in size and shape, thus enabling the treatment of critical-sized bone defects.[7–9] While 3D printing of material-based bone implants has progressed, the generation of bioprinted constructs containing vital cells is still a challenging task.

In 3D bioprinting, various printing techniques exist, including extrusion-based bioprinting.[10] Another technical principle for bioprinting is the use of digital light processing (DLP).[11–16] A significant advantage of DLP bioprinting lies in its high printing resolution, enabling the creation of complex and biomimetic shapes, along with controlled and precise positioning of pores within the cell-loaded hydrogel-based constructs. The porous structure of the constructs, along with the high fluid content in the hydrogel bioinks, facilitates the supply of nutrients and oxygen.[17–20] The hydrogels applied as bioinks need to fulfill a broad spectrum of prerequisites, ranging from rheological properties for the printing process up to creating an environment for cell survival, proliferation, migration, and highly cell-type-specific bioactivities.[21–24] Collagen type 1, the major constitutional protein in the bone, is rich in arginine-glycine-aspartic acid (RGD) sequences, thus promoting cell adhesion.[25,26] After hydrolyzation and methacrylation of collagen, the resulting derivate gelatin methacrylamide (GelMa) enables ultraviolet (UV)-light-mediated formation of a stable hydrogel with tunable mechanical properties, high biocompatibility, and biodegradability.[15,27–36] Optimization of basic GelMa bioinks, in terms of the methacrylation degree and the application of photo-initiators or photo-absorbers, is often a fine-tuning process that needs to be aligned with the printing technology, the parameters applied in the printing process, and the desired biomedical goal.[37–41] To fulfill specific biological and mechanical requirements, additional functionalization of GelMa bioinks is often desirable to enhance their potential for bone tissue bioprinting.

Bioinks used for bone constructs can be modified with a series of different nanomaterials, including graphene oxide (GO) or different variants of calcium phosphate (CaP), to tailor their properties for bone regeneration.[32,42–55] The use of these nanomaterials has been mainly applied to extrusion-based or other printing technologies.[56–59] However, for DLP-based bioprinting, the functionalization of bioinks using nanomaterials has hardly been reported. In addition, data on nanomaterial-modified bioinks are often not directly comparable due to different printing technologies, bioinks, implant designs, and general experimental conditions. Nonetheless, these nanomaterials exhibit highly diverse effects on cellular viability and cell-specific functions, which are not yet fully understood.

Calcium phosphate (CaP) demonstrates excellent bioactivity and provides a mineral component, resembling the bone matrix.[60,61] Calcium and phosphate ions released from CaP are important inorganic materials known to activate new bone formation.[62–64] In the context of nanomaterials applied for 3D printing, we have recently demonstrated that CaP nanoparticles, integrated into 3D-printed polycaprolactone bone scaffolds, improve osteoinductive properties.[65] In addition, we have demonstrated that GO nanomaterials, particularly their non-reduced form, can improve cell adhesion of mesenchymal stem cells and support vascularization by active binding of vascular endothelial growth factor in clinically used bone substitute materials.[66]

In this study, we developed GelMa bioinks that contain the nanomaterials CaP and GO to investigate their suitability for DLP bioprinting. The impact of the scaffold design and the different nanomaterials was assessed in direct comparison but has not yet been reported. The study aims to compare the impact of the individual nanomaterials on the DLP printing process, the mechanical properties of the constructs, and the cellular viability and osteogenic differentiation of human mesenchymal stem cells (hMSCs).

2. Methods

2.1. Design of 3D model with a cancellous bone-inspired structure

A 3D model with a bone-inspired structure was designed using Shapr3D software (version 5.290). The 3D model (Figure 1) provides a cylindrical shape featuring a diameter of 7 mm and a height of 3.64 mm. The implant design includes interconnected pores with a diameter of 500 µm, which are evenly distributed throughout the model (Figure 1). In addition, larger-sized channels with a diameter of up to 2500 µm with irregular-shaped structures were integrated into the 3D model, aiming to facilitate the ingrowth of vascular structures after the implantation.

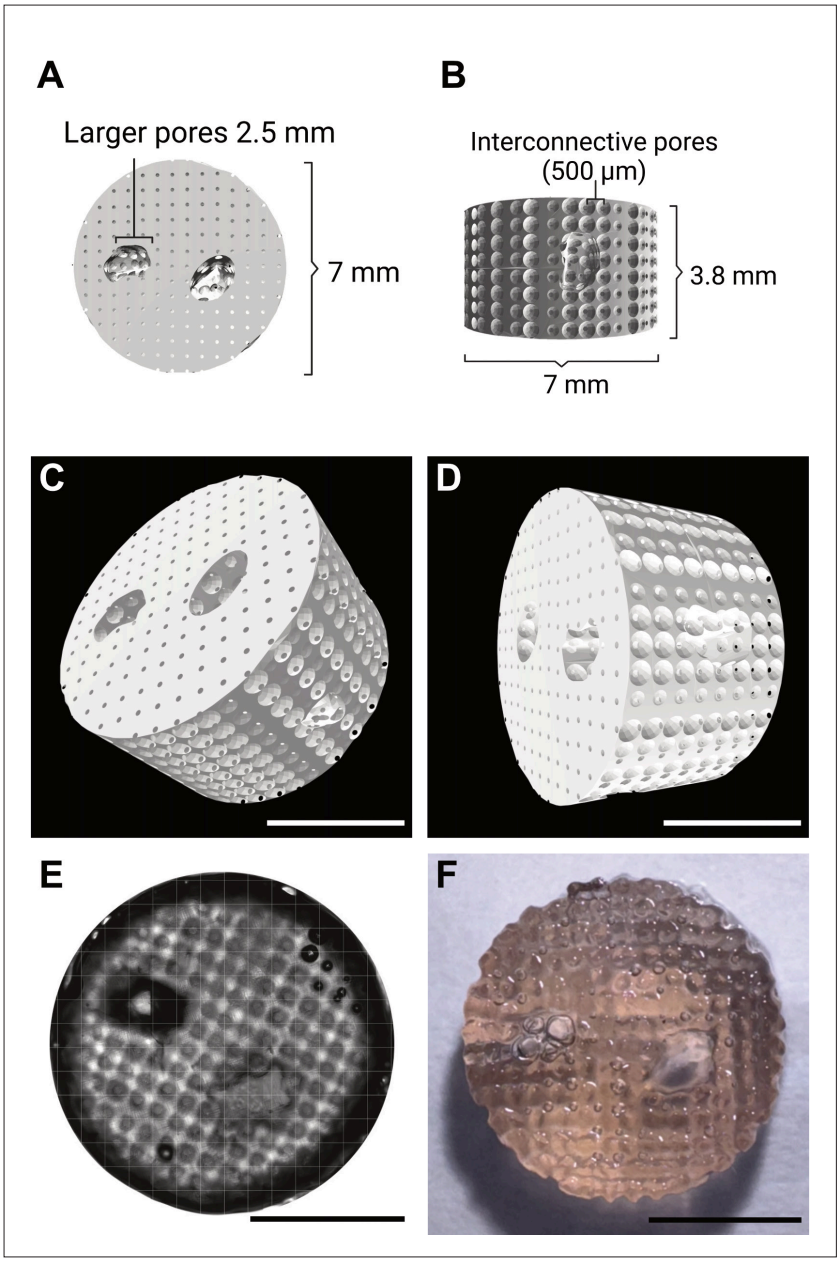

Figure 1. Design and dimension of the 3D model. (A and B) A cylindrical 3D model with interconnective pores (pore diameter: 500 μm) arranged in a regular grid and larger pores (pore diameter: 2.5 mm): top view (A) and front view (B). (C and D) The 3D model from different perspectives: Figure 1C (perspective A) and Figure 1D (perspective B). (E) Light microscopy image of a printed GelMaBB construct. (F) Image of the printed GelMaBB construct. Scale bars: 3.5 cm (C–F). Magnification: 4×. Abbreviations: GelMa: Gelatin methacrylamide; BB: Brilliant Black.

2.2. Volume, surface area, and base area of the 3D model

The overall volume, surface area, and base area of the porous 3D model were calculated using Blender (version 2.93.4) with the "3D Print Toolbox" add-on. For reference, a solid 3D model with the same overall geometry but without pores was created, and its volume, surface area, and base area were calculated using the same method. Additionally, the porous 3D model was sliced into sections at 100 μm intervals, and the surface area of each section was calculated to determine the minimum, mean, and maximum areas of the sections.

2.3. Isolation and culture of human mesenchymal stem cells

Human mesenchymal stem cells (hMSCs) were isolated from the femoral heads of adult patients, as previously

described.[67,68] The use of human tissue was approved by the local ethical advisory board of the University Medical Center in Kiel (approval number: D459/13) and included the consent of the individual donors. Cells were precultured in osteogenic differentiation medium (ODM), i.e., DMEM F12 (PAN Biotech, Germany), supplemented with 10% fetal bovine serum (FBS; PAN Biotech, Germany), 1% penicillin/streptomycin (Biochrom, Germany), 0.1 µM dexamethasone (Sigma-Aldrich, United States of America [USA]), 50 µM ascorbic acid (Sigma-Aldrich, USA), and 10 µM ß-glycerolphosphate (Sigma-Aldrich, USA), to induce osteogenic differentiation. For the printing process, hMSCs (passages 3 and 4) were added to different types of bioinks.

2.4. Formulation and modifications of different bioinks

Different types of GelMa-based bioinks were formulated and compared in terms of their printability and biocompatibility, both before and after modification with nanomaterials. In this context, a commercially available GelMa bioink (GelMa PhotoInk; Cellink, Sweden) served as reference material for the evaluation process. The basis of the different bioinks was formulated using sterile GelMa with a methacrylation degree of 80% (GelMa; Gelomics, Australia). In brief, GelMa was dissolved in ODM at a concentration of 100 mg/mL. Lithium-phenyl-2,4,6-tri-methylbenzoylphosphinate (LAP; Sigma-Aldrich, USA) was used in all bioinks as a photo-initiator at a final concentration of 5 mg/mL.[69] In contrast, the photo-absorber concentration varied between the different bioinks (Table 1). As indicated in Table 1, Brilliant Black (BB) (Sigma-Aldrich, USA) was used as a photo-absorber at a final concentration of 0.5 mg/mL, dissolved in ODM. The components of the bioink (LAP and BB) were individually filtered (Filtropur 0.2 µm; Sarstedt, Germany) for sterilization.

Different nanomaterials were investigated for further functionalization of the GelMa-based bioink. To enhance the osteoinductive properties of the GelMa bioink, CaP nanoparticles (particle size: < 150 nm) (Sigma-Aldrich, USA) were added to the bioink at a concentration of 50 mg/mL. Before printing, the resulting ink (GelMaBB-CaP) was incubated at 37°C for 2 h to allow swelling of CaP particles and a homogeneous consistency of the bioink. In addition, the GelMa bioink was modified with GO, provided by the technical faculty at Kiel University. GO was added at a final concentration of 0.5 mg/mL to the bioink (GelMaGO). The bioinks were loaded with 3×10^6 hMSC/mL bioink before the DLP bioprinting process.

2.5. Bioprinting of constructs using DLP technology

Tissue constructs were printed by DLP using LumenX (Cellink, Sweden) equipped with LightField software. To print under sterile conditions, the Lumen X printer was placed under a laminar flow bench, and sterile equipment was used. The printbed and printhead were further treated with 70% ethanol. For the printing process, 1 mL bioink was loaded into the printer, resulting in three constructs for the given design. The printbed temperature was set to 37°C. Details of the printing parameters are listed in **Table S2, Supporting Information** and were identical for all bioinks. The 3D model was sliced into layers of 100 µm height. The first layer was exposed with a factor of 4. The exposure time of the light was 9 s, with an intensity of 70% (33.6 mW/cm^2). After the printing process, gel-based tissue constructs were transferred to a 24-well plate (Sarstedt, Germany) and washed three times with phosphate-buffered saline (PBS) (Gibco by Life Technologies, USA) for 10 min each. Each construct was then placed in 2 mL of ODM and further cultured at 37°C and 5% CO_2 for the indicated time points. For the controls, samples with and without cells were printed as indicated in the sections for the individual analyzing methods. Scaffolds with or without cells were treated and cultured in the same way for a better comparison.

2.6. Diameter and weight of the GelMa constructs

The weight and the diameter of the constructs consisting of the different GelMa-based inks (GelMaBB, GelMaBB-CaP,

Table 1. Ingredients of different modified bioinks.

Ingredient	Modified bioinks		
	GelMaBB	GelMaBB-CaP	GelMaGO
GelMa (mg/mL)	100	100	100
LAP (mg/mL)	5	5	5
BB (mg/mL)	0.5	0.5	—
CaP (mg/mL)	—	50	—
GO (mg/mL)	—	—	0.5

Abbreviations: GelMa: Gelatin methacrylamide; LAP: Lithium-phenyl-2,4,6-trimethylbenzoylphosphinate; BB: Brilliant Black; CaP: Calcium phosphate; GO: Graphene oxide.

GelMaGO, and the commercial ink) without cells were measured every day for seven days (n = 6). To measure the diameter of the construct, an image of the construct was taken. Using a ruler and the program ImageJ (version 2.3.0/1.53q), the pixel aspect ratio was calculated. In addition, the weight of the constructs was measured with a precision scale (BP 211 D; Sartorius Lab Instruments GmbH & Co. KG, Germany) every day for seven days. After printing, constructs were directly weighted, which accounted for day 0. The measurements were performed at room temperature.

2.7. Micro-computed tomography and data analysis

Freeze-dried samples were mounted on custom-built holders, imaged with a micro-computed tomography (micro-CT) scanner (VivaCT-80; Scanco Medical AG, Switzerland), and reconstructed using the manufacturer's tomography software (V. 6.4-2). All freeze-dried samples were embedded in foam and scanned at a tube voltage of 45 kVp, beam current of 177 µA, with a 0.1 mm aluminum filter, an integration time of 300 ms, a field of view (FOV) with a diameter of 34.4 mm, 1500 projections/180 °, using 3072 × 3072 sample size, resulting in an isotropic voxel size of (11.2 µm)^3.

For primary visualization and inspection of the DICOM datasets, the free, open-source software 3D slicer (https://www.slicer.org/) was used.[70] Histogram-based segmentations of the constructs in 3D Slicer were exported as 3D meshes (.stl format), which were then cleaned and visualized using MeshLab (https://www.meshlab.net).[71]

ImageJ was used to measure the pore sizes by visually identifying a region of interest (ROI) along the Z-axis. For noise reduction, 3D Gaussian blur filter (1 px) was applied, before the maximum intensity projections in the ROIs were created using a limited number of images (GelMaBB = 26 images; GelMaGO = 20 images; GelMaBB-CaP = 18 images). The peak positions of line profile plots were used to measure the pore wall distances; for GelMaGO and GelMaBB-CaP constructs, only pores with small cell wall length ratios were used.

2.8. Water absorption of the GelMa-based constructs

The water absorption capacity of the printed GelMaBB, GelMaBB-CaP, and GelMaGO constructs (n = 12) was evaluated. After printing and subsequent washing steps, cell-free constructs were weighed. The samples were then subjected to freeze-drying using a Scanvac Coolsafe 55-9 PRO freeze dryer (Labogene, Denmark), and the dry weight was determined. The water absorption capacity was calculated by the difference between the initial wet weight and the dry weight.

2.9. Porosity of the GelMa-based constructs

The density of the GelMa-based constructs (GelMaBB, GelMaBB-CaP, and GelMaGO) (n = 12) was analyzed using a specific gravity measurement kit (Shimadzu Corporation, Japan). The solid density in ultra-pure water at 24°C for cell-free constructs was measured (water density: 0.9973 g/cm^3). The density ρ was calculated according to **Equation I**. The density of the materials using GelMaBB, GelMaBB-CaP, and GelMaGO was determined by printing solid constructs with the same dimensions as the porous constructs. These solid constructs were measured using the gravimetry method (n = 4).

$$\rho = \frac{Wa}{(Wa - Wl)} * \rho l \quad (I)$$

Wa: Solid specimen weight in air, Wl: Solid specimen weight in the liquid medium, ρl: Density of the medium liquid. The porosity was calculated with **Equation II.**

$$P = 1 - \frac{\rho p}{\rho m} \quad (II)$$

P: Porosity, ρp: Density of the porous construct, ρm Density of the material (solid construct).

2.10. Scanning electron microscopy and surface structure of printed samples

Cell-free constructs consisting of the different GelMa-based bioinks (GelMaBB, GelMaBB-CaP, GelMaGO, and commercial ink) were dehydrated in an increasing alcohol series of 50, 60, 70, 80, 90, 95, and 100% ethanol. The final step with 100% ethanol was repeated three times to prepare the samples for critical point drying (LEICA EM CPD 300; Leica Microsystems GmbH, Germany). The samples were critical point dried at 40°C and 79–80 bars of CO_2. The samples were mounted onto a holder with a carbon Leit-Tab (Plano GmbH, Germany) and sputter-coated with gold-palladium (10 nm thickness) using a Leica EM SCD 500 High-Vacuum sputter-coater (Leica Microsystems GmbH, Germany). The samples were scanned at 15 kV using the scanning electron microscope (SEM) Hitachi TM300 (Hitachi High-Tech, Japan).

2.11. Live/dead and actin cytoskeleton staining analyzed by confocal laser scanning microscopy

Live/dead staining after 7 and 14 days of culture was performed by adding 5 µg/mL calcein AM (Sigma-Aldrich, USA) to the culture medium to stain living cells; 2 µg/mL propidium iodide (Sigma-Aldrich, USA) was added to stain dead cells. The samples were incubated in the staining solution for 30 min before washing with a new medium and

observing them with a confocal laser scanning microscope (CLSM) (LSM 800; Zeiss, Germany).

In addition, phalloidin TRITC and Hoechst 33258 (Sigma-Aldrich, USA) staining was applied to analyze the morphology of the cells and the appearance of the actin cytoskeleton. For this purpose, the constructs were fixed in 4% paraformaldehyde (PFA) and 3% glutaraldehyde for 30 min and washed three times for 10 min with PBS. The samples were permeabilized using 0.5% Triton™ X-100 (Sigma-Aldrich, USA) for 30 min and washed with PBS three times for 10 min. To block unspecific binding sites, the samples were pretreated with 1% bovine serum albumin (BSA; Millipore, USA), dissolved in PBS for 30 min, followed by three washing steps for 10 min each. Thereafter, 0.5 µg/mL phalloidin TRITC (Sigma-Aldrich, USA) and 2 µg/mL Hoechst 33258 were added to the samples for 30 min and washed three times for 10 min each. Samples were analyzed using CLSM.

2.12. DNA quantification

The DNA content, correlating to the number of hMSCs in the different GelMa-based constructs, was determined using a Quant-iT PicoGreen dsDNA assay kit (Molecular Probes, USA) after 7 and 14 days of culture. For this purpose, constructs were harvested in 1 mL of nuclease-free water (Nalgene; Thermo Fisher Scientific, USA) in tissue homogenization tubes (Bertin Technologies, France). Using the homogenizer (Precellys 24 Lysis; Bertin Technologies, France) and homogenization kit (Soft tissue homogenizing CK14; Bertin Technologies, France), the samples were grounded. Then samples were frozen at −80°C and thawed for three repeating cycles. Samples were additionally sonicated (MSE; Henderson Biomedical, United Kingdom) three times for 30 s at 20 kHz. The DNA content was determined in accordance with the manufacturer's protocol using PicoGreen. The fluorescence of the DNA amount of each sample was measured using a microplate reader, SpectraMax iD3 (Molecular Devices, USA), at an excitation wavelength of 485 nm and an emission wavelength of 535 nm. Four different donor samples were measured using three biological replicates (constructs) and technical triplicates.

2.13. Mechanical properties of the printed constructs

Compressive strength was determined using a compact modular rheometer with a linear actuator (MCR 702e MultiDrive; Anton Paar, Austria). Tests were performed at room temperature for all samples after the indicated culture and incubation times. The porous, cell-laden constructs and cell-free porous reference scaffolds were printed and cultivated for 7 or 14 days. The diameter and height of the individual samples were measured with calipers before the mechanical tests. The maximum compression distance was 25% of the initial height of the samples. The tests were performed with two replicates from four donors in total and three cycles of measurement. We assumed the material to be ideally elastic and calculated the mean of three repetitive measurements. Young's modulus was calculated from the stress-strain curve using the first 8% of measurement points. This was performed using linear regression from the "scikit-learn" library in Python. For curves where this was not feasible, the start of the linear region was determined manually, and the subsequent 8% of measurement points were used. This approach accounted for surface roughness and non-planar surfaces due to swelling of the construct, resulting in delayed onset of the compression curve.

2.14. Evaluation of cell distribution and differentiation using cryosections of printed constructs

The printed constructs consisting of different cell-laden GelMa-based bioinks and cell-free control scaffolds were fixed with 4% PFA for 30 min. Afterwards, the constructs were embedded in TissueTek (Sakura Finetek, Japan) and frozen on dry ice. The samples were cut into 7 µm slices using a cryostat (Thermo Fischer Scientific, USA).

Alizarin Red staining (ARS) was performed to evaluate the integration of CaP nanoparticles in the bioink, as well as the osteogenic differentiation of cells within the scaffolds. The sections were overlaid with ARS solution (Osteogenesis Quantitation Kit; Merck KGaA, Germany), incubated for 30 min, and subsequently washed three times with PBS. Picrosirius red staining (Morphisto GmbH, Germany) was performed according to the manufacturer's specifications to monitor collagen deposition within the scaffolds over time. The stained sections were examined with the microscope EVOS FL Auto 2 (Invitrogen by Thermo Fisher Scientific, USA).

2.15. Alizarin Red staining and calcification assessment

The calcification of constructs, including GelMaBB, GelMaBB-CaP, and GelMaGO, with and without cells, was evaluated through ARS using the osteogenesis assay kit (ECM 815; Millipore, USA) after 7 and 14 days of culture. For ARS, the constructs were fixed in 4 % PFA, followed by three washing steps with PBS. Subsequently, the constructs were stained with ARS solution (40 mM) for 30 min. The samples were then washed with distilled water until the supernatant was clear. The stained constructs were finally photographed. To quantitatively assess mineralization, the stained constructs were freeze-dried. The lyophilized samples were homogenized using Precellys tubes (soft tissue homogenizing kit CK14) and the Precellys soft

tissue program (6500 rpm for 30 s with 20 s rest) in three cycles with 800 µL of 10% acetic acid. ARS extraction from the homogenized samples was achieved by shaking them for 24 h. Following extraction, the samples were heated at 85°C for 10 min, then transferred to ice for 5 min, and centrifuged at 20 × 10^3 g for 15 min. The supernatants were collected, and the pH was adjusted to 4.1 using 10% ammonium hydroxide. The samples were applied in duplicates. The absorbance of the samples was measured at a wavelength of 405 nm using a microplate reader.

2.16. Quantitative real-time polymerase chain reaction for osteogenic differentiation in GelMaBB-CaP

To evaluate the influence of the CaP-modified GelMaBB bioink on osteogenic differentiation, polymerase chain reaction (PCR) was performed for osteogenic differentiation markers. For RNA isolation, the RNA advanced isolation kit (RNAdvance Tissue; Beckman Coulter, Canada) was used. The printed tissue constructs were frozen at −80°C in 1 mL of nuclease-free water and subsequently lyophilized with a freeze dryer. Two lyophilized samples were pooled and homogenized with 380 µL lysis buffer (RNAdvance Tissue; Beckman Coulter, Canada) and 20 µL proteinase K (RNAdvance Tissue; Beckman Coulter, Canada) for 2 h at 37°C. Magnetic beads were added in accordance with the manufacturer's protocol. The protocol includes DNAse treatment for 15 min. The RNA concentration was then measured with a microplate reader (SpectraMax iD3, USA) at an excitation/emission wavelength of 260/280 nm. For each sample, 500 ng of RNA was transcribed into cDNA using the High-Capacity RNA-to-cDNA™ kit (Applied Biosystems, Lithuania) according to the manufacturer's instructions. PCR was performed using a volume of 20 µL for each reaction; 3.2 µL of cDNA was mixed with 10 µL of SYBR™ Select Master Mix (Applied Biosystems, Lithuania), 2 µL of Quanti-Tect Primer Assay (Qiagen, Germany) (**Table S3, Supporting Information**), and 4.8 µL of nuclease-free water. The ribosomal protein 13A (RPL13A) gene was used as a housekeeping gene. A two-step PCR program using a Q-PCR-cycler (Rotor-Gene Q; Qiagen, Germany) was applied for the amplification (50°C for 2 min; 95°C for 2 min; 40 cycles; 95°C for 15 s; and 60°C for 60 s). Relative gene expression was calculated using the ΔΔCt method.

2.17. Statistical analysis

Statistics were evaluated using GraphPad Prism 10 (GraphPad Software, USA) software. For statistical analysis, a two-way analysis of variance (ANOVA) with a Tukey multiple comparison test was used. Data in this article depicts results from different technical and biological replicates. Statistical significance was determined as $^*p < 0.05$, $^{**}p < 0.01$, $^{***}p < 0.001$, and $^{****}p < 0.0001$.

3. Results

3.1. Implant design of DLP-printed constructs

The virtual model of the 3D-printed constructs was generated using Shapr3D software, creating a cylindrically shaped implant (Figure 1). An interconnected porous structure (pore size diameter: 500 µm) and some larger pores were created to support the exchange of nutrients and oxygen (Figure 1A–F). Both are necessary to facilitate cell survival within the construct after printing or implantation. In addition, the interconnected porous structure creates a larger construct-tissue interface, facilitating the ingrowth of cells and tissue components in the implant. Besides the small pores, larger pores with a diameter of up to 2.5 mm were included (Figure 1A–F). The rationale for using small and larger-sized pores was to support construct-tissue interaction on different-sized scales without compromising mechanical stability. The 3D model used for printing provides an overall porosity of 42%, as described in Table S1, Supporting Information. The printed construct displayed high macroscopic fidelity in comparison to the actual model (Figure 1E and F), whereas microscopic details vary depending on the applied bioinks.

3.2. Porous structure of the printed constructs

The overall porosities of the printed constructs were first determined using gravimetric measurement of cell-free native constructs (Figure S1, Supporting Information). The highest porosity was observed for GelMaGO (20%) (Figure S1E, Supporting Information), which was lower than the calculated porosity of the porous 3D model, which is likely due to the swelling of the hydrogels. In this context, GelMaGO also indicated the highest water absorption capacity, which was significantly higher compared to GelMaBB. To assess the pore sizes within the scaffolds, micro-CT analysis was performed using freeze-dried samples to ensure sufficient contrast (Figure 2).

Micro-CT scanning revealed that there was no discernable contrast between the printed structures and the solvent for the models in solution (no apparent difference in Houndsfield units, as the model mostly consists of water). Freeze-dried models, however, yielded high-contrast CT images (Figure 2). Both 2D reconstructions and rendered 3D models revealed differences in surface topology. GelMaBB and GelMaGO surfaces exhibited regular porosity and distinct pore anatomy, whereas the GelMaBB-CaP surface appeared more compact and less regular. Virtual sections in the XY-plane of the printed constructs displayed significant differences in the internal

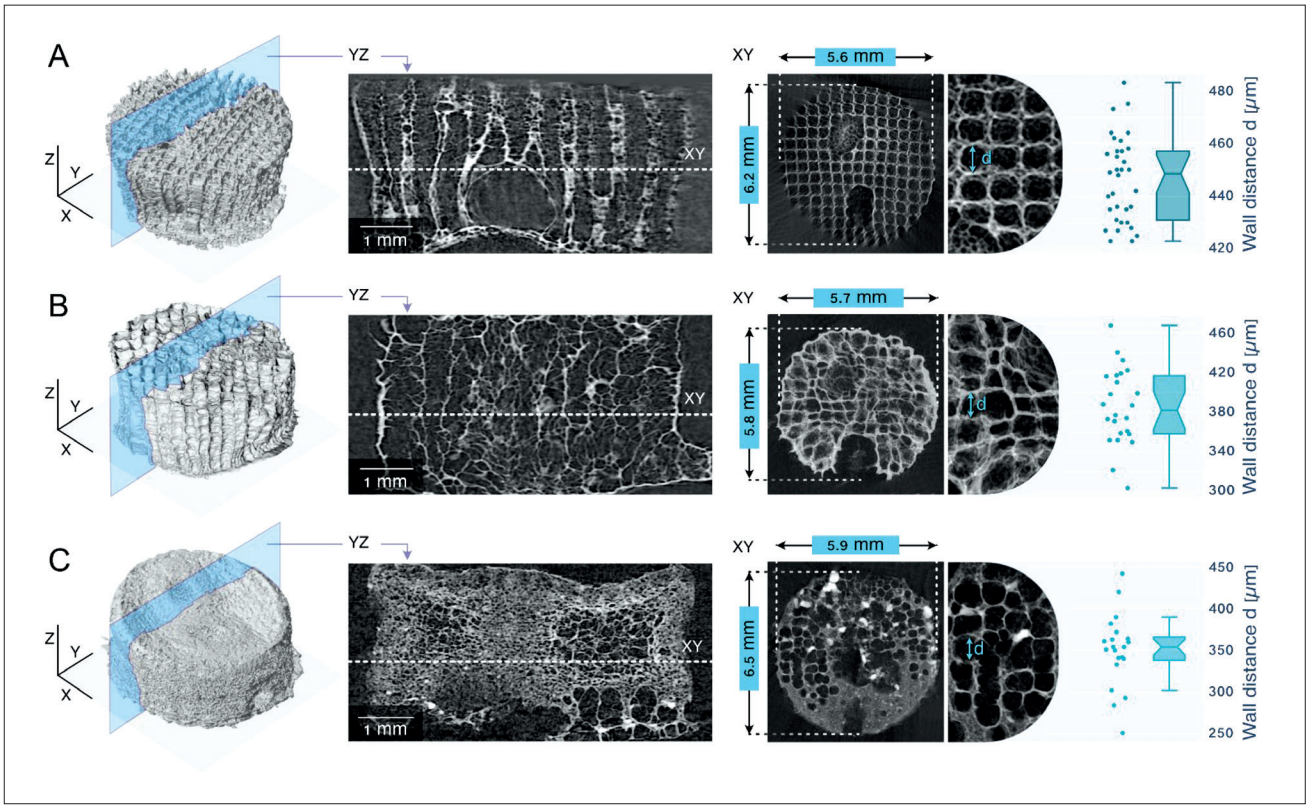

Figure 2. Micro-computed tomography (microCT) of freeze-dried bone tissue constructs. Analysis of the effect of bioink composition on the pore size in three printed constructs: (A) GelMaBB, (B) GelMaGO, and (C) GelMaBB-CaP. 3D models of the freeze-dried constructs display the surface topology and geometric differences in pore appearance (far left); the position of the printbed is indicated as a grey base plane. Virtual sections in the YZ plane (orthogonal to the printbed), display the internal structure and differences in pore network appearance (left middle). Z-stack projections (maximum intensity projections: 18–26 consecutive images) in the XY plane, revealing the structured organization of the gels and allowing for distance measurements of the pore walls in 2D (center). Magnification of the pores (right middle). Measurements of cell wall distances (d) based on pore sizes (mean ± standard deviation) (far right): 446.3 ± 13.6 µm in GelMaBB (n = 34), 385.4 ± 32.1 µm in GelMaGO (n = 24), and 336.7 ± 28.9 µm in GelMaBB-CaP (n = 19). Scale bars: 1 mm. Abbreviations: GelMa: Gelatin methacrylamide; BB: Brilliant Black; CaP: Calcium phosphate; GO: Graphene oxide.

organization. The appearance of the pores varied among the constructs and within different regions of each construct.

Maximum intensity projections (MIPs) in the z-direction of a limited number (n) of adjacent images in the XY-plane (parallel to the print bed) allowed, to varying degrees, the visualization of the pore arrangement within the constructs. In the Z-stack MIP of GelMaBB, the pore system appeared more intact compared to the other gels, displaying a rectangular network of pore walls. In GelMaGO, the network of pore walls resembled the rectangular network in GelMaBB but with more variations in pore shape and size, whereas the pores in GelMaBB-CaP appeared more rounded than rectangular.

For size measurements, pores with small cell wall length ratios were used. Due to strong variations in the appearance of the samples, including irregular pore networks in both GelMaGO and GelMaBB-CaP, there was a high variation in pore sizes and fewer intact pores identified for size measurement: 34 pores in GelMaBB, 24 pores in GelMaGO, and 19 pores in GelMaBB-CaP. The pore sizes (mean ± standard deviation) measured based on cell wall distances in MIPs were 446.3 ± 13.6 µm in GelMaBB (n = 34), 385.4 ± 32.1 µm in GelMaGO (n = 24), and 336.7 ± 28.9 µm in GelMaBB-CaP (n = 19). Although these data refer to specific regions of the samples, they provide insights into the influence of the nanomaterials on the porous appearance of the DLP-printed constructs.

3.3. Surface and morphology of DLP-printed constructs

The bioinks were prepared as summarized in Table 1. Cell-free 3D-printed constructs were subjected to SEM to analyze the effects of CaP and GO on the implant surface and the structure of the DLP-printed constructs (Figure 3). Commercial GelMa bioink (Figure 3A, E, and I) and

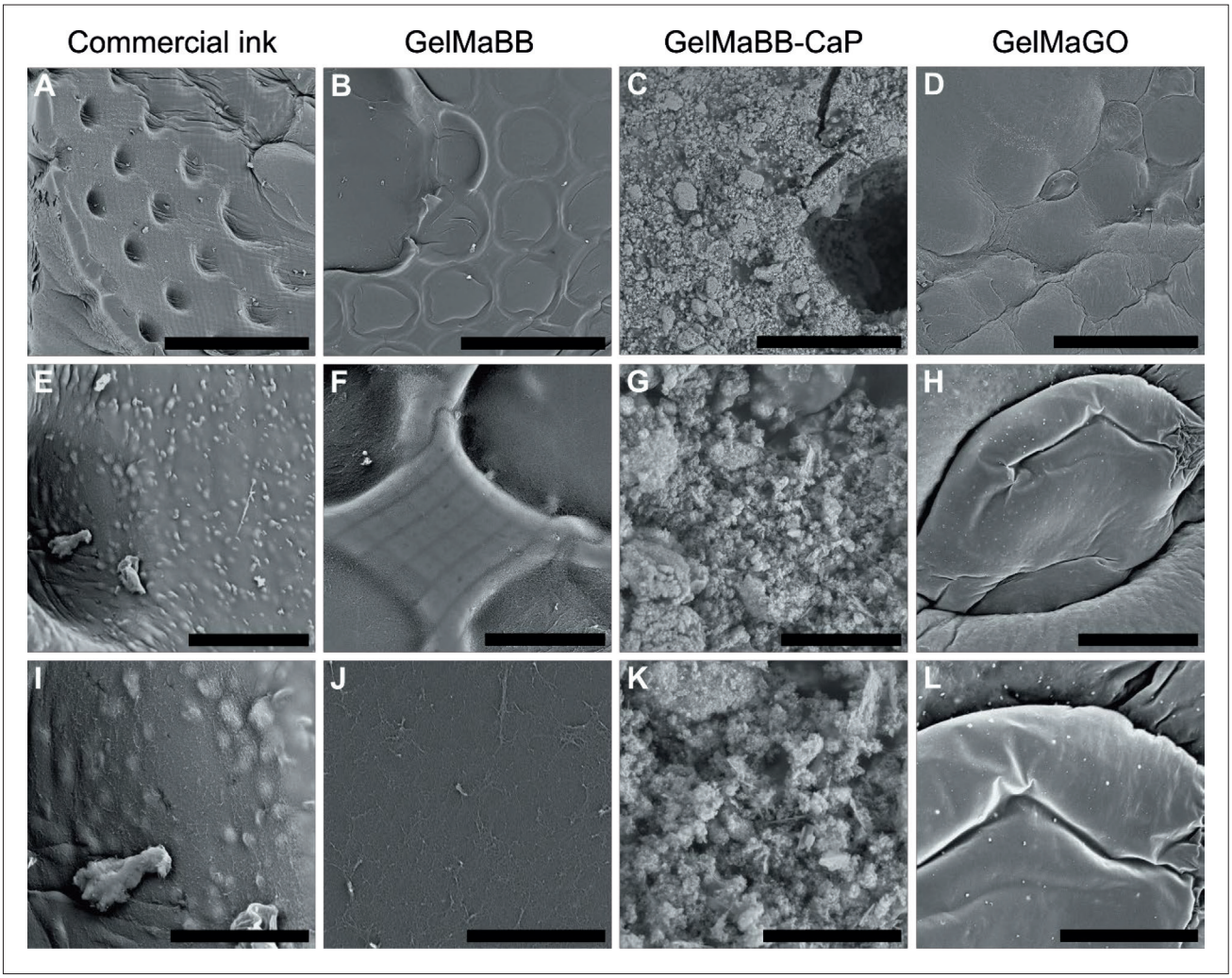

Figure 3. Scanning electron microscopy for digital light processing (DLP)-printed gelatin methacrylamide (GelMa)-based constructs: (A, E, and I) commercial ink; (B, F, and J) GelMaBB; (C, G, and K) GelMaBB-CaP; and (D, H, and L) GelMaGO. Scale bars: 800 µm (A–D); 80 µm (E–H); 40 µm (I–L). Abbreviations: BB: Brilliant Black; CaP: Calcium phosphate; GO: Graphene oxide.

GelMaBB (Figure 3B, F, and J) displayed high similarities and a smooth surface for the printed constructs. The commercial sample presented a small integration of bulk material of unknown origin. As expected, the integration of CaP nanoparticles (Figure 3C, G, and K) resulted in a rough surface with clearly visible CaP particles in the printed constructs. In contrast, the integration of GO (Figure 3D, H, and I) was characterized by a highly smooth surface.

3.4. Cellular viability and morphology of hMSCs in DLP-printed constructs

Calcein AM and propidium-iodide staining (Figure 4A–H) indicated high cellular viability in GelMaBB bioink-based constructs over 14 days, especially when compared to the reference commercial GelMa bioink (Figure 4A, E, I, and M). Encapsulation of CaP indicated a higher number of propidium-iodide-positive cells, which seem to increase over time from day 7 to 14, thus indicating an increased rate of dead cells. However, vital cells in GelMaBB-CaP still revealed an elongated and hMSC-typical morphology. In comparison, the reference bioink had nearly no vital cells present, independent of the time point. Similar findings were observed after staining with phalloidin TRITC (Figure 4I–P) to highlight the cellular cytoskeleton. In contrast to other GelMaBB bioinks, the cells in GO-modified bioink had a broader morphology with more pronounced actin fibers, potentially resembling stress fibers becoming more evident over the culture period.

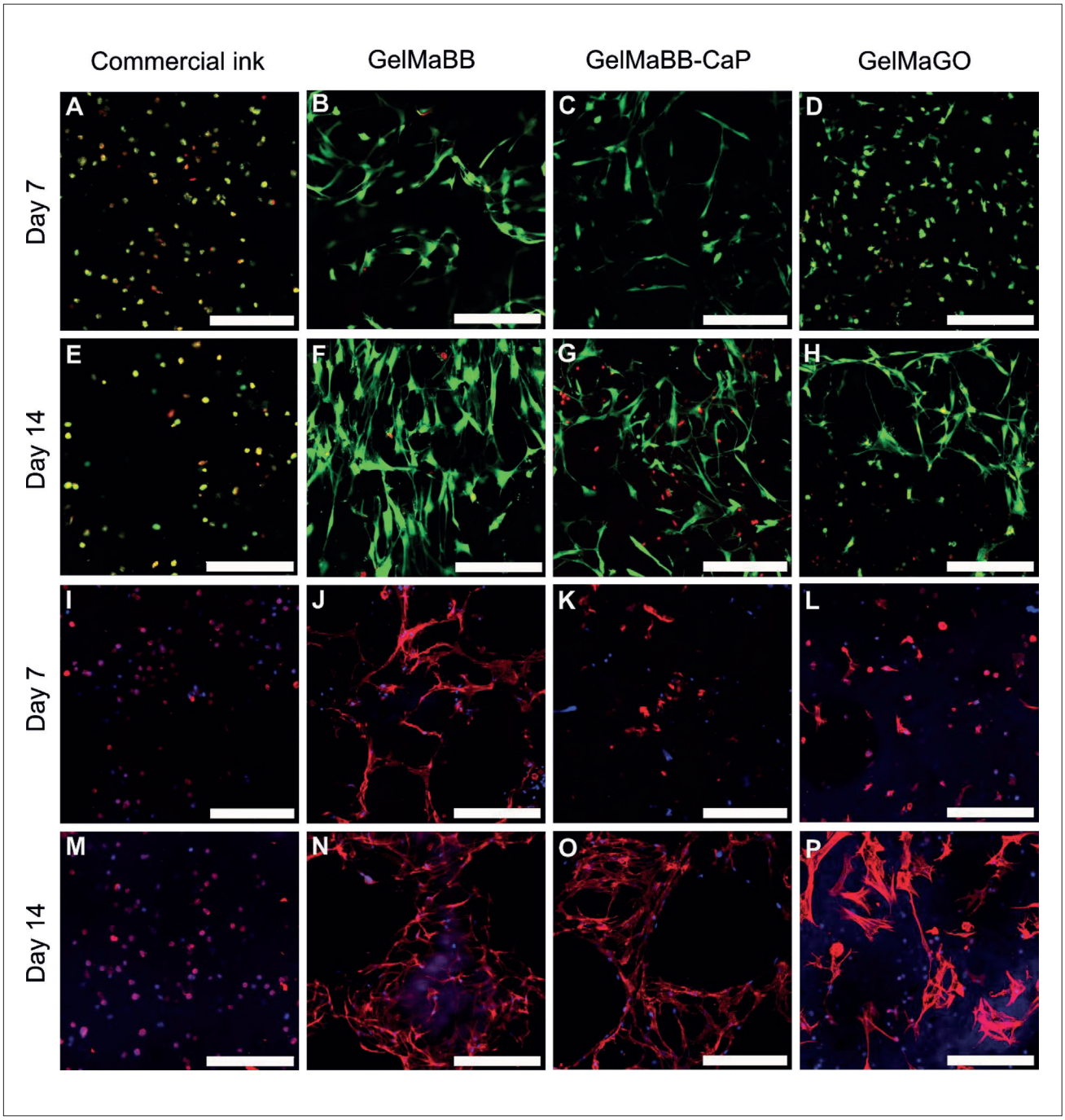

Figure 4. Confocal microscopy of human mesenchymal stem cells (hMSCs) encapsulated in the printed constructs: commercial ink (A, E, I, and M), GelMaBB (B, F, J, and N), GelMaBB-CaP (C, G, K, and O), and GelMaGO (D, H, L, and P). (A–H) Live/dead staining with calcein AM (green) and propidium-iodide (red) after 7 (A–D) and 14 (E–H) days. (I–P) Staining with Phalloidin TRITC (red) and Hoechst 33258 (blue) after 7 (I–L) and 14 (M–P) days. Scale bars: 250 μm. Abbreviations: GelMa: Gelatin methacrylamide; BB: Brilliant Black; CaP: Calcium phosphate; GO: Graphene oxide.

3.5. Influence of nanomaterial-modified bioinks on cell number and proliferation

To assess the cellular performance in the different bioinks quantitatively, we determined the DNA amount in the DLP-printed constructs over time and for several donors of hMSC (Figure 5). The reference GelMa bioink (commercial), however, had the lowest DNA amount in pilot studies in accordance with the morphological data as described above. Thus, we focused on the GelMaBB bioink and its modifications in the upcoming experiments.

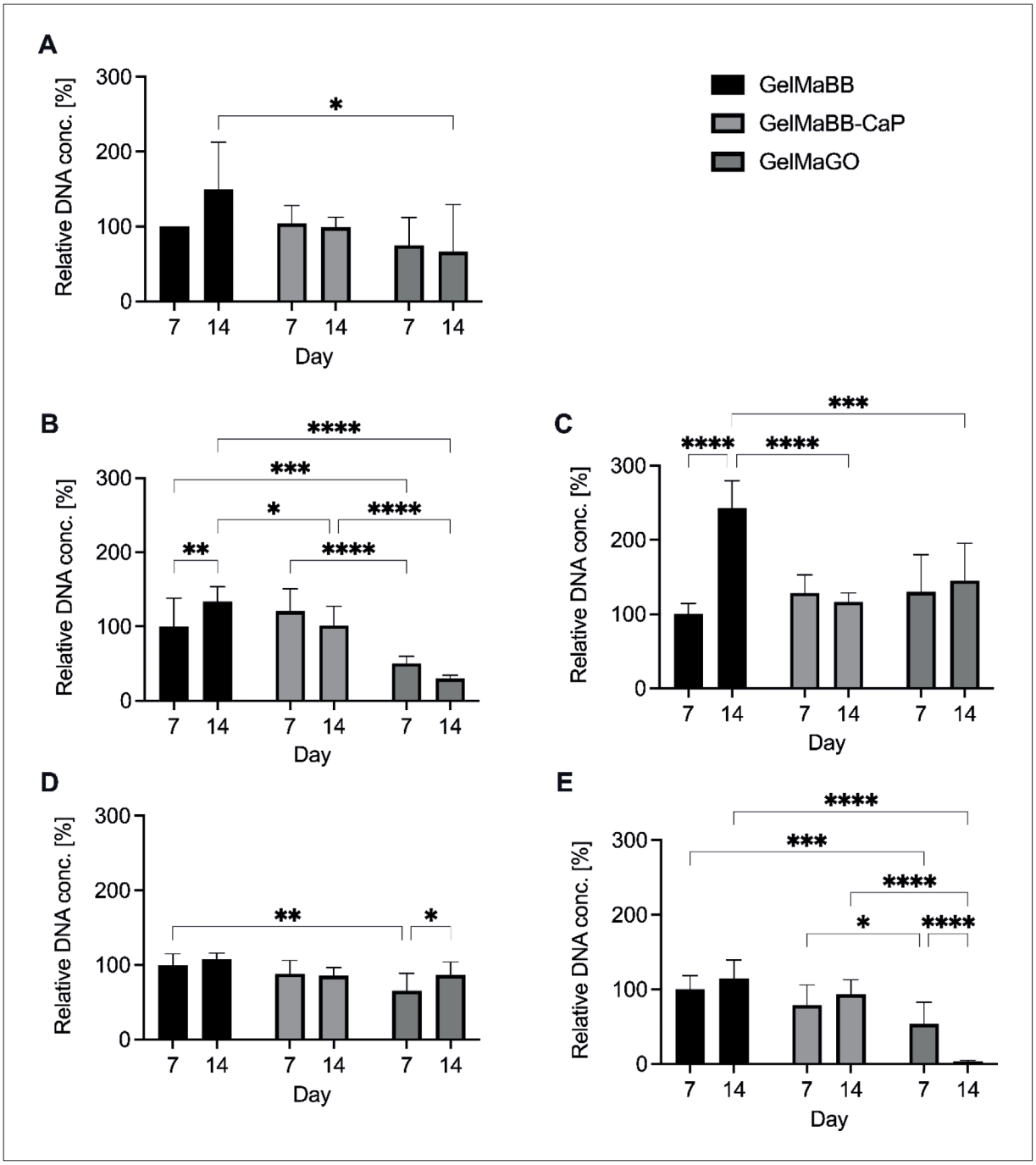

Figure 5. (A) DNA quantification of human mesenchymal stem cells (hMSCs) in printed gelatin methacrylamide (GelMa)-based bioinks after 7 and 14 days (n = 4 donors). (B–E) Results of DNA quantification of hMSCs in printed GelMa-based bioinks for four different donors after 7 and 14 days (n = 3 technical replicates). Two-way ANOVA was used for statistical evaluation; $^{*}p < 0.05$, $^{**}p < 0.01$; $^{***}p < 0.001$; $^{****}p < 0.0001$. Abbreviations: ANOVA: Analysis of variance; BB: Brilliant Black; CaP: Calcium phosphate; GO: Graphene oxide.

The amount of DNA in GelMa-based constructs was assessed on days 7 and 14 to analyze the impact of the nanomaterial and the temporal development of cell growth over the tested time frame. GelMaBB samples displayed, on average, the highest DNA content at day 14 compared to the nanomaterial-modified variants, as well as a significant increase in the DNA amount over time, thus indicating cellular proliferation in GelMaBB (Figure 5A).

Although not consistently significant for all individual donors, the same trend was observed in the DNA amount across the individual donors (Figure 5B–E). For CaP- and GO-modified bioinks, no increase in DNA content (i.e., cell proliferation) was observed, independent of the donor. DNA content indicated relatively stable cell numbers with slight variations between nanomaterials and time points, but no clear trend.

3.6. Mechanical properties of the printed constructs

3D-printed constructs (with or without cells) were subjected to compression strength tests at different time points to compare the impact of the nanomaterials, temporal development, and the impact of cells on mechanical stability (Figure 6). Young's modulus was first assessed for constructs printed without cells to focus on the impact of the nanomaterials (Figure 6A). On day 14, the GO-modified GelMa exhibited the highest values for Young's modulus in the cell-free constructs maintained in the culture medium before assessment. Conversely, the cell-laden constructs, i.e., closely mimicking physiological conditions, revealed no clear trend for Young's modulus between nanomaterials or across the two tested time points, both in the average of all donors (Figure 6B) and for individual donors (Figure 6C–F). When comparing Young's modulus in cell-loaded and cell-free constructs at different time points of culture, the GO-modified GelMa bioink exhibited improved stability compared to GelMaBB and GelMaBB-CaP, with no significant differences with or without cells (Figure 6H). Overall, these data indicate that GO increases Young's modulus of the cell-free GelMaGO constructs over culture time. Although the cells seem to have a certain influence, their effect on the mechanical properties did not indicate a clear trend.

3.7. Collagen deposition in DLP-printed constructs independent of the bioink

Ensuring appropriate cell bioactivity after integration into the bioink and within the final 3D-printed construct is crucial for successful bioprinting. To assess the activity of cells internalized into the bioink and the DLP construct, we used cryosections and staining of typical osteogenic activities. Collagen production was analyzed by picrosirius red staining using cell-free constructs as controls for background staining (Figure 7). Collagen matrix production associated or localized with embedded cells was observed for all types of bioinks. No background staining for picrosirius red was observed in cell-free constructs. Collagen deposition is more pronounced along the pores or on the surface of the constructs (arrows in Figure 7B, C, E, F, H, and I). However, no clear differences were observed for the different bioinks. The collagen deposition by embedded hMSCs underlines their bioactivity.

3.8. Calcification in DLP-printed constructs independent of the nanomaterials

In addition to collagen production, the calcification of hMSCs was first investigated on the morphological level after staining the whole constructs or the derived cryosections with ARS (Figure 8). Cell-free constructs served as controls and are depicted in Figure 8A–C (whole constructs) and Figure S3, Supporting Information (cryosections). As expected, CaP-modified GelMaBB resulted in a high background for calcium signals (Figure 8B). In contrast, the cryosections indicated distinct calcification areas associated with embedded cells, which were highly pronounced in cell-laden GelMaBB-CaP constructs (Figures 8H; and Figure S3I–L, Supporting Information) but not observed in the cell-free controls (Figure S3G and H, Supporting Information). Pronounced areas of calcium deposition were associated with cells in the construct and most prominent in GelMaBB-CaP compared to GelMaBB or GelMaGO, thus indicating the remarkable osteoinductive properties of GelMaBB-CaP.

To quantify the calcification process in DLP-printed constructs, alizarin red was extracted and assessed quantitatively on days 7 and 14 (Figure 9). Cell-free constructs consisting of different bioinks are depicted in Figure 9A with high ratios of calcium in GelMaBB-CaP bioinks. In samples with hMSCs from several donors, alizarin red values were significantly higher in GelMaBB-CaP samples than in the corresponding samples from the other bioinks (Figure 9B). Values are depicted as total values without subtracting the values from the cell-free scaffolds. Data for individual donors of hMSCs resulted in a tentative temporal increase in alizarin red for two individual donors (Figure 9C and E), whereas two other donors displayed a tentative decrease in alizarin red over time (Figure 9D and F). When comparing the alizarin red values of cell-free and cell-laden samples as average values for all donors, the GelMaBB-CaP samples presented significantly higher alizarin red values than the other bioink samples. These quantitative data suggest that GelMaBB-CaP has osteoinductive properties, despite the donor-donor variation in ARS over time.

3.9. Osteogenic differentiation in the printed constructs

To further analyze the osteoinductive potential of the GelMaBB-CaP vs. GelMaBB bioinks, semi-quantitative real-time PCR was performed (Figure 10). RNA extraction from constructs consisting of GelMaGO was not feasible and resulted in low RNA quantities. Thus, GelMaGO was excluded from PCR analysis. For the average of all tested donors (Figure 10A) and the individual donors (Figure 10B–D), GelMaBB-CaP-derived samples indicated

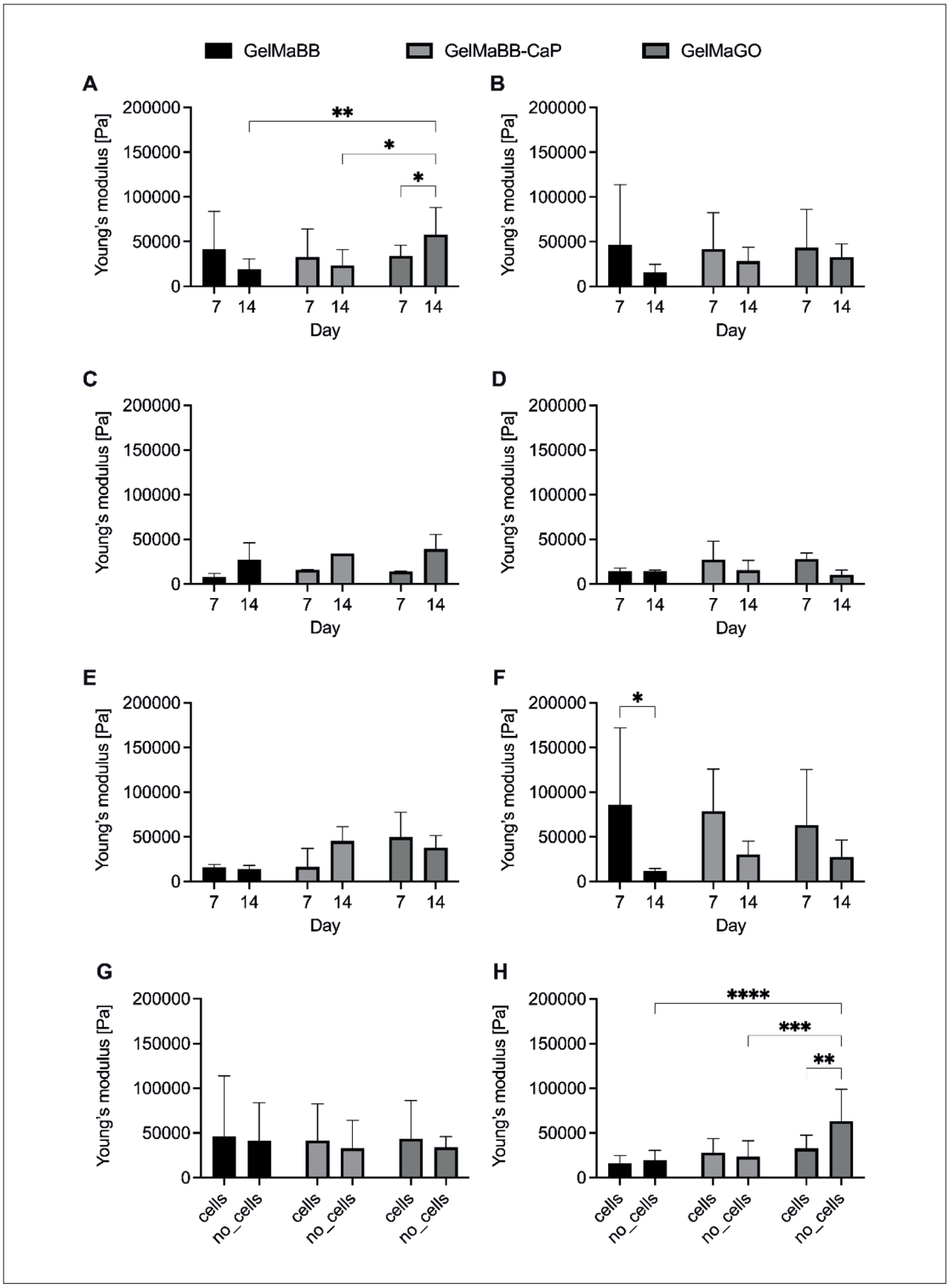

Figure 6. Young's modulus of constructs composed of different bioinks (GelMaBB, GelMaBB-CaP, and GelMaGO) with or without human mesenchymal stem cells (hMSCs). (A) Young's modulus of cell-free scaffolds (n = 4). (B) Young's modulus of constructs with hMSCs (in average) (n = 4 Donors). (C–F) Young's modulus for each of the four donors on days 7 and 14 (n = 3 technical replicates). (G) Young's modulus of printed constructs with (cells) and without (no_cells) hMSCs on day 7 (n = 4 donors). (H) Young's modulus of printed constructs with (cells) and without (no_cells) hMSCs on day 14 (n = 4 donors). Statistics were evaluated using two-way ANOVA; *p < 0.05; **p < 0.01; ***p < 0.001; ****p < 0.0001. Abbreviations: ANOVA: Analysis of variance; GelMa: Gelatin methacrylamide; BB: Brilliant Black; CaP: Calcium phosphate; GO: Graphene oxide.

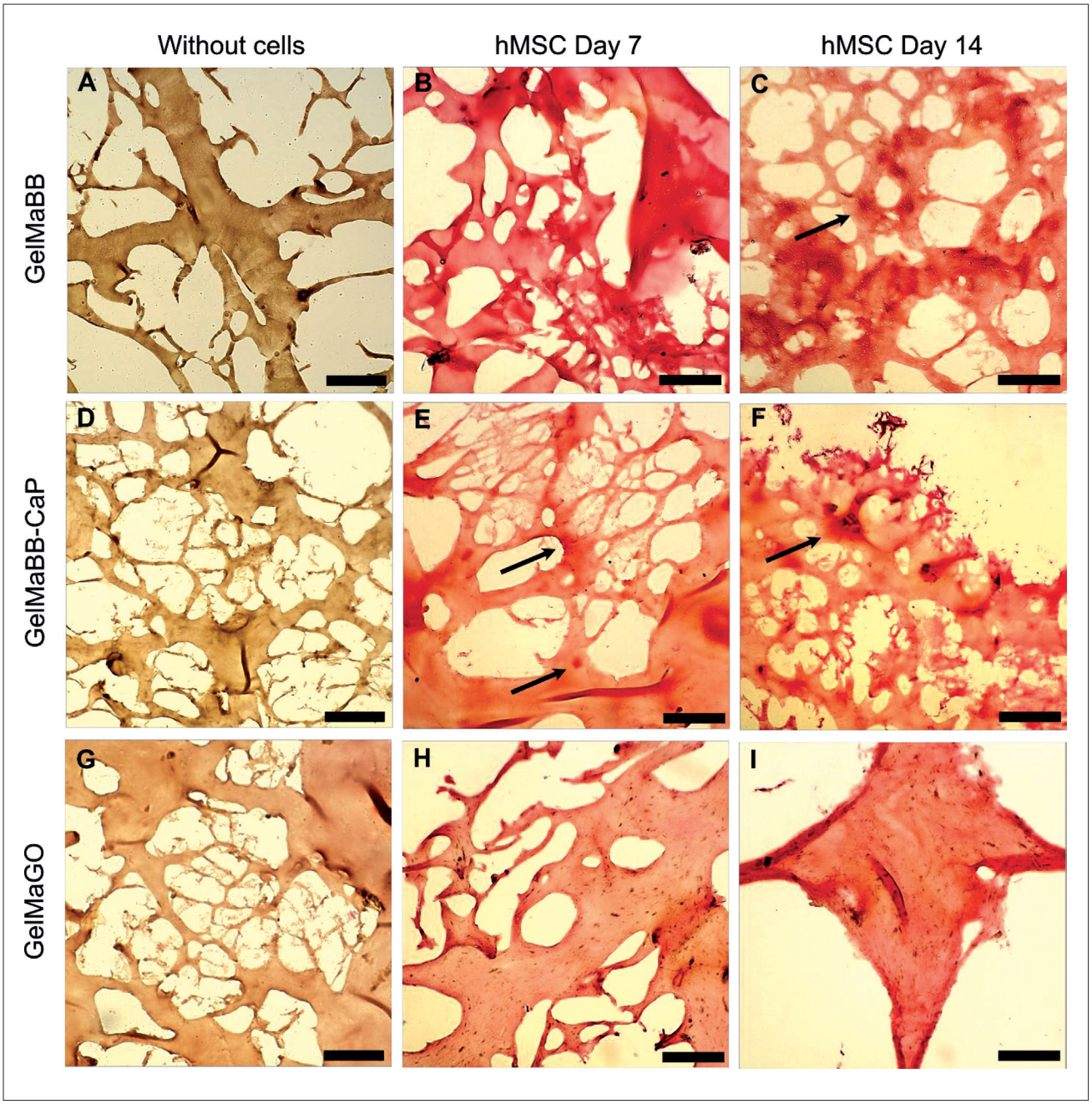

Figure 7. Picrosirius red staining of GelMaBB (A–C), GelMaBB-CaP (D–F), and GelMaGO (G–I) after 7 and 14 days. Comparison between human mesenchymal stem cell (hMSC)-free scaffolds (A, D, and G) and hMSC-containing constructs (B, C, E, F, H, and I) after 7 and 14 days. Scaffolds printed without cells serve as controls for the staining process to determine material-based background staining. Arrows indicate collagen deposition by cells in the bioink. Scale bars: 100 μm. Abbreviations: GelMa: Gelatin methacrylamide; BB: Brilliant Black; CaP: Calcium phosphate; GO: Graphene oxide.

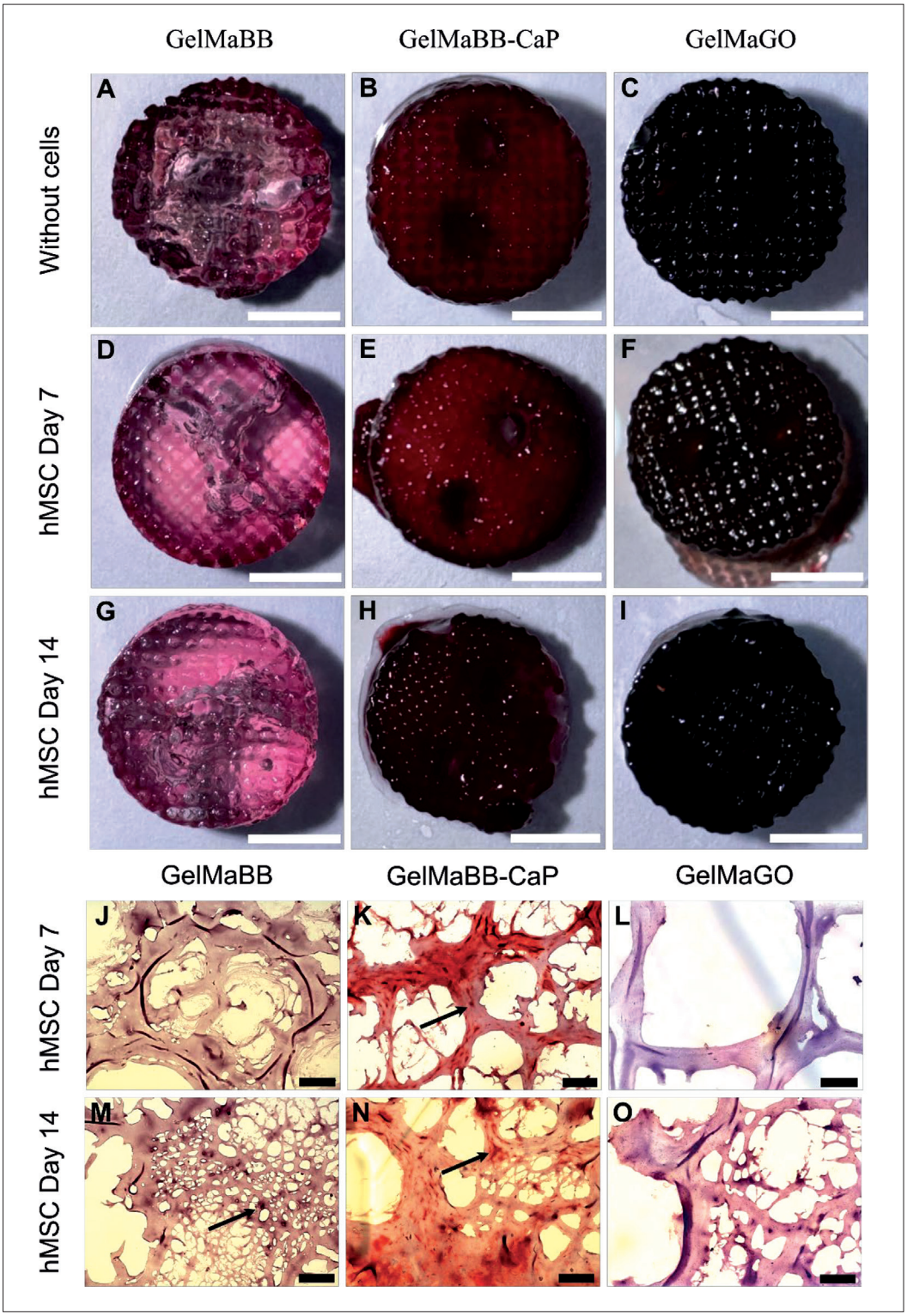

Figure 8. Alizarin Red (AR) staining of constructs and cryo-sections of printed constructs after 7 and 14 days. (A–I) Images of AR-stained constructs with (D–I) or without (A–C) cells. (J–O) AR-stained cryo-sections of cell-laden GelMaBB (J and M), GelMaBB-CaP (K and N) and GelMaGO (L and O) constructs after 7 (J–L) and 14 (M–O) days. Arrows indicate calcified matrix deposition by cells in the bioink. Scale bars: 100 μm. Abbreviations: GelMa: Gelatin methacrylamide; BB: Brilliant Black; CaP: Calcium phosphate; GO: Graphene oxide.

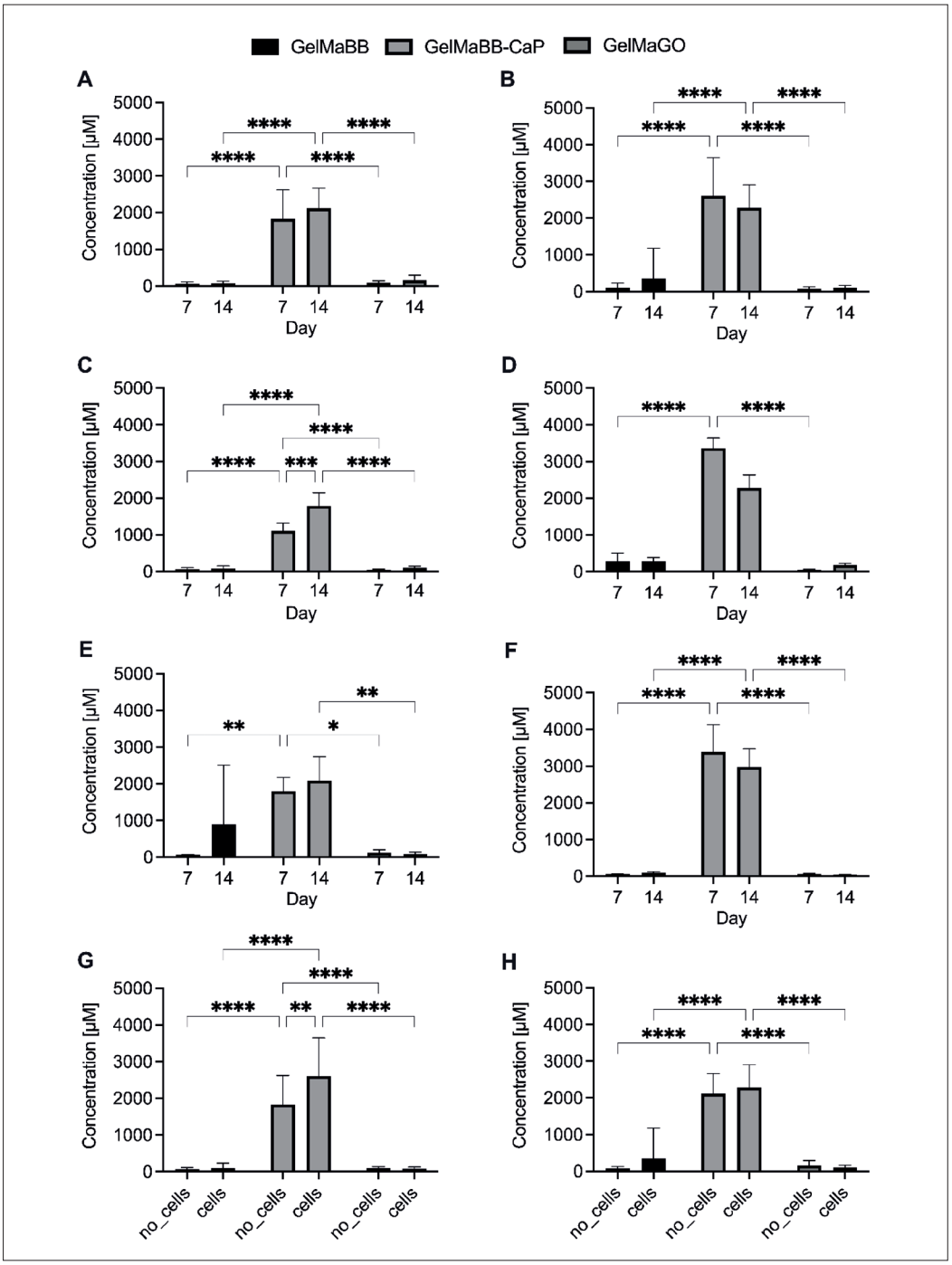

Figure 9. Quantification of Alizarin Red staining (ARS) for GelMa-based constructs with and without human mesenchymal stem cells (hMSCs) after 7 and 14 days. (A) ARS quantification of cell-free scaffolds (n = 4). (B) ARS quantification of cell-loaded constructs for four donors on days 7 and 14. (C–F) Individual ARS quantification of the constructs for four donors, respectively (n =3 technical replicates). (G) Comparison of GelMa-based constructs with (cells) and without (no_cells) hMSCs on day 7 (n =4 donors). (H) Comparison of GelMa-based constructs with (cells) and without (no_cells) hMSCs on day 14 (n = 4 donors). Statistics were evaluated using two-way ANOVA; *$p < 0.05$; **$p < 0.01$; ***$p < 0.001$; ****$p < 0.0001$. Abbreviations: ANOVA: Analysis of variance; GelMa: Gelatin methacrylamide; BB: Brilliant Black; CaP: Calcium phosphate; GO: Graphene oxide.

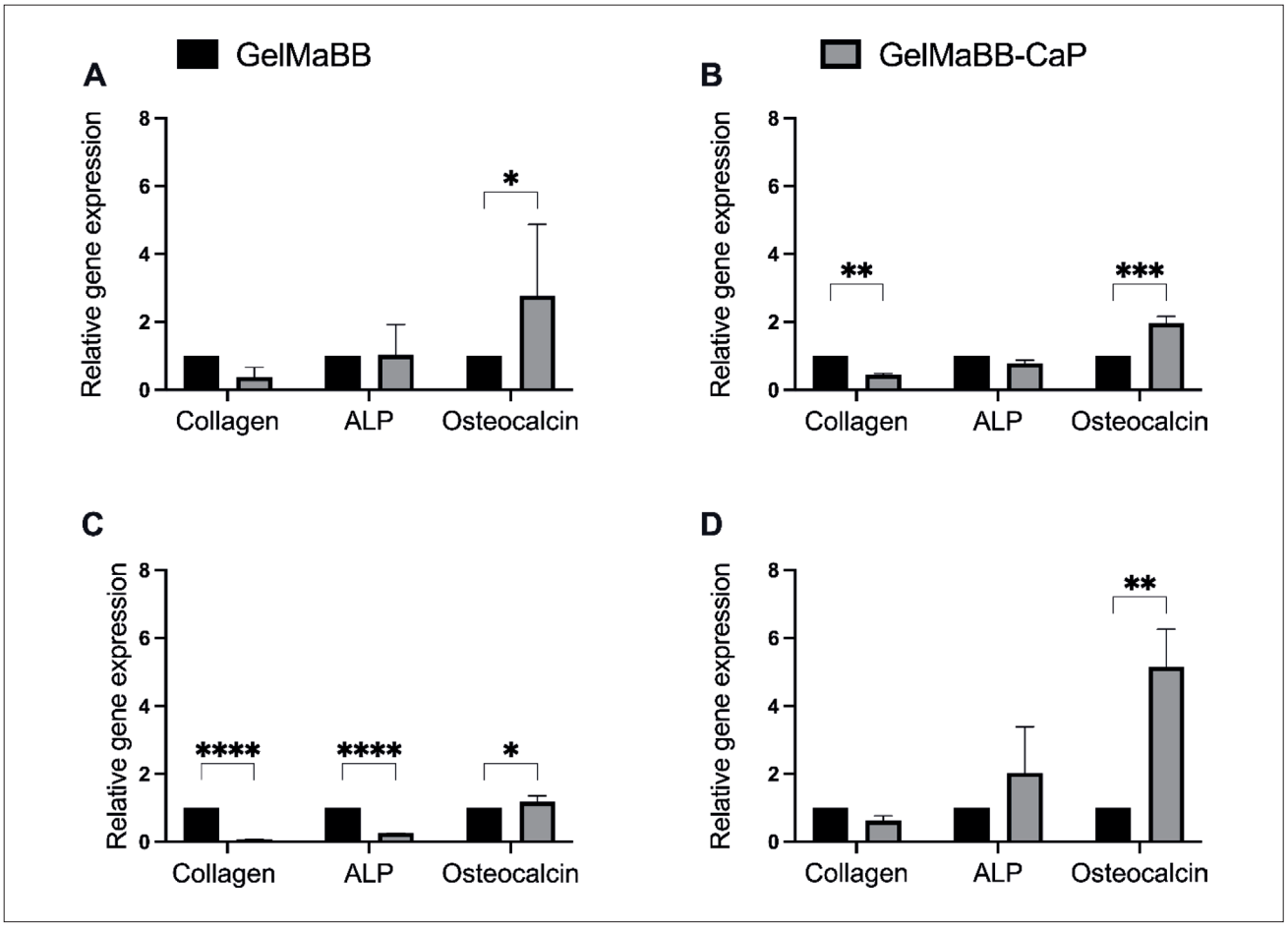

Figure 10. Gene expression of osteogenic differentiation markers in constructs composed of GelMaBB or GelMaBB-CaP. (A) PCR results for all four donors on day 14 (n = 3 donors). (B–D) PCR results for each of the three donors on day 14 (n = 3 donors). Statistics were evaluated using two-way ANOVA; *$p < 0.05$; **$p < 0.01$; ***$p < 0.001$; ****$p < 0.0001$. Abbreviations: ALP: Alkaline phosphatase; ANOVA: Analysis of variance; GelMa: Gelatin methacrylamide; BB: Brilliant Black; CaP: Calcium phosphate; GO: Graphene oxide.

a higher gene expression of osteocalcin, which is a marker associated with osteogenic differentiation. Other markers associated with early osteogenic differentiation, such as alkaline phosphatase (ALP) or collagen gene expression, exhibited less consistent trends. However, the gene expression data obtained highlight the osteogenic impact of GelMaBB-CaP on hMSCs in DLP-bioprinted constructs.

4. Discussion

In this study, we developed different bioink formulations based on GelMa and the nanomaterials CaP and GO for DLP-bioprinting. The influence of the GelMa-based bioink in combination with the nanomaterials on mechanical properties and cellular parameters, such as cell viability, proliferation, and differentiation, was directly compared using a variety of methods. GelMaBB samples displayed the highest cell viability and proliferation of hMSCs within the construct. Notably, GO increased the stiffness of cell-free DLP-printed GelMa constructs. However, we observed that the slightly increased stiffness of GelMaGO enhanced the actin cytoskeleton structure. Incorporation of CaP nanoparticles improved the osteogenic differentiation of hMSCs, indicated by calcification and gene expression, and revealed the highest impact on osteogenic differentiation compared to the other samples. In general, the application of nanomaterials in DLP-printed constructs did not interfere with the printing process, though slight changes in pore sizes and porosity were observed.

In bioprinting, the selection of printing technology and the design of bioprinted constructs are highly interdependent factors. DLP offers a high printing resolution, enabling precise and defined printing of biomimetic implants that conform to the shape of specific bone defects.[30,72] In addition, DLP provides flexibility in designing internal implant structures with various pore sizes, shapes, and patterns. The integration of smaller

and larger pores in this present study facilitated the efficient exchange of nutrients and oxygen within the construct. The pore size (pore diameter: 500 μm) in the 3D model is close to the size of pores in cancellous bone *in vivo* with a typical range of 300–600 μm, which is also the recommended range (200–600 μm) for bone tissue engineering applications.[51,73–78] The final porous structure in the printed construct differed slightly due to the bioink, as observed from the cryosections, overall porosity, and micro-CT results. Accurately depicting the internal structure of printed tissues is key for assessing the success of the print but challenging. It should be noted that freeze-drying affects the samples' internal structure, and imaging samples in solution would provide a more realistic view. However, native, non-contrast-enhanced micro-CT could not distinguish between the constructs and the solution due to similar absorption. Hence, future studies should explore tailored CT contrast agents to facilitate the imaging of constructs in solution.

Structural differences are probably due to variations in water binding capacities and the type of nanomaterial used in the DLP printing process. Besides the porous structure, the exchange of nutrients and oxygen is supported by the high-water content in bioinks, evident from the high cellular bioactivity along the pores and within the bioink. Suitable pore sizes and high interconnectivity facilitate successful implantation by enabling the ingrowth of cells and vascular structures from the peri-implant tissue. Although tissue cells and vascular structures might be directly integrated into bioprinted constructs, their physiological interaction with the host tissue remains a decisive factor for the vitality and functionality of bioprinted constructs. In this context, the biomechanical properties of bioinks and the overall construct design control cell migration and differentiation, while simultaneously providing structural stability in a dynamic, biologically active environment.

Bioinks need to be formulated according to specific technological requirements, mainly defined by the printing technology and implant design. A series of bioinks for bone bioprinting have been reported.[11,29,50,79–83] However, bioprinting of vital and more complex tissue constructs, especially for hard and highly vascularized tissues like the bone, is far away from being a standardized procedure. In addition, the impact of bioinks on the cellular and molecular performance of encapsulated cells remains unclear. Moreover, there is a lack of direct comparisons of the effects caused by different bioink formulations or nanomaterials.

In this study, we developed the GelMaBB bioink and studied the influence of nanomaterial integration on the functional parameters in the DLP-printed constructs. GelMa was selected as the base bioink for its high biocompatibility and biodegradability, thereby providing an excellent matrix for cell growth due to its RGD sequences.[15,25,27–36] The high degree of methacrylation (80%) in GelMa also supports the crosslinking process and enhances the stability of the construct. LAP was used as the photo-initiator due to its high-water solubility and high polymerization rates, favoring good biocompatibility.[37,69,84–86] BB was used as a photo-absorber to prevent light scattering, thereby enhancing the printing accuracy.[14] These components provide the basis for the GelMaBB bioink, which was further modified using GO and CaP nanomaterials to enhance its mechanical and osteoinductive properties.

Graphene oxide (GO) is a nanomaterial with various beneficial functions for DLP bioprinting and functionalizing 3D-printed scaffolds.[58,59] GO acts as a photo-absorber due to its black color, and its functional groups introduce new functionalities in bioinks or biomaterials, such as improving cell performance in biological inert alginate bioinks and enhancing hMSC adhesion in decellularized biomaterials.[44,66] In addition, GO stabilizes materials and constructs by increasing the stiffness of bioinks.[83,87]

Various nanomaterials have been reported for modifying bioinks for bone bioprinting, including other forms of CaP such as α-tricalcium phosphate (TCP), β-TCP, and biomimetic hydroxyapatite particles, that enhance the osteoinductive properties of bioinks.[88–90] In our study, we have selected CaP nanoparticles due to their osteoinductive potential in extrusion-based 3D-printed polycaprolactone scaffolds, recently reported by our group.[65,91]

In the SEM images of DLP-printed constructs, CaP nanoparticles exhibited cloud-like bulk structures, which might be attributed to their agglomeration within the bioink and could be improved by other dispersion methods like shear mixing. Upon comparison of the surface characteristics between the samples, it was noted that GelMaGO and GelMaBB exhibited a smooth surface, while GelMaBB-CaP displayed a rougher surface texture. This difference might be partly attributed to the particle sizes, with CaP particles up to 150 nm in size and GO particles of approximately 10 nm in size. Furthermore, the concentration of CaP nanoparticles (50 mg/mL) was 100-fold higher than that of GO (0.5 mg/mL), which was selected based on the concentration of the photo-absorber BB. In other studies, GO concentrations ranging from 0.1 to 2 mg/mL in hydrogels induced diverse effects on cells and mechanical parameters.[44,46,83,92]

In this present study, GO and CaP displayed slightly different effects on the vitality and morphological appearance of cells in the DLP-printed constructs. Besides the influence of the nanomaterials, the GelMaBB bioink alone had a significant impact on the cells compared to commercial GelMa bioink. The viability of hMSCs in commercial GelMa bioink was surprisingly low, with high rates of rounded and dead cells, while cell viability and proliferation were the highest in GelMaBB amongst all tested bioinks, as indicated by morphological data and DNA quantification. Both added nanomaterials resulted in diverse effects on the cell morphology or viability staining. For GelMaBB-CaP, we observed the presence of some dead cells morphologically, but none on the quantitative level; many cells still maintained a typical elongated hMSC morphology. Cells within GelMaGO were, especially in the later phase, characterized by a more broadened morphology with distinct stress fibers, probably associated with the increased stiffness of these samples. Stress fibers, as a result of the higher stiffness of hydrogels containing GO, have been reported by other groups, probably associated with the need for a robust actin skeleton to facilitate stretching or movement within a stiffer matrix.[93] Besides these morphological differences, DNA quantification revealed no clear trends regarding the negative or positive effects of CaP or GO on cell growth over time. In addition, the inherent donor-to-donor variation of hMSCs, such as differences in cell growth or population heterogeneity, will contribute to variations in DNA assessment and overall biological evaluations.[94,95]

Although nanoparticles might be taken up by hMSCs, DNA quantification did not reveal significant cytotoxic effects caused by the nanomaterials in the investigated time frame. Previous studies have demonstrated that concentrations exceeding 50 µg/mL of GO can induce cytotoxic effects in hMSCs.[96] Our data, however, indicate that the much higher concentration of 500 µg/mL in our bioink did not cause severe negative effects in comparison to the unmodified GelMaBB or the commercial GelMa bioink. In our previous study, we have demonstrated that the same CaP nanoparticles used in this study and integrated into polycaprolactone (PCL) can induce an increase in lactate dehydrogenase as an indicator for cellular cytotoxicity in the early phases of culture after seeding of hMSCs.[65] In the context of our present study, no quantitative cytotoxic effects were indicated. In addition to cytotoxicity, differentiation processes, often attenuating cellular proliferation, can contribute to differences in cell numbers over time.[97–100] Thus, we can also assume that differentiation processes affect the results of DNA quantification in the present study.

The nanomaterials CaP and GO have both been associated with the ability to enhance mechanical properties, such as stiffness and compression strength in hydrogels.[46,47,50,52–54,69,92,101–105] Despite the lower concentration of GO (0.5 mg/mL) compared to CaP (50 mg/mL), GelMaGO exhibited the highest value for Young's modulus. These data from cell-free scaffolds verified the stabilizing effect of GO on the material, i.e., the overall constructs, as previously reported in the literature. It may be surmised that GO acts as a photo-absorber and facilitates proper crosslinking of the bioink during printing and subsequent storage.

The mechanical properties of bioinks are typically evaluated based on the materials or constructs themselves. Although this is necessary to assess the impact of material composition without other influencing factors, integrated cells or physiological processes (e.g., degradation, differentiation, or matrix deposition) can actively change the biomechanical properties in bioprinted constructs. However, measuring Young's modulus in biological-based soft samples is a complex endeavor to determine the points of the first contact. Therefore, the algorithm for fitting a linear curve can only be based on the linearity of compression curves, which may lead to a large scatter in the evaluation of Young's modulus. In the investigated time frame, we did not observe significant differences in the biomechanical properties between samples without cells (~20–60 kPa) or integrated with cells (~16–50 kPa). In this context, it was demonstrated that mechanical stability increases with calcium deposition in cell-laden hydrogels. Hydrogels based on the fibrillating peptide FEFEFKFK or alginate in combination with gelatin and GO display an increase in elasticity, compressive modulus, or stiffness over time, particularly when cells are encapsulated. These studies suggest that the production of extracellular matrix proteins and mineralization correlate with mechanical properties.[80,83,106] Although in our study samples from donors with a high calcification also displayed a temporal increase in the mechanical properties, the donor-to-donor variation was too high to validate this effect in our studies.

The compressive strength of cancellous bone ranges between 0.1 and 16 MPa, and Young's modulus ranges between 0.05 and 0.5 GPa.[107,108] In contrast, hydrogel-based bioprinted constructs containing living cells, typically have significantly lower compression strength than that of bone, i.e., 1–30 kPa.[83,84,106] Thus, they are unable to act as load-bearing implants, if applied on their own. During the physiological processes of cellular differentiation and bone formation *in vivo*, collagen deposition and calcification processes will continuously change the biomechanical properties from soft to hard tissue in long-term processes over several weeks or months. Thus far, a mechanically

stable bone construct has not been achieved for hydrogel-based bioprinted constructs. In addition, the mechanical behavior of such constructs is documented over much shorter time frames.[80]

In this study, we used different methods to assess the osteogenic differentiation of hMSCs under the influence of GO or CaP in GelMa-based bioink. In this context, we analyzed the functionality of cells in the internal parts of the constructs by applying cryosections in combination with quantitative evaluation methods, assessing the entire constructs. The formation of typical bone matrix components by the cells in the internal parts of the construct was assessed using picrosirius red staining of the cryosections to detect collagen production, and ARS to monitor the calcification process. Observations from picrosirius red indicate active collagen synthesis within the printed constructs by hMSCs, reflecting a high bioactivity of encapsulated cells after the printing process. The production of collagen was additionally investigated using PCR, with no clear differences between the tested samples. ARS-stained cryosections confirmed calcium deposition and late osteogenic differentiation by bioactive cells in GelMaBB-CaP, despite background calcium signals from the bioink.[42,97,99] In agreement with this morphological observation of osteogenic differentiation in GelMaBB-CaP, quantitative analysis of ARS from whole constructs revealed notably higher calcium content in GelMaBB-CaP samples. When comparing cell-laden and cell-free samples, hMSC-loaded samples exhibited higher calcium content on days 7 and 14, highlighting cell differentiation and their active role in calcification. This was further supported by an increase in osteocalcin expression in the PCR data for GelMaBB-CaP compared to GelMaBB. Osteocalcin, which is expressed more during later phases of bone mineralization, exhibited a consistent trend in gene expression across all individual hMSC donors, highlighting the osteoinductive properties of GelMaBB-CaP.[109]

5. Conclusion

This study presents a GelMa-based bioink formulation tailored for DLP printing and enabling a high viability and biological activity of hMSC after the bioprinting process. The incorporation of nanomaterials, CaP and GO, enhanced the functionality of the bioink in different ways, while no significant cytotoxicity was observed. CaP nanoparticles exhibited osteoinductive properties within the bioink, while GO primarily increased the material's Young's modulus. The nanomaterials did not interfere significantly with the DLP printing process. However, slight changes in the microscopical structure of the construct were observed. Future studies will focus on using nanomaterials for bioink functionalization strategies.

Acknowledgments

We would like to thank Esther Appel and Dr. Alexander Kovalev for their technical support with SEM. We acknowledge Lennard Arp's excellent technical support. We would like to also thank Dr. Sebastian Wille, Frank Lehmann, and Timo Damm for their support with gravimetry and μCT.

Funding

This work was supported by the Federal Ministry of Education and Research (BMBF), Germany, through the WIR! program for BlueHealthTech and BlueBioPol (FKZ 03WIR6207A.BMBF). MOIN CC was founded by a grant from the European Regional Development Fund (ERDF) and the Zukunftsprogramm Wirtschaft of Schleswig-Holstein (project no. 122-09-053).

Conflict of interest

The authors declare they have no competing interests.

Author contributions

Conceptualization: Julie Kühl, Sven Malte Krümpelmann, Leonard Siebert, Sabine Fuchs

Formal analysis: Julie Kühl, Sven Malte Krümpelmann, Malte Bruhn, Ronald Seidel

Investigation: Julie Kühl, Sven Malte Krümpelmann, Larissa Hildebrandt

Methodology: Julie Kühl, Sven Malte Krümpelmann, Rainer Adelung, Malte Bruhn, Fabian Schütt, Stanislav Gorb, Ronald Seidel, Jan-Bernd Hövener

Writing – original draft: Julie Kühl, Sabine Fuchs

Writing – review & editing: Sabine Fuchs, Andreas Seekamp, Stanislav Gorb, Leonard Siebert

Ethics approval and consent to participate

The use of human tissue was approved by the local ethical advisory board of the University Medical Center in Kiel (approval number: D459/13) and included the consent of the individual donors.

Consent for publication

Not applicable.

Availability of data

All relevant data are included in the manuscript, for further information please refer to the authors.

Further disclosure

Part of the findings have been presented Additive Manufacturing Meets Medicine (AMMM 2022) - Lübeck, Deutschland, 13–15. September 2022.

References

1. Maruyama M, Rhee C, Utsunomiya T, et al. Modulation of the inflammatory response and bone healingr Review. *Front Endocrinol*. 2020;11:386. doi: 10.3389/fendo.2020.00386
2. Ko HF, Sfeir C, Kumta PN. Novel synthesis strategies for natural polymer and composite biomaterials as potential scaffolds for tissue engineering. *Philos Trans A Math Phys Eng Sci*. 2010;368(1917):1981-1997. doi: 10.1098/rsta.2010.0009
3. LeGeros RZ. Properties of osteoconductive biomaterials: calcium phosphates. *Clin Orthop Relat Res*. 2002;395:81-98. doi: 10.1097/00003086-200202000-00009
4. Dimitriou R, Mataliotakis GI, Angoules AG, Kanakaris NK, Giannoudis PV. Complications following autologous bone graft harvesting from the iliac crest and using the RIA: a systematic review. *Injury*. 2011;42:S3-S15. doi: 10.1016/j.injury.2011.06.015
5. Nauth A, Schemitsch E, Norris B, Nollin Z, Watson JT. Critical-size bone defects: is there a consensus for diagnosis and treatment? *J Orthop Trauma*. 2018;32(Suppl 1):S7-S11. doi: 10.1097/bot.0000000000001115
6. Aktuglu K, Erol K, Vahabi A. Ilizarov bone transport and treatment of critical-sized tibial bone defects: a narrative review. *J Orthop Traumatol*. 2019;20(1):22. doi: 10.1186/s10195-019-0527-1
7. Zhu W, Ma X, Gou M, Mei D, Zhang K, Chen S. 3D printing of functional biomaterials for tissue engineering. *Curr Opin Biotechnol*. 2016;40:103-112. doi: 10.1016/j.copbio.2016.03.014
8. Haglin JM, Eltorai AE, Gil JA, Marcaccio SE, Botero-Hincapie J, Daniels AH. Patient-specific orthopaedic implants. *Orthop Surg*. 2016;8(4):417-424. doi: 10.1111/os.12282
9. Mobbs RJ, Parr WCH, Huang C, Amin T. Rapid personalised virtual planning and on-demand surgery for acute spinal trauma using 3D-printing, biomodelling and patient-specific implant manufacture. *J Pers Med*. 2022; 12(6):997. doi: 10.3390/jpm12060997
10. Ozbolat IT, Hospodiuk M. Current advances and future perspectives in extrusion-based bioprinting. *Biomaterials*. 2016;76:321-343. doi: 10.1016/j.biomaterials.2015.10.076
11. Liang R, Gu Y, Wu Y, Bunpetch V, Zhang S. Lithography-based 3D bioprinting and bioinks for bone repair and regeneration. *ACS Biomater Sci Eng*. 2021;7(3): 806-816. doi: 10.1021/acsbiomaterials.9b01818
12. Kim SH, Kim DY, Lim TH, Park CH. Silk fibroin bioinks for digital light processing (DLP) 3D bioprinting. *Adv Exp Med Biol*. 2020;1249:53-66. doi: 10.1007/978-981-15-3258-0_4
13. Shen Y, Tang H, Huang X, et al. DLP printing photocurable chitosan to build bio-constructs for tissue engineering. *Carbohydr Polym*. 2020;235:115970. doi: 10.1016/j.carbpol.2020.115970
14. Sheng L, Li M, Zheng S, Qi J. Adjusting the accuracy of PEGDA-GelMA vascular network by dark pigments via digital light processing printing. *J. Biomater Appl*. 2022;36(7):1173-1187. doi: 10.1177/08853282211053081
15. Song P, Gui X, Wu L, et al. DLP fabrication of multiple hierarchical biomimetic GelMA/SilMA/HAp scaffolds for enhancing bone regeneration. *Biomacromolecules*. 2024;25(3):1871-1886. doi: 10.1021/acs.biomac.3c01318
16. Tao J, Zhu S, Liao X, et al. DLP-based bioprinting of void-forming hydrogels for enhanced stem-cell-mediated bone regeneration. *Mater Today Bio*. 2022;17:100487. doi: 10.1016/j.mtbio.2022.100487
17. Park SH, Park DS, Shin JW, et al. Scaffolds for bone tissue engineering fabricated from two different materials by the rapid prototyping technique: PCL versus PLGA. *J Mater Sci Mater Med*. 2012;23(11):2671-2678. doi: 10.1007/s10856-012-4738-8
18. Tibbitt MW, Rodell CB, Burdick JA, Anseth KS. Progress in material design for biomedical applications. *Proc Natl Acad Sci*. 2015;112(47):14444-14451. doi: 10.1073/pnas.1516247112
19. Nguyen DG, Funk J, Robbins JB, et al. Bioprinted 3D primary liver tissues allow assessment of organ-level response to clinical drug induced toxicity in vitro. *Plos One*. 2016;11(7):e0158674. doi: 10.1371/journal.pone.0158674
20. Lee KY, Mooney DJ. Hydrogels for tissue engineering. *Chem Rev*. 2001;101(7):1869-1880. doi: 10.1021/cr000108x
21. Levato R, Visser J, Planell JA, Engel E, Malda J, Mateos-Timoneda MA. Biofabrication of tissue constructs by 3D bioprinting of cell-laden microcarriers. *Biofabrication*. 2014;6(3):035020. doi: 10.1088/1758-5082/6/3/035020
22. Leijten J, Rouwkema J, Zhang YS, Nasajpour A, Dokmeci MR, Khademhosseini A. Advancing tissue engineering:

a tale of nano-, micro-, and macroscale integration. *Small*. 2016;12(16):2130-2145.
doi: 10.1002/smll.201501798

23. Wüst S, Müller R, Hofmann S. Controlled positioning of cells in biomaterials—approaches towards 3D tissue printing. *J Funct Biomater*. 2011;2(3):119-154.
doi: 10.3390/jfb2030119

24. Murphy SV, Atala A. 3D bioprinting of tissues and organs. *Nat Biotechnol*. 2014;32(8):773-785.
doi: 10.1038/nbt.2958

25. Liu Y, Chan-Park MB. A biomimetic hydrogel based on methacrylated dextran-graft-lysine and gelatin for 3D smooth muscle cell culture. *Biomaterials*. 2010;31(6):1158-1170.
doi: 10.1016/j.biomaterials.2009.10.040

26. Jeong HJ, Nam H, Jang J, Lee SJ. 3D Bioprinting strategies for the regeneration of functional tubular tissues and organs. *Bioengineering (Basel)*. 2020;7(2):32.
doi: 10.3390/bioengineering7020032

27. Xu T, Zhao W, Zhu J-M, Albanna MZ, Yoo JJ, Atala A. Complex heterogeneous tissue constructs containing multiple cell types prepared by inkjet printing technology. *Biomaterials*. 2013;34(1):130-139.
doi: 10.1016/j.biomaterials.2012.09.035

28. Li J, Mooney DJ. Designing hydrogels for controlled drug delivery. *Nat Rev Mater*. 2016;1(12):16071.
doi: 10.1038/natrevmats.2016.71

29. Gao J, Li M, Cheng J, et al. 3D-printed GelMA/PEGDA/F127DA scaffolds for bone regeneration. *J Funct Biomater*. 2023;14(2):96.
doi: 10.3390/jfb14020096

30. Gao J, Wang H, Li M, et al. DLP-printed GelMA-PMAA scaffold for bone regeneration through endochondral ossification. *Int J Bioprint*. 2023;9(5):754.
doi: 10.18063/ijb.754

31. Shi H, Li Y, Xu K, Yin J. Advantages of photo-curable collagen-based cell-laden bioinks compared to methacrylated gelatin (GelMA) in digital light processing (DLP) and extrusion bioprinting. *Mater Today Bio*. 2023;23:100799.
doi: 10.1016/j.mtbio.2023.100799

32. Kurian AG, Singh RK, Patel KD, Lee JH, Kim HW. Multifunctional GelMA platforms with nanomaterials for advanced tissue therapeutics. *Bioact Mater*. 2022;8:267-295.
doi: 10.1016/j.bioactmat.2021.06.027

33. Li J, Moeinzadeh S, Kim C, et al. Development and systematic characterization of GelMA/alginate/PEGDMA/xanthan gum hydrogel bioink system for extrusion bioprinting. *Biomaterials*. 2023;293:121969.
doi: 10.1016/j.biomaterials.2022.121969

34. Pérez-Cortez JE, Sánchez-Rodríguez VH, Gallegos-Martínez S, et al. Low-cost light-based GelMA 3D bioprinting via retrofitting: manufacturability test and cell culture assessment. *Micromachines (Basel)*. 2022;14(1):55.
doi: 10.3390/mi14010055

35. Sun X, Ma Z, Zhao X, et al. Three-dimensional bioprinting of multicell-laden scaffolds containing bone morphogenic protein-4 for promoting M2 macrophage polarization and accelerating bone defect repair in diabetes mellitus. *Bioact Mater*. 2021;6(3):757-769.
doi: 10.1016/j.bioactmat.2020.08.030

36. Yi S, Liu Q, Luo Z, et al. Micropore-forming gelatin methacryloyl (GelMA) bioink toolbox 2.0: designable tunability and adaptability for 3D bioprinting applications. *Small*. 2022;18(25):e2106357.
doi: 10.1002/smll.202106357

37. Billiet T, Gevaert E, De Schryver T, Cornelissen M, Dubruel P. The 3D printing of gelatin methacrylamide cell-laden tissue-engineered constructs with high cell viability. *Biomaterials*. 2014;35(1):49-62.
doi: 10.1016/j.biomaterials.2013.09.078

38. Hospodiuk M, Dey M, Sosnoski D, Ozbolat IT. The bioink: a comprehensive review on bioprintable materials. *Biotechnol Adv*. 2017;35(2):217-239.
doi: 10.1016/j.biotechadv.2016.12.006

39. Gopinathan J, Noh I. Recent trends in bioinks for 3D printing. *Biomater Res*. 2018/04/06 2018;22(1):11.
doi: 10.1186/s40824-018-0122-1

40. Jammalamadaka U, Tappa K. Recent advances in biomaterials for 3D printing and tissue engineering. *J Funct Biomater*. 2018;9(1):22.
doi: 10.3390/jfb9010022

41. Huh J, Moon YW, Park J, Atala A, Yoo JJ, Lee SJ. Combinations of photoinitiator and UV absorber for cell-based digital light processing (DLP) bioprinting. *Biofabrication*. 2021;13(3):034103.
doi: 10.1088/1758-5090/abfd7a

42. Peng X, Liu X, Yang Y, et al. Graphene oxide functionalized gelatin methacryloyl microgel for enhanced biomimetic mineralization and in situ bone repair. *Int J Nanomedicine*. 2023;18:6725-6741.
doi: 10.2147/ijn.S433624

43. Dinescu S, Ionita M, Ignat SR, Costache M, Hermenean A. Graphene oxide enhances chitosan-based 3D scaffold properties for bone tissue engineering. *Int J Mol Sci*. 2019;20(20):5077.
doi: 10.3390/ijms20205077

44. Li J, Liu X, Crook JM, Wallace GG. Development of 3D printable graphene oxide based bio-ink for cell support and tissue engineering. *Front Bioeng Biotechnol*. 2022;10:994776.
doi: 10.3389/fbioe.2022.994776

45. Wang C, Mallela J, Garapati US, et al. A chitosan-modified graphene nanogel for noninvasive controlled drug release. *Nanomed Nanotechnol Biol Med*. 2013;9(7):903-911.
doi: 10.1016/j.nano.2013.01.003

46. Zhang L, Li X, Shi C, et al. Biocompatibility and angiogenic effect of chitosan/graphene oxide hydrogel scaffolds on EPCs. *Stem Cells International*. 2021;2021:5594370. doi: 10.1155/2021/5594370

47. Zhihui K, Min D. Application of graphene oxide-based hydrogels in bone tissue engineering. *ACS Biomater Sci Eng*. 2022;8(7):2849-2857. doi: 10.1021/acsbiomaterials.2c00396

48. Zhou C, Liu S, Li J, et al. Collagen functionalized with graphene oxide enhanced biomimetic mineralization and in situ bone defect repair. *ACS Appl Mater Interfaces*. 2018;10(50):44080-44091. doi: 10.1021/acsami.8b17636

49. Jeong J-T, Choi M-K, Sim Y, et al. Effect of graphene oxide ratio on the cell adhesion and growth behavior on a graphene oxide-coated silicon substrate. *Sci Rep*. 2016;6(1):33835. doi: 10.1038/srep33835

50. Choe G, Oh S, Seok JM, Park SA, Lee JY. Graphene oxide/alginate composites as novel bioinks for three-dimensional mesenchymal stem cell printing and bone regeneration applications. *Nanoscale*. 2019;11(48):23275-23285. doi: 10.1039/C9NR07643C

51. Schmidleithner C, Malferrari S, Palgrave R, Bomze D, Schwentenwein M, Kalaskar DM. Application of high resolution DLP stereolithography for fabrication of tricalcium phosphate scaffolds for bone regeneration. *Biomed Mater*. 2019;14(4):045018. doi: 10.1088/1748-605X/ab279d

52. Bhattacharyya A, Janarthanan G, Kim T, et al. Modulation of bioactive calcium phosphate micro/nanoparticle size and shape during in situ synthesis of photo-crosslinkable gelatin methacryloyl based nanocomposite hydrogels for 3D bioprinting and tissue engineering. *Biomater Res*. 2022;26(1):54. doi: 10.1186/s40824-022-00301-6

53. Choi JB, Kim YK, Byeon SM, et al. Fabrication and characterization of biodegradable gelatin methacrylate/biphasic calcium phosphate composite hydrogel for bone tissue engineering. *Nanomaterials (Basel)*. 2021;11(3):617. doi: 10.3390/nano11030617

54. Lee DN, Park JY, Seo YW, et al. Photo-crosslinked gelatin methacryloyl hydrogel strengthened with calcium phosphate-based nanoparticles for early healing of rabbit calvarial defects. *J Periodontal Implant Sci*. 2023;53(5):321-335. doi: 10.5051/jpis.2203220161

55. Ren-Jie X, Jin-Jin M, Yu X, et al. A biphasic calcium phosphate/acylated methacrylate gelatin composite hydrogel promotes osteogenesis and bone repair. *Connect Tissue Res*. 2023;64(5):445-456. doi: 10.1080/03008207.2023.2212067

56. Zhang X, Zhang H, Zhang Y, et al. 3D printed reduced graphene oxide-GelMA hybrid hydrogel scaffolds for potential neuralized bone regeneration. *J Mater Chem B*. 2023;11(6):1288-1301. doi: 10.1039/D2TB01979E

57. Khan MUA, Razak SIA, Rehman S, Hasan A, Qureshi S, Stojanovic GM. Bioactive scaffold (sodium alginate)-g-(nHAp@SiO(2)@GO) for bone tissue engineering. *Int J Biol Macromol*. 2022;222(Pt A):462-472. doi: 10.1016/j.ijbiomac.2022.09.153

58. Qi F, Wang C, Peng S, Shuai C, Yang W, Zhao Z. A co-dispersed nanosystem of strontium-anchored reduced graphene oxide to enhance the bioactivity and mechanical property of polymer scaffolds. *Mater Chem Front*. 2021;5(5):2373-2386. doi: 10.1039/D0QM00958J

59. Shuai C, Guo W, Wu P, et al. A graphene oxide-Ag co-dispersing nanosystem: dual synergistic effects on antibacterial activities and mechanical properties of polymer scaffolds. *Chem Eng J*. 2018;347:322-333. doi: 10.1016/j.cej.2018.04.092

60. Saini G, Segaran N, Mayer JL, Saini A, Albadawi H, Oklu R. Applications of 3D bioprinting in tissue engineering and regenerative medicine. *J Clin Med*. 2021;10(21):4966. doi: 10.3390/jcm10214966

61. Vallet-Regí M, González-Calbet JM. Calcium phosphates as substitution of bone tissues. *Progress in Solid State Chemistry*. 2004;32(1):1-31. doi: 10.1016/j.progsolidstchem.2004.07.001

62. Zhou B, Jiang X, Zhou X, et al. GelMA-based bioactive hydrogel scaffolds with multiple bone defect repair functions: therapeutic strategies and recent advances. *Biomater Res*. 2023;27(1):86. doi: 10.1186/s40824-023-00422-6

63. Ginebra M-P, Espanol M, Maazouz Y, Bergez V, Pastorino D. Bioceramics and bone healing. *EFORT Open Rev*. 2018;3(5):173-183. doi: 10.1302/2058-5241.3.170056

64. Alvarez K, Nakajima H. Metallic scaffolds for bone regeneration. *Materials*. 2009;2(3):790-832. doi: 10.3390/ma2030790

65. Kühl J, Gorb S, Kern M, et al. Extrusion-based 3D printing of osteoinductive scaffolds with a spongiosa-inspired structure. *Front Bioeng Biotechnol*. 2023;11:1268049. doi: 10.3389/fbioe.2023.1268049

66. Wang F, Saure LM, Schütt F, et al. Graphene oxide framework structures and coatings: impact on cell adhesion and pre-vascularization processes for bone grafts. *Int J Mol Sci*. 2022;23(6):3379. doi: 10.3390/ijms23063379

67. Kolbe M, Xiang Z, Dohle E, Tonak M, Kirkpatrick CJ, Fuchs S. Paracrine effects influenced by cell culture medium and consequences on microvessel-like structures in cocultures

of mesenchymal stem cells and outgrowth endothelial cells. *Tissue Eng A*. 2011;17(17–18):2199-2212. doi: 10.1089/ten.TEA.2010.0474

68. Fuchs S, Hermanns MI, Kirkpatrick CJ. Retention of a differentiated endothelial phenotype by outgrowth endothelial cells isolated from human peripheral blood and expanded in long-term cultures. *Cell Tissue Res*. 2006;326:79-92. doi: 10.1007/s00441-006-0222-4

69. Yue K, Trujillo-de Santiago G, Alvarez MM, Tamayol A, Annabi N, Khademhosseini A. Synthesis, properties, and biomedical applications of gelatin methacryloyl (GelMA) hydrogels. *Biomaterials*. 2015;73:254-271. doi: 10.1016/j.biomaterials.2015.08.045

70. Fedorov A, Beichel R, Kalpathy-Cramer J, et al. 3D slicer as an image computing platform for the quantitative imaging network. *Magn Reson Imaging*. 2012;30(9):1323-1341. doi: 10.1016/j.mri.2012.05.001

71. Cignoni P, Callieri M, Corsini M, Dellepiane M, Ganovelli F, Ranzuglia G. MeshLab: an Open-Source Mesh Processing Tool. The Eurographics Association. 2008; 129-136. doi: 10.2312/LocalChapterEvents/ItalChap/ItalianChapConf2008/129-136

72. Choi CE, Chakraborty A, Adzija H, et al. Metal organic framework-incorporated three-dimensional (3D) bio-printable hydrogels to facilitate bone repair: preparation and in vitro bioactivity analysis. *Gels*. 2023;9(12):923. doi: 10.3390/gels9120923

73. Hildebrand T, Laib A, Müller R, Dequeker J, Rüegsegger P. Direct three-dimensional morphometric analysis of human cancellous bone: microstructural data from spine, femur, iliac crest, and calcaneus. *J Bone Miner Res*. 1999;14(7):1167-1174. doi: 10.1359/jbmr.1999.14.7.1167

74. Doktor T, Valach J, Kytyr D, Jiroušek O. *Pore Size Distribution of Human Trabecular Bone – Comparison of Intrusion Measurements with Image Analysis*. 2011:115-118.

75. Lim TC, Chian KS, Leong KF. Cryogenic prototyping of chitosan scaffolds with controlled micro and macro architecture and their effect on in vivo neo-vascularization and cellular infiltration. *J Biomed Mater Res A*. 2010;94A(4):1303-1311. doi: 10.1002/jbm.a.32747

76. Zhou K, Yu P, Shi X, et al. Hierarchically porous hydroxyapatite hybrid scaffold incorporated with reduced graphene oxide for rapid bone ingrowth and repair. *ACS Nano*. 2019;13(8):9595-9606. doi: 10.1021/acsnano.9b04723

77. Taniguchi N, Fujibayashi S, Takemoto M, et al. Effect of pore size on bone ingrowth into porous titanium implants fabricated by additive manufacturing: an in vivo experiment. *Mater Sci Eng C*. 2016;59:690-701. doi: 10.1016/j.msec.2015.10.069

78. Xia P, Luo Y. Vascularization in tissue engineering: the architecture cues of pores in scaffolds. *J Biomed Mater Res B Appl Biomater*. 2022;110(5):1206-1214. doi: 10.1002/jbm.b.34979

79. Abdollahiyan P, Oroojalian F, Mokhtarzadeh A, de la Guardia M. Hydrogel-Based 3D Bioprinting for bone and cartilage tissue engineering. *Biotechnol J*. 2020;15(12):e2000095. doi: 10.1002/biot.202000095

80. de Leeuw AM, Graf R, Lim PJ, et al. Physiological cell bioprinting density in human bone-derived cell-laden scaffolds enhances matrix mineralization rate and stiffness under dynamic loading. Original research. *Front Bioeng Biotechnol*. 2024;12:1310289. doi: 10.3389/fbioe.2024.1310289

81. Dhawan A, Kennedy PM, Rizk EB, Ozbolat IT. Three-dimensional bioprinting for bone and cartilage restoration in orthopaedic surgery. *J Am Acad Orthop Surg*. 2019;27(5):e215-e226. doi: 10.5435/jaaos-d-17-00632

82. Midha S, Dalela M, Sybil D, Patra P, Mohanty S. Advances in three-dimensional bioprinting of bone: progress and challenges. *J Tissue Eng Regen Med*. 2019;13(6):925-945. doi: 10.1002/term.2847

83. Zhang J, Eyisoylu H, Qin X-H, Rubert M, Müller R. 3D bioprinting of graphene oxide-incorporated cell-laden bone mimicking scaffolds for promoting scaffold fidelity, osteogenic differentiation and mineralization. *Acta Biomaterialia*. 2021;121:637-652. doi: 10.1016/j.actbio.2020.12.026

84. Chen YC, Lin RZ, Qi H, et al. Functional human vascular network generated in photocrosslinkable gelatin methacrylate hydrogels. *Adv Funct Mater*. 2012;22(10):2027-2039. doi: 10.1002/adfm.201101662

85. Tigner TJ, Rajput S, Gaharwar AK, Alge DL. Comparison of photo cross linkable gelatin derivatives and initiators for three-dimensional extrusion bioprinting. *Biomacromolecules*. 2020;21(2):454-463. doi: 10.1021/acs.biomac.9b01204

86. Im G-B, Lin R-Z. Bioengineering for vascularization: trends and directions of photocrosslinkable gelatin methacrylate hydrogels. Review. *Front Bioeng Biotechnol*. 2022;10:1053491. doi: 10.3389/fbioe.2022.1053491

87. Ahmed J, Mulla M, Maniruzzaman M. Rheological and dielectric behavior of 3D-printable chitosan/graphene oxide hydrogels. *ACS Biomater Sci Eng*. 2020;6(1):88-99. doi: 10.1021/acsbiomaterials.9b00201

88. Kim J, Raja N, Choi YJ, et al. Enhancement of properties of a cell-laden GelMA hydrogel-based bioink via calcium phosphate phase transition. *Biofabrication*. 2023;16(1):ad05e2. doi: 10.1088/1758-5090/ad05e2

89. Montelongo SA, Chiou G, Ong JL, Bizios R, Guda T. Development of bioinks for 3D printing microporous, sintered calcium phosphate scaffolds. *J Mater Sci Mater Med*. 2021;32(8):94. doi: 10.1007/s10856-021-06569-9

90. Fischetti T, Borciani G, Avnet S, et al. Incorporation/enrichment of 3D bioprinted constructs by biomimetic nanoparticles: tuning printability and cell behavior in bone models. *Nanomaterials (Basel)*. 2023;13(14):2040. doi: 10.3390/nano13142040

91. Raghav PK, Mann Z, Ahlawat S, Mohanty S. Mesenchymal stem cell-based nanoparticles and scaffolds in regenerative medicine. *Eur J Pharmacol*. 2022;918:174657. doi: 10.1016/j.ejphar.2021.174657

92. Cernencu AI, Vlasceanu GM, Serafim A, Pircalabioru G, Ionita M. 3D double-reinforced graphene oxide – nanocellulose biomaterial inks for tissue engineered constructs. *RSC Adv*. 2023;13(34):24053-24063. doi: 10.1039/D3RA02786D

93. Steward AJ, Kelly DJ. Mechanical regulation of mesenchymal stem cell differentiation. *J Anat*. 2015;227(6):717-731. doi: 10.1111/joa.12243

94. Phinney DG. Functional heterogeneity of mesenchymal stem cells: implications for cell therapy. *J Cell Biochem*. 2012;113(9):2806-2812. doi: 10.1002/jcb.24166

95. Costa LA, Eiro N, Fraile M, et al. Functional heterogeneity of mesenchymal stem cells from natural niches to culture conditions: implications for further clinical uses. *Cell Mol Life Sci*. 2021;78(2):447-467. doi: 10.1007/s00018-020-03600-0

96. Talukdar Y, Rashkow J, Lalwani G, Kanakia S, Sitharaman B. The effects of graphene nanostructures on mesenchymal stem cells. *Biomaterials*. 2014;35(18):4863-4877. doi: 10.1016/j.biomaterials.2014.02.054

97. Golub EE, Boesze-Battaglia K. The role of alkaline phosphatase in mineralization. *Curr Opin Orthopaed*. 2007;18(5):444-448. doi: 10.1097/BCO.0b013e3282630851

98. Sharma U, Pal D, Prasad R. Alkaline phosphatase: an overview. *Indian J Clin Biochem*. 2014;29(3):269-278. doi: 10.1007/s12291-013-0408-y

99. Rutkovskiy A, Stensløkken KO, Vaage IJ. Osteoblast differentiation at a glance. *Med Sci Monit Basic Res*. 2016;22:95-106. doi: 10.12659/msmbr.901142

100. Ma H, Feng C, Chang J, Wu C. 3D-printed bioceramic scaffolds: from bone tissue engineering to tumor therapy. *Acta Biomaterialia*. 2018;79:37-59. doi: 10.1016/j.actbio.2018.08.026

101. Wu M, Zou L, Jiang L, Zhao Z, Liu J. Osteoinductive and antimicrobial mechanisms of graphene-based materials for enhancing bone tissue engineering. *J Tissue Eng Regen Med*. 2021;15(11):915-935. doi: 10.1002/term.3239

102. Shin SR, Li YC, Jang HL, et al. Graphene-based materials for tissue engineering. *Adv Drug Deliv Rev*. 2016;105(Pt B):255-274. doi: 10.1016/j.addr.2016.03.007

103. Farshid B, Lalwani G, Mohammadi MS, et al. Two-dimensional graphene oxide-reinforced porous biodegradable polymeric nanocomposites for bone tissue engineering. *J Biomed Mater Res A*. 2019;107(6):1143-1153. doi: 10.1002/jbm.a.36606

104. Catoira MC, Fusaro L, Di Francesco D, Ramella M, Boccafoschi F. Overview of natural hydrogels for regenerative medicine applications. *J Mater Sci Mater Med*. 2019;30(10):115. doi: 10.1007/s10856-019-6318-7

105. Zhou L, Tan G, Tan Y, Wang H, Liao J, Ning C. Biomimetic mineralization of anionic gelatin hydrogels: Effect of degree of methacrylation. *RSC Adv*. 2014;4:21997. doi: 10.1039/c4ra02271h

106. Castillo Diaz LA, Saiani A, Gough JE, Miller AF. Human osteoblasts within soft peptide hydrogels promote mineralisation in vitro. *J Tissue Eng*. 2014;5:2041731414539344. doi: 10.1177/2041731414539344

107. Gerhardt LC, Boccaccini AR. Bioactive glass and glass-ceramic scaffolds for bone tissue engineering. *Materials*. 2010;3(7):3867-3910. doi: 10.3390/ma3073867

108. Morgan EF, Unnikrisnan GU, Hussein AI. Bone mechanical properties in healthy and diseased states. *Annu Rev Biomed Eng*. 2018;20(2018):119-143. doi: 10.1146/annurev-bioeng-062117-121139

109. Diaz-Rodriguez P, Sánchez M, Landin M. Drug-loaded biomimetic ceramics for tissue engineering. *Pharmaceutics*. 2018;10(4):272. doi: 10.3390/pharmaceutics10040272

ACCSCIENCE PUBLISHING

International Journal of Bioprinting

RESEARCH ARTICLE

Collagen bioinks redefined: Optimizing ionic strength and growth factor delivery for cartilage tissue engineering

Murad Redzheb[1†*], Yordan Sbirkov[2,3†], Atanas Valev[1], Vasil Dzharov[3], Hristi Petrova[1], Tatyana Damyanova[2], Ani Georgieva[1,4], and Victoria Sarafian[2,3]

[1]MatriChem Ltd., Sofia, Bulgaria

[2]Department of Medical Biology, Faculty of Medicine, Medical University of Plovdiv, Plovdiv, Bulgaria

[3]Department of Molecular and Regenerative Medicine, Research Institute at Medical University of Plovdiv (RIMU-Plovdiv), Plovdiv, Bulgaria

[4]Section Pathology, Institute of Experimental Morphology, Pathology and Anthropology with Museum, Bulgarian Academy of Sciences, Sofia, Bulgaria

Abstract

Tissue engineering of hyaline cartilage for regenerative medicine and the treatment of osteoarthritis has advanced significantly over the past decade, driven by developments in 3D bioprinting and biomaterials science. Despite these advances, standardized biofabrication protocols approved for clinical applications remain elusive, underscoring the need for research into widely accessible, non-immunogenic, and biocompatible bioinks that support chondrogenesis. This study proposes a strategy to improve the gelation kinetics of collagen bioinks by fine-tuning their ionic strength and reports a highly efficient sequestration of TGF-β1 within them, alongside their compatibility with bioprinting live chondrocytes and adipose-derived stem cells for cartilage tissue engineering. By adjusting sodium chloride and phosphate-buffered saline (PBS) concentrations, we demonstrate that reduced ionic strengths accelerate gelation, facilitating high-fidelity bioprinting while supporting high cell viability and proliferation. Furthermore, at 1% collagen concentration, the hydrogel effectively immobilized TGF-β1, with less than 0.5% released over two weeks, indicating potent sequestration capability. Using adipose-derived mesenchymal stromal cells, histomorphological and transcriptomic analyses reveal that the presence of TGF-β1 significantly enhances chondrogenesis. These results underscore the neglected role of ionic strength in optimizing collagen ink properties for advanced bioprinting applications and highlight the potential of collagen hydrogels as effective carriers for sustained growth factor delivery, paving the way for successful cartilage tissue engineering strategies.

Keywords: Collagen; Bioink; Bioprinting; Cartilage; Chondrocytes; Gelation kinetics; TGF-β1

[†]These authors contributed equally to this work.

***Corresponding authors:**
Murad Redzheb
(m.redzheb@matrichem.com)

Citation: Redzheb M, Sbirkov Y, Valev A, et al. Collagen bioinks redefined: Optimizing ionic strength and growth factor delivery for cartilage tissue engineering. *Int J Bioprint*. 2024;10(6):4566. doi: 10.36922/ijb.4566

Received: August 18, 2024
Revised: September 15, 2024
Accepted: September 29, 2024
Published Online: September 29, 2024

Copyright: © 2024 Author(s). This is an Open Access article distributed under the terms of the Creative Commons Attribution License, permitting distribution, and reproduction in any medium, provided the original work is properly cited.

Publisher's Note: AccScience Publishing remains neutral with regard to jurisdictional claims in published maps and institutional affiliations.

1. Introduction

Additive manufacturing, encompassing 3D printing and bioprinting, has become a mainstay in biomedical research, with technologies like custom implant, prosthesis, and surgical guide fabrication already integrated into clinical practice, enhancing personalized care.[1] However, areas like bioprinting for tissue and organ regeneration remain largely in research and development. This field is advancing, yet it faces ongoing challenges related to replicating the intricacies of biological structures, ensuring cell viability, and fine-tuning material properties to meet the stringent demands of biological compatibility and functionality. Before bioprinting can be applied clinically, it is crucial to develop materials that comply with local laws and regulations. For example, in the European Union (EU), per Regulation (EU) 2017/745, medical devices are defined as products or equipment intended for medical purposes. In bioprinting, the bioink can be considered a medical device when it serves a function similar to that of established clinical scaffolds used in tissue engineering. Thus, the development and availability of compliant materials and standardized procedures are foundational to the clinical adoption of bioprinting-based therapeutic solutions.

Collagen is the most abundant extracellular matrix (ECM) protein in the human body.[2] Its structural and functional importance for cell function and homeostasis has made it a popular biomaterial for biomedical applications, including *in vitro* tissue engineering and regenerative medicine. For instance, collagen promotes cell adhesion, differentiation, and many functions governing regeneration and embryonic development. However, collagen is also involved in various cell pathologies. For instance, overproduction of collagen and subsequent ECM stiffening accelerate cancer progression by activating signaling pathways for tumor invasion and metastasis and impede T-cell anti-tumor activity. In the context of biomedical applications, this intricate balance highlights collagen's pivotal role in both advancing regenerative therapies and necessitating careful consideration of its potential in pathological tissue remodeling.

Type I collagen bioinks are central to extrusion bioprinting.[3-6] However, their use is challenging due to low viscosity and slow gelation, which can hinder high-fidelity 3D printing. Strategies like blending collagen with other biomaterials or printing in support materials, i.e. suspended bioprinting, help enhance printability.[7] Fine-tuning parameters like pH,[8,9] concentration,10 ionic strength,[11,12] ion type,11 and temperature[12] is essential for optimizing the fibrillation, morphology, porosity, and mechanical properties.[13-19] Moreover, its self-assembly is accelerated at lower ionic strength,[20] increased concentration,[15] and higher temperature,[21] while a basic pH slows it down.[22] However, the numerous studies on collagen fibrillogenesis have had limited impact on its bioink formulations, which is apparent in the most recent reviews.[3-6] For instance, no bioprinting study has utilized, as we have done in this study, the acceleration of the gelation kinetics by decreasing the ionic strength below the physiological range. Furthermore, most of the accumulated data on fibrillogenesis may be applicable in suspended bioprinting, but its utility in direct bioprinting is limited due to the narrow window of gelation kinetics, enabling sufficiently good printability. In particular, many studies were not conducted at 37°C,[8,11,13-15,23,24] at which the fastest gelation occurs, or at high ionic strength, further slowing down the fibrillation process.[8] This is important because lower polymerization temperatures produce stiffer, less flexible fibers, slowing down cell spreading, while higher temperatures yield more compact structures with thinner fibers.[25,26] Additionally, the gelation temperature determines the fibrillar and network structure independent of subsequent increases in temperature.[23] Another shortcoming is that most studies utilize turbidity measurements that can mislead the estimation of the gelation kinetics, as the induction and gelation times, as determined by rheology, are systematically shorter than the induction and fibrillation times seen in turbidity measurements.[9,21] Worse still, fibrillation, deduced by fast and large turbidity change, might not correspond to any change in storage modulus during rheology or result in a weak gel[9] even at very high concentrations.[14] Similarly, calcium ions may inhibit gelation1[5] even if fibrillation takes place.[11]

Growth factors (GFs) are vital for cellular processes, such as proliferation, maturation, and differentiation, making them essential in tissue regeneration. However, their application in tissue engineering is challenging due to difficulties in maintaining GF activity and ensuring consistent, controlled exposure over time. Collagen-based hydrogels can serve as reservoirs for GFs, but their effectiveness varies, with GF retention ranging from 5 to 50% after seven days, depending on the specific chemical affinities of the GFs.[27] Although GFs have been incorporated into various bioinks, reports on TGF-β1, a key regulator of cartilage homeostasis and repair,[28] in collagen bioinks are lacking. TGF-β1 plays a crucial role in chondrocyte proliferation, differentiation, and ECM production, making it a therapeutic target for osteoarthritis.[29] A single day of TGF-β exposure can trigger chondrogenic induction in bone marrow-derived mesenchymal stromal cells (BM-MSCs).[30] Previous reports on TGF-β bioinks include a polycaprolactone (PCL)-alginate scaffold, which promoted nasal chondrocyte proliferation and glycosaminoglycan deposition,[31] Gelatin methacryloyl-Polyethylene glycol

diacrylate (GelMA-PEGDA) nanospheres enhancing BM-MSC chondrogenesis,[32] and a hyaluronic acid-Polyethylene glycol (PEG) bioink inducing dose-dependent chondrogenesis over 21 days.[33] These studies highlight the importance of TGF-β in cartilage tissue engineering, but none have investigated collagen type I as a carrier or its combined effect with TGF-β on chondrogenesis of adipose-derived mesenchymal stem cells (MSCs).

In this work, we consider various aspects of collagen-based bioinks suitable for direct and suspended extrusion 3D (bio)printing. Utilizing rotational rheometry, we demonstrate the neglected relevance of the ionic strength and composition to the ink's gelation kinetics. We demonstrate that engineering the ionic strength is compatible with bioprinting live cells while maintaining high post-printing viability. The mechanical properties and stability against collagenase are also documented. We report remarkably high retention of TGF-β1 within a 1% collagen hydrogel of over 99% for incubation of up to 14 days. Thus, given that collagen type I is a well-established biomaterial in the field of cartilage repair, we consider the bioink for the treatment of osteoarthritis. As a result, we demonstrate that functionalizing collagen-based bioinks significantly affects the fate of adipose tissue MSCs.

2. Materials and methods

2.1. Materials

Pepsin from porcine gastric mucosa (600–1200 units/mg), dialysis tubing (molecular weight cut-off [MWCO]: 14 kDa), bromophenol blue, collagen type I from calfskin, glycine, ammonium persulfate (APS), tris(hydroxymethyl) aminomethane, sodium dodecyl sulfate (SDS), brilliant blue, 2-mercaptoethanol, 30% solution of acrylamide/bis-acrylamide (37.5:1), bovine serum albumin (BSA), collagenase type I from *Clostridium histolyticum*, fluorescamine, molecular weight (MW) marker (27–180 kDa), N,N,N′,N′-tetramethyl ethylenediamine (TEMED), and hydroxyproline assay kit were obtained from Sigma-Aldrich (Germany). Acetic acid, hydrochloric acid, ethanol, sodium hydroxide, methanol, and acetone were supplied by Valerus (Bulgaria). Recombinant human TGF-β1 was purchased from Proteintech (Germany). The Human TGF-β1 ELISA kit was obtained from Boster Bio (United States of America [USA]). Metallic needles 22GA and 25GA and plastic conical nozzles 22GA and 25GA were purchased from Nordson (USA).

2.2. Collagen type I extraction and characterization

In compliance with Regulation (EC) 1069/2009, the handling of animal byproducts, bovine tendons, and collagen extraction was carried out in a facility registered with the local competent authority. In contrast, the extraction procedure was developed in compliance with Regulation (EU) 142/2011. Crucially, a procedure has been established where the supplied tendons are accompanied by information about the age, sex, breed, rearing conditions, and animal's diet.

The collagen extraction procedure was carried out on ice and using solutions cooled to 5°C. First, the tendons were cut into small pieces of a few millimeters, washed in organic solvent(s) and a neutral buffer, and wet milled in a blender. The milling was performed in cold dilute acetic acid. The milling was followed by acidic extraction at 4°C for 72 h. Next, pepsin-assisted extraction was carried out, followed by purification via salting out and resuspension in dilute acetic acid. The resulting solution was dialyzed through tubing with a MWCO 14 kDa until complete removal of the salt. Finally, the dialyzed solution was frozen at −20°C and lyophilized for 24 h.

The quality of the collagen was ascertained by sodium dodecyl sulfate-polyacrylamide gel electrophoresis (SDS-PAGE) and hydroxyproline assay. SDS-PAGE was performed, followed by protein-specific staining using Coomassie Brilliant Blue. Collagen solutions of 0.5 mg/mL were prepared, where the protein was denatured by Laemmli buffer containing SDS and mercaptoethanol, and heated at 95°C for 5 min. The analysis used a 7% separating and 5% stacking gel and ran at a constant voltage of 100V. A protein marker was included to determine molecular weights, containing proteins down to 97.4 kDa. After electrophoresis, the gel was stained with Coomassie Brilliant Blue for 2 h and destained overnight. The relative content of collagen was determined using the well-established hydroxyproline assay according to the manufacturer's instructions. Spectrophotometric measurements were then performed at 560 nm to determine the amount of hydroxyproline using a standard curve. The collagen mass was calculated by dividing the obtained result by 13.5%. The calculated mass corresponds to the dry mass of the lyophilized collagen used to prepare the initial collagen solution, which was used to determine the percentage content of collagen.

Differential scanning calorimetry (DSC) measurements were conducted using a calorimeter from DASM4 (Privalov; BioPribor, Russia) as previously described.[34] In brief, while maintaining a constant pressure of 2 atm, 2 mg/mL collagen solutions in 0.05 M acetic acid were heated from 20 to 65°C at a rate of 1°C/min, following a baseline run with buffer-filled cells. Each collagen solution underwent a second heating after initial cooling to assess the reversibility of thermal transitions, using the reheating scan as an instrumental baseline for subtraction, given that collagen thermal denaturation is irreversible. The

obtained excess heat capacity profiles were normalized to the protein content.

2.3. Collagen bioink formulation and printability

Neutral collagen bioinks were prepared by keeping the solutions at a low temperature of around 5°C. First, the dry collagen was dissolved in cold dilute acetic acid. Thereafter, a suitably selected concentration of phosphate-buffered saline (PBS) was added. Finally, the solution was neutralized with NaOH solution. For instance, to prepare a 5 mg/mL collagen solution, 25 mg dry collagen was dissolved in 3.5 mL 0.05 M acetic acid; 0.5 mL 10× PBS was then added; and finally, the solution was neutralized with about 0.9 mL 0.2 M NaOH. The neutralization process was closely monitored using the pH indicator phenol red.

The effect of various components of a typical collagen bioink on thermal gelation kinetics and complex modulus was investigated. In particular, 0.5% collagen solution with neutral pH and with various concentrations of NaCl, Na_2SO_4, $CaCl_2$, phosphate buffer (Na_2HPO_4 and KH_2PO_4 in a molar ratio 5.6:1), PBS (i.e., 1× PBS contains 1.37 M NaCl, 0.027 M KCl, 0.1 M Na_2HPO_4, and 0.018 M KH_2PO_4), and glucose were prepared and studied by rotational rheometry in oscillation mode (Table 1).

Printability of a 2% collagen ink was evaluated on a newly developed mechanical extrusion bioprinter capable of maintaining a cartridge temperature of ≤5°C indefinitely and independent of the ambient temperature. Additionally, the bioprinter maintains a platform temperature of 37°C. The system uses 3 mL syringes with a Luer lock, which are widely available in sterile packaging.

The printability of the formulated bioinks was characterized by their extrudability and capacity for continuous uninterrupted extrusion. The resolution was established by screening various extrusion factors, which effectively and directly determined the flow rate until filament thinning resulted in the deposition of non-continuous filaments. The effect of filament spreading was evaluated by the smallest pore that could be achieved. The tendency for filament collapse was observed by printing over gaps with sizes of 1–16 mm. Finally, height maintenance was evaluated by printing a 10-layer "wall" and following its height for 30 min at ambient conditions of 45% humidity and 20°C.

Table 1. Tested concentrations of various components in the collagen bioink.

Component	Concentrations
NaCl	75, 100, and 150 mM
Na_2SO_4	75, 100, and 150 mM
$CaCl_2$	75, 100, and 150 mM
Phosphate buffer	6, 12, and 18 mM
PBS	0.5×, 0.75×, and 1×
Glucose	5, 15, and 30 mM

Note: The concentrations of glucose were tested in 1× phosphate-buffered saline (PBS); phosphate buffer was prepared with 0.1 M NaCl.

2.4. Enzymatic hydrolysis of high-collagen concentration hydrogels

Stability against enzymatic digestion was established *in vitro* by dipping in a 2 mL 0.1 M Tris-HCl buffer containing 5 mM $CaCl_2$ solution of collagenase from *Clostridium histolyticum*, with an activity of 49 CDUs/mL (collagen digestion units) at 37°C. Three different collagen concentrations were investigated, i.e., 1.0, 2.0, and 4.0% (w/v). The neutralized hydrogels were thermally crosslinked at 37°C overnight before introducing them to the collagenase solutions. Changes in the biopolymer mass were monitored for up to 8 h by washing the remaining gels with EDTA solution, freezing the hydrogels at −20°C, freeze-drying, and weighing the dry mass. This approach eliminates the effect of mass increase due to hydrogel swelling, providing direct information on biopolymer degradation kinetics.

2.5. Characterization of elastic properties

Rheological analysis of neutralized collagen solutions and inks was performed using Thermo Scientific HAAKE RHEOSTRESS 600 with parallel plate (20 mm diameter; 1 mm distance) geometry. Rotational controlled-shear-stress oscillatory measurements at 1 Hz and amplitude of 1 Pa were utilized to monitor thermal crosslinking and viscoelastic properties. Thermal gelation was induced with two different temperature ramps at 1°C/min and 30°C/min.

2.6. Bioink functionalization with TGF-β1 and release studies

The release of two different concentrations of TGF-β1 from thermally crosslinked collagen hydrogels with two different biopolymer concentrations was investigated at 37°C. Initially, 5 ng/mL GF was tested, as it is within the range of typical concentrations employed in chondrogenic media. Simultaneously, for consistency with the bioprinting studies described below, the collagen concentration used was 2%. In light of the repeatedly observed results, the GF concentration was increased to 100 ng/mL, and the collagen concentration was decreased to 1% to ensure release within the sensitivity range of the ELISA kit.

Functionalization was performed in a laminar hood by adding TGF-β1 to a freshly neutralized collagen solution, prepared aseptically, and homogenizing the solution with a spatula while cooling on ice. The full volume of the functionalized collagen solution was then distributed into

the wells of a 12-well plate and thermally gelled at 37°C for 2 h. Next, the hydrogels were weighed aseptically, without washing, and immersed in 4 mL PBS in the wells of a 6-well plate, which was then placed in a CO_2 incubator at 37°C. This procedure ensured that all of the added TGF-β1 was in the hydrogel and/or in the PBS with insignificant losses to the walls of the wells where the gelation occurred. The PBS was sampled for ELISA analysis and replaced by the same volume of 4 mL PBS on days 0 (after 2 h of incubation), 1, 2, 3, 7, and 14. The sampled solution was stored at −20°C until ELISA analysis. For ELISA, the frozen solutions were brought to ambient temperature naturally, and the analysis was performed according to the manufacturer's protocol. Finally, statistical analysis of the absorbance from triplicates was performed after normalization to the documented mass.

Additionally, the effect of freezing a TGF-β1 solution at a selected concentration of 312.5 pg/mL, which is a value close to the middle of the standard curve, at −20°C for 2 h on the observed absorbance values was established.

2.7. Cell culture, 3D bioprinting, and live/dead staining

Two of the established cell lines used in this study, Caco-2 (colorectal cancer) and CHON-001 (human chondrocytes), were generously donated by Associate Professor Marian Draganov (Medical University of Plovdiv) and Dr. Agniezska Panek (Institute of Nuclear Physics, Krakow, Poland), respectively; hTERT A41hWAT-SVF (immortalized white adipose tissue stromal vascular fraction [SVF] cells) were purchased from ATCC (CRL-3386). All cell lines were cultured under standard conditions as recommended by the original protocols or the ATCC. In brief, the conditions for Caco-2 included DMEM/F12 (P04-41250), fetal bovine serum (FBS; at 10% final concentration; P40-37500), and 0.5% penicillin-streptomycin (Pen/Strep; P06-07100) (all purchased from PAN-Biotech, Germany). For CHON-001 and the SVF cell lines, we used DMEM (P04-05550), 10% FBS, and 0.5% Pen/Strep. For bioprinting, 8–10 million cells/mL of 2% freshly neutralized collagen ink (prepared as described above) were collected (by using Accutase cell detachment solution, 423201; Biolegend, USA) and bioprinted at 8–12 kPa pressure and 8–10 mm/s printing speed, using a pre-cooled (4°C) printing head of the BioX extrusion bioprinter (Cellink, Sweden). The design of the models was a 5 × 0.82 mm disc. Thermal crosslinking was enhanced by initially preheating (to 37°C) both the 24-well plates, which served as the platform for bioprinting the constructs, and the respective growth medium, which was added to the wells after the bioprinting process. Cell viability was assessed by fluorescent microscopy of bioprints taken on days 1, 3, 7, and 14 after printing and stained with calcein AM and propidium iodide (PI) (live/dead staining). Manual counting of cells with Nikon software NIS-Elements v 4.3 ("measure" and "count" functions) was carried out for Caco-2, CHON-001, and SVF cells at 10× magnification. The percentage of viable cells was calculated by subtracting the percentage of dead cells (the number of dead PI-positive cells divided by the total number of cells) from 100%. At least two separate fields of view (~1 mm^2) from two representative images were used. Bright-field time-lapse microscopy for the evaluation of viability, migration, and proliferation of CHON-001 cells was carried out with a CytoSmart Lux2 inverted microscope (CytoSmart, Netherlands), with images taken every 15 min over one week.

2.8. Histomorphological and immunohistochemistry analyses

Bioprints were taken at different time points (between days 1 and 14) after printing and were fixed in 10% neutral buffered paraformaldehyde; the bioprints were then kept at 4°C before embedding in formalin and sectioning (at 4 μm thickness). After being mounted on microscopic slides, the sections were deparaffinized with xylol and re-hydrated. Standard hematoxylin and eosin (H&E) staining (05-06015/L and 05-10002/L; Bio-Optica, Italy) was carried out for morphological assessment. Alcian blue staining was performed to detect the presence of proteo- and glycosaminoglycans. The sections were mixed in 3% acetic acid for 3 min, followed by 30 min incubation with Alcian blue (1% in 3% acetic acid, pH 2.5; cat# B8438-250ML; Sigma-Aldrich, USA) and washing.

Immunohistochemistry (IHC) was carried out following the manufacturer's protocol of the Novocastra Peroxidase Detection System (RE7110-K; Leica, Germany) with an anti-collagen II rabbit polyclonal antibody (SAB4500366; Sigma-Aldrich, USA) at a final dilution of 1:100. Micrographs were taken with Nikon Eclipse Ni (Nikon, Japan).

2.9. RNA extraction, sequencing, and transcriptomic analysis

RNA extraction was carried out with a Pure Link RNA Mini kit (cat # 12183018A; ThermoFisher Scientific, USA) following the manufacturer's protocol with one modification, i.e., bioprints were left in 500 μL lysis buffer for 10 min on ice before lysis. Total RNA concentration was then measured with Nanodrop (ThermoFisher Scientific, USA) and frozen at −20°C before shipping for library preparation and sequencing to Novogene (United Kingdom [UK]). Differentially expressed genes were estimated by Fragments Per Kilobase per Million mapped fragments, which was used in the subsequent gene set enrichment

analysis (GSEA). Curated gene sets from the (molecular signature database of the Broad Institute) for cartilage development and chondrocyte development (GOBP_CHONDROCYTE_DEVELOPMENT, M11483, and GOBP_CARTILAGE_DEVELOPMENT, M10512) were used to assess chondrogenesis and compare between cells printed in pure collagen and biofunctionalized collagen of genes with >1.5-fold change expression compared to 2D control (SVF cells grown under standard monolayer conditions) and <0.05 false discovery rate (FDR) adjusted *p*-value. Gene ontology (GO) analyses with ShinyGO 0.80[35] and StringDB[36] were used with upregulated genes, while Venny 2.1 (https://bioinfogp.cnb.csic.es/tools/venny/) was used to create Venn diagrams.

2.10. Statistical analysis

Raw data from post-printing cell viability, collagenase stability, and printed strand spreading analyses, as well as rheometry and optical extinction, were imported into Microsoft Excel. They were analyzed by the in-built functions for single factor analysis of variation (ANOVA), followed by a post-hoc Student's *t*-test, taking into account homoscedasticity as determined by *F*-tests. Confidence intervals for the means at a 95% confidence level were calculated and plotted as error bars. GO analyses were performed with ShinyGO 0.80[35] and StringDB[36]; Venn diagrams were plotted using Venny 2.1.

3. Results and discussion

3.1. Characterization of the extract

The quality of the extracted collagen was ascertained by Coomassie-stained SDS-PAGE, DSC, and hydroxyproline assay (Figure S1, Supporting Information). The electrophoretogram contains typical collagen type I bands around 115–120 kDa, corresponding to the α1 and α2 chains, and two bands at >200 kDa, attributed to β dimers.[37] The thermogram also contains a typical narrow endothermic transition centered at 41.6°C. The total collagen content is >90% of the dry mass.

3.2. Kinetics of thermal crosslinking and hydrogel properties

The gelation temperature affects collagen fibril length and thickness, both of which are relevant to collagen inks printed without and within a supporting medium.[25] In direct bioprinting, without a supporting medium, the extruded filament is instantly exposed to 37°C, which corresponds to a fast ramp rate, rapidly stabilizing the printed structure. In contrast, bioprinting within a supporting medium is typically performed initially at room temperature, with a subsequent increase in the temperature to 37°C at a slow rate of 1°/min. Despite differences in fiber morphology, our rheological analysis did not identify significant differences between the equilibrium G′ values of collagen solutions crosslinked at 37°C after a ramp rate of ~30°/min and 1°/min (Figure 1). In both cases, a G′ of ~1 kPa

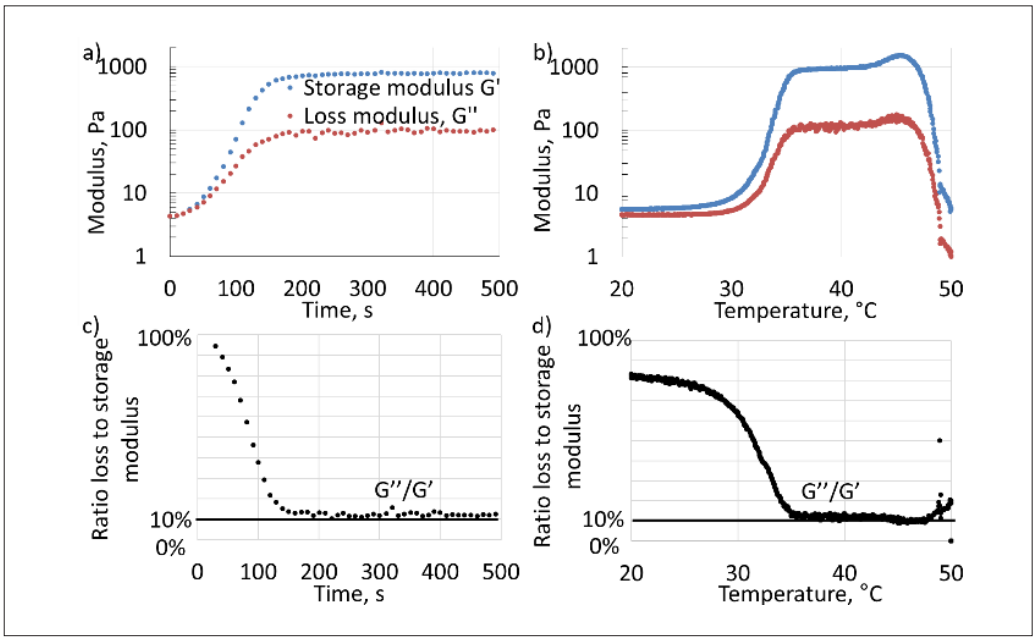

Figure 1. Rheometry results in oscillation mode, i.e., storage modulus (G′; blue) and loss modulus (G′; red), revealing thermal gelation of 0.5% collagen solution after heating (a) to 37°C at 30°/min and (b) to 50°C at 1°/min. Inset plots display the ratio of loss modulus to storage modulus, presented in %, marking the biomimetic value of 10%.

was observed for a 0.5% hydrogel, comparable to values in the literature.[38] However, about 3 min was required for a hydrogel with a thickness of 1 mm (i.e., the distance between the rheometer plates) to reach G′ saturation at 37°C (Figure 1a). Although this is considered too long for high-precision extrusion bioprinting, extruded filaments are typically only a few hundred micrometers, facilitating quicker thermal activation of gelation. Furthermore, to retain its shape, the extruded fiber does not need to be completely crosslinked; rather, the crosslinking needs to progress to the point of sufficient viscosity to resist flowing, corresponding to the state of biopolymer arrest well-documented by Tran-Ba et al.,[26] thereby ensuring shape retention during the deposition of the subsequent layers and the concurrent stiffening.

In extrusion (bio)printing, rapid crosslinking of the extruded and deposited strands is crucial for a high-fidelity printing process, both within and without a supporting medium, but the timescales are different. Various strategies can accelerate crosslinking, including controlling the temperature and pH or adding riboflavin, tannic acid, and genipin.[5] However, modifying the ionic strength of the collagen inks, which has been documented to affect the kinetics and fiber morphology during fibrillogenesis, has received little attention from the bioprinting community.[19] Our rheological findings agree with studies highlighting chloride ions' effectiveness in facilitating collagen crosslinking (Figure S2a, Supporting Information), whereas divalent phosphate ions, which form salt bridges in positively charged regions, slow down the gelation process, which we observed as a trend of slower gelation when increasing the phosphate buffer concentration from 6 to 12 and 18 mM in the presence of 1 M NaCl (data not shown).[39,40] A key insight from this study is that fibril formation is expedited at lower ionic strengths due to the minimization of salting-out effects and enhanced electrostatic interactions among amino acids.[18] We observed it by decreasing the concentration of NaCl or KCl from 150 to 100 and 75 mM or that of PBS from 1× to 0.75× and 0.5× (Figure 2a). In addition to the faster gelation at 37°C, the neutral collagen solution becomes more sensitive to temperature, initiating gelation at a lower temperature at lower PBS concentrations (Figure 2b). Hence, the solution with 75 mM NaCl could not be tested even while maintaining a low temperature.

The study of the effect of $CaCl_2$ revealed that, in line with the literature, divalent cations like Ca^{2+} inhibit gelation despite the chloride ions' presence.[15,41] The addition of 75, 100, and 150 mM $CaCl_2$ to a 0.5% collagen solution did not result in gelation, corroborating reports that Ca^{2+} inhibits the formation of native fibrils probably due to the shift in the isoelectric point to the basic pH above 9.0.[42] In contrast, the lack of gelation of a solution containing Na_2SO_4 seems inconsistent with previously reported fibrillogenesis, including a proportional thickening of the assembled fibrils with the increase in the Na_2SO_4 concentration.[20,43] However, Xing et al.[20] reported the optical density of the collagen solution without discussing its gelation, while Oh et al.[43] added Na_2SO_4 to a collagen solution that already contained PBS, i.e., phosphate buffer and Cl^- ions.

In our study, glucose had a negligible effect on collagen gelation kinetics. In contrast, Lien et al. demonstrated glucose-induced inhibition at a concentration as low as 5 mM with half-maximal inhibition occurring at 50 mM and

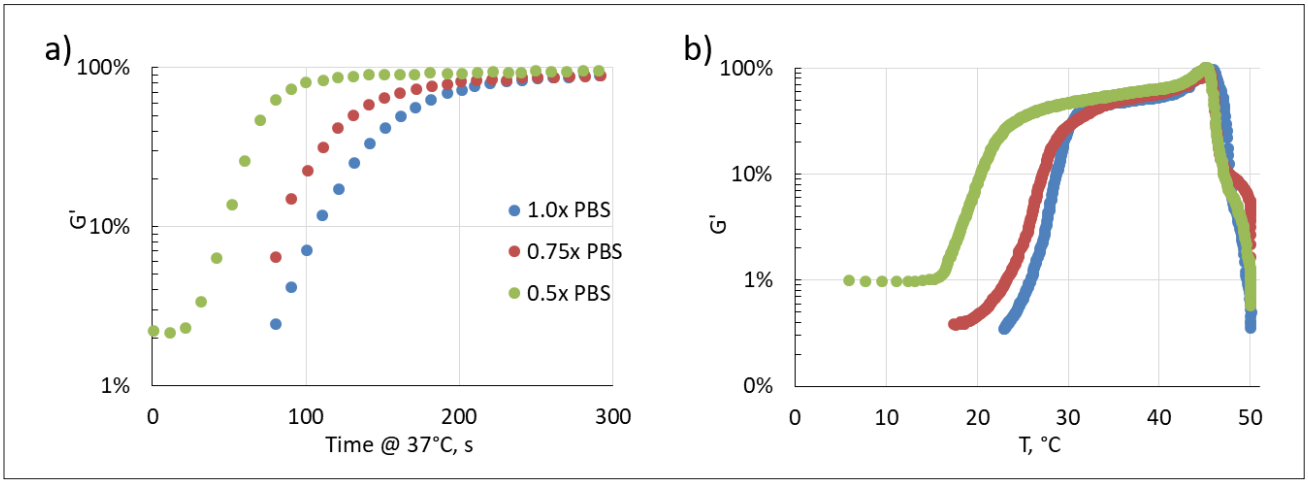

Figure 2. Rheological investigation in oscillation mode, normalized storage modulus (G′), of the effect of various concentrations of phosphate-buffered saline (PBS) at a neutral pH on the gelation of 0.5% collagen solution during (a) an incubation at 37°C after a temperature ramp rate of 30°/min, and (b) a temperature ramp (T) with a rate of 1°/min. G′ has been normalized to the highest value observed during rheometry (100%) to aid the reader in distinguishing the different gelation kinetics.

maximum inhibition at 200 mM.[44] At a concentration range of 5–30 mM, common in low- and high-glucose media, we observed negligible differences in gelation kinetics with largely overlapping G′(t) curves across glucose concentrations (Figure S2c, Supporting Information), suggesting that PBS mitigates its inhibitory effect.

A collagen ink with subphysiological ionic strength will impose stress on cells already subjected to shear stresses during the extrusion. To assess its impact on cell viability and proliferation during bioprinting, as initial tests, we conducted a study with 1% collagen bioinks and a rapidly proliferating cancer cell line (Caco-2 cells). We selected proliferating cells instead of slowly dividing chondrocytes because any negative effect would be observed readily in metabolically active cells going through the cell cycle more rapidly.[45] Results indicated high cell viability, approximately 90%, after incubation for up to seven days, affirming the suitability of this approach for bioprinting live cells (Figure 3). Although there was a slight reduction in cell viability between days 3 and 7, possibly due to the thickness of the bioprinted constructs exceeding 0.5 mm, we observed cell proliferation (Figure S3, Supporting Information). This suggests that the initial stress conditions did not significantly compromise cell functionality.

3.3. Bioink mechanical properties

Dynamic analytical techniques (e.g., rheometry in oscillation mode), in contrast to conventional static tests, are the most appropriate for characterizing viscoelastic materials like collagen-based hydrogels, which exhibit solid- and fluid-like responses. The proportion between these characteristics, quantified by the storage (G′) and loss (G′) moduli, is around 10% in natural tissues.[46] This is reproduced in the collagen gels (insets of Figure 1), mirroring the viscoelastic properties of natural cartilage and indicating an optimal balance between viscosity and elasticity. This balance is essential for supporting cellular functions, such as proliferation, differentiation, and migration, providing an ideal ECM-simulating environment for bioprinted cells.

We performed *in situ* rheological analysis during thermal crosslinking with a ramp rate of 1°/min, and we report the storage moduli G′ achieved at 37°C for collagen hydrogels with various concentrations up to 7% (Figure 4). We observed the expected concentration-dependent stiffening. The apparent exponential dependence, however, is partly a measurement artifact due to increased sensitivity to temperature with higher concentrations; gelation starts at a lower temperature as collagen concentration increases (data not shown). This implies that at 37°C, the G′ of higher-concentration hydrogels were closer to saturation than those of lower concentration. For a more robust comparison, atmosphere-controlled rheometry should be performed to exclude the effect of sample drying while maintaining the sample at 37°C until saturation of G′ is reached. Nonetheless, the 7% hydrogel after thermal crosslinking closely aligns with the mechanical properties of the articular cartilage's surface layer.[47]. For the bioprinting studies, we selected the 2% collagen ink to ensure high cell viability following extrusion bioprinting.[48,49] The wide range of storage moduli underscores the potential of collagen type I bioink in cartilage tissue engineering.

3.4. Enzymatic hydrolysis kinetics of the hydrogels

Tissue engineering with high-concentration collagen inks/hydrogels above 1% is a relatively recent strategy,

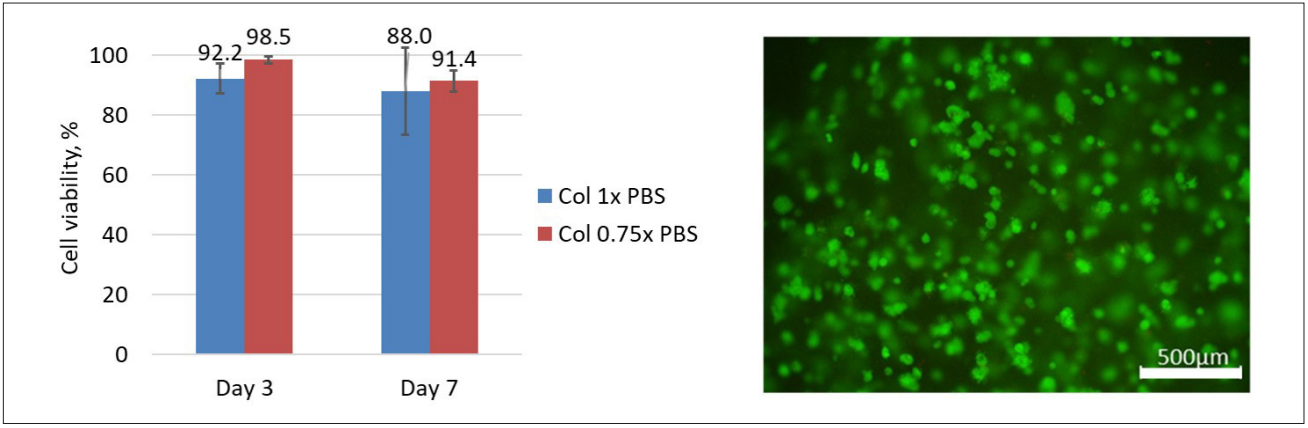

Figure 3. Viability of Caco-2 cells bioprinted in collagen (Col) inks with physiological (1× phosphate-buffered saline [PBS]; blue bars) and subphysiological (0.75× PBS; red bars) ionic strength after 3 and 7 days of incubation (left) and a representative fluorescence micrograph depicting live (green) and dead (red) cells after 7 days of incubation (right). Error bars represent the 95% confidence interval for the mean after at least four representative areas were counted. Scale bar: 500 µm.

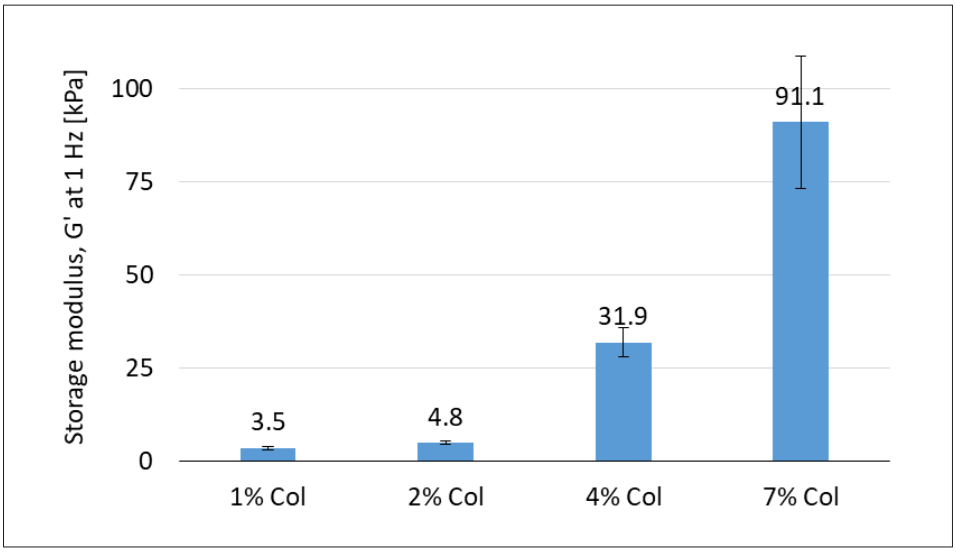

Figure 4. Storage moduli were observed at 37°C after thermal crosslinking at a heating rate of 1°/min of 1–7% collagen (Col) bioinks. Error bars represent the 95% confidence interval for the mean from three replicates.

with limited information about their characteristics. This includes *in vitro* degradation rates and how they correspond to *in vivo* rates, which are also dependent on the implantation site.[3] Increasing the collagen concentration is a straightforward way to increase the hydrogel's resistance against enzymatic digestion. The kinetic analysis of collagen hydrogel degradation confirms the concentration-dependent degradation rates for 1, 2, and 4% thermally crosslinked hydrogels (Figure 5). A first-order kinetic model, substantiated by the linear relationship between the natural logarithm of the relative mass and time, accurately describes the degradation process. Rate constants derived from the slopes are −0.5130, −0.4462, and −0.2482 h^{-1}, respectively, with R^2 values above 0.94 indicating a robust fit. We note that these rate constants were obtained under conditions of significant enzymatic activity, where hydrogels with 10–40 mg dry collagen mass were exposed to a solution with 98 CDU collagenase. These results confirm that lower collagen concentrations correspond to accelerated degradation within the hydrogel matrix, a crucial consideration for designing biodegradable scaffolds in biomedical applications.

3.5. Bioink printability

Despite the increasing interest in collagen for bioink preparation,[3,5,49] comprehensive printability data for single-component bioinks remains scarce. While its biocompatibility and biodegradability make it an ideal

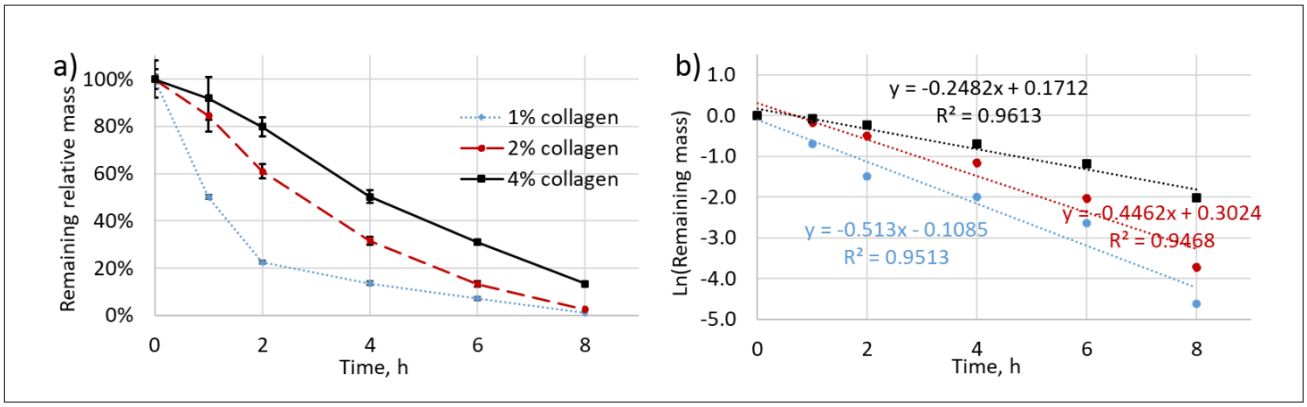

Figure 5. Collagenase degradation of thermally crosslinked high-collagen concentration hydrogels: (a) changes in the relative mass of the biopolymer, and (b) fitting to first-order kinetics with the corresponding equations. The error bars represent the standard deviation of a sample of three replicates.

candidate for creating scaffolds, most studies focus on mechanical properties, degradation rates, and biological performance rather than printability. This gap in the literature underscores the need for more rigorous assessments of printability, such as extrusion parameters, viscosity measurements, and post-printing stability, to fully realize the potential of pure collagen bioinks in 3D bioprinting applications. Following preliminary printability tests and to avoid extensive cell death due to a too-high density, the 2% collagen ink was selected for the bioprinting experiments reported below. Thus, here, we describe the comprehensive characterization of its printability.

The good extrudability of the 2% collagen ink was ascertained using a pneumatic extrusion bioprinter (BioX) to facilitate comparison with the prevalent literature, which predominantly utilizes pneumatic systems. The ink was successfully extruded through a 420 µm conical nozzle (22GA) at a pressure as low as 10 kPa, yielding continuous strands. The subsequent printability tests were conducted on a mechanical extrusion bioprinter (FiBotBio), which offers a distinct advantage in terms of direct control over the flow rate. Unlike pneumatic systems where the flow rate is influenced by different variables (applied pressure, nozzle geometry, bioink viscosity under shear, and piston friction) and must be determined experimentally, mechanical systems directly control the plunger's displacement rate. This feature allows for precise management of the flow rate, independent of the bioink's rheological properties and other factors, enhancing reproducibility and accuracy in bioprinting applications. As a result, the width of the extruded strand consistently decreases as the flow percentage is reduced from 100 to 8%, controlled by the M221 instruction in the machine code (.gcode file) (Figure 6). Utilizing the 22GA 420 µm conical nozzle, the finest strand diameter achieved without repeated interruptions was approximately 440 µm (Figure 6).

The 2% collagen ink exhibits exceptional shape fidelity during 3D printing, primarily due to its optimal viscosity and effective water retention capacity. Notably, a 10-layer construct maintains its height with minimal change within the first 5 min and only a slight decrease of up to 10% after 20 min at ambient conditions (20°C, 45% relative humidity [RH]) (Figure S4a, Supporting Information). This contrasts with previous studies where a 50% reduction in height was observed within 10 min, but in this study, the ink preserves structural integrity for up to 90 min, akin to hydroxyethyl cellulose – sodium alginate (HEC-SA) ink in water-vapor-saturated environments.[50] Thus, humidity control could further enhance the integrity of the collagen strands.

Additionally, the ink's precision is demonstrated by forming pores as narrow as around 80 µm wide (Figure S4b, Supporting Information). This capability, along with the test results from printing a strand over various gap spans (Figure 7), where collagen strands maintain structural integrity across gaps of 1 to 16 mm with minimal sagging except at the widest span, underscores the robustness of its formulation. The ink's higher viscosity curtails the initial spread upon deposition, effectively preserving height and form, while its ability to retain moisture prevents deformation or collapse. Taken together, these properties are crucial for achieving high resolution and maintaining the structural fidelity of bioprinted tissues, illustrating how the ink adapts to different stresses and maintains

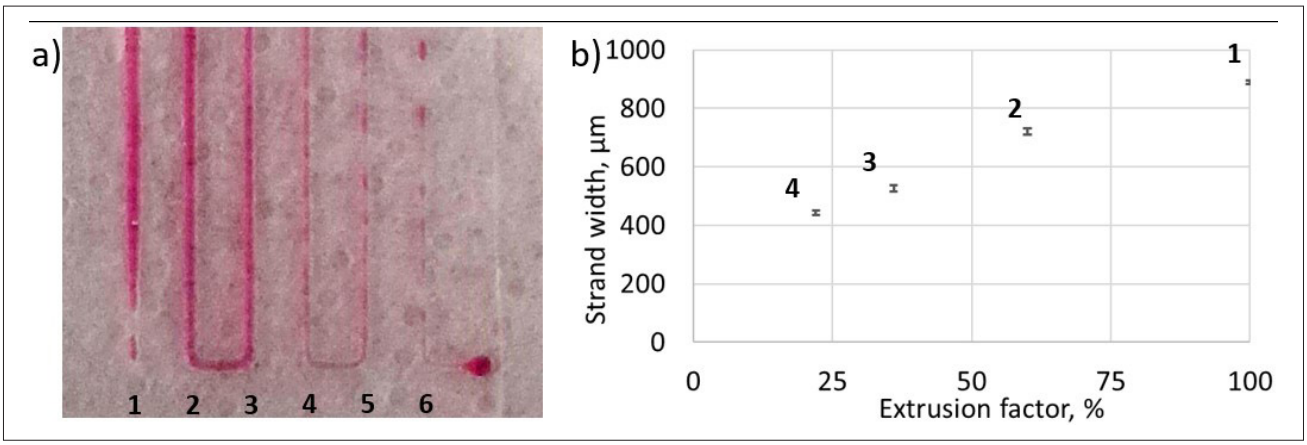

Figure 6. Printing 2% collagen ink with decreasing flow rates as defined by an extrusion factor. (a) A photograph of the resulting strands; The extrusion factor (EF) was 1: 100%; 2: 60%; 3: 36%; 4: 22%; 5: 13%; 6: 8%. (b) Average width of the continuous non-interrupted strands with EF 1: 100%; 2: 60%; 3: 36%; 4: 22%. Error bars represent the 95% confidence interval for the mean from five replicates.

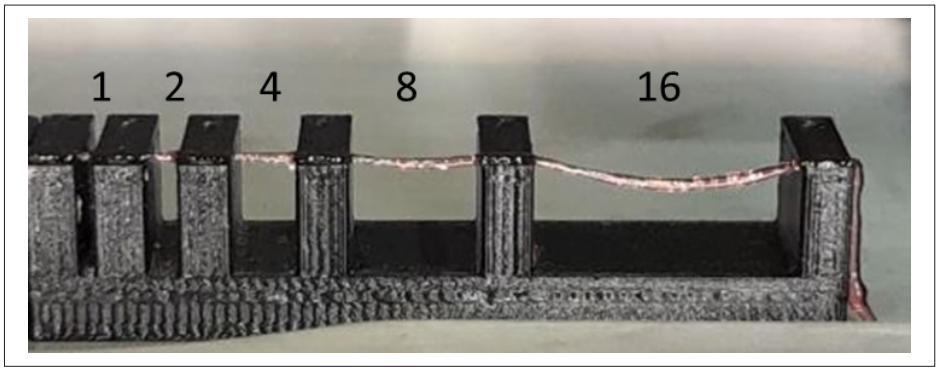

Figure 7. Collagen ink (2%) deposited over gaps of 1, 2, 4, 8, and 16 mm.

precise geometries essential for functional outcomes in tissue engineering.

3.6. Biofunctionalization and growth factor release

Despite the substantial role of collagen hydrogels in tissue engineering, their application in GF delivery has been limited by the absence of specific binding sites for GFs, which are essential for effective cell signaling and tissue regeneration.[27] Here, we report the effective biofunctionalization of the collagen ink with TGF-β1, utilizing direct loading, followed by a thermal crosslinking strategy to entrap the GF. Preliminary investigations of the release of TGF-β1 with a concentration of 5 ng/mL, typical for chondrogenic media, from a 2% thermally crosslinked collagen hydrogel yielded no detectable amount of GF release for a two-week incubation. Thus, the more porous 1% formulation was selected, and the TGF-β1 concentration was increased 20 times to establish its release kinetics.

Less than 0.5% of the total TGF-β1 content, initially at a concentration of 100 ng/mL in the 1% collagen hydrogel, is released over two weeks of incubation in PBS at 37°C (Figure 8). Moreover, nearly 90% of the released amount is found in the supernatant within three days. After day 7, the signal from TGF-β1 becomes indistinguishable from the noise, which could reflect minimal release or limited stability of the GF under the incubation conditions. Regardless, the saturation of the release profile indicates effective immobilization by the hydrogel.

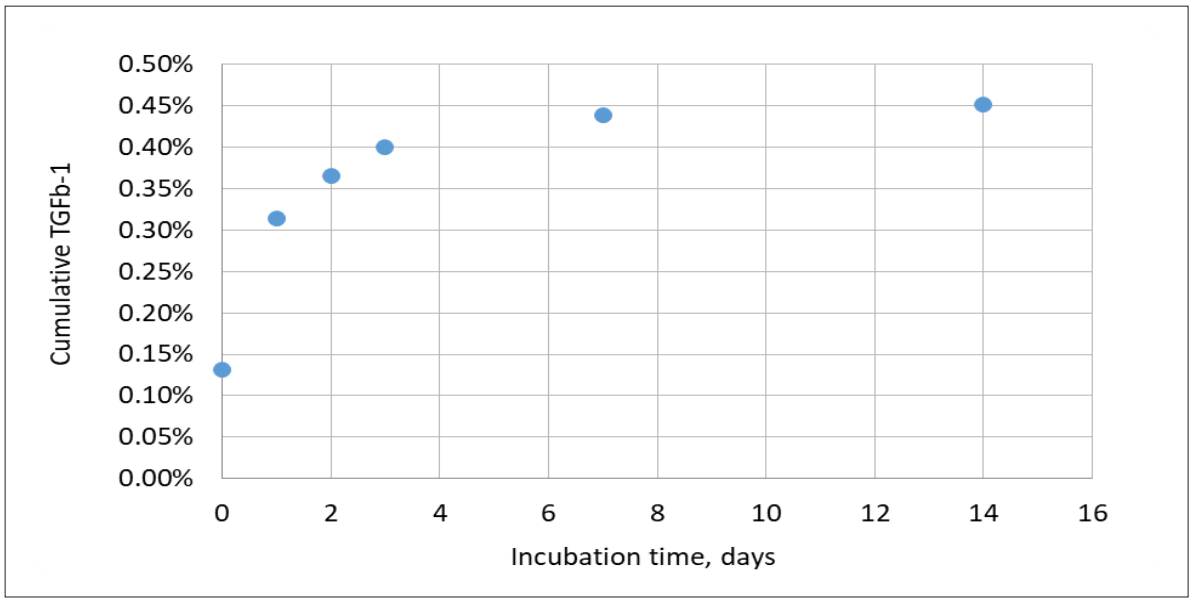

Figure 8. Release profile of TGF-*β1* displaying high retention of the growth factor within a 1% collagen hydrogel. Less than 0.5% of the total mass of TGF-*β1 added to the collagen hydrogel is released into the incubation solution* before saturation. The TGF-*β1 concentrations up to* and including day 7 exceed baseline levels and are significant (n = 3; α = 0.05). Error bars are not included, as no statistical analysis was performed on the cumulative values.

Notably, error bars are deliberately omitted from the cumulative values reported in Figure 8 to avoid misleading the reader. One of the reasons is that the concentration of TGF-β1 was determined in freshly added PBS, i.e., its statistically significant detection in the supernatant ($n = 3$; $\alpha = 0.05$) up to and including day 7 is proof of GF release. The calculated values are then summed, and the relative concentration is plotted. The second reason is that the values may systematically underestimate the true concentration due to the impact of freezing the supernatant containing the released GF. A preliminary study indicated that absorbance values can halve when a solution containing 312.5 pg/mL TGF-β1 is frozen at −20°C for 2 h, compared to the same solution maintained at 4°C without undergoing the freeze-thaw cycle. Consequently, the actual total amount of released GF could be as high as 0.9%, still indicating an effective immobilization.

However, the absence of detectable TGF-β1 release from the 2% hydrogel at a typical chondrogenic media concentration of 5 ng/mL, used in the subsequent bioprinting experiments, suggests a strong immobilization of the GF. At this significantly lower concentration, release may be slower or less evident due to weaker concentration gradients and stronger interactions with hydrogel molecules. To our knowledge, this is the first demonstration of an efficient TGF-β1 sequestration within a collagen hydrogel, highlighting its potential for sustained delivery to embedded cells in bioprinted tissue engineering.[51]

3.7. Biological effects of collagen I-based and collagen I-biofunctionalized hydrogels on chondrogenesis

To assess the potential use of collagen I-based bioinks in cartilage tissue engineering, we first tested the biocompatibility of the hydrogel with a typical chondrocyte cell line, CHON-001. Using bright field time-lapse microscopy, we observed excellent viability and motility of the cells within the bioprint over one week (Figure 9a; Video S1, Supporting Information). These initial results were confirmed and extended by live/dead staining (Figure 9b),

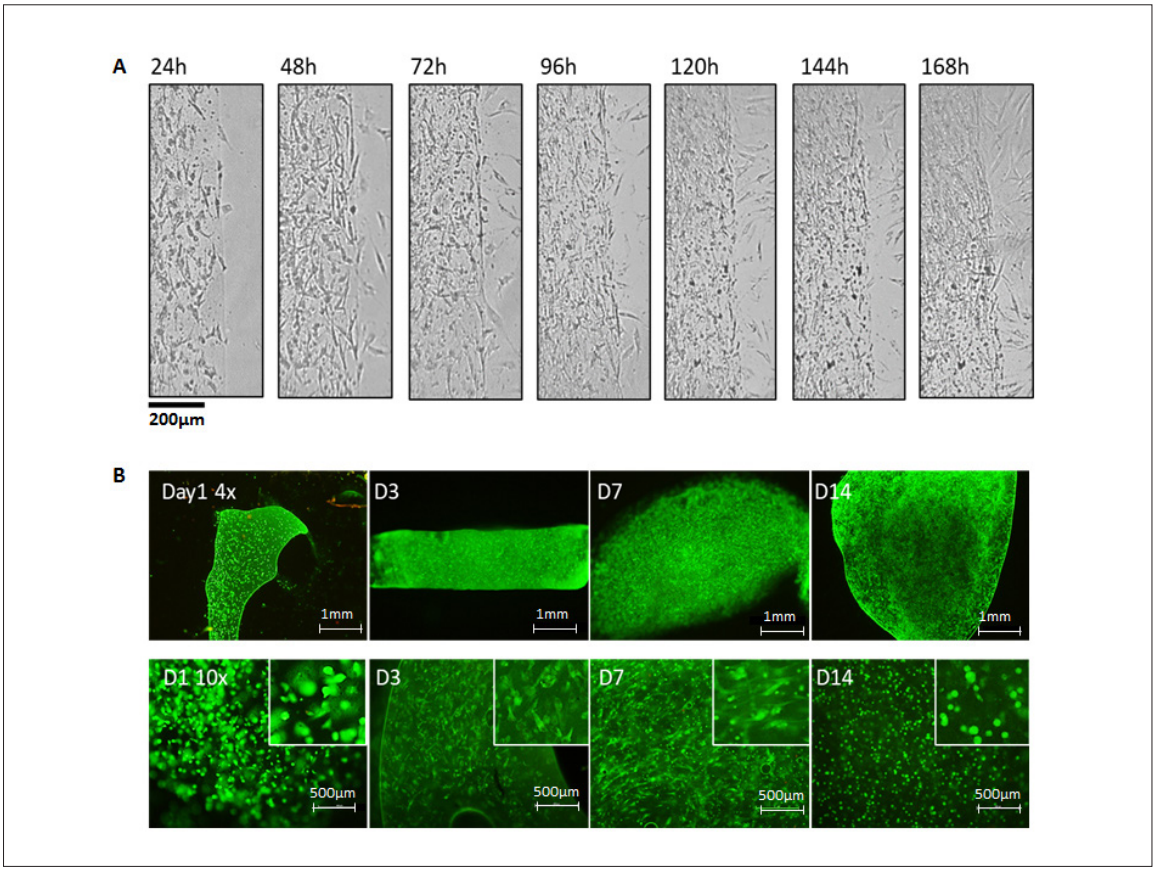

Figure 9. Assessment of biocompatibility of 1% collagen type I with chondrocytes (CHON-001 cell line) through (a) bright field time-lapse microscopy over seven days, displaying cell migration and proliferation, and (b) live-dead staining with calcein AM (green) and propidium iodide (red), respectively. Scale bar at 4× – 1mm, at 10× 500 µm.

demonstrating an insignificant number of dying cells even three weeks after bioprinting (data not shown).

The study was then expanded to test the bioinks' potential to induce and support chondrogenesis, as both collagen type I and TGF-β1 are important for cartilage development. To assess this, we used an *in vitro* model cell line of MSCs derived from white adipose tissue (or SVF cells), hTERT A41hWAT-SVF. Cells in both bioinks demonstrated good viability of around 90% on day 1 and 80% on day 14, even if there were more dying cells compared to CHON-001 (Figure 10a).

Next, we assessed the morphology of the SVF cells compared to chondrocytes in terms of the formation of lacunae, secretion of proteoglycans (Alcian blue staining), and collagen type II (IHC). We found that both bioinks induced chondrogenesis in at least a portion of the SVF cells as observed from H&E and staining for typical cartilage ECM components. Notably, weaker staining for proteoglycans and collagen II was observed in the collagen bioink compared to CHON-001 (printed in collagen) and SVF cells in the biofunctionalized bioink (Figure 10b), suggesting that TGF-β1 release enhances the chondrogenic properties of the biomaterial.

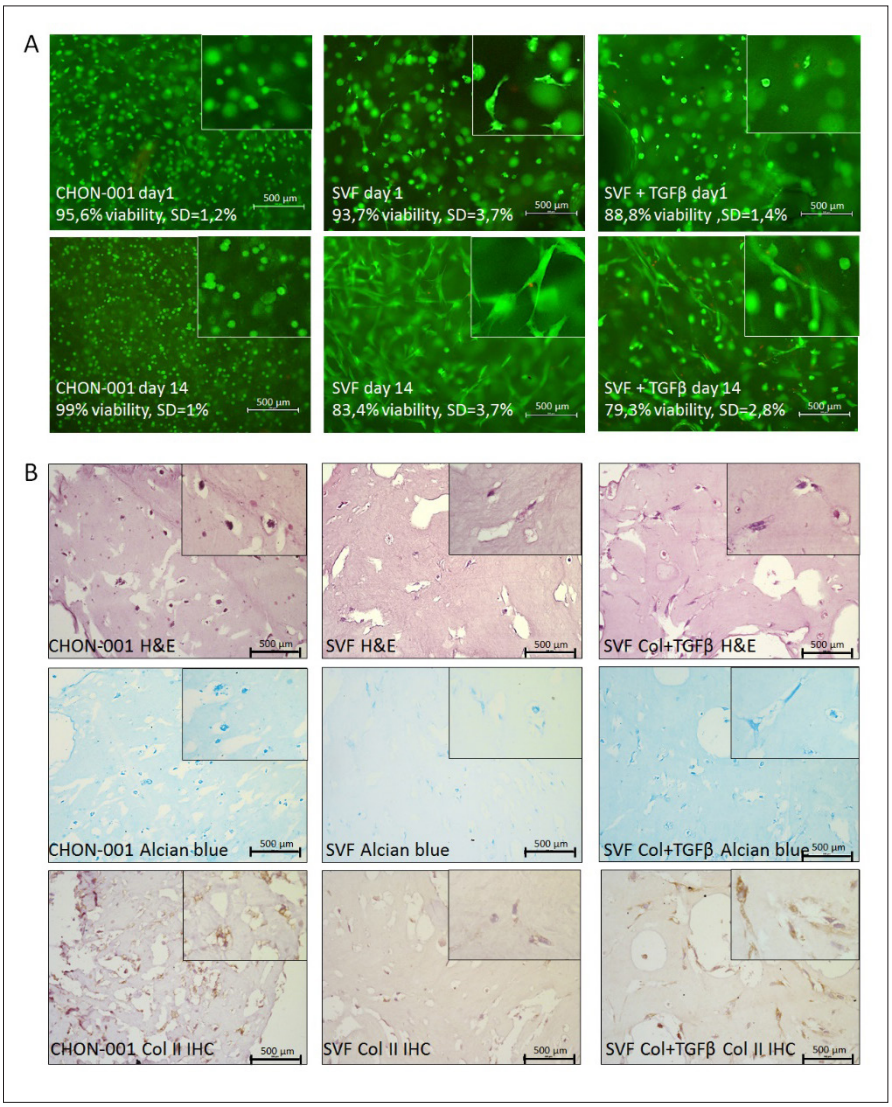

Figure 10. Evaluation of chondrogenesis support of pure and biofunctionalized collagen bioinks. (a) Live-dead staining of CHON-001 cells (left) and stromal vascular fraction (SVF) cells in pure collagen (middle) and in collagen biofunctionalized with TGF-β (right) on days 1 (top panel) and 14 (bottom panel). (b) Histomorphology of chondrogenesis in CHON-001 (left column) and SVF cells in pure collagen (middle column) and biofunctionalized collagen (right column) through hematoxylin and eosin (H&E) staining, staining with Alcian blue for proteoglycans and glycosaminoglycans, and immunohistochemistry (IHC) for the cartilage biomarker collagen II (Col II) (top, middle, and bottom rows, respectively). The inset images denote regions of interest that are at 2× higher magnification (digital for (a) and taken with a 20× objective for (b).

Thus, this is the first report suggesting that 2% collagen type I bioinks provide an excellent microenvironment for human chondrocytes (CHON-001 cells) in terms of motility, proliferation, long-term growth, and retention of morphology. Thus far, there have been only two studies using collagen type I (both at 4% concentration) by Beketov et al. and Isaeva et al. – one with rat chondrocytes, while the second mixing the collagen with ECM and another one where ECM granules from rat costal cartilage were mixed into the hydrogel and bioprinted with primary adipose-derived MSCs (similar to the SVF cells).[48,49] Therefore, strategies, where primary human chondrocytes are used for cartilage biofabrication, as previously demonstrated with synthetic materials (PEGDA[52] and PCL-alginate[31]), may exploit the implementation of collagen I bioinks.

Furthermore, we demonstrate that collagen type I possesses good biocompatibility properties with respect to human SVF cells (Figure 10a) and is sufficient to induce differentiation at least in part of the cells *in vitro* (Figure 10b), as we observed both morphologies of chondrocytes in lacunae and fibroblast-like cells. It is important to note that SVF cells comprise a heterogeneous mixture of several cell types, including pre-adipocytes, MSCs, fibroblasts, pericytes, and others.[53] Therefore, differentiation of all cells may be difficult to achieve, even more so by simply adding one component of the ECM (collagen I) or transcription factor (TGF-β).

3.8. Transcriptomic assessment of the biofunctionalization of collagen type I with TGF-β1

To assess the molecular changes that growing SVF cells in 3D-bioprinted structures induce and make an unbiased comparison between the effects of the two hydrogels (collagen alone and collagen functionalized with TGF-β1), we carried out transcriptomic analysis two weeks post-printing. We used SVF cells grown under the gold standard for chondrogenic induction (3D culture micromasses or spheroids) as controls for data comparison. After filtering for ≥1.5-fold change in gene expression (and adjusted p-value ≤0.05), we observed a total of 3364 (1893 upregulated and 1471 downregulated) differentially expressed genes (DEGs) in SVF cells bioprinted in collagen and 4138 (2240 upregulated and 1898 downregulated) DEGs with functionalized hydrogel compared to 2D cells. With regards to 3D-cultured cells, the DEGs were 4271 (2197 upregulated and 2074 downregulated). To obtain an objective overview of whether these conditions can affect chondrogenesis, we performed GSEA using curated datasets from MsigDB related to cartilage and chondrocytes. Of note, both collagen and collagen/TGF-β could successfully induce chondrogenesis to a similar extent (Figure 11), with normalized enrichment scores (NES) of above 2 for "cartilage development" and above 1.8 for "chondrocyte development," and with very significant FDR-adjusted p-values, while growing SVF cells in micromasses could activate the same transcriptional programs much more poorly (both in terms of NES of around 1.5 and FDR-adjusted p-values of 0.297 and 0.67, respectively).

Thus, we confirmed the chondrogenic potential of both collagen-based bioinks. However, to elucidate the effect of the entrapped TGF-β (besides the larger number of DEGs), we conducted GO analysis of the upregulated genes in the two bioinks (Figure 12a). Under both conditions, the cells activated transcription programs for ECM remodeling, typical of cartilage, and the top hit in both cases was for the upregulation of glycosaminoglycans and chondroitin sulfate genes (Figures 12a; Figures S5 and S6, Supporting Information). Importantly, one of the top 10 enriched processes, when cells were bioprinted with the functionalized bioink, was for TGF-β activation (Figure 12b), suggesting that the entrapped transcription factor was indeed taken up by the cells and induced measurable and significant changes (at two weeks).

To assess the specific effects that functionalization with TGF-β1 has, we analyzed the genes that are uniquely upregulated in the cells bioprinted with this bioink compared to collagen only (1057 DEGs). The results revealed enrichment for activation of TGF-β signaling (17 of the 29 total genes previously found upregulated in Figure 12b). Of note, the findings were also confirmed by another GO analysis with STRING DB, which indicated that these 1057 uniquely upregulated by TGF-β1 genes are strongly implicated in cartilage development, proteoglycan, and glycosaminoglycan biogenesis, among other pathways and processes (Figures 13 and S7, Supporting Information).

Thus, by transcriptomic analysis, we confirmed that bioprinting SVF cells with either pure or biofunctionalized collagen can induce chondrogenesis (Figures 11 and 12a). This serves as a crucial independent and objective validation of the histomorphological results (Figure 10b), highlighting the presence of lacunae typical of cartilage formation and the specific ECM composition. To our knowledge, this is one of the few examples using such an evaluation approach in 3D-bioprinted cartilage, as we could find only one other study where the biological effects of biofunctionalized GelMA (also with TGF-β1) were also investigated through sequencing.[54]

The key finding of this work is the biological effectiveness of biofunctionalizing a collagen hydrogel with TGF-β1. The successful retention of the GF through thermal crosslinking and its subsequent utilization by the cells was demonstrated unequivocally through transcriptomic analysis. The enrichment of genes involved in the TGF-β

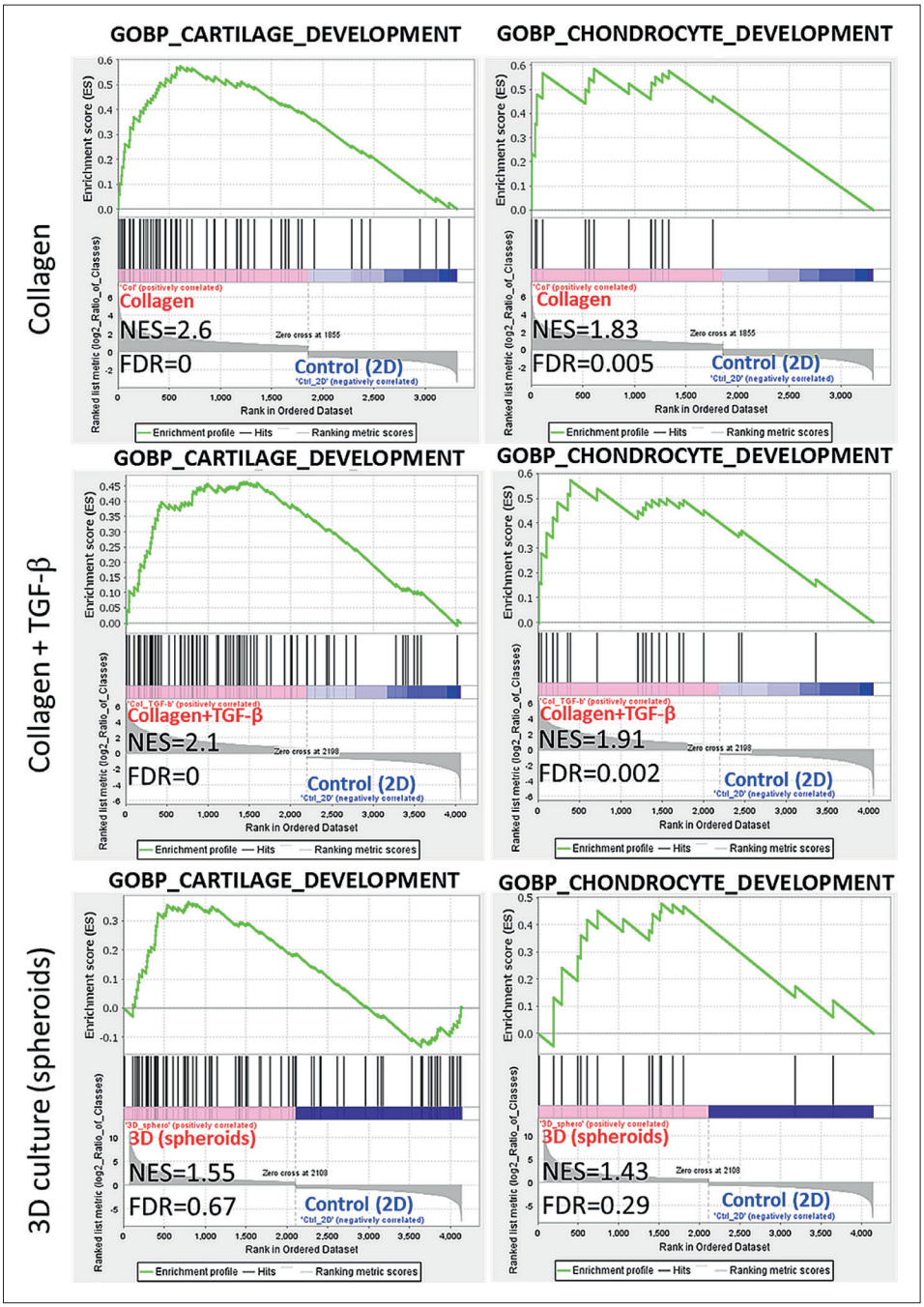

Figure 11. Gene set enrichment analysis of stromal vascular fraction (SVF) cells for chondrogenesis-related transcriptional programs. Enrichment for cartilage and chondrocyte development of SVF cells bioprinted in collagen (left column), in biofunctionalized collagen (middle), and of SVF cells cultured in 3D culture (spheroids/micromasses). Abbreviations: NES: Normalized enrichment score; FDR: False discovery rate adjusted *p*-values.

signaling pathway (17 genes are uniquely upregulated in that bioink; Figure S6, Supporting Information right-hand side) strongly suggests the uptake of the GF by the cells within the prints. Likewise, the enrichment of genes related to cartilage morphogenesis and development, particularly those related to proteoglycan and glycosaminoglycan metabolic processes (Figure 13), reveals the effect of biofunctionalization.

Of note, the transcriptomic analysis also suggested another important point if SVF cells were to be differentiated into chondrocytes; TGF-β induces chondrogenesis gene expression, but it can also drive cell differentiation via other

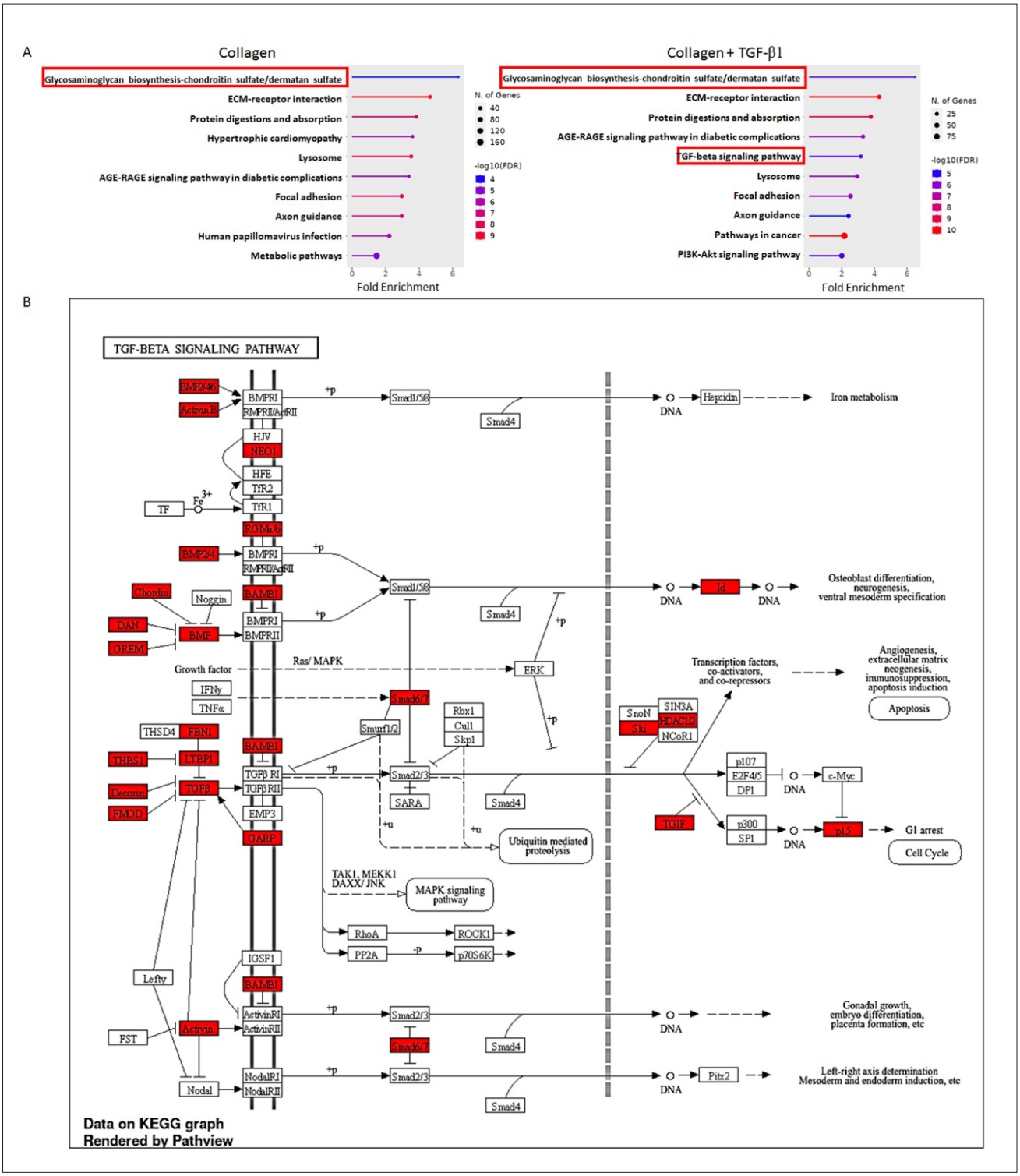

Figure 12. Analysis of upregulated genes in bioprinted stromal vascular fraction (SVF) cells. (a) Gene ontology analysis of the upregulated genes in cells printed in collagen or collagen and TGF-β1, featuring the top 10 enriched processes these genes are involved in. (b) Pathway visualization (KEGG pathways) of the upregulated genes involved in TGF-β signaling in SVF cells bioprinted in functionalized collagen. Red boxes highlight pathways of interest relevant to chondrogenesis. Abbreviation: FDR: False discovery rate.

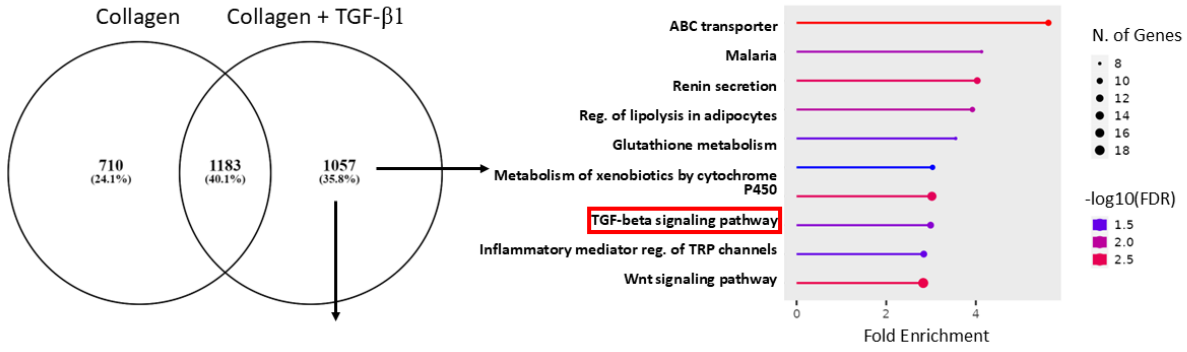

GO-term	Description	Count in network	Strength (log10 enrichment)	FDR
GO:0060536	Cartilage morphogenesis	5 of 10	1.01	0.0426
GO:0030501	Positive regulation of bone mineralisation	11 or 44	0.71	0.0079
GO:0045667	Regulation of osteoblast differentiation	22 of 125	0.56	0.0006
GO:0006029	Proteoglycan metabolic process	13 of 80	0.52	0.0381
GO:0051216	Cartilage development	22 of 167	0.43	0.0121
GO:0060348	Bone development	30 of 216	0.45	0.00067
GO:0030203	Glycosaminoglycan metabolic process	16 of 115	0.45	0.0406

Figure 13. Analysis of the genes that are uniquely upregulated by biofunctionalized collagen. (a) Venn diagram (left) of upregulated genes in stromal vascular fraction (SVF) cells bioprinted in pure collagen or collagen and TGF-β, displaying 1057 genes uniquely expressed after 3D bioprinting with functionalized collagen. GO analysis (right) of the unique genes, displaying the top 10 enriched pathways/processes, including enrichment for TGF-β signaling. (b) GO analysis with STRING DB of the abovementioned genes confirms the activation of genes involved in cartilage formation. Abbreviation: FDR: False discovery rate.

undesired pathways (e.g., bone development; Figure 13). This GF has been reported to play different roles in bone morphogenesis, adipogenesis,[55] and carcinogenesis.[56] Therefore, using only TGF-β1 to biofunctionalize bioinks instead of a whole cocktail for the differentiation of MSCs into chondrocytes (as commonly used in standard culture protocols[57]) may be insufficient and may elicit unwanted consequences when applied *in vivo*.

In summary, our research provides compelling evidence that collagen I bioinks robustly support chondrocyte development and can be effectively functionalized with TGF-β1 to significantly enhance chondrogenesis in 3D-bioprinted SVF cells. This represents a crucial advancement in the pursuit of efficient cartilage bioengineering processes, laying a solid foundation for the development of more sophisticated biomaterial formulation strategies.

4. Conclusion

Our study underscores the neglected role of ionic strength in the gelation kinetics of collagen bioinks, demonstrating that modulation of NaCl and PBS concentrations significantly affects gelation. Furthermore, we established the exceptional capability of collagen hydrogels to sequester TGF-β1, a growth factor pivotal in regenerative medicine, achieving over 99% retention with minimal release over an extended period. This stable sequestration provides a robust matrix for therapeutic applications, as evidenced by the successful induction of chondrogenesis in bioinks, confirmed through histomorphological and transcriptomic analyses. These insights not only deepen our understanding of the physical properties that govern bioink behavior but also pave the way for the development of advanced collagen-based hydrogels as effective carriers for the controlled delivery of bioactive molecules, progressing the field of tissue engineering and regenerative medicine.

Acknowledgments

The authors would like to thank (i) Prof. S. Todinova from the Institute of Biophysics and Biomedical Engineering, Bulgarian Academy of Sciences, for her assistance with DSC analysis, and (ii) Assoc. Prof. L. Simova from the Institute

of Plant Physiology and Genetics, Bulgarian Academy of Sciences, for her assistance with SDS-PAGE analysis.

Funding

This work was supported by the Bulgarian National Innovation Fund (grant number: 13IF-02-9/07.12.2022).

Conflict of interest

The authors declared the following potential conflicts of interest concerning the research, authorship, and/or publication of this article: M.R. is the majority owner and Managing Director of MatriChem, Ltd., which markets the collagen used in this study. A.V., H.P., and A.G. are MatriChem employees. No conflicts of interest concerning the research, authorship, and/or publications exist for all other authors.

Author contributions

Conceptualization: Murad Redzheb, Yordan Sbirkov, Victoria Sarafian

Formal analysis: Murad Redzheb, Yordan Sbirkov

Funding Acquisition: Murad Redzheb, Yordan Sbirkov, Victoria Sarafian

Investigation: Murad Redzheb, Yordan Sbirkov, Atanas Valev, Vasil Dzharov, Hristi Petrova, Tatyana Damyanova, Ani Georgieva

Project Administration: Murad Redzheb, Yordan Sbirkov, Victoria Sarafian

Writing – Original Draft: Murad Redzheb, Yordan Sbirkov

Writing – Review & Editing: Murad Redzheb, Yordan Sbirkov, Victoria Sarafian

Ethics approval and consent to participate

Not applicable.

Consent for publication

Not applicable.

Availability of data

Sequencing data is available on the Gene Expression Ombinus (GEO) under accession number GSE271638. (https://www.ncbi.nlm.nih.gov/geo/query/acc.cgi?acc=GSE271638).

References

1. Dhavalikar P, Lan Z, Kar R, Salhadar K, Gaharwar AK, Cosgriff-Hernandez E. Biomedical applications of additive manufacturing. In: *Biomaterials Science*. 4th ed. San Diego, USA: Elsevier; 2020:623-639. doi: 10.1016/B978-0-12-816137-1.00040-4

2. Sagi I, Afratis NA. *Collagen*. Vol 1944. In: Sagi I, Afratis NA, eds. New York, NY: Springer; 2019. doi: 10.1007/978-1-4939-9095-5

3. Osidak EO, Kozhukhov VI, Osidak MS, Domogatsky SP. Collagen as bioink for bioprinting: a comprehensive review. *Int J Bioprint*. 2024;6(3):270. doi: 10.18063/ijb.v6i3.270

4. Li Z, Ruan C, Niu X. Collagen-based bioinks for regenerative medicine: fabrication, application and prospective. *Med Nov Technol Devices*. 2023;17(37):100211. doi: 10.1016/j.medntd.2023.100211

5. Stepanovska J, Supova M, Hanzalek K, Broz A, Matejka R. Collagen bioinks for bioprinting: a systematic review of hydrogel properties, bioprinting parameters, protocols, and bioprinted structure characteristics. *Biomedicines*. 2021;9(9):1137. doi: 10.3390/biomedicines9091137

6. Marques CF, Diogo GS, Pina S, Oliveira JM, Silva TH, Reis RL. Collagen-based bioinks for hard tissue engineering applications: a comprehensive review. *J Mater Sci Mater Med*. 2019;30(3):32. doi: 10.1007/s10856-019-6234-x

7. Li Y, Asadi A, Monroe MR, Douglas EP. pH effects on collagen fibrillogenesis *in vitro*: electrostatic interactions and phosphate binding. *Mater Sci Eng C*. 2009;29(5):1643-1649. doi: 10.1016/j.msec.2009.01.001

8. Rezabeigi E, Griffanti G, Nazhat SN. Effect of fibrillization ph on gelation viscoelasticity and properties of biofabricated dense collagen matrices via gel aspiration-ejection. *Int J Mol Sci*. 2023;24(4):3889. doi: 10.3390/ijms24043889

9. Kalbitzer L, Pompe T. Fibril growth kinetics link buffer conditions and topology of 3D collagen I networks. *Acta Biomater*. 2018;67:206-214. doi: 10.1016/j.actbio.2017.11.051

10. Li Y, Douglas EP. Effects of various salts on structural polymorphism of reconstituted type I collagen fibrils. *Colloids Surf B Biointerfaces*. 2013;112:42-50. doi: 10.1016/j.colsurfb.2013.07.037

11. Achilli M, Mantovani D. Tailoring mechanical properties of collagen-based scaffolds for vascular tissue engineering: the effects of pH, temperature and ionic strength on gelation. *Polymers (Basel)*. 2010;2(4):664-680. doi: 10.3390/polym2040664

12. Stamov DR, Stock E, Franz CM, Jähnke T, Haschke H. Imaging collagen type I fibrillogenesis with high spatiotemporal resolution. *Ultramicroscopy*. 2015;149:86-94. doi: 10.1016/j.ultramic.2014.10.003

13. Gobeaux F, Mosser G, Anglo A, et al. Fibrillogenesis in dense collagen solutions: a physicochemical study. *J Mol Biol*. 2008;376(5):1509-1522. doi: 10.1016/j.jmb.2007.12.047

14. Zhang J, Wei B, He L, et al. Systematic modulation of gelation dynamics of snakehead (Channa argus) skin collagen by environmental parameters. *Macromol Res*. 2017;25(11):1105-1114. doi: 10.1007/s13233-017-5149-y

15. Harris JR, Reiber A. Influence of saline and pH on collagen type I fibrillogenesis *in vitro*: fibril polymorphism and colloidal gold labelling. *Micron*. 2007;38(5):513-521. doi: 10.1016/j.micron.2006.07.026

16. Harris JR, Soliakov A, Lewis RJ. *In vitro* fibrillogenesis of collagen type I in varying ionic and pH conditions. *Micron*. 2013;49:60-68. doi: 10.1016/j.micron.2013.03.004

17. Salinas-Fernandez S, Garcia O, Kelly DJ, Buckley CT. The influence of pH and salt concentration on the microstructure and mechanical properties of meniscus extracellular matrix-derived implants. *J Biomed Mater Res A*. 2024;112(3):359-372. doi: 10.1002/jbm.a.37634

18. Zhu S, Yuan Q, Yin T, et al. Self-assembly of collagen-based biomaterials: preparation, characterizations and biomedical applications. *J Mater Chem B*. 2018;6(18):2650-2676. doi: 10.1039/c7tb02999c

19. Cooke ME, Rosenzweig DH. The rheology of direct and suspended extrusion bioprinting. *APL Bioeng*. 2021;5(1):011502. doi: 10.1063/5.0031475

20. Xing JY, Yang L, Li YL. Effect of anions on type I collagen fibrillogenesis in aqueous solution. *ISWREP 2011 – Proc 2011 Int Symp Water Resour Environ Prot*. 2011;4: 2975-2978. doi: 10.1109/ISWREP.2011.5893502

21. Zhu J, Kaufman LJ. Collagen I self-assembly: revealing the developing structures that generate turbidity. *Biophys J*. 2014;106(8):1822-1831. doi: 10.1016/j.bpj.2014.03.011

22. Diamantides N, Wang L, Pruiksma T, et al. Correlating rheological properties and printability of collagen bioinks: the effects of riboflavin photocrosslinking and pH. *Biofabrication*. 2017;9(3):034102. doi: 10.1088/1758-5090/aa780f

23. Yang YL, Motte S, Kaufman LJ. Pore size variable type I collagen gels and their interaction with glioma cells. *Biomaterials*. 2010;31(21):5678-5688. doi: 10.1016/j.biomaterials.2010.03.039

24. Lai G, Li Y, Li G. Effect of concentration and temperature on the rheological behavior of collagen solution. *Int J Biol Macromol*. 2008;42(3):285-291. doi: 10.1016/j.ijbiomac.2007.12.010

25. Xie J, Bao M, Bruekers SMC, Huck WTS. Collagen gels with different fibrillar microarchitectures elicit different cellular responses. *ACS Appl Mater Interfaces*. 2017;9(23):19630-19637. doi: 10.1021/acsami.7b03883

26. Tran-Ba KH, Lee DJ, Zhu J, Paeng K, Kaufman LJ. Confocal rheology probes the structure and mechanics of collagen through the sol-gel transition. *Biophys J*. 2017;113(8): 1882-1892. doi: 10.1016/j.bpj.2017.08.025

27. Sarrigiannidis SO, Rey JM, Dobre O, González-García C, Dalby MJ, Salmeron-Sanchez M. A tough act to follow: collagen hydrogel modifications to improve mechanical and growth factor loading capabilities. *Mater Today Bio*. 2021;10(January):100098. doi: 10.1016/j.mtbio.2021.100098

28. Goebel EJ, Hart KN, McCoy JC, Thompson TB. Structural biology of the TGFβ family. *Exp Biol Med*. 2019;244(17): 1530-1546. doi: 10.1177/1535370219880894

29. Shah SS, Mithoefer K. Current applications of growth factors for knee cartilage repair and osteoarthritis treatment. *Curr Rev Musculoskelet Med*. 2020;13(6):641-650. doi: 10.1007/s12178-020-09664-6

30. Johnstone B, Hering TM, Caplan AI, Goldberg VM, Yoo JU. *In vitro* chondrogenesis of bone marrow-derived mesenchymal progenitor cells. *Exp Cell Res*. 1998;238(1):265-272. doi: 10.1006/excr.1997.3858

31. Kundu J, Shim JH, Jang J, Kim SW, Cho DW. An additive manufacturing-based PCL-alginate-chondrocyte bioprinted scaffold for cartilage tissue engineering. *J Tissue Eng Regen Med*. 2015;9(11):1286-1297. doi: 10.1002/term.1682

32. Zhu W, Cui H, Boualam B, et al. 3D bioprinting mesenchymal stem cell-laden construct with core–shell nanospheres for cartilage tissue engineering. *Nanotechnology*. 2018;29(18):185101. doi: 10.1088/1361-6528/aaafa1

33. Hauptstein J, Forster L, Nadernezhad A, Groll J, Teßmar J, Blunk T. Tethered TGF-β1 in a hyaluronic acid-based bioink for bioprinting cartilaginous tissues. *Int J Mol Sci*. 2022;23(2):924. doi: 10.3390/ijms23020924

34. Komsa-Penkova R, Stavreva G, Belemezova K, Kyurkchiev S, Todinova S, Altankov G. Mesenchymal stem-cell remodeling of adsorbed type-I collagen – the effect of collagen oxidation. *Int J Mol Sci*. 2022;23(6):3058. doi: 10.3390/ijms23063058

35. Ge SX, Jung D, Jung D, Yao R. ShinyGO: a graphical gene-set enrichment tool for animals and plants. *Bioinformatics*. 2020;36(8):2628-2629. doi: 10.1093/bioinformatics/btz931

36. Szklarczyk D, Kirsch R, Koutrouli M, et al. The STRING database in 2023: protein-protein association networks and functional enrichment analyses for any sequenced genome of interest. *Nucleic Acids Res*. 2023;51(1D):D638-D646. doi: 10.1093/nar/gkac1000

37. Deyl Z, Mikšík I, Eckhardt A. Preparative procedures and purity assessment of collagen proteins. *J Chromatogr B Anal Technol Biomed Life Sci*. 2003;790(1-2):245-275. doi: 10.1016/S1570-0232(03)00158-2

38. Drzewiecki KE, Grisham DR, Parmar AS, Nanda V, Shreiber DI. Circular dichroism spectroscopy of collagen fibrillogenesis: a new use for an old technique. *Biophys J*. 2016;111(11):2377-2386. doi: 10.1016/j.bpj.2016.10.023

39. Mertz EL, Leikin S. Interactions of inorganic phosphate and sulfate anions with collagen. *Biochemistry*. 2004;43(47):14901-14912. doi: 10.1021/bi048788b

40. Hayashi T, Nagai Y. Factors affecting the interactions of collagen molecules as observed by *in vitro* fibril formation: III. non-helical regions of the collagen molecules. *J Biochem*. 1974;76(1):177-186. doi: 10.1093/oxfordjournals.jbchem.a130543

41. Weinstock A, King PC, Wuthier RE. The ion-binding characteristics of reconstituted collagen. *Biochem J*. 1967;104(3):705_b1-705_b1. doi: 10.1042/bj1040705_b1a

42. Freudenberg U, Behrens SH, Welzel PB, et al. Electrostatic interactions modulate the conformation of collagen I. *Biophys J*. 2007;92(6):2108-2119. doi: 10.1529/biophysj.106.094284

43. Oh S, Nguyen QD, Chung KH, Lee H. Bundling of collagen fibrils using sodium sulfate for biomimetic cell culturing. *ACS Omega*. 2020;5(7):3444-3452. doi: 10.1021/acsomega.9b03704

44. Lien YH, Stern R, Fu JCC, Siegel RC. Inhibition of collagen fibril formation *in vitro* and subsequent cross-linking by glucose. *Science*. 1984;225(4669):1489-1491. doi: 10.1126/science.6147899

45. Sbirkov Y, Molander D, Milet C, et al. A colorectal cancer 3D bioprinting workflow as a platform for disease modeling and chemotherapeuticsScreening. *Front Bioeng Biotechnol*. 2021;9(November):1-12. doi: 10.3389/fbioe.2021.755563

46. Chaudhuri O, Cooper-White J, Janmey PA, Mooney DJ, Shenoy VB. Effects of extracellular matrix viscoelasticity on cellular behaviour. *Nature*. 2020;584(7822):535-546. doi: 10.1038/s41586-020-2612-2

47. Schinagl RM, Gurskis D, Chen AC, Sah RL. Depth-dependent confined compression modulus of full-thickness bovine articular cartilage. *J Orthop Res*. 1997;15(4):499-506. doi: 10.1002/jor.1100150404

48. Beketov EE, Isaeva EV, Yakovleva ND, et al. Bioprinting of cartilage with bioink based on high-concentration collagen and chondrocytes. *Int J Mol Sci*. 2021;22(21):11351. doi: 10.3390/ijms222111351

49. Isaeva EV, Beketov EE, Demyashkin GA, et al. Cartilage formation *in vivo* using high concentration collagen-based bioink with MSC and decellularized ECM granules. *Int J Mol Sci*. 2022;23(5):2703. doi: 10.3390/ijms23052703

50. Gospodinova A, Nankov V, Tomov S, Redzheb M, Petrov PD. Extrusion bioprinting of hydroxyethylcellulose-based bioink for cervical tumor model. *Carbohydr Polym*. 2021;260(February):117793. doi: 10.1016/j.carbpol.2021.117793

51. Sbirkov Y, Redzheb M, Forraz N, McGuckin C, Sarafian V. High hopes for the biofabrication of articular cartilage – what lies beyond the horizon of tissue engineering and 3D bioprinting? *Biomedicines*. 2024;12(3):665. doi: 10.3390/biomedicines12030665

52. Cui X, Gao G, Yonezawa T, Dai G. Human cartilage tissue fabrication using three-dimensional inkjet printing technology. *J Vis Exp*. 2014;(88):1-5. doi: 10.3791/51294

53. Bourin P, Bunnell BA, Casteilla L, et al. Stromal cells from the adipose tissue-derived stromal vascular fraction and culture expanded adipose tissue-derived stromal/stem cells: a joint statement of the International Federation for Adipose Therapeutics and Science (IFATS) and the International So. *Cytotherapy*. 2013;15(6):641-648. doi: 10.1016/j.jcyt.2013.02.006

54. Sang S, Mao X, Cao Y, et al. 3D bioprinting using synovium-derived MSC-laden photo-cross-linked ECM bioink for cartilage regeneration. *ACS Appl Mater Interfaces*. 2023;15(7):8895-8913. doi: 10.1021/acsami.2c19058

55. Grafe I, Alexander S, Peterson JR, et al. TGF-β family signaling in mesenchymal differentiation. *Cold Spring Harb Perspect Biol*. 2018;10(5):1-50. doi: 10.1101/cshperspect.a022202

56. Baba AB, Rah B, Bhat GR, et al. Transforming growth factor-beta (TGF-β) signaling in cancer-A betrayal within. *Front Pharmacol*. 2022;13(February):1-16. doi: 10.3389/fphar.2022.791272

57. Stromps JP, Paul NE, Rath B, Nourbakhsh M, Bernhagen J, Pallua N. Chondrogenic differentiation of human adipose-derived stem cells: a new path in articular cartilage defect management? *Biomed Res Int*. 2014;2014:740926. doi: 10.1155/2014/740926

ACCSCIENCE PUBLISHING

International Journal of Bioprinting

RESEARCH ARTICLE

Fabrication of bacteriorhodopsin-embedded hydrogel construct for biocompatible photosensitive device

Mian Wu[1,2,3], Feng Lin[1,2,3], and Yu Song [1,2,3]*

[1] Department of Mechanical Engineering, Tsinghua University, Beijing, China

[2] Biomanufacturing and Rapid Forming Technology Key Laboratory of Beijing, Beijing, China

[3] Key Laboratory of Advanced Materials Processing Technology of Ministry of Education, Beijing, China

Abstract

Bacteriorhodopsin (br) is a promising photosensitive material with applications in energy conversion, biosensors, and optoelectronic devices due to its bio-sourced origin and photoelectrical properties. Despite advancements in recent years, the integration of br-based devices necessitates the use of materials with little biocompatibility and fabrication techniques with restricted customizability, limiting potential applications such as optocontrol of cell behavior, implants with 3D patterning for retinal disease treatment, and light-sensitive cell robots. To solve this limitation, this study presents a novel approach by embedding br into a hydrogel matrix. It utilizes an extrusion-based and 3D bioprinting technique, showcasing its light-sensitive characteristics within a fully biocompatible construct. The hydrogel, comprising gelatin and sodium alginate, offers excellent printability for generating structured designs with versatile patterns. Photoelectrical properties of the fabricated br-embedded hydrogel construct, such as differential response, light intensity sensitivity, and br concentration sensitivity, are identified through electrochemical characterization. The temporal and spatial pattern recognition ability, based on the photoelectrical characteristics, is demonstrated through modulated light illumination and different patterns of printed hydrogel construct. Pattern recognition ability was then applied to reconstruct images containing different Latin letters. This research presents a novel method for the fabrication of patterned hydrogel constructs with high biocompatibility and distinctive light-responsive properties, expanding the potential applications of br in bio-related scenarios.

Keywords: Bacteriorhodopsin; Hydrogel construct; Photoelectrical response; Pattern recognition

***Corresponding author:**
Yu Song
(y-song@mail.tsinghua.edu.cn)

Citation: Wu M, Lin F, Song Y. Fabrication of bacteriorhodopsin-embedded hydrogel construct for biocompatible photosensitive device. *Int J Bioprint*. 2024;10(6):4454. doi: 10.36922/ijb.4454

Received: August 6, 2024
Revised: September 11, 2024
Accepted: September 24, 2024
Published Online: September 25, 2024

Copyright: © 2024 Author(s). This is an Open Access article distributed under the terms of the Creative Commons Attribution License, permitting distribution, and reproduction in any medium, provided the original work is properly cited.

Publisher's Note: AccScience Publishing remains neutral with regard to jurisdictional claims in published maps and institutional affiliations.

1. Introduction

Devices fabricated from biomaterials offer significant advantages in terms of biocompatibility, low toxicity, and minimal environmental impact.[1,2] An effective strategy for developing biomaterial-based devices involves integrating functional proteins, including photosensitive,[3] thermosensitive,[4] and pressure-sensitive.[5] proteins.

Bacteriorhodopsin (br), a photosensitive membrane protein derived from *Halobacterium salinarum*,[6-13] serves as a key component in the development of biosensors,[14-26] energy harvesters[27-43] and other applications.[44-49] Integrating br into functional devices leverages its inherent structural and functional, enabling operation under varying temperatures, pH levels, and environmental conditions, thereby providing a robust foundation for sustained performance. Additionally, br's responsiveness to the entire visible light spectrum enhances its utility in applications such as optical sensing and renewable energy conversion, marking it as a versatile and resilient component in photosensitive protein-based devices.

The bio-sourced nature of br makes it an ideal material for the optocontrol of cell behavior, offering an alternative to optogenetic tools for manipulating cellular functions, such as the contraction of cardiomyocytes and the activity of nerve cells. Furthermore, the structural and functional similarities between br and rhodopsin in human retinal photoreceptor cells[50] suggest br's potential in treating retinal diseases through the fabrication of biodegradable hydrogel implants. These implants would allow precise control over both their shape and the concentration of br. Moreover, integrating br-embedded hydrogel into cell-robot assembly introduces the possibility of opto-controlled systems, which could provide significant advantages over direct electrical stimulation, including non-intrusiveness and electrode-free operation, thus expanding the potential for biohybrid robotic applications. However, these potential applications introduce specific requirements for br integration, including biocompatibility, 3D patterning ability, and versatility in the design and fabrication of br-based devices. The absence of these properties in current research limits the adaptability and broader application of br. In ongoing studies, br is typically used as a photo-responsive catalyst, applied as a coating on substrates to create a photoanode. These photoanodes typically consist of inflexible and non-biocompatible substrates, including materials such as indium tin oxide (ITO)/fluorine-doped tin oxide (FTO) glass,[21,30,41,51,52] anodic alumina oxide (AAO) nanochannel,[37] gallium nitride (GaN) nanowall network (NWN),[28] TiO_2,[31,35,51-54] etc. In addition to non-biocompatible material, current research is also limited due to the lack of study on the concentration of br molecule and its impact on photoelectrical performance. Hasegawa et al.[19] demonstrated the contribution of br concentration to the photocurrent via 2D inkjet patterning, whereas the 3D patterning of br, which is essential to its biomaterial-related applications, required more research. Despite the application in various fields, the lack of research on br integrated with highly biocompatible materials prompts the need for exploring alternative materials and configurations, and the lack of research on 3D patterning of br with varying concentration warrants an accurate, efficient, and versatile fabrication technique to realize the controlled spatial distribution. Only by solving the problems mentioned above can br be better integrated into devices to suit scenarios such as tissue engineering, organoids, and regenerative implants. The photoelectrical properties of br stand at the center of the application of br-based devices. In past research, br films have demonstrated a consistent and distinctive photoelectrical response that is differential and light intensity-sensitive[55]; the photoelectrical properties of br embedded in 3D-printed hydrogel rather than immobilized as films require more characterization to demonstrate the preservation of its function. While studies have demonstrated the photosensitive feature of br in hydrogel,[56-58] the performance of br-embedded hydrogel, including the light intensity sensitivity, and the structure-property relationship needs more detailed research.

This study addressed the aforementioned challenges through the fabrication of a br-embedded hydrogel construct. This was achieved through the integration of br with a highly printable composite hydrogel, using extrusion printing to create a hydrogel-based construct. Hydrogels, due to their ease of molding, high biocompatibility, and flexible composition, have found extensive applications in tissue engineering and regenerative medicine. In the field of biosensing, hydrogels, benefiting from their flexibility and high biocompatibility, are utilized for the fabrication of hydrogel-based wearable epidermal sensors, emerging as popular choices in digital healthcare.[59-62] The hydrogel used in this study, composed of alginate and gelatin, exhibited commendable biocompatibility and mechanical properties, comparable to those of human tissues, making it suitable for the fabrication of cell-friendly structures. The fabrication technique involving extrusion-based 3D printing of hydrogel is widely used in the field of tissue engineering, where cells are embedded in the hydrogel and printed to form a 3D pattern. This 3D printing method is believed to be advantageous to 2D patterning, as it provides an environment similar to *in vivo*[63,64]; the protein-based ink, such as the composite hydrogel mentioned above, exhibits desired structural strength, chemical component, and other features such as bio-combability and degradability.[60] However, the 3D printing of functional protein rather than structural protein remains understudied, calling for more research on the fabrication technique of functional protein and the structure-property relationships. In this study, a br-embedded hydrogel construct was fabricated using extrusion-based 3D printing. The excellent printability and biocompatibility of hydrogel, combined with the versatility of the fabrication technique, provide a novel method for the device integration of functional proteins such as br. The

fabricated structure preserves the photosensitive nature of br and exhibits desirable photoelectrical properties, such as light intensity sensitivity, concentration sensitivity, and advanced functions such as pattern recognition. These results lay the groundwork for further innovative applications of br through biocompatible material, versatile fabrication techniques, and comprehensive photoelectrical characterization.

2. Methods

2.1. Fabrication of br-embedded hydrogel construct

Figure 1A illustrates the fabrication process of the hydrogel construct. Bacteriorhodopsin (br; lyophilized powder; Sigma-Aldrich, USA) was dissolved in Dulbecco's phosphate-buffered saline (DPBS; Sigma-Aldrich, USA) at a concentration of 1 mg/mL, resulting in a uniformly pale purple solution after ultrasonic oscillation. The printing material containing br was prepared by combining 400 μLof the solution with 200 μL of gelatin solution (20 wt% in DPBS) and 100 μL of sodium alginate solution (1 wt% in DPBS). The mixture was heated to 45°C and thoroughly mixed for 20 s using a vortex mixer. An ITO glass measuring 30 × 20 mm with a surface resistance of 8 Ω/m^2 was sonicated in ethanol, acetone, and deionized (DI) water to prepare the printing substrate. The well-mixed printing system was drawn into a 1 mL syringe, pre-chilled in a 4°C refrigerator for 10 min, and then loaded into a printer (Biomakers; SunP Biotech, China). The nozzle and the ITO glass substrate were cooled to 13 and 10°C, respectively, before printing. The printing speed was set to 5 mm/s, and the extrusion speed was set to 0.8 mm^3/min. Following printing, 500 μL of $CaCl_2$ solution (2% wt in DI water) was applied to immerse the printed structures to facilitate the crosslinking of sodium alginate. After 3 min, the $CaCl_2$ solution was aspirated, and the ITO glass with the printed structures was placed in a 65 mm Petri dish. DI water was added to prevent the structures from dehydrating. The Petri dish was sealed with Parafilm and stored in the dark at 4°C for future use.

2.2. Characterization of printing material and structure

The printed br-embedded hydrogel structure was observed under an optical microscope (SMZ800N; Nikon, Japan) to determine if it was crosslinked properly. To distinguish hydrogel structure with varying br concentration, hydrogel with high br concentration was dyed with Coomassie brilliant blue G-250, while hydrogel with low br concentration was dyed with grape skin anthocyanin. The printed construct was freeze-dried at −60° overnight in a lyophilizer (LGJ-12; SONGYUANHUAXING Technology, China) and then observed using a scanning electron microscope (SEM; Zeiss GeminiSEM 300; Zeiss, Germany). The surface of the freeze-dried construct was carefully trimmed to reveal part of the internal structure. The UV-VIS absorption spectrum of printing material containing br was measured using a spectrometer (U-3900; HITACHI, Japan) with hydrogel containing no br as a reference. The scan range was set to 250–700 nm. The material to be measured was heated up to 45° in a metal bath to increase its liquidity. Subsequently, it was transferred to an Eppendorf UVett™ and cooled to room temperature before conducting the absorption spectrum test.

Rheological measurement was performed using a rotational rheometer (MCR302; Anton Paar, Austria) in oscillatory mode. The strain and frequency were set to 1% and 1 Hz, respectively. Cone-plate geometry with a 25 mm diameter, 2' cone, and a 99 μm truncation gap was used. G′ is defined as the storage modulus, and G′ is defined as the loss modulus. The printing material was heated up to 30° using a metal bath before being transferred to the rheometer. The temperature sweep was performed at 20–30°, and 70 sample points were recorded. A shear rate-viscosity test was then performed at 21°. The shear rate ranges from 0.1 to 1000 1/s, and 100 sample points were recorded.

Biocompatibility was assessed by loading neural progenitor cells (NPCs) obtained through the method described in previous research[65] onto the br-embedded hydrogel. A cell suspension was mixed with gelatin/sodium alginate hydrogel containing br, and fibrinogen was added to enhance NPC adaptability. To evaluate cell viability using a live-dead assay, Calcein AM and propidium iodide (PI) (DOJINDO, Japan) were applied to the construct, and images were captured using laser scanning confocal microscopy (TI-FL; Nikon, Japan). A calcium assay was subsequently conducted to assess neural function. Fluo 4-AM (DOJINDO, Japan) was applied to the construct, and time-lapse images were acquired using a laser confocal microscope (FV3000; Olympus, Japan) under 488 nm laser excitation. Further details regarding the biocompatibility assessment methods can be found in Gai's work.[65]

2.3. Photoelectrochemical characterization

The br-embedded hydrogel construct on the ITO glass substrate was positioned on the sample stage of a probe workstation (Chuangpu Instrument, China) and examined using a microscope. A droplet of electrolyte (DPBS, pH 8) was dispersed onto the br-embedded hydrogel and covered with another ITO glass, constructing a photovoltaic cell with a layered structure. The photovoltaic cell was then connected to an electrochemical workstation (CHI660E; Shanghai ChenHua, China), with the br-embedded hydrogel-attached ITO glass connected to the working electrode, and the other ITO glass connected to the counter and reference electrode. A white light-emitting diode (LED) with adjustable light

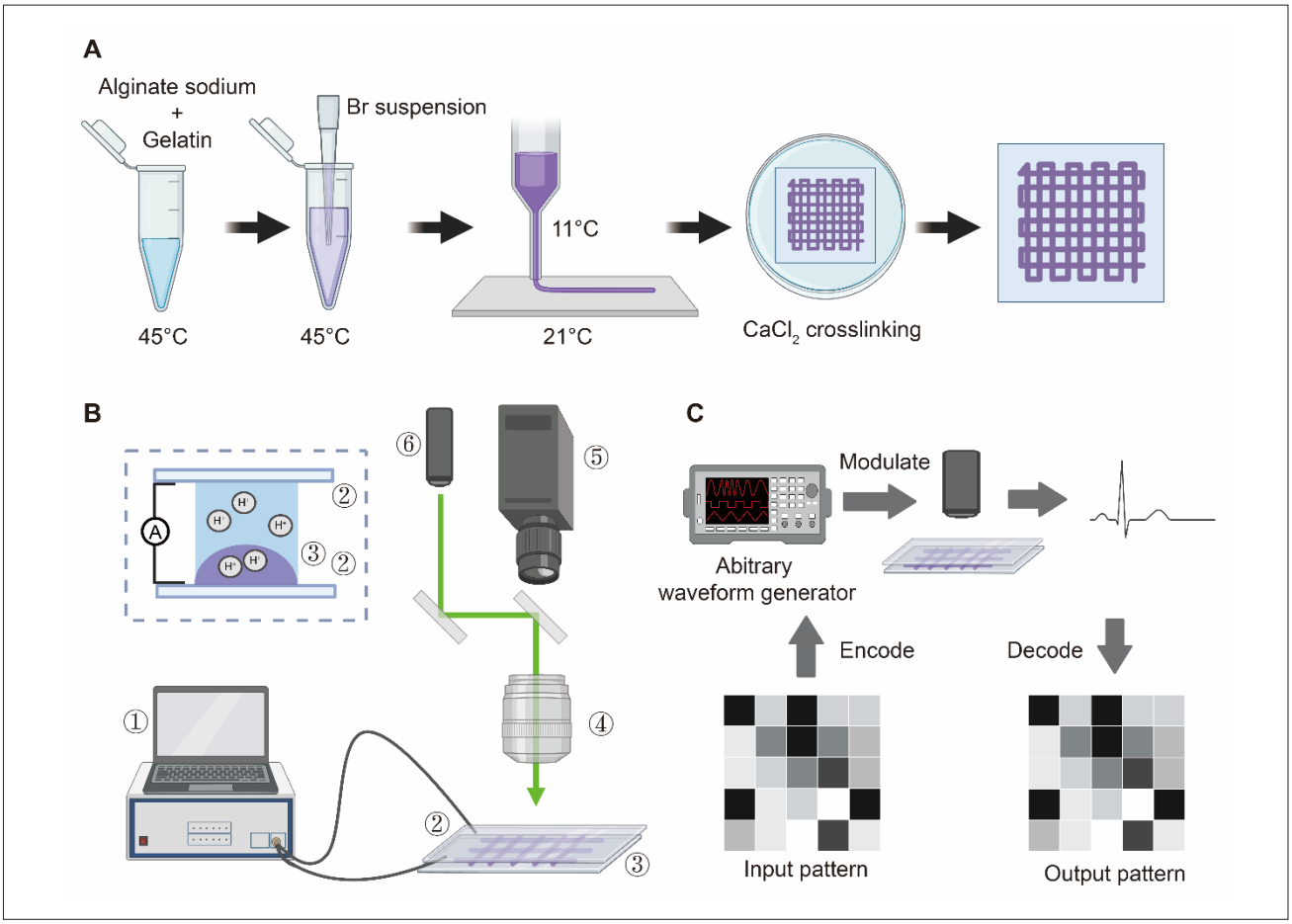

Figure 1. Schematics of fabrication, characterization, and application of bacteriorhodopsin (br)-embedded hydrogel construct. (A) Schematics of the fabrication process of the br-embedded hydrogel construct. Alginate sodium, gelatin, and br solution were mixed at 45°C to ensure thorough blending. The mixed material was then loaded into the nozzle of a 3D printer and cooled to 21°C, which is close to the sol–gel transformation temperature. The substrate was cooled to 11°C to initiate thermal crosslinking of gelatin, and the printed structure was immersed in a $CaCl_2$ solution to further ionic crosslink sodium alginate. The dual-crosslinking procedure ensures a stable structure and excellent printability. (B) The setup for photoelectrochemical characterization of br-embedded hydrogel. A microscope objective was connected to a 543 nm laser generator to illuminate the hydrogel. The surface of the bottom and the top indium tin oxide (ITO) glass were connected to the electrochemical workstation for data acquisition: 1: electrochemical workstation; 2: ITO glass; 3: br-embedded construct; 4: objective reflector; 5: charge-coupled device (CCD) camera; 6: laser generator. (C) Schematics of the pattern recognition setup utilizing the photoelectrical properties of br-embedded hydrogel. The input pattern was pixelized to a 5 × 5 grid, and each line consisting of 5 pixels was encoded to a specific waveform, which was generated through the arbitrary wave generator and transmitted to the temporal modulation of the laser. The photoelectric response of br-embedded hydrogel corresponding to the modulated laser was then recorded and decoded to an output pattern that stores the pixelized information of light intensity of the input pattern.

intensity served as the continuous-wave light source, and a green laser generator (λ = 543 nm; Yuanming Laser Technology, China) was used as the monochromatic light source (Figure 1B). Light intensity was measured using a spectrometer (HP330; Duotone Cloud, China). For photoelectrochemical tests, the photocurrent of the hydrogel construct was recorded employing the i-t mode (sensitivity: 10^{-7}, sampling rate: 50 Hz). Additionally, the linear sweep voltammetry tests were conducted in both dark and light illumination conditions (voltage range: 0–0.2 V). Hydrogel constructs with varying br concentrations were prepared by adjusting the volume of br suspension in the printing material (1×: 100 μL in 700 μL; 2×: 200 μL in 700 μL; 3×: 300 μL in 700 μL; 4×: 400 μL in 700 μL) and then fabricated onto an ITO glass substrate. The photoelectrical response was subsequently measured for different concentrations of br under the same light-intensity conditions.

2.4. Pattern recognition

Temporal pattern recognition was accomplished by encoding pixelized images into time-modulated illumination and decoding photocurrent responses. An arbitrary waveform generator (AWG; SDG 1022X; Siglent, China) was configured to produce square waves and

staircase waves with various waveform characteristics. The AWG was linked to the 543 nm green laser generator to modulate the light source using transistor-transistor logic (TTL) and AC modulation. The modulated light was subsequently employed as light stimuli on the photovoltaic cell based on the br-embedded hydrogel construct. This hydrogel construct was then connected to the electrochemical workstation to record the photocurrent data. To characterize the spatial pattern recognition function, br-embedded hydrogel was fabricated into distinctive patterns, and the photocurrent data of the captured under the illumination of a moving laser spot. Three hydrogel patterns, containing one to three parallel hydrogel filaments, respectively, were fabricated onto an ITO glass substrate and constructed to form three photovoltaic cells. The 543 nm green laser was focused to form a laser spot of 2 mm diameter and moved across the photovoltaic cells at a constant speed. The photoelectrical response was then recorded using the electrochemical workstation, which was used to reconstruct the spatial pattern of the hydrogel construct (Figure 1C).

2.5. Statistical analysis

All values are expressed as the mean ± standard deviation and were analyzed using Prism software (GraphPad Inc., USA). Statistical analysis was performed using Student's *t*-test or one-way analysis of variance (ANOVA).

3. Results

3.1. Hydrogel construct fabrication and characterization

The hydrogel exhibited excellent printability, resulting in a clear, patterned construct with varying br concentration (Figure 2A). The blue hydrogel filament indicates high br concentration, while the red filament represents low br concentration, demonstrating the capability of fabricating hydrogel structure with varying br concentration using extrusion-based printing. A slightly over-crosslinked hydrogel construct (Figure 2B) demonstrated suitability for functional devices due to its high mechanical strength.[66] Over-crosslinked (Figure 2B), well-crosslinked, (Figure 2C), and under-crosslinked (Figure 2D) hydrogel filaments were fabricated by adjusting the temperature of the printing nozzle, leveraging gelatin's thermal crosslinking properties. In addition to flexibility, the porous structure of the hydrogel pattern (Figure 2E–G) facilitates proton transfer.

The rheological characteristics are crucial for printing materials undergoing sol–gel transformation. The hydrogel, composed of sodium alginate and gelatin, underwent dual crosslinking to optimize both printability and structural integrity. Gelatin's thermal crosslinking allowed for precise viscosity control via temperature adjustment. The printing material with and without br exhibited similar rheological behavior, with only a 1°C difference in sol–gel transformation temperature. In this study, the nozzle temperature was set at 20°C, slightly lower than the sol–gel transformation point (Figure 2H), resulting in a slightly over-crosslinked structure. Meanwhile, the substrate was cooled to 11°C, accelerating the gelatin's crosslinking kinetics. Sodium alginate was selected for its suitability in extrusion-based printing due to its shear-thinning properties (Figure 2I). The incorporation of Ca^{2+} ionic crosslinking further enhanced the structural robustness, ensuring stability above the sol–gel transition temperature. The calcium alginate (Figure 2F), formed during ionic crosslinking, protected the construct from environmental effects. The rheological profile supports sodium alginate/gelatin dual-crosslinking as an excellent choice for the intricate fabrication of the br-embedded hydrogel construct. With the hydrogel's exceptional printability and the versatility of extrusion-based printing, various structural patterns can be achieved. Furthermore, the characteristic absorption peak of br was well-preserved, and the crosslinking process did not affect the absorption spectrum (Figure 2J). The absorption spectrum confirmed the retention of the br molecule within the hydrogel, displaying minimal changes in peak absorption wavelength and intensity after immersing the br-embedded hydrogel in DPBS for seven days (Figure S1, Supplementary File). This indicates the functional stability of the br-embedded hydrogel in aqueous environments. A swelling experiment was conducted to assess the morphological stability of the hydrogel. The weight and diameter of the hydrogel structure increased significantly following ionic crosslinking of sodium alginate and remained relatively stable for 36 h, with no significant changes observed (Figure S2, Supplementary File). These findings demonstrate that the br-embedded hydrogel maintains structural integrity and consistent morphology post-fabrication.

In addition to its excellent printability, the br-embedded hydrogel demonstrated high biocompatibility when combined with NPCs (Figure S3, Supplementary File). A live-dead assay conducted on day 1 revealed an average cell viability of 91.09%, indicating that the br-embedded hydrogel is well-suited as a supportive matrix for cell encapsulation. Moreover, a calcium assay confirmed neural activity in NPCs embedded within the hydrogel after six days of culture. These results highlight the br-embedded hydrogel as a promising biocompatible material for biological applications.

3.2. Photoelectrochemical characterization

When exposed to light, br induces a flow of protons through protonation and deprotonation, resulting in

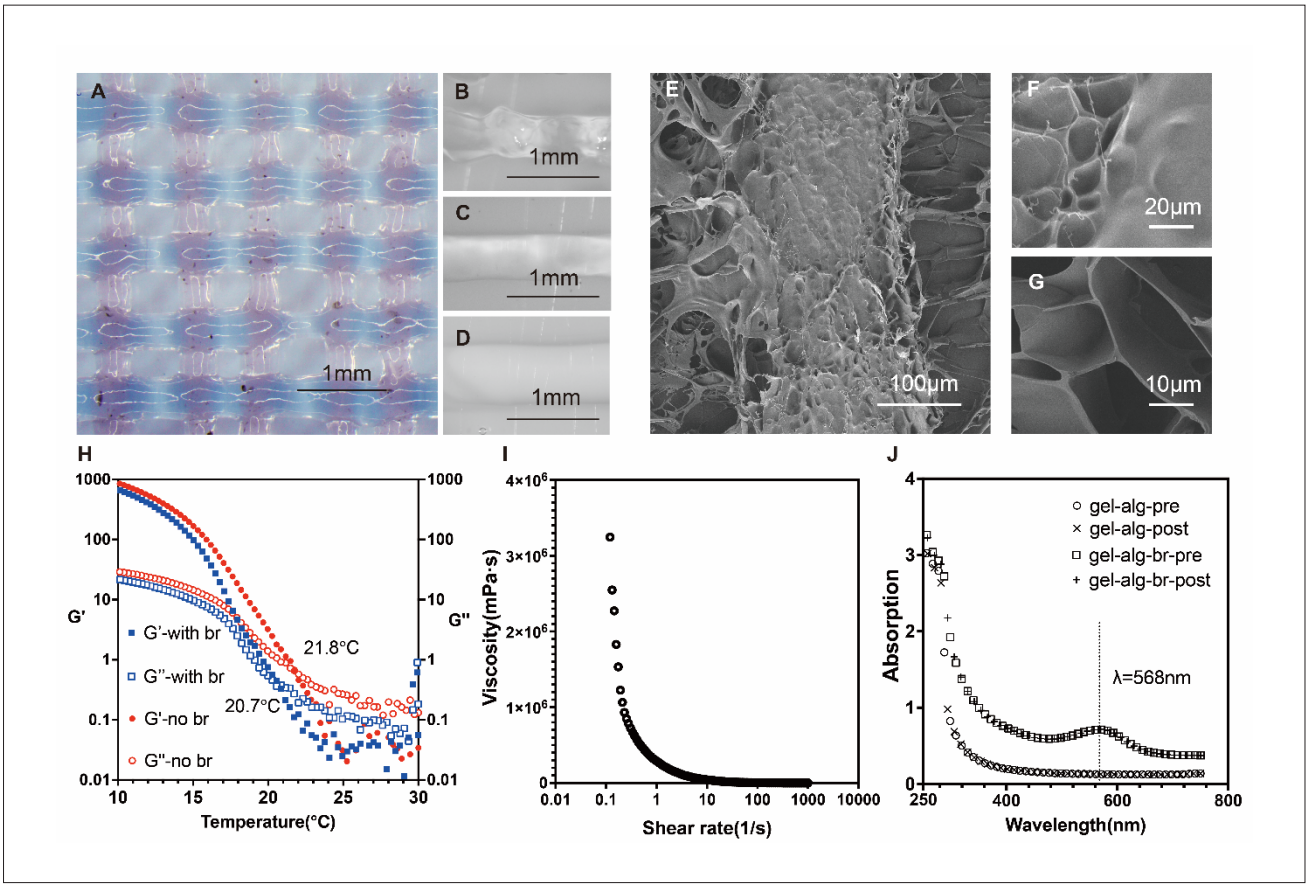

Figure 2. Topographical characterization of the fabricated hydrogel construct and the printability of the hydrogel. (A) Fabricated bacteriorhodopsin (br)-embedded hydrogel construct with varying br concentrations. The blue filament represents a high concentration, while the red filament represents a low br concentration. (B) Hydrogel filament printed at 19°C, where a lower crosslinking temperature resulted in an over-crosslinked filament. (C) Hydrogel filament printed at 21°C, resulting in a well-crosslinked filament. (D) Hydrogel filament printed at 23°C, where a higher crosslinking temperature resulted in an under-crosslinked filament. (E) Scanning electron microscopy (SEM) image of the br-embedded hydrogel construct. (F) SEM image of the dried hydrogel filament from the br-embedded hydrogel construct. The sodium alginate film (right half of the image) formed through ionic crosslinking provides additional mechanical strength. (G) The porous hydrogel structure allows free proton transfer within the construct. (H) The relationship between loss modulus (G″) and storage modulus (G′) with respect to temperature. (I) The printing material exhibits shear-thinning behavior due to the presence of sodium alginate. Shear-thinning is critical for extrusion-based printing methods, as it allows the material to flow through the nozzle while maintaining its structure after printing. (J) UV-VIS absorption spectrum of hydrogels with and without br. The br-embedded hydrogel exhibits an absorption peak around 568 nm, corresponding to the retinal absorption peak in br. No significant difference in the absorption spectrum was observed before and after crosslinking. Scale bars: 1 mm (A–D); 100 μm (E); 20 μm (F); 10 μm (G). Abbreviations: gel-alg-pre: Hydrogel without br before crosslinking; gel-alg-post: Hydrogel without br after crosslinking; gel-alg-br-pre: Hydrogel with br before crosslinking; gel-alg-br-post: Hydrogel with br after crosslinking.

the generation of a photocurrent when utilized as a photoanode, as evidenced in prior studies.[19,21,29,55] In a constructed three-electrode photovoltaic cell with br integrated into a hydrogel acting as the working electrode, the photoelectrochemical analysis revealed a differential pattern of photocurrent under continuous illumination, corresponding to the differential response associated with br-based photovoltaic cells in which br functions in the form of thin films. The typical photoelectrical response (Figure 3A) is a composite waveform consisting of a differential response and a square wave-like response. This response does not come solely from the photosensitive character of br, but rather the combination of the proton pumping function of br and the effect of ITO conduction change. Specifically, the differential part of the response comes from the br molecule in the hydrogel, and the square-wave part of the response comes from the change of the potential of ITO glass under illumination (Figure 3B). The ITO glass, even without photosensitive protein, exhibits a square-wave photoelectric response in our experiment. This could potentially stem from the heat effect of light, as heating the ITO glass directly leads to a similar result. Therefore, a white LED, with a peak spectrum of 443 nm, could contribute to the square

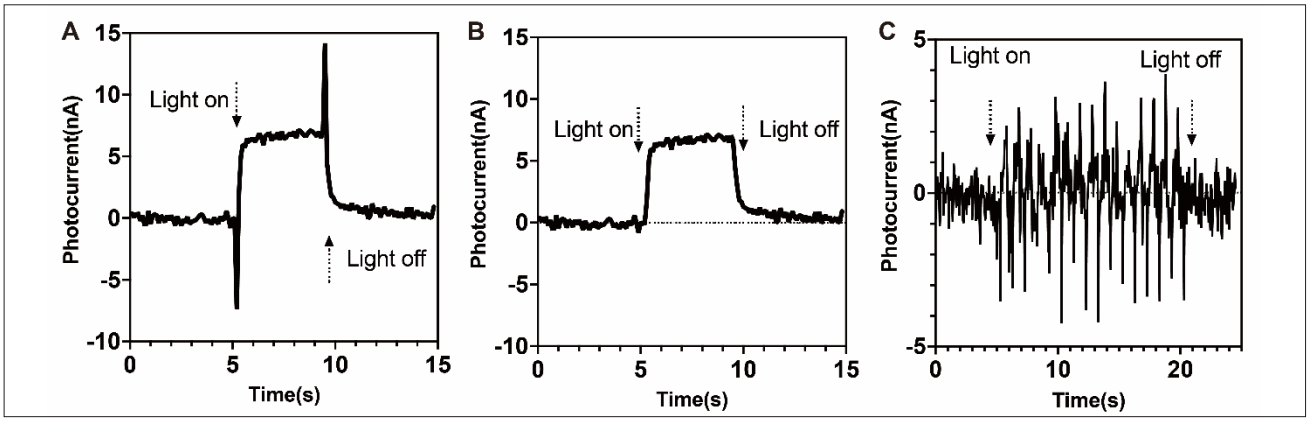

Figure 3. Photoelectric response of bacteriorhodopsin (br)-embedded hydrogel construct. (A) The composite square-differential photoelectrical response of hydrogel construct containing br. A constant photocurrent and a differential response were observed when the construct was illuminated by white LED with a wavelength span of 420–700 nm. (B) The square-wave photoelectric response of a hydrogel construct containing no br. The square-wave response originated from the indium tin oxide (ITO) glass substrate under the illumination of white LED. (C) The pure differential photoelectrical response of the br-embedded hydrogel construct under pulsing light with 1 Hz frequency from a 543 nm laser. No square-wave photoelectrical response was observed.

wave response of ITO glass due to the heating effect of its blue light component. To validate this hypothesis, a 543 nm green laser, containing no blue light component and having significantly less heat effect, was utilized for the photoelectrical characterization, and pure differential photoelectrical response was observed (Figure 3C). These results explained the composite photoelectrical response of the br-embedded hydrogel construct immobilized on the ITO glass substrate under the illumination of a white LED light source. Therefore, the 543 nm green laser light source was used in the pattern recognition experiment as it introduces no observable artifacts.

The differential response, which refers to the response of the material to changes in light intensity rather than the light itself, is a critical characteristic of the photoelectrical response of br. This phenomenon is commonly observed in devices incorporating br films as photosensitive elements.[21,26,55,67] When br is immobilized as thin films on an electrode, exposure to light leads to the transfer of protons to the electrode, resulting in the generation of a potential difference between the electrodes. This potential difference gradually diminishes as it drives the electron movement, thereby causing the differential response.[68] The photovoltaic mechanism of the br molecule in the hydrogel is thus very similar, if not identical, to that of the br molecule in a solid film, where the br molecule facilitates proton transfer between the working electrode and the electrolyte. Nevertheless, there are several distinctions between br-embedded hydrogel and br films. For instance, in a three-electrode photovoltaic cell configuration in this study, the br molecules embedded in the hydrogel can only produce detectable photocurrent when they are closely attached to the working electrode, whereas in a br film-based device, nearly all br molecules contribute to the photoelectric response as they are all attached to the working electrode. Additionally, in the br-embedded hydrogel, protonation and deprotonation occur within the hydrogel environment, while in a br film-based photovoltaic cell, these processes take place in the liquid aqueous environment. Since proton mobility is restricted in the hydrogel matrix, this could also lead to a reduction in the photocurrent of br-embedded hydrogel. Consequently, the photocurrent generated by the br-embedded hydrogel in a three-electrode photovoltaic setup is notably lower than the photocurrent produced by the br film under the same light intensity.

In addition to the amperometric i-t mode, linear sweep voltammetry and open circuit potential-time mode were employed to further characterize the photoelectrochemical properties of the br-embedded hydrogel. In the linear sweep voltammetry test, a 5 Hz pulsing laser served as the light source, and data was recorded both with and without illumination. The difference between the two linear sweep voltammetry curves is illustrated in Figure 4A, displaying an alternating photocurrent under illumination. The open circuit potential-time analysis (Figure 4B) displayed a differential response pattern similar to the photocurrent curve in Figure 3A, where an initial upward peak was noted at the onset of illumination, followed by a subsequent downward peak after the illumination period.

The relationship between light intensity and the amplitude of photocurrent is illustrated in Figure 4C. The photocurrent increased as the light intensity increased, and a linear correlation was observed as presented in the following equation:

$$I = 0.1422 \times P + 0.3518 \quad \text{(I)}$$

The equation relates the photocurrent (measured in nA) to the light intensity (measured in mW/cm²), while I represents the photocurrent and P represents the light intensity. The obtained correlation coefficient of 0.9885 suggests a reliable fit, demonstrating a linear association. The linear relationship reveals the potential of the br-embedded hydrogel as light intensity-sensitive. This feature can be advantageous for light power-sensitive devices. After calibration of the br-embedded hydrogel, it can be used as a light sensor to detect light intensity. It can also function as a nanocurrent generator, producing the required current or voltage by controlling light intensity.

The extrusion-based fabrication technique offers great versatility and convenience in terms of creating hydrogel patterns with controlled spatial distribution of br concentration. Therefore, the relationship between the photoelectrical properties and the br concentration is crucial to the device integration of br. The photocurrent in the br-embedded hydrogel construct demonstrates a positive correlation with the concentration of br (Figure 4D). A linear correlation was identified, with a high coefficient of determination (R^2 = 0.9289). The rationale behind this linear correlation is self-evident: an increase in the concentration of br results in a higher number of activated br molecules within the same volume when exposed to light, leading to a higher photocurrent. This property is significant for applications such as opto-controlled electrodes, as hydrogels with different br

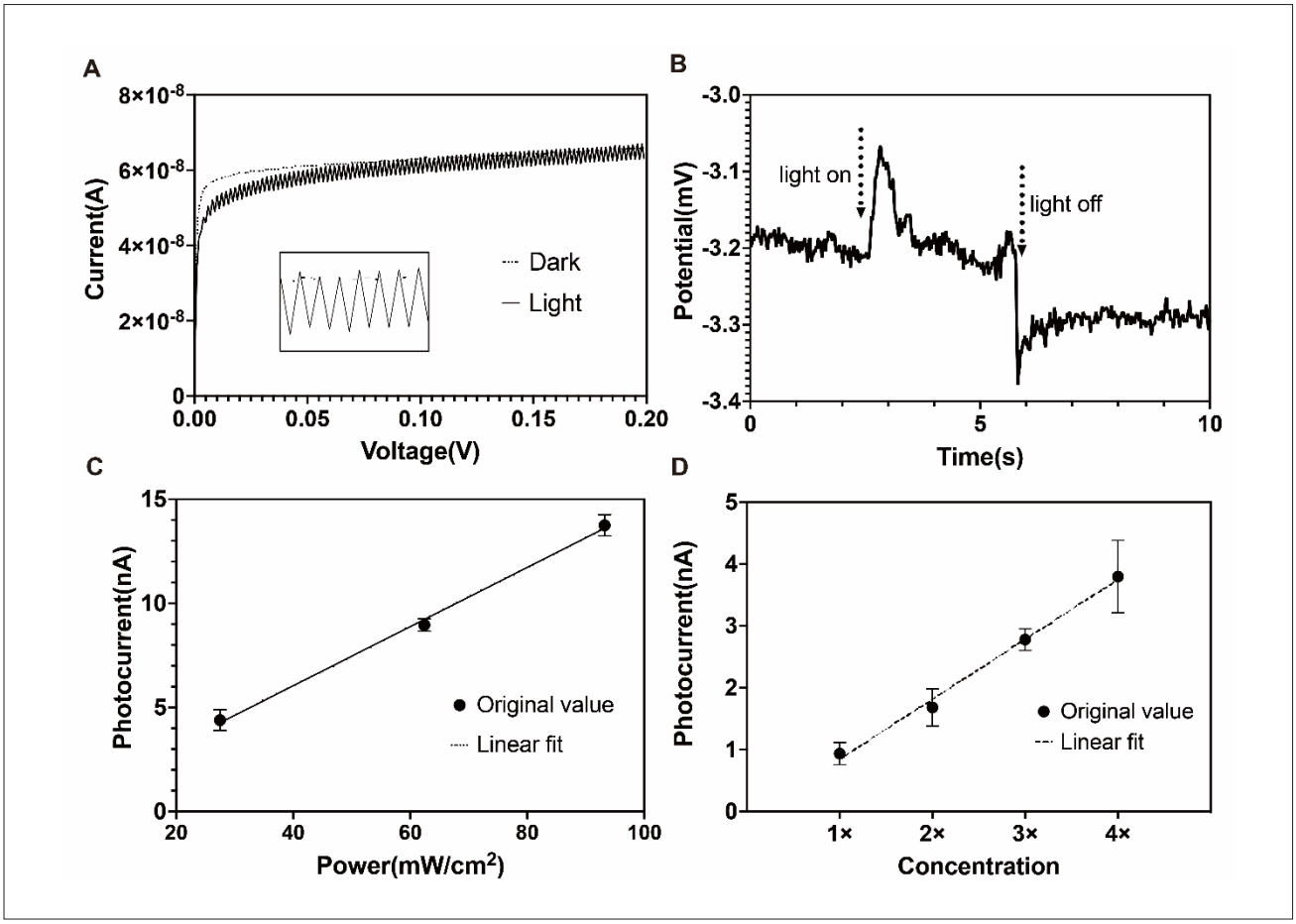

Figure 4. The photoelectrical characteristic of bacteriorhodopsin (br)-embedded hydrogel construct. (A) The linear sweep voltammetry result of br-embedded hydrogel. Under pulsing illumination, the voltammetry curve deviated from that of the dark condition due to the photocurrent. (B) The open circuit potential-time curve of the br-embedded hydrogel construct. Two differential responses were observed at the beginning and the end of the illumination. (C) The relationship between the power of light and peak photocurrent. The photocurrent increases as the power of light increases, and a linear relationship was observed. (D) The relationship between the concentration of br in the hydrogel and the amplitude of photocurrent. Four br-embedded hydrogel constructs containing different concentrations of br were tested for the photocurrent under the same illumination, and a linear relationship was observed.

concentrations can be structured into specific patterns, allowing for spatially diverse stimulation.

The light intensity-sensitive characteristic of br-embedded hydrogel was further verified by grayscale pattern recognition, as illustrated in Figure 5. The grayscale pattern was encoded to different voltage levels corresponding to varying grayscale values. The signal containing time-modulated voltage levels was generated using the arbitrary waveform generator and used to modulate the power of the laser source using AC modulation. The information contained in the grayscale pattern was therefore converted to time-modulated illumination with varying intensity, with each pixel corresponding to one second of illumination and the gray value corresponding to the light intensity. Due to the differential response and the light intensity-sensitive characteristic of br-embedded hydrogel, the gray value of each pixel can be determined based on the gray value of its preceding pixels (e.g., for pixel 1, the brightness of the preceding pixel is 0) and the value of the photocurrent at the onset of the pixel, and a quantitative relationship can be determined after calibration. Considering a pixel *i*, its gray value P_i can be obtained through the following equation:

$$P_i = P_{i-1} + C \times I_i, P_0 = 0 \quad \text{(II)}$$

In this equation, I_i represents the magnitude of the photocurrent at the onset of pixel *i* and takes a positive value when the photocurrent flows from the anode to the cathode and a negative value when the photocurrent flows from the cathode to the anode. *C* is the constant obtained after calibration that represents the linear relationship between the amplitude of light intensity change and the magnitude of the photocurrent. The constant *C* is positively correlated with the concentration of br in the br-embedded hydrogel and is influenced by other factors, such as the composition

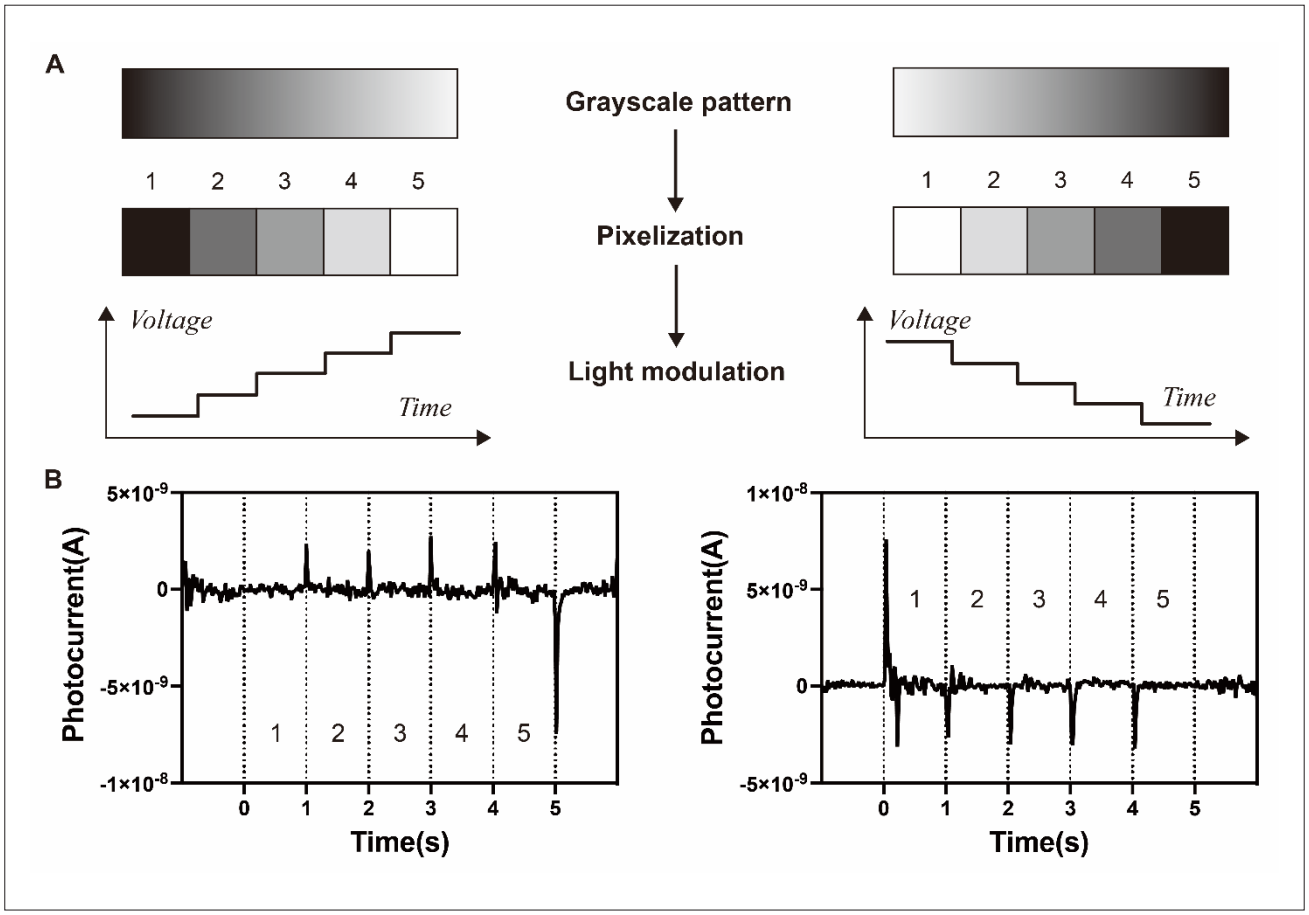

Figure 5. The grayscale pattern recognition demonstrates the light intensity-sensitive property of bacteriorhodopsin (br)-embedded hydrogel. (A) The 1D grayscale pattern was pixelized and encoded into a staircase wave signal with voltage levels corresponding to the gray value of each pixel. The signals were generated using an arbitrary wave generator and used to modulate the laser generator through AC modulation. (B) The photocurrent response of the encoded patterns. The two response curves correspond to the pattern with ascending brightness and descending gray values, respectively. A positive photocurrent indicates an increase in gray value, while a negative photocurrent indicates a decrease in gray value.

of the hydrogel, the morphological characteristics of the structure, materials of the electrodes, the pH and ionic concentration of electrolyte, etc. Therefore, this offers great versatility in terms of controlling the photoelectric properties of br-embedded hydrogels by adjusting the aforementioned factors.

3.3. Pattern recognition

In previous results, the br-embedded hydrogel demonstrated excellent photoelectric performance. Specifically, this biomaterial-based photosensitive hydrogel-based device can respond to changes in light intensity, and this response is related to two factors: (i) the amplitude of light intensity changes and (ii) the concentration of br molecules in the hydrogel.

Leveraging these properties, the br-embedded hydrogel can be utilized to fabricate devices that can respond to temporally modulated light stimulation patterns and convert them into electrical patterns. Figure 6A illustrates the temporal pattern recognition function. A 1D binary image pattern, consisting of a 1 × 5 pixel array, was encoded into an electrical signal. This electrical signal is a square wave signal, with pixels valued at 1 corresponding to a high voltage level (5 V) and pixels valued at 0 corresponding to a low voltage level (0 V). The signal lasted for 5 s, with each second corresponding to a single pixel in the 1 × 5 pixel array. This electrical signal generated by the AWG was then input into the laser generator, and TTL modulation was employed to operate the laser generator at full power when at a high voltage level and cease operating at a low voltage level. After the encoding process was completed, the laser signal carrying image data was used as the illuminating source, and the photoelectric response signal of the br-embedded hydrogel was recorded. The photoelectric response was produced by the laser signal encoded with a 1D image pattern as illustrated. This response exhibits differential response characteristics. In this pattern, where the laser signal includes two "1" pixels, the resulting photoelectric response displays four peaks. The positive photocurrent corresponds to the increasing light intensity, while the negative photocurrent aligns with the decreasing light intensity.

In addition to temporal pattern recognition of light signals with varying intensity, spatial pattern recognition was also achieved using br-embedded hydrogel constructs with different spatial patterns. All three patterns were fabricated under the same conditions using extrusion-based printing. When the laser spot moved across the hydrogel patterns in a direction perpendicular to the hydrogel filaments, the photocurrent response captured was able to reveal the spatial pattern of the hydrogel construct. The photocurrent was observed only when the total light intensity projected on the hydrogel filaments changed. For a single hydrogel filament, as seen in the first pattern, the light intensity changes when the laser spot starts to overlay with the filament and subsequently leaves it, causing the light intensity to first increase and then decrease. Therefore, two photocurrent peaks with opposite directions were observed when the laser spot moved across a single br-embedded hydrogel filament. Similarly, four and six photocurrent peaks were observed for hydrogel patterns with two and three filaments, respectively (Figure 6B). The spatial pattern recognition was achieved by reconstructing the pattern of br-embedded hydrogel constructs with a photocurrent pattern, utilizing the differential response of br.

The pattern recognition function can be utilized for capturing and reconstructing image information, such as images containing Latin letters (Figure 7). To validate this functionality, three images, composed of the letters T, H, and U, respectively, were used as the input patterns. To convert the image information into light signals recognizable by the br-embedded hydrogel, a progressive row-by-row encoding process was implemented to process the images (Figure 7A). First, the image information was pixelized and converted into binary images. In this experiment, each letter was converted into a 5 × 5 pixel grid, with each pixel containing brightness information assigned a value of 1 and each pixel without brightness information assigned a value of 0. The pixel resolution can be adjusted based on specific needs, but a 5 × 5 resolution is sufficient to distinguish most English letters. For the image patterns that have been segmented into a 5 × 5 pixel grid, the process involves encoding each row individually and subsequently reconstructing it using five photoelectric response signals to restore the original image pattern, as illustrated in Figure 7. Finally, every 1D image pattern was converted into a time-modulated laser signal, where each second corresponds to a pixel in the pattern. The laser was on when representing a pixel value of 1 and off when representing a pixel value of 0. For each letter, five photocurrent signals, each corresponding to a row in the image, were captured to reconstruct the image pattern. Due to the differential response characteristic, a photocurrent peak was observed when the pixel went from 0 to 1, or black to white in a binary image, and another peak with the opposite direction was observed when the pixel went from 1 to 0, or white to black in a binary image. One row of a binary image was reconstructed based on this principle, and the whole image can be reconstructed by repeating the process above (Figure 7B).

The pattern recognition of Latin letters provides an example of how the photovoltaic property of br-embedded hydrogel can convert light signals into electrical signals. By

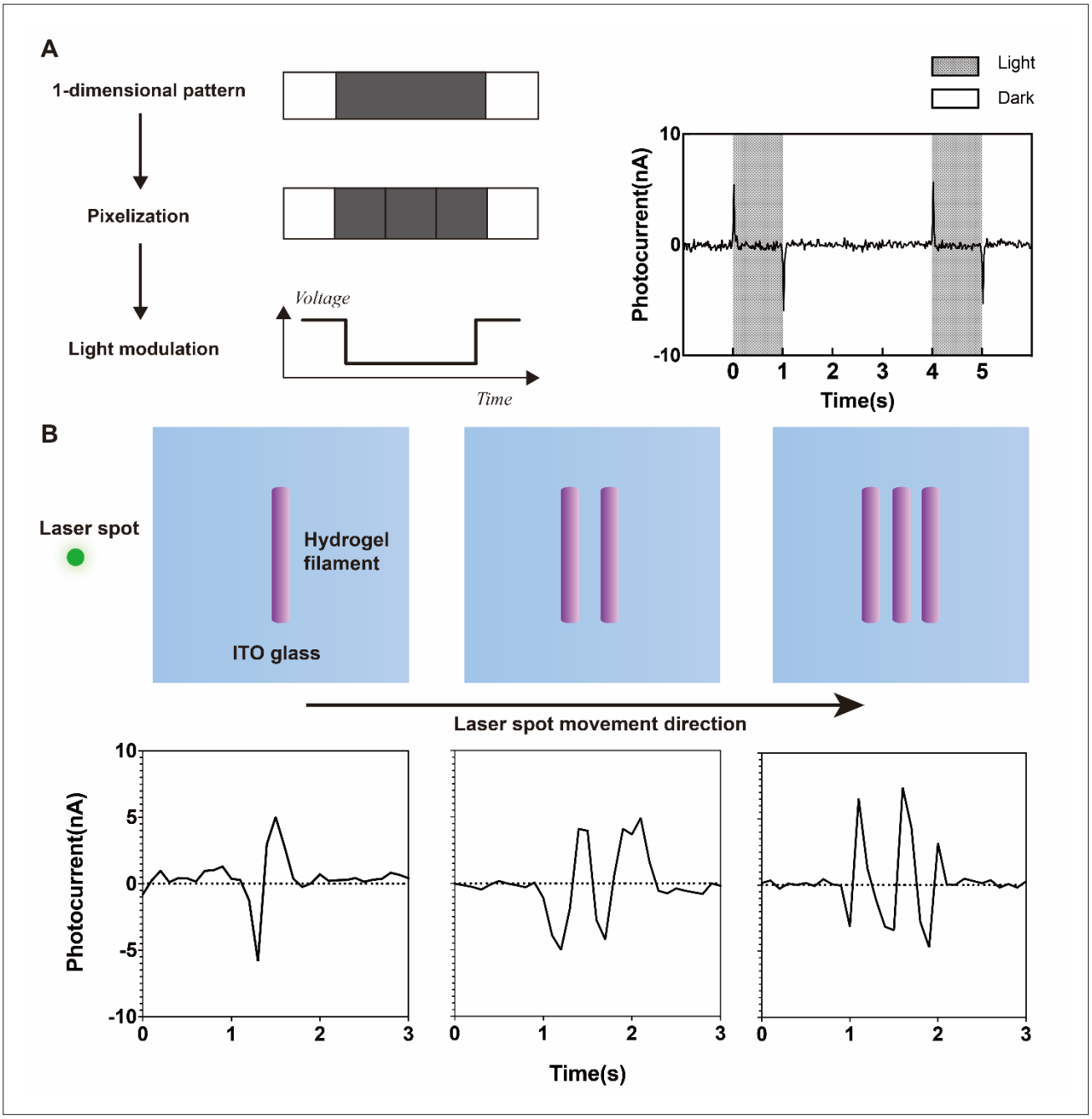

Figure 6. Temporal and spatial pattern recognition by the bacteriorhodopsin (br)-embedded hydrogel filament. (A) Schematic and result of temporal pattern recognition. A binary pattern was pixelized to a 5-pixel group, whereas the "light" pixel corresponds to the high voltage (5 V), and the "dark" pixel corresponds to the low voltage (0 V) to form a square-wave-like waveform. The waveform was then used to modulate the laser light source using TTL modulation, resulting in a time-modulated laser signal. This signal was used as the input stimuli of the br-embedded hydrogel, and the photocurrent response was captured to reconstruct the temporal pattern. (B) Schematic and result of spatial pattern recognition. Three br-embedded hydrogels with different patterns, i.e., with one to three hydrogel filaments, respectively, were fabricated, and the laser spot, as the light source, moved across the photovoltaic cells based on the patterns. The photocurrent response was recorded. The relationship between the number of photocurrent peaks and the number of hydrogel filaments, due to the differential response property, was demonstrated.

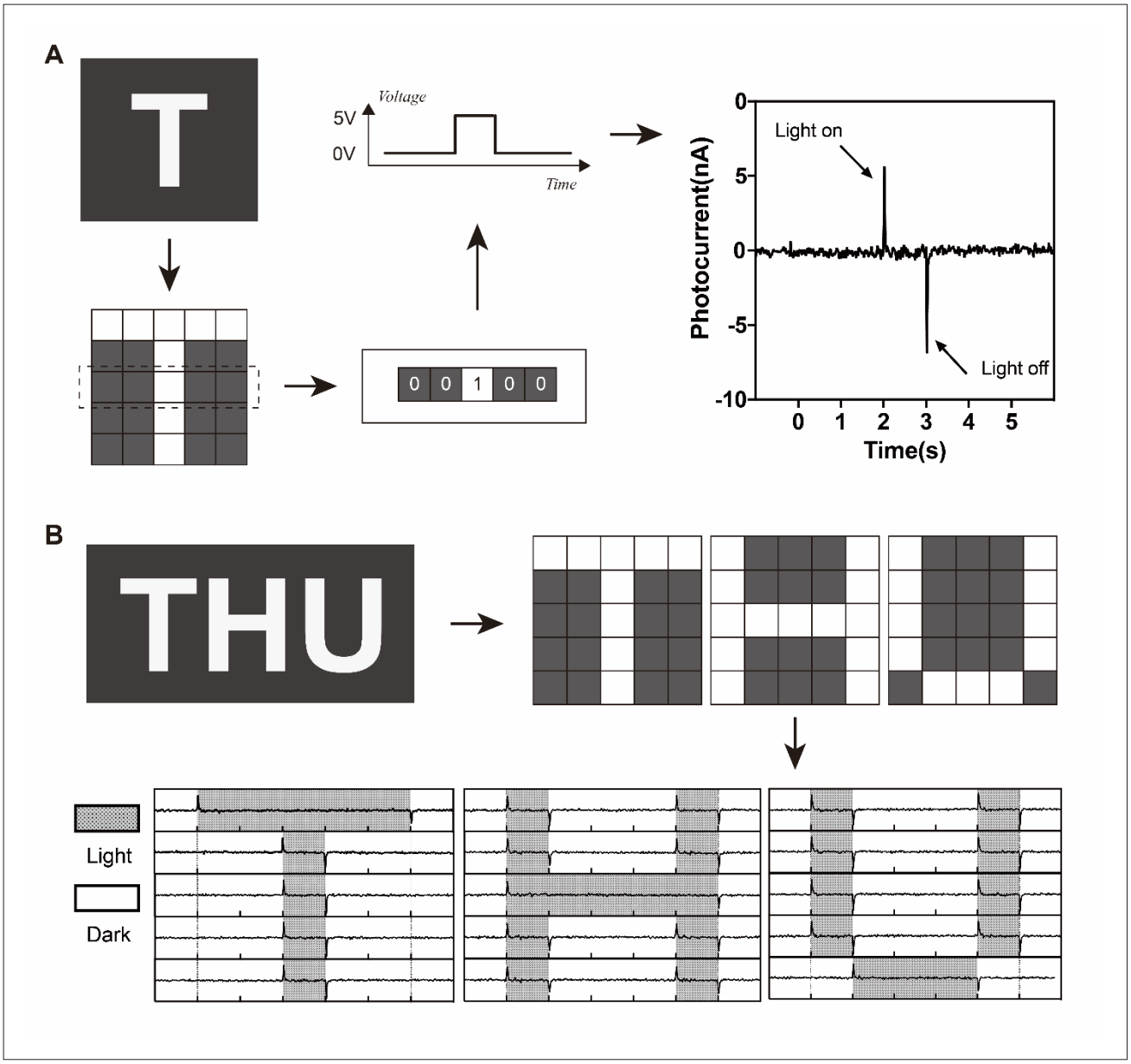

Figure 7. Pattern recognition of images containing Latin letters. (A) Schematic of image pattern recognition. An image containing the letter "T" was pixelized into a 5 × 5 pixel array, and each row of pixels was encoded into a series of Boolean values. The pixel values were transformed into a square wave signal, where "0" corresponded to a low voltage level and "1" corresponded to a high voltage level. The signal was then sent to the laser generator, and the photocurrent response was recorded. (B) Pattern recognition results of Latin letters. The letter combination "THU" was pixelized, encoded, and used as the light stimulus. A total of 15 photocurrent response signals were utilized to reconstruct the image pattern.

encoding the image pattern, it is possible to transform it into a light signal with varying light intensity for binary or grayscale images using TTL or AC modulation of a laser generator. This process converts spatial-encoded brightness information into temporal-encoded brightness information. The varying light intensity aligns effectively with the differential response characteristics of the br, thereby encoding the information regarding changes in brightness within the photocurrent produced by the br-embedded hydrogel. The amplitude and the temporal layout of the electrical stimuli can be customized by modulating the light source's intensity, while the spatial layout can be achieved through alterations in the shape of the br-embedded hydrogel structure and the concentration of br.

4. Discussion

Bacteriorhodopsin (br) has displayed significant promise in biosensors and energy harvesters due to its photosensitive properties. However, previous research has relied on the incorporation of inorganic materials that are not biocompatible or environmentally friendly to develop br-based photosensitive devices. This study successfully integrated br into a hydrogel matrix, creating a light-sensitive device that is fully biocompatible, environmentally friendly, and flexible. The hydrogel matrix offers excellent printability, high biocompatibility, and precise spatial resolution, making it suitable for applications involving living cells and tissues. The extrusion-based printing technique also enables 3D patterning with varying br concentrations, making it suitable for fabricating br-based devices with complex spatial structures. Photoelectrochemical assessments revealed unique characteristics, including differential responses to light intensity, sensitivity to br concentration, and the performance of complex functions such as pattern recognition. These distinctive mechanical, biological, and photoelectrical properties of br-embedded hydrogel introduce innovative prospects for integrating br into various kinds of devices, providing a versatile and biocompatible alternative to br film-based devices and potentially expanding the application of br to the fields of tissue engineering, soft interface electrode, and photosensitive implantable biosensor.

Future research should focus on several aspects to maximize the potential of br-embedded hydrogels, such as exploring the interactions between the hydrogel and electrosensitive living cells (e.g., cardiomyocytes and neurons) under different conditions. Additionally, validating the photoelectrical functionality of br-embedded hydrogel *in vivo*, including evaluating the stability of br and the degradability of hydrogel, would be beneficial for the development of photosensitive implants and other applications *in vivo*.

5. Conclusion

The br-embedded hydrogel exhibits remarkable photoelectric response capabilities, attributable to its sensitivity to light intensity and the concentration of br molecules. The extrusion-based fabrication method offers great versatility in creating distinctive patterns with the spatial distribution of varying br concentrations in the 3D hydrogel. The br-embedded hydrogel demonstrated both temporal and spatial pattern recognition abilities due to its photoelectric properties, highlighting its potential for applications in biocompatible light-sensitive devices and paving the way for innovative uses in biosensors.

Acknowledgments

Not applicable.

Funding

Not applicable.

Conflict of interest

The authors declare they have no competing interests.

Author contributions

Conceptualization: All authors
Formal analysis: Mian Wu
Investigation: All authors
Methodology: All authors
Writing – original draft: Mian Wu
Writing – review & editing: All authors

Ethics approval and consent to participate

Not applicable.

Consent for publication

Not applicable.

Availability of data

Data is available from the corresponding author upon reasonable request.

References

1. Marin E, Boschetto F, Pezzotti G. Biomaterials and biocompatibility: an historical overview. *J Biomed Mater Res A*. 2020;108(8):1617-1633. doi: 10.1002/jbm.a.36930
2. Biswal T, BadJena SK, Pradhan D. Sustainable biomaterials and their applications: a short review. *Mater Today Proc*. 2020;30:274-282. doi: 10.1016/j.matpr.2020.01.437
3. Li YT, Tian Y, Tian H, et al. A review on bacteriorhodopsin-based bioelectronic devices. *Sensors (Basel)*. 2018;18(5):1368. doi: 10.3390/s18051368
4. Shin N, Lee SH, Cho Y, Park TH, Hong S. Bioelectronic skin based on nociceptive ion channel for human-like perception of cold pains. *Small*. 2020;16(30):2001469. doi: 10.1002/smll.202001469

5. Kim D, Han SA, Kim JH, Lee JH, Kim SW, Lee SW. Biomolecular piezoelectric materials: from amino acids to living tissues. *Adv Mater.* 2020;32(14):1906989. doi: 10.1002/adma.201906989

6. Lanyi JK. Understanding structure and function in the light-driven proton pump bacteriorhodopsin. *J Struct Biol.* 1998;124(2):164-178. doi: 10.1006/jsbi.1998.4044

7. Oesterhelt D, Stoeckenius W. Rhodopsin-like protein from the purple membrane of *Halobacterium halobium*. *Nat New Biol.* 1971;233(39):149-152. doi: 10.1038/newbio233149a0

8. Lozier RH, Bogomolni RA, Stoeckenius W. Bacteriorhodopsin: a light-driven proton pump in *Halobacterium halobium*. *Biophys J.* 1975;15(9):955-962. doi: 10.1016/S0006-3495(75)85875-9

9. Oesterhelt D. The purple membrane of *Halobacterium halobium*: a new system for light energy conversion. *Ciba Found Symp.* 1975;(31):147-167. doi: 10.1002/9780470720134.ch9

10. Oesterhelt D. Bacteriorhodopsin as an example of a light-driven proton pump. *Angew Chem Int Ed Engl.* 1976;15(1):17-24. doi: 10.1002/anie.197600171

11. Stoeckenius W, Lozier RH, Bogomolni RA. Bacteriorhodopsin and the purple membrane of halobacteria. *Biochim Biophys Acta* 1979;505(3–4):215-278. doi: 10.1016/0304-4173(79)90006-5

12. Váró G, Keszthelyi L. Photoelectric signals from dried oriented purple membranes of *Halobacterium halobium*. *Biophys J.* 1983;43(1):47-51. doi: 10.1016/S0006-3495(83)84322-7

13. Kouyama T, Kouyama AN, Ikegami A. Bacteriorhodopsin is a powerful light-driven proton pump. *Biophys J.* 1987;51(5):839-841. doi: 10.1016/S0006-3495(87)83411-2

14. Kikukawa T, Araiso T, Mukasa K, Shimozawa T, Kamo N. The molecular motion of bacteriorhodopsin mutant D96N in the purple membrane. *FEBS Lett.* 1995;377(3): 502-504. doi: 10.1016/0014-5793(95)01408-X

15. Miyasaka TMT. Design of intelligent optical sensors with organized bacteriorhodopsin films. *Jpn J Appl Phys.* 1995;34(7S):3920. doi: 10.1143/JJAP.34.3920

16. Miyasaka T, Koyama K, Itoh I. Quantum conversion and image detection by a bacteriorhodopsin-based artificial photoreceptor. *Science.* 1992;255(5042):342-344. doi: 10.1126/science.255.5042.342

17. Lu Z, Wang J, Xiang X, Li R, Qiao Y, Li CM. Integration of bacteriorhodopsin with upconversion nanoparticles for NIR-triggered photoelectrical response. *Chem Commun (Camb).* 2015;51(29):6373-6376. doi: 10.1039/c5cc00457h

18. Choi HG, Min J, Choi JW, Lee WH. Molecular photoreceptor consisting of bacteriorhodopsin/flavin complex Langmuir–Blodgett films. *Biosensor Bioelectron.* 1998;13(10):1069-1075. doi: 10.1016/S0956-5663(98)00073-6

19. Hasegawa H, Sakamoto K, Shomura K, et al. Biomaterial-based biomimetic visual sensors: inkjet patterning of bacteriorhodopsin. *ACS Appl Mater Interfaces.* 2023;15(38):45137-45145. doi: 10.1021/acsami.3c07540

20. Okada-Shudo Y, Tanabe T, Mukai T, Kasai K, Zhang Y, Watanabe M. Directionally selective motion detection with bacteriorhodopsin patterned sensor. *Synth Met.* 2016;222:249-254. doi: 10.1016/j.synthmet.2016.10.020

21. Lv Y, Yang N, Li S, Lu S, Xiang Y. A novel light-driven pH-biosensor based on bacteriorhodopsin. *Nano Energy.* 2019;66:104129. doi: 10.1016/j.nanoen.2019.104129

22. Walczak KA, Bergstrom PL, Friedrich CR. Light sensor platform based on the integration of bacteriorhodopsin with a single electron transistor. *Act Passive Electron Compon.* 2011;2011:1-7. doi: 10.1155/2011/586924

23. Chen HM, Jheng KR, Yu AD. Direct, label-free, selective, and sensitive microbial detection using a bacteriorhodopsin-based photoelectric immunosensor. *Biosens Bioelectron.* 2017;91:24-31. doi: 10.1016/j.bios.2016.12.032

24. Ahmadi M, Yeow JTW. Fabrication and characterization of a radiation sensor based on bacteriorhodopsin. *Biosens Bioelectron.* 2011;26(5):2171-2176. doi: 10.1016/j.bios.2010.09.029

25. Ahmadi M, Osei EK, Yeow JTW. Bacteriorhodopsin for superficial X-ray sensing. *Sens Actuat B Chem.* 2012;166-167:177-183. doi: 10.1016/j.snb.2012.02.037

26. Choi HG, Jung WC, Min J, Lee WH, Choi JW. Color image detection by biomolecular photoreceptor using bacteriorhodopsin-based complex LB films. *Biosens Bioelectron.* 2001;16(9):925-935. doi: 10.1016/s0956-5663(01)00211-1

27. Kim JH, Kim DH, So JH, Koo HJ. Toward eco-friendly dye-sensitized solar cells (DSSCs): natural dyes and aqueous electrolytes. *Energies.* 2021;15(1):219. doi: 10.3390/en15010219

28. Devi P, Thakur A, Ghosh D, et al. Boosting photoelectrochemical performance of GaN nanowall

network photoanode with bacteriorhodopsin. *Int J Hydrogen Energy.* 2020;45(1):103-111.
doi: 10.1016/j.ijhydene.2019.10.184

29. Wu M, Lin F, Song Y. Engineered bacteriorhodopsin film with oriented patterns for the improvement of the photoelectric response. *Int J Mol Sci.* 2022;23(24):16079.
doi: 10.3390/ijms232416079

30. Molaeirad A, Rezaeian N. Oriented assembly of bacteriorhodopsin on ZnO nanostructured electrode for enhanced photocurrent generation. *Biotechnol Appl Biochem.* 2015;62(4):489-493.
doi: 10.1002/bab.1294

31. Renugopalakrishnan V, Barbiellini B, King C, et al. Engineering a robust photovoltaic device with quantum dots and bacteriorhodopsin. *J Phys Chem C Nanomater Interfaces.* 2014;118(30):16710-16717.
doi: 10.1021/jp502885s

32. Lu S, Guo Z, Xiang Y, Jiang L. Photoelectric frequency response in a bioinspired bacteriorhodopsin/alumina nanochannel hybrid nanosystem. *Adv Mater.* 2016;28(44):9851-9856.
doi: 10.1002/adma.201603809

33. Chellamuthu J, Nagaraj P, Chidambaram SG, Sambandam A, Muthupandian A. Enhanced photocurrent generation in bacteriorhodopsin based bio-sensitized solar cells using gel electrolyte. *J Photochem Photobiol B.* 2016;162:208-212.
doi: 10.1016/j.jphotobiol.2016.06.044

34. Naseri N, Janfaza S, Irani R. Visible light switchable bR/TiO2 nanostructured photoanodes for bio-inspired solar energy conversion. *RSC Adv.* 2015;5(24):18642-18646.
doi: 10.1039/C4RA16188B

35. Molaeirad A, Janfaza S, Karimi-Fard A, Mahyad B. Photocurrent generation by adsorption of two main pigments of *Halobacterium salinarum* on TiO2 nanostructured electrode. *Biotechnol Appl Biochem.* 2015;62(1):121-125.
doi: 10.1002/bab.1244

36. Mohammadpour R, Janfaza S. Efficient nanostructured biophotovoltaic cell based on bacteriorhodopsin as biophotosensitizer. *ACS Sustain Chem Eng.* 2015;3(5):809-813.
doi: 10.1021/sc500617w

37. Guo Z, Liang D, Rao S, Xiang Y. Heterogeneous bacteriorhodopsin/gold nanoparticle stacks as a photovoltaic system. *Nano Energy.* 2015;11:654-661.
doi: 10.1016/j.nanoen.2014.11.026

38. Hug H, Bader M, Mair P, Glatzel T. Biophotovoltaics: natural pigments in dye-sensitized solar cells. *Appl Energy.* 2014;115:216-225.
doi: 10.1016/j.apenergy.2013.10.055

39. Kumara NTRN, Ekanayake P, Lim A, et al. Layered co-sensitization for enhancement of conversion efficiency of natural dye sensitized solar cells. *J Alloys Compoun.* 2013;581:186-191.
doi: 10.1016/j.jallcom.2013.07.039

40. Yen CW, Hayden SC, Dreaden EC, Szymanski P, El-Sayed MA. Tailoring plasmonic and electrostatic field effects to maximize solar energy conversion by bacteriorhodopsin, the other natural photosynthetic system. *Nano Lett.* 2011;11(9):3821-3826.
doi: 10.1021/nl2018959

41. Thavasi V, Lazarova T, Filipek S, et al. Study on the feasibility of bacteriorhodopsin as bio-photosensitizer in excitonic solar cell: a first report. *J Nanosci Nanotech.* 2009;9(3):1679-1687.
doi: 10.1166/jnn.2009.si07

42. Li R, Hu F, Bao Q, et al. Enhancement of photoelectric response of bacteriorhodopsin by multilayered WO3·H2O nanocrystals/PVA membrane. *Chem Commun.* 2010;46(5):689-691.
doi: 10.1039/b923354g

43. Zabut B, Elkahlout K, Yücel M, Gunduz U, Turker L, Eroglu I. Hydrogen gas production by combined systems of *Rhodobacter sphaeroides* O.U.001 and *Halobacterium salinarum* in a photobioreactor. *Int J Hydrogen Energy.* 2006;31:1553-1562.
doi: 10.1016/j.ijhydene.2006.06.023

44. Chen F, Qing Y, Wu H, Hou X. Optical storage characters of bacteriorhodopsin molecule film. *Proc SPIE.* 2002;4536.
doi: 10.1117/12.409233

45. Yu X, Yao B, Lei M, Gao P, Ma B. Femtosecond laser-induced permanent anisotropy in bacteriorhodopsin films and applications in optical data storage. *J Modern Optic.* 2013;60(4):309-314.
doi: 10.1080/09500340.2013.774067

46. Yao B, Lei M, Ren L, et al. Polarization multiplexed write-once–read-many optical data storage in bacteriorhodopsin films. *Opt Lett.* 2005;30(22):3060-3062.
doi: 10.1364/ol.30.003060

47. Chen F, Hou X, Li BF, Jiang L, Hammp N. Optical information storage of bacteriorhodopsin molecule film: experimental study. *Mater Sci Eng B.* 2000;76(1):76-78.
doi: 10.1016/S0921-5107(00)00399-8

48. Hampp NA, Neebe M, Seitz A. Printing inks containing the photochromic protein bacteriorhodopsin. In: *Optical Security and Counterfeit Deterrence Techniques III*. SPIE, 2000;3973:118-125.
doi: 10.1117/12.382181

49. Hampp N, Neebe M. Bacteriorhodopsin-based multilevel optical security features. In: *Optical Security and Counterfeit Deterrence Techniques VI*. SPIE, 2006;6075:256-264.
doi: 10.1117/12.642627

50. Ostrovsky MA, Smitienko OA, Bochenkova AV, Feldman TB. Similarities and differences in photochemistry of Type

I and Type II rhodopsins. *Biochem Moscow.* 2023;88(10): 1528-1543.
doi: 10.1134/S0006297923100097

51. Sabari Girisun TC, Jeganathan C, Pavithra N, Anandan S. Structurally modified bacteriorhodopsin as an efficient bio-sensitizer for solar cell applications. *Eur Biophys J.* 2019;48(1):61-71.
doi: 10.1007/s00249-018-1331-1

52. Janfaza S, Molaeirad A, Mohamadpour R, Khayati M, Mehrvand J. Efficient bio-nano hybrid solar cells via purple membrane as sensitizer. *BioNanoSci.* 2014;4(1):71-77.
doi: 10.1007/s12668-013-0118-1

53. Das S, Wu C, Song Z, et al. Bacteriorhodopsin enhances efficiency of perovskite solar cells. *ACS Appl Mater Interfaces.* 2019;11(34):30728-30734.
doi: 10.1021/acsami.9b06372

54. Jeganathan C, Sabari Girisun TC, Vijaya S, Anandan S. Bacteriorhodopsin-sensitized preferentially oriented one-dimensional TiO2 nanorod polymorphs as efficient photoanodes for high-performance bio-sensitized solar cells. *Appl Nanosci*. 2019;9(2):189-208.
doi: 10.1007/s13204-018-0905-7

55. Yao B, Wang Y, Lei M, Zheng Y. Characteristics and mechanisms of the two types of photoelectric differential response of bacteriorhodopsin-based photocell. *Biosens Bioelectron.* 2003;19(4):283-287.
doi: 10.1016/S0956-5663(03)00211-2

56. Wang Y, Wu J, Ma D, Ding J. Preparation of a cross-linked gelatin/bacteriorhodopsin film and its photochromic properties. *Sci China Chem*. 2011;54(2):405-409.
doi: 10.1007/s11426-010-4213-7

57. Ma D, Zhao Y, Wu J, Cui T, Ding J. A block-copolymer hydrogel encapsulates bacteriorhodopsin and produces the longest photochromic response of the membrane protein under high water content conditions. *Soft Matter*. 2009;5(23):4635-4637.
doi: 10.1039/b917438a

58. Hsieh FY, Han HW, Chen XR, Yang CS, Wei Y, Hsu SH. Non-viral delivery of an optogenetic tool into cells with self-healing hydrogel. *Biomaterials*. 2018;174:31-40.
doi: 10.1016/j.biomaterials.2018.05.014

59. Ma Y, Zhang Y, Cai S, et al. Flexible hybrid electronics for digital healthcare. *Adv Mater.* 2020;32(15):1902062.
doi: 10.1002/adma.201902062

60. Wang L, Xu T, Zhang X. Multifunctional conductive hydrogel-based flexible wearable sensors. *TrAC Trends Anal Chem*. 2021;134:116130.
doi: 10.1016/j.trac.2020.116130

61. Ling Y, An T, Yap LW, Zhu B, Gong S, Cheng W. Disruptive, soft, wearable sensors. *Adv Mater.* 2020;32(18):1904664.
doi: 10.1002/adma.201904664

62. Han F, Xie X, Wang T, et al. Wearable hydrogel-based epidermal sensor with thermal compatibility and long term stability for smart colorimetric multi-signals monitoring. *Adv Healthc Mater*. 2023;12(3):2201730.
doi: 10.1002/adhm.202201730

63. Persaud A, Maus A, Strait L, Zhu D. 3D bioprinting with live cells. *Eng Regen.* 2022;3(3):292-309.
doi: 10.1016/j.engreg.2022.07.002

64. Dey M, Ozbolat IT. 3D bioprinting of cells, tissues and organs. *Sci Rep*. 2020;10(1):14023.
doi: 10.1038/s41598-020-70086-y

65. Gai K, Yang M, Chen W, et al. Development of neural cells and spontaneous neural activities in engineered brain-like constructs for transplantation. *Adv Healthc Mater*. 2024;2401419.
doi: 10.1002/adhm.202401419

66. Lien SM, Ko LY, Huang TJ. Effect of crosslinking temperature on compression strength of gelatin scaffold for articular cartilage tissue engineering. *Mater Sci Eng C.* 2010;30(4):631-635.
doi: 10.1016/j.msec.2010.02.019

67. Chu LK, Yen CW, El-Sayed MA. Bacteriorhodopsin-based photo-electrochemical cell. *Biosens Bioelectron.* 2010;26(2):620-626.
doi: 10.1016/j.bios.2010.07.01

68. Liu W, Liu F, Zhang T. An optoelectronic device based on bacteriorhodopsin with modulated photocurrent waveform. *Opt Mater.* 2022;133:112937.
doi: 10.1016/j.optmat.2022.112937

ACCSCIENCE PUBLISHING

International Journal of Bioprinting

RESEARCH ARTICLE

Design, fabrication, and biocompatibility of 3D-printed poly(LLA-ran-PDO-ran-GA)/poly (D-lactide) composite scaffolds for bone tissue engineering

Tiantang Fan[1†], Xiao Meng[5†], Ruishen Zhuge[3†], Jingwen Qin[4], Yutong Wang[1], Chunyu Zhang[1], Yiqiao Yin[1], Jianru Liu[3*], Tianyun Fan[2*], and Dongya Liu[1*]

[1]College of Medical Engineering and the Key Laboratory for Medical Functional Nanomaterials, Jining Medical University, Jining, Shandong, China

[2]Dongguan Maternal and Child Health Care Hospital, Postdoctoral Innovation Practice Base of Southern Medical University, Dongguan, Guangdong, China

[3]Peking University School and Hospital of Stomatology & National Center for Stomatology & National Clinical Research Center for Oral Diseases & National Engineering Research Center of Oral Biomaterials and Digital Medical Devices, Beijing, China

[4]The Institute for Translational Nanomedicine, Shanghai East Hospital, the Institute for Biomedical Engineering & Nano Science, Tongji University School of Medicine, Shanghai, China

[5]School of Energy, Power, and Mechanical Engineering, North China Electric Power University, Beijing, China

(This article belongs to the Special Issue: *Advances in Bioprinting and Organ-on-a-chip and Applications for Precision Medicine*)

Abstract

The long-term nonunion of bone defects remains a significant challenge in the field of orthopedics. Poly(L-lactic acid) (PLLA), widely used in bone tissue engineering, offers hope for addressing this issue. In our previous study, we aimed to enhance the poor toughness and slow degradation of PLLA by introducing flexible p-dioxanone (PDO) and highly reactive glycolic acid units into the molecular chain of PLLA to prepare PLLA-*ran*-PDO-*ran*-GA (PLPG) scaffolds, effectively mitigating the limitations of PLLA. However, the crystallization capacity of PLPG copolymers was weakened, resulting in insufficient mechanical properties. Therefore, in this study, poly(D-lactic acid) (PDLA) was introduced into PLPG via solution blending to enhance its crystallization properties through the *in situ* generation of stereocomplex poly(lactic acid) (SC-PLA). Subsequently, PLPG/PDLA scaffolds were prepared using 3D printing technology. The results demonstrated that PLPG/PDLA composites exhibited good machinability, while the scaffolds exhibited satisfactory mechanical and degradation properties. Additionally, cell experiments indicated that PLPG/PDLA scaffolds are biocompatible, supporting cell growth and proliferation on their surfaces. We believe that PLPG/PDLA scaffolds have significant potential for application in bone tissue engineering, effectively addressing the issue of long-term non-healing bone defects.

Keywords: 3D bioprinting; Poly(L-lactide acid); Poly(D-lactide acid); Scaffolds; Tissue engineering

[†]These authors contributed equally to this work

***Corresponding authors:**
Jianru Liu
(lensang@163.com)

Tianyun Fan
(fty1668@163.com)

Dongya Liu
(liudongya@mail.jnmc.edu.cn)

Citation: Fan T, Meng X, Zhuge R, et al. Design, fabrication, and biocompatibility of 3D-printed poly(LLA-ran-PDO-ran-GA)/poly (D-lactide) composite scaffolds for bone tissue engineering. *Int J Bioprint*. 2024;10(6):4645. doi: 10.36922/ijb.4645

Received: August 23, 2024
1st revised: September 28, 2024
2nd revised: October 7, 2024
Accepted: October 8, 2024
Published Online: October 8, 2024

Copyright: © 2024 Author(s). This is an Open Access article distributed under the terms of the Creative Commons Attribution License, permitting distribution, and reproduction in any medium, provided the original work is properly cited.

Publisher's Note: AccScience Publishing remains neutral with regard to jurisdictional claims in published maps and institutional affiliations.

1. Introduction

Bone tissue defects caused by trauma, infection, and congenital diseases significantly impact individuals' health.[1-3] Currently, bone tissue engineering is regarded as one of the most promising methods for repairing bone tissue defects. Bone scaffolds can be achieved by adjusting the shape, hole size, and density of the scaffold, as well as providing cells with the 3D space needed for survival like natural bone. This allows the cells to absorb sufficient nutrients, exchange gases, and eliminate waste, enabling them to grow on the bone scaffolds according to the prefabricated form. This approach combines cells, biological materials, or scaffolds to create biological constructs, implants, or tissues that restore the structure and function of damaged tissues *in vivo*.[4,5] Generally, bone scaffolds need to have high mechanical properties and provide stable mechanical support for bone defects, which significantly prevent fractures or joint instability caused by bone defects. Besides, in order to form a good interface combination with the tissues around the defect site, the scaffold also needs to have good biocompatibility and reduce inflammation and rejection. In addition, the stent can be gradually degraded and absorbed in the human body, avoiding the pain and risk associated with a second operation to remove it. Meanwhile, the shape and structure of the scaffolds could be customized to the specific needs of the patients, which helps to personalize treatment plans and improve treatment outcomes and patient satisfaction. Various synthetic polymers have been extensively used in the fabrication of bone tissue engineering scaffolds due to their favorable processing, mechanical properties, biocompatibility, and biodegradability.[6-8] Among these, poly(L-lactic acid) (PLLA), a thermoplastic elastomer, possesses good processability, mechanical properties, and degradation characteristics, and has been approved by the United States Food and Drug Administration (FDA) for clinical applications, such as vascular prostheses, peripheral nerve repair, and urethral reconstruction.[9,10] However, PLLA has notable shortcomings, including poor toughness and a slow degradation rate, which impede its medical applications.[11,12] In our previous study, PLLA-*ran*-PDO-*ran*-GA (PLPG) copolymers were synthesized using poly(p-dioxanone) (PPDO) for its flexibility and mechanical strength, along with glycolic acid (GA) for its reactivity, through ring-opening polymerization. Subsequently, PLPG scaffolds were fabricated using 3D printing technology, demonstrating good mechanical performance, degradation properties, and biocompatibility.[13]

Although PLPG copolymers exhibit excellent degradation and toughness, the introduction of p-dioxanone (PDO) and GA reduces the crystallization capacity of PLPG. Previous studies have indicated that nucleating agents can significantly enhance the crystallization capacity of PLLA copolymers.[14,15] Stereocomplex poly(lactic acid) (SC-PLA), known for its good biocompatibility, can be formed *in situ* by the interaction of PLLA and poly(D-lactic acid) (PDLA) segments through hydrogen bonding.[16-18] The melting temperature (*776*) of SC-PLA is approximately 220°C, considerably higher than that of PLLA.[19,20] Thus, when the temperature reaches the T_m of PLLA during processing, SC-PLA remains in a granular form within the system. Additionally, SC-PLA crystals can be generated by introducing a small amount of PDLA, thereby increasing the overall crystallization rate of PLLA. SC-PLA has been widely utilized as a nucleating agent to enhance the crystallinity of PLLA copolymers due to its high growth rate.[21-23]

Currently, 3D printing technology has emerged as a crucial method for manufacturing porous scaffolds with high surface areas and mechanical performance.[24,25] This technology allows for alterations in surface roughness and fiber arrangement, particularly in the creation of interconnected pore structures, enabling the production of complex 3D architectures.[26] When an ideal 3D scaffold is implanted at bone defect sites, it regulates cell migration, adhesion, and proliferation by mimicking the micro-nano structure of bone tissue, thus promoting new bone regeneration.[27,28] In our previous published article, we studied the performances of PLPG/PDLA blends, and the results indicate that SC-PLA crystals could be *in situ* generated by the H bond between PLPG and PDLA.[29] Therefore, the primary aim of this study is to investigate the influence of *in situ* SC-PLA formation on the properties of PLPG/PDLA scaffolds resulting from the introduction of PDLA into the PLPG matrix. PLPG/PDLA blends were prepared *via* solution blending and subsequently processed into scaffolds using 3D printing technology. The selected processing temperature of 170°C ensures that PLPG is fully melted while the *in situ*-formed SC-PLA remains in granular form, effectively enhancing the crystallization capacity of the PLLA chain segments in the PLPG copolymers. For clarity, the PLPG/PDLA scaffolds are designated as PLPG/PDLA-3, PLPG/PDLA-5, PLPG/PDLA-7, and PLPG/PDLA-10 based on the amount of PDLA used. For example, PLPG/PDLA-3 represents a mass ratio of 97:3 between PLPG and PDLA. The surface morphology, degradation and mechanical properties, and *in vitro* biocompatibility of the PLPG/PDLA scaffolds were studied to assess their potential applications in bone tissue regeneration.

2. Materials and methods

2.1. Materials

L-lactic acid (LLA), D-lactic acid (D-LA), and GA were obtained from Jinan Daigang Biomaterial (China). p-Dioxanone (PDO) was sourced from Bangcheng Chems (China), and $Sn(Oct)_2$ was purchased from Adamas Reagent Co. Ltd. (China).

2.2. Preparation of the PLPG copolymers

The PLPG copolymers with a molar ratio of 90:5:5 for LLA, GA, and PDO were synthesized using the same method described in our previously published article.[29] Specifically, the PLPG copolymers were prepared by ring-opening polymerization of the following amounts: 184 g of LLA, 8.3 g of GA, and 7.3 g of PDO. $Sn(Oct)_2$ was used as the catalyst, and the polymerization process was conducted at 135°C for three days. The resulting copolymers were treated with dichloromethane (CH_2Cl_2) and precipitated with ethanol. Finally, the obtained PLPG copolymers were dried at 70°C until their mass remained unchanged.

2.3. Fabrication of the PLPG/PDLA scaffolds

The synthesized PLPG and PDLA polymers were thoroughly dissolved in CH_2Cl_2 for 0.5 h. The resulting solutions were then placed at 30°C until the solvent evaporated. The PLPG/PDLA composites were placed in a vacuum-drying oven until their mass stabilized and were subsequently cut into pellets. Later, the PLPG/PDLA pellets were processed into powders using a wall crusher.

The PLPG/PDLA scaffolds were fabricated using a 3D bioprinter (Beijing Advanced Medical Technologies Inc., Beijing, China). The job program was designed in SolidWorks and saved in STL format. To ensure good porosity, the fiber diameter and layer spacing of the PLPG/PDLA scaffolds were set to 300 μm.

The preparation and manufacturing process of the PLPG/PDLA scaffolds is illustrated in Scheme 1.

2.4. Characterization of the PLPG/PDLA scaffolds

The surface morphology of the PLPG/PDLA scaffolds was examined using scanning electron microscopy (SEM). The porosity of the scaffolds was calculated using the ethanol liquid displacement method according to **Equation I**:

$$Porosity\ (\%) = \frac{V_1 - V_3}{V_2 - V_1} \times 100 \quad \text{(I)}$$

where V_1 and V_2 refer to the ethanol volume before and after soaking in the PLPG/PDLA scaffolds, respectively, while V_3 represents the ethanol volume after wiping off the scaffolds. Each experiment had three parallel samples.

2.5. Mechanical performance of the PLPG/PDLA scaffolds

The mechanical performance of the PLPG/PDLA scaffolds ($5 \times 5 \times 5$ mm^3) was measured using a static and dynamic material testing machine (CMT2502; Shandong Wanchen

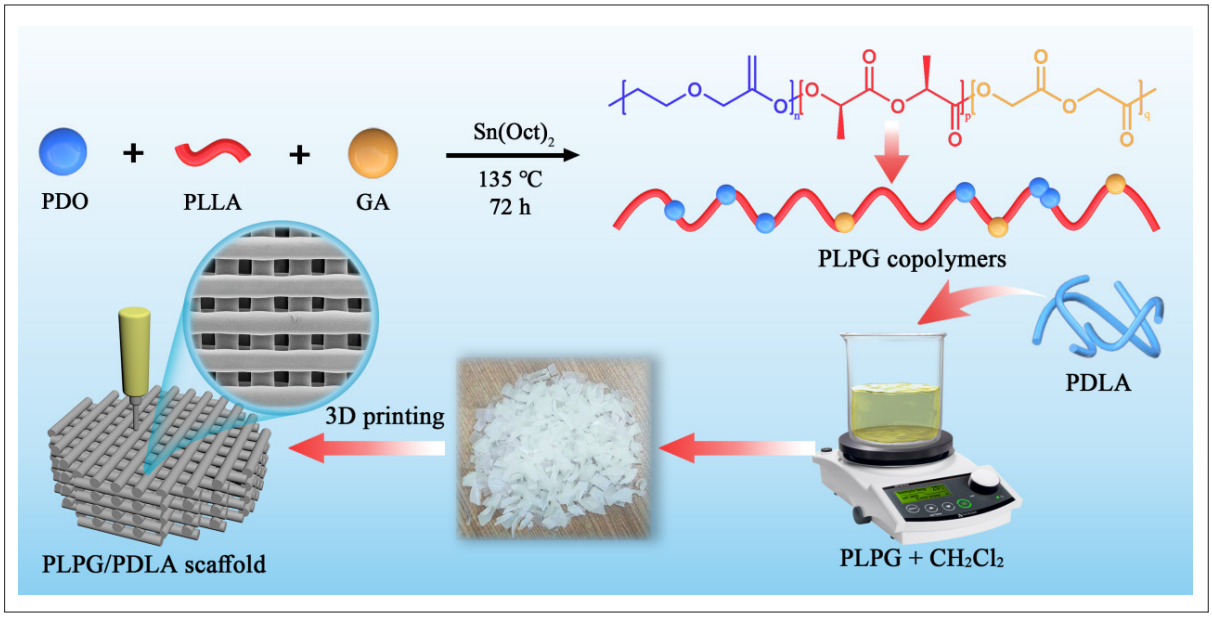

Scheme 1. Schematic illustration of the fabrication of PLPG/PDLA scaffolds for bone regeneration. Abbreviations: PDO: p-Dioxanone; PLLA: Poly(L-lactic acid); GA: Glycolic acid; PDLA: Poly(D-lactic acid); PLPG: PLLA-ran-PDO-ran-GA.

Testing Machine Co., LTD, China) at a compression speed of 1 mm/min. Each experiment had three parallel samples.

2.6. Degradation behavior of the PLPG/PDLA scaffolds

The enzymatic degradation behavior of the PLPG/PDLA scaffolds was assessed in a proteinase K solution over 15 days. Initially, the PLPG/PDLA scaffolds were immersed in 3 mL of proteinase K solution containing tris buffer (0.05 M; pH 8.5). To maintain enzyme activity, the proteinase K-tris buffer was replaced every two days. The scaffolds were removed at specified time points, washed with plenty of water, and then placed in a vacuum drying oven (37°C) until their mass stabilized. Mass loss was calculated using **Equation II**:

$$Mass\ loss\ (\%) = \frac{(M_i - M_d)}{M_i} \times 100 \quad \text{(II)}$$

where M_i and M_d are the initial dry mass and final dry mass, respectively. Each experiment had three parallel samples.

2.7. Biocompatibility of the PLPG/PDLA scaffolds

MC3T3-E1 cells were cultured in an incubator (5% CO_2) at 37°C for 5 h. The PLPG/PDLA scaffolds were sterilized under ultraviolet light for two days. MC3T3-E1 cells were then detached from the culture plates using trypsin and subsequently centrifuged. The cell concentration was adjusted to 6×10^5 cells/mL. A 30 μL cell suspension was inoculated onto the PLPG/PDLA scaffolds. After incubation for 6 h, a fresh medium was added to each well, fully immersing the scaffolds.

2.7.1. Cell proliferation

A cell counting kit-8 (CCK-8) assay was used to quantitatively assess the proliferation of MC3T3-E1 cells at 6×10^4 cells per mL in the PLPG/PDLA scaffolds. MC3T3-E1 cells and the scaffolds were co-cultured for 1, 3, and 5 days in a 48-well plate. 10 μL of CCK-8 reagent (100 μL, 10%), diluted 10 times, was then added to the wells and incubated in the cell incubator for 2 h. The optical density (OD) was measured at 450 nm using a multifunctional microplate reader (Infinite M200PRO; Tecan, Switzerland). Each experiment had three parallel samples.

2.7.2. Live/dead viability assay

The live/dead staining assay was performed to evaluate the viability of MC3T3-E1 cells cultured with the PLPG/PDLA scaffolds. The cells and scaffolds were co-cultured for 1, 2, and 3 days in the incubator. Calcein-AM and propidium iodide solutions were then added, and the samples were cultured for 0.5 h. Finally, the cells were washed with phosphate-buffered saline (PBS) and analyzed using a fluorescence microscope (LEICA DMi8; LEICA, Germany). Each experiment had three parallel samples.

2.7.3. Immunofluorescent staining

MC3T3-E1 cells (3×10^4 cells per mL) co-cultured on the PLPG/PDLA scaffolds for 12 and 72 h were fixed with paraformaldehyde for 0.5 h and then permeabilized with Triton X-100 solution. The cells were co-cultured with an anti-vinculin antibody for 12 h at 4°C. Cell actin stress fibers were stained using a rhodamine-phalloidin solution for 0.5 h, and cell nuclei were stained with 10 μg/mL DAPI. The adhesion morphology of the MC3T3-E1 cells cultured on the scaffolds was analyzed using a confocal laser scanning microscope (LEICA DMi8 S; LEICA, Germany). Each experiment had three parallel samples.

2.7.4. Alkaline phosphatase staining

To assess alkaline phosphatase (ALP) activity, MC3T3-E1 cells (6×10^4 cells per mL) were co-cultured with the PLPG/PDLA scaffolds for 7 and 14 days at 37°C. After fixing the cells with paraformaldehyde and rinsing with PBS, a certain amount of BCIP/NBT solution was added, and the samples were incubated in the dark for 24 h. Finally, the staining was captured using an inverted microscope (LEICA DMi8 S; LEICA, Germany). Each experiment had three parallel samples.

For the assessment of ALP, MC3T3-E1 cells (6×10^4 cells per mL) were co-cultured with the PLPG/PDLA scaffolds for 14 days. Post-incubation, RIPA lysis buffer was added to each well. The resulting supernatants with 150 μL were mixed with 150 μL pNPP and incubated in the dark for 1 h. The supernatants of 20 μL were then introduced into a 200 μL BCA detection solution and incubated for another hour in the dark. Finally, the OD of the solution was measured at 405 and 562 nm using a multifunctional enzyme-labeled instrument (TECAN Infinite M200 PRO; Tecan, Switzerland), and the relative activity of ALP (R_{ALP}) was calculated using **Equation III**:

$$R_{ALP} = OD_{405}/OD_{562} \times 100\% \quad \text{(III)}$$

3. Results and discussion

3.1. Characterization of the PLPG/PDLA scaffolds

The morphology of the PLPG/PDLA scaffolds was observed *via* SEM. As displayed in Figure 1a–d, the PLPG/PDLA scaffolds, with pore sizes of 200–300 μm, exhibited a regular network structure and uniform struts, indicating that the PLPG/PDLA composites are suitable for 3D printing to fabricate complex scaffolds. The top and side views of the pore structure inside the scaffold demonstrated

that the pores were interconnected, ensuring complete connectivity. Moreover, as the mass of PDLA increased to 7 wt.%, the PLPG/PDLA scaffolds gradually appeared uneven, and the surface of the struts changed from smooth to rough. This change can be attributed to the formation of SC-PLA, which significantly influences the melt flow of PLPG copolymers, leading to unstable fluid behavior and turbulence.

Additionally, the influence of PDLA content on the porosity of the PLPG/PDLA scaffolds was assessed (Figure 1e). Notably, there was no significant difference in the porosity of all the scaffolds, indicating that the generated SC-PLA did not affect the scaffolds' porosity. Compared to the theoretical porosity of 58% set before printing, the actual measured porosity of the PLPG/PDLA scaffolds was slightly higher, at about 65%. This can be explained by the formation of SC-PLA, which resulted in reduced melt flow and thinner supporting struts. Importantly, higher porosity in the scaffolds is beneficial for the proliferation, adhesion, and growth of related cells, as well as for providing oxygen and nutrients to those cells.[30,31]

The mechanical properties of the scaffolds are another crucial factor for *in vivo* implantation. The mechanical properties of the PLPG/PDLA scaffolds are depicted in Figure 1f–g. It is evident that the compressive strength of the PLPG/PDLA scaffolds significantly increased with the addition of PDLA to the PLPG matrix. This enhancement can be attributed to the generated SC-PLA acting as a heterogeneous nucleation site, improving the crystallinity of the PLPG/PDLA scaffold materials and thus enhancing their mechanical properties. Furthermore, the compressive modulus remained stable at about 110 MPa as the PDLA content reached 7 wt.%. These results imply that the PLPG/PDLA-7 scaffolds possess excellent mechanical properties suitable for providing support.

3.2. Degradation behavior of the PLPG/PDLA scaffolds

The mass loss of the PLPG/PDLA scaffolds was analyzed after immersion in PBS for 12 weeks (Figure 2a). The

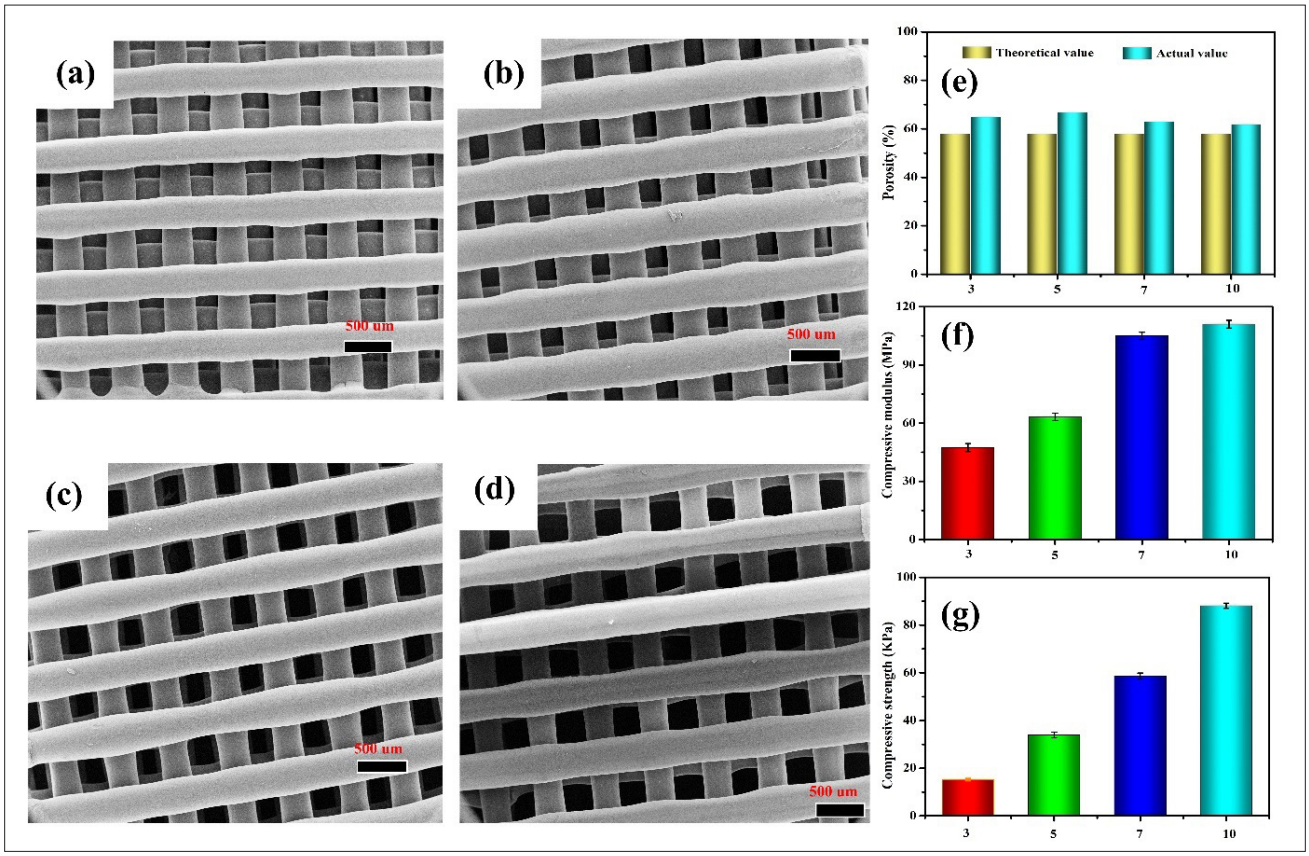

Figure 1. The physical properties of the PLPG/PDLA scaffolds. (a–d) scanning electron microscopy (SEM) images of PLPG/PDLA scaffolds: (a) PLPG/PDLA-3, (b) PLPG/PDLA-5, (c) PLPG/PDLA-7, (d) PLPG/PDLA-10, (e) theoretical and actual porosity of PLPG/PDLA scaffolds, (f) compressive modulus of PLPG/PDLA scaffolds, and (g) compressive strength of PLPG/PDLA scaffolds. $n = 3$. Scale bars: 500 μm. Abbreviations: PDLA: Poly(D-lactic acid); PLPG: PLLA-ran-PDO-ran-GA.

degradation behavior of polymers typically results from the solubilization of components generated during the degradation process. As displayed in Figure 2a, the PLPG/PDLA scaffolds exhibited similar weight loss behavior. Compared to PLPG scaffolds,[18] the degradation of PLPG/PDLA scaffolds decreased with increasing PDLA mass. For example, the mass loss for PLPG/PDLA-7 and PLPG/PDLA-10 scaffolds was approximately 2.1 and 3.2%, respectively, attributed to the enhanced crystallinity. Additionally, surface morphology data was not provided since the surface changes of the PLPG/PDLA scaffolds were not significant during the degradation process.

To further analyze the enzymatic degradation behavior, PLPG/PDLA scaffolds were placed in proteinase K solution for 15 days. The weight loss of the PLPG/PDLA scaffolds exhibited a linear increase over this period (Figure 2b). Notably, compared to previously studied PLPG/PDLA membrane samples,[24] the degradation of the PLPG/PDLA scaffolds was significantly higher. The enzymatic degradation mechanism follows surface erosion.[32-34] The PLPG/PDLA scaffolds had a higher specific surface area, making them more conducive to adsorbing protease K. Furthermore, the degradation rate of approximately 60.3% for the PLPG/PDLA scaffolds was slightly slower than that of the PLPG scaffolds evaluated in previous studies.[29] Proteinase K cannot degrade the crystalline regions, and the formation of SC-PLA enhances the crystallinity of the PLPG/PDLA scaffold materials.

To thoroughly observe the degradation behavior of the PLPG/PDLA scaffolds, the surface morphology was examined via SEM (Figure 2c). Notably, the amorphous regions of the PLPG/PDLA scaffolds were degraded

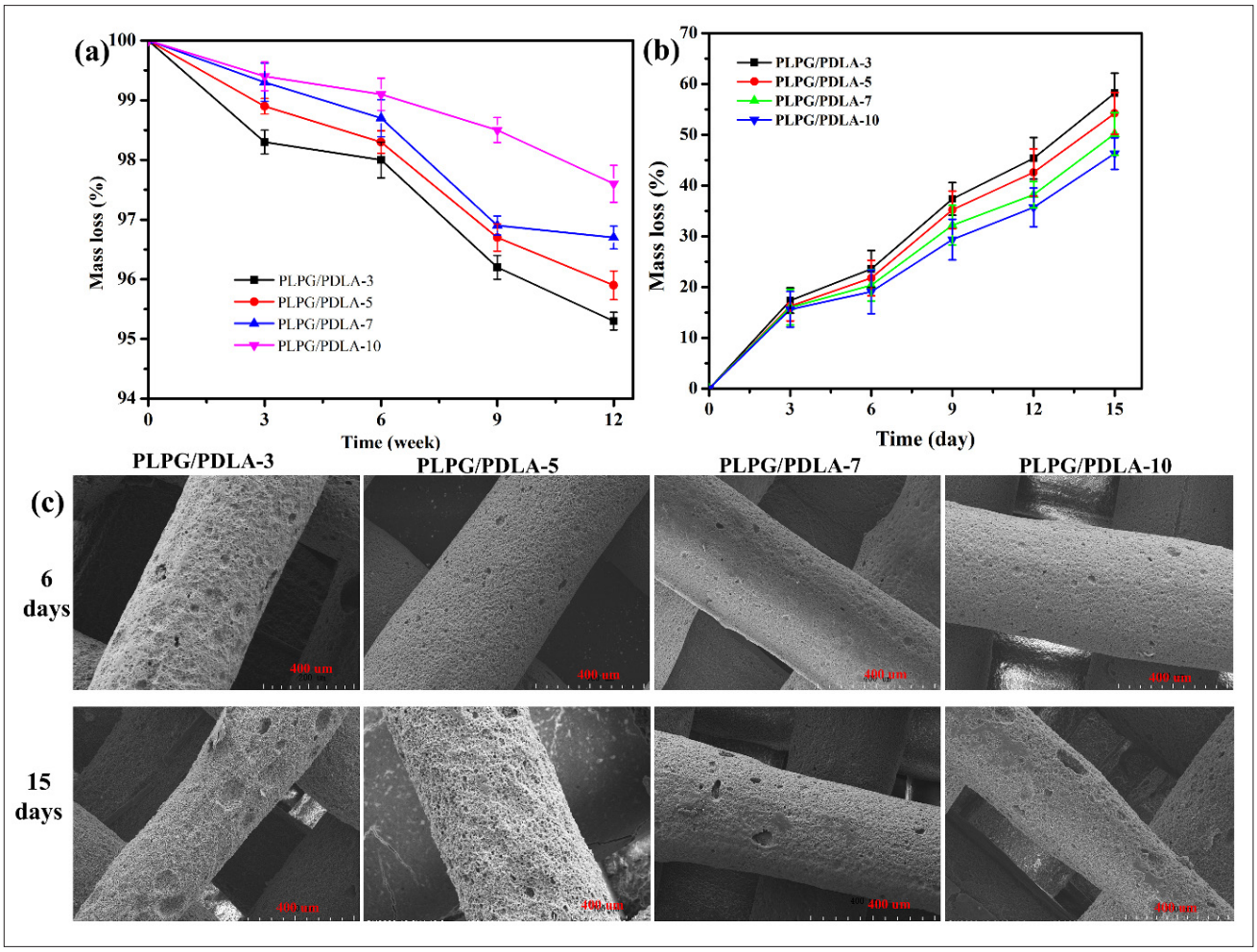

Figure 2. The hydrolytic degradation behavior of the PLPG/PDLA scaffolds. (a) Weight loss of PLPG/PDLA scaffolds after hydrolytic degradation for 12 weeks. (b) Weight loss of PLPG/PDLA scaffolds after enzymatic degradation for 15 days. (c) Scanning electron microscopy (SEM) images of PLPG/PDLA scaffolds after enzymatic degradation for 15 days. $n = 3$. Scale bars: 400 μm. Abbreviations: PDLA: Poly(D-lactic acid); PLPG: PLLA-ran-PDO-ran-GA.

after six days of enzymatic degradation. By day 15, the PLPG/PDLA scaffolds exhibited significant degradation. Additionally, as the PDLA mass increased, numerous voids appeared on the strut surfaces, while the undegraded areas remained relatively smooth. This can be attributed to the fact that proteinase K primarily degraded the amorphous regions surrounding the spherulites.[35,36] The SEM results are consistent with the weight loss data. Therefore, based on the mechanical properties and degradation behavior, the PLPG/PDLA-7 scaffolds demonstrate potential for use in tissue engineering.

3.3. *In vitro* cellular assay

To analyze the biocompatibility and proliferation of MC3T3-E1 cells co-cultured with PLPG/PDLA scaffolds for five days, a CCK-8 assay was conducted (Figure 3). The OD values gradually increased, indicating that the number of MC3T3-E1 cells increased over time. This suggests that the PLPG/PDLA scaffolds have good biocompatibility, supporting the proliferation of MC3T3-E1 cells. Additionally, no significant difference in cell viability was observed in the PLPG/PDLA scaffolds after three days of co-culture, further demonstrating the good cytocompatibility of these scaffolds.

Furthermore, the viability of MC3T3-E1 cells co-cultured with PLPG/PDLA scaffolds was assessed using live/dead staining over five days (Figure 4). Only a few cells stained red (indicating dead cells) were detected, while a large number of living cells stained green attached to the struts of the PLPG/PDLA scaffolds, indicating that the PLPG/PDLA scaffolds promote the growth and proliferation of MC3T3-E1 cells.

The proliferation capacity of MC3T3-E1 cells co-cultured with PLPG/PDLA scaffolds was further evaluated using confocal laser scanning microscopy (CLSM) images taken after a day. As displayed in Figure 5a, many cells adhered to the struts of the PLPG/PDLA scaffolds, with the cytoskeleton clearly visible. The expression of the adhesion protein vinculin (green) indicated that MC3T3-E1 cells exhibited substantial cytoplasmic spreading on the PLPG/PDLA scaffolds and were well-attached to F-actin (red), demonstrating that the PLPG/PDLA scaffolds promote cell proliferation and growth. Additionally, MC3T3-E1 cells were able to spread through the pores in the PLPG/PDLA scaffolds. The growth capacity of cells through these pores was also assessed using CLSM scanning along the Z-axis (Figure 5b). The 3D reconstruction images displayed that MC3T3-E1 cells were distributed along the

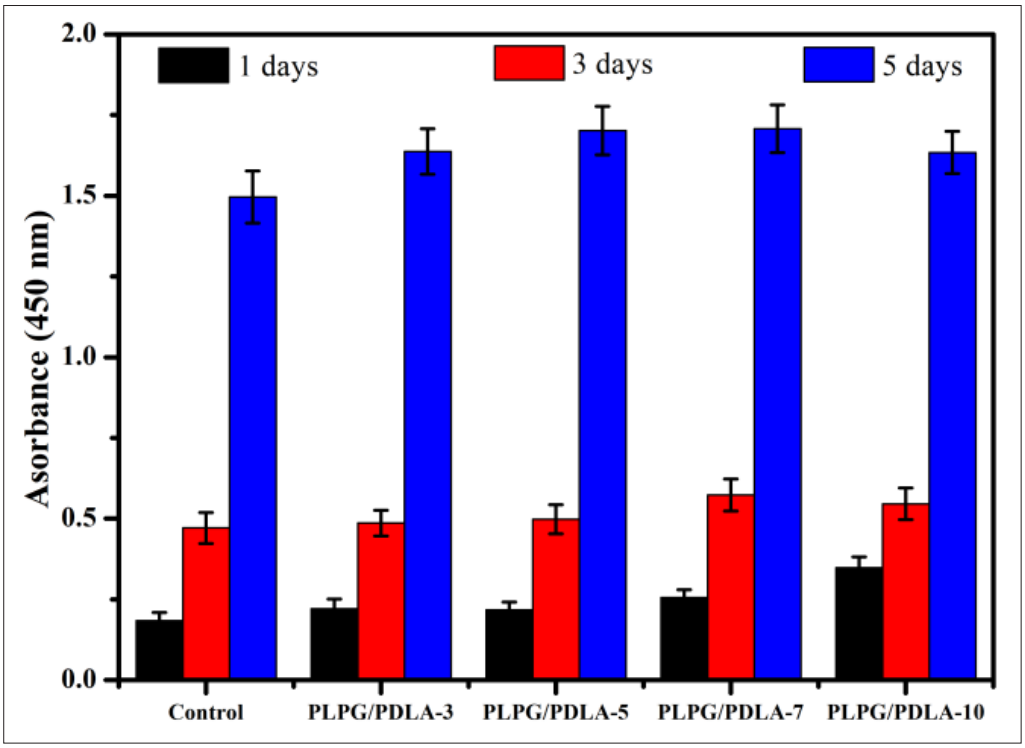

Figure 3. CCK-8 assay of MC3T3-E1 cells cultured on PLPG/PDLA scaffolds (n = 3). Abbreviations: PDLA: Poly(D-lactic acid); PLPG: PLLA-ran-PDO-ran-GA.

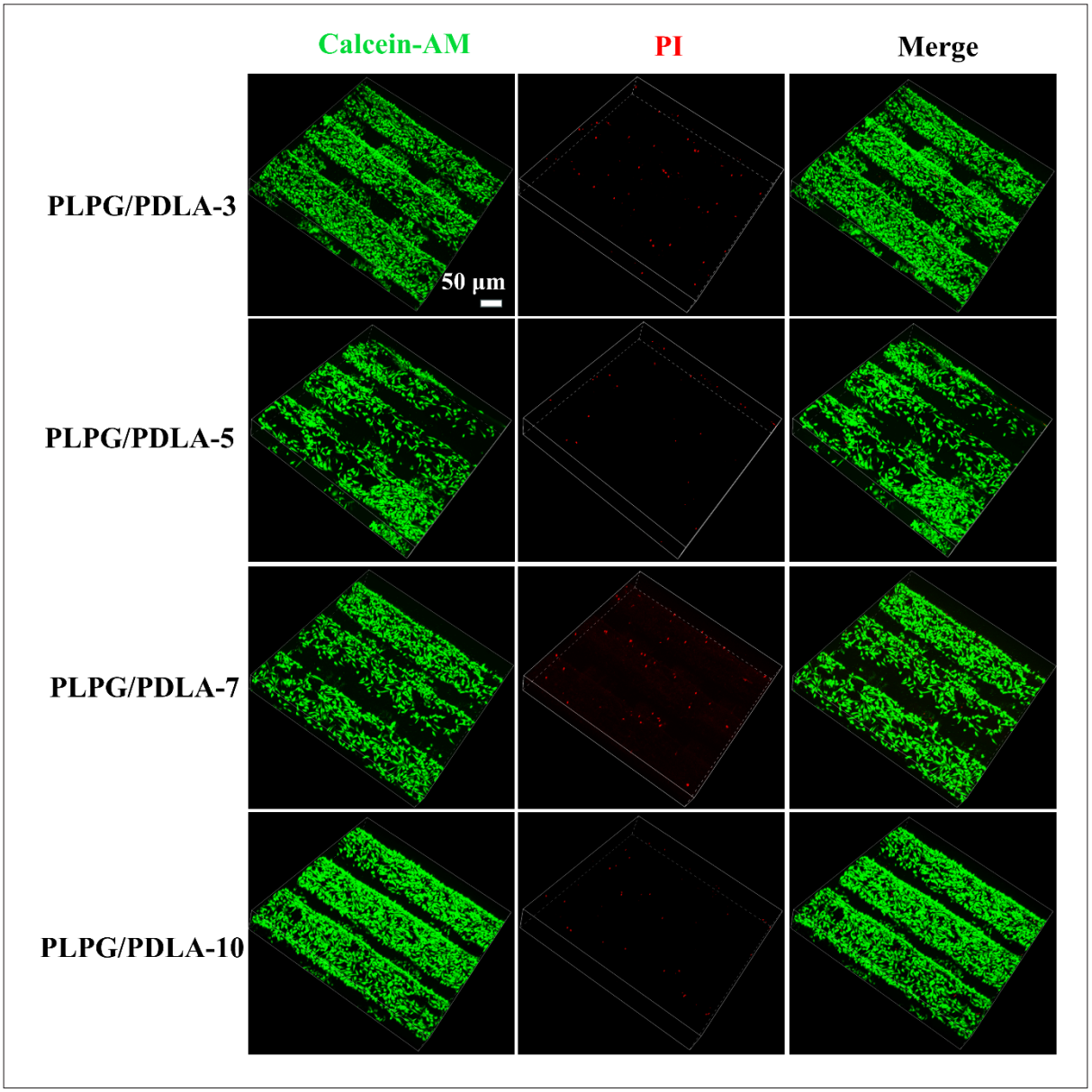

Figure 4. Live/dead staining of MC3T3-E1 cells co-cultured with PLPG/PDLA scaffolds. Scale bars: 50 μm. Abbreviations: PDLA: Poly(D-lactic acid); PLPG: PLLA-ran-PDO-ran-GA; PI: Propidium iodide.

Z-axis of the pores. Moreover, the density observed in the overhead view was much higher than that of the 2D results, indicating that the PLPG/PDLA scaffolds favor the growth and proliferation of MC3T3-E1 cells.

Alkaline phosphatase (ALP) staining of MC3T3-E1 cells co-cultured on PLPG/PDLA scaffolds was performed to assess early osteogenic activity over 14 days (Figure 6). As presented in Figure 6a, a few gray deposits appeared after 14 days. Quantitative analysis indicated that ALP expression was approximately 1.8 (Figure 6b). This is primarily due to the fact that the PLPG/PDLA scaffolds, being biodegradable polymer materials, have limited ability to promote bone formation. In light of this, future work will involve introducing bioactive materials into the PLPG/PDLA scaffolds to enhance their osteogenic properties.

4. Conclusion

In this study, we demonstrated that the addition of PDO and GA monomers negatively affects the crystallization capacity of PLPG copolymers, resulting in insufficient

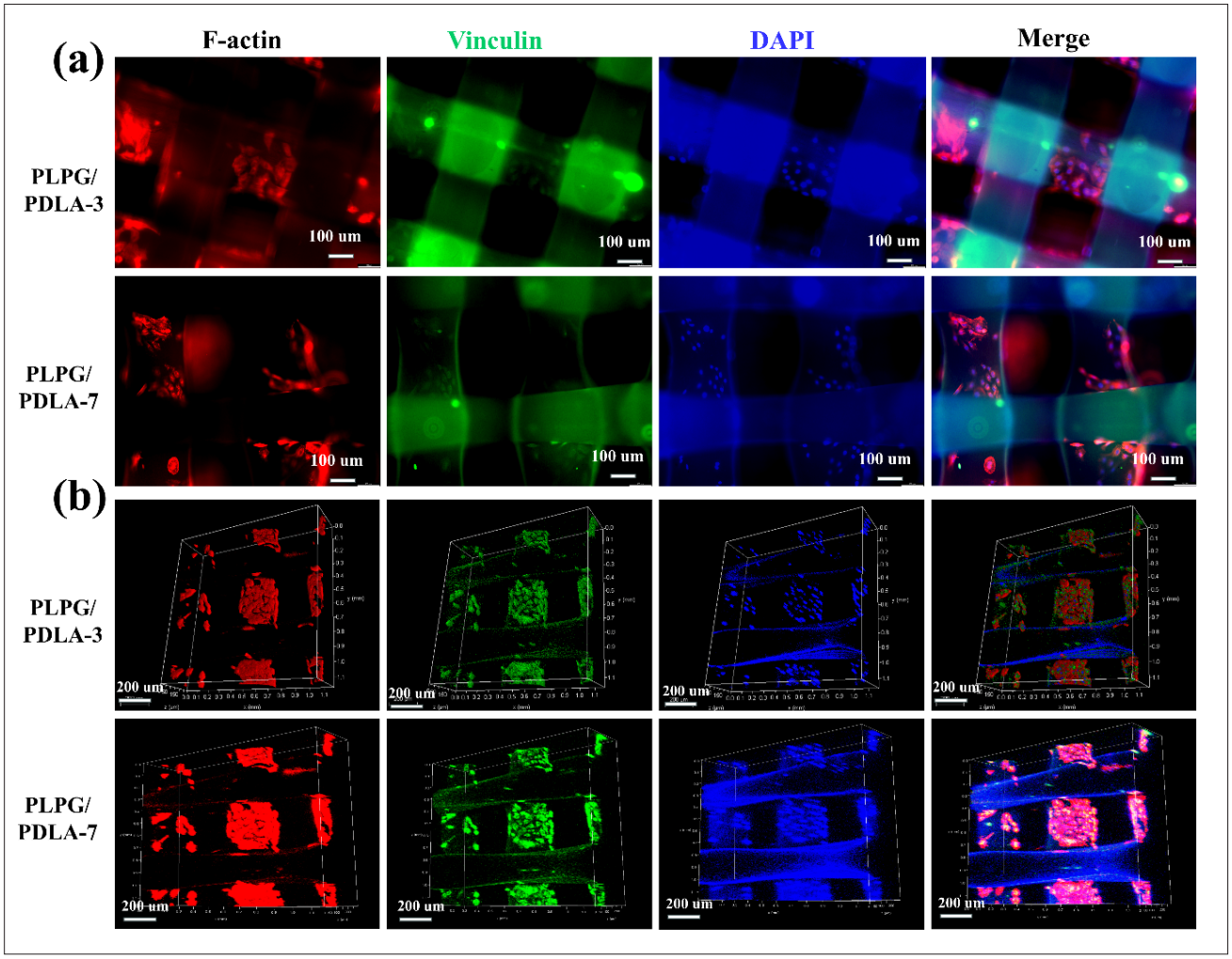

Figure 5. The distribution and growth of MC3T3-E1 cells on the PLPG/PDLA scaffolds (a) Confocal laser scanning microscopy (CLSM) images of MC3T3-E1 cells cultured with PLPG/PDLA scaffolds for one day. Scale bar = 100 μm. (b) 3D reconstruction of CLSM images of MC3T3-E1 cells cultured on PLPG/PDLA scaffolds for three days. Scale bar = 200 μm. Abbreviations: PDLA: Poly(D-lactic acid); PLPG: PLLA-ran-PDO-ran-GA.

mechanical properties. PLPG/PDLA composites were prepared using a solution method, followed by the fabrication of PLPG/PDLA scaffolds through 3D printing technology, based on the *in situ* formation of SC-PLA between PLLA and PDLA. SEM results displayed that the struts of the PLPG/PDLA scaffolds became increasingly uneven as the mass of PDLA increased to 7 wt.%. The findings indicate that the addition of PDLA enhances the mechanical properties of the PLPG/PDLA scaffolds. Compared to other scaffolds, the PLPG/PDLA-7 scaffolds exhibited superior mechanical and degradation abilities. Furthermore, *in vitro* experiments confirmed that PLPG/PDLA scaffolds possess good biocompatibility, supporting the growth and proliferation of MC3T3-E1 cells. It is important to note that the PLPG/PDLA scaffolds, being biodegradable polymer materials, have limited capabilities in promoting bone formation. Therefore, future studies will focus on incorporating bioactive materials into PLPG/PDLA scaffolds to improve their osteogenic properties. Overall, we believe that PLPG/PDLA scaffolds may be effectively applied in the field of bone tissue engineering to treat bone defects.

Acknowledgments

None.

Funding

This work was supported by the Research Fund for Academician Lin He New Medicine, Natural Science Foundation of Shandong Province (no. ZR2021QC205),

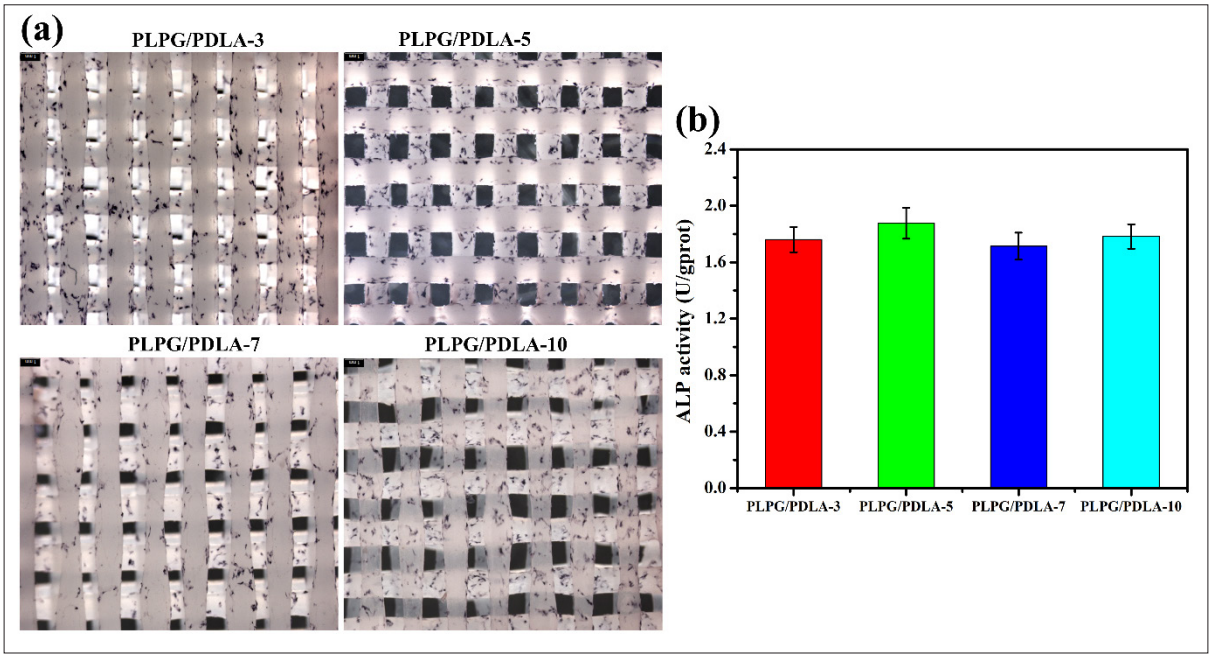

Figure 6. Osteosynthesis induction in MC3T3-E1 cells co-cultured on the PLPG/PDLA scaffolds. (a) Alkaline phosphatase (ALP) staining of PLPG/PDLA scaffolds for 14 days. (b) Quantitative analysis of MC3T3-E1 cells co-cultured on PLPG/PDLA scaffolds for 14 days (n = 3). Abbreviations: PDLA: Poly(D-lactic acid); PLPG: PLLA-ran-PDO-ran-GA.

and the National Natural Science Foundation of China-Young Scientists Fund (No. 81600867).

Conflict of interest

The authors declare that they have no competing interests.

Author contributions

Conceptualization: Tiantang Fan, Dongya Liu
Data curation: Tiantang Fan, Xiao Meng, Jingwen Qin, Ruishen Zhuge
Formal analysis: Tiantang Fan, Xiao Meng, Jingwen Qin, Ruishen Zhuge, Ruishen Zhuge
Funding: Tiantang Fan, Jianru Liu
Investigation: Tiantang Fan
Methodology: Yutong Wang, Chunyu Zhang, Yiqiao Yin
Resources: Jianru Liu, Tianyun Fan
Supervision: Tianyun Fan, Dongya Liu
Writing – original draft: Tiantang Fan
Writing – review & editing: Tianyun Fan, Dongya Liu

Ethics approval and consent to participate

Not applicable.

Consent for publication

Not applicable.

Availability of data

The data presented in this study are available upon request from the corresponding author.

References

1. Chen Y, Huang J, Liu J, et al. Tuning filament composition and microstructure of 3D-printed bioceramic scaffolds facilitate bone defect regeneration and repair. *Regen Biomater*. 2021;8:rbab007. doi: 10.1093/rb/rbab007
2. Wei S, Ma J, Xu L, et al. Biodegradable materials for bone defect repair. *Military Med Res*. 2020;7:1-25. doi: 10.1186/s40779-020-00280-6
3. Xu L, Ma F, Leung FK, et al. Chitosan-strontium chondroitin sulfate scaffolds for reconstruction of bone defects in aged rats. *Carbohyd Polym*. 2021;273:118532. doi: 10.1016/j.carbpol.2021.118532
4. Cendrero AM, Martínez FF, Requejo WGS, et al. Open-source library of tissue engineering scaffolds. *Mater Design*. 2022;223:111154. doi: 10.1016/j.matdes.2022.111154
5. Wang C, Huang W, Zhou Y, et al. 3D printing of bone tissue engineering scaffolds. *Bioact Mater*. 2020;5:82-91. doi: 10.1016/j.bioactmat.2020.01.004
6. Asghari F, Faradonbeh DR, Malekshahi ZV, et al. Hybrid PCL/chitosan-PEO nanofibrous scaffolds incorporated with

A. euchroma extract for skin tissue engineering application. *Carbohyd Polym*. 2022;278:118926.
doi: 10.1016/j.carbpol.2021.118926

7. Kuang T, Chen F, Chang L, et al. Facile preparation of open-cellular porous poly (l-lactic acid) scaffold by supercritical carbon dioxide foaming for potential tissue engineering applications. *Chem Eng J*. 2017;307:1017-1025.
doi: 10.1016/j.cej.2016.09.023

8. Bertsch C, Maréchal H, Gribova V, et al. Biomimetic bilayered scaffolds for tissue engineering: from current design strategies to medical applications. *Adv Healthc Mater*. 2023;12:2203115.
doi: 10.1002/adhm.202203115

9. Nigmatullin R, Taylor CS, Basnett P, et al. Medium chain length polyhydroxyalkanoates as potential matrix materials for peripheral nerve regeneration. *Regen Biomater*. 2023;10:rbad063.
doi: 10.1093/rb/rbad063

10. Duan R, Wang Y, Su D, et al. The effect of blending poly(l-lactic acid) on *in vivo* performance of 3D-printed poly(l-lactide-co-caprolactone)/PLLA scaffolds. *Biomater Adv*. 2022;138:212948.
doi: 10.1016/j.bioadv.2022.212948

11. Zheng S, Li W, Chen Y, et al. Synergistic effect of stereo-complexation and interfacial compatibility in ammonium polyphosphate grafted polylactic acid fibers for simultaneously improved toughness and flame retardancy. *Int J Biol Macromol*. 2024;261(Pt 2):129943.
doi: 10.1016/j.ijbiomac.2024.129943

12. Yang Y, Zan J, Yang W, et al. Metal organic frameworks as a compatible reinforcement in a biopolymer bone scaffold. *Mater Chem Front*. 2020;4:973-984.
doi: 10.1039/C9QM00772E

13. Fan T, Qin J, Li J, et al. Fabrication and evaluation of 3D printed poly(l-lactide) copolymer scaffolds for bone tissue engineering. *Int J Biol Macromol*. 2023;245:125525.
doi: 10.1016/j.ijbiomac.2023.125525

14. Liu H, Bai D, Bai H, et al. Constructing stereocomplex structures at the interface for remarkably accelerating matrix crystallization and enhancing the mechanical properties of poly(L-lactide)/multi-walled carbon nanotube nanocomposites. *J Mater Chem A*. 2015;3:13835-13847.
doi: 10.1039/c5ta02017d

15. Cheng Y, Jiao Z, Li M, et al. A new class of nucleating agents for poly(L-lactic acid): environmentally-friendly metal salts with biomass-derived ligands and advanced nucleation ability. *Int J Biol Macromol*. 2023;225:1599-1606.
doi: 10.1016/j.ijbiomac.2022.11.216

16. Yu B, Meng L, Fu S, et al. Morphology and internal structure control over PLA microspheres by compounding PLLA and PDLA and effects on drug release behavior. *Colloid Surface B*. 2018;172:105-112.
doi: 10.1016/j.colsurfb.2018.08.037

17. Zhang Y, Wang Y, Wang B, et al. Exclusive formation of poly(lactide) stereocomplexes with enhanced melt stability via regenerated cellulose assisted Pickering emulsion approach. *Compos Commun*. 2022;32:101138.
doi: 10.1016/j.coco.2022.101138

18. Zhou W, Chen X, Yang K, et al. Achieving morphological evolution and interfacial enhancement in fully degradable and supertough polylactide/polyurethane elastomer blends by interfacial stereocomplexation. *Appl Surf Sci*. 2022;572:151393.
doi: 10.1016/j.apsusc.2021.151393

19. Zhang H, Bai H, Deng S, et al. Achieving all-polylactide fibers with significantly enhanced heat resistance and tensile strength via *in situ* formation of nanofibrilized stereocomplex polylactide. *Polymer*. 2019;166:13-20.
doi: 10.1016/j.polymer.2019.01.040

20. Jalali A, Romero-Diez S, Nofar M, et al. Entirely environment-friendly polylactide composites with outstanding heat resistance and superior mechanical performance fabricated by spunbond technology: exploring the role of nanofibrillated stereocomplex polylactide crystals. *Int J Biol Macromol*. 2021;193:2210-2220.
doi: 10.1016/j.ijbiomac.2021.11.052

21. Li J, Ye W, Fan Z, et al. A novel stereocomplex poly (lactic acid) with shish-kebab crystals and bionic surface structures as bioimplant materials for tissue engineering applications. *ACS Appl Mater Interfaces*. 2021;13:5469-5477.
doi: 10.1021/acsami.0c17465

22. Feng L, Bian X, Li G, et al. Thermal properties and structural evolution of poly(l-lactide)/poly(d-lactide) blends. *Macromolecules*. 2021;54:10163-10176.
doi: 10.1021/acs.macromol.1c01866

23. Körber S, Moser K, Diemert J. Development of high temperature resistant stereocomplex PLA for injection moulding. *Polymers*. 2022;14:384.
doi: 10.3390/polym14030384

24. Yan Q, Dong H, Su J, et al. A review of 3D printing technology for medical applications. *Engineering*. 2018;4:729-742.
doi: 10.1016/j.eng.2018.07.021

25. Liu X, Zhang J, Cheng X, et al. Integrated printed BDNF-stimulated HUCMSCs-derived exosomes/collagen/chitosan biological scaffolds with 3D printing technology promoted the remodelling of neural networks after traumatic brain injury. *Regen Biomater*. 2023;10:rbac085.
doi: 10.1093/rb/rbac085

26. Jiang S, Wang M, He J. A review of biomimetic scaffolds for bone regeneration: toward a cell-free strategy. *Bioeng Transl Med*. 2021;6:e10206.
doi: 10.1002/btm2.10206

27. Jia W, Li H, Wang Z, et al. 3D composite lithium metal with multilevel micro-nano structure combined with surface modification for stable lithium metal anodes. *Appl Surf Sci*. 2021;570:151159.

doi: 10.1016/j.apsusc.2021.151159

28. Feng C, Ma B, Xu M, et al. Three-dimensional printing of scaffolds with synergistic effects of micro–nano surfaces and hollow channels for bone regeneration. *ACS Biomater Sci Eng*. 2020;7:872-880.
doi: 10.1021/acsbiomaterials.9b01824

29. Fan T, Qin J, Dong F, et al. Effects on the crystallization behavior and biocompatibility of poly(LLA-ran-PDO-ran-GA) with poly(d-lactide) as nucleating agents. *RSC Adv*. 2022;12:10711-10724.
doi: 10.1039/d2ra00525e

30. Yu H, Chen X, Cai J, et al. Novel porous three-dimensional nanofibrous scaffolds for accelerating wound healing. *Chem Eng J*. 2019;369:253-262.
doi: 10.1016/j.cej.2019.03.091

31. Peng MW, Yu XL, Guan Y, et al. Underlying promotion mechanism of high concentration of silver nanoparticles on anammox process. *ACS Nano*. 2019;13:14500-14510.
doi: 10.1021/acsnano.9b08263

32. Zhang Y, Ge T, Li Y, et al. Anti-fouling and anti-biofilm performance of self-polishing waterborne polyurethane with Gemini quaternary ammonium salts. *Polymers*. 2023;15:317.
doi: 10.3390/polym15020317

33. Zhao Z, Yang L, Hu Y, et al. Enzymatic degradation of block copolymers obtained by sequential ring opening polymerization of l-lactide and ε-caprolactone. *Polym Degrad Stabil*. 2007;92:1769-1777.
doi: 10.1016/j.polymdegradstab.2007.07.012

34. Chen Z, Ding D, Yu T, et al. Enzymatic degradation behaviors and kinetics of bio-degradable jute/poly (lactic acid)(PLA) composites. *Compos Commun*. 2022;33:101227.
doi: 10.1016/j.coco.2022.101227

35. Huang Q, Hiyama M, Kabe T, et al. Enzymatic self-biodegradation of poly(l-lactic acid) films by embedded heat-treated and immobilized proteinase K. *Biomacromolecules*. 2020;21:3301-3307.
doi: 10.1021/acs.biomac.0c00759

36. Arbeiter D, Lebahn K, Reske T, et al. Comparison of accelerated and enzyme-associated real-time degradation of HMW PLLA and HMW P3HB films. *Polym Test*. 2022;107:107471.
doi: 10.1016/j.polymertesting.2021.107471

ACCSCIENCE PUBLISHING

International Journal of Bioprinting

RESEARCH ARTICLE

Internally-crosslinked alginate dialdehyde/alginate/gelatin-based hydrogels as bioinks for prospective cardiac tissue engineering applications

Giovanni Paolo Stola[1,2], Camilla Paoletti[1,2], Letizia Nicoletti[1,2], Geo Paul[3], Claudio Cassino[3], Leonardo Marchese[3], Valeria Chiono[1,2*], and Elena Marcello[1,2*]

[1]Department of Mechanical and Aerospace Engineering, POLITO BioMedLab, Politecnico di Torino, Turin, Italy

[2]Interuniversity Center for the Promotion of the 3Rs Principles in Teaching and Research (Centro 3R), Pisa, Italy

[3]Department of Science and Technological Innovation and "Centro Interdisciplinare Nano-SiSTeMI", Università del Piemonte Orientale, Alessandria, Italy

Abstract

Cardiovascular diseases represent a global challenge due to heart-limited regenerative capabilities. 3D-bioprinted cell-laden constructs are a promising approach as cardiac patches or *in vitro* models. However, developing bioinks with optimal mechanical, rheological, and biological properties remains challenging. Although alginate (Alg)-based bioinks have been extensively explored, such hydrogels lack cell adhesion properties and degradability. Additionally, 3D Alg structures are usually obtained by microextrusion bioprinting, exploiting conventional external crosslinking methods, which introduce inhomogeneities and unpredictability in construct formation. This work exploits Alg internal ionic gelation mechanism to obtain homogeneous self-standing multilayered 3D-printed constructs without employing support baths or post-printing crosslinking treatments. Alg was blended with oxidized alginate (ADA) and gelatin (Gel) to achieve degradable and cell-adhesive hydrogels for cardiac tissue engineering. Firstly, ADA/Alg bioink composition was tailored to achieve cardiac tissue-like viscoelastic properties. Then, the amount of Gel in ADA/Alg hydrogels was optimized to support cell adhesion, producing shear thinning inks with tunable viscoelastic properties (storage modulus [G']: 650–1300 Pa) and degradation profile (40–80% weight loss after 21 days in phosphate-buffered saline [PBS]) by varying Gel concentration. ADA/Alg/Gel hydrogels displayed shear thinning behavior, suitable for 3D bioprinting depending on the ink stabilization time, due to the gradual pH-triggered release of calcium ions over time. Adult human cardiac fibroblast (AHCF) and H9C2-laden ADA/Alg/Gel bioinks were successfully printed, producing scaffolds with high shape fidelity and good cell viability post-printing. Finally, the highest Gel content (25% [w/w]) supported cell adhesion after 24 h of incubation, displaying potential for cardiac tissue modeling. This research presents a comprehensive framework for advancing the design of bioink.

Keywords: Alginate dialdehyde; Gelatin; Bioink; Internal gelation; *In vitro* cardiac models

***Corresponding authors:**
Valeria Chiono (valeria.chiono@polito.it)

Elena Marcello (elena.marcello@polito.it)

Citation: Stola GP, Paoletti C, Nicoletti L, et al. Internally-crosslinked alginate dialdehyde/alginate/gelatin-based hydrogels as bioinks for prospective cardiac tissue engineering applications. *Int J Bioprint*. 2024;10(6):4014. doi: 10.36922/ijb.4014

Received: June 21, 2024
1st revised: August 1, 2024
2nd revised: September 10, 2024
Accepted: September 18, 2024
Published Online: September 18, 2024

Copyright: © 2024 Author(s). This is an Open Access article distributed under the terms of the Creative Commons Attribution License, permitting distribution, and reproduction in any medium, provided the original work is properly cited.

Publisher's Note: AccScience Publishing remains neutral with regard to jurisdictional claims in published maps and institutional affiliations.

1. Introduction

3D bioprinting has radically transformed the manufacturing process of scaffolds for tissue engineering (TE) applications by converting computer-aided design models into layered structures, bypassing traditional molding methods.[1] Highly reproducible and customizable 3D-printed scaffolds can be employed as a potential approach to meet the increasing global demand for organ replacement and tissue regeneration.[2,3] In this scenario, the heart ranks as the third most transplanted organ worldwide, primarily because it represents the only therapeutic option in case of end-stage heart failure due to its poor intrinsic regenerative capacity. In the last three decades, cardiac TE has emerged as a potential new therapeutic and *in vitro* modeling approach, based on the use of biomaterials, eventually combined with bioactive factors, with/without cells for regeneration.[4] 3D-bioprinted constructs can be exploited as therapeutic patches[5,6] to favor heart regeneration or as *in vitro* models of human cardiac tissue for preclinical validation of drugs and therapies, in agreement with the 3Rs principles.[7]

Among 3D bioprinting techniques, microextrusion bioprinting is based on the layer-by-layer deposition of cell-laden bioinks to create intricate 3D structures. This technique has emerged as a promising tool in TE, owing to its scalability, versatility, and the capability to incorporate various cell types, growth factors, and biomolecules within the bioink matrix.[8] Microextrusion printing relies on hydrogels as ideal bioink materials for 3D printing cell-laden constructs, allowing the production of hydrated constructs mimicking the natural extracellular matrix (ECM) of tissues.[9] Despite considerable efforts, one key challenge in micro-extrusion bioprinting is the availability of suitable bioinks able to fulfill all the following requirements: (i) biocompatibility; (ii) biomimetic properties comparable to the ECM of the target tissue, in order to favor cell adhesion, spreading, and differentiation; (iii) controlled degradability, ideally matching the cell-mediated ECM deposition rate; and (iv) proper rheological characteristics for printing.[10-12]

Among the materials investigated for microextrusion bioprinting applications, alginate (Alg) has been widely employed due to its tunable properties, cost-effectiveness,[10,11] non-immunogenicity, and non-toxicity. Hence, Alg represents an excellent candidate for regenerative medicine and has been recently tested in preclinical research and clinical trials for cardiovascular diseases.[12,13] Algysil-LVR (LoneStar Heart Inc., United States of America [USA]) is an Alg-based injectable hydrogel designed for the treatment of heart failure by reshaping the left ventricle geometry, preventing or reversing ventricular enlargement.[12,14] Once injected, the biopolymer thickens and forms gel bodies that remain in the heart muscle as permanent internal support implants for the injured heart, preventing disease progression.[12,14] The device has been tested in three clinical trials: two were completed (ClinicalTrials.gov identifier: NCT00847964; NCT01311791 [AUGMENT-HF]) and one has been published but is still not recruiting (ClinicalTrials.gov identifier: NCT03082508 [AUGMENT-HF II]). However, Algysil-LVR is defined as a permanent device that only offers mechanical support to the left ventricle without providing full restoration of cardiac functionality.[12,13]

One of the most interesting properties of Alg is the ability to complex with divalent cations, particularly calcium ions, to form hydrogels through physical crosslinking under physiological conditions, forming an "egg box" model.[15] Depending on the source of calcium ions, two different modes of ionic crosslinking have been investigated: internal and external methods.[16-18] External gelation is characterized by the use of highly soluble calcium salts (i.e., $CaCl_2$) and consists of the diffusion of multivalent cations from the outside into the Alg solution phase, forming a crosslinked Alg matrix. Most studies on microextrusion bioprinting of Alg bioinks have exploited such external mechanism.[19-21] The use of external crosslinking leads to the formation of a non-homogeneous filament, characterized by a highly crosslinked surface, as the rapid gelation is confined at the interface between the calcium solution and Alg phase.[22,23] Such highly crosslinked surface might affect the behavior of embedded cells, limiting the diffusion of nutrients and oxygen.[24,25] Moreover, the application of the external crosslinking technique is usually associated with the use of coagulation baths, in which the Alg phase is extruded. Such baths (e.g., freeform reversible embedding of suspended hydrogels [FRESH] printing[19]) physically support the extruded bioink filaments and allow crosslinking of its polymeric chains to obtain constructs with high shape fidelity and resolution. However, the use of such a support bath, which involves a microparticle slurry, adds complexity to the bioprinting process, as particle size and shape can significantly affect bioprinting resolution and the morphology of the printed filaments.[26] Lastly, the use of external gelation can be a drawback for drug delivery applications, as the cargo embedded within the bioink might be partially released during the coagulation step.

Recently, internal gelation of Alg solutions has been studied to develop 3D self-standing constructs without the need for a support bath. Internal gelation involves the dispersion of water-insoluble calcium salt, such as calcium carbonate ($CaCO_3$), within the Alg solution, followed by the gradual release of calcium ions through a decrease in pH that is induced by an acidic compound, usually

D-(+)-glucono-1,5-lactone (GDL).[16,18] Internal gelation allows a more uniform distribution of multivalent cations within the Alg phase during gelation, resulting in a more homogeneous gel and allowing 3D printing of uniform self-supporting hydrogel fibers, without the need for post-crosslinking or supporting materials or baths.[27,28] However, internal crosslinking of Alg-based bioinks has been often used as a pre-crosslinking mechanism to improve the printability of the hydrogel by increasing its viscosity.[22,29] Hence, in such studies, an external gelation mechanism has been added to fully crosslink the construct and improve hydrogel stability. The application of the secondary external crosslinking mechanism can lead to the release of water-soluble components present in the bioink, such as proteins (e.g., gelatin or collagen) or small hydrophilic molecules (added for drug release applications).[27,30] Limited research has been conducted on solely utilizing internal crosslinking to print self-standing uniform Alg-based 3D constructs.[27,28] Remaggi et al. investigated the printability of Alg bioinks with $CaCO_3$ and GDL to be used as a platform for the delivery of Epirubicin, a water-soluble drug for the treatment of breast cancer.[27] However, in that study, selected printing conditions comprised a curing time of three days at 2°C, which is not suitable for *in vitro* cell cultures. Sardelli et al. performed an extensive investigation on the printability of Alg inks by internal gelation, exploring the rheological properties of the material and fiber printability.[28] Guagliano et al. recently developed a bioink composed of internally crosslinked Alg and ECM for bioprinting volumetric hepatic tissue models. The scaffold design was optimized to achieve 14-layered printed constructs using internal gelation alone, demonstrating the bioink capability to support mid/long-term cultures of human liver cancer cells (HepG2) in static conditions for up to 12 days.[31-33]

Although Alg has been extensively used for biomedical applications, it is limited by two main drawbacks: (i) poor *in vivo* degradability due to the lack of enzymes in mammals that can induce the degradation of Alg, and (ii) lack of adhesive moieties for cells.[10,11] To overcome the first drawback, Alg dialdehyde (ADA), an oxidized form of Alg, has been obtained by partial oxidation with sodium metaperiodate.[34,35] Literature studies suggested that ADA has a lower molecular weight (MW) compared to Alg, and its degradation occurs by alkaline β-elimination.[34,35] To improve cell adhesion and proliferation, Alg hydrogels have been previously blended with gelatin (Gel)[36,37] and stabilized by an external physical gelation or a double crosslinking mechanism via chemical reactions (i.e., Schiff base formation between the aldehyde groups of ADA and the amino groups of Gel) and external ionic gelation.[36,38,39] Recently, Heid et al. evaluated the possibility of printing ADA/Gel hydrogels via an internal crosslinking mechanism through the incorporation of bioactive inorganic fillers that can slowly release bivalent calcium ions.[40] Nevertheless, the addition of external gelation was necessary to achieve well-defined 3D-printed ADA/Gel constructs, and internal gelation only improved ADA/Gel *in vitro* stability for long periods (i.e., up to 21 days).

The novelty of this work lies in the combination of ADA, Alg, and Gel hydrogels with an internal crosslinking mechanism to develop bioinks for prospective applications in *in vitro* cardiac TE. Although studies have already investigated the use of internal gelation for Alg bioprinting,[28,32,33] we reported the possibility of exploiting such crosslinking for ADA-based hydrogels, in combination with Alg and Gel, with ADA as the main component. Moreover, we investigated the possibility of applying these materials for the development of self-standing homogeneous structures for future applications in cardiac TE. Firstly, ADA/Alg hydrogel composition was optimized by varying the content of calcium ions ($CaCO_3$) and GDL to achieve cardiac tissue-like viscoelastic properties. Then, the amount of Gel in ADA/Alg hydrogels was optimized to achieve tunable viscoelastic and degradation properties, cytocompatibility, and cell-adhesive properties. All hydrogel formulations were characterized through rheological and *in vitro* degradation studies. Three gelatin concentrations were then selected for 3D microextrusion printing, and material printability was investigated over time to evaluate the effect of time-dependent pH-triggered release of calcium ions. Specifically, the composition and crosslinking kinetics were fine-tuned to achieve an optimal printability window suitable for application in 3D bioprinting (i.e., 15–90 min) without using curing or post-processing strategies. *In vitro* biocompatibility of the three hydrogel systems was investigated using adult human cardiac fibroblasts (AHCFs). Finally, as a proof of concept for cardiac TE applications, bioprinting of AHCF-laden and H9C2-laden hydrogels was investigated, and cell viability after printing was studied.

2. Materials and methods

2.1. Materials

Sodium Alg (alginic acid sodium salt, medium viscosity) was purchased from MP Biomedicals (USA). Calcium carbonate ($CaCO_3$), GDL (C6H1006), potassium iodide (KI), and soluble starch solution were obtained from Alfa Aesar (USA). Sodium metaperiodate ($NaIO_4$; MW: 213.98), sodium chloride (NaCl), Gel (Bloom 300, Type A, porcine skin, suitable for cell culture), 2,4,6-trinitrobenzene sulfonate (TNBS), tert-butyl carbazate (t-BC), phosphate-buffered saline (PBS) tablets, and Trypsin/EDTA solution were supplied from Sigma-Aldrich (USA). Dialysis

membrane tubings were acquired from Spectrum Lab (Spectrum™ Spectra/Por™, New Zealand), based on regenerated cellulose with MW cut-off (MWCO) of 6–8 kDa. Ethanol absolute, anhydrous ethylene glycol and hydrochloric acid (37% [w/v]) were obtained from Carlo Erba (Italy). Dulbecco's modified Eagle medium (DMEM), fetal bovine serum (FBS), sodium pyruvate, and L-glutamine solution were acquired from GIBCO (USA). CellTiter Blue and CytoTOX-ONE™ assay were acquired from Promega (USA). Live/Dead™ Viability/Cytotoxicity Kit was obtained from Invitrogen (USA).

2.2. Production and characterization of alginate dialdehyde

2.2.1. Production of alginate dialdehyde

Alginate dialdehyde (ADA) was prepared by controlled oxidation of sodium Alg via sodium metaperiodate according to the protocol by Sarker et al.[41] Briefly, a 20% (w/v) sodium Alg dispersion in ethanol was prepared and stirred for 1 h at room temperature. A 0.3 M solution of sodium metaperiodate in deionized water was then added dropwise to the sodium Alg dispersion under magnetic stirring in the dark at room temperature. After 6 h, the reaction was quenched by adding 0.2% (v/v) ethylene glycol solution under continuous stirring for 30 min. The resulting solution was dialyzed (Spectrum™ Spectra/Por™ membrane; MWCO: 6–8 kDa) in deionized water for seven days to remove all traces of unreacted sodium metaperiodate and then lyophilized.

Two methods were used to determine ADA degree of oxidation: an indirect and a direct method. For the indirect method, the degree of oxidation was determined by measuring the unreacted sodium metaperiodate before quenching the reaction with ethylene glycol. A soluble starch indicator solution was prepared by mixing equal volumes of KI (20% [w/v]) and soluble starch (1% [w/v]) solutions using PBS as the solvent. Reaction mixture (1 mL) was added to 250 mL of deionized water. Then, 3 mL of the diluted solution was mixed with 1.5 mL of indicator solution and 0.5 mL of distilled water. The absorbance of the tri-iodine-starch complex was measured using a UV-Vis spectrophotometer (Varioskan LUX multimode microplate, Thermofisher, Italy) at 486 nm. The concentration of periodate in the sample was obtained using a calibration curve previously obtained with different concentrations of sodium metaperiodate (0.0016–0.02 mg/mL). The difference between the initial and final amount of sodium metaperiodate corresponds to the hydroxyl groups converted into aldehyde groups.

For the direct method, the quantification of aldehyde groups was performed using the TNBS assay, following a protocol described by Wang et al.[42] Briefly, 25 µL of ADA solution (1% [w/v]) was mixed with 25 µL t-BC (30 mM in acetic acid) and allowed to react overnight. Subsequently, 0.5 mL of TNBS solution (6 mM in 0.1 M sodium bicarbonate) was added and allowed to react for 1 h. The reaction was quenched by adding 0.55 mL of HCl (0.5 N), and the absorbance was measured at 340 nm using the UV-Vis spectrophotometer (Varioskan LUX multimode microplate, Thermofisher, Italy). The concentration of unreacted t-BC was calculated using a calibration curve obtained using t-BC standards and aldehyde groups determined by calculating the reacted t-BC.

2.2.2. Determination of viscosity average molecular weight

The viscosity average molecular weight (Mv) of Alg and ADA was determined by viscometric analysis using an Ubbelohde viscometer (Poulten Selfe & Lee Limited, England).[43] Briefly, Alg and ADA solutions were prepared at different concentrations (0.025–0.2 and 0.2–0.6% [w/v], respectively). Inherent and reduced viscosity were calculated and plotted against concentration. Finally, after checking the linearity, the intrinsic viscosity (η) was derived, and Mv was calculated according to the Mark-Houwink-Sakurada equation (Equation I).[44]

$$[\eta] = K\,\mathrm{Mv}^{\alpha} \quad \text{(I)}$$

where $K = 0.0073 cm^3/g$ and $\alpha = 0.92$ are the Mark-Houwink-Sakurada parameters considered for Alg and ADA.[44]

2.2.3. Attenuated total reflectance Fourier transform infrared spectroscopy

Attenuated total reflectance Fourier transform infrared (ATR-FTIR) was carried out to investigate the formation of aldehyde groups in the Alg chains. The analyses were performed in a spectral range of 4000–600 cm^{-1} with a resolution of 4 cm^{-1} using ATR-FTIR Frontier FT-IR Perkin Elmer instrument (PerkinElmer Inc., USA).

2.2.4. Nuclear magnetic resonance spectroscopy analysis

^{13}C cross polarization under magic angle spinning (CP-MAS) nuclear magnetic resonance spectroscopy (NMR) of Alg powder and ADA lyophilized samples was performed using a Bruker AVANCE III HD NMR spectrometer (Bruker, Germany) equipped with an 11.74 T superconducting magnet (500 MHz ^{1}H Larmor frequency; Bruker, Germany) to investigate the presence of aldehyde groups. Moreover, Alg and ADA block composition (M/G ratios) was calculated from ^{13}C CP-MAS NMR spectra deconvoluted using Gaussian and/or Lorentzian line

shapes.[45] Thus, the M/G ratio was estimated according to **Equation II**:

$$\frac{M}{G}ratio = \frac{E+F}{D+G+H} \quad \text{(II)}$$

where E and F are the integrated intensities of signals at 76.4 and 71.6 ppm, respectively, to estimate the mannuronate content; and D, G, and H are the integrated intensities of signals at 82.8, 68.4, and 65.5 ppm, respectively, to estimate the guluronate content.

2.3. Hydrogel composition and preparation

All the hydrogels were obtained using a dual-syringe mixing method starting from 8% (w/v) Alg, ADA, and Gel stock solutions in PBS.

2.3.1. ADA/Alg hydrogels

The ADA/Alg hydrogels were optimized by varying the ADA:Alg polymer ratio (2:1 and 1:1) and the final $CaCO_3$ concentration (1.5, 3, and 6%), while keeping the GDL content (5% [w/v]) and the final polymer concentration (6% [w/v]) constant, as described in **Table 1**. Hydrogels were prepared in subsequential steps using the dual-syringe luer-lock mixing method. Firstly, ADA and Alg solutions were mixed according to the specific ratio; $CaCO_3$ in powder form was then added and mixed thoroughly. Finally, an aqueous GDL solution was added to the ADA/Alg/$CaCO_3$ systems at a fixed proportion of 1:4 (GDL volume: total volume).

The GDL content was then optimized on ADA/Alg_50/50_C6 hydrogels by varying the final GDL concentration (1, 1.5, 2, 2.5, and 5% [w/v]), keeping the total polymer (6% [w/v]) and $CaCO_3$ concentrations (6% [w/v]) constant.

2.3.2. ADA/Alg/Gel hydrogels

Gelatin (Bloom 300, Type A, porcine skin; Merck, USA) was added to selected ADA/Alg_50/50 samples with 6% (w/v) $CaCO_3$ and 1.5% (w/v) GDL final concentration. The Gel content of ADA/Alg/Gel samples was optimized, keeping the final ADA concentration at 3% (w/v) and varying Alg:Gel polymer weight ratios from 100:0 to 50:50 (w/w), while maintaining the final concentration of Alg/Gel at 3% (w/v), as described in **Table 2**. ADA/Alg/Gel hydrogels were produced as described in **Section 2.3.1** using the dual-syringe luer-lock mixing method. Specifically, Gel solution was mixed with ADA/Alg blend solution before the addition of $CaCO_3$.

2.4. Rheological characterization

The rheological characterization of hydrogels (2 mm height) was performed at 37°C using an MCR 302 rheometer (Anton Paar, Austria) equipped with a parallel plate geometry (25 mm diameter). Oscillatory time sweep analyses were performed immediately after component mixing at a frequency of 5 Hz and a strain of 1% to evaluate the gel point of the hydrogels. The gel point was calculated as the time in which storage modulus (G′) is equal to loss modulus (G″). Strain sweep analyses of hydrogels (2 mm height) were performed 2 h after hydrogel formation to ensure the complete crosslinking at a frequency of 5 Hz, varying the strain from 0.1 to 100% to determine the linear viscoelastic (LVE) region. Frequency sweep analyses of hydrogels (2 mm height) were performed 2 h after hydrogel formation to ensure the complete crosslinking at a constant strain of 1%, varying the frequency from 0.1 to 100 rad/s, and were used to determine G′ and G″. The tests were performed in triplicate. Frequency analyses were used to estimate the elastic modulus (E), according to **Equation III**[46]:

$$E = 2G \cdot (1 + \nu) \quad \text{(III)}$$

where ν is the Poisson's ratio (i.e., 0.5 for alginate) and G is the storage modulus at 1 rad/s. Shear rate sweep tests were performed immediately after component mixing to investigate the non-Newtonian behavior of bioinks. Apparent viscosity (η) was recorded at selected time points

Table 1. Composition of tested ADA/Alg hydrogels with varying ADA:Alg polymer ratio and $CaCO_3$ (%w/v) concentration.

Code	Composition (wt%)		Final concentration (% [w/v])			
	ADA	Alg	ADA	Alg	$CaCO_3$	GDL
ADA/Alg_66/33_C1.5	66.6	33.3	4	2	1.5	5
ADA/Alg_66/33_C3	66.6	33.3	4	2	3	5
ADA/Alg_66/33_C6	66.6	33.3	4	2	6	5
ADA/Alg_50/50_C3	50	50	3	3	3	5
ADA/Alg_50/50_C6	50	50	3	3	6	5

Note: GDL (5% [w/v]) and total polymer (6% [w/v]) concentrations were kept constant. Abbreviations: ADA: Alginate dialdehyde; Alg: Alginate; GDL: D-(+)-glucono-1,5-lactone.

Table 2. ADA/Alg/Gel hydrogel compositions investigated.

Code	Composition (wt.%)			Final concentrations (% [w/v])				
	ADA	Alg	Gel	ADA	Alg	Gel	$CaCO_3$	GDL
ADA/Alg/Gel_50/50/0	50	50	0	3	3	0	6	1.5
ADA/Alg/Gel_50/47.5/2.5	50	47.5	2.5	3	2.85	0.15	6	1.5
ADA/Alg/Gel_50/45/5	50	45	5	3	2.7	0.3	6	1.5
ADA/Alg/Gel_50/40/10	50	40	10	3	2.4	0.6	6	1.5
ADA/Alg/Gel_50/35/15	50	35	15	3	2.1	0.9	6	1.5
ADA/Alg/Gel_50/30/20	50	30	20	3	1.8	1.2	6	1.5
ADA/Alg/Gel_50/25/25	50	25	25	3	1.5	1.5	6	1.5

Note: The final content of ADA was kept constant at 3% (w/v); Alg:Gel polymer weight ratios varied from 100:0 to 50:50; the final content of Alg+Gel was equivalent to 3% (w/v); the final concentrations of $CaCO_3$ and GDL were 6 and 1.5% (w/v), respectively. Abbreviations: Gel: Gelatin; ADA: Alginate dialdehyde; Alg: Alginate; GDL: D-(+)-glucono-1,5-lactone.

(2, 10, 20, 30, 45, 60, and 90 min) by varying the shear rate from 0.1 to 500 1/s to investigate the flow properties of the ink during extrusion.

2.5. *In vitro* stability studies

In vitro stability analysis of ADA/Alg/Gel hydrogels was performed upon incubation in PBS at 37°C. Samples (0.5 mL) were incubated in 500 µL PBS for 1, 5, 7, 14, and 21 days. At each time point, the weight of the wet hydrogel ($w_{s,t}$) was measured; the samples were then frozen at −20°C, lyophilized, and weighed again ($w_{d,t}$). The wet weight variation percentage is defined in **Equation IV**:

$$Wet\ weight\ variation(\%) = \frac{w_{s,t} - w_{s,0}}{w_{s,0}} \times 100 \quad \text{(IV)}$$

where $w_{s,t}$ is the weight of the swollen hydrogel and $w_{s,0}$ the initial wet weight of the hydrogel. The dry weight loss percentage at the time *i* was calculated using **Equation V**:

$$Dry\ weight\ loss(\%) = \frac{w_{d,0} - w_{d,t}}{w_{d,0}} \times 100 \quad \text{(V)}$$

where $w_{d,t}$ and $w_{d,0}$ are the weight of the dried hydrogel at time *t* and 0, respectively.

2.6. Printing process and printability evaluation

The printability of hydrogels was evaluated using the RegenHU – 3DDiscovery™ bioprinter (RegenHU, Switzerland) upon optimizing printing parameters. All printability tests were performed using cylindrical nozzles (250 µm inner diameter), at 37°C, a printing speed of 15 mm/s, and minimal pressure (30–70 kPa) for continuous filament deposition.

To investigate hydrogel printability as a function of time, ADA/Alg/Gel_50/50/0, ADA/Alg/Gel_50/40/10, and ADA/Alg/Gel_50/25/25 were printed at selected time points (10, 20, 30, 45, 60, and 90 min) into square grid structures (15 × 15 mm^2), with strand spacing of 2.5 mm. Brightfield images (4× magnification) were taken using a Nikon Eclipse Ti2 spinning disk confocal microscope equipped with NIS-Elements software (Nikon, Japan), and data were analyzed by ImageJ software. At the selected time points, two grids for each composition were printed; for each grid, five images were taken. The filament width of the printed structures was measured in five different locations for each collected image. Moreover, the filament spreading ratio (S),[47] defined as the width of the printed filament divided by the needle diameter, and the printability index (Pr),[48] defined by comparing the circularity of a square (π/4) with the outcome pores, were measured for each bioink at each time point using **Equations VI** and **VII**:

$$Spreading\ ratio(S) = \frac{width\ of\ the\ printed\ filament}{nozzle\ diameter} \quad \text{(VI)}$$

$$Printability\ index(Pr) = \frac{Pore\ perimeter^2}{16\ Pore\ Area} \quad \text{(VII)}$$

Finally, to assess the possibility of developing self-standing internally crosslinked structures using the optimized bioink, ADA/Alg/Gel_50/25/25 formulation was printed into 3D grid structures with square mesh geometry (strand distance: 5 mm), obtaining 3D square samples (10 × 10 mm^2; five layers), and into hollow 3D cylindrical structures (diameter ∅: 3 mm; 10 layers).

2.7. *In vitro* biological characterization

2.7.1. Cell culture

AHCFs were purchased from Lonza (CC-2903; Lonza, Switzerland) and maintained in culture using Fibroblasts Growth Medium-3 (PromoCell, Germany) containing 10% FBS, 1% (v/v) insulin, 1% (v/v) human basal fibroblast growth factor (hFGF-B), and 1% (v/v) gentamicin. Cells were expanded until the fourth passage and then used for experiments. H9C2 heart myoblasts were purchased from the American Type Culture Collection (ATCC, USA) and maintained in culture using DMEM, supplemented with 10% FBS, 2% L-glutamine, 1% sodium pyruvate, and 1% penicillin/streptomycin.

In vitro experiments with AHCFs were conducted in complete medium composed of DMEM, supplemented with 10% FBS, 1% L-glutamine, and 1% penicillin/streptomycin, at 37°C in 5% CO_2 atmosphere. *In vitro* experiments with H9C2 were conducted in a complete medium composed of DMEM, supplemented with 10% FBS, 2% L-glutamine, 1% sodium pyruvate, and 1% penicillin/streptomycin.

2.7.2. Indirect cell viability and cytotoxicity assays

In vitro cell viability by indirect contact with ADA/Alg/Gel_50/50/0, ADA/Alg/Gel_50/40/10, and ADA/Alg/Gel_50/25/25 hydrogels was studied using AHCFs following ISO 10993. AHCFs were seeded in a tissue culture 96-well at a cell density of 6×10^3 cells/well in a complete medium and maintained in a humified incubator at 37°C and 5% CO_2. For each sample, hydrogels with 6.4 mm diameter and 2 mm thickness were prepared and incubated (37°C and 5% CO_2) with 500 µL medium per 100 mg hydrogel for 24 h. Eluates were then collected and added to the AHCF cultures. Then, AHCFs were cultured for 24 h at 37°C with 5% CO_2. After 24 h, cell viability and cytotoxicity were measured using Cell TiterBlue and CytoTox-ONE™ assay, respectively. For cell viability, the control group consists of cells cultured in fresh complete medium. For cytotoxicity, the control group consists of cells cultured in fresh complete medium and treated with CytoTox-ONE™ lysis solution (to achieve 100% cell death) according to manufacturer instructions. Samples were analyzed using a Varioskan spectrophotometer (Thermofisher, Italy) at excitation and emission wavelengths of 560 and 590 nm, respectively.

2.7.3. Cell printing

Bioprinting of ADA/Alg/Gel_50/50/0, ADA/Alg/Gel_50/40/10, and ADA/Alg/Gel_50/25/25 hydrogels embedding AHCFs was investigated. Briefly, cultured AHCFs were detached using 0.05% Trypsin/EDTA and centrifuged. The cell pellet was resuspended in PBS and incorporated into bioinks at a concentration of 5×10^5 cells/mL. Subsequently, for each bioink composition, two-layered grid structures (10×10 mm^2) with 2 mm strand spacing were printed using a RegenHU-3DDiscovery™ bioprinter (RegenHU, Switzerland) with optimized parameters, including the printability window. Cell viability was investigated using the live/dead assay at 1 and 24 h post-printing by culturing constructs in complete media at 37°C with 5% CO_2.

As a proof-of-concept for cardiac TE, bioprinting of ADA/Alg/Gel_50/25/25 embedding H9C2 was investigated. Cultured H9C2 were detached using 0.05% Trypsin/EDTA and centrifuged. The cell pellet was resuspended in PBS and incorporated into bioinks at a concentration of 5×10^5 cells/mL. Subsequently, two-layered grid structures (10×10 mm^2) with 5 mm strand spacing were printed using the RegenHU-3DDiscovery™ bioprinter (RegenHU, Switzerland) with optimized parameters, including the printability window. Cell viability was investigated using the live/dead assay at 1 and 24 h post-printing by culturing constructs in complete media at 37°C with 5% CO_2.

2.8. Statistical analysis

All measurements were made in triplicate, and data are presented as the mean ± standard deviation. One-way analysis of variance (ANOVA) was performed with GraphPad Prism 6 software; differences were considered statistically significant at $p < 0.05$. Tukey post-hoc test was conducted between two or more groups to determine if there were statistically significant differences between populations. In particular, $^*p < 0.05$, $^{**}p < 0.01$, $^{***}p < 0.001$, and $^{****}p < 0.0001$.

3. Results and discussion

This work aimed to develop novel bioinks based on a combination of ADA with Alg and Gel, exploiting an internal crosslinking mechanism to achieve 3D-printed cell-supporting and self-standing constructs without the need for a support bath or external crosslinking. Alg-based hydrogels were selected, as Alg has already been widely investigated for biomedical applications, specifically in cardiac regeneration.[12,20] In this work, ADA was employed to improve the degradability of Alg. Firstly, ADA was combined with Alg, and internal crosslinking was exploited to achieve cardiac tissue-like viscoelastic properties, tailoring both the ADA/Alg ratio and calcium ion ($CaCO_3$) content. GDL content was then optimized to reduce potential detrimental effects on cell viability caused by environmental acidification. Then, the incorporation of Gel within the ADA/Alg hydrogels was optimized to improve cytocompatibility and impart cell adhesive properties. Printability of ADA/Alg/Gel bioinks was investigated over time to evaluate the effect of time-dependent pH-triggered release of calcium ions. Finally,

bioprinting of AHCFs-and H9C2/laden hydrogels was investigated, and cell viability after printing was studied.

3.1. ADA production and characterization

Alginate dialdehyde (ADA) was prepared via oxidation of Alg using sodium metaperiodate, achieving a production yield of 70 ± 5%. Oxidation reaction causes the cleavage of a carbon–carbon bond and the formation of two aldehyde groups.[49,50] Following previous literature reports,[41,50] a theoretical oxidation degree of 25% was targeted by controlling the stoichiometric addition of $NaIO_4$. ADA oxidation degree was measured by both indirect and direct methods. The indirect method was used as a preliminary assessment of the oxidation degree by measuring the amount of unreacted sodium metaperiodate.[41,51] As 99% sodium metaperiodate was consumed in the reaction, the theoretical oxidation degree was calculated to be 23 ± 1%. Conversely, the direct method is based on the direct quantification of aldehyde groups in ADA using the TNBS assay. This method yielded an oxidation degree of 25 ± 4% (mol aldehyde group/mol polymer).

The initial chemical characterization of ADA and Alg was analyzed using ATR-FTIR (Figure 1A). ATR-FITR spectra of Alg and ADA displayed the typical absorption bands of the Alg structure: 1318 cm^{-1} due to C-O stretching; 1126 cm^{-1} indicating C-C stretching; 1021 cm^{-1} attributed to C-O-C stretching; 1590 and 1414 cm^{-1} due to the asymmetric and symmetric stretching vibrations of carboxylate salt groups (-C=(O)O-) of Alg.[41] In the ADA ATR-FTIR spectrum, additional bands with very low intensity were detected at 2850 and 1740 cm^{-1} associated respectively with the C-H and C=O vibrations in aldehyde groups suggesting successful ADA production.[41]

To further assess aldehyde group formation, ^{13}C CP-MAS NMR spectroscopy was performed on Alg and ADA lyophilized samples (Figure 1B). Both Alg and ADA spectra displayed peaks associated with the carbon atoms present in mannuronate (M1: 99.5 ppm; M2, M3: 71.6 ppm; M4, M5: 76.4 ppm; M6: 172.6 ppm) and guluronate (G1: 102.2 ppm; G2: 65.5; G3, G5: 68.4 ppm; G4: 82.8 ppm; G6: 172.6 ppm).[52] The spectra of ADA exhibited an additional peak at 92.2 ppm, attributed to hemiacetalic groups originating from aldehydic groups.[53] Moreover, the resonance of both M-6 and G-6 at 176.2 ppm, attributed to carboxylate groups, were not altered, proving that sodium metaperiodate can convert diols to aldehydes without affecting the carboxylate groups.[53] Deconvolution of the ^{13}C CP-MAS-NMR (Figure S1A and B, Supporting Information) spectra of Alg and ADA allow to determine the M/G ratio in both polymers; 1.2 ± 0.3 for Alg and 1.5 ± 0.5 for ADA. ADA displayed a slight reduction of G groups compared to Alg, though no significant differences were detected in the M/G ratio between the two materials. Literature studies have

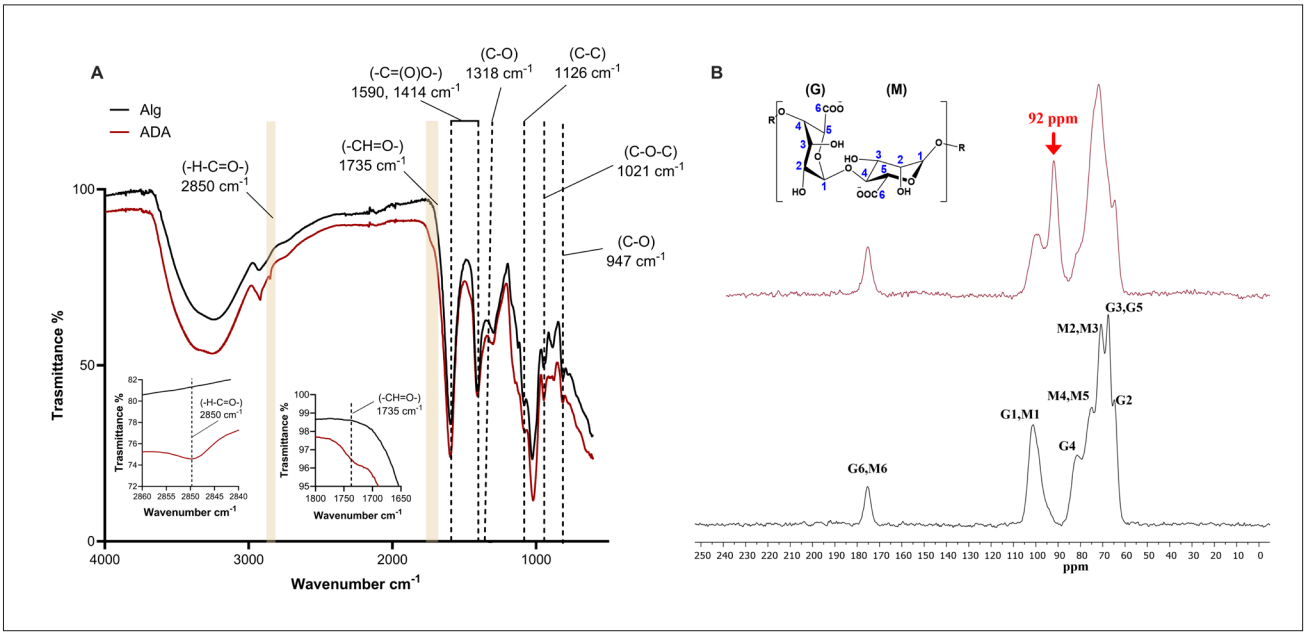

Figure 1. Characterization of ADA and Alg (A) Attenuated total reflectance Fourier transform infrared (ATR-FTIR) spectra of alginate (Alg; black) and lyophilized Alg dialdehyde (ADA; red). The inset figures represent magnifications of the spectra areas at 2840–2860 cm^{-1} (left) and 1650–1800 cm^{-1} (right). (B) ^{13}C cross polarization under magic angle spinning nuclear magnetic resonance (CP-MAS NMR) spectra of Alg (black) and lyophilized ADA (red). G and M represents guluronate and mannuronate groups, respectively.

reported contradictory results on the effect of oxidation on G and M groups, suggesting either a preferential reaction of G groups to oxidation[52,53] or no difference between the two groups.[54] Differences in the results might be associated with the different M/G ratios of the starting Alg being oxidized and other factors, such as M and G block distribution.

Finally, ADA Mv was calculated to be 22 ± 1 kDa based on the Mark-Houwink-Sakurada equation, corresponding to a 93.5% reduction relative to Alg Mv (340 ± 5 kDa). Oxidation by sodium periodate triggers the scission of polysaccharide chains, causing a decrease in ADA MW and intermolecular interactions.[55] Coherently to the literature, MW reduction between 80 and 90% was thus expected with an oxidation degree of 25–30%.[51,56]

3.2. ADA/Alg-based hydrogels

The ADA/Alg samples were first optimized by varying the Alg:ADA ratio, as well as $CaCO_3$ and GDL concentrations, to obtain suitable stiffness for potential cardiac TE applications. Hydrogels with the compositions reported in Table 1 were characterized through frequency sweep tests. Initially, the influence of the Alg:ADA ratio and calcium concentration was studied at fixed GDL content (Figure 2A and B). As displayed in Figure 2A, all compositions exhibited higher G′ than G″, demonstrating their hydrogel state. G′ increased as a function of both Alg content and $CaCO_3$ concentration (Table S2, Supporting Information). At 3% (w/v) $CaCO_3$, samples with the highest Alg content (ADA/Alg_50/50_C3) exhibited higher G′ compared to ADA/Alg_66/33_C3 ($p < 0.0002$). Indeed, Alg is primarily responsible for the internal crosslinking mechanism of ADA/Alg hydrogels. ADA has a reduced ability to undergo crosslinking with calcium ions due to the chemical modification of its chains and reduced MW.[50,51,57] Ring-opening of ADA chains upon oxidation weakens or even hinders ionic crosslinking, which requires the presence of approximately 20 consecutive guluronate groups for forming egg-box ionic junctions with calcium ions.[34,58] In this work, an initial characterization of ADA (data not shown) confirmed its low ionic crosslinking ability in the presence of $CaCO_3$ and GDL, as suggested by the formation of soft hydrogels with low G′ (< 100 Pa) even at high polymer concentrations (i.e., 10% [w/v]).

At the same Alg:ADA ratio, hydrogels with higher calcium content (i.e., ADA/Alg_50/50_C6) exhibited higher G′ compared to those with lower $CaCO_3$ content (i.e., ADA/Alg_50/50_C3) ($p < 0.0001$). Overall, the ADA/Alg_50/50_C6 composition was selected as it displayed the

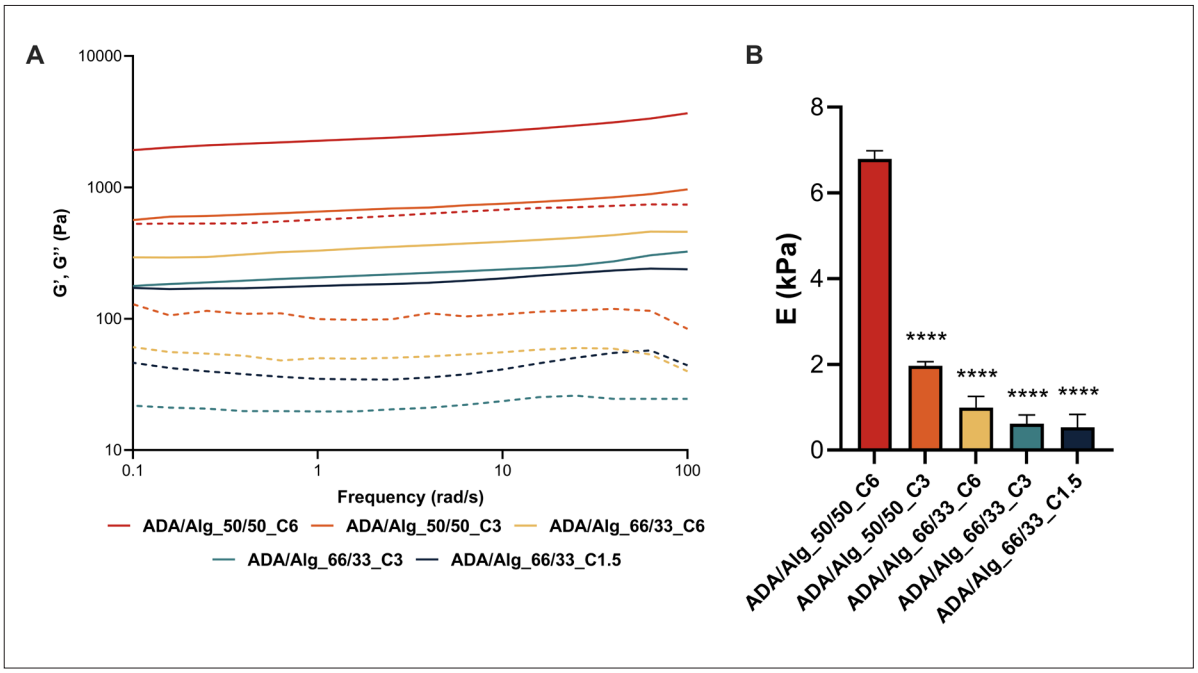

Figure 2. Rheological analysis of Alg/ADA hydrogels. (A) Storage modulus (G′; continuous line) and loss modulus (G″; dotted line) of ADA/Alg_50/50_C6 (red), ADA/Alg_50/50_C3 (orange), ADA/Alg_66/33_C6 (yellow), ADA/Alg_66/33_C3 (light blue), and ADA/Alg_66/33_C1.5 (blue) as a function of angular frequency (0.1 and 100 rad/s) at 37°C ($n = 3$). (B) Elastic modulus (E) of ADA/Alg_50/50_C6 (red), ADA/Alg_50/50_C3 (orange), ADA/Alg_66/33_C6 (yellow), ADA/Alg_66/33_C3 (light blue), and ADA/Alg_66/33_C1.5 (blue), derived from frequency sweep tests ($n = 3$). **** $p < 0.0001$ indicates a statistically significant difference with ADA/Alg_50/50_C6. Abbreviations: Alg: Alginate; ADA: Alginate dialdehyde.

closest G′ (2300 ± 65 Pa) to that of Algysil-LVR,[59] the Alg-based hydrogel currently investigated in cardiac clinical trials. Moreover, ADA/Alg_50/50_C6 exhibited an average E (derived from **Equation III**) of 6.8 ± 0.2 kPa (Figure 2B**;** Table S2, Supporting Information), which is within the range of embryonic cardiac tissue stiffness (≈1–6 kPa)[60] and close to that of adult tissue (≈10–30 kPa).[61]

The influence of GDL on ADA/Alg_50/50_C6 composition was then investigated. GDL hydrolysis into gluconic acid leads to the release of protons, which in turn induces the gradual release of calcium ions from $CaCO_3$ particles.[62] Therefore, GDL content in the matrix needs to be tailored to trigger the release of calcium ions from $CaCO_3$. However, the decrease in pH should not have a detrimental effect on cell viability[63] and should be maintained within physiological values. Hydrogels with five different concentrations of GDL (1, 1.5, 2, 2.5, and 5% [w/v])) were characterized for their rheological properties. Time sweep analysis was performed to evaluate the influence of GDL on crosslinking kinetics. As presented in Figure 3E and Table S1, Supporting Information, an increase in GDL content caused a reduction in crosslinking time (defined as the time in which G′ = G″).[18,27,62] Frequency sweep tests were performed in the LVE region, and the results are reported in Figure 3A and Table S3, Supporting Information. Elastic modulus values for all the samples were derived from the rheological data and reported in Figure 3B and Table S3, Supporting Information. Samples with reduced GDL concentration (1 and 1.5% [w/v]) expressed a significant G′ (and consequently E) decrease compared to the sample with the highest GDL amount (5% [w/v]) ($p < 0.0021$ and $p < 0.0001$ for *GDL1* and *GDL1.5*, respectively).

The pH of eluates from hydrogels with increasing GDL content was measured over time (i.e., after 1, 5, 7, 14, and 21 days). The pH variation is reported in Figure 3C and D. The composition with the highest GDL concentrations (i.e., 5, 2.5, and 2% [w/v]) exhibited a rapid pH decrease after one day of incubation (6.1 ± 0.2, 6.2 ± 0.1, and 6.56 ± 0.03, respectively), and physiological values of pH (i.e., 7.4) were achieved only after seven days. In contrast, compositions with a lower content of GDL (1.5 and 1% [w/v]) displayed a smaller decrease in pH after one day (6.78 ± 0.04 and 6.8 ± 0.02, respectively; $p < 0.0001$). Additionally, the pH of the supernatant for these compositions returned to physiological levels within five days of incubation.

Based on the rheological properties and pH variation study, hydrogel composition with 3% (w/v) Alg, 3% (w/v) ADA, 6% (w/v) $CaCO_3$, and 1.5% (w/v) GDL was selected as optimal. This formulation displayed an average G′ of 1.5 kPa (corresponding to an E of 4.5 kPa), suitable for cardiac TE applications while maintaining the pH close to *in vitro* physiological values.

3.3. ADA/Alg/Gel hydrogels

We then investigated the possibility of introducing Gel into the optimized ADA/Alg composition to improve cell adhesion. ADA/Alg/Gel hydrogels with constant 50% ADA composition were optimized by varying the Alg:Gel relative weight ratios from 50:0 to 25:25, while maintaining their overall amount at 50% (Table 2).

3.3.1. Rheological characterization

The ADA/Alg/Gel hydrogels were characterized for their rheological properties by evaluating the G′ and G″ values as a function of time (time sweep), strain (strain sweep), and frequency (frequency sweep) at 37°C.

Time sweep analysis showed that the introduction of Gel caused a faster gelation: the gel point, evaluated as the crossover of G′ and G″ curves versus time, could not be detected (data not shown) as the materials were already in a gel state (G′ higher than G″).

Frequency sweep tests were performed within the LVE range of each hydrogel to evaluate the influence of Gel on the viscoelastic behavior of the hydrogels. As displayed in Figure 4A, all hydrogels expressed a G′ higher than G″, demonstrating viscoelastic solid-like properties. Samples with the lowest Gel contents (ADA/Alg/Gel_50/47.5/2.5 and ADA/Alg/Gel_50/45/5) exhibited an average G′ (1300 ± 190 Pa and 1170 ± 115 Pa at 1 rad/s, respectively) similar to that of ADA/Alg/Gel_50/50/0, with no statistically significant differences. In contrast, hydrogel samples with a Gel content higher than 10% (ADA/Alg/Gel_50/40/10, ADA/Alg/Gel_50/35/15, ADA/Alg/Gel_50/30/20, and ADA/Alg/Gel_50/25/25) expressed a G′ significantly lower than ADA/Alg/Gel_50/50/, with ADA/Alg/Gel_50/25/25 reaching the lowest G′ value of 650 ± 55 Pa ($p < 0.0001$, when compared to ADA/Alg/Gel_50/50/0). Based on G′ from the frequency sweep analysis, the E of ADA/Alg/Gel samples was calculated to range between 2.0 ± 0.2 and 3.9 ± 0.6 kPa (Figure 4B**;** Table S4, Supporting Information). Such values are still within the range of embryonic cardiac tissue (≈1–6 kPa).[60]

In previous literature, injectable hydrogels and 3D-printed constructs based on Gel and Alg hydrogels have been obtained by an external crosslinking method.[64-69] Alg/Gel hydrogels have been commonly described as interpenetrated (IPN) or semi-interpenetrated (semi-IPN) hydrogel networks, depending on the involved crosslinking mechanism. Semi-IPN hydrogels have been generally obtained by ionic crosslinking of Alg chains through calcium ions from $CaCl_2$ dissociation, with Gel physically entrapped in the Alg crosslinked network.[70-72] IPN hydrogels have also been obtained by combining ionic crosslinking of Alg, with additional Gel crosslinking

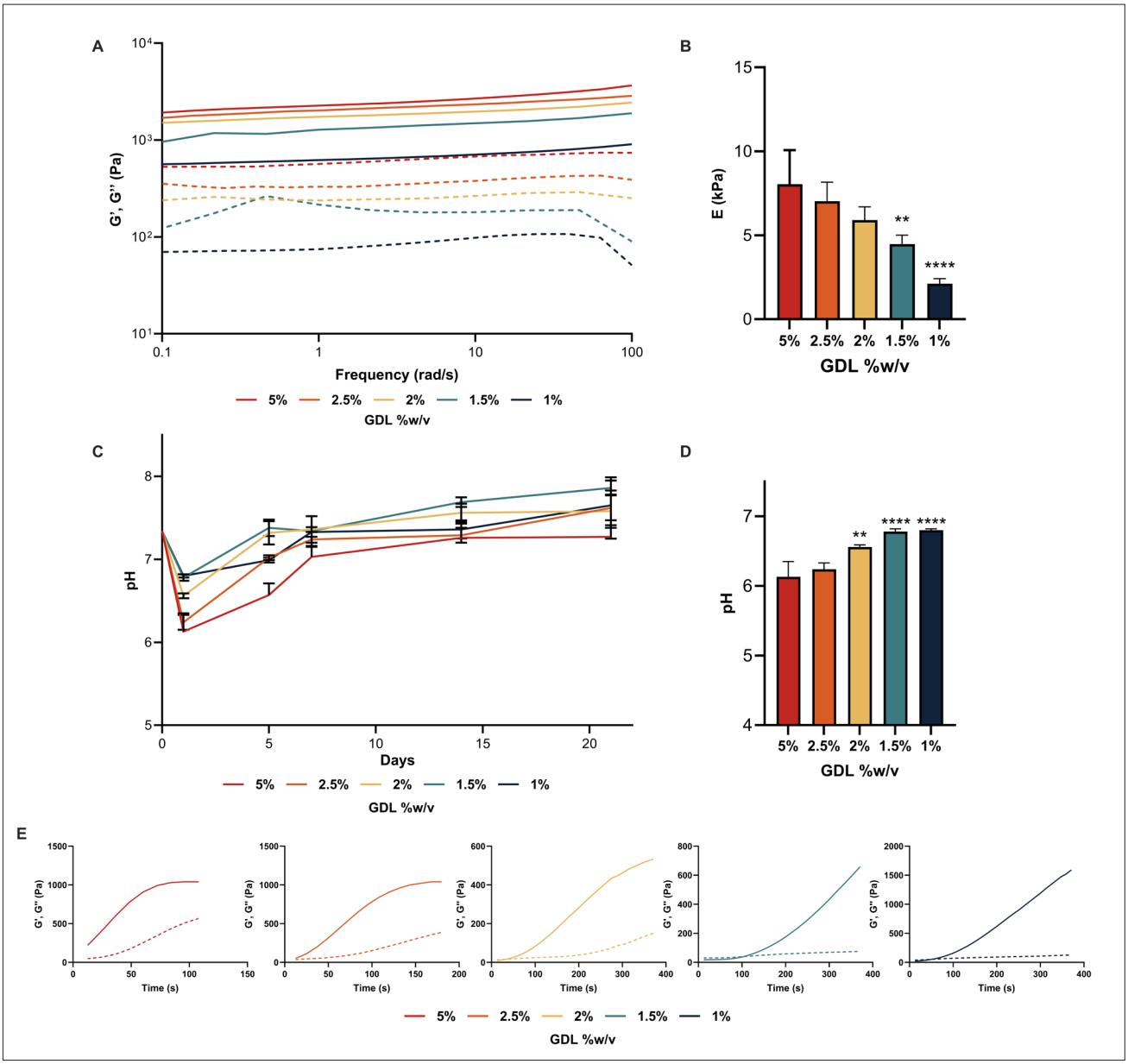

Figure 3. Rheological analyses and pH evaluation of ADA/Alg/Gel hydrogels. (A) Storage modulus (G′; continuous line) and loss modulus (G″; dotted line) of ADA/Alg_50/50_C6 with different concentrations of GDL (5% [w/v], red; 2.5% [w/v], orange; 2% [w/v], yellow; 1.5% [w/v], light blue; and 1% [w/v], blue) as a function of angular frequency (0.1 and 100 rad/s) at 37°C ($n = 3$). (B) Elastic modulus (E) of ADA/Alg_50/50_C6 with different concentrations of GDL (5% [w/v], red; 2.5% [w/v], orange; 2% [w/v], yellow; 1.5% [w/v], light blue; and 1% [w/v], blue) derived from frequency sweep test ($n = 3$). $^{**}p < 0.01$ and **** $p < 0.0001$ indicate statistically significant difference with 5% (w/v) GDL samples. (C–D) pH variation of ADA/Alg_50/50_C6 with different concentrations of GDL (5% [w/v], red; 2.5% [w/v], orange; 2% [w/v], yellow; 1.5% [w/v], light blue; and 1% [w/v], blue) measured after incubation at 37°C for 21 days (C) and after 24h (D) ($n = 3$). $^{**}p < 0.01$ and $^{****}p < 0.0001$ indicate statistically significant difference with 5% (w/v) GDL samples. (E) Time sweep analyses; evaluation of G′ (continuous line) and G″ (dotted line) as a function of time for ADA/Alg_50/50_C6 hydrogels with 5% (w/v) GDL (red), 2.5% (w/v) GDL (orange), 2% (w/v) GDL (yellow), 1.5% (w/v) GDL (light blue), and 1% (w/v) GDL (blue) at 37°C ($n = 2$). Abbreviations: Alg: Alginate; ADA: Alginate dialdehyde; GDL: D-(+)-glucono-1,5-lactone.

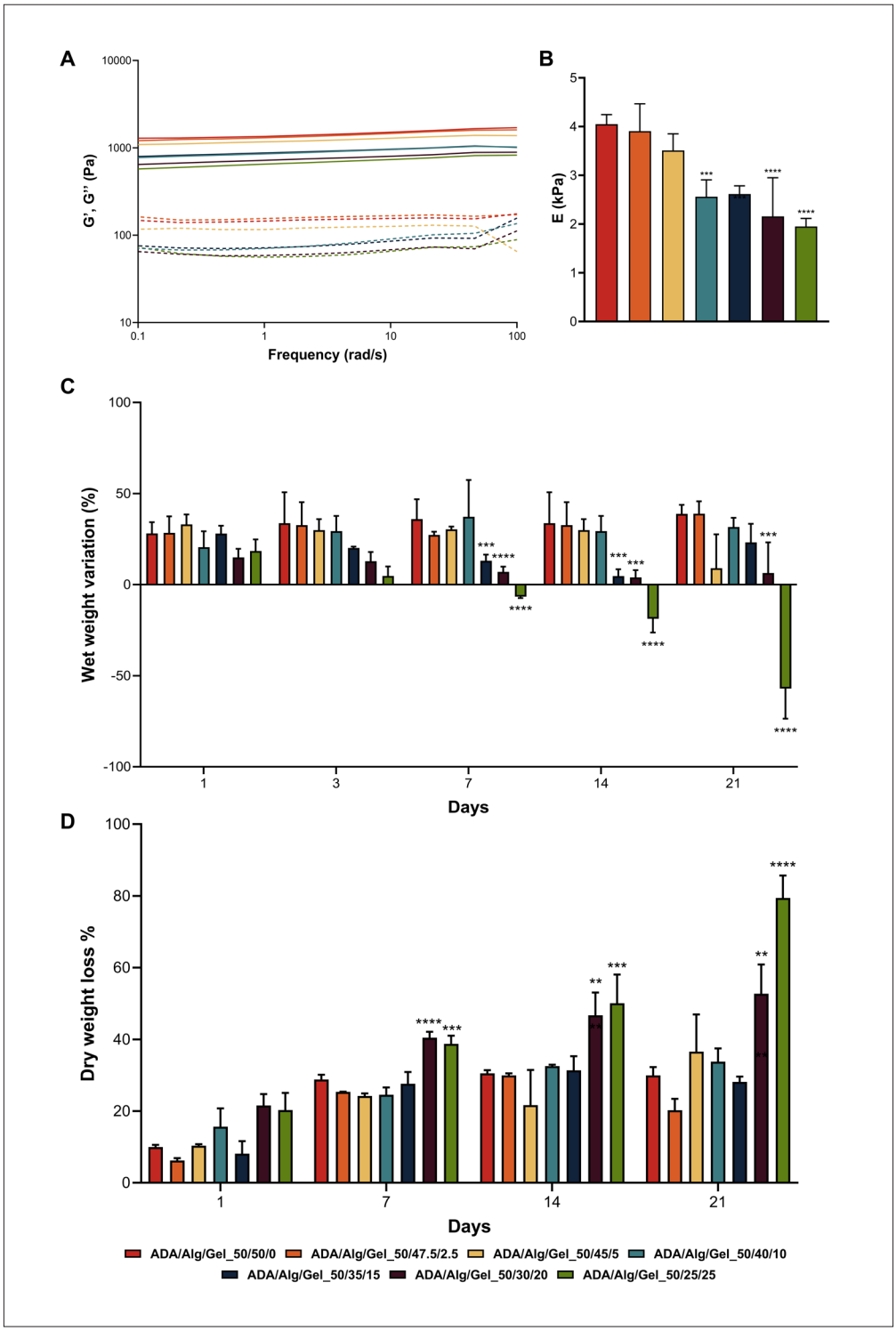

Figure 4. Rheological characterization and *in vitro* stability analysis of ADA/Alg/Gel hydrogels. (A) Storage modulus (G′; continuous line) and loss modulus (G″; dotted line) of ADA/Alg/Gel hydrogels as a function of angular frequency (0.1–100 rad/s) at 37°C (n = 3). (B) Elastic modulus (E) derived from frequency sweep test (n = 3). (C) Wet weight variation (%) of ADA-Alg/Gel hydrogels measured at 1, 3, 7, 14, and 21 days after incubation at 37°C (n = 3). (D) Dry weight loss (%) of ADA/Alg/Gel hydrogels measured at 1, 7, 14, and 21 days after incubation at 37°C (n = 3). In all graphs, the samples are ADA/Alg/Gel_50/50/0 (red), ADA/Alg/Gel_50/47.5/2.5 (orange), ADA/Alg/Gel_50/45/5 (yellow), ADA/Alg/Gel_50/40/10 (light blue), ADA/Alg/Gel_50/35/15 (blue), ADA/Alg/Gel_50/30/2 (purple), and ADA/Alg/Gel_50/25/25 (green). *$p < 0.05$, **$p < 0.01$, ***$p < 0.001$, and ****$p < 0.0001$ indicate statistically significant difference with ADA/Alg/Gel_50/50/0. Abbreviations: Alg: Alginate; ADA: Alginate dialdehyde; Gel: Gelatin.

triggered by an enzyme, such as transglutaminase,[73,74] or a chemical agent, such as carbodiimides,[65] glutaraldehyde,[66] or genipin.[67] In ADA/Alg/Gel-based hydrogels, chemical crosslinking between ADA and Gel could be achieved by Schiff base formation between ADA aldehyde groups and Gel amino groups. However, ADA/Gel hydrogels crosslinked by Schiff base reaction are weak and unstable due to the reversible nature of the formed chemical bonds and poor mechanical properties of Gel at physiological temperature. Therefore, ADA/Gel hydrogels are usually further crosslinked by external ionic crosslinking of ADA[68,69] and/or Gel crosslinking by transglutaminase.[73] To our knowledge, the herein investigated formulation of ADA/Alg/Gel hydrogels using only an internal ionic crosslinking mechanism has not been proposed so far. In this work, the rheological characterization of ADA/Alg/Gel hydrogels suggested the formation of a semi-INP network based on physically crosslinked ADA/Alg chains by calcium ions and non-crosslinked Gel chains. Indeed, the G′ of ADA/Alg/Gel hydrogels decreased proportionally with decreasing Alg content in the hydrogels. On the contrary, an increase in Gel amount did not increase the mechanical stiffness of hydrogels. To better understand ADA/Gel interactions, ATR-FTIR analysis and rheological characterization of only ADA/Gel hydrogels were conducted, selecting the highest ADA:Gel (~70:30) ratio investigated in this study for samples ADA/Alg/Gel_50/25/25. In the ADA/Gel FTIR spectrum (Figure S2A, Supporting Information), a broad peak at 1625 cm^{-1} was detected, associated with the overlapping of C=N vibration of Schiff base at 1620 cm^{-1} and amide I of uncrosslinked Gel at 1630 cm^{-1}.[41,75] Additionally, the shift of the amide II band from 1522 to 1540 cm^{-1}, characteristic of Gel, along with the complete absence of the 1740 cm^{-1} band, associated with the carbonyl groups of ADA in the ADA/Gel spectrum, indicated the possible involvement of these groups in Schiff bond formation.[76] Nonetheless, further rheological characterization of ADA/Gel hydrogels (Figure S2B, Supporting Information) suggested that these interactions were not sufficient to form a fully crosslinked chemical network at the investigated concentrations. A possible explanation of these contrasting results could be associated with the hypothesis of having Gel chains linked to ADA through Schiff base interactions (ADA-modified Gel chains) without forming a fully crosslinked chemical network. Hydrogel formation via Schiff base reactions depends on ADA oxidation degree and MW, and the molar ratio between ADA aldehyde groups and Gel amino moieties.[68,77] Results from this work are in agreement with previous literature studies on ADA/Gel hydrogels based on ADA with a similar oxidation degree of around 25%. In those studies, fully formed ADA/Gel hydrogels were only obtained through an additional ionic crosslinking strategy.[41,73,77] Therefore, previous findings further support our hypothesis that ADA/Alg/Gel hydrogels with internal ionic crosslinking are based on a semi-IPN network.

Future work will focus on optimizing ADA production to achieve oxidation degrees and MW suitable to form fully crosslinked ADA/Gel Schiff-base hydrogels, investigating the development of fully interpenetrated time-dependent ADA/Alg/Gel systems. In this regard, ADA with different oxidation degrees will be tested for efficient crosslinking of Gel chains. Additionally, the amination reaction between ADA and Gel (through sodium borohydride or sodium cyanoborohydride) could further improve network stability but would require a careful evaluation of its implementation to avoid cell cytotoxicity.[78]

3.3.2. In vitro stability studies

Hydrogel stability was studied by evaluating wet and dry weight changes upon incubation in PBS for 21 days. Both wet and dry weight loss were monitored to obtain comprehensive insights into hydrogel stability and degradation rate. Wet weight assessment provides immediate information on the total mass of the hydrogel, allowing the evaluation of swelling behavior and hydration dynamics. In contrast, dry weight assessment enables precise tracking of material degradation, offering a clearer understanding of the hydrogel's long-term stability and structural integrity.

Wet weight variation percentage over time is reported in Figure 4C. ADA/Alg/Gel_50/50/0 hydrogel displayed an increase in wet weight after 24 h of incubation, reaching an average wet weight variation percentage of 21 ± 9%, which then remained constant for up to 21 days. The introduction of Gel induced composition-dependent variations in the wet weight profile. Samples with the lowest Gel content (ADA/Alg/Gel_50/47.5/2.5, ADA/Alg/Gel_50/45/5, and ADA/Alg/Gel_50/40/10) exhibited a behavior similar to ADA/Alg/Gel_50/50/0. Hydrogels with a higher Gel content (ADA/Alg/Gel_50/35/15 and ADA/Alg/Gel_50/30/20) reached a lower wet variation percentage (13 ± 9% and 7 ± 3%, respectively) compared to ADA/Alg/Gel_50/50/0 after seven days ($p < 0.0002$ and $p < 0.0001$, respectively). Finally, the hydrogel composition with the highest Gel content (ADA/Alg/Gel_50/25/25) exhibited a decrease in wet weight over time, with a negative wet weight variation percentage after seven days of incubation in PBS. This behavior suggested that the samples released polymeric components while absorbing PBS, with prevalent dissolution over swelling starting from day 7 of incubation in PBS.

The dry weight loss on day 21 of incubation in PBS is reported in Figure 4D. After seven days, ADA/Alg/Gel_50/50/0 displayed a 30 ± 1% dry weight loss, which remained constant over time. Hydrogels with the lowest Gel content (ADA/Alg/Gel_50/47.5/2.5, ADA/Alg/Gel_50/45/5, ADA/Alg/Gel_50/40/10, and ADA/Alg/Gel_50/35/15) behaved similarly to ADA/Alg/Gel_50/50/0, with no statistically significant differences. On the contrary, hydrogels with the highest Gel contents (ADA/Alg/Gel_50/30/20 and ADA/Alg/Gel_50/25/25) presented significantly higher dry weight loss compared to ADA/Alg/Gel_50/50/0 at all the evaluated time points ($p < 0.0021$ on days 1, 14, and 21 and $p < 0.0001$ on day 7 for ADA/Alg/Gel_50/30/20; $p < 0.0332$ on day 1, $p < 0.0002$ on days 7 and 14, and $p < 0.0001$ on day 21 for ADA/Alg/Gel_50/25/25). Moreover, ADA/Alg/Gel_50/30/20 and ADA/Alg/Gel_50/25/25 dry weight loss increased over time, reaching 53 ± 8% for ADA/Alg/Gel_50/30/20 and 80 ± 6% for ADA/Alg/Gel_50/25/25 after 21 days.

Biodegradability is a critical requirement in TE applications, both for regenerative applications and *in vitro* models. Dissolution of ionically crosslinked Alg-based hydrogels in the aqueous environment is regulated by the exchange between divalent calcium ions and monovalent cations (e.g., Na^+), inducing calcium ion release into the surrounding media.[10,11,37] The dissolution process is usually long-lasting and depends on Alg concentration and degree of crosslinking, requiring at least a month to achieve significant initial weight loss.[11,57] The introduction of ADA within the matrix has the advantage of increasing the dissolution rate due to the higher susceptibility of ADA to hydrolytic scission and β-elimination at physiological pH.[58,79] Moreover, for prospective *in vivo* applications, ADA with MW lower than 50 kDa (like the one produced in this work) can be removed from the human body by kidney clearance.[34,57] In our work, ADA/Alg/Gel featured a tunable degradation profile depending on the Gel concentration selected, providing a versatile hydrogel platform for TE applications. The dependence of hydrogel stability on Gel content is probably associated with the release of Gel from the ADA/Alg/Gel semi-IPN network at 37°C (with Gel in sol state). Specifically, hydrogels with the highest Gel content (20% and 25% wt.; Table 2) exhibited a dry weight loss exceeding the initial Gel percentage, namely 53% and 80% wt., respectively, after 21 days of incubation in PBS. This behavior suggests the release of Gel linked to ADA chains (i.e., ADA-modified Gel chains), which were not integrated into a broader chemical network. Therefore, the release of such ADA-modified Gel chains could explain the higher dry weight loss observed. In addition, decreased stability of ADA/Alg/Gel systems could also be associated with the reduction of the total Alg content (from 50 to 25% [w/w]) within the system proportional to the increment of Gel (from 0 to 25% [w/w]). In the ADA/Alg/Gel semi-IPN network, Alg is the main component that interacts with calcium ions; hence, the reduction of this component could also lead to decreased hydrogel stability. The presence of Gel in the ADA/Alg/Gel network is also expected to enhance the enzymatic degradation of the hydrogel, though not tested in this work. Thus, forthcoming investigations should involve *in vitro* degradation studies in the presence of relevant enzymes (e.g., collagenase).

3.3.3. Printability evaluation of Alg/ADA/Gel bioinks

Based on the rheological and stability properties of ADA/Alg/Gel samples, three compositions were selected to be investigated as hydrogel inks for 3D microextrusion printing: ADA/Alg/Gel_50/50/0 with no Gel in the network; ADA/Alg/Gel_50/40/10 having intermediate Gel concentration; and ADA/Alg/Gel_50/25/25 with the highest Gel content. The three compositions were selected to evaluate the printability of Alg/ADA/Gel bioinks as a platform with tunable degradability, stiffness, and cell adhesive properties. Due to the time-dependance of the internal crosslinking mechanism, printability was investigated over time through viscosity tests and microscopy analyses of 3D-printed structures.

Figure 5A–C presents the variations in apparent viscosity over time, studied by shear sweep tests. Regarding the composition without Gel (ADA/Alg/Gel_50/50/0), a Newtonian region was detected immediately after hydrogel preparation (i.e., t = 2 min; time required to load the sample on the rheometer and start the measurement), corresponding to a constant viscosity at low shear rates (< 1 rad/s). Conversely, a shear-thinning behavior was observed for shear rates higher than 1 rad/s.[80,81] This behavior is typically displayed by non-crosslinked Alg solutions or hydrogels.[70,80] After 10 min, ADA/Alg/Gel_50/50/0 displayed a shear-thinning behavior at all the shear rates investigated, and this trend remained constant over time. The other two hydrogel compositions containing Gel exhibited a shear-thinning behavior for all the time points investigated, without Newtonian behavior even immediately after hydrogel preparation.

Thereafter, 2D grid structures (15 × 15 mm^2) with a strand spacing of 2.5 mm were then printed at selected time points, and variations in average fiber dimension, spreading ratio (S), and printability index (Pr) were evaluated as a function of time.

All the compositions displayed a variation in fiber diameter as a function of time (Figure 5D–F). ADA/Alg/Gel_50/50/0 bioinks could be printed at the shortest time points (i.e., 10 and 20 min), resulting in well-defined 2D

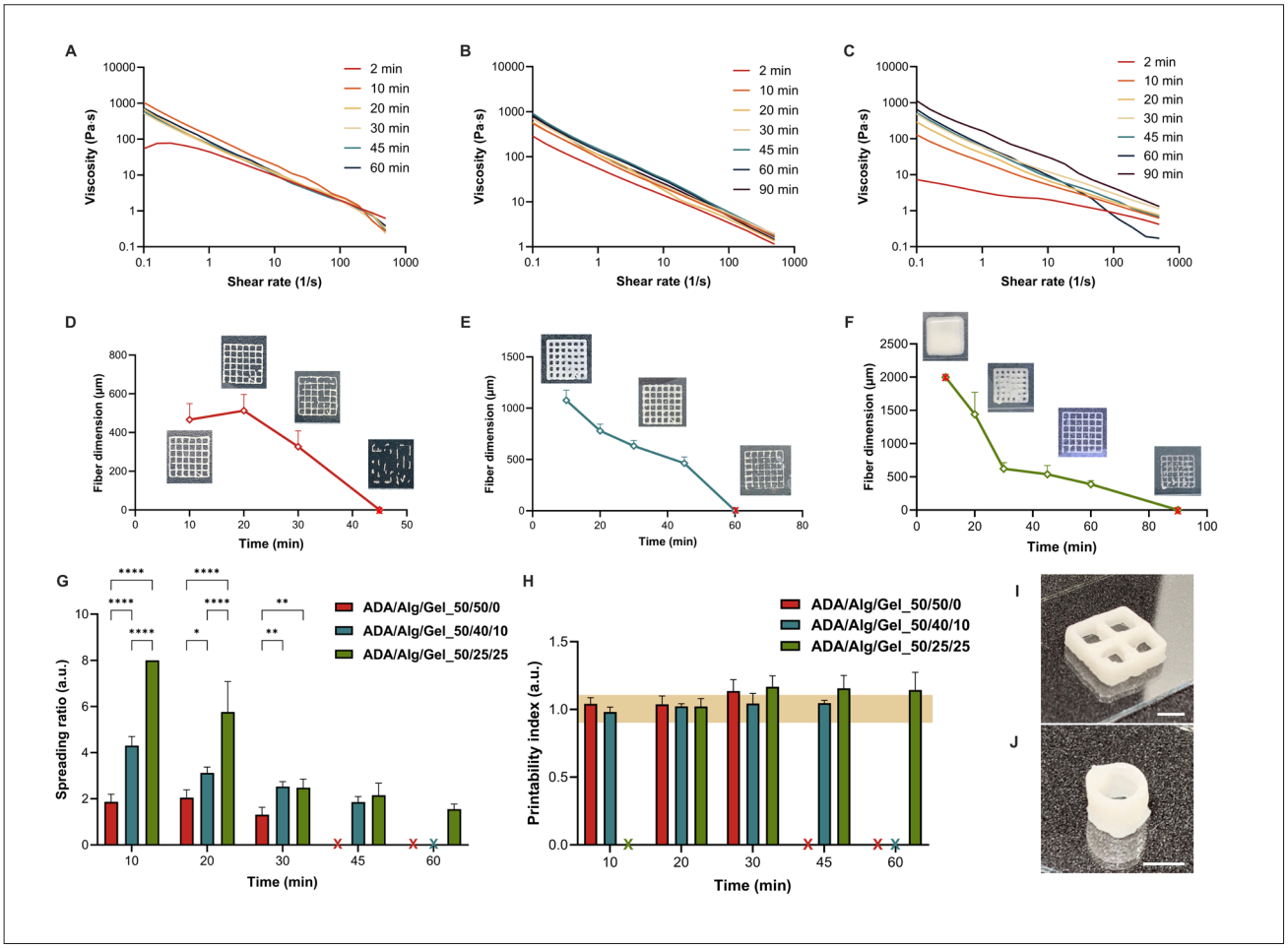

Figure 5. Printability characterization of ADA/Alg/Gel hydrogels (A–C) Viscosity curve as a function of the shear rate for ADA/Alg/Gel_50/50/0 (A), ADA/Alg/Gel_50/40/10 (B), and ADA/Alg/Gel_50/25/25 (C) measured at 2, 10, 20, 30, 45, 60, and 90 min after hydrogel preparation. (D–F) Variations in fiber diameter over time for ADA/Alg/Gel_50/50/0 (D), ADA/Alg/Gel_50/40/10 (E), and ADA/Alg/Gel_50/25/25 (F) (n = 10). (G) Spreading ratio over time for ADA/Alg/Gel_50/50/0 (red), ADA/Alg/Gel_50/40/10 (light blue), and ADA/Alg/Gel_50/25/25 (green) (n = 10). *p < 0.05, **p < 0.01, and ****p <0.0001 indicate statistically significant differences with ADA/Alg/Gel_50/50/0. (H) Printability index over time for ADA/Alg/Gel_50/50/0 (red), ADA/Alg/Gel_50/40/10 (light blue), and ADA/Alg/Gel_50/25/25 (green) (n = 10). (I and J) Optical images of self-standing (I) 3D square samples (10 × 10 mm^2; five layers) and (J) hollow 3D cylindrical structures (diameter, ∅: 3 mm; 10 layers). Scale bars: 5 mm. Abbreviations: Alg: Alginate; ADA: Alginate dialdehyde; Gel: Gelatin.

grid structures with an average filament diameter of 465 ± 80 µm at 10 min and 510.0 ± 85 µm at 20 min. After 30 min, the average fiber diameter decreased to 330 ± 80 µm, closer to the ideal value of 250 µm (i.e., similar to the nozzle diameter); however, inhomogeneities were observed (Figure 5D). Finally, after 45 min, a continuous grid structure could not be printed due to complete hydrogel crosslinking. The samples containing Gel displayed a significantly higher fiber size immediately after printing due to bioink overflow and delayed crosslinking onset. Particularly, well-defined grid structures with spaced individual filaments of ADA/Alg/Gel_50/40/10 could only be printed 20 min after hydrogel preparation (Figure 5E), while 30 min was required for ADA/Alg/Gel_50/25/25 (Figure 5F). The smallest fiber diameter was achieved after 45 min for ADA/Alg/Gel_50/40/10 (464 ± 60 µm) and after 60 min for ADA/Alg/Gel_50/25/25 (390 ± 55 µm). As for ADA/Alg/Gel_50/50/0 hydrogel, continuous grid structures could not be obtained even after longer durations, i.e., 60 min for ADA/Alg/Gel_50/40/10 hydrogel and 90 min for ADA/Alg/Gel_50/25/25 hydrogel.

The ADA/Alg/Gel samples demonstrated a similar trend for variations in spreading ratio over time as fiber dimensions (Figure 5G). For ADA/Alg/Gel_50/50/0 hydrogel, a spreading ratio between 1.3 and 2.05 was obtained between 10 and 30 min. The spreading ratio of

Gel containing hydrogel was significantly higher than that for ADA/Alg/Gel_50/50/0 at all the evaluated time points. At longer times, well-defined 3D structures could not be printed, and both compositions exhibited spreading ratios above 3 (4.3 ± 0.5 for ADA/Alg/Gel_50/40/10 after 10 min; 8 and 5.8 ± 1.3 for ADA/Alg/Gel_50/25/25 after 10 and 20 min, respectively). For ADA/Alg/Gel_50/40/10 hydrogel, the average spreading ratio decreased from 3.1 ± 0.3 to 1.8 ± 0.2 between 20 and 45 min (i.e., 3.1 ± 0.3, 2.5 ± 0.2, and 1.8 ± 0.2 after 20, 30, and 45 min); while the spreading ratio for ADA/Alg/Gel_50/25/25 decreased from 2.5 to 1.5 between 30 and 60 min (2.5 ± 0.4, 2.1 ± 0.5, and 1.5 ± 0.2 after 30, 45, and 60 min).

Finally, the Pr was measured to evaluate possible under- or over-gelation phenomena of the inks (Figure 5H). At conditions allowing the printing of continuous filaments and well-defined grid structures (10–30 min for ADA/Alg/Gel_50/50/0; 10–45 min for ADA/Alg/Gel_50/40/10; and 20–60 min for ADA/Alg/Gel_50/25/25), the three compositions exhibited a Pr between 0.9 and 1.1, indicating the formation of square-shaped pores[82] (Pr = 1, indicates perfectly square-shaped pores), with no statistically significant differences among the samples with/without Gel (Figure 5H).

Microextrusion printing of Alg-based hydrogel was previously investigated using external ionic crosslinking with calcium ions and supporting baths. The process requires optimization of the hydrogel ink and supporting bath to print complex 3D structures.[20] Moreover, external gelation is inherently associated with the formation of non-homogeneous filaments with a highly crosslinked surface, causing potential detrimental effects on nutrient exchange.[24,25] Additionally, for drug delivery applications, the use of a crosslinking solution can lead to a fast release of the encapsulated molecules during the gelation phase.[27] To overcome these drawbacks, internal ionic crosslinking represents a promising approach for the development of Alg-based ink. Only a few studies have investigated internal gelation for Alg-based inks, highlighting its ability to generate homogeneous scaffolds without the need for post-crosslinking strategies or supporting baths. Specifically, Remaggi et al. investigated the application of internally crosslinked Alg inks for drug delivery for breast cancer treatment, using printing conditions (i.e., curing time of three days at 2°C) not suitable for cell bioprinting.[27] Sardelli et al. explored Alg ink printability via internal gelation, evaluating material properties and fiber printability over 24 h, but without biological characterization. To our knowledge, only three studies by the same group developed a bioink for cell bioprinting based on an internally crosslinked Alg hydrogel added with porcine liver-derived decellularized ECM to design *in vitro* models of hepatic tissue.[31,32] In these reports, the authors demonstrated the hydrogel ability to support mid/long-term cultures of human liver cancer cells (HepG2).[31-33] In this work, we investigated the bioprinting of ADA/Alg/Gel hydrogels, exploiting an internal crosslinking mechanism to fabricate biodegradable, biocompatible, and self-standing ADA-based 3D-printed scaffolds for prospective cardiac TE. Considering the time-dependent nature of the internal crosslinking mechanism,[28] an in-depth investigation of ADA/Alg/Gel printability was performed, evaluating viscosity and shape fidelity (i.e., spreading ratio and Pr) over time. Specifically, printability was optimized within short time intervals (i.e., below 90 min), as long printing times can severely decrease the viability of cells embedded in the bioink.[83,84] ADA/Alg/Gel_50/50/0, ADA/Alg/Gel_50/40/10, and ADA/Alg/Gel_50/25/25 hydrogels demonstrated suitable printability times of 10, 20, and 30 min, respectively. Given the internal gelation mechanism exploited in the study, the printability of the hydrogels is attributed to the gradual pH-triggered release of calcium ions, leading to time-dependent crosslinking, as evidenced by printability studies. The delay in printability observed for the samples with higher Gel content was probably related to the steric hindrance of uncrosslinked Gel within the semi-IPN network, slowing down the crosslinking process.[39] Indeed, the presence of additives in internally crosslinked Alg-based hydrogels significantly affected their rheological behavior, including gelation.[33,85,86] However, it is not possible to exclude other factors that might concur to determine such delay.

Finally, as a proof-of-concept, Figure 5I and J features 3D structures based on ADA/Alg/Gel_50/25/25, printed after 60 min from hydrogel components, having a grid (1.25 mm height, five layers; Figure 5I) and cylindrical geometry (2.25 mm height, 10 layers; Figure 5J). Hence, ADA/Alg/Gel hydrogels can be used for printing self-standing 3D structures with various shapes by internal crosslinking with no need for a supporting bath. Unlike previous works,[32] multilayer structures were developed without the need for curing or post-processing of the bioink.

3.3.4. Bioink in vitro cytocompatibility and printability

In vitro indirect cell cytocompatibility tests were carried out to investigate the potential cytotoxic effect of eluates from ADA/Alg/Gel_50/50/0, ADA/Alg/Gel_50/40/10, and ADA/Alg/Gel_50/25/25 hydrogels by *in vitro* culture of AHCFs for 24 h in the presence of eluates, following ISO 10993. Results indicated increasing cell viability for hydrogels with increasing Gel content (Figure 6A). Indeed, AHCFs cultured with eluates from ADA/Alg/Gel_50/50/0,

ADA/Alg/Gel_50/40/10, and ADA/Alg/Gel_50/25/25 hydrogels reported 70% ($p < 0.0021$), 83% ($p < 0.0332$), and 87% cell viability compared to control AHCFs, respectively. Cell cytotoxicity assay (Figure 6B) confirmed low (< 6% in ADA/Alg/Gel_50/50/0 and ADA/Alg/Gel_50/40/10) or no cytotoxic effects (in ADA/Alg/Gel_50/25/25) for hydrogel eluates with AHCFs, demonstrating hydrogel cytocompatibility ($p < 0.0001$).

Then, bioprinting of AHCFs embedded into ADA/Alg/Gel_50/50/0, ADA/Alg/Gel_50/40/10, and ADA/Alg/Gel_50/25/25 hydrogels was investigated. Live/dead assay performed 1 h post-printing displayed high cell viability for all samples (Figure 6C). However, after 24 h post-printing (Figure 6D and E), the viability of AHCFs embedded into ADA/Alg/Gel_50/50/0, ADA/Alg/Gel_50/40/10, and ADA/Alg/Gel_50/25/25 hydrogel was 45, 50, and 92% ($p < 0.0001$ compared to red-stained dead cells), respectively. To further validate the developed bioink suitability for cardiac TE, the bioprinting of H9C2 cells embedded in ADA/Alg/Gel_50/25/25 hydrogels was examined. Live/dead assays demonstrated excellent cell viability 1 h after printing (Figure 6F) and indicated high viability 24 h post-printing (Figure 6F and G), with 83% of viable cells ($p < 0.0001$ compared to red-stained dead cells).

In this work, Gel was added within the system to overcome one of the main limitations of Alg and ADA-based hydrogels, i.e., the lack of cell adhesive moieties. Moreover, as reported in previous studies, ADA-based hydrogels may elicit cell cytotoxicity due to oxidative stresses induced by the presence of free aldehyde groups.[75,87] Specifically, ADA-based hydrogels can affect the viability of both primary human fibroblasts and endothelial cells by depleting cellular thiols, increasing reactive oxygen species (ROS) generation.[75] The combination of ADA with Gel reportedly reduces ADA cytotoxicity due to aldehyde group shielding by Gel primary amine groups via Schiff base formation.[75,87] In this work, low cell viability within ADA/Alg/Gel_50/50/0 and ADA/Alg/Gel_50/40/10 hydrogel at 24 h post-printing was probably caused by the combination of the lack of cell adhesion moieties and the cytotoxic effects of aldehyde groups in the hydrogel. Indeed, in the sample without Gel, ADA aldehyde groups are free to interact with cellular components, inducing cytotoxicity. Cell viability results indicated that the addition of 10% Gel was not sufficient to improve the cytocompatibility of the system, suggesting the persistence of a high number of free aldehyde groups within the matrix, combined with insufficient addition of cell adhesive groups. On the contrary, increasing Gel concentration to 25% (w/w) (ADA/Alg/Gel_50/25/25) drastically improved cell viability at 24 h post-printing. The improved cell viability could be associated with an increase in cell adhesive moieties present within the hydrogel matrix. Moreover, as ADA content was kept constant in all the formulations, increasing the Gel content could be directly correlated with a higher number of Gel primary amine groups that can interact with free aldehyde groups in ADA, decreasing their cytotoxicity. As a proof-of- concept, we demonstrated the bioink suitability for prospective cardiac TE by bioprinting H9C2 cells in ADA/Alg/Gel_50/25/25 hydrogels, with excellent cell viability at 1 and 24 h post-printing.

In this study, a bioink supporting cardiac cell printing and initial adhesion was designed based on time-dependent internal ionic crosslinking. Future studies will evaluate longer culture times for bioinks cellularized with AHCFs, human induced pluripotent stem cells derived cardiomyocytes. and their co-cultures to assess the effect of hydrogel on cell proliferation, maturation, and matrix remodeling with the deposition of new ECM. New knowledge will be obtained for the *in vitro* engineering of 3D cardiac tissue with controlled and reproducible structure by bioprinting, which can be exploited as *in vitro* cardiac tissue models or cardiac patches.

4. Conclusion

In this study, we investigated, for the first time, the development of novel ADA/Alg/Gel-based bioinks, exploiting an internal crosslinking mechanism method to achieve self-standing 3D scaffolds for prospective applications in *in vitro* cardiac TE. Polymer concentration, as well as $CaCO_3$ and GDL content, were tuned to obtain 3D-printed constructs with a faster degradation rate (imparted by ADA and Gel) and the ability to support cell adhesion (due to Gel adhesive moieties). Printability studies revealed that all ADA/Alg/Gel formulations demonstrated time-dependent shear-thinning behavior suitable for 3D bioprinting. This behavior is attributed to the gradual pH-triggered release of calcium ions over time and is influenced by Gel content. Notably, self-standing and multilayer 3D structures could be printed, exploiting internal gelation without the addition of any post-crosslinking agents or supporting baths. *In vitro* biological tests confirmed that the bioinks and selected printing process parameters preserved cell viability. Hydrogel composition with the highest Gel content was able to support the viability of AHCFs and H9C2 embedded in the hydrogels, at 24 h post-printing.

Such innovative bioinks are promising in the field of soft TE, particularly for prospective cardiac TE, due to the cardiac tissue-like stiffness of the inks and their ability

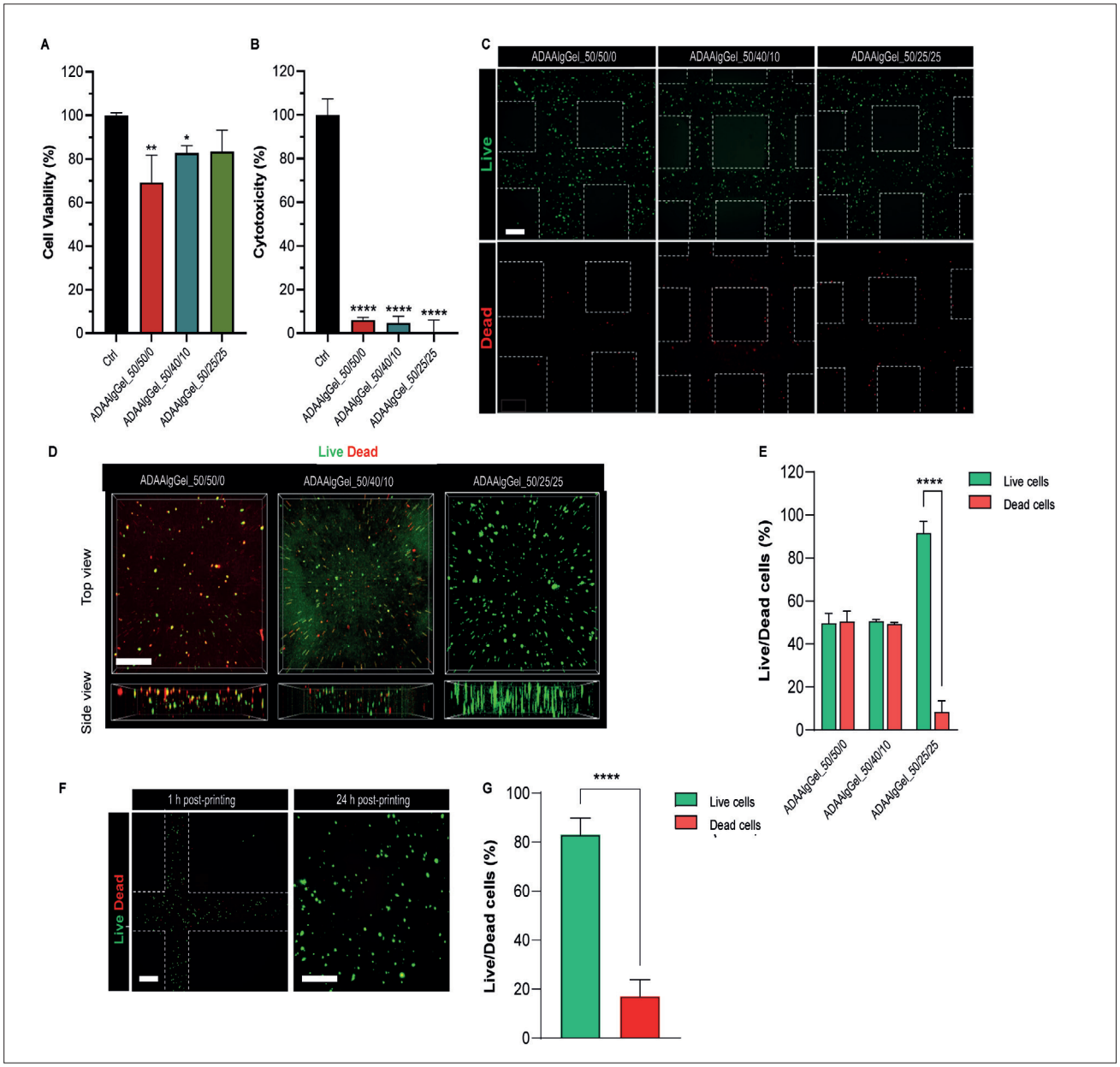

Figure 6. *In vitro* characterization of ADA/Alg/Gel hydrogels (A and B) Viability (A) and toxicity (B) studies ($n = 3$) of ADA/Alg/Gel_50/50/0 (red), ADA/Alg/Gel_50/40/10 (blue), and ADA/Alg/Gel_50/25/25 (green); for viability studies (A), the control group consists of AHCFs cultured on tissue culture plastic with untreated media; for toxicity studies (B), the control group consists of AHCFs cultured on tissue culture plastic with 100% of cell death induced by CytoTox-ONE™ lysis solution (grey). $^{*}p < 0.05$, $^{**}p < 0.01$, and $^{****}p < 0.0001$ indicate statistically significant differences between the compositions and the control group. (C and D) Live/dead assay performed on AHCF-laden ADA/Alg/Gel_50/50/0, ADA/Alg/Gel_50/40/10, and ADA/Alg/Gel_50/25/25 hydrogels at 1 h (C) and 24 h (D) after printing. Scale bars: 100 μm (C) and 500 μm (D). (E) Quantification of live (green) and dead (red) AHCFs at 24 h after printing. $^{****}p < 0.0001$ indicates a statistically significant difference between the live and dead cells for ADA/Alg/Gel_50/25/25 ($n = 9$). (F) Live/dead assay performed on H9C2-laden ADA/Alg/Gel_50/25/25 hydrogels after 1 and 24 h. Scale bars: 100 μm (1h, left image) 500 μm (24h, right image). (G) Quantification of live (green) and dead (red) H9C2 at 24 h after printing. $^{****}p < 0.0001$ indicates a statistically significant difference between the live and dead cells for ADA/Alg/Gel_50/25/25 ($n = 9$). Abbreviations: AHCF: Adult human cardiac fibroblast; Alg: Alginate; ADA: Alginate dialdehyde; Gel: Gelatin.

to support AHCF and H9C2 viability. In conclusion, this work provides valuable insights toward overcoming the limitations associated with traditional Alg-based hydrogel bioinks.

Acknowledgments

Not applicable.

Funding

This work was supported by the European Research Council (ERC) under the European Union's Horizon 2020 research and innovation program (BIORECAR, grant agreement number 772168).

Conflict of interest

Elena Marcello serves as the Editorial Board Member of the journal, but was not in any way involved in the editorial and peer-review process conducted for this paper, directly or indirectly. Other authors declare they have no competing interests.

Author contributions

Conceptualization: Elena Marcello, Valeria Chiono
Funding acquisition: Valeria Chiono
Investigation: Giovanni Paolo Stola, Camilla Paoletti, Letizia Nicoletti, Elena Marcello, Geo Paul, Claudio Cassino, Leonardo Marchese
Writing – original draft: Elena Marcello, Giovanni Paolo Stola, Camilla Paoletti
Writing – review & editing: Elena Marcello, Valeria Chiono

Ethics approval and consent to participate

Not applicable.

Consent for publication

Not applicable.

Availability of data

Data are available from the corresponding author upon reasonable request.

References

1. Fatimi A, Okoro OV, Podstawczyk D, Siminska-Stanny J, Shavandi A. Natural hydrogel-based bio-inks for 3D bioprinting in tissue engineering: a review. *Gels*. 2022;8(3):179. doi: 10.3390/gels8030179
2. Ramiah P, du Toit LC, Choonara YE, Kondiah PPD, Pillay V. Hydrogel-based bioinks for 3D bioprinting in tissue regeneration. *Front Mater*. 2020;7:506968. doi: 10.3389/FMATS.2020.00076/BIBTEX
3. Taneja H, Salodkar SM, Singh Parmar A, Chaudhary S. Hydrogel based 3D printing: bio ink for tissue engineering. *J Mol Liq*. 2022;367:120390. doi: 10.1016/J.MOLLIQ.2022.120390
4. Wissing TB, Bonito V, Bouten CVC, Smits AIPM. Biomaterial-driven *in situ* cardiovascular tissue engineering—a multi-disciplinary perspective. *NPJ Regen Med*. 2017;2(1):1-20. doi: 10.1038/s41536-017-0023-2
5. Mei X, Cheng K. Recent development in therapeutic cardiac patches. *Front Cardiovasc Med*. 2020;7:610364. doi: 10.3389/fcvm.2020.610364
6. Testore D, Zoso A, Kortaberria G, Sangermano M, Chiono V. Electroconductive photo-curable PEGDA-Gelatin/PEDOT: PSS hydrogels for prospective cardiac tissue engineering application. *Front Bioeng Biotechnol*. 2022;10:897575. doi: 10.3389/fbioe.2022.897575
7. Neuhaus W, Reininger-Gutmann B, Rinner B, et al. The rise of three rs centres and platforms in Europe*. *Altern Lab Anim*. 2022;50(2):90-120. doi: 10.1177/02611929221099165
8. Panwar A, Tan LP. Current status of bioinks for micro-extrusion-based 3D bioprinting. *Molecules*. 2016;21(6):685. doi: 10.3390/molecules21060685
9. He Y, Yang F, Zhao H, Gao Q, Xia B, Fu J. Research on the printability of hydrogels in 3D bioprinting. *Sci Rep*. 2016;6(1):1-13. doi: 10.1038/srep29977
10. Sun J, Tan H. Alginate-based biomaterials for regenerative medicine applications. *Materials*. 2013;6(4):1285-1309. doi: 10.3390/ma6041285
11. Lee KY, Mooney DJ. Alginate: properties and biomedical applications. *Prog Polym Sci (Oxford)*. 2012;37(1):106-126. doi: 10.1016/j.progpolymsci.2011.06.003
12. Lee RJ, Hinson A, Bauernschmitt R, et al. The feasibility and safety of Algisyl-LVR™ as a method of left ventricular augmentation in patients with dilated cardiomyopathy: initial first in man clinical results. *Int J Cardiol*. 2015;199:18-24. doi: 10.1016/j.ijcard.2015.06.111
13. Ruvinov E, Cohen S. Alginate biomaterial for the treatment of myocardial infarction: progress, translational strategies, and clinical outlook. From ocean algae to patient bedside. *Adv Drug Deliv Rev*. 2016;96:54-76. doi: 10.1016/j.addr.2015.04.021
14. Choy JS, Leng S, Acevedo-Bolton G, et al. Efficacy of intramyocardial injection of Algisyl-LVR for the

treatment of ischemic heart failure in swine. *Int J Cardiol*. 2018;255:129-135.
doi: 10.1016/j.ijcard.2017.09.179

15. Cao L, Lu W, Mata A, Nishinari K, Fang Y. Egg-box model-based gelation of alginate and pectin: a review. *Carbohydr Polym*. 2020;242:116389.
doi: 10.1016/j.carbpol.2020.116389

16. Hu C, Lu W, Mata A, Nishinari K, Fang Y. Ions-induced gelation of alginate: mechanisms and applications. *Int J Biol Macromol*. 2021;177:578-588.
doi: 10.1016/j.ijbiomac.2021.02.086

17. Paques JP. Alginate nanospheres prepared by internal or external gelation with nanoparticles. In: *Microencapsulation and Microspheres for Food Applications*. Cambridge, USA: Academic Press; 2015:39-55.
doi: 10.1016/B978-0-12-800350-3.00004-2

18. Chan LW, Lee HY, Heng PWS. Mechanisms of external and internal gelation and their impact on the functions of alginate as a coat and delivery system. *Carbohydr Polym*. 2006;63(2):176-187.
doi: 10.1016/j.carbpol.2005.07.033

19. Hinton TJ, Jallerat Q, Palchesko RN, et al. Three-dimensional printing of complex biological structures by freeform reversible embedding of suspended hydrogels. *Sci Adv*. 2015;1(9):e1500758.
doi: 10.1126/sciadv.1500758

20. Mirdamadi E, Tashman JW, Shiwarski DJ, Palchesko RN, Feinberg AW. FRESH 3D bioprinting a full-size model of the human heart. *ACS Biomater Sci Eng*. 2020;6(11):6453-6459.
doi: 10.1021/acsbiomaterials.0c01133

21. Mirdamadi E, Muselimyan N, Koti P, Asfour H, Sarvazyan N. Agarose slurry as a support medium for bioprinting and culturing freestanding cell-laden hydrogel constructs. *3D Print Addit Manuf*. 2019;6(3):158-164.
doi: 10.1089/3dp.2018.0175

22. Hazur J, Detsch R, Karakaya E, et al. Improving alginate printability for biofabrication: establishment of a universal and homogeneous pre-crosslinking technique. *Biofabrication*. 2020;12(4):045004.
doi: 10.1088/1758-5090/ab98e5

23. Girón-Hernández J, Gentile P, Benlloch-Tinoco M. Impact of heterogeneously crosslinked calcium alginate networks on the encapsulation of β-carotene-loaded beads. *Carbohydr Polym*. 2021;271:118429.
doi: 10.1016/j.carbpol.2021.118429

24. Baker BM, Chen CS. Deconstructing the third dimension-how 3D culture microenvironments alter cellular cues. *J Cell Sci*. 2012;125(13):3015-3024.
doi: 10.1242/jcs.079509

25. Marchioli G, Van Gurp L, Van Krieken PP, et al. Fabrication of three-dimensional bioplotted hydrogel scaffolds for islets of Langerhans transplantation. *Biofabrication*. 2015;7(2).
doi: 10.1088/1758-5090/7/2/025009

26. Lee A, Hudson AR, Shiwarski DJ, et al. 3D bioprinting of collagen to rebuild components of the human heart. *Science*. 2019;365(6452):482-487.
http://science.sciencemag.org/.

27. Remaggi G, Catanzano O, Quaglia F, Elviri L. Alginate self-crosslinking ink for 3D extrusion-based cryoprinting and application for epirubicin-HCl delivery on MCF-7 cells. *Molecules*. 2022;27(3):882.
doi: 10.3390/molecules27030882

28. Sardelli L, Tunesi M, Briatico-Vangosa F, Petrini P. 3D-reactive printing of engineered alginate inks. *Soft Matter*. 2021;17(35):8105-8117.
doi: 10.1039/d1sm00604e

29. Kim E, Seok JM, Bae SB, Park SA, Park WH. Silk fibroin enhances cytocompatibilty and dimensional stability of alginate hydrogels for light-based three-dimensional bioprinting. *Biomacromolecules*. 2021;22(5):1921-1931.
doi: 10.1021/acs.biomac.1c00034

30. Falcone G, Mazzei P, Piccolo A, et al. Advanced printable hydrogels from pre-crosslinked alginate as a new tool in semi solid extrusion 3D printing process. *Carbohydr Polym*. 2022;276:118746.
doi: 10.1016/j.carbpol.2021.118746

31. Guagliano G, Volpini C, Camilletti J, et al. Internally crosslinked alginate-based bioinks for the fabrication of *in vitro* hepatic tissue models. *Biofabrication*. 2023;15(3):035018.
doi: 10.1088/1758-5090/acd872

32. Guagliano G, Volpini C, Sardelli L, et al. Hep3Gel: a shape-shifting extracellular matrix-based, three-dimensional liver model adaptable to different culture systems. *ACS Biomater Sci Eng*. 2023;9(1):211-229.
doi: 10.1021/ACSBIOMATERIALS.2C01226

33. Guagliano G, Volpini C, Sardelli L, Briatico Vangosa F, Visai L, Petrini P. Bioinspired bioinks for the fabrication of chemomechanically relevant standalone disease models of hepatic steatosis. *Adv Healthc Mater*. 2024;13(14):e2303349.
doi: 10.1002/ADHM.202303349

34. Bouhadir KH, Lee KY, Alsberg E, Damm KL, Anderson KW, Mooney DJ. Degradation of partially oxidized alginate and its potential application for tissue engineering. *Biotechnol Prog*. 2001;17(5):945-950.
doi: 10.1021/bp010070p

35. Liberski A, Latif N, Raynaud C, Bollensdorff C, Yacoub M. Alginate for cardiac regeneration: from seaweed to clinical trials. *Glob Cardiol Sci Pract*. 2016;2016(1):e201604.
doi: 10.21542/gcsp.2016.4

36. Łabowska MB, Cierluk K, Jankowska AM, Kulbacka J, Detyna J, Michalak I. A review on the adaption of alginate-gelatin hydrogels for 3D cultures and bioprinting. *Materials*. 2021;14(4):1-28.
doi: 10.3390/ma14040858

37. Cattelan G, Guerrero Gerbolés A, Foresti R, et al. Alginate formulations: current developments in the race for hydrogel-

based cardiac regeneration. *Front Bioeng Biotechnol*. 2020;8:414.
doi: 10.3389/fbioe.2020.00414

38. Roche CD, Lin H, Huang Y, et al. 3D bioprinted alginate-gelatin hydrogel patches containing cardiac spheroids recover heart function in a mouse model of myocardial infarction. *Bioprinting*. 2023;30:e00263.
doi: 10.1016/j.bprint.2023.e00263

39. Sonaye SY, Ertugral EG, Kothapalli CR, Sikder P. Extrusion 3D (Bio)printing of alginate-gelatin-based composite scaffolds for skeletal muscle tissue engineering. *Materials*. 2022;15(22):7945.
doi: 10.3390/ma15227945

40. Heid S, Becker K, Byun J, et al. Bioprinting with bioactive alginate dialdehyde-gelatin (ADA-GEL) composite bioinks: time-dependent *in-situ* crosslinking via addition of calcium-silicate particles tunes *in vitro* stability of 3D bioprinted constructs. *Bioprinting*. 2022;26:e00200.
doi: 10.1016/j.bprint.2022.e00200

41. Sarker B, Papageorgiou DG, Silva R, et al. Fabrication of alginate-gelatin crosslinked hydrogel microcapsules and evaluation of the microstructure and physico-chemical properties. *J Mater Chem B*. 2014;2(11):1470-1482.
doi: 10.1039/c3tb21509a

42. Wang LL, Highley CB, Yeh YC, Galarraga JH, Uman S, Burdick JA. Three-dimensional extrusion bioprinting of single- and double-network hydrogels containing dynamic covalent crosslinks. *J Biomed Mater Res A*. 2018;106(4):865-875.
doi: 10.1002/jbm.a.36323

43. Neira-Velàzquez MG, Rodríguez-Hernández MT, Hernández-Hernández E, Ruiz-Martínez AR. Polymer molecular weight measurement. *Handbook of polymer synthesis, characterization, and processing*. 2013;355-366.

44. Pamies R, Schmidt RR, Martínez MDCL and de la Torre JG. The influence of mono and divalent cations on dilute and non-dilute aqueous solutions of sodium alginates. *Carbohydr Polym*. 2010;80(1):248-253.
https://www.researchgate.net/publication/272785338

45. Forgács AF, Papp V, Paul G, et al. Mechanism of hydration and hydration induced structural changes of calcium alginate aerogel. *ACS Appl Mater Interfaces*. 2021;13:2997-3010.
doi: 10.1021/acsami.0c17012

46. Kaklamani G, Cheneler D, Grover LM, Adams MJ, Bowen J. Mechanical properties of alginate hydrogels manufactured using external gelation. *J Mech Behav Biomed Mater*. 2014;36:135-142.
doi: 10.1016/j.jmbbm.2014.04.013

47. Daly AC, Critchley SE, Rencsok EM, Kelly DJ. A comparison of different bioinks for 3D bioprinting of fibrocartilage and hyaline cartilage. *Biofabrication*. 2016;8(4):045002.
doi: 10.1088/1758-5090/8/4/045002

48. Wang Q, Backman O, Nuopponen M, Xu C, Wang X. Rheological and printability assessments on biomaterial inks of nanocellulose/photo-crosslinkable biopolymer in light-aided 3D printing. *Front Chem Eng*. 2021;3:723429.
doi: 10.3389/fceng.2021.723429

49. Barceló X, Eichholz KF, Garcia O, Kelly DJ. Tuning the degradation rate of alginate-based bioinks for bioprinting functional cartilage tissue. *Biomedicines*. 2022;10(7):1621.
doi: 10.3390/biomedicines10071621

50. Reakasame S, Boccaccini AR. Oxidized alginate-based hydrogels for tissue engineering applications: a review. *Biomacromolecules*. 2018;19(1):3-21.
doi: 10.1021/acs.biomac.7b01331

51. Gomez CG, Rinaudo M, Villar MA. Oxidation of sodium alginate and characterization of the oxidized derivatives. *Carbohydr Polym*. 2007;67(3):296-304.
doi: 10.1016/J.CARBPOL.2006.05.025

52. Salomonsen T, Jensen HM, Larsen FH, Steuernagel S, Engelsen SB. Direct quantification of M/G ratio from 13C CP-MAS NMR spectra of alginate powders by multivariate curve resolution. *Carbohydr Res*. 2009;344(15):2014-2022.
doi: 10.1016/j.carres.2009.06.025

53. Huamani-Palomino RG, Córdova BM, Elvis Renzo Pichilingue L, Venâncio T, Valderrama AC. Functionalization of an alginate-based material by oxidation and reductive amination. *Polymers (Basel)*. 2021;13(2):1-15.
doi: 10.3390/polym13020255

54. Banks SR, Enck K, Wright M, Opara EC, Welker ME. Chemical modification of alginate for controlled oral drug delivery. *J Agric Food Chem*. 2019;67(37):10481-10488.
doi: 10.1021/acs.jafc.9b01911

55. Sarker B, Singh R, Silva R, et al. Evaluation of fibroblasts adhesion and proliferation on alginate-gelatin crosslinked hydrogel. *PLoS One*. 2014;9(9):e107952.
doi: 10.1371/JOURNAL.PONE.0107952

56. Zhao C, Latif A, Williams KJ, Tirella A. The characterization of molecular weight distribution and aggregation by asymmetrical flow field-flow fractionation of unmodified and oxidized alginate. *React Funct Polym*. 2022;175:105292.
doi: 10.1016/j.reactfunctpolym.2022.105292

57. Wang H, Chen X, Wen Y, et al. A study on the correlation between the oxidation degree of oxidized sodium alginate on its degradability and gelation. *Polymers (Basel)*. 2022;14(9):1679.
doi: 10.3390/polym14091679

58. Kristiansen KA, Tomren HB, Christensen BE. Periodate oxidized alginates: depolymerization kinetics. *Carbohydr Polym*. 2011;86(4):1595-1601.
doi: 10.1016/J.CARBPOL.2011.06.069

59. Larsen BE, Bjørnstad J, Pettersen EO, Tønnesen HH, Melvik JE. Rheological characterization of an injectable alginate gel system. *BMC Biotechnol*. 2015;15(1):29.
doi: 10.1186/s12896-015-0147-7

60. Mccain ML, Lee H, Aratyn-Schaus Y, Kléber AG, Parker KK. Cooperative coupling of cell-matrix and cell–cell adhesions in cardiac muscle. *Biophys Comput Biol*. 2012;109(25):9881-9886.
doi: 10.1073/pnas.1203007109/-/DCSupplemental

61. Deddens JC, Sadeghi AH, Hjortnaes J, et al. Modeling the human scarred heart *in vitro*: toward new tissue engineered models. *Adv Healthc Mater*. 2017;6(3):1600571.
doi: 10.1002/adhm.201600571

62. Maxwell CJ, Soltisz AM, Rich WW, Choi A, Reilly MA, Swindle-Reilly KE. Tunable alginate hydrogels as injectable drug delivery vehicles for optic neuropathy. *J Biomed Mater Res A*. 2022;110(10):1621-1635.
doi: 10.1002/jbm.a.37412

63. Park H, Lyons J, Ohtsubo T, Song CW. Acidic environment causes apoptosis by increasing caspase activity. *Br J Cancer*. 1999;80:1892-1897
doi: 10.1038/sj.bjc.6690617

64. Mirek A, Belaid H, Barranger F, et al. Development of a new 3D bioprinted antibiotic delivery system based on a cross-linked gelatin-alginate hydrogel. *J Mater Chem B*. 2022;10(43):8862-8874.
doi: 10.1039/d2tb01268e

65. Li Z, Liao Y, Li D, et al. Design and properties of alginate/gelatin/cellulose nanocrystals interpenetrating polymer network composite hydrogels based on *in situ* cross-linking. *Eur Polym J*. 2023;201:112556
doi: 10.21203/rs.3.rs-2215053/v1

66. Saarai A, Kasparkova V, Sedlacek T, Saha P. On the development and characterisation of crosslinked sodium alginate/gelatine hydrogels. *J Mech Behav Biomed Mater*. 2013;18:152-166.
doi: 10.1016/j.jmbbm.2012.11.010

67. Hackenhaar CR, Rosa CF, Flores EEE, Santagapita PR, Klein MP, Hertz PF. Development of a biocomposite based on alginate/gelatin crosslinked with genipin for β-galactosidase immobilization: performance and characteristics. *Carbohydr Polym*. 2022;291:119483.
doi: 10.1016/j.carbpol.2022.119483

68. Karakaya E, Schöbel L, Zhong Y, et al. How to determine a suitable alginate for biofabrication approaches using an extensive alginate library? *Biomacromolecules*. 2023;24(7):2982-2997.
doi: 10.1021/acs.biomac.2c01282

69. Zehnder T, Sarker B, Boccaccini AR, Detsch R. Evaluation of an alginate-gelatine crosslinked hydrogel for bioplotting. *Biofabrication*. 2015;7(2):025001.
doi: 10.1088/1758-5090/7/2/025001

70. Bociaga D, Bartniak M, Grabarczyk J, Przybyszewska K. Sodium alginate/gelatine hydrogels for direct bioprinting-the effect of composition selection and applied solvents on the bioink properties. *Materials*. 2019;12(7):2669.
doi: 10.3390/ma12172669

71. Li Z, Huang S, Liu Y, et al. Tuning alginate-gelatin bioink properties by varying solvent and their impact on stem cell behavior. *Sci Rep*. 2018;8(1):8020.
doi: 10.1038/s41598-018-26407-3

72. Mondal A, Gebeyehu A, Miranda M, et al. Author correction: characterization and printability of sodium alginate -gelatin hydrogel for bioprinting NSCLC co-culture. *Sci Rep*. 2020;10(1):1732.
doi: 10.1038/s41598-020-58952-1

73. Distler T, Mcdonald K, Heid S, Karakaya E, Detsch R, Boccaccini AR. Ionically and enzymatically dual cross-linked oxidized alginate gelatin hydrogels with tunable stiffness and degradation behavior for tissue engineering. *ACS Biomater Sci Eng*. 2020;6(7): 3899-3914.
doi: 10.1021/acsbiomaterials.0c00677

74. Bider F, Miola M, Clejanu CE, et al. 3D bioprinting of multifunctional alginate dialdehyde (ADA)–gelatin (GEL) (ADA-GEL) hydrogels incorporating ferulic acid. *Int J Biol Macromol*. 2024;257:128449.
doi: 10.1016/j.ijbiomac.2023.128449

75. Genç H, Hazur J, Karakaya E, et al. Differential responses to bioink-induced oxidative stress in endothelial cells and fibroblasts. *Int J Mol Sci*. 2021;22(5):2358.
doi: 10.3390/IJMS22052358

76. Wu Y, Yuan L, Sheng N, et al. A soft tissue adhesive based on aldehyde-sodium alginate and amino-carboxymethyl chitosan preparation through the Schiff reaction. *Front Mater Sci*. 2017;11(3):215-222.
doi: 10.1007/S11706-017-0392-X

77. Emami Z, Ehsani M, Zandi M, Foudazi R. Controlling alginate oxidation conditions for making alginate-gelatin hydrogels. *Carbohydr Polym*. 2018;198: 509-517.
doi: 10.1016/j.carbpol.2018.06.080

78. Dalheim M, Vanacker J, Najmi MA, Aachmann FL, Strand BL, Christensen BE. Efficient functionalization of alginate biomaterials. *Biomaterials*. 2016;80:146-156.
doi: 10.1016/J.BIOMATERIALS.2015.11.043

79. Boontheekul T, Kong HJ, Mooney DJ. Controlling alginate gel degradation utilizing partial oxidation and bimodal molecular weight distribution. *Biomaterials*. 2005;26:2455-2465.
doi: 10.1016/j.biomaterials.2004.06.044

80. Cuomo F, Cofelice M, Lopez F. Rheological characterization of hydrogels from alginate-based nanodispersion. *Polymers (Basel)*. 2019;11(2):259.
doi: 10.3390/polym11020259

81. Cooke ME, Rosenzweig DH. The rheology of direct and suspended extrusion bioprinting. *APL Bioeng*. 2021;5(1):011502.
doi: 10.1063/5.0031475

82. Schwab A, Levato R, D'este M, Piluso S, Eglin D, Malda J. Printability and shape fidelity of bioinks in 3D bioprinting. *Chem Rev*. 2020;120(19):11028-11055. doi: 10.1021/acs.chemrev.0c00084

83. Zhao Y, Li Y, Mao S, Sun W, Yao R. The influence of printing parameters on cell survival rate and printability in microextrusion-based 3D cell printing technology. *Biofabrication*. 2015;7(4):045002. doi: 10.1088/1758-5090/7/4/045002

84. Malekpour A, Chen X. Printability and cell viability in extrusion-based bioprinting from experimental, computational, and machine learning views. *J Funct Biomater*. 2022;13(2):40. doi: 10.3390/jfb13020040

85. Kim E, Seok JM, Bae S Bin, Park SA, Park WH. Silk fibroin enhances cytocompatibilty and dimensional stability of alginate hydrogels for light-based three-dimensional bioprinting. *Biomacromolecules*. 2021;22(5):1921-1931. doi: 10.1021/acs.biomac.1c00034

86. Li A, Guo C, Li X, Li P, Yang X, Guo Y. Gelation mechanism and physical properties of glucono-δ-lactone induced alginate sodium/casein composite gels. *Food Hydrocoll*. 2021;118:106775. doi: 10.1016/J.FOODHYD.2021.106775

87. Jia J, Richards DJ, Pollard S, et al. Engineering alginate as bioink for bioprinting. *Acta Biomater*. 2014;10(10):4323-4331. doi: 10.1016/j.actbio.2014.06.034

ACCSCIENCE PUBLISHING

International Journal of Bioprinting

RESEARCH ARTICLE

Biomechanical analysis of partial mandibular implants with various lattice designs of different material properties: *In vitro* study and finite element analysis

Hao Zhang[1], Lih Jyh Fuh[1,2], Jui Ting Hsu[3], Zhe Min Lim[1], and Heng Li Huang [1,4]*

[1] School of Dentistry, China Medical University, Taichung, Taiwan

[2] Department of Dentistry, China Medical University Hospital, Taichung, Taiwan

[3] Department of Biomedical Engineering, China Medical University, Taichung, Taiwan

[4] Department of Bioinformatics and Medical Engineering, Asia University, Taichung, Taiwan

(This article belongs to the Special Issue: *3D Printing of Composite Materials in Bone Tissue Engineering Applications*)

Abstract

For patients with mandibular bone defects, although reconstruction plates can be used for repair, achieving both occlusal function and facial aesthetics is challenging. In the present study, *in vitro* experiments and finite element analysis (FEA) were conducted to determine the biomechanical characteristics of multiple porous lattice structures of varying shapes and diameters that were used for mandibular implants. Additionally, an abutment designed to carry occlusal forces was added to the top of the implants. The stress distribution of four lattice designs (tetrahedron, quad-diametral-cross, hex-star, and hex-vase) of three sizes (2.5, 3.0, and 3.5 mm) in cubic porous models were analyzed by FEA. Subsequently, two optimal designs for 3D-printed titanium alloy were selected. These designs, featuring different lattice diameters (0.5, 0.7, and 0.9 mm), were tested to determine their elastic modulus, which was used in another FEA of a mandibular implant designed for a patient with a malignant tumor in the right mandible. This model, which included an abutment design, was subjected to a vertical force of 100 N and muscle forces generated by biting. This analysis was conducted to determine the elastic modulus of the implant and the values of stress and strain on the implant and surrounding bone. The lattice designs of quad-diametral-cross and hex-vase exhibited smaller high-stress regions than those of tetrahedron and hex-star. *In vitro* tests revealed that the elastic modulus of the lattices increased with the rod diameter. When these values were applied to mandibular implants, Young's modulus decreased, which in turn increased the frictional stress observed at the interface between the abutment and the implant. However, the implant's maximum stress remained below its yield strength (910 MPa), and the strain on the surrounding bone varied between 1500 and 3000 μstrain. As indicated by Frost's theory, these implants are unlikely to damage the surrounding bone tissue and are likely to support bone growth.

Keywords: Mandibular segmental resection; Porous lattice design; Lattice size; Rod diameter; Mandibular implant; Abutment; *In vitro* experiment; Finite element analysis

***Corresponding author:**
Heng-Li Huang
(hlhuang@mail.cmu.edu.tw)

Citation: Zhang H, Fuh LJ, Hsu JT, Lim ZM, Huang HL. Biomechanical analysis of partial mandibular implants with various lattice designs of different material properties: *In vitro* study and finite element analysis. *Int J Bioprint*. 2024;10(6):3943. doi: 10.36922/ijb.3943

Received: June 14, 2024
1st revised: July 29, 2024
2nd revised: August 27, 2024
3rd revised: August 29, 2024
Accepted: September 2, 2024
Published Online: September 2, 2024

Copyright: © 2024 Author(s). This is an Open Access article distributed under the terms of the Creative Commons Attribution License, permitting distribution, and reproduction in any medium, provided the original work is properly cited.

Publisher's Note: AccScience Publishing remains neutral with regard to jurisdictional claims in published maps and institutional affiliations.

1. Introduction

Mandibular segmental defects often result from trauma, congenital disorders, and benign or malignant tumors. If left untreated, these defects may lead to difficulties in daily activities such as speaking or eating. Currently, vascularized and non-vascularized bone grafting are regarded as primary surgical techniques for repairing mandibular segmental defects. However, these techniques require the surgeon to manually shape the grafted bone and subsequent transplantation into the patient's oral cavity. Likewise, these procedures are associated with prolonged surgical duration and carry the risk of complications related to bone transplantation.[1,2]

Advancements in additive manufacturing technology have enabled the customization of facial reconstruction for patients with facial defects through the integration of images from computed tomography and magnetic resonance imaging. This approach not only enables greater customization of reconstruction but also mitigates the likelihood of errors occurring during surgery, thereby increasing the success rate of these procedures.[3,4]

Titanium alloys have excellent mechanical properties, corrosion resistance, and biocompatibility.[5] These alloys are used to manufacture complex geometric shapes that match anatomical structures, and they are used to construct porous titanium scaffolds with mechanical properties similar to those of trabecular bone. Utilizing the pore characteristics of titanium alloys can enhance the integration of implants with surrounding bone and thereby enhance the long-term stability of the implants.[6,7] Therefore, porous titanium alloys are regarded as a suitable option for the repair of mandibular defects.[8,9] In particular, Ti6Al4V not only possesses the advantages of titanium alloys but also features a high strength-to-weight ratio, excellent fatigue resistance, and a lower elastic modulus. This makes it more capable of simulating the elastic modulus of human bone in medical implants, reducing the stress-shielding effect between the implant and the surrounding bone, which contributes to more effective and durable implant outcomes.[10]

Multiple studies have indicated that designing mandibular implants with porous structures can reduce the weight of the implants and promote their long-term integration with surrounding tissues, thereby facilitating inward bone growth.[11–13] In lattice structures, adjusting the rod diameter of the tetrahedron unit cell enables the porous structures to achieve higher mechanical strength.[14] However, the use of porous structures alone may not fully restore biting function. Therefore, many researchers have attempted to integrate abutment structures into mandibular implants,[15,16] with several successful cases reported in the literature.[17–19]

Although multiple studies have investigated the biomechanical characteristics of porous mandibular implants, the impact of internal lattice design – specifically the shapes, sizes, and rod diameters – on the biomechanics of these implants remains unclear. Therefore, the present study determined the effects of different lattice shapes, sizes, and rod diameters on mandibular implants and identified good design parameters. To facilitate the attachment of dental crowns postoperatively and restore biting function, we designed a mandibular implant with an abutment structure on its top. Selected porous lattice structures with suitable elastic modulus were used to improve the stress distribution of the titanium alloy mandibular implant and surrounding bone, providing insights into its biomechanical design while reducing its overall weight.

2. Methods

2.1. Design of a 3D lattice model

The solid models of lattice structures with four porous shapes, namely tetrahedron, hex-star, hex-vase, and quad-diametral-cross,[20] were designed in accordance with the specifications of ASTM F2077 by SolidWorks 2024 (Dassault Systèmes SolidWorks Corporation, United States of America [USA]) and other related software. As presented in Figure 1a, these models were compared based on three lattice sizes (2.5, 3.0, and 3.5 mm) and three rod diameters (0.5, 0.7, and 0.9 mm). Each lattice model is 10 mm in length, 10 mm in width, and 10 mm in height.

2.2. Finite element analysis of lattice model

After the porous lattice models were imported into the finite element analysis (FEA) software Ansys 2021 R2 (Ansys, USA), they were placed within a 3D model with upper and lower platens with a length of 12 mm, a width of 12 mm, and a height of 2 mm for computer-simulated compression experiments. Boundary conditions were established with zero displacement in the x-, y-, and z-directions on the lower plane, and the interface between the lattice model and the upper and lower platens was defined as a bonding interface.

As indicated in Figure 1b, the loading conditions involved the application of an axial downward force with a displacement of 0.1 mm on the upper plane. The material properties were uniformly set as linear elastic, homogeneous, and isotropic (Table 1).[21]

2.3. *In vitro* experiments of the lattice model

Based on the stress distribution results, two sets of lattice shapes and sizes with more favorable stress distribution

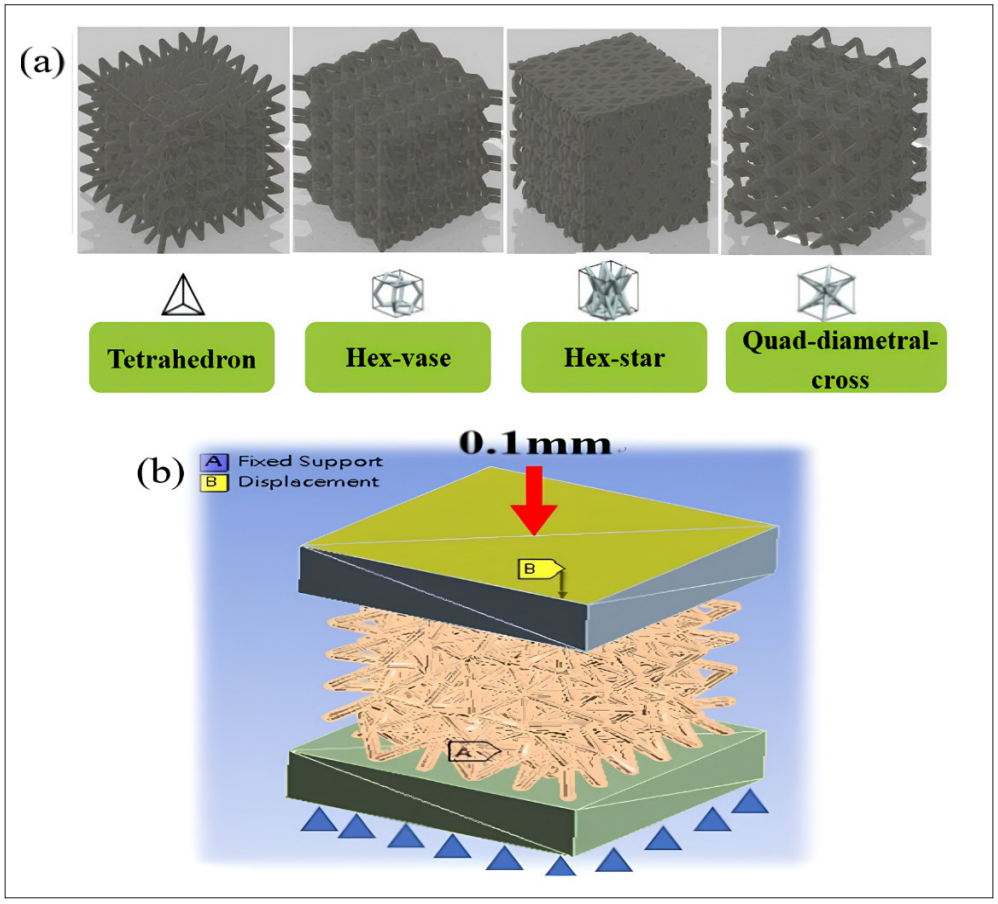

Figure 1. The finite element analysis (FEA) of 3D titanium alloy lattice models: (a) the 3D porous structures of four different lattice models and (b) the loading and boundary conditions applied to the FE lattice model.

Table 1. Material properties of the finite element (FE) lattice model.

Material	Elastic modulus (MPa)	Poisson's ratio	Reference
Ti6Al4V	96,000	0.36	[21]

were selected. A ZRapid iSLM280 metal 3D printer (ZRapid Technologies, China) was used to print the 3D titanium alloy lattice models required for *in vitro* compression experiments (Figure 2). To ensure the quality of 3D printing, the production speed was set to 4 cm^3/h; the printing layer thickness was 0.02 mm. Additionally, all samples underwent sandblasting and fine sandpaper polishing to make the lattice interior and cubit surface smoother. Each set included three distinct lattice rod diameters (0.5, 0.7, and 0.9 mm), with five samples per set.

After the 3D-printed titanium alloy lattice samples were placed on the platform of an MTS QTest/10 load frame (MTS Systems, USA), axial pressure was applied at a rate of 1 mm/min until the yield point of each sample was reached (Figure 3). To determine the elastic modulus of the three lattice rod diameters, the load force and displacement data were recorded to plot a stress–strain curve and calculate its slope (Figure 4).

2.4. Designing a customized mandibular model

This study was approved by the Institutional Review Board of the China Medical University Hospital (approval no. CMUH110-REC2-247). Cone-beam computed tomography images were obtained from the mandible of a patient with a right-sided malignant tumor. The images were imported into the medical imaging software Mimics (version 14.0; Materialise, Belgium) to obtain the mandible's outline and the contours of cortical and cancellous bone based on grayscale intensity values. The resulting data were exported as STL files and imported into the reverse-engineering software SpaceClaim (Ansys, USA) to reconstruct the 3D surface mesh of the mandible. Subsequently, the data were imported into the computer-aided design software SolidWorks 2024 (Dassault Systèmes

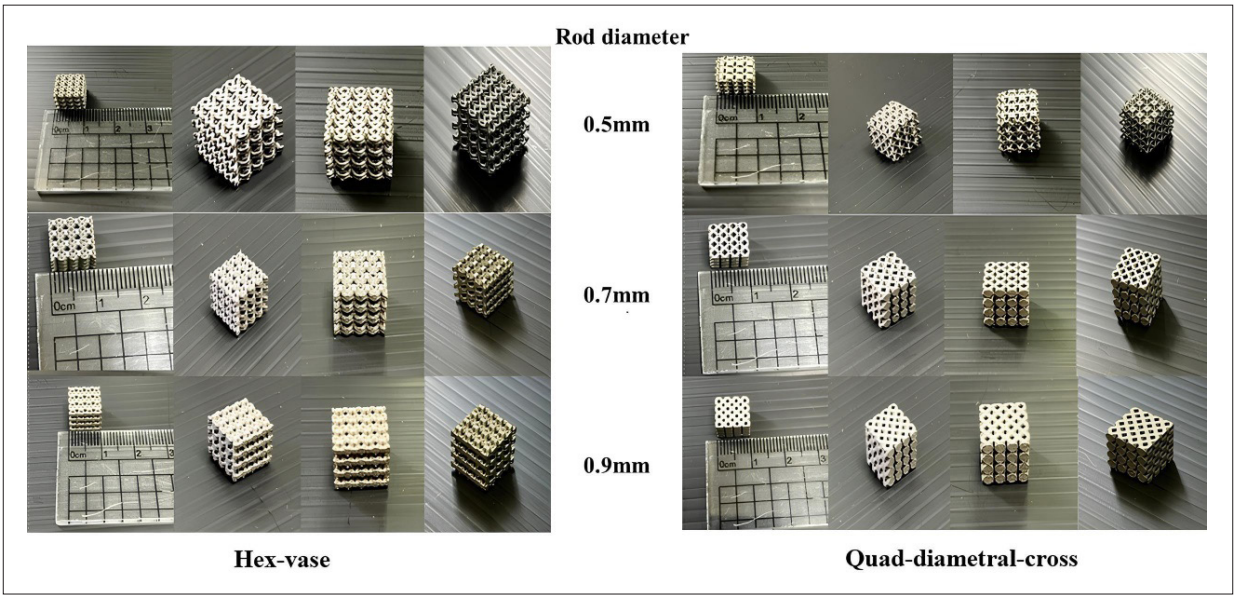

Figure 2. 3D-printed titanium alloy lattice samples.

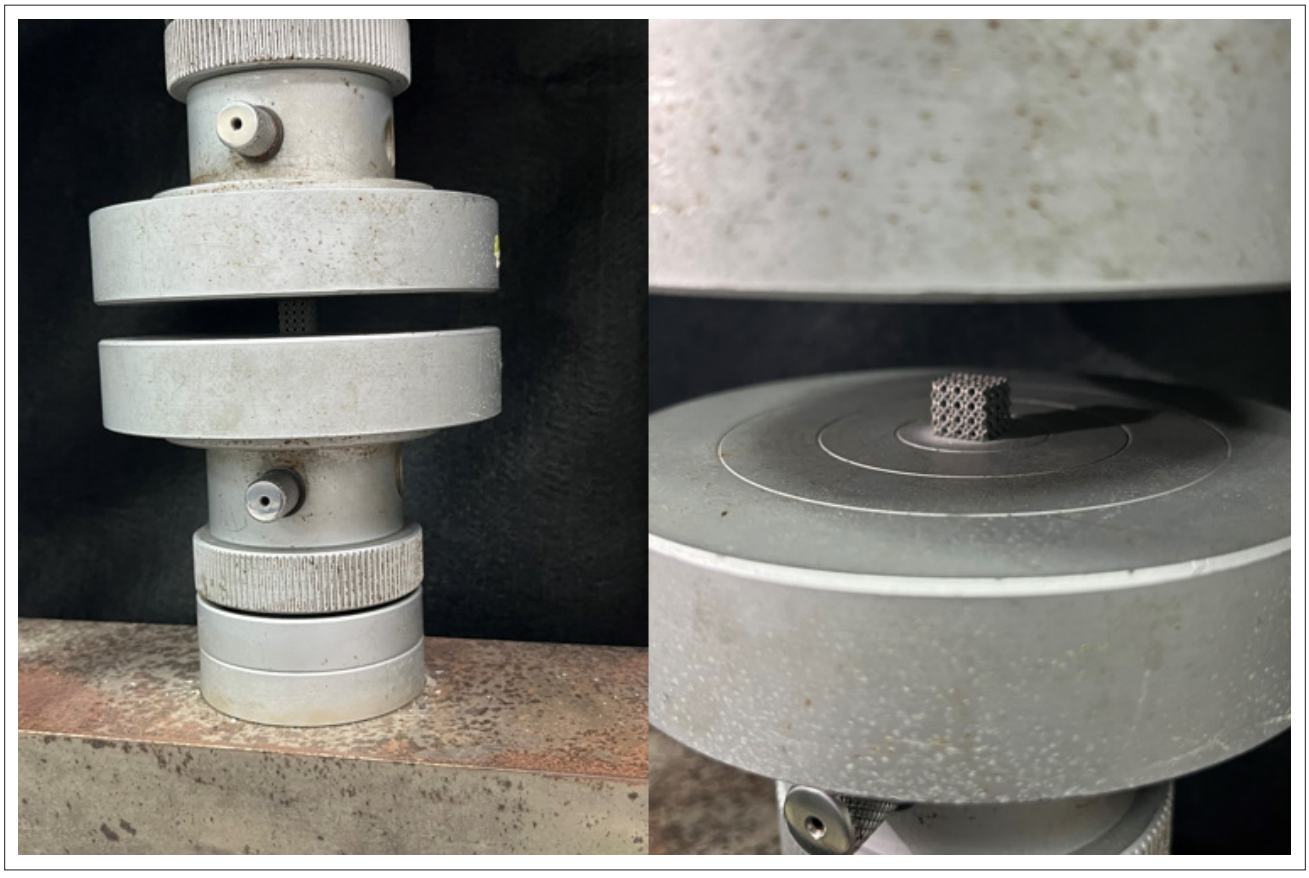

Figure 3. *In vitro* compression test.

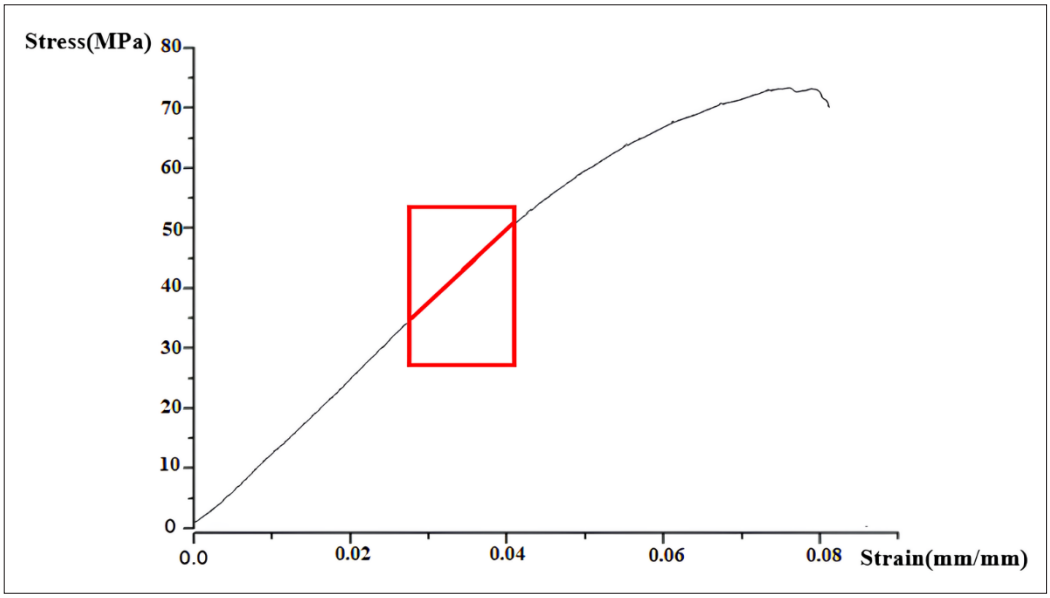

Figure 4. Stress–strain plot of HV-d1. The slop of the curve in the red box is measured as elastic modulus. Abbreviations: HV: Hex-vase; d1: Rod diameter of 0.5 mm.

SolidWorks Corporation, USA) to create a 3D solid model of the resected mandible (Figure 5d).

A mandibular implant model measuring approximately 45 × 35 × 12 mm was designed using the resected right mandibular bone with the malignant tumor. To secure the implant in the mandible with bone screws, each side of the implant included two 4-mm screw holes. Each bone screw was 12 mm in length, with a head diameter of 4 mm, a neck diameter of 2.7 mm, and a pitch of 1.26 mm (Figure 5). In addition, four abutments were designed above the implant to facilitate future attachment of dentures for biting function. The design of the abutment placed on the mandibular implant is similar to a Zest LOCATOR (Zest Anchors, USA), with a length of 7.88 mm, a head diameter of 3.86 mm, a neck diameter of 1.8 mm, and a pitch of 1.2 mm (Figure 5).

2.5. Finite element analysis of mandibular implants

After the proposed model was imported into Ansys 2021 R2 (Ansys, USA) for further analysis, the material properties were uniformly set as linear elastic, homogeneous, and isotropic (Table 2).[22] Table 3, which presents data from Result 3.2 of the *in vitro* experimental test, presents the elastic modulus values of the three lattice rod diameters of the 3D-printed titanium alloy lattice samples. These properties were used to set the elastic modulus of the mandibular implant for subsequent analyses. The mesh sizes for FEA were set as follows: 1 mm for the posterior segment of the mandible, 0.8 mm for the surrounding bone, 0.6 mm for the mandibular implant and fixation screws, and 0.5 mm for the abutment. The total number of elements of the FE model was 1,238,926 (Figure 6).

The frictional coefficient at the interface between the mandibular implant and bone was set to 0.4,[23] and the frictional coefficient between the implant and bone screws was set to 0.3.[24] These values were specified for nonlinear surface-to-surface contact elements to simulate the frictional contact behavior, including sliding and sticking, at these interfaces.

The loading conditions primarily involved the three major muscles responsible for mandibular movement (Figure 7). Since reconstruction was performed on the right side of the mandible, the loading conditions involved right group function (RGF) and right unilateral molar clench (RMOL). In addition, a vertical force of 100 N was applied to the plane above the abutment to simulate the force exerted by the patient on the right side.[25,26] Boundary conditions were set at the temporomandibular joint on both sides of the mandible, with zero displacement in the x-, y-, and z-directions.

3. Results

3.1. Finite element analysis of lattice structures

Figure 8 depicts the stress results for the different lattice shapes and sizes. Among the lattice designs, that of hex-star exhibited the highest stress distribution, followed by that of tetrahedron. The lattice designs hex-vase and quad-diametral-cross exhibited lower stress distributions. When the size of the lattice decreased, the amount of stress

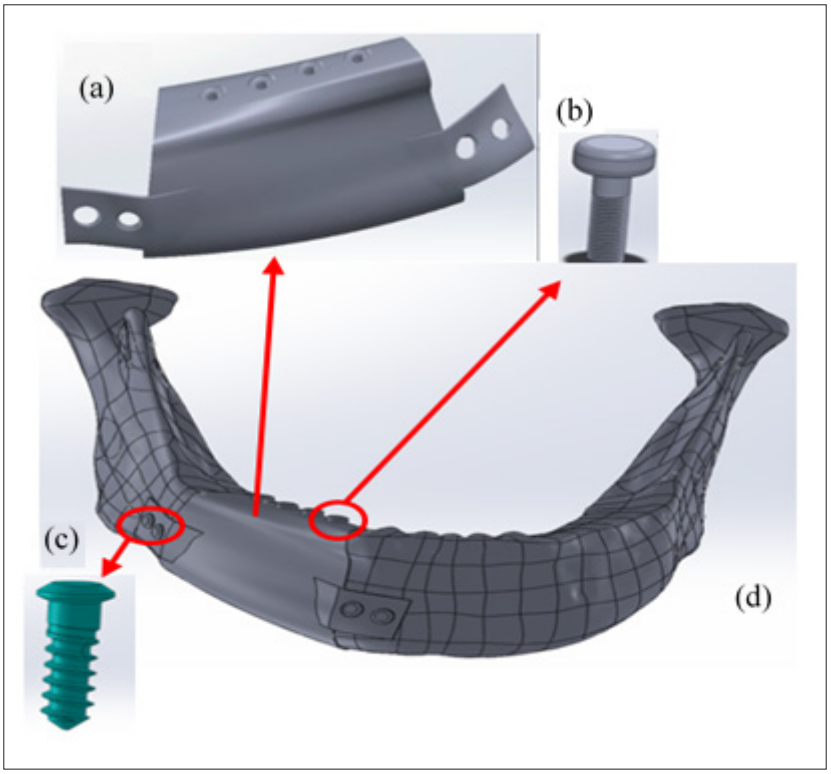

Figure 5. Simulated finite element (FE) model of the (a) mandibular implant with wing plate, (b) abutment, (c) bone screws, and (d) mandibular.

Table 2. Material properties of the finite element (FE) models involving the mandibular implant, abutment, screws, and bone.

Material	Elastic modulus (MPa)	Poisson's ratio	Reference
Trabecular bone	1600	0.3	[22]
Cortical bone	14,800	0.3	[22]
Abutment and screws	110,000	0.35	[22]
Mandibular implant	From **Table 3**	0.3	

Note: The values of the elastic modulus are adapted from **Table 3**, which were obtained through *in vitro* experimental testing.

Table 3. Elastic modulus of six lattice designs.

Sample	Elastic modulus (MPa)					
	HV-d1	HV-d2	HV-d3	QDC-d1	QDC-d2	QDC-d3
Sample 1	1247.50	2226.67	2253.59	773.08	1720.69	2175.43
Sample 2	1254.40	1999.00	2349.18	768.46	1705.64	2191.63
Sample 3	1251.30	2072.27	2288.51	763.08	1683.56	2178.26
Sample 4	1242.50	2064.85	2280.57	768.46	1758.86	2187.47
Sample 5	1171.80	2216.11	2254.21	669.33	1726.21	2212.33
Average	1233.50	2115.80	2285.20	748.48	1719.00	2189.03
Standard deviation	34.77	100.61	39.00	44.39	27.74	14.60

Abbreviations: HV: Hex-vase; QDC: Quad-diametral-cross; d1: Rod diameter of 0.5 mm; d2: Rod diameter of 0.7 mm; d3: Rod diameter of 0.9 mm.

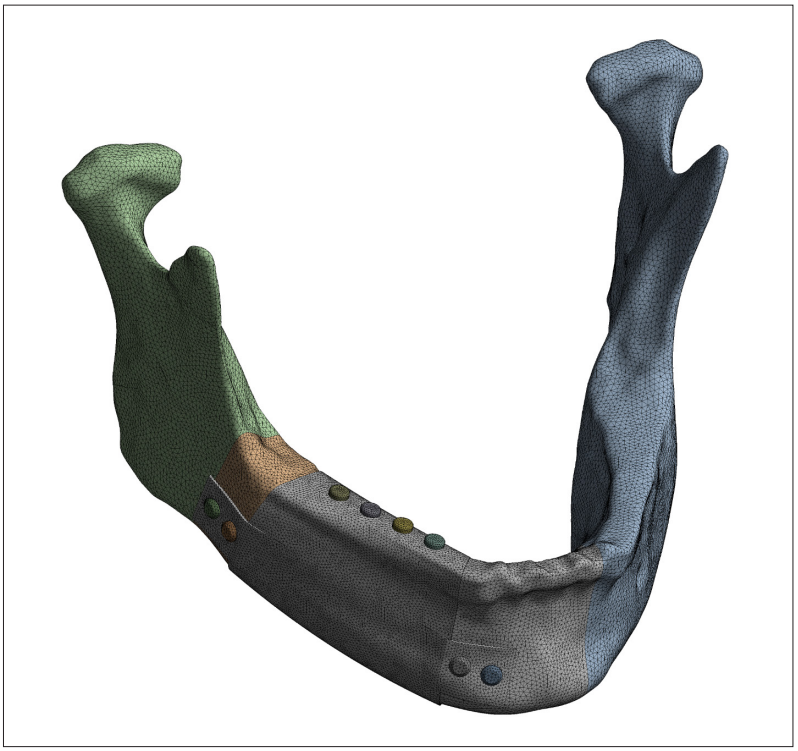

Figure 6. Mesh status of the finite element model of the mandibular implant.

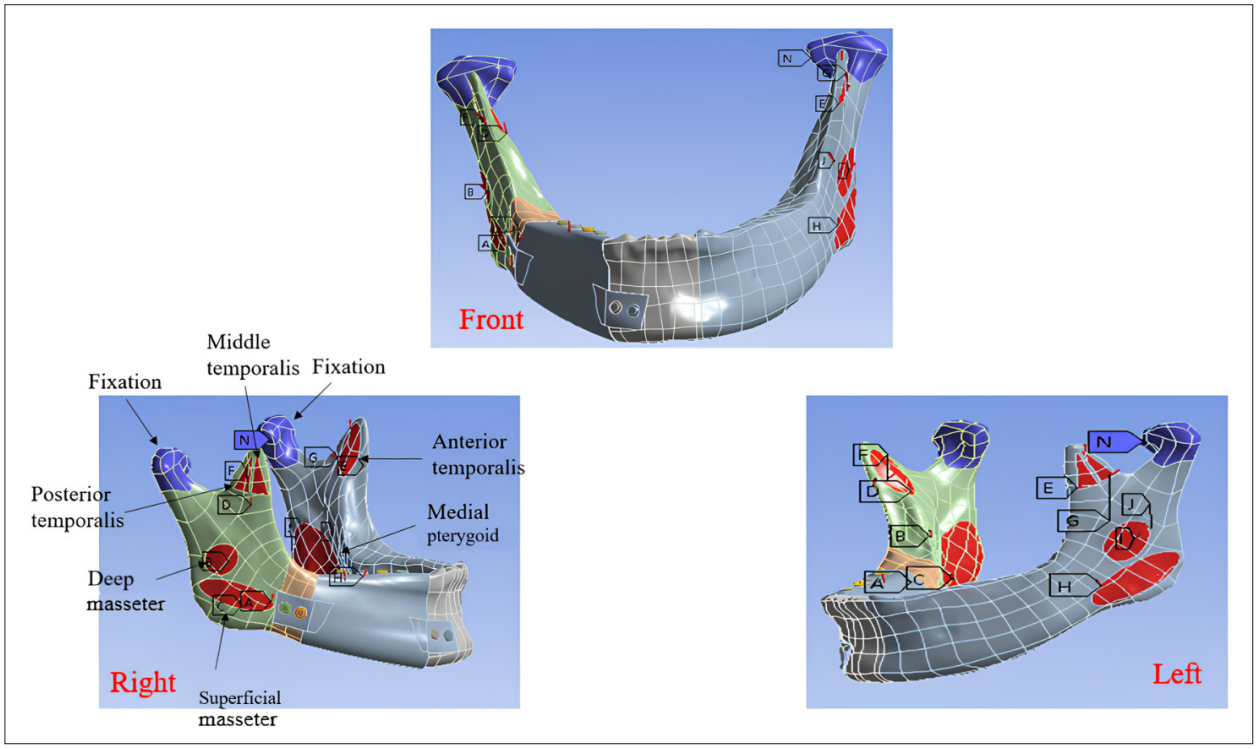

Figure 7. Loading and boundary conditions of the finite element (FE) model. The blue section represents the fixed area and the red section represents the loading position of the mandibular muscle. A: Superficial masseter; B: Deep masseter; C: Medial pterygoid; D: Anterior temporalis; E: Middle temporalis; F: Posterior temporalis; G: Posterior temporalis; H: Superficial masseter; I: Deep masseter; J: Medial pterygoid; and N: Fixation.

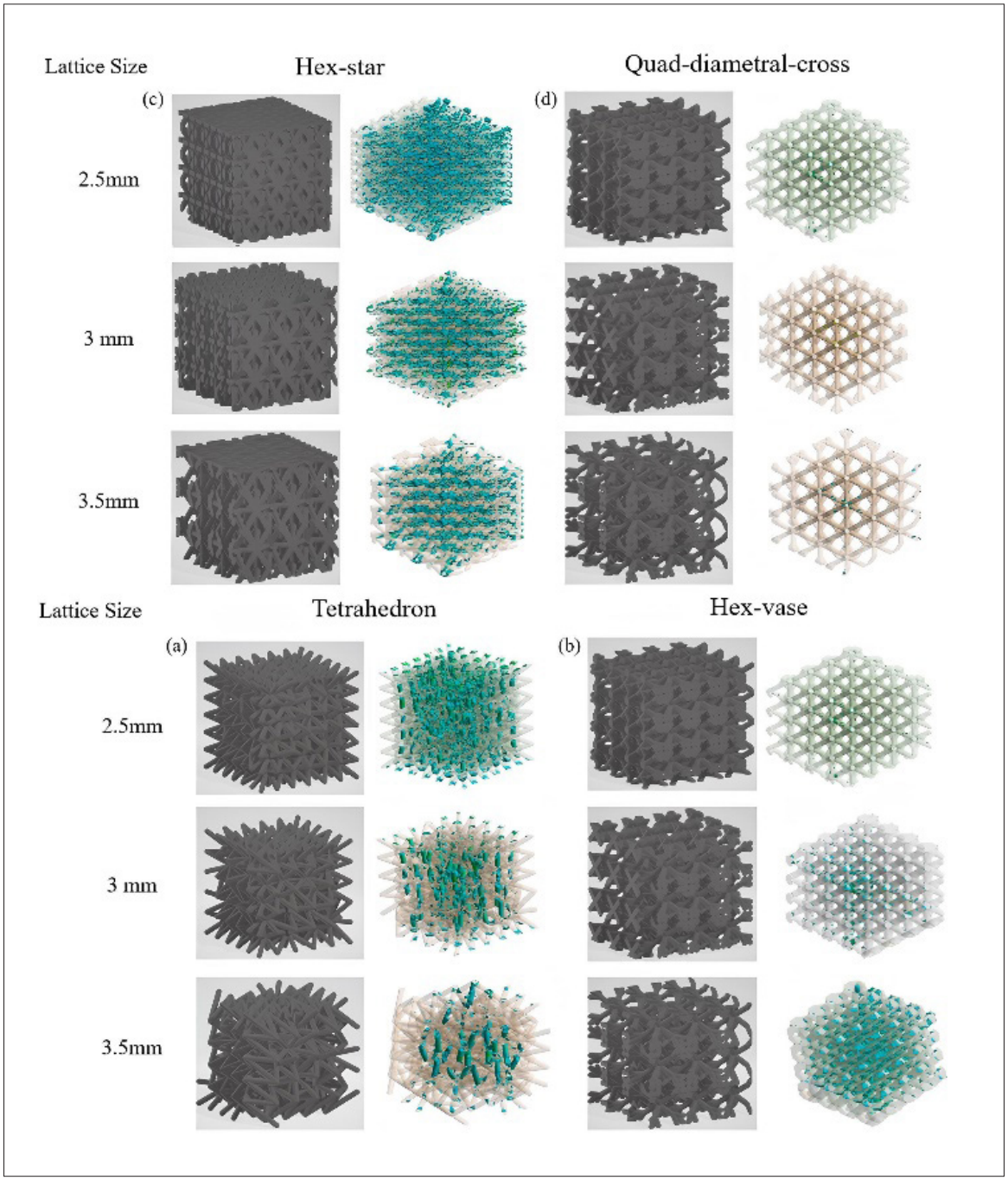

Figure 8. High-stress distribution in samples with various lattice shapes and sizes: (a) for tetrahedron lattice designs, only stresses exceeding 1000 MPa are displayed, (b) for hex-vase lattice designs, only stresses exceeding 1000 MPa are displayed, (c) for hex-star lattice designs, only stresses exceeding 1000 MPa are displayed, and (d) for quad-diametral-cross lattice designs, only stresses exceeding 1000 MPa are displayed.

within the lattice gradually increased, and the regions with high-stress distributions gradually expanded for all four lattice shapes.

With consideration of the results regarding the lattice rod diameters (Figure 9), the lattice designs of quad-diametral-cross and hex-vase, both of which exhibited relatively low high-stress distributions, were compared. Therefore, these two designs were selected for the next phase of experimentation.

3.2. *In vitro* experimental test

In the lattice designs of quad-diametral-cross and hex-vase, a significant increase was observed in the elastic

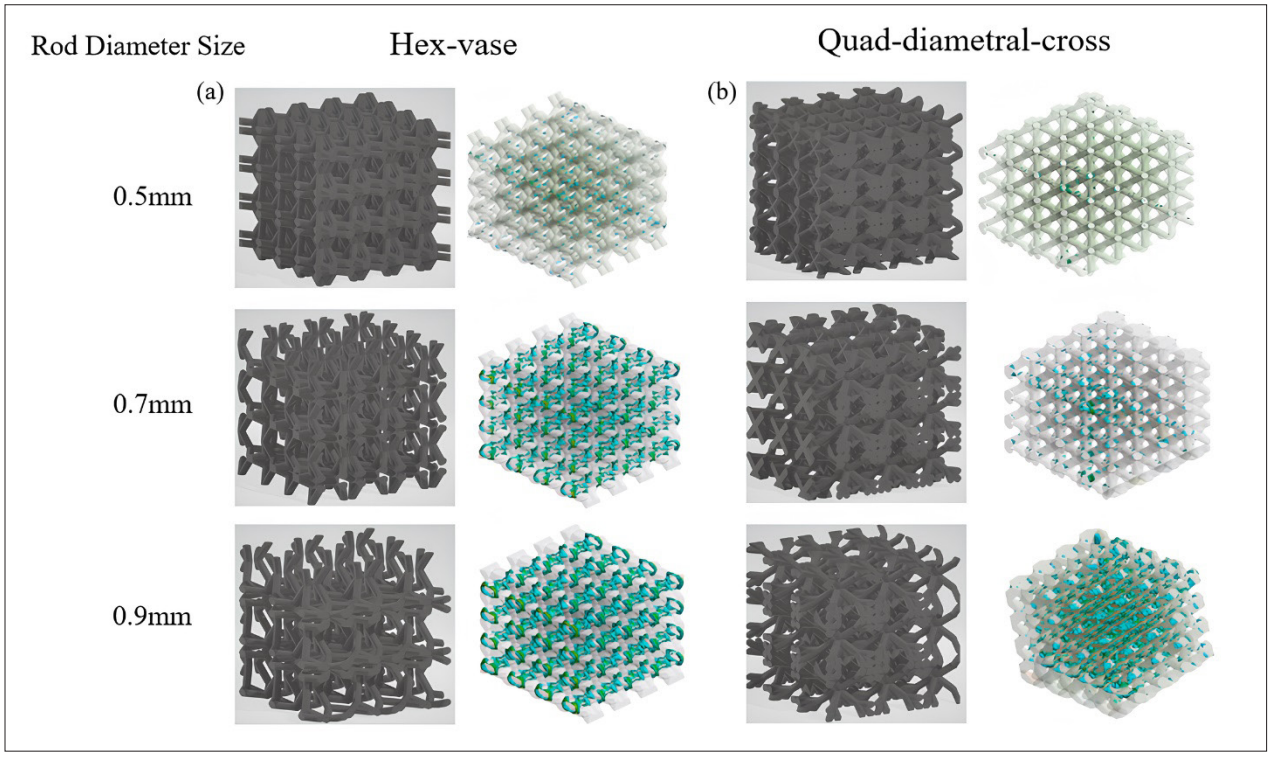

Figure 9. High-stress distribution in two lattice structures with various rod diameters: (a) for hex-vase lattice designs, only stresses exceeding 1000 MPa are displayed and (b) for quad-diametral-cross lattice designs, only stresses exceeding 1000 MPa are displayed.

modulus as the lattice rod diameter increased (Table 3). In the lattice structure of hex-vase, the elastic modulus reached approximately 1233 MPa at a rod diameter of 0.5 mm and approximately 2285 MPa at a rod diameter of 0.9 mm, indicating that the elastic modulus for a rod diameter of 0.5 mm was nearly half of that for a diameter of 0.9 mm.

In the lattice structure of quad-diametral-cross, major changes were observed in the elastic modulus, indicating a strong effect of the lattice rod diameter on the material strength of the lattice, particularly in terms of the elastic range. Given that the elastic modulus of cancellous bone in the human body is approximately 1600 MPa,[22] three models were selected in this study with consideration of a threshold of 1600 MPa. These models were QDC-d1, with an elastic modulus of approximately 749 MPa, representing low cancellous bone strength; QDC-d2, with an elastic modulus of approximately 1719 MPa, representing near cancellous bone strength; and HV-d3, with an elastic modulus of approximately 2285 MPa, representing high cancellous bone strength. These three values were applied to the mandibular implant model to determine the stress and strain effects on both the implant itself and the surrounding bone.

3.3. Finite element analysis of the mandibular implant

As displayed in Figure 10, under both RMOL and RGF loading conditions, the location of the maximum frictional stress was consistently on the right side of the abutment. Regardless of the loading conditions, when the elastic modulus of the mandibular implant decreased, the frictional stress between the abutment and the implant significantly increased.

As presented in Figure 11, under both RMOL and RGF loading conditions, the maximum stress in the implant was observed at the junction of the screw and the screw hole of the inner wing plate. Under RMOL loading conditions, when the elastic modulus of the mandibular implant decreased, the stress in the implant itself also decreased. By contrast, under RGF loading conditions, when the elastic modulus decreased, the stress in the implant itself increased.

In terms of bone strain (Figure 12), under both RMOL and RGF loading conditions, the maximum values of bone strain were observed near the dense bone adjacent to the left screw of the implant. Under RMOL loading conditions, the mandibular implant with the same elastic modulus as that of the HV-d3 lattice sample exhibited higher strain

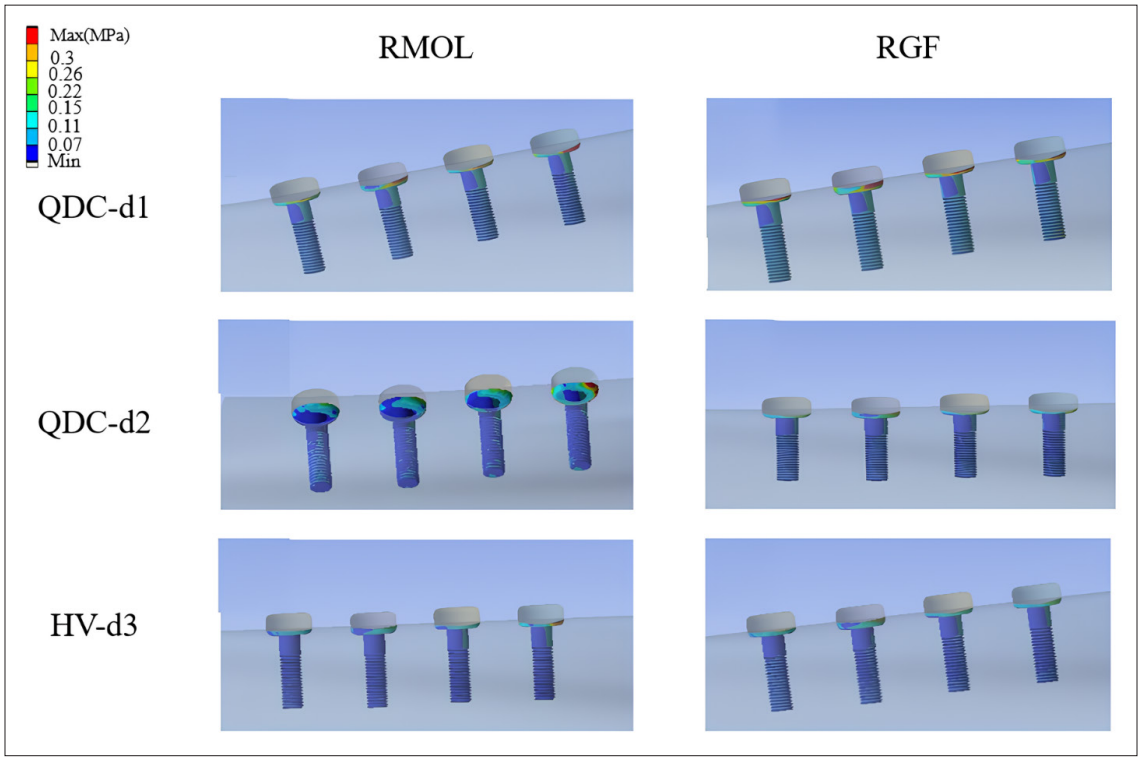

Figure 10. Distribution of frictional stress at the interface between the abutment and mandibular implant. Abbreviations: HV: Hex-vase; QDC: Quad-diametral-cross; d1: Rod diameter of 0.5 mm; d2: Rod diameter of 0.7 mm; d3: Rod diameter of 0.9 mm; RGF: Right group function; RMOL: Right unilateral molar clench.

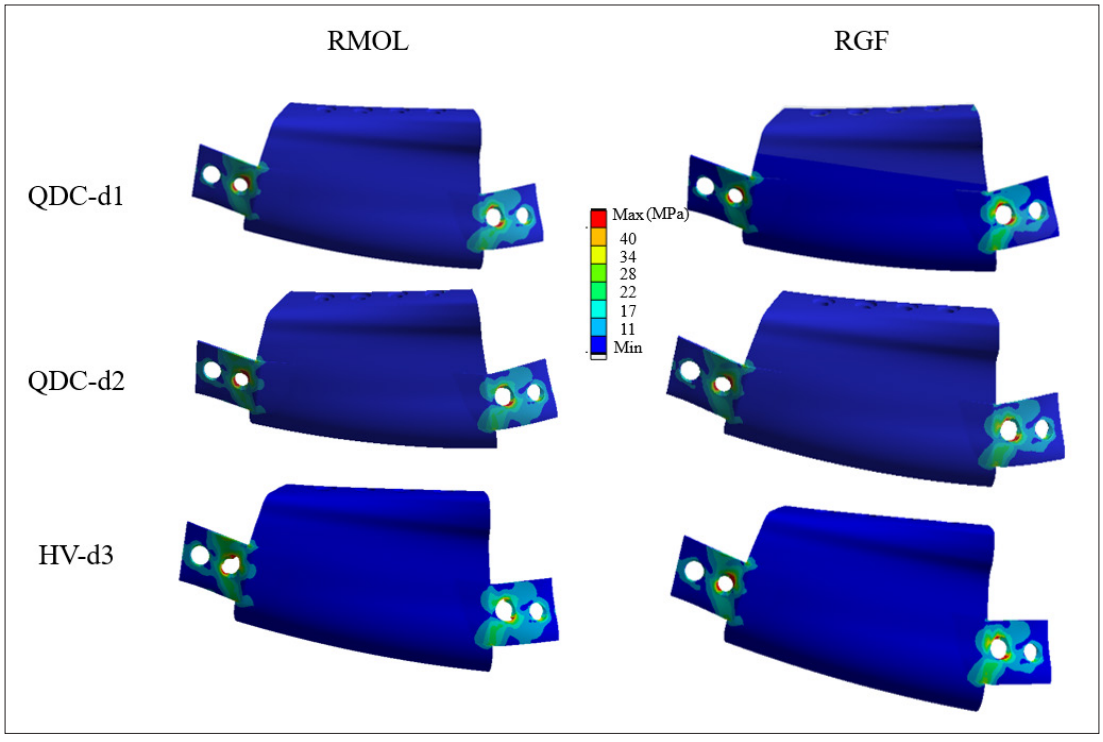

Figure 11. Von Mises stress distribution of mandibular implants. Abbreviations: HV: Hex-vase; QDC: Quad-diametral-cross; d1: Rod diameter of 0.5 mm; d2: Rod diameter of 0.7 mm; d3: Rod diameter of 0.9 mm; RGF: Right group function; RMOL: Right unilateral molar clench.

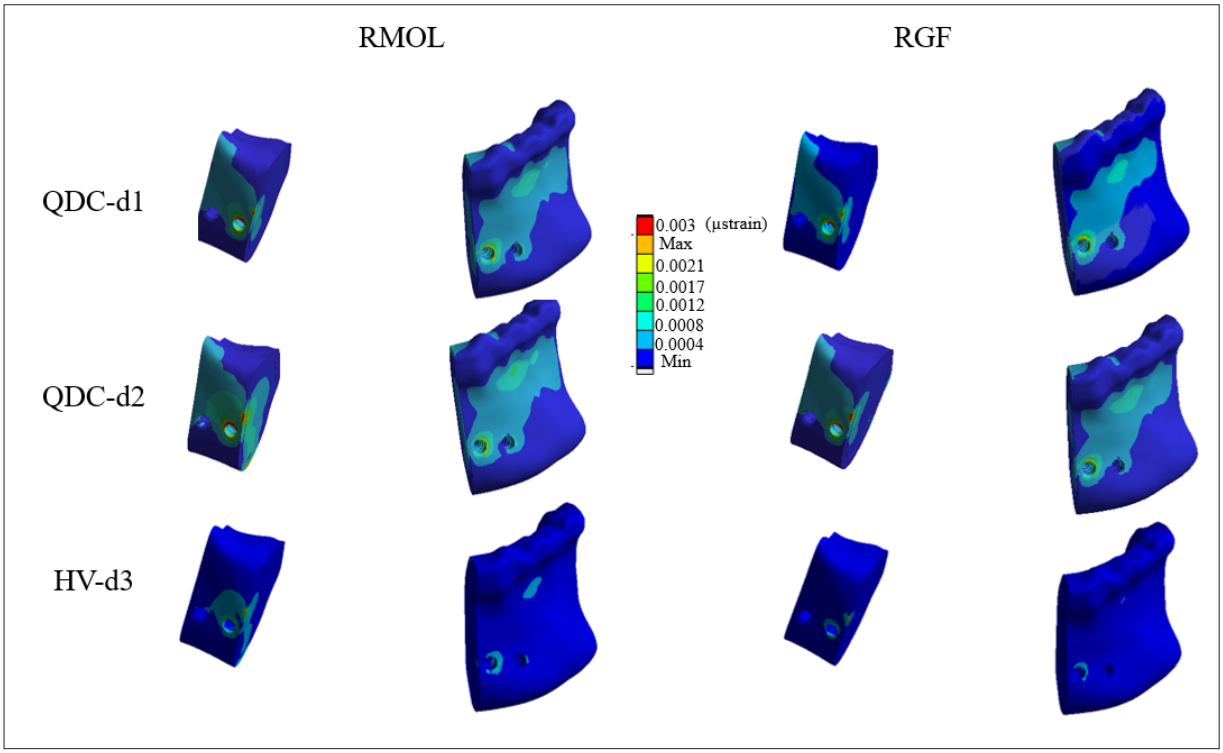

Figure 12. Von Mises strain distribution of bone near the mandibular implant. Abbreviations: HV: Hex-vase; QDC: Quad-diametral-cross; d1: Rod diameter of 0.5 mm; d2: Rod diameter of 0.7 mm; d3: Rod diameter of 0.9 mm; RGF: Right group function; RMOL: Right unilateral molar clench.

values compared with those for the mandibular implants with the same elastic modulus as those of the QDC-d1 or QDC-d2 lattice samples. However, under RGF loading conditions, the mandibular implant with the same elastic modulus as that of the QDC-d2 lattice sample exhibited the highest bone strain values (Table 4).

4. Discussion

This study designed a mandibular implant involving a titanium alloy with unique characteristics. The contour of this mandibular implant was derived from the shape of human mandible bone, which is likely to enhance facial appearance restoration upon implantation. In addition, the implant is made from a titanium alloy and features a porous lattice structure, which is likely to provide excellent mechanical and biological properties. The porous structure of the lattice is also expected to provide space for bone cell migration, proliferation, and differentiation,[14] while reducing the weight of the 3D-printed metal implant.[27] Unlike previous mandibular implants,[14,28] the proposed mandibular implant has an abutment design, similar to that of a dental implant, allowing for the direct placement of a prosthetic crown, which could potentially improve both facial appearance restoration and the patient's occlusal function.

4.1. *In vitro* experiments

In vitro experiments were conducted in accordance with the specifications of ISO 13314 to measure the elastic modulus of the proposed implant within the elastic

Table 4. The peak value of frictional stress between abutment and implant, maximum stress of mandibular implant, and maximum strain of bone around mandibular implant under RMOL and RGF loading conditions.

Parameter	QDC-d1	QDC-d2	HV-d3
Frictional stress between abutment and implant (MPa)			
RMOL	1.315	0.824	0.671
RGF	1.074	0.723	0.578
Implant maximum stress (MPa)			
RMOL	113.72	125.42	127.95
RGF	107.06	106.99	106.32
Bone maximum strain (μstrain)			
RMOL	2137.6	1941.8	2836.6
RGF	1558.9	2708.9	2697.3

Abbreviations: HV: Hex-vase; QDC: Quad-diametral-cross; d1: Rod diameter of 0.5 mm; d2: Rod diameter of 0.7 mm; d3: Rod diameter of 0.9 mm; RGF: Right group function; RMOL: Right unilateral molar clench.

range. The results indicate that the lattice rod diameter significantly influenced the material strength of the lattice, particularly in terms of the elastic range. When the lattice rod diameter increased, the elastic modulus of the samples significantly increased, a finding consistent with the results of previous studies.[29]

In addition, a significant positive correlation was observed between the lattice rod diameter and the porosity of the lattice structure. Generally, high porosity reduces the weight of mandibular implants, promotes the integration of implants with surrounding bone,[30] and mitigates the risk of bone loss induced by stress shielding.[31]

In this study, three titanium porous lattices were selected to represent elastic modulus lower than, close to, and higher than the strength of cancellous bone. The values of the lattices were applied to the finite element model of the proposed implant for advanced biomechanical analysis. The aim of the analysis was to determine the stress and strain effects on both the implant and the surrounding bone in the presence of different elastic modulus.

4.2. Finite element analysis

For the lattice rod diameters, it was observed that both the quad-diametral-cross and hex-vase lattice designs exhibited relatively low high-stress distributions. A comparison between these two designs revealed that as the lattice rod diameter increased from 0.5 to 0.9 mm, the regions experiencing high stress within the lattice structures gradually expanded. This suggests that larger rod diameters may contribute to a broader distribution of high-stress areas, potentially affecting the overall structure of the lattice designs (Figure 9). In addition, increasing the lattice rod diameter not only raises high stress but also increases the elastic modulus value of the lattice structure, as observed in the *in vitro* experiments (Table 3). Since the rod diameter of the lattice has a significant impact on both the internal stress and material properties of the lattice, careful consideration is essential when designing lattice structures.

Reconstruction plate failure due to stress-induced fractures is the most common reason for mandibular reconstruction failure.[32] In this study, analysis considering three distinct modulus values revealed that the maximum stress values of both the implant and the bone screws remained below the yield strength of Ti6Al4V (910 MPa).[33] These results indicated that under appropriate occlusal force conditions (RMOL and RGF), plastic deformations or fractures posed no immediate risk in the simulated mandibular implant. However, the high stress in the mandibular implants is primarily concentrated in the wing plates, which may lead to fatigue failure of the wing plates. Nevertheless, the high-stress values are still below the strength of Ti6Al4V, ensuring that there is no immediate risk of fracture. In addition, when the elastic modulus of the mandibular implant decreased, the frictional stress observed at the interface between the abutment and the implant increased, which presumably increased the likelihood of interface wear.

Consistent with Frost's mechanostat theory, the values of strain observed in the bone surrounding the implant remained below 3000 μstrain, indicating that the proposed mandibular implant did not cause the possibility of unrepaired microscopic fatigue damage accumulated in the bone under appropriate occlusal force conditions.[34] In addition, the maximum strain values observed in some regions of the bone exceeded 1500 μstrain, indicating the ability of the proposed implant to promote growth of surrounding bone.[34,35]

4.3. Limitations

This study faced several limitations:

(i) The material properties, boundary conditions, and loading conditions of the bone model used in FEA were somewhat simplified.

(ii) The bone material used in the FE model was assumed to be homogeneous and isotropic, which differs from actual human conditions.

(iii) The boundary conditions used involved zero displacement at the condyle in the x-, y-, and z-directions. In real-world scenarios, the mandible exhibits some displacement during movement.

(iv) The biomechanical analysis conducted in this study involved static occlusal conditions, assuming the absence of immediate implant fracture or bone damage. During the bone healing process, physiological changes may affect the stability of the resection site. The wing plates of the mandibular implants are the primary locations of high stress. Although the stress is below the yield strength of Ti6Al4V, future research must continue to optimize this part of the design to reduce the risk of the possibility of fatigue failure.

(v) The study did not include a non-destructive quality check after the production of the specimens. Although the settings for optimizing production and postprocessing actions were carefully considered, the absence of a thorough evaluation of the internal structure and detection of potential defects could affect the mechanical behavior of the specimens. Incorporating non-destructive evaluations in

future research is essential to ensure the internal integrity of the specimens and accurately assess their mechanical performance. In addition, future studies should involve more comprehensive analyses, such as dynamic occlusion tests, animal experiments, and even clinical research, to explore the long-term usability and success rate of mandibular implants in animals or humans.

5. Conclusion

Compared with the tetrahedron and hex-star lattice designs, the quad-diametral-cross and hex-vase designs exhibited fewer high-stress regions. According to the *in vitro* experimental results, when the rod diameter of the lattice structure increased, the overall elastic modulus of the structure significantly increased. Regardless of whether quad-diametral-cross or hex-vase design was used, the maximum stress observed in the mandibular implant did not exceed the yield strength of Ti6Al4V (910 MPa). These findings indicate that the proposed mandibular implant was not at risk of plastic deformation or immediate failure. When the elastic modulus of the mandibular implant decreased, the frictional stress observed at the interface between the abutment and the implant increased, which presumably increased the risk of interface wear. In addition, the maximum strain observed in the surrounding bone of the mandibular implant was within 1500–3000 μstrain. These results indicate that, in the presence of appropriate occlusal forces, the proposed mandibular implant did not cause immediate damage and promoted growth of the surrounding bone. However, there are still some limitations in this study, particularly in the final step where the finite element simulation of the mandibular implants was conducted using only the material properties of different lattice structures for biomechanical analysis. In this regard, future research can incorporate the actual 3D structure of the lattice into the finite element model for more advanced analysis, as well as include *in vitro* or animal experiments to verify the clinical applicability of the findings. Additionally, simulating the biomechanical properties of the implant warrants further evaluation through *in vitro* testing and printing of its final configuration.

Acknowledgments

None

Funding

This study was supported by the Ministry of Science and Technology, Taiwan (Project No. MOST 111-2221-E-039-008-MY2).

Conflict of interest

All authors declare that they have no conflict of interest.

Author contributions

Conceptualization: Lih-Jyh Fuh, Heng-Li Huang
Data curation: Hao Zhang
Formal analysis: Hao Zhang
Funding acquisition: Heng-Li Huang
Investigation: Hao Zhang, Heng-Li Huang
Methodology: Hao Zhang, Heng-Li Huang
Project administration: Heng-Li Huang
Resources: Lih-Jyh Fuh
Software: Jui-Ting Hsu, Lih-Jyh Fuh
Supervision: Heng-Li Huang
Validation: Jui-Ting Hsu, Heng-Li Huang
Writing – original draft: Hao Zhang, Heng-Li Huang
Writing – review & editing: Hao Zhang, Zhe-Min Lim, Heng-Li Huang

Ethics approval and consent to participate

The study was conducted according to the guidelines of the Declaration of Helsinki and approved by the Institutional Review Board of China Medical University Hospital (protocol code: CMUH110-REC2-247).

Consent for publication

Not applicable.

Availability of data

The datasets generated and/or analyzed in this study are available from the corresponding author upon reasonable request.

References

1. Seikaly H, Chau J, Li F, et al. Bone that best matches the properties of the mandible. *J Otolaryngol*. 2003;32(4):262-265. doi: 10.2310/7070.2003.41646
2. Bak M, Jacobson AS, Buchbinder D, Urken ML. Contemporary reconstruction of the mandible. *Oral Oncol*. 2010;46(2):71-76. doi: 10.1016/j.oraloncology.2009.11.006
3. Schlueter B, Kim KB, Oliver D, Sortiropoulos G. Cone beam computed tomography 3D reconstruction of the mandibular condyle. *Angle Orthod*. 2008;78(5):880-888. doi: 10.2319/072007-339.1
4. van Baar GJC, Forouzanfar T, Liberton NPTJ, Winters HAH, Leusink FKJ. Accuracy of computer-assisted surgery in mandibular reconstruction: a systematic review. *Oral Oncol*. 2018;84:52-60.

doi: 10.1016/j.oraloncology.2018.07.004

5. Baltatu MS, Tugui CA, Perju MC, et al. Biocompatible titanium alloys used in medical applications. *Rev Chim*. 2019;70(4):1302-1306.
doi: 10.37358/RC.19.4.7114

6. Ran Q, Yang W, Hu Y, et al. Osteogenesis of 3D printed porous Ti6Al4V implants with different pore sizes. *J Mech Behav Biomed Mater*. 2018;84:1-11.
doi: 10.1016/j.jmbbm.2018.04.010

7. Taniguchi N, Fujibayashi S, Takemoto M, et al. Effect of pore size on bone ingrowth into porous titanium implants fabricated by additive manufacturing: An *in vivo* experiment. *Mater Sci Eng C Mater Biol Appl*. 2016;59:690-701.
doi: 10.1016/j.msec.2015.10.069

8. Eshkalak SK, Ghomi ER, Dai Y, Choudhury D, Ramakrishna S. The role of three-dimensional printing in healthcare and medicine. *Mater Des*. 2020;194:108940.
doi: 10.1016/j.matdes.2020.108940

9. Gao H, Li X, Wang C, Ji P, Wang C. Mechanobiologically optimization of a 3D titanium-mesh implant for mandibular large defect: a simulated study. *Mater Sci Eng C Mater Biol Appl*. 2019;104:109934.
doi: 10.1016/j.msec.2019.109934

10. Hosseini S, Hudak R, Penhaker M, Majernik J. Fatigue of Ti-6Al-4V. In: *Biomedical Engineering-Technical Applications in Medicine*. London, UK: IntechOpen; 2012:75-92.
doi: 10.5772/45753

11. Davoodi E, Montazerian H, Esmaeilizadeh R, et al. Additively manufactured gradient porous Ti-6Al-4V hip replacement implants embedded with cell-laden gelatin methacryloyl hydrogels. *ACS Appl Mater Interfaces*. 2021;13(19):22110-22123.
doi: 10.1021/acsami.0c20751

12. Farajpour H, Bastami F, Bohlouli M, Khojasteh A. Reconstruction of bilateral ramus-condyle unit defect using custom titanium prosthesis with preservation of both condyles. *J Mech Behav Biomed Mater*. 2021;124:104765.
doi: 10.1016/j.jmbbm.2021.104765

13. Luo D, Rong Q, Chen Q. Finite-element design and optimization of a three-dimensional tetrahedral porous titanium scaffold for the reconstruction of mandibular defects. *Med Eng Phys*. 2017;47:176-183.
doi: 10.1016/j.medengphy.2017.06.015

14. Liu R, Su Y, Yang W, et al. Novel design and optimization of porous titanium structure for mandibular reconstruction. *Appl Bionics Biomech*. 2022;2022:8686670.
doi: 10.1155/2022/8686670

15. Touré G, Gouet E. Use of a 3-dimensional custom-made porous titanium prosthesis for mandibular body reconstruction with prosthetic dental rehabilitation and lipofilling. *J Oral Maxillofac Surg*. 2019;77(6):1305-1313.
doi: 10.1016/j.joms.2018.12.026

16. Cheng KJ, Liu YF, Wang R, et al. Topological optimization of 3D printed bone analog with PEKK for surgical mandibular reconstruction. *J Mech Behav Biomed Mater*. 2020;107:103758.
doi: 10.1016/j.jmbbm.2020.103758

17. Qassemyar Q, Assouly N, Temam S, Kolb F. Use of a three-dimensional custom-made porous titanium prosthesis for mandibular body reconstruction. *Int J Oral Maxillofac Surg*. 2017;46(10):1248-1251.
doi: 10.1016/j.ijom.2017.06.001

18. Ardila CM, Hernández-Arenas Y, Álvarez-Martínez E. Mandibular body reconstruction utilizing a three-dimensional custom-made porous titanium plate: a four-year follow-up clinical report. *Case Rep Dent*. 2022; 2022:5702066.
doi: 10.1155/2022/5702066

19. Park JH, Odkhuu M, Cho S, Li J, Park BY, Kim JW. 3D-printed titanium implant with pre-mounted dental implants for mandible reconstruction: a case report. *Maxillofac Plast Reconstr Surg*. 2020;42(1):28.
doi: 10.1186/s40902-020-00272-5

20. Raz K, Chval Z, Sedlacek F. Compressive strength prediction of quad-diametral lattice structures. *Key Eng Mater*. 2020;847:69-74.
doi: 10.4028/www.scientific.net/KEM.847.69

21. Kim JW, Oh CW, Kim BS, Jeong SL, Jung GH, Lee DH. Structure-mechanical analysis of various fixation constructs for basicervical fractures of the proximal femur and clinical implications; finite element analysis. *Injury*. 2023;54(2):370-378.
doi: 10.1016/j.injury.2022.12.004

22. Huang HL, Lin TW, Tsai HL, Wu YL, Wu AYJ. Biomechanical effects of bone atrophy, implant design, and vertical or tilted of posterior implant on all-on-four concept implantation: finite element analysis. *J Med Biol Eng*. 2022;42(4):488-497.
doi: 10.1007/s40846-022-00725-4

23. Grant JA, Bishop NE, Götzen N, Sprecher C, Honl M, Morlock MM. Artificial composite bone as a model of human trabecular bone: the implant-bone interface. *J Biomech*. 2007;40(5):1158-1164.
doi: 10.1016/j.jbiomech.2006.04.007

24. Bozkaya D, Müftü S. Mechanics of the taper integrated screwed-in (TIS) abutments used in dental implants. *J Biomech*. 2005;38(1):87-97.
doi: 10.1016/j.jbiomech.2004.03.006

25. Huang HL, Su KC, Fuh LJ, et al. Biomechanical analysis of a temporomandibular joint condylar prosthesis during various clenching tasks. *J Craniomaxillofac Surg*. 2015;43(7):1194-1201.
doi: 10.1016/j.jcms.2015.04.016

26. Korioth TW, Hannam AG. Mandibular forces during simulated tooth clenching. *J Orofac Pain*. 1994;8(2):178-189.

27. Moiduddin K, Anwar S, Ahmed N, Ashfaq M, Al-Ahmari A. Computer assisted design and analysis of customized porous plate for mandibular reconstruction. *Irbm*. 2017;38(2):78-89. doi: 10.1016/j.irbm.2017.01.003

28. Peng WM, Cheng KJ, Liu YF, et al. Biomechanical and mechanostat analysis of a titanium layered porous implant for mandibular reconstruction: the effect of the topology optimization design. *Mater Sci Eng C Mater Biol Appl*. 2021;124:112056. doi: 10.1016/j.msec.2021.112056

29. Liu Y, Wang H, Li S, et al. Compressive and fatigue behavior of beta-type titanium porous structures fabricated by electron beam melting. *Acta Mater*. 2017;126:58-66. doi: 10.1016/j.actamat.2016.12.052

30. Torres-Sanchez C, Al Mushref FRA, Norrito M, Yendall K, Liu Y, Conway PP. The effect of pore size and porosity on mechanical properties and biological response of porous titanium scaffolds. *Mater Sci Eng C Mater Biol Appl*. 2017;77:219-228. doi: 10.1016/j.msec.2017.03.249

31. Arabnejad S, Johnston B, Tanzer M, Pasini D. Fully porous 3D printed titanium femoral stem to reduce stress-shielding following total hip arthroplasty. *J Orthop Res*. 2017;35(8):1774-1783. doi: 10.1002/jor.23445

32. Knoll WD, Gaida A, Maurer P. Analysis of mechanical stress in reconstruction plates for bridging mandibular angle defects. *J Craniomaxillofac Surg*. 2006;34(4):201-209. doi: 10.1016/j.jcms.2006.01.004

33. Afazov S, Denmark WA, Toralles BL, Holloway A, Yaghi A. Distortion prediction and compensation in selective laser melting. *Addit Manuf*. 2017;17:15-22. doi: 10.1016/j.addma.2017.07.005

34. Frost HM. A 2003 update of bone physiology and Wolff's Law for clinicians. *Angle Orthod*. 2004;74(1):3-15. doi:10.1043/0003-3219(2004)074<0003:AUOBPA>2.0.CO;2

35. Biewener AA. Safety factors in bone strength. *Calcif Tissue Int*. 1993;53(Suppl 1):S68-S74. doi: 10.1007/BF01673406

International Journal of Bioprinting

Special Issue Alerts

Invitation for Special Issue Proposals

Organizing and editing for a Special Issue helps Guest Editors gain editorial experience and improve academic profile, in addition to being a part of organizing scientific communication of contemporary topics.

If you are published researcher and have an idea for a Special Issue, please write in via email to our Managing Editor (ijb.office@accscience.sg). Please provide your CV, professional profile page and a topic of interest in your email. Our colleague will guide you in the process of writing a Special Issue proposal.

Visit Special Issues site for the list of Special Issues featured in *International Journal of Bioprinting*.

Frequently Asked Questions

1. **Are Special Issue submissions processed in the same way how Regular Issue papers are being pre-screened and reviewed?**
   Yes, all full-length article submissions to a Special Issue will go through the same editorial and peer-review process. The distinct difference here is that the Guest Editors will replace the usual editors and get involved in the making professional decisions on papers after peer review. Note that the specific roles of a Guest Editor could vary across Special Issues.

2. **How many Guest Editors are required to organize a Special Issue?**
   There is no fixed number; however, we suggest no more than 4 Guest Editors per Special Issue. More importantly, all Guest Editors should have excellent publication track records and demonstrated expertise in the topic(s) being proposed.

3. **Is the Special Issue governed by important deadlines?**
   Yes.

Benefits of Being A Guest Editor

- A chance to get involved in the conception and development of a specialty, contemporary topic that is of interest to the readers
- A chance to expand your professional network to the scholars and researchers who are similarly involved in the research of specialty topic
- A chance to hone your editorial skills
- A chance to gain first-hand experience of editing a thematic issue publication, which is a very valuable experience for those who aspire to edit their own journal in future
- A chance to improve your academic profile and help establish your academic influence within your discipline

Our Journals

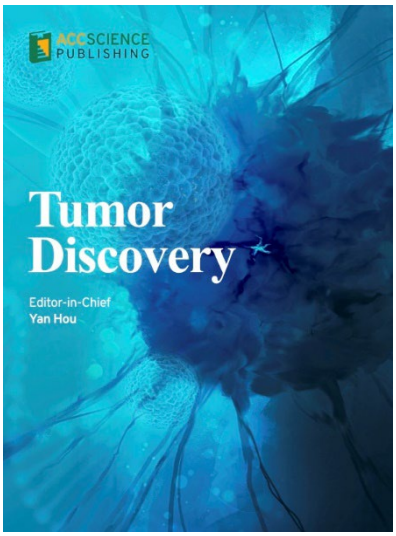

Tumor Discovery is a peer-reviewed and open-access journal that aims to present new cancer research with strong emphasis on fundamental and translational studies. *Tumor Discovery* covers topics, including but not limited to the following:

- Etiology and pathogenesis of cancer
- Mechanisms and molecular pathways underlying cancer initiation and progression
- Tumor metastasis
- Tumor evolution and heterogeneity
- Tumor microenvironment and tumor-host interactions
- Cancer genetics and genomics
- Cancer characterization using omics approaches
- Discovery and validation of cancer biomarker
- Discovery of new therapeutic targets
- New approaches of diagnostic and treatment modalities
- Statistical methods in cancer research

Global Translational Medicine is a quarterly journal that focuses on medicine, biological sciences, and biomaterials engineering. The goal of *Global Translational Medicine* is to provide a platform to researchers for showcasing their latest research works in translational medicine so as to advance the field towards the betterment of human health. Despite the advancement of omics and new technologies, the process of transforming these technologies and scientific research results into effective therapies and putting them into clinical use still has a long way to go. *Global Translational Medicine* provides a platform to fill the gaps in preclinical and inter-disciplinary research, to promote clinical translation of scientific research results, and to contribute to the conception of new and improved preventive measures as well as diagnostic and therapeutic techniques of diseases.

Global Translational Medicine covers the following themes: cardiovascular disease, metabolism/diabetes/obesity, neuroscience/neurology, cancer, biomaterials and their applications in medicine, proteomics/metabolomics, pharmacogenomics, biomarkers, bioinformatics and data mining, animal and clinical research, and medical methods arising from interdisciplinary crossover.

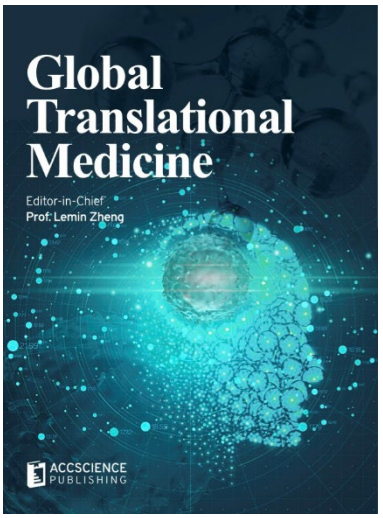

Start a new journal

Write to us via email if you are interested to start a new journal with AccScience Publishing. Please attach your CV, professional profile page and a brief pitch proposal in your email. We shall inform you of our decision whether we are interested to collaborate in starting a new journal.

Contact: info@accscience.com

ACCSCIENCE PUBLISHING

ACCSCIENCE PUBLISHING

Publishing Office:
8 Burn Road, #15-03 Trivex, Singapore 369977.
Editorial Office:
30-2, Jalan BS 1/2, Olive Hill Business Park, 43300 Seri Kembangan, Selangor. Malaysia.

Editorial Office: editor.ijb@accscience.com
General Inquires: info@accscience.com

https://accscience.com/journal/IJB